PROCEEDINGS OF THE 17TH ANNUAL SEISMIC RESEARCH SYMPOSIUM ON MONITORING A COMPREHENSIVE TEST BAN TREATY, 12-15 SEPTEMBER 1995

Editors:
James F. Lewkowicz
Jeanne M. McPhetres
Delaine T. Reiter

14 August 1995

APPROVED FOR PUBLIC RELEASE; DISTRIBUTION UNLIMITED.

PHILLIPS LABORATORY
DIRECTORATE OF GEOPHYSICS
AIR FORCE MATERIEL COMMAND
HANSCOM AIR FORCE BASE, MA 01731-3010

AIR FORCE OFFICE OF SCIENTIFIC RESEARCH
DIRECTORATE OF MATHEMATICS & GEOSCIENCES
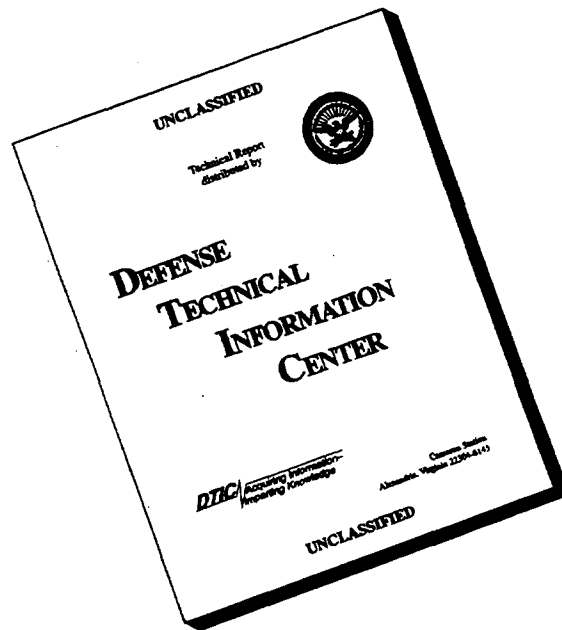AIR FORCE MATERIEL COMMAND
BOLLING AIR FORCE BASE, DC 20332-0001

HQ AIR FORCE TECHNICAL APPLICATIONS CENTER
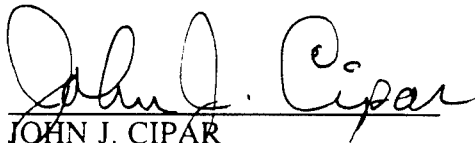**NUCLEAR TREATY MONITORING DIRECTORATE**
PATRICK AIR FORCE BASE, FL 32925-3002

DEPARTMENT OF ENERGY
OFFICE OF NONPROLIFERATION & NATIONAL SECURITY
WASHINGTON, DC 20585

DISCLAIMER NOTICE

UNCLASSIFIED

Technical Report
distributed by

**DEFENSE
TECHNICAL
INFORMATION
CENTER**

DTIC/ Acquiring Information—
Imparting Knowledge

Cameron Station
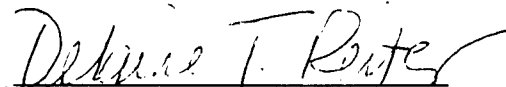Alexandria, Virginia 22304-6145

UNCLASSIFIED

**THIS DOCUMENT IS BEST
QUALITY AVAILABLE. THE
COPY FURNISHED TO DTIC
CONTAINED A SIGNIFICANT
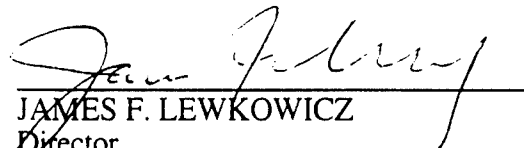NUMBER OF PAGES WHICH DO
NOT REPRODUCE LEGIBLY.**

"This technical report has been reviewed and is approved for publication."

JOHN J. CIPAR
Task Scientist
Earth Sciences Division

DELAINE T. REITER
Program Manager
Earth Sciences Division

JAMES F. LEWKOWICZ
Director
Earth Sciences Division

This report has been reviewed by the ESC Public Affairs Office (PA) and is releasable to the National Technical Information Service (NTIS).

Qualified requestors may obtain additional copies from the Defense Technical Information Center. All others should apply to the National Technical Information Service.

If your address has changed, or if you wish to be removed from the mailing list, or if the addressee is no longer employed by your organization, please notify PL/IM, 29 Randolph Road, Hanscom AFB, MA 01731-3010. This will assist us in maintaining a current mailing list.

Do not return copies of this report unless contractual obligations or notices on a specific document requires that it be returned.

REPORT DOCUMENTATION PAGE

Form Approved
OMB No. 0704-0188

Public reporting burden for this collection of information is estimated to average 1 hour per response, including the time for reviewing instructions, searching existing data sources, gathering and maintaining the data needed, and completing and reviewing the collection of information. Send comments regarding this burden estimate or any other aspect of this collection of information, including suggestions for reducing this burden, to Washington Headquarters Services, Directorate for Information Operations and Reports, 1215 Jefferson Davis Highway, Suite 1204, Arlington, VA 22202-4302, and to the Office of Management and Budget, Paperwork Reduction Project (0704-0188), Washington, DC 20503.

1. AGENCY USE ONLY (Leave blank)	2. REPORT DATE 14 August 1995	3. REPORT TYPE AND DATES COVERED Scientific, Final

4. TITLE AND SUBTITLE Proceedings of the 17th Annual Seismic Research Symposium on Monitoring a Comprehensive Test Ban Treaty, 12 -15 September 1995

5. FUNDING NUMBERS

PE 61102F 621010
PR 2309 7600
TA G2 09
WU 10 08

6. AUTHOR(S) James F. Lewkowicz

Editors: Jeanne M. McPhetres
Delaine T. Reiter

7. PERFORMING ORGANIZATION NAME(S) AND ADDRESS(ES)

Phillips Laboratory (GPE)
29 Randolph Road
Hanscom AFB, MA 01731-3010

8. PERFORMING ORGANIZATION REPORT NUMBER

PL-TR-95-2108
ERP, No. 1173

9. SPONSORING / MONITORING AGENCY NAME(S) AND ADDRESS(ES)
Air Force Office of Scientific Research
HQ Air Force Technical Applications Center
Department of Energy

19960607 035

11. SUPPLEMENTARY NOTES
This research was supported by PL under PE 621010, by AFOSR under PE 61102F, by AFTAC under PE 35999F, ARPA under PE 62301E, DOE and ACDA.

12a. DISTRIBUTION / AVAILABILITY STATEMENT

Approved for Public Release; distribution unlimited

12b. DISTRIBUTION CODE

DTIC QUALITY INSPECTED 4

13. ABSTRACT (Maximum 200 words)

These Proceedings contain papers presented at the Seventeenth Annual Seismic Research Symposium on Monitoring a Comprehensive Test Ban Treaty (CTBT), held 12-15 September 1995, in Scottsdale, Arizona. This Symposium represents the combined annual review for the basic seismology program funded by the Air Force Office of Scientific Research (AFOSR) and the regional verification program funded by the Phillips Laboratory (PL), Hq Air Force Technical Applications Center (AFTAC), Department of Energy (DOE), the Advanced Research Projects Agency (ARPA) and the Arms Control and Disarmament Agency (ACDA). The scientific objectives of the research programs are to improve the Air Force's capability to seismically detect, locate, identify, and characterize underground nuclear explosions under a potential CTBT. The purpose of these Symposia, organized annually by GPE, is to provide the sponsoring agencies an opportunity to review research, particularly contractor research, accomplished during the preceding year and to

14. SUBJECT TERMS
underground nuclear explosions, discrimination, regional seismology, seismic sources, structure of the crust and upper mantle, mining practices, hydroacoustics, data processing and analysis

15. NUMBER OF PAGES

16. PRICE CODE

17. SECURITY CLASSIFICATION OF REPORT	18. SECURITY CLASSIFICATION OF THIS PAGE	19. SECURITY CLASSIFICATION OF ABSTRACT	20. LIMITATION OF ABSTRACT
UNCLASSIFIED	UNCLASSIFIED	UNCLASSIFIED	UL

Block 9 continued

AFOSR/NM
110 Duncan Avenue, Suite B115
Bolling AFB, DC 20332-0001

HQ AFTAC/TT
1030 South Highway A1A
Patrick AFB, FL 32925-3002

DOE
Office of R&D, NN-20
1000 Independence Avenue, S.W.
Washington, DC 20585

Block 13 continued

outline areas of investigation for the coming year. For the researchers, it provides a forum for the exchange of scientific information to help achieve program goals, and an opportunity to meet AFOSR, PL, HQ AFTAC, DOE, ARPA and ACDA staff to discuss results and future plans. In addition, the Symposium and the technical presentations serve as an important avenue for technology transition to the Air Force user. The papers include studies of the identification and characterization of seismic sources (discrimination), the factors affecting regional wave propagation in various geological/geophysical settings, regional seismic wave propagation from both theoretical and empirical viewpoints, the determination of earth structure in selected areas of the world, various models of the physics of earthquake and explosion sources, hydroacoustic wave propagation, and data processing and analysis.

TABLE OF CONTENTS

CTBT TALKS

DISCRIMINATION

SEISMIC REGIONALIZATION

SEISMIC WAVE PROPAGATION

MINING PRACTICES

SEISMIC SOURCES AND STRUCTURE

DATA PROCESSING AND ANALYSIS

DETECTION/LOCATION/IDENTIFICATION

HYDROACOUSTICS, INFRASOUND, RADIONUCLIDES AND ON-SITE INSPECTION

LATE SUBMISSIONS

MONITORING RESEARCH IN THE CONTEXT OF
CTBT NEGOTIATIONS AND NETWORKS

Robert Blandford
HQ AFTAC/TT
Center for Monitoring Research
1300 North 17th Street, Suite 1450
Arlington, VA 22209

ABSTRACT
Since the last Phillips Laboratory conference there has been substantial progress at the Geneva Negotiations in the United Nations Conference on Disarmament on the subject of which types of detecting networks will be implemented as part of an international monitoring system (IMS), used to monitor a CTBT.

At the present time the United States is supporting the deployment of 4 networks, seismic, radio-nuclide, hydroacoustic, and infrasonic. In addition the US is supporting a strong on-site inspection regime, mandatory baseline notifications of the locations and blasting practices of mines which detonate explosions above some yield, and voluntary transparency measures such as calibration experiments and mine monitoring.

In this paper I will first briefly discuss the nature of these networks and practices, and discuss how they fit together to help the international community to deny an evader an opportunity to test. I then plan to step back and brieflydiscuss how the geophysical research community in the US can make a contribution to the CTBT.

Keywords: networks, monitoring, event detection, characterization

SEISMIC NETWORK

The seismic network, like the radionuclide network, the hydroacoustic network, and the infrasound network are described in the United Nations Conference on Disarmament Working Paper CD/NTB/WP.224 of 16 March 1995. The network comprises approximately 50 stations of which approximately 30 are seismic arrays. These stations are termed the "primary seismic network" and are to transmit their data continuously to an international data center (IDC). At the moment Vienna is the leading candidate for the location of the center. At the IDC the data will be used to produce a seismic bulletin in less than 2 days.

In addition to the primary network there is to be an auxiliary network of 100-150 3-component stations. The stations in the auxiliary network which are near the preliminary event location will be dialed up by the IDC at some point in the bulletin preparation and used to refine the bulletin. Data from these stations can be used to confirm the reality of the event, to improve the event location, and to supply additional data so that event discrimination can be performed.

The IDC-created bulletins and the seismic data recovered by the IDC will be available to National Data Centers (NDCs). (Not only the seismic data will be available by this route but also the data from the other networks and data sources.) Each nation which signs the treaty, if it wants the data, will set up an NDC; however, an NDC could range from a mailbox which receives monthly bulletins to an NDC which receives all the raw data and intermediate and final computed results of the IDC over a satellite link between the IDC and NDC. The US NDC at AFTAC is planned to be such an NDC.

DATA COLLECTION AND DISTRIBUTION

The current US concept of data collection and distribution of all the network's data revolves around a constellation of 3 geostationary satellites on which the international organization owns transponders. There are also to be 3 dedicated ground relay stations in the 3 regions of overlap of the satellite's footprints. The uplink antennas can be inexpensive and could be located at each station or perhaps at the NDC where a country's data are concentrated before transmission.

After uplink the data are subsequently relayed so that each satellite and relay station has available all the data. At this point it is clear that the IDC could be located at or near any of the relay stations; Vienna would be a suitable location. The relay stations could be at secure locations, perhaps as one example at an Austrian military base near Vienna with an optical fiber link to the IDC, so that the overall system would be less vulnerable to sabotage. The system will function without interruption if the IDC and any one of the 3 ground stations is destroyed, and, should a satellite malfunction it is possible to quickly substitute an alternate.

The data can be broadcast by the satellites, so that, with a relatively expensive receiving antenna and a small back-uplink for error control, any location could be the site of an alternate IDC. Or, since the US NDC plans to acquire all the data, it may acquire the data directly from the satellite, removing the risk that a disruption at the central point of failure potentially represented by the IDC would prevent access to all data.

After a few $M up-front costs, the total yearly costs to the international organization for data gath-

ering would be less than $1M.

Each NDC will be responsible for distributing data to the citizens of its country; it may be that the treaty will permit an NDC to distribute the data to whomever it pleases. It is currently envisioned that the USNDC will use an interface similar to the World-Wide-Web page currently operating at the IDC to provide data access to all data received from the IDC. Data from other stations, and continuous data from the auxiliary stations, could only be obtained from other sources, for example from the IRIS DMC.

HYDROACOUSTIC NETWORK

There are several plans for hydroacoustic networks before the CD, one currently of interest to the US is one in which there are 6 single hydrophone stations with cabled connections to land The coverage of the six stations is strongly biased toward the Southern Hemisphere in part for the reason that testing in the oceans in the Northern Hemisphere is far less favorable to the evader due to the high concentration of inhabited land masses, ship traffic, and air-line traffic, as well as the proposed high density of radionuclide sensors.

The principal daily use of the hydroacoustic network is for purposes of simple discrimination of those oceanic earthquakes detected by the seismic system and which are clearly located away from land. The arrival time of the water-borne signal is predicted and if the signal does not have the high-frequency characteristics of an underwater explosion, then it is concluded that the event must have been an earthquake. A record at a single hydrophone is sufficient for this discrimination.

A lower-atmosphere explosion may not be detected by the seismic system, but may be detected by the hydroacoustic system. However, we do not yet know what the spectral or time domain characteristics of such a hydroacoustic signal will be so that we do not know if simple examination of the signal can reveal the type of source. The amplitudes of such a signal can be similar to those of various industrial explosions in the oceans, and since the single hydrophones provide no directional information, using such a sparse network to create a hydroacoustic bulletin with a low false alarm rate could be a daunting task. However, as we shall see, in conjunction with an infrasound system, the hydroacoustic system can greatly improve the locations of those events which it does detect.

INFRASOUND NETWORK

The Geneva Technical Experts have suggested a 60 or 70 station worldwide network of 4 element infrasonic arrays with spacings of 1-3 km. In theory this network can reliably detect a 1 kt atmospheric burst anywhere in the world. The US is currently interested in the possibilities of a much less expensive network, concentrated in the Southern Hemisphere for the same reasons discussed above for the hydroacoustic network.

This network would be comprised of 12 16-element stations in the Southern Hemisphere, and this network has a threshold below 1 kt in the Southern Hemisphere and less than 3 kt in the Northern Hemisphere.

It is thought that the false alarm rate for an infrasound network is quite low. Although storms do

3

create acoustic waves, the resulting waves are continuous, not transient. Volcanos emit infrasound signals rarely, but it is usually clear that a volcano is the source. On the occasions when earthquakes or quarry blasts emit signals, the seismic source will also be located by the system and the source can be accounted for in that way.

The occasional multikiloton conventional blast in the atmosphere can be expected to be in inhabited areas, and to be pre-announced or to be the subject of extensive newspaper coverage.

The most serious potential false alarm problem is probably the signals generated by meteorites; these sources are also known as bolides. ReVelle (1995) estimates, using infrasound and satellite data, that these sources generate explosion-like signals worldwide at a rate of approximately 1/yr at 10 kt, and 10/year at 1 kt. On the occasion of detection of such a signal emanating from most locations, a plausible response would be closer inspection of downwind radionuclide sensors and the querying of ships, planes, and human habitations in the area. In locations, such as the oceanic Southern Hemisphere, where such resources are few, in addition to more closely inspecting the downwind radionuclide stations, there may be good reason to dispatch a plane to the general area to gather additional radionuclide data.

One would also want to closely inspect the hydroacoustic data and, if a signal is detected on the hydroacoustic sensors, to instruct the plane to drop a calibration explosive source into the SOFAR channel. This should enable absolute location of the original hydroacoustic source to within a few kilometers which can further direct the plane's search in real time. Detection by 3 hydrophones should pinpoint the location, and detection by two hydrophones should greatly reduce the area of the infrasound confidence ellipse.

If even a single sighting from a satellite were available, it would be very likely conclusively identify the event as non-nuclear, thus reducing infrasound false alarms to near-zero. It is to be expected that all such bolides will be detected since there is little possibility that a bolide would be hidden by clouds. Any such events not shown to be a bolide would presumptively be a kiloton-level atmospheric explosion, if not conventional then perhaps a nuclear explosion under heavy cloud cover or with a signal distorted by other means.

RADIONUCLIDE DETECTION NETWORK
The US has proposed a network of approximately 100 radionuclide detectors for the detection of radioactive particles, and 100 co-located radioactive xenon detectors for the detection of the xenon created by nuclear explosions.

The principal use of the particle detectors would be for detecting atmospheric explosions; the xenon detectors are aimed at the evasive underground test. It is thought that a decoupled test would be especially likely to leak, due to the absence of the explosion-created stress cage which serves to constrain leakage in fully tamped shots. Thus the xenon detectors are especially important in a comprehensive system.

Both systems, as planned, would be substantial advances in the state of the art of automation; both would produce and communicate data while unattended for many months.

4

BASELINE DATA, CALIBRATION AND MINE MONITORING

The US has also considered requiring that mines which plan to detonate explosives above a yield limit of several tens of tons reveal after the treaty enters into force the locations of these mines and the typical types of explosive practices at that mine. These mines would also be required to reveal the details of three of the largest shots in the year after entry into force; the idea here is, of course that these shots will be detected by the international seismic system and can serve as a calibration.

The US also wants to encourage voluntary calibration and mine monitoring on a bilateral basis in order to resolve questions which may arise about ambiguous results.

SUMMARY

The systems outlined above provide the infrastructure required to close the door, at some threshold, on the possibility of evasive testing underground, in the ocean and in the atmosphere.

However, in each field there are important research requirements. Just to cite a few, in seismic there is the challenge of discriminating poor S/N events at regional distances. In hydroacoustic there is the question of the hydroacoustic coupling and the waveform appearance of atmospheric explosions. In infrasound there is the development of new array designs and of new automatic detection algorithms. In radionuclide there is the excitement to come from an unprecedented look at world-wide background data, who knows what natural processes may be revealed?

REFERENCES

Expert Group (1995). Working Group 1 - Verification, International Monitoring System Expert Group Report based on Technical Discussions held from 6 February to 3 March 1995, CD/NTB/WP.224, 16 March 1995.

ReVelle, D.O. (1995). Historical detection of atmospheric impacts by large bolides using acoustic-gravity waves, submitted to International Conference on Near-Earth Objects, April 24-25 1995, New York Cit

US CONCEPT FOR A CTBT INTERNATIONAL DATA CENTER

STEVEN R. BRATT
ADVANCED RESEARCH PROJECTS AGENCY
NUCLEAR MONITORING RESEARCH OFFICE
e-mail: sbratt@arpa.mil;   phone: 703-696-2238;   fax: 703-696-2203

ABSTRACT

The Advanced Research Projects Agency (ARPA) has been tasked by the Administration to prototype a Comprehensive Test Ban Treaty (CTBT) International Data Center (IDC) -- a central element of the proposed CTBT verification regime. The IDC would support and make more affordable the verification responsibilities of States Parties by performing the computationally intensive tasks necessary for effective, global monitoring. The IDC would collect and archive large volumes of data from hundreds of worldwide seismic, radionuclide, hydroacoustic and infrasound sensor sites of the CTBT International Monitoring System (IMS). Analyses, performed both by automated systems and human experts, would rapidly reduce this large volume of data by computing key parameters that estimate the existence, location and character of detected events. In the US model, the IDC would stop short of providing a final identification of these events. However, all States Parties would have open and convenient access to all raw data and IDC products, with customized interfaces that allow interested States Parties to apply national criteria to screen for the subsets of data of interest to them.

To meet the requirements for a CTBT IDC, ARPA, together with an international team of developers and operators, is expanding the framework of the Center for Monitoring Research, with an increased focus on data authentication, automated fusion of multi-sensor data, regional knowledge acquisition, reliable and secure distributed processing on UNIX systems, advanced data management technologies, effective data visualization and access, and an open and modular system architecture. The still-evolving prototype IDC is the centerpiece of an on-going Group of Scientific Experts seismic monitoring experiment (called GSETT-3) that began full-scale operations in January 1995. The IDC is producing a daily bulletin containing 50 - 200 seismic events. Radionuclide data are also being collected, processed and disseminated as part of a separate multi-lateral technical experiment. The processing of hydroacoustic and infrasound data will follow later this year. On-going transition of the IDC software to the prototype US National Data Center at the Air Force Technical Applications Center (AFTAC) is expected to improve the US capability to monitor to the low thresholds required to verify a CTBT without increasing the number of human analysts. The US has also offered to transition the product of ARPA's work to the Conference on Disarmament (CD, the body negotiating the CTBT in Geneva) for use within the future international CTBT verification organization. This transition is expected to begin and continue over the next two or three years.

KEY WORDS: automation, data processing, knowledgebased systems, seismology, radionuclide, hydroacoustic, infrasound,

SYNOPSIS

In the view of the US, the fundamental task of the International Data Center (IDC) for the Comprehensive Test Ban Treaty (CTBT) is to provide States Parties with equal, open and convenient access to standard products and services to support their national CTBT verification requirements. In doing so, the IDC would perform a large fraction of the computationally-intensive, technical work required by most States Parties. This would include collecting and archiving data from the International Monitoring System (IMS) sensors and other sources (e.g., associated measures, on-site inspections), performing data analysis to detect and locate events and to compute parameters useful for event identification, and customized provision to States Parties of the subsets of data of interest to them. It would be the responsibility of States Parties to apply national criteria to the technical products from the IDC and other sources to make verification decisions regarding the identification of events, the attribution of those events, and the options for responding within or outside of the CTBT. All products and services would be objective and technical in nature, and would aim to facilitate cost-effective compliance assessments by States Parties. Advanced physical and computer science technologies would be incorporated to allow the IDC to perform its work with as high a degree of security, reliability, cost-efficiency and automation as possible.

The vision for the CTBT IMS is shown in Figure 1. Data from sensors certified as part of the IMS would be transmitted to the IDC either directly or through National Data Centers (NDC) operated by States Parties. It is likely that the IDC would collect and archive a daily volume of up to 10 Gbytes of raw and partially-processed data from over 1,500 channels of data received from 40 - 150 seismic, 50 - 100 radionuclide, 5 - 20 hydroacoustic and 60 - 70 infrasound stations. The IMS sensors would be divided into two categories: primary and auxiliary. The primary sensors would establish a detection threshold by automatically forwarding continuous and/or preprocessed data that would be used to detect and initially locate events. The IDC could automatically or interactively retrieve additional data from auxiliary sensors to improve event location and characterization. Primary, and perhaps auxiliary, sensors would provide digital signatures with each data package which could be authenticated by the IDC or States Parties as a means of increasing confidence in the integrity of the data.
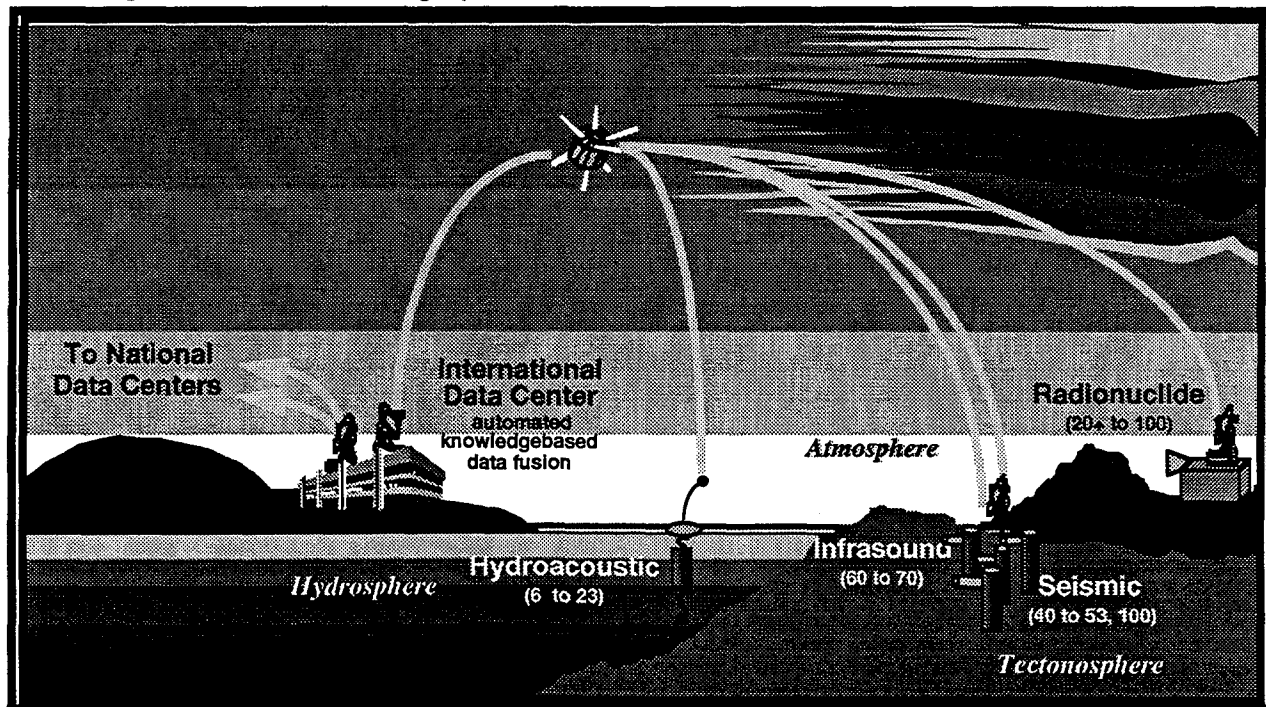
Figure 1. Elements of the proposed CTBT International Monitoring System.

The analysis objective of the IDC would be to produce global bulletins and other products that support the CTBT verification objectives of States Parties. The differences between the techniques would typically be related to the schedules for processing, the particular algorithms applied during processing, and whether or not there is a need for both primary and auxiliary data processing. Seismic, hydroacoustic and infrasound are timeseries data that are similar enough that they could be analyzed with variants of the same software. However, radionuclide analyses diverge somewhat from the others, in that the propagation of radionuclides from the causative event to the sensors can take days, location of events requires temporally-varying meteorological models, there may be some degree of in-field processing, physical filter and gas samples may need archiving and additional analyses, and coordination with certified labs may be required. In general, an initial, automatically-computed event list would be available as rapidly as possible, depending on the monitoring technique, after the event's occurrence. An analyst-reviewed bulletin for each technique would be available hours or days later, again depending on the technique. In addition to the single technique products, "fused" event lists, which contain correlated signals and located events based on different techniques, would be compiled automatically and updated over time (Figure 2). The final product would be an analyzed, "fused" event bulletin. The processing and analysis procedures at the IDC would be scientifically validated and documented in the Operational Manual for the International Data Center. This manual would provide for IDC procedures to meet changing requirements and to improve operational quality and efficiency.
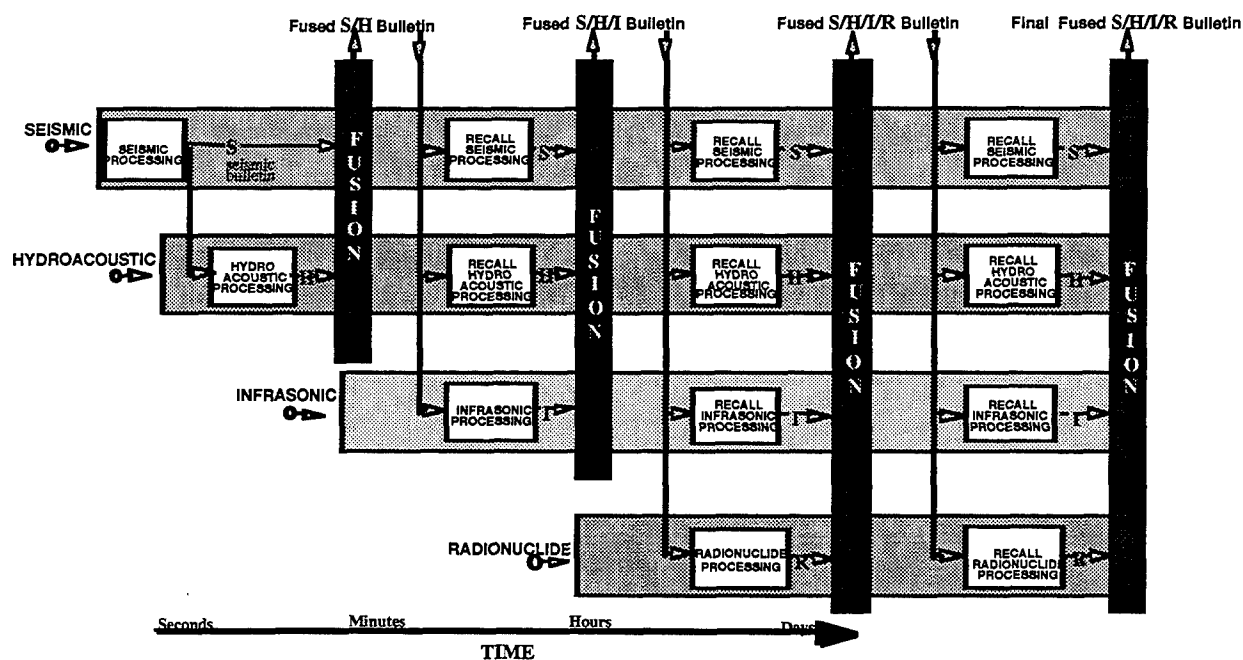
Figure 2. IDC fusion architecture and data flow.

The IDC would provide data access services that make it convenient for States Parties to find and retrieve, only those data of interest to them. Services would range from the re-transmission of large volumes of continuous, raw data, to provision of select, relatively small, subsets of data and products. For the latter, the IDC would allow States Parties to establish "subscriptions" that apply their own national criteria to screen for and automatically forward the subsets of data necessary to meet national verification needs. These tools would generally use the parameters computed from the raw data by the IDC as a basis for the screening.

The US is leading an international effort to prototype and test an IDC for processing seismic data during the Group of Scientific Experts Third Technical Test (GSETT-3). GSETT-3 began full-scale operations in January 1995 (CD/1296). The US is building upon the GSETT-3 system to prototype and test a more general IDC for processing data from all CTBT monitoring techniques. The US has offered to transition this prototype to the future CTBT organization (CD/NTB/WP.192). ARPA continues to transfer elements of the IDC to the prototype US National Data Center at AFTAC. The schedule for development, testing and transfer is shown in Figure 3.

TASK	FY 94	FY 95	FY 96	FY 97	FY 98
Seismic	5 + 10 stations	25 + 25 stations	40 + 75 stations	50 + 100 stations	
Radionuclide		11 stations	20 stations	25+ stations	
Hydroacoustic			2 stations	4+ stations	
Infrasound			1 stations	5+ stations	
Fusion			S/H location	S/H/R/I location & char	
Visualization					
Testbed					
Knowledge Acq.					
CTBT Int'l Org					
US AEDS					

Legend:
- Concept Definition
- Unit Prototyping
- System Integration
- Ops Testing and Knowledge Acq.
- Final Prototype Testing
- Transition & Testing

(Side label: Automated, Knowledgebased Processing)

Bottom markers: Start CTBT Negotiations · US Congressionally-Mandated Signature · Preparatory Commission? · Entry Into Force?

Figure 3. Schedule for development, testing and transition of the prototype IDC.

The IDC is being prototyped and tested at the Center for Monitoring Research (formerly, the Center for Seismic Studies) in Arlington, Virginia. The hardware and software infrastructure has been designed to be flexible enough to support sophisticated, knowledge-driven fusion of data collected from seismic, hydroacoustic, infrasound and radionuclide sensors. The seismic processing capability being developed in support of GSETT-3 is the most mature at this time, and is quite unique. Signal processing and event location systems will incorporate station- and path-specific knowledge (e.g., detection parameters and phase identification parameters, time and amplitude path corrections). The knowledge base and the resulting quality of the products are improving with experience. Signal and event parameters not normally presented in earthquake bulletins (e.g., spectral ratios, spectral variance, complexity, and measures of similarity to previous events) are also routinely computed. The detection capability of the network is permitting calibration of regional magnitude scales around the world. New concepts for maintaining the integrity of the facilities, the data, the products and the systems are being tested. All products are being archived on-line at the IDC and made available to NDCs via the variety of data access services. Seismic bulletins and a wide range of information are also available to the public through the IDC's World Wide Web pages at http://www.cdidc.org/.

Presented in Figure 4 are the primary and auxiliary seismic stations planned for GSETT-3. Figure 5 shows the locations and error ellipses (most too small to be seen) of events from the first almost seven months of the GSETT-3 Reviewed Event Bulletins (REB). These events were analyzed and available within about two days after the end of the data day. There are on average 60 events, and up to 200 events during large aftershock sequences, in the REB each day. Estimates of the 90% threshold for detection by three Alpha stations range from m_b 3.1 in northern Europe up to m_b 4.7 in the southern oceans. Typical location uncertainties for events within 2000

km of the closest station are between 40 and 50 km. Completion of the station network and calibration through the use of regional, rather than globally-averaged travel times, will reduce the location uncertainty. Table 1 demonstrates some of the progress that has been made during the preparation for and conduct of full-scale GSETT-3 operations.

	1 Feb 1994	20 Aug 1994	20 Feb 1995	1 Aug 1995	Plan
Nations	10	13	28	38	>40
Alpha Stations	6	12	32	35	60
Beta Stations	13	21	44	71	~150
Coverage	European	Sparse Global	Global	Global	Global
NDCs -> Gamma data	1	5	11	14	20-30
Data Vol/day to IDC	0.2 Gbytes	1.5 Gbytes	2.5 Gbytes	2.5 Gbytes	>5 Gbytes
Data Days/week	2	3	7	7 (24hrs/day)	7 (24hrs/day)
REB Events/day	20	20	60	60	>100
REB Events Total	1500	2700	6800	11000	
IDC Staff (int'l)	27(0)	27(0)	47(9)	49(10)	50(9)

Table 1. Key statistics for GSETT-3 as a function of time.

Over the past year, increasing effort has been focused on adapting the GSETT-3 IDC infrastructure to support prompt, secure and reliable collection, processing, analysis, storage and provision of data derived from the diverse types of sensors envisaged for the CTBT IMS. Shown in Figure 4 is the suite of hydroacoustic, infrasound and radionuclide sensors expected to be providing realtime data to the prototype IDC during 1995. The first phase of this effort has been to integrate atmospheric radionuclide processing into the IDC. The data flow in this system, at a high-level, is similar to that for seismic, in the sense that signal detection, location, characterization and timely reporting are important requirements. The prototype radionuclide processing system is testing new concepts that focus on automating and accelerating these processes. By the end of 1995, the IDC will likely be collecting and analyzing data from stations in the US, Australia, Canada, Finland, Germany, Kuwait, Russia, South Korea, Sweden and Turkmenistan. Future work will focus on integrating into the prototype IDC innovative concepts for hydroacoustic and infrasound monitoring, and for fusion of data from multiple techniques to improve event detection, location and characterization. It is expected that data from hydroacoustic stations near Wake and Ascension Islands, and from infrasound sensors in New Mexico and Utah will start arriving at the IDC during the fall of 1995.

Credits

The principal contributors to the success of the International Data Center include Science Applications International Corporation, Pacific Sierra Research Corporation, AFTAC, Atlantic Aerospace, Australian National University, Autometric, Canberra, Cornell University, Digital Systems Research, Ensco, Harvard University, Mission Research, Multimax, NOAA, NORSAR, Planing Research Incorporated, Ruhr University, Science Horizons Incorporated, S-CUBED/Maxwell Industries, Southern Methodist University, Teledyne-Brown, Torrey Sciences, Trusted Information Systems, University of California - San Diego, University of Virginia, Woodward-Clyde Federal Services and the many international experts who have provided service, software and analyses.

REFERENCES

References

CD/1296 (1995) *Progress Report to the Conference on Disarmament on the Fortieth Session of the Ad Hoc Group of Scientific Experts to Consider International Cooperative Measures to Detect and Identify Seismic Events*, Conference On Disarmament, Geneva, 17 pp.

CD/NTB/WP.192 (1994) *U.S. Approach for the Comprehensive Test Ban Treaty International Data Center*, Conference On Disarmament, Geneva, 25 pp.

Figure 4. Prototype International Data Center Sensor Network for 1995.

11
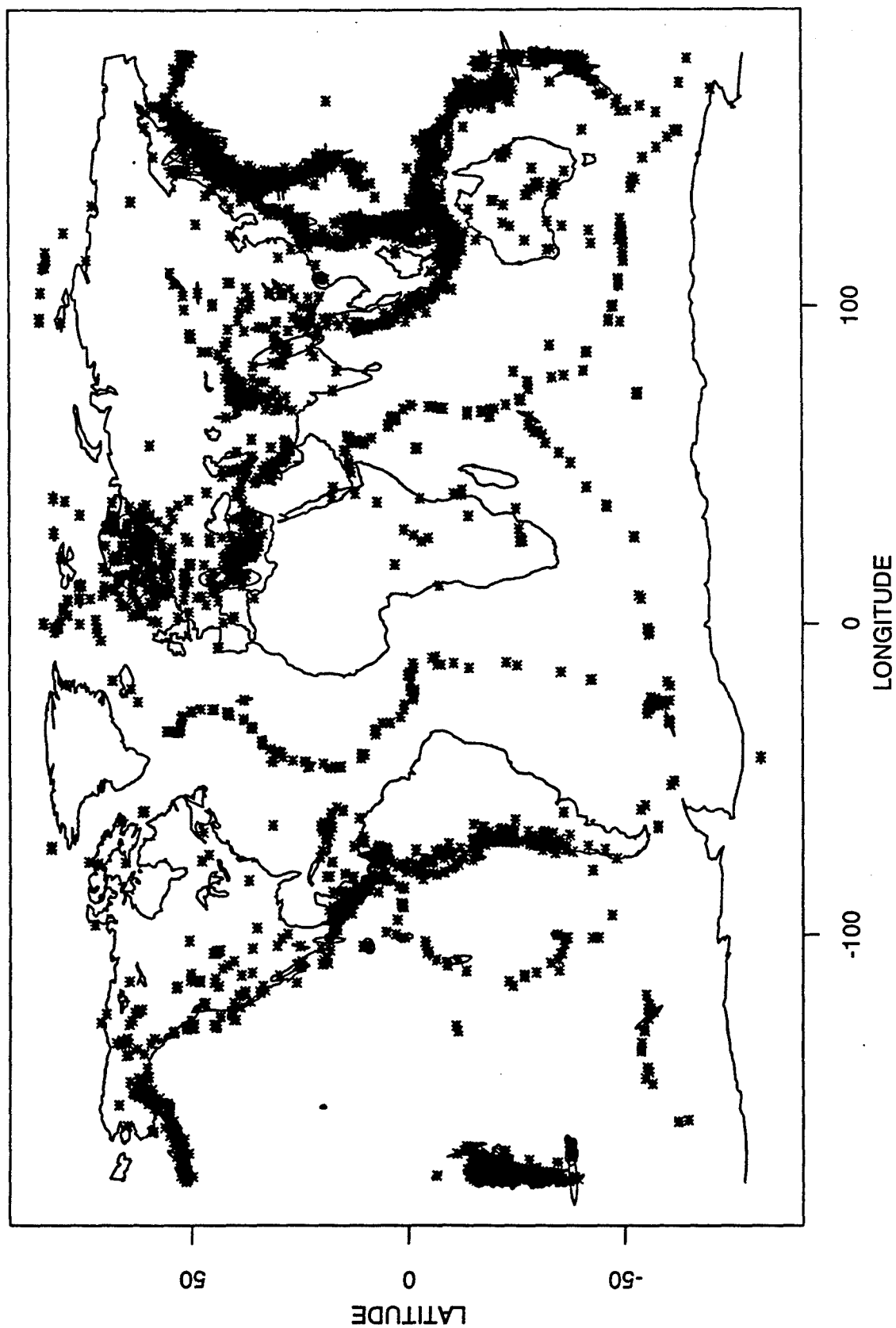
Figure 5. GSETT-3 Reviewed Event Bulletin events from January 1 through July 23, 1995, with at least 6 defining phases.

A STATUS REPORT ON THE CTBT NEGOTIATIONS:
A LOOK FORWARD TO 1995
JAY H. NORMAN
NONPROLIFERATION & INTERNATIONAL SECURITY DIVISION
LOS ALAMOS NATIONAL LABORATORY
ON ASSIGNMENT TO
OFFICE OF ARMS CONTROL AND NONPROLIFERATION
DEPARTMENT OF ENERGY

Abstract

A Comprehensive Ban on Nuclear Testing has been a goal for decades with formal negotiations commencing in January of 1994. The most contentious issues are agreement on the scope of the treaty and the nature and scope of the proposed International Monitoring System. Further issues of concern are on-site inspection and entry-into-force. Without important compromises, it seems unlikely that the treaty will be ready for signature before the end of 1996; however, all of the nuclear weapons states have stated that they will be prepared to sign a Comprehensive Test Ban Treaty by that time. Thus we continue to be hopeful that a successful treaty will be completed.

A STATUS REPORT ON THE CTBT NEGOTIATIONS:
A LOOK FORWARD TO 1995

A Comprehensive Ban on Nuclear Testing has been the subject of discussion, debate, and at times, negotiation for decades. But with the end of the Cold War, and the resulting change in political climate, this elusive goal at last appears to be within our grasp. Early in 1993, circumstances favoring the completion of a CTBT were evident: France, Russia, the United Kingdom, and the U.S. had unilaterally declared moratoria on their nuclear testing programs; the U.S. had passed legislation calling for the completion of a CTBT by the end of 1996; a U.N. resolution calling for the negotiation of a multilaterally verifiable CTBT was unanimously adopted, and all the "Nuclear Weapon States" as well as Israel, Pakistan, and India (the nuclear capable states that are not party to the NPT) were prepared to join in the negotiation of a CTBT at the Conference on Disarmament.

Formal negotiation of the CTBT began in January of 1994 at the Conference on Disarmament (CD) in Geneva. The CD has 38 member states and some 50 observer nations. As of this summer, the CD has published the third version of the "rolling" treaty text which is slowly evolving into what will become the final treaty document. In the negotiation there are some areas where there are few disputes and the treaty language is largely agreed. However, there are four significant areas where there are fundamental differences of opinion among the states. These areas which will require particular attention and significant compromises by some states are: the scope of the treaty, the International Monitoring System, On-Site Inspection provisions, and the mechanism for Entry-Into-Force.

The area most important to the achievement of a treaty is agreement on the scope of the treaty. By scope we mean the set of prohibitions or requirements which are the basic reason for the treaty. Resolving this issue will require agreement on what is generally understood to be a nuclear test (even if this is not explicitly stated in the treaty) and whether certain activities will be excluded from the general prohibition (for example some ICF experiments may be considered by certain states to be nuclear explosions but they may agree that it should not be considered within the scope of the treaty). Alternatively, the treaty might simply be silent allowing countries some latitude in interpretation (for example the conduct of hydronuclear experiments could be approached this way). However, even if the treaty itself does not spell out in detail what will be allowed for "activities not prohibited" (ANP), there will certainly be a sensitivity among the nuclear weapon states that such activities are conducted within agreed limits to ensure that asymmetries in the capability for long-term maintenance of stockpiles and nuclear deterrent do not develop. Thus, if there are ANTP, verification of these activities among the five nuclear weapon states may be required. This could be expensive, and intrusive. There are ideas on approaches to such verification or confidence building measures, but they must be worked out by a consensus within the Nuclear Weapon States. This could add another significant aspect to the final resolution of the treaty.

The second important area is nearer to the interests of the participants of this symposium and involves the nature and scope of the proposed International Monitoring System (IMS). Again there are a spectrum of positions taken by states participating in the negotiation that range from a token IMS to a comprehensive system with the best possible capabilities. At the one extreme are countries who feel that the political commitment of a CTBT is all that is required. For them, the

debate over verification only slows the process of completing the treaty, and in their view the Partial Test Ban Treat (PTBT) (also called the Limited Test Ban Treaty [LTBT]) worked well for some 30 years without a verification system other than the NTM of the U.S. and Russia so why waste time and resources on an IMS for the CTBT. At the other extreme one of the P-5 has proposed a more comprehensive international monitoring system, that would give the international community access to monitoring capabilities similar to those of the U.S. and Russia. However, the cost of such a system seems to be higher than the international community is willing to pay. The largest segment of the CD seems to be focusing on a system of modest capability that would fulfill the mandate of an internationally-verifiable treaty. Of the current negotiating problems the definition of the IMS is the least likely to derail the treaty negotiations, but it is an area that will require significant technical work to finalize the treaty test. Resolution of some of the remaining issues of the IMS is unlikely without some significant compromises on the part of the U.S.

The third hot topic area is that of On-Site Inspections (OSI). For the U.S. there are two sides to this issue. First, we would like to be able to conduct inspections at any location where we have a concern about compliance with the CTBT. On the other hand, we want to be able to limit the potential for inspection at our sensitive military and defense R&D installations. These opposing viewpoints have led the U.S. to propose a compromise position between these extremes. China, France, and Israel have clearly chosen in favor of protection of their sensitive military and defense R&D installations over the right to unimpeded access for OSI. Several other influential countries including Germany and Australia are promoting a presumption of access with some limitations following a "managed access" approach similar to that of the Chemical Weapons Convention (CWC). This conflict between the right of access for OSI and the right to protect sensitive information unrelated to the treaty will result in some sort of compromise using "managed access" provisions or restricted zones. Some delegations have advocated adoption of the challenge inspection provisions of the CWC as the approach to OSI. However, several states had reservations about the intrusiveness of the challenge inspection regime of the CWC at the time of its negotiation. The work at the CWC PrepCom has only heightened their concerns about challenge OSI and created a backlash against the CWC approach for the CTBT. The technical work on OSI has been limited to date in the negotiation. There is a substantial amount of technical input on OSI that still needs to be considered before this issue will be reduced to simply finishing the treaty text.

The fourth sticky issue concerns provisions for Entry-Into-Force (EIF) of the treaty. The EIF provision will define which countries and/or how many countries will have to complete their legislative process (ratification by the Senate in the U.S.) to accept the provisions of the treaty before the treaty will actually enter into force. For the CWC EIF is defined as ratification of the treaty by 65 states (the CWC is still waiting for ratification by about 30 additional states, the U.S. included, to achieve EIF). The issues for the CTBT CIF are much more difficult as most states want all of the nuclear weapon states to have ratified the treaty before it enters into force. Some states have clearly stated that they will insist on the nuclear threshold states, India, Pakistan and Israel, having ratified the treaty as a condition for EIF. Other states such as India and Pakistan are unlikely to accept EIF of the treaty unless their regional rivals have also ratified the treaty. The U.S. has proposed a provisional acceptance of the treaty (similar in nature to the EIF provisions of the Treaty of Tlatelolco, the South American Nuclear Free Zone Agreement) as a way to achieve EIF for those states that have ratified the treaty while other states complete their legislative process as a way to move forward. But no matter what the approach, this process of defining which states must have ratified the treaty before EIF will take time and artful negotiation to reach a formula acceptable to all participating states.

Finally, there is an interplay between these final three issues. In the push to achieve the CTBT as soon as possible there will be a desire to minimize the negotiation of details of the IMS and OSI and leave the resolution of such details to a Preparatory Commission that will become responsible to prepare for implementation of the treaty after EIF. If the CWC PrepCom is an

15

example of how this works, one could expect lengthy debates and strong differences of opinion in the PrepCom on the details of operations and equipment for OSI; what constitutes the required operational capabilities of the IMS; and the schedule for deployment of sensors and equipment for the IMS. If the current U.S. position holds sway (all IMS stations are owned and operated by the host country) the initial operational capabilities of the IMS could be subject to manipulation by states not installing equipment or dedicating resources in a timely fashion to delay EIF. Thus, the requirements for EIF could become hostage to completion of the required PrepCom work.

The above litany would seem very pessimistic and often when one works very hard to achieve a particular goal it is only the obstacles that stick out in one's mind rather than all the positive progress. There has been much progress on the CTBT and the prospects for a signed and ratified CTBT are still good. Without some important compromises, it seems unlikely that the treaty will be ready for signature before the end of 1996. However, all of the nuclear weapon states have clearly stated that they will be prepared to sign a CTBT by the end of 1996. Thus, the work of this group continues to be vital to the successful negotiation of the treaty, the work of the PrepCom that will follow, and ultimately to the operation of the treaty verification regime.

THE UNITED STATES NATIONAL DATA CENTER

BY

Bruce R. Varnum

Director of US NDC

Abstract

This report initially summarizes the progress made in the development of the U.S. National Data Center (NDC) at the Air Force Technical Applications Center (AFTAC) and its on-going support to the Group of Scientific Experts (GSE) 3rd large-scale technical test (GSETT-3).

Under the GSE concept for an International Monitoring System (IMS), each participating member-state has several options from which they may choose in developing their own NDC. The US is participating in GSETT-3 by prototyping and operating a full-scale NDC.

The GSETT-3 experiment has been in progress for eight months with significant progress having been made during this time-period. The US NDC is currently forwarding data to the IDC from six primary (alpha) stations located in the United States, one primary station located in Antarctica, and eleven US auxiliary (beta) stations. In addition, the US NDC is transmitting, per each country's request, data to the IDC from participating Southern hemisphere stations including PLCA in Argentina, LPAZ in Bolivia, BDFB in Brazil, BGCA in the Central African Republic, DBIC in the Ivory Coast, CPUP in Paraguay, BOSA in South Africa, and CMAR in Thailand.

The remaining portion of the report addresses the system for providing data services at the NDC. The National Data Center Archive (NDCA) is being developed to include archiving large quantities of geophysical data (primarily seismic) for nuclear monitoring. Raw seismic waveform data will comprise the bulk of the NDCA, but it will also include supporting alpha-numeric tables and files, as well as raw hydroacoustic, infrasonic, and radionuclide data. Specifically, mechanisms through which NDCA data will be made available to US researchers and other authorized users, formats and content for all data contained in the archives, the scope of the data archives, mode of data submission, and types and priority of request handling are addressed in this report.

This Page
Intentionally Blank

Statistical Frameworks for Seismic Discrimination

DN Anderson   KK Anderson   DN Hagedorn   SR Sain[1]   CJ Young[2]

Pacific Northwest Laboratory

Contract No. DE-AC06-76RLO 1830

Abstract

To verify compliance with a Comprehensive Test Ban Treaty (CTBT), low energy seismic activity must be detected and discriminated. Monitoring small-scale seismic activity will require regional monitoring capabilities (within $\approx$ 2000 km, U.S. Congress (1988)). The reliable discrimination of small-scale seismic events requires a multi-dimensional representation of the seismic signal. A multi-dimensional characterization might include wave arrival times, magnitudes, and incidence and azimuth angles. These measurements can be used singly or combined to form discriminants, which are then subjected to a set of discrimination rules to categorize the source event. Statistical discrimination methods of this type require a *training sample*, i.e., a set of real or simulated seismic data used to optimize or tune the discrimination algorithm by assigning weights to the various discriminants, or by modifying the structure of the algorithm. Identifying the signatures of various seismic sources also requires a geologic characterization of the shallow structure of the earth in each particular region of interest. The results can be used to construct seismic signals representing nuclear test sources. These synthetic or simulated signals can be combined with empirical signals of earthquakes and mining activities to form a training sample for each region. This paper identifies several statistical issues that must be resolved in order to address the CTBT verification mission. These are all associated with uncertainties in the multidimensional characterization measurements or in the correlations among them. In particular, further research is needed on the statistical properties of:

- wave arrival time estimates, especially for regional wave arrivals, which sometimes tend to be emergent;

- regional velocity tables, i.e., the travel time tables that characterize the regional geology;

- measurements from regional seismic arrays, which can theoretically be combined to provide better estimates of wave arrival times, magnitudes, and direction;

- evasion scenarios (see U.S. Congress, 1988, Chapter 6);

- association, i.e., the agreement among seismic stations or between global and regional seismic networks that a seismic event has occurred and how to classify it;

- training samples, especially how to eliminate bias in the sample;

- robust discrimination algorithms, e.g., algorithms that are less sensitive to data with a poor signal-to-noise ratio;

- Bayesian discrimination algorithms e.g., algorithms that utilize expert opinion to substitute for missing data;

- statistical interdependencies in a regional seismic analysis, e.g., the relationship between the uncertainties in detection, phase identification, event association and discrimination.

Also discussed are several common statistical discrimination methods including linear discrimination, classification and regression trees (CART) and logistic regression.

Key Words: statistical discrimination, CART, logistic regression, nearest neighbor

---

[1] Department of Statistical Sciences, Southern Methodist University

[2] Sandia National Laboratories

Objective

To meet the exacting demands of monitoring a CTBT, tools that integrate both seismic and statistical technologies are needed. Discriminating small seismic events in a region of interest requires a geological characterization of the crust of the earth in that region. This characterization leads to an understanding of the unique seismic signatures that will be produced by different seismic sources. Characterization of regions of interest to the United States (U.S.) is currently being studied as a part of the U.S. Department of Energy (DOE) CTBT R & D program (DOE, 1994). The findings from this research could conceivably be used to construct synthetic or simulated seismic signals representing the behavior of a nuclear source. These simulated signals can be combined with empirical signals from earthquakes and mining activities to form a *training sample* for the region. Discrimination for low energy seismic events will require a multi-dimensional representation of a seismic signal. Multi-dimensional measurements from a seismic signal (discriminants) can be combined by a variety of statistical techniques to form a unified discrimination method. With a training sample, a statistical discrimination technique is trained to optimally combine discriminants. For example, a discrimination rule might make use of a sum of weighted discriminants with the weights estimated from a regional training sample. Several common statistical discrimination methods are:

- linear discrimination, including Fisher's linear discriminant function

- quadratic discrimination

- nonparametric discrimination, including nonparametric likelihood methods and kth nearest-neighbor methods

- classification and regression trees (CART)

- logistic regression.

The objective of this research is to identify and resolve the statistical issues associated with monitoring a CTBT and to identify and research various statistical discrimination methods appropriate for regional seismic discrimination.

Preliminary Research Results

Statistical Issues in Seismic Analysis

Several general statistical issues need to be resolved in order to effectively verify a CTBT. Addressing them will undoubtedly uncover more detailed statistical questions. These issues include:

- Statistical properties of wave arrival time estimates—Arrival times of various seismic waves can be estimated in several ways, with associated uncertainties. Hypocenter estimation techniques are based on arrival times of different types of waves from a seismic disturbance. Estimates of depth and epicenter are used as discrimination tools. To ascribe uncertainty to a hypocenter estimate, the uncertainty in a wave arrival time estimate must be resolved. The seismic community is fully aware of the problem of ascribing uncertainty to a wave arrival time estimate in a teleseismic setting. This issue will need to be revisited in a regional setting because regional wave arrivals often exhibit a gradual transition from noise to wave signal, i.e., they are emergent.

- Statistical properties of regional travel time tables—To develop a U.S. CTBT seismic monitoring system, regional travel time tables will need to be developed. At regional distances, small variations in the velocity structure of the earth can have a significant impact on location and source characterization. To construct an uncertainty statement for a regional hypocenter estimate, the uncertainty in a regional travel time table will need to be combined with wave-arrival time uncertainties. Travel time tables provide the single largest source of systematic error in a hypocenter estimate.

- Statistical properties of seismic measurements from arrays—The proposed CTBT monitoring system will use seismic arrays to monitor regions of interest. The statistical properties of teleseismic array data are well understood in the seismic community. The statistical issues associated with using array data in regional seismic analysis will need to be researched. Regional seismic array data will be combined to estimate wave arrival times. The uncertainty in this process will need to be evaluated. Also, calculating wave magnitudes from regional array data will form the foundation for some regional discriminants. The statistical properties of regional array magnitudes and the discriminative power of these magnitudes should be researched.

- Statistical issues of evasion scenarios—The U.S. Congress (1988, Chapter 6) Office of Technology Assessment discusses several viable evasion scenarios that need to be addressed to effectively implement a CTBT. One of these scenarios involves masking or decoupling the energy release from a nuclear weapon test by performing the test in an open underground cavity. The parameters (decoupling factors) associated with an evasive decoupled weapon test need to be estimated. As noted in the congressional report, decoupling factors are needed to establish CTBT monitoring thresholds. The statistical properties of decoupling factors for various geologies and test cavity configurations should be researched in order to effectively establish CTBT monitoring thresholds.

- Statistical properties of association—Errors in the association process often lead to the cataloging of spurious events, or the degradation of the accuracy of seismic event locations. A quantitative measure of the strength of association is necessary. The creation of such a measure is a statistical challenge because it would have to combine measures of the similarity of the associated waveforms, the agreement of the back azimuths and slowness, and the agreement of the phase arrival times, all weighted by some type of observed signal-to-noise ratio. The measure must include penalties for missing data; for example, an analyst may wonder why a high quality, low noise station, which usually detects events from the area in question, did not detect it. If the station is operational, such non-data is strong evidence against the event being a true event. The problem of misassociation of individual events aside, another statistical issue is the estimation of the overall rate of misassociations reported in seismic bulletins and catalogs of events. Perhaps region-by-region rates of misassociation can be estimated by comparison of global seismic catalogs with the seismic catalogs from regional networks. Such regional networks may provide more complete catalogs of the region's events; i.e., the region's near-ground-truth.

- Statistical issues in constructing a training sample—Any regional discrimination process will need a training sample to build individual discriminant weights and possibly the structure of the discrimination algorithm. A proper regional training sample will be similar in every respect to data that would be analyzed in an operational setting. A training sample must not be biased by the elimination of information. Using only "clean" events in a training sample will seriously misrepresent misclassification rates and uncertainties in a discrimination algorithm. A training sample can further misrepresent these misclassification rates and uncertainties if the size of an event is confounded with the source of the event; e.g., if all large magnitude events in a training sample are earthquakes (or conversely if all are explosions). Finally, a training sample may include designed nuclear weapon tests or mining explosions (calibration events) in regions of interest. Statistical experimental design techniques can contribute to an optimally designed calibration event.

- Robustness of statistical discrimination algorithms—The ability of a statistical discrimination method to accurately perform under a less than optimal operational setting (its robustness) should be researched. The statistical discrimination methods discussed below should be considered when developing a U.S. CTBT seismic monitoring system because the robustness properties of these methods can be readily studied. These methods can be synergistically used as evidence when identifying the source of a seismic event. Complementary to research on the robustness of statistical discrimination methods, there should be research on statistical methods to address missing data. It is conceivable that it may not be possible to construct an appropriate training sample for a future region of interest. Expert opinion may be required to construct an initial discrimination algorithm for such a region. In the

20

statistical community, methods of integrating expert opinion into a statistical methodology are known as Bayesian methods. Determining if a statistical discrimination technique is amenable to Bayesian methods should be an important CTBT research task.

- Statistical interdependencies in a seismic analysis—All aspects of a regional seismic analysis are related or interdependent. These interdependencies will most likely produce statistical correlations that must be addressed. For example, a hypocenter estimate is used in forming some seismic discriminants. Understanding the correlations between various seismic measurements and sub-analyses is necessary to develop general uncertainty statements.

Statistical Techniques for Seismic Discrimination

In a seismological setting, statistical discrimination is the process of classifying a candidate seismic event as an earthquake, a chemical explosion, or a nuclear detonation using information from seismic discriminants (variables containing information derived from a seismic waveform). For a lucid discussion of potential regional seismic discriminants see Blandford (1995). The goal of discriminant analysis is not only to identify important or relevant discriminants but also to design a procedure incorporating these discriminants that accurately classifies the source of a seismic disturbance. In this section, some basic statistical multivariate discrimination methods are reviewed. Examples that illustrate each of these statistical discrimination methods are included. The data used in these examples were collected by Walter, Mayeda, and Patton (1994). *It is important to remember that these examples are not intended to be an authoritative seismic analysis of these data. Rather, the goal is to use data with seismic characteristics to illustrate the features of statistical discrimination methods. When presented with these examples, the reader should focus on the potential utility of the statistical discrimination methods and not the specific inferences from this small data set.*

For a seismic event, a vector of p discriminants, $\mathbf{x} = (x_1, \ldots, x_p)'$, is measured or derived from a seismic waveform. The vector $\mathbf{x}$ might include wave arrival times, magnitudes, incidence and azimuth angles and other potential discriminants. Note that these discriminants, x_i, $i = 1, \ldots, p$, can take on any value, real (e.g., focal depth) or categorical (e.g., polarity of first motion). A classifier or discrimination rule is defined as a function $d(\mathbf{x})$ that mathematically combines the discriminants in $\mathbf{x}$. The value of the function $d(\mathbf{x})$ indicates the most likely source of a seismic event. An alternative formulation of the discrimination rule is to consider the vector of discriminants, $\mathbf{x}$, as a point in a p-dimensional space. The discrimination rule $d(\mathbf{x})$ can then be thought of as partitioning or dividing this p-dimensional space into sections. Each section would then be associated with a particular seismic source. For example, if a single real discriminant is considered, then $d(\mathbf{x})$ represents a "cut" on that discriminant, dividing the real line into "right" and "left" sections. All candidate events with values of this discriminant to the left of the cut could be labeled as explosions, while all values to the right could be labeled as earthquakes. If two discriminants are considered, then $d(\mathbf{x})$ is a line dividing the plane of real numbers into "left" and "right" areas. If three discriminants are considered, then $d(\mathbf{x})$ is a plane slicing through three-dimensional space. Note that more complex rules are not restricted to a single partition, nor are the partition boundaries always straight lines.

The error involved in a classification scheme is governed by the rule that partitions the relevant multivariable space. Some insight into the sources and behavior of the misclassification error can be found by studying how a classification rule partitions the space of possible discriminant values. Let the discriminants $\mathbf{x}$ for a particular seismic source be generated from a probability model (distribution) that is distinct from the probability model describing another seismic source. A classification rule divides the variable space into sections, with each section representing a seismic source. The probability of misclassification is simply the probability of making an incorrect classification. The total misclassification probability is a sum of the individual source misclassification probabilities.

Discrimination rules are constructed based on past experience in the form of a training sample. A training sample is a set of discriminant vectors $\mathbf{x}$ with known classification that is representative of the distribution of the seismic sources. This set of data is used to "train" the discrimination rule. A training sample is used to build a discrimination rule and to test its performance or accuracy with cross-validation methods. The

performance of a discrimination rule is generally ascertained through some measure of misclassification cost. For example, Taylor et.al. (1989) and Glaser et.al. (1986) discuss the cost function

$$C(x|q)\pi_q P(x|q) + C(q|x)\pi_x P(q|x), \tag{1}$$

where π_q and π_x are the prior probability of an earthquake and explosion, $C(x|q)$ and $C(q|x)$ are the costs or penalties associated with mislabeling an explosion as an earthquake or an earthquake as an explosion, and $P(x|q)$ and $P(q|x)$ are the misclassification probabilities.

Such a criterion allows considerable flexibility to account for a variety of situations. For example, in a CTBT setting, the relative frequency of nuclear explosions versus earthquakes should be quite small. Hence, π_x should be set quite small relative to π_q in a CTBT setting. Perhaps more important is the cost associated with the different types of error. A false alarm (labeling an event as an explosion when in fact it is an earthquake) may be thought of as less serious than the failure to detect a violation of the CTBT (labeling an event as an earthquake when in fact it is an explosion). Hence, the cost associated with failure to detect a violation, $C(q|x)$, would be set higher than the cost of a false alarm, $C(x|q)$. The probabilities in Equation (1) are generally unknown quantities, but they can easily be estimated with cross-validation methods.

Linear Discrimination

One of the most conceptually simple rules, linear discrimination, is based on the assumption that the sources exhibit Gaussian distributions with identical covariance structure (i.e., differing only in location). A linear discrimination rule assigns a candidate event to the source with centroid closest to the position of the x in the sample space. Many distance metrics are possible, but the most natural is the Mahalanobis distance, using the pooled within-group sample variances (an unbiased estimator of the common covariance matrix of the groups). For example, consider two sources, earthquake and nuclear detonation (NUDET). Then the estimated covariance is written as $s = (n_x s_x + n_q s_q)/(n_x + n_q - 2)$, where s_x and s_q are the sample covariances estimated from the training sample and n_x and n_q are the sample sizes of the training sample for the two sources. A new observation x is labeled as a NUDET if $(\bar{x}_x - \bar{x}_q)s^{-1}(x - \frac{1}{2}(\bar{x}_x + \bar{x}_q)) > 0$, where $\bar{x}_x$ and $\bar{x}_q$ are the means of the training sample for the two sources. A quadratic discrimination rule is possible if the covariances are not equal.

Nonparametric Discrimination

The classical approach to statistical discrimination involves assuming a parametric form for the probability distribution of each group and using a training sample to estimate the relevant parameters. A candidate event is then classified to the group with the largest likelihood. For example, one might choose the Gaussian distribution to model the earthquakes. A training sample would then be used to estimate the mean and covariance. The distribution for NUDETs would be handled similarly. A candidate event would then be classified as an earthquake if $\hat{f}_q(x; \bar{x}_q, s_q^2)$ is greater than $\hat{f}_x(x; \bar{x}_x, s_x^2)$ or as a NUDET otherwise. Here, $\hat{f}_q$ and $\hat{f}_x$ are the earthquake and NUDET distributions with parameters $\bar{x}_q$, $\bar{x}_x$, s_q^2, and s_x^2 estimated from training data.

Hand (1981) and Silverman (1986) have studied the use of nonparametric methods for use in classification problems, replacing the parametric probability models in the classical procedure with nonparametric density estimates. Examples of nonparametric density estimates include the histogram and the kernel estimator. Recent advances in multivariate probability density estimation (see Scott (1992)) have led to further work in nonparametric methods for discrimination. Hall and Wand (1988) study the use of nonparametric methods with probability model differences as a discrimination tool. Holmstrom and Sain (1993) successfully apply a ratio of nonparametric probability models to applications in particle physics.

An example of nonparametric discrimination is shown in Figure 1. The plot on the right shows decision boundaries based on a bivariate product kernel estimator of the distributions of the earthquakes and the NUDETs. New events are classified according to which model yields a higher density value at the new point,
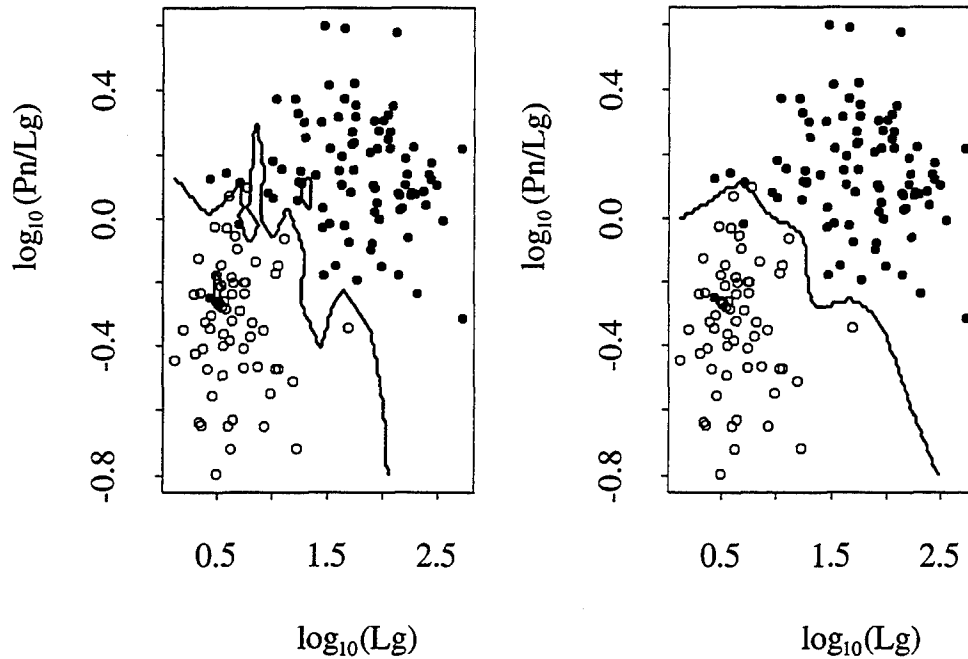
Figure 1: Example of nearest neighbor (left plot) and kernel (right plot) discrimination.

x. Note that the boundaries are highly nonlinear, offering greater flexibility. This flexibility can become increasingly important for situations with more complex structure or as the dimensionality increases.

The plot on the left illustrates a discrimination method in which new events are classified according to a kth nearest-neighbor rule (Fix and Hodges, 1951) with $k = 1$. Here a candidate event is classified to the group in which the nearest point to that event belongs. The boundaries in this case are highly irregular due to the lack of "smoothing". This single nearest-neighbor method represents an extreme case, when no smoothing is performed. The decision boundary for the kth nearest-neighbor rule will "smooth" as the value of k increases.

Tree-Based Methods

Binary tree methods represent an important improvement over some of the basic methods of statistical discrimination and in the use of standard linear and additive models for classification problems. First and foremost, binary tree methods can incorporate both numeric and categorical discriminants. Complicated discriminant behavior can also be modeled easily. Furthermore, binary tree methods are conceptually simple and yield a nice graphical representation of the final decision tree and the resulting classifications. This is especially valuable when dealing multi-dimensional data. For an overview of the theory and methodology, see Breiman et.al. (1984). Artificial Neural Networks (ANN) also have these features, however binary tree methods have advantages over ANN in seismic discrimination applications. For a comparison of binary trees and neural networks see Blough and Anderson(1994).

Binary tree methods are based on the notion of recursive partitioning. To illustrate, consider again the notion of a vector of discriminants, x, as a distinct point lying in a multivariate space. To build a binary decision tree, the discrimination algorithm recursively divides this multivariate space into smaller and smaller subregions. This dividing process is based on the training sample, and continues until each subregion is homogeneous with respect to one of the sources.

This tree-growing process leads to a large number of regions and can overfit by becoming overly representative of the training sample. To prevent overfitting and extreme complexity, a tree is grown and then pruned
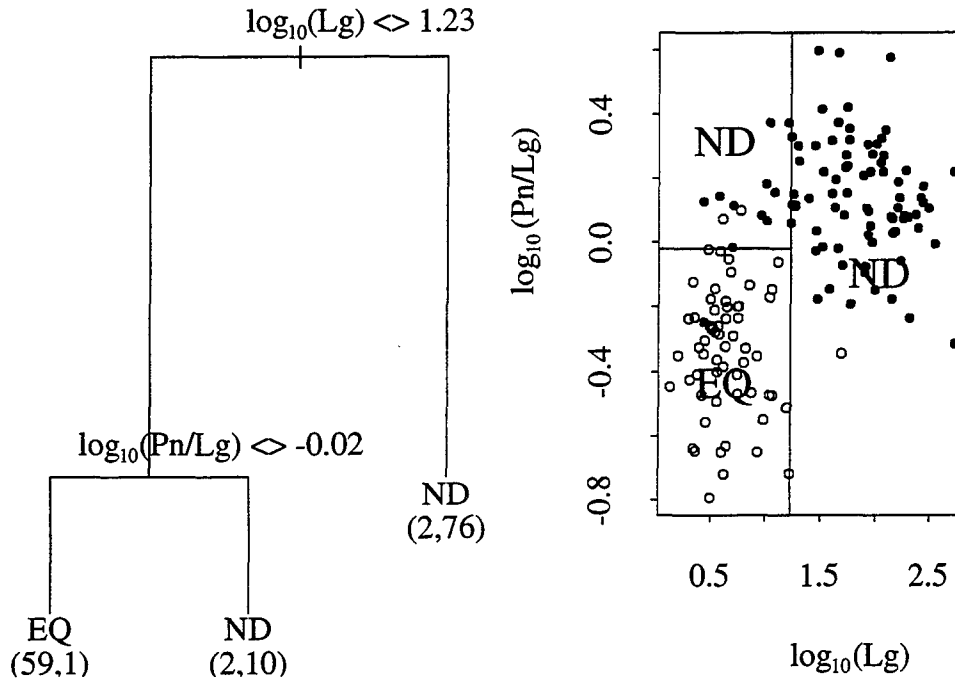
Figure 2: Binary tree example.

or shrunk to a more manageable size. This pruning is generally done by removing the least important splits, based on a cost-complexity measure that is designed to balance the homogeneity of the final regions and the complexity of the tree. This pruning can be thought of as combining adjacent regions of the multivariate space that are very much alike.

Graphically, the splitting of the discriminant space into regions can be displayed as a binary tree. An example is shown in Figure 2, using the data from Walter, Mayeda, and Patton (1995). The figure on the left shows a tree that has been grown and then pruned using a cost-complexity function as discussed in the previous paragraph. The final partitioning of the discriminant space is shown in the figure on the right. In this example, 59 earthquakes were correctly identified as earthquakes and 1 nuclear detonation was incorrectly identified as an earthquake. The counts at the "ND" branches of the tree are interpreted similarly.

Logistic Regression

Standard linear regression techniques have also been used extensively for discrimination tasks. The procedure is to model the responses, in this case a dummy variable taking on values of 0 or 1 depending on the candidate event being an earthquake or NUDET, as a linear function of the predictor variables, in this case the discriminants. In the simplest form, the model is written as

$$\ln \frac{p}{1-p} = \beta_0 + \beta_1 x_1, \tag{2}$$

where p is the probability of NUDET as calculated using the training sample and x_1 is a discriminant measured from a waveform. The parameters β_0 and β_1 are estimated using an iterative maximum likelihood procedure. The form of the left hand side of Equation (2) is used to ensure that predicted values for p are bona fide probabilities, i.e., that they lie in the interval $[0, 1]$. Once the parameters are estimated from a training sample, a new candidate event is classified as a NUDET if the estimated probability is greater than 0.5.
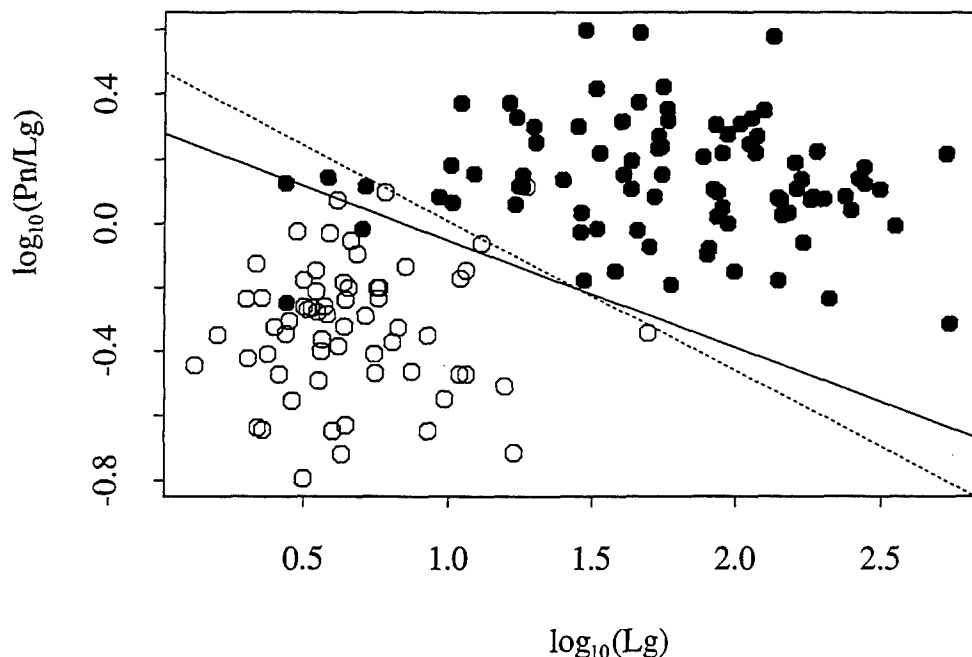
Figure 3: Logistic regression example. Dotted line represents linear discrimination.

Note that the model given by Equation (2) can easily be extended to include multiple discriminants as well as interaction terms. Furthermore, categorical variables can also be included as variables in the model. An example is shown in Figure 3, again using the data collected by Walter, Mayeda, and Patton (1995). The solid line represents the partition of the discriminant space based on the logistic regression approach. The dotted line represents the partition based on linear discrimination, and is shown for comparison. The two methods are quite similar since the fitted logistic model, in this case, included no interaction terms. Logistic regression methods are easily extended to the CTBT problem of discriminating between earthquakes, NUDETs and commercial explosions.

Recommendations and Future Plans

Research to address the statistical issues discussed above is an integral part of the DOE CTBT R & D program (DOE, 1994). In collaboration with AFTAC, PNL plans to research and resolve the statistical issues associated with regional discrimination. This research is comprised of two major issues. First, the operational capabilities of a CTBT monitoring system must be fully understood when monitoring regions of interest. Realistic training samples can be used accurately assess misclassification rates and uncertainties in a discrimination algorithm. Developing appropriate regional training samples is critical to the regional discrimination problem. Second, the statistical discrimination discussed above can be synergistically used by AFTAC as ancillary or corroborative evidence when identifying the source of a seismic event. PNL will continue research on statistical discrimination methods as a collaborative effort with AFTAC and Sandia National Laboratory.

References

1. Blandford, R. R. (1995), *Regional Seismic Event Discrimination*, Monitoring a Comprehensive Test Ban Treaty, NATO Advanced Studies Institute, Series E, (in press).

2. Blough, D. K., and K. K. Anderson (1994), *A Comparison of Artificial Neural Networks and Statistical Analyses*, Technical Report PNL-9050 UC-705, Pacific Northwest Laboratory.

3. Breiman, L., J. Friedman, R. Olshen, and C. Stone (1984), *Classification and Regression Trees*, Wadsworth International Group.

4. DOE (1994), *Comprehensive Test Ban Treaty Research an Development FY95-96 Program Plan*, United States Department of Energy, Report DOE/NN-0003.

5. Fix, E., and J. L. Hodges (1951), *Nonparametric Discrimination: Consistency Properties*, Project No. 21-49-004, Report No. 4, U.S. Air Force School of Aviation Medicine, Randolph Field, TX.

6. Glaser, R. E., S. R. Taylor, M. D. Denny and E. S. Vergino (1986), *Regional Discrimination of NTS Explosions and Western U.S. Earthquakes: Multivariate Discriminants*, Technical Report UCID-20930, Lawrence Livermore National Laboratory.

7. Hall, P. and M. Wand (1988), *On Nonparametric Discrimination using Density Differences*, Biometrika, 75, 541-547.

8. Hand, D. J. (1981) *Discrimination and Classification*, John Wiley & Sons.

9. Holmstrom, L. and S. Sain (1993), *Searching for the Top Quark Using Multivariate Density Estimates*, Technical Report, Department of Statistics, Rice University.

10. Scott, D. W. (1992), *Multivariate Density Estimation*, John Wiley & Sons.

11. Silverman, B. W. (1986), *Density Estimation for Statistics and Data Analysis*, Chapman and Hall.

12. Taylor, S. R., Denny, M. D., Vergino, E. S., and Glaser, R. E. (1989), *Regional Discrimination Between NTS Explosions and Western U.S. Earthquakes*, Bull. Seism. Soc. Am., 79, 1142-1176.

13. U.S. Congress (1988), *Seismic Verification of Nuclear Testing Treaties*, Office of Technology Assessment, OTA-ISC-361.

14. Walter, W. R., K. M. Mayeda and H. J. Patton (1995), *Phase and Spectral Ratio Discrimination between NTS Earthquakes and Explosions, Part I: Empirical Observations*, Bull. Seism. Soc. Am., (in press).

CROSS REGION ANALYSIS, PATH CORRECTIONS AND THE TRANSPORTABILITY OF REGIONAL SEISMIC DISCRIMINANTS

Douglas R. Baumgardt
ENSCO, Inc.
5400 Port Royal Road
Springfield, Virginia 22151

ABSTRACT

This study has investigated the problem of transporting regional discriminants, principally the regional *P/S* amplitude ratio and *Lg* spectral discriminants, between regions of differing tectonic type. The effects of differential regional phase attenuation and propagation blockages need to be taken into account and corrected before decision criteria for discriminants developed in one tectonic region can be transported to a different tectonic region. We have developed a set of frequency-dependent distance correction curves to correct the *Pn/Sn* and *Pn/Lg* amplitude ratio to a standard distance. Similar corrections have been developed for the *Lg* spectral ratio using a standard *Lg* attenuation model. Also, we have developed a method, called *cross-region seismic event characterization*, to characterize and identify new events which occur in aseismic regions or regions lacking known source types. Discrimination processing results of the Intelligent Seismic Event Identification System (ISEIS) for many different regions are stored in an Oracle database and can be called up on a regionalized basis. When a new event occurs, the method of cross-region seismic event characterization tries to find reference events from different regions, probably recorded at different stations than the new event, but at comparable distance for comparison which can be used as reference or training events to identify the new event. We construct crustal cross sections for the different propagation paths and determine if the new event has similar cross sections as the reference events. If the paths are not too different, the discriminants can be directly compared, after correcting for differences in distance. For paths that are very different, canonical correlation analysis of waveform features, such as the *Pn/Lg* amplitude ratio in different frequency bands, with propagation path parameters provides an empirical method for predicting the change in the feature, due to differences in propagation path effects (e.g., blockage and scattering). These correlations can be used to calibrate different tectonic regions and correct the discriminants being transported from one region to another. We have used this method to characterize a recent event of high interest, the January 5, 1995 Urals event, which was located in a known Russian mine. *Pn/Lg* ratios, measured at the Russian station Arti (ARU), were compared with earthquakes and nuclear explosions recorded at the Chinese station Urumchi (WMQ). Analysis of the propagation path cross section in China and Russia seemed similar, although seismic attenuation may be greater in China. This comparison revealed that the event had large shear waves, and therefore lower *Pn/Lg* ratio comparable to earthquakes but much lower than nuclear blasts. Therefore, the event has been identified as either a rockburst or mine collapse, and not an explosion.

OBJECTIVES

The objective of this project has been to investigate regional seismic waveform discriminants in a number of diverse tectonic regions to investigate the problem of discriminant transportability. Global seismic event identification for a CTBT requires discriminants which are insensitive to propagation path effects or can be corrected for propagation effects. In our research, we have tried to understand the effects of propagation path variations on regional waveform discriminants, to derive path corrections for discriminants, and to calibrate discriminants to different tectonic regions. Also, this study has investigated the performance of various regional discriminants to the different regions. This paper discusses the results of a just completed study of the transportability of regional seismic discriminants and presents plans for research in a new project on discriminant transportability which is pending.

RESEARCH ACCOMPLISHED

Cross-Region Seismic Event Characterization

Past studies of regional seismic discriminants have revealed that certain simple seismic measurements can be used as discriminants between classes of known earthquakes and explosions, including conventional economic explosions (mine blasts) and nuclear explosion tests. These include frequency dependent ratios of amplitudes of different phases, in particular, regional *P/S* (e.g., Bennett et al, 1989; Baumgardt and Young, 1990; Kim et al, 1993), spectral ratios on individual regional seismic phases (Murphy and Bennett, 1982; Bennett and Murphy, 1986; Taylor et al, 1988; Taylor et al, 1989; Walter et al, 1994), and the detection of ripplefire by the identification of spectral scalloping (Baumgardt and Ziegler, 1988; Hedlin et al, 1989; Hedlin et al, 1990; Kim et al, 1994). Most discrimination studies have sought events of different source types in the same, geographically confined region, in order to quantify the source discriminants and eliminate any differences due to propagation path.

However, a major problem with monitoring afuture CTBT will be characterizing and identifying seismic events that can occur anywhere in the world. Thus, we may not have the luxury of identifying new events with training or reference events in the same region with common propagation paths. To address this problem, we have analyzed these discriminants, implemented in the Intelligent Seismic Event Identification System (ISEIS) (Baumgardt et al, 1991), and applied to many mine blasts, rock bursts, and nuclear explosions and earthquakes in Russia, Scandinavia, Germany, Poland, and China. ISEIS discrimination-analysis results are stored in an Oracle database, and these results can be recalled on a regional basis. Thus, we can compare discrimination results in different regions with each other, which provides useful insights about regional performance of discriminants. Our approach has been to compare seismic events recorded at different stations in different region but at comparable distances. We then attempt to characterize and quantify differences in discriminant performance with differences in the propagation path effects due to differences in the tectonic regions.

Figure 1 shows a flow diagram for our concept for cross-region seismic discriminant characterization and calibration. Given a new event to characterize, we check the database for reference events located in the same region and recorded at the same station. Quite often, however, few events may be available. Thus, to characterize the event, it will be necessary to access events from another region by a different station but at the same distance.
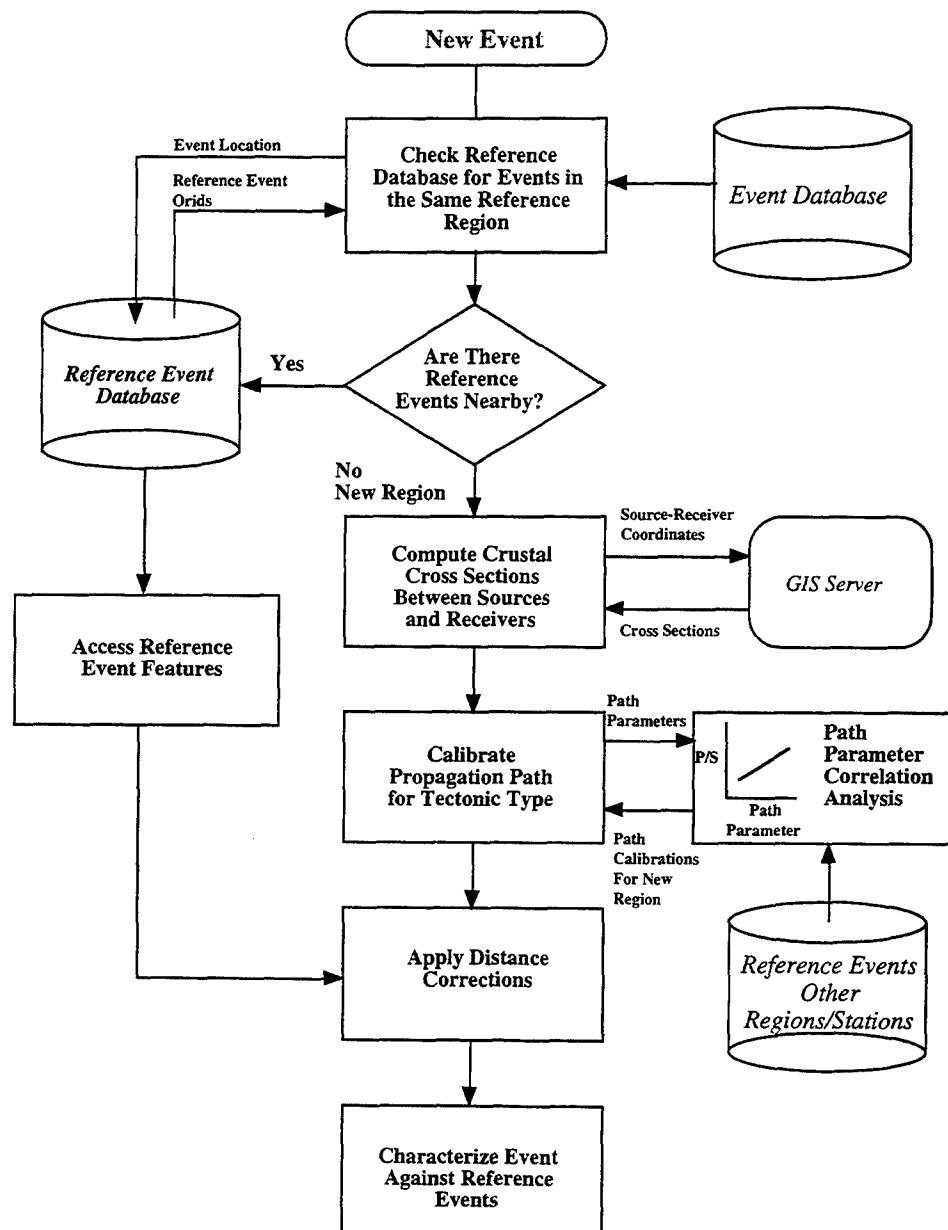
Figure 1: Method for accessing and utilizing reference events for event characterization. If the event occurs in a region where previously identified events have been studied, these events can be used to characterize the event. If not, events from other regions, perhaps recorded at other stations, must be used. Path parameter and seismic waveform feature correlations are then used to calibrate the P/S ratio discriminant from one tectonic region to another.

However, discriminants may be biased from one region to another because of differences in the seismic propagation in the different regions. We attempt to quantify these differences by comparing crustal cross sections for the propagation paths in the different regions utilizing crustal structure information now available from on-line GIS servers (e.g., Barazangi et al, 1995). Propagation paths can be parameterized in terms of elevations, crustal thicknesses, depth to sediments, and variations in these quantities (Zhang et al, 1994; Baumgardt and Der, 1994). If the different propagation paths have similar parameters, seismic discrminants in the same regions may be directly compared, provided they have been corrected for distance. If they differ, canonical correlation analysis (e.g., Zhang et al, 1994; Baumgardt and Der, 1994) can be used to calibrate discriminants for different regions prior to distance correction.

Cross-region characterization was used to analyze and identify a recent event which occurred on January 5, 1995 near a mine in Russia (Baumgardt, 1995). Figure 2 shows the location of the event and the stations which recorded it .The Russian media announced that the event was "tectonic", i.e., associated with an earthquake which apparently induced considerable damage in the mine. Also shown are a number of historical PNEs which occurred in the same region. Aside from these PNEs, we know of no other seismicity in the region. Also, the PNEs occurred before the nearest alpha station ARU was installed, so we have no reference events in the same region recorded at ARU to compare with the January 5 event.

■ Magnitude 4.3 event which occurred in a Russian mine.

■ Announced by Russians as "tectonic" rock burst or collapse

■ Closest recording Alpha station was ARU.
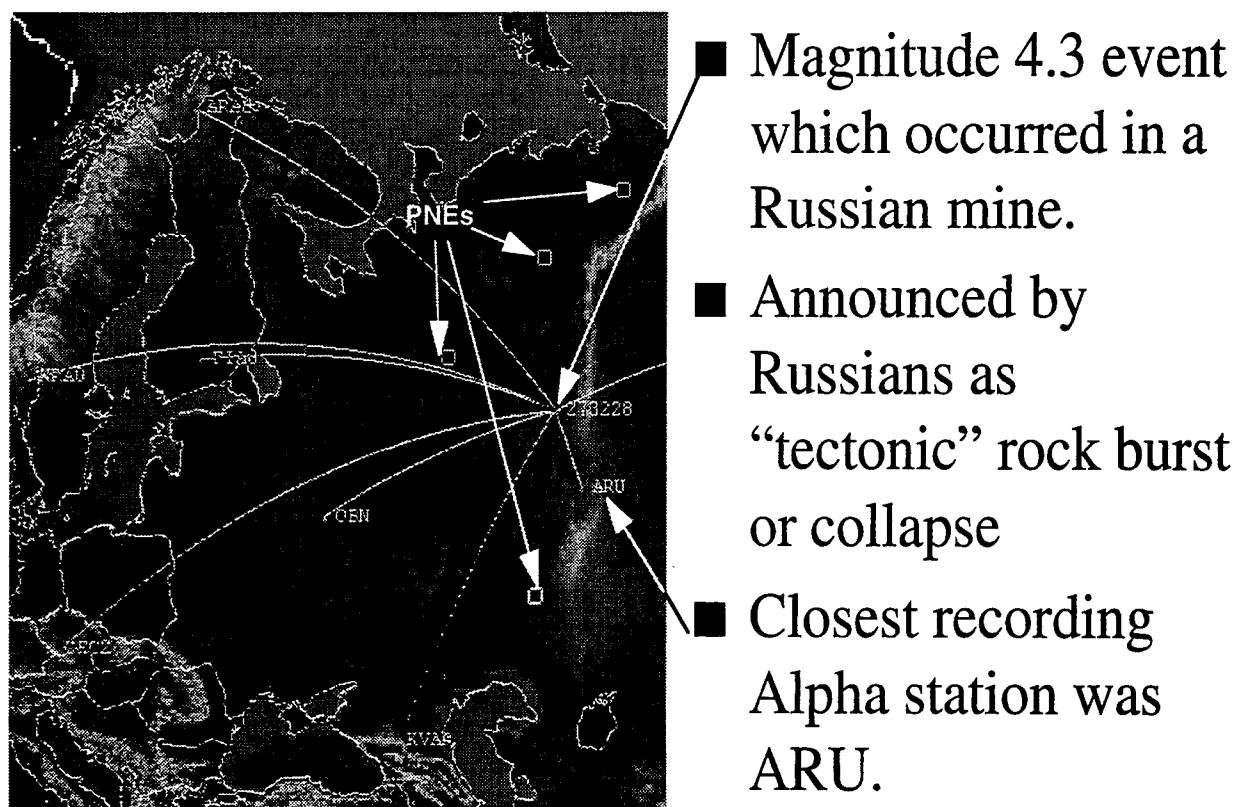
Figure 2: Map showing location of the January 5, 1995 S. Urals events and the alpha stations which recorded the event. Also shown are location of nearby PNEs.

This event was of high interest because it was located in a known Russian mine and also in a region where PNEs have been detonated in the past. Because of the lack of reference events in the region recorded at ARU (no PNEs have been recorded at ARU), Baumgardt (1995) compared the event with earthquakes and explosions in China and Russia recorded at the station Urumchi (WMQ) in China, originally studied by Baumgardt and Der (1994) and shown on the map in Figure 3. The justification for this comparison, even though the Ural and Chinese events occurred in different regions and were recorded at different stations, is that the distances and propagation paths in the ARU and WMQ regions are similar. Also, because we are comparing ratios between phases in the same frequency band, the difference in the ARU and WMQ instrument response is not a factor. However, we may expect greater attenuation in the crust of China than in the more shield-like Russian Platform, which may result in large Pn/Lg ratios in China than in Russia at the same distances.
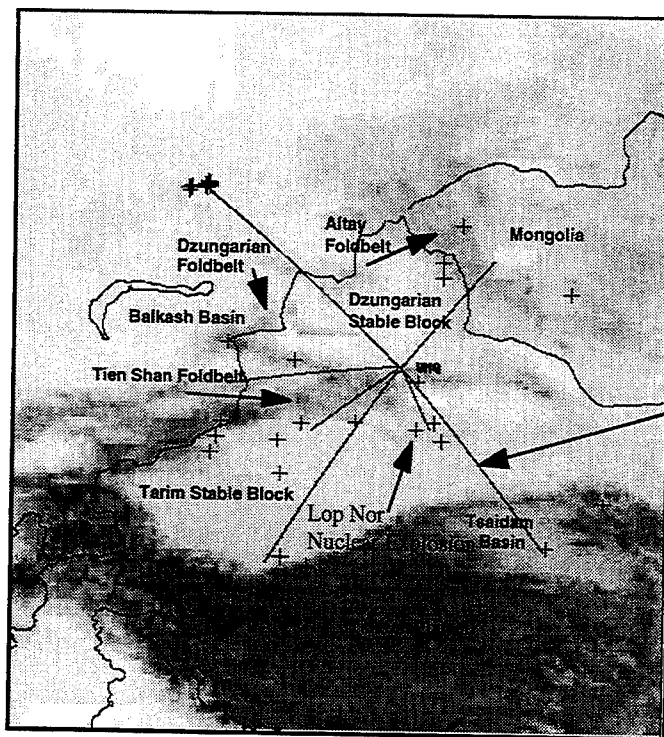
- Lack of reference events in Eurasia for Urals event requires comparison with Chinese events.

- Geology of propagation paths from earthquakes to Chinese station WMQ comparable to Urals path to ARU.

- Greater attenuation in China may produce larger Pn/Lg ratios (greater Lg attenuation) than in Russia.

Figure 3: Chinese events recorded at the stations WMQ which are compared to the S. Urals event recorded at ARU.

Figure 4 shows a distance plot of the measured Pn/Lg ratios in the 6 to 8 Hz band from the Ural event at ARU and the WMQ recordings of Chinese earthquakes and nuclear explosions recorded at the WMQ station. In Figure 4 (a), the distance-dependence of the Baumgardt and Der (1994) correction is superimposed. Over this distance range, the slope of the correction curve is small. Thus, as shown in Figure 4 (b), correcting for distance with this function has little effect. After distance corrections, the Urals event appears to have Pn/Lg ratios, measured at ARU, which are comparable to earthquakes in China and much lower than those observed for nuclear blasts. This comparison strongly suggests that the Urals event was a tectonic event, such as a rockburst or mine collapse, since we would expect such events to have larger shear waves and lower Pn/Lg ratios.
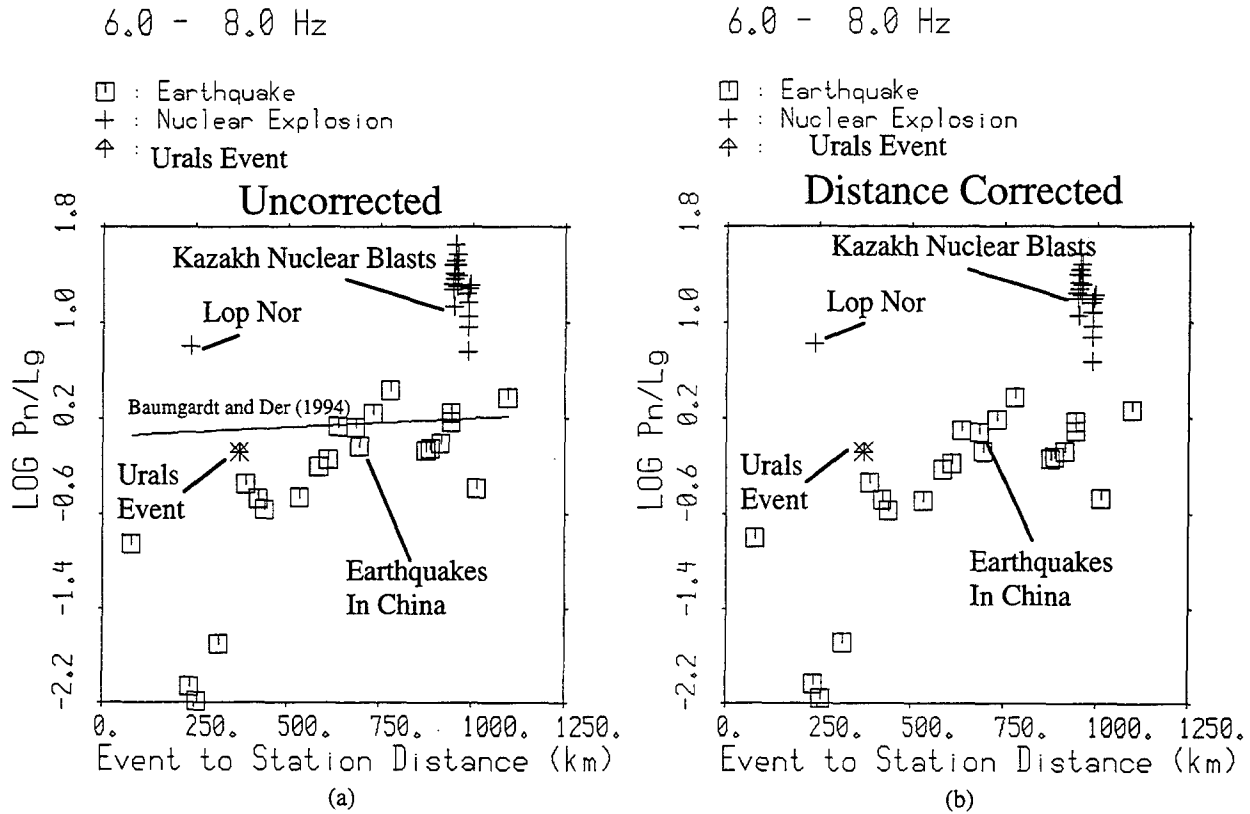
Figure 4: *PnlLg* ratios plotted versus distance for the WMQ recordings of Chinese earthquakes and Lop Nor and Kazakh nuclear blasts recorded at WMQ compared with the January 5, 1995 Urals event recorded at ARU. Distance correction of Baumgardt and Der (1994) is shown on the left and applied on the right.

Path Corrections for Regional *P/S* Ratio and *Lg* Spectral

During this project, a set of distance corrections were developed for the *P/S* ratio discriminant (Baumgardt and Der, 1994) and the *Lg* spectral ratio (Baumgardt, 1995). The *P/S* ratio corrections were developed empirically for several frequency bands from data in Scandinavia and Europe, and implemented in ISEIS for corrections of the *Pn/Sn* and *Pn/Lg* ratio discriminants. Figure 4 shows an example of the application of this correction for the 6-8 Hz band. For correction of the *Lg* spectral ratio, the affect of attenuation must be taken into account. We model the amplitude of a regional phase with the standard anelastic attenuation relation

$$A^{TH}(f,D) = A_o(f)\exp\left[\frac{-\pi f D}{QU}\right],$$

where A^{TH} is the theoretical spectral amplitude at frequency f and distance D, A_o is the initial source excitation, D is the distance in km, Q is the attenuation quality factor, U is the group velocity of the regional phase and f is the frequency in Hz. We assume the commonly used power-law frequency dependence for attenuation

32

$$Q = Q_o \left(\frac{f}{f_o} \right)^\zeta$$

where Q_o is quality factor at the reference frequency f_o and ζ specifies the frequency dependence. Generally, f_o is 1 Hz and ζ ranges from 0.0 to 1.0. Given observed values of the rms spectral ratio between the low frequency band (Δf_1) and the high frequency band (Δf_2), $R(\Delta f_1, \Delta f_2, D)$, at distances D, we wish to correct the ratios to the same reference distance, D_{ref}. Assuming values of Q_o, ζ, and U, we have for the distance corrected spectral ratio

$$R(\Delta f_1, \Delta f_2, D_{ref}) = R(\Delta f_1, \Delta f_2, D) \frac{R^{TH}(\Delta f_1, \Delta f_2, D_{ref})}{R^{TH}(\Delta f_1, \Delta f_2, D)} .$$

Group velocities, U, of 8.1, 6.5, 4.7, and 4.0 km/sec were assumed for major regional phases, Pn, Pg, Sn, and Lg, respectively. Values of Q_o and ζ are dependent on the path and must be determined by direct inversion of Lg spectra or coda, or by trial and error by fitting trends by eye to spectral-ratio-versus-distance plots. In this study, we use the latter approach.

Figure 5 shows measurements of Lg spectral ratios for Vogtland mineblasts and earthquake in Germany and Polish rockbursts, originally studied by Baumgardt (1993).
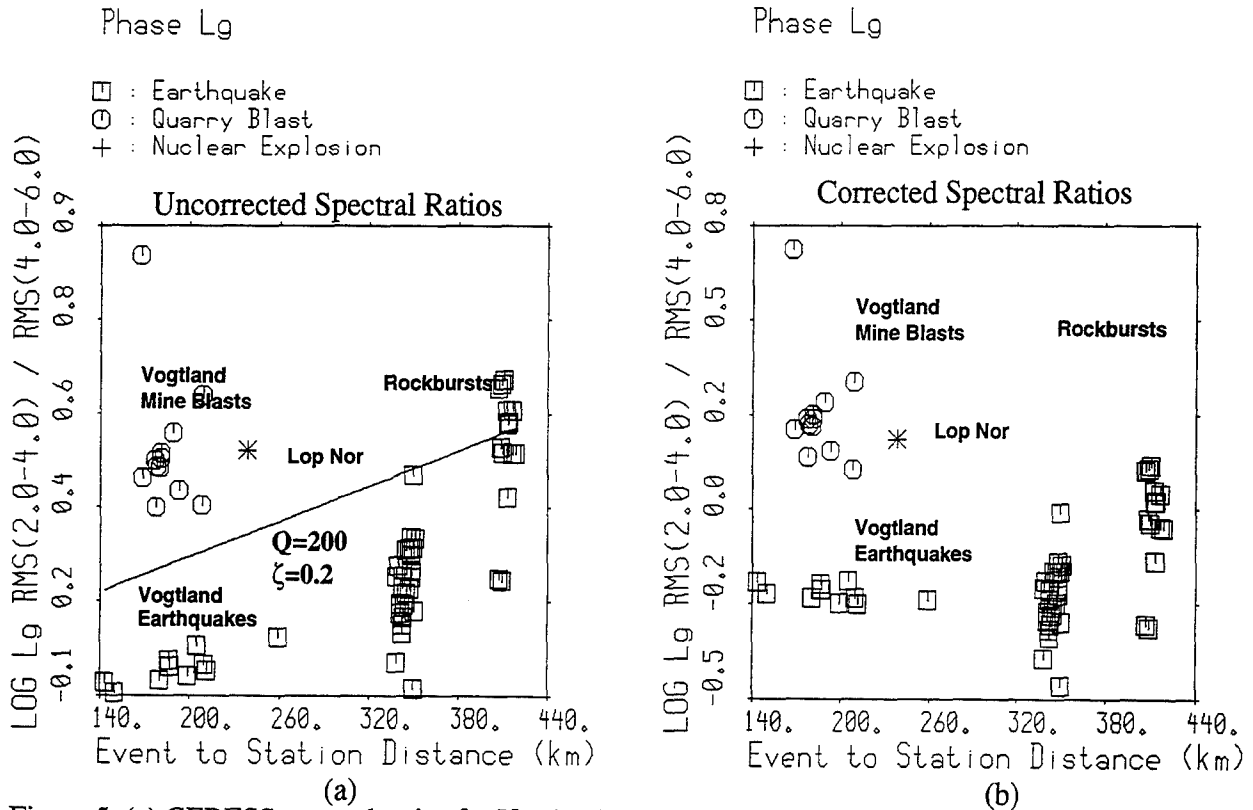
Figure 5: (a) GERESS spectral ratios for Vogtland and Polish rockbursts with distance correction curve for Q=200 and ζ=0.2. (b) Result of correcting the spectral ratios for anelastic attenuation. Note now that the rockburst points are lowered and now discriminate from the mine blasts after the distance correction is applied.

33

This discriminant easily separated the Vogtland mineblasts and earthquakes. However, as shown in Figure 5 (a), the more distant rockburst points have larger values and greater scatter than the mineblasts. The rockbursts, being similar to earthquakes, might be expected to discriminate from mine blasts in the same way as earthquakes, and the increasing spectral ratios with distance may be due to anelastic attenuation. Based on trial and error plotting of different attenuation correction curves, we conclude that the curve for $Qo = 200$ and $\zeta = 0.2$ seems to pass through the extreme values of the earthquakes and rockbursts, as shown in Figure 5 (a). Assuming this correction curve, we get the distance-corrected spectral ratios shown plotted in Figure 5 (b). After correction, the rockburst points at larger distance are shifted downward and more closely resemble the values of Vogtland earthquakes. Thus, in this instance at least, the increased scatter of the rockbursts may have been due to their increased distance. We conclude that, after distance corrections, the rockbursts in Poland are similar to earthquakes and that both Pn/Lg ratios and Lg spectral ratios can classify events in this region.

CONCLUSIONS AND RECOMMENDATIONS

We have found cross-region discriminant analysis to be a useful method for characterizing seismic events which have occurred in regions with limited historical record of explosions and earthquakes. When corrections for distance are made, events in different regions can be used to identify events in other regions, even when recorded at the same stations. We have determined path corrections for P/S amplitude ratios and Lg spectral which reduce systematic bias due to distance effects and improve the performance in separating explosions and earthquakes.

There still remains the problem of calibration of regional discriminants when transporting them between extremes of tectonic type. For example, waveform discriminants developed in the Scandinavian shield cannot be directly used to discriminate events in the tectonically active regions China, even after distance correction, without proper calibration for the differences in propagation in the two tectonic regions. The canonical correlation analysis of Zhang et al (1994) and Baumgardt and Der (1994) may be a promising first step towards developing these calibrations. Modeling studies may also be a useful means for determining sensitivities of regional discriminants to crustal parameters which can be used for calibration. In future reearch, we plan to continue investigating this approach, extending it to propagation paths and regions in the Middle East as data becomes available.

REFERENCES

Barazangi, M. D. Seber, M. Vallve, E. Fielding, and B. Isacks (1995). A geological and geophysical information system for Eurasia, the Middle East, and North Africa, PL-TR-94-2092, Cornell University, Ithaca, NY.   ADA297018

Baumgardt, D.R. (1990). Investigation of teleseismic Lg blockage and scattering using regional arrays, *Bull. Seism. Soc. Am.*, **80**, 2261-2281.

Baumgardt, D.R. (1993). Regional characteristics of mine blasts, earthquakes, mine tremors, and nuclear explosions using the Intelligent Seismic Event Identification System, Final Report, *SAS-TR-94-12*, ENSCO, Inc., Springfield, Va.

Baumgardt, D.R. (1995). Case studies of seismic discriination problems and reginal disriminant transportability, Final Report (Draft), 31 July 1995, ENSCO, Inc., Springfield, VA.

Baumgardt, D.R. and Z.A. Der (1994). Investigation of the transportability of the P/S ratio discriminant to different tectonic regions, Scientific Report No. 1, PL-TR-94-2299, ENSCO, Inc., Springfield, VA. ADA292944

Baumgardt, D.R. and G.B. Young (1990). Regional seismic waveform discriminants and case-based event identification using regional arrays, *Bull. Seism. Soc. Am*, **80**, 1874-1892.

Baumgardt, D.R. and K.A. Ziegler (1988). Spectral evidence of source multiplicity in explosions: application to regional discrimination of earthquakes and explosions, *Bull. Seism. Soc. Am.*, **78**, 1773-1795.

Baumgardt, D.R., S. Carter, M. Maxson, J. Carney, K. Ziegler, and N. Matson (1991). Design and development of the intelligent event identification system, *PL-TR-91- 22298(I)*, Final Report, Volumes I,II, and III, ENSCO, Inc., Springfield, Va. ADA248381

Bennett, T.J. and J.R. Murphy (1986). Analysis of seismic discrimination capabilities using regional data from western United States events, *Bull. Seism. Soc. Am.*, **76**, 1069-1086.

Bennett, T.J., B.W. Barker, K.L. McLaughlin, and J.R. Murphy (1989). Regional discrimination of quarry blasts, earthquakes, and underground nuclear explosions, Final Report, *GL-TR-89-0114*, S-Cubed, La Jolla, Ca. ADA223148

Hedlin, M.A., J.B. Minster, and J.A. Orcutt (1989). The time-frequency characteristics of quarry blasts and calibration explosions recorded in Kazakhstan, USSR, *Geophys. J. Int.*, **99**, 109-121.

Hedlin, M.A., J.B. Minster, and J.A. Orcutt (1990). An automatic means to discriminate between earthquakes and quarry blasts, *Bull. Seism. Soc. Am.*, **80**, 2143-2160.

Kim, W.Y., D.W. Simpson, and P.G. Richards (1993). Discrimination of earthquakes and explosions in the eastern United States using regional high-frequency data, *Geophys. Res. Lett.*, **20**, 1507-1510.

Taylor, S.R., N.W. Sherman, and M.D. Denny (1988). Spectral discrimination between NTS explosion and western United States earthquakes at regional distances, *Bull. Seism. Soc. Am.*, **78**, 1563-1579.

Taylor, S.R., M.D. Denny, E.S. Vergino, and R.E. Glaser (1989). Regional discrimination between NTS explosion and western United States earthquakes, *Bull. Seism. Soc. Am.*, **79**, 1142-1176.

Walter, W.R., K. Mayeda, and H.J. Patton (1994). Phase and spectra ratio discrimination between NTS earthquakes and explosions, Part 1: Empirical observations, UCRL-JC-118551 Part 1, Lawrence Livermore National Laboratory, September 1994.

Zhang, T. S.Y. Schwartz, and T. Lay (1994). Multivariate analysis of waveguide effects on short-period regional wave propagation in Eurasia and its application in seismic discrimination, *J. Geophys. Res.*, **99**, 211929-21945.

The Physical Basis for the Lg/P Discriminant

T. J. Bennett and K. L. McLaughlin
S-CUBED
11800 Sunrise Valley Dr., Suite 1212
Reston, Virginia 22091
Contract No. F 19628-95-C-0107
Sponsored by AFTAC

Abstract

Recent interest in a Comprehensive Test Ban Treaty (CTBT) has stimulated a desire to detect and identify much smaller seismic events. Furthermore, concern for possible proliferation of nuclear weapons into countries where nuclear weapons testing was not previously at issue requires extending seismic capabilities into new geographic regions. To reach these goals at magnitude levels of interest will require utilization of regional seismic signals. Unfortunately, implementation of effective regional discriminants has proven to be elusive due to the complexity of regional signals and incomplete physical understanding of their dependence on regional propagation and excitation. The objective of this research program is to improve fundamental understanding of the L_g/P ratio regional discriminant, which over the years has proven to be one of the most promising and enduring measures at regional stations for distinguishing between explosions and earthquakes. This investigation includes an empirical element to review and formalize the salient features of the L_g/P measure for distinct tectonic environments and different source types and a theoretical element to explain the observed features in terms of source mechanism, source size, depth, and propagation path influences on the regional signals.

The empirical element of this research program utilizes a traditional analytic approach including time-domain measurements and spectral analyses of L_g and regional P signals from large, high-quality databases representative of different source types and geographic regions. We are performing time-domain, bandpass filter, and spectral analyses on these regional signals recorded from underground nuclear explosions, earthquakes, non-nuclear blasts, and rockbursts using the digital seismic data collected over the years and currently being collected for the western U.S., eastern North America, central Asia, and central Europe. The theoretical part of this research program draws upon published information on the velocity and attenuation structures for each of the regions considered to generate ensembles of propagation models. Synthetic seismograms determined for the various models can then be used to predict the behavior of the L_g/P ratios and their variations for suites of source mechanism, size, and taking into account model uncertainties. Comparisons of the predicted behavior with the empirical results will be used to modify the regional models and refine predictive capability for the L_g/P discriminants. Finally, the results of these comparisons will be used to document and codify the procedures needed to define a more general predictive capability for the L_g/P ratio and to perform sensitivity analyses which will help determine which methodologies are most useful for transporting an L_g/P ratio into uncalibrated regions.

Key Words: Seismic, Discrimination, Regional, Explosion, Earthquake, Mechanism

Transportability of Regional Phase Spectral Ratio Discriminants

T. J. Bennett and J. R. Murphy
S-CUBED
11800 Sunrise Valley Dr., Suite 1212
Reston, Virginia 22091

Abstract

This research program is intended to provide a thorough assessment of the transportability of regional phase spectral ratios as discriminants between underground nuclear explosions and other source types. Although L_g spectral ratios appeared to offer considerable promise for distinguishing between nuclear explosions and nearby earthquakes based on experience from the vicinity of the Nevada Test Site, attempts to extend this spectral ratio discriminant into other geographic regions (e.g. the vicinity of the Semipalatinsk/Balapan test site) have not always proven to be successful. One of the main obstacles to demonstrating the value of regional phase spectral ratios as discriminants has been difficulty in finding events of different source types with similar magnitudes and like propagation paths to enable direct comparisons of spectral ratio measurements. In addition, attempts to provide theoretical bases for understanding differences in regional phase signals from different source types have proven to be of only limited success.

The principal objectives of this research program are to develop more complete understanding of the influences of source excitation and propagation on the transportability of regional phase spectral ratio discriminants and to define criteria for application of spectral ratio discrimination methods in uncalibrated areas. For these studies we are looking at spectral ratios for all types of regional phases including P_n, P_g, and S_n in addition to L_g. We are performing a thorough empirical analysis of available regional data from different event types in distinct source environments. Signal spectra for the different phases are to be adjusted for influences of attenuation and source size using empirical models developed from information on regional propagation characteristics and source excitation appropriate to the specific tectonic regions. The empirical models used for these corrections will be tested for selected cases using theoretical modeling techniques. We anticipate that by applying appropriate corrections we will be able to more reliably discern source-dependent differences in the regional phase spectral ratios and define characteristics which are transportable into different, uncalibrated monitoring environments.

Key Words: Seismic, Discrimination, Regional, Calibration, Explosion, Earthquake.

STUDY OF BROADBAND Lg/P AND ITS APPLICATION TO SOURCE DISCRIMINATION

Indra N. Gupta
Multimax, Inc.
1441 McCormick Drive, Landover, Maryland 20785
Contract No. F19628-95-C-0176
Sponsored by DOE (Start Date 17 July 1995)

ABSTRACT

Several investigations have shown the ratio Lg/P to be an effective regional discriminant, but its limitations and spectral characteristics under various geological settings and near-source parameters are largely unknown. This research will analyze representative sets of broadband three-component data for regional phases Pn, Pg, Sn, Lg, and Rg from both explosion and earthquake sources belonging to several distinct regions. The main sources of data will be the large amount of regional, near-regional, and near-field data available from several Department of Energy Labs and the primary (Alpha) and auxiliary (Beta) stations of the GSETT-3. A considerable amount of in-country regional data from seismic sources with ground-truth information is also available from the former USSR. These data include not only shots with large variations in their near-source parameters (such as geology, yield, and depth of burial) but also a few decoupled shots, so their analysis will provide an improved understanding of the role of various near-source parameters in shaping the broadband characteristics of regional phases. Data from decoupled shots, identification of which perhaps constitutes the greatest challenge to U. S. efforts, will be used to investigate whether such explosions may be identified on the basis of their relative deficiency in higher frequency S or Lg. The mechanism of generation of Lg and its influence on the ratio Lg/P will be determined by using several methods, including synthetic seismograms and finite-difference investigations. Results of the study will significantly improve source discrimination of small events, including identification of decoupled shots.

Preliminary studies since the start of the Contract about two weeks ago, include an examination of the low-frequency Lg from East Kazakh nuclear explosions for spectral nulls associated with CLVD sources and a comparison of three-component observations of Lg by narrow-bandpass filtering of regional data. An effective CLVD source may be present not only for Lg from Yucca Flats (NTS) explosions but also for East Kazakh explosions. Analysis of data from a Yucca Flats explosion indicates that the spectral null frequency varies significantly not only among the three orthogonal components of motion but also among the recording stations. It seems that although the near-source scattering of explosion-generated Rg into S (with both SV and SH components) may be principally responsible for the low-frequency Lg, several other factors (such as source asymmetry) also have important roles.

Key Words:
Explosion-generated Lg, scattering of Rg, low-frequency Lg, source discrimination, Lg/P ratio, decoupled explosions, overburied shots

OBJECTIVE

The Lg/P ratio has been found to be one of the most promising regional discriminants for earthquakes and explosions, but its full potential has not been exploited because the physics behind this discriminant is largely lacking and source discrimination has been found to be strongly region-dependent. For example, the failure of Lg/Pn amplitude ratio to discriminate at frequencies around 1 Hz and its excellent discrimination performance at higher frequencies are not well understood. A clear understanding of the broadband characteristics of the regional phases Pn, Pg, Sn, Lg, and Rg and their dependence on various near-source parameters must be obtained if successful techniques developed in one region are to be used in other locations. Analysis of a large amount of broadband data recorded at regional and closer distances will not only improve our understanding of the Lg/P ratio but will also provide information on the relative advantages of using low- or high-frequency data. One of the most difficult problems in treaty monitoring will be the identification of decoupled shots. Differences in the mechanisms of seismic wave generation from decoupled and normal explosions will be investigated by analyzing broadband regional and closer-distance data from decoupled shots and others (such as overburied shots) that may help resolve the lack of agreement regarding the generation of S waves at higher (above 3 Hz) frequencies. Results of the proposed research will lead to an improved understanding of the broadband characteristics of the ratio Lg/P and consequently to more effective and reliable discrimination of small events, including identification of decoupled explosions, in various geological settings.

PRELIMINARY RESEARCH RESULTS

Recent Related Work

Several recent studies have provided new insight into the generation of Lg from explosions. According to Patton and Taylor's (1994) study of several closely-spaced Yucca Flats (NTS), explosions, "a prominent spectral null between 0.5-0.6 Hz comes about from an excitation null of Rg waves when the source is a CLVD, and Lg waves are generated by the scattering of Rg near the source. Previous studies (Gupta *et al.*, 1991, 1992) have argued that this scattering imprints the Rg source spectrum onto the scattered P and S waves. Scattered S waves with slowness appropriate for trapping in the crust will generate Lg waves observed at regional distances (Xie and Lay, 1994). The null in the Rg spectrum is due to the centroid depth of the CLVD source." Israelsson (1992) analyzed in-country regional data from a large number of Kazakh and Novaya Zemlya nuclear explosions. His study of the Lg spectra led him to conclude that "the source spectra and their scaling are consistent with the hypothesis advanced by Gupta *et al.* (1992) that low-frequency Lg waves are produced from scattering of explosion-generated Rg into S waves". These results suggest that an analysis of the low-frequency Lg may be useful for estimating source depth if one can establish a relationship between the centroid depth of the CLVD source and the explosion depth. Rg is stronger for shallow sources such as mining explosions and rockbursts than for deeper sources such as earthquakes. Investigation of the frequency-dependent excitation of Lg should therefore lead to improved identification of such events.

Cavity decoupling (the use of large cavities to reduce the seismic signal) presents one of the most difficult problems in treaty monitoring. It is therefore important to understand differences in the mechanism of generation of seismic waves from decoupled and tamped explosions. A knowledge of shot depth can be useful in the identification of decoupled shots which are likely to behave like shots with greater than normal shot depth, or overburied shots. Evidence supporting this method of identification, obtained from 56 NTS explosions of known depths and yields, is presented in Figure 1 which includes data from 7 overburied shots. Average ratios of Pn/Lg and Pg/Lg versus m_b from observations at the broadband station, ELK indicate most overburied shots to have unusually high values, suggesting abnormally large shot depths. Figure 1c suggests that the Lg spectral ratio may also be useful for identifying overburied/decoupled explosions.

Spectral Nulls in Lg from Kazakh Explosions:

Regional data from the Soviet underground nuclear explosion of the Joint Verification Experiment (JVE, 14 September 1988, m_b = 6.0) are available at the three Natural Resources Defense Council (NRDC) stations, KSU, KKL, and BAY. These three stations lie at epicentral distances of about 160 km east, 255 km southwest, and 255 km northwest, respectively. Narrow bandpass filtering (NBF) of these regional data indicated a spectral null in Lg at a period of about 0.7 sec, implying that an effective CLVD source is present not only for explosions at Yucca Flats (as demonstrated by Patton and Taylor, 1995) but also at the East Kazakh test site with completely different crustal structure and tectonics (Gupta and Salzberg, 1995).

Regional data from the JVE and several other nuclear explosions are also available at the digital broadband station WMQ, located about 950 km southeast of the Kazakh test site (Gupta *et al.*, 1992). Spectral ratios of Lg from the JVE and the much smaller explosion of 12 March 1987, 87071 (m_b = 5.3), both recorded at WMQ so that path effects are minimized, are shown in Figure 2 for Lg windows of 76.8, 51.2, and 25.6 sec. Each of the three plots shows a spectral null at about 1.4 Hz which corresponds to the null at period of 0.7 sec observed in the NRDC regional data. Furthermore, the plots suggest a maximum at frequency of about 1.9 Hz which may be due to the shallower CLVD source associated with Lg from the smaller explosion, 87071. Spectral ratios of Lg from the explosion of 3 April 1987 (87093), with m_b = 6.1 (somewhat larger than the JVE) and the smaller explosion 87071, shown in Figure 3, also indicate a spectral null at frequency of about 1.1 Hz, likely to be due to the CLVD source associated with the larger explosion 87093. These preliminary results suggest that shot depth may be important in defining the spectral null in Lg and a determination of the spectral nulls in Lg may be useful for precise estimates of shot depths.

Comparison of Three-component Data from NTS Shots:

Earlier NBF analysis of vertical-component regional data from the Yucca Flats explosion, Texarkana (10 February 1989, m_b = 5.2, depth 503 m) indicated a spectral null at a period of about 1.5 sec (Gupta and Salzberg, 1995). Analysis of three-component data from several regional stations indicates that the spectral null and other characteristics of the low-frequency Lg
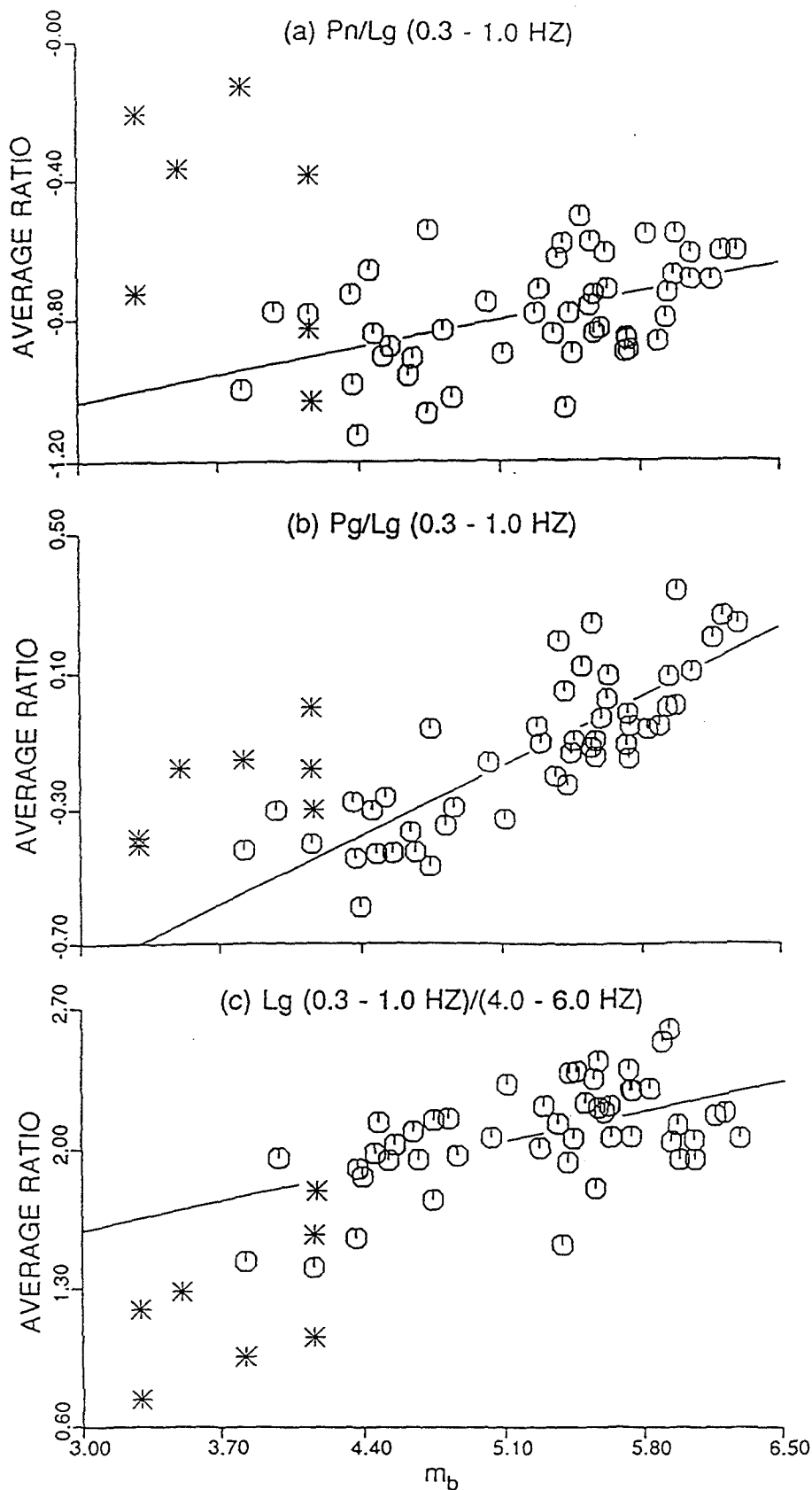
Figure 1. Amplitude ratios (a) Pn/Lg and (b) Pg/Lg, averaged over the frequency range of 0.3-1.0 Hz, and (c) Lg spectral ratio plotted versus m_b for 56 NTS explosions recorded at ELK. The 7 overburied shots, denoted by *, are not included in the linear regression lines.

Lg JVE/87071
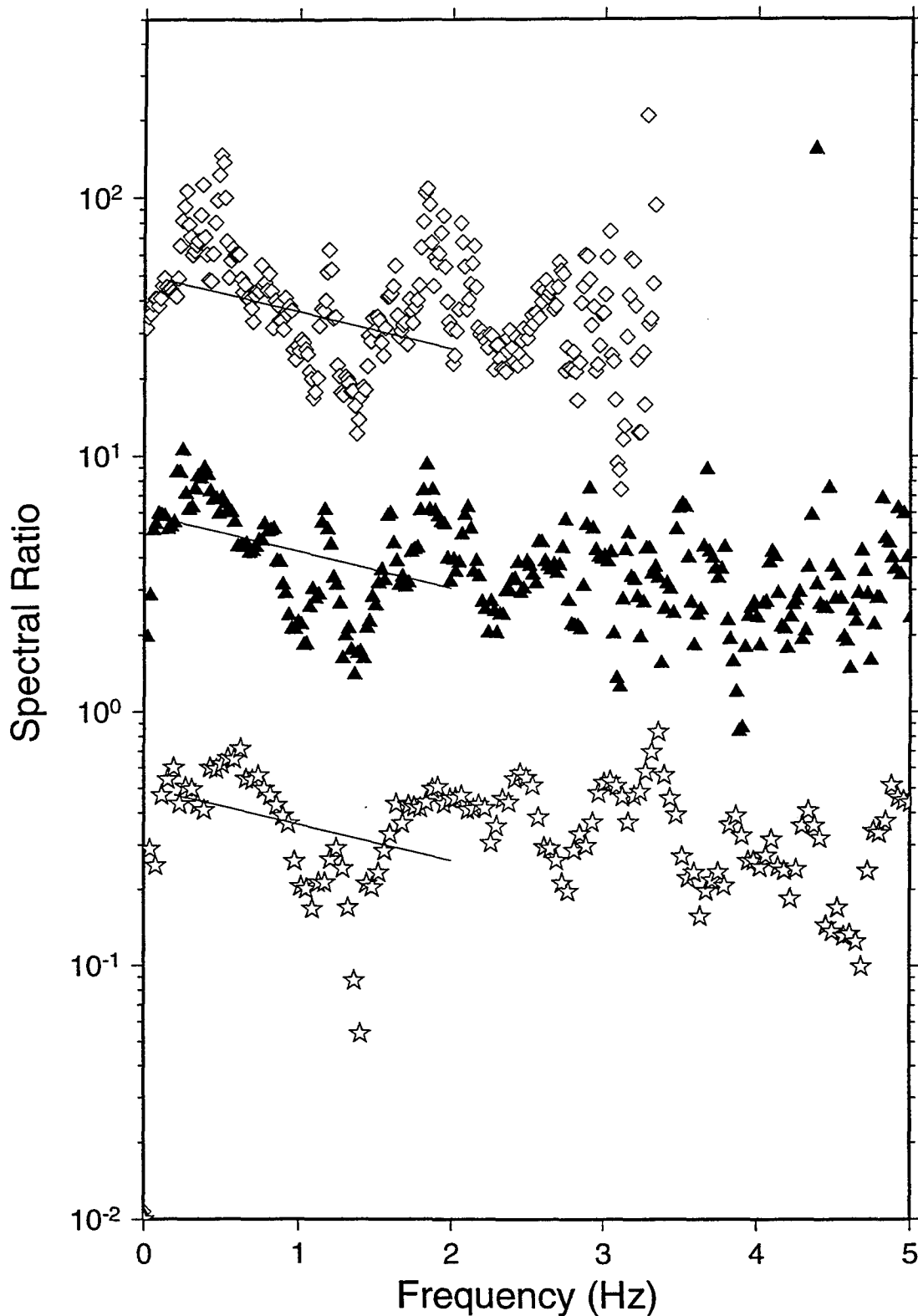
Figure 2. Spectral ratios of Lg JVE/87071 for window lengths of 76.8 sec (top), 51.2 sec (middle), and 25.6 sec (bottom). Each plot shows a spectral minimum at about 1.4 Hz and a maximum at frequency of about 1.9 Hz, probably due to spectral nulls associated with the CLVD sources representing the two explosions.

42
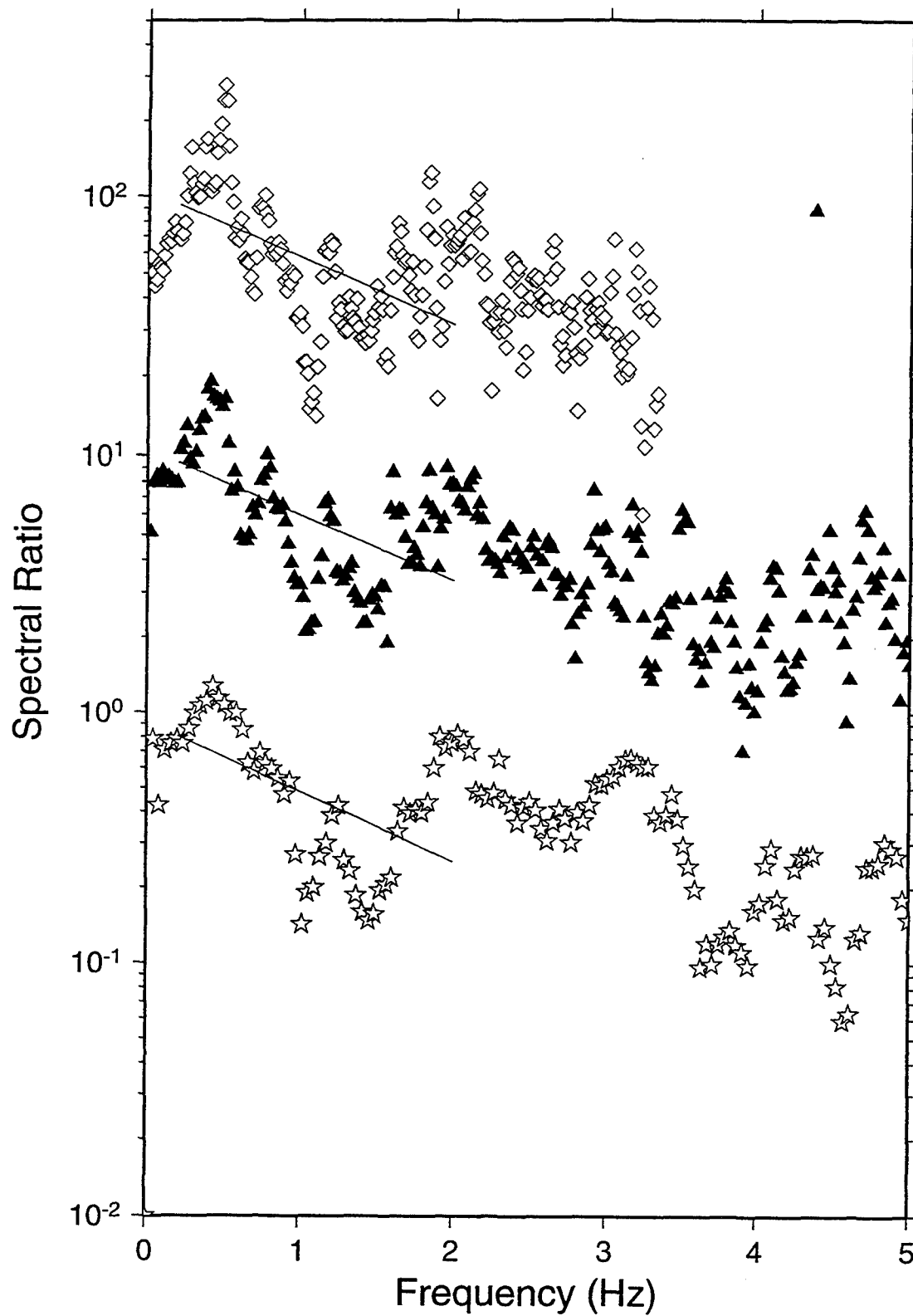
Lg 87093/87071

Figure 3. Similar to Figure 2 for Lg 87093/87071. Each of the three plots shows a spectral minimum at about 1.1 Hz, probably due to the spectral null associated with the CLVD source representing the larger explosion, 87093.

vary significantly from one recording station to another. For example, NBF analysis of the vertical (Z), radial (R), and transverse (T) component data at stations TON and DRW, located at distances of about 155 km northwest and 168 km southwest, shown in Figure 4, show large differences in the spectral nulls and relative amplitudes of the low-frequency Lg and Rg. At TON, Z and R components (Figures 4a, b) show spectral null at about 1.5 Hz and fairly similar distribution of energy in both the Lg (velocity about 3.0-3.5 km/sec) and Rg (velocity about 1.0-2.0 km/sec) arrivals. On T component (Figure 4c), the maximum-amplitude-Lg arrival is considerably later than those on the other two components. The delay is significantly more pronounced for Lg of period about 2 sec than for the dominant Lg of period about 1 sec. A possible explanation is that the conversion of Rg into SH motion requires three-dimensional variations which are perhaps less common and smaller than two-dimensional variations along the source-receiver path. At DRW, Z and R components (Figures 4d, e) are not similar and the spectral nulls are not distinct. On T component (Figure 4f), a spectral null is clearly observed at about 2.0 sec and the distribution of energy in Lg is remarkably similar to that on T component at TON (Figure 4c). It is, however, interesting to note that, as compared to TON (Figure 4c), the maximum-amplitude-Lg arrival on transverse component at DRW (Figure 4c) is of higher frequency and is not delayed but actually somewhat earlier than those on Z and R components (Figures 4d, f). A possible explanation is source asymmetry with strong SH component at or very near the source. It is also interesting to note that the low-frequency (less than about 1Hz) Lg at DRW is smaller than that at TON by a factor of about 5, suggesting strong azimuthal variations in the CLVD source function, perhaps consistent with the Rayleigh wave amplitude radiation pattern for Yucca Valley explosions suggested by Masse (1981, see his Figure 4). It seems therefore that the concept of a simple vertically-oriented CLVD source as the principal contributor to the low-frequency Lg may not be always valid. There is clearly a need to understand these large differences in the observed low-frequency Lg by examining three-component broadband data from several explosions with known source parameters and known near-source geology and crustal structure along propagation paths.

CONCLUSIONS AND RECOMMENDATIONS

Near-source scattering of explosion-generated Rg may be an important contributor to the low-frequency Lg from explosions at NTS and other test sites. The observed results, however, appear to be severely contaminated by various complexities, probably due to source anisotropy, path and recording site effects, and other factors largely unknown at this time. Narrow bandpass filtering, combined with synthetics, may provide a useful tool for understanding some of the complexities of the generation and propagation of Lg.

It is recommended that the generation, propagation, and spectral characteristics of Lg under various geological settings be investigated by analyzing large amounts of data from (1) nuclear explosions at the NTS and other test sites with ground-truth information, (2) chemical explosions with known source information, and (3) earthquakes located close to the explosions. Representative sets of seismic data covering a wide range of known near-source parameters should be analyzed to understand the generation of both low and high frequency Lg from tamped as well as decoupled and overburied explosions. A comparison of the observations with synthetic seismograms for various basic sources in layered structures should be useful in understanding why
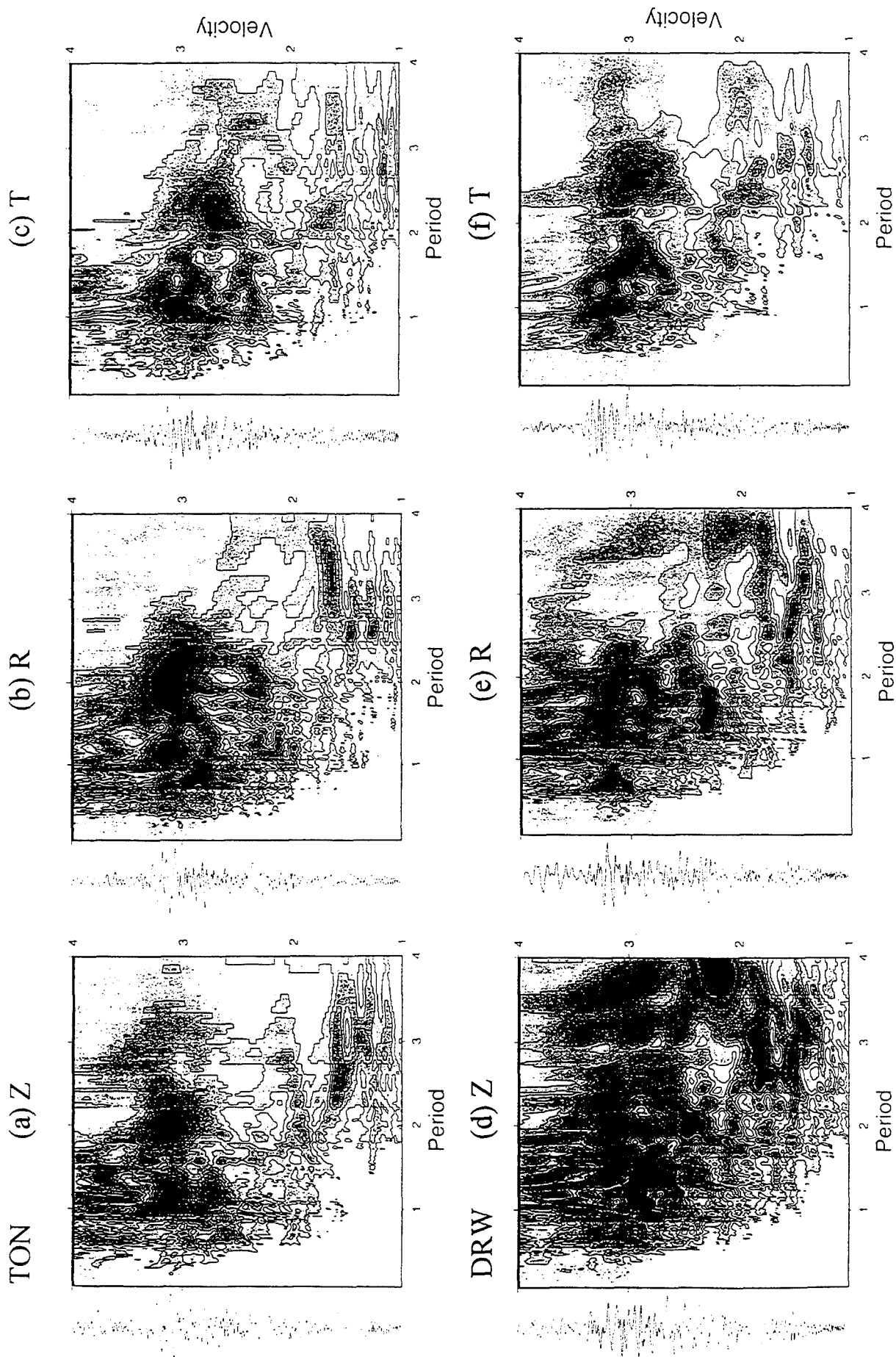
Figure 4. Narrow bandpass filtering of vertical (Z), radial (R), and transverse (T) component data from the Yucca Flats explosion, Texarkana, recorded at stations TON and DRW for the period range of 0.1-4.0 sec. Darker regions represent larger amplitudes. The group velocity (in km/sec) and the corresponding seismograms are also shown.

a discriminant is or is not working. Finite-difference investigations, such as those described by Xie and Lay (1994) can be useful in improving our understanding of the role of scattering due to near-source complexities. Results related to the understanding of broadband Lg/P from these studies should be applied to discriminate earthquakes and explosions of various types recorded at the Alpha and Beta stations of the GSETT-3. Data from the Alpha array at Pinedale, Wyoming, which lies within a region of intense coal mining activity (probably both underground and near-surface blasts) and earthquakes, should be specially useful for this purpose.

ACKNOWLEDGMENT

REFERENCES

Gupta, I. N., W. W. Chan, and R. A. Wagner (1992). A comparison of regional phases from underground nuclear explosions at East Kazakh and Nevada test sites, *Bull. Seism. Soc. Am.* 82, 352-382.

Gupta, I. N., T. W. McElfresh, and R. A. Wagner (1991). Near-source scattering of Rayleigh to P in teleseismic arrivals from Pahute Mesa (NTS) shots, in *Explosion Source Phenomenology*, Am. Geophys. Union Monograph 65, 151-159.

Gupta, I. N. and D. H. Salzberg (1995). Observations of spectral nulls in Lg from underground explosions at the Nevada and Kazakh test sites, *EOS* 76, no. 17, S205 (abstract).

Israelsson, H. (1992). A spectral decomposition of Lg waves from explosions and scaling of RMS magnitudes, *in* RMS Lg as a yield estimator in Eurasia, PL-TR-92-2117(I), 143-166, Phillips Laboratory, Hanscom Air Force Base, Massachusetts. ADA256692

Masse, R. P. (1981). Review of seismic source models for underground nuclear explosions, *Bull. Seism. Soc. Am.* 71, 1249-1268.

Patton, H. J. and S. R. Taylor (1995). Analysis of Lg spectral ratios from NTS explosions: implications for the source mechanisms of spall and the generation of Lg waves, *Bull. Seism. Soc. Am.* 85, 220-236.

Xie, X. B. and T. Lay (1994). The excitation of Lg waves by explosions: a finite-difference investigation, *Bull. Seism. Soc. Am.* 84, 324-342.

Preliminary Results of Discrimination Studies in Western China

Hans E. Hartse, Steven R. Taylor, and George E. Randall
Geophysics Group - EES-3, Los Alamos National Lab

ABSTRACT

As a part of the Comprehensive Test Ban Treaty Research and Development Program, we have started to evaluate regional seismic discriminants for western China. Our primary objective is to appraise the current seismic discrimination capability for central and south-central Asia. We have been testing several discriminants using short-period and broadband waveforms recorded at the Chinese Digital Seismic Network station WMQ. Our preliminary results cover four classes of discriminants: (1) short-period ratios, (2) short-period spectral ratios, (3) long-period ratios, and (4) long-period to short-period ratios. For each discriminant tested, we have measured waveforms from over 140 earthquakes to find ratio-distance relationships, and we have used these relationships to correct our final ratio-m_b discrimination plots for distance effects.

To date, we have evaluated earthquakes that range in magnitude (m_b) between 3.8 and 6.2 and occurred up to 1200 km from WMQ. We have evaluated about 15 underground nuclear explosions from the Kazakh test site ($4.5 < m_b < 6.1$ and $\Delta \approx 960$ km) and a single nuclear explosion from the Lop Nor test site ($m_b = 4.6$ and $\Delta = 260$ km). For this range of magnitudes and distances, we find that most of the discriminants outlined above (with the exception of the spectral discriminant) separate the explosion and earthquake populations. We find that the absence of a Love wave accompanied by the presence of a Rayleigh wave is a strong indicator of an explosion. Such an occurrence is apparently rare for central Asian earthquakes. We plan to continue this study by, processing other regional data, developing regional m_b, M_s, and coda magnitude scales, and testing the m_b / M_s and coda discriminants. We will be applying multivariate techniques to combine discriminants and assess discrimination capabilities.

OBJECTIVE

As a part of the Comprehensive Test Ban Treaty (CTBT) Research and Development Program, we have started to evaluate regional seismic discriminants for western China. Our primary objective is to appraise the current seismic discrimination capability for central and south-central Asia. We have been testing several known discriminants (cf. Pomeroy et al., 1982; Taylor et al., 1989) using waveforms recorded with the Chinese Digital Seismic Network (CDSN). Here we present results for station WMQ in northwest China. These preliminary results cover four classes of discriminants: (1) short-period ratios (such as P_g/L_g), (2) short-period spectral ratios (such as L_g (1–2 Hz) / L_g (6–8 Hz)), (3) long-period ratios (Love wave (L) / Rayleigh wave (R), and (4) long-period to short-period ratios (such as L/P_g). We compute distance corrections by linear regression of earthquake ratios on the logarithm of distance and apply the corrections to both earthquake and explosion ratios. To date, we have analyzed about 140 earthquakes that range in magnitude (m_b) between 3.8 and 6.2 and range in epicentral distance between about 100 and 1200 km. We have evaluated about 15 underground nuclear explosions from the Kazakh test site (KTS) and a single nuclear explosion from the Lop Nor test site. The explosions range in magnitude between 4.6 and 6.1 and range in epicentral distance between about 260 and 980 km. For this range of magnitudes and distances, we find that most of the discriminants outlined above (with the exception of the spectral discriminant) separate the explosion and earthquake populations.

RESEARCH ACCOMPLISHED

Waveforms obtained. Our data source for this project has been the IRIS Data Management Center (DMC). Using NEIC/ISC event catalogs maintained at the IRIS DMC, we have requested and obtained short-period (SH, 40 sps) and broadband (BH, 20 sps) waveforms from about 140 earthquakes and 16 nuclear explosions recorded at station WMQ. The locations of these events, along with station locations and some geographic features, are shown in Figure 1. We obtained and processed data from events shown in the box surrounding station WMQ. Waveforms of a single explosion from Lop Nor are available through IRIS. This explosion is about 260 km from WMQ and has a reported m_b of 4.6. About 15 nuclear explosions from KTS have been recorded at WMQ. The KTS explosions are between about 950 and 980 km from WMQ. Magnitudes of these explosions range between 4.6 and 6.1. Most earthquakes composing our data set occurred to the south, southwest, and west of WMQ. They range in magnitude between 3.8 and 6.2. Maximum epicentral distance for the earthquakes is about 1200 km.

Waveforms and Processing - Short Periods. To evaluate short-period discriminants, we measured bandpass filtered velocity records for P_n, P_g, S_n, and L_g rms amplitudes. Prior to measuring phase amplitudes, we handpicked the clearest arrivals for each phase on unfiltered, three-component records, and measured velocities for each phase. Using the velocities of each phase, we defined group velocity windows centered on each phase, and then automatically measured rms amplitudes within the windows. The centers of the frequency bands evaluated range between 1 and 9 Hz.

An earthquake from January, 1990 has nearly the same epicenter and m_b as the Lop Nor explosion (Figure 1). As an example of our data processing procedure, we compare short-period records of this explosion and earthquake in Figure 2. Each event shows the unfiltered SHZ velocity record and two bandpass filtered waveforms. Also shown are the P_g and L_g measurement windows. P_n and S_n were not measured on these records because the event-station distance is too short for a clear head wave arrival from the crust-mantle boundary. Note that for the 1-2 Hz band the P_g and L_g amplitudes of the explosion are about the same. However, for the 4-8 Hz band, the P_g amplitude is much greater than the L_g amplitude. For the earthquake, the L_g amplitude is always greater than the P_g amplitude.

Waveforms and Processing - Long Periods. Figure 3 shows Rayleigh waves and Love waves from the same explosion and earthquake discussed above. Here, we show broadband

displacement records filtered between 8 and 16 seconds. By visually inspecting many long-period records, we selected L and R group velocities that allowed us to automatically pick peak-to-peak maximum amplitudes for each surface wave phase. We also processed surface waves for 6-12 s, 12-24 s, and 16-32 s periods. L and R from the earthquake have about the same maximum amplitudes, while R for the explosions is about four times greater than L. Indeed, L from the explosion source is such a weak, poorly developed phase, that it often barely exceeds noise levels. Although these events have the same m_b, the amplitudes of the earthquake surface waves are more than a factor of 10 greater the the amplitudes of the explosion surface waves.

Short-Period Discriminants. Many short-period regional discriminants that exploit a P/S ratio have been discussed in the literature (*cf. Pomeroy et al.*, 1982). Figure 4 shows two of our examples from China. For each discriminant, we show the ratio-distance trend obtained from earthquake data, and we present a ratio-m_b discrimination plot where all been been corrected for distance. All ratios shown have signal that is at least 2.5 times the measured noise level. The 1-2 Hz P_g/L_g ratio does not separate the explosion and earthquake populations nearly as well as the 4-8 Hz ratio. We find that for frequency bands above 3 Hz, the populations can be separated for P_g/L_g, P_n/L_g, and P_n/S_n ratios. However, considering signal-to-noise ratios of these four body wave phases, we find that the P_g/L_g ratio is most useful.

Short-Period Spectral Discriminants. Spectral discriminants have been successfully applied to relatively small events from the western United States. *Taylor et al.* (1988) used the $L_g(1-2\,Hz)\ /\ L_g(6-8\,Hz)$ ratio, *Bennett and Murphy* (1986) used the $L_g(0.5-1\,Hz)\ /\ L_g(2-4\,Hz)$ ratio, and *Hartse et al.* (1995) used the coda $(0.5-1\,Hz)/(2-4\,Hz)$ ratio to separate nuclear explosions from earthquakes. However, Figure 5 shows that the spectral discriminant for western China may not be as successful. The $L_g(1-2\,Hz)\ /\ L_g(6-8\,Hz)$ ratio fails to separate the events. We also have tried $L_g(0.5-1\,Hz)\ /\ L_g(2-4\,Hz)$ ratios and various P_g/L_g spectral ratios with results similar to those in Figure 5. The western U.S. studies generally examined small explosions ($m_b<4.8$) that were detonated above the water table. Most explosions from Asia are thought to be detonated below the water table (*Matzko*, 1994). As discussed by *Taylor and Denny* (1991), the amount of gas-filled porosity near the explosion appears to control the performance of the spectral-ratio discriminant.

Long-Period Discriminants. We tested long-period L/R discriminants in four frequency bands, and found that the 8-16 s period shows the best separation and least scatter (Figure 6). The L/R discriminant was mentioned by *Pomeroy et al.* (1982), but has not been widely applied. The problem is that the weak L of the explosions often fail to exceed noise levels. The Kazakh explosions had to be large ($m_b>5.5$) to generate L that was above the noise at WMQ, over 950 km from the station. However, for smaller events, the absence of L combined with the presence of R can be used as an explosion indicator. We measured L and R of over 100 earthquakes and found only four events ($<4\%$) where L was below the noise while R was above the noise. At the same time, of the 15 Kazakh explosions we processed, we found four ($>25\%$) with L below the noise and R above the noise.

Short-Period/Long-Period Discriminants. We tested P_g/L and P_g/R ratios. These discriminants are analogous to the m_b/M_s discriminant that has been successfully applied in the western U.S (*Taylor et al.*, 1989). Because we have not yet developed regional m_b and M_s scales for station WMQ, we have simply tested P_g / surface wave ratios. We measured peak-to-peak displacement amplitudes from broadband records to test this discriminant. Figure 7 shows the $P_g(2-4\,Hz)\ /\ L(8-16\,s)$ and the $P_g(2-4\,Hz)\ /\ R(8-16\,s)$ ratios versus m_b. We also tested $P_g(1-2\,Hz)$, but found that $P_g(2-4\,Hz)$ produces better separation. L performs better than R, but, as in the case of the long-period discriminants, L for smaller explosions is difficult to measure above the noise.

RECOMMENDATIONS AND FUTURE PLANS

We have started a comprehensive seismic discrimination study of western China. Using waveforms from over 100 earthquakes and 16 nuclear explosions recorded at CDSN station WMQ, we have tested short-period phase ratios, short-period spectral ratios, long-period ratios, and short-period/long-period ratios as event discriminants. We have estimated and applied distance corrections for every discriminant tested. We find that the absence of a Love wave accompanied by the presence of a Rayleigh wave is a strong indicator of an explosion. This appears to be a rare occurrence for central Asian earthquakes. With the exceptions of the short-period spectral ratio, we have been able to separate earthquakes from underground nuclear explosions for events down to $m_b \approx 4.5$ at distances of about 1000 km. However, we have not yet processed any chemical explosion data. We do not know what our discrimination capabilities will be for smaller explosions.

Our study has progressed to where the performance of some discriminants can be compared between the western China region and the western U.S. In Figure 8 we compare event separation for these two regions using the P_g / L_g ratio. The figure shows average ratios and one standard deviation for earthquakes and nuclear explosions plotted against frequency. Compared to the U.S., in western China, separation is greater and occurs at lower frequencies. As more events are processed from Asia, the separation may decrease. However, the good separation at about 3 Hz implies that this regional discriminant can be applied at greater distances in central Asia than in the western U.S. Additionally, the scatter of the P_g / L_g ratio appears to less for western China than for the western U.S. at higher frequencies.

Furture work will involve expanding outward from western China. We have obtained, but have not yet processed, waveforms recorded at stations AAK and TLY (Figure 1), and we will obtain and process other regional data. We will develop regional m_b, M_s, and coda magnitude scales, and test the m_b / M_s and coda discriminants. Because we have tested several different discriminants, we have been preparing multivariate techniques that combine discriminants and discrimination capabilities. We will analyze smaller magnitude events by acquiring Chinese provincial catalogs and obtaining these events from the IRIS DMC.

REFERENCES

Bennett, T., and J. Murphy, Analysis of seismic discrimination using regional data from western United States events, *Bull. Seis. Soc. Am.*, *76*, 1069-1086, 1986.

Hartse, H. E., W. S. Phillips, M. C. Fehler, and L. S. House, Single-station spectral discrimination using coda waves, *Bull. Seis. Soc. Am.*, *85*, in-press, 1995.

Matzko, J. R., Geology of the Chinese nuclear test site near Lop Nor, Xinjiang Uygur Autonomous Region, China, *Engineering Geology*, *36*, 173-181, 1994.

Pomeroy, P. W., J. B. Best, and T. V. McEvilly, Test ban treaty verification with regional data - a review, *Bull. Seis. Soc. Am.*, *72*, S89-S129, 1982.

Taylor, S. R., N. W. Sherman, and D. D. Marvin, Spectral discrimination between NTS explosions and western United States earthquakes at regional distances, *Bull. Seis. Soc. Am.*, *78*, 1563-1579, 1988.

Taylor, S. R., M. D. Denny, E. S. Vergino, and R. E. Glaser, Regional discrimination between NTS explosions and western U.S. earthquakes, *Bull. Seis. Soc. Am.*, *79*, 1142-1176, 1989.

Taylor, S. R., and M. D. Denny, An analysis of spectral differences between Nevada Test Site and Shagan River nuclear explosions, *J. Geophys. Res.*, *96*, 6237-6245, 1991.
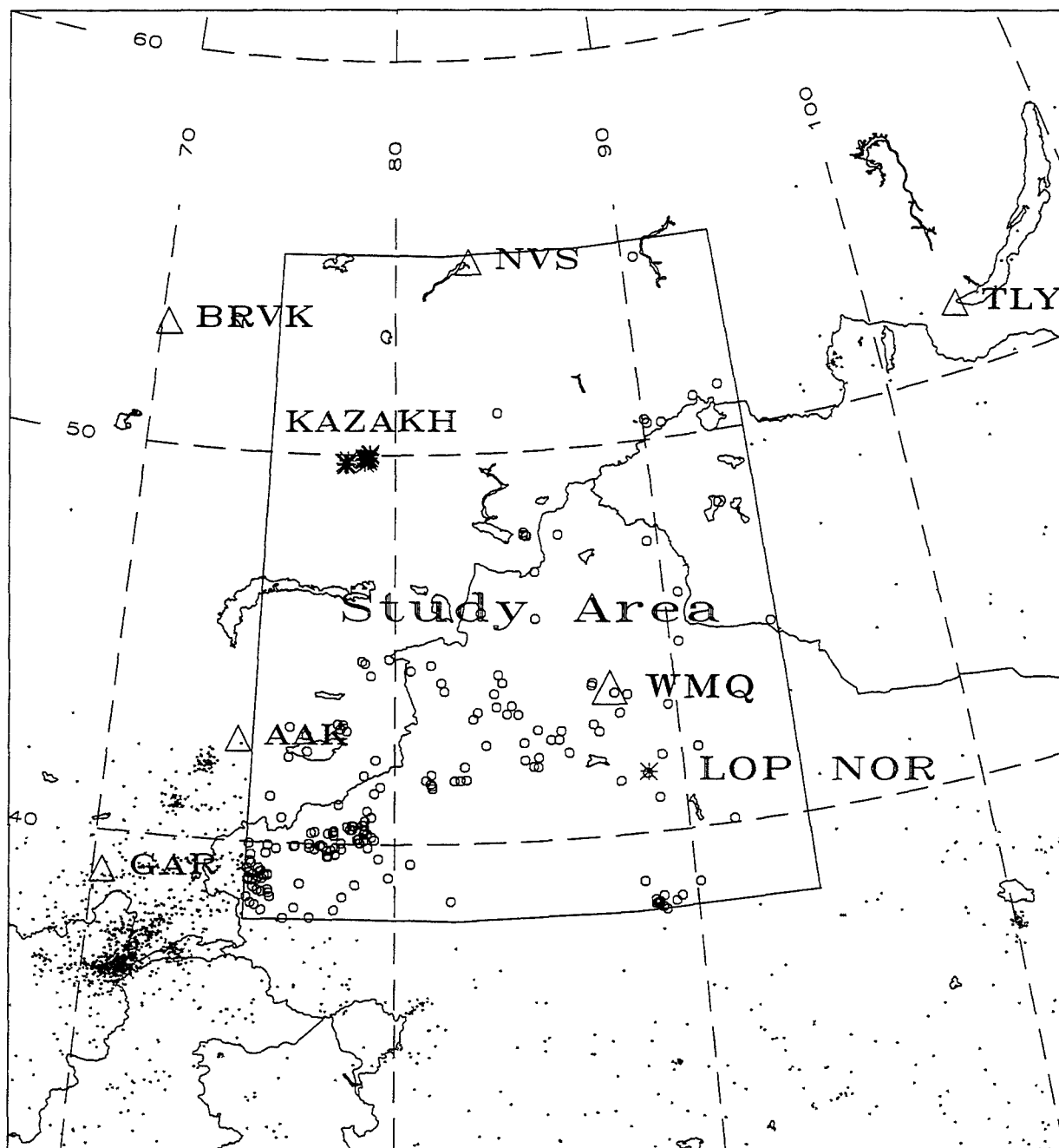
Figure 1. Event location map of central Asia for the years 1989-1994. Large symbols inside study area box denote events for which we have obtained and processed waveforms. Asterisks denote nuclear explosions and circles denote earthquakes. Small dots outside study area represent earthquakes that we have not investigated. For scale, it is about 260 km from Lop Nor to station WMQ and about 970 km from the Kazakh test site to station WMQ. Locations are from the National Earthquake Information Center catalogs maintained at the IRIS Data Management Center.

Lop Nor Explosion - mb = 4.6
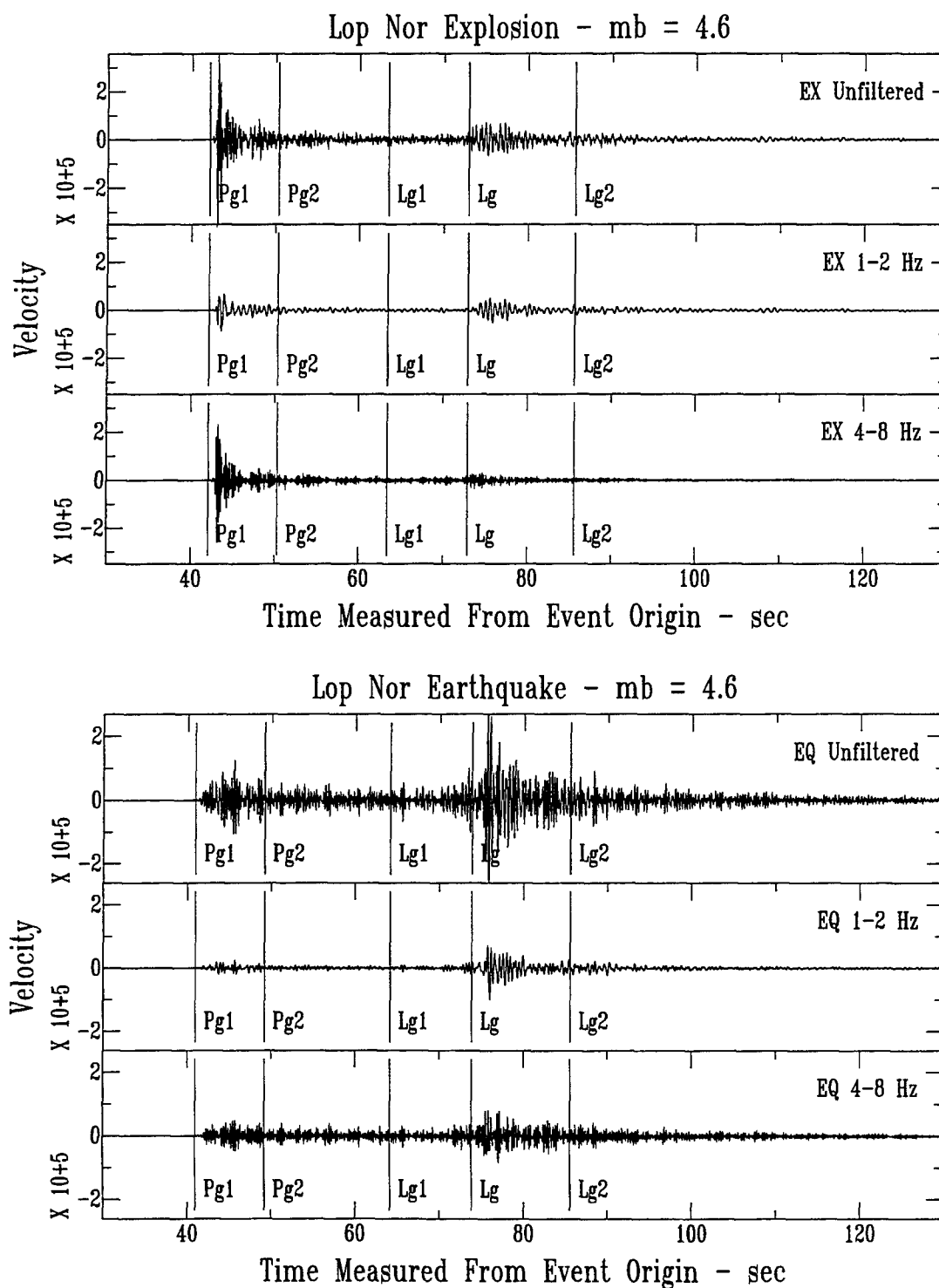
Figure 2. Short-period, vertical component (SHZ) waveforms recorded at station WMQ for the September 29, 1988 Lop Nor nuclear explosion (*top*) and a nearby earthquake from 1990 (*bottom*) (see Figure 1 for locations). Unfiltered, bandpass filtered from 1-2 Hz, and bandpass filtered from 4-8 Hz waveforms are displayed in velocity. P_g and L_g measurement windows are marked by Pg1, Pg2, Lg1, and Lg2. For both events, $m_b \approx 4.6$ and event-station distance is about 260 km. Note the strong P_g phase of the explosions and that the P_g / L_g ratio of the explosion increases as passbands are increased to above 4 Hz.

52
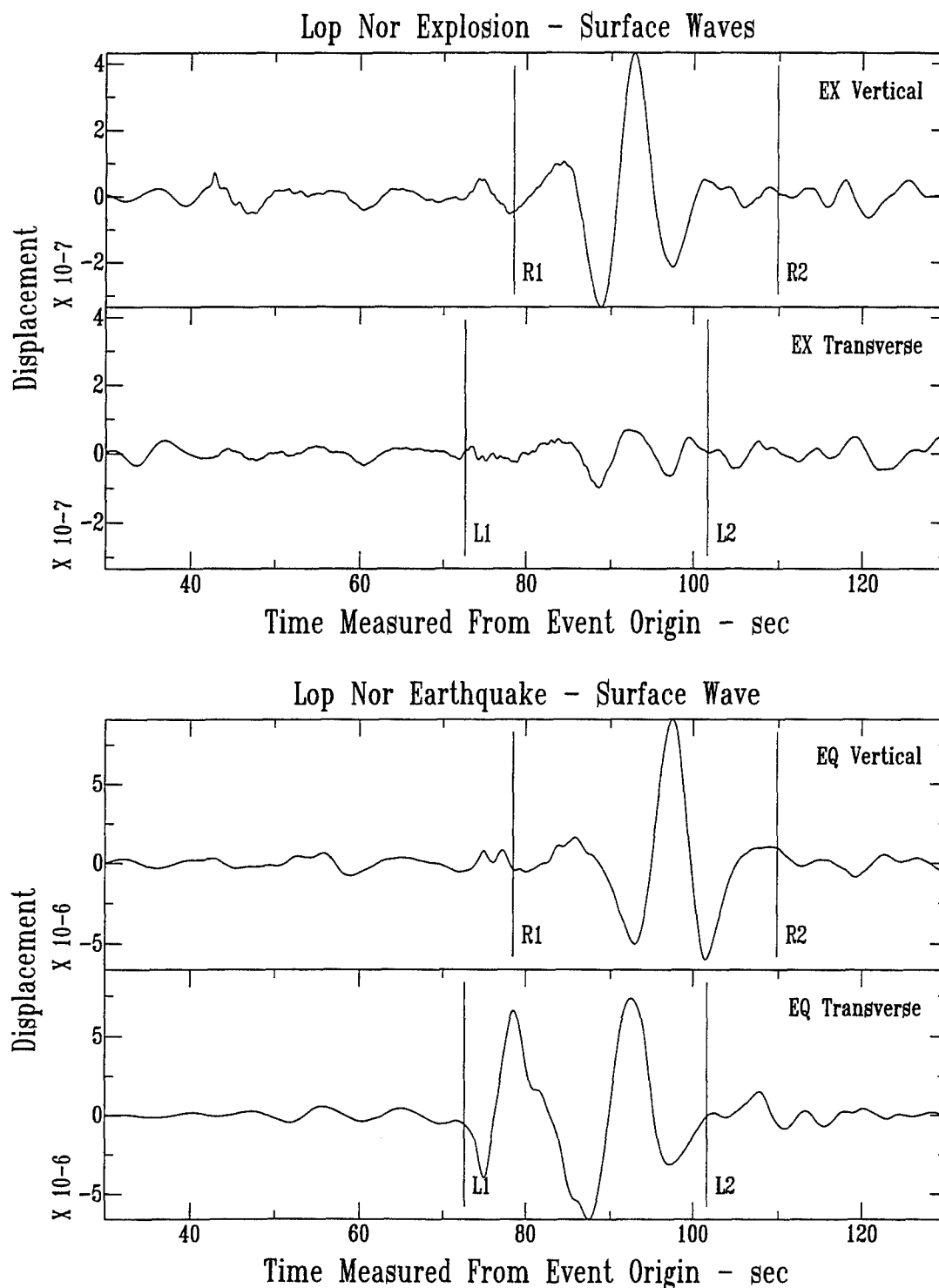
Figure 3. Long-period (8-16 s) surface waves recorded with broadband seismometers at station WMQ. These are the same events shown in Figure 2, but the long periods are displayed in displacement. *Top* shows the explosion Rayleigh wave between R1 and R2 markers and the Love wave between L1 and L2 markers. *Bottom* shows the Rayleigh and Love wave of the earthquake. Note that the Love wave for the explosion is extremely weak relative to the Rayleigh wave, while the Love and Rayleigh wave of the earthquake have comparable amplitudes. Also, despite the similar magnitudes (≈ 4.6), the surface waves of the explosion are much weaker than those of the earthquake.

53
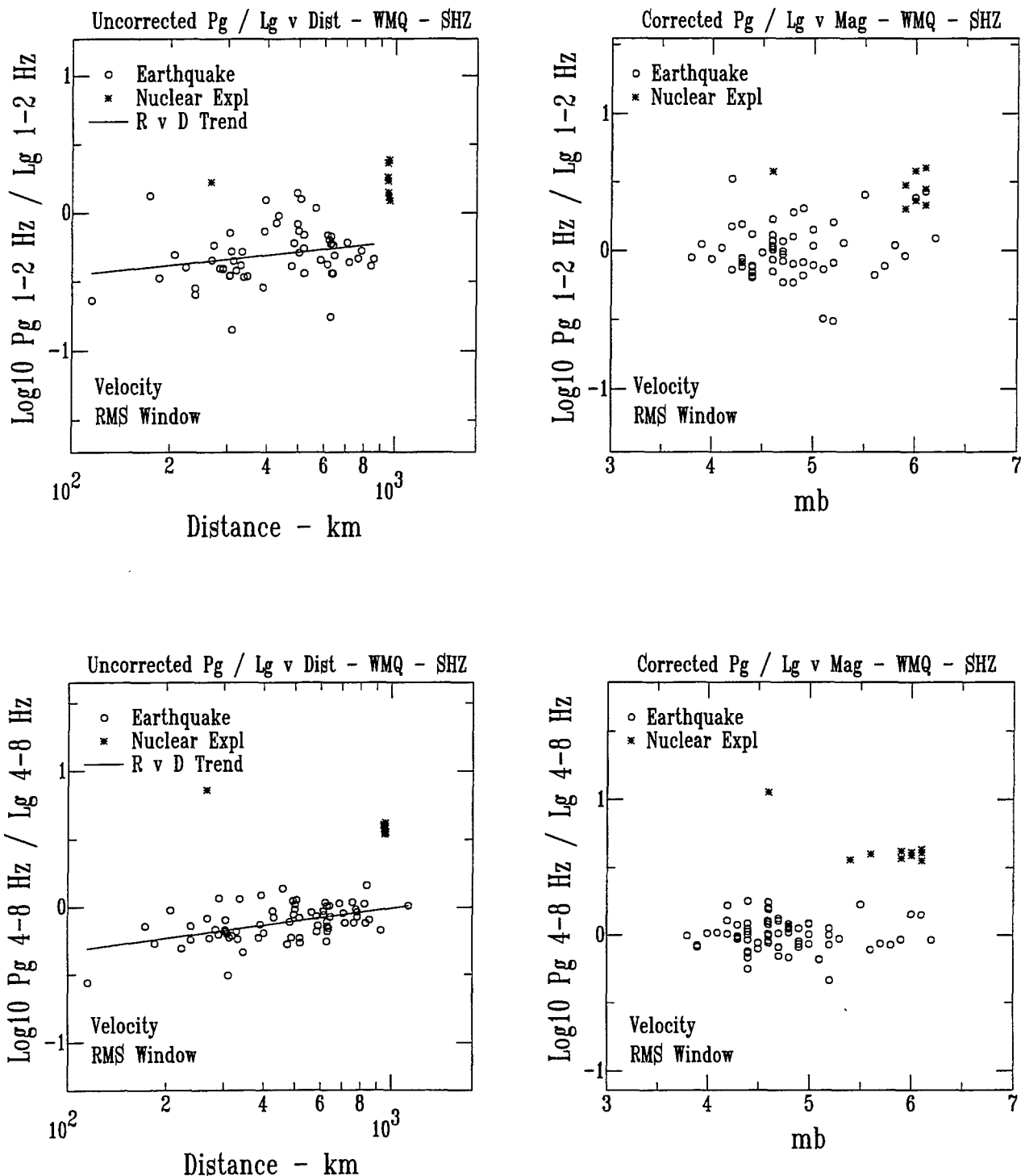
Figure 4. Short-period discrimination plots for station WMQ. *Top* shows P_g (1–2 Hz)/L_g (1–2 Hz) results, and *bottom* shows P_g (4–8 Hz)/L_g (4–8 Hz) results. Ratio-distance trend (slope and intercept) is obtained from the earthquake measurements, and trend is removed in the ratio-magnitude discrimination plots (on *right*). Waveform rms amplitudes are measured from short-period, vertical component (SHZ) velocity records. Note increased separation between earthquakes and explosions as frequency increases.

54
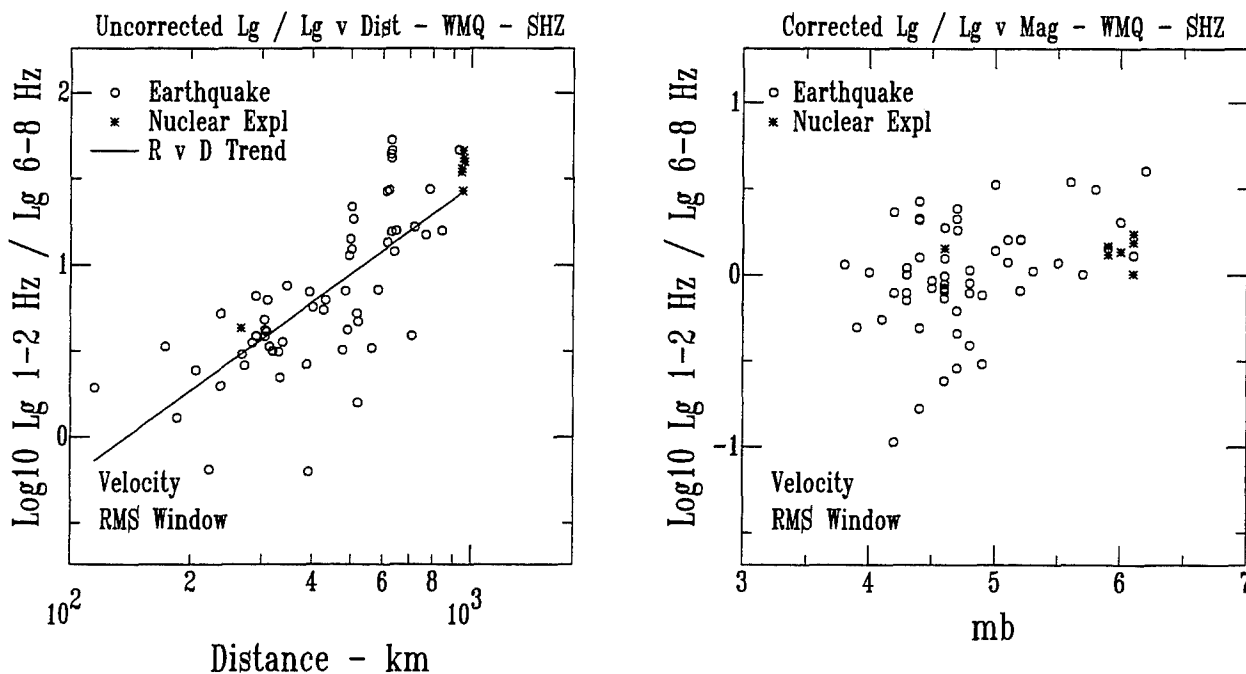
Figure 5. Short-period spectral discrimination plots for station WMQ. The L_g (1–2) / L_g (6–8) spectral discriminant was successfully applied to events from the western U.S. by *Taylor et al.* (1988), but, for south-central Asia, the L_g (1–2)/L_g (6–8) spectral ratio apparently does not perform well. Distance corrections have been applied to the ratio-magnitude plot as described in Figure 4. Waveform rms amplitudes are measured from short-period, vertical-component (SHZ) velocity records.
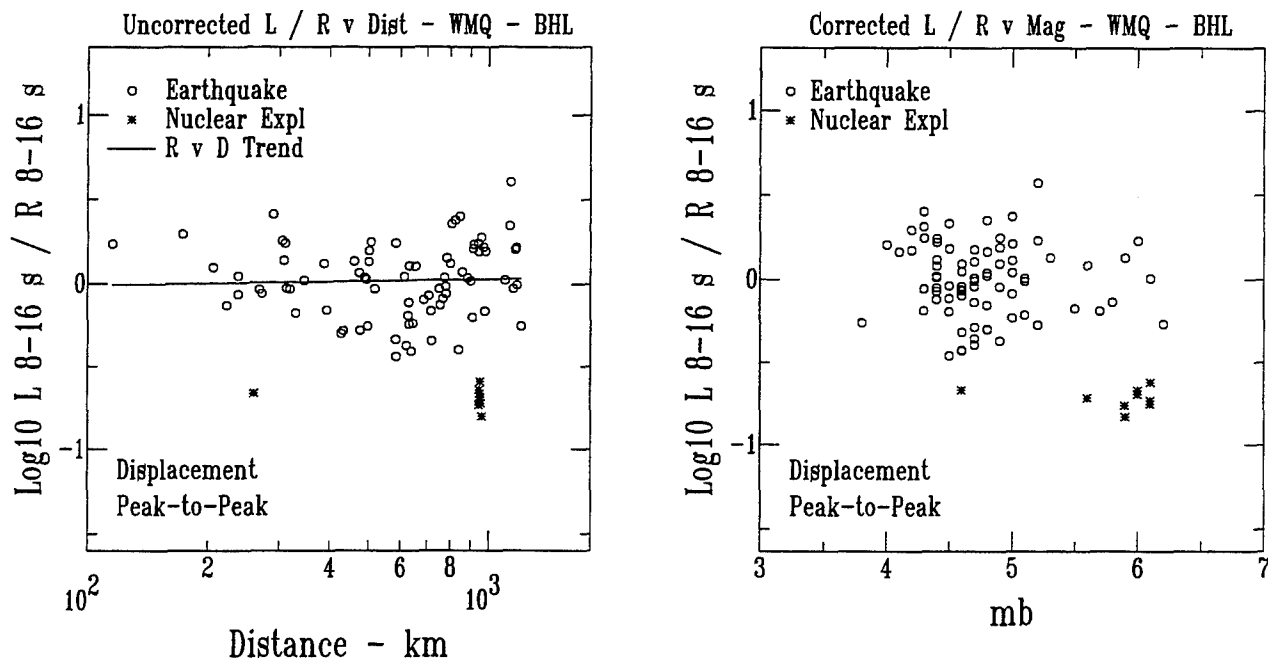
Figure 6. Long-period (8-16 s) discrimination plots for station WMQ. Rayleigh wave (R) is measured from vertical component, and Love wave (L) is measured from tangential component of broadband (BH) displacement records. Distance corrections have been applied to the ratio-magnitude plot as described under Figure 4. When Love-wave energy exceeds signal-to-noise levels, the L / R ratio is a viable discriminant.
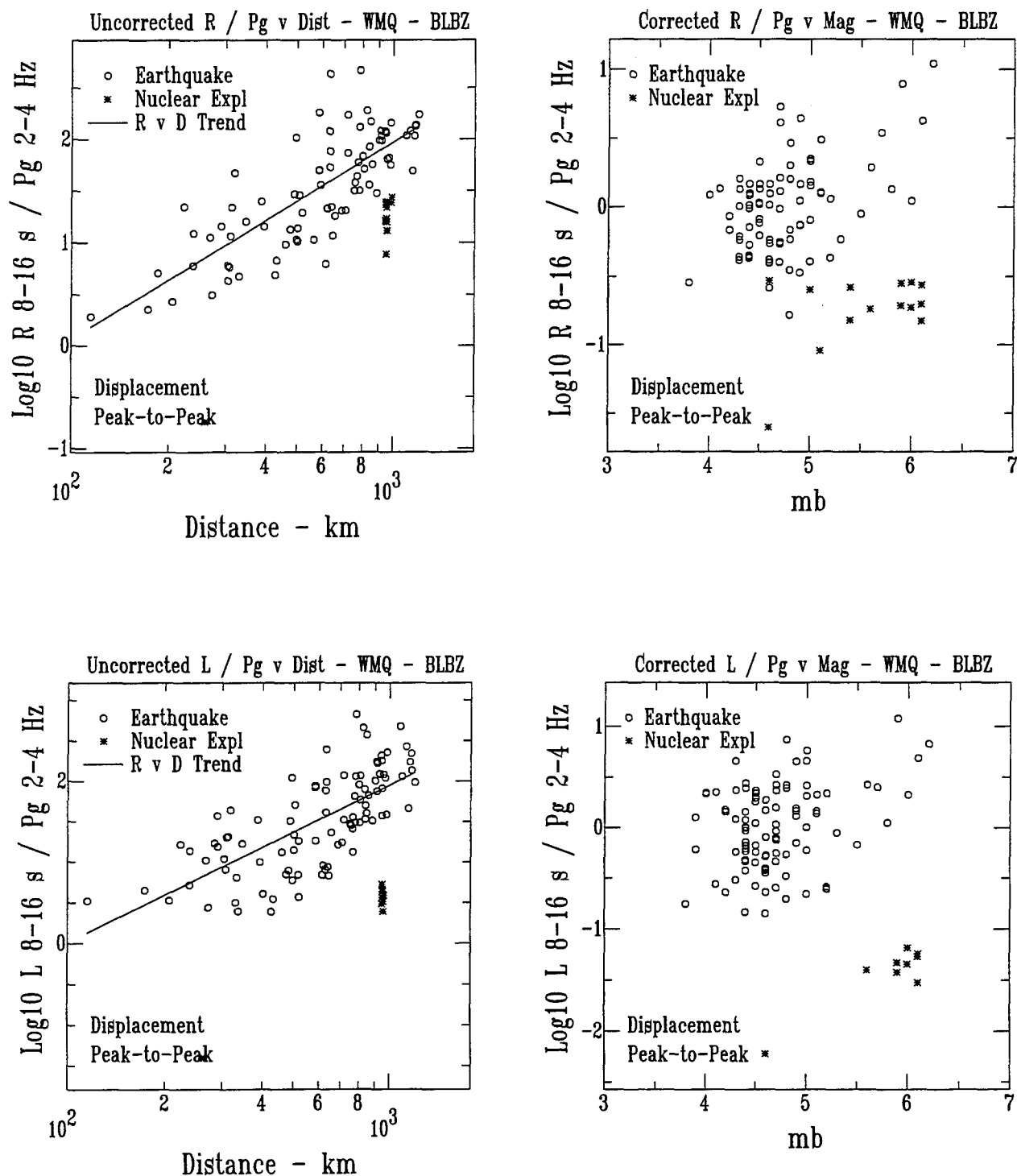
Figure 7. Long-period / short-period discrimination plots for station WMQ. *Top* shows R (8–16 s)/P_g (2–4 Hz) results, and *bottom* shows L (8–16 s)/P_g (2–4 Hz) results. Distance corrections have been applied to the ratio-magnitude plot as described under Figure 4. Waveform peak-to-peak amplitudes are measured from broadband (BH) displacement records.

Western China
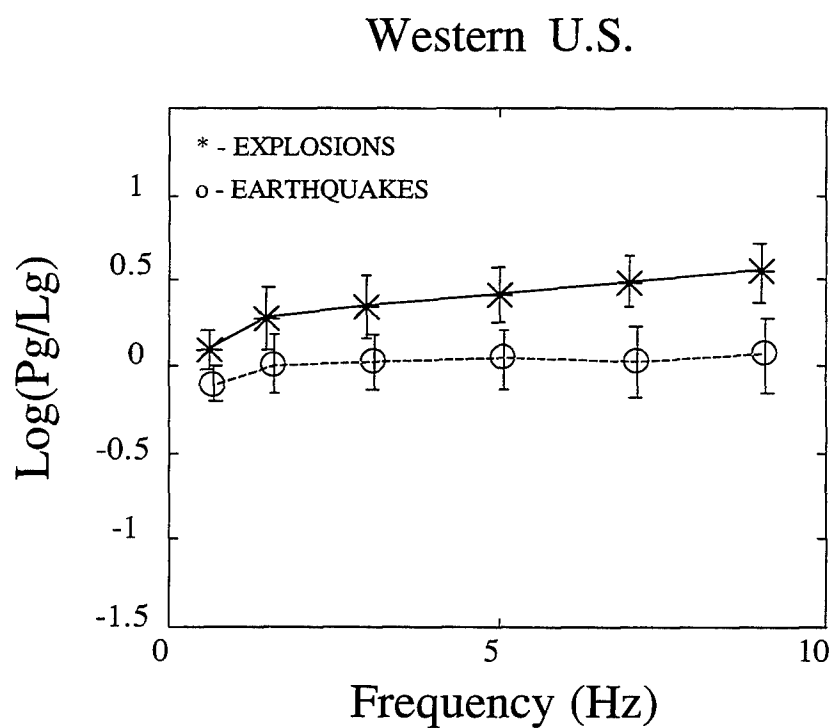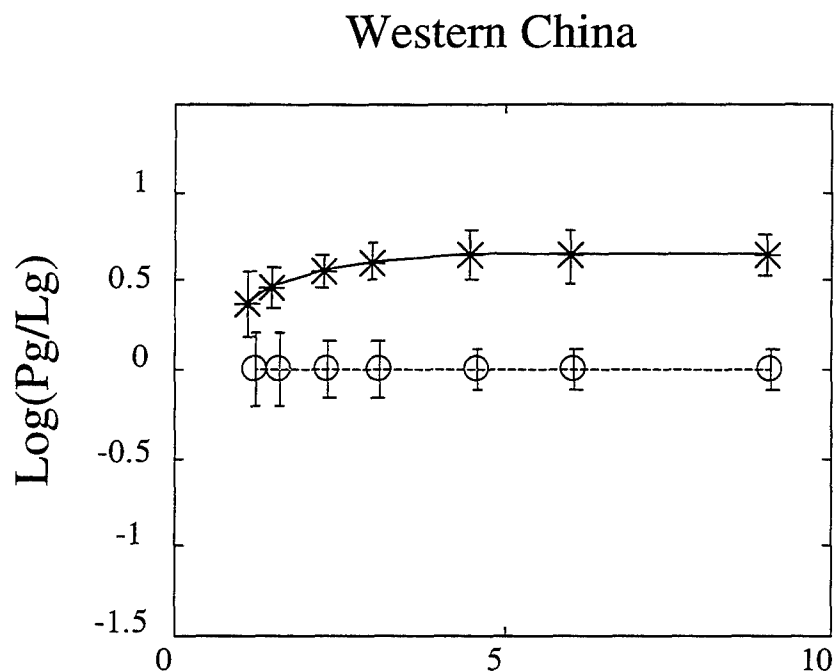
Western U.S.

Figure 8. Short-period (P_g / L_g) ratio versus frequency for western China (*top*) and western United States (*bottom*). Circles show average ratios for earthquakes and asterisks show average ratios for nuclear explosions. Error bars are for 1 standard deviation. Above about 3 Hz separation between earthquakes and explosions for China is greater than for U.S. and scatter appears to be reduced.

DEVELOPMENT OF REGIONAL DISCRIMINANTS

Don V. Helmberger and Xi Song
Seismological Laboratory
California Institute of Technology, Pasadena, CA 91125

ABSTRACT

With the installation of broadband, high dynamic range instruments, it has become possible to compare the regional waveforms of earthquakes and explosions at magnitudes 3 to 6. These waveforms are similar for event sequences in many situations and can be inverted for source mechanisms. We find that flat-layered models are sufficient for inverting seismograms at periods greater than a few seconds. This paper presents three studies aimed at determining crustal models, source finiteness and modeling complex structure near a receiver.

We have conducted a set of sensitivity tests on the parameters of 1-D models to compare their impact on different segments of regional seismograms. We found that P_{nl} waves (extended P-waves) are controlled in broadband character by the mid-crust while the top layer contributes to the long-period motions. The SV wave is mostly controlled by the shear wave velocity of the lower crust, especially the crustal layer just below the source depth. The top crustal layer controls the shape of the surface waves at ranges from 300 to 600 km, and the upper crust, especially the crustal layer just above the source depth, controls their timing. Applying these tests in modeling three earthquakes in the Basin-and-Range province, we found that a simple two-layer crustal model could effectively explain the data both in timing and in shape. The main crustal layer has P and S velocities of 6.1 km/sec and 3.6 km/sec, similar to those found by Langston and Helmberger (1974). A surface layer of thickness 2.5 to 3.5 km is required to fit the Rayleigh waves.

Fast estimation of point-source parameters for earthquakes has witnessed much progress in recent years due to the development of broadband seismic networks. The expansion of these networks now provides the opportunity to address second order effects such as source directivity and finiteness for regional and local events on a routine basis. To study the directivity for a finite source, we discretize the fault region into a set of elements represented as point-sources. We then generate the generalized rays for the best-fitting point-source location and derive for each separate ray the response for neighboring point-sources with power series expansions. The total response for a finite fault then becomes a double summation over rays and elements. If we sum over elements first, we obtain an effective far-field source-time function for each ray, which becomes quite sensitive to the direction of rupture. These far-field source-time functions are convolved with the corresponding rays and the results summed to form the total response. A simple application of the above method is demonstrated with the tangential motions observed from the 1991 Sierra Madre earthquake.

A 2-D SH hybrid method was developed, which combines finite-difference applied in the inhomogeneous region and an analytic method, GRT, outside. GRT enables us to study basin effects and complex receiver structure for different types of incident energy. The comparison of hybrid method seismograms, GRT seismograms, and regular finite-difference seismograms yields good agreement.

OBJECTIVE

Recent advances in instrumentation allowing low amplitude Rayleigh wave detection coupled with new analytical techniques has demonstrated the capability of inverting regional waveform data for source excitation down to relatively low magnitudes. To achieve this requires the determination of regional crustal models and path calibrations from master events. This approach can be applied in many countries of interest where earthquakes are plentiful and event discrimination is difficult. However, once these models are determined, we still need to address the question of what criterion do we use to distinguish the "first blast"? We propose to address this issue by a detailed study of US explosions and earthquakes as observed in Southern California by nearly 300 short-period stations and TERRAscope. Thus, separating propagation features from true source phenomenon should be greatly aided by the completeness of the observations. That is, we can see observationally what happens to broadband signals as they encounter ridges, valleys, faults, etc. This region is rich in sources with quarry blasts, NTS shots, and many different types of earthquakes, thus providing ample data for definitive testing and the development of regional discriminants.

RESEARCH ACCOMPLISHED

We have examined broadband waveforms from a large number of NTS explosions and earthquakes throughout the southwestern United States in order to characterize seismic sources. Explosions were found to be richer in coda energy than earthquakes. Most earthquakes show relatively little long-period (T>4 sec) coda energy and tend to be richer in long-period and shear-wave energy than explosions. We have developed several seismic discriminants based on these observations and our modeling experience. One promising discriminant is the ratio of short-period vertical component, P-wavetrain energy, to long-period surface wave energy, averaged over three components. Explosions tend to have a higher ratio than do earthquakes, essentially an extension of m_b:M_S. Magnitude threshold for this discriminant is about 3.5. Another useful discriminant is based on the total broadband energy to moment ratio where explosions are distinguished by their stronger energy levels relative to their long-period amplitudes. This approach requires Green's functions, a source estimator program, and processes all events as earthquakes. For this method to be effective requires the calibration of the region using relatively large earthquakes, M>5, but does not require calibrations of explosions, see last year's research report and references; Helmberger and Woods (1995), Woods et al., (1993), Woods and Helmberger (1994), Zhao and Helmberger (1995).

In this year's report, we will address three topics involving studies that help refine earthquake source effects (depth, directivity, etc.) and regional modeling of structure. Note that we detect explosions because they do not look like earthquakes.

a) Estimation Of Earthquake Parameters

The approach followed here, Zhao and Helmberger (1995), uses a direct grid search and does not require stable partial derivative of waveforms. This method matches complete broadband observed seismograms against synthetics over discrete phases so that timing shifts between particular arrivals are allowed. This feature desensitizes the crustal model used in generating the synthetic waveforms used.

An application of this procedure is displayed in figure 1 along with depth sensitivity of regional phases versus teleseismic waveforms. In this example, only one station is used to determine the three source parameters which yields various solutions as a function of depth. The solution obtained from TERRAscope is displayed as BB which is at a depth of 10 kms. This depth agrees well with teleseismic depth phases, namely sP as displayed in figure 1. The individual depth phases in the regional data, $p^P m^P$, $s^P m^P$, $s^S m^S$, etc. are quite obvious at higher frequency as pointed out by Helmberger et al., (1992), although they are strongly affected by

source directivity, Dreger and Helmberger (1993). The importance of source directivity is becoming increasingly clear in TERRAscope data, see Song et al., (1995) and others, and methods of estimating these effects by analytical means is discussed by Saikia and Helmberger (1995).

In short, the expansion of broadband networks such as TERRAscope is providing the opportunity to address second order effects such as source directivity and finiteness for teleseismic, regional and local events on a routine basis. Making this practical motivates the development of methods to quickly generate synthetic seismograms for finite sources. This proves possible when the fault dimension is small compared to the source-receiver distance and when the structure around the source region is relatively simple. To study the directivity for a finite source, we discretize the fault region into a set of elements represented as point-sources. We then generate the generalized rays for the best-fitting point-source location and derive for each separate ray the response for neighboring point-sources with power series expansions. The total response for a finite fault then becomes a double summation over rays and elements. If we sum over elements first, we obtain an effective far-field source-time function for each ray, which becomes quite sensitive to the direction of rupture, see figure 2. As displayed in the upper panel, the goodness of fit to a particular record becomes strongly dependent on rupture direction and easily included in source inversion, see Song and Helmberger (1995). These far-field source-time functions are convolved with the corresponding rays and the results summed to form the total response.

b) Crustal structure

The source estimation code used in modeling the regional records such as in figure 1 is used routinely to obtain fault parameters from TERRAscope data, i.e., Jones (1995). It uses a store of Green's functions computed on a range interval of 5 kms, and on a depth interval of 3 kms starting at a depth of 5 km, see last year's Seismic Research Symposium summaries, and Zhao and Helmberger (1995). While the SC model proves effective because of the shifting specialized models or regionalized local models work even better as displayed in figure 3. A simple two-layer crustal model is found for this basin-and-range region that fits the events very well as reported on by Song and Helmberger (1995). To find an average model that fits the data in both absolute time and waveform, we generate broadband reflectivity synthetics and conduct sensitivity tests on different parts of a layered crustal model, where only a few layers are involved. Generalized rays are used to help identify the various phases. It proves useful to decompose a regional seismogram into segments so that the impact of model parameters on each segment is the most direct. Thus, it is established that the top crustal layer controls the Rayleigh wave, the Airy phase, in shape over the range from 300 to 600 km, and the crustal layer just above the source depth controls its timing. The P_{nl} waves, the P_n and PL portion, are controlled in broadband character by the mid-crust while the top layer contributes to its long period motion. These crustal parameters control the tangential motion similarly. The SV wave, the segment between the P_{nl} wave and the Rayleigh wave, is mostly controlled by the shear velocity of the lower crust. In judging the goodness of fit between the array observations and synthetic waveforms, we allow individual data segments to shift relative to the 1-D synthetics a few seconds to account for some lateral variation. The amount of time shift is found by the cross-correlation in displacement between the data segment and the synthetics. Applying these tests in a forward modeling approach, we find that a simple two-layer crustal model is effective in explaining a Basin-and-Range data set. In this model, the main crustal layer has P and S velocities of 6.1 km/sec and 3.6 km/sec, similar to those found by Langston and Helmberger (1974). A surface layer of thickness 2.5 to 3.5 km is required to fit the Rayleigh waves. The refined model can be used as a reference model for locating source inversions for other events. We find that two-layer crustal models prove effective in many regions, see Zhu and Helmberger, and Woods and Saikia of this report.

60

c) Analytical and Numerical Interfacing

Our present regional source estimator program works reasonably well because it allows for lateral variation. This is achieved by allowing small shifts in timing between phases. Some physical basis for this rather ad hoc procedure is given in figure 4, where we display the effects of 2-D structures. Model (a) is a typical 1-D Southern California structure. Model (b) is similar to (a) but with the addition of a soft surface structure (basin-like materials). Models (c) and (d) contain basins in the source region. The synthetics are the most similar on the vertical component, especially (a), (c) and (d). Thus, we can roughly predict (c) and (d) from (a) by slightly separating the P-wave from the Rayleigh wave. The source code handles this nicely in its present form. The radial component does not work so well both in waveform and amplitude. The Love-wave portion of the tangential motion is not very well developed at this range but we can still see a shift developing. Thus, we can add this feature to the code by generating the Love-wave (top structure), as discussed in Helmberger et al., (1992), and shifting the bodywaves separately.

Another important issue is how to treat local scattering near the receiver. This is very important at the shorter periods and we probably need help from other investigators to do this right. However, one possible approach is to treat the receiver as a separate operator and introduce a separate structure at the receiver. Figure 5 displays such a procedure, where we can propagate the field analytically up to the receiver and introduce a local structure. Since finite-differencing does not need to propagate far, this becomes a viable approach. The method would allow us to model some of the obvious shifts in radial vs. vertical Rayleigh waves and their strange amplitude ratios. We could also use this technique to account for high frequency energy enhancement at particular stations that is commonly observed.

RECOMMENDATIONS

In the calibration of new regions, we must develop some "master events" which are well recorded teleseismically, and thus their source parameters can be determined. The regional records of these known events can then be used to develop the local structure, Zhao and Helmberger (1993), and others. This approach seems to work but for small events in isolated regions with only a few regional records, it would be useful to include other short-period array stacks of the P-waves (say, first 50 secs), especially if the event can be seen teleseismically. Thus, we recommend better communication links between array processors and waveform source estimators.

REFERENCES

Dreger, D. S. and D. V. Helmberger (1993). Determination of Source parameters at Regional Distances with Three-Component Sparse Network Data, *J. Geophys. Res.*, **98**, No. B5, 8107-8125.

Helmberger, D. V., and B. B. Woods (1995). Regional Source Parameters, Seismic Energy, and Discrimination, Proceedings in the NATO ASI Conference, Series E, Alvor, Portugal.

Helmberger, D. V., D. Dreger, R. Stead, and H. Kanamori (1992c). Impact of broadband seismology on strong motion attenuation, *Bull. Seism. Soc. Am.*, **83**, 830-850.

Jones, L. Part I: Broadband modeling of aftershocks from the Joshua Tree Landers and Big Bear sequences, Southern California. Part II: Characteristics of the June 28, 1992, Big Bear mainshock from TERRAscope data: evidence for a multiple event source, Ph.D. Thesis, Caltech, Pasadena, CA, June 1995.

Langston, C. A. and D. V. Helmberger (1974). Interpretation of Body and Rayleigh waves from NTS to Tucson, *Bull. Seism. Soc. Am.*, **64**, 1919-1929.

Saikia, C. K. and D. V. Helmberger (1995). An algorithm to compute-up and down-going wavefields for seismic sources, submitted to *BSSA*.

Song, X. J. and D. V. Helmberger (1995). Broadband modeling of regional seismograms; constraints on Basin and Range crustal structure, Spring Abstr., SSA (in preparation).

Song, Xi, L. Jones, and D. V. Helmberger (1995). Source characteristics of the January 17, 1994 Northridge, California earthquake from regional broadband modeling, *BSSA* (in press).

Wen, L., C. Scrivner, and D. V. Helmberger (1995). 2-D SH Hybrid method study of the Los Angeles Basin effects (in preparation).

Woods, B. B., S. Kedar, and D. V. Helmberger (1993). M_L:M_O as a Regional Seismic Discriminant, *Bull. Seism. Soc. Am.*, **83**, 11677-11683.

Woods, B. B. and D. V. Helmberger (1994). Regional Seismic Discriminants using Wavetrain energy ratios, submitted to *BSSA*.

Zhao, L. S. and D. V. Helmberger (1993). Source retrieval from broadband regional seismograms: Hindu Kush region, *Phys. of the Earth and Planet. Inter.*, **78**, 69-95.

Zhao, L. S. and D. V. Helmberger (1994). Source estimation from broadband regional seismograms, *Bull. Seism. Soc. Am.*, **84**, 91-104.

Zhao, L. S. and D. V. Helmberger (1995). Regional Moments, Energy Levels, and a New Discriminant, submitted to *BSSA* (in press).
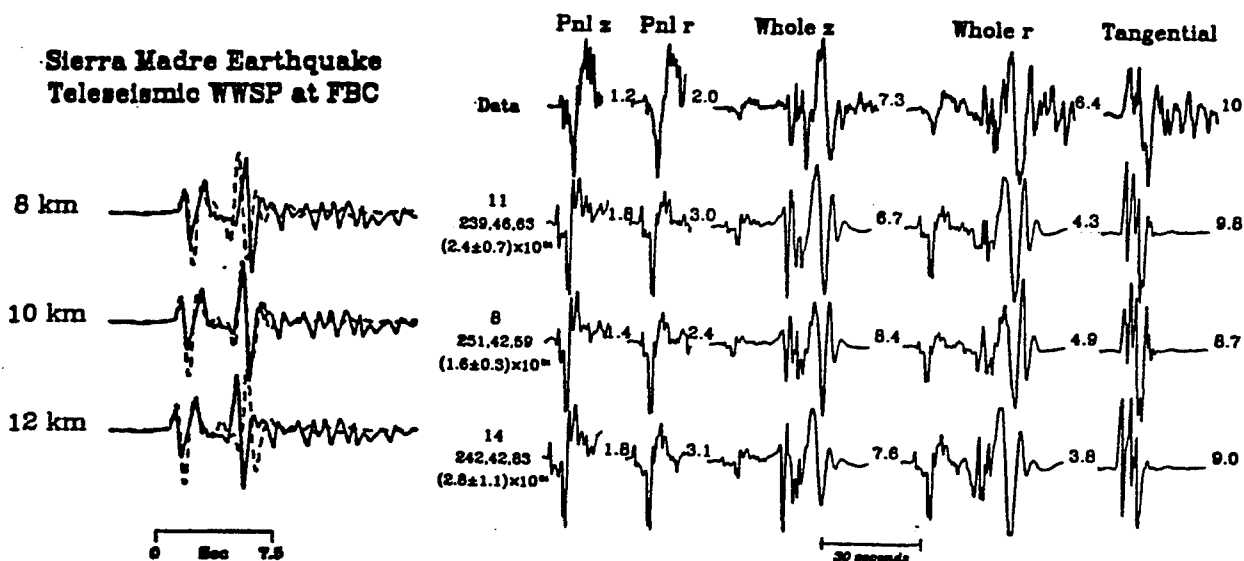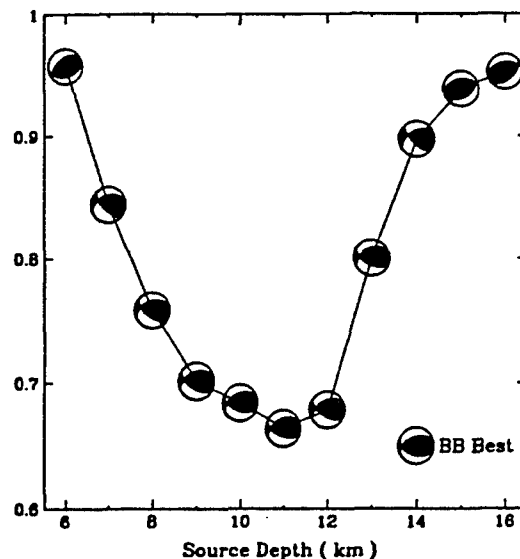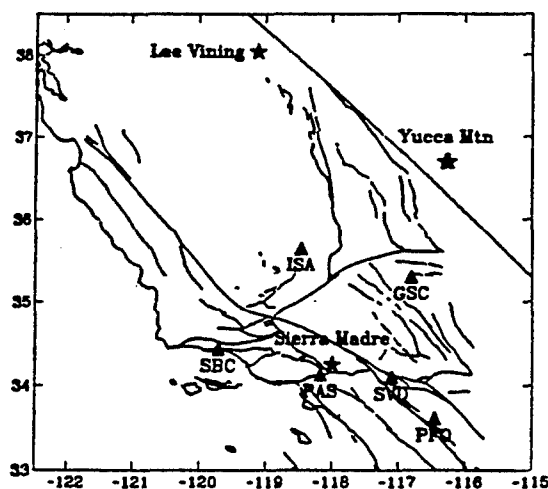
Figure 1. Results from modeling the Sierra Madre Earthquake as displayed in the upper corner. Comparison of synthetics and data at teleseismic distant (FBC, short-period waveforms displaying P and sP) and regional (GSC, Δ = 160 kms, three components). The plot in the upper right hand corner displays the sensitivity (error vs. depth) and the corresponding mechanisms.
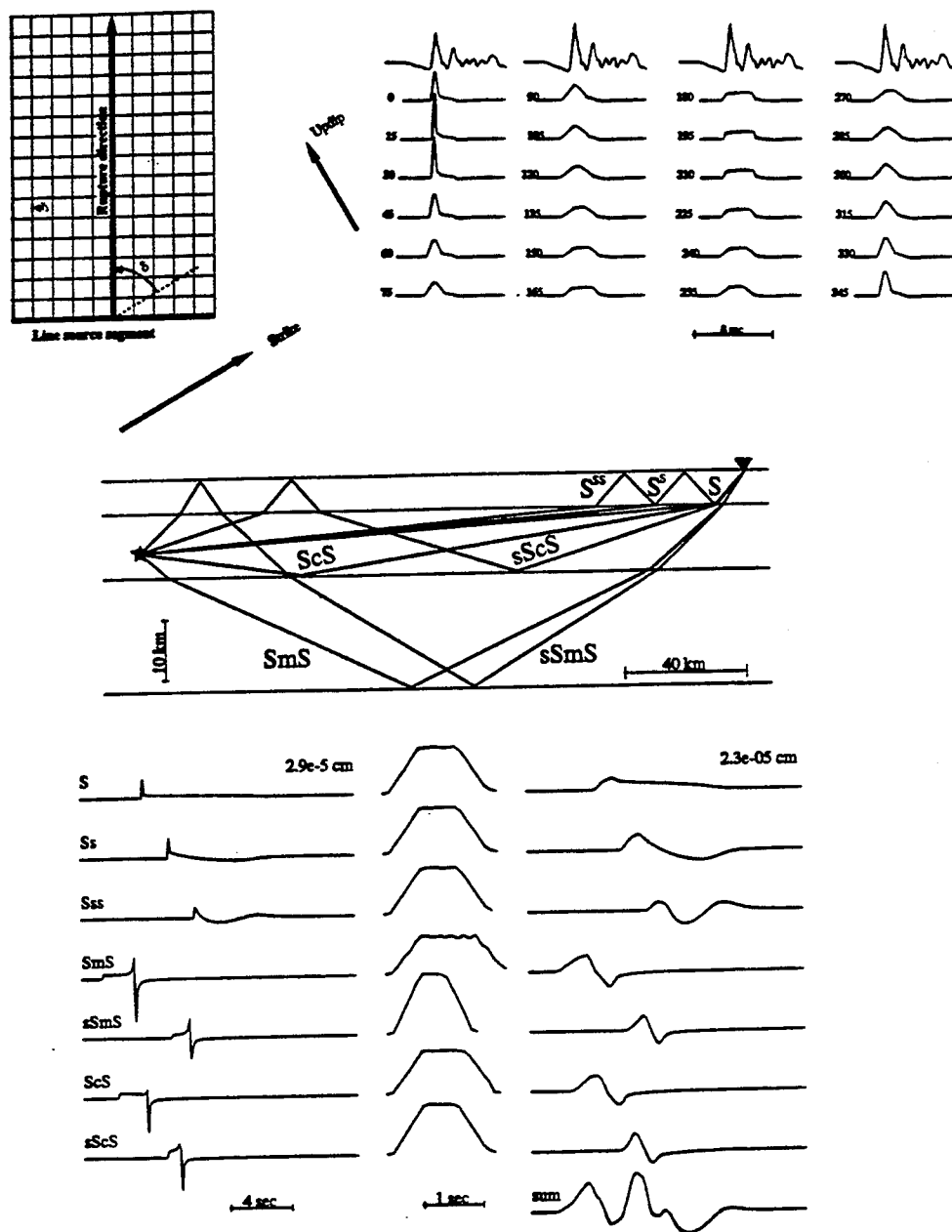
Figure 2. The upper panel (left) displays a map view of a discretized fault. Rupture is simulated by a line source segment propagating perpendicular to itself. The rupture angle δ is defined here to specify the rupture direction. When calculating the synthetic seismograms, each element of the fault is represented by a point-source with a weighting factor w_j. Upper panel (right) displays the comparison between data (PAS, tangential motion, the first trace in each column) and synthetics for fault size 5 x 5 km and varying rupture angles. Seismograms in each column are aligned in absolute timing and scaled with respect to peak amplitude. Numbers indicate rupture angles. Middle panel shows paths of some of the important rays. The star indicates the source and the triangle indicates the receiver. The lower panel displays the ray responses (left column, displacement) and the corresponding unit-area far-field source-time functions (middle column). Each ray is convolved with its corresponding far-field source-time function and the results (right column) are summed to form the total response (the right bottom trace) from the complex source. In this example, a 3-km-long line source segment propagates 2 km up-dip from a depth of 12 km at a constant velocity 3.0 km/sec on a fault plane striking 242° and dipping 50°. Source-receiver distance is 200 km and the station azimuth is 44°. Seismograms are scaled by peak amplitude. A source-time function (0.1, 0.1, 0.1) is used for each point-source, after Song & Helmberger (1995).

64
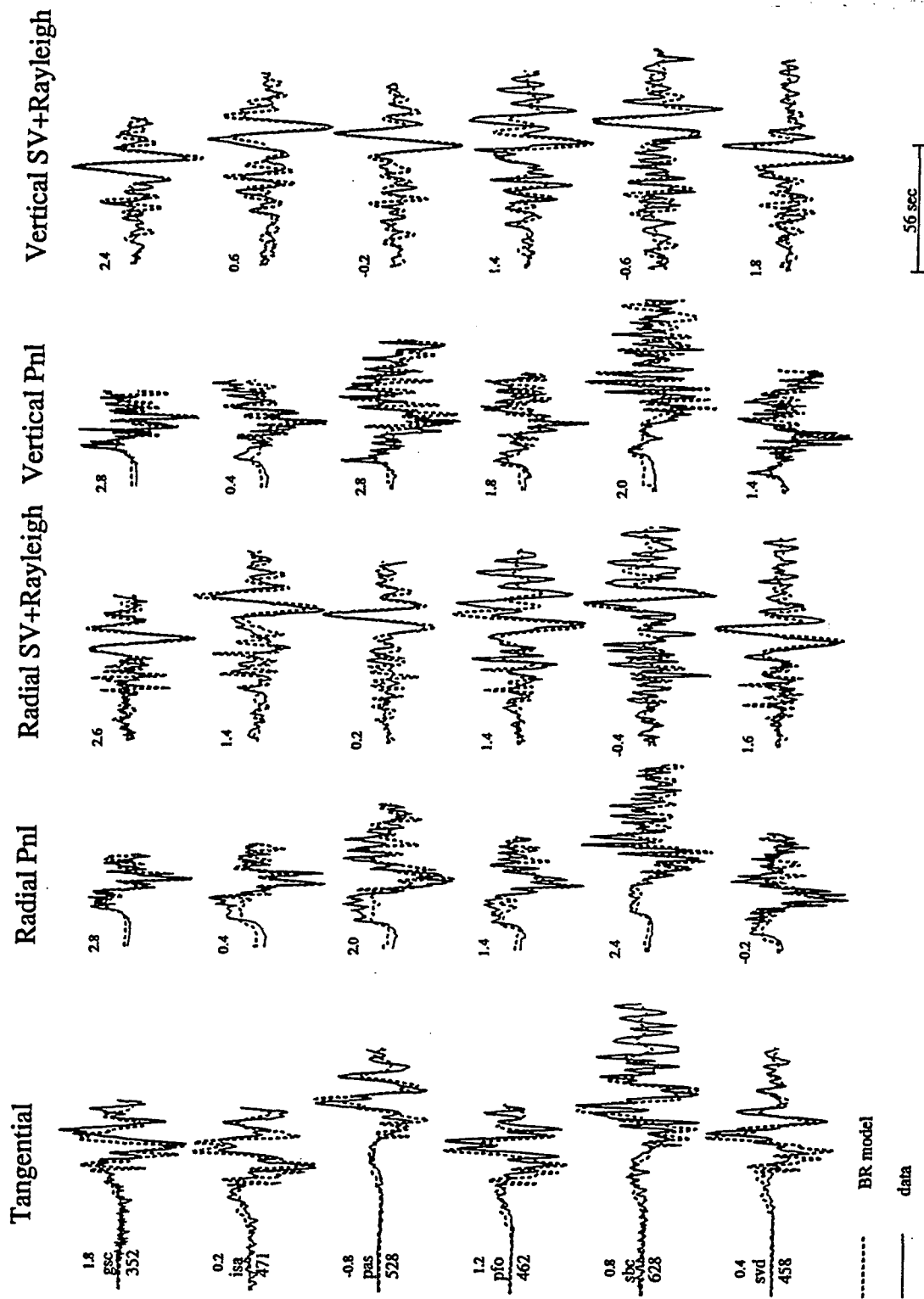
Figure 3. Comparison between data and synthetics (2-layer model) for a Utah event, Song and Helmberger (1995). The P-velocities are 3.6, 5.8, 7.85; the S-velocities are 2.05, 3.57, 4.53; thicknesses are 2.5 and 32.5 km. The numbers indicate the relative shift of the synthetic to align with data.
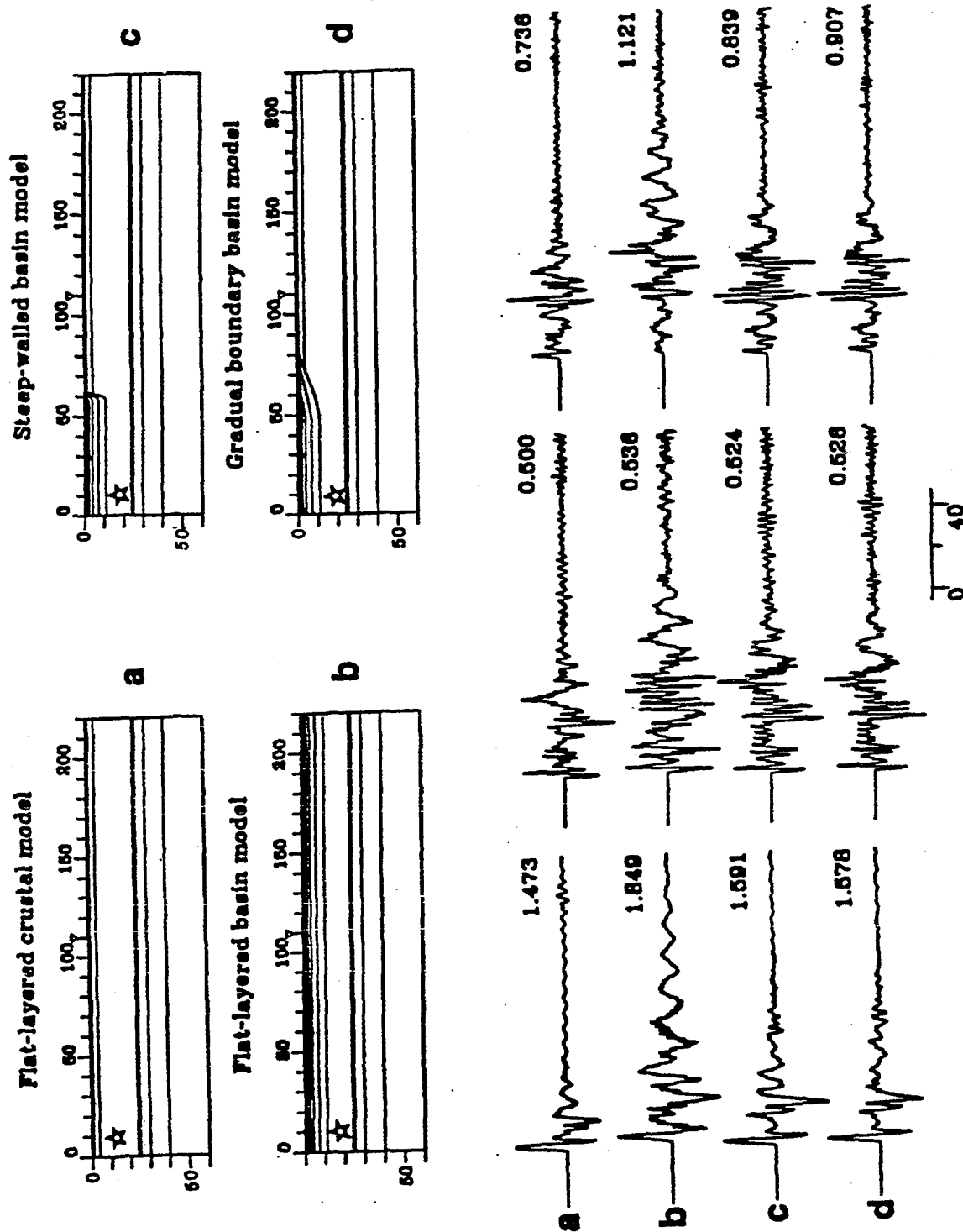
Figure 4. Four crustal models (upper panel) and corresponding three-component seismograms (lower panel) computed with finite difference method, assuming a strike-slip source. The source location is indicated by a star and the receiver is indicated by a triangle Δ = 100 km, after Song et al. (1995).

66

Figure 5. Comparison of synthetics generated by two finite-difference codes for a set of stations crossing the edge of a basin (actually Los Angeles basin, Scrivner & Helmberger, 1994). Those on the left generated the entire distance by FD (Vidale & Helmberger) while the profile on the right contains the results of interfacing the analytical solution with FD at the box boundary (Wen & Helmberger, 1995).

67

DISCRIMINATION OF EARTHQUAKES AND EXPLOSIONS IN SOUTHERN RUSSIA USING REGIONAL HIGH-FREQUENCY DATA FROM IRIS/JSP CAUCASUS NETWORK

W.-Y. Kim, V. Aharonian, G. Abbers[1], A. Lerner-Lam[2] and P. Richards[2]
Lamont-Doherty Earth Observatory of Columbia University, Palisades, NY 10964
[1] Department of Geology, University of Kansas, Lawrence, KS 66045
([2] also, Department of Geological Sciences, Columbia University)

Abstract

High-frequency regional records from small earthquakes (magnitude < 4.5), and comparable magnitude chemical explosions, are analyzed to find a reliable seismic discriminant in the Northern Caucasus region in Southern Russia. About 130 digital, vertical-component seismograms recorded during 1992 by the IRIS/JSP North Caucasus Network operated by Lamont-Doherty Earth Observatory since 1991 in the distance ranges 10 to 250 km are used. Mean *Pg/Lg* spectral ratios in the high frequency band 10 – 20 Hz are about 1 and 3 for earthquakes and explosions, respectively, in the Northern Caucasus region, Southern Russia. These ratios are much higher than those observed in tectonically stable eastern U. S. where Kim et al. (1993) reported the mean *Pg/Lg* ratios of 0.5 and 1.25 for earthquakes and explosions, respectively in the similar high frequency band.

We find that the high-frequency *Pg/Lg* spectral amplitude ratio in the frequency band 10 – 20 Hz is an adequate discriminant for classifying these events. A linear discriminant function analysis indicates that the *Pg/Lg* spectral amplitude ratio method provides discrimination power with a total misclassification probability of about 7%. The *Pg/Lg* spectral amplitude ratio method we used is sufficiently reliable and robust that it can be used in discriminating chemical explosions (especially numerous mining and quarry blasts) from small regional earthquakes in the routine analysis of regional earthquake monitoring networks.

We are evaluating the *P/Lg* spectral ratio and other potential discriminants using three component regional records. A key to our use of three component regional records for discrimination analysis is correction of the free surface interaction, which allows direct comparison between the *P-*, *SV-* and *SH*-wave amplitudes and reveals clear radiation characteristics from the source.

Keywords: regional crustal waves, seismic discrimination, Caucasus region

OBJECTIVE

Main objective of this research is to improve our knowledge of seismic sources and structure in central Asia including Iran, Caspian Sea and Caucasus Mountains, by analyzing regional high-frequency signals recorded at North Caucasus Network and other regional networks.

Our goals are; 1) to characterize seismic sources in the region and to evaluate reliable seismic discriminants, 2) to determine attenuation of regional phases and to map propagation efficiencies of regional phases along various paths, 3) to determine crust and uppermost mantle velocity structure beneath the Caucasus Network and to locate accurately small events in the region.

Results of our work assist in the monitoring of small seismic events at regional distances for CTBT monitoring.

RESEARCH ACCOMPLISHED

The discrimination of small earthquakes from large chemical explosions (from mines and quarries) based on seismic signals recorded at regional distances (10 – 1000 km) is an important issue facing numerous regional seismic networks. The seismic discrimination problem becomes especially severe in an area with poorly known seismicity such as the southern Russia (Fig. 1). It would be extremely useful to have a reliable and robust criterion that could be used to discriminate earthquakes from explosions in the context of global seismic monitoring.

Most of the previous work on seismic discrimination has focused on separating large underground nuclear explosions from earthquakes in the context of a future comprehensive test ban (e.g., Pomeroy et al., 1982; Evernden et al., 1986; Taylor et al., 1989). In most earlier studies, data available for discrimination analyses were limited to frequencies below 10 Hz, and previous work on regional signals from earthquakes and explosions in the western U. S. suggested that P and S waves from earthquakes have higher frequency content than signals from explosions (e.g., Murphy & Bennett, 1982; Bennett & Murphy, 1986; Taylor et al., 1988; Chael, 1988). Kim et al. (1993) reported that the mean Pg/Lg spectral ratios in the band 1 – 25 Hz are about 0.5 and 1.25 for earthquakes and explosions, respectively, in the eastern U. S. ($\Delta \approx 10$ - 610 km). Further, they found that the high-frequency Pg/Lg spectral amplitude ratio in the frequency band 5 – 25 Hz was an adequate discriminant for classifying these events. In the eastern U. S., the Pg/Lg spectral amplitude ratio method provides discrimination power with a total misclassification probability of about 1% (Kim et al., 1993).

In the following sections, we report the results of our evaluation of Pg/Lg spectral ratio discriminant for the regional earthquakes and explosions in Northern Caucasus region, Southern Russia using digital seismograms recorded at IRIS/JSP North Caucasus Network (Fig. 1).

Characteristics of Regional Seismograms in Southern Russia

A typical vertical-component seismograms from a small earthquake are plotted in a group velocity section in Figure 2. The first P and S onset arrives with group velocities of about 5.8 km/s and 3.2 km/s, respectively at a distance of about 60 km. This indicates very low P- and S-wave speeds in the region around the North Caucasus Network. Further, strong S to P converted phases (Sp) observed at stations KUB and MIC suggest the presence of a relatively thick sedimentary layer beneath these stations (see Fig. 2).

Frequency content of regional seismic signals from an earthquake and a quarry blast is

examined using spectrograms (frequency-time display; Fig. 3). Both events are at a comparable distance ranges from KIV ($\Delta \approx 65$ km). The earthquake record is characterized by a strong S wave amplitude at low frequencies (below about 7 Hz), and P and S waves with comparable amplitude at higher frequencies (10-15 Hz). The spectrogram of the quarry blast record shows predominant P wave energy over a wide frequency band 3 - 20 Hz and a weak S waves in this band (Fig. 3). The spectrogram of the earthquake record shows random distribution of seismic wave energy, while the spectrogram of the ripple-fired quarry blast record shows clear spectral banding due to source multiplicity. Time series of these events also show clear differences between the earthquake and explosion records (Fig. 3).
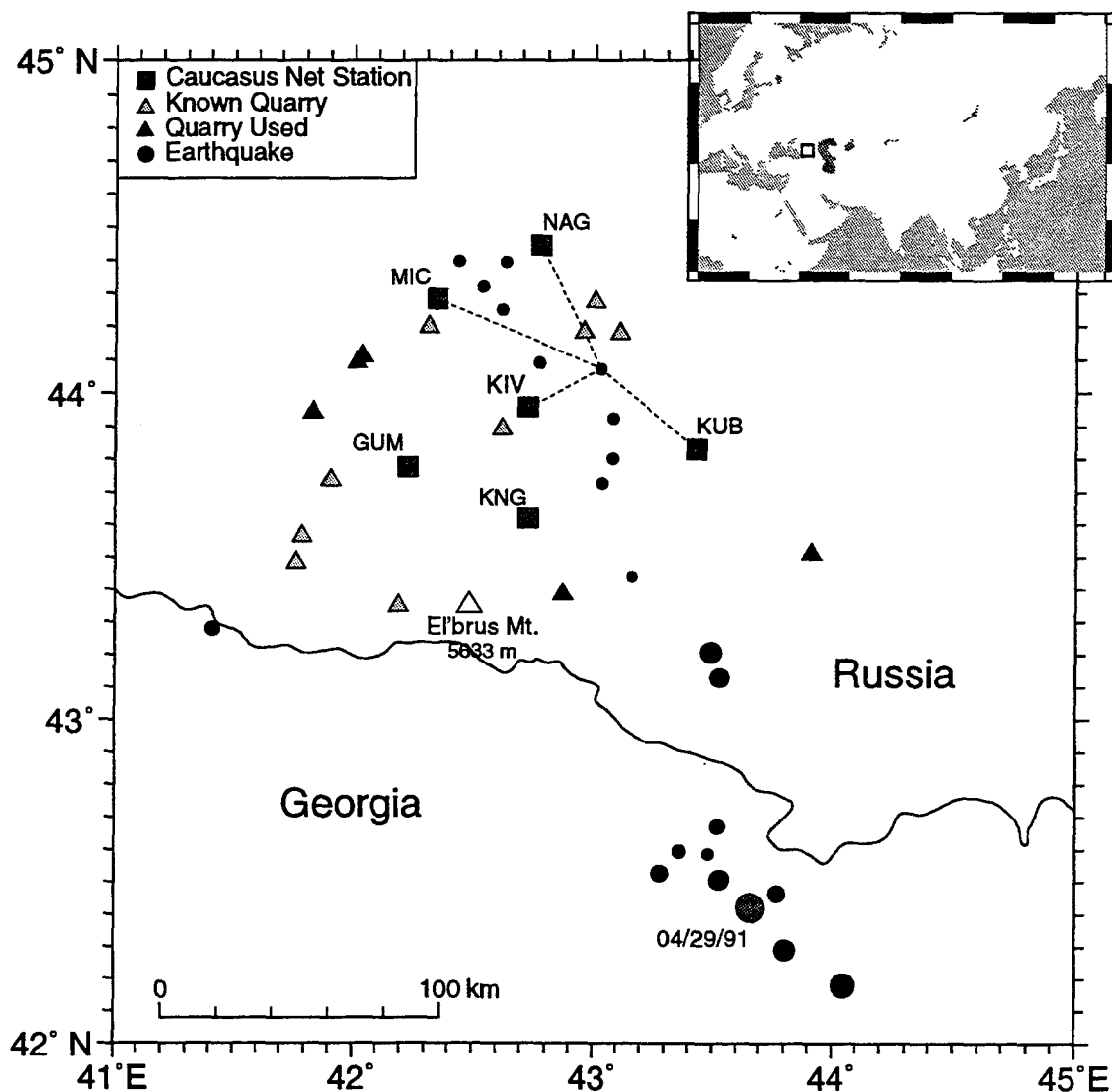
Fig. 1. Locations of earthquakes (*solid circles*), mines and quarries identified and used in this study (*solid triangles*), other known quarries (*open triangles*) and Caucasus Network stations (*shaded squares*). Circle size is proportional to the magnitude of the earthquakes.

03/07/92 03:06:42.8, 44.072°N, 43.028°E, h=20 km, Local Earthquake, Caucasus region
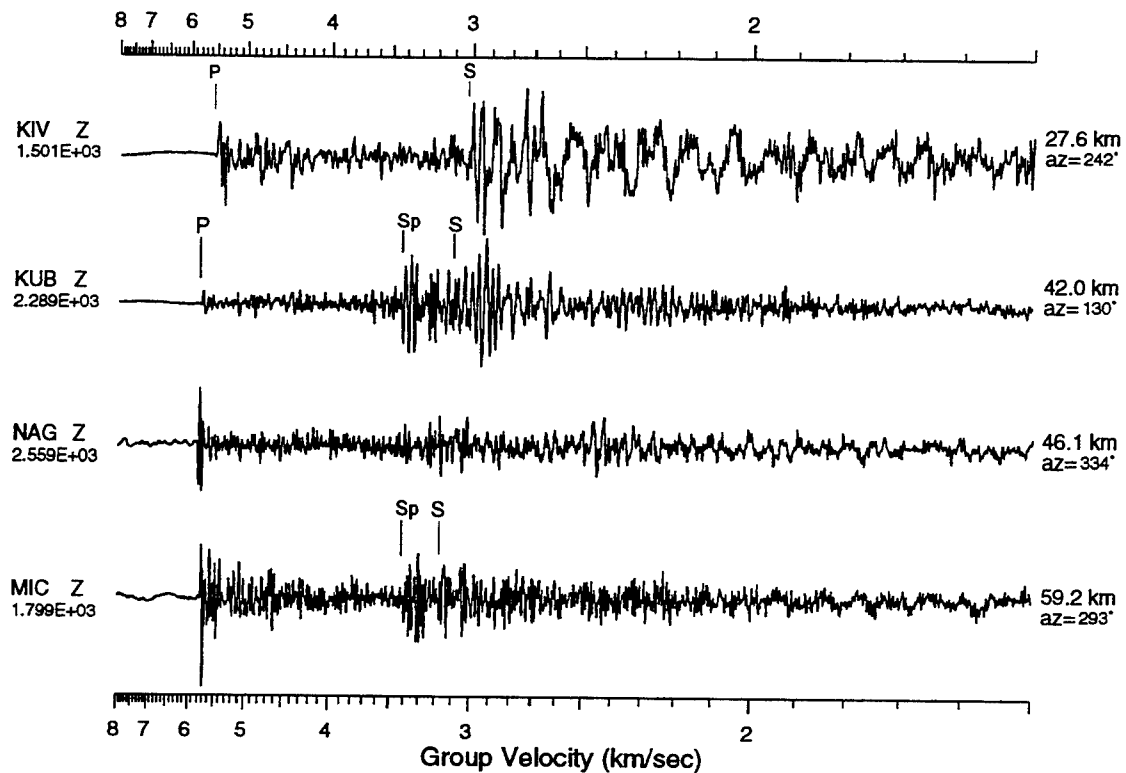
Fig. 2. A group velocity record section of typical vertical-component seismograms from a small local earthquake recorded at the Caucasus Network. Notice strong *P* to *S* converted phases (*Sp*) at stations KUB and MIC.
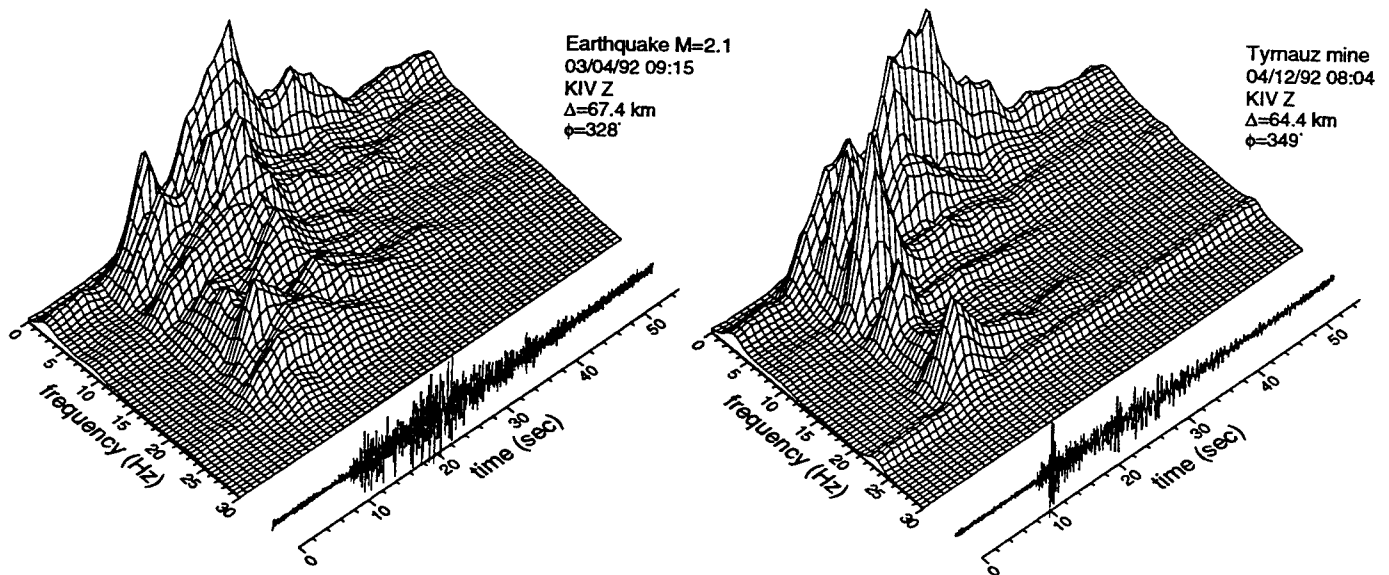
Fig. 3. A comparison of regional seismic signals from an earthquake and a ripple-fired quarry blast. Spectrogram of the earthquake record (*upper panel*) shows random distribution of seismic wave energy, while the spectrogram of the quarry blast record (*lower panel*) shows clear spectral banding due to source multiplicity (ripple-firing). Note that a spectral band at about 22 Hz is due to noise signal, since it appears even before the first arrival *P* wave.

71

Our observations of high-frequency (1-25 Hz) regional signals from earthquakes and explosions in the southern Russia may be summarized as: 1) P waves from the explosions have higher frequency content than S waves, while S waves from the earthquakes have comparable frequency content as P waves (see Fig. 3); 2) P and S waves from known quarry blasts show frequency banding due to spectral modulation from source multiplicity; 3) records from explosions often show a strong Rg phase out to about 100 km.

These examples indicate that high-frequency seismograms show distinctively different patterns in the spectral content of the P and S signals between earthquakes and explosions. Such high-frequency seismograms suggest that the Pg/Lg spectral amplitude ratio can be made the basis of a useful discriminant. The overall differences in frequency content of the P and S waves from different source types are the basis of our Pg/Lg spectral amplitude ratio discriminant.

We report our measurements of the Pg/Lg spectral amplitude ratio, using high-frequency, vertical-component digital seismograms from earthquakes and chemical explosions recorded by the Caucasus Network and we evaluate its discrimination capability.

Data

We first present the analysis of digital seismograms from 21 explosions (presumably quarry blasts) and 21 earthquakes to obtain a specific discriminant, which later is applied to other events. Most of the earthquakes are in the magnitude range 1 to 4 and are reported by the Joint Seismic Program Center (JSPC) and the U.S. Geological Survey (PDE). Events are selected to sample a wide range of propagation paths around the network. All quarry blasts are from three known quarry sites plus a previously unknown site identified in this study by calculating spectrograms. Locations of mines and quarries in the region are depicted in Figure 1.

Only explosions for which we had information about the blast characteristics (usually blast time and location) or the blasts whose signals were clearly identified as quarry blast are included. Blast time is one of the most practical discriminant for large chemical explosions. About 87% of events, 71 out of 82 events, located near the Tyrnauz mine are clustered at two peak times (10 am & 4 pm local time) while all events located near the Ust-Djeguta quarry are clustered at 2 pm local time. Distance ranges of the data are 5 to 200 km with means of 120 km and 100 km for earthquakes and explosions, respectively.

Pg and Lg signals are windowed with a Gaussian weighting function centered at group velocities around 5.6 km/s and 3.2 km/s, respectively (see Fig. 2). Digital seismograms from the Caucasus Network are sampled at 60 samples/sec and instrument responses of the stations are nearly flat to ground velocity in the frequency band 0.2 to 24 Hz (-3 db level). The Pg and Lg signals, weighted by the Gaussian functions, are fast Fourier transformed. The resulting amplitude spectra are smoothed with another Gaussian function having $\sigma = 1$ Hz and are re-sampled at every 2 Hz interval from 2 to 24 Hz. Noise analyses indicate that the signal-to-noise (S/N) ratios are quite high in most of the records, but in some cases the signals fall to the background noise level above about 20 Hz. The S/N ratio becomes less than 2 at about 15 Hz for records from distant events ($\Delta > 150$ km). The $\log_{10}(Pg/Lg)$ spectral ratios at discrete frequency points are obtained for each record. Network averaged $\log_{10} (Pg/Lg)$ ratios are then obtained for each event by averaging the discrete frequency values from all stations. Earthquake and explosion populations are well separated in the frequency band 10 to 24 Hz. At frequencies lower than 10 Hz, there is some overlap. Thus, the frequency band 2 – 20 Hz is used in discrimination analysis.

Applications of Discriminant Analysis

To test the discriminant power of the high-frequency *Pg/Lg* spectral ratio, we performed multivariate discriminant analysis on $\log_{10}(Pg/Lg)$ spectral ratios for the data set of earthquakes and explosions. Each training group of 21 events (i.e. 21 explosions, 21 earthquakes) is described by a matrix of 6 rows [($\log_{10}(Pg/Lg)$ at 2 Hz frequency intervals from 10 to 20 Hz] and 21 columns. Details of the linear discriminant function is given for example, Seber (1984) and Kim et al. (1993).

High-frequency network averaged Pg/Lg ratio: The sample data sets consisting of 21 earthquakes and 21 explosions were analyzed using the linear discriminant function. For each event, network averaged $\log_{10}$ *(Pg/Lg)* ratios at frequencies of 10, 12, 14, 16, 18 and 20 Hz correspond to the variables r_1, r_2, r_3, r_4, r_5 and r_6. The linear discriminant function obtained is

$$D(r) = 5.608 + 1.459\, r_1 - 5.140 r_2 - 5.123 r_3 - 0.217 r_4 + 11.773 r_5 - 20.432 r_6$$

and the Mahalanobis D-squared measure is $\Delta^2 = 8.640$. Assuming equal prior probabilities for the two groups, we assign event **r** to the earthquake class if $D(r) > 0$. Applying this rule to the earthquake and explosion data, we find that all events are classified correctly and the misclassification probability is 0.071. Values of $D(r)$ may be called the discriminant score and are plotted in Fig. 4 with respect to the mean $\log_{10}$ *(Pg/Lg)* spectral amplitude ratio of each event. Vertical lines in the figure denoted as Eq and Ex are the projection of the multivariate mean of the earthquake and explosion populations, respectively. The vertical line, D_0, is the line $D(r) = 0$, which serves to classify the events when the *a priori* probability of the two populations is the same. The distance between Eq and Ex is the Mahalanobis D-squared measure of distance between two populations. It is shown in Figure 4 that all the earthquake records from various paths in the Northern Caucasus, southern Russia have a mean *Pg/Lg* spectral ratio of about 1, while the explosion records show a mean of about 3. The F statistic for this analysis indicates that there is a statistically significant difference in *Pg/Lg* spectral ratios of signals from the two groups of events.

Discussion and Conclusions

We find that *Pg* waves from explosions have stronger high frequency content than *Lg* waves over the broad high-frequency band 10 – 20 Hz at regional distances in southern Russia near Kislovodsk: the mean ratio for 64 explosion records is about 3. The opposite is true for signals from earthquakes with magnitudes 1–4: the mean *Pg/Lg* ratio for 69 earthquake records in the frequency band 10–20 Hz is about 1. These mean *Pg/Lg* ratios are much higher than the ratios observed in the eastern U. S., where the ratios are 0.5 and 1.25 for the earthquakes and explosions, respectively (Kim et al., 1993). The observed high *Pg/Lg* ratios may suggest stronger attenuation of *S* waves in southern Russia than in the eastern U. S. Very low near surface *S* wave velocity may channel *SV* waves from vertical component into radial component.

The *Pg/Lg* spectral amplitude ratio in the frequency band 10–20 Hz provides discrimination power with a total misclassification probability of about 7%. In a lower frequency band, 2-10 Hz, *Pg/Lg* ratios show poor results and the separation between explosions and earthquakes is less

clear. The *Pg/Lg* ratio is robust as a discriminant to the extent that there is cancellation of spectral reinforcement due to source multiplicity as well as other characteristics, such as event size, corner frequency, some effects of focal depth, and instrument response.

We have shown that the *Pg/Lg* ratio is an adequate discriminant for explosions from earthquakes (magnitude smaller than 4.5) in the southern Russia. The stability of the *Pg/Lg* ratio in discriminating ripple-fired explosions from small regional earthquakes is significant for seismic monitoring in southern Russia. Our results demonstrate the importance of data at frequencies up to at least 20 Hz.

One basis for the empirical success of our proposed high-frequency *Pg/Lg* ratio method is that, if selected spectral amplitude reinforcement occurs at the source (as is the case for ripple-fired blasts), it will affect both early *P* phases as well as later-arriving *Lg* phases. Such spectral scalloping will largely cancel in the ratio we have used. The ratio is robust as a discriminant
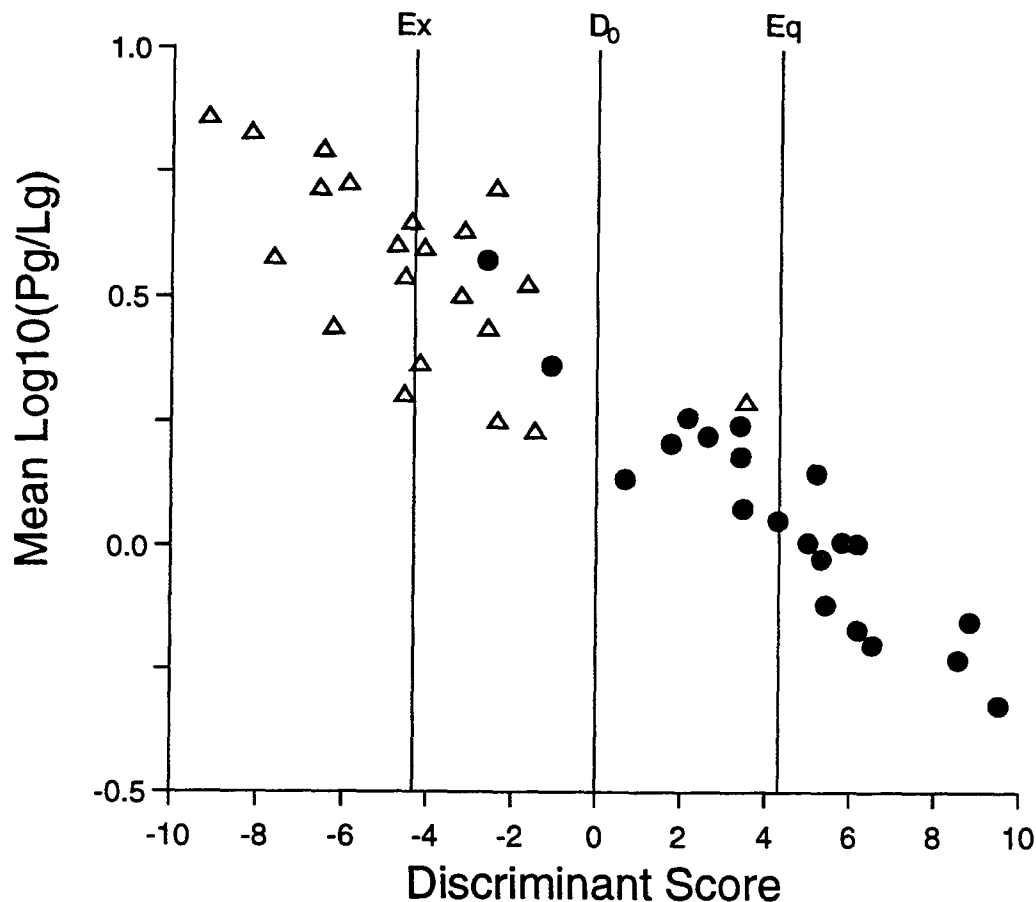
Fig. 4. Discriminant scores of earthquakes (*shaded circles*) and explosions (*triangles*) of the sample data are plotted with their mean network averaged $\log_{10}(Pg/Lg)$ ratios. Note that two populations are also separated by mean $\log_{10}(Pg/Lg)$ ratio ≈ 0.25. Vertical lines denoted as **Ex** and **Eq** are the projection of the multivariate mean of the earthquake and explosion population, respectively. The vertical line D_0 is the classification line. Two earthquakes and an explosion are incorrectly classified and the total misclassification probability is 7.1 %.

to the extent that there is cancellation of other characteristics, such as event size, corner frequency, some effects of focal depth, and instrument response.

We have used only vertical-component seismograms for the discrimination analysis, however inclusion of horizontal components records may improve discrimination power of regional high-frequency records. We observed that *Pg/Lg* ratio of many earthquake horizontal component records show stronger contrast than vertical components. We are working on to include both horizontal component records into discrimination analysis.

It has been reported by some researchers (R. Blandford, person. comm., April, 1994) that correction of anelastic attenuation for both the *P* and *S* signals may enhance the discriminant power of *Pg/Lg* ratio discriminant. However, we believe that it is extremely difficult to correct the signals for attenuation with confidence, at least for the regions with poorly known seismicity.

RECOMMENDATIONS AND FUTURE PLANS

Removal of free surface effect on regional records

Although, high-frequency regional signals on vertical-component show reasonable discrimination power for classifying earthquakes from explosions, use of 3-component records has great potential to discriminate different types of source. Recently, Kennett (1991) showed that interpretation of the regional signals on 3-component records can be facilitated by removing free surface interaction of the incoming wavefield. Kennett (1991) demonstrated that a set of approximate free surface correction operators can be formed to remove the free surface effects over the slowness bands for the main regional phases (see also Aki and Richards, page 190).

An example 3-component records from an underground nuclear explosion recorded at Borovoye (BRVK), Kazakhstan are shown in Figure 5. The rotated seismograms (Z, R, T) show that the *P* waves on Z and R components as well as *Lg* waves on T-component have nearly identical peak amplitude (Fig. 5). However, when the free surface effects are removed from the rotated seismograms by successively applying free surface correction operators appropriate for major regional phases, *P*, *Sn* and *Lg*, the recovered incident wavevector estimates allow us to make direct comparison between the *P*-, *SV*- and *SH*-wave amplitudes along the trace.

The composite incident wavevector traces shows that the *P* waves are mainly on *P*-wavevector component, while *S* waves (*Sn* and *Lg*) are dominantly on *SV*-wavevector component (Fig. 5), hence the amplitudes of major crustal phases reveal clearer radiation characteristics from the source. In particular, the amplitude ratio of *SV* to *SH* in the regional *S* waves clearly indicates the signal being generated by an explosion source.

A very useful result of the free surface correction is that we can make direct comparison between the *P*-, *SV*- and *SH*-wave amplitude in a particular group velocity window and so get closer to the radiation characteristics from the source. This is of potential significance for discriminating different types of sources.

We are working to form a set of simple free surface correction operators suitable for regional signals in the Caucasus region and to evaluate *P/Lg* spectral ratios and other potential discriminants using three component regional records.
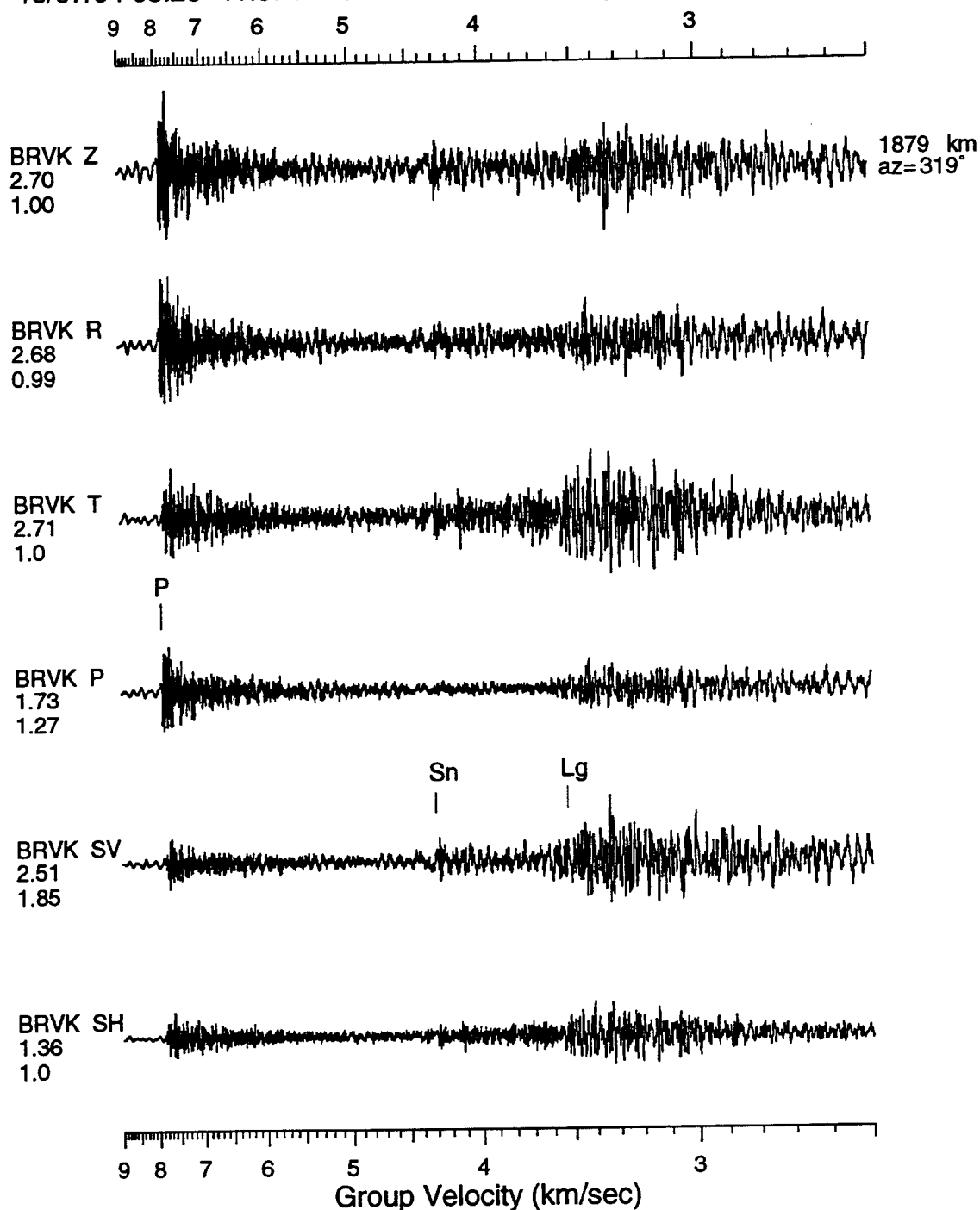
Figure 5. (*Upper three traces*) Rotated 3-component records from an explosion in Lop Nor test site (Z, R and T). The *S* waves are dominantly on T-component, while *P* waves are on Z- and R-component; (*Lower three traces*) Composite incident wavevector component traces (*P*, *SV* and *SH*) produced by applying free surface correction operators successively along the trace. Note that radiation characteristics of the source are more clearly depicted on the decomposed incident wavevector components. Amplitude ratios, Z/T, R/T and P/SH, SV/SH are indicated.

Acknowledgments

References

Aki, K. and P. G. Richards (1980). *Quantitative Seismology: Theory and methods*, vol. 1, W. H. Freeman and Co., 1980.

Bennett, T. J. and J. R. Murphy (1986). Analysis of seismic discrimination capabilities using regional data from western United States events, *Bull. Seism. Soc. Am.*, **76**, 1069-1086.

Chael, E. P. (1988). Spectral discrimination of NTS explosions and earthquakes in the southwestern United States using high-frequency regional data, *Geophys. Res.Lett.*, **15**, 625-628.

Davis, J. C. (1986). *Statistics and Data Analysis in Geology*, 2nd ed., John Wiley & Sons, Inc., New York, 646pp.

Evernden, J. F., C. B. Archambeau and E. Cranswick (1986). An evaluation of seismic decoupling and underground nuclear test monitoring using high-frequency seismic data, *Review Geophys.*, **24**, 143-215.

Kennett, B. L. N. (1991). The removal of free surface interactions from three-component seismograms, *Geophys. J. Int.*, **104**, 153-163.

Kim, W. Y., D. W. Simpson and P. G. Richards (1993). Discrimination of regional earthquakes and explosions in eastern United States using high-frequency data, *Geophys. Res. Lett.*, **20**, 1507-1510.

Murphy, J. R. and T. J. Bennett (1982). A discrimination analysis of short-period regional data at Tonto Forest Observatory, *Bull. Seism. Soc. Am.*, **72**, 1351-1366.

Pomeroy, P. W., W. J. Best, and T. V. McEvilly (1982). Test ban treaty verification with regional data – A review, *Bull. Seism. Soc. Am.*, **72**, S89-S129.

Seber, G. A. F. (1984). *Multivariate Observations*, John Wiley & Sons, Inc., New York, 686pp.

Taylor, S. R., N. W. Sherman and M. D. Denny (1988). Spectral discrimination between NTS explosions and western United States earthquakes at regional distances, *Bull. Seism. Soc. Am.*, **78**, 1563-1579.

Taylor, S. R., M. D. Denny, E. S. Vergino and R. E. Glaser (1989). Regional discrimination between NTS explosions and western U.S. earthquakes, *Bull. Seism. Soc. Am.*, **79**, 1142-1176.

DISCRIMINATION OF EARTHQUAKES, EXPLOSIONS, AND MINING TREMORS USING THE EMPIRICAL GREEN'S FUNCTION METHOD

Y. Li, W. Rodi and M. N. Toksöz

Earth Resources Laboratory
Department of Earth, Atmospheric, and Planetary Sciences
Massachusetts Institute of Technology, Cambridge, MA 02139

ABSTRACT

Using the empirical Green's function (EGF) method, we have estimated source time functions for earthquakes, industrial blasts, nuclear explosions, and mining tremors covering the magnitude range 0.9 – 6.6. The results show that, for events with magnitudes less than 2.5 or greater than 4.5, the time duration of the source time function can discriminate earthquakes from explosions. For large magnitude events source duration is longer for earthquakes than explosions, but at small magnitudes explosions have longer duration. For the remaining magnitude range (2.5 to 4.5) the earthquake, explosion and mining tremor populations overlap in the source duration vs. magnitude plane. However, the source time functions themselves display features that are indicative of event type, such as source directivity, spall phases, and multiple pulses in industrial blasts and mining tremors. Therefore, we conclude that source time functions inferred by the EGF method are potentially useful for regional event discrimination under a CTBT, and we recommend that further work be done to develop effective EGF-based discriminants for events in the magnitude range 2.5 to 4.5.

OBJECTIVE

The objective of this work is to develop discriminants for small events based on the empirical Green's function (EGF) method. The EGF method yields an estimate of the source time function (STF) of an event relative to that of a smaller, reference event (the "EGF event"). The result is referred to as the *relative* source time function (RSTF) of the larger event and can be interpreted as a scaled version of its STF when the EGF event has similar location and focal mechanism. The advantage of the EGF approach is that, by using the waveforms of the smaller event as approximate Green's functions, it does not require detailed 3D earth models and computation of propagation effects between source and receiver.

The focus of the research reported here is events having magnitudes less than 5 and detectable at regional distances. The characterization and discrimination of such events is crucial to achieving the goals of the Comprehensive Test Ban Treaty.

RESEARCH ACCOMPLISHED

In previously reported work (Toksöz et al., 1993; Li et al., 1994, 1995) we applied the empirical Green's function method to teleseismic and regional waveform data from moderate to large ($m_b > 5$) earthquakes and explosions in central Asia to test whether the EGF method was a useful technique for characterizing seismic sources. The results showed that, when suitable event pairs are available, the EGF method reliably determines the RSTF of $m_b > 5$ events and reveals important details about their energy release processes. For example, the RSTF of some of the explosions studied displayed clear indication of a spall phase following the main energy pulse. It was also seen that a very simple property of the RSTF—its time duration—discriminated earthquakes and explosions of similar magnitude. Since the rupture process of moderate and large earthquakes is generally more complex than the energy release from a nuclear explosion, the RSTF time durations of the central Asian earthquakes analyzed were about a factor of 10 longer than those of the nuclear explosions (Figure 1).

We turn our attention now to events having magnitudes below 5. To apply the EGF method to such events it is necessary to use regional or local waveform data. In the first example, we apply the EGF method to small quarry blasts at Kaiser Quarry in northern California recorded at station CCYM. Both blasts (891028-1830 and 891031-1915) were assigned a body-wave magnitude of 0.9. We used a nearby smaller event (891031-1946) with magnitude 0.6 as the EGF event for each. The blasts occurred about 25 km south of station CCYM, and the spatial separation among the three is about 50 m. Figure 2 shows the RSTFs of the two M0.9 blasts. We see that they have different source time functions. The RSTF of the top event can be approximated as a simple pulse with source duration less than 0.1 s. The bottom event, in contrast, is interpreted as a multiply detonated blast with three distinct pulses. The total source duration of the bottom blast is 0.3 s, at least three times longer than the simple blast.

Figure 3 shows further examples of multiply detonated blasts. The events in this case are two construction blasts (labeled 920409-0956 and 920702-0405) located near Deer
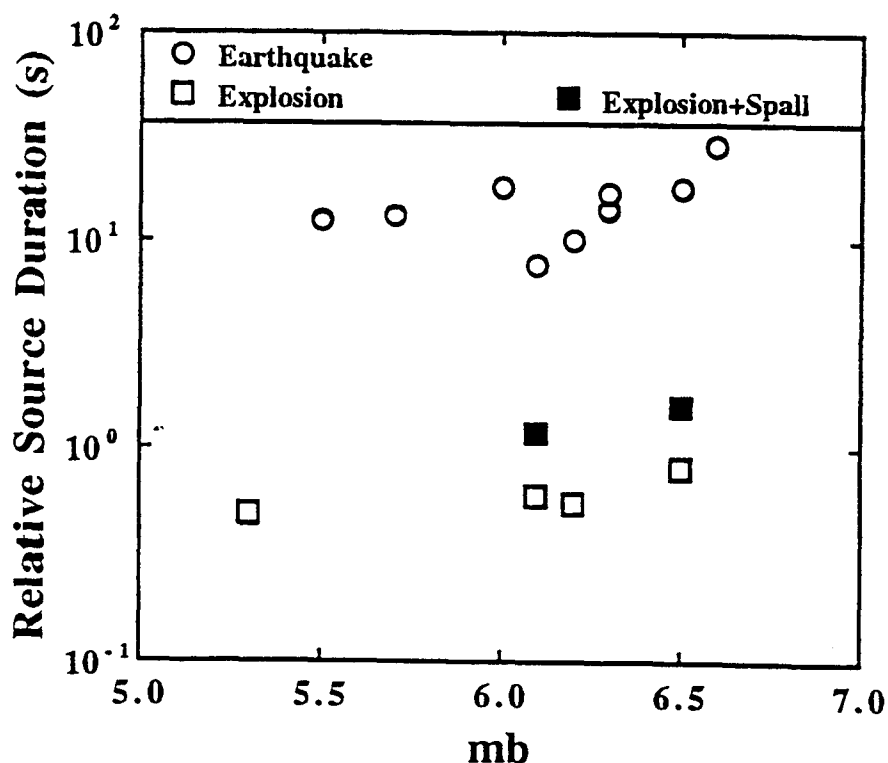
Figure 1: Comparison of source durations of earthquakes and nuclear explosions in central Asia. Source duration of each event was measured from its relative source time function, retrieved using the EGF method. (From Li et al., 1995.)

Island, Boston. The two events have magnitudes of 2.6 and 2.4, respectively. Taking a smaller, nearby blast with M=2.1 as the EGF event, we determined the RSTFs of the two larger blasts using waveform data recorded at station WFM of the M.I.T. seismic network, about 50 km from the epicenters. In Figure 3 we see that the top event has two distinct pulses with total duration of about 0.25 s, while the bottom event consists of four continuous pulses with a total duration of 0.75 s.

These examples (Figures 2 and 3) show that the source duration of industrial blasts is often controlled by shooting practices, such as multiple detonation and ripple firing. This may explain why blasts differing by about 1.5 magnitude units (Deer Island vs. Kaiser Quarry examples) do not differ greatly in source duration. The differences seen between the two locations are comparable to the variation within each location (about a factor of 3). Further, the time durations of the blasts in each example are longer than those of typical earthquakes of comparable magnitude. A typical M=3 earthquake in New England, for example, has a source duration of only about 0.1 to 0.2 s.

In the next example (Figure 4) we look at three nuclear explosions at the Nevada Test Site: JUNCTION (M5.4), MINERAL QUARRY (M4.7) and DISKO ELM (M4.2). We determined their RSTFs using smaller explosions as the respective EGF events, as labeled on the figure. The RSTFs were obtained from regional data from Southern California

RSTFs of Quarry Blasts in Northern California
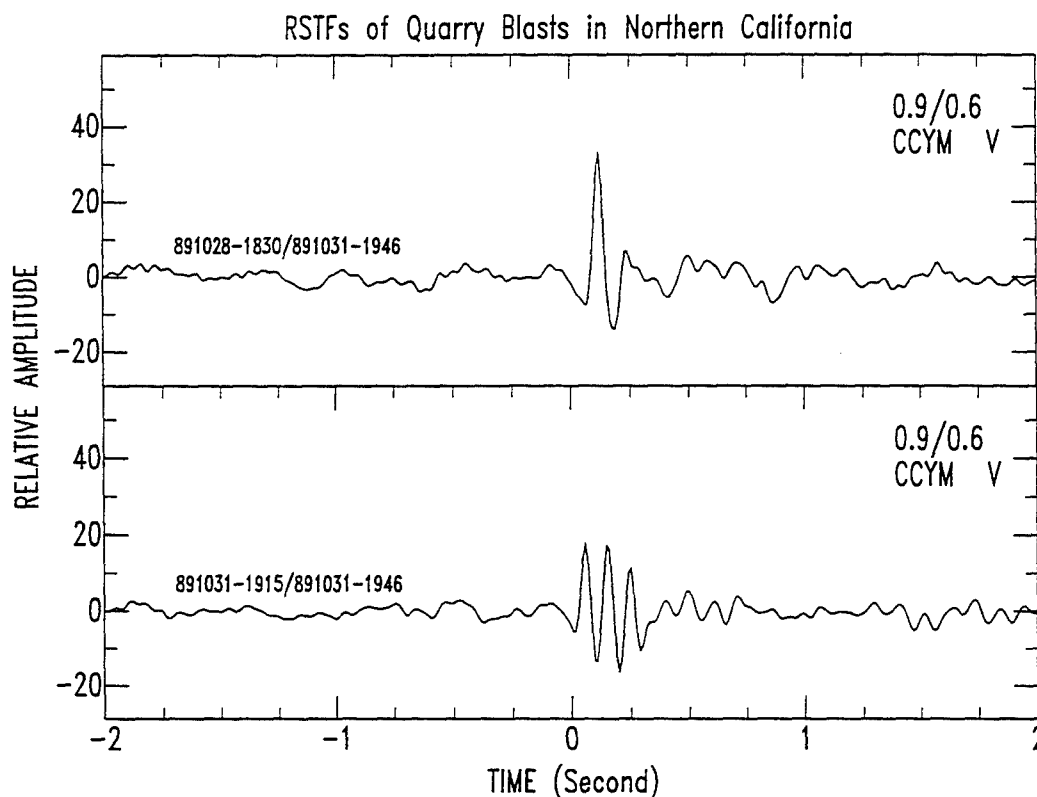
Figure 2: Estimated relative source time functions (RSTFs) of two small blasts (M=0.9) in Kaiser Quarry, California. Both RSTFs were determined relative to the same EGF event. The date and time of each blast and the EGF event are labeled on the left part of each frame. The numbers on the right are the magnitudes of the event and EGF event.

Earthquake Center stations PTQ and BRG, located between 450 and 500 km from NTS. The RSTF of explosion MINERAL QUARRY (middle of Figure 4) is a relatively simple pulse with a source duration of 0.4 s. The RSTF for JUNCTION has a complex structure comprising two pulses. The width of the first pulse is about 0.35 s and the total duration of the event is about 0.65 s. The RSTF of DISKO ELM also has two pulses with a total duration of 0.35 s. Thus, including secondary pulses, the source durations of these explosions increase with magnitude and are significantly shorter than those determined by Li et al. (1995) for larger nuclear explosions in central Asia. As in the case of the central Asia explosions, we interpret the secondary pulses of the NTS explosions (Figure 4) as spall phases.

Next, we examine the source time function of an earthquake with magnitude somewhat smaller than the NTS explosions just considered. The earthquake is a M3.7 event that occurred in central Massachusetts on 2 October 1994. Using a M3.3 aftershock as the EGF event, we determined an RSTF at each of 17 stations varying in epicentral distance from about 60 to 450 km. Figure 5 shows the RSTF from each station, ordered by azimuth from the epicenter. The bottom trace is a stacked RSTF obtained by sum-

RSTFs of Blasts near Deer Island, Boston
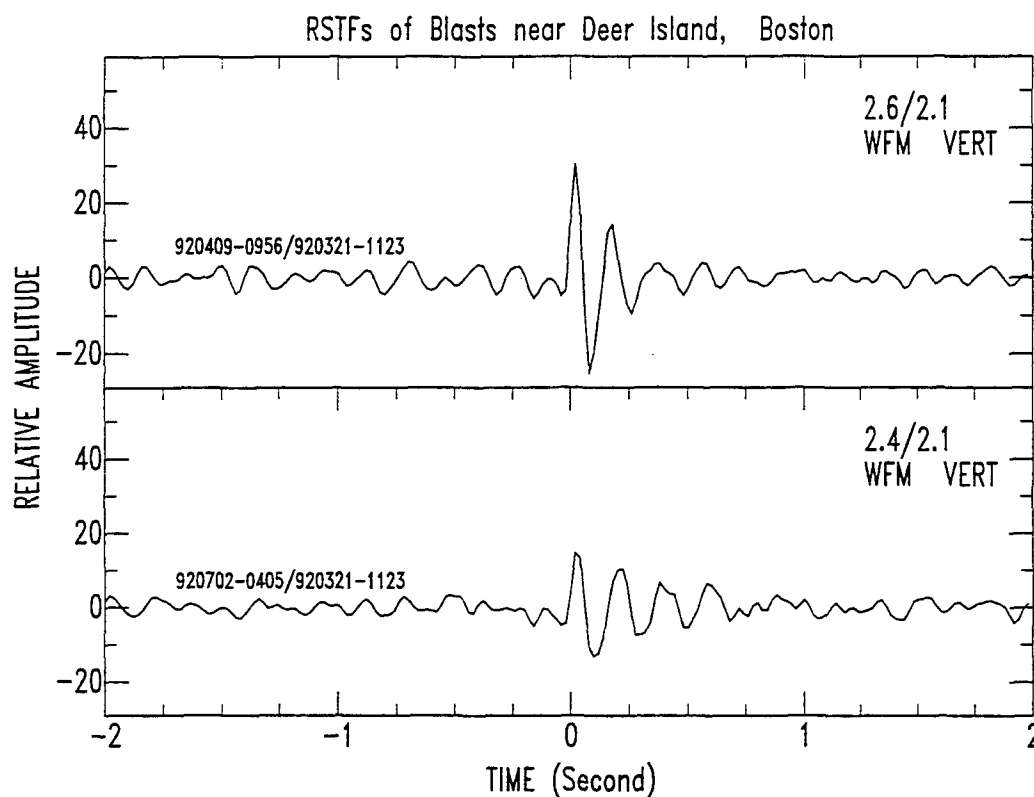
Figure 3: RSTFs of two construction blasts near Deer Island, Boston. The events have magnitudes 2.6 and 2.4, respectively. Note the multiple detonations of the events.

ming the individual station estimates. The stacked RSTF comprises a single pulse with a width of approximately 0.15 s. The individual station RSTFs show evidence of source directivity, i.e. the time duration and amplitude vary systematically with azimuth. From this variation we infer that the rupture propagated toward the southwest.

Our final example, shown in Figure 6, studies six mining tremors in the Lubin copper mining district of Poland. The events were recorded at station KSP, about 80 km away, operated by the Polish Academy of Sciences. The magnitudes of the tremors range from 2.8 to 4.1. For three of the events (second, fifth and sixth) the RSTF is a simple pulse with duration of less than 0.2 s. The other three events (first, third and fourth) are more complex with source durations varying from about 0.4 to 0.55 s. The double pulse RSTFs may be a result of multiple collapses of pillars.

Figure 7 displays source time duration, as inferred by the EGF method, as a function of event magnitude for all the events we have studied to date. Different event types are plotted with different symbols: open circles for natural earthquakes, open squares for explosions (nuclear and chemical), and filled triangles for mining tremors. The events included on this plot include the examples from Figures 2–6, the large events studied by Li et al. (1995), and additional events of each type that we have analyzed but not discussed here. The data for magnitude less than 2.5 include several earthquakes and

82
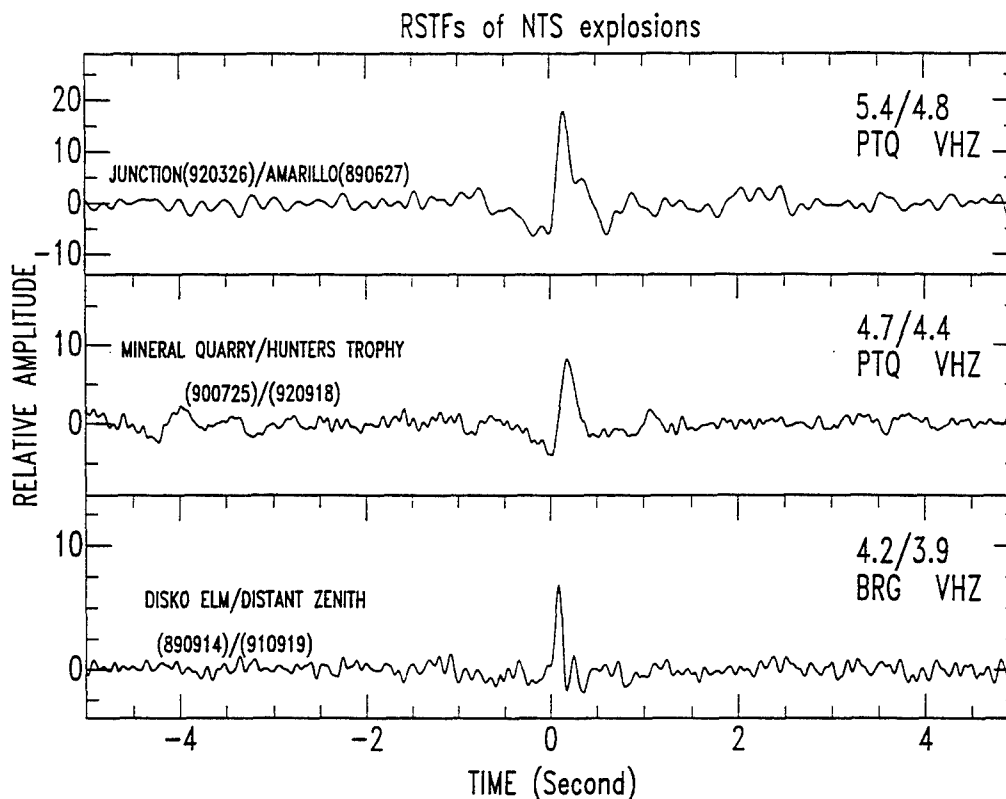
Figure 4: RSTFs of three nuclear explosions at the Nevada Test Site, determined from regional waveform data. The source durations of the explosions range from 0.35 to 0.65 s. The two bottom events are tunnel shots. Note the 'spall phase' of the explosions JUNCTION and DISKO ELM.

industrial explosions from a variety of areas with differing tectonic settings. In addition, some earthquake data from Mori and Frankel (1990) are included in the plot.

From Figure 7 we see that source duration vs. magnitude works as a discriminant between explosions and earthquakes for both the largest (M>4.5) and smallest (M<2.5) events. The earthquake population appears to obey some scaling relation, determined by the dependence of source duration and magnitude on the spatial dimension of the source. If such a relation exists for explosions, it implies a weaker variation of duration with magnitude and perhaps separate relations for nuclear and industrial explosions. For the small (M<2.5) events we analyzed, the discriminant works because the source duration of quarry and construction blasts is significantly longer than that of earthquakes with similar magnitudes. This is consistent with results of Herrin et al. (1994), who found that spectra of small magnitude earthquakes have relatively higher peak frequencies compared to explosions with similar magnitudes. However, as noted earlier, the time duration of industrial explosions may depend on factors, like firing pattern, that are not determined by any underlying physical process.

For magnitudes between 2.5 and 4.5, the earthquake, explosion and mining tremor

Figure 5: Estimated RSTFs of the 941002-1127 M=3.7 earthquake in central Massachusetts. Shown is the RSTF obtained at each of 17 stations together with the stack of the individual station estimates. The average source duration is about 0.15 s. The columns at the right show the code, azimuth and epicentral distance of each station. The variation of the source pulse width and amplitude with azimuth suggests that the rupture propagates to the southwest.

Figure 6: RSTFs of six mining tremors in Lubin, Poland. The magnitudes of the events range from 2.8 to 4.1. The source durations inferred from the RSTFS range from 0.15 to 0.6 s.

Earthquakes, Explosions & Mining Tremors
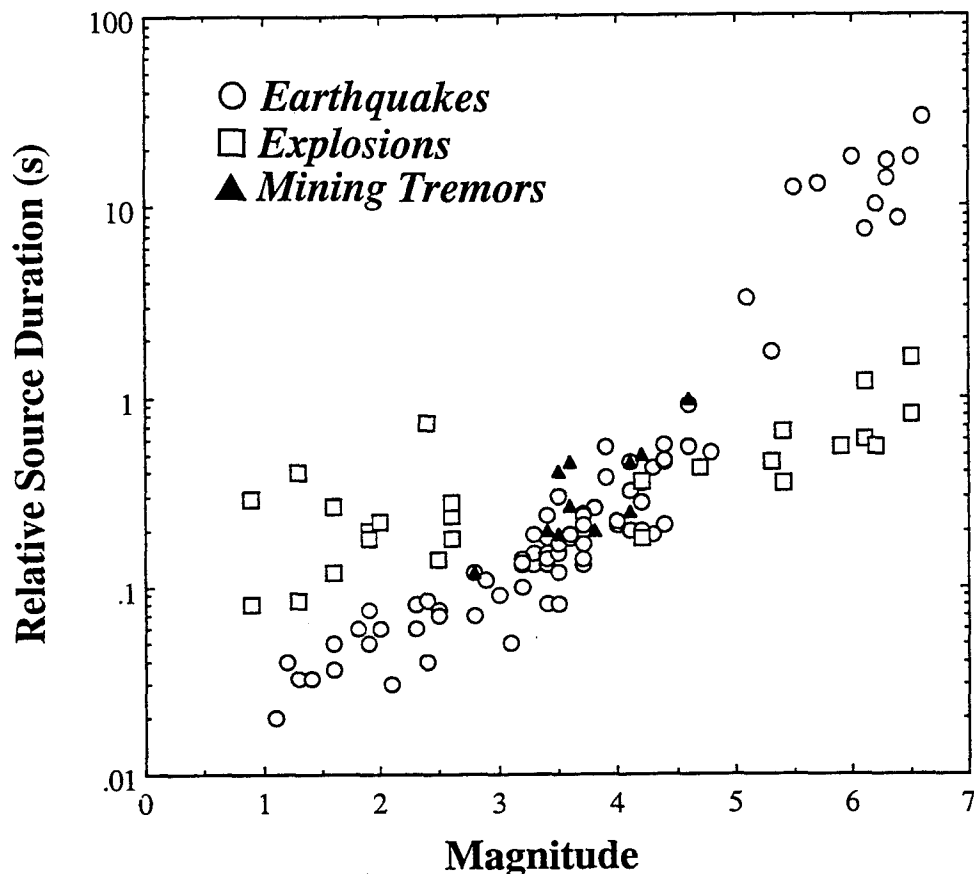
Figure 7: Source duration vs. magnitude for natural earthquakes (circles), explosions (squares), and mining tremors (filled triangles), determined by EGF analysis. For events having magnitude less than 2.5 or greater than 4.5, the source duration is a good discriminator between earthquakes and explosions. In the remaining magnitude range (2.5 to 4.5) the earthquake, explosion and mining tremor populations overlap.

populations overlap, as shown in Figure 7, indicating that simple source duration is not a good discriminant in this magnitude range. However, while source time duration may not be a good discriminant for magnitude 2.5–4.5 events, the examples shown above suggest that other properties of the RSTF may be useful for discrimination. In Figures 2 and 3, for example, the RSTFs show evidence of multiple detonation, characteristic of industrial blasting practices. The RSTFs of two of the nuclear explosions analyzed (Figure 4) show evidence of the spall phase, while the earthquake example (Figure 5) shows clear directivity effects in the RSTF as a function of azimuth. Finally, for three of the mining tremors analyzed (Figure 6), the RSTF shows multiple pulses that are different from both the secondary spall phase of a nuclear explosion and the multiple pulses of multiply detonated blasts.

CONCLUSIONS AND RECOMMENDATIONS

Our results demonstrate that source time functions retrieved with the EGF method provide valuable information about the energy release process of seismic events of all magnitudes. Source duration vs. magnitude, however, is only capable of distinguishing large (M>4.5) or very small (M<2.5) earthquakes from explosions. Nonetheless, many of the source time functions examined in this study display features that are indicative of event type, such as source directivity, spall phases, and multiple pulses in industrial blasts and mining tremors. Therefore, we conclude that the source time functions inferred by the empirical Green's function method make a useful contribution to the difficult problem of regional event discrimination. We recommend that further work be done to find better EGF-based discriminants for events in the magnitude range 2.5 to 4.5. The effort should include both empirical studies, such as presented here, and theoretical modeling of relevant source types.

REFERENCES

Herrin, E., Burlacu, V., Gray, H.L., Swanson, J., Golden, P., and Myers, B., 1994. Research in regional event discrimination using Ms:mb and autoregressive modeling of Lg waves, *Proceedings*, 16th Annual Seismic Research Symposium, Thornwood, New York, Phillips Laboratory, Hanscom AFB, Massachusetts, 152–158. ADA284667

Li, Y., Rodi, W., and Toksöz, M.N., 1994. Seismic source characterization with empirical Green's function and relative location techniques, *Proceedings*, 16th Annual Seismic Research Symposium, Thornwood, New York, Phillips Laboratory, Hanscom AFB, Massachusetts, 231–237. PL-TR-94-2217, ADA284667

Li, Y., Toksöz, M.N., and Rodi, W., 1995. Source time functions of nuclear explosions and earthquakes in central Asia determined using empirical Green's functions, *J. Geophys. Res.*, *100*, 659–674.

Mori, J., and Frankel, A., 1990. Source parameters for small events associated with the 1986 North Palm Springs, California, earthquake determined using empirical Green functions, *Bull. Seism. Soc. Am.*, *80*, 278–295.

Toksöz, M.N., Li, Y., and Rodi, W., 1993. Seismic source characterization with empirical Green's function and relative location techniques, *Proceedings*, 15th Annual Seismic Research Symposium, Vail, Colorado, Phillips Laboratory, Hanscom AFB, Massachusetts, 398–404. PL-TR-93-2160, ADA271458

An Overview of Seismic Discrimination Issues Relevant to CTBT Monitoring

J. R. Murphy

Maxwell Laboratories, Inc.,S-CUBED Division
11800 Sunrise Valley Dr., Suite 1212
Reston, Virginia 22091

Abstract

The Conference on Disarmament of the U.N. General Assembly is currently working to draft a Comprehensive Test Ban Treaty (CTBT) which will prohibit all nuclear testing. Because seismology remains as the primary monitoring technique for verifying treaty compliance with respect to underground nuclear tests, it is appropriate at this time to once again review the current state of understanding regarding the seismic identification of such explosions. It is evident that no practical seismic monitoring system will ever insure identification of all conceivable underground nuclear tests and, therefore, it is important to begin any such assessment of capability by recognizing that it is first necessary to establish a monitoring threshold goal, which will ultimately represent some compromise between system cost and various political and military considerations. This goal may vary depending on the perspectives of the groups designing the monitoring systems. For example, the stated design objective of the proposed International Monitoring System (IMS) is to insure the capability to identify all well-coupled underground nuclear tests having yields greater than 1 kt, while the ultimate design threshold of the U.S. NTM system has often been expressed in terms of monitoring evasively tested 1 kt explosions. Such differences in design thresholds have profound implications with respect to the associated required seismic discrimination capabilities. That is, since well-coupled 1 kt nuclear explosions correspond to m_b values of 4.0 or more, most events with magnitudes above the IMS threshold can be effectively identified using data from a capable teleseismic network alone. Moreover, since there are virtually no chemical explosions which generate seismic signals of this magnitude, the IMS identification task is greatly simplified in that the range of source types to be considered is limited. On the other hand, cavity decoupled 1 kt explosions are expected to produce seismic signals corresponding to magnitudes in the range $2.0 < m_b < 2.5$, and such events will not be detected teleseismically. It follows that regional seismic data and associated discrimination techniques will be required to monitor any such U.S. NTM threshold level. Furthermore, current estimates indicate that tamped chemical explosions with yields of less than 10 tons and ripple-fired quarry blasts with yields in the range of 75-100 tons will produce regional seismic signals comparable to those expected from fully decoupled 1 kt nuclear explosions. Since chemical explosions of such sizes are common in many areas of the world, they will have to be routinely discriminated from nuclear explosions in order to monitor at such low threshold levels. More generally, seismic monitoring of any eventual CTBT will likely involve a combination of teleseismic and regional data and will require the routine, confident identification of underground nuclear explosion signatures from a background of signals produced by numerous earthquake, mine blast and rockburst sources. The most reliable seismic discriminants continue to be those based on fundamental source properties such as location (especially depth), geometry and source dynamics. The current status of the development of such discriminants will be summarized and their implications with respect to effective teleseismic and regional monitoring of a CTBT will be assessed.

Key Words: Seismic, Discrimination, CTBT

Application of Soviet PNE Data to the Assessment of the Transportability of Regional Discriminants

J. R. Murphy, I. O. Kitov*, B. W. Barker and D. D. Sultanov*
Maxwell Laboratories, Inc.,S-CUBED Division
11800 Sunrise Valley Dr., Suite 1212
Reston, Virginia 22091
Contract No. F19628-95-C-0109
Sponsored by AFTAC

Abstract

In order to discriminate the regional seismic signals produced by underground nuclear explosions from those produced by earthquakes, rockbursts and conventional mining explosions of comparable magnitude, it is necessary to know the range of nuclear explosion signal variation that can be expected as a function of source and propagation path conditions over the entire ranges of these conditions which may be encountered in global test monitoring. However, most research conducted to date has focused on analyses of regional signals recorded from explosions conducted at the few major nuclear test sites and these sample only limited ranges of the variables of interest. On the other hand, the extensive Soviet PNE testing program provides a source of regional seismic data recorded over much broader ranges of source and propagation path variables. More specifically, over 120 tests were conducted in this series and these explosions were detonated in a wide variety of geologic emplacement media (e.g., salt, clay, sandstone, granite, limestone) and are representative of wide ranges in yield (0.01 to 300 kt) and source depth (130 to 2860 m). Moreover, because of the tremendous geologic and tectonic diversity represented within the territories of the former Soviet Union, regional data recorded from these tests sample propagation path characteristics encompassing a range extending from tectonically active to stable continental interior regimes. S-CUBED plans to work with scientists from the Russian Institute For Dynamics of the Geospheres (IDG) to improve regional seismic discrimination capability by using data recorded from these Soviet PNE tests to derive improved, quantitative bounds on the ranges of seismic signal characteristics which can be expected from underground nuclear explosions which might be conducted under the wide variety of source and propagation path conditions which must be considered in global test monitoring.

Key Words: Seismic, Discrimination, Regional, Soviet, PNE

* Institute For Dynamics of the Geospheres, Russian Academy of Sciences

TRANSPORTABLE SEISMIC DISCRIMINANTS: THE USE OF CROSS- SPECTRAL MEASUREMENTS TO REDUCE PARAMETER SCATTER AND IDENTIFICATION ERROR

Jay J. Pulli
Radix Systems, Inc.
6 Taft Court, Rockville, Maryland 20850
pulli@radix.com
Contract No. F19628-95-C-0175, Sponsored by DOE

Abstract

Much progress has been made in regional seismic discrimination over the past ten years. Aided by the availability of high-quality waveforms and ground-truth databases, researchers discovered the discrimination capabilities of Lg/P and S/P spectral ratios, especially at high frequencies. However, when spectral ratios or signal parameters which perform well in one geographic area are applied to events in another, the results are typically uncertain or erroneous. This was illustrated during the identification analysis of the Dec. 31, 1992 Novaya Zemlya event: the same data were analyzed by a number of researchers who came to uncertain or conflicting conclusions. For regional discrimination to work in a CTBT context, this problem must be overcome.

The most obvious factors contributing to transportability failure include geographic variability of source and path effects. However, noise and the inherent instability of spectral ratio calculations at low SNR's and restricted bandwidths are also likely factors. Regional seismic spectra rarely follow the model of a flat low-frequency spectrum with smooth high-frequency rolloff. This is especially true for quarry explosions, where long time-delay ripple firing can add harmonic distortion. Good signal processing practice dictates that measurements be made only at frequencies where there is sufficient SNR, which often means the use of cross spectral and system identification methods. This project will extend the discrimination research conducted to date to include these methods. The specific tasks include:

- analysis of existing ground-truth databases using cross-spectral methods,
- a systematic search of cross spectral parameters with discrimination capability,
- discrimination performance comparison of cross-spectral methods with those already made for existing ground-truth databases,
- analysis of new ground truth databases as they are made available by other contractors in this program, and
- statistical assessment of transportability of the cross spectral methods.

Key Words: Discrimination, Spectral Ratios, Cross-Spectra, Ground-Truth Databases

1. OBJECTIVES

The overall objective of this research is to improve regional seismic event discrimination capabilities, reduce identification uncertainty, and search for discriminants which can be transported from one geographic region to another. This is relevant to CTBT verification given the degree of identification uncertainty which has been shown to exist for events in areas with little prior data (Ryall, 1993). Reducing the variability in parameter estimation will be attempted using cross spectral measurements of seismic phases, the motivation for which is described in this paper. The specific tasks are

- to apply cross-spectral measurements to ground truth databases already studied,

- to evaluate the discrimination capability of the extracted cross-spectra,

- to apply and evaluate this discrimination capability for new ground truth databases as they are compiled by other contractors during this program.

2. PRELIMINARY RESEARCH RESULTS

2.1 Overview of the Parameterization Approach

Regional seismic discrimination had been the subject of intense study for the past 15 years. Many approaches have been taken, most notably the parameterization approach, where numerous signal parameters are extracted from waveforms for events with known source type. Other approaches are the machine learning approach (e.g. Dysart and Pulli, 1990; Dowla et al., 1990) and the statistical approach (Shumway, 1995). The parameterization approach receives the most attention because the specific parameters measured are typically chosen on the basis of source physics and seismic understanding (Pulli, 1995).

In the parameterization approach, the ability of a parameter to distinguish between source types is usually expressed in terms of the Mahalanobis Distance for the normal distribution (Duda and Hart, 1973),

$$M_p = \frac{(\mu_{p1} - \mu_{p2})^2}{\sigma_{p1}^2 + \sigma_{p2}^2}$$

where μ and σ are the means and variances, respectively, for parameter p measured for source types 1 and 2. The larger the Mahalanobis Distance, the smaller the overlap in parameter distributions and identification uncertainty (see *Figure 1*).
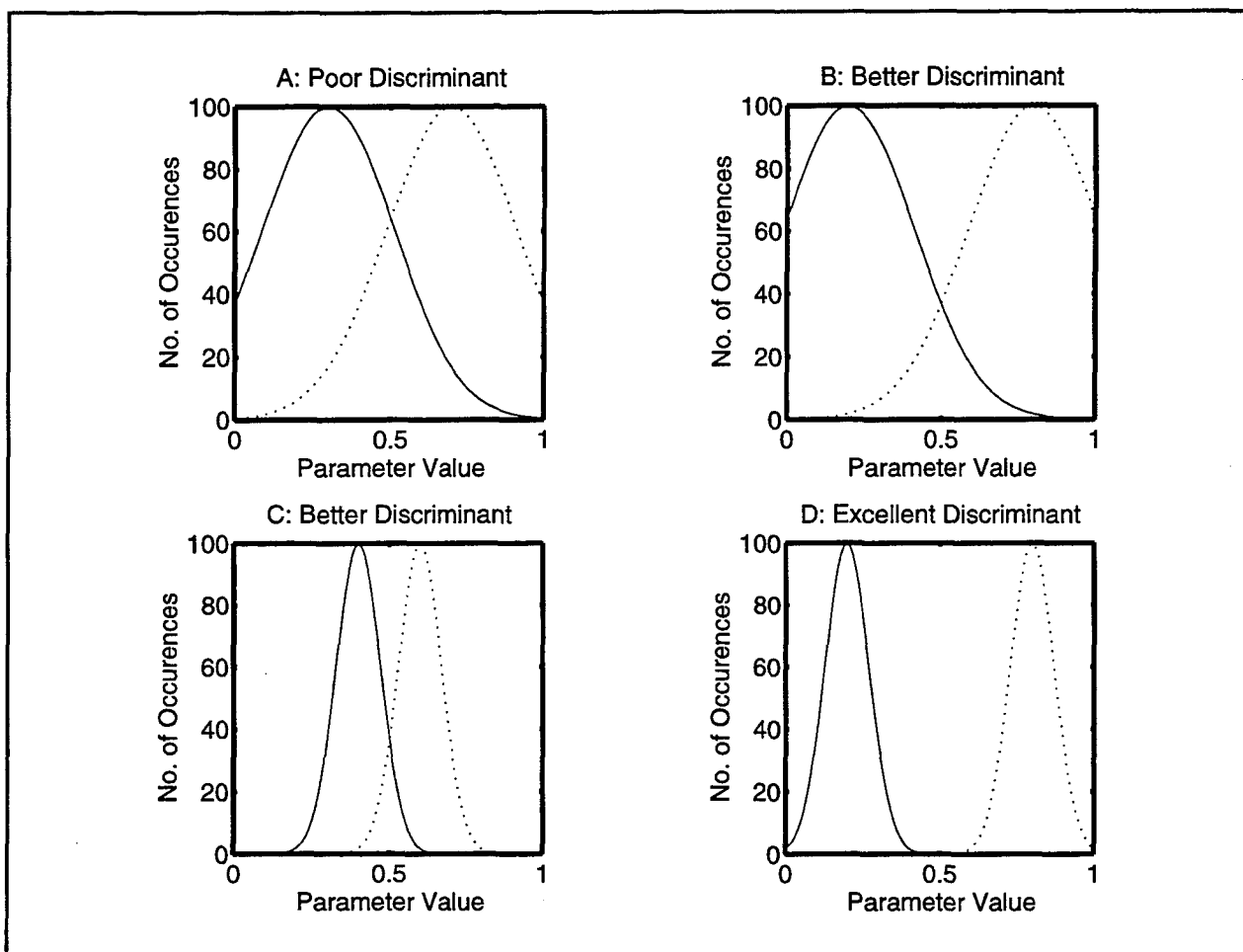
Figure 1. Four hypothetical parameter distributions for two classes of seismic events. In case A, the distributions have similar means and variances, and provide poor discrimination capability. Case B is better, with a larger separation of means but still large variances and overlap. Case C has close means but small variances, with some overlap. Case D is the best, with a large difference in means and small variances.

2.2 Examples of Discriminants at NORESS

To illustrate this concept, consider the 14 discriminant parameter dataset measured at the NORESS array by Pulli and Dysart (1993). *Figure* 2 shows examples of both good and bad parameters for distinguishing local earthquakes from small quarry explosions. The Pn/Lg spectral ratio measured from 10-20 Hz (*Figure 2a*) provides good separation of event types, though there is some overlap in the distributions and an earthquake outlier. The Lg cepstral variance (*Figure 2b*) provides little discriminant capability given the large degree of overlap. *Figure 3* shows the Mahalanobis Distances for all 14 parameters. Clearly, parameters 13, 12, and 14 provide no discrimination capability; parameters 2, 11, 9, 6, and 4 provide some discrimination; parameters 1, 3, 10, 5, and 8 provide the best capability.
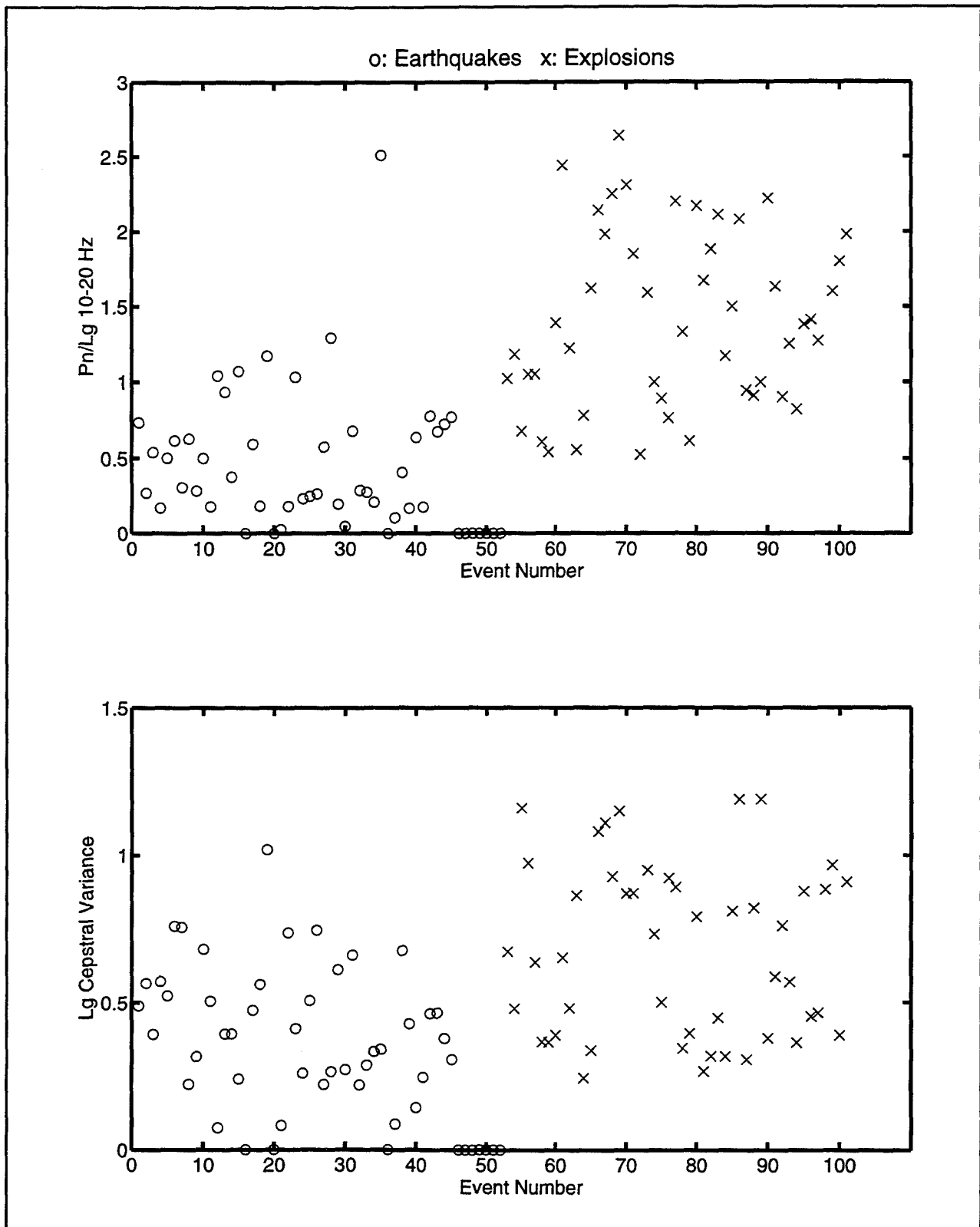
Figure 2. Examples of two spectral parameters measured at the NORESS array, tested for their ability to discriminate small earthquakes and explosions. The *Pn/Lg* spectral ratio measured from 10-20 Hz (top) provides good discrimination, though there is some overlap and one outlier. The *Lg* cepstral variance (bottom) is a poor discriminant.
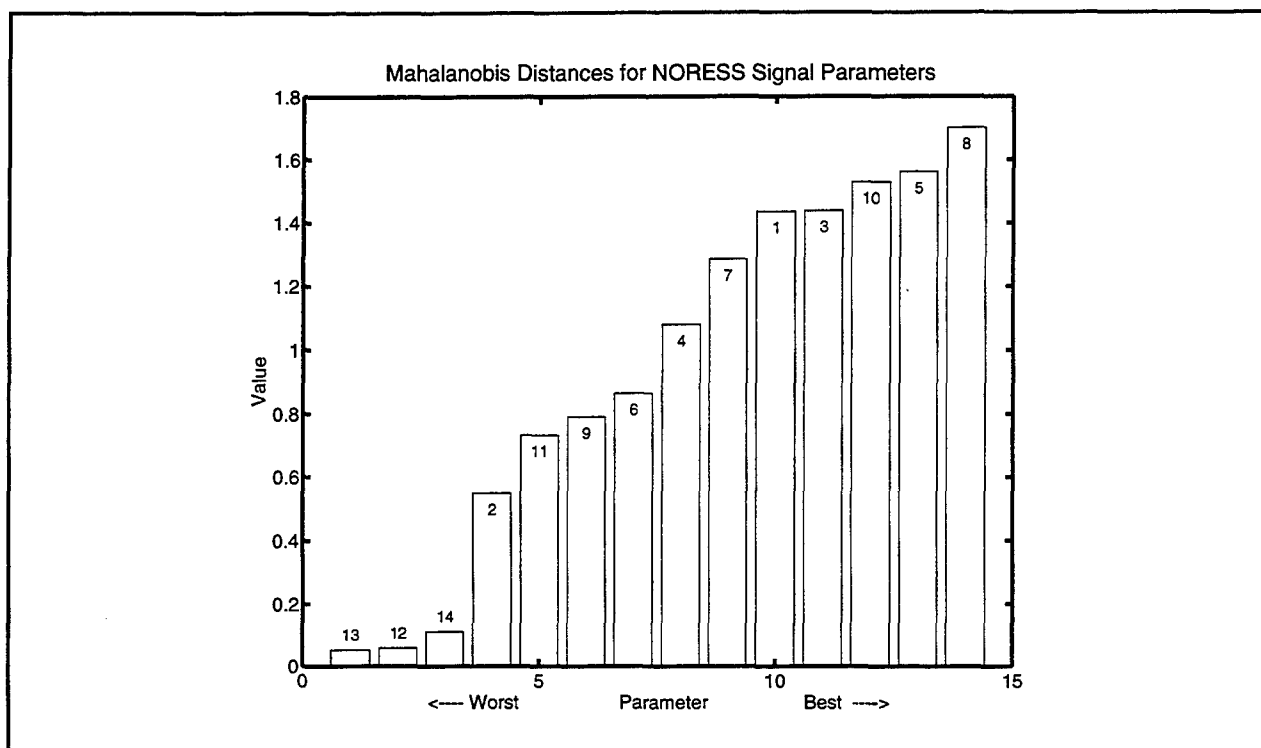
Figure 3. Mahalanobis Distances for the 14 signal parameters measured at the NORESS array. The parameters are: 1 - broadband *Pn/Sn* spectral ratio; 2 - *Pn/Sn* spectral ratio from 2-5 Hz; 3 - *Pn/Sn* spectral ratio from 5-10 Hz; 4 - *Pn/Sn* spectral ratio from 10-20 Hz; 5 - broadband *Pn/Lg* spectral ratio; 6 - *Pn/Lg* spectral ratio from 2-5 Hz; 7 - *Pn/Lg* spectral ratio from 5-10 Hz; 8 - *Pn/Lg* spectral ratio from 10-20 Hz; 9 - *Pn* cepstral variance; 10 - *Sn* cepstral variance; 11 - *Lg* cepstral variance; 12 - *Pn* third moment of frequency (TMF); 13 - *Sn* TMF; 14 - *Lg* TMF.

Real seismic signal parameter measurements are unlikely to ever replicate the ideal case shown in *Figure 1D*. There will always be scatter in the measurements. This scatter can either be real or due to measurement error. Real factors contributing to the scatter can be either source effects (source radiation patterns, source corner frequencies, etc.) or path effects (attenuation, scattering, or blockage). These factors can sometimes be accounted for using a larger azimuthal distribution of signal measurement or corrections to the data based on known effects (like Q). Measurement errors include both the effects of noise and the inaccuracy of the actual measurements, especially for spectral ratios.

2.3 Noise

Seismic measurements are (almost) always contaminated by noise. When we compute the *Lg/P* spectral ratio, we are actually computing the *(Lg+noise)/(P+noise)* ratio. This is an important consideration for small magnitude events, as illustrated in *Figure 4*. The figure shows a simple model calculation of *Lg/P* vs. noise for an *Lg/P* of 2.0, typical for a small earthquake near NORESS. The noise, which is additive for both phases, varies from 1 to 30 (with respect to *P*). It is only when the

94

SNR reaches 5 that the measured spectral ratio is in error by less than 10%. Regional P-wave SNR's are generally lower than 10 in most frequency bands.
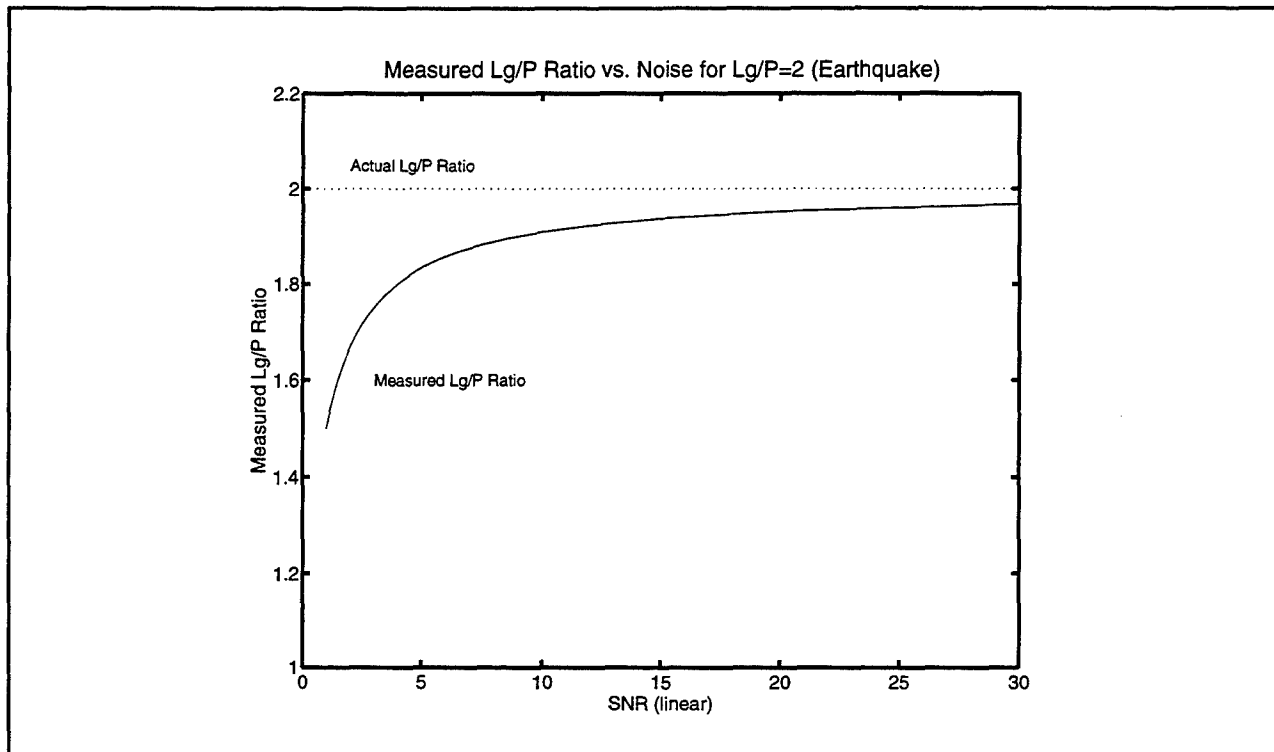
Figure 4. Predicted *Lg/P* spectral ratios vs. noise for a typical regional earthquake at NORESS where the actual *Lg/P* is 2. The noise, which is additive for both phases, varies from an SNR of 1 to 30 (with respect to *P*). When the SNR is low, the measurement is likely to be in error, adding to identification uncertainty.

2.4 Instability of Spectral Ratios and the Motivation for Cross Spectra

The use of spectral ratios in the parameterization approach is certainly appropriate, given the nature of source excitation for earthquakes and explosions. But regional seismic spectra rarely follow the model of a flat low-frequency spectrum with smooth high-frequency rolloff. This is especially true for quarry explosions, where long time-delay ripple firing can add harmonic distortion. Good signal processing practice dictates that measurements be made only at frequencies where there is sufficient SNR, which often means the use of cross spectral and system identification methods.

Even earthquakes and mining-induced events can exhibit enough spectral complexity to render common-band spectral ratios unrealistically too large or small. For example, *Figure 5* shows *Lg* and *Pn* spectra for a mining-induced earthquake in the Lubin Copper Basin, recorded at GERESS. Because of spectral complexity, the spectral ratio shows peaks at narrow bands. Smoothing the spectra, a common practice in seismology, would help but would result in an inaccurate representation of the true ratios.
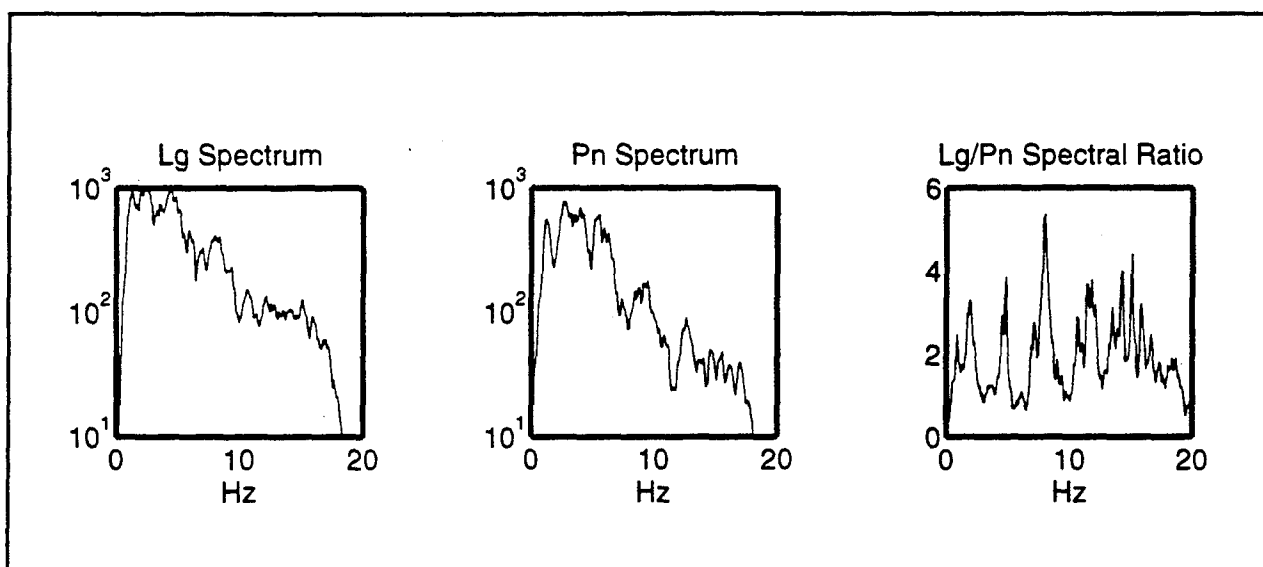
Figure 5. Lg and *Pn* spectra for a mining-induced earthquake in the Lubin Copper Basin, recorded at GERESS. Because of spectral complexity, the spectral ratio shows peaks at narrow bands. Smoothing the spectra, a common practice in seismology, would help but would result in an inaccurate representation of the true ratios.

Figure 6 shows another view of these same spectra, this time with the f^2 spectral decay removed. Note that the *Lg* and *Pn* spectra have peaks at different frequencies. Prudent signal processing dictates that measurements be made where there is signal energy. Use of cross band spectral ratios at energetic frequencies should reduce parameter variance and increase the certainty of source identification.
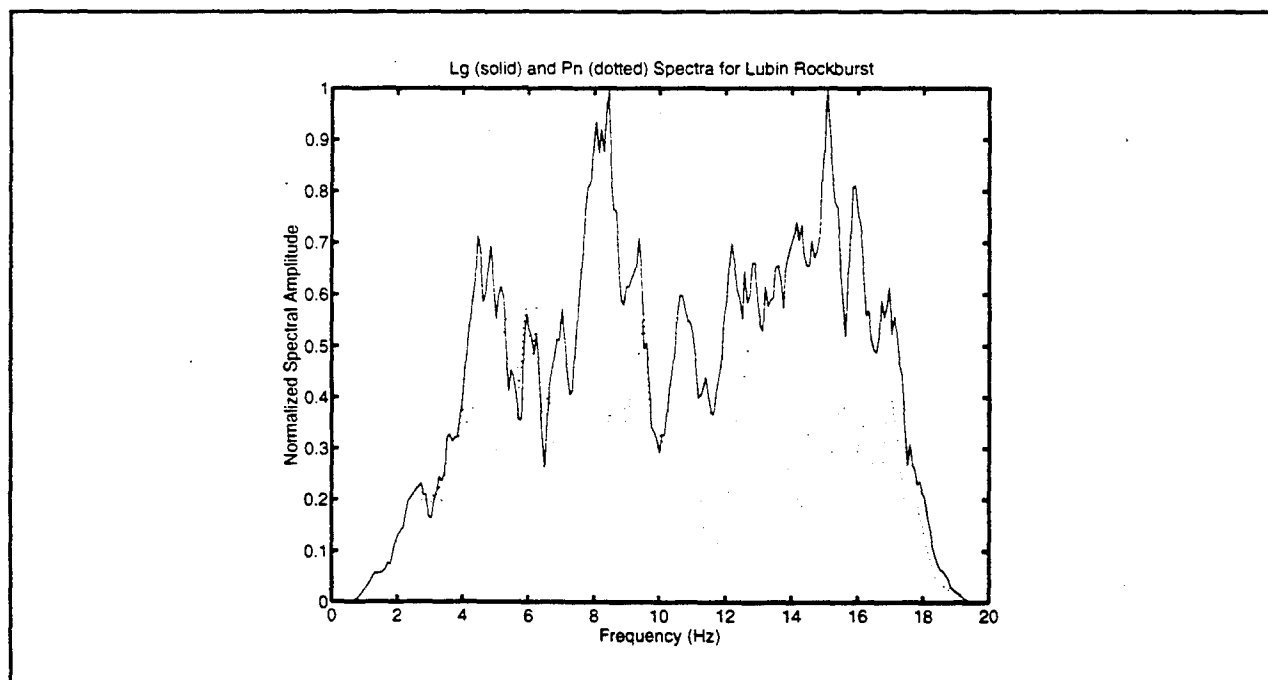
Figure 6. Lg and *Pn* spectra for a mining-induced earthquake in the Lubin Copper Basin (same as *Figure* 5). Both spectra have been corrected for f^2 spectral decay. The *Lg* and *Pn* spectral energy is concentrated in narrow bands which are not coincident, leading to peaks in the common-band spectral ratio.

96

3. RECOMMENDATIONS AND FUTURE PLANS

This project is just beginning, and the author solicits the assistance of any researchers in this program who have seismic waveform data for events with independently verified source type.

4. REFERENCES

Dowla, F.S., S. Taylor, and R. Anderson (1990), Seismic discrimination with artificial neural networks: preliminary results with spectral ratio data, *Bull. Seis. Soc. Amer., 80*, 1346-1373.

Dysart, P.S. and J.J. Pulli (1990), Regional seismic event classification at the NORESS array: seismological observations and the use of artificial neural networks, *Bull. Seis. Soc. Amer., 80*, 1910-1933.

Duda, R.O. and P.E. Hart (1973), *Pattern Recognition and Classification*, John Wiley & Sons, New York, 482 pp.

Pulli, J.J. and P.S. Dysart (1994), Development and testing of a methodology for regional seismic event identification in Eurasia, ARPA Final Report, 126 pp.

Pulli, J.J. (1995), Extracting and processing signal parameters for regional seismic event identification, *in Monitoring a Comprehensive Test Ban Treaty*, ed. Dainty and Husebye, Kluwer Press, in press.

Ryall, A. (1993), The Novaya Zemlya event of December 31, 1992 and seismic identification issues, handout from the 15th Annual Seismic Research Symposium, Vail, CO.   PL-TR-93-2160, ADA271458

Shumway, R. (1995), Statistical approaches to seismic discrimination, *in Monitoring a Comprehensive Test Ban Treaty*, ed. Dainty and Husebye, Kluwer Press, in press.

Path Calibration and Regional Discriminants in North Africa and the Middle East

Chandan K. Saikia (PI) and B. B. Woods (Co-PI)
Woodward-Clyde Federal Services
Pasadena, CA 91101

ABSTRACT

Reviews on the effectiveness of regional discriminants suggest that discriminant rules developed for one region do not readily apply to another. However, it is feasible to apply these discriminants in a new region provided relative path corrections for various seismic phases (i.e., P_n, L_g, and R_g) are available. We are presently investigating path corrections for the North Africa and other Middle East regions around the GSETT-3 stations. Our objective is to develop regional magnitude relationships using the amplitude distance corrections that will be obtained from the crustal models. To this end, regional broadband seismograms recorded by the operational GSETT-3 stations in these regions will be modeled by calibrating the regional waveguide to establish path corrections for individual phases. For those GSETT-3 stations which have not become operational yet, regional seismograms from the nearby WWSSN stations will be analyzed. Whenever possible, we will select large earthquakes which are recorded regionally and teleseismically, and for which their focal mechanisms have been determined previously. To date, we have collected regional waveforms recorded at KEG (Kottamiya, Egypt, operating since 1990), HLW (Halwan, Egypt) and KIV (Kislovodsk, CIS), and modeling of these waveforms has just started. This study also includes finding path corrections for regional phases around a newest GSETT-3 array, PAKO deployed near Nilore (NIL, location of a former WWSSN station) in Pakistan. This array is also located southwest of a recent PASCAL experiment which consisted of nine broadband stations. Initial success in modeling regional seismograms from this PASCAL experiment is quite promising and we have already obtained a preliminary crustal structure model near the PAKO array. Based on this initial crustal structure, we present results discussing various trade-offs between depth and focal mechanism for observed earthquakes and demonstrate that these trade-offs are real by comparing our preferred solutions with those of CMT.

OBJECTIVES

A recent review of effective regional discriminants and their transportability indicates that a discriminant rule established in one region does not readily apply to another (Fisk et al., 1994); consequently, establishing relative path corrections for the various phases (P_n, L_g, R_g etc.) are essential for new regions. To this end, we are calibrating paths in North Africa and other Middle East regions for the IDC event indentification subsystem. We envision providing travel-time and amplitude-distance curves or relations for each of the GSETT-3 stations operating in these regions. Directly related to the amplitude distance corrections are regional magnitude relationships which will also be developed. We will determine short-period magnitude relationships for P_n ($m_b(P_n)$), $L_g(m_b(L_g))$, and $S_g(m_b(S_g))$ vs distance. We will also estimate the effective t* beneath our source region by comparing teleseismic and regional derived source histories. Special calibrations to ARPA's short-period arrays with respect to regional source strengths will be established. Such t* values will then be used to predict teleseismic m_b and obtain a calibration for regional m_b versus teleseismic m_b.

Developing the above travel-time and amplitude-magnitude distance curves involves waveform modeling of regional seismograms and advanced processing techniques for regional array data, such as modeling of specific depth phases, as well as developing softwares for automated real-time source discrimination routines. While small earthquakes (m_b < 4.5) can cause difficulties in discrimination, larger events (m_b > 5.5) can be used to calibrate paths and establish source estimation techniques useful for all sizes of events. Our strategy is to find a set of intermediate to large magnitude earthquakes in the study regions which have been recorded both regionally and teleseismically with the emphasis placed on events recorded by GSETT-3 stations or by stations located near the proposed GSETT-3 sites. Accurate source parameters can be obtained from the teleseismic observations and these earthquakes can be used as "teleseismic master" events. The composition of teleseismic down-going P and up-going pP waves can be modeled for each teleseismic master event to determine source complexity and depth. Using these derived source parameters, broadband characteristics of P_{nl}, S_{nl} and surface waves recorded on regional waveforms consequently can be modeled for calibration of source to receiver paths. After calibrating these regional paths, regional waveforms recorded from other smaller events are inverted to determine their source mechanism and seismic moment M_o. For the purpose of path calibration around the GSETT-3 stations, we are also looking for a set of "regional master" earthquakes when the teleseismic ones are not available. These earthquakes must be recorded with good signal to noise ratio. We use long-period regional seismograms from the "regional masters" and a simplified initial crustal structure consistent with the local geology to determine source parameters. Once source mechanisms are determined, the regional long-period data can be modeled to improve the crustal structure. Structure models obtained

from the long-period records are later refined to fit the short-period signals which are observed in the broadband data. We shall also invert for the broadband source time function for each of these regional events. We expect regional master events to be small but of large enough magnitude to be recorded by various operational arrays at teleseismic distances. We shall stack P waveforms recorded by these arrays to enhance the signal quality and will attempt to model the enhanced P wave by convolving the inverted source time function with a suitable t* operator.

An additional focus of this study is to further develop energy-based regional discriminants that can be integrated into an operational environment to monitor North Africa and the Middle East (including western Iran, the southern-most states of the former Soviet Union and Pakistan). The main difficulty in applying discriminants to these regions is the recognition of a "first blast", since these regions have high natural seismicity but few, if any, large explosions. Besides calibrating these regions with respect to regional and teleseismic phases, we intend to test the applicability of regional discriminants we developed using earthquakes and explosions from western United States and many parts of central Asia (Woods et al., 1993; Woods and Saikia, 1995) and investigate the factors influencing their transportability. It should be noted that parameters obtained from modeling regional seismograms are used to determine the following regional discriminants: M_L vs M_o and $M_E/M_B:M_o$ or $M_E:M_B$ vs M_o where M_E is the energy required to match the total energy in the recorded data to that in the synthetic waveforms and M_B is the moment determined by modeling broadband P_{nl} data.

PRELIMINARY RESULTS

One of the newest arrays to be developed is in Pakistan, PAKO. It is located just southwest of a recent PASCAL experiment near the old WWSSN station NIL (Nilore) as displayed in Figure 1. Thus this broadband array provides an excellent opportunity to examine the wave propagation characteristics of this region. The array was operated only for a few months, September to December 1992, but recorded a number of significant events since this region is seismically very active (Ni et al., 1993). Some preliminary mechanisms are displayed in Figure 1 indicating strike-slip type mechanism expected from the west and mixed mechanisms from the north. These latter events are from the Hindu-Kush region and generally show such diversity in depth and mechanisms (Chatelain et al., 1980). This event diversity was also found in a recent study of the broadband regional recordings from GAR, see Figure 1. Zhao and Helmberger (1993) derived two crustal models for the region, one with uniform crust and one containing a gradient. A similar but simpler model is displayed in Table 1 which proved effective in modeling events beneath Tibet, Zhu and Helmberger (1995) of this report.

100

As discussed in Song and Helmberger (1995) one can generally model regional records at frequencies above a few Hz for ranges from 300 to 800 km with very simple two layer models. The top layer controls the surface waves while the moho controls the body phases. Since we are beyond critical angle, the relative sharpness of the crust mantle transition is not important. Crustal gradients do affect the time separation between the P_{nl} waves (extended P wave), the S_{nl} and surface waves, but this effect can be handled by the so-called "cut-and-paste" method of Zhao and Helmberger (1994). This method uses a direct grid-search approach and matches the complete seismograms against synthetic over discrete phases, so that timing shift between particular arrivals are allowed. This feature eliminates the need for an accurate crustal model for computing the fundamental Green's functions. Figure 2 and 3 display the fits obtained by this method. To improve the method, we introduce more sensitivity to amplitudes by fitting absolute motions, see Zhu and Helmberger (1995) of this report. Thus, examining the SH waves one can easily see the enhancement of amplitudes going from stations SHAB to DASU where the latter is near the maximum of the radiation pattern. Note that the Pnl's have been fit separately as discussed above. The model appears to be too slow for this region and so the complete synthetics have been shifted 4s forward in Figure 2 and 3s in Figure 3. The additional shifts are then made per trace. For the Pnl synthetics at SHAB has been shifted a total of 5.8s, or the synthetic is late by 5.8s. Note that the path to DASU is only 4.4s late. The observed love wave is 8.8s early relative to the synthetics, etc. At this stage these shifts are viewed as a baseline since we do not necessarily know the origin time. Trade-offs between depth and origin time is discussed in Zhao and Helmberger (1991). They find that throughout the Tibetan Plateau region events systematically are located too deep by about 20 km and occur about 4s earlier than given in PDE estimates.

These events are too small to be well recorded teleseismically and do not have CMT type solutions. One of the crustal events studied to date does have a Harvard solution, namely the 328.2 (M=5.6) event. Their mechanism versus our estimates are given in Figure 4 where we have tested four depths, 10, 20, 30 and 40 kms. The best fits occur for depths 10 and 20 kms, while the fits for depths 30 and 40 kms yield about double the error. These results are essentially a simple station solution given the azimuth of the event and these trade-offs of mechanism versus depths appear to be real as discussed in Zhao and Helmberger (1993). The CMT depth determination was 43 km, but this must be checked since their solutions have a 20 km bias in this region as determined from identifying depth phases in teleseismic body waves, see Zhao and Helmberger (1993). Deep events are particularly simple at these ranges and occur often in this region. An example is displayed in Figure 5. This event is near M=5 and causes some difficulty in m_b:M_s discrimination because the surface waves are relatively small. Teleseismically, an event of this size can also be difficult to analyze since depth phases become less obvious, see Figure 6. Short-period array stacks could prove very helpful for such events

and this type of data will be added to our source inversion technique in the near future.

REFERENCES

Fisk, M. D., G. L. Henry and G. D. McCartor (1994). Preliminary assessment of seismic CTBT/NPT monitoring capability, Scientific Report No 1. PL-TR-94-2300, 39p. ADA293188

Ni, J. F., A. Ibenbrahim and S. W. Roecker (1991). Three-dimensional velocity structure and hypocenters of earthquakes beneath the Hazara Arc, Pakistan: Geometry of the underthrusting Indian Plate, J. Geophys. Res., Vol 94, 19,865-19,877.

Song, X. and D. V. Helmberger (1995). Broadband modeling of regional seismograms: the basin and range crustal structure, submitted to Bull. Seis. Soc. Am.

Woods, B. B., S. Kedar, and D. V. Helmberger (1993). ML:Mo as regional seismic discriminant, Bull. Seis. Soc. Am., 83, pp 1167-1183.

Woods, B.B. and C. K. Saikia (1995). The portability of some regional seismic discriminants and related broadband waveform monitoring, Paper presented in the 17th Annual Research Symposium on CTBT monitoring at Scottsdale, Arizona. PL-TR-95-2108

Zhao, L. Z. and D. V. Helmberger (1991). Geophysical implication from relocations of Tibetan earthquakes - Hot lithosphere, Geophys. Res. Lett. 18, pp 2205-2208.

Zhao, L. Z. and D. V. Helmberger (1993). Source retrieval from broadband regional seismograms: Hindu-Kush region, Phys. Earth Planet. Inter., 78, 69-95, 1993.

Zhao, L. Z. and D. V. Helmberger (1994). Source estimation from broadband regional seismograms, Bull Seis. Soc. Am., 84, 91-104.
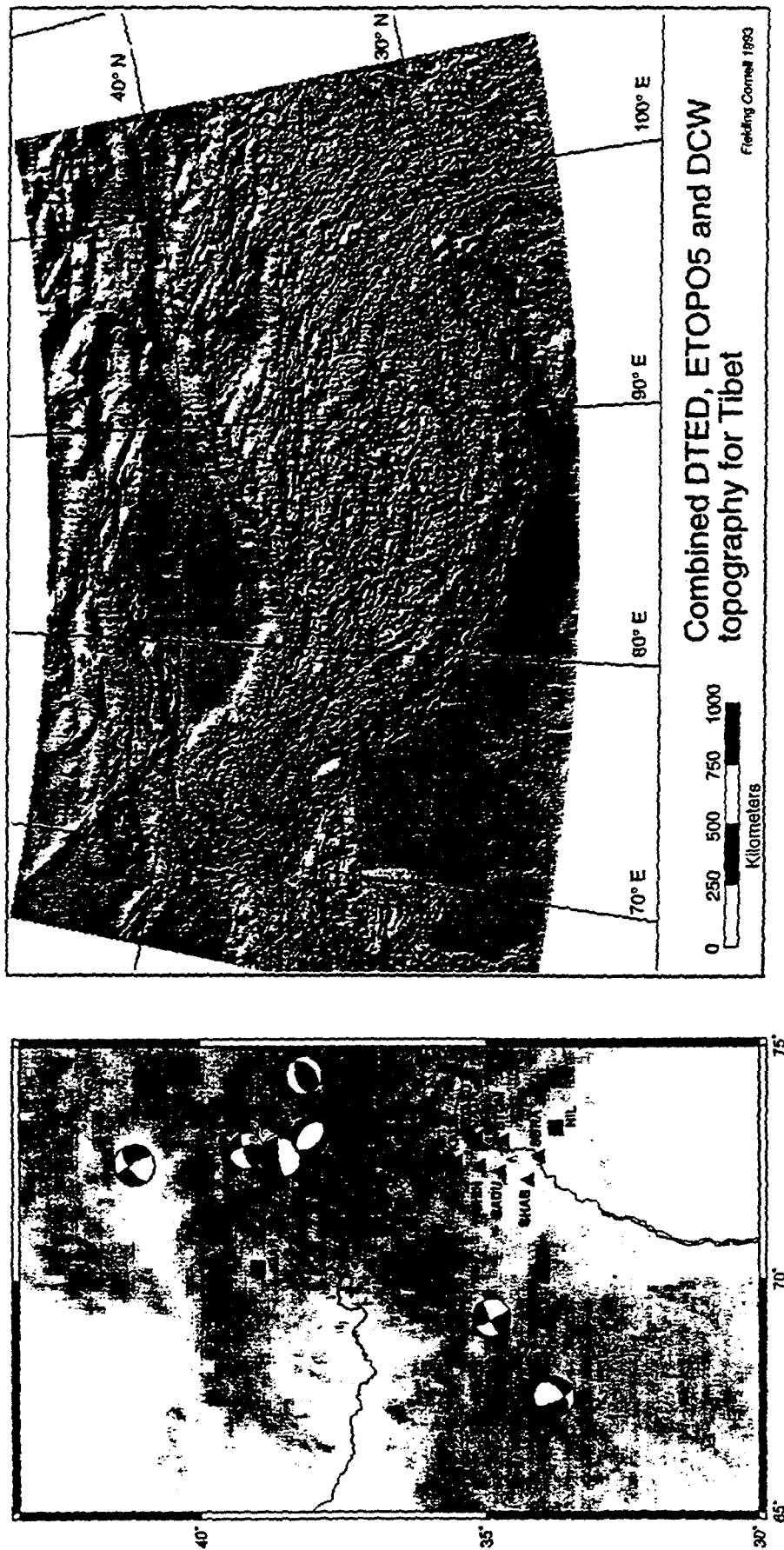
Figure 1. Panel on the right displays the shaded relief for the Tibet region, after Fielding et al. (1993) and panel on the left displays the PASCAL array location relative to NIL (PAKO), the IRIS station GAR (now closed down) and a number of events.
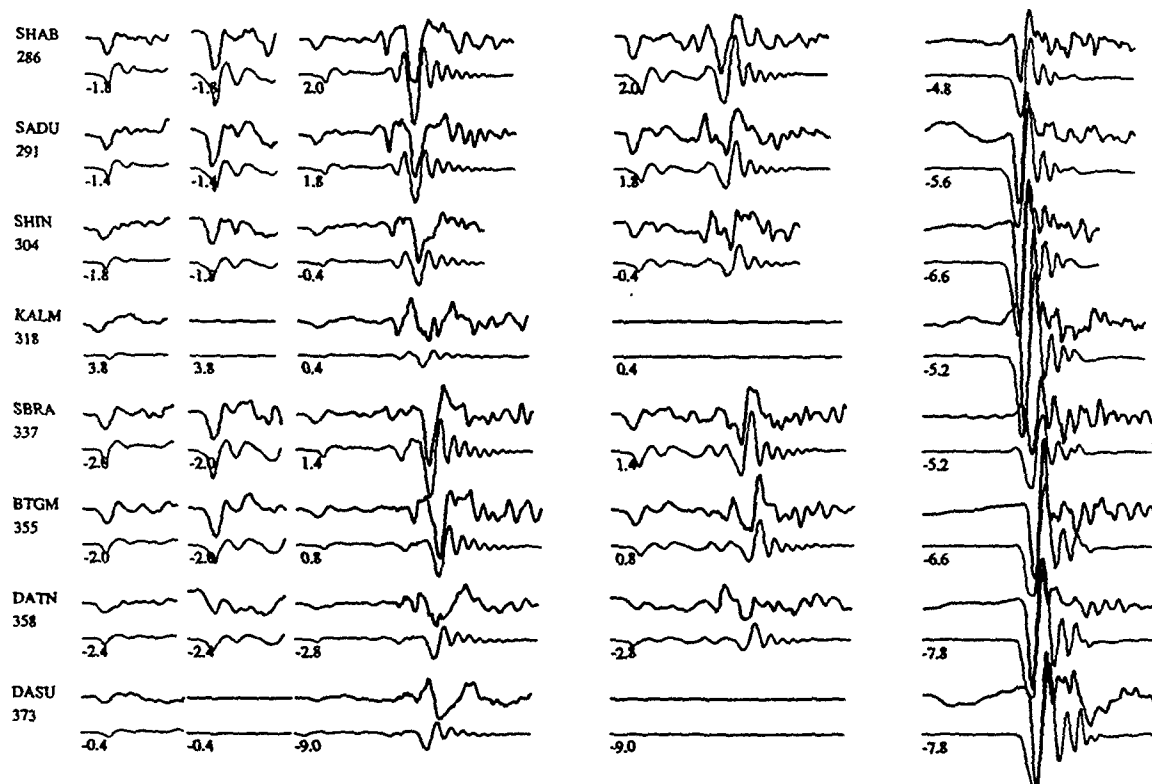
Figure 2. Comparison of synthetics and observations for the 311.1758 event (M=5). The synthetics and observations are relative to SHAB (Peak-to-peak amplitude of tangential is 0.011 Qcm). The seismic moment estimate is 7.9×10^{23} ergs, depth of 10 km, strike, dip and rake (70°, 90°, 230°).
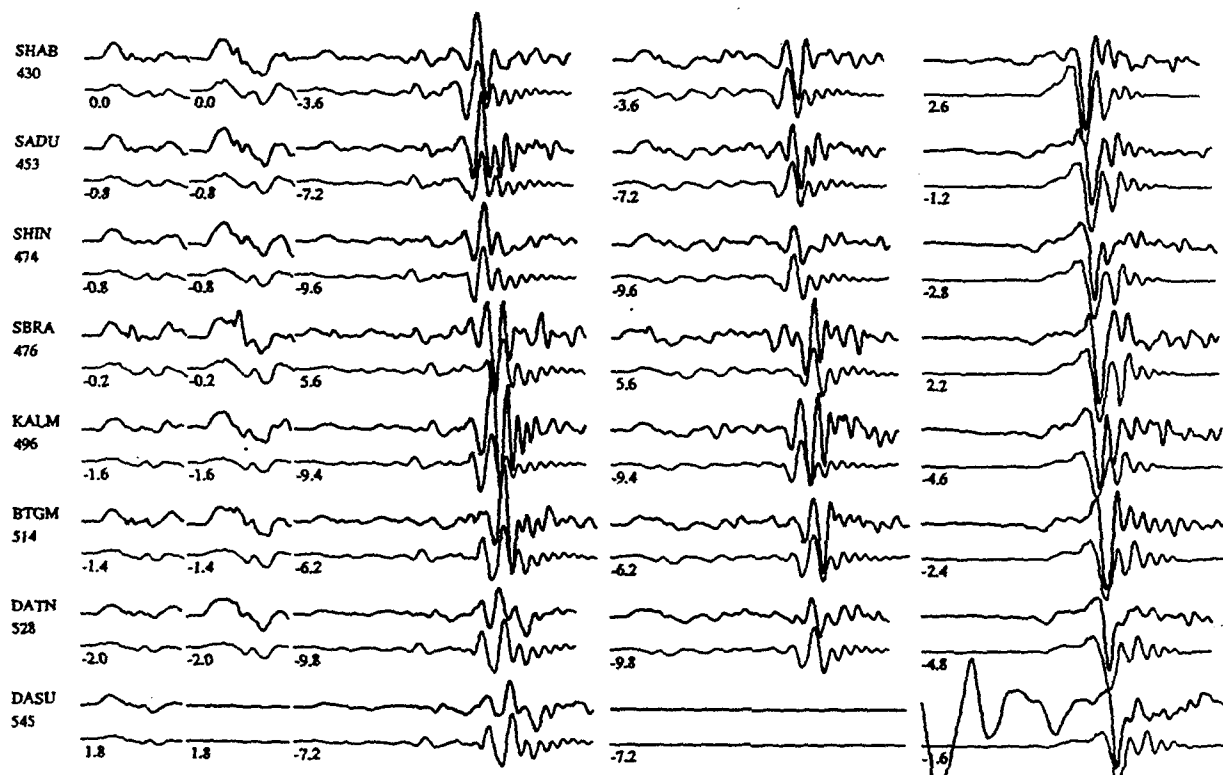
Figure 3. Comparison of synthetics and observations for 322.0238 event, $M_o = 3.2 \times 10^{24}$ ergs, h=10 kms, mechanism (30°, 50°, 250°), peak-to-peak amplitude at SHAB tangential is 0.0042 cm.
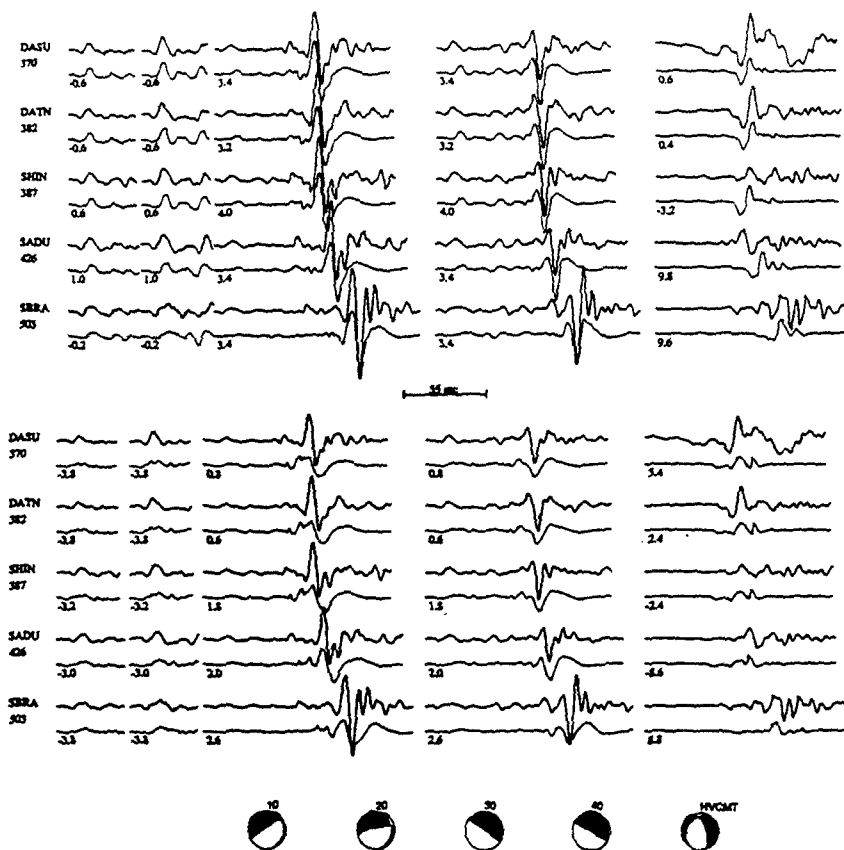
Figure 4. Comparison of solutions of the 328.2311 event (M=5.6) with the CMT solution. Upper panel displays results assuming a depth of 20 km (M_o=6.3 x 10^{24} ergs). Lower panel displays results for a depth of 40 km (M_o= 8.9 x 10^{24} ergs).

Figure 5. Comparison of observations and synthetics for a deep event (h=150 kms), 276.1438.

d276
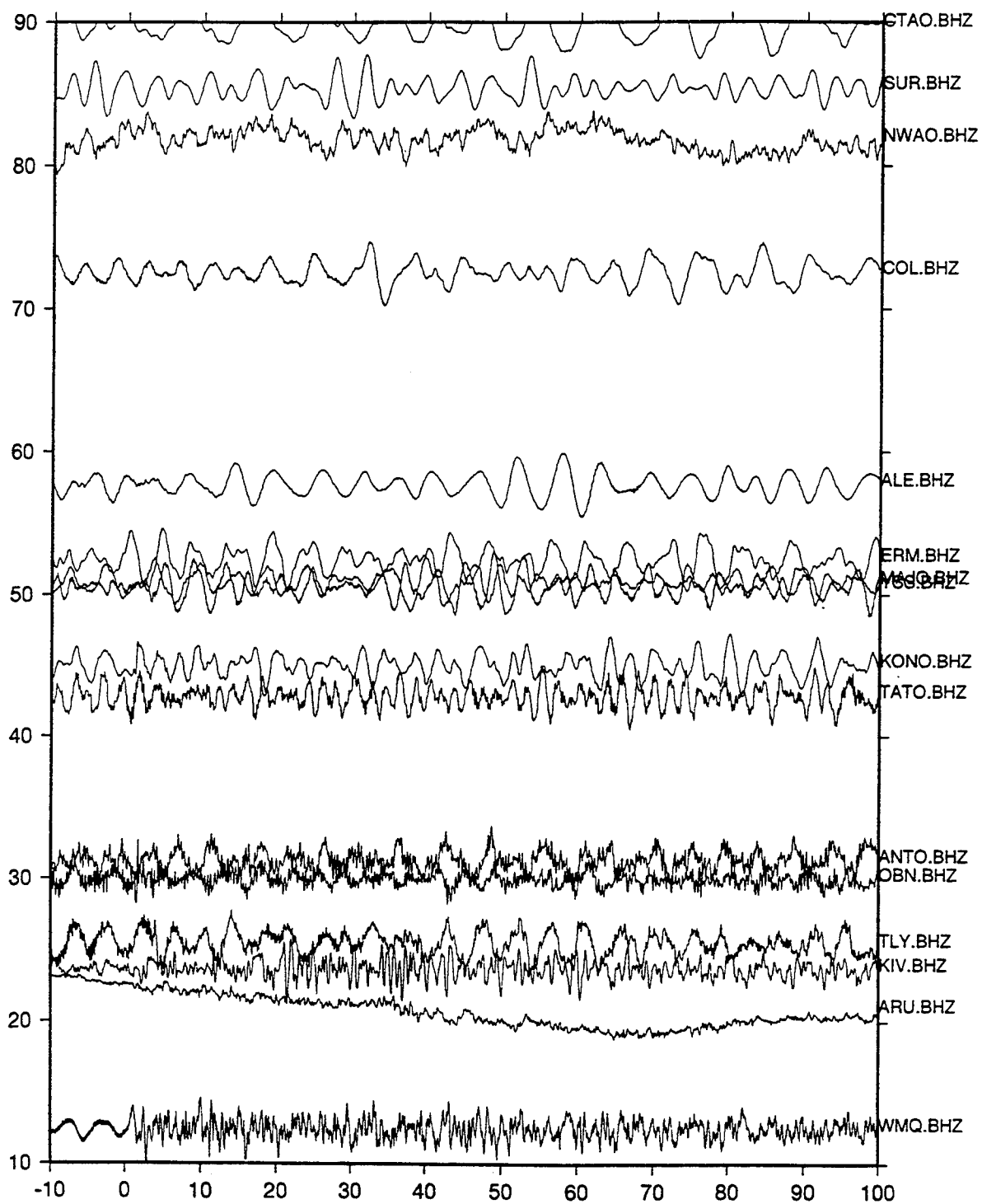
Figure 6. Output of FARM preview of IRIS data, vertical broadband for the 276 event (M=5.2) displayed in Figure 5. Only a few stations have useful data.

Table 1. Average velocity model of the Tibetan Plateau

layer	Thickness (km)	V_p (km/s)	V_s (km/s)
1	4	4.70	2.70
2	60	6.20	3.50
3	–	8.14	4.70

Table 2. Locations of the events from PDE catalog

Event	Date	Origin time	*lat.*	*lon.*	h (km)	M_b
355	12-21-91	$19^h52^m45.5$	27.90N	88.14E	57	4.9
067	03-07-92	$22^h41^m50.8$	29.44N	89.37E	113	4.3
095	04-04-92	$17^h43^m20.7$	28.15N	87.98E	33	4.9

Table 3. Focal depths and fault plane solutions from waveform modeling

Event	P axis [a]	T axis [a]	h (km)	M_w
355	341±9/57± 8	81±7/ 6± 4	75±10	4.9
067	225±4/31±10	125±4/16±11	75±10	4.4
095	8±7/30± 9	270±9/18± 9	75±10	4.9

[a]Azimuth/Plunge, all in degrees

Regional Wave Attenuation and the Lg/P Discriminant

Thomas J. Sereno, Jr., Darrin D. Wahl, Richard D. Jenkins and Donna J. Williams
Science Applications International Corporation
10260 Campus Point Drive
San Diego, California 92121

ABSTRACT

Results from previous empirical studies indicate that the high-frequency Lg/P ratio is one of the most promising discriminants at regional distances. However, many of these studies are based on co-located earthquakes and explosions in limited geographic regions, and their results must be recalibrated for each new source region. We just started a two-year research project to develop frequency-dependent attenuation models for regional phases and to use them to generalize the high-frequency Lg/P discriminant for use in uncalibrated source regions.We plan to develop attenuation models for up to 10 primary (or Alpha) stations from the Group of Scientific Experts Technical Test (GSETT-3). These models will be used to normalize frequency-dependent Lg/P amplitude ratios for thousands of events recorded during GSETT-3 to a common reference distance. We will develop discriminants based on these distance-corrected ratios, and we will evaluate their effectiveness and limitations (including the sensitivity to the accuracy of the attenuation models). We will obtain *ground-truth* identification for as many of the events as possible, and we will use knowledge of the local natural and industrial seismicity to qualitatively evaluate effectiveness when this information is not available. We will attempt to generalize the distance-corrected Lg/P ratio by geological and tectonic environment so that this discriminant can be extrapolated with confidence to uncalibrated regions.

KEY WORDS: Generalized Inversion, GSETT-3, Regional Discrimination, Regional Wave Attenuation, Regionalization, Software Development, Transportability

Regional Wave Attenuation and the Lg/P Discriminant

INTRODUCTION

Results from previous empirical studies indicate that the high-frequency Lg/P ratio is one of the most promising discriminants at regional distances. However, many of these studies are based on co-located earthquakes and explosions in limited geographic regions, and their results must be recalibrated for each new source region. We just started a two-year research project to develop frequency-dependent attenuation models for regional phases and to use them to generalize the high-frequency Lg/P discriminant for use in uncalibrated source regions. This paper presents our research plan.

1.0 OBJECTIVE

The primary objective of this project is to develop frequency-dependent regional wave attenuation models and use them to generalize the high-frequency Lg/P discriminant. Table 1 lists the primary technical tasks.

Table 1: Task Description

Task	Description
1.0	Develop processing parameters for measuring regional wave amplitudes
2.0	Develop software for regional wave amplitude inversion
3.0	Develop regional wave attenuation models for up to 10 GSETT-3 stations
4.0	Assemble data sets for testing the Lg/P discriminant
5.0	Calculate the distance-corrected Lg/P amplitude ratios
6.0	Determine the identification accuracy of the Lg/P discriminant
7.0	Determine the sensitivity of the Lg/P discriminant to the accuracy of the attenuation models
8.0	Generalize the results in terms of geologic and tectonic environment

We plan to develop attenuation models for up to 10 primary (or Alpha) stations from the Group of Scientific Experts Technical Test (GSETT-3). These models will be used to normalize frequency-dependent Lg/P amplitude ratios for thousands of events recorded during GSETT-3 to a common

reference distance. We will develop discriminants based on these distance-corrected ratios, and we will evaluate their effectiveness and limitations (including the sensitivity to the accuracy of the attenuation models). We will obtain *ground-truth* identification for as many of the events as possible, and we will use knowledge of the local natural and industrial seismicity to qualitatively evaluate effectiveness when this information is not available. We will attempt to generalize the distance-corrected Lg/P ratio by geological and tectonic environment so that this discriminant can be extrapolated with confidence to uncalibrated regions.

2.0 PRELIMINARY RESEARCH RESULTS

We started development of software to invert frequency-dependent regional wave amplitudes for attenuation models (Task 2.0). Figure 1 shows the major software components. DFX was developed for the International Data Center (IDC) to perform seismic signal detection and feature extraction. It will be used in this study to compute frequency-dependent regional wave amplitudes in the time and frequency domains. AmpInv is a new program being developed under this contract to invert regional wave amplitudes for attenuation models.
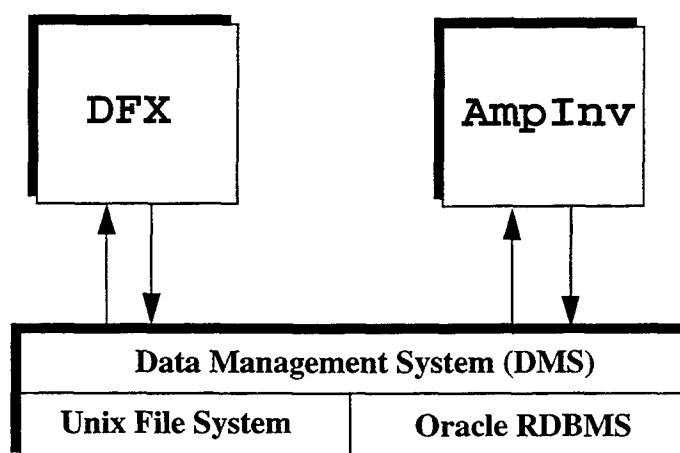
Figure 1. This shows the two major software components for the attenuation study, DFX and AmpInv. These components share a common library for access to the centralized data management system.

3.0 RECOMMENDATIONS AND FUTURE PLANS

Our plans for this two-year project are divided into two categories: (1) frequency-dependent regional wave attenuation, and (2) the Lg/P discriminant. After a brief introduction, this section describes the work to be completed in each category.

3.1 Introduction

Several early studies propose the use of Lg/P ratios as a regional event discriminant for earthquakes and nuclear explosions [e.g., *Willis et al.*, 1963; *Blandford*, 1981; *Gupta and Burnetti*, 1981; *Nuttli*, 1981; *Pomeroy et al.*, 1982; *Murphy and Bennett*, 1982; *Bennett and Murphy*, 1986; *Taylor et al.*, 1989]. These studies found that Lg/P discriminants provide some separation between nuclear explosions and earthquakes, but that there is significant overlap between the two populations. More recent studies have exploited higher frequencies to improve the Lg/P discrimi-

nant and have extended the application to include industrial chemical explosions. For example, high-frequency (2-16 Hz) Lg/P ratios have shown to be successful in discriminating between earthquakes and mining explosions in northern and central Europe [e.g., *Baumgardt and Young*, 1990; *Dysart and Pulli*, 1990; *Baumgardt et al.*, 1992; *Wuster*, 1993], and earthquakes and underground nuclear explosions in Eurasia [e.g., *Bennett et al.*, 1989; *Chan et al.*, 1990; *Bennett et al.* 1992]. The practice of mining can also induce stress-release events such as rockbursts. Often these stress-release events are much larger than the actual mining explosions. *Bennett et al.* [1993] show that stress-release events in central Europe and South Africa have similar Lg/P ratios (> 1.0) to earthquakes across broad frequency bands, and these are higher than the ratios for underground nuclear explosions (< 1.0) at frequencies above 2 Hz. Most of these studies use co-located explosions and earthquakes to minimize propagation effects. A major concern expressed in the recent research is that propagation characteristics may have a significant affect on the Lg/P discriminant, and that transportability may be problematic [e.g,. *Lynnes and Baumstark*, 1991; *Bennett et al.*, 1992]. In the next section, we describe how we propose to account for the path effects by developing frequency-dependent regional wave attenuation models.

3.2 Frequency-Dependent Regional Wave Attenuation

Amplitude Measures (Task 1.0). Frequency-dependent amplitudes will be computed automatically using DFX. We will investigate the use of both spectral and time-domain amplitude measurements. For either type, the time window will depend on which regional phase is being measured. Part of this task will be to determine the optimal time windows for P and Lg phases. We will experiment with fixed group velocity windows with respect to the estimated location and origin time of the event, and shorter, fixed-duration time windows near the arrival time of associated P and Lg phases. The time windows will be selected on the basis of the consistency of the log amplitudes with magnitudes in independent bulletins. The spectra computed by DFX will be stored in Unix ASCII files and indexed in an Oracle relational database management system (RDBMS). The time-domain amplitudes will be stored in the Oracle RDBMS.

Amplitude Inversion (Task 2.0). Our parameterization and inversion method are described in detail by *Sereno* [1990]. Briefly, the frequency-dependent (either time-domain or spectral) amplitude of the *kth* wave recorded at the *ith* station from the *jth* source is parameterized as:

$$\log A_{ijk}(f) = \log A^0_{jk}(f) + B_k(\Delta_{ij}, \Delta_0, f) + \delta_{ik} \tag{1}$$

where $A^0_{jk}(f)$ is the amplitude at a reference distance Δ_0, $B_k(\Delta_{ij}, \Delta_0, f)$ is the attenuation from the reference distance to the epicentral distance Δ_{ij}, and δ_{ik} is a station correction. The amplitude at the reference distance is expressed in terms of the material properties at the source and the receiver, source parameters such as the seismic moment, the shape of the source spectrum, and a wave-dependent excitation factor. We use the *Mueller and Murphy* [1971] and *Brune* [1970, 1971] models to parameterize the shape of the source function.

The attenuation is parameterized in terms of a power-law distance dependence with a frequency-dependent exponent:

$$B_k(\Delta_{ij}, \Delta_0, f) = -\log e \cdot \alpha^0_k \cdot f + n_k(f) \cdot \log(\Delta_0/\Delta_{jk}) \tag{2}$$

where the first term accounts for anelastic attenuation from the source to the reference distance, and the second term is the total attenuation from the reference distance to the epicentral distance.

The total attenuation includes geometrical spreading, scattering and anelasticity. It is difficult to separate these terms since the geometrical spreading of regional phases is a complicated function of the crustal and upper mantle velocity structure [e.g., Sereno and Given, 1990]. Fortunately, it is not important to separate these terms for application to the Lg/P discriminant. The exponent, $n_k(f)$, is parameterized as a linear function of frequency. Chun et al. [1989] used this parameterization to estimate Pn attenuation in the Canadian Shield.

Frequency-Dependent Attenuation Models (Task 3.0). This parameterization will be used to develop frequency-dependent attenuation models for regional phases recorded by up to 10 stations in the primary (or Alpha) network for GSETT-3. An example is provided by our earlier work with data from the NORESS and ARCESS arrays in Norway [Sereno, 1990]. We inverted frequency-dependent amplitudes of four regional phases for source scaling parameters, frequency-dependent attenuation models, and station corrections. The data set included nearly 100 events with magnitudes between 2.0 and 3.6, and epicentral distances between 200 and 1600 km. Our results for the frequency-dependent attenuation of Pn, Pg, Sn, and Lg are plotted in Figure 2. The model provides a reasonable fit to the observed data.

3.3 Lg/P Discriminant

Data Sets (Task 4.0). The data sets for testing the Lg/P discriminant will include the events used to develop the attenuation models, but they must also include others. The attenuation models are based on the highest quality data that are available. However, the Lg/P discriminant must be tested on typical events in the GSETT-3 analyst-reviewed bulletin (i.e., not just the highest-quality events). We propose to assemble two test data sets to evaluate the effectiveness of the Lg/P discriminant for each station. We will call the first one the ground-truth data set because it will consist of events whose identifications are known with high confidence. It will be assembled by gathering information from operators of local networks, universities, and government agencies. The second data set will include a large number of events (>1000 per station) intended to represent the type of events that must be routinely identified by a seismic monitoring system. In general, we will not have ground-truth information for these events. Instead, we will rely on knowledge of the local natural and industrial seismicity to qualitatively evaluate the effectiveness of the Lg/P discriminant.

We used this approach to evaluate the performance of the Event Identification System that we developed for ARPA's Intelligent Monitoring System (IMS) [Sereno and Wahl, 1993]. We used a local bulletin produced by the University of Helsinki as our ground-truth data set. The events in the Helsinki Bulletin are identified as mine blasts or earthquakes by experienced analysts based on data from a dense network of stations in northern Europe. The second data set that we used to evaluate the Event Identification System consisted of >6000 events in the IMS bulletin between November 1990 and June 1991. The results are plotted on a map in Figure 3. All of the events that were identified as mine blasts occurred in areas of active mining. Most of the events that were identified as earthquakes are in areas with the highest natural seismicity in this region: the southwest coast of Norway and the Mid-Atlantic Ridge. Many of the events that were identified as explosions are in active mining areas, but our case-based approach failed to associate them with a known mine. Several of the offshore clusters are known to be explosions from military exercises. Some of the events are obviously identified incorrectly by the automated system (like the events that were identified as explosions on the Mid-Atlantic Ridge). This example shows how we are able to gain valuable information regarding the performance of a discriminant (or set of discrimi-
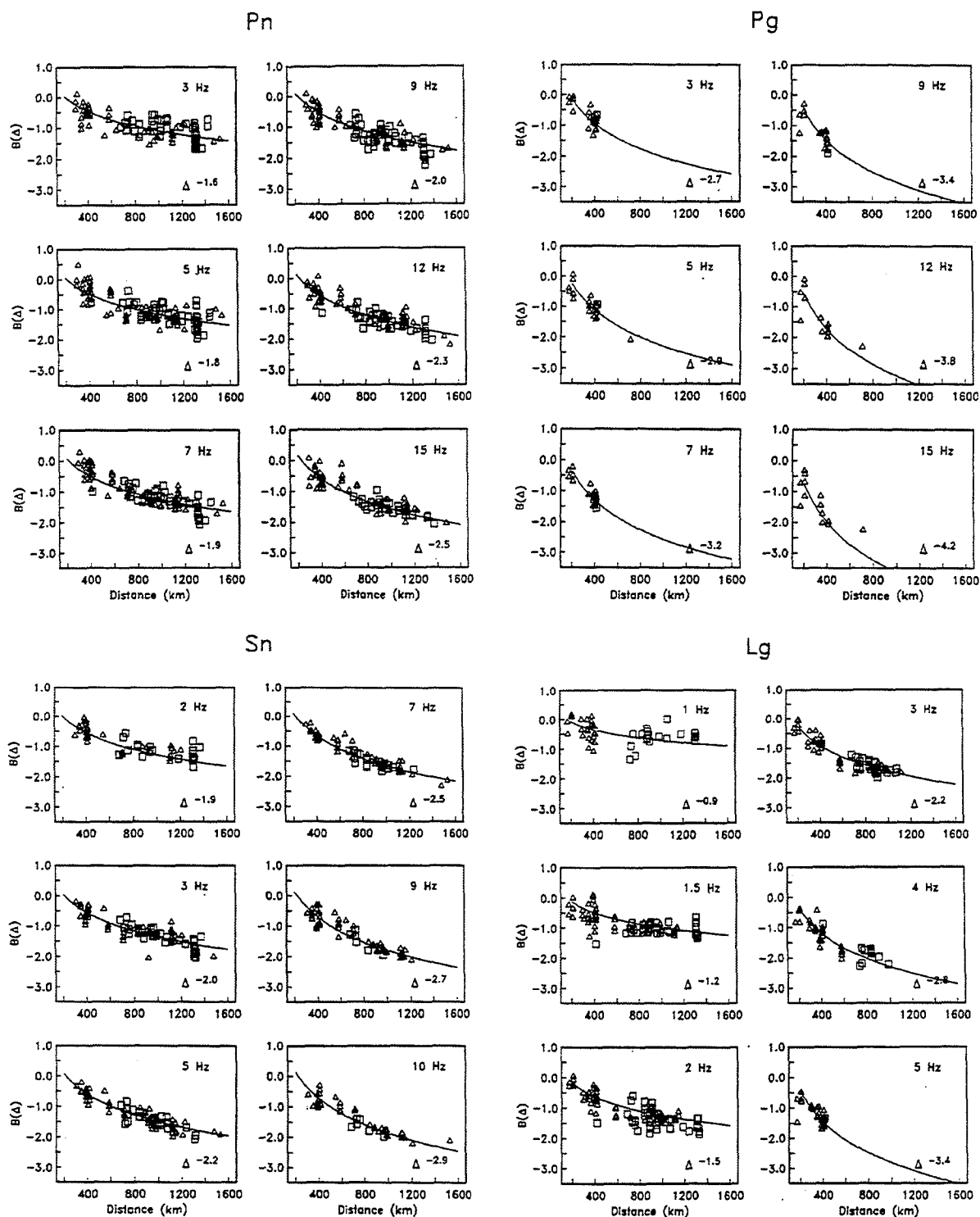
Figure 2. Attenuation is plotted at six frequencies for Pn, Pg, Sn and Lg. The attenuation is parameterized in terms of a power-law dependence on distance. The exponent, *n(f)*, is modeled with a linear dependence on frequency. The solid curves show the attenuation models derived by generalized inversion. The symbols are used to plot source-corrected data recorded at NORESS and ARCESS.

Earthquakes
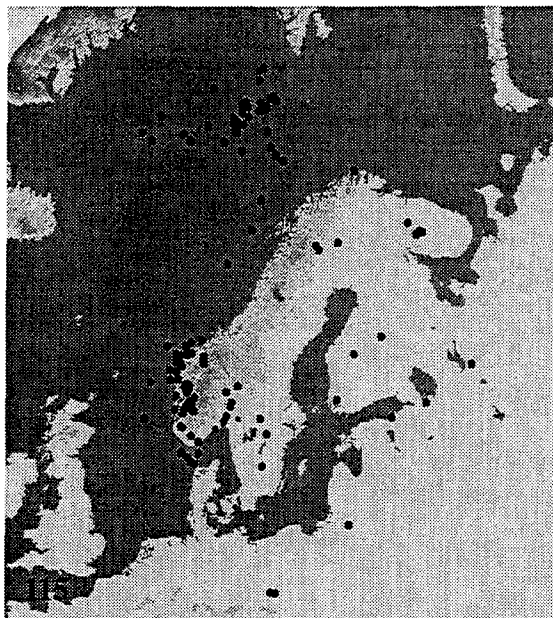
Mine Blasts
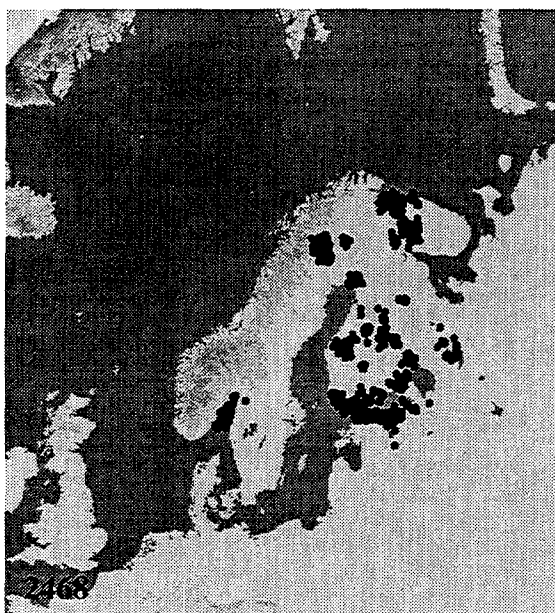
Explosions (ML > 2.0)
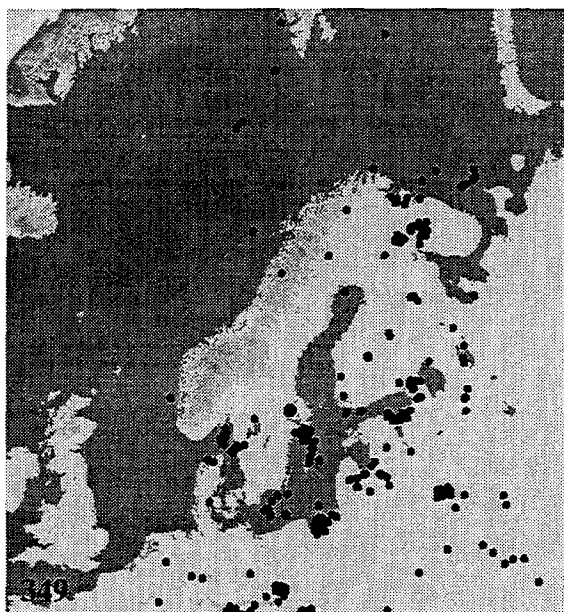
Figure 3. These maps show the location of events that were identified as earthquakes, mine blasts and explosions by the IMS Event Identification System. Ground-truth information is not available for these events, but is it clear that most of the events are identified correctly. The number of events is listed in the lower left corner of each map.

nants) using the general properties of a large number sampling of events without the *ground-truth* information that can be difficult and time-consuming to compile. We plan to use this same approach to evaluate the performance of the Lg/P discriminant.

Distance-Corrected Lg/P Ratios (Task 5.0). The Lg/P ratios will be corrected for distance using the attenuation models. The distance-corrected Lg/P ratios will be compared with the uncorrected ratios to verify that the dependence on distance has been eliminated. For example, Figure 4 shows uncorrected and distance-corrected ratios for events recorded by the high-frequency arrays in northern Europe.
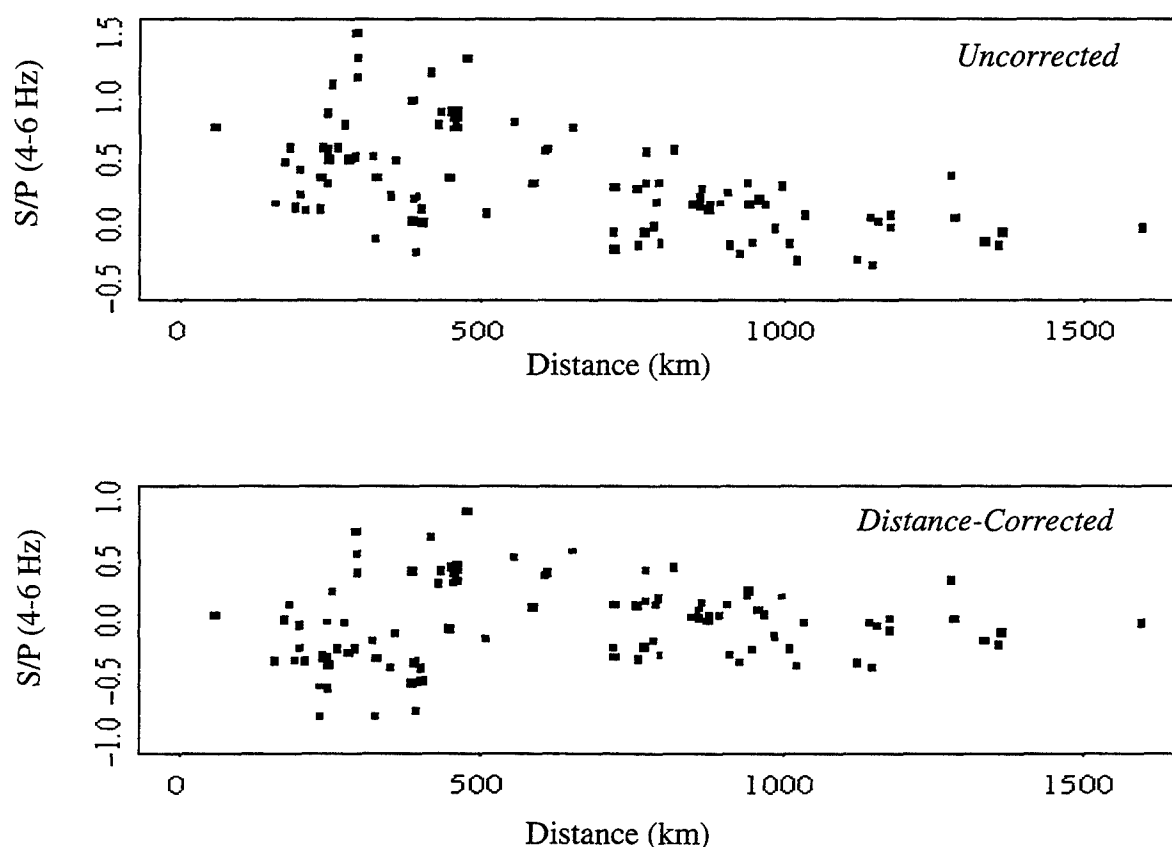
Figure 4. The top panel shows the S/P amplitude ratio in the 4-6 Hz band as a function of distance for events recorded in northern Europe. The bottom panel shows the same events after applying distance corrections developed by *Sereno* [1990].

Identification Accuracy (Task 6.0). The next step is to determine the identification accuracy of the distance-corrected Lg/P discriminant for the data sets described above. We will compare the distributions of the distance-corrected Lg/P amplitude ratios for earthquakes and explosions in our *ground-truth* data set. We have already performed this type of analysis using data from the IMS high-frequency arrays in northern and central Europe. For example, Figure 5 shows the distribution of the distance-corrected *Largest-S/First-P* ratio for earthquakes and explosions recorded by the NORESS, ARCESS, and FINESA arrays in northern Europe, and by the GERESS array in central Europe. The identifications of the events in northern Europe are from the University of

Northern Europe
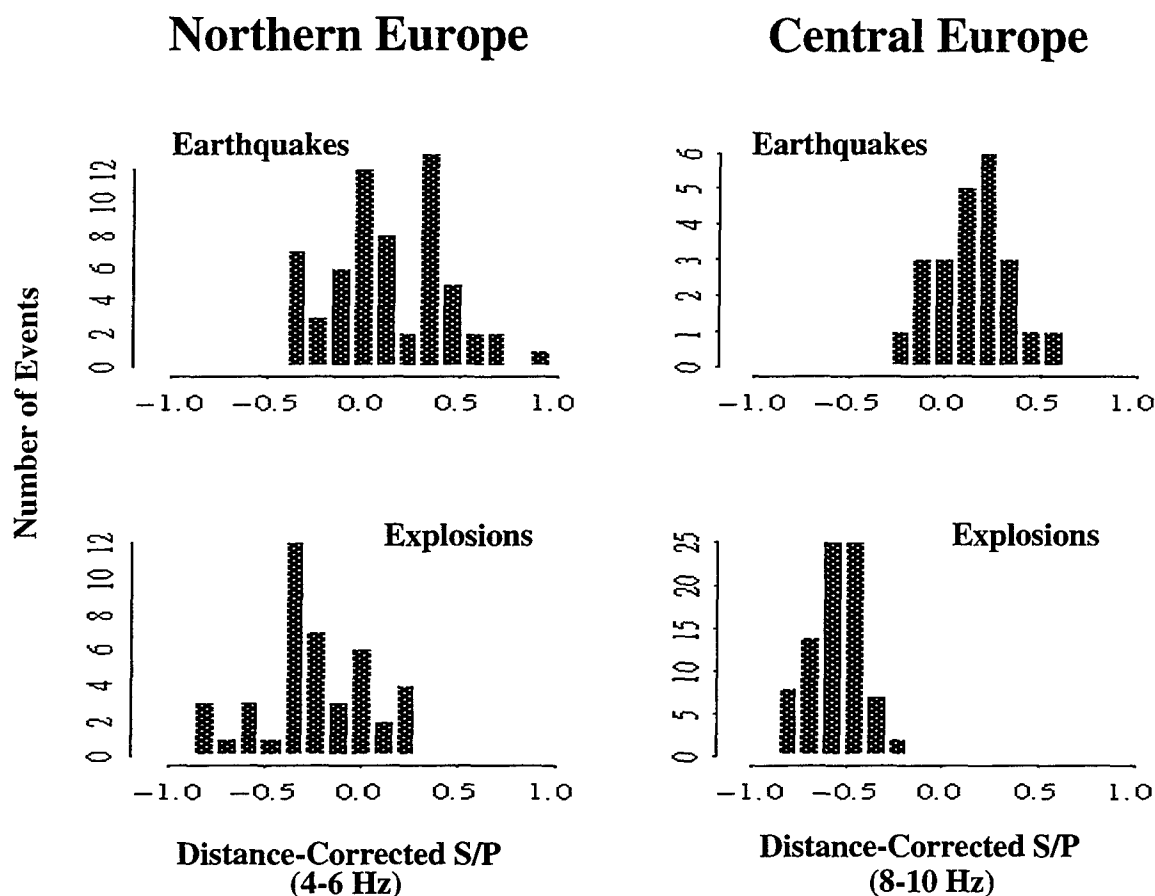
Central Europe

Figure 5. Distance-corrected *Largest-S/First-P* ratios are plotted for earthquakes and explosions in northern Europe (4-6 Hz) and Central Europe (8-10 Hz).

Helsinki and from the *ground-truth* event identification data set developed by *Grant et al.* [1993]. The earthquakes are primarily from the west coast of Norway (near Bergen and Steigen), and on the Mid-Atlantic Ridge. The mining explosions are in the Kola Peninsula, northern Sweden, Finland, St. Petersburg and Estonia. Many of the events in central Europe were also identified in the *ground-truth* database at the Center for Monitoring Research (CMR). They include mining explosions and earthquakes in Vogtland, Germany [*Wuster*, 1993], presumed mining explosions in Austria about 175 km south of GERESS [H. P. Harjes, personal communication], and mining-induced tremors in Lubin, Poland [*Grant et al.*, 1993].

The distance-corrected *Largest-S/First-P* amplitude ratio is higher for earthquakes than for explosions recorded at GERESS in the 8-10 Hz band. *Baumgardt et al.* [1992] previously found that the Lg/P ratio in this band was successful for identifying events in Vogtland, Germany, and we showed that it could be extrapolated to other source regions by applying distance corrections. The Lg/P amplitude ratio does not appear to work as well for events in northern Europe (Figure 5). We found the best discrimination for these data was provided by ratios in the 4-6 Hz band. It is likely that a multivariate approach that combines results from several frequency bands will provide better results in these cases. We will investigate these and other alternatives for deriving a composite identification from Lg/P ratios.

Sensitivity to Attenuation Models (Task 7.0). The sensitivity of the distance-corrected Lg/P discriminant to the accuracy of the attenuation model will directly address the issue of the transportability of this discriminant to uncalibrated regions. We plan to evaluate the effectiveness of the discriminant at each station when distance corrections derived from data recorded at other stations are used. The final result will be an estimate of the identification accuracy of the Lg/P discriminant at each station as a function of the attenuation model.

Regionalization (Task 8.0). This task is to generalize the distance-corrected Lg/P discriminant in terms of geologic and tectonic environment. Like the previous task, it addresses the issue of transportability to uncalibrated regions. First, we will group the data by tectonic province [e.g., *Jordan*, 1981]. Next, we will derive new attenuation models for each province using the method described in earlier Sections. The average attenuation models for each province will be used to compute new distance-corrected Lg/P ratios. The identification accuracy for each province will be compared to the results when station-specific attenuation models were used.

REFERENCES

Baumgardt, D., and G. Young, Regional seismic waveform discriminants and case-based event identification using regional arrays, *Bull. Seismol. Soc. Am.*, *80*, 1874-1892, 1990.

Baumgardt, D., J. Carney, M. Maxson and S. Carter, Evaluation of regional seismic discriminants using the Intelligent Seismic Event Identification System, Tech. Rep. *SAS-TR-93-38*, ENSCO, Inc., Springfield, Virginia, 96 pp., 1992.

Bennett, J., B. Barker, K. McLaughlin, and J. Murphy, Regional discrimination of quarry blasts, earthquakes, and underground nuclear explosions, Final Rep. *GL-TR-89-0114*, 146 pp., 1989. ADA223148

Bennett, J., A. Campanella, J. Scheimer, and J. Murphy, Demonstration of regional discrimination of Eurasian seismic events using observations at Soviet IRIS and CDSN stations, Final Rep. *PL-TR-92-2090*, 122 pp., 1992. ADA253275

Bennett, J., and J. Murphy, Analysis of seismic discrimination capabilities using regional data from western United States events, *Bull. Seismol. Soc. Am.*, *76*, 1069-1086, 1986.

Bennett, J., J. Scheimer, A. Campanella, and J. Murphy, Seismic characteristics of rockbursts for use in discrimination, Sci. Rep. *PL-TR-93-2059*, 89 pp., 1993. ADA266063

Blandford, R., Seismic discrimination problems at regional distances, in *Identification of Seismic Sources - Earthquake or Nuclear Explosion*, E. S. Husebye and S. Mykkeltveit (Ed.), D. Reidel Publishing Co., Dordrecht, The Netherlands, 695-740, 1981.

Brune, J., Tectonic stress and the spectra of seismic shear waves from earthquakes, *J. Geophys. Res.*, *75*, 4997-5009, 1970.

Brune, J., Correction to tectonic stress and the spectra of seismic shear waves from earthquakes, *J. Geophys. Res.*, *76*, 5002, 1971.

Chan, W., R. Baumstark, and R. Cessaro, Spectral discrimination between explosions and earthquakes in central Eurasia, Tech. Rep. *GL-TR-90-0217*, 38 pp., 1990. ADA230048

Chun, K., R. Kokoski, and G. West, High-frequency Pn attenuation in the Canadian Shield, *Bull. Seismol. Soc. Am.*, *79*, 1039-1053, 1989.

Dysart, P., and J. Pulli, Regional seismic event classification at the NORESS array: seismological measurements and the use of trained neural networks, *Bull. Seismol. Soc. Am.*, *80*, 1910-1933, 1990.

Grant, L., F. Ryall, and J. Coyne, CSS ground-truth database: update and case study, Proceedings of the 15th Annual Seismic Research Symposium, *PL-TR-93-2160*, 114-120, 1993. ADA271458

Gupta, I., and J. Burnetti, An investigation of discriminants for events in Western USSR based on regional phases recorded at station Kabul, *Bull. Seismol. Soc. Am., 71*, 263-274, 1981.

Jordan, T., Global tectonic regionalization for seismological data analysis, *Bull. Seismol. Soc. Am., 71*, 1131-1141, 1981.

Lynnes, C., and R. Baumstark, Phase and spectral ratio discrimination in North America, Tech. Rep. *PL-TR-91-2212(II)*, 68 pp., 1991. ADA246673

Mueller, R., and J. Murphy, Seismic characteristics of underground nuclear detonations, *Bull. Seismol. Soc. Am., 61*, 1675-1692, 1971.

Murphy, J., and J. Bennett, A discrimination analysis of short-period regional seismic data recorded at Tonto Forest Observatory, *Bull. Seismol. Soc. Am., 72*, 1351-1366, 1982.

Nuttli, O., On the attenuation of Lg waves in western and central Asia and their use as a discriminant between earthquakes and explosions, *Bull. Seismol. Soc. Am., 71*, 249-261, 1981.

Pomeroy, P., W. Best, and T. McEvilly, Test ban treaty verification with regional data - a review, *Bull. Seismol. Soc. Am., 72*, S89-S129, 1982.

Sereno, T., Attenuation of regional seismic phases in Fennoscandia and estimates of arrival time and azimuth uncertainty using data recorded by regional arrays, Tech. Rep. *SAIC-90/1472*, 115 pp., 1990.

Sereno, T., and J. Given, Pn attenuation for a spherically symmetric earth model, *Geophys. Res. Lett., 17*, 1141-1144, 1990.

Sereno, T. and D. Wahl, A fuzzy logic approach to regional seismic event identification: application to the Novaya Zemlya event on 31 December 1992, Tech. Rep. *SAIC-93/1156*, 24 pp., 1993.

Taylor, S., M. Denny, E. Vergino, and R. Glaser, Regional discrimination between NTS explosions and western United States earthquakes at regional distances, *Bull. Seismol. Soc. Am., 79*, 1142-1176, 1989.

Willis, D., J. DeNoyer, and J. Wilson, Differentiation of earthquakes and underground nuclear explosions on the basis of amplitude characteristics, *Bull. Seismol. Soc. Am., 53*, 979-987, 1963.

Wuster, J., Discrimination of chemical explosions and earthquakes in central Europe - a case study, *Bull. Seismol. Soc. Am., 83*, 1184-1212, 1993.

A Transportable Regional Discriminant Using a Maximum Likelihood Analysis of Surface Waves

J. L. Stevens and K. L. McLaughlin
S-CUBED
P. O. Box 1620
La Jolla, CA 92038
Contract No. F19628-95-C-0110
Sponsored by AFTAC

Abstract

The objective of this research is to develop a robust extension of the mb:Ms discriminant that is:

1. transportable from region to region,
2. optimizeable for each region,
3. frequency independent,
4. usable at regional and teleseismic distances,
5. applicable to small magnitude events,
6. able to determine an upper bound in the absence of surface wave data,
7. robust with respect to regional variations and operational considerations,
8. usable in an operational system.

The product of this research will be a procedure to analyze surface waves from earthquakes, explosions, and other seismic sources, and to form a discriminant, an extension of the mb:Ms discriminant, that can be implemented in an automated, semi-automated, or interactive system. The research will test the procedure on a broad range of data to determine the range of reliability, minimum magnitude for which the method provides reliable results, limitations and unusual conditions that might cause the analysis procedure or discriminant to fail.

In brief, the method that we plan to implement works as follows: In place of Ms, we use path corrected spectral magnitudes (scalar moment) combined with a maximum likelihood procedure. The path corrections include phase-matched filtering which compress the data into a relatively small time window, reducing the problem of interfering arrivals. The scalar moment is essentially a spectral magnitude, averaged over a range of frequencies and corrected for source and path effects. An explosion Green's function is used for path correction for both explosions and earthquakes. Since it is not necessary to know the source type in advance, the method can be used for discrimination in the same manner as mb:Ms. An upper bound on the scalar moment can be found even if no surface wave data is measureable. Stevens and McLaughlin (1988) applied this procedure to a large number of explosions and earthquakes in Central Asia and the Western United States.

Keywords: Seismic, Discrimination, Surface Wave, Explosion, Earthquake, Ms

LLNL's Regional Seismic Discrimination Research

William R. Walter, Kevin M. Mayeda, Peter Goldstein, Howard J. Patton,
Steve Jarpe and Lew Glenn

Earth Sciences Division, Lawrence Livermore National Laboratory

Abstract

The ability to negotiate and verify a Comprehensive Test Ban Treaty (CTBT) depends in part on the ability to seismically detect and discriminate between potential clandestine underground nuclear tests and other seismic sources, including earthquakes and mining activities. Regional techniques are necessary to push detection and discrimination levels down to small magnitudes, but existing methods of event discrimination are mainly empirical and show much variability from region to region. The goals of Lawrence Livermore National Laboratory's (LLNL's) regional discriminant research are to evaluate the most promising discriminants, improve our understanding of their physical basis and use this information to develop new and more effective discriminants that can be transported to new regions of high monitoring interest.

In this report we discuss our preliminary efforts to geophysically characterize two regions, the Korean Peninsula and the Middle East-North Africa. We show that the remarkable stability of coda allows us to develop physically based, stable single station magnitude scales in new regions. We then discuss our progress to date on evaluating and improving our physical understanding and ability to model regional discriminants, focusing on the comprehensive NTS dataset. We apply this modeling ability to develop improved discriminants including slopes of *P* to *S* ratios. We find combining disparate discriminant techniques is particularly effective in identifying consistent outliers such as shallow earthquakes and mine seismicity. Finally we discuss our development and use of new coda and waveform modeling tools to investigate special events.

Objectives

The ability to negotiate and verify a Comprehensive Test Ban Treaty (CTBT) depends in part on the ability to seismically detect and discriminate between potential clandestine underground nuclear tests and other seismic sources, including earthquakes and mine related events. While large magnitude events can be detected and discriminated teleseismically using well established techniques, events smaller than about magnitude 4.5 may not have adequate signal above the noise to identify definitively. Regional records offer stronger signals and broader frequency content, both of which have the potential to push the identification threshold to a much lower magnitude. However regional methods of event discrimination are mainly empirical and show much variability from region to region. The aim of LLNL's seismic monitoring research is to evaluate the most promising regional discriminants, improve our understanding of their physical basis and use this information to develop new and more effective discriminants that can be transported to new regions. We are applying these regional discriminants in two regions of monitoring interest, the Korean Peninsula and the Middle East-North Africa.

Research Accomplished

As part of the overall Department of Energy CTBT Research and Development program, LLNL is pursuing a broad and comprehensive research effort to improve our capabilities to seismically discriminate potential underground nuclear tests from other natural and man-made source of seismicity. We present here four aspects of this work: Geophysical Characterization, Discriminant Transportability, Improved Discriminants and Special Event Analysis.

Geophysical Characterization

Before beginning to apply regional discriminant techniques to data in an uncalibrated area of the world, several very basic steps need to be taken. These include determining and evaluating some geophysical parameters which are not readily available in the geophysical literature for regions outside of the well calibrated areas of North America, Europe and the nuclear testing sites, where most discriminant studies have been done. Examples include but are not limited to: 1) identifying the regions where the regional phases P_n, P_g, S_n, L_g and the surface waves propagate and where they are blocked; 2) developing a regional magnitude scale consistent with teleseismic magnitude scales and/or physical properties of the events; 3) developing basic regional 1-D velocity models for subregions to predict phase crossovers (e.g. P_n-P_g), relative amplitudes and to locate small events; 4) developing simple frequency dependent attenuation relations for the regional phases to allow a comparison of events at different distances; and 5) building up a ground truth database of known event types in order to begin to evaluate discriminant performance.

To illustrate this process we focus on number (2) above, the example of developing a regional magnitude scale for a new area. It is well known that regional magnitude scales such as $m_b(P_n)$, $m_b(L_g)$, and M_L often differ from each other within a region, with regional magnitude scales in other regions and with teleseismic magnitudes such as m_b and M_s. None of these magnitude scales are based directly on a physical property of the source itself. Recently Mayeda and Walter (1995) have developed a stable single station implementation of the moment magnitude scale, M_w (Hanks and Kanamori, 1979), using coda envelopes. This technique takes advantage of the remarkable stability of coda amplitudes as shown in Figure 1. This figure compares coda amplitudes at two stations (left) with L_g amplitudes at the same two stations for the same set of

Basin and Range earthquakes. The coda amplitudes show more than a factor of 8 less scatter than the direct L_g at 1 Hz, a remarkable result considering that L_g is usually thought of as a fairly stable phase (e.g. Hansen et al., 1990). This stability means that we achieve the same accuracy of magnitude estimation with a single station as a network of well distributed stations using L_g. Because moment is a physical quantity, moment magnitude can be compared with moments in other regions directly. We have used the technique to estimate events as small as $M_w=2.2$, with the lower limit determined only by signal above the noise of the regional coda.

We recently applied this coda magnitude technique to a small set of events recorded at a single 3-component station on the Korean Peninsula. It requires a small set of events covering a range of distances which are used to determine the coda attenuation properties to obtain path and relative site corrections. We then determine the moment of several of the larger events using a waveform modeling technique (Walter, 1993) to calibrate the scale and make an absolute site correction. The waveform modeling also directly contributes to the geophysical characterization since it allows an evaluation of published 1-D velocity structures and event locations. The waveform modeling also allows us to begin to build up a ground truth database since we can use it to begin to identify the larger events via their depth and focal mechanism. We illustrate the coda magnitude results in Figure 2 for the few events we have that were large enough to have teleseismic m_b magnitudes or for which we determined moments. Note that the coda based magnitudes correlate better with these independent results than a more simplistic regional magnitude scale based on the amplitude of P_g.

Discriminant Transportability

The general increase in seismicity on the Nevada Test Site (NTS) following the Landers $M_w=7.3$ earthquake on June 28, 1992 along with the historical database of underground nuclear tests forms a nearly ideal dataset for studying the physical basis of earthquake-explosion discrimination. Figure 3 shows the location of these events and illustrates an example of the type of earthquake-explosion difference in the high frequency L_g phase typically observed. We are doing a two part study of discrimination using this dataset. We have recently completed the first part, an empirical study of the most promising small magnitude discriminants (Walter et al., 1995). We are working on the second part, improving our physical understanding of regional discriminants. We approach this problem by modeling the path corrected regional phase spectra as the product of a source spectrum with a transfer function spectrum. The transfer function spectrum represents the near source scattering efficiencies of phase conversions, particularly P to S and R_g to S conversions. Then we model the dependence of the source time function on the material properties at the shot point. We also model the frequency dependence of the transfer function on the depth, mechanism and material properties of the event. An example is shown in Figure 4. where we have successfully matched the general behavior of the high/low spectral ratio discriminant for L_g. This type of physically based modeling ability is crucial to understanding where and under what circumstances a discriminant may fail, especially when it is transported to regions outside of where it was developed and empirical data are insufficient to fully validate it.

Improved Discriminants

As a result of our NTS discrimination work we have begun developing new discriminants that are more effective at separating particular types of events from the explosions. In the original study (Walter et al., 1995) we noted that the P/S ratios P_n/L_g and P_g/L_g appeared to show much variability between the two stations examined, MNV and KNB. While the discrimination

performance improved as the frequency band increased, even at the highest band for reasonable signal, 6-8 Hz, the P_n/L_g discriminant shows many overlapping events, particularly for the shallow earthquakes at station KNB as shown in Figure 5a. We also noted the P/S ratios showed the explosion material dependence was the opposite of the spectral ratios shown in Figure 3. Averaging over stations and taking a simple product of these phase and spectral ratios discriminants to reduce the material property dependence, we improve the discrimination performance greatly (Figure 5 b). Shallow earthquakes still remain somewhat problematic.

Another type of regional discriminant that shows promise is based on comparisons of moment to magnitude (Patton and Walter, 1993; Woods et al., 1993). This is a regional extension of the traditional long-period:short-period discriminants like M_s:m_b but is not limited only to those events large enough to generate surface waves. Moment can potentially be measured on any size event. We are presently investigating techniques to measure moment using the very stable coda methods described in the Geophysical Characterization section. In our initial studies M_o:$m_b(P_n)$ appears to have the potential to correctly classify shallow earthquakes, but it appears to have trouble with mine collapses as shown in Figure 5c (Patton and Walter, 1994). Note that mine collapses are correctly classified in the 6-8 Hz P_n/L_g ratios in Figure 5a.

Discrimination studies in a variety of regions have shown that explosion P/S ratios tend to increase and discrimination improves as frequency increases (e.g. Scandinavia: Dysart and Pulli, 1987, Baumgardt et al, 1992; Central Asia: Bennett et al, 1989; Eastern U.S.: Kim et al; Western U.S.: Walter et al., 1995; and others). These observations suggests that this increasing slope of P/S may be useful as an identifier of explosions. Goldstein (1995) has developed this idea as a discriminant by examining the slope of the P_n/L_g ratio for the NTS data plus other western U.S. earthquakes. The P/S slope results as shown in Figure 5d are quite good, only a few events are misclassified and this discriminant appears to have the best single station performance of those tested. Of particular interest is the improvement in the correct classification of the shallow earthquakes compared with the direct P_n/L_g ratio in Figure 5a. The overall impression in comparing these disparate discriminants in Figure 5 is that because they have different outliers, combinations of discriminants may offer the best hope of improving event identification.

Special Event Analysis

Events that fail one or more discriminants ("special events") may require a more detailed investigation to positively identify. In addition they offer the opportunity to learn more about the physical basis of a particular discriminant by demonstrating how it can fail. As discussed above these are often shallow events with unusual mechanisms. In order to understand some of these persistent special events, namely mine blasts and mine collapses we are carrying out a field program to record and study both of these types of events in detail.

We have been investigating the use of two tools to help identify and understand special events. The first is the coda derived source spectra. While normal depth earthquake spectra have a typically constant low frequency level and rolloff above a corner frequency, unusually shallow events have peaked spectra as shown in Figure 6. The frequency of this peak, at least for explosions scales with absolute depth of burial. In addition, for events with non-earthquake mechanisms the spectra appear to decrease significantly from the peak as frequency decreases. We believe this peaking and rolldown is related to the Rayleigh wave excitation which is a function of depth, velocity structure and mechanism.

123

We have also had good success using waveform modeling techniques (e.g. Walter, 1993) for large events with unusual mechanisms. If the event has detectable surface waves and a reasonable 1-D velocity structure is known, it is possible to discriminate between a collapse and an explosion using the phase of the Rayleigh waves. Ruling out an earthquake is more difficult but if sufficient azimuthal coverage is available, the presence or lack of Love waves can be used. This process is shown in Figure 7. We used this method with good results on two recent large mine collapses, one in Wyoming (Pechmann et al., 1995) and one in the Ural region of Russia.

Conclusions and Recommendations

LLNL is making good progress in characterizing regions of monitoring interest as well as in evaluating and understanding the regional discriminant behavior. We have used this information to develop improved discriminant techniques. Combining different regional discriminants appears to have the potential to achieve very high rates of event identification and discrimination. We are continuing to develop new tools and collect field data to study special events (outliers on discriminant plots). We are optimistic that combining all this information will make discriminant transportability practical, even in regions that presently have little ground truth data.

References

Baumgardt, D. R., J. Carney, M. Maxson, and S. Carter (1992). Evaluation of regional seismic discriminants using the intelligent seismic event identification system, ENSCO Technical Report SAS-TR-93-38, October, 1992.

Bennett, T. J., B. W. Barker, K. L. McLaughlin, J. R. Murphy (1989). Regional discrimination of quarry blasts, earthquakes, and underground nuclear explosions, SCUBED Technical Report SSS-TR-89-10395, April, 1989.

Dysart, P. S. and J. J. Pulli (1987), Spectral study of regional earthquakes and chemical explosions recorded at the NORESS array, SAIC Technical Report C87-03.

Goldstein, P. (1995). Slopes of P to S wave spectral ratios: a broadband regional seismic discriminant and a physical model, *LLNL UCRL-JC-121223*, (submitted to *Geophys Res. Lett.*)

Hanks, T. C. and H. Kanamori (1979). A moment magnitude scale, *J. Geophys. Res.* **84**, 2348-2350.

Hansen, R. A., F. Ringdal, and P. G. Richards (1990). The stability of rms L_g measurements and their potential for accurate estimation of the yields of Soviet underground nuclear explosions, *Bull. Seism. Soc. Am.* **80**, 2106-2126.

Kim, W.-Y., D. W. Simpson, and P. G. Richards (1993), Discrimination of earthquakes and explosions in eastern United States using regional high-frequency data, *Geophys. Res. Lett.*, **20**, 1507-1510.

Mayeda, K. and W. R. Walter (1995). Source parameters of western U.S. earthquakes: moment energy, stress drop and source spectra from regional coda envelopes, *LLNL UCRL-JC-121234* (submitted to *J. Geophys. Res.*).

Patton, H. J. and W. R. Walter (1993). Regional moment:magnitude relations for earthquakes and explosions, *Geophys. Res. Lett.* **20**, 277-280.

Patton, H. J. and W. R. Walter (1994). Correction to "Regional moment:magnitude relations for earthquakes and explosions", *Geophys. Res. Lett.* **21**, 743.

Pechmann, J. C., W. R. Walter, S. J. Nava, and W. J. Arabasz (1995). The February 3, 1995 M_L 5.1 seismic event in the trona mining district of southwestern Wyoming, *Seism. Res. Lett.* **66**, 25-34.

Walter, W. R. (1993). Source parameters of the June 29, 1992 Little Skull Mountain earthquake from complete regional waveforms at a single station, *Geophys. Res. Lett.* **20**, 403-406.

Walter, W. R., K. Mayeda, and H. J. Patton (1995). Phase and spectral ratio discrimination between NTS earthquakes and explosions Part 1: Empirical observations, in press *Bull. Seism. Soc. Am.,* **85**.

Woods, B. B., S. Kedar, and D. Helmberger (1993). $M_L:M_0$ as a regional seismic discriminant, *Bull. Seism. Soc. Am.*, **83**, 1167-1183.
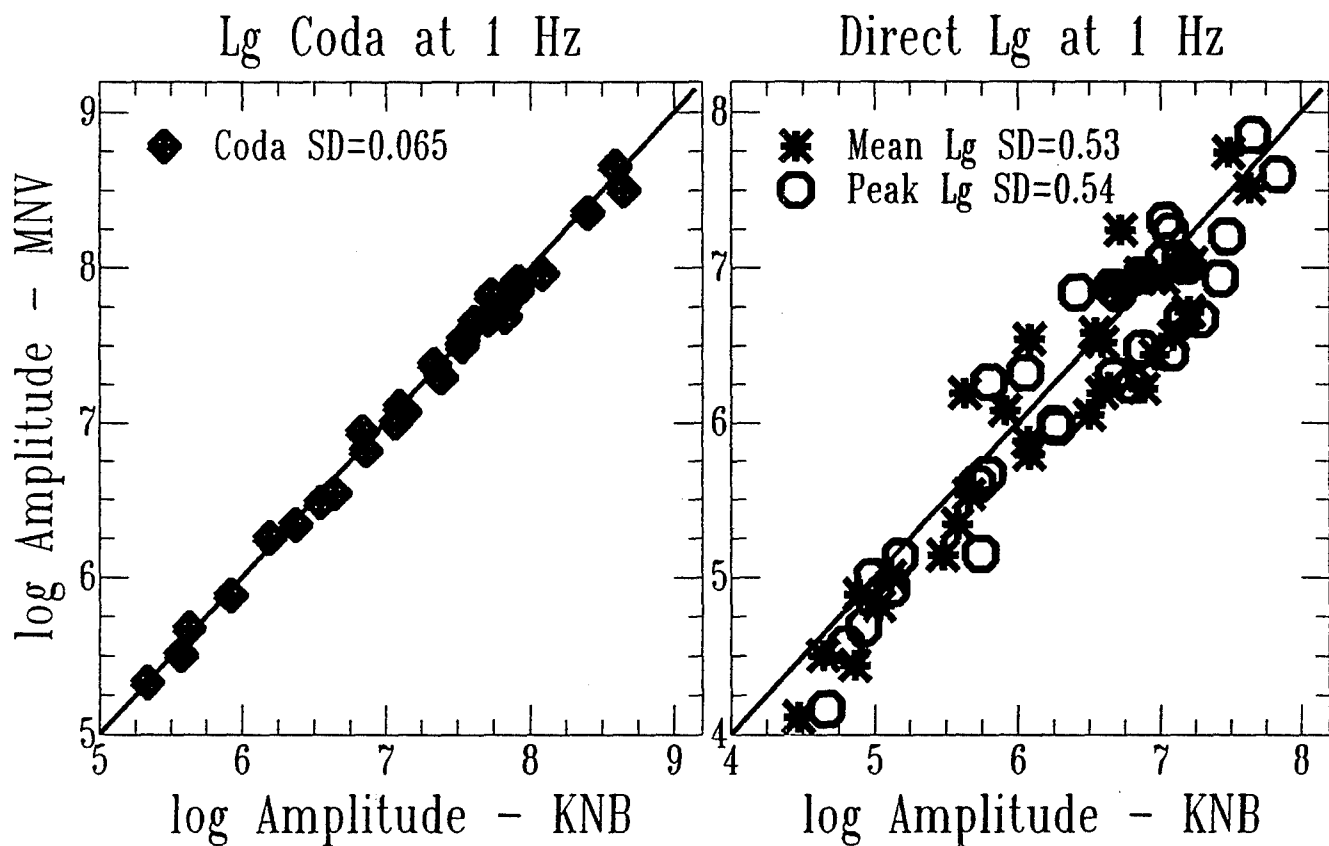
Fig. 1. A comparison of the interstation stability of amplitudes determined from coda with those determined from the direct L_g phase. The regional coda amplitudes are 8 times more stable than direct L_g at 1 Hz, as indicated by the standard deviation from the line. We use this stability to obtain accurate single station estimates of seismic source parameters such as the moment magnitude, M_w (Mayeda and Walter, 1995).
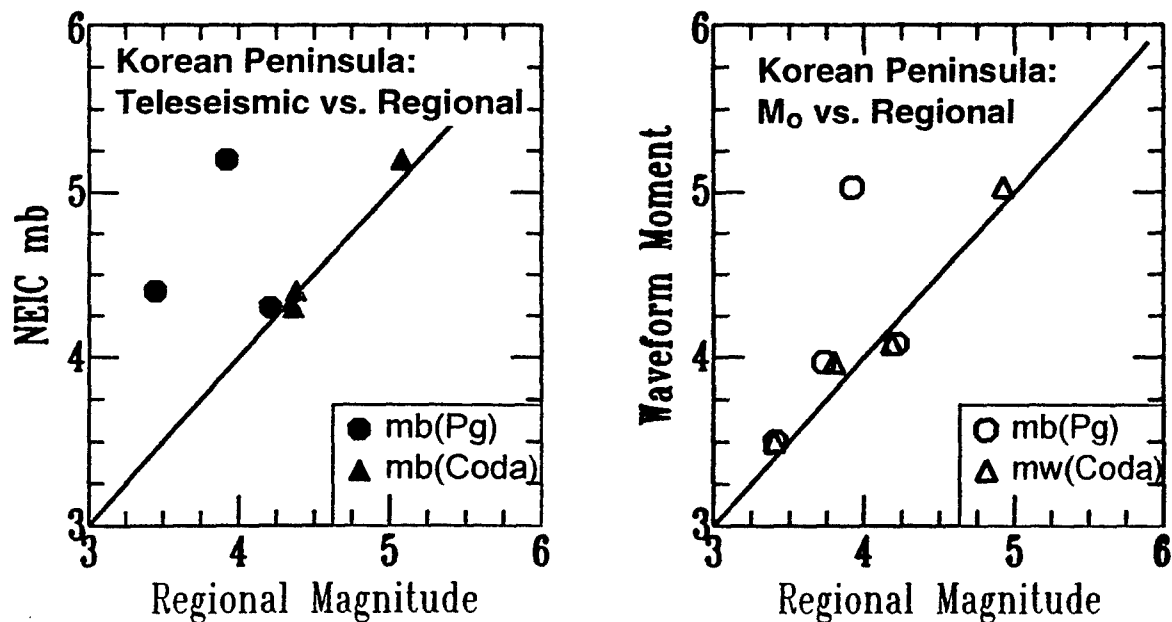
Fig. 2. Preliminary results show the stability of calibrated, single station coda magnitudes are transportable to the Korean Peninsula. The coda results correlate better with independent estimates of size than those based on the amplitude of regional phase P_g. Moments are estimated from regional waveform modeling.
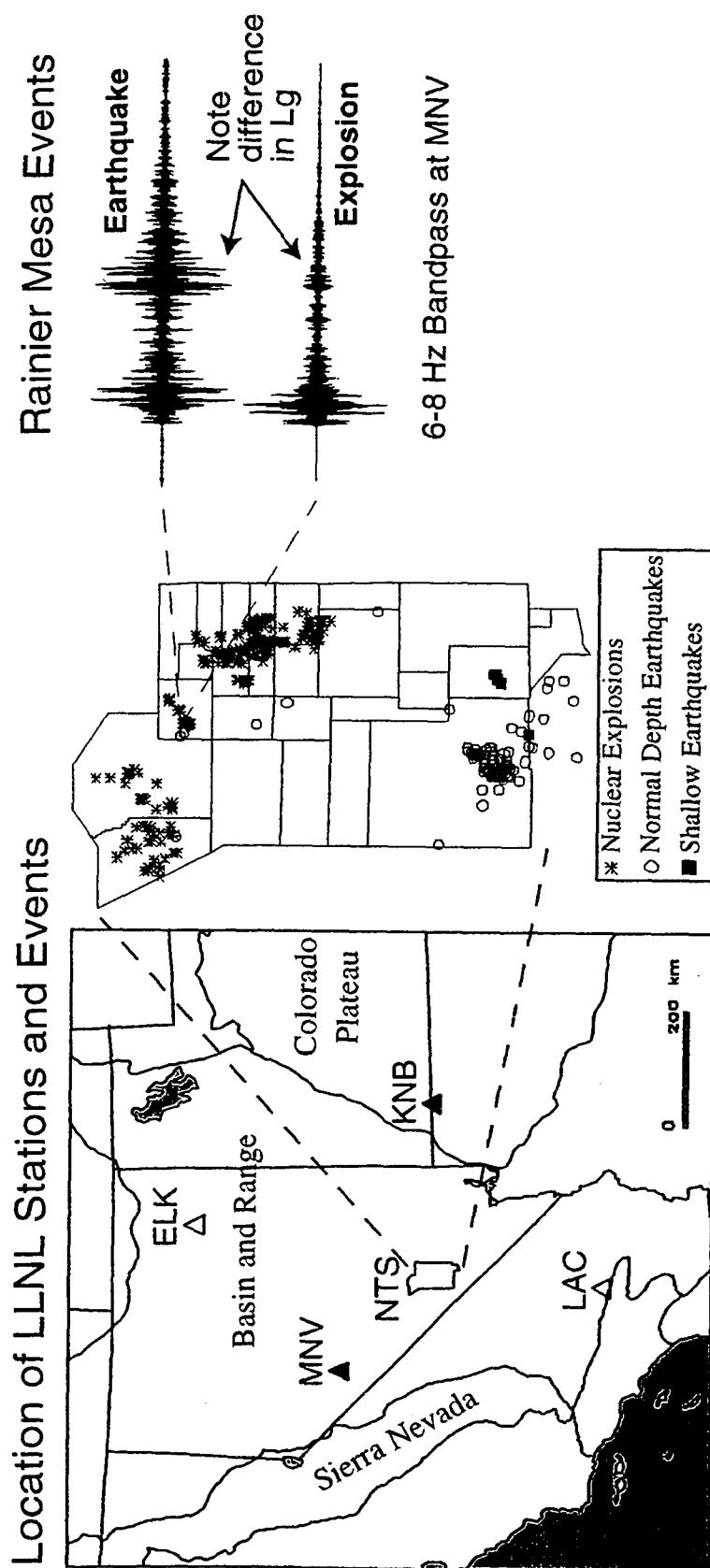
Fig. 3. NTS events form a nearly ideal data set for examining the physical basis of earthquake-explosion discrimination. Map on left shows the locations of NTS and the stations that recorded these events. Center map shows location of earthquakes and explosions at NTS. Right hand traces show the differences in high frequency recordings of a similar sized earthquake and explosion with similar epicenters and magnitudes. Because of the similarity of the paths we can ascribe the observed differences in L_g to depth, mechanism, source time function and material property differences. The data cover a range of depths, magnitudes, mechanisms and material properties allowing us to evaluate the relative importance of each for discrimination.

Spectral Ratio Discrimination Depends on Two Effects:
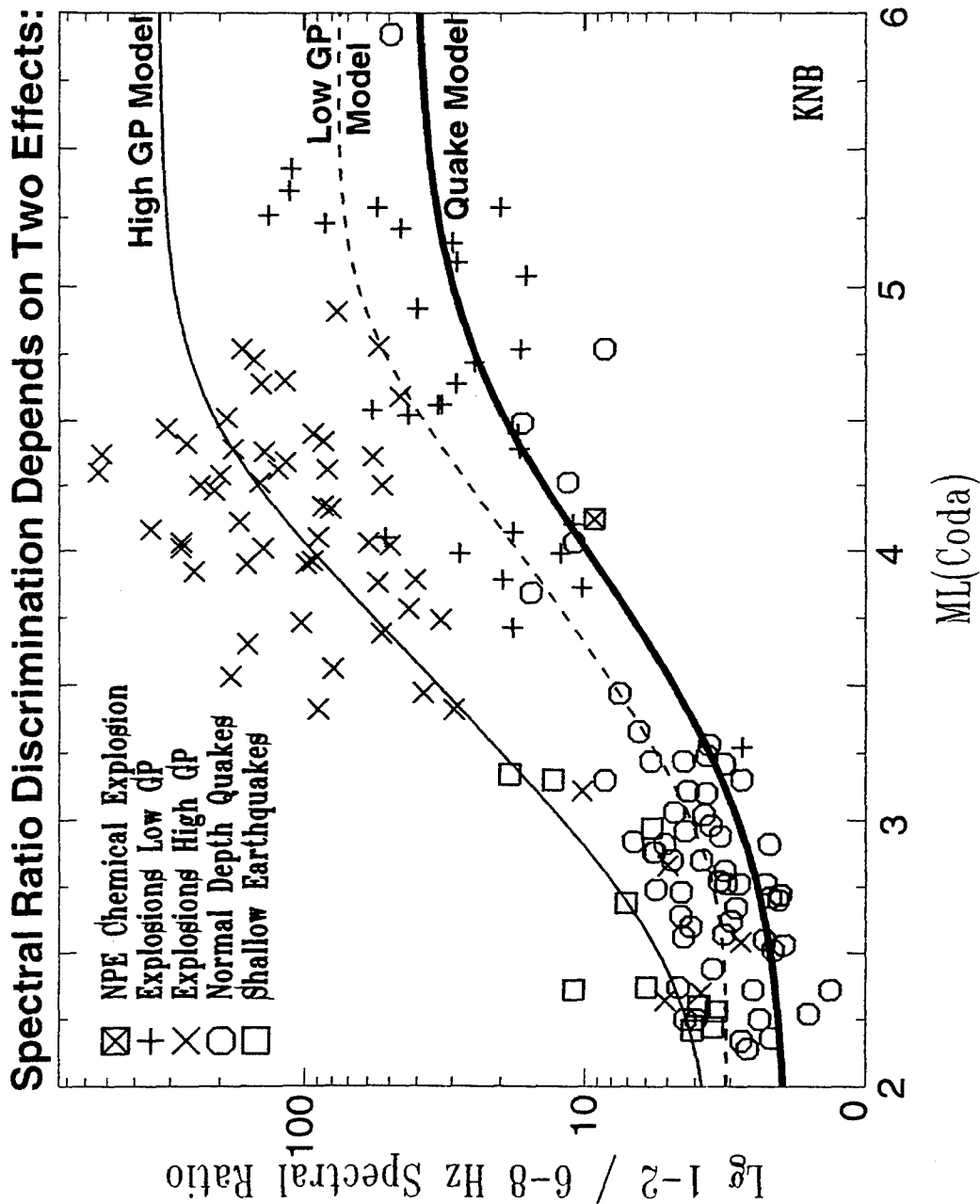
Fig. 4. A model for the L_g low/high or (1-2 Hz)/(6-8 Hz) spectral ratio discriminant. We model the path and site corrected L_g spectrum as the product of source and transfer function terms. Each of these terms is modeled as follows: 1) source spectrum sensitivity to material property effects as illustrated on the upper right. Explosions in high gas porosity low strength materials have source spectra with steeper high frequency falloff than earthquakes or low gas porosity explosions. 2) transfer function (frequency dependent measure of S source plus $P+R_g$ scattering into S) is nearly constant for earthquakes but varies strongly for explosions.
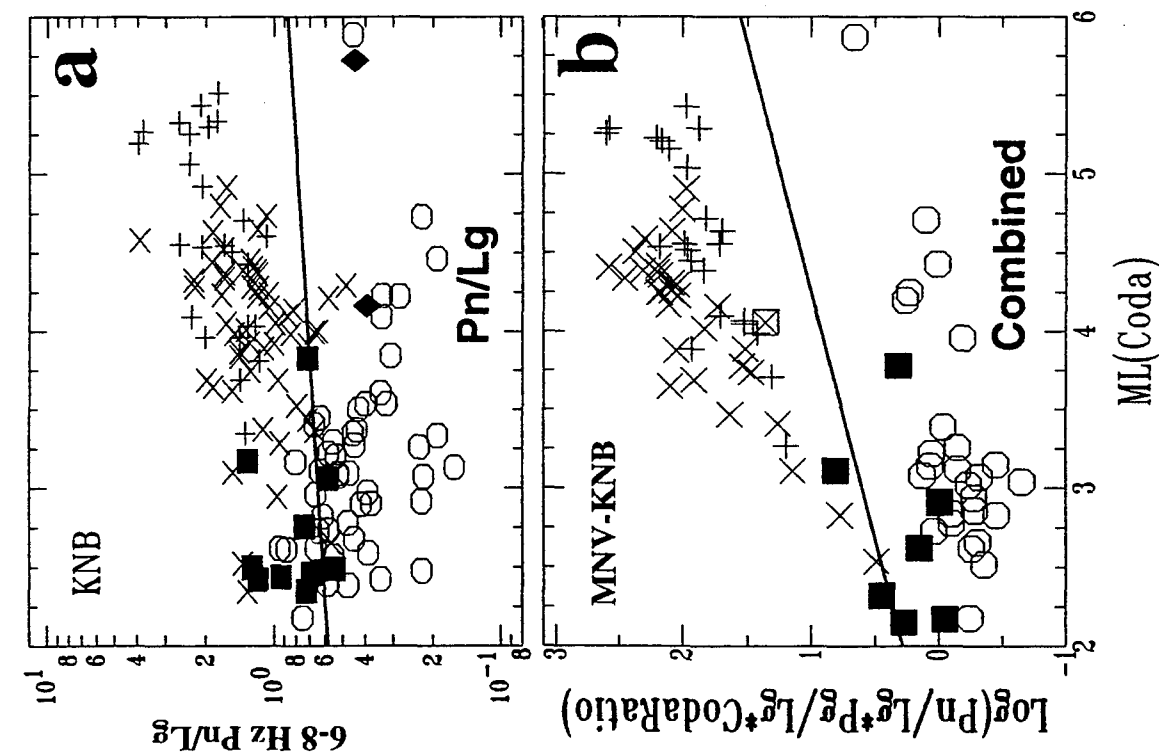
Fig. 5. A comparison of regional discriminants in the western U.S. (a) 6-8 Hz P_n/L_g at KNB (Walter et al., 1995). (b) Combined 6-8 Hz P_n/L_g, P_g/L_g and 1-2/6-8 Hz L_g coda ratio averaged for MNV-KNB (Walter et al., 1995). (c) Regional M_o versus $m_b(P_n)$ (Patton and Walter, 1993). (d) Slope of P_n/L_g at KNB (Goldstein, 1995). Note shallow earthquakes (filled squares) are a problem for (a) and (b) but not (c) and (d), while collapses are a problem for (c) but not (a) and (d). Combinations of regional discriminants can best identify events.

128

Explosion Spectra

Non-Explosion Spectra
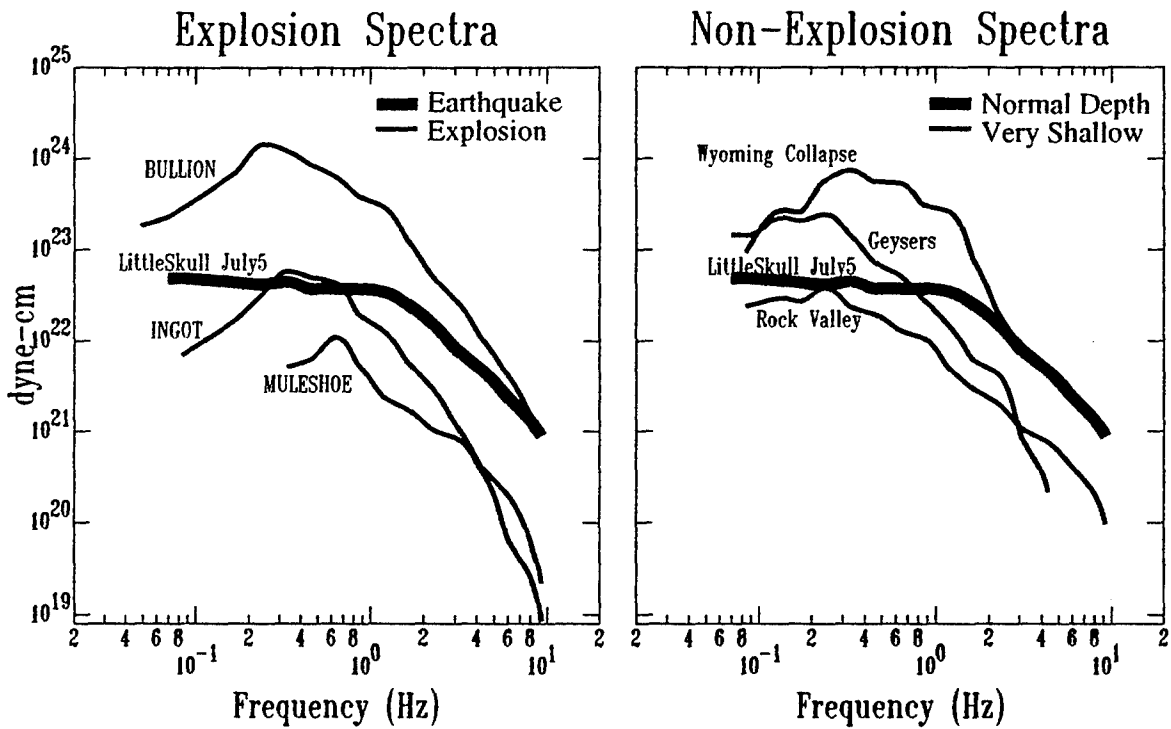
Fig. 6. Coda derived source spectra compared for a normal depth earthquake and a variety of very shallow events. Note the normal depth earthquake source spectra looks simple: constant at long periods and falling off above a corner frequency. In contrast the shallow events when processed in an identical manner look unusual and are peaked. The frequency of the peaked spectra scales with absolute depth for explosions.

Waveform modeling 2/3/95 Wyoming collapse at ELK for 20-50 s Period Band
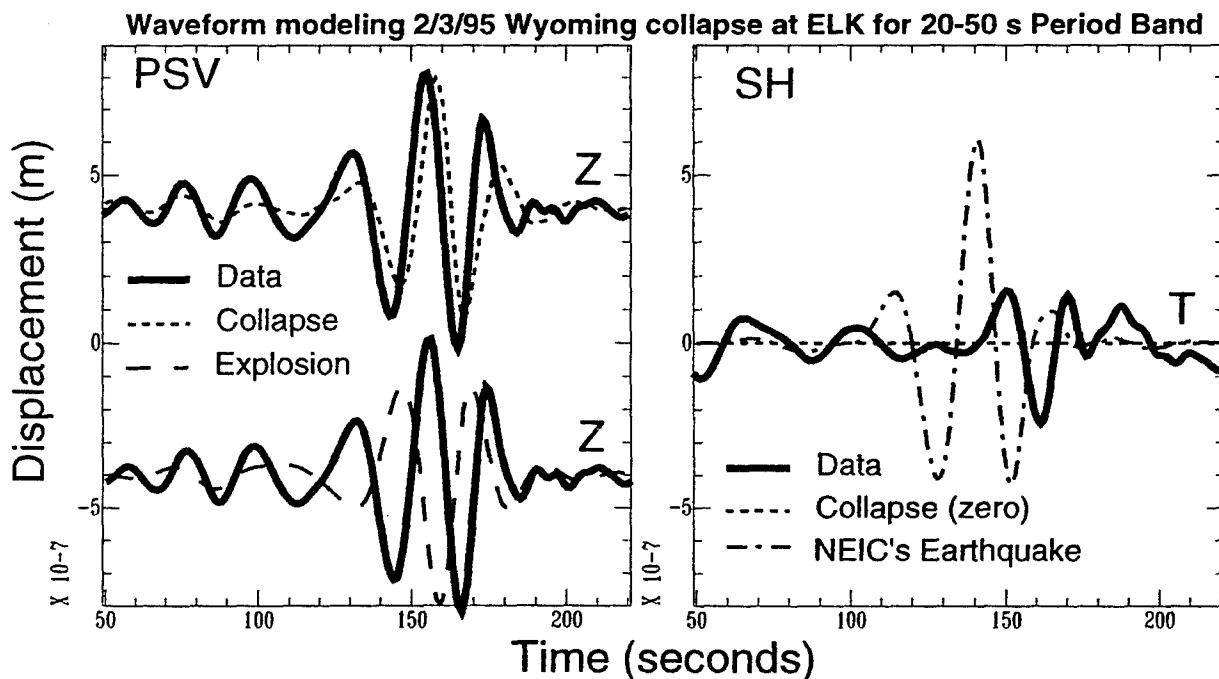
Fig. 7. Intermediate period waveform modeling can identify seismic source when the path is known. Explosions and earthquakes can be distinguished at one station on the basis of their Rayleigh wave phase as shown on the left. Ruling out an earthquake is more difficult and requires at least two stations with differing azimuths. The presence or absence of Love waves is then an indicator of whether the event was an earthquake.

129

Isotropic and Deviatoric Moment Inversion of Regional Surface Waves from Nevada Test Site Explosions: Implications for Yield Estimation and Seismic Discrimination

Bradley B. Woods and David. G. Harkrider
Seismological Laboratory, California Institute of Technology,
Pasadena, CA 91125
AFOSR F49620-93-1-0221

ABSTRACT:

Seismic moments of Nevada Test Site (NTS) explosions were determined from regional surface wave spectra. Two methods were used. In one the moment is solved for assuming only an explosive source, or average scalar moment; in the other a joint inversion for an isotropic (explosive) source plus a constrained double couple moment component representing tectonic strain release (TSR). Although the general moment tensor solution to this joint inversion problem is non-unique, if some assumptions are made concerning the non-isotropic moment components, then the remaining source parameters can be solved by a linear least-squares inversion scheme. We examined the errors in determining the isotropic moment component (M_I) by this latter method of constrained linear inversion solutions in a canonical study using a theoretical network of long-period (6-60 sec.) surface wave data. The network azimuthal coverage was chosen to represent that of a long-period North American super-network of 55 stations used for the actual NTS events. We compared these errors in moment estimate to those obtained from surface wave magnitude (M_S) and spectral scalar moment (M_0) measurements for the same surface wave observations. For a ratio of $M_{(expl)}/M_{(eq)}$ less than 1.0 we found that the inverted M_I solution is a much better estimate of the actual isotropic moment than either M_S or M_0, and the standard deviation in this estimate is substantially less than that using the other two methods for the great majority of isotropic source + double couple sources. Even when the inversion constraints are off in dip and rake each by 30°, the mis-estimate of the isotropic moment is less than 35 percent of the actual value. In the case of a vertical strike-slip fault, the inverted isotropic moment solution which assumes this fault orientation is exact to three figures, whereas M_S and M_0 under-estimate the moment by 45 percent and 32 percent, respectively because of uneven azimuthal coverage.

This moment tensor inversion method was applied to determine the isotropic source for 111 NTS underground explosions using vertical and tangential component surface wave data from this regional network. We also calculated M_S and M_0 for these same events and compared the results. Isotropic source errors were smallest using the spectral domain inversion method. However, this spectral domain method cannot attain as low a magnitude threshold as the time domain moment or M_S method. The extensive moment data set analyzed were combined with larger yield explosions from prior moment studies to create a comprehensive data set with which to obtain conclusive, well-constrained long-period explosion source scaling relationships at the separate NTS sub-sites.

Regressing on the results presented here and the results of others for larger events with published yields, we obtained a M_I versus yield relation with which we were to estimate the surface wave inferred yields of the 111 NTS events.

Key Words Rayleigh and Love wave seismic moments, yields, NTS

OBJECTIVE:

To develop regional surface wave techniques for estimating seismic yield and to use these techniques to obtain a set of surface wave magnitudes, moments and inferred yields in as diverse an environment as possible at NTS in terms of yield, source location and shot medium. To relate the observed variations over NTS with known site characteristics inorder to transport or modify the relations for future test regions.

RECENT RESEARCH RESULTS:

The abstract summarises the results previously obtained under this grant which have been published in various reports and thesis. Here we present in tabular form our best estimates of the surface wave determined moments for 111 NTS events. Using published yields and the results of others for larger yields, we obtain a formula for log moment versus log yield. The figure shows the 6 fixed slope regressions based on subsets of the extended yield moment data set. The values of Given and Mellman (1986) were adjusted to correspond to the same shot point properties as used by us. The shot point independent values of Stevens (1985) were converted to our assumed source region velocity ratios. The order of the author names in the regression titles indicate that the first authors values were used instead of the other authors values if there was a discrepancy. It is interesting that the overlapping values of Given and Mellman were in agreement with Stevens eventhough Stevens used an azimuthally averaged value and Given and Mellman used a moment tensor inversion for the isotropic or explosion moment as in our analysis. In order to estimate yield, we used the regression formula determined from supplementing our values with those of Given and Mellman. The second sub-figure uses Stevens Piledriver value instead of ours and replaces our values by those of Given and Mellman when in conflict with ours. The difference in the regression constants is only 0.02. The regression formula is

$$\log M_I = LogY + 13.78$$

and was used to obtain the estimated yield Y_{SW} in the table.

Combining this log moment versus log yield relation with previous deteremined M_S versus log moment formulas, we obtain

$$M_S = \log Y + 2.34$$

or

$$M_S = \log Y + 1.91$$

depending on whether one uses regression formulas based on the Woods and Harkrider (1995) M_S magnitude values or those of Marshall *etal.* (1979). It shoulds noted that the latter formula is close to the commonly assumed formula for source regions of unknown geologic and seismic properties.

CONCLUSIONS AND RECOMMENSATIONS:

Until further NTS yields are published by the Department of Energy, especially below 10 kt, this set of surface wave estimated yields are about as good as one can accomplish from surface wave data and published yields at NTS. The moments are useful in testing ones ability to form and transport regional surface wave based discriminants and yield determination to other sites. These moments should not be considered as different from surface wave magnitudes but as more accurate and reliable

magnitudes. Their conversion formula to M_s has been presented in reports sponsored by this AFOSR grant.

References

Given, J.W., and Mellman,G.R., 1986. Estimating explosion and tectonic release source parameters of underground nuclear explosions from Rayleigh and Love wave observations,Sierra Geophysics Inc. Rept. No. SGI-R-86-126, AFGL-TR-86-0171, Kirkland, WA. ADB110040

Stevens, J.L., 1986. Estimation of scalar moments from explosion-generated surface waves, Bull. Seism. Soc. Am., v.76 , pp.123-151.

Woods, Bradley B., and Harkrider, D. G., 1995. Determining surface-wave magnitudes from regional Nevada Test Site data, Geophys. J. Int., v.120, pp.474-498.

Woods&Harkrider, NTS

Given&Mellman+Stevens+Woods&Harkrider, NTS

Stevens, NTS
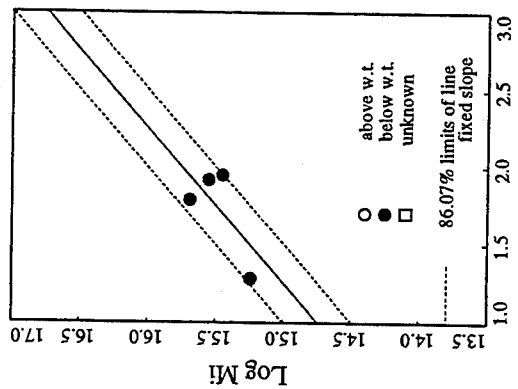
Woods&Harkrider+Given&Mellman, NTS
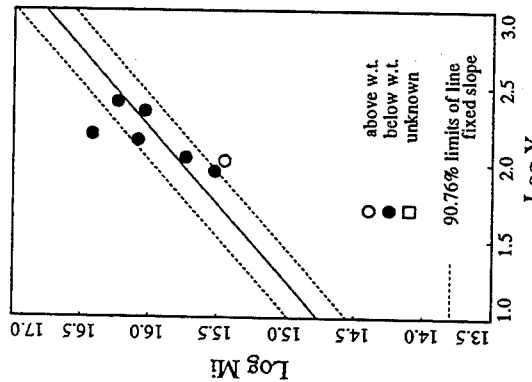
Given&Mellman+Stevens, NTS

Given&Mellman, NTS

133
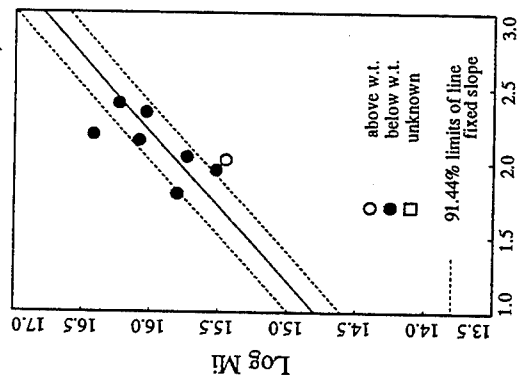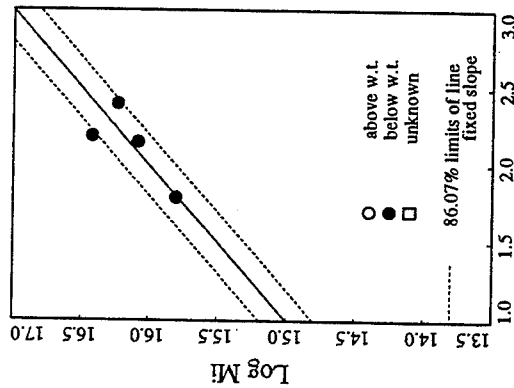
NAME	Date	M_0	σ	$M_{I(R)}$	σ	$M_{I(R+L)}$	σ	Y_{SW}
Table (a): Best log moments and inferred yields								
WAGTAIL	65062	15.25	0.03	15.35	0.02	15.35	0.02	37
LAMPBLACK	66018	15.24	0.02	15.22	0.02	15.22	0.01	28
REX	66055	14.98	0.03	15.24	0.01	15.25	0.02	29
PIRANHA	66133	15.77	0.04	15.75	0.04	15.74	0.04	98
PILEDRIVER	66153	15.63	0.06	15.69	0.05	15.58	0.12	81
TAN	66154	15.74	0.04	15.73	0.04	15.72	0.04	91
MIDIMIST	67177	14.84	0.01	14.80	0.01	14.39	0.01	11
DOORMIST	67243	14.47	0.12					5
COBBLER	67312	15.05	0.01	14.98	0.02	14.94	0.02	19
DORSALFIN	68060	14.81	0.01	14.86	0.01			12
HUDSONSEAL	68268	14.84	0.01	14.81	0.01			11
WINESKIN	69015	15.41	0.02	15.47	0.05	15.46	0.07	43
CYPRESS	69043	14.65						7
BLENTON	69120	15.50	0.02	15.48	0.03	15.47	0.03	52
DIANAMIST	70042	14.77	0.05					10
SHAPER	70082	15.73	0.06	15.76	0.06	15.75	0.05	93
MINTLEAF	70125	14.93	0.01	16.85	0.01	14.59	0.01	14
HUDSONMOON	70146	14.55	0.01					6
CAMPHOR	71180	14.46	0.01	14.56	0.01			6
MINIATA	71189	15.55	0.02	15.59	0.03	15.54	0.03	59
ALGODONES	71230	15.15	0.01	15.14	0.01	15.11	0.01	23
MISTYNORTH	72123	14.65	0.01	14.85	0.01	14.82	0.01	12
MONERO	72140	14.76	0.01	14.78	0.01	14.76	0.01	10
DIAMONDSCULLS	72202	14.68	0.01	14.68	0.01			8
MIERA	73067	15.51	0.02	15.53	0.04	15.44	0.03	54
STARWORT	73116	15.45	0.03	15.46	0.04	15.46	0.04	47
DIDOQUEEN	73156	14.80	0.01	14.76	0.01			10
LATIR	74058	15.78	0.05	15.74	0.04	15.73	0.04	89

Table (b): Best log moments and inferred yields								
NAME	Date	M_0	σ	$M_{I(R)}$	σ	$M_{I(R+L)}$	σ	Y_{SW}
MINGBLADE	74170	14.84	0.01	14.88	0.01	14.92	0.01	14
ESCABOSA	74191	16.02	0.09	16.02	0.08	16.02	0.08	174
STANYAN	74269	15.36	0.01	15.34	0.02	15.34	0.02	38
CABRILLO	75066	15.43	0.02	15.39	0.02			45
DININGCAR	75095	14.72	0.18					9
OBAR	75120	15.17	0.01	15.17	0.01			25
MIZZEN	75154	15.95	0.08	15.93	0.08	15.94	0.09	148
HUSKYPUP	75297	14.46						11
KEELSON	76035	15.86	0.06	15.89	0.06	15.86	0.06	129
MIGHTYEPIC	76133	14.70	0.16					8
RUDDER	76363	15.68	0.03	15.64	0.03			72
BULKHEAD	77117	15.52	0.03	15.59	0.04	15.50	0.04	55
CREWLINE	77145	15.61	0.03	15.67	0.04			68
LOWBALL	78193	15.67	0.05	15.72	0.04	15.71	0.05	87
QUARGEL	78322	15.28	0.02	15.28	0.02			32
QUINELLA	79039	15.42	0.07	15.64	0.08			72
PYRAMID	80107	15.49	0.05	15.51	0.04	15.49	0.05	54
MINERSIRON	80305	14.72	0.01	14.79	0.01	14.91	0.01	13
BASEBALL	81015	15.90	0.05	15.88	0.07	15.87	0.05	132
JORNADO	82028	16.05	0.04	16.06	0.03	16.06	0.03	191
MOLBO	82043	16.01	0.07	16.01	0.09	15.92	0.05	138
HOSTA	82044	15.87	0.04	15.84	0.04	15.85	0.03	117
TENAJA	82107	14.32	0.01	14.29	0.01	14.32	0.01	3
GIBNE	82115	15.82	0.03	15.82	0.03	15.82	0.03	110
KRYDDOST	82126	14.04	0.01	14.05	0.01			2
BOUSCHET	82127	15.69	0.03	15.70	0.02	15.70	0.02	83
NEBBIOLO	82175	15.99	0.05	15.96	0.04	15.96	0.03	151
MONTEREY	82210	14.45	0.01	14.44	0.01	14.42	0.01	5

Table (c): Best log moments and inferred yields								
NAME	Date	M_0	σ	$M_{I(R)}$	σ	$M_{I(R+L)}$	σ	Y_{SW}
ATRISCO	82217	16.11	0.04	16.10	0.04	16.10	0.04	209
HURONLANDING	82266	14.77	0.01	14.80	0.02	14.59	0.01	10
FRISCO	82267	14.99	0.01	14.98	0.01	14.87	0.01	16
BORREGO	82272	13.98	0.01	13.96	0.01			2
MANTECA	82344	14.55	0.01	14.50	0.01	14.45	0.01	6
CABRA	83085	15.54	0.03	15.52	0.01	15.49	0.02	55
TORQUOISE	83104	15.55	0.03	15.56	0.03	15.55	0.02	59
CROWDIE	83125	14.08	0.01	14.28	0.01			3
FAHADA	83146	14.74	0.01	14.72	0.01	14.72	0.01	9
DANABLU	83160	14.47	0.01	14.48	0.01	14.48	0.01	5
CHANCELLOR	83244	15.59	0.05	15.63	0.02	15.63	0.02	71
MIDNITEZEPHYR	83264	14.21	0.01					3
TECHADO	83265	13.89	0.01	13.96	0.01	13.94	0.01	1
ROMANO	83350	15.30	0.01	15.28	0.01	15.27	0.01	31
MILAGRO	84046	14.77	0.01	14.80	0.01	14.80	0.01	10
TORTUGAS	84122	15.87	0.04	15.80	0.05	15.80	0.03	132
MUNDO	84061	15.92	0.06	15.90	0.03	15.90	0.03	105
CAPROCK	84152	15.91	0.04	15.91	0.04	15.91	0.03	135
DUORO	84172	14.82	0.01	14.70	0.01	14.70	0.01	8
KAPPELI	84207	15.56	0.07	15.68	0.02	15.69	0.02	81
CORREO	84215	14.32	0.01	14.31	0.01	14.31	0.01	3
DOLCETTO	84243	14.55	0.01	14.59	0.01	14.59	0.01	6
BRETON	84257	15.07	0.01	15.08	0.01	15.08	0.01	20
VILLITA	84315	14.10	0.01	14.15	0.01	14.20	0.01	2
EGMONT	84344	15.64	0.04	15.64	0.02	15.64	0.02	72
TIERRA	84350	15.72	0.05	15.71	0.03	15.69	0.03	85
VAUGHN	85074	14.92	0.01	14.90	0.03			14
COTTAGE	85082	15.63	0.06			15.48	0.04	50

Table (d): Best log moments and inferred yields								
NAME	Date	M_0	σ	$M_{I(R)}$	σ	$M_{I(R+L)}$	σ	Y_{SW}
HERMOSA	85092	16.10	0.08	16.12	0.10	16.12	0.07	219
MISTYRAIN	85096	15.05	0.01			14.78	0.04	19
TOWANDA	85122	15.81	0.06	15.77	0.05	15.76	0.03	96
SALUT	85163	15.91	0.05	15.92	0.04	15.93	0.03	141
SERENA	85206	15.50	0.06	15.63	0.05	15.53	0.05	71
PONIL	85270	14.71	0.01					9
ROQUEFORT	85289	14.74	0.01					9
KINIBITO	85339	15.71	0.08	15.71	0.07	15.70	0.05	83
GOLDSTONE	85362	15.67	0.05	15.63	0.04	15.65	0.04	74
GLENCOE	86081	15.50	0.02	15.46	0.04	15.35	0.02	52
MIGHTYOAK	86100	14.81	0.01	14.78	0.01	14.77	0.01	10
JEFFERSON	86112	15.68	0.06	15.78	0.04	15.78	0.03	100
PANAMINT	86141	13.97	0.11					2
TAJO	86156	15.67	0.06	15.66	0.06	15.66	0.05	76
DARWIN	86176	15.60	0.04	15.72	0.04	15.69	0.02	81
CYBAR	86198	15.84	0.07	15.83	0.05	15.83	0.04	112
CORNUCOPIA	86205	14.40	0.02					4
LABQUARK	86273	15.87	0.08	15.83	0.02	15.83	0.03	112
BELMONT	86289	15.84	0.05	15.89	0.02	15.88	0.02	126
GASCON	86318	15.91	0.04	16.00	0.09	16.00	0.07	135
BODIE	86347	15.97	0.07	15.94	0.14	15.89	0.07	155
DELAMAR	87108	15.90	0.04	15.79	0.03	15.72	0.02	87
HARDIN	87120	16.05	0.07	15.94	0.05	15.90	0.05	145
PANCHUELA	87181	14.17	0.01					2
TAHOKA	87225	16.03	0.05	16.07	0.01	16.02	0.06	195
LOCKNEY	87267	16.03	0.03	16.01	0.01	15.94	0.03	170
BORATE	87296	15.22	0.01	15.30	0.01			33

The Portability of Some Regional Seismic Discriminants And Related Broadband Waveform Modeling

Bradley B. Woods and Chandan K. Saikia
Woodward-Clyde Federal Services,
Pasadena, CA

ABSTRACT

We are investigating the portability of regional seismic discriminants which were developed from the analysis of data for southwestern U.S. earthquakes and NTS explosions. Besides determining whether or not these discriminants are effective for seismic events in other tectonically active regions, it will be possible to calibrate the effective discriminant parameters for these different regions, so that an event from any such area can be incorporated into a unified database. Events studied are the U.S. PNE's and earthquakes in the Colorado Plateau/Rockies region, explosions at the Kazakh (CIS) and Lop Nor (PRC) test sites, as well as earthquakes in and around this region of Asia. Events in Pakistan are analyzed by these discriminants, too, although no explosion data are available. This region includes significant deep seismicity (d>50km). The discriminants being used here are the ratio of integrated short-period P-wave to long-period energy (predominantly surface wave) summed over the three components (sp_z-P/lp_3) (Woods and Helmberger, 1994), the ratio of integrated short-period vertical component energy between the P and S wavetrains (sp_z-P/sp_z-S), and the ratio of M_L to scalar seismic moment (M_0). For the Colorado Plateau data set the energy ratio discriminants were modified to use peak amplitudes, as many of the records could not be digitized. The sp_z-P/lp_3 discriminant is most effective at distinguishing source-types. The sp_z-P/sp_z-S energy ratio appears to be useful to identify deep events from shallower crustal earthquakes. The M_L:M_0 discriminant is deterministic, requiring Green's functions that reflect the crustal structure of a region with which to invert waveform data to obtain the source parameters for any event. To this end we have modeled broadband regional records at WMQ and those recorded by the PASCAL array in Pakistan. Initial modeling of the Pakistan region has been successful using a thick crustal model developed for the Tibetan Plateau. Well-constrained source mechanisms have been obtained for deep and shallow events. One potential use of regional waveform modeling in areas of deep seismicity is to calibrate t^* for teleseismic m_b measurements. Once the source parameters and source time function are determined by regional source inversion, then teleseismic body-waves can be fit by varying Q in the mantle source region.

OBJECTIVE:

We are investigating the portability of regional seismic discriminants which were developed from the analysis of data for southwestern U.S. earthquakes and NTS explosions. Besides determining whether or not these discriminants are effective for seismic events in other tectonically active regions, it will be possible to calibrate the effective discriminant parameters for these different regions, so that an event from any such area can be incorporated into a unified database.

Events studied are the U.S. PNE's and earthquakes in the Colorado Plateau/Rockies region, explosions at the Kazakh (CIS) and Lop Nor (PRC) test sites, as well as earthquakes in and around this region of Asia. The discriminants being used here are the ratio of integrated short-period P-wave to long-period energy (predominantly surface wave) summed over the three components (sp_z-P/lp_3) (Woods and Helmberger, 1994), the ratio of integrated short-period vertical component energy between the P and S wavetrains (sp_z-P/sp_z-S), and the ratio of M_L to scalar seismic moment (M_0), M_L:M_0 (Woods $et\ al$, 1994).

The energy ratio discriminants are empirical and only require the velocity records, whereas the M_L:M_0 discriminant is deterministic in that it involves waveform inversion for source parameters, which in turn requires establishing crustal models for these regions. Besides being used for source inversion, such Green's functions can be used to calibrate paths with respect to specific regional phases used for magnitude measurements and other discriminants. This study is primarily concerned with calibrating the regional crustal structure centered about the station WMQ in central Asia, and the region encompassing Pakistan and eastern Iran. These path calibrations are particularly useful for regions where no large explosions have taken place, as it is then possible to predict waveforms for such sources, thus helping to establish criterion for a "first-blast" in the region.

These discriminants and waveform modeling techniques have an effective threshold at or above M_L=4, for regional events, so that they fit the monitoring criteria of the CTBT.

RESEARCH ACCOMPLISHED:

Figure 1 plots the sp_z-P/lp_3 integrated energy ratio vs. distance for central Asian events. Explosions are circles and earthquakes are crosses, and each datum point represents one station - event pair. This method yields good separation of the two populations. Note also the Ural event (triangles) which plots in the earthquake population. It is now believed that this event was a mine collapse. More explosion data at a range of distances would help to establish the efficacy of this discriminant. In comparing these results to the original study (Woods and Helmberger, 1994) using regional TERRAscope data, we find that earthquakes and explosions demonstrate the same trends in Asia as they do in North America, although several Asian earthquakes near 500 km do have relatively high sp_z-P/lp_3 ratios. The Asian explosions also plot fairly high, suggesting the the regional crustal structure and Q may be responsible for these differences by increasing the relative high-frequency content of the wavefield.

This discriminant was also applied to events in the Colorado Plateau - Rocky Mountain region, hereafter referred to as the Colorado data. Source information for these events is given in table 1. The data obtained was primarily from WWSN analog records. The short-period records are of generally low quality, so that they could not be digitized. So instead of calculating the integrated energy, the peak short-period P-wave amplitude was taken, as well as the sum of the peak amplitude of the three long-period components. Figure 2 is the plot of the ratio of short-period P-wave amplitude to the sum of the three long-period components vs.

distance. For this version of the discriminant, the two source type populations also have different trending data, although there is some overlap. The fact this alternate method works makes it a promising discriminant to use on historical analog data, of even poor visual quality, to calibrate the sp_z-P/lp_3 ratio vs. distance for regions with sparse modern data coverage. In the original study of TERRAscope data (Woods and Helmberger, 1994), it was found that peak amplitude measurements worked nearly as well as integrated energy at discriminating events.

Another promising empirical discriminant is the ratio of integrated sp_z-P/sp_z-S. Figure 3 plots this ratio vs. distance for Asian events. Each datum point represents one station - event pair. The populations are well separated, although, again the data sets are too small to make any firm conclusions. This time the Ural event plots in the explosion population. A similar discriminant had been applied to regional TERRAscope data, with poorer results, however the seismograms had not been narrow-band filtered. It is believed that this step significantly enhances the separation of source types. Waveforms for central Asian events display more high-frequency energy than do those in the Basin and Range and neighboring provinces. These observation has been reported by Given *et al* (1990) as well.

A modified, peak-amplitude version of the sp_z-P/sp_z-S was performed on the Colorado data, the results of which are shown in figure 4. Here, also, the two source-type populations are separated by this discriminant. This again suggests that the modified discriminant can be used to calibrate regional sp_z-P/sp_z-S ratios for regions without adequate digital data.

Another use of the sp_z-P/sp_z-S ratio is as depth discriminant. Deep events waveforms can appear explosion-like in that the body-waves have sharp onsets and surface waves generated are relatively small. Also deeper events often are relatively high-frequency rich, again making them look explosion-like by some criteria. These differences can be seen in figure 5 which compares velocity records of a shallow (d=15km) and a deep (d=135km) event recorded in Pakistan. Both events are recorded at nearly the same range. Body-waves for the shallow event (top set of traces) are quite small compared to the surface wave and coda wavetrain. The deep event has strong, high-frequency rich, body waves and virtually no long-period (T>4 sec) coda. The bottom figure plots the integrated energy for each component of the two events. A large proportion (35 to 50 %) of the total energy arrives within the P-wavetrain for the deep event, whereas less than 10 percent of the total energy of the shallow event arrives in this time. This difference is most evident on the vertical components. Without treating this event as a deep source, it well could be misidentified as an explosion using some discrimination criteria such as m_b:MsubsS.

Using regional M_0 lowers the long-period measurement threshold to m_b=4, which is also near the threshold for teleseismic m_b measurements. Figure 6 plots M_L vs. M_0 for events in central Asia. Moments have been determined by us as well as taken from other studies, while M_L's have been taken from such studies or from bulletins where available.

We are also studying the area encompassing Pakistan and eastern Iran, see figure 7. As there are no large explosions recorded in this region, emphasis has been placed on broadband waveform modeling of the crustal structure instead. By modeling and understanding the propagational characteristics of a region using available earthquake data, one will be able to identify anomalous events when they do occur. As an example, figure 8 shows records from two stations of an event in Pakistan. The records are played-out as broadband displacement, under which are succeedingly higher bandpasses of the same record. In the bottom set of tangential traces, vertical bars have been placed just to the left of the Pn and Sn arrival times. At higher frequencies these phases become quite prominent. Typically the broadband record or even a longer-period waveform would be used to model this path. Secondary modeling of Q would be achieved by fitting the amplitude or energy of the high-frequency waveforms. Thus the path can be calibrated for both long- and short-period data.

To model waveforms one needs constraints on the sources. To this end, events were first inverted for the source mechanism using Green's functions developed for the Tibetan Plateau (TB) (Zhu and Helmberger, 1995; elsewhere in these proceedings). This model has a thick crust like that which is believed to underlie this mountainous region of Pakistan. The "cut and paste" method of inverting seismograms (Zhao and Helmberger, 1994), by fitting the Pnl and surface wavetrains separately, makes it possible to obtain good source inversions without requiring the use of a crustal model that correctly predicts the relative arrival time between the body waves and the surface waves. Figure 9 show array data and synthetic fits for one event (d=20km) using the inverted source parameters and the TB model. All waveforms have been low-pass filtered at 0.1 Hz. The first two columns of traces are the Pnl windows (Z and R, respectively), while the last three columns are for the surface waves (Z, R and T, respectively). The waveform fits are good for the body waves and surface waves. The number below each set of traces is the time shift of the data to synthetic, with a positive number indicating the synthetic being too fast by that amount. The source mechanism obtained also agrees with that for the Harvard CMT solution. The CMT solution places the depth at 44km. We found a depth of 20 km by cycling through Green's functions for the least-error inversion. As found in an earlier study by Zhao and Helmberger (1993) most crustal events are shallower than generally reported in this region of thickened crust as determined from teleseismic depth phases. Figure 10 shows fits of the array data for a deep (d=139) event. Again the waveform fits are good. Thus we have been successful in modeling both crustal and deep earthquakes. The next step is to refine the crustal structure by modeling the broadband waveforms of events for which their long-period source mechanism has been obtained.

CONCLUSIONS AND RECOMMENDATIONS:

All the discriminants discussed above all show promise with the Asian and Colorado data sets. The success of the narrow-band sp_z-P/sp_z-S ratio suggests that narrower-band measurements for any empirical discriminants may be in order. This passband will be applied to TERRAscope sp_z-P/sp_z-S data to compare with that for Asia. Furthermore this energy ratio can be used to identify deep events where there is such seismicity. Analysis of the Ural mine collapse using these discriminants suggests that it was rich in long-period energy and deficient in shear-wave energy. The success of modeling regional deep events with fairly simple 1-D crustal models suggests that it will be possible to accurately determine teleseismic t^* for such regions. One can obtain the source time function and other source parameters from regional data. With these parameters known, one can then match teleseismic records by varying t^*, thus calibrating m_b measurements for the region. Moreover, we can probably calibrate far regional data, upper-mantle phases, and perform joint source inversions to help resolve events poorly constrained in depth and origin time by using depth phases.

REFERENCES:

Given, H. K., N. Tarasov, V. Zhuravlev, F. L. Vernon, J. Berger, and I. L. Nersesov, 1990. High-Frequency Seismic Observations in Eastern Kazakhstan, USSR, with Emphasis on Chemical Explosion Experiments, *J. Geophys. Res.*, **95**, pp. 295-307.

Woods, B. B., S. Kedar, and D. V. Helmberger, 1993. M_L:M_0 as a Regional Seismic Discriminant, *Bull. Seism. Soc. Am.*, **83**, pp. 1167-1183.

Woods, B. B. and D. V. Helmberger, 1994. Regional Seismic Discriminants Using Wavetrain Energy Ratios, submitted to *Bull. Seism. Soc. Am.*

Zhao, L. Z. and D. V. Helmberger, 1993. Geophysical Implication from Relocations of Tibetan Earthquakes - Hot Lithosphere, *Geophys. Res. Let.* **18** pp.2205-2208.

Zhao, L. Z. and D. V. Helmberger, 1994. Source Estimation from Broadband Regional Seismograms, *Bull. Seism. Soc. Am.*, **84**, pp. 91-104

Zhu, L. and D. V. Helmberger, 1995. Intermediate Depth Earthquakes beneath the India-Tibet Collision Zone, submitted to *Geophys. Res. Let.*

Table 1:

U.S. PNE's and nearby earthquakes studied					
Event	Date	Time	Lat.	Lon.	m_b
GNOME	61/12/10	19:00	32.26	-103.87	-
GASBUGGY	67/12/10	19:30	36.7	-107.2	5.1
RULISON	70/08/28	21:00	39.4	-107.9	5.3
Colorado EQ	66/01/05	00:37	39.8	-104.7	5.0
Colorado EQ	67/08/09	12:25	39.9	-104.7	5.3
N. Mexico EQ	66/01/23	01:56	37.0	-107.0	5.5
N. Mexico AS	66/01/23	06:14	"	"	4.3
N. Mexico AS	66/01/23	07:49	"	"	4.6
N. Mexico AS	66/01/23	11:01	"	"	4.3
N. Mexico AS	66/01/23	19:43	36.9	-107.1	4.5
N. Mexico AS	66/01/23	23:48	36.9	-107.0	4.6

SP-LP(3-comp) Ratio vs. Distance, Asia
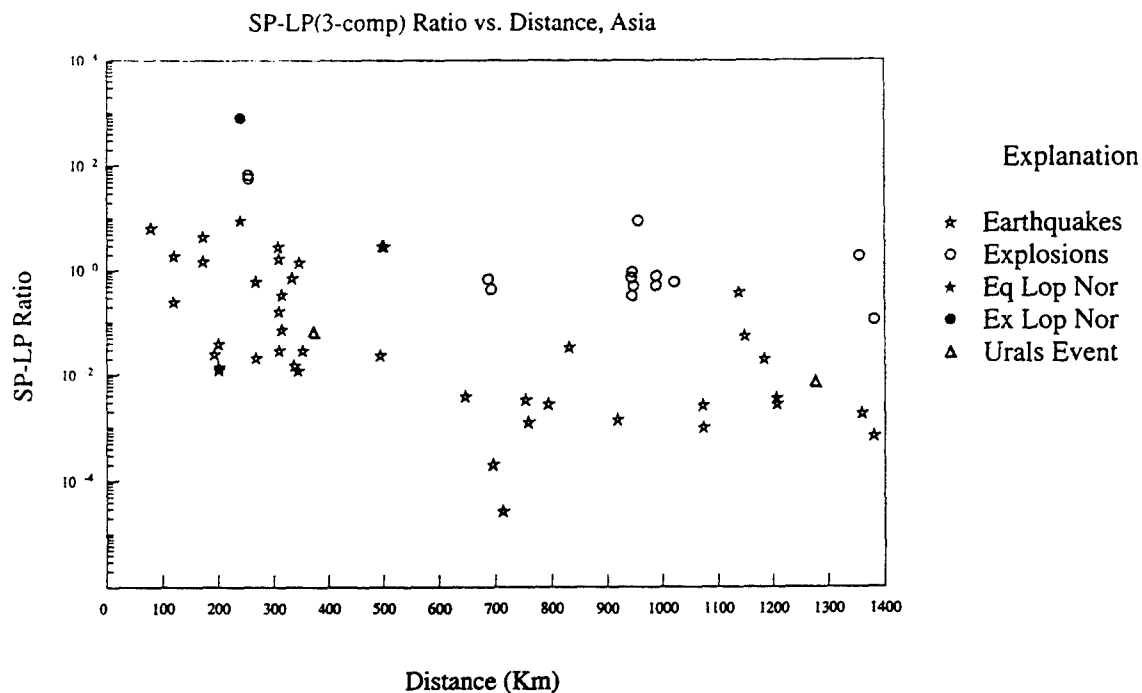
Figure 1. sp_z-P/lp_3 vs. distance for events in Asia. Explosions are circles, stars are earthquakes, and triangles represent the Ural mine collpase.

SP-LP(3-comp) Ratio vs. Distance, North America
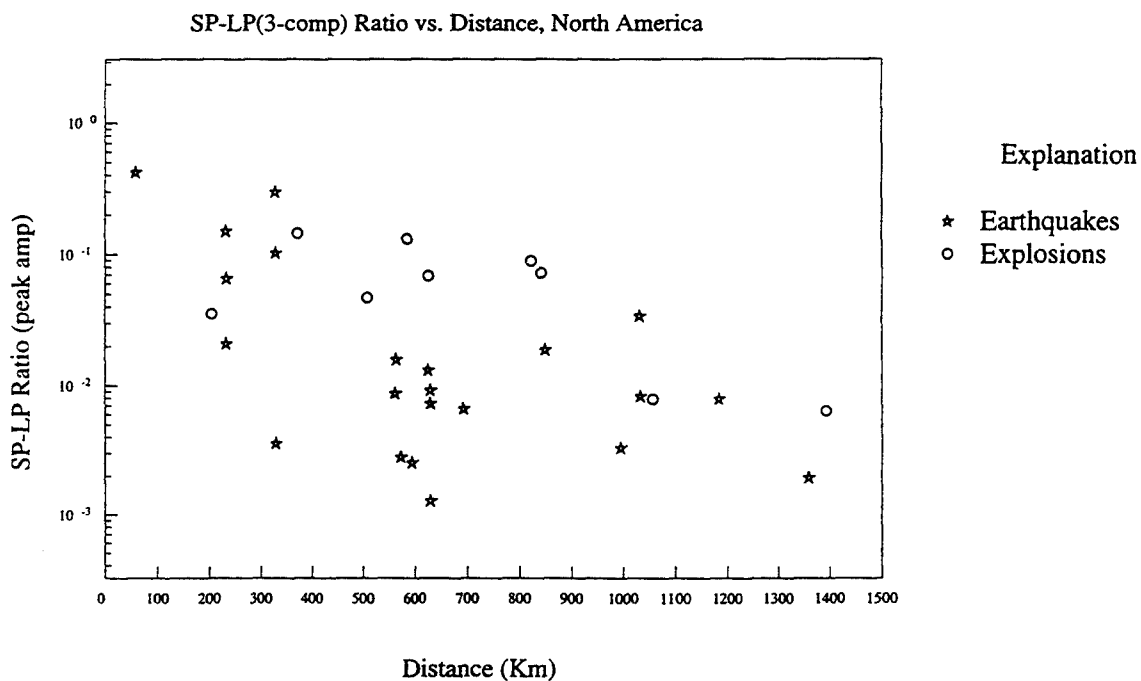
Figure 2. sp_z-P(peak amp.)/lp_3(peak amp) vs. distance for events in the Colorado Plateau region. Explosions are circles and stars are earthquakes.

Short-period P:S energy ratio vs. distance, Asia
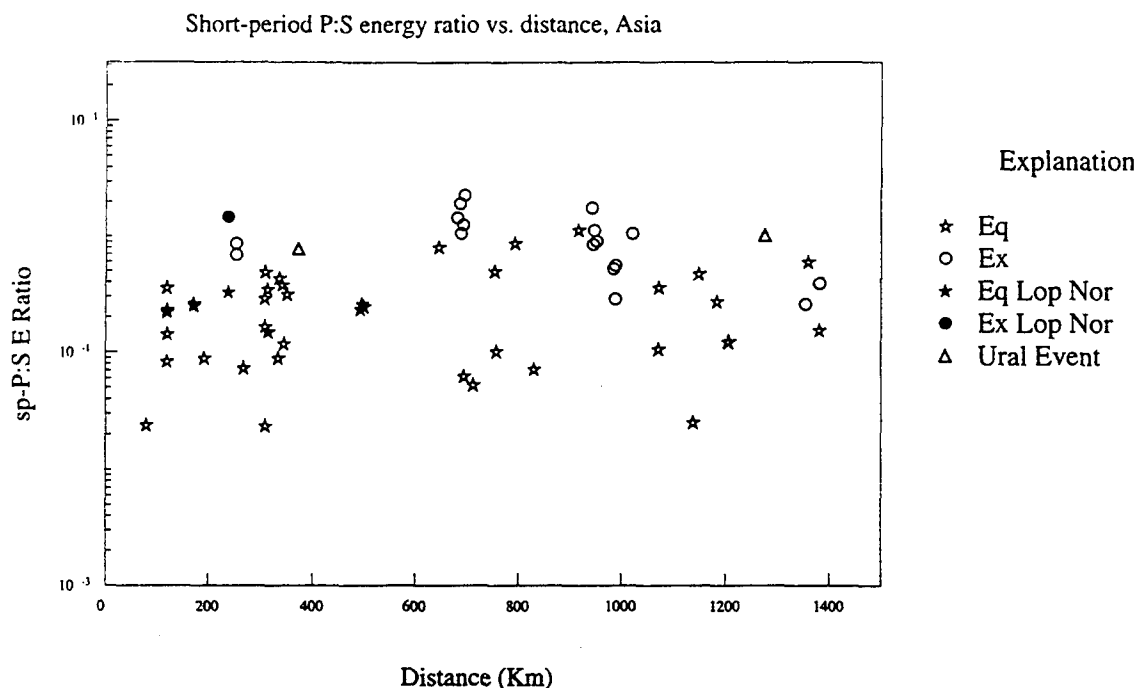
Figure 3. sp_z-P/sp_z-S energy ratio vs. distance for the Lop Nor and Kazakh explosions and nearby earthquakes.

Short-period P:S energy ratio vs. distance, North America
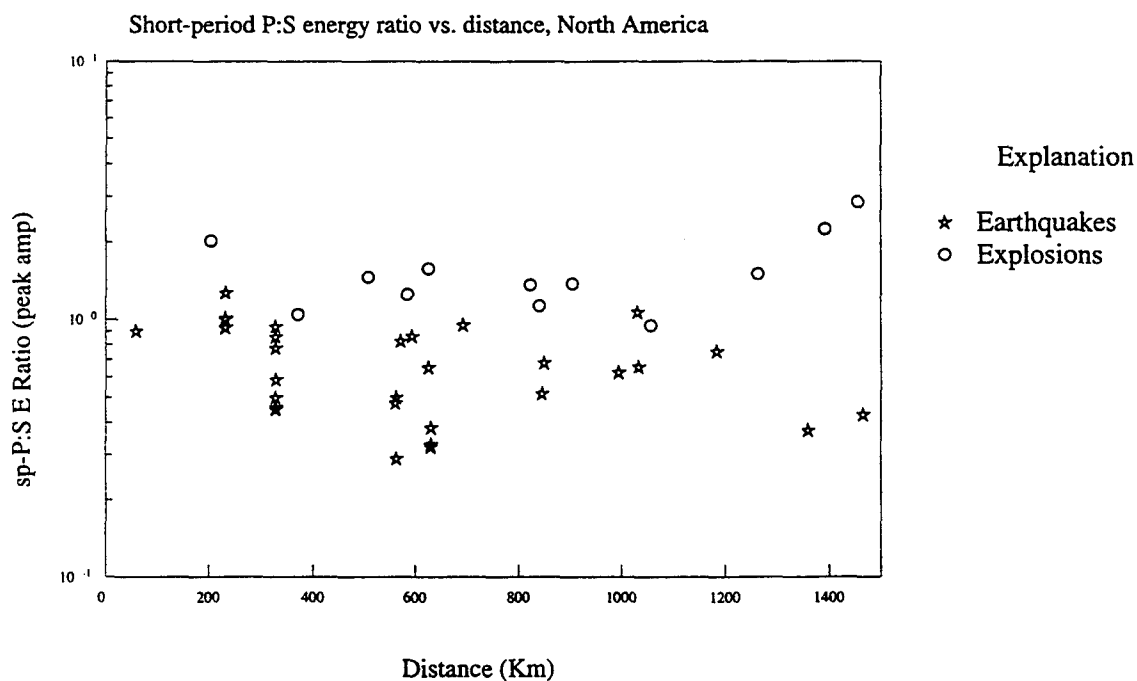
Figure 4. sp_z-P/sp_z-S energy ratio vs. distance for the U.S. PNE's and nearby earthquakes.

144
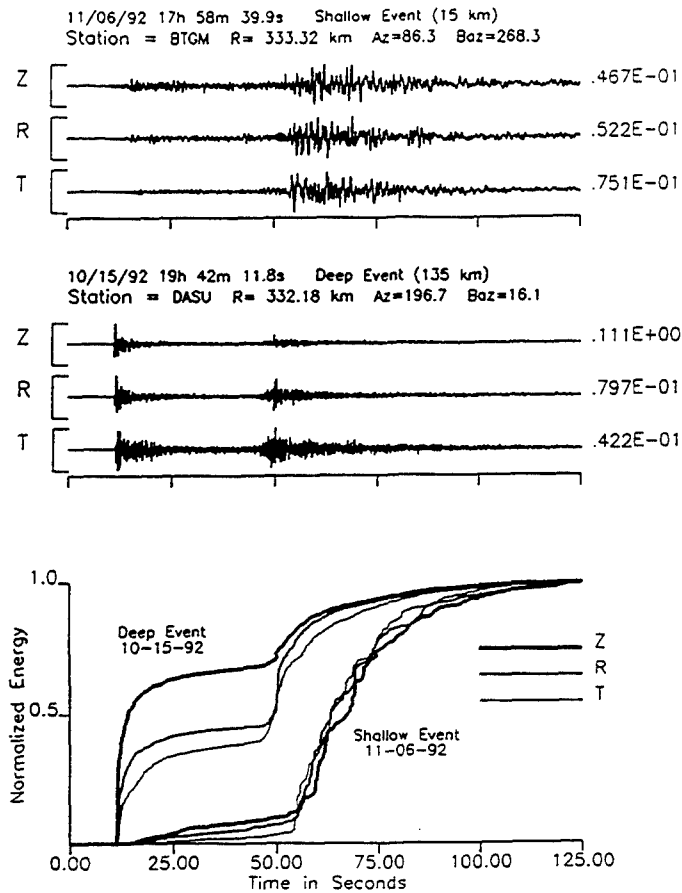
Figure 5. Broadband velocity records for a shallow event (top traces) and a deep event (middle traces) recorded by the Pakistan PASCAL array. The botttom figure plots the integrated energy curves for these records.
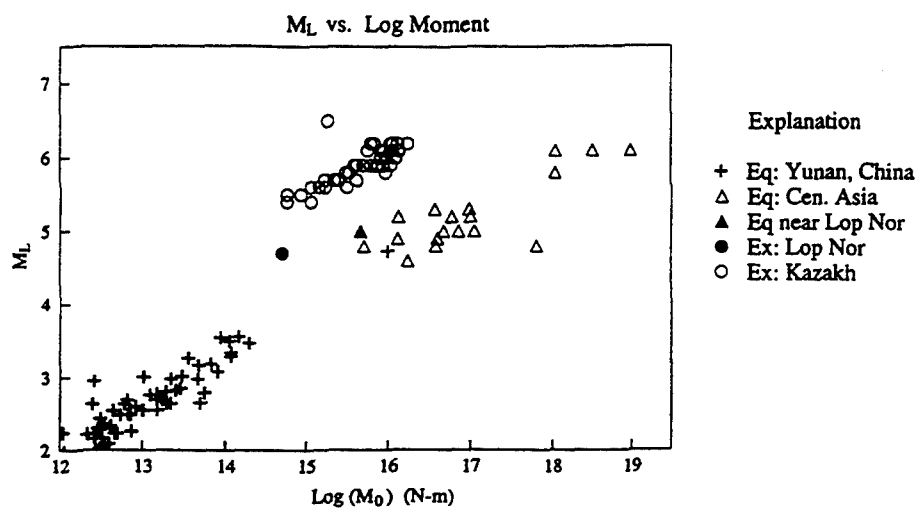
Figure 6. M_L vs. M_0 for Eurasian events.

Broadband Integrated Waveforms from Pakistani Array

Event — 11/06/92 07h 21m 57.8s
Lat= 40.99° Lon= 72.51° M=4.5

Figure 8. Regional wavefroms from Pakistan played-out at different different bandwidths.

Figure 7. Map of Pakistan/eastern Iran study area and events studied. The Harvard CMT solution is for the event 328.2.
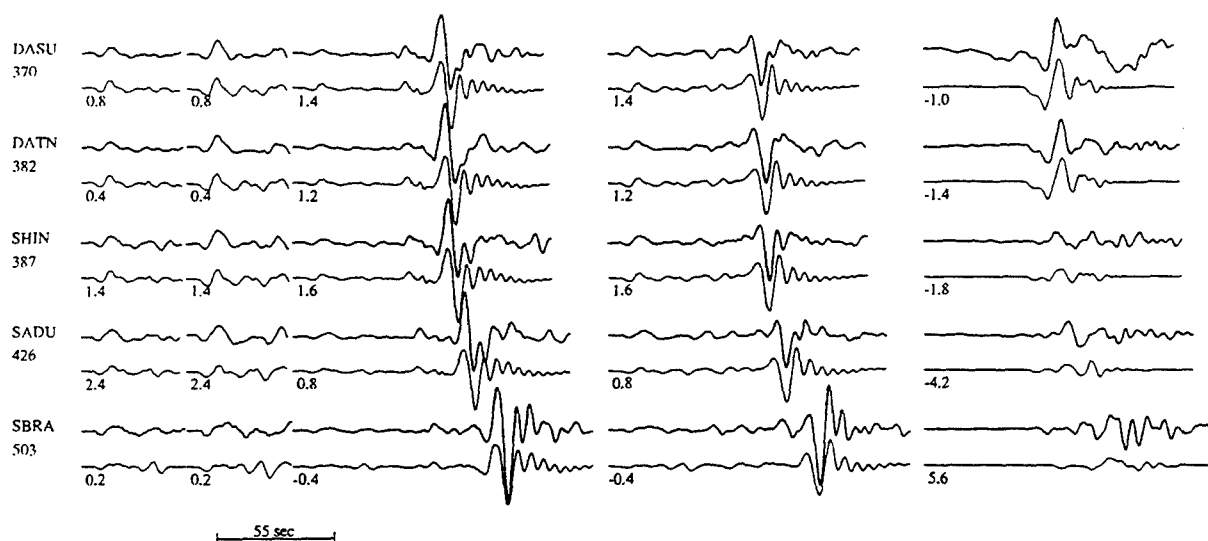
Figure 9. Data to synthetic waveform comparisons for the inversion of event 328.2 (240,60,240; M_w=6.0; d=20km). The data is the top, heavier trace. The number below the trace is the time-shift of the synthetic, with positive numbers indicating fast synthetics.
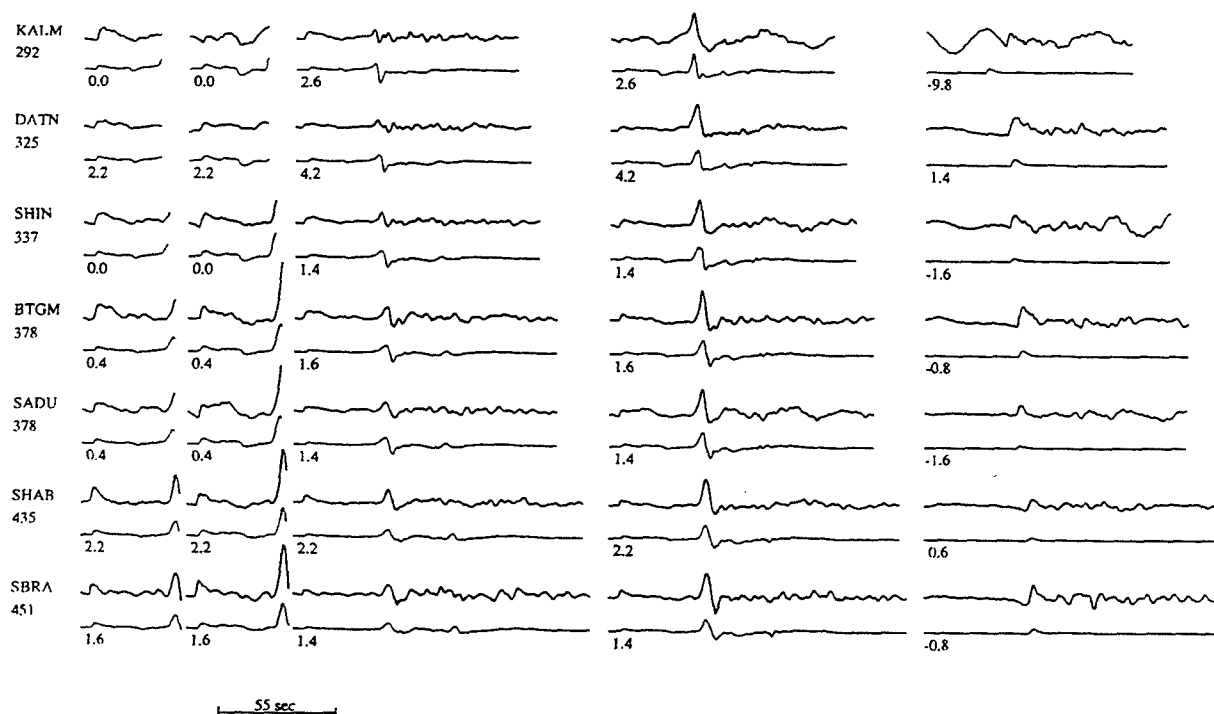
Figure 10. Data to synthetic waveform comparisons for the inversion of event 276.1 (110,50,270; M_w=5.1; d=150km).

Calibration of Regional Wave Discriminants in Diverse Geological Environments: Topographic Correlations

Tian-Run Zhang and Thorne Lay
University of California, Santa Cruz

ABSTRACT

- It has long been recognized that L_g waves are not observed on paths traversing oceanic crust, but this has not yet been fully explained. Using normal mode analysis and finite-difference simulations, we demonstrate that: (1) the overall thickness of the crustal waveguide affects the number of normal modes in a given frequency range; in general, thinner crust accommodates fewer modes; (2) 6-km thick oceanic crust does not allow L_g to develop as a significant phase in the frequency band 0.3-2 Hz due to the limited number of modes that exist; (3) in continental crust thicker than 15 km there are usually sufficient modes that L_g is stable; (4) the shallow sediment layer plays important roles in crustal guided wave propagation; trapping energy near the surface, separating L_g and R_g waves; (5) a 100-km long segment of oceanic structure on a mixed ocean/continent path can block P–SV type L_g propagation. The primary reason why L_g does not travel through oceanic crust thus lies in the structure of the crustal waveguide, with the decisive factor being the crustal thickness. The detailed shape of ocean to continent crustal transitions can influence L_g blockage, but the general inefficiency of L_g propagation in the oceanic structure is the dominant effect.

- Regional P and S waves decay with different rates due to complex geometric spreading and attenuation factors, hence discriminants based on P/S ratios are distance dependent. In a region without L_g blockage, the distance dependence, γ, of P_g/L_g ratios and the factors influencing the distance dependence are of concern for the correction of the path effect. 80 earthquakes in the Western U.S. recorded at four stations of the Livermore NTS Network are used to determine the regional distance dependence of P_g/L_g ratios. $\log P_g/L_g$ is found to be significantly correlated with both propagation distance and surface roughness. The correlation is strongest when the product of distance and roughness is used as an independent variable. The distance dependence γ can be approximately expressed as a linear function of surface roughness. The ratio data in the frequency range 2.0-6.0 Hz have the most distance dependence. Corrections based on the inferred relations for distance and roughness can reduce the variance of the discriminant $\log P_g/L_g$ by 20%. Analysis of the P_n/L_g ratio is underway.

OBJECTIVE:

This research is directed at improving the performance of regional wave discriminants by developing empirical and, potentially, theoretical wave propagation corrections for P_g/L_g and P_n/L_g ratios, as well as for L_g amplitudes. It will hopefully provide fundamental advances in our understanding of the regional wavefield. The basic idea is that by establishing the influence of large-scale crustal waveguide structure on the amplitude ratios of regional phases, the scatter in those ratios can be reduced, thereby enhancing the discriminant performance. We have explored the influence of irregularities in the crustal waveguide, such as surface topography, bathymetry characteristics, Moho depth, sediment depth, and attenuation term in the first year of the project. In the second year, a numerical simulation study has been undertaken to understand the role of crustal thickness in propagation of L_g waves. We are also studying the variation of P_g/L_g and P_n/L_g with distance and surface roughness.

RESEARCH ACCOMPLISHED

We have carried out two projects:

Why the Lg Phase does not Traverse Oceanic Crust

L_g only propagates in continental crust. The dominant opinion has been that the disappearance of L_g in oceanic regions might be due to the effect of propagation across a continent-ocean margin. If this is the main reason, the structure of the continental margins would play a more important role than the structure of the oceanic crust itself in disrupting L_g propagation. Our previous work has established that there is significant correlation between regional phase amplitude ratios and minimum crustal thickness along some propagation paths (Zhang and Lay, 1994ab; Zhang et al., 1994). This motivated us to explore the role of crustal thickness in guided wave (L_g) propagation, which may help us understand the observed phenomena related to path effects (Zhang and Lay, 1995). Because L_g can be viewed as the sum of higher Rayleigh and Love modes, we use a normal mode method to construct dispersion curves for Rayleigh waves in layer over a halfspace models with various crustal thickness (Figure 1). It is conspicuous that the number of normal modes in the 0-2 Hz range decreases for thinner crust. For a 32-km thick crust (Figure 1a), the group velocity minima (or Airy phases) concentrate within a narrow group velocity range between 3 and 3.5 km/s. The concentrated L_g phase develops by constructive interference of these higher mode Airy phases. According to our finite difference calculations, there is significant energy within the "L_g window", marked by the two lines in Figure 2 for both radial and vertical components. However, there are only 5 modes for the 6-km thick (oceanic) crust in the same frequency range (Figure 1d). The synthetics shown in Figure 3 illustrate that there is almost no energy within the L_g window, due to the limited number of modes that exist in the thin oceanic crust. Our calculations indicate that the lack of L_g signals for oceanic paths is primarily a gross structural effect, intrinsic to the thin waveguide. Zhang and Lay (1995) also shows that L_g and R_g waves are separated in the time domain given the existence of a low-velocity sediment layer. Two-dimensional models show that a 100-km long segment of oceanic crust can reduce L_g amplitudes significantly, whereas a 50-km long segment does not. This phenomenon can be simulated without having to introduce a water layer, as did Cao and Muirhead (1993).

149

How P/Lg Ratios Change with Distance and Surface Roughness

In regions with crustal structures that cause L_g blockage, P/L_g ratios can change drastically on some propagation paths, and one must correct for, or at least recognize this effect. In regions without L_g blockage, the distance dependence of P/L_g ratios and the factors that influence distance dependence should be corrected for. We chose 80 earthquakes in the Western U.S. recorded at four stations of the Livermore NTS Network to determine the distance dependence of P_g/L_g. No L_g blockage is observed in this region, even in areas with strong relief like near the Sierra Nevada Mountains and Death Valley. Log P_g/L_g ratios are calculated following Lynnes and Baumstark (1991). Figure 4a shows the result obtained in the 2-4 Hz band. CC means correlation coefficient, SIG standard deviation, and SLO the slope of the regression line. Following Baumgardt and Der (1994), we assume

$$R(\Delta) = 10^{\gamma\Delta} \tag{1}$$

where R is the P_g/L_g ratio, Δ the distance in unit of km, γ the slope of the regression line. It is interesting that while log R increases with Δ at frequencies higher than 1 Hz, it decreases at low frequency (0.3-1.0 Hz). The low frequency result is not shown here, but the results of all regressions for different frequency bands are summarized in Figure 5. Figure 5a shows that the slope for the low frequency band is negative, contrasting with the positive slopes at higher frequency bands.

Previous work has indicated that surface topography may provide a surrogate for crustal variations that influence regional phases. log R correlates with RMS surface roughness over the path almost as strongly as with distance. The 2-4 Hz band result is shown in Figure 4b. Figure 5c is a summary of the correlation coefficients of log R with distance (hollow circles), roughness (hollow triangles), and their product (solid squares) for 6 frequency bands. The slope of log R vs. roughness in the low-frequency band is also negative, this is consistent with our observation based on the data from Semipalatinsk, Kazakhstan (Zhang and Lay, 1994a). Although the correlation patterns of Figure 4a and 4b are similar, the two independent variables distance and roughness are not correlated. Their correlation coefficient is only 0.08.

We consider an end-member case in which the distance behaviors of P_g and/or L_g are controlled by path roughness. Taking the simplest assumption, we let γ be a linear function of roughness, i.e.

$$\gamma(\mu) = \alpha\mu \tag{2}$$

where μ stands for roughness, α is a proportional coefficient. Then (1) becomes

$$R(\Delta) = 10^{\alpha\,(\Delta\mu)} \tag{3}$$

In actuality, we expect that γ involves contributions from intrinsic attenuation, scattering and geometric spreading, but the separate contributions are very difficult to isolate. Figure 4c reflects the correlation of log R with the product of distance and roughness. The correlation coefficient is higher than that of each variable respectively (solid squares in Figure 5c). The slopes (α) for various bands are summarized in Figure 5b. Figure 5d illustrates the variations of another parameter, coefficient of determination, which is interpreted as the proportion of the variability of the data explained by the regression on the independent variable (see Zhang et al., 1994). The product of distance and roughness (solid squares) explains more variability than either distance (hollow circles) or roughness (hollow triangles) alone.

In the frequency range 2.0-6.0 Hz log R shows the greatest distance and roughness dependence. Thus the correction for the two variables and their product in this range produces more reduction in the variances of log R data than in other frequency range.

CONCLUSIONS AND RECOMMENDATIONS:

Finite-difference and normal mode calculations for simple crustal models clearly demonstrate that waveguide structure, especially the overall thickness of the crust and the presence of any low-velocity surface layer, strongly affect the propagation of regional waves like L_g and R_g. The correction based on distance and roughness dependence of the P_g/L_g ratio can reduce the data variance up to 20%. This correction may improve practical discrimination. A discrimination test between NTS explosions and Western U.S. earthquakes will be performed to verify the effect of correction for propagation distance and surface roughness. A regression study on the P_n/L_g ratio is being performed. To obtain more insight into the observed patterns, simulations with reflectivity and finite difference methods are to be done in the near future.

REFERENCES

Baumgardt, D. R. and Z. Der (1994), Investigation of the transportability of the P/S ratio discriminant to different tectonic regions. *PL-TR-94-2299*. ENSCO, Inc., Sprinfield, VA. ADA292944

Cao, S. and K. J. Muirhead (1993). Finite difference modeling of L_g blockage, *Geophys. J. Int.*, **116**, 85-96.

Lynnes, C. and R. Baumstark (1991). Phase and spectral discrimination in North America, *PL-TR-91-2212(II)*. Teledyne Geotech, Alexandria, VA. ADA246673

Zhang, T.-R. and T. Lay (1994a). Analysis of short-period regional phase path effects associated with topography in Eurasia, *Bull. Seism. Soc. Am.*, **84**, 119-132.

Zhang, T.-R. and T. Lay (1994b). Effects of crustal structure under the Barents and Kara seas on short-period regional wave propagation for Novaya Zemlya explosions: empirical relations, *Bull. Seism. Soc. Am.* **84**, 1132-1147.

Zhang, T.-R., S. Y. Schwartz, and T. Lay (1994). Multivariate analysis of waveguide effects on short-period regional wave propagation in Eurasia and its application in seismic discrimination, *J. Geophys. Res.*, **99**, 21929-21945.

Zhang, T.-R. and T. Lay (1995). Why the Lg Phase does not Traverse Oceanic Crust, *Bull. Seism. Soc. Am.*, in press

Zhang, T.-R., S. Y. Schwartz, and T. Lay (1994). Distance and roughness dependence of P/L_g ratios in the Western United States, *Bull. Seism. Soc. Am.*, in preparation
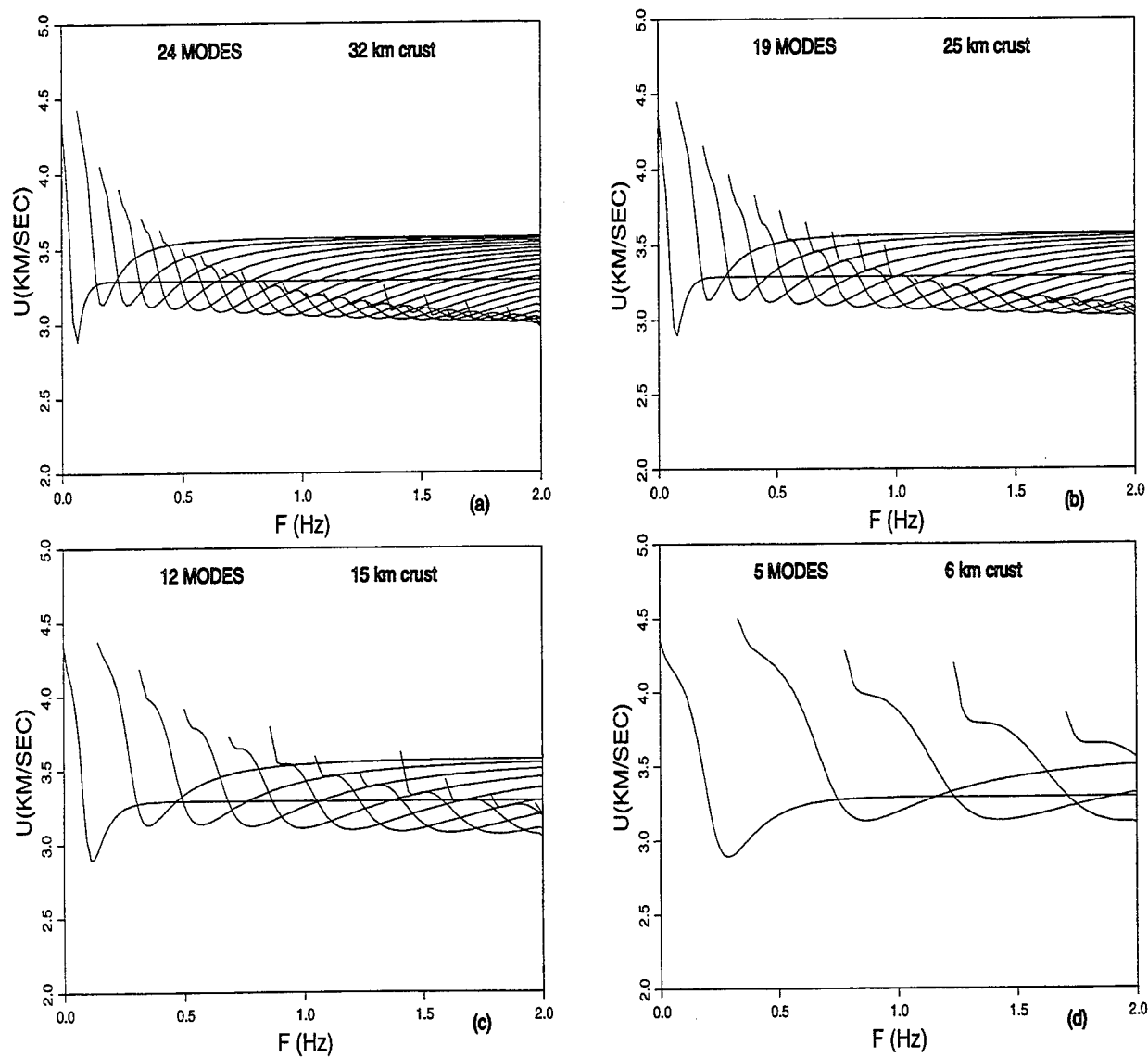
Figure 1: Dispersion curves for Rayleigh waves in layer over a halfspace models with crustal thickness of (a) 32 km, (b) 25 km, (c) 15 km, and (d) 6 km. U stands for group velocity. The number of normal modes in the 0-2 Hz range decreases for thinner crust.

Figure 2: Synthetic seismograms for a layer over halfspace model with 32 km thick crust. Both radial and vertical components are shown. Two lines mark the group velocity window 3.7-to-3.1 km/s used for calculation of RMS L_g amplitudes (called the L_g window). The RMS amplitude values in the L_g window are shown for each waveform.
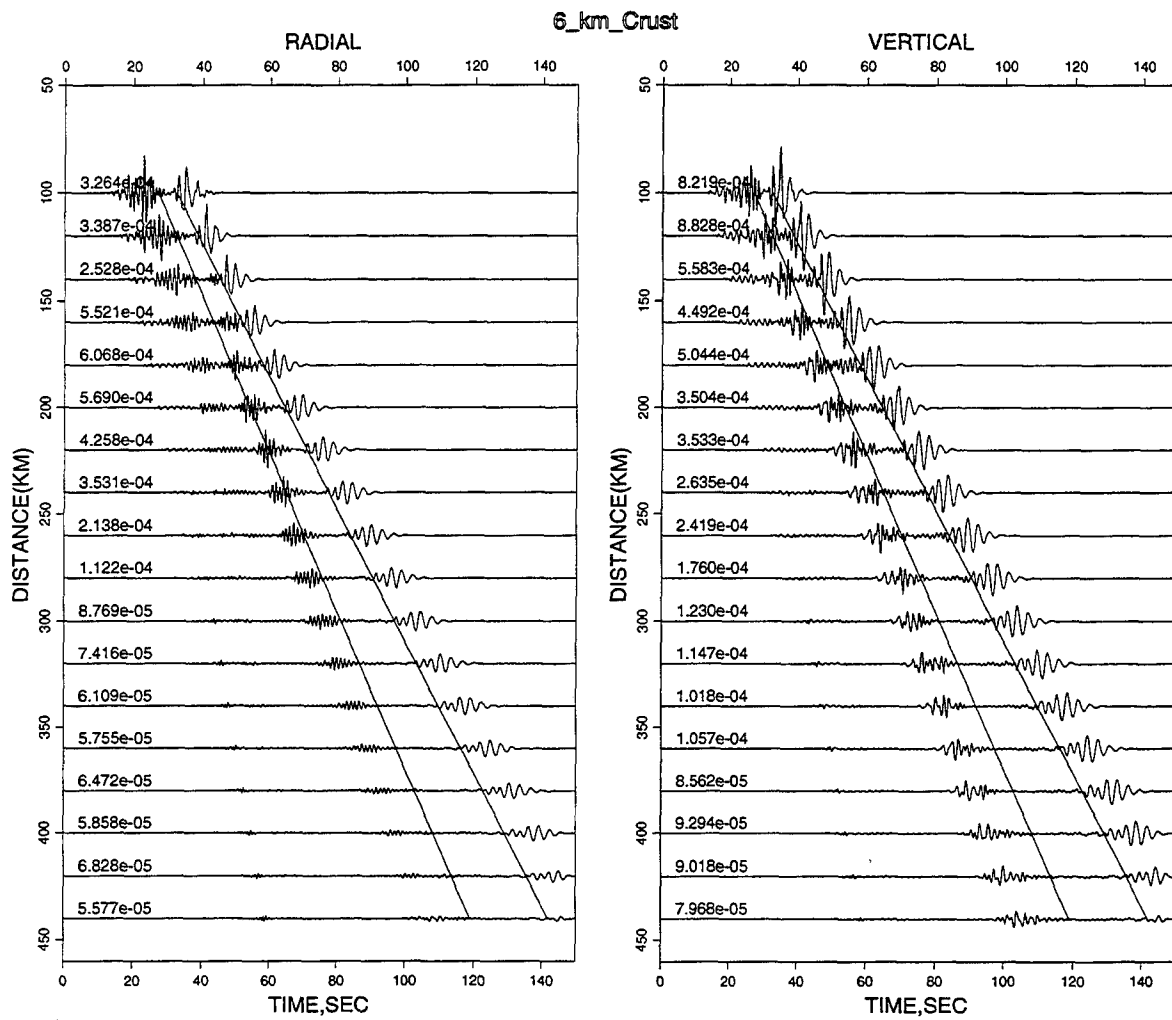
Figure 3: Synthetic seismograms for a layer over halfspace model with 6-km crustal thickness. The arrivals within the L_g window are weak. The R_g waves are delayed, and most of their energy is outside the L_g window.
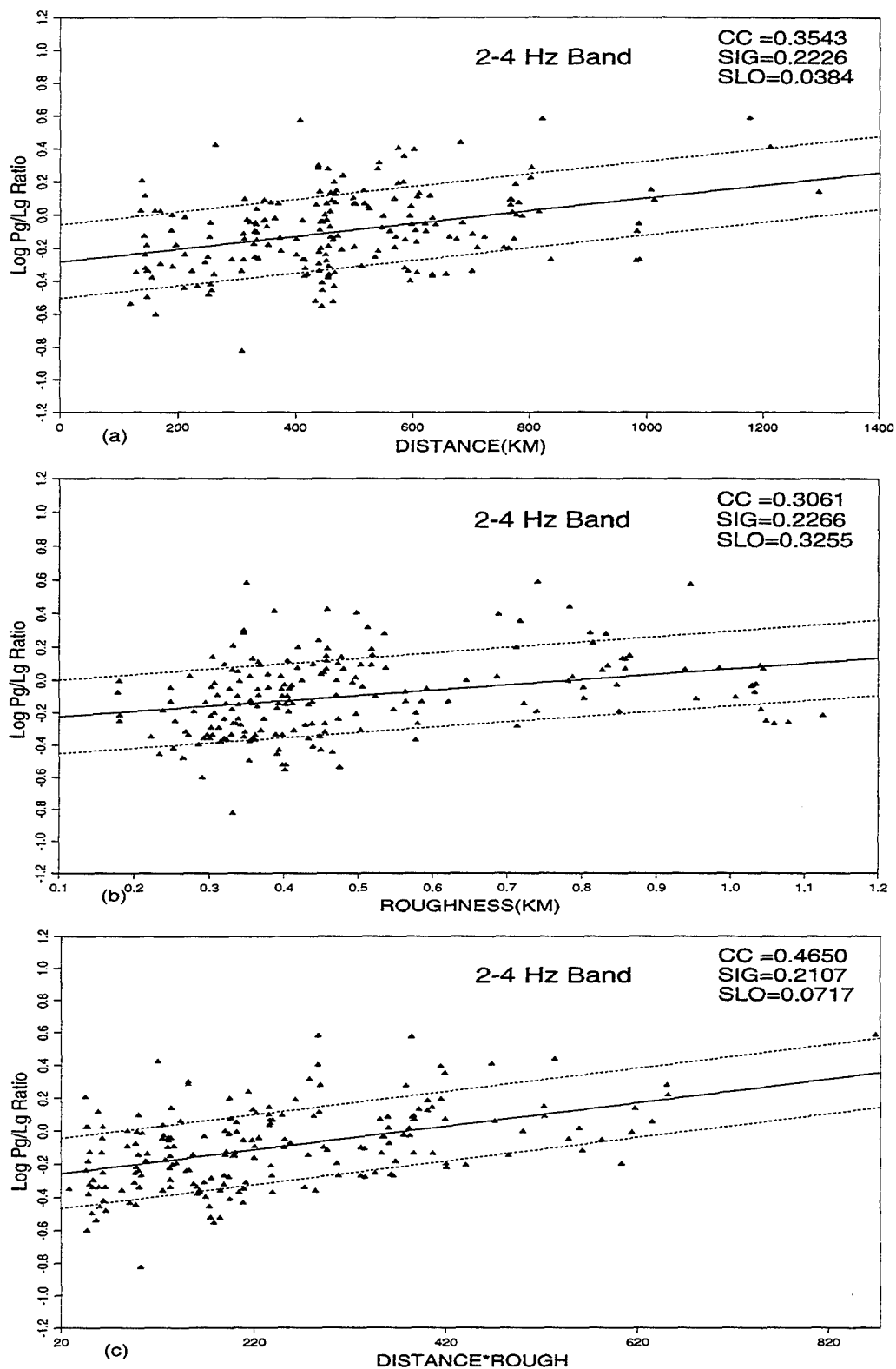
Figure 4: $Log(P_g/L_g)$ as a function of (a) distance, (b) roughness, and (c) distance*roughness for Western U.S. data in the frequency band 2-4 Hz.
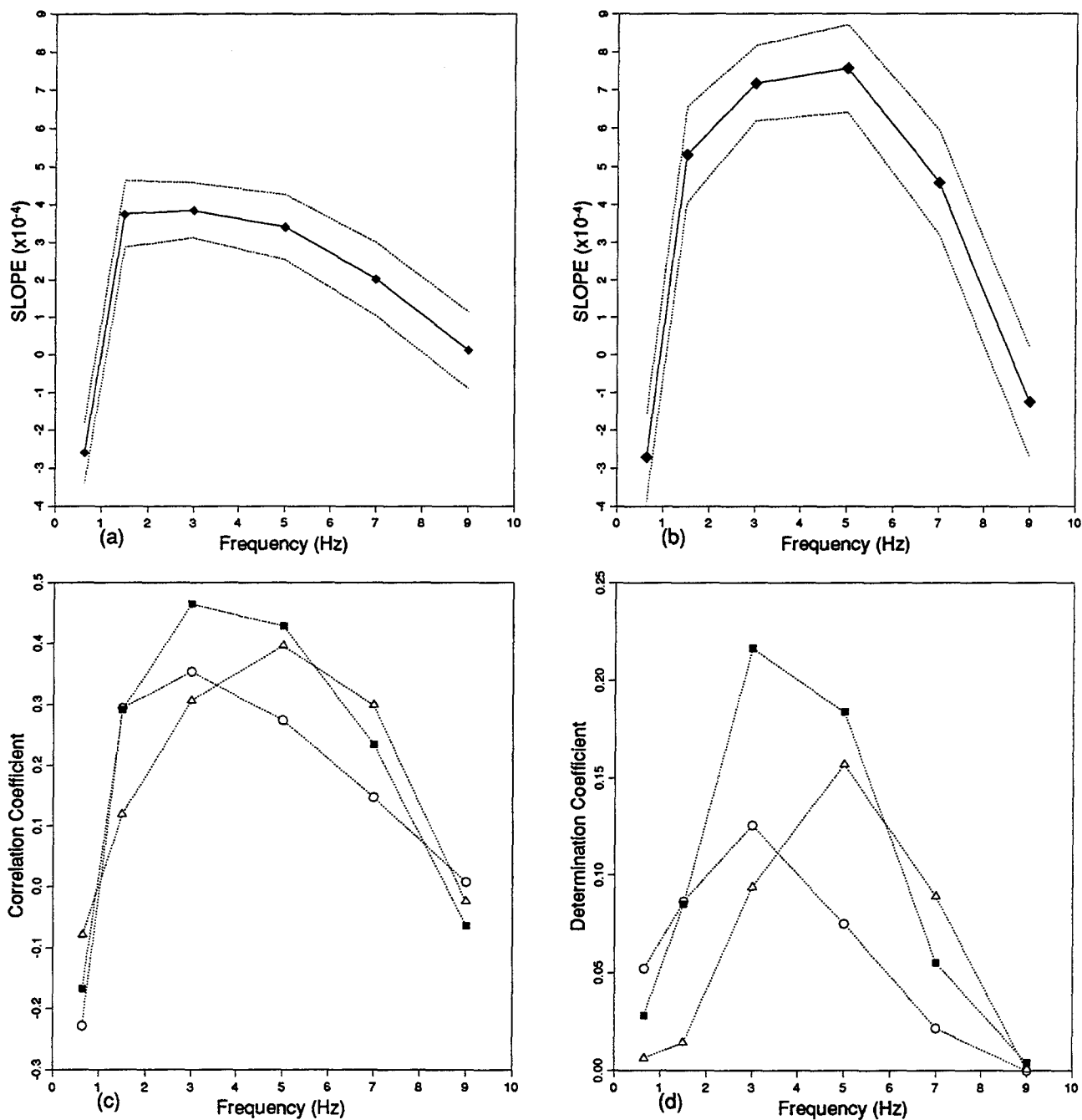
Figure 5: Summary of the correlation results of $\log(P_g/L_g)$ with distance, roughness, and distance*roughness. (a) shows the slopes of the fitting lines of $\log(P_g/L_g)$ with distance in various frequency bands. (b) shows the slopes with distance*roughness. (c) the correlation coefficients of $\log(P_g/L_g)$ with distance (diamonds), roughness (triangles), and distance*roughness (squares). (d) the coefficients of determination of the regressions of $\log(P_g/L_g)$ with distance (diamonds), roughness (triangles), and distance*roughness (squares).

156

BROADBAND SEISMIC RECORDINGS OF MINING EXPLOSIONS AND EARTHQUAKES IN SOUTH AMERICA

Susan L. Beck and Terry C. Wallace
Southern Arizona Seismic Observatory
Department of Geosciences
University of Arizona
Tucson, AZ 85721

ABSTRACT

S/P ratios have shown great promise as discriminants for explosions and earthquakes recorded at regional distances. Spectrograms, or the frequency–time displays of seismograms, have been used to separate explosion populations into those which are single-shot or multiple-hole instantaneous explosions and those which are ripple-fired explosions. However, despite the promise of these discriminants, there are problems of transportability. The character of regional phases is extremely sensitive to differences in propagation paths, and it is essential to calibrate regions of monitoring interest.

We have investigated the seismicity (both natural and man-made) in central Chile recorded on a high-frequency seismic network. We are developing a data base to quantify distance-dependent spectral ratios and other potential discriminants. Within the seismic network is a large open-pit copper mine which has occasional multiple-shot explosions with magnitudes as large as 3.7. We find at close epicentral distances (<~60 km) that mining explosions show spectral scalloping indicative of "ripple-fire" sources and that *S–P* amplitude ratios indicate enhanced *P* wave radiation. However, at epicentral distances of ~100 km the frequency content has decreased, with little energy above 5 Hz. Preliminary analysis indicates that spectral discriminants for earthquakes and ripple-fire explosions at close epicentral distances operate as other investigators have reported for other regions in the world.

KEYWORDS: discrimination, regional distance, spectral ratios

INTRODUCTION

The spectral characteristics of seismograms recorded at regional distances have been extensively studied in recent years (Bennett *et al.*, 1989; Taylor *et al.*, 1989; Lilwall, 1988) and are some of the most promising discriminants. Most spectral discriminants are based on two conditions: (1) Given the same zero frequency moment, an earthquake will be enriched in high frequencies as compared to an explosion, and (2) earthquakes excite more S wave type energy than explosions. Typical spectral discriminants ratio the spectral level or amplitude of S and P waves. In general, there is good separation of earthquakes and explosion populations, especially at high frequencies ($f > 6$ Hz) (Kim *et al.*, 1994). Unfortunately, travel path has a strong influence on the "base line" of the trend which separates the explosion and earthquake populations (Lynnes *et al.*, 1990), and travel paths must be carefully calibrated for spectral discriminants to work.

One of the most pressing problems in monitoring a comprehensive test ban is identification of industrial explosions. Richards *et al.* (1992) report that there are literally thousands of industrial explosions in the U.S. every year, many of which have local magnitudes between 2.5 and 3.0 Presently there is considerable discussion on the possibility of clandestine testing using decoupling scenarios. A fully decoupled explosion could produce seismic signals much smaller (factor of 30 to 70) than that of fully tamped events. Thus, clandestine tests of a few kilotons may produce magnitudes of 2.5 to 3.0 and must be discriminated from the mining activity. In general, industrial explosions have spatial–temporal characteristics which can be used to discriminate them from nuclear explosions. Most large mining explosions have a unique signature in the frequency domain due to the "ripple-fire" detonation of "sub" explosions separated by small distances and times. This spectral scalloping is diagnostic of an industrial explosion, but it is most pronounced at frequencies above 10 Hz. In some regions of high seismic attenuation (such as the Basin and Range in the western U.S.), the spectral scalloping disappears beyond a few hundred kilometers. Most of our experience with industrial explosions is limited to a few areas, especially within the U.S. Blasting practice varies dramatically from country to country, so it is essential to calibrate path and source effects in any region of potential monitoring interest.

In this phase of this project we have focused on studying the high-frequency characteristics of seismic events in western South America. In both Chile and Argentina there are very large copper mines which have had chemical explosions in excess of 400 tons. In addition, there are several mines which are in excess of 3 km depth. Many of the mines are in regions of moderate to high natural seismicity, and there are occasional rock bursts with large magnitudes.

PRELIMINARY RESEARCH RESULTS

The character of regional distance seismograms in South America is extremely complex and poorly mapped. The Andes are regions of *Lg* blockage, and further, some regions show extreme crustal seismic attenuation. For this report we have studied the shallow seismicity in southern Chile recorded in a digital seismic network operated by the University of Chile. The network, known as the Central Chile Seismic Network (CCSN), consists of 16 short-period seismic stations located near Santiago (see Figure 1) between 32.5° and 34.5°S. The network employs 2-Hz sensors which are flat to velocity between 2 and 20 Hz; the data are sampled at 50 Hz. The Disputada de las Condes Mine is one of the largest copper mines in Chile and is located within the CCSN. The mine is mainly an open pit operation, but there is an older section which continues underground operations. The mine produces a significant number of explosions per week, many of which have magnitudes of between 3.4 and 3.6 as reported by the University of Chile. Further, the mine is located in a region of moderate background seismicity. We have analyzed data recorded on the CCSN to investigate regional discrimination.

Industrial explosions are generally classified as three types: (1) single shots, (2) multiple shots, with near instantaneous detonation, and (3) multiple shots, with delayed detonations. This last category is called a "ripple-fired" explosion, and it is the most common blasting practice for large amounts of explosives. Ripple fire maximizes the rock volume fracture and reduces ground

roll vibration which can cause damage to nearby structures and equipment. Since the vast majority of large industrial explosions are ripple-fired, it is essential to develop seismic discriminants which identify single-shot events (potential clandestine underground nuclear explosions) and earthquakes.

The spatial–temporal pattern of ripple-fire explosions produces a characteristic pattern in the frequency domain. Hedlin et al. (1989) used spectrograms which show the frequency content of an entire regional distant waveform to map "banding" characteristics of ripple fire. Figure 2 shows the waveforms on spectrograms for four events from the Disputada Mine recorded at a digital station located at an epicentral distance of approximately 20 km. The shaped spectrograms show the frequency content in a window centered on a given point on the time axis. The shading is scaled with ground velocity amplitude, so dark spots correspond to large amplitudes.

In Figure 2, events a, b, and c are thought to be ripple-fired explosions. Note that the amplitude ratio of S to P energy suggests enhanced P wave radiation, especially at high frequencies. Note also the banding or scalloping in a given time window; high amplitudes are followed by spectral holes. For all three of these events, the S-to-P ratio discriminates the events from earthquake populations, and the scalloping indicates industrial explosions. However, event d is problematic. The S-to-P ratio fits well within the earthquake population, but the event was located near all the explosions (events a, b, c).

The observation of regular spectral banding at high frequencies for the waveforms in Figure 2 is a reliable indicator of industrial explosions. Kim et al. (1994) report that this banding persists out to distances of several hundred kilometers for explosions in Norway. However, this is not the case for central Chile. Figure 3 shows the spectrograms of mining explosions recorded at successively increasing epicentral distances. The closest station, FCH (21 km) shows strong banding, particularly at 10 Hz. The most distant station, CACH (114 km) has almost no seismic energy above 5 Hz, and hence evidence of spectral scalloping has disappeared. Further, the S/P ratio increases with distance, perhaps due to Rg to Lg scattering. The removal of high-frequency energy is probably due to the extreme crustal attenuation. Wigger (1988) used mine explosions in northern Chile (Chuquicamata Mine) as seismic sources for a refraction profile. Each mine blast was 250 tons, and it was expected that seismic energy could be seen to distances of 300 km or greater. However, for a refraction profile into the Andes, coherent seismic energy was recorded out to only 100 km.

CONCLUSIONS AND RECOMMENDATIONS

We are developing a large data base of digital recordings of shallow seismic sources in central Chile. The sources include earthquakes, mining explosions, and rock bursts. We are investigating the behavior of spectral discriminants as a function of both epicentral distance and azimuth. In addition to high crustal attenuation, the large variations in topography (station FCH is at 2770 m and station PCH is at 1010 m) and crustal structure also appear to contribute to the behavior of the spectral discriminants. Preliminary analysis indicates that spectral discriminants for earthquakes and ripple-fire explosions at close epicentral distances operate as other investigators have reported for other regions in the world. However, the discriminants appear to be severely limited by high levels of crustal attenuation and/or scattering.

REFERENCES

Bennett, T. J., B. W. Barker, K. L. McLaughlin, and J. R. Murphy (1989). Regional discrimination of quarry blasts, earthquakes and underground explosions, *S-Cubed Report, SSS-TR-89-10395*.

Kim, W., D. W. Simpson and P. G. Richards (1994). High frequency spectra of regional phases from earthquakes and chemical explosions, *Bull. Seism. Soc. Am.*, **84**.

Lilwall, R. C. (1988). Regional m_b:M_S, Lg and Pg amplitude ratio and Lg spectral ratio as criteria for distinguishing between earthquakes and explosions: A theoretical study, *Geophys. J.*, **93**, 137–147.

Lynnes, C. S., R. Baumstark, R. K. Cessaro and W. W. Chan (1990). *Pg/Lg* discrimination in the western United States, in *12th annual DARPA/GL Seismic Research Symposium*, Lewkowicz and McPhetres, editors, 123–129. GLTR-90-0212, ADA226635

Richards, P. G., D. A. Anderson and D. W. Simpson (1992). A survey of blasting activity in the United States, *Bull. Seism. Soc. Am.*, **82**, 1416–1433.

Taylor, S. R., and M. D. Denny, E. S. Vergino and R. E. Glaser (1989). Regional discrimination between NTS explosions and western United States earthquakes, *Bull. Seism. Soc. Am.*, **79**, 1143–1176.
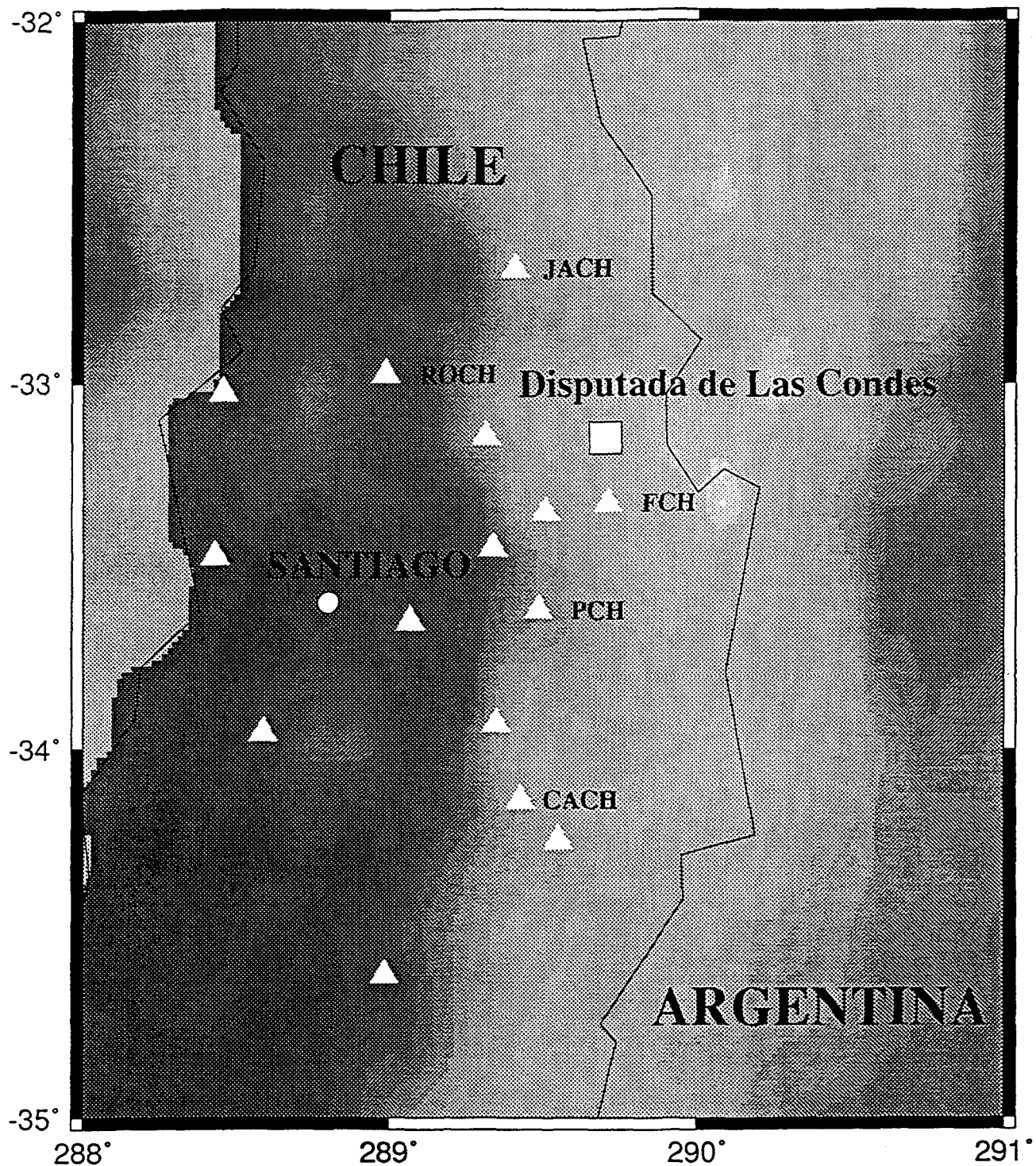
Figure 1. Map showing the location of the Central Chile Seismic Network stations (triangles) and the Disputada de las Condes copper mine (square). Shading indicates elevations with light regions above 2 km.
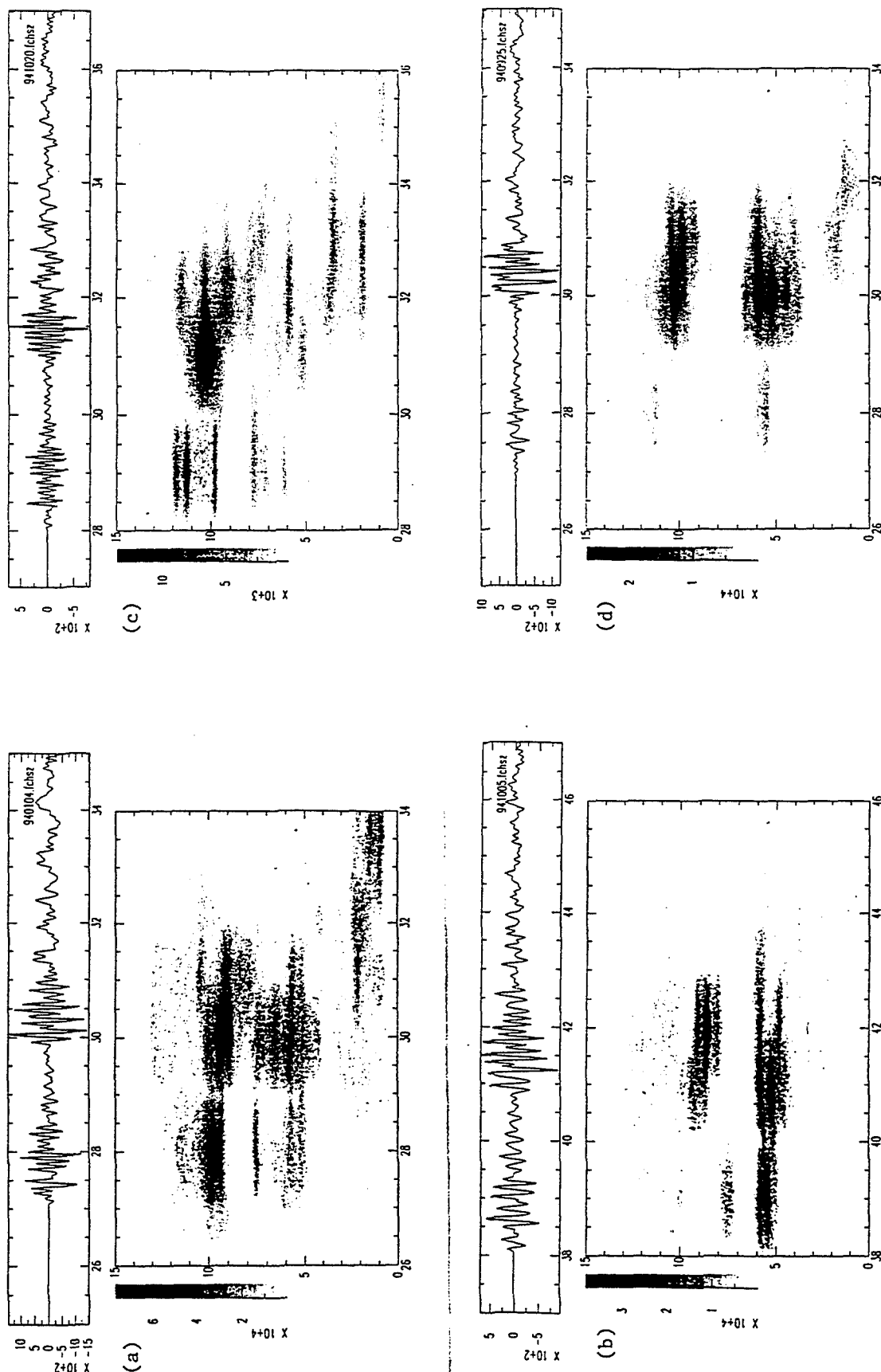
Figure 2. Plots showing seismograms and spectrograms (X,Y,Z plot with time, frequency, amplitude axes respectively) for four different events and recorded at station FCH at a distance of 20 km. In each case 10 seconds of time is plotted. Events A (M_L=3.51), B (M_L=3.63) and C (M_L=3.27) show spectral banding indicative of a ripple fire sources. Event D (M_L=3.48) shows very weak Pg relative to Lg.

162
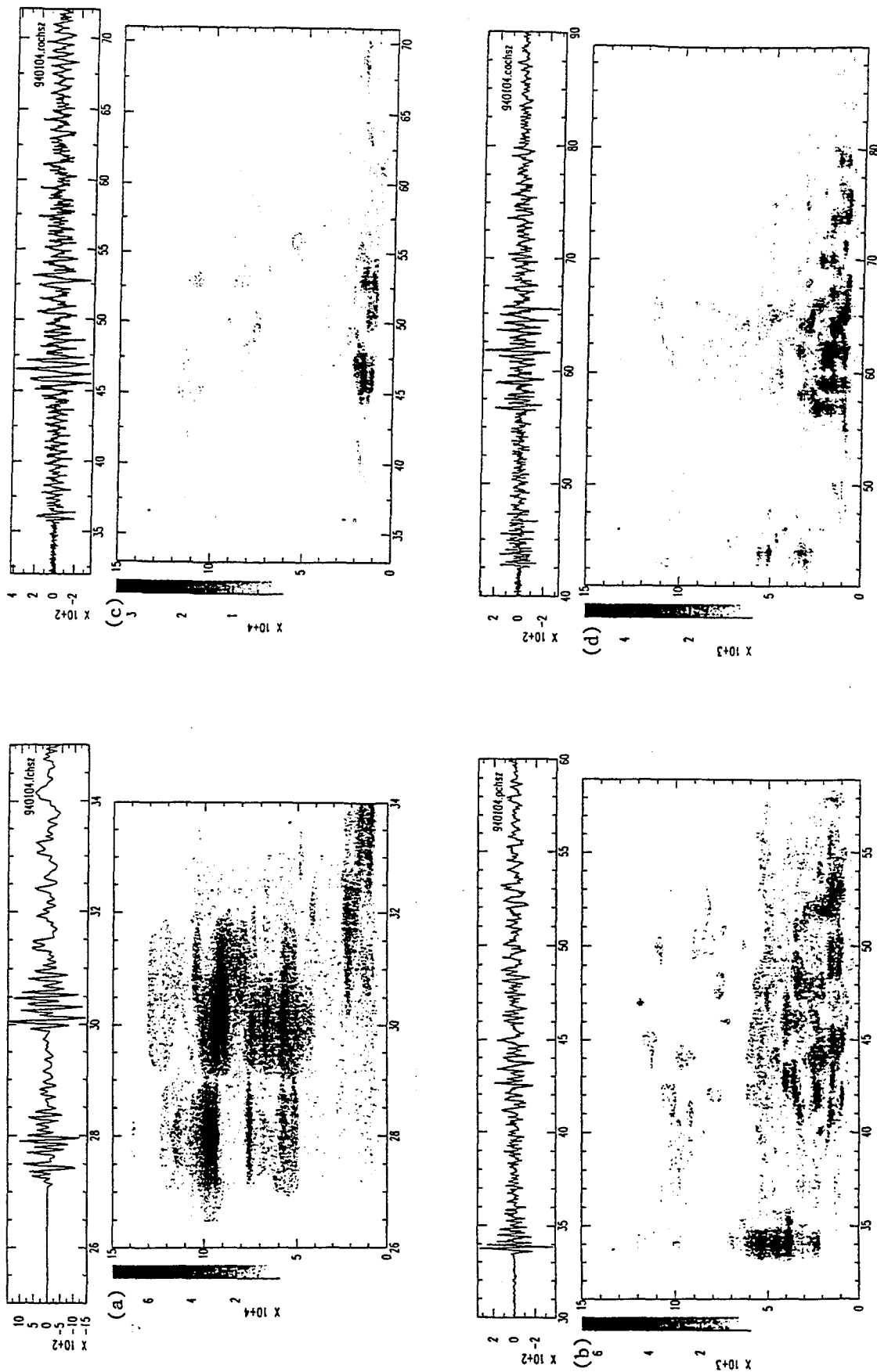
Figure 3. Seismograms and spectrograms for a mine blast on 01/04/94 recorded at four stations with increasing distance. (A) FCH (dist=21 km), (B) PCH (dist=58 km), (C) ROCH (dist=70 km) and (D) CACH (dist=114 km). At a recording distance of 20 km the spectral banding is prominent but decreases quickly with distance.

Constraints on the Upper Mantle Velocity Beneath the Yellow Sea, Eastern China

John J. Cipar
Earth Sciences Division (PL/GPE)
Phillips Laboratory

Abstract. Detailed models of the crust and upper mantle are crucial for precise event location and computation of realistic synthetic seismograms for earthquake/explosion identification. However, such models are not available for most of the globe, including eastern China. In this report, data from the 1992 Yellow Sea earthquake is used to put constraints on the upper mantle velocity beneath the Yellow Sea and eastern China. The average velocity in the upper mantle is measured at 8.06 km/sec. Comparison of observed waveforms to synthetics suggests that the upper mantle P-wave velocity gradient is 0.0013 km./sec/km, with a higher gradient in the uppermost mantle just beneath the Moho. Availability of array data for a suite of events could be used to place strong constraints on the velocity structure.

Keywords: Seismology, Body wave propagation, Lithosphere and upper mantle, Asia

OBJECTIVE: To determine the crustal and upper mantle structure beneath eastern China

PRELIMINARY RESEARCH RESULTS:

Introduction

The details of the crust and upper mantle structure of eastern China have been measured in only a few places (Mangino and Ebel, 1992 and references cited therein). Mangino and Ebel (1992) used teleseismic receiver function observations to estimate the shear velocity of the crust at stations of the Chinese Digital Seismographic Network (CDSN). Nguyen and Hsu (1993) inverted surface wave group velocity dispersion curves from the 1992 Yellow Sea earthquake to obtain models for each of the CDSN stations. Cipar (1995) refined their focal mechanism using a grid search procedure and proposed a new crustal structure model for the Yellow Sea.

The 1992 Yellow Sea, China, Earthquake

A moderate earthquake occurred in the Yellow Sea off the coast of eastern China on 3 November 1992 at 17h 31m 23.7s. Coordinates are 35.328°N, 123.312°E; focal depth is 10 km, m_b = 4.8 (Preliminary Determination of Epicenters, November, 1992, Monthly Listing). Figure 1 shows the earthquake location and the locations of the CDSN stations used in this study (Table 1). Each station recorded the data in three pass bands: long-period (LH), broadband (BH), and short-period (SH) (Peterson and Tilgner, 1985). Nguyen (1994) used CDSN surface wave observations to determine the mechanism of the 1992 Yellow Sea earthquake to be nearly strike-slip with a minor amount of dip-slip. His mechanism, shown in Figure 1, is consistent with first-motion measurements observed on CDSN short-period records. The fault plane has the parameters: strike = 15°, dip = 80°, and rake = 155°. He determined the source depth and seismic moment to be 9 km and 8.42×10^{22} dyne-cm, respectively.

In this report, I use the CDSN broadband data (the BH band) to place an additional constraint on the upper mantle velocity. The data set is less than ideal. The earthquake was of moderate magnitude located at sea far from the nearest seismic station, hence its location is imprecisely known and teleseismic observations are poor. In the context of nuclear treaty

Table 1. CDSN Station Information

Station Location	Latitude (°N)	Longitude (°E)	Elevation (m)	Delta (deg)	Distance (km)	Azimuth (deg)	Back Azimuth (deg)	
BJI	40.0403	116.1750	43.0	7.357	817.958	311.860	127.490	Beijing
ENH	30.2800	109.4975	487.0	12.661	1408.070	250.471	62.954	Enshi
HIA	49.2667	119.7417	610.0	14.175	1575.558	350.415	167.994	Hailar
HKC	22.3036	114.1719	0.0	15.238	1694.948	214.049	29.608	Hong Kong
KMI	25.1500	102.7500	1952.0	20.421	2271.258	245.854	55.375	Kunming
LZH	36.0867	103.8444	1560.0	15.836	1760.627	278.427	86.992	Lanzhou
MDJ	44.6164	129.5919	250.0	10.449	1161.622	25.507	209.557	Mudanjiang
SSE	31.0956	121.1867	10.0	4.581	509.467	203.475	22.310	Sheshan

monitoring, however, it is precisely these weak signals which will be of prime importance for discrimination of suspect events.
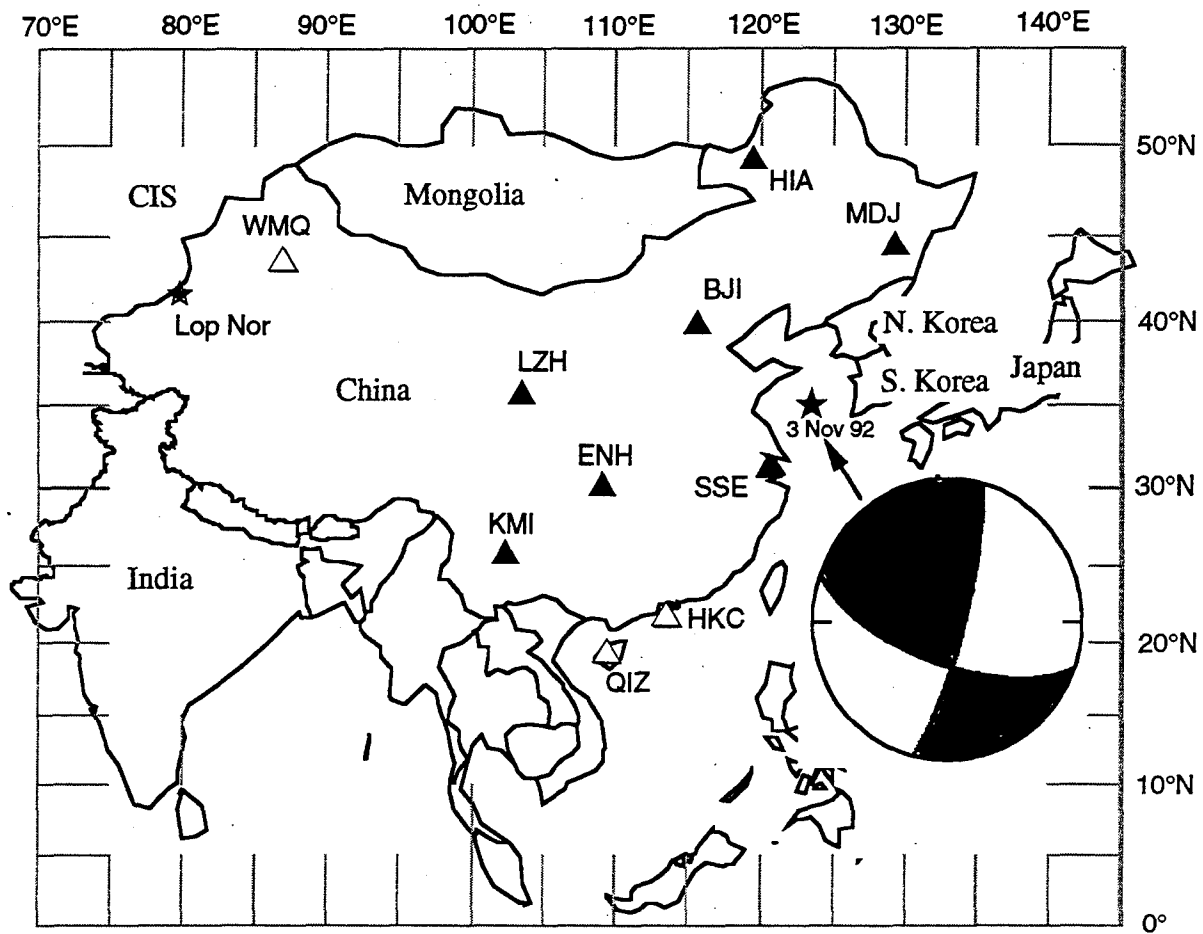
Figure 1. Map of the location of the Yellow Sea earthquake (star) and stations (filled triangles) used in this study. Open triangles denote other stations in the area. The inset shows the focal mechanism reported by Nguyen (1994); shaded quadrants are compressional.

Model for Crustal Structure

The starting velocity model for the crust was determined by Nguyen and Hsu (1993) as their MDJ model. The model was extended into the upper mantle using a constant velocity gradient. Although the attenuation was set rather high, the values are broadly consistent with previous measurements for the continental crust (Cheng and Mitchell, 1981). This starting model is designated A5 and is given in Table 2a.

Cipar (1995) used model A5 and the long-period (LH) channels at CDSN stations SSE, MDJ, BJI, HIA, LZH, and ENH to determine the focal mechanism by a gird search inversion procedure. The best fitting depth is 15 km, 6 km deeper than the depth determined by Nguyen (1994). The inferred mechanism is slightly different as well with a strike = 19°, dip = 90°, and rake = 173°. This mechanism is broadly consistent with the results reported by Nguyen (1994) especially given the fact that this inversion did not use any constraints such as P-wave polarities. It should be noted, however, that the focal mechanism reported by Nguyen (1994) produced rather large misfits at all source depths. The inferred source depth, 15 km, is well within the depths expected for a continental earthquake.

The focal mechanism grid search provides a source model that produces overall better agreement between observed and synthetic seismograms. Further improvement can be gained by modifying the crustal structure. Cipar (1995) tried several simple modifications of the MDJ path model (model A5). The most successful was dubbed A8 (Table 2b) in which the lower crustal velocity is reduced from 7.16 km/sec for A5 to 6.8 km/sec, and the Q reduced. The Pn velocity of A5 seems to be quite low compared to other continental regions, however, synthetics computed for higher Pn velocity values produced larger misfits than A8. Cipar (1995) adopted the Nguyen and Hsu (1993) Pn velocity as correct.

Upper Mantle Velocity

The broadband (BH band) data for the Yellow Sea earthquake are shown in record section format in Figure 2. The seismograms have been high-pass filtered to remove long-period noise and are plotted as trace normalized. Prominent phases are a clear Pn, especially at close distances, and Lg. A straight line fit to the first arrival observations at SSE, BJI, ENH, and HIA (see Figure 1), over the distance range 509 to 1575 km, indicates the average Pn velocity is 8.06 km/sec.

Broadband vertical seismograms for the two closest CDSN stations (SSE and BJI) are shown in the left panel of Figure 3, along with travel time curves computed for model A8 (Table 2b). We are looking at the first 60 seconds of record, that is, the P wave group. At these ranges, the first arrival is a strong, clear Pn. The travel time curves were computed for a surface source, whereas the earthquake occurred at 10 to 15 km depth. Nevertheless, the arrival times of the observed Pn phases closely match the theoretical curves in time. The A8 synthetics (right panel) were computed using the reflectivity method (Fuchs and Muller, 1971) for a 15-km deep source, hence the time discrepancy between travel time curves and synthetics. This implies that the travel times of the synthetics are early compared to the data. One obvious explanation is uncertainty in location and origin time. Alternatively, model A8 may be too fast relative to the true structure.

The synthetic waveforms provide a further constraint on the structure. One of the features of model A8 is high velocity gradients in the upper mantle which turn energy back to the surface, leading to strong first arrivals compared to later phases. The data, on the other hand, show strong first arrivals followed by a long coda, punctuated by several distinct phases. Unlike the A8 synthetics, however, the observed Pn phases are comparable in amplitude to later phases.

A range of models with constant gradients in the upper 160 km were tested by computing synthetics and comparing these to the observed seismograms. Synthetics for model A20 (Table 2c) with a gradient 0.0013 km/sec/km are shown in Figure 4. The Pn amplitude at BJI is comparable qualitatively to the observed record. The synthetic Pn at SSE,
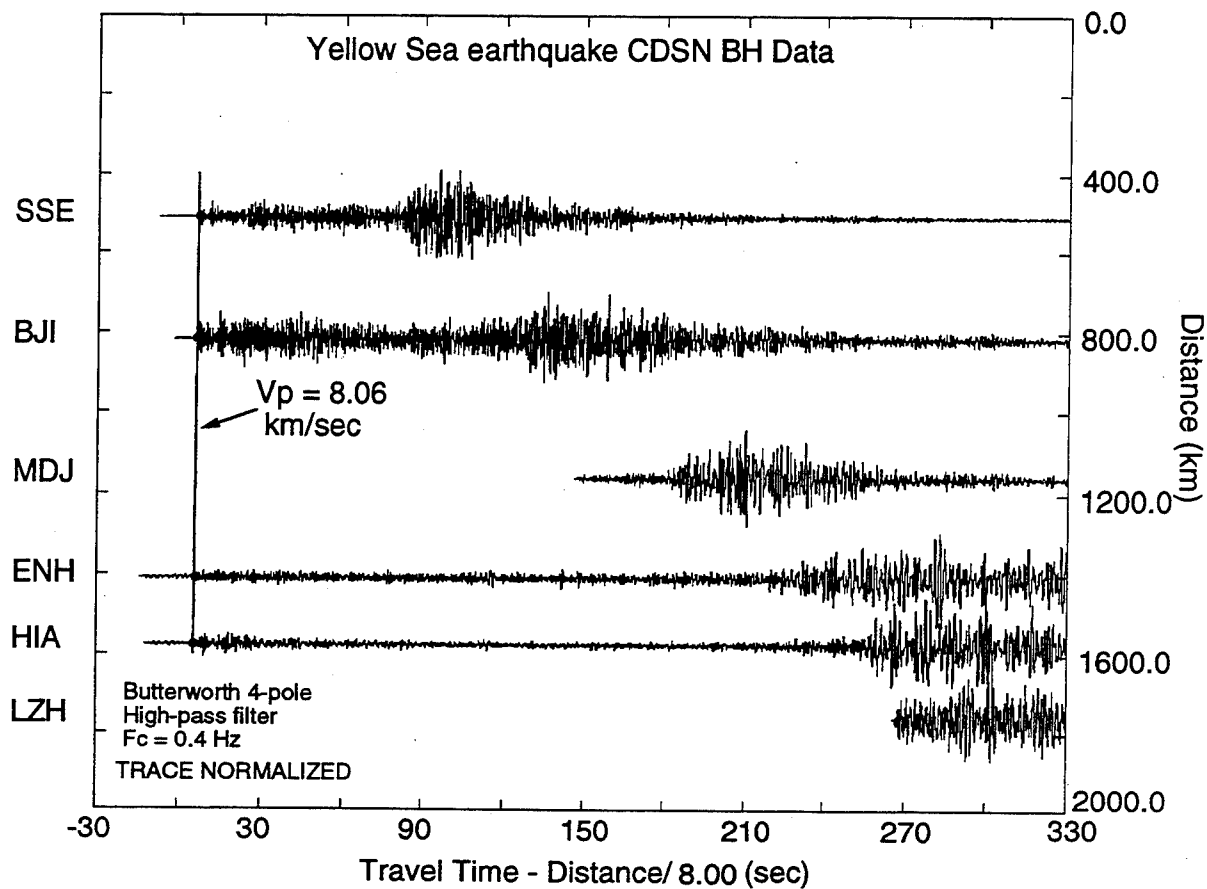
Figure 2. Broadband CDSN seismograms of the 1992 Yellow Sea earthquake displayed as trace normalized records. The seismograms have been high-passed filtered using a 4-pole Butterworth filter with a corner frequency of 0.4 Hz. The line marked 8.06 km/sec indicates the best fit straight line to measured first arrival times.

on the other hand, is too small compared to the observed Pn.   The original MDJ model (A5) has a Moho velocity of 7.76 km/sec and we have already measured the average Pn velocity to be 8.06 km/sec. These observations suggest a strong gradient just below the Moho, which decreases with depth.   Note that

Table 2. Crustal Models

Depth km	P-velocity km/s	Q_p	S-velocity km/s	Q_s	Density g/cm^3
		(a) Model A5			
0.0	4.06	200.0000	2.3500	100.0000	2.3300
1.0	4.06	200.0000	2.3500	100.0000	2.3300
1.0	5.42	1000.0000	3.1300	500.0000	2.5800
3.0	5.42	1000.0000	3.1300	500.0000	2.5800
3.0	6.16	1000.0000	3.5600	500.0000	2.7500
16.0	6.16	1000.0000	3.5600	500.0000	2.7500
16.0	7.16	1000.0000	4.1400	500.0000	3.0300
40.0	7.16	1000.0000	4.1400	500.0000	3.0300
40.0	7.76	1000.0000	4.4800	500.0000	3.2300
70.0	8.10	1000.0000	4.6767	500.0000	3.3203
100.0	8.20	1000.0000	4.7344	500.0000	3.3582
130.0	8.40	1000.0000	4.8499	500.0000	3.4339
160.0	8.50	1000.0000	4.9076	500.0000	3.4718
		(b) Model A8			
0.0	4.0600	50.0000	2.3500	25.0000	2.3300
1.0	4.0600	50.0000	2.3500	25.0000	2.3300
1.0	5.4200	100.0000	3.1300	50.0000	2.5800
3.0	5.4200	100.0000	3.1300	50.0000	2.5800
3.0	6.1600	525.0000	3.5600	263.0000	2.7500
16.0	6.1600	525.0000	3.5600	263.0000	2.7500
16.0	6.8000	525.0000	3.9261	263.0000	2.8278
40.0	6.8000	525.0000	3.9261	263.0000	2.8278
40.0	7.7600	525.0000	4.4800	263.0000	3.2300
70.0	8.1000	525.0000	4.6767	263.0000	3.3203
100.0	8.2000	525.0000	4.7344	263.0000	3.3582
130.0	8.4000	525.0000	4.8499	263.0000	3.4339
160.0	8.5000	525.0000	4.9076	263.0000	3.4718
		(c) Model A20 (same as A8 above 40 km)			
40.0	8.0000	525.0000	4.6200	263.0000	3.2300
70.0	8.0400	525.0000	4.6200	263.0000	3.3203
100.0	8.0800	525.0000	4.6300	263.0000	3.3582
130.0	8.1200	525.0000	4.6400	263.0000	3.4339
160.0	8.1600	525.0000	4.6415	263.0000	3.4718

169

Yellow Sea BH Data + YSA-A8 Synthetics & Travel-Time Curves

SSE

BJI

TRACE NORMALIZED

Travel Time - Distance/8.00 (sec)

Distance (km)
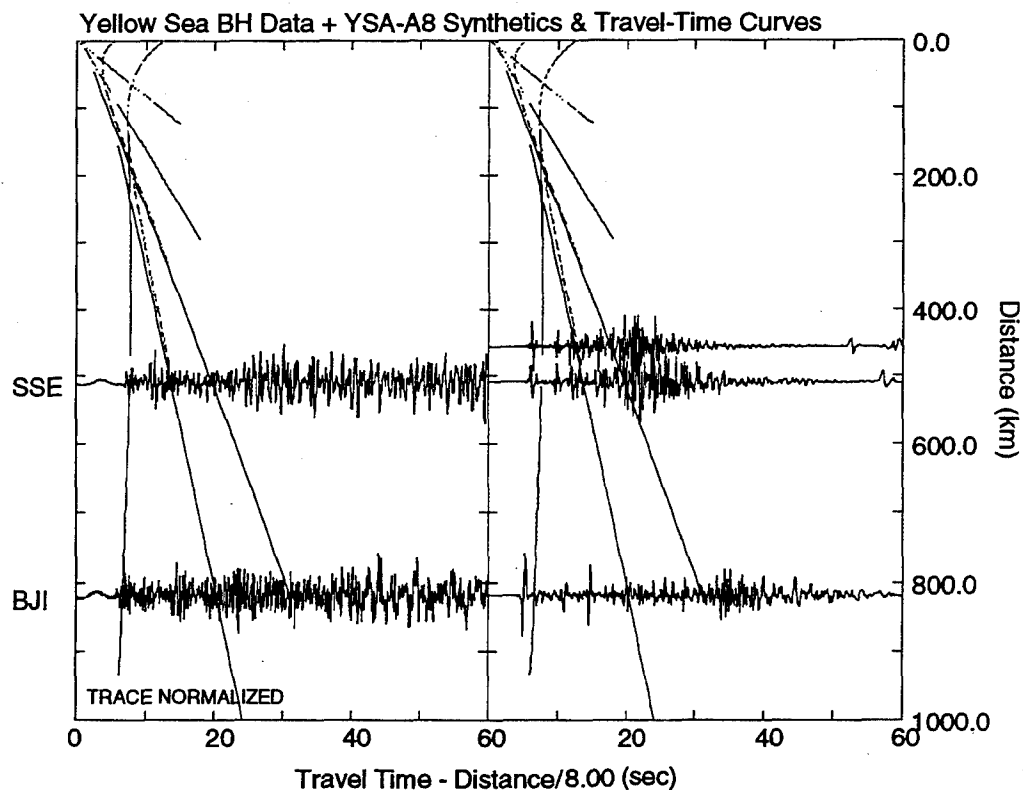
Figure 3. Broadband data of the Yellow Sea earthquake (left panel) and synthetic seismograms computed for model A8. Travel time curves are calculated for model A8 at zero source depth.

Yellow Sea BH Data + YSA-A20 Synthetics & Travel-Time Curves

SSE

BJI

Travel Time - Distance/8.00 (sec)

Distance (km)
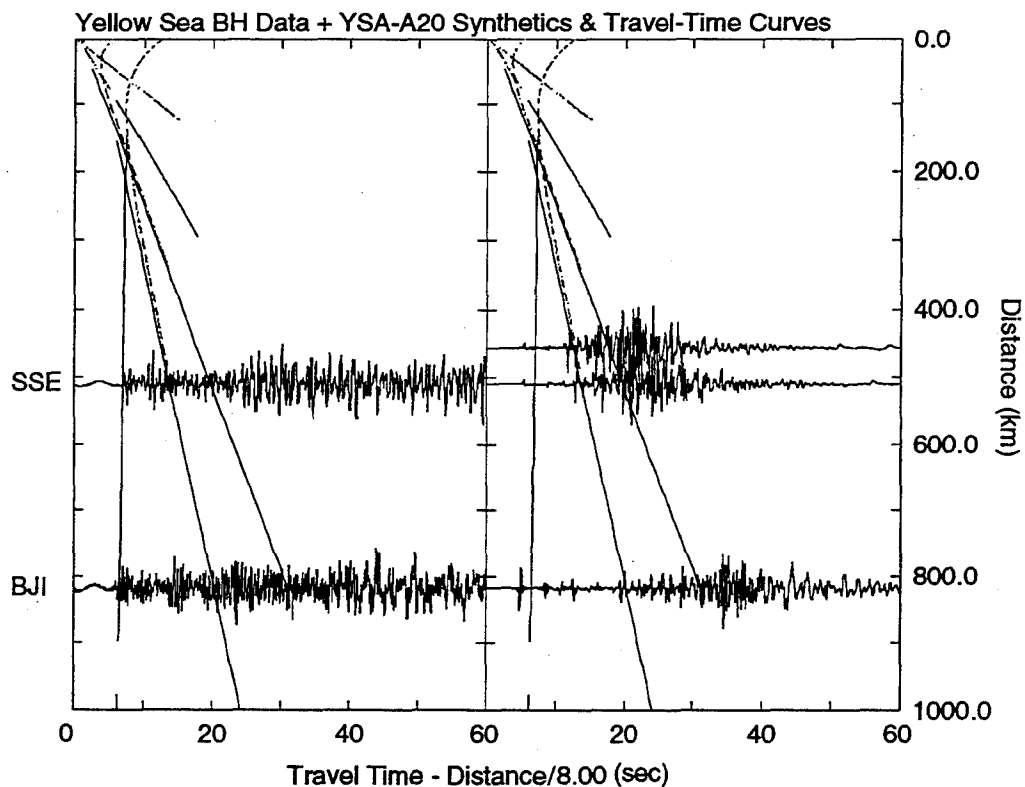
Figure 4. Broadband data of the Yellow Sea earthquake (left panel) and synthetic seismograms computed for model A20. Travel time curves are calculated for model A20.

20-JUL-95

170

the travel time curves for model A20 nearly overlay the observed Pn first arrivals.

<u>CONCLUSIONS AND RECOMMENDATIONS:</u>

The average upper mantle Pn velocity beneath the Yellow Sea and eastern China is 8.06 km/sec, determined using data from the 1992 Yellow Sea earthquake, and is consistent with other stable platform regions (Meissner, 1986). The P wave velocity gradient is 0.0013 km/sec/km, although it may be higher in the uppermost mantle just below the Moho. Array observations of a suite of events at a range of distances and azimuths could be invaluable in putting constraints on crust and upper mantle velocities.

References

Cheng, Chiung-Chuan and Brian J. Mitchell, Crustal Q structure in the United States from Multi-Mode Surface waves, *Bull. Seism. Soc. Am., 71,* 161-181 (February, 1981)

Cipar, John, A Grid Search Algorithm to Determine Earthquake Source Parameters - Application to the 1992 Yellow Sea, China, Earthquake, in press, PL-TR-95-2082

Fuchs, K. and G. Muller, Computation of Synthetic Seismograms with the Reflectivity Method and Comparison with Observations, *Geophys. J. Roy. Astron. Soc., 23,* 417-433 (1971)

Mangino, Stephen and John Ebel, The Receiver Structure Beneath the Chinese Digital Seismograph Network (CDSN) Stations: Preliminary Results, PL-TR-92-2149, Phillips Laboratory, Hanscom AFB, MA (30 April 1992) ADA256681

Meissner, Rolf, *The Continental Crust - A Geophysical Approach,* Academic Press, 1986, 426p.

Nguyen, Bao V. Surface-Wave Focal Mechanism of the 03 November 1992 Yellow-Sea Main Shock, *EoS (Trans. Am. Geophys. Union), 75,* 241, (April 19, 1994)

Nguyen, Bao V. and Vindell Hsu, Shear Path Structures from Inversions of Surface waves of the 03 November 1992 Yellow-Sea Main shock, *EoS (Trans. Am. Geophys. Union), 74,* 426 (Oct. 26, 1993)

Peterson, J. and E. E. Tilgner, Description and preliminary testing of the CDSN Seismic sensor systems, USGS Open File report 83-288, 37p., 1985.

EXCITATION AND PROPAGATION OF Lg IN CENTRAL EURASIA

Lianli Cong, Jiakang Xie and B.J. Mitchell
Department of Earth and Atmospheric Sciences, St. Louis University
3507 Laclede Ave., St. Louis, MO 63103

Abstract

Lg spectra from 20 underground nuclear explosions and 52 shallow earthquakes in central Eurasia have been collected at 21 broad band IRIS, CDSN and KNET stations. Using the non-linear method of Xie (1993), we simultaneously invert for Lg source spectral parameters and path-variable Lg Q_0 and η values (Lg Q at 1 Hz and its power-law frequency dependence, respectively). The inversions yield Lg seismic moments (M_0), corner frequencies (f_c) for the events, as well as Lg Q_0 and η values for numerous paths in central Eurasia.

Grossly speaking, Lg Q and Lg coda Q are similar in central Eurasia, although minor discrepancies exist between (a) Lg η and Lg coda η at large (> about 2700 km) distances, and (b) Lg Q_0 and Lg coda Q_0 values in a sub-region northeast of the Lop Nor test site. For both explosions and earthquakes Lg M_0 values correlate linearly with the ISC M_b values, both having slopes slightly greater than 1.0. For the same Lg M_0 values, M_b values from explosions tend to be larger than those from earthquakes. Lg M_0 tend to scale with $f_c^{-\alpha}$, with α closer to 4 than to 3. Regression analysis over M_0 and f_c values suggest that for the same M_0 values, explosions tend to have higher f_c values. This may form a basis of an explosion discriminant, but the fact the there is a slight overlap among M_0 and f_c values from explosions and those from earthquakes suggests that the use of this discriminant should be used with caution.

Applications of the methodology used in this study to other regional phases, such as Pn, may contribute to our understanding of regional wave excitation/propagation by various types of seismic source, and to the evaluation of various discriminants using regional waves.

Key words: Lg, Q, source spectral parameters, explosion discrimination.

Research Accomplished

Over the past two years we have collected Lg spectra from 20 underground nuclear explosions in the Balapan and Lop Nor test sites, recorded by 17 broad-band IRIS, CDSN and KNET stations (Figures 1, 4, also *cf.* Xie *et al.*, 1995). We have also collected Lg spectra from 52 shallow earthquakes (5-33 km) that occurred in the areas of the central Asian Republics of the F.S.U. and southern Xinjiang, China, recorded by 11 broad band stations (Figures 1, 5). These spectra are used to invert for Lg source spectral parameters (M_0, f_c) and path variable Lg Q_0 and η values (Lg Q at 1 Hz and its power-law frequency dependence, respectively), with the non-linear inverse method of Xie (1993). Figures 2 and 3 show examples of the fit of the optimal source/path parameters to the observed Lg spectra, where the inverted Q_0, η values for multiple stations that recorded an explosion (Figure 2) and earthquake (Figure 3) are used to remove path effects, resulting in reduced Lg spectra at the source. It appears that the fit for the explosion event (Figure 2) is better than for the earthquake event (Figure 3), particularly for the station averages (lower right panels). The main findings of this study are:

(1) Importance of the number of stations recording Lg: During the spectral inversions using Lg, we found that when the number of stations recording the same event is less than 3, the available Lg spectra is typically not sufficient for a simultaneous inversion of source M_0, f_c and path Q_0, η values. Accordingly, *a priori* information on the Q_0, η values obtained in previous simultaneous inversions must be used. It also appears that the M_0 and f_c values obtained with Lg spectra from only one or two stations are less reliable than those obtained with Lg spectra from more stations. Much of the scatter in Figure 9 is due to the M_0, f_c values obtained using only 1 or 2 stations.

(2) Effects of radiation pattern by earthquake sources: For paths connecting the Lop Nor test site and stations AAK, GAR and ARU, there are two sets of Lg Q_0 values obtained, one using earthquake data and the other using explosion data (Figures 5 an 6). These Lg Q_0 values are very similar, suggesting that the radiation patterns for the earthquake sources are insignificant.

(3) Comparison between Lg Q_0 and and Lg coda Q_0: For most of the paths used in this study, the Lg Q_0 obtained in this study are highly consistent with the Lg coda Q_0 map of Xie & Mitchell (1991) and Pan *et al.* (1992) (see Figures 4, 5, 6). For three paths that run from the earthquake in Xinjiang northeastward to stations MDJ, HIA and TLY (Figure 6(a)), the Lg Q_0 values are somewhat higher than the Lg coda Q_0 values (Figure 4). The most likely cause of this discrepancy is that the direct Lg phase and Lg coda are affected by 3D structural complexities in different manners in the area, causing the two Q_0 values differ.

(4) *Comparison between Lg η and and Lg coda η:* When the epicentral distance (Δ) is less than about 2700 km, the frequency dependence of Lg Q, η, obtained in this study agrees (within an uncertainty level of about 0.1 to 0.2) with the Lg coda η. At larger distances ($\Delta > 2700$ km), the η values obtained in this study tend to be low (often down to ~ 0.0). This discrepancy is most likely due to imprecisely estimated Lg η in this study due to narrower frequency bands, or effects of the earth's curvature at large Δ.

(5) *Scaling of Lg M_0 with ISC M_b:* For both explosions and earthquakes, the Lg M_0 values correlate linearly with ISC M_b (Figure 7). Linear regression over the points in Figure 7 yield

$$\log M_0 = 1.19(\pm 0.11) M_b + 8.85(\pm 0.64) \qquad (1)$$

for explosions, and

$$\log M_0 = 1.04(\pm 0.09) M_b + 10.66(\pm 0.51) \qquad (2)$$

for earthquakes. These are straight lines that parallel each other (Figure 7), but are offset such that for the same M_0 values, M_b values tend to be systematically higher for explosions.

(6) *Scaling of Lg M_0 with f_c for explosions:* Figure 8 shows Lg M_0 versus f_c obtained in this study obtained for the 20 underground nuclear explosions studied, with the explosion source model [*i.e.*, the model with an overshoot effect; see equation (2) of Sereno *et al.* (1988) or equation (10) of Xie, (1993)]. Lg M_0 values correlate linearly with ISC M_b and a linear regression yields

$$\log M_0 = 15.12(\pm 0.22) - 3.98(\pm 0.43) \log f_c \quad . \qquad (3)$$

This suggests that Lg M_0 scales with f_c^{-4}, instead of with f_c^{-3} (*i.e.*, constant stress drop scaling).

(7) *Scaling of Lg M_0 with f_c for earthquakes:* Figure 9 shows Lg M_0 versus f_c obtained for the 53 earthquakes obtained in this study, using an earthquake source model (*i.e.*, the ω^2 model without overshoot). A linear regression over the points in Figure 9 yields

$$\log M_0 = 14.85(\pm 0.29) - 3.56(\pm 0.29) \log f_c \quad . \qquad (4)$$

(8) *Difference between the M_0, f_c scaling for earthquakes and explosions:* Equation (3) is obtained for Lg M_0 and f_c values of explosion sources, obtained in inversions using the *explosion* source model. On the other hand, equation (4) is obtained for Lg M_0 and f_c values of earthquakes using the *earthquake* source model. For the purpose of discriminating explosions from earthquakes, it is desirable to obtain M_0 and f_c for explosions using the earthquake source model, thus simulating a situation where we do not know that the explosions under study are explosions. The resulting Lg M_0 and f_c values for the explosions, obtained using the earthquake source model, are plotted in Figure 9, and a linear regression over these values yields

$$\log M_0 = 15.69(\pm 0.23) - 3.83(\pm 0.45) \log f_c \quad . \quad (5)$$

The straight lines represented by equations (4) and (5) are subparallel, both being closer to $M_0 \sim f_c^{-4}$ scaling than to $M_0 \sim f_c^{-3}$ scaling. However, the two lines are offset and for a given M_0, the explosions tend to have higher f_c values. This suggests greater high-frequency content of Lg from explosions, as compared to that from earthquakes of similar moments. The M_0 and f_c values may therefore be used to discriminate explosions from earthquakes. However, Figure 9 shows that there is some slight overlap of the M_0 and f_c values for the two groups of events at smaller moments, indicating that this discriminant should be used with caution.

Conclusions and Recommendations

Grossly speaking, Lg Q and Lg coda Q are similar in central Eurasia, although minor discrepancies exist between (a) Lg η and Lg coda η at large (> about 2700 km) distances, and (b) Lg Q_0 and Lg coda Q_0 values in a sub-region northeast of the Lop Nor test site. For both earthquake and explosion sources, Lg M_0 values correlate linearly with the ISC M_b values, both having slopes that are slightly greater than 1.0. Lg M_0 tends to scale with $f_c^{-\alpha}$, with α being closer to 4 than to 3. Regression analysis over M_0 and f_c values suggests that for the same M_0 values, explosions tend to have higher f_c values. This may form a basis of a explosion discriminant, but the fact the there is a slight overlap among M_0 and f_c values from explosions and those from earthquakes suggests that the use of this discriminant should be used with caution.

Future research is recommended in the following areas:

(1) Establish more precise, perhaps distance and frequency dependent geometrical spreading for the Lg phase and other regional phases based on synthetics using realistic velocity structures.

(2) Conduct experiments to see if the ω^2 source model needs to be modified for Lg excitation by earthquake sources.

(3) Apply the same methodology in this study to the spectral characteristics of excitation and propagation of other regional phases, particularly the Pn phase, and systematically evaluate the Pn/Lg spectral ratio discriminant. Also, test to see if the Pn/Lg discriminant is more reliable than the Lg discriminant.

References

Pan, Y., Mitchell, B.J. & Xie, J., 1992. Lg coda Q across Northern Eurasia, paper presented at the 14th annual PL/DARPA research symposium, September 1992. PL-TR-92-2210, ADA256711

Sereno, T.J., S.R. Bratt and T.C. Bache, 1988. Simultaneous inversion of regional wave

spectra for attenuation and seismic moment in Scandinavia, *J. Geophys. Res.*, **93**, 2019-2036.

Xie, J. and B.J. Mitchell B.J. 1991. Lg coda Q across Eurasia, in *Yield and discrimination studies in stable continental regions*, B.J. Mitchell (ed). Report PL-TR-91-2286, Phillips Laboratory, Hanscom Air Force Base, MA, 77-91. ADA251590

Xie, J. 1993. Simultaneous inversion of source spectra and path Q using Lg with applications to three Semipalatisk explosions, *Bull. Seism. Soc. Am.*, **83**, 1547-1562.

Xie, J., Cong, L., Ni, J. and B.J. Mitchell, 1994. Source scaling and depth determination from Lg spectra, *Proc. 16th Annual Seismic Research Symposium*, 7-9 September 1994, Thornwood Conference Center, New York, Edited by Phillips Lab, Hanscom AFB and Air Force Office of Scientific Research, Bolling AFB, 386-392. PL-TR-94-2217, ADA284667

Xie, J., Cong, L. and B.J. Mitchell, 1995. Spectral characteristics of the excitation and propagation of Lg from underground nuclear explosions in Central Asia, *J. Geophys. Res.*, in press.
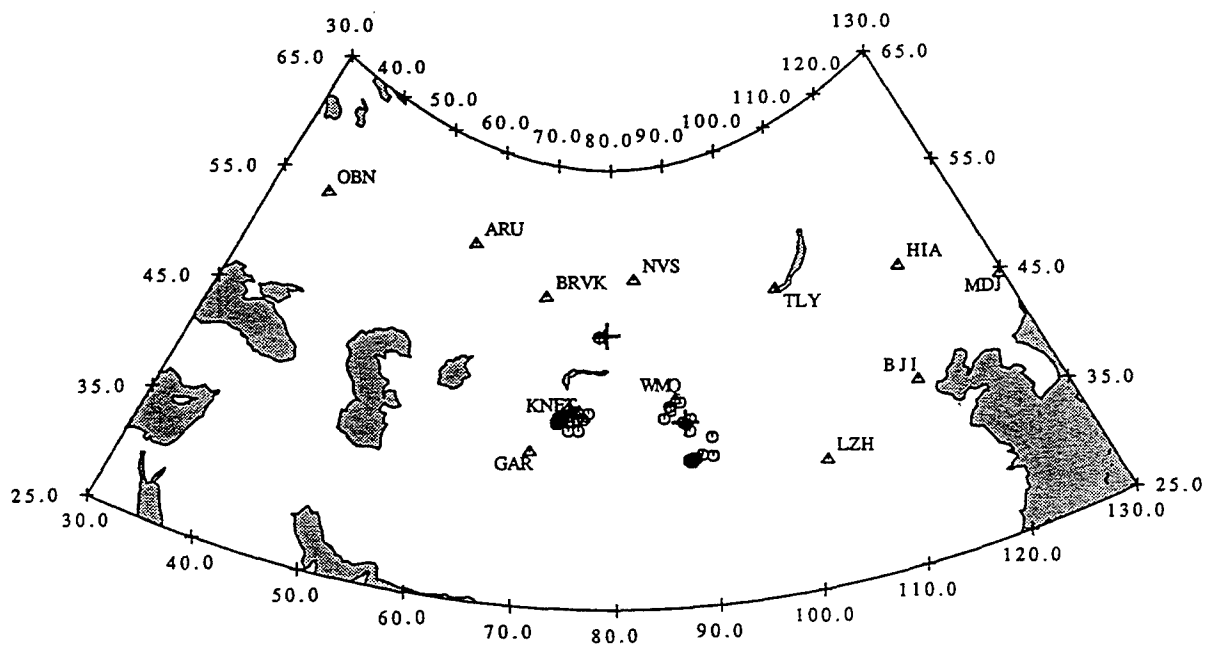
Fig. 1. Locations of the 20 underground nuclear explosions (crosses), 52 earthquakes (circles) and 21 seismic stations (triangles) used in this study. The numbers of stations providing Lg records are 17 for the explosions, and 11 for the earthquakes.
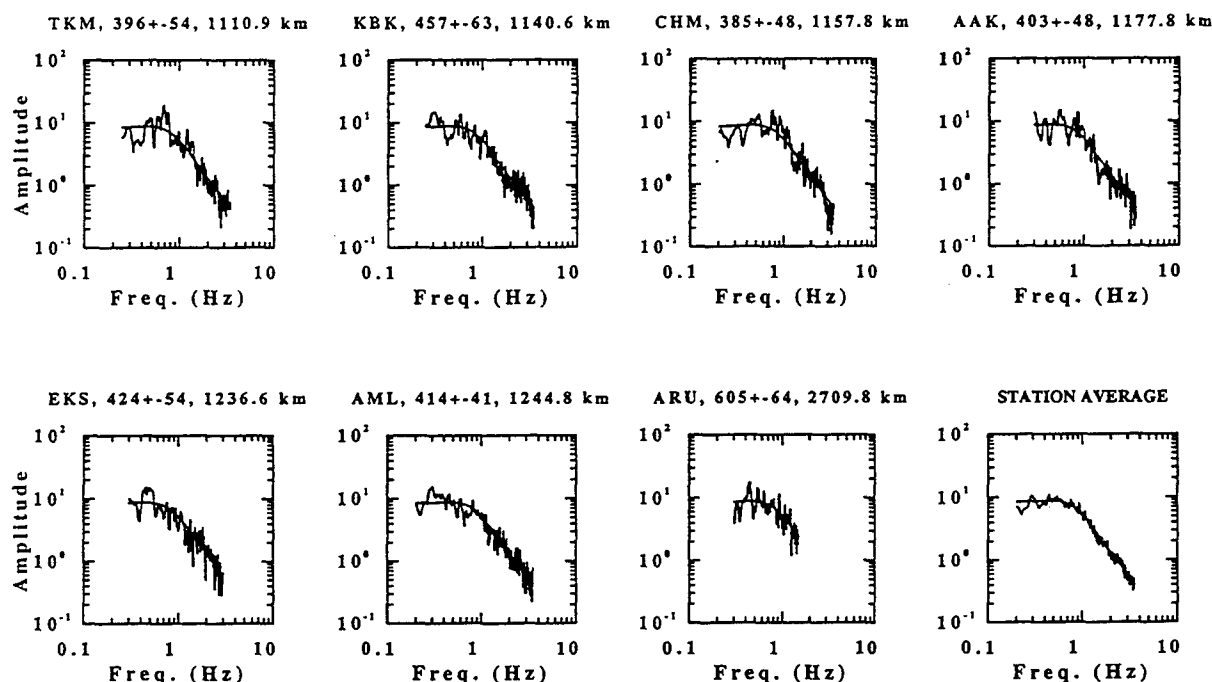
Fig. 2. Synthetic Lg source spectra for seven KNET and IRIS stations recording the October 5, 1993, Lop Nor explosion, versus the observed Lg spectra that are reduced to source by removing path effects. The lower right panel is the average for all of the seven stations. The synthetic spectra are calculated using optimal source spectral parameters ($M_0 = 8.3\times10^{15}$ Nm, f_c=0.68 Hz) obtained in the inversion. Path Q_0 values obtained in the inversion are written on the top of the panels, together with the epicentral distances.
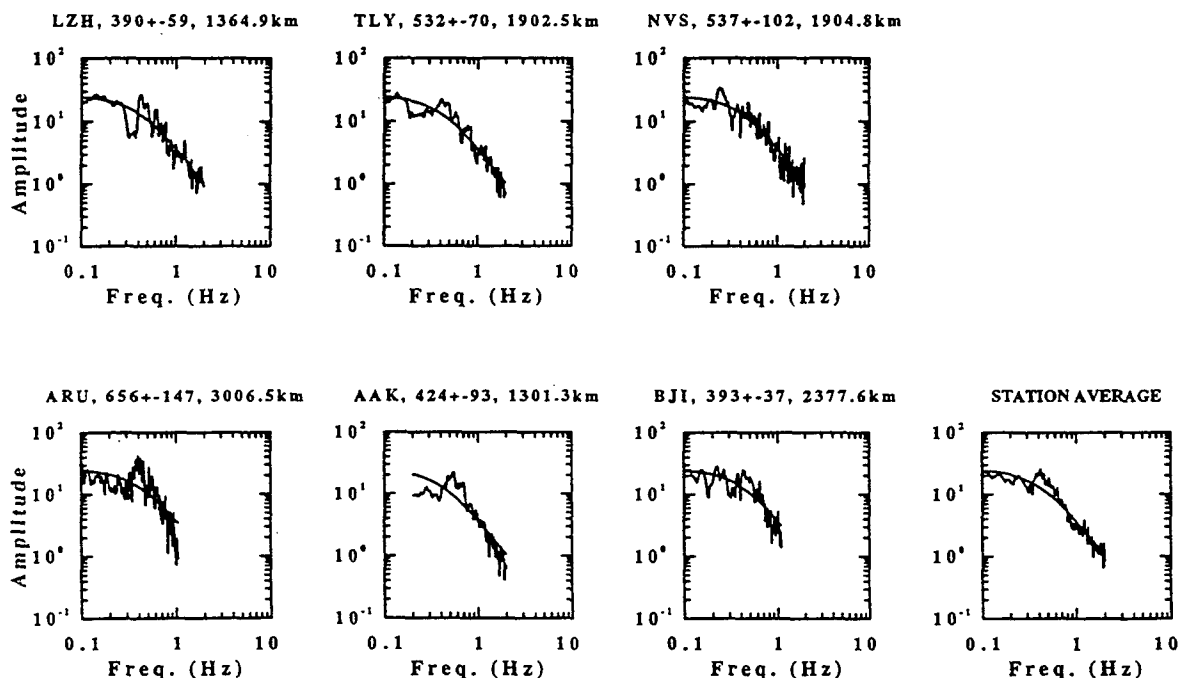
Fig. 3. Synthetic Lg source spectra for six IRIS and CDSN stations recording the October 2, 1993, southern Xinjiang earthquake (Mb = 5.6), versus the observed. The synthetic spectra are calculated using optimal source spectral parameters (M_0=2.6$\times 10^{16}$ Nm, f_c=0.41 Hz) obtained in the inversion.
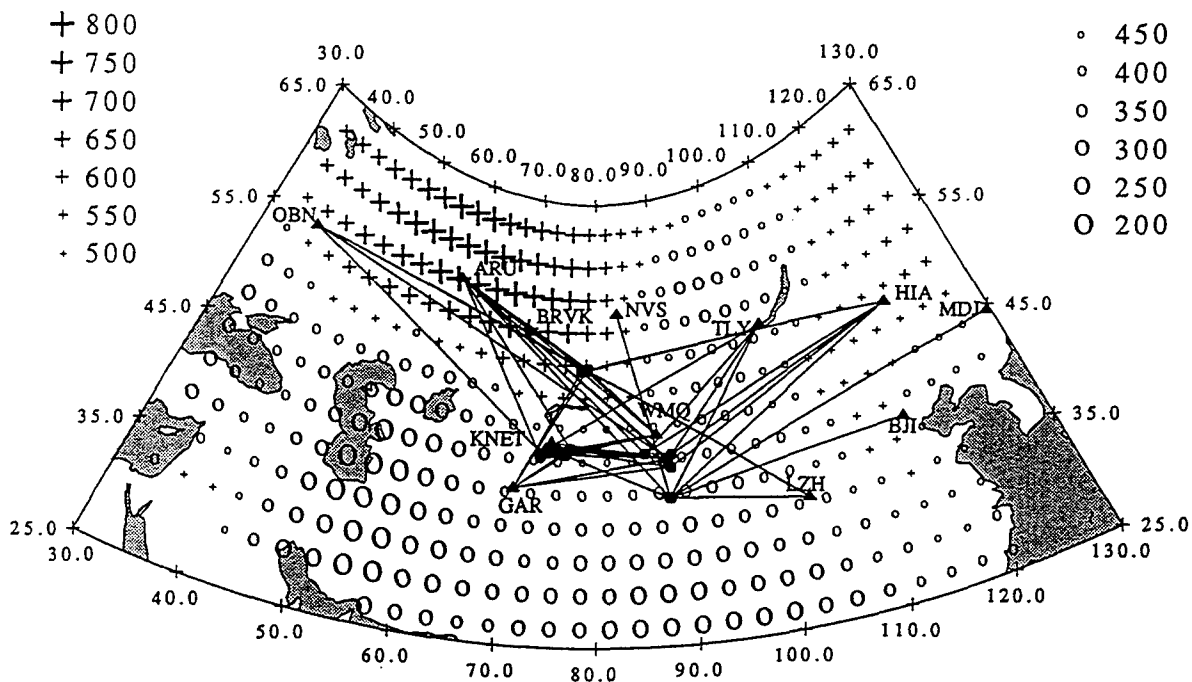
Fig. 4. The Lg paths for which Q values are measured in this study, plotted with the Lg coda Q_0 values from the tomographic inversion by Xie and Mitchell (1991). Solid dots and triangles are sources and stations, respectively.
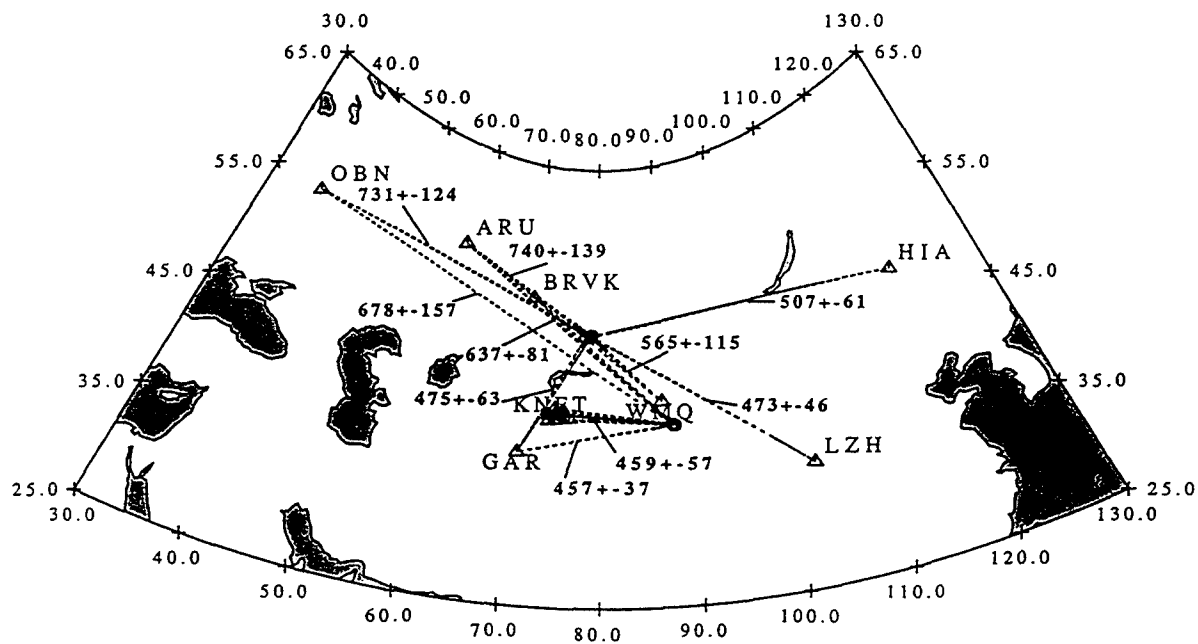
Fig. 5 Lg Q_0 values obtained for the great circle paths from the Lop Nor and Balapan test sites to the 17 IRIS, CDSN and KNET stations. Water-covered areas are shaded.
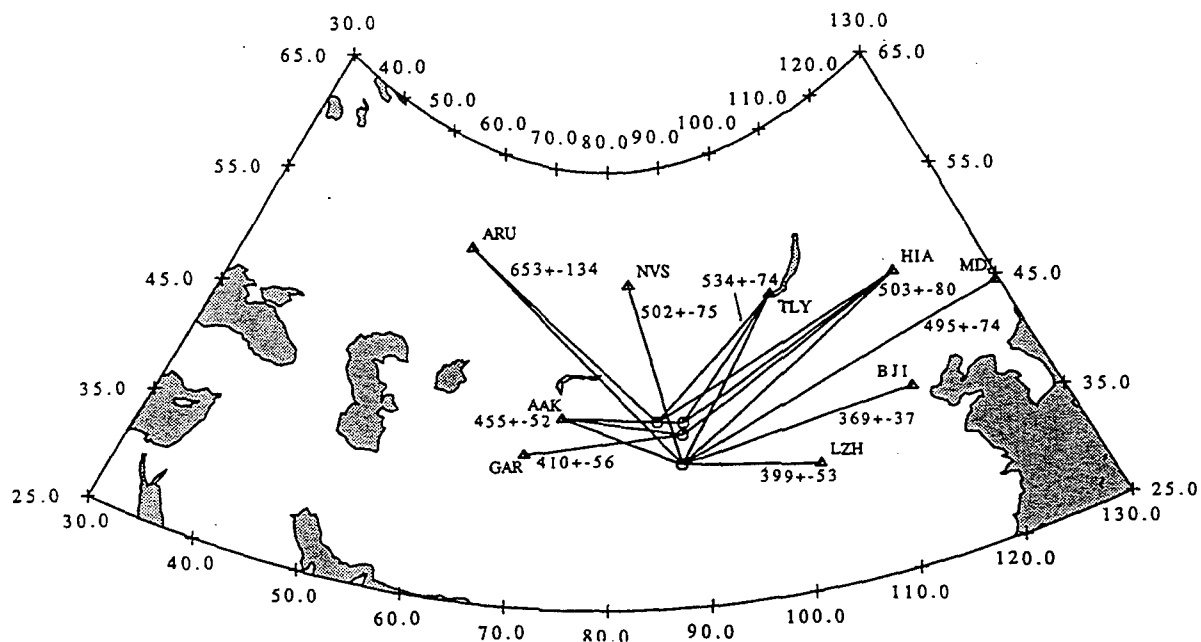
Fig. 6(a) Lg Q_0 values obtained for the great circle paths from the Xinjiang earthquakes to IRIS and CDSN stations.
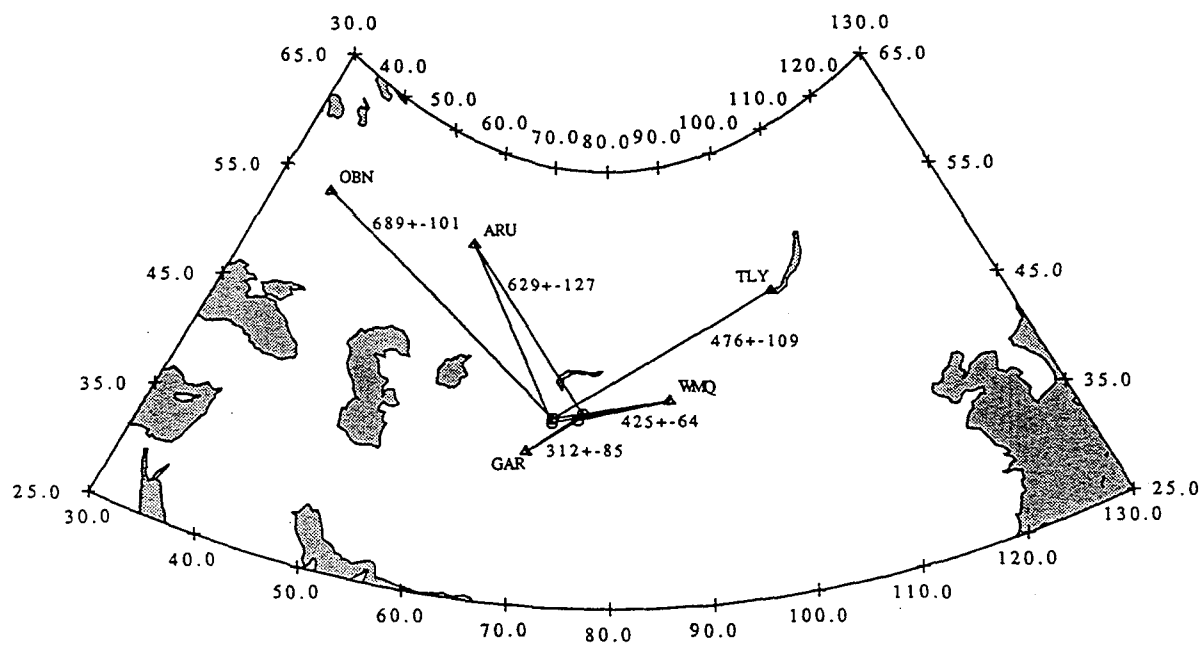
Fig. 6(b) Lg Q_0 values obtained for the great circle paths from earthquakes in the central Asian Republics of the F.S.U. to IRIS and CDSN stations.

179

mb versus Mo
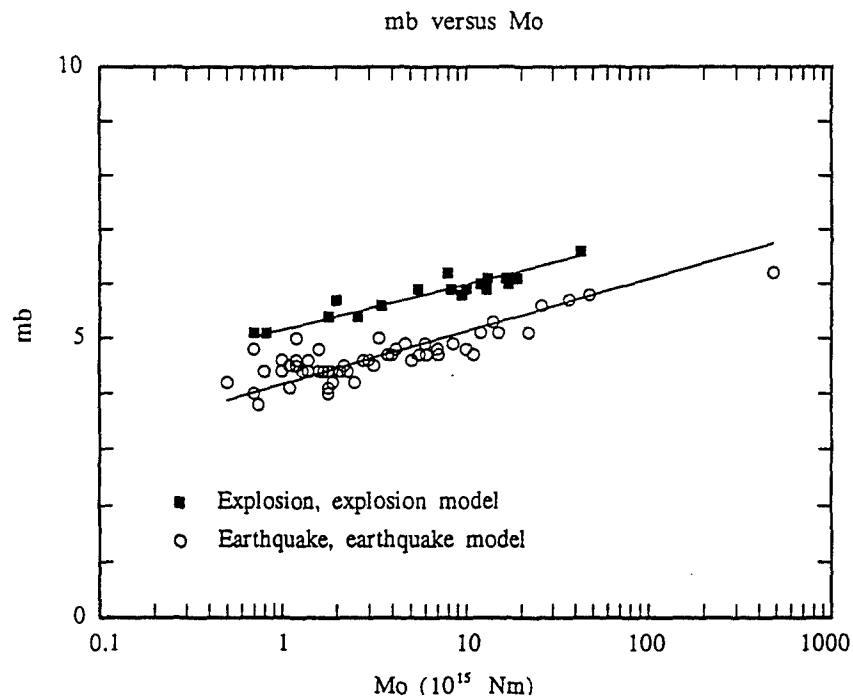
Fig. 7. M_b values versus logarithm of M_0 values (in 10^{15} Nm) obtained for explosions and earthquakes. Straight lines represent the linear regression fitting.

fc versus Mo (Explosion Model)
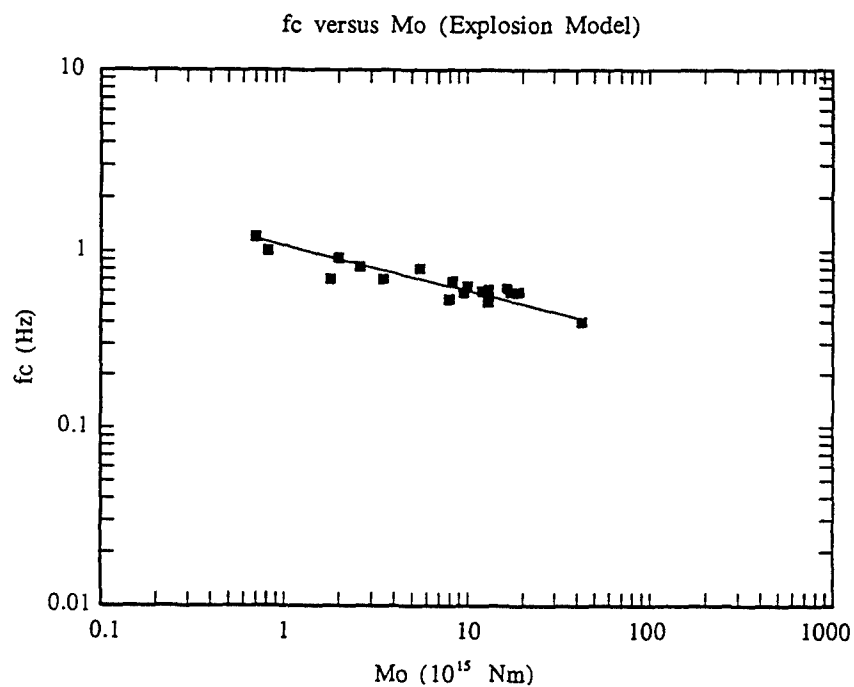
Fig. 8. Logarithm of M_0 (in 10^{15} Nm) versus logarithm of f_c values for the explosions studied, obtained by inverting the Lg spectra using the explosion source model. Straight line represents the linear regression fitting.

180
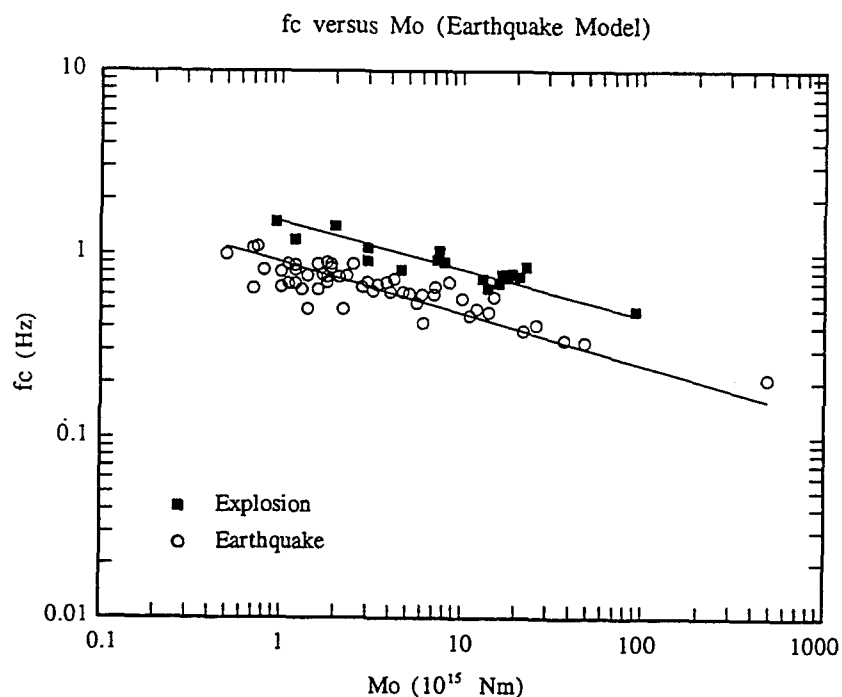
Fig. 9. Logarithm of M_0 (in 10^{15} Nm) versus logarithm of f_c values for the earthquakes and explosions studied, both obtained by inverting the Lg spectra using the earthquake source model. Straight lines represent the linear regression fitting.

INVESTIGATION OF ATTENUATION AND BLOCKAGE OF LG IN THE VICINITY OF THE KYRGYZ ARRAY

Vernon F. Cormier and Tom Anderson
Department of Geology and Geophysics
University of Connecticut
Storrs, CT 06269-2045

ABSTRACT:

Synthetic seismograms and ray paths obtained by 3-D dynamic ray tracing are compared with regional seismograms from the KNET array in the Republic of Kyrgyzstan, in the former Soviet Union. Variations in regional waveforms recorded by the KNET array in the Republic of Kyrgyzstan are compared with predicted variations in the paths of multiple SmS waves comprising the Lg phase using the database of Moho topography by Fielding et al. (1993). Ray diagrams predict strong regional variations Lg efficiency in Kyrgyz area. The strongest variations in observed Lg amplitudes and predicted Lg paths are associated with strong gradients in Moho topography along the Hindu Kush and Pamir mountain ranges. Lg is nearly extinguished for paths from shallow events to the southwest of the Kyrgyz array, which traverse regions of strong Moho gradient. Detailed variations of waveforms across the Kyrgyz array are consistent with Lg efficiency being proportional to the length and number of times SmS ray paths traverse regions of strong Moho gradient. Synthetic seismograms predict that crustal thickness variations will either compress or stretch the Lg coda compared to that predicted in a crust of uniform thickness.

OBJECTIVE:

The crust and uppermost mantle are the most strongly laterally varying and heterogeneous regions of the Earth. The seismic phases Pn, Pg, Sn, Lg, and Rg, which are important to nuclear verification of small sources, are all strongly affected by this heterogeneity, complicating the transportability of methods to detect, discriminate and yield estimate in different regions. There is a need to predict the effects of heterogeneous crustal structure on regional phase propagation using geological and geophysical information for regions in which little or no seismic recording has occurred. The computational expense of a numerical solution of the wave equation in an arbitrarily heterogeneous model have thus far limited such predictions to primarily 2-D structure and low frequency bands. Ray based techniques of forward modeling, however, are sufficiently fast to allow practical predictions of efficiency of the propagation of regional phases in detailed 3-D structures. The effects of scattering by statistically distributed heterogeneity can also be incorporated in ray methods by single scattering theory. The objective of this project is to develop and apply the methods of dynamic ray tracing and superposition of Gaussian beams to forward model regional seismic phases in three-dimensionally varying models of the Earth's crust. Goals include (a) an understanding of what crustal structures are most important in determining the efficiency of regional phase propagation, (b) determining what type of non-seismic data (topography, surficially mapped geology, gravity, magnetics) are most useful in inferring 3-D crustal structure, and (c) testing the success of a fast ray-based modeling procedure in modeling detailed features of regional waveform

RESEARCH ACCOMPLISHED:

Crustal Models and Dynamic Ray Tracing

Regional seismograms are synthesized by summing dynamically traced rays and/or superposing Gaussian beams (e.g., Cerveny, 1985) in models of the crust for the vicinity of the Kyrgyz array. Moho turning points of the rays comprising the Lg and Pg phase are projected in a map view to illustrate predicted efficiency of propagation. To simplify the description of rays and reduce model storage, the model parameters are assumed to be continuous functions of space. P and S velocity and density are parameterized by functions:

$$v(x,y,z) = a + b\tanh(z - h_1(x,y) / s_1) + c\tanh(z - h_2(x,y) / s_2)$$

where $h_1(x,y)$ and $h_2(x,y)$ specify the depth of the sedimentary basin/basement contact and depth of the Moho, respectively. The functions h_1 and h_2 are given as continuous functions of horizontal coordinates by interpolating digitized surfaces by splines under tension. Additional tanh functions can be added, as needed, to model more interfaces. In the vicinity of the Kyrgyz array, h_1 and h_2 are taken from databases assembled by Fielding et al. (1993). A plot of ray trajectories useful in the interpretation of structural effects on Lg. A useful plot is a map view of SmS turning points and surface bounce points (Bostock and Kennett, 1991). Several of these types of plots are discussed in the interpretation of Kyrgyz data.

Data Interpretation

Regional data shown were recorded in Kyrgyzstan by a 10 station network that was installed in the summer of 1991 (JSPC, 1993). Stations EKS2 and TKM are located on piers in underground vaults. Station AAK is located approximately 40 m inside a tunnel constructed specifically for geophysical observations. Station CHM s located in a small building at the bottom of a hill.

Events were selected based on the following criteria: shallow depth and published JSPC location. (JSPC locations are more precise than the PDE locations for the events in this region.) Events are selected in the distance range 300 to 1200 km. in epicentral distance. From the events that met these criteria, four were chosen based on the quality and azimuthal paths that traversed regions of strong Moho topography in the Fielding database (figures 1b-c).

Data are band pass filtered from .5 to 5 Hz. using a butterworth filter with 4 poles. The data are displayed in record section plots in SAC.

Event 3. 25 Mar 92. This event traverses a region of Moho east of the array that is relatively flat and 47 km deep (figures1a-c). The record sections (figure 2) show similarities in both Lg coda length, shape, and amplitude ratio to Pg. The similarities in Lg coda are consistent with the expected effect of the flat Moho between the source and array. Dynamic ray tracing shows that the rays passing through this region are not greatly affected by the slight changes in Moho topography. The ray tracing results (figures 3 ,4) are shown in map view of SmS bounce points and 2-D cross sections of ray paths projected onto vertical planes through the back azimuths to stations. Figure 3 shows relatively coherent wavefronts of bounce points reaching out to the Kyrgyz array. The rays calculated for this event shown in figure 4 illustrate that in a region of nearly flat Moho, the rays remain coherent over regional distances, in this case out to approximately 600 km. At longer range, figure 4 and subsequent ray plots show that many rays experience azimuthal bending.

Event 1. 6 May 92. This event was chosen for the ray paths that pass through a region north of the Pamir Mountains where the depth of the Moho increases to 70 km with steep gradients. The array had a back azimuthal range (baz) of 198.02-209.86 degrees and ranged in distance from 527.91-611.25 km. The effects of the steep Moho gradients are seen in the Lg which differs greatly across the array (figure 5). Station TKM (baz 209.86 dist 599 km) shows almost no sign of Lg coda, station CHM (baz 204.86 dist. 592 km) has very little Lg, while AAK(baz 204.47 dist 546km) has noticeable Lg and station EKS2 (baz 198.02; dist. 527km) has significant Lg. Ray tracing shows similarly strong variations for rays passing this region. The map view (figure 6) of ray bounce points for this source receiver scenario shows that the wave front is distorted by the second bounce and a 2-D caustic develops which transects the array. This correlates well with the differences seen in Lg from one side of the array to the other. Two-dimensional vertical cross sections of rays for this event (figure 7) illustrate the same degree of variation. The rays diverge after the first bounce and the 'range of coherency' can be said to be less than 100 km.

Event 2. 27 Jun 92. The array had a back azimuthal range of 139.17-146.57 degrees and ranged in distance from 987-1047 km. This event originated over the deep Moho b(70 km) associated with the Hindu Kush region. The record section plot (figure 8) shows the variation across the array in Lg coda shape and amplitude ratio to Pg consistent with the changes in Moho topography. The Lg coda at station EKS2 has a different shape and a much lower Lg/Pg ratio than the rest of the array. The ray tracing depicts similar effects

from the Moho gradients in this region. The map view of SmS bounce points (figure9) shows the distortion of the wavefront as it crosses the Moho and a 2-d caustic aligned over station EKS2. The ray tracing (figure 10) shows rays shot at azimuths to the stations EKS2 and TKM. The slight difference in azimuth yields totally different ray paths through this region.

RECOMMENDATIONS AND FUTURE PLANS:

Ray synthetics in simple crustal models do not have the complexity exhibited in recorded Lg coda. Realistic complexity can be introduced by fine plane layering in 1-D structure. It would be a mistake, however, to attribute the observed complexity to 1-D structure even if good matches between observed and synthetic waveforms can be obtained. Array analysis of regional phases have made it clear that the coda of regional phases contains scattered arrivals, including energy arriving off-azimuth.

Up to frequencies as high as 5 Hz, the details of local S coda can be well explained by first order scattering by heterogeneities distributed within the crust and uppermost mantle. In the poster accompaning this paper, the results of experiments in modeling the realistic complexity of Lg coda are shown using a first-order Born approximation. Experiments are shown using single scattering incorporated in a superposition of locked modes. Future experiments will include single scattering in the ray approached described in this paper. A recommended approach to modeling the effects of 3-D structure on regional seismograms would be a ray approach to include the effects of large scale deterministic structures, such as Moho topography having scale lengths greater than 10 km, coupled with single scattering theory applied to small scale statistical structure.

CONCLUSIONS AND RECOMMENDATIONS:

Synthetics and ray diagrams predict the strong regional variations in Lg efficiency seen in data collected at the Kyrgyz array. The plots of SmS turning points for the events in this study strongly suggests that a strong transition Lg amplitudes occurs for paths traversing regions of strong Moho gradient along the Hindu Kush and Pamir mountains. A common effect of crustal thickness variation is either compression or stretching of the Lg coda compared to that predicted in a crust of uniform thickness. It may be possible to incorporate this effect in the refinement of regional discriminants.

REFERENCES:

Bostock, M.G., and B.L.N. Kennett, The effect of 3-dimensional structure on Lg propagation patterns, *Geophys. J. Int.*, 355-365, 1991.

Cerveny, V., The application of ray tracing to the propagation of shear waves in complex media, in *Seismic Exploration* pp. 1-124, Treitel and Helbig, Vol. on Seismic Shear Waves, G. Dohr, ed., Geophysical Press, 1985.

Fielding, E., M. Barazangi, and B. Isacks, A network-accessible geological and geophysical database for Eurasia, North Africa, and the Middle East, *Proceedings 15th Annual Seismic Research Symposium*, AFOSR/DARPA, PL-TR-93-2160, ADA-271458, 1993

Joint Seismic Program Center, Kyrgyz Network Information Product, Technical Reference Manual, Version 1.0, 1993.

Figure 1. (a) Top left: Kyrgyz array and events on a contour map of Moho topography. (b) Top right: Kyrgyz seismic network (JSPC KNET technical reference manual). (c) Bottom: contour map of Moho topography with 4 events in this study.

Time (sec)   [VM OFF]

0   50   100   150

8.CHM.HHZ

550

555

Distance (km)

560

565

570

8.AAK.HHZ

60   70   80   90

50

40

30

700

600

500

400   CHM

300

200   AAK

100

0

0   100   200   300   400   500   600   700
Kilometers

Figure 2. Top left: record section of event #3, 6 May 92. Data were band passed filtered 1-5 Hz.

Figure 3. Top right: map view of bounce points from dynamic ray tracing for event #3. Wave front remains coherent for 5 turning rays in the Moho transition.

Figure 4. Bottom: rays for event #3 for a range of vertical take-off angles of 61-69 degrees for paths to stations AAK and CHM. Due to the relatively flat Moho along the ray path, the turning rays in the Moho transition remain similar in form to a horizontal range of 500-600 km.

Time (sec)   [VM OFF]

0   50   100   150

EKS2.HHZ

9.AAK.HHZ

8.CHM.HHZ

8.TKM.HHZ

8.USP.HHZ

Distance (km)

520
540
560
580
600
620

60   70   80   90

50

40

30

600
500
400
300
200
100
0

EKS

TKM

0   100   200   300   400   500   600   700
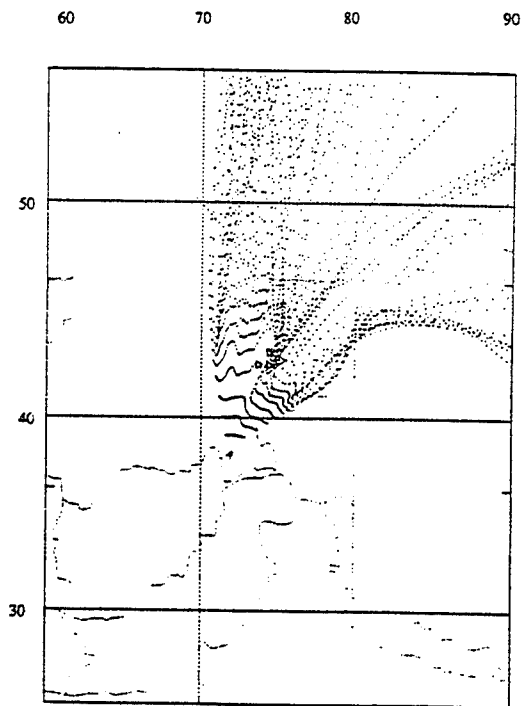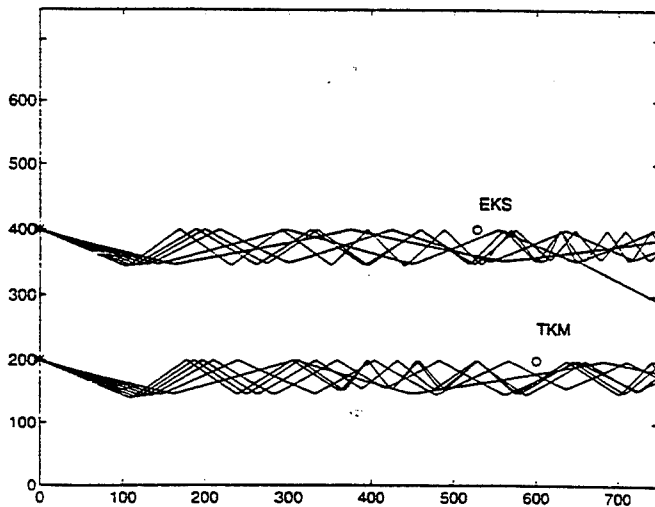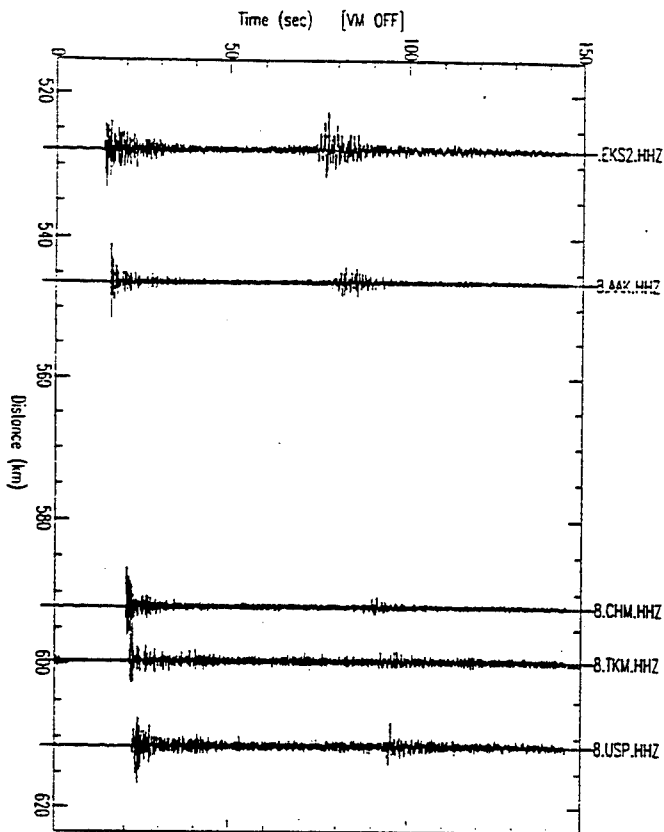
Figure 5. Top left: record section of event #1, 6 May 92. Data were band passed filtered 1-5 Hz. The signals vary greatly across the array; station TKM has little or no Lg.

Figure 6. Top right: map view of ray bounce points from dynamic ray tracing for event #1. The wavefront is strongly affected by the steep Moho topography. A casutic surface appears to pass through the middle of the array.

Figure 7. Bottom: rays for event#1 at vertical take-off angles of 63-71 degrees for paths to stations TKM and EKS2. Both paths show focusing and defocusing due to gradients in Moho topography.
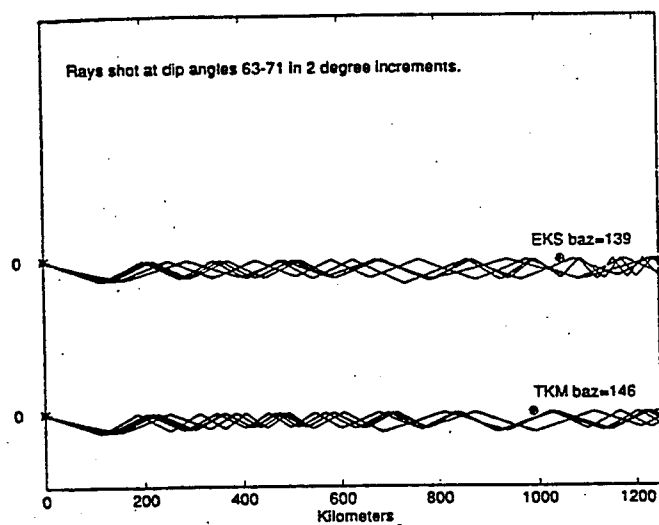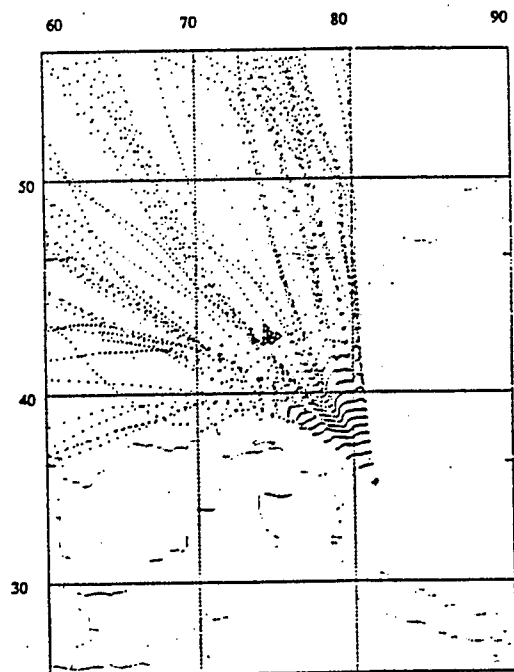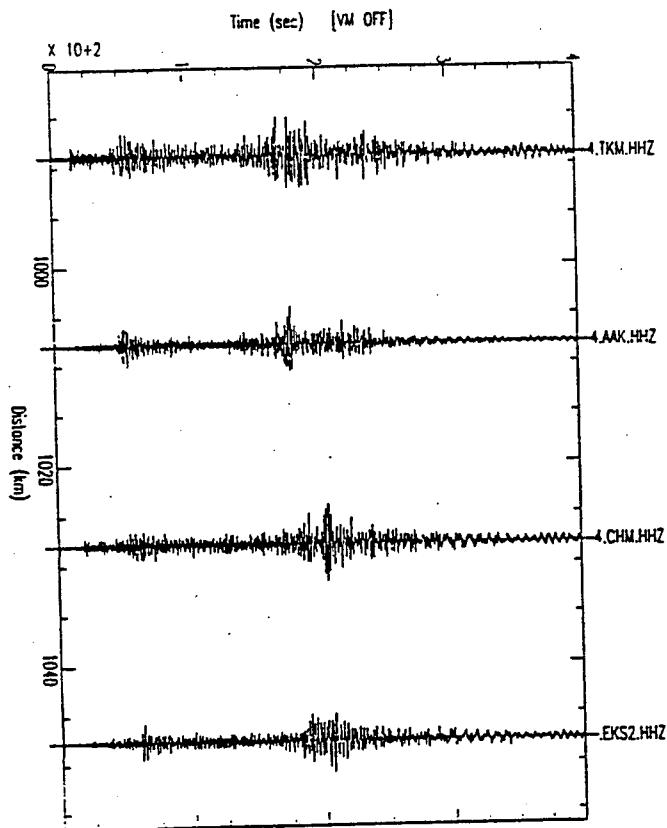
Figure 8 Top left: record section of event #2, 6 May 92. Data were band passed filtered 1-5 Hz. The Lg coda varies across the array.

Figure 9 . Top right: map view of ray bounce points from dynamic ray tracing for event #2. Rays beend sharply due to steep gradients in the Moho.

Figure 10 Bottom: rays for event #2 at vertical take-off angles of 63-71 degrees for paths to stations TKM and EKS2. Both paths show development of focusing and defocusing due to gradients in the Moho topography.

189

Seismic Propagation in the Baikal Rift Zone:
A Transition from a Craton to an Orogenic Zone

P.M. DAVIS AND S. GAO
Department of Earth and Space Sciences
University of California, Los Angeles, CA 90095
Contract No. F49620-94-1-0161
Sponsored by AFOSR

ABSTRACT

Most nuclear tests occur on continents. Continental geology can broadly be separated into stable shields and orogenic zones. Recently it has been recognized that large variations in the seismic properties of the upper mantle occur beneath the continents and these need to be taken into account when using seismograms to discriminate explosions from earthquakes, to measure seismic yield and to locate events. This report documents lateral variation in attenuation, anisotropy, and seismic velocity in a 1200x1500 km area centered on the Baikal rift zone in Siberia, based on two portable array experiments we carried out with colleagues from University of Wisconsin and the Institute of the Earth's Crust, Irkutsk in the summers of 91 and 92 as well as analog regional network data collected in 94 which we have digitized. The attenuation analysis finds that relative t^* has a 0.1 second anomaly at the rift zone and increases to the east into the Sayan-Baikal fold belt. Explosions detonated in this area would have reduced body wave amplitudes at arrays at teleseismic distances such as NORESS with a concomitant underestimate in yield. We have observed S wave splitting of on average 1 s at virtually every station, implying that significant anisotropy is present in the uppermost mantle. Though fast directions are spatially coherent in local regions there is significant variation region to region. Travel time delays shown an unusual pattern of a central peak of about 1 sec surrounded by two troughs of about 0.5 secs. We attribute the combination of low Q, anisotropy and travel time anomalies to small scale convective upwelling beneath the rift zone. Comparison with similar experiments and the global Earth models is taken as evidence that these effects are present worldwide beneath orogenic zones on the continents and should be taken into account as part of any global seismic monitoring system.

(Mantle Anomaly Attenuation Anisotropy Baikal Continental Rift Zone)

OBJECTIVE

The objective is to study the propagation of seismic waves in a region of anisotropy and lateral heterogeneity using digital data that we, along with colleagues from the University of California, Los Angeles (UCLA), University of Wisconsin (UW), and the Institute of Earth's Crust of Russian Academy of Sciences at Irkutsk (IEC) collected in the summers of 91 and 92 in south central Siberia and Mongolia, and local array network data collected in the summer of 94. Continental rifts lie in regions of some of the largest lateral heterogeneity in velocity and attenuation in the continental crust and mantle. It is therefore important for nuclear monitoring purposes to quantify how seismic waves are affected by such lateral heterogeneities so that estimates of yield and location are accurate, and source type discrimination is reliable.

RESEARCH ACCOMPLISHED

Introduction

This report is a continuation of previous ones [Davis et al., 1992; Gao et al., 1994a; 1994b; 1994c; Gao, 1995] on seismic propagation in the Baikal rift zone (BRZ) of Siberia and in northern Mongolia. During the last year we added to our data set by digitizing (Nxscan) analog seismograms from 27 stations of the Russian S. Siberian network (Figure 1), in order to extend the area over that covered by our portable array installations. Data from our experiments have been submitted to the Iris Data Management Center[Davis et al., 1992; 1993a; 1994].

The Baikal rift zone extends 1500 km along the transition from the stable Siberian platform to the Sayan-Baikal mobile fold belt (Figure 1). It is the most seismically active continental rift in the world. Lake Baikal contains 1/5 of the world's fresh water, with the maximum depth 1600 m. The maximum width of the lake is about 50 km. The sediments are up to 6 km deep [Zorin, 1971; Logatchev and Florensov, 1978].

Various lines of geophysical evidence suggest the asthenosphere upwarps beneath a broad region surrounding lake Baikal giving rise to a significant lateral heterogeneity in the upper mantle. At the lake, the crust thins. The combination of thinned lithosphere and crust, and a graben filled with a thick layer of sediments affects the propagation of seismic waves at most of the frequences of interest for nuclear monitoring. Active and ancient failed rift structures are found on every continent. It is therefore important to establish their deep structure and document its effect on seismic waves from nuclear explosions, including tests that might be carried out in a rift zone which, because of its absorptive properties, may disguise yield.

Effect of P-Wave Attenuation on Yield of a Rift Zone Explosion

We calculate relative t^* using a spectral inversion method developed by *Halderman and Davis* [1991] for P wave coda from the 1991 array [Gao et al., 1994b]. Figure 2 shows the spatial distribution of t^* across the profile W to E. A localized t^* anomaly of 0.1 seconds occurs at the lake with an increase of 0.05 seconds to the east (where t^* is the relative attenuation). The results are consistent with the pattern published by Murphy et al [1993] who find high $t^* = 0.60$ in the region about lake Baikal with an

increase of 0.05 to 0.065 to the southeast. Thus in the vicinity of the lake the total t^* reaches 0.7, i.e., among the highest values in Eurasia. We calculate that estimates of yield from a rift zone nuclear explosion based on body waves at NORESS [e.g., Ringdal 1990] would be 70% too low because of attenuation.

Interpretation of Teleseismic P-wave Travel Time Residuals

The data consist of 2128 P-wave travel times from 155 teleseismic events, corrected by subtracting theoretical arrival times [from the IASPEI 1991 Earth model, Kennett and Engdahl, 1991]. Relative residuals were formed for each event by subtracting the event's mean residual from the raw residuals and detrended to isolate velocity anomalies having wavelengths less than the array length (1260 km).

To examine the dependence of the relative travel time residuals on event location, we group the events into 26 groups by azimuth (ϕ) and epicentral distance (Δ) of the sources. This gave 517 mean travel time residuals from 26 groups which were then used in an inversion for structure.

Most of the event clusters recorded by the 1992 profile (Figures 3) display a peak in their travel time residual curves approximately in the region -30 km $< x <$ 60 km with troughs on either side. A similar structure is seen in the attenuation data (Figure 2). The peaks are interpreted to arise from upwarped low-velocity structure associated with convective upwelling in the mantle. The relatively uniform distance between the valleys, and the large shift in their location as a function of incoming azimuth are interpreted to be caused by two high velocity structures located about 200 km deep.

We used both isotropic and vertically anisotropic upper mantle models to interpret the travel time data [Gao, 1995]. The models have a curved lithosphere/asthenosphere boundary that upwarps beneath the rift and in the isotropic model downwarps on the flanks. For the isotropic model the asthenosphere upwarps from 200 km to about 45 km. The magnitudes of the downwarps are about 120 km in the west and 40 km in the east. The velocity contrast between the lithosphere and the asthenosphere is about -2.4% (Figure 4).

The anisotropic model has an asthenospheric upwarp from 232 km to about 42 km with a velocity contrast of -2.7% . At the base, the upwarp is about 260 km wide. The maximum vertical anisotropy is 2.8% (Figure 4) and decays exponentially away from the rift.

SKS Splitting Measurements and Interpretation

The ubiquity of SKS splitting [e.g., Kind et al, 1985; Silver and Chan, 1988, 1991; Silver and Kaneshima, 1993; Gao et al., 1994a; Liu et al., 1995; Gao, 1995] strongly suggests that variations in anisotropy need to be included in models of upper mantle propagation. It is generally believed that the main cause for SKS splitting in the mantle is flow-induced preferred orientation of crystallographic axes of elastically anisotropic minerals such as olivine. SKS splitting measurements are shown in Figure 5 which is divided into 4 zones A-D based on the tectonics (A: rift- shear zone, B: rift, C: craton,

D: Fold belt). The splitting ranges from 0.3 to 2.1 seconds consistent with a layer of 30 to 210 km thick characterized by 4% anisotropy.

In area A, the fast directions are scattered with an average approximately ENE-WSW. Five stations in area B (B01-02, B07, B17, and B24) near the rift axis show NE fast directions, i.e., parallel to the surface expression of the rift and the strike of the two dimensional low velocity structure. Most of the rest of the stations show fast directions perpendicular to the rift axis. The rapid change of the fast directions on station B17 and B18, which are 30 km apart, may indicate that the source of anisotropy in the area is shallow, at a maximum depth of 100 km, as revealed by the Fresnel zone forward modeling [Gao, 1995]. Any deeper the spatial variation at the surface would be more spread out.

The fast direction in area C is dominantly NW-SE which is perpendicular to the rift axis. In the northern part of area D, the fast directions are dominantly perpendicular to the rift axis, while at the transition to the fold belt in northern Mongolia, fast directions change to nearly E-W, i.e. parallel to the faulting and fold axis. The transition takes places between stations D07 and D09, over a distance of about 90 km suggesting a source for the transition in the upper few hundred km.

Mobility of olivine crystals at temperatures above 900°C is high and therefore the survival of fossil anisotropy is very unlikely at about 150 km and deeper beneath PreCambrian platforms such as the Siberian Craton [Vinnik et al., 1992]. Beneath present-day continental rifts such as the BRZ, the 900°C isotherm is thought to upwarp to a depth of about 50 km [Zorin and Osokina, 1984]. The thickness of the layer cooler than 900°C ('rigid layer') is about 50 km in the vicinity of the BRZ. Near the rift axis (in area B), the thickness of the rigid layer is too small to generate the observed splitting, if all the anisotropy is fossil anisotropy. Therefore at least part and probably most of the observed splitting must originate in the asthenosphere sustained by mantle flow. The fast direction for the southern part of the profile is roughly E-W which is consistent with the dominant direction found across the Tibetan Plateau [McNamara et al., 1994]. Both the Tibetan and the Mongolian Plateaus have been deformed by Cenozoic deformation related to the collision of India with Asia. The observed fast directions in both regions may have the same origin.

A Small-Scale Mantle Convection Model for the Baikal Rift Zone

Based on these observations a small-scale mantle convection model is constructed (Figure 6). According to the model, there is an asthenospheric upwarp in the vicinity of the BRZ. The low velocity upwarp starts approximately at the base of the lithosphere, which has a thickness of about 200 km and reaches the base of the crust. The flow induces anisotropy orienting a, b, and c axes of olivine crystals as shown in figure 6. In the vicinity of the rift zone, vertical flow dominates; In the areas away from the rift zone the dominant flow direction is horizontal and perpendicular to the rift axis. Further testing of this model is in progress.

CONCLUSIONS AND RECOMMENDATIONS

Convection in the mantle beneath continents brings hot material from depth which has the effect of lowering P and S wave velocities as well as Q, and inducing anisotropy. As a result, estimates of yield based on body waves could be as much as a factor of three too low for events detonated above such an upwelling current. Global tomography maps [Woodhouse, 1995 in Press, personal communication] indicate such low velocity regions are common beneath orogenic zones on the continents. Accurate location of nuclear events will eventually have to take both lateral heterogeneity in velocity from such thermal effects as well as effects from anisotropy induced by the flow. Seismic anisotropy can result in converted phases, and has strong effects on surface waves [e.g., Park et al., 1994]. Further work needs to be done on this unique data set, including searching for Lg blocking, characterizing effects on surface waves, S wave attenuation and travel times and receiver function analyses.

This work provides a calibration for extension to other orogenic continental regions where global models (of order 20) have insufficient resolution, but geophysical signatures such as gravity, topography, heat flow as well as tectonic history could be used to infer lateral variations in the upper mantle, thereby extending the global models. The resulting model of the continents would then serve as a basis for inverting seismograms from potential test sites for location and yield, when monitoring a CTBT.

REFERENCES

Davis, P. M., S. Gao, H. Liu, and P. D. Slack, Seismic array study of the Baikal rift zone, Siberia, in *Proceedings of the 14 Annual PL/DARPA Seismic Research Symposium, 16-18 September, 1992*, PL-TR-92-2210, editors James F. Lewkowicz and Jeanne M. McPhetres, pp. 99-110, 1992. ADA256711

Davis, P. M., S. Gao, H. Liu, and P. D. Slack, Baikal 1991 Seismic Array Project data report, *submitted to IRIS DMC and DARPA*, 1993a.

Davis, P. M., P. Slack, H.-A. Dahlheim, W. V. Green, R. P. Meyer, U. Achauer, A. Glahn, and M. Granet, Teleseismic Tomography of Continental Rift Zones, in H. M. Iyer and H. Hirata (editors) *Seismic Tomography: Theory and Practice*, pp. 397-439, Chapman Hall, 1993b.

Davis, P. M., S. Gao, H. Liu, P. D. Slack, M. Benthien, and D. Daniels, Baikal 1992 Seismic Array Project data report, *submitted to IRIS DMC and DARPA*,1994.

Gao, S., P. M. Davis, H. Liu, P. D. Slack, Yu. A. Zorin, V. V. Mordvinova, V. M. Kozhevnikov, and R. P. Meyer, Seismic Anisotropy and Mantle Flow beneath the Baikal Rift Zone, *Nature, 371*, 149-151, 1994a.

Gao, S., P. M. Davis, H. Liu, P. Slack, Y. A. Zorin, N. A. Logatchev, M. Kogan, P. Burkholder, and R. P. Meyer, Asymmetric upwarp of the Asthenosphere beneath the Baikal Rift zone, Siberia, *J. Geophys. Res., 99*, 15,319-15,330, 1994b.

Gao, S., P.M. Davis, H. Liu, P.D. Slack, Yu.A. Zorin, N.A. Logatchev, M.G. Kogan, P.D. Burkholder, and R.P. Meyer, Preliminary results of teleseismic studies of

the mantle of the Baikal rift, (in Russian), *Fizika Zemli (Physics of the Earth)*, *N7-8*, 113-122, Moscow, 1994c.

Gao, S., *Seismic Evidence for Small Scale Mantle Convection under the Baikal Rift Zone, Siberia*, PhD thesis, University of California, Los Angeles, 1995.

Halderman, T. P., and P. M. Davis, Q_p beneath the Rio Grande and east African rift zones, *J. Geophys. Res., 96,* 10,113-10,128, 1991.

Kennett, B. L. N., and E. R. Engdahl, Travel times for global earthquake location and phase identification, *Geophys. J. Int., 105,* 429-465, 1991.

Kind, R., G. L. Kosarev, L. I. Makeyeva, and L. P. Vinnik, Observations of laterally inhomogeneous anisotropy in the continental lithosphere, *Nature, 318,* 358-361, 1985.

Liu, H., P. M. Davis, and S. Gao, SKS splitting beneath southern California, *Geophys. Res. Lett. 22,* 767-770, 1995.

Logatchev, N. A., and N. A. Florensov, The Baikal system of rift valleys, *Tectonophysics, 45,* 1-13, 1978.

McNamara, D. E., T. J. Owens, P. G. Silver, and F. T. Wu, Shear wave anisotropy beneath the Tibetan Plateau, *J. Geophys. Res., 99,* 13,655-13,665, 1994.

Murphy, J.R., M. E. Marshall, and B. W. Barker, Application of network-averaged teleseismic P wave spectra to seismic yield estimation of Soviet PNE explosions, *Proceedings of the 16 Annual PL/AFOSR Seismic Research Symposium, 7-9 September, 1993,* PL-TR-93-2160, John Ciper, James Lewkowicz, and Jeanne McPhetres, pp. 284-290, 1993. ADA271458

Park, J., Yu, Y., Su, L., Lilly, J., and Fischer, R., The effects of anisotropy on regional seismic wave propagation, in *Proceedings of the 16 Annual PL/AFOSR Seismic Research Symposium, 7-9 September, 1994,* PL-TR-94-2217, editors John Ciper, James Lewkowicz, and Jeanne McPhetres, pp. 284-290, 1994. ADA284667

Ringdal, F., Teleseismic event detection using the NORESS array, with special reference to low-yield semipalatinsk explosions, *Bull. Seismo. Soc. Ame., 80,* 2127-2142, 1990.

Silver, P. G., and W. W. Chan, Implications for continental structure and evolution from seismic anisotropy, *Nature, 335,* 34-39, 1988.

Silver, P. G., and W. W. Chan, Shear wave splitting and subcontinental mantle deformation, *J. Geophys. Res. 96,* 16,429-16,454, 1991.

Zorin, Yu. A., 1971, *Recent structure and isostasy of the Baikal rift zone and adjacent areas*, Moscow, 168pp. (in Russian), 1971.

195

Figure 2: Spatial distribution of t* along the 1991 profile estimated from 13 events. Note the greater attenuation beneath Lake Baikal. Zero on the horizontal coordinate corresponds to the center of the lake [Gao et al., 1994b].

Figure 1: A Mercator projection map showing location and type of stations used and topography of the area under investigation. Elevations are part of the global ETOPO-5 data set and are smoothed with a two-dimensional boxcar filter.

Figure 4: Isotropic (top diagram) and anisotropic velocity model determined from Bayesian non-linear inversion of the travel time residuals.

NW Distance (km) SE

Figure 3: Mean travel time residual curves from the 1992 array event groups. Each vertical unit represents one second. Each horizontal grid line is the zero line of a group, with group name written on the right side of the diagram. The two vertical curves connect the location of the two minima on the residual curves. The insert on the right shows average arrival direction of each event group.

Figure 5: Maps showing SKS splitting measurement results. The diagram on the top is an enlargement of the rectangle in the lower diagram. Stations with well-defined measurements are represented by single circles with size proportional to the splitting. The line drawn through each circle gives the fast polarization direction.
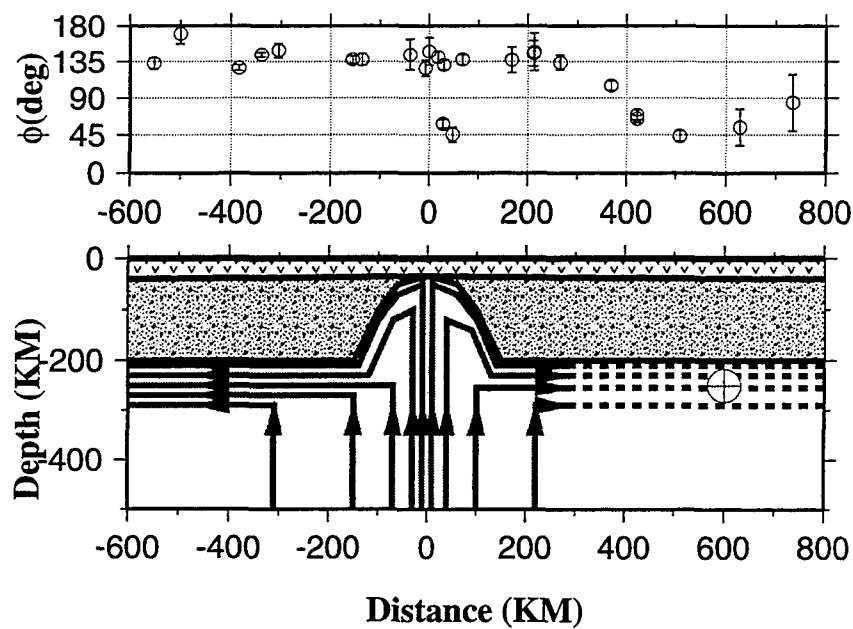
Figure 6: A small-scale convection model for the Baikal rift zone (middle diagram), fast SKS directions along the 1992 profile (top diagram), and orientation of olivine (a-fast, b-slow, c- intermediate) crystallographic axes in vertical and horizontal mantle flows (bottom diagram).

Development of a Lithospheric Model and Geophysical Data Base for North Africa

Diane I. Doser, G. Randy Keller, Kate C. Miller, and Steven Harder, Department of Geological Sciences, University of Texas at El Paso, El Paso, TX 79968-0555

ABSTRACT:

We have begun to develop a model of the North African lithosphere via an integrated analysis of seismic, potential field, and geologic data. These data will be used to construct detailed 2-D models of the region and a geological and geophysical data base which will be made available to the scientific community. The detailed 2-D lithospheric models will be verified through modeling of regional seismic phases. Recent results of ongoing gravity, heat flow, and earthquake source parameter studies of Libya, and surface wave dispersion studies of North Africa using WWSSN stations are presented as examples of the types of data that will be used to develop regional lithospheric models.

key words: geophysical data base, North African lithosphere

OBJECTIVE:

We will develop a model of North African lithosphere via an integrated analysis of seismic, potential field, and geologic data. In particular, we will construct detailed 2-D models from known earthquake source regions to key seismic monitoring stations in the region. An outgrowth of this effort will be a data base of geological and geophysical information which will be made available to the community through electronic access.

PRELIMINARY RESULTS:

A first step in this process is the collection of pertinent geological and geophysical data for North Africa. The coverage of any one type of data is insufficient to formulate a lithospheric model. Thus, we are using an integrated approach to the problem in which all possible data are used to derive a model. As an example of this process, we use the results of recent geophysical studies of Libya, a region whose present day structure is primarily a result of Late Cretaceous and Early Tertiary age rifting.

Gravity data can be useful in extrapolating below and between regions in which seismic data provide good constraints on structure. Figure 1 shows that we have been able to compile a good database of gravity readings in Libya (Suleiman, 1993). The large anomalies present (Figure 2) attest to the complex subsurface structure of this rifted region. Modeling of gravity data suggest a total sedimentary section of more than 5 km in the Sirt basin deep (Figure 3). The crust in the region is relatively thin (< 40 km thick) with the thinnest crust found underneath the Cyrenaica shelf.

Borehole data are also useful, as demonstrated by bottom hole temperature, stratigraphic, and well log information we have gathered for Libya. These data were used in conjunction with thermal conductivity and radioactive heat production measurements of formations to estimate heat flow values (Figure 4, Nyblade et al., 1995). Heat flow in the Sirt Basin is elevated by about 10 mW/m^2 from the global mean for unrifted Proterozoic terrains. This small heat flow anomaly could be due to either enhanced crustal heat production or residual heat from Cretaceous rifting (Nyblade et al., 1995).

Waveform modeling studies of the 1935 Hun graben earthquake sequence, including the largest magnitude (moment-magnitude 6.9) earthquake in Libyan history, suggest the crust supports brittle failure to depths of at least 20 km (Suleiman and Doser, 1995). Normal faults formed during Cretaceous rifting appear to have been reactivated as strike-slip faults in the present day stress regime (Figure 5).

Surface wave dispersion studies between WWSSN stations MAL and HLW and MAL and JER (Figure 6) (Yousef, 1986) sample the average crust and mantle structure across much of extreme northern Africa. These results suggest a mantle lid at about 60 km depth and a possible crustal low velocity zone at a depth of 10 to 15 km. As part of present study we will be reanalyzing these data

201

using updated processing techniques (Dean and Keller, 1991) and extend the analysis using new digital stations in the region.

Integration of these geophysical studies of Libya would suggest that the crust is best modeled as being no more than 40 km thick, thinning slightly from west to east. The brittle-ductile transition in the crust appears to occur at 20 km depth, with an expected velocity change corresponding to this transition. Heat flow results suggest only small decreases in crustal velocity relative to velocities associated with unrifted Proterozoic terrains, while surface wave dispersion studies suggest an asthenospheric thickness of about 60 km. This preliminary crustal/upper mantle model will need to be validated through waveform modeling studies of regional seismic phases of Libyan earthquakes.

FUTURE PLANS:

We have begun to collect geophysical and geological data sets for other regions of North Africa that will be used to determine preliminary lithospheric models in a manner similar to that demonstrated for Libya. Regional seismic waveforms are also being collected and will be modeled in order to validate and update these preliminary lithospheric models. Our final results will be a geophysical and geological data base for North Africa that will be easily accessible to the scientific community and a series of "best" lithospheric models for regions of North Africa that have been validated through waveform modeling of regional seismic phases.

REFERENCES:

Dean, E.A., and G.R. Keller, 1991. Interactive processing to obtain interstation surface wave dispersion, Bull. Seismol. Soc. Am. 81, 931-947.

Nyblade, A.A., I.S. Suleiman, B. Pursell, A.S. Suleiman, D.I. Doser, and G.R. Keller, 1995, Terrestrial heat flow in the Sirt Basin, Libya, submitted to J. Geophys. Res.

Suleiman, A.S., and D.I. Doser, 1995. Seismotectonics of Libya and the 1935 Hun graben earthquake sequence, Geophys. J. Int. 116, 605-607.

Suleiman, A.S., 1993. Geophysics of the rifts associated with the Sirt Basin (North Africa) and the Anadarko Basin (North America), Ph.D. Dissertation, The University of Texas at El Paso, 150 pp.

Yousef, A., 1986. A surface wave dispersion study of the lithospheric structure of Africa, Ph.D. Dissertation, The University of Texas at El Paso, 115 pp.
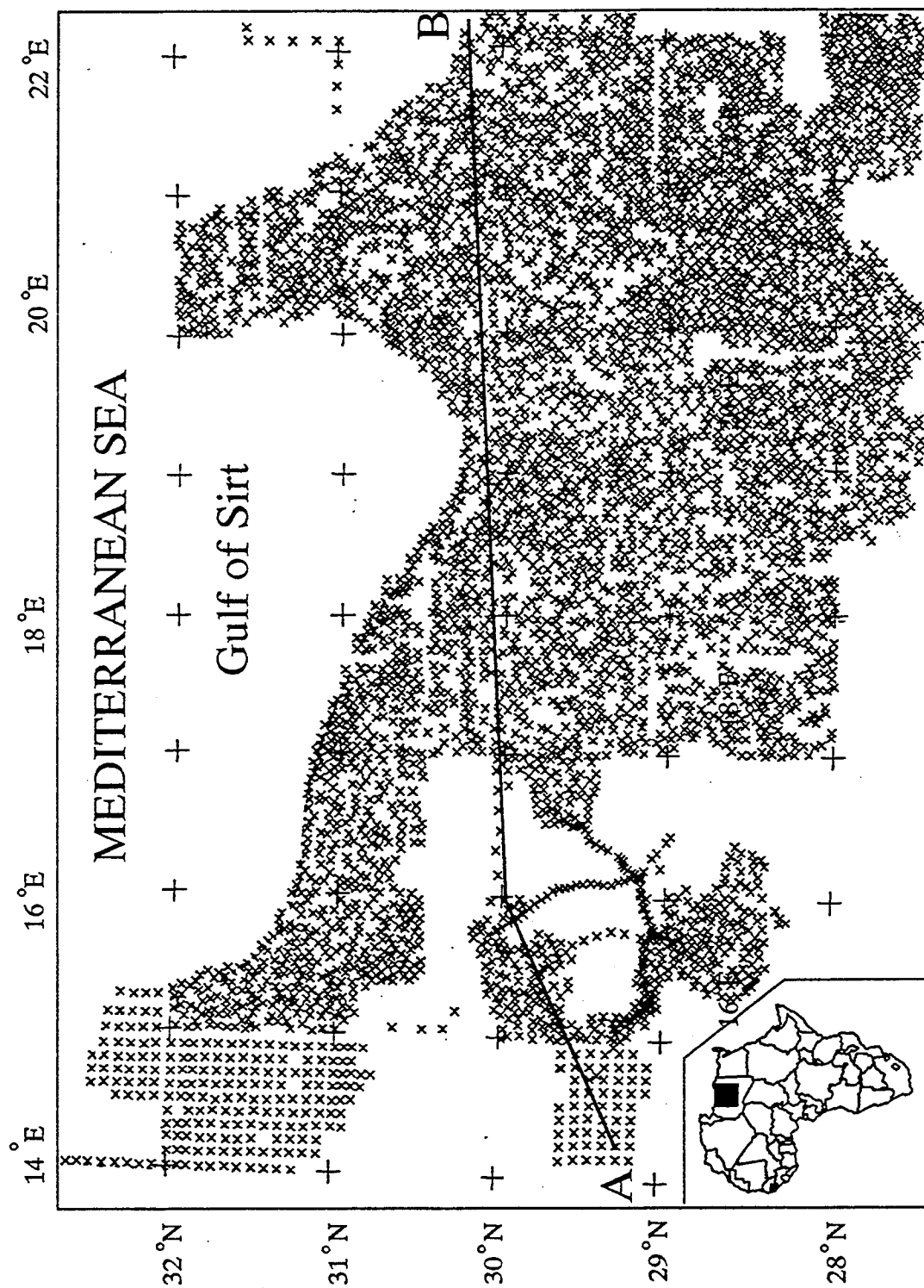
Figure 1. Map showing the gravity station distribution in the Sirt basin area. Interpretation of gravity data along profile A-B is shown in Figure 3.
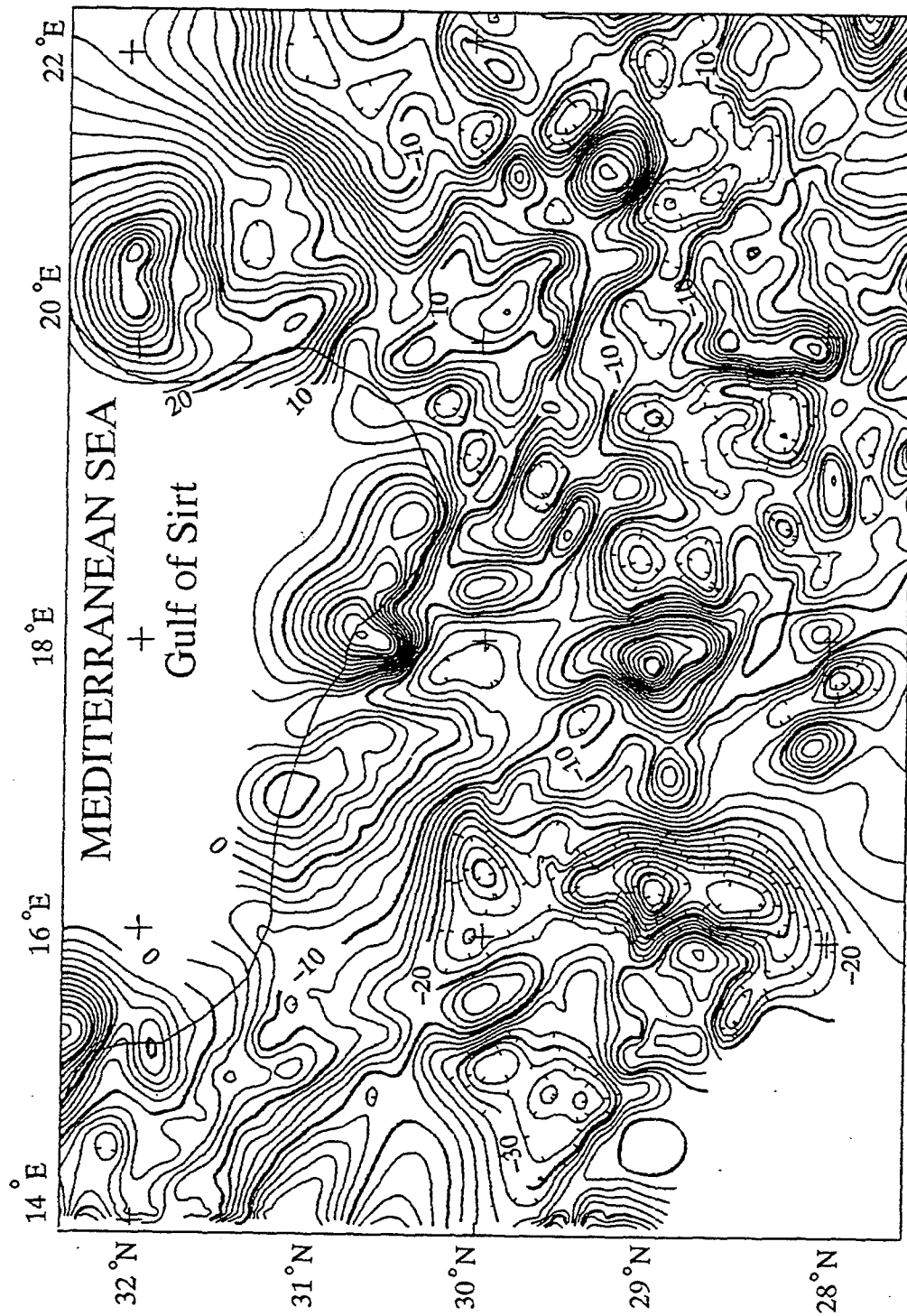
Figure 2. Bouguer anomaly map of the Sirt basin rift system from Suleiman (1993). Contour interval is 2 mgals.
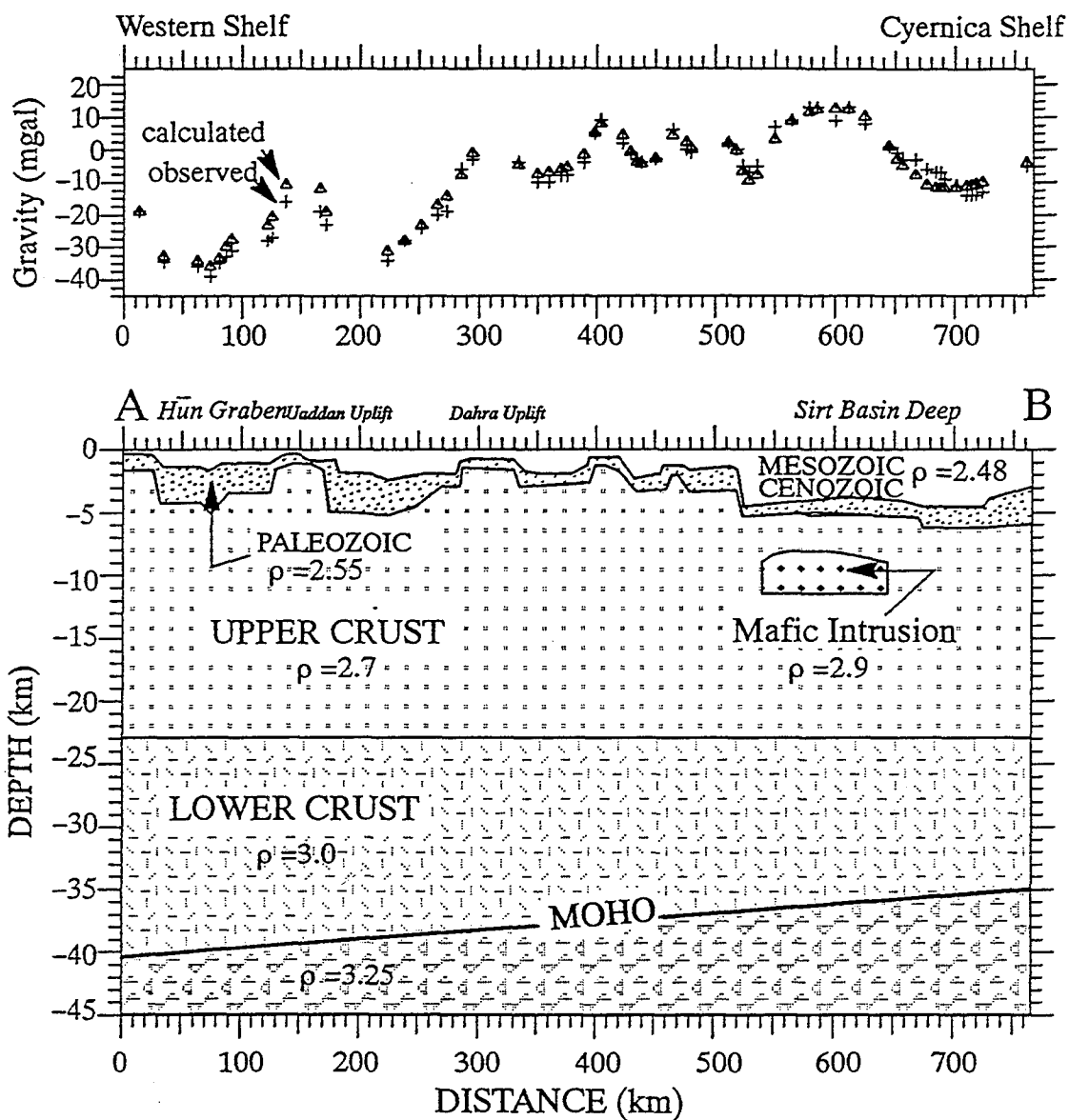
Figure 3. Interpretation of gravity profile across the Sirt basin rift system along profile A-B (see Figure 1) and corresponding computer model of crustal structure (Suleiman, 1993). Densities shown in model are in g/cm^3.
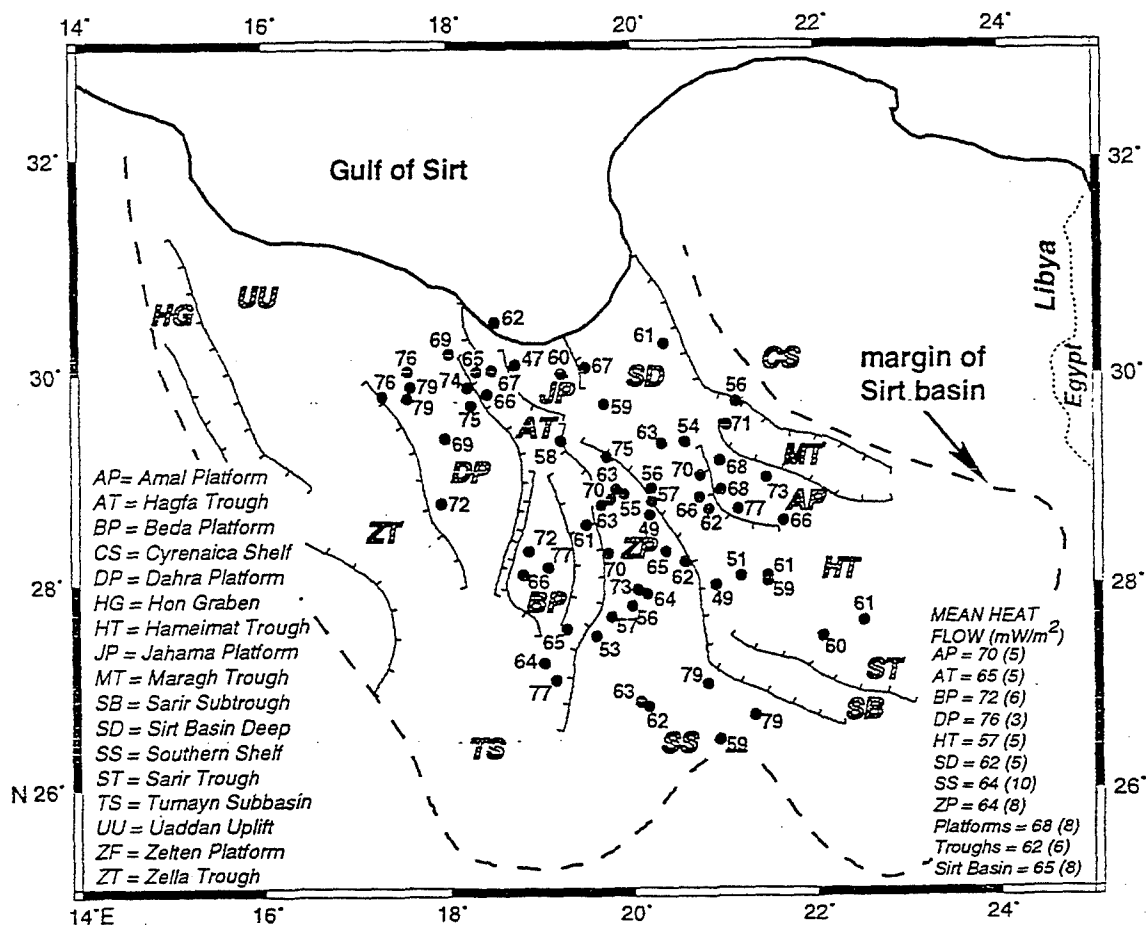
Figure 4. Map of Sirt basin showing heat flow (in mW/m²) at wells
(solid circles), major rift faults, and prominent structural
features (from Nyblade et al., 1995). Mean heat flow values are
given in the lower right corner, with standard deviations of the
mean given in parentheses.
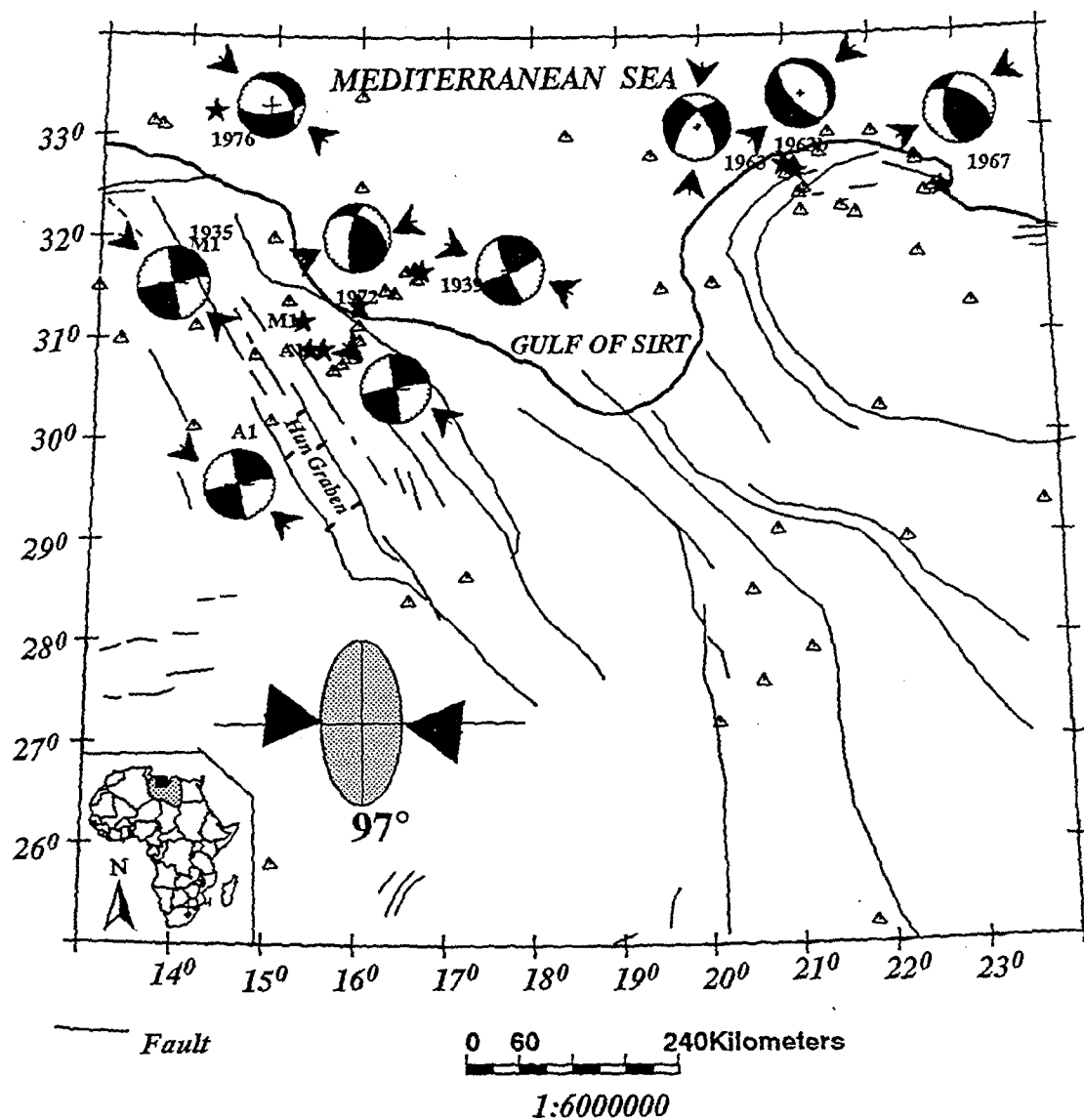
Figure 5. Northern Libya earthquakes (triangles and stars) and focal mechanisms (from Suleiman and Doser, 1995). Arrows denote strike of P-axes. Large arrows in left corner denote strike of maximum compressive stress direction determined from the inversion of northwestern Libya focal mechanisms.
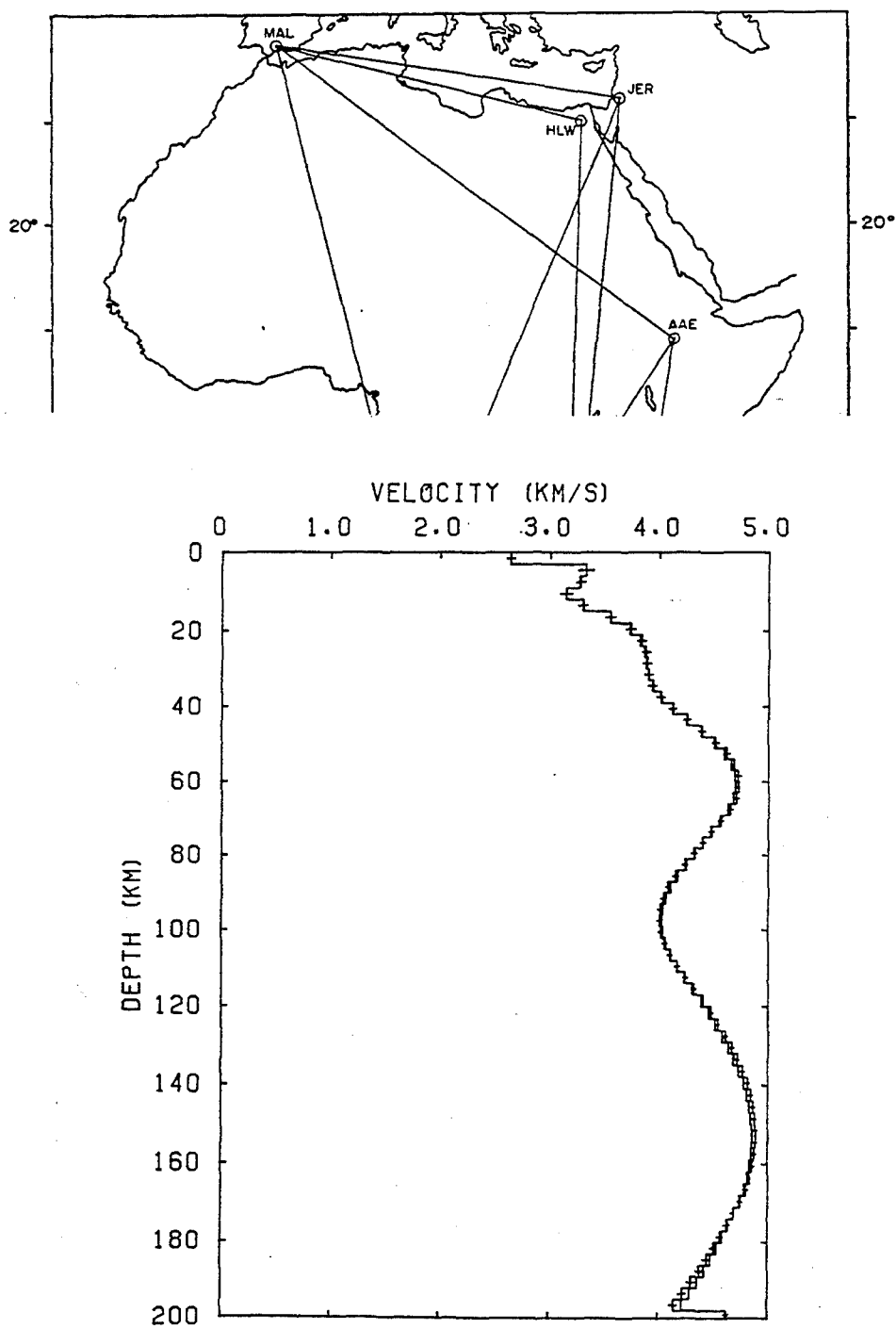
Figure 6. Location of North African travel paths and WWSSN
stations used in surface wave dispersion analysis (top). Velocity
model determined from inversion of dispersion data for the paths
HLW-MAL and JER-MAL (from Yousef, 1986) are shown at bottom.

Lower Crustal and Upper-most Mantle Structure beneath Station WMQ, China by using teleseismic P-wave Polarization signals

Liping Gao and Paul G. Richards*
Lamont-Doherty Earth Observatory, Palisades, NY 10964
(*also, Dept. of Geological Sciences, Columbia University)

Abstract

We have applied a polarization tomographic inversion to the single station WMQ to retrieve the velocity structure of the lower crust and upper-most mantle in the vicinity of Lop Nor. 828 teleseismic P-wave waveforms with event magnitude $M_b \geq 5.0$ around the world with excellent coverage of back azimuth were collected and are used to measure polarization anomalies. In addition, 39 PKP signals are used. Inversion results reveal a low velocity region or a depressed Moho to the northwest of the WMQ station.

Keywords: polarization tomography, crust and mantle velocity structure.

Objective

The Chinese Digital Seismographic Network (CDSN) station WMQ (Urumqi) is the closest digital station to Lop Nor, known as the Chinese nuclear test site, in Xinjiang Province, China. It is also the only station for this area from which we can get data from the IRIS DMC. With limited resources of seismic signals, analysis of the crustal and upper mantle structure has been very difficult. Yet, understanding the velocity structure in the area is crucial in analyzing the seismic signals of both earthquakes and explosions. Also, the station WMQ is in a region of great interest geological and tectonically, being affected by the collision of India with Asia and the resulting continental deformation. In this paper, we have used the single station teleseismic polarization anomalies to study the lower crust and upper-most mantle structure, mainly in the vicinity of the Moho.

Research Accomplished

We have used the newly developed polarization tomography method [Hu and Menke, 1992] to study laterally varying velocity structure in the vicinity of the Chinese nuclear site in Xinjiang Province. Compared with teleseismic travel-time inversion, polarization tomography takes advantage of the facts that: (1) the measurement of polarization (i.e. ray arrival direction) does not depend upon the origin time of earthquakes; and (2) the polarization has little dependence on the structure near the source, the location error of the source, or the deep mantle structures, because the sensitivity of polarization to a velocity structure is, in a rough sense, inversely proportional to the distance between the structure and the station measured along the ray path. For instance, a 10 km location error, which may cause a 1 second delay in travel-time, only causes 0.1° anomaly on arriving azimuth at 60° distance. To get high quality polarization data at a station, requires high quality of the original waveform data. From 1988-mid 1994 (the data for WMQ starts from 1988 in IRIS), we obtained over 1500 broad band P-wave waveforms of events ($M_b \geq 5.0$) around the world with excellent back azimuth coverage (0°-360°). Among them, 828 teleseismic events with high signal to noise ratio and 39 high quality PKP signals are chosen to measure the polarization anomalies. Figure 1 shows the 867 event locations relative to the station, and Figure 2 shows two examples of the waveform data, one event from the Philippines with distance of 76° and azimuth 135° and the other from Greece with distance of 42° and azimuth 228°.

We adopted a very simple time domain least square fit [Hu, 1994] to measure the P-wave polarization — the azimuth and incident angles. For a signal (z, n, e), where data vectors have the components (z_i, n_i, e_i) with i=1, ..., N and N is the total number of points

in the digital time series, we calculate azimuth angle by fitting **n** and **e** with a linear relationship, $e = a + bn$. The azimuth is $\phi = \tan^{-1}$ (b). The radial component is then $r = n\cos(\phi) + e\sin(\phi)$. By fitting the linear relationship $r = c + dz$, we get the apparent incidence angle $\delta' = \tan^{-1}$ (d). Then, the true incidence angle, after correction for free surface reflections, is $\delta = \sin^{-1} [V_p^2(1-\cos\delta')/2V_s^2]^{1/2}$. Only the first few cycles of the P arrival are used to avoid noise introduced by later arrivals. The polarization residuals are with reference to the iasp91 global Earth model [Kennett and Engdahl, 1991] and locations are taken from the PDE catalog (Figure 3).

There have been some previous efforts by western scientists to study crustal structure in the area [for example, Mangino and Ebel, 1992; Roecker, et al., 1993; and Gao and Richards, 1994]. We chose a regional crust velocity model from our previous studies [Gao and Richards, 1994] as our reference, with which to develop the velocity variations. Our reference model was obtained by fitting regional seismic records (recorded at WMQ) from an explosion in Lop Nor. It has three layers in the crust, and Moho depth is at 46 km (Figure 4). This model represents an average structure along the path from the Lop Nor test site to the station WMQ (distance ~240km), which does not necessarily reflect the structure right underneath the station. In the inversion, we limited the three-dimensional velocity variation to be within a 15 km thick layer centered at Moho depth (46 km). The P-wave velocity at the top and bottom of this layer is fixed to join continuously with the one-dimensional background velocity (reference model). We represent the velocity in this layer with B splines and invert for the three-dimensional P-wave velocity variation in this layer by the method from Hu [1994] using only the polarization measurements (azimuth and incidence angles at WMQ). Our data distribution is not uniform in the back azimuth (Figure 3), because the data from 20° - 135° are much denser than those from the remaining directions (ratio is 3:1). We therefore gave the latter directions of the data a weight three times larger than the former. Our preliminary results (Figure 5) show that the general trend of the velocity isopaths is west-southwest for much of the region, which is also the trend of the Tian Shan mountain range in the same general location. There is a velocity depression (low velocity, more than 7% lower than the reference model) to the northwest of the station WMQ. This is consistent with the observation from Mangino and Ebel [1992] that there is a NW dipping structure underneath the station WMQ. Our studies indicate that this dipping structure could be the Moho.

Future Work and Recommendations

Our studies show that polarization tomography is effective although our data resources are limited (because there is only one station in Tian Shan - Lop Nor vicinity).

With help from the US Geological Survey and the State Seismological Bureau (SSB) of China, we have obtained a comprehensive catalog of local and regional earthquakes in the Lop Nor region (Xinjiang Province). This catalog provides additional information on seismicity. Some of the events have records available from IRIS. With the help of local and regional data, the understanding of the structure parameters, such as velocities and Q values of the region can be greatly improved. This effort is well underway here in Lamont.

References

Hu, G. and W. Menke, Formal inversion of laterally herogeneous velocity structure from P-wave polarization data, Geophys. J. Int., 110, 63-69, 1992.

Hu, G., Polarization Tomography, Ph.D. Thesis, Department of Geological Science, Columbia University, 1994.

Gao, L. and P. G. Richards, Studies of earthquakes on and near the Lop Nor, China, Nuclear test site, Proceedings of the 16th Annual Research Symposium, 7-9 September, 106-112, 1994. PL-TR-94-2217, ADA284667

Kennett, B. L. N., and E. R. Engdahl, Traveltimes for global earthquake location and phase identification, Geophys. J. Int., 105, 429-465, 1991.

Mangino S. and J. Ebel, The receiver structure beneath the Chinese Digital Seismography Network (CDSN) stations: preliminary results, Phillips Laboratory, PL-TR-92-2149, 1992. ADA256681

Roecker, S. W., T. M. Sabitova, L. P. Vinnik, Y. A. Burmakov, M. I. Golvanov, R. Mamatkanova, and L. Munirova, Three-Dimensional elastic wave velocity structure of the western and central Tien Shan, J. Geophys. Res., 98, 15779-15796, 1993.
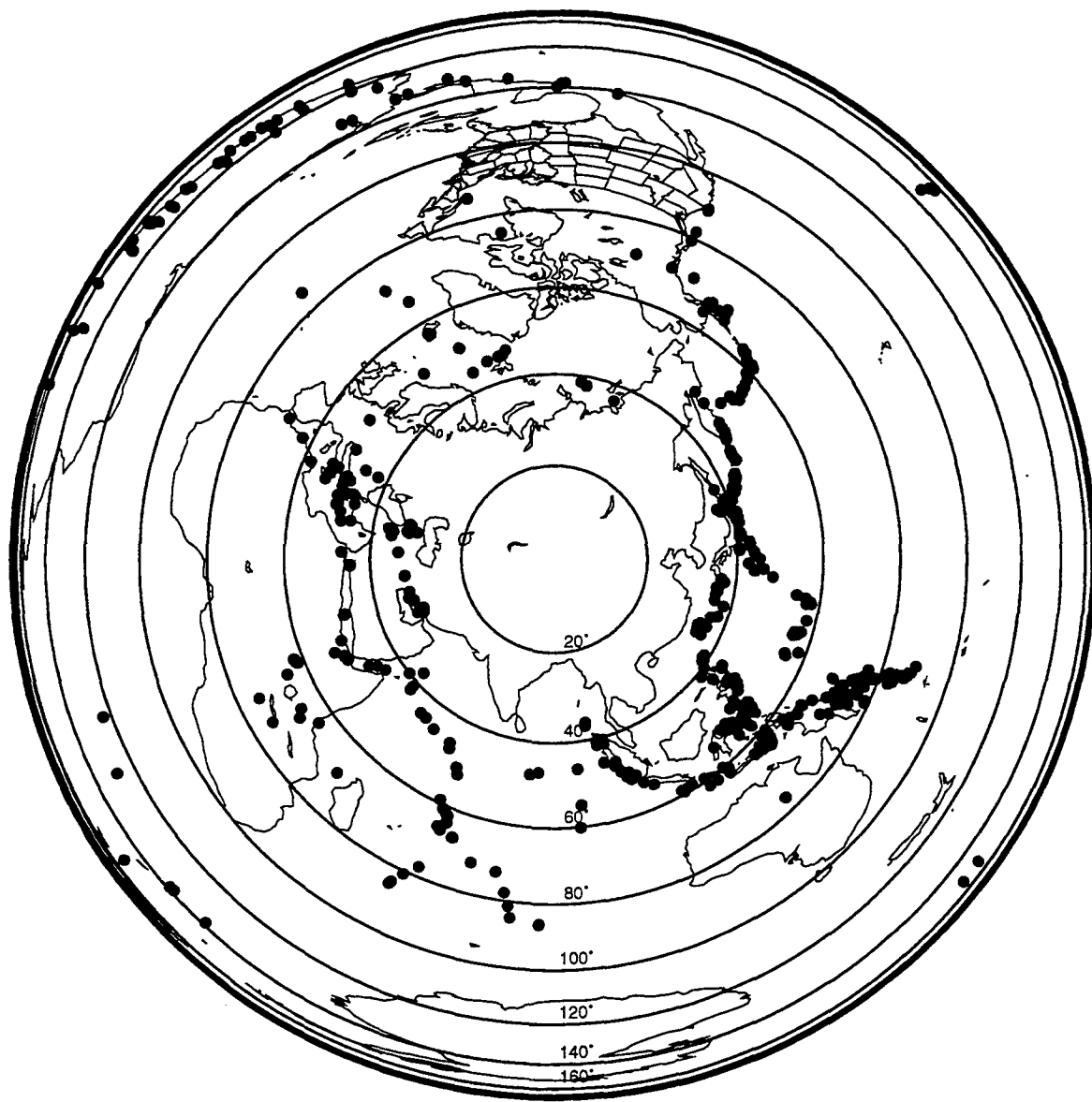
Figure 1. Location map showing the events used in the study.
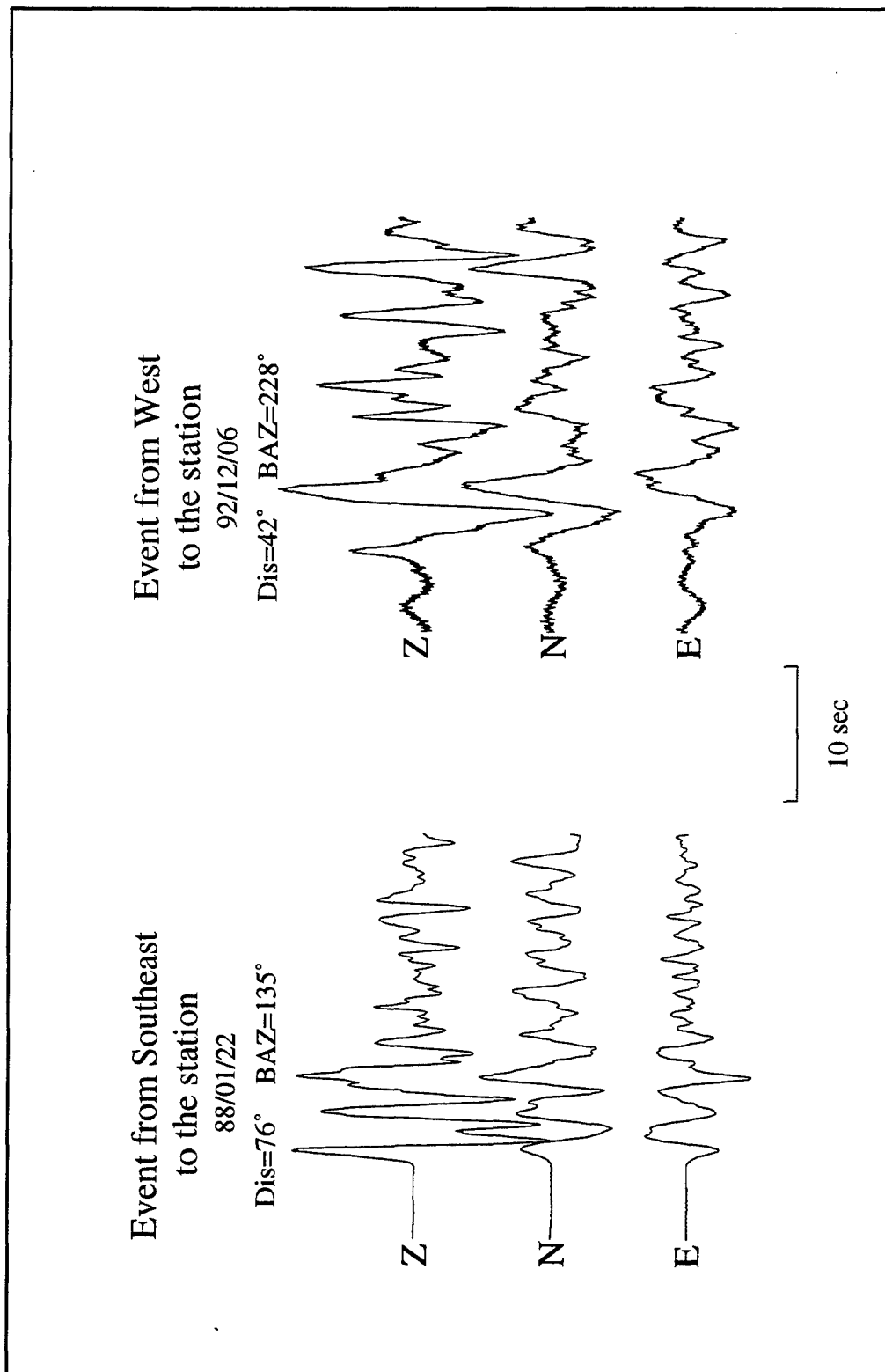
Figure 2. Two examples of the teleseismic records recorded at WMQ station. One event is from the southeast to the station (88/01/22) and the other is from the west to the station (92/12/06).

file: pol.total

dp=0.05

dp vs. event inc and back-azi
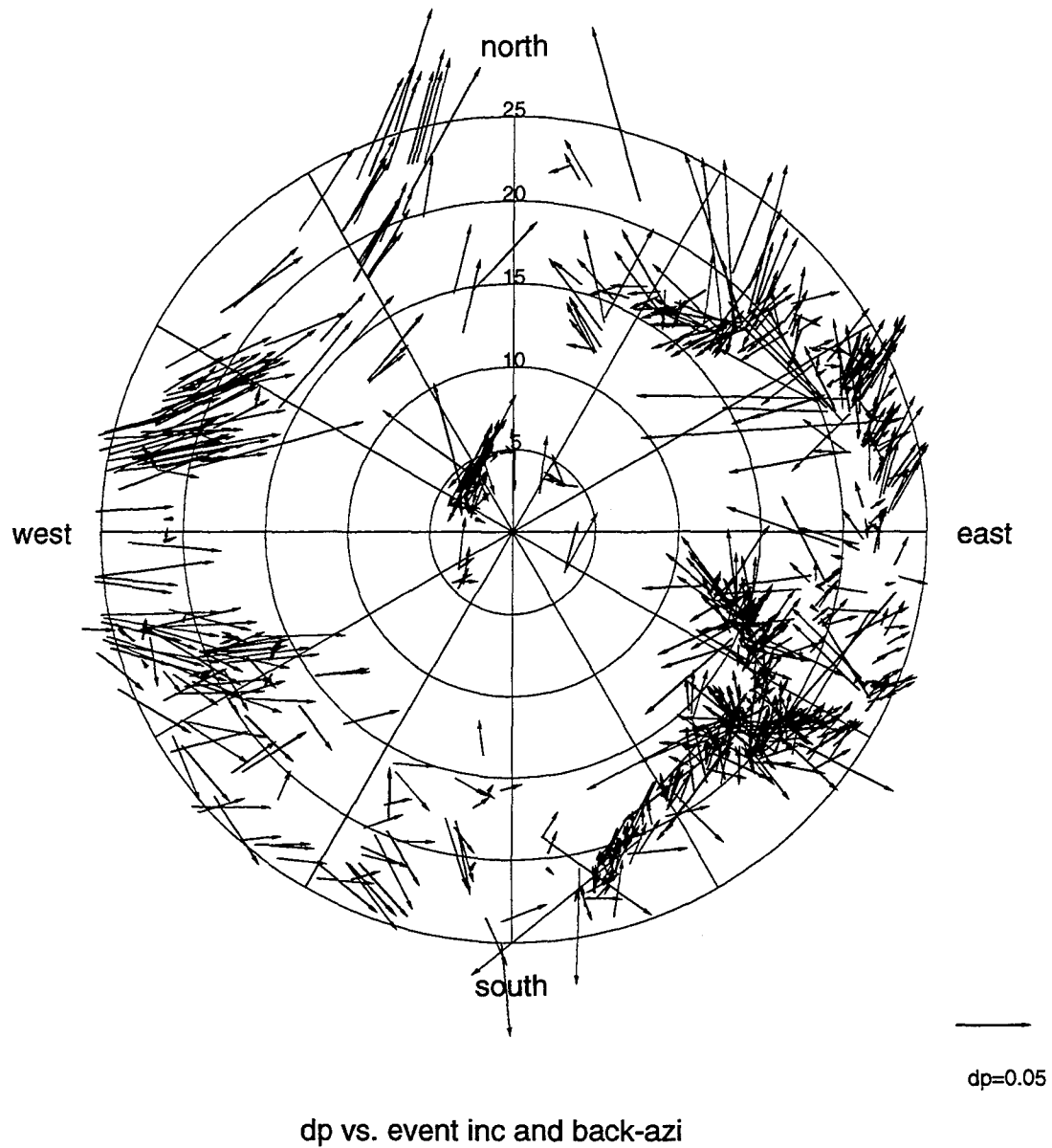
Figure 3. Polar plot of the polarization residuals. The radial axis shows the incident angle of the polarization vector and the position of each vector is plotted according the back-azimuth.
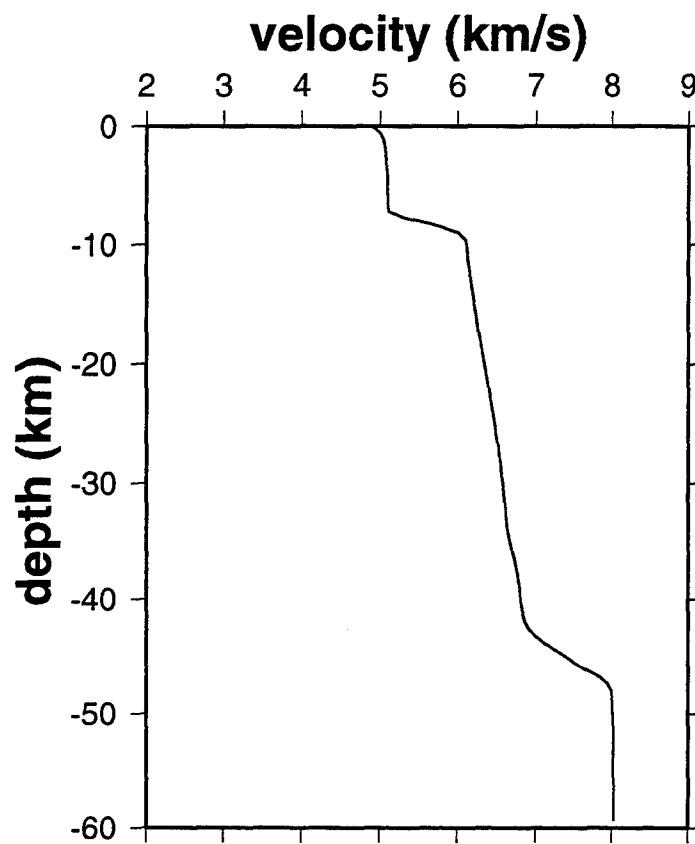
Figure 4. Reference (starting) 1-Dimensional model from Gao and Richards [1994].

velocity contrast (%)

newmod_my - my_mod1 z=46 km
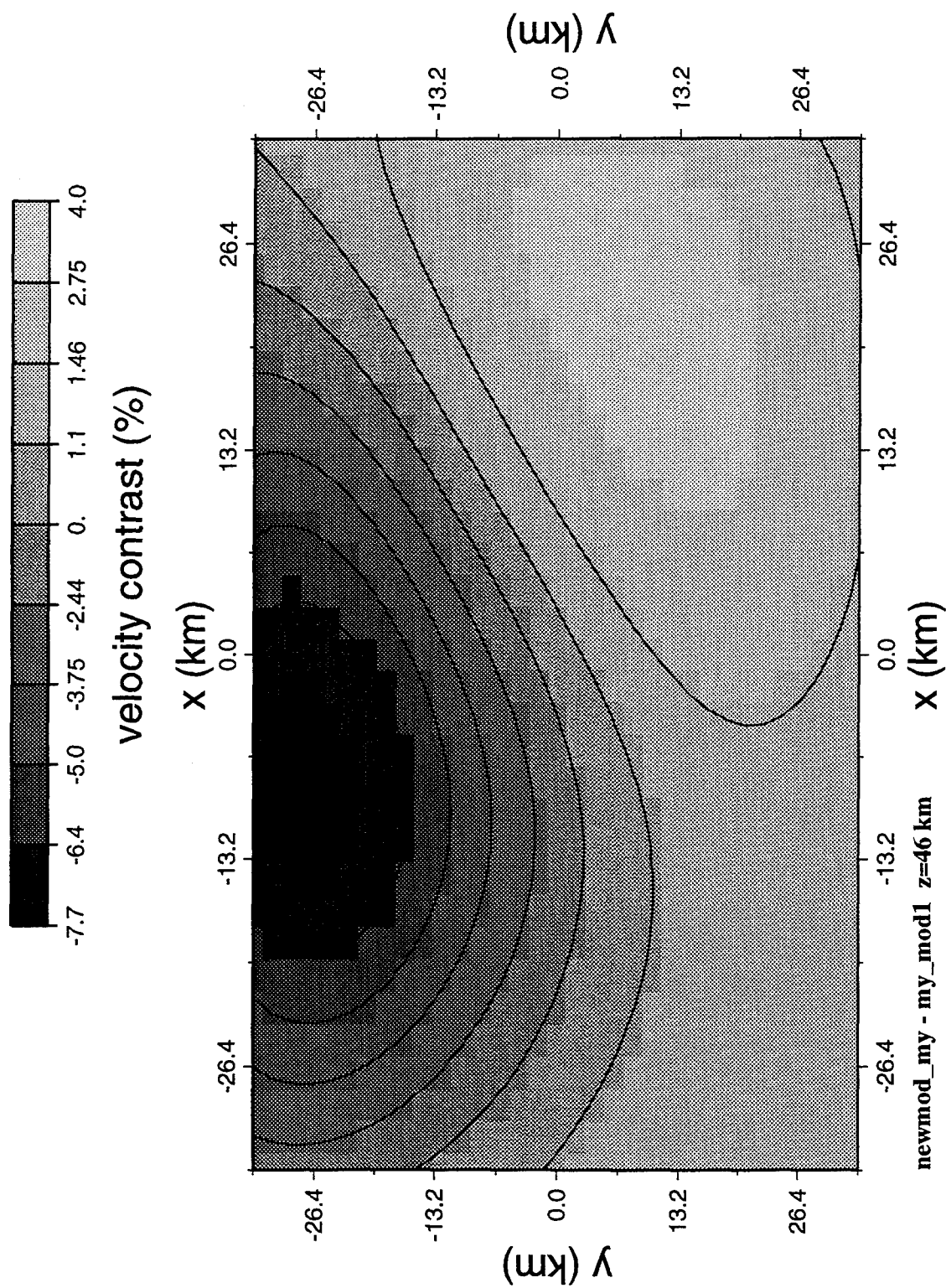
Figure 5. A horizontal slice at depth 46 km of the model resulting from the inversion showing a low velocity depression to the NW of station WMQ (centered at (0,0)).

217

Lithospheric Profiles in Western North America

G. Randy Keller, Kate C. Miller, and Diane I. Doser, Department of
Geological Sciences, University of Texas at El Paso, El Paso, TX
79968-0555

ABSTRACT:

As we move toward a Comprehensive Test Ban Treaty for nuclear
weapons, it has become increasingly clear that detailed knowledge
of lithospheric structure is necessary to verification efforts.
Key seismic phases which are being used as discriminants (Pn,Pg,
Lg, etc.) to identify suspicious seismic signals travel
exclusively in the lithosphere and are thus much affected by its
structure. However, the studies needed to acquire detailed
knowledge of lithospheric structure require large explosions,
recorded by hundreds of seismograph systems. In the former Soviet
Union, a series of Peaceful Nuclear Explosions (PNE) were exploded
to provide such data. There have been very few PNE in the U.S.,
and these experiments took place in the 1960's and 1970's long
before there were large numbers of digital seismograph systems
available to provide detailed recordings. Thus, these few PNE
events do not provide detailed pictures of lithospheric structure
and propagation of regional phases and cannot serve as effective
benchmarks for comparison with other continents. Large chemical
explosions can provide suitable sources for lithospheric
experiments as proven by the EARLY RISE experiment in the Great
Lakes region in the 1960's and the recent Non-Proliferation
Experiment at the Nevada Test site (NTS). However, we have not
had an opportunity to conduct a large-scale lithospheric
experiment with modern equipment except with NTS sources. The
UTEP geophysics group has been conducting a series of
investigations in the southwestern U.S. The most recent was
undertaken in the summer of 1995 and is the closest thing to a PNE
experiment that we will see taking place outside of NTS for the
foreseeable future. In cooperation with the Canadian program
called LITHOPROBE, we and Rice University recorded along a profile
extending from Great Slave Lake to New Mexico, a distance of about
2500 km. This experiment is a unique opportunity to gather
seismic data at regional distances with large numbers of modern
seismograph systems. In addition to preliminary information on
this 1995 experiment (termed "Deep Probe") we will present results
of the May 1994 Colorado Plateau/Basin and Range transition
experiment ("Delta Force"), tomographic studies of the eastern
Mojave using earthquake and explosion sources, and passive seismic
studies of the El Paso and Lubbock, Texas regions.

key words: western North America lithosphere

OBJECTIVE:

Determine the lithospheric structure of western North America including structure of the western Colorado Plateau/eastern Basin and Range transition, eastern Mojave Desert region, Rio Grande rift/Great Plains transition, and deep structure of Archean and Proterozoic crust of the northern and central Rocky Mountains. These objectives will be accomplished through active and passive seismic experiments in the regions of interest.

PRELIMINARY RESULTS:

Delta Force:

The May 1994 Delta Force refraction/wide angle reflection seismic project was designed to sample the eastern edge of the Basin and Range province at the latitude of Las Vegas, NV, to Blythe, CA, and into the Colorado Plateau of northwestern Arizona. A group of 474 digital instruments were installed on a single deployment covering two main lines at an average spacing of 2 km and a group of recorders were set loosely as a third line (Figure 1). Four explosive sources were set up near Hurricane, UT (Shot 1), Death Valley Junction (Shot 2), Kingman, AZ (Shot 3), and Blythe (Shot 4). The shots were fired in succession at 4 minute intervals providing in-line as well as fan-type coverage. Seismic recording occurred along Line 1 (Blythe to Death Valley Junction), Line 2 (Death Valley Junction to Kingman), and Line 3 (Hurricane to Kingman).

Preliminary results of the interpretation of Line 1 suggest Pn velocities of 7.8 km/s, which is consistent with previous studies. Upper and lower crustal velocities of 6.0 and 6.6 km/sec, respectively, are also interpreted. The crust appears to be 30 km thick. No major variation in crustal thickness is indicated along this line. The Pn crossover distance from Shot 2 along Line 2 is about 180 km, and the data indicate crustal thickening beginning at the Grand Wash Cliffs. On Line 3 the apparent Pn crossover distance is ~140 km from Shot 1.

Eastern Mojave:

We have collected travel-time data from nuclear and chemical explosions and earthquakes of magnitude > 3.0 within the eastern Mojave Desert region (Figure 2). These data have been used in a 3-D tomographic inversion to determine the velocity structure beneath the region, as well as the effects of anisotropy on wave propagation. The earthquakes and explosions used in the study were recorded by stations operated by Caltech, the University of Nevada-Reno, and the University of California at Berkeley. Travel times of P arrivals from the 1994 Delta Force and 1993 Southern Sierra Nevada Continental Dynamics seismic refraction experiments have also been incorporated into the data set. Two different starting models have been tested to see which provided the best fit with the data: a) a smooth, homogeneous model, and b) a priori velocity constraints obtained from the results of seismic refraction profiles in the Mojave and southern Basin and Range region. Preliminary inversion results suggest that anisotropy develops from both starting models, with the horizontal velocities generally being 1 to 2 % faster than the vertical velocities.

Both starting models give average velocities of 6.1 to 6.3 km/sec in the upper 15 km of the crust.

Passive Seismic Studies:

We have installed broadband, digital seismographs at Lubbock and El Paso, TX, (January, 1995) and more recently at Canyon de Chelly, AZ, and Chaco Canyon, NM (June, 1995) to examine the structure of the southeastern Colorado Plateau, the eastern Rio Grande rift and western Great Plains (Figure 3). In addition to recording teleseismic data for surface wave dispersion and teleseismic receiver function studies, we have recorded a number of regional events including the April 1995 Alpine-Marathon (M~5.5) earthquake (Figure 4). Data analysis for the two Texas stations has just begun.

Deep Probe:

Collection of data for this experiment is currently underway. Figure 5 indicates the deployments in the U.S. and the shotpoints. The first deployment in Montana and southern Wyoming is scheduled for the night of August 1.

FUTURE PLANS:

The whole wavefield data for the Delta Force experiment will be modeled using the reflectivity method and a finite difference wave equation algorithm. The results will be complemented by gravity data modeling using earth structure derived from the seismic model.

Travel-time information from the University of Nevada-Reno seismic network is currently being merged with other travel-time data for the eastern Mojave region. Final results of the tomographic studies are expected by late fall.

Interpretation of broadband data collected in Texas is just beginning. We plan to continue operation of the Texas stations for at least another year. Since stations on the southeastern Colorado Plateau have only begun operation, we plan to continue data collection at these sites through at least the fall and winter of 1995.

Data from the Deep Probe experiment and preliminary interpretations will be presented at the Fall 1995 AGU meeting.
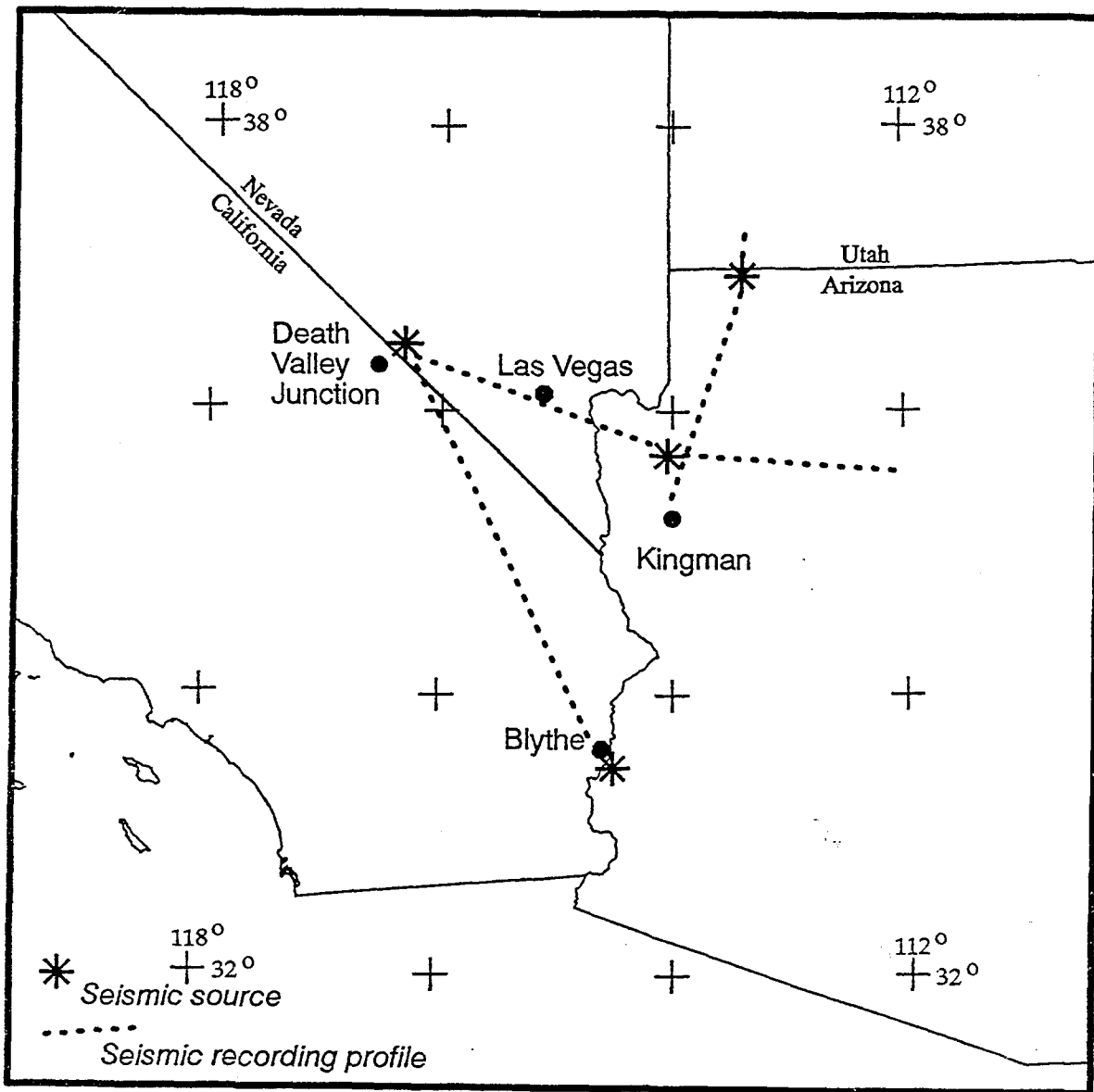
Figure 1. Index map of the Delta Force seismic experiment.
Seismic sources are indicated as asterisks, receiver deployments
as dashed lines.
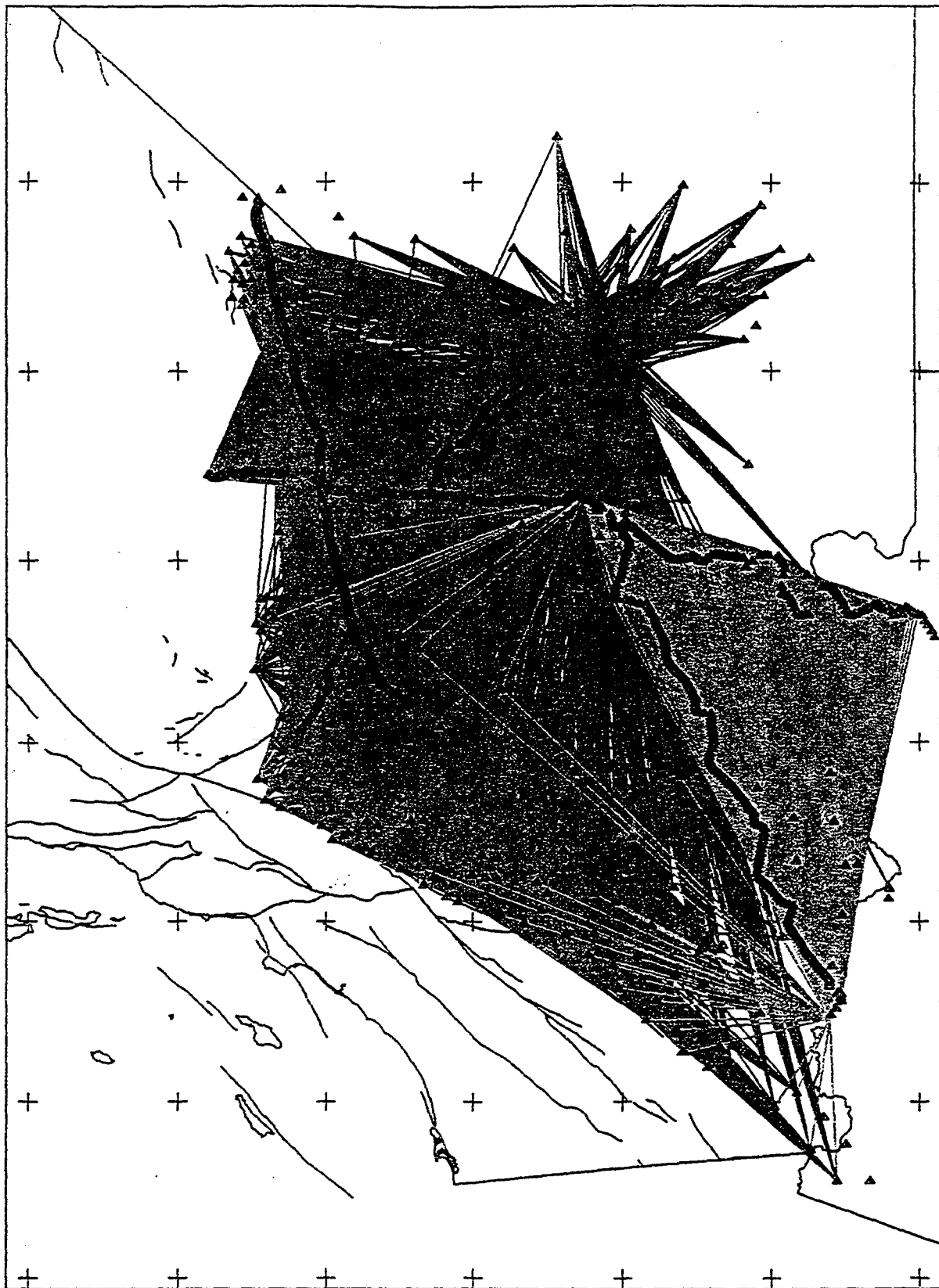
Figure 2. Index map of the eastern Mojave study region showing seismograph stations (triangles) and raypath coverage.
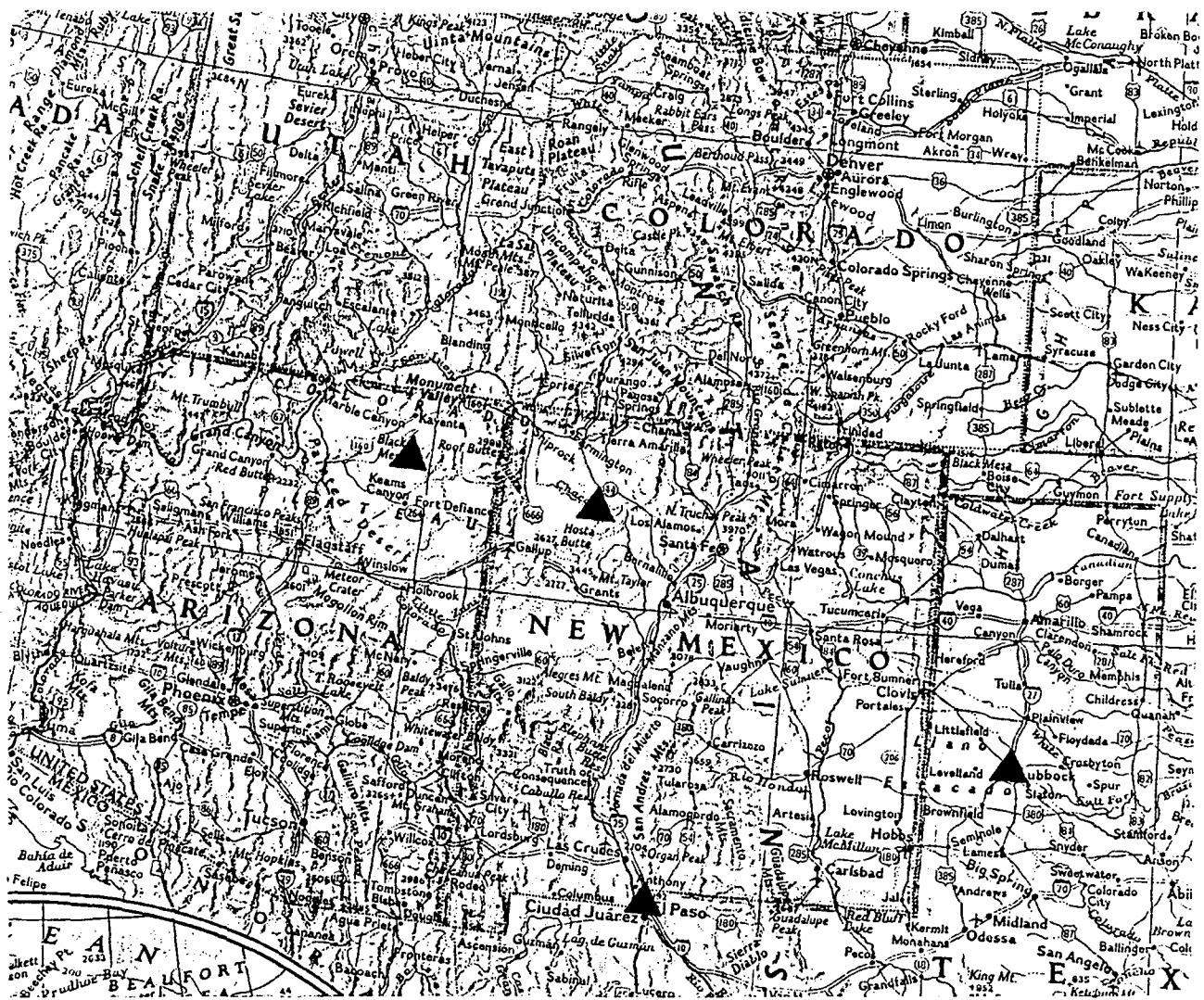
Figure 3. Index map of broadband seismograph stations (triangles) currently deployed in a passive seismic study of the southeastern Colorado Plateau, eastern Rio Grande rift and western Great Plains.

223
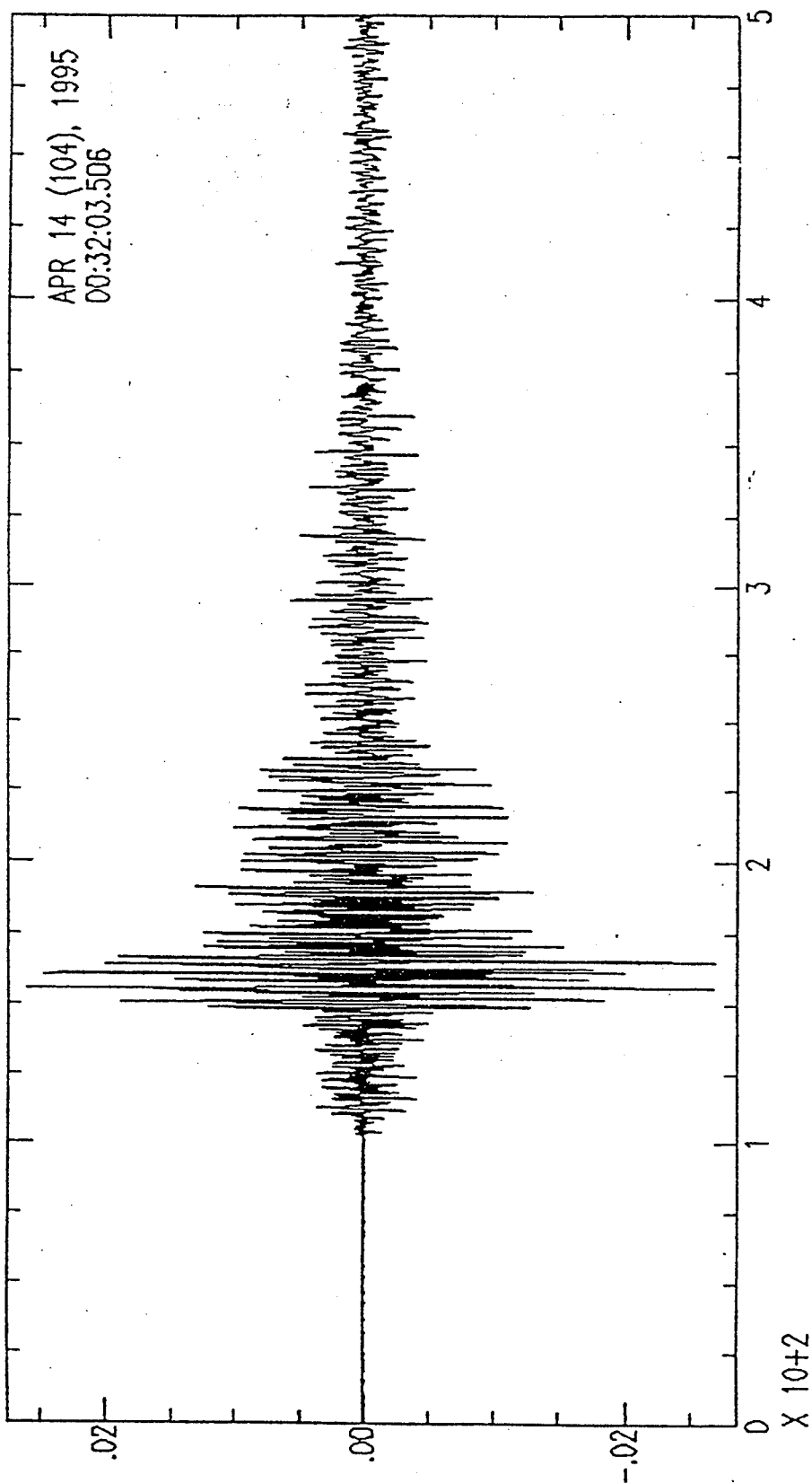
Figure 4. Seismogram of the April 13, 1994, Alpine-Marathon, Texas, earthquake (magnitude ~5.5) recorded in El Paso.
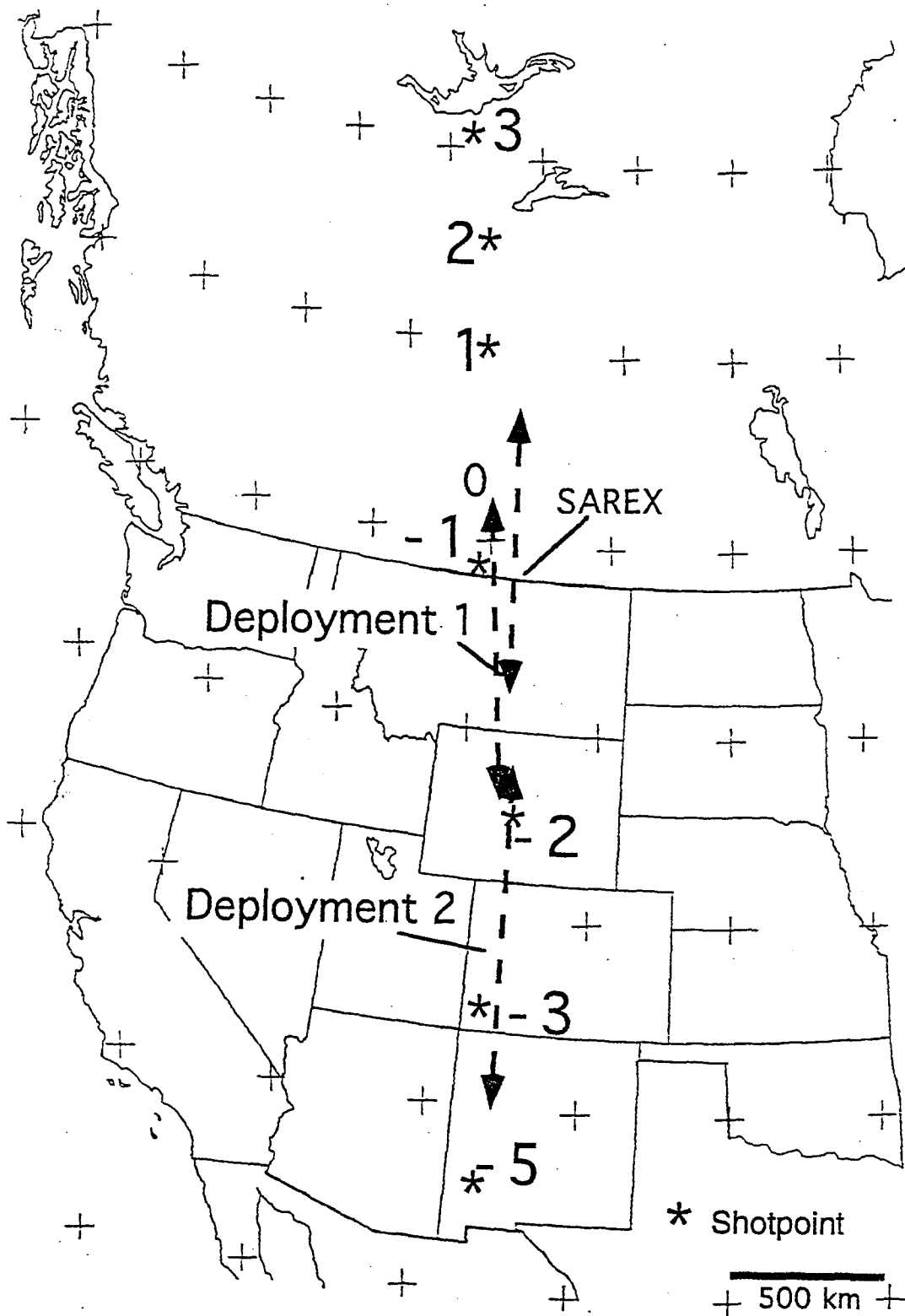
Figure 5. Index map showing U.S. deployments and all shot points for the August 1995 Deep Probe seismic experiment.

SURFACE WAVE GROUP VELOCITY MEASUREMENTS ACROSS EURASIA

A. L. Levshin, M. H. Ritzwoller, and L. I. Ratnikova

Department of Physics, University of Colorado at Boulder
Contract Number F49620-95-1-0139
Sponsored by AFOSR

Abstract

Earthquake and nuclear explosion data recorded by the GSN, GEOSCOPE, CDSN, and MED-NET broadband networks and the IRIS/Kyrghyz regional network (KNET) during 1988-1995 have been used to study the characteristics of surface wave propagation across Eurasia. More than 3500 three-component records for different epicenter - station pairs have been processed. Group and phase velocity dispersion curves, spectral amplitude curves, as well as frequency - dependent azimuthal particle - motion anomalies for fundamental Rayleigh and Love waves in the range of periods between about 20 and 300 s have been obtained by means of frequency-time analysis and floating filtering. Data on group velocities have been used to obtain preliminary group velocity maps of the region under study for a broad set of periods. Spatial resolution of these maps depends on the ray coverage, and appears to vary from 600 to 1000 km. Significant lateral variations of Rayleigh and Love group velocities seen on the maps indicate drastic changes of lithospheric shear velocity structure across the region. The Tibetan Plateau, the mountain regions of Central Asia, the Siberian Platform, the Indian Shield, as well as some smaller tectonic features, appear on maps as regions of relatively high or low group velocities. The 2D-inversion of all data into group velocity maps and 3D-inversion for the lithospheric structure of the region is in progress.
key words: Eurasia, seismic wave propagation, Love waves, Rayleigh waves, group velocity, polarization

OBJECTIVE

This research concentrates on making robust measurements of properties of surface waves propagating across Eurasia for periods ranging from 20 to 300 s, and on inverting the observations for elastic structures in the crust and upper mantle of Eurasia. Earthquake and nuclear explosion data recorded by several global and regional broadband networks and arrays in 1988-1995 are used to measure phase and group velocity dispersion, spectral amplitudes and polarization properties of fundamental Rayleigh and Love waves. Tomographic inversion of measurements into 2D-maps of observed wave parameters and 3D-elastic and anelastic structures should allow us to focus existing long-wavelength seismic models to tectonic wavelengths. Such models could be used to enhance the detection and location capabilities of seismic monitoring for complex tectonic regions of Eurasia.

PRELIMINARY RESEARCH RESULTS

Studies of the crustal and upper mantle structure of the Eurasian continent have a comparatively long history. Global tomographic models of Nataf *et al.* (1986), Woodhouse & Dziewonski (1989), Masters (1989), Su *et al.* (1994), Zhang & Tanimoto (1993) discovered the presence of significant long-wave lateral inhomogeneities in the Eurasian mantle. Inversion of body wave data for different regions of Eurasia was a subject of numerous papers (e.g., Vinnik & Ryaboy, 1981; Pavlenkova & Egorkin, 1983; Grand & Helmberger, 1985; Goldstein *et al.*, 1992). Surface waves propagating across Eurasia have been analyzed by Nolet (1977), Patton (1980), Feng & Teng (1983), Lerner-Lam & Jordan (1983), Snieder (1988), Zielhuis & Nolet (1993), among others. These studies provided important information about the crustal and upper mantle structure of the continent as a whole and some of its parts. However, the recent dramatic increase in the number of broadband seismic stations deployed in Eurasia opens the opportunity to focus these models and obtain much more detailed 3D elastic and anelastic models of the continent. Of especial interest are the poorly studied regions of Northern, Central and Southern Asia. A natural subject for this scrutiny are surface waves propagating across the Eurasian continent.

Data. Earthquake and nuclear explosion data recorded by the GSN, GEOSCOPE, CDSN, MEDNET broadband networks and the IRIS/Kyrghyz regional network (KNET) during 1988-1995 have been used to study the characteristics of surface wave propagation across Eurasia. Events with surface wave magnitude $M_s > 5.5$ and source depth less than 100 km in and around Eurasia were selected for this purpose. All waveforms which passed quality control and related information were transformed into the CSS 3.0 relational database format before processing. The measurement techniques and data are described in more detail in a companion paper (Ritzwoller *et al.*, 1995). More than 3500 three-component records for different epicenter - station pairs have been analyzed to date. Great circle wave paths corresponding to selected epicenter-station pairs are shown at Figure 1.

Processing. Selected records were processed by means of a frequency-time analysis and floating filtering (Levshin *et al.*, 1989, 1994; Ritzwoller *et al.*, 1995). Results of measurements are group and phase velocity dispersion curves of fundamental Rayleigh and Love waves, so-called "cleaned" waveforms, corresponding to these waves, their amplitude spectra and frequency-dependent azimuthal polarization anomalies. All these measurements are stored in an extension of the CSS 3.0 database system.

Inversion . Group velocity observations were used for constructing preliminary group velocity maps for the region under study for a set of periods between 25 and 250 s with an increment of 25 s. The technique developed by Yanovskaya and Ditmar (1990), and applied to Central Asia group

velocity data by Wu & Levshin (1994), and Wu *et al.* (1995), was used for these purposes. This technique is based on a two-dimensional Backus-Gilbert formalism with some specific smoothness constrains. This method allows the estimation of the spatial resolution for a given path coverage of a studied region.

Group velocity maps. About half of all group velocity measurements were used for preliminary 2D-inversion into group velocity maps. Some resulting maps for Rayleigh and Love waves are shown in Figures 2-7. Significant lateral variations of Rayleigh and Love wave group velocities seen on these maps indicate dramatic changes of lithospheric shear velocity structure across the region. The Tibetan Plateau, the mountain regions of Central Asia, the Siberian Platform, the Indian Shield, as well as some smaller tectonic features, appear on maps as regions of relatively low or high group velocities. The 2D-inversion of all data and 3D-inversion for lithospheric structure of the region is in progress.

CONCLUSIONS AND RECOMMENDATIONS

Analysis of part of the surface wave data compiled from broadband seismological networks and arrays deployed in Eurasia during last 8 years shows a close relation between group velocity maps and tectonic regimes forming the Eurasian continent. We expect further significant improvement in the resolution of these maps when all available data will be used for inversion.

We plan to concentrate our further efforts in the following directions:
(1) Increase by a factor of 2 or 3 the amount of measurements by using the latest available data and continuing to lower the magnitude threshold for event selection.
(2) Enhance and automate the quality control of measurements.
(3) Estimate the internal consistency of group velocity maps by evaluating group time residuals between predicted and observed group arrival times.
(4) Develop techniques for the 3D structural inversion of observed data, including group and phase velocities and polarization anomalies.
(5) Apply these techniques for imaging different tectonic regimes forming Eurasia, with special attention to Central and Southern Asia.

REFERENCES

Feng, C-C., and T-L. Teng, 1983. Three-dimensional crust and upper mantle structure of the Eurasian continent. *J. Geoph. Res.*, **88**, 2261-2272.

Goldstein, P., W. R. Walter, and G. Zandt, 1992. Upper mantle structure beneath Central Eurasia using a source array of nuclear explosions and waveforms at regional distances. *J. Geoph. Res.*, **97**, 14,097-14,113.

Grand, S. P., and D. V. Helmberger, 1985. Uppermantle shear structure beneath Asia from multibounce S waves. *Phys. of the Earth and Planet. Inter.* , **41**, 154-169.

Lerner-Lam, A. L., and T. J. Jordan ,1983. Earth structure from fundamental and higher-mode waveform analysis. *Geoph. J. R. Astron. Soc.*, **76**, 759-797.

Levshin, A. L., T. B. Yanovskaya, A. V. Lander, B. G. Bukchin, M. P. Barmin, L. I. Ratnikova, and E. N. Its, 1989. *Seismic surface waves in a laterally inhomogeneous Earth* , (ed. V. I. Keilis-Borok), Kluwer Publ., Dordrecht.

Levshin, A. L., M. H. Ritzwoller, and L. I. Ratnikova, 1994. The nature and cause of polarization anomalies of surface waves crossing northern and central Eurasia. *Geophys. J. Int.* , **117**, 577-590.

Masters, G., 1989. Seismic modelling of the Earth's large-scale three-dimensional structure. *Phil. Trans. R. Soc. Lond. A*, **328**, 329-349.

Nataf, H. C., I. Nakanishi, and D. L. Anderson, 1986. Measurement of mantle wave velocity and inversion for lateral heterogeneity and anisotropy. III. Inversion. *J. Geophys. Res.*, **91**, 7261-7307.

Patton, H., 1980. Crust and upper mantle structure of the Eurasian continent from the phase velocity and Q of surface waves. *Rev. Geophys. and Space Phys.*, **18**, 605-625.

Pavlenkova, N. I., and A. V. Egorkin, 1983. Upper mantle heterogeneity in the northern part of Eurasia. *Phys. of the Earth and Planet. Inter.* , **33**, 180-193.

Ritzwoller, M. H., A. L. Levshin, S. S. Smith, and C. S. Lee, 1995. Making accurate continental broadband surface wave measurements. *This Volume.*

Snieder, R., 1988. Large-scale waveform inversions of surface waves for lateral heterogeneity. 2. Application to surface waves in Europe and the Mediterranean. *J. Geoph. Res.*, **93**, 12,067-12,080.

Su, W., R. L. Woodward, and A. M. Dziewonski, 1994. Degree-12 Model of shear velocity heterogeneity in the mantle. *J. Geoph. Res.*, *J. Geophys. Res.*, **99**, 6945-6980.

Vinnik, L. P., and V. Z. Ryaboy, 1981. Deep structure of the East European Platform according to seismic data. *Physics of the Earth and Planet. Inter.* , **25**, 27-37.

Woodhouse, J. H., and A. M. Dziewonski, 1986. Seismic modelling of the Earth's large scale three-dimensional structure. *Phil. Trans. R. Soc. Lond. A*, **328**, 291-308.

Wu, F. T., and A. Levshin, 1994. Surface-wave group velocity tomography of East Asia. *Physics of the Earth and Planet. Inter.* , **84**, 59-77.

Wu, F. T., A. L. Levshin, and V. M. Kozhevnikov, 1995. Rayleigh wave group velocity tomography of Siberia, China and the Vicinity. *Geoph. J. Int.* , in press.

Yanovskaya, T. B., and P. G. Ditmar, 1990. Smoothness criteria in surface wave tomography. *Geoph. J. Int.* , **102**, 63-72.

Zhang, Y.-S., and T. Tanimoto, 1993. High-resolution global upper mantle structure and plate tectonics. *J. Geophys. Res.*, **98**, 9793-9823.

Zielhuis, A., and G. Nolet, 1993. Shear-wave velocity variations in the upper mantle beneath Central Europe. *Geophysl. J.Int.*, **117**, 695-715.
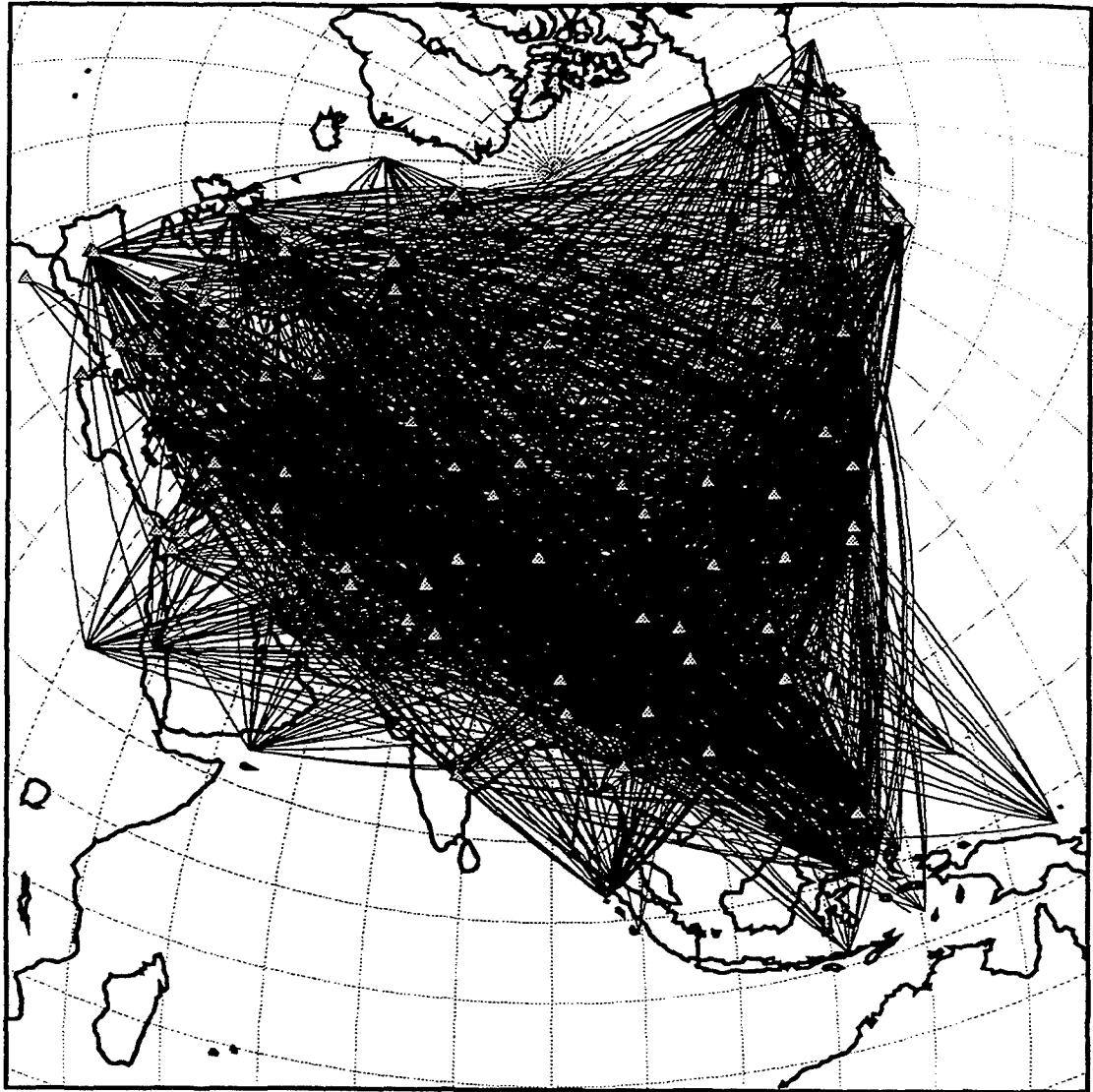
Figure 1. Source-Station Paths used for
Tomographic Inversion of Group
Velocity Data.
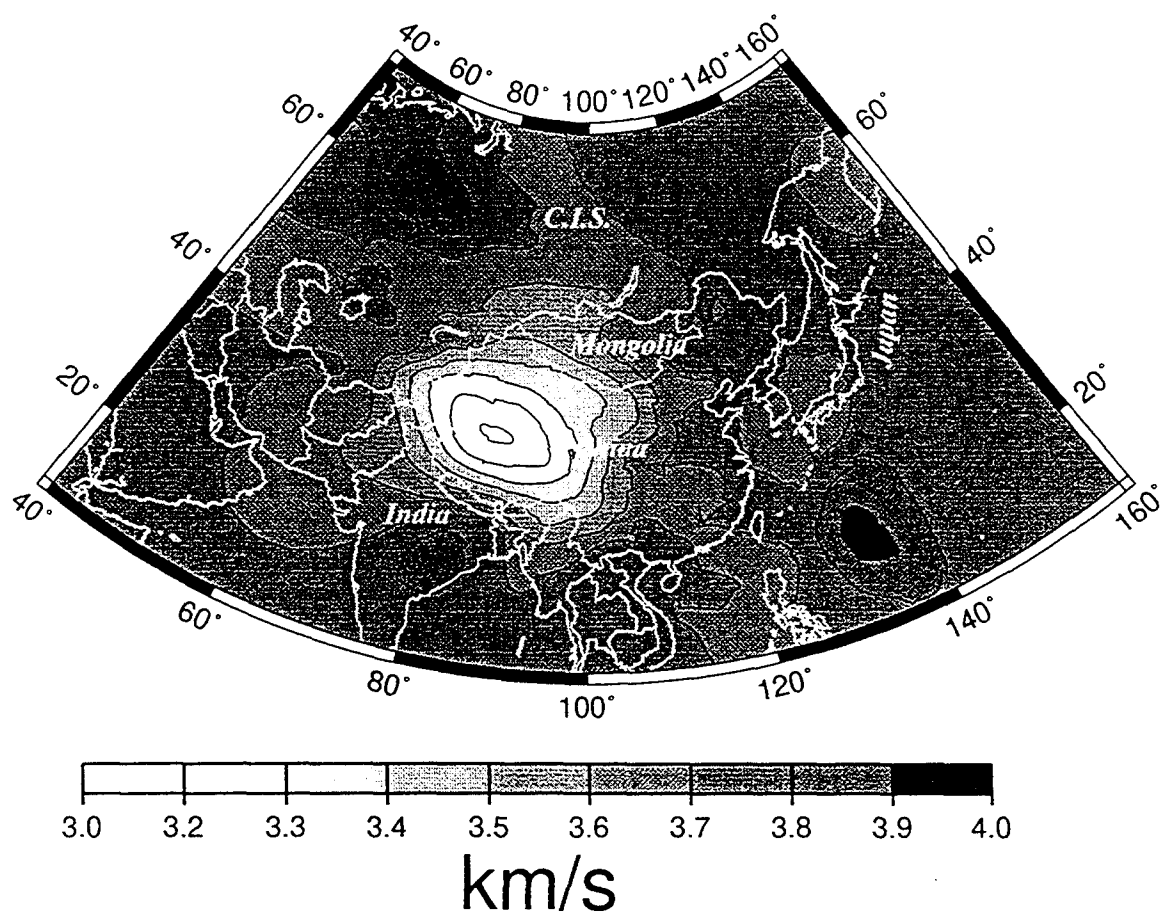
Figure 2. Rayleigh Wave Group
Velocity for T=50 s.
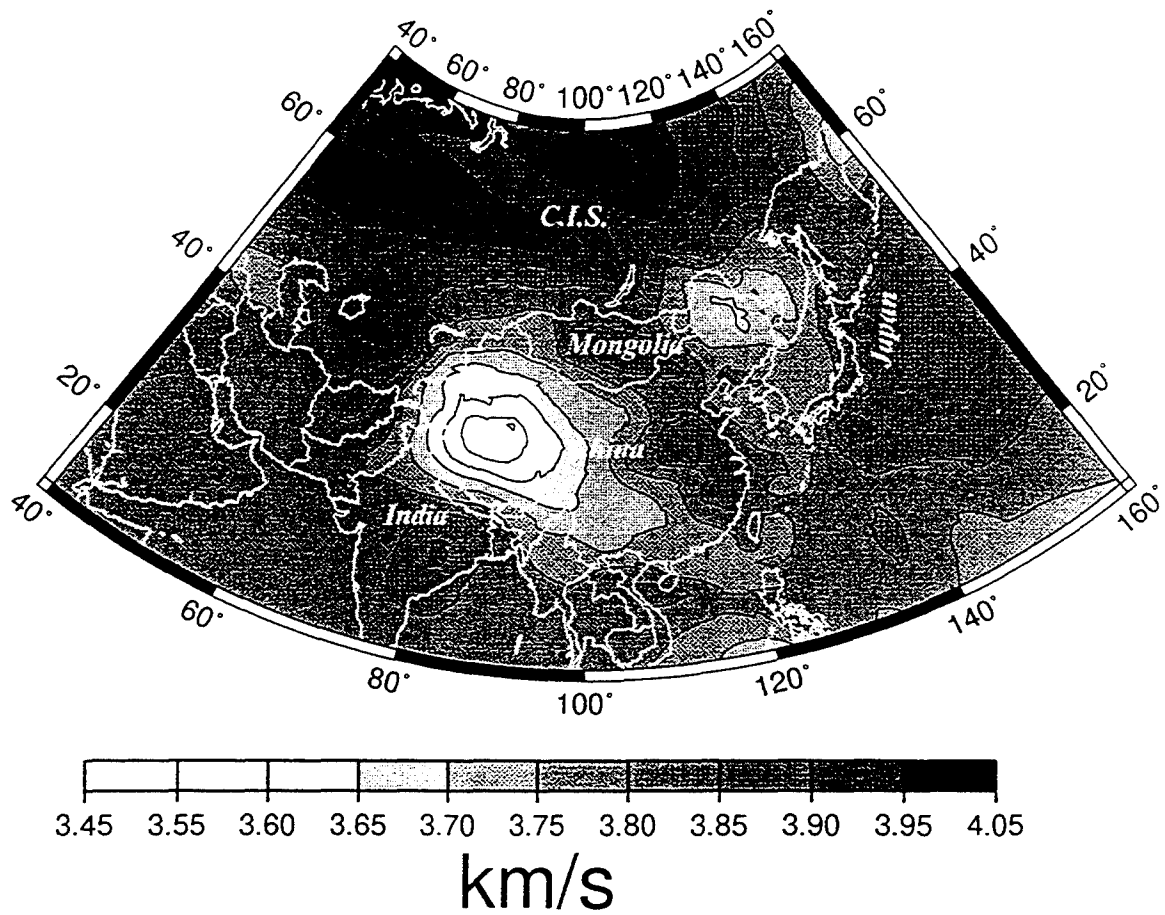
Figure 3. Rayleigh Wave Group
Velocity for T=75 s.
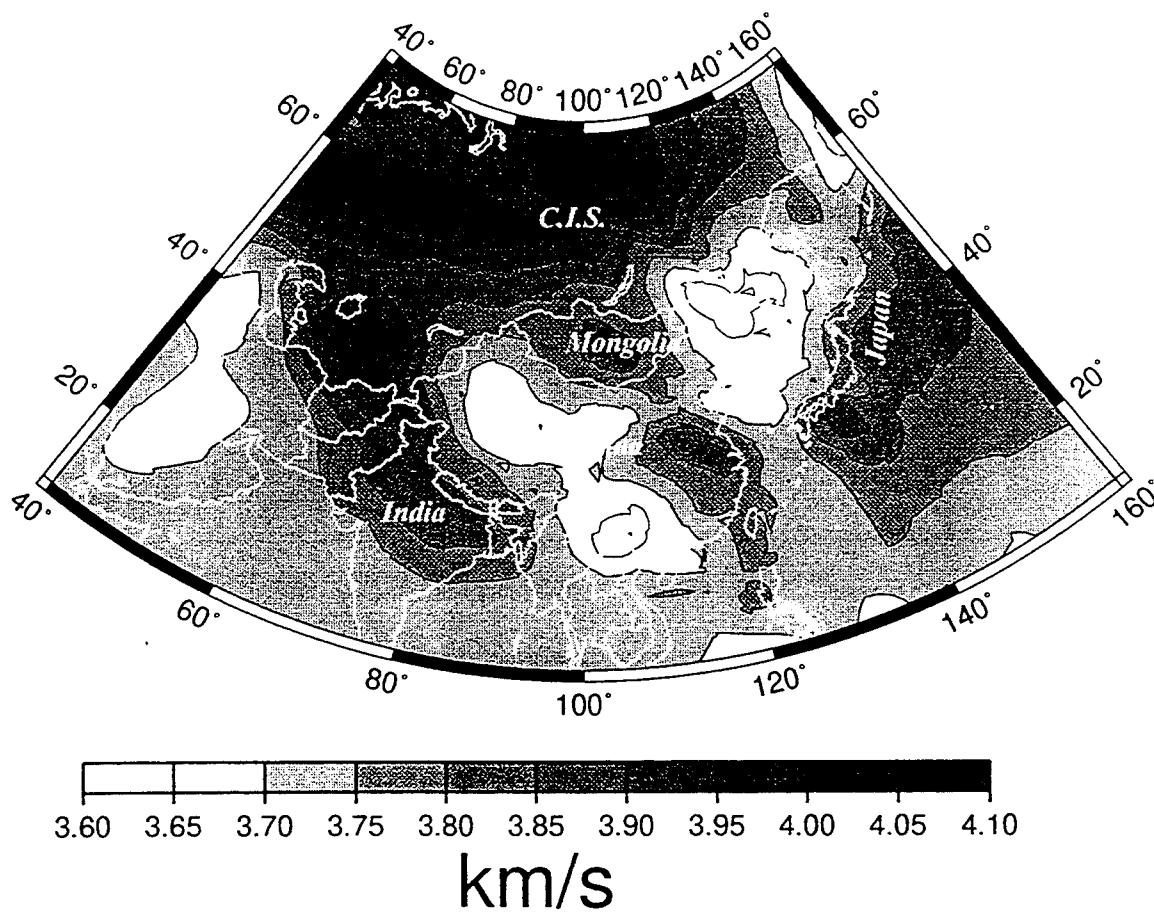
Figure 4. Rayleigh Wave Group
Velocity for T=100 s.
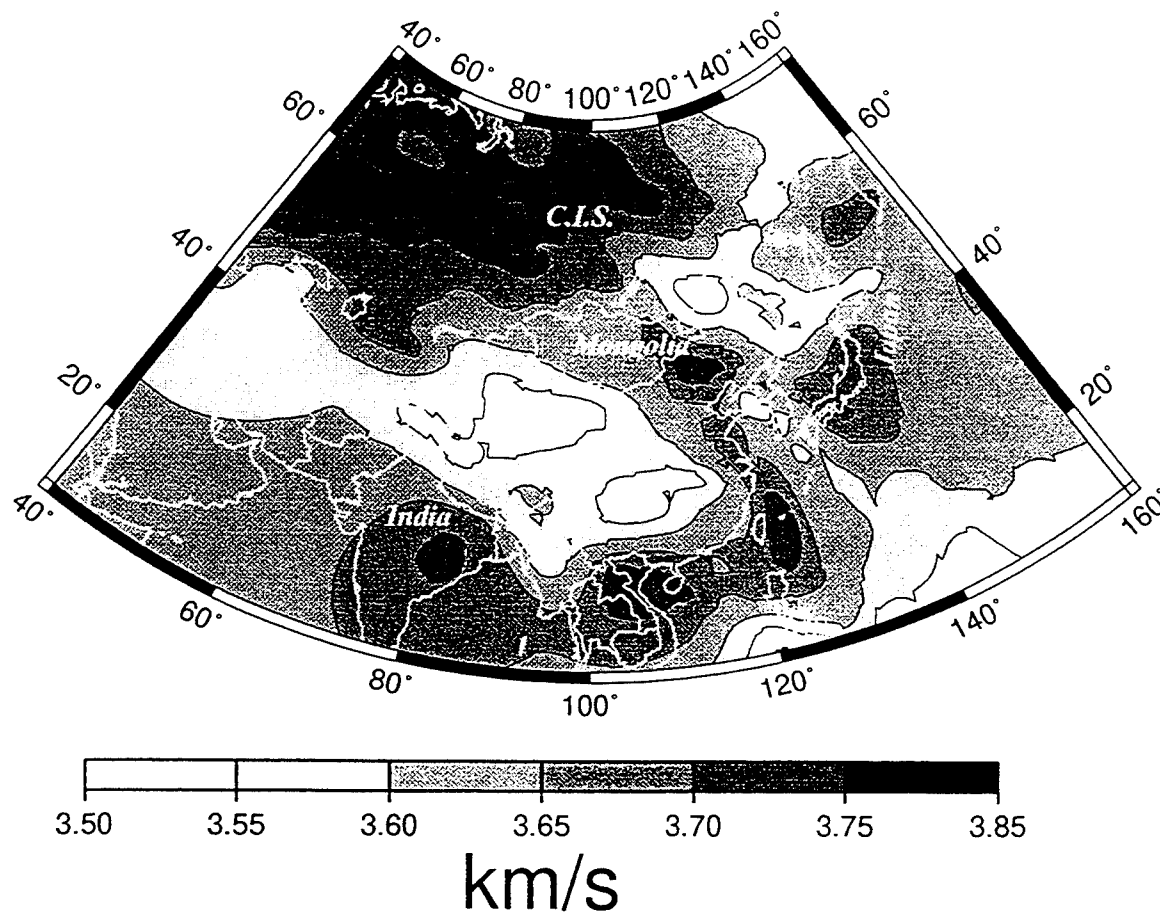
Figure 5. Rayleigh Wave Group
Velocity for T=200 s.
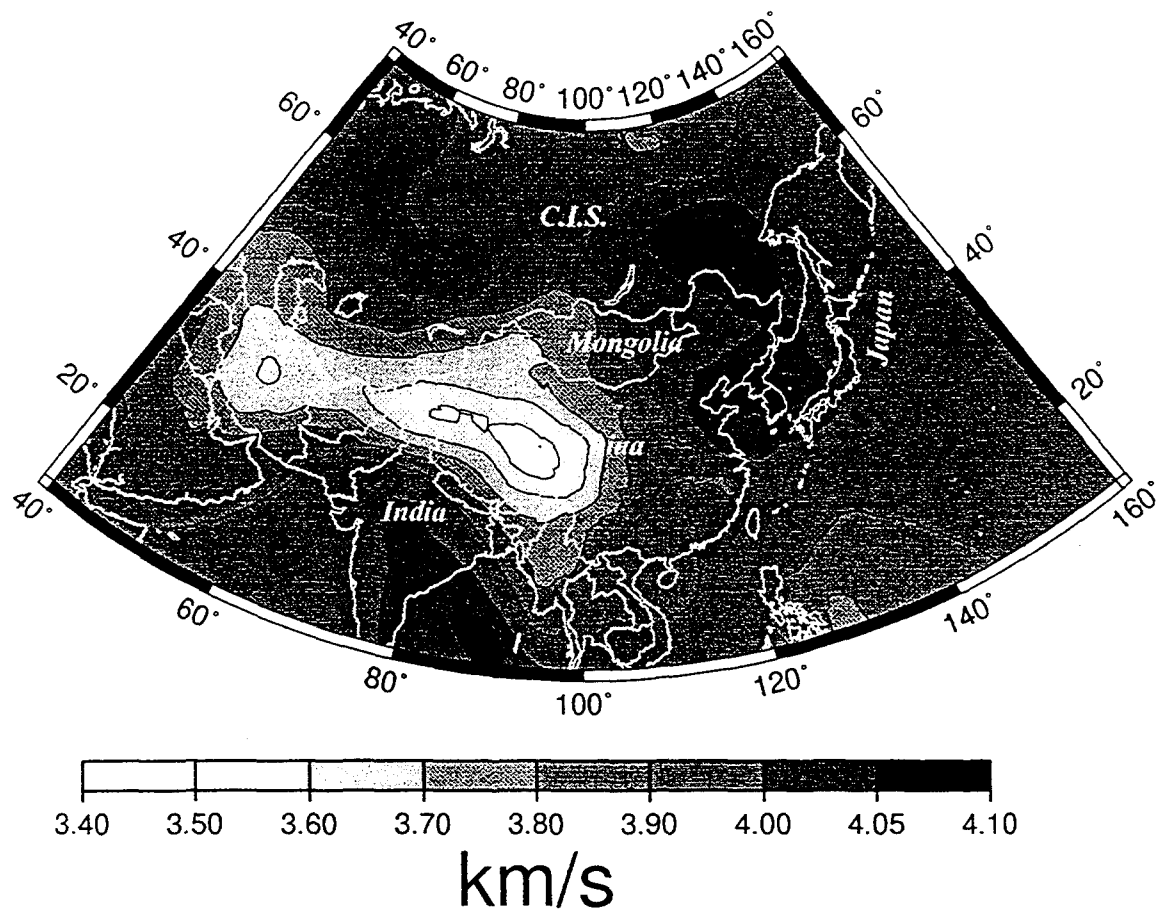
Figure 6. Love Wave Group
Velocity for T=50 s.
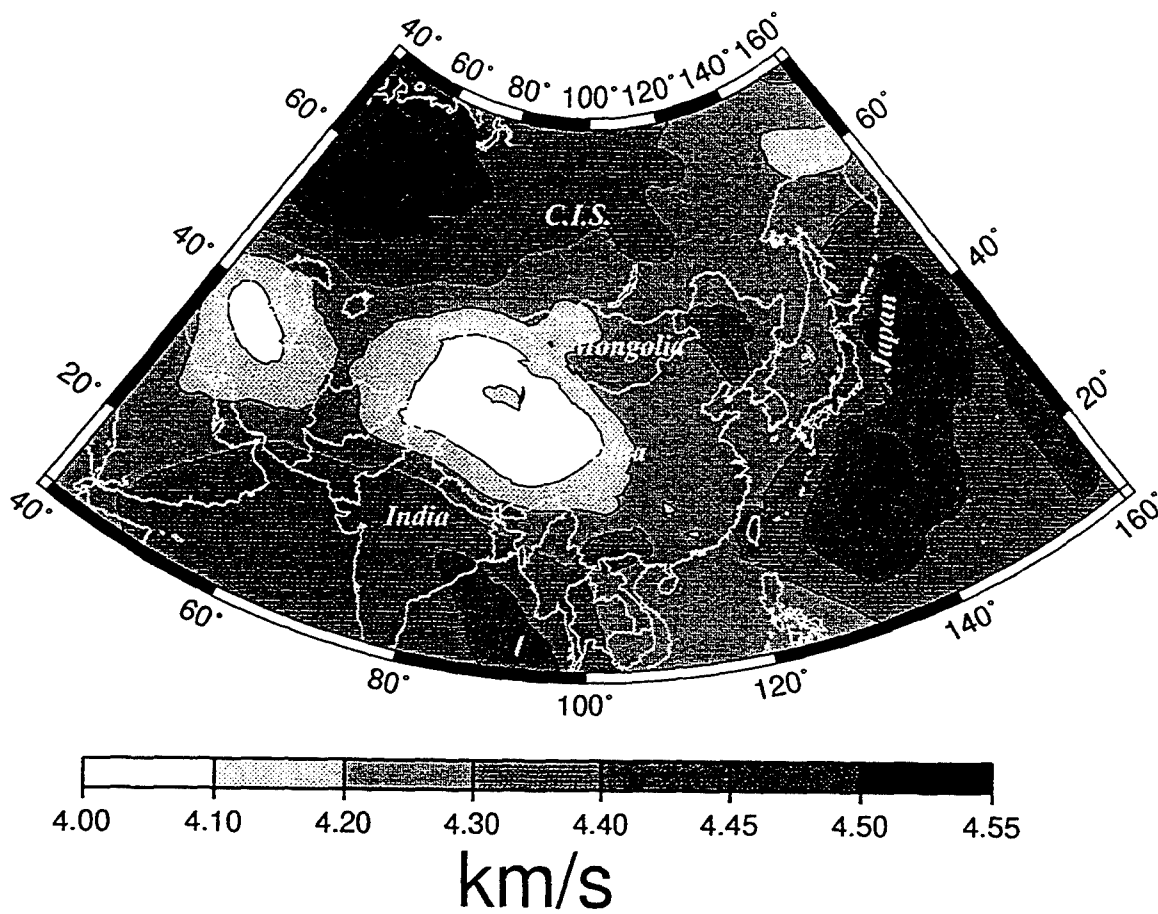
Figure 7. Love Wave Group
Velocity for T=100 s.

Seismic Studies of the Caspian Basin and Surrounding Regions

Stephen Mangino and Keith Priestley

Department of Earth Sciences, Bullard Laboratories, University of Cambridge
Cambridge CB3 0EZ, England

Abstract:

The crust and upper mantle structure of the south Caspian Basin and the Turkmenian Lowlands is enigmatic. From Soviet deep seismic sounding data collected in the 1960's, the crust appears to consists of two layers: a thick sedimentary section (15–25 km) with low P–wave velocity (3.5–4.0 km/s) overlying a 12–18 km thick basaltic lower crust. It has been suggested that this basaltic lower crust is "oceanic–like" crust and that the south Caspian Basin represents a section of relic ocean from a Paleozoic – Triassic ocean or a Mesozoic – Paleogene marginal sea. Improved knowledge of the crust and upper mantle velocity structure of the south Caspian Basin is important in a seismic verification context because of the anomalous effect it has on regional seismic waveforms. To investigate the crust and upper mantle structure of the south Caspian Basin, we have installed six three–component seismograph stations within the former Soviet Republics of Turkmenia and Azerbaijan. Our objective is to determine the velocity structure of this region using both body wave receiver function and surface wave modeling techniques. We present receiver function inversion results for four sites and fundamental mode Rayleigh wave observations for two great circle paths across this region.

Key Words: South Caspian Basin, crust and upper mantle structure, receiver functions, surface wave dispersion

Objectives:

The objective of the research funded by the existing AFOSR grant is to develop models for the crust and upper mantle velocity structure of the south Caspian Basin using body wave receiver function and surface wave dispersion techniques. To accomplish this we have installed six digital three-component seismic stations in the former Soviet republics of Turkmenia and Azerbaijan and have operated these for almost two years. The research objectives of the pending DOE grant are to utilize the seismic data collected under the AFOSR grant and the seismic velocity models developed for the south Caspian Basin for seismic event characterization, regional wave propagation, and discriminant transportability in the Middle East.

Preliminary Research Results and Research Accomplished:

The south Caspian Basin and the Turkmenian Lowlands form an anomalous aseismic depression that is bounded to the north by the Apsheron-Balkhan Sill, a narrow seismogenic zone extending from the Caucuses Mountains in Azerbaijan to the Kopet Dagh Mountains of Turkmenia; and to the west in Azerbaijan and to the south along the Iranian border by the active fold and thrust belts of the Talesh and Alborz Mountains, respectively. The northward movement of the Iranian plate with respect to the Eurasian plate is causing compressional deformation throughout the Caspian region (Jackson and McKenzie, 1984). Mechanisms of earthquakes occurring within the bounding seismic belts of the south Caspian Basin suggest that the crust of the south Caspian Basin is being overriden by the continental crust of the Iranian plateau in the south, and to a lesser extent, by the northern Caspian continental crust (Priestley et al, 1994). In addition, the velocity structure of the south Caspian Basin is poorly known. Deep seismic sounding data collected in the early 1960's suggests that the crust of the south Caspian Basin and west Turkmenian Lowlands consists of two layers: a thick sedimentary layer (15–20 km) with a P-wave velocity of 3.5–4.0 km/s which overlies a 12–18 km thick "basaltic" layer with a P-wave velocity of 6.6–7.0 km/s (Neprochnov 1968; Rezanov and Chamo, 1969). It has been suggested that the south Caspian Basin represents a section of "ocean-like" crust that may be either a relic of an older Paleozoic-Triassic ocean, or a marginal sea which developed behind a Mesozoic-Paleogene ocean (Berberian and King 1981; Berberian 1983). The south Caspian Basin strongly affects the propagation of regional seismic waves. For example, the seismic phase Lg is blocked for paths crossing the south Caspian Basin (Kadinsky-Cade et al, 1981). This has important ramifications for seismic monitoring in the Middle East.

The Caspian Seismic Network: To better understand the crust and upper mantle structure in the south Caspian region and its effect on regional seismic wave propagation, we have installed six, three-component broadband digital seismographs around the south Caspian Sea in the former Soviet republics of Turkmenia and Azerbaijan (Fig. 1). The Turkmenian stations are located near Krasnovosdk (KRV), Nebit Dag (NBD), Dana Tag (DTA) and Kizyl Atrek (KAT); the Azerbaijan the stations are located near Lenkoran (LNK) and Baku (BAK). In June 1994 BAK was relocated 100 km west to Shemaha (SHE). The Turkmenian stations are operated in cooperation with Dr. B. Karryev from the Institute of Seismology of Turkmenia, and the Azerbaijan stations are operated in cooperation with Dr. S. Agamirzoev from the Geophysical Expedition of Azerbaijan. Dr. Mikhail Rozhkov of SYNAPSE oversees the station operation from Moscow. Data at each site is recorded on a Refraction Technology 72a–02 data logger that is equipped with either

238

Omega or GPS timing. Stations KRV, DTA, KAT and LNK have Guralp CMG–3T sensors and stations NBD, BAK and SHE have Geotech SL–210/220 long period sensors. All stations record data continuously at 10 samples per second and some have a triggered data stream at 50 samples per second. We are calibrating each station with a pseudo–random binary input on an annual basis and with a step function at each station visit ($\sim$ 6 weeks). Data is received at Cambridge from Moscow six to nine months after recording.

Analysis of Teleseismic Body Waves: We are using teleseismic body waves to determine the velocity structure beneath the CSN stations and the IRIS station ABKT (Fig. 1). We have measured the backazimuth of the teleseismic P–waves as a function of frequency using a maximum likelihood (Harris, 1990) and multi–taper (Park et al, 1987) approach to determine the magnitude of scattering in the teleseismic P–waveform at each site. This comparison shows that, except at KRV, the majority of the scattering occurs at high frequency ($> \sim 0.5Hz$), which provides a guide in the receiver function analysis.

For each Caspian station we isolated the P to S converted phases in the 30 seconds following the P–wave arrival using the source equalization method (Langston, 1979; Ammon, 1991). Receiver functions were computed to include frequencies up to 0.4 Hz and only the most stable deconvolutions (those with averaging functions that approximate a narrow band Gaussian pulse) were used to infer structure. Events from common source regions were stacked and the variance of the stacked data is used as a measure of coherence of individual Ps arrivals. We studied the response by examining the radial and tangential components as a function of azimuth, and determined a 1–D estimate of the receiver structure using the receiver function inversion method of Ammon et al. (1990). Figure 2 shows the model solutions for ABKT, KRV, NBD, and LNK.

ABKT is located 400 km east of the south Caspian Basin in the Kopet Dag Mountains. The velocity models show a relatively simple structure compared to the south Caspian Basin models. The crust can be divided into two layers separated by a prominent 1 km/s step in velocity between 16–20 km depth. The upper–crust between 2–16 km depth has an average velocity of 5.75 km/s. The lower crust between 20–38 km depth has an average velocity of 7.1 km/s. The crust–mantle transition is gradational and the upper–mantle has a P–wave velocity 8.2 km/s. KRV is located on the eastern shore of the Caspian on the trend of the Apsheron–Balkhan Sill. The velocity models have a strong gradient from 3.7 km/s at the surface to 4 km depth. Between 4 and 17 km depth the average velocity is 6.5 km/s. A step in velocity occurs from 17–21.5 km depth. This very thin crust overlies a relatively constant upper–most mantle with an average velocity of 7.9 km/s. NBD is the only site which may be located within the "ocean–like" crustal region. The velocity models are based on only two events; however, the particle motion between the radial and tangential receiver functions indicate little scattered energy. The shallow crust has a strong gradient from 3.1 km/s at the surface to 7.2 km/s at to 6 km depth. Beneath this layer the average velocity is 5.6 km/s between 10–20 km depth. A step in velocity is present at 20 km depth (similar magnitude to ABKT), followed by a positive gradient that reaches 8.0 km/s at 38–40 km depth. LNK is along the southwestern shore of the Caspian Sea, in the foothills of the Talesh Mountains. The velocity models show a low–velocity upper crust varying from 2.25 km/s at the surface to 4.1 km/s at 6 km depth. Starting at 6 km depth there is a strong positive gradient with a velocity of 7.2 km/s at 12 km depth. Below this the velocity is high but does not reach an upper mantle velocity of 8.0 km/s at 50–52 km depth.

The velocity models beneath each station are considerably different. For KRV, NBD and LNK,

the shallow low velocity upper crust fits the delay of the first pulse on the radial component with respect to the direct P–wave arrival on the vertical component. This delay is not present in the ABKT data. This low velocity uppermost crust is consistent with a sedimentary layer, but beneath NBD it is much less than the previously reported 15–20 km thick. Only at LNK is a relatively thick sedimentary pile present. The 7.2 km/s layer between 6–10 km depth beneath NBD is the most prominent feature of all Caspian models. The velocity of this layer is consistent with ultra–mafic rock velocities and may represent the remnant oceanic crust. It is unlikely that this layer has remained laterally continuous throughout the Turkmenian Lowlands since emplacement, given the level of scattering observed at KAT, where we have so far been unable to obtain a physically realistic 1–D model estimate.

Surface Wave Analysis: The study of Kadinsky–Cade et al. (1981) demonstrated that the seismic phase Lg is largely blocked for paths crossing the south Caspian Basin and this is also apparent in the data we have collected in the region immediately surrounding the Caspian. However, Figure 3 shows that the south Caspian Basin also severely disrupts low frequency fundamental mode surface wave trains. Figure 3a compares broadband seismograms for a mid–Atlantic ridge earthquake propagating along a great circle path between LNK and KAT. The LNK seismogram shows a dispersed fundamental mode wave train ($\sim$ 2400–3000 seconds) followed by scattered surface wave arrivals. The lowest frequency fundamental mode surface wave arrival seen in the LNK seismogram is clear in the KAT seismogram ($\sim$2600–2700 seconds) but the dispersed wave train observed at LNK is largely missing from the KAT seismogram and the overall surface wave amplitude has decreased significantly. Figure 3b compares seismograms for a north Mulucca Sea earthquake propagating along a great circle path between KAT and LNK, i.e., reversing the path of the event in Figure 3a. These seismograms exhibit the same degradation of the surface wave train and show that this is not, for example, an instrumental effect. We have observed this phenomenon for all events propagating along great circle paths across the central portion of the south Caspian Basin.

The great circle path between KRV and KAT crosses the Turkmenian Lowlands. Russian earth scientists have suggested that this region is structurally part of the south Caspian Basin and that the crust in the region consists of 10–15 km of sediment lying on "ocean–like" crust. The deep thickness of sediments is verified from well logs (Sengor, personal communications, 1995). Surface waves propagating along the KRV–KAT great circle path do not show the same disruption (Fig. 4a) as those propagating across the main part of the basin (Fig. 3). Figure 4b shows the fundamental mode Rayleigh wave phase velocity dispersion curve for this path. This curve was computed from four seismogram pairs using a constrained least–squares algorithm (Gomberg et al, 1988). The KRV–KAT phase velocity curve is compared with observed dispersion curves for an ocean basin (Kuo et al, 1962) and a continental tectonic (Knopoff et al, 1966) region. The KRV–KAT phase velocity is high for periods greater than 40 seconds and exceptionally low for periods less than 30 seconds. We do not feel comfortable in interpreting the KRV–KAT phase velocity curve at this time until we have included the past year's data which we have recently received.

Effects on Regional Wave Propagation: The velocity structures from body wave modeling provide some insight of the effects of crustal structure on regional seismic waves propagating across the south Caspian Basin. It is clear from the Caspian data that both longer and shorter

period surface wave trains are greatly scattered or attenuated for travel paths across the Caspian Sea, and to a lesser degree for paths across the Turkmenian Lowlands. The Lg phase is blocked for travel paths across oceanic crust, as well as in regions where the crustal structure includes rapid changes in thickness. If we consider the Lg phase to consist of multiple reflected S waves trapped within the crustal wave guide, then the receiver function modeling results suggest that the blockage is due to the abrupt change in crustal structure from a relatively simple model beneath ABKT to complex models beneath NBD and LNK. Although these are 1–D models and the basin is a 3–D structure, these observations support a scattering mechanism. Recent analysis of the logarithmic rms amplitude ratio of Sn/Lg (Zhang and Lay 1994) has shown that this ratio can be linearly related to changes in surface topography. The southern margins of the Basin and the eastern margin of the Turkmenian Lowlands range from below sea level at LNK up to 2 km in the Alborz Mountains. These features probably contribute to the Lg blockage, but these effects have not been examined to date.

Recommendations and Future Plans:

The research focus under the existing AFOSR grant is for the operation of the digital seismographs in the region surrounding the south Caspian Basin and the analysis of the teleseismic body wave and surface wave data to determine the velocity structure of the crust and upper mantle. Our study has shown that the south Caspian has an anomalous crustal structure and this has a pronounced effect on not only higher frequency regional seismic waveforms but also lower frequency surface waves. The research focus of our new grant will be to use this structural information and the data recorded on the CSN and other seismograph stations in the Middle East to improve understanding of (1) the crust and upper mantle velocity structure of the region south of the Caspian, (2) the amplitude and frequency characteristics of regional seismic phases Pn, Pg, Sn, and Lg, and (3) the source characteristics of moderate size seismic events in the region surrounding and to the south of the Caspian Sea.

We intend to continue work on the crustal structure of the Caspian Basin. Much of our current knowledge of the crustal structure of the south Caspian Basin has come from analyses of Soviet DSS data collected primarily in the 1960's. Little of this data has been available to western seismologists. We have recently obtained funds to digitize these data and reinterpret them with more modern techniques than those available to Soviet seismologists in the 1960's. This work should commence this autumn. While these data are not of comparable quality to modern refraction data, they should help in understanding the crustal structure of this anomalous region.

References

Ammon, C. J., The isolation of receiver effects from teleseismic P waveforms, *Bull. Seism. Soc. Am.*, **81**, 2504–2510, 1991.

Ammon, C. J., G. E. Randall and G. Zandt, On the resolution and non–uniqueness of receiver function inversions, *J. Geophys. Res.*, **95**, 15303–15318, 1990.

Berberian, M., The southern Caspian: A compressional depression floored by trapped, modified oceanic crust, *Can. J. Earth Sci.*, **20**, 163–183, 1983.

Berberian, M. and G. C. P. King, Towards a paleogeography and tectonic evolution of Iran, *Can.*

J. Earth Sci., **18**, 210–265, 1981.

Gomberg, J.S., K.F. Priestley, T.G. Masters, and J.N. Brune, The structure of the crust and upper mantle of northern Mexico, *Geophys. J.*, **94**, 1–20.

Harris, D.B., Comparison of the direction estimation performance of high–frequency seismic arrays and three–component stations, *Bull. Seis. Soc. Am.*, *80*, 1951–1968, 1990.

Jackson, J. A., and D. McKenzie, Active tectonics of the Alpine–Himalayan Belt between western Turkey and Pakistan, *Geophys. J. R. Astr. Soc.*, **77**, 185–264, 1984.

Kadinsky–Cade, K., M. Barazangi, J. Oliver, and B. Isacks, Lateral variations of high–frequency seismic wave propagation at regional distances across the Turkish and Iranian Plateaus, *J. Geophys. Res.*, **86**, 9377–9369, 1981.

Knopoff, L., S. Mueller, and W.L. Pilant, Structure of the crust and upper mantle in the Alps from the phase velocity of Rayleigh waves, *Bull. Seis. Soc. Am.*, *56*, 1009–1044, 1966.

Kuo, J., J. Brune, and M. Major, Rayleigh wave dispersion in the Pacific Ocean for the period range 20 to 140 seconds, *Bull. Seis. Soc. Am.*, *52*, 338–357, 1962.

Langston, C. A., Structure under Mount Rainier, Washington inferred from teleseismic body waves, *J. Geophys. Res.*, **84**, 4749–4762, 1979.

Neprochnov, Y. P., Structure of the earth's crust of epi–continental seas: Caspian, Black, and Mediterranean, *Can. J. Earth Sci.*, **5**, 1037–1043, 1968.

Park, J., F. Vernon and C. R. Lindberg, Frequency dependent polarization analysis of high–frequency seismograms, *J. Geophys. Res.*, **92**, 12,664–12,674, 1987.

Priestley, K., C. Baker and J. Jackson, Implications of earthquake focal mechanism data for the active tectonics of the south Caspian Basin and surrounding regions, *Geophys. J. Int.*, **118**, 111–141, 1994.

Rezanov, I. A. and S. S. Chamo, Reasons for absence of a granitic layer in basins of the South Caspian and Black Sea type, *Can. J. Earth Sci.*, **6**, 671–678, 1969.

Zhang, T., and T. Lay, Analysis of short period regional phase path effects associated with topography in Eurasia, *Bull. Seis. Soc. Am.*, *84*, 119–132, 1994.
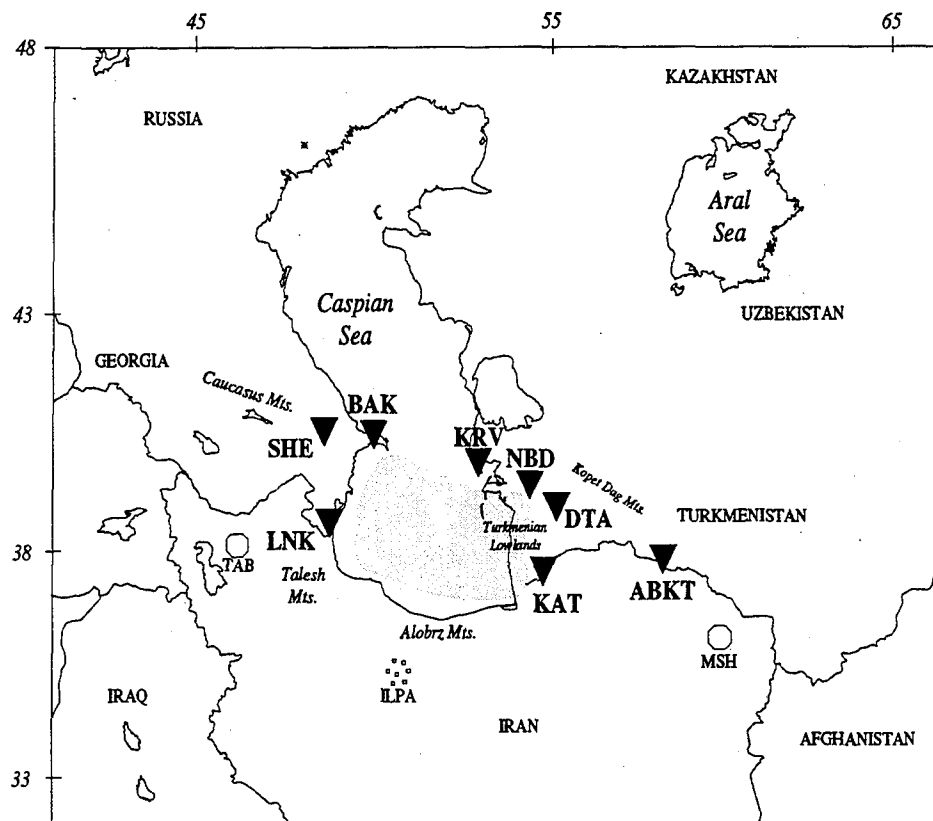
Figure 1. Caspian Seismograph Network stations Krasnovosdk (KRV), Nebit Dag (NBD), Kizyl Atrek (KAT), Dana Tag (DTA), Lenkoran (LNK), Baku (BAK) and Shemaha (SHE). Also shown are WWSSN stations TAB and MSH, the Iranian Long Period Array (ILPA) and IRIS station ABKT. The shaded region denotes the subsurface lateral extent of the suspected "ocean-like" crust.
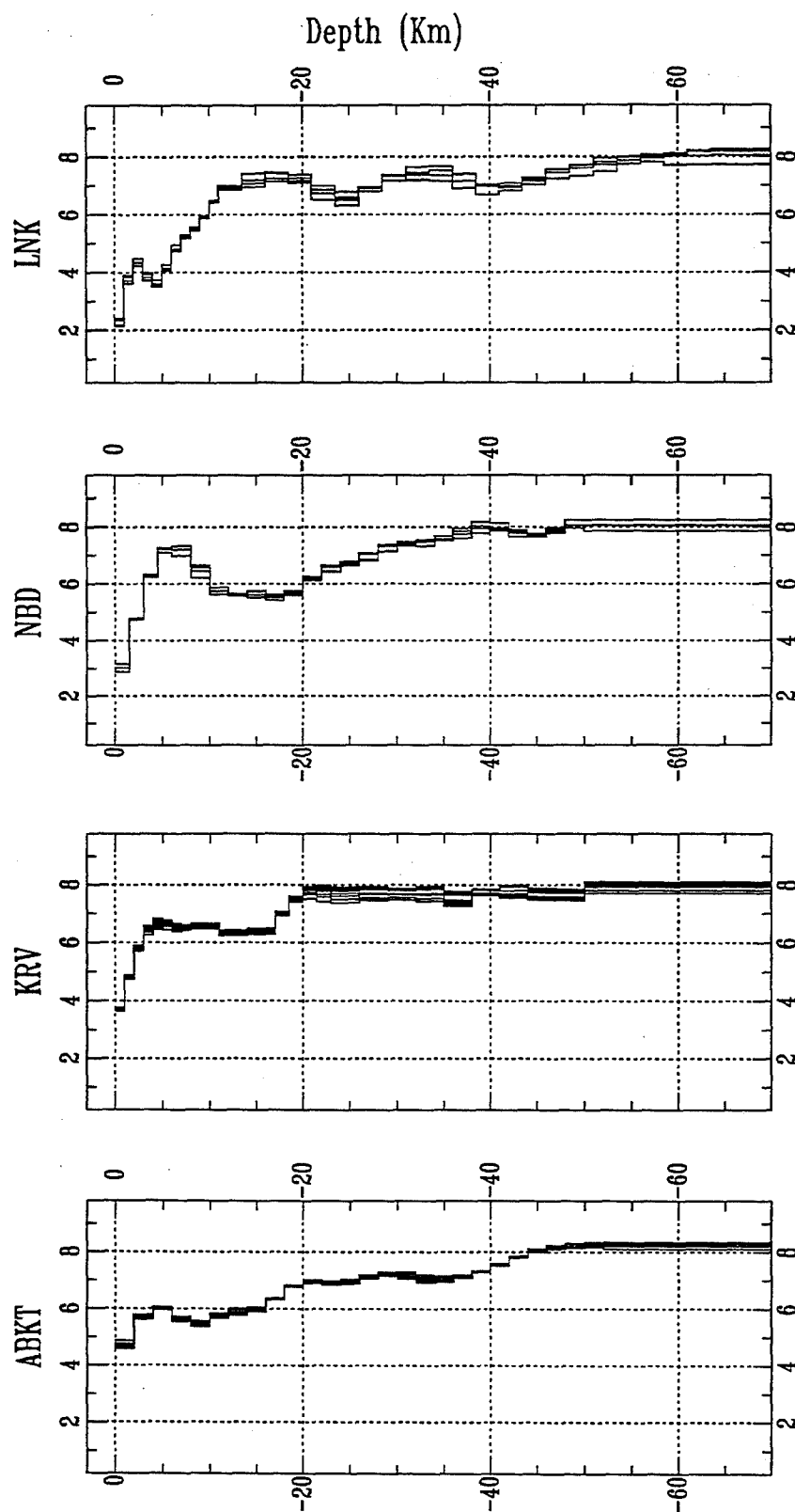
Figure 2. P-wave velocity receiver function modeling results for stations ABKT, KRV, NBD, and LNK
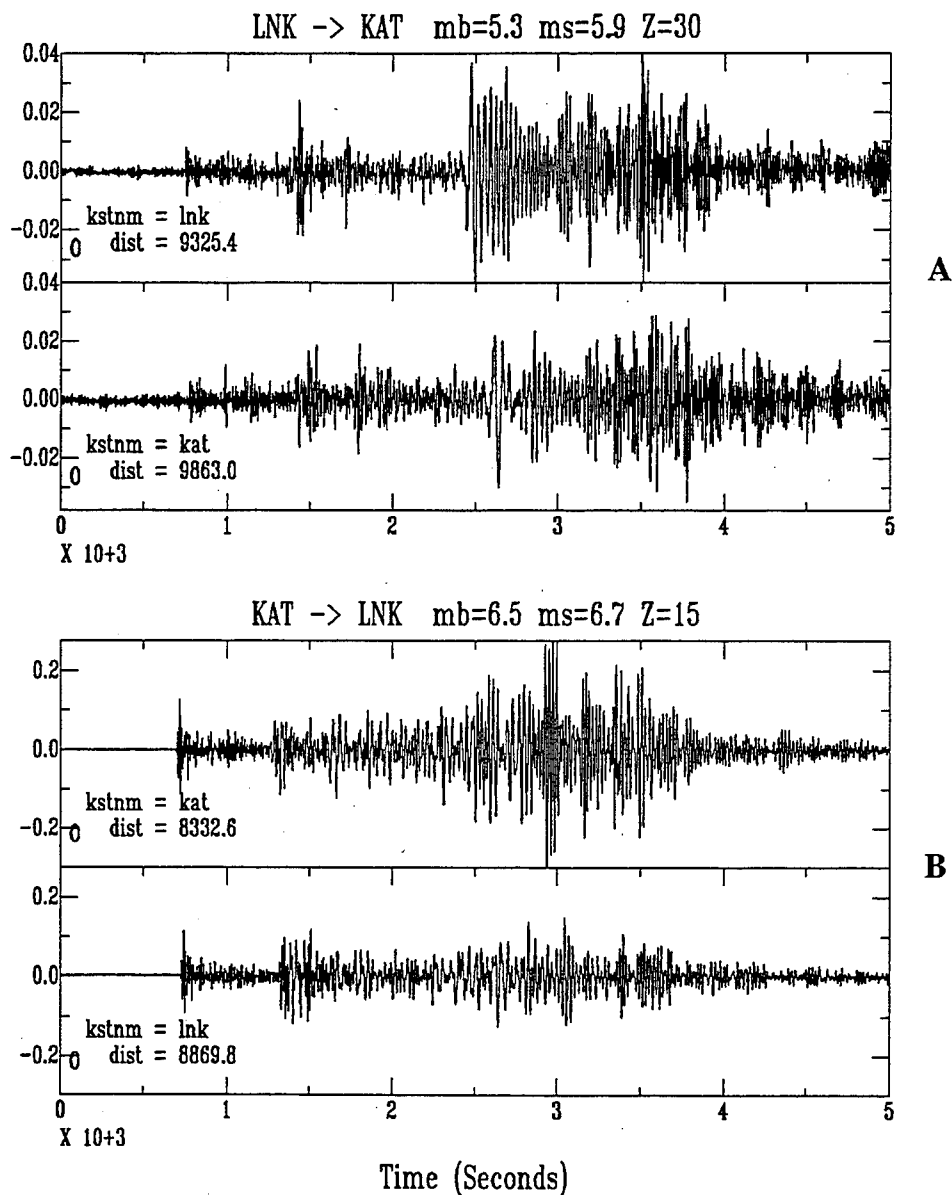
Figure3. Reversed, great circle path vertical component seismograms recorded at CSN stations LNK and KAT. The top figure (A) is a record of a mid-Atlantic ridge earthquake propagating from west to east across the south Caspian Basin, while the lower figure (B) is a larger event from the Mulucca Sea which propagates across the Basin from east to west. Both pairs show considerable degradation of the surface wave train after propagating across the south Caspian Basin. These seismograms are characteristic of all great circle path events across the central portion of the south Caspian Basin.
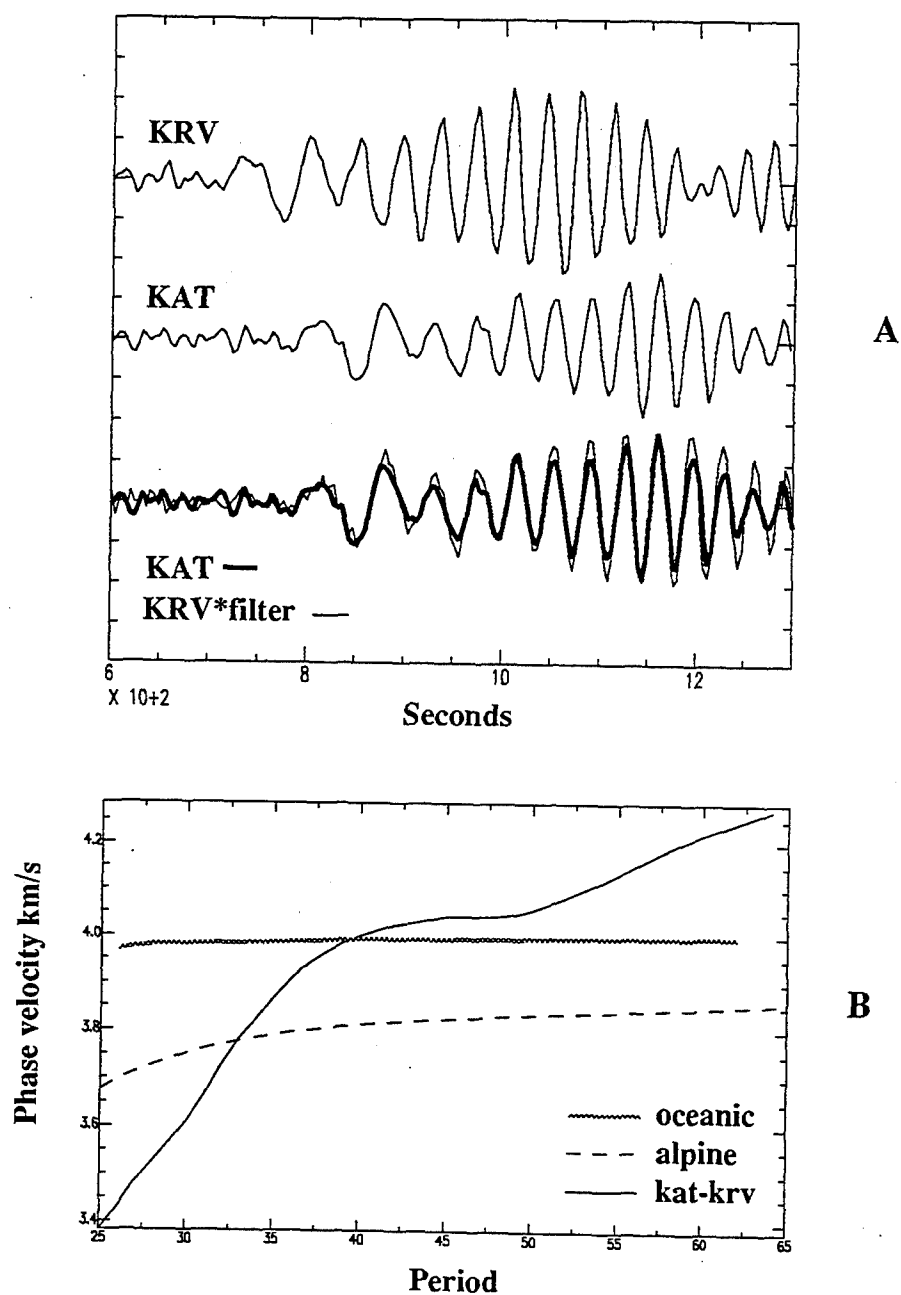
Figure 4. The upper figure (A) shows one of four common great circle path fundamental mode Rayleigh wave pairs used to compute the dispersion results shown in the lower figure (B). Also shown in (A) is the close station filtered with the resulting phase velocity transfer function. The lower figure (B) compares our preliminary results with typical oceanic (Kuo et al. 1962) and Alpine (Knopoff et al. 1966) models.

Propagation of Regional Phases
in Southern Asia and the Middle East

B. J. Mitchell and Y. Pan
Department of Earth & Atmospheric Sciences
Saint Louis University

ABSTRACT

New Lg coda Q values have been determined for Iran using the stacked spectral ratio method. These, combined with values obtained earlier by Ghalib (1992) in the Arabian penninsula and by John (1983) in India, allow us to extend Lg coda Q coverage through much of southern Asia and the Middle East. With the exception of the Indian shield, Q is low throughout all of the region of study. Lg coda Q in the Indian shield is about 1000 but observed values decrease rapidly with distance to the north and west of the shield, being as low as 200 in Pakistan. Lg coda Q is low throughout all of the Middle East with values ranging between about 150 and 300. That variability may be partly due the lateral structural complexity of the region. Portions of some scattering ellipses for the Lg coda data overlap oceanic regions (the Red Sea and the eastern Mediterranean Sea), a situation that has been shown to systematically affect Lg coda Q measurements. We plan to incorporate these Lg coda Q results into inversions of fundamental-mode Rayleigh wave attenuation to obtain frequency-dependent models of shear-wave internal friction for various regions of the Middle East.

Key words: Lg, Lg coda, Q, attenuation

OBJECTIVE

The overall objective of this project is to characterize the efficiency of propagation of regional seismic phases across a broad region extending from India in the east to Turkey and the eastern Mediterranean in the west. Countries in this region include India, Pakistan, Iran, Iraq, Saudi Arabia, Syria, Jordan, Israel, Lebanon, and Turkey. The efficiency of propagation there is likely to be poor, both because instrinsic anelasticity of the crust is low almost everywhere, and because the structure is laterally complex. The number of published studies on seismic wave propagation in that region are still very few. We are studying attenuation over a broad frequency range between about 0.02 and 20 Hz or higher, thus providing information which can be used to ascertain which frequencies will be best for detection and discrimination of small seismic events. In addition to measuring the attenuation of various seismic phases, we will invert surface wave data (in about the 0.02-0.2 Hz range) in selected sub-regions to obtain models of crustal Q and use those models to predict the attenuation of several regional phases at frequencies between 1 and 20 Hz or more. We will compare the attenuation of those predicted phases with corresponding observed phases to determine if attenuation along various paths is due to intrinsic Q or to damping produced by lateral complexities in crustal structure.

PRELIMINARY RESEARCH RESULTS

In order to complete our map of Lg coda Q for Eurasia (Pan, *et al.*, 1992), we have collected seismograms for several paths across the Middle East. We found that many of the seismograms are unusable because the attenuative properties in this region are so high that Lg coda is almost entirely obliterated before it reaches the recording station. We found, however, well-recorded coda for several relatively short paths across Iran. These produced coda Q values of about 200 using the stacked spectral ratio method of Xie and Nuttli (1988).

We have also incorporated the Lg coda Q values of John (1983), for India, and of Ghalib (1992), for the Arabian Peninsula, into our data base. This has allowed us to expand coverage of Lg coda Q to include those regions. Figure 1 displays the scattering ellipses (for a time window late in the coda) for the coda we have studied. For each source-station pair, the source is at one focus and the recording station is at the other focus of the ellipse. Inversion of the measured Lg coda Q values using the tomographic method of Xie and Mitchell (1990a) leads to a new map of regionalized Lg coda Q for Eurasia. The new results indicate that Lg coda Q is about 1000 in the Indian shield but decreases rapidly to both the north and west of the shield. Lg coda Q is very low throughout all of the Middle East, ranging between about 150 and 300. Individual measurements of Lg coda Q are highly variable, even for nearby paths, probably because of the lateral structural complexity of the region. Both the Red Sea and the western end of the Mediterranean Sea lie near the shield and probably bias the Lg coda Q results for some paths. A similar phenomenon was observed by Xie and Mitchell (1990b) in the western United States for paths in which scattering ellipses significantly overlapped the Pacific basin.

The results obtained in the Middle East are consistent with the conclusion of Mitchell (1995) that the degree of seismic attenuation is proportional to the time which has elapsed since the last period of intense tectonic activity in a region. It does not appear to be affected by the age of formation of continental rock. This is especially well illustrated by the Arabian shield where the rocks are of Precambrian age but the region has undergone extensive recent deformation that causes low Q values.

RECOMMENDATIONS AND FUTURE PLANS

We plan to combine the 1-Hz Lg coda Q results with wave attenuation measured for fundamental-mode Rayleigh waves in various parts of the Middle East. The models that result from this process should provide information on how crustal Q varies with depth and with frequency in this complex region.

Because of the complexity of this broad region, it is likely that we will not be able to obtain a one-dimensional model which satisfies all of the data which we hope to collect. In particular, the margins of the Mediterranean and the Red Sea rift may distort or extinguish seismic phases which traverse them. We have tentative plans to install temporary broad-band seismic stations on Cyprus and near the Red Sea to evaluate the degree to which those features affect regional seismic wave forms.

REFERENCES

Ghalib, H.A.A., Seismic Velocity Structure and Attenuation of the Arabian Plate, Ph.D. Diss., Saint Louis University, 313 pp., 1992.

John, V., Coda-Q Studies in the Indian Subcontinent, M.S. Thesis, Saint Louis University, 99 pp., 1983.

Mitchell, B.J., Anelastic structure and evolution of the continental crust and upper mantle from seismic wave attenuation, *Rev. Geophys.*, in press, 1995.

Pan, Y., B.J. Mitchell, J. Xie, and J. Ni, Lg coda Q across northern Eurasia, in Proc. 14th Ann. PL/DARPA Seismic Research Symp., Rpt. No. PL-TR-92-2210, 311-317, 1992, ADA256711.

Xie, J., and O.W. Nuttli, Interpretation of high-frequency coda at large distances: Stochastic modeling and method of inversion, *Geophys. J.*, 95, 579-595, 1988.

Xie, J., and B.J. Mitchell, A back-projection method for imaging large-scale lateral variations of Lg coda Q with application to continental Africa, Geophys. J. Int., 100, 161-181, 1990a.

Xie, J., and B.J. Mitchell, Attenuation of multiphase surface waves in the Basin and Range province, Part I: Lg and Lg coda, *Geophys. J. Int.*, 102, 121-137, 1990b.
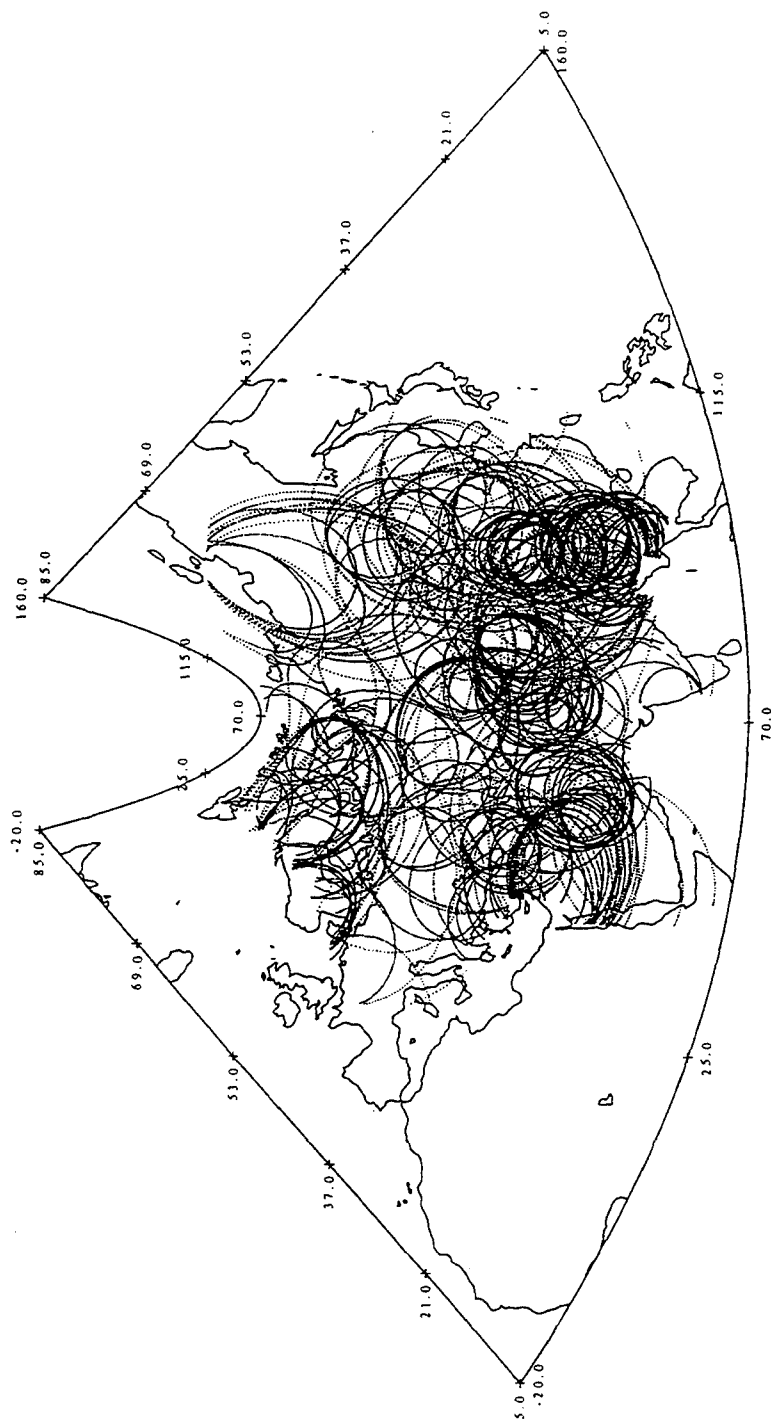
Figure 1. Scattering ellipses for all source-station pairs used to construct the Lg coda map in Figure 2.
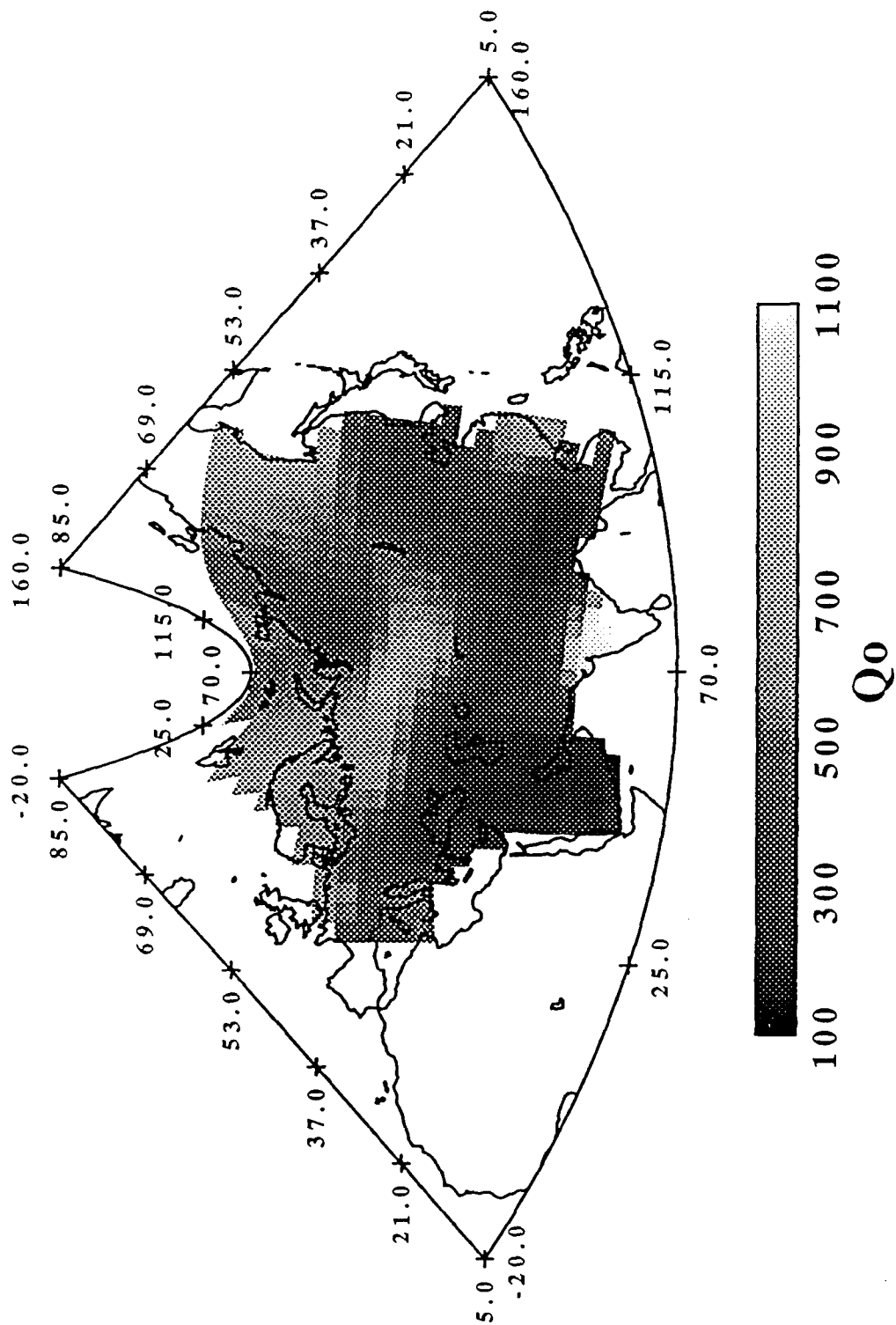
Figure 2. New Lg coda Q map of Eurasia at frequencies near 1 Hz.

Calibration of Local Magnitude Scales For Use in Seismic Monitoring

J. R. Murphy, M. E. Marshall, B. W. Barker, T. J. Bennett,
W. Rivers* and L. Grant*

Maxwell Laboratories, Inc., S-CUBED Division
11800 Sunrise Valley Dr., Suite 1212
Reston, Virginia 22091
Contract No. F19628-91-C-0186
Sponsored by ACDA

Abstract

In situations where cavity decoupling is a plausible evasion scenario, comprehensive monitoring of any eventual CTBT will require the routine identification of many small seismic events with magnitudes in the range $2.0 < m_b < 3.5$. Thus, an important issue in the assessment of monitoring requirements concerns the definition of the numbers and types of events which will generate seismic signals in this magnitude range. This has proved to be a difficult question to answer with any real degree of confidence, because the magnitude values reported for most small events are based on a variety of regional magnitude scales which may not be consistent with the teleseismic m_b magnitude scale which is used to specify seismic monitoring capability. Under this project, we are attempting to quantitatively relate such regional magnitude measures to m_b. This is being accomplished by theoretically scaling observed regional seismic data recorded from tamped underground nuclear tests to obtain estimates of the corresponding seismic signals to be expected from small cavity decoupled nuclear explosions at those same source locations. These synthetic data are processed to determine various local magnitude measures which can then be directly correlated with the known m_b values of these synthetic explosions. This theoretical scaling procedure has now been applied to regional seismic data recorded at the Scandinavian NORESS and ARCESS arrays from tamped Soviet nuclear explosions at the Novaya Zemlya and selected PNE sites and to data recorded at IRIS stations from explosions at the Semipalatinsk and Lop Nor test sites. Results of analyses of these synthetic data indicate that, even for the well-calibrated Scandinavian arrays, regional magnitude measures can show a pronounced dependence on source location and type. For example, since regional magnitude scales are typically calibrated using data recorded from small earthquakes and mine blasts, differences between explosion and earthquake regional phase characteristics, such as the L_g/P ratio, can lead to consistent bias in regional magnitude determinations for explosions. Analyses of the phase and frequency dependence of such biases are currently being conducted in an attempt to define an optimum regional magnitude measure for use in seismic monitoring.

Key Words: Seismic, Magnitude, Regional, Explosion, Cavity Decoupling

* Multimax, Inc., Landover, Maryland

Objective

A central issue in current discussions of the seismic monitoring capability required to adequately verify any eventual Comprehensive Test Ban Treaty (CTBT) concerns the definition of the threshold level of seismic event size or magnitude down to which seismic events will have to be detected and identified. It is generally agreed that the capability currently exists to unambiguously identify almost all seismic events having magnitudes characteristic of well-coupled underground nuclear explosions with yields greater than a few kilotons (i.e., $m_b \sim 4$, OTA (1988)). However, in the context of monitoring a CTBT, consideration has to be given to the requirement to characterize the much smaller signals which would be expected to result from various evasive testing practices which might be employed by a nation pursuing a clandestine nuclear weapons development program. For example, since it has been experimentally demonstrated that it is possible to reduce the amplitude of the radiated seismic signal of an underground nuclear explosion by at least a factor of 70 by employing the cavity decoupling evasion scenario, it follows that comprehensive monitoring of underground nuclear tests in the 1 to 10 kt range will necessarily involve identification analyses of small seismic events with magnitudes in the range $2.0 < m_b < 3.5$. However, since such small events are generally not recorded teleseismically, their magnitudes are typically determined using one of the many proposed regional magnitude scales (M_L). This constitutes a problem in that such regional magnitude measures are defined in terms of seismic phases and frequency bands which are different from those associated with the traditional teleseismic m_b magnitude measure and, consequently, it is not always clear how they relate to the corresponding m_b values which are used to specify seismic monitoring capability. The objective of this project has been to attempt to develop an improved quantitative understanding of the relationship between M_L and m_b for small underground nuclear tests. This has been accomplished through analyses of synthetic data obtained by theoretically scaling observed regional seismic data recorded from tamped underground nuclear tests to obtain estimates of the corresponding seismic signals to be expected from small cavity decoupled nuclear tests at those same source locations.

Research Accomplishments

The scaling procedure used to derive the synthetic regional seismic data analyzed in this study has been described in detail by Murphy and Barker (1994). In this approximation, if the elastic radius of the seismic source of the tamped

reference explosion of yield W_T is denoted as rel_2, then the elastic radius for the corresponding cavity decoupled explosion is

$$rel_1 = \frac{rel_2}{(DF)^{1/3}}$$

where DF denotes the decoupling factor for a particular yield/cavity volume ratio. For each selected tamped explosion we have considered a range of decoupling factors which increase incrementally by factors of 2 such that DF = 2,4,8,..., 70 W_T where 70 W_T corresponds to the case of 1 kt fully decoupled with a low frequency decoupling factor of 70. Now, for values of W_T < 100 kt, the corner frequency of the tamped explosion source generally lies above 1 Hz and, consequently, the m_b values corresponding to such a sequence of partially decoupled synthetic explosions can be approximated simply as

$$m_{bi} = m_b(T) - \log (2,4,8,..., 70 \ W_T)$$

where $m_b(T)$ is the observed m_b value of the tamped explosion with yield W_T. A typical sequence of such source spectrum scaling operators is shown in Figure 1 for the Soviet JVE event, where a nominal seismic yield of about 115 kt has been used for that explosion. It can be seen from this figure that the scaling is strongly frequency dependent over this regional band extending from 0.1 to 20 Hz, particularly for the operators corresponding to the lower yield decoupled explosions. Not surprisingly, such frequency dependent scaling can have some pronounced effects on the characteristics of the corresponding broadband regional seismograms. This is illustrated in Figure 2 which shows the results of scaling the IRIS station GARM recording of the Soviet JVE (Δ = 1380 km) using the range of source scaling operators from Figure 1. It can be seen that in this case the lower frequency L_g and R_g signals are progressively attenuated with respect to the higher frequency P signals as the data are scaled to lower m_b values. Clearly, such large variations in relative phase amplitudes can be expected to have pronounced effects on at least some regional magnitude measures.

The sample of tamped underground nuclear explosions for which regional seismic data were scaled using the above procedures is summarized in Table 1. It can be seen that the first two events in Table 1 were recorded at the ARPA array stations ARCESS and NORESS in Scandinavia, for which extensive magnitude calibration studies have been carried out, leading to a regional magnitude measure which is expressed as a weighted average of individual phase magnitudes determined from measured amplitudes of the P_n, P_g, S_n and L_g arrivals (Bache et al., 1991). The individual phase magnitudes for the scaled

Table 1
Tamped Explosion Data Sample

Event		Station	Estimated Yield, kt	Δ, km
Novaya Zemlya	10/24/90	ARCESS	65	1110
PNE (Archangel)	7/18/85	NORESS	8.5	1564
Soviet JVE	9/14/88	WMQ	115	950
Soviet JVE	9/14/88	GARM	115	1380
Soviet JVE	9/14/88	ARU	115	1530
Lop Nor	8/16/90	GARM	215	1590

Novaya Zemlya 10/24/90 explosion recordings at ARCESS determined using these algorithms are plotted as functions of m_b in Figure 3 where the corresponding $M_L = m_b$ nominal relations are also shown for reference purposes. It can be seen that these individual phase magnitude values show some significant divergences from the expected $M_L = m_b$ relations, with the P_n and S_n values biased high by about 0.6 magnitude units and the L_g values biased low by about 0.4 magnitude units for the smaller events. This broad scatter is presumably due to the fact that the propagation path from Novaya Zemlya to ARCESS is quite different from those of the regional earthquakes and mine blasts used to calibrate the ARCESS magnitude determination algorithms. This example graphically illustrates the fact that, even for well calibrated stations, significant biases can occur for events in locations not represented in the calibration database. Another notable feature illustrated by Figure 3 is the tendency for the explosion Lg magnitudes to be lower than those determined from the other phases. This has been found to be a consistent result of the study, even for well calibrated propagation paths. This fact is illustrated in Figure 4 which shows the various magnitude measures determined from the scaled recordings of Table 1, evaluated at a fixed m_b value of 3.0. Note from the left panel of this figure that the L_g magnitude is lower than the others, even for the well calibrated PNE to NORESS path. It seems likely that this consistent bias is due to differences in the relative phase excitation levels associated with the different source types. That is, since the magnitude determination algorithms are generally calibrated using earthquake and mine blast data, it can be expected that the L_g magnitudes will be biased low for explosion sources due to characteristic differences in the average L_g/P amplitude ratios for these different source types. The right hand panel of Figure 4 illustrates the range of variation in regional phase characteristics for explosions recorded along selected paths in Central Asia. In these examples, the individual

phase magnitudes were again estimated using the Scandinavian algorithms to provide a constant reference base and, consequently, it can be expected that careful path calibration studies could be expected to significantly reduce the variability displayed here. However, these results do serve to emphasize once again the very strong dependence of regional phase characteristics on the properties of the propagation paths. Analyses of the phase and frequency dependence of such biases are continuing in an attempt to define a more optimal regional magnitude measure for use in seismic monitoring.

Conclusions and Recommendations

The definition of meaningful magnitude measures for small seismic events remains as a major unsolved issue affecting assessments of CTBT monitoring requirements. That is, since such events are not expected to be detected teleseismically, their magnitudes will have to be estimated from regional recordings using seismic phases and frequency bands which are different from those employed in the teleseismic m_b scale which is generally used to specify seismic monitoring capability. In this study, we have attempted to quantitatively relate these different magnitude measures by theoretically scaling regional seismic data observed from tamped underground nuclear explosions to obtain improved estimates of the corresponding signals to be expected from low yield cavity decoupled explosions at a variety of different source locations. Analyses of these synthetic data have indicated that, even for well calibrated stations such as the ARPA Scandinavian arrays, traditional regional magnitude measures can show a pronounced dependence on source type and location. In particular, it has been demonstrated that differences between explosion and earthquake regional phase characteristics, such as the average L_g/P ratio, can lead to consistent biases between regional magnitude estimates for explosions and earthquakes having comparable m_b values. Such biases and associated uncertainties should be carefully considered in the definition of required magnitude monitoring thresholds for any eventual CTBT.

References

Bache, T. C., S. R. Bratt, J. W. Given, T. D. Schroeder, H. J. Swanger, and J. Wang (1991), The Intelligent Monitoring System Version 2, NMRD Quarterly Technical Report #7, October 1991, SAIC Report, San Diego.

Murphy, J. R. and B. W. Barker (1994), "Seismic Identification Analyses of Cavity Decoupled Nuclear and Chemical Explosions," S-CUBED Technical Report SSS-TR-94-14399 (PL-TR-94-2036). ADA280947

Office of Technology Assessment (1988), "Seismic Verification of Nuclear Testing Treaties," OTA-SC-361, Government Printing Office, Washington, DC.
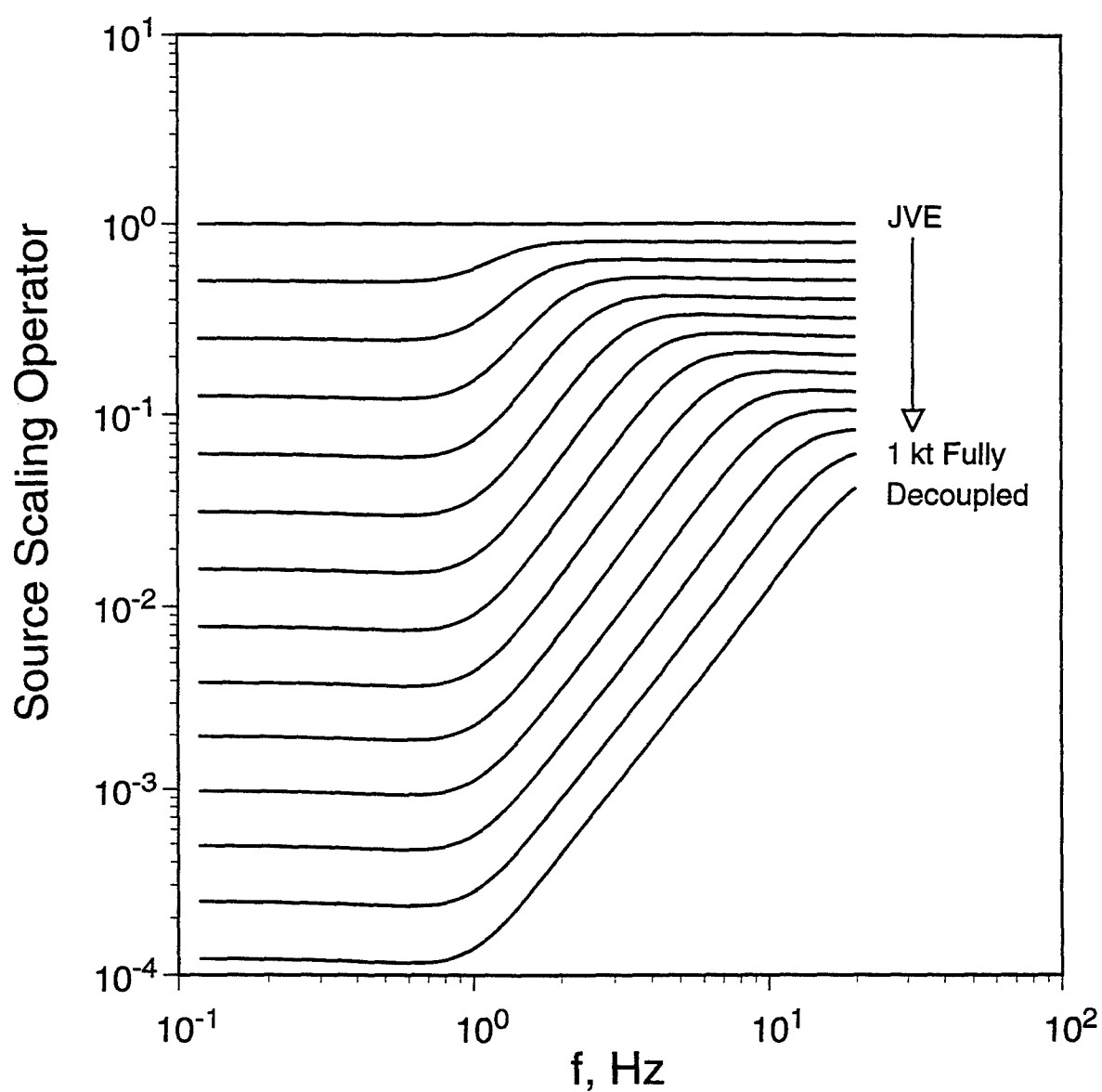
Figure 1. Frequency dependent source scaling operators used to theoretically scale observed regional recordings from the Soviet JVE to simulate the signals expected from various cavity decoupling scenarios.
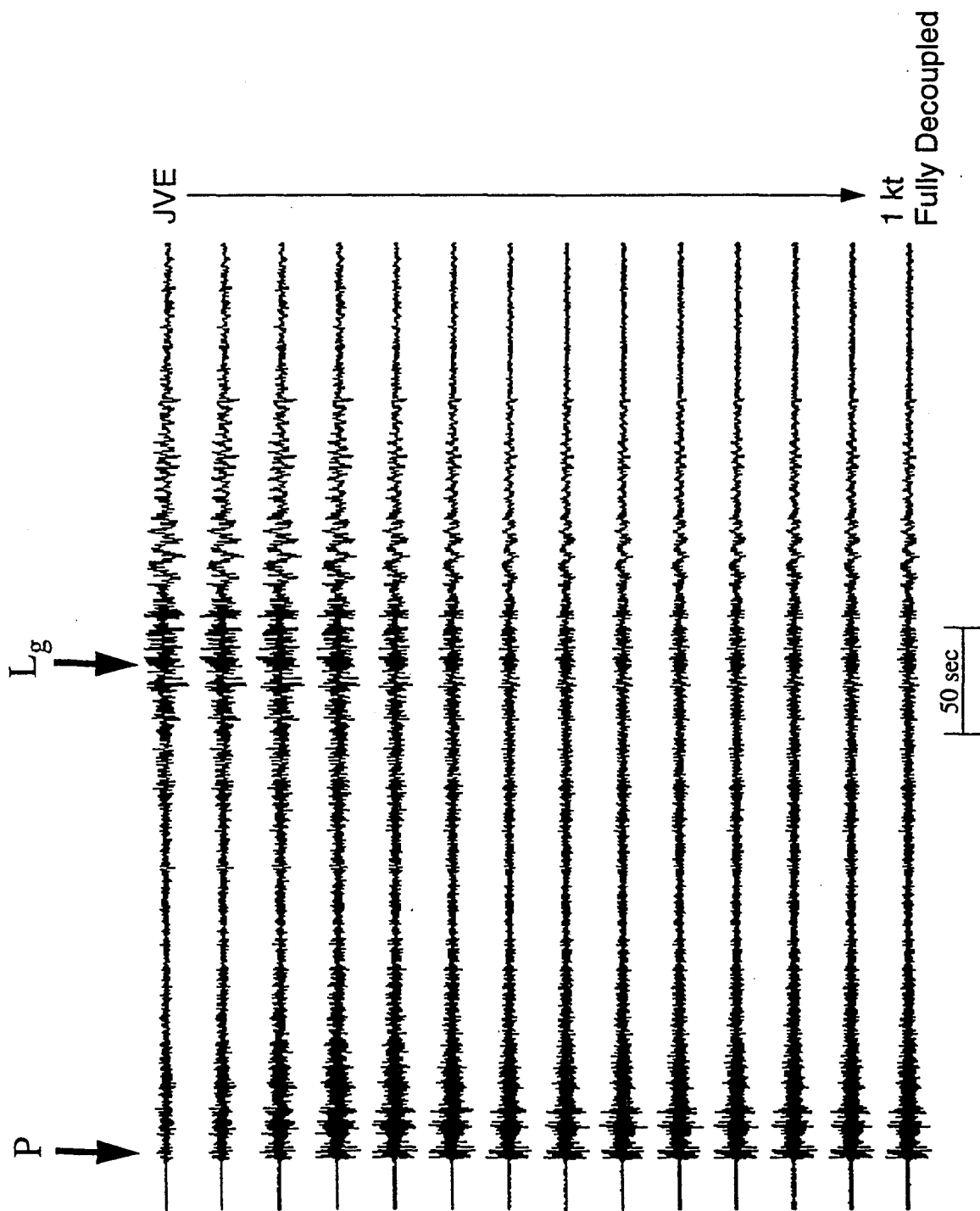
Figure 2. Synthetic cavity decoupled regional seismograms obtained by applying the theoretical source scaling operators of Figure 1 to the IRIS station GARM (Δ = 1380 km) recording of the Soviet JVE.
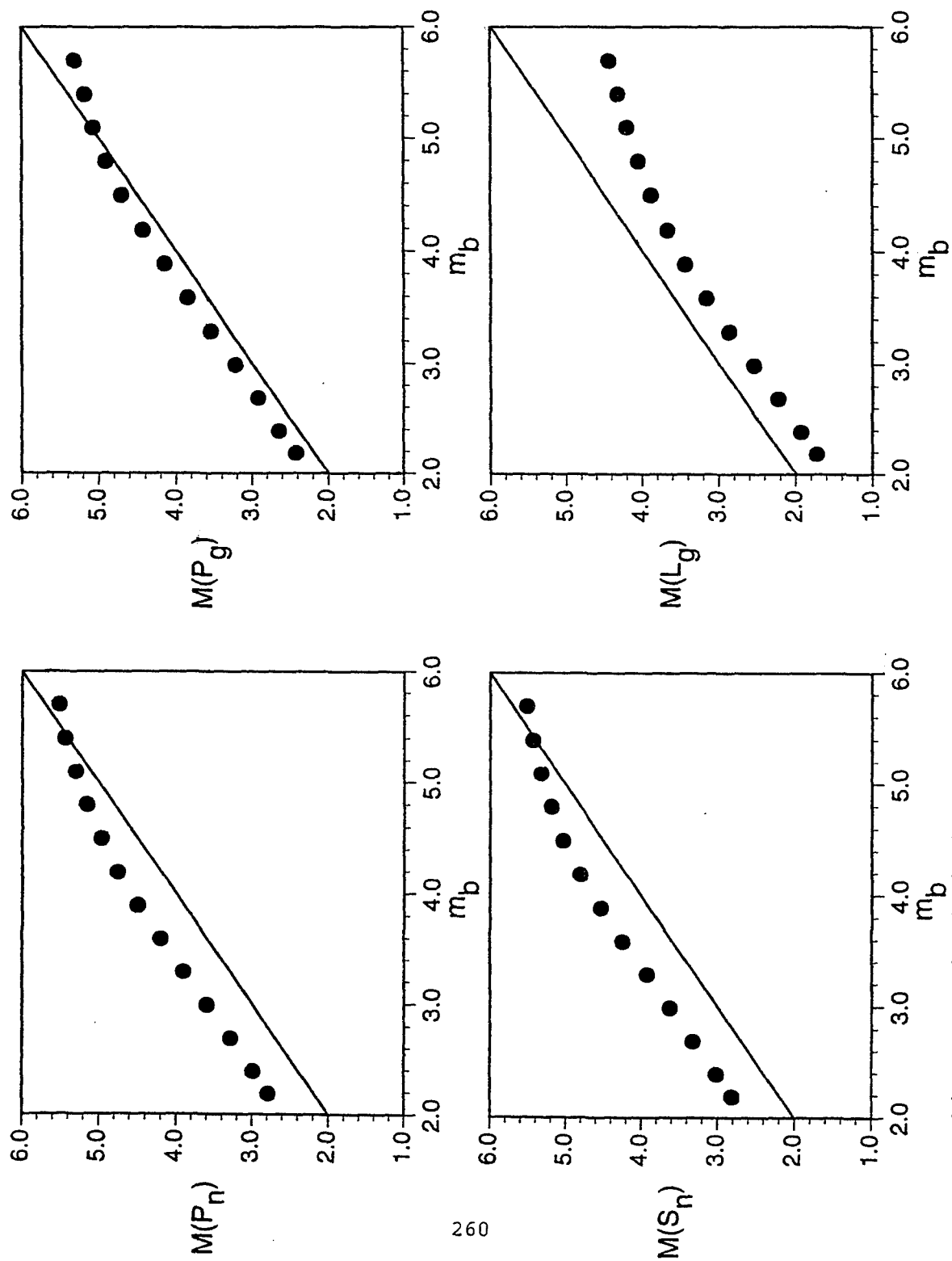
Figure 3. Regional seismic magnitudes as functions of m_b derived from source scaled versions of the ARCESS recording of the Novaya Zemlya nuclear explosion of 10/24/90.
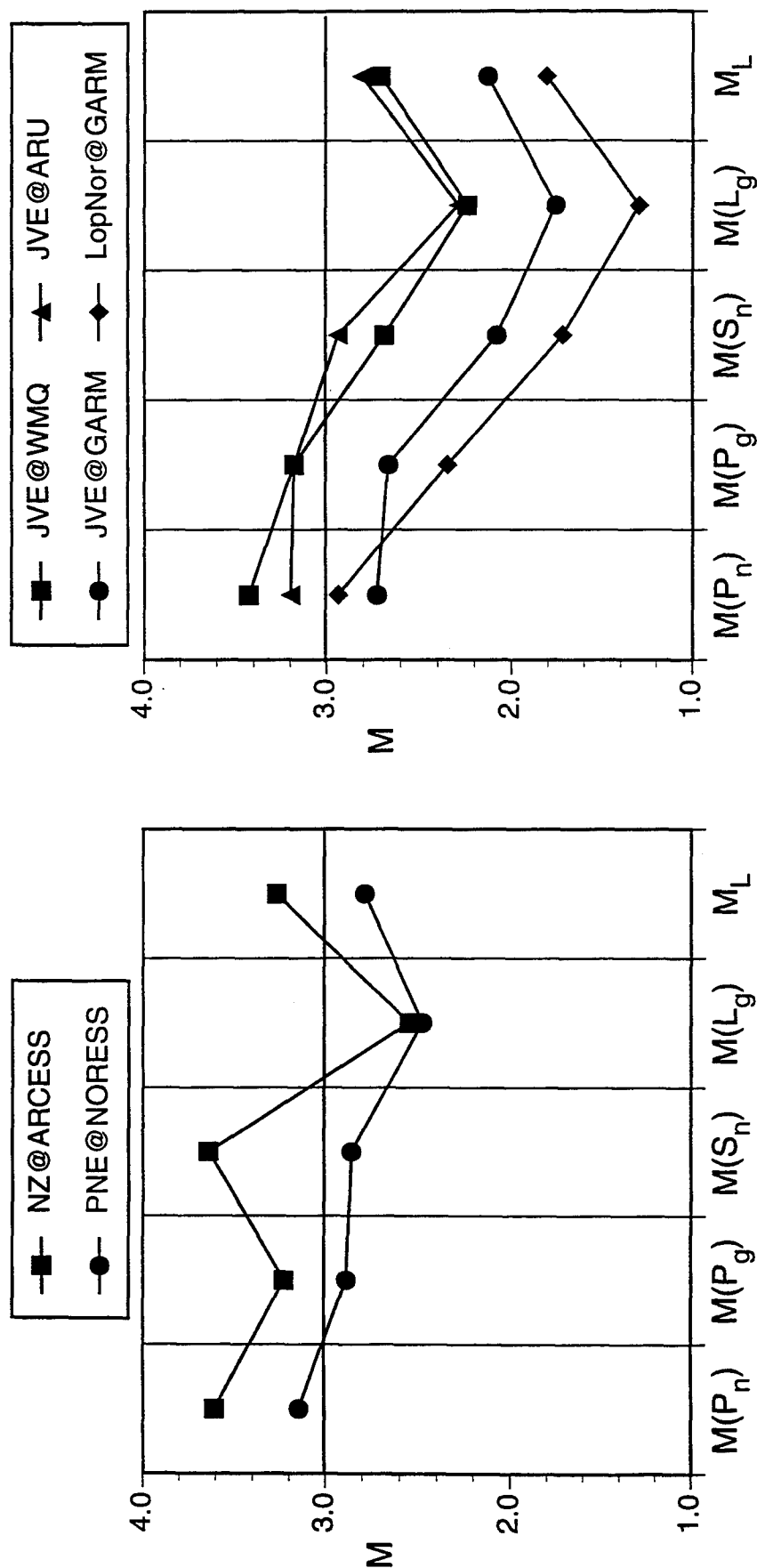
Figure 4. Variations of regional seismic magnitude measures for $m_b = 3.0$ explosions in Scandinavia (left) and Central Asia (right).

Regional Wave Propagation Characteristics in China and Southern Asia

James Ni, Richard Rapine, Jianxin Wu and Thomas Hearn
New Mexico State University, Department of Physics
Las Cruces, NM 88003

Abstract

Regional wave propagation studies are currently an important focus of research because of concerns over proliferation of nuclear weapons. Regional studies serve a twofold purpose: (1) regional data can provide stable yield estimates for underground nuclear explosions, and (2) regional data can discriminate between explosions and earthquakes. Yield and discrimination studies have often used the Sn and Lg regional phases. However, discriminants based on these types of regional data are generally not transportable and must be individually calibrated for a particular region. For China and Southern Asia the problem has been a lack of recorded local and regional events. The first step to alleviate this problem is to increase the database of regional seismic data and their associated ground truth information. To achieve this goal we have documented the regional waveform characteristics of bandpassed (0.5 -5 Hz) digital data collected by the Chinese Digital Seismic Network (CDSN). Our current work has concentrated mostly on mapping Sn and Lg propagation efficiencies, especially beneath the continental plateaus.

The northern Tibet Plateau seems to attenuate most Sn, but southern and eastern Tibet often have weak, but visible, Sn propagation. Sn also does not propagate efficiently beneath the Mongolian Plateau, southeast China, the Baikal Rift, the east China Rift, and Indochina. Events occurring on the Pacific Rim also lack the Sn phase. Paths of efficient Sn propagation exist in central China , in northeast China, and within the Tarim Basin and the Tien Shan. With some notable exceptions, we observe, then, that Sn seems to be attenuated for most tectonically active regions (Tibet, Mongolia, Indochina, the east China Rift, and the west Pacific), while it is not attenuated within the more stable regions of eastern China. Since Sn is often attenuated where Pn velocities are low, we conclude that a small amount of partial melt within the mantle may be responsible for much of the Sn attenuation within Asia. Alternatively, a very thin mantle lid with a negative S-velocity gradient could also diminish Sn.

Lg propagates efficiently for ray paths that are nearly perpendicular to the Himalayas, but it is rapidly attenuated for paths traveling parallel to the mountain range. Lg does, however, propagate well for paths within the Tien Shan and the Tarim Basin. Within the Tibetan Plateau, Lg is observed for paths with distances less than about 6 degrees. Lg is highly attenuated when ray paths cross western or northern Tibet, the eastern Himalayan Syntaxis or Indochina. Lg propagates well for northeast and north central China as well as Mongolia. Lg propagates efficiently across the Taiwan strait, but is clearly attenuated for all raypaths crossing any oceanic crust. In general, Lg is seen more often than Sn. Our observations are consistent with Lg being attenuated primarily by rapid variations in crustal structure such as changes from continental crust to oceanic crust. Crustal changes across the Himalayan front are not enough to fully attenuate Lg unless a substantial portion of the Himalayas is crossed.

Key words: China, Tibet, Sn, Lg, attenuation.

Regional Wave Propagation Characteristics in China and Southern Asia

Objective

Regional wave propagation studies are currently an important focus of research because of concerns over proliferation of nuclear weapons. Regional studies serve a twofold purpose: (1) regional data can provide stable yield estimates for underground nuclear explosions, and (2) regional data can discriminate between explosions and earthquakes. Yield and discrimination studies have often used the Sn and Lg regional phases. However, discriminants based on these types of regional data are generally not transportable and must be individually calibrated for a particular region. For China and Southern Asia the problem has been a lack of recorded local and regional events. The first step to alleviate this problem is to increase the database of regional seismic data and their associated ground truth information. To achieve this goal we have documented the regional waveform characteristics of bandpassed (0.5 -5 Hz) digital data collected by the Chinese Digital Seismic Network (CDSN) (Figure 1). Our current work has concentrated mostly on mapping Sn and Lg propagation efficiencies, especially beneath the continental plateaus. We are interested in the relationship between the propagation of these phases and regional tectonics.

Research Accomplished

The character of Pn, Pg, Sn and Lg propagation was used to constrain structure and provide insights into the tectonic processes, most notably in structurally complex areas such as the Middle East, Central Asia and the Tibetan Plateau (Ruzaikan et al., 1977, Kadinsky-Cade et al., 1981, Ni and Barazangi, 1983, 1984). In these studies short-period analog seismograms were used to qualitatively characterize broad tectonic provinces and subprovinces in terms of either efficient or inefficient Sn and Lg propagation. Quantitative analysis of the Lg phases and the Pnl phase was also conducted (e.g. Kennett 1986; Xie and Lay, 1994). Our approach to documenting the characteristics of observed regional phases is empirical. When propagation paths cross some tectonic regions, the amplitudes of particular regional phases are dramatically reduced.

During the past year we have nearly completed analyzing regional wave propagation characteristics from broadband data recorded by the CDSN stations (Figure 1). We examined over 8000 seismograms. Sn and Lg propagation efficiencies from regional events to each station are mapped. These maps rank Sn and Lg propagation efficiency based on the amplitude of Sn or Lg relative to Pn: "A" classification is for very efficient propagation where the amplitude of either Sn or Lg is similar to or larger than half the amplitude of the Pn wave; "B" classification is for attenuated Sn or Lg phases with amplitudes less than half that of the Pn wave; "C" classification is used when Sn or Lg are not observed. We present results from eight CDSN stations.

For station LSA (Lhasa; Figure 2), Sn propagates efficiently across the Himalayas. In contrast, Sn does not propagate through a large portion of the central and northern Tibet. In southern Tibet, Sn propagation efficiency is reduced when compared with those traversing

mainly the Himalayas. Lg does not propagate efficiently (B and C classification) across the Himalayas when the ray path is subparallel to the Himalayas; however, Lg is observed for those ray paths that are more perpendicular to the strike of the mountain belt. Within the Tibetan Plateau, Lg is observed only for paths with distances less than about 6 degrees. We also observed that the Indus Tsangpo Suture attenuates most crustal phases. The attenuation is probably due to a partially melted upper crust rather than the complex structure in the suture.

For station WMQ (Urumqi; Figure 3), Sn is observed from crustal events originating in the western Himalayas, the Pamirs and the Tien Shan. Paths crossing the Tarim Basin are all efficient. A few paths from eastern Tibet show efficient Sn propagation, but the majority of events in Tibet do not show Sn. The Mongolian Plateau does not allow Sn to propagate either. Lack of efficient Sn propagation beneath these plateaus indicates that the uppermost mantle beneath them may be partially melted; possibly analogous with the mantle beneath the Turkish-Iranian Plateau or the Basin and Range Province (Hearn & Ni, 1994; Rodgers et al, 1995). Lg is observed for most raypaths, especially those ray paths that cross Mongolia, Tien Shan and Tarim Basin. Only a few of the longer paths from Tibet have Lg completely eliminated.

For station LZH (Lanzhou; Figure 4), Sn is observed for those crustal events originating from the Tarim Basin and the southern Tien Shan. Most events north and east of the station also show good Sn; however, there are a few events occurring in eastern China that also show no Sn. Events crossing Tibet from the southwest also have no Sn. Lg is observed from northern China events with epicentral distances less than about 10 degrees. Lg records for rays originating at all azimuths except the southwest azimuth (eastern Tibet). For those ray paths traversing a large portion of western Tibet, Lg is no longer observed.

For station BJI (Beijing; Figure 5), Sn is only observed for some nearby events. This is probably due to the fact that BJI is located in the eastern China rift system which may be underlain by an attenuated upper mantle. In contrast to Sn, Lg propagates efficiently from all the events we looked at.

For station MDJ (Mudnjiang; Figure 6), in northeast China, Sn is weak for events occurring near Lake Baikal and is not seen from events in Mongolia or north-central China. Sn is almost never detected from any of the many western Pacific events. Lg propagates efficiently to station MDJ from all continental paths, but is fully attenuated for all west Pacific events. This is consistent with other observations that have repeatedly shown Lg to be attenuated when crossing any oceanic crust.

For station QIZ (Qiongzhong; on Hainan Island; Figure 7), Sn is not observed for those ray paths crossing Indochina. In late Cenozoic, a large part of the Indochina is a back-arc and the uppermantle may still be hot there. Thus, the observed Sn propagation is consistent with known geology. Sn is also not usually seen for events in the west Pacific (Philippines and Borneo) although a few events with weak Sn do arrive from near Taiwan. Lg is seen from earthquake travel from Taiwan; these events travel beneath the continental shelf and do not cross any oceanic crust. Events that do lie across oceanic crust (Philippines and Borneo) always have Lg completely extinguished. Lg propagates weakly from paths that traverse Burma and most of the Indochina.

Station KMI (Kunming; Figure 8), sees Sn only from paths from eastern China, but all other paths (from Tibet and Indochina) do not have Sn. This is most likely due to the attenuation associated with the eastern China rift system. Lg is seen from nearly all azimuths at this station, but longer Lg raypaths (>10 degrees) are more attenuated.

Station TLY (Talaya; Figure 9), at the southern end of Lake Baikal, has paths that travel along Lake Baikal or cross Mongolia. All of these paths have no Sn propagation but do have efficient Lg propagation. We suspect that the Sn phase may be attenuating due to partial melt

264

within the uppermost mantle beneath the Baikal Rift and beneath the Mongolian Plateau. Lg propagates efficiently since there are no major changes in crustal thickness for any of these paths.

Conclusions and Recommendations

The northern Tibet Plateau seems to attenuate most Sn, but southern and eastern Tibet often have weak, but visible, Sn propagation. This zone of Sn attenuation roughly corresponds to a zone of low Pn velocity in central Tibet (e.g., Zhao and Helmberger, 1992). Sn also does not propagate efficiently beneath the Mongolian Plateau, southeast China, the Baikal Rift, the east China Rift, and Indochina. Events occurring on the Pacific Rim also lack the Sn phase. Paths of efficient Sn propagation exist in central China (near station LZH), in northeast China, and within the Tarim Basin and the Tien Shan. With some notable exceptions, we observe, then, that Sn seems to be attenuated for most tectonically active regions (Tibet, Mongolia, Indochina, the east China Rift, and the west Pacific), while it is not attenuated within the more stable regions of eastern China. Since Sn is often attenuated where Pn velocities are low, we conclude that a small amount of partial melt within the mantle may be responsible for much of the Sn attenuation within Asia. Alternatively, a very thin mantle lid with a negative S-velocity gradient could also diminish Sn.

Lg propagates efficiently for ray paths that are nearly perpendicular to the Himalayas, but it is rapidly attenuated for paths traveling parallel to the mountain range. Lg does, however, propagate well for paths within the Tien Shan and the Tarim Basin. Within the Tibetan Plateau, Lg is observed for paths with distances less than about 6 degrees. Lg is highly attenuated when ray paths cross western or northern Tibet, the eastern Himalayan Syntaxis or Indochina. Lg propagates well for northeast and north central China as well as Mongolia. Lg propagates efficiently across the Taiwan strait, but is clearly attenuated for all raypaths crossing any oceanic crust. In general, Lg is seen more often than Sn. Our observations are consistent with Lg being attenuated primarily by rapid variations in crustal structure such as changes from continental crust to oceanic crust. Crustal changes across the Himalayan front are not enough to fully attenuate Lg unless a substantial portion of the Himalayas is crossed.

The Sn data in China is sufficiently large now and we plan to do a Sn tomography map for this geologically very interesting region. We are also planning to compare the Sn attenuation results to apparent Pn velocities in the region. The Lg data set is also suited for a tomographic study of Lg attenuation in China.

References

Kadinsky-Cade, K., M. Barazangi, J. Oliver, & B. Isacks, Lateral variations of high-frequency seismic wave propagation at regional distances across the Turkish and Iranian Plateaus, *J. Geophys. Res., 86,* 9377-9396, 1981.

Kennett, B., Lg waves and structural boundaries, *Bull. Seism. Soc. Am., 76,* 1133-1141, 1986.

Hearn, T. and J. Ni, Pn velocities beneath continental collision zones: the Turkish-Iranian Plateau, *Geophys. J. Int.,* 117, 273-283, 1994

Ni, J., & M. Barazangi, Seismicity and tectonics of the Zagros and a comparison with the Himalayas, *J. Geophys. Res., 91,* 8205-8218, 1986.

Ni, J., & M. Barazangi, Seismotectonics of the Himalaya Collision Zone: Geometry of the underthrusting Indian Plate beneath the Himalaya, *J. Geophys. Res., 89,* 1147-1164, 1984.

Ni, J., & M. Barazangi, Velocities and propagation characteristics of Pn, Pg, Sn, and Lg seismic waves beneath the Indian Shield, Himalayan Arc, Tibetan Plateau, and surrounding regions:

High uppermost mantle velocities and efficient Sn propagation beneath Tibet, *Geophys. J. R. Astr. Soc. 72,* 665-689, 1983.

Nuttli, O., Seismic wave attenuation and magnitude relations for eastern North America, *J. Geophys. Res., 78,* 876-885, 1973.

Rodgers, A., J. Ni, & T. Hearn, Pn, Sn and Lg propagation in the Middle East, submitted to the *Bull. Seis. Soc. Am.,* 1995.

Ruzaikin, A., I. Nersesov, V. Khalturin, V, & P. Molnar, Propagation of Lg, and lateral variations in crustal structure in Asia, *J. Geophys. Res., 82,* 307-316.

Xie, X., & T. Lay, The excitation of Lg waves by explosions: A finite-difference investigation, *Bull. Seism. Soc. Am., 84,* 324-342, 1994.

Zhao, L., J. Xie, & D. Helmberger, Tomography of the Tibetan Plateau from Pn travel times, Seis. Res. Lett., 63, 43, 1992.
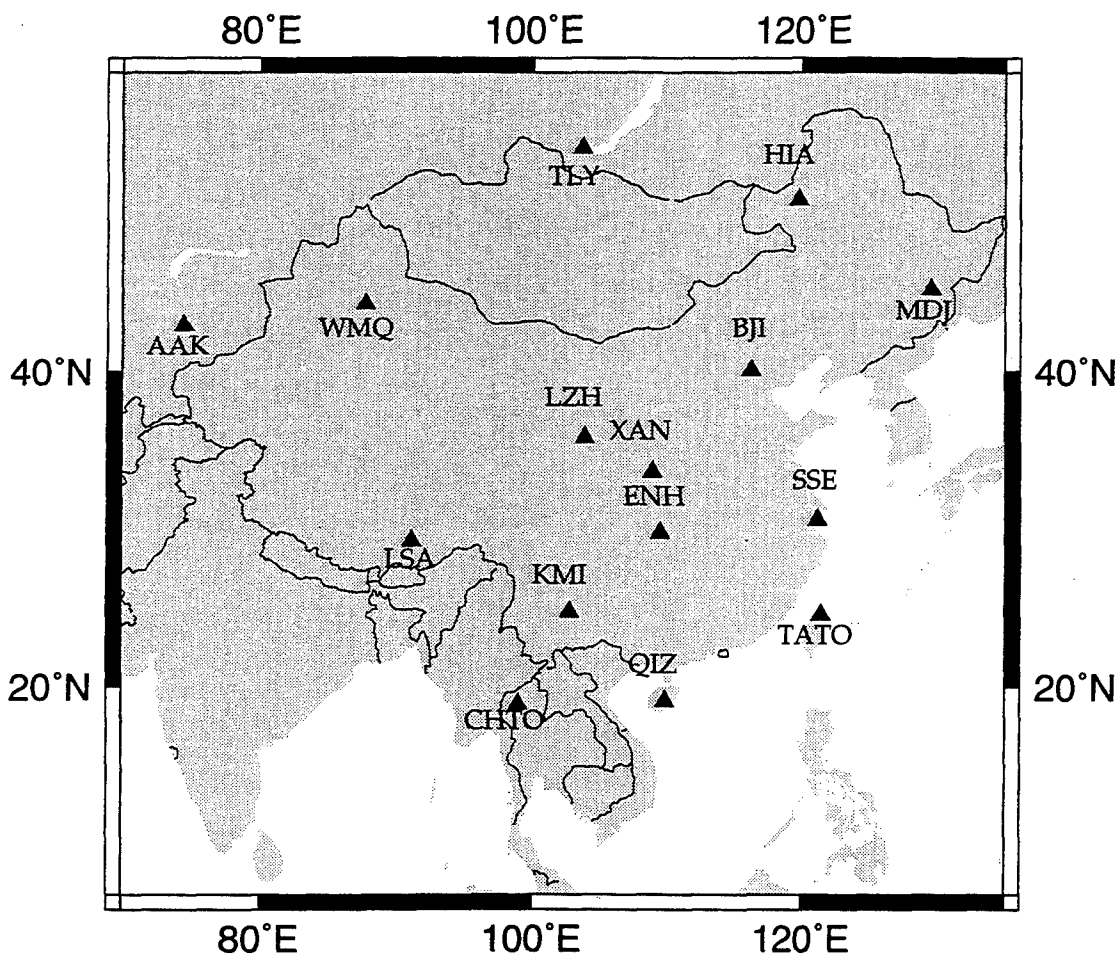
Figure 1. Locations of seismic stations in and around China.
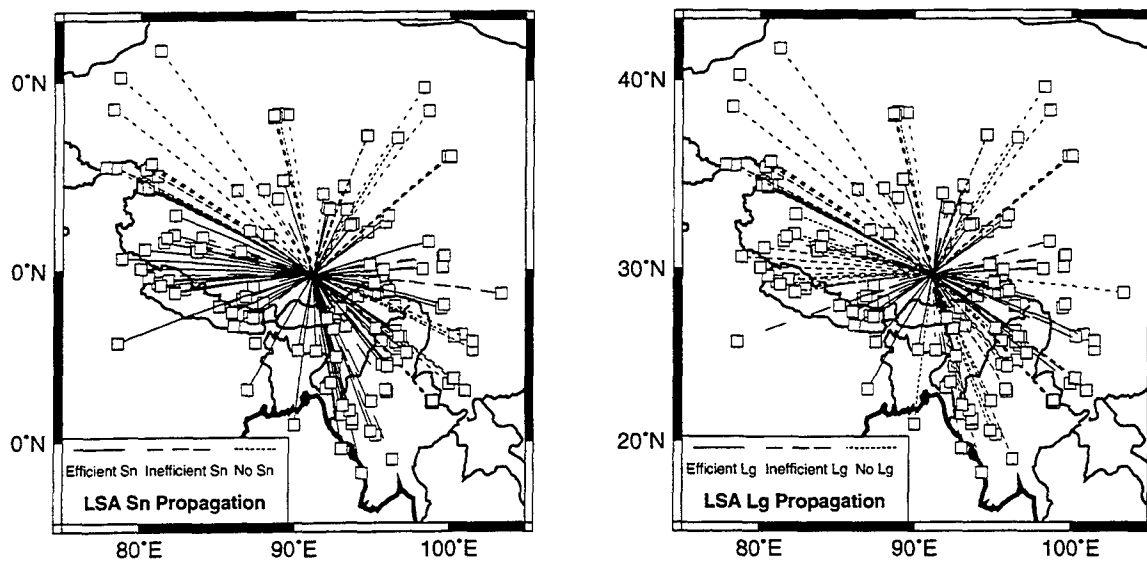
Figure 2. Sn and Lg propagation efficiencies for station LSA (Lhasa).
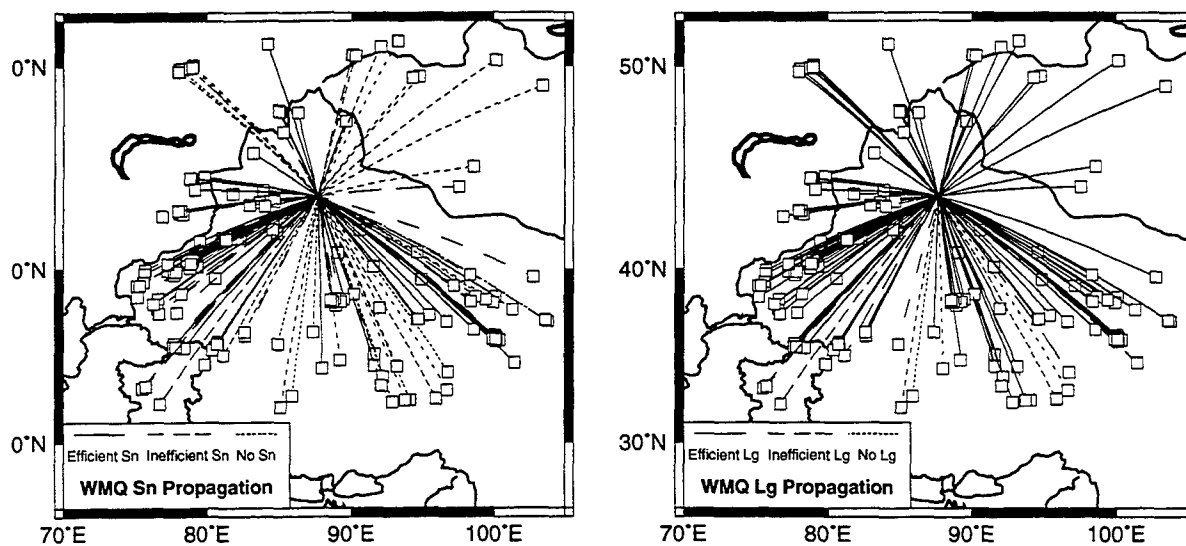
Figure 3. Sn and Lg propagation efficiencies for station WMQ (Urumqi).
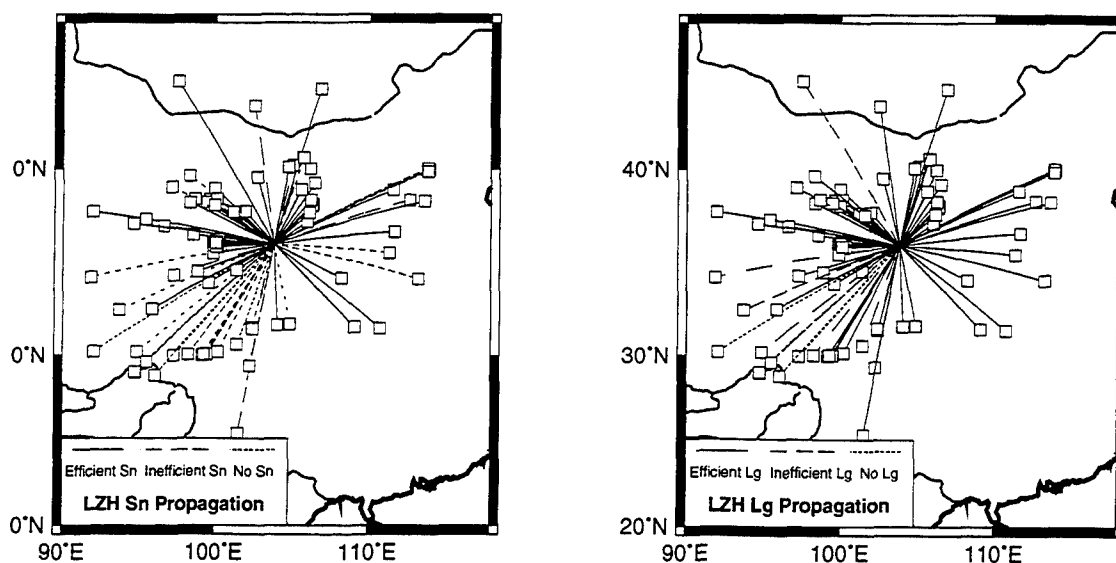
Figure 4. Sn and Lg propagation efficiencies for station LZH (Lanzhou).
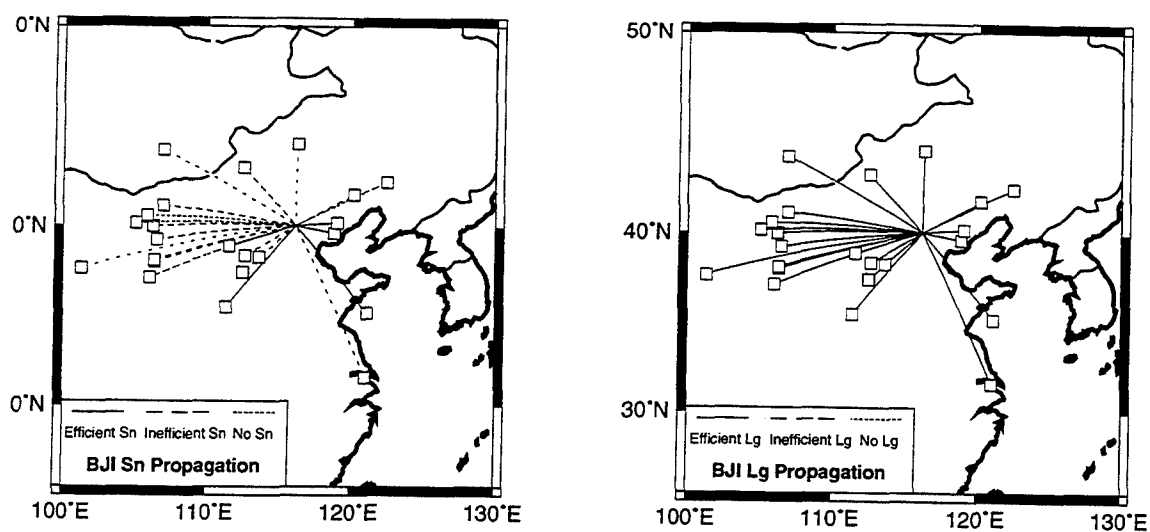
Figure 5. Sn and Lg propagation efficiencies for station BJI (Beijing).
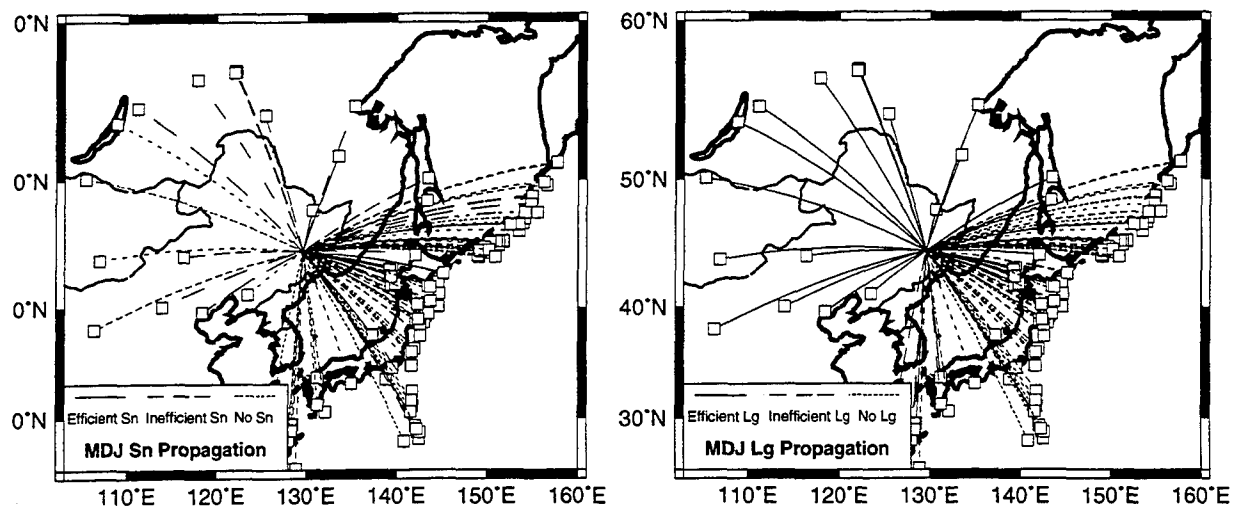
Figure 6. Sn and Lg propagation efficiencies for station MDJ (Mudanjiang).
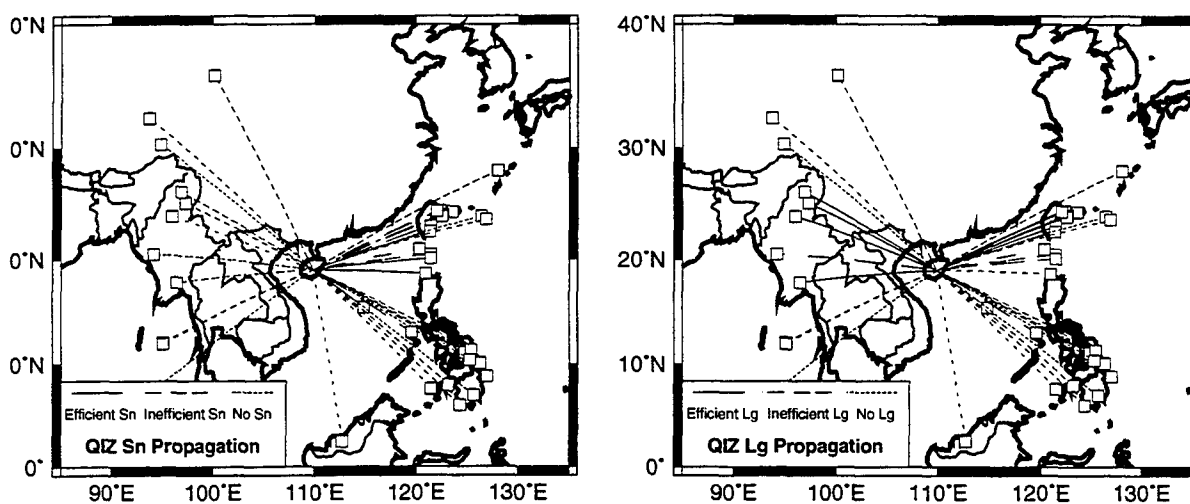
Figure 7. Sn and Lg propagation efficiencies for station QIZ (Qiongzhong).
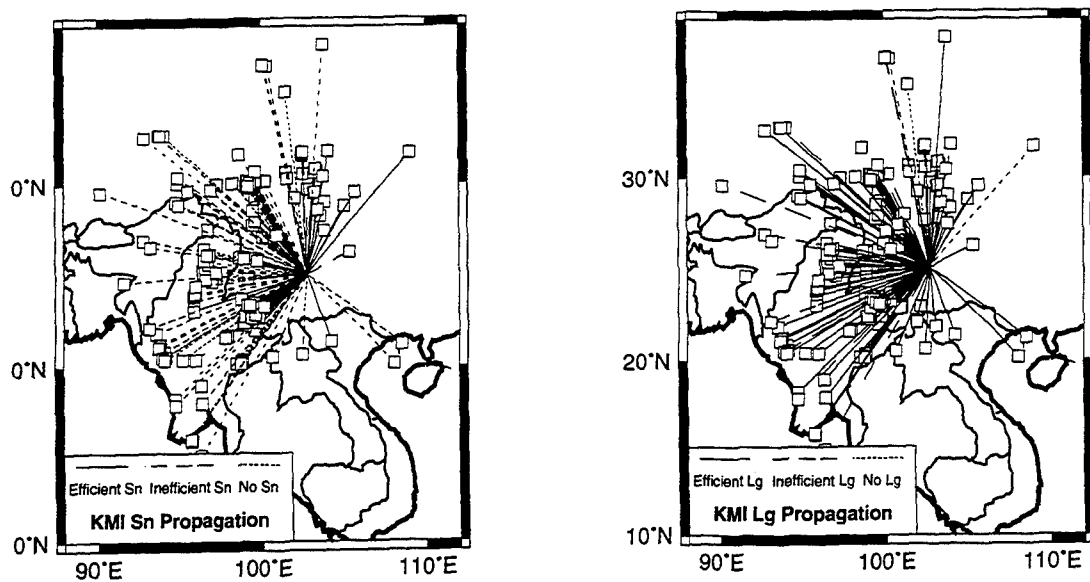
Figure 8. Sn and Lg propagation efficiencies for station KMI (Kunming).
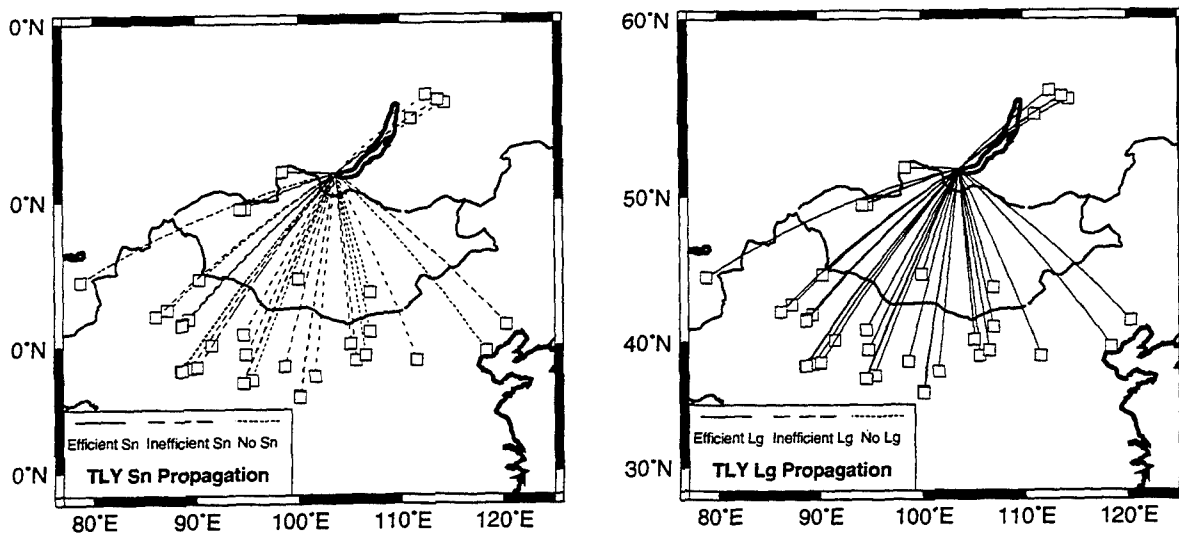
Figure 9. Sn and Lg propagation efficiencies for station TLY (Talaya).

Implications for Lithospheric Reheating Beneath the African Superswell from P_{nl} Wave Propagation in Central and Southern Africa

Andrew A. Nyblade[1], Kristin S. Vogfjord[2], and Charles A. Langston[1]

[1]Department of Geosciences
Penn State University
University Park, PA 16802

[2]Department of Geological and Geophysical Sciences
Princeton Univeristy
Princeton, NJ

ABSTRACT

The African superswell is an extensive topographic anomaly comprising the eastern and southern African plateaus, and an area of elevated bathymetry in the southeastern Atlantic Ocean basin. By comparing the P-wave velocity structure of unrifted Proterozoic lithosphere beneath (e.g., southern Africa) and away from (e.g., central Africa) the African superswell, we investigate the hypothesis that uplift within the superswell distal to the Cenozoic East African rift valleys has been caused by lithospheric reheating. If lithospheric reheating is the primary cause of uplift within the superswell, then P-wave velocity gradients beneath the southern Africa should be about 0.001 s^{-1} lower than beneath central Africa. Lithospheric P-wave velocity structure is obtained by forward modeling of P_{nl} waveforms from four moderate sized earthquakes. Results suggest that upper mantle beneath central and southern Africa is similar, characterized by a lid structure with a constant velocity. There appears to be little evidence for (1) mantle velocity gradients beneath southern Africa that are lower than beneath central Africa, (2) a low velocity zone as shallow as 120 km beneath central Africa, and (3) the existence of a pronounced, shallow ($\leq$ 80 km depth) low velocity zone beneath southern Africa. Additionally, modeling results yield an average thickness of 45 km for Proterozoic crust beneath central Africa and 40 km beneath southern Africa, and somewhat slower crustal velocities beneath central Africa compared to southern Africa. The similarity in upper mantle structure between central and southern Africa suggests that uplift away from the Cenozoic East African rifts is not caused entirely by reheating of the lithosphere, but the possibility that a small amount of lithospheric reheating may have occurred cannot be ruled out. If, as our results suggest, uplift away from the East African rifts is not due primarily to lithospheric reheating, then additional explanations for the origin of the African superswell must be sought, either in conjunction with a small amount of lithospheric reheating or in isolation.

OBJECTIVE

The African superswell is one of the largest (areally) topographic anomalies on Earth, comprising three contiguous regions, each characterized by about 500 m of positive residual elevation; the eastern African plateau, the southern African plateau, and an area of the southeastern Atlantic Ocean basin southwest of the African continent (Nyblade and Robinson, 1994). The eastern and southern African plateaus have mean elevations of ~1 km, roughly 500 m higher than the mean global elevation of continents not covered by ice caps, while bathymetry in the southeastern Atlantic Ocean basin is about 500 m shallower than predicted by boundary layer cooling models (e.g., half-space and plate models) describing the age-dependence of bathymetry (Nyblade and Robinson, 1994). The northern boundary of the superswell on the African continent is shown in Figure 1.

Recent seismic work in Kenya, East Africa, clearly reveals that rifted lithosphere within the African superswell has been perturbed thermally (e.g., Green et al., 1991; KRISP working group, 1991; Braile et al., 1994; Slack et al., 1994; Keller et al., 1994), and therefore much of the superswell topography proximal to the Cenozoic East African rifts can be attributed to isostatic uplift from lithospheric reheating and also possibly to a component of dynamic support. However, the origin of elevated topography in unrifted areas of the African superswell is less certain. One possibility is that lithospheric reheating has also caused isostatic uplift away from the Cenozoic rifts, and in this paper we investigate that possibility. Reheating of the lithosphere as a possible explanation for superswell topography away from the Cenozoic rifts was previously suggested by Nyblade and Robinson (1994) based on the observation that heat flow from Proterozoic terrains in southern Africa, as well as from seafloor older than ~80 Ma in the oceanic portion of the African superswell, is slightly elevated. Similarly, interpretations of long-wavelength (> 1000 km) Bouguer gravity anomalies in eastern and southern Africa also suggest that unrifted superswell lithosphere may be thermally altered (e.g., Wohlenberg, 1975; Fairhead, 1976; Fairhead and Revees, 1977; Brown and Girdler, 1980; Ebinger et al., 1989).

To investigate the lithospheric reheating hypothesis for the origin of the African superswell, we first model the P-wave velocity structure of Proterozoic lithosphere inside (southern Africa) and outside (central Africa) the African superswell, and then compare velocity models to identify structural differences caused by reheating. If the superswell lithosphere has been reheated, then the P-wave velocity structure of uppermost mantle beneath the African superswell should be different from that of "normal" (i.e., thermally unperturbed) upper mantle outside the superswell. Importantly, in this approach we focus on terrains of similar age (Proterozoic) beneath and away from the African superswell so that we can minimize the possibility of confusing structure resulting from lithospheric reheating with structure resulting from age-dependent thermal and compositional variations, such as those typically found between thinner, warmer Proterozoic lithosphere and thicker, colder Archean lithosphere (Jordan, 1988; Nyblade and Pollack, 1993a).

RESEARCH RESULTS

The P-wave velocity models that we use in this study are derived by forward modeling of P_{nl} waveforms from four earthquakes. The P_{nl} phase is a long-period waveform recorded at regional distances (< ~15°). It begins with the initial P arrival, continues through to the S wave arrival, and consists of two parts, upper mantle phases (Pn), and partially trapped crustal phases (PL). Hence the name P_{nl} (Helmberger and Engen, 1980; Wallace, 1983; Shaw and Orcutt, 1984). More specifically, the P_n portion of the waveform comprises P wave interactions with the uppermost mantle, for example, the headwave along the Moho and turning waves within the lid, while PL is a long-period wavetrain following P_n that propagates as partially trapped P-SV reverberations in the

crust, leaking SV wave energy into the mantle. In comparison to P_n wave propagation, PL wave propagation is relatively insensitive to mantle structure (Shaw and Orcutt, 1984).

The source-receiver paths used in this study can be seen in Figure 1 and details of the earthquakes are given in Table 1. Event 1 is located on the eastern flank of the Lake Tanganyika Rift and was recorded 1626 km to the northwest at Bangui (BCAO) in the Central African Republic. The ray path for Event 1 crosses the northern margin of the Congo Basin, lying outside the African superswell. Event 2 occurred in the tip of South Africa and was recorded at Windhoek (WIN), Namibia, 1193 km to the north. Events 3 and 4 occurred in Zambia and were recorded, respectively, 1183 and 1203 km to the southwest at Windhoek. The ray paths for these events cross Proterozoic mobile belts within the African superswell. Focal mechanisms show normal faulting with primarily E-W extension for Events 1, 3, and 4, and sinistral strike-slip motion for Event 2.

Green's functions were calculated using the wave number integration algorithm of Barker (1984) for point sources in elastic plane-layered structure. Anelastic attenuation was included by assuming complex layer velocities, with complex phase to produce a causal attenuation operator (Baag and Langston, 1986). Helmberger's (1973) earth flattening transformation was applied to velocity models prior to inclusion in the Green's functions calculations.

We begin by modeling lithospheric structure away from the African superswell to establish a reference model for thermally unperturbed lithosphere and then examine structure beneath the superswell. Two criteria are used to evaluate the "goodness" of fit between the observed and synthetic waveforms, (1) the P_n/PL amplitude ratio, and (2) the overall similarity between the observed and synthetic waveforms. The P_n/PL amplitude ratio, which we take as the ratio of the largest amplitude (peak to trough) within the P_n phase to the largest amplitude within the PL phase, is particularly sensitive to mantle velocity gradients because any P wave energy turning within the upper mantle, as a result of a positive velocity gradient, will boost the P_n amplitude relative to the PL amplitude.

Starting model parameters have been taken from two seismic refraction surveys across the Namaqua and Damara Belts (Figure 1) (Green and Durrheim, 1990; Baier et al., 1983). Velocities and layer thicknesses from these surveys have been averaged to produce a model with three crustal layers, a crustal thickness of 40 km, and an uppermost mantle velocity of 8.05 km s^{-1} (Table 2). For crustal attenuation, we assigned values of 1000 and 440 to Qp and Qs, respectively, and for the mantle we used values of 500 and 220 for Qp and Qs, respectively. Although the mantle Qp and Qs values are higher than average continental values, they are not unreasonable for Precambrian shield areas (e.g., Brune and Dorman, 1963).

The vertical and radial seismograms for Event 1 together with the synthetics from several models are shown in Figure 2. Distinct P_n and PL phases are seen on both components of motion. Figure 3 gives details of the velocity models, where Model 1 is the starting model described in Table 2. The synthetic waveforms for Model 1 show good resemblance to the data, with the P_n/PL amplitude ratio on both components of motion only slightly underestimating the observed ratios. However, the PL phase arrives ~10 seconds early relative to P_n (Figure 2), suggesting that the model can be improved.

The PL-P_n time can be increased in a number of ways. For example, crustal velocities can be lowered, making PL arrive later in the wavetrain, the crust can be thickened, also making PL arrive later, or the upper mantle velocity can be increased, making P_n arrive earlier. Combinations of these possibilities would also increase the PL-P_n time. To test these and other possibilities, synthetics for models with various crustal thicknesses and velocities were generated, and the three models which best match the data are shown in Figure 3a (Models 2, 3 and 4). Our preferred crustal model (Model 4,

Figure 3a) has a 45 km thick crust and velocities that are slightly lower than those in our starting model.

In Model 4, the P_n/PL amplitude ratio is only slightly overestimated on the vertical component of motion and only slightly underestimated on the radial component of motion, suggesting that a constant velocity lid may be a reasonable characterization of uppermost mantle structure beneath central Africa. But can alternative upper mantle models produce a better match in the P_n/PL amplitude ratios? Based on structure modeling in other Precambrian shield areas (e.g., King and Calcagnile, 1979; LeFevre and Helmberger, 1989), there are two likely possibilities; (1) the upper mantle might have a positive velocity gradient, and (2) the upper mantle could comprise a lid with a positive velocity gradient overlying a low velocity zone (LVZ).

Three alternative upper mantle models are shown in Figure 3b (Models 5, 6 and 7). To examine the effects of an upper mantle velocity gradient, a small velocity gradient of 0.001 s^{-1} was incorporated in Model 5. In this model the bottoming depth of P-waves is ~140 km. To examine the effects of a LVZ, Models 6 and 7 contain mantle lids with positive velocity gradients of 0.001 s^{-1} and 0.003 s^{-1}, respectively, overlying 30 km thick low velocity zones that begin at a depth representative of the base of the lithosphere, 120 km. In Model 6 rays bottom just below the LVZ, while in Model 7 rays bottom somewhat deeper. In all three models (5, 6 and 7) the P_n/PL amplitude ratio is significantly overestimated for both components of motion (Figure 2), and we therefore conclude that there is little evidence for (1) a mantle lid beneath central Africa containing a positive velocity gradient or (2) a low velocity zone as shallow as 120 km depth. Thus, our preferred model for the upper mantle beneath central Africa is a half-space (Model 4, Figure 6a). The existence of a low velocity zone deeper than 120 km, however, cannot be ruled out, given the depths at which the P-waves bottom in our models.

The data and synthetics for the source-receiver paths inside the African superswell (Events 2, 3 and 4) are shown in Figures 4, 5 and 6, and the accompanying velocity models are illustrated in Figure 7. Similar to Event 1, clear P_n and PL phases can be seen for Events 2, 3 and 4. Model 1 comprises the starting crustal model (Table 2), and examination of Figures 4, 5 and 6 reveals that for this model there is good resemblance between the synthetics and the data; the synthetic PL-P_n times are similar to the observed times, and the observed and calculated P_n/PL amplitude ratios are in reasonable agreement. The starting model is sufficient for explaining the major features of the data. Alternative models were tested and are shown; these models have various undesirable characteristics.

CONCLUSIONS AND RECOMMENDATIONS

Forward modeling of P_{nl} waveforms from four earthquakes within the southern African subcontinent suggest that Proterozoic upper mantle beneath central and southern Africa is similar, characterized by a constant velocity. Modeling results do not support the presence of a low velocity zone as shallow as 120 km beneath central Africa or the existence of a pronounced, shallow ($\leq$ 80 km depth) low velocity zone beneath southern Africa. The presence of deeper low velocity zones beneath central and southern Africa cannot be ruled out. These results are broadly consistent with the velocity models published by Clouser and Langston (1990), as well as the results of global tomography studies showing fast regions within the upper mantle beneath southern and central Africa (Su et al., 1994; Woodward and Masters, 1991). Additionally, our modeling results suggest an average thickness of 45 km for Proterozoic crust beneath central Africa and 40 km beneath southern Africa, and somewhat slower crustal velocities beneath central Africa compared to southern Africa.

The lack of evidence in our modeling analysis for mantle velocity gradients beneath Proterozoic terrains in southern Africa that are lower than beneath Proterozoic

terrains in central Africa suggests that the African superswell away from the Cenozoic East African rifts is not caused solely by reheating of the lithosphere. Furthermore, the lack of evidence in our modeling analysis for a pronounced low velocity zone beneath southern Africa, when combined with global seismic tomography models, suggests, albeit weakly, that significant thermal erosion of the base of the superswell lithosphere has also not occurred.

References

Baag, C-E., and C.A. Langston, Diffracted Sp generated under the Australian Shield, *J. Geophys. Res., 91*, 9507-9516, 1986.

Baier, B., H. Berckhemer, D. Gajewski, R.W. Green, C. Grimsel, and C. Prodehl, Deep seismic soundings in the area of the Damara Orogen, Namibia, South West Africa, in Intercontinental Fold Belts, edited by by H, Martin and F. Eder, Springer-Verlag, Berlin, pp. 885-900, 1983.

Barker, J.S., A seismological analysis of the May 1980 Mammoth Lakes, California earthquakes, Ph.D. thesis, Penn State Univ., University Park, 1984.

Braile, L.W., B. Wang, C.R. Daudt, G.R. Keller, and J.P. Patel, Modeling the 2-D seismic velocity structure across the Kenya rift, *Tectonophysics, 236*, 251-269, 1994.

Brown, C., and R.W. Girdler, Interpretation of African gravity and its implication for the breakup of the continents, *J. Geophys. Res., 85*, 6443-6455, 1980.

Brune, J., and J. Dorman, Seismic waves and Earth structure in the Canadian Shield, *Bull. Seis. Soc. Am., 53*, 167-209, 1963.

Clouser, R.H., and C.A. Langston, Upper mantle structure of southern Africa from P_{nl} waves, *J. Geophys. Res., 95*, 17403-17415, 1990.

Ebinger, C.J., T.D. Bechtel, D.W. Forsyth, and C.O. Bowin, Effective elastic plate thickness beneath the East African and Afar plateaus and dynamic compensation of the uplifts, *J. Geophys. Res., 94*, 2883-2901, 1989.

Fairhead, J.D., The structure of the lithosphere beneath the eastern rift, East Africa, deduced from gravity studies, *Tectonophys., 30*, 269-298, 1976.

Fairhead, J.D., and C.V. Reeves, Teleseismic delay times, Bouguer anomalies and inferred thickness of the African lithosphere, *Earth Planet. Sci. Lett., 36*, 63-76, 1977.

Green, R.W.E., and R.J. Durrhiem, A seismic refraction investigation of the Namaqualand Metamorphic Complex, South Africa, *J. Geophys. Res., 95*, 19927-19932, 1990.

Green, W.V., U. Achauer, and R.P. Meyer, A three-dimensional seismic image of the crust and upper mantle beneath the Kenya rift, *Nature, 354*, 199-203, 1991.

Helmberger, D.V., and G.R. Engen, Modeling the long-period body waves from shallow earthquakes at regional ranges, *Bull. Seis. Soc. Am., 70*, 1699-1714, 1980.

Helmberger, D.V., Numerical seismograms of long-period body waves from seventeen to forty degrees, *Bull. Seis. Soc. Am., 62*, 325-341, 1973.

Jordan, T.H., Structure and formation of the continental tectosphere, *J. Petrol., Spec. Lithosphere Issue*, 11-37, 1988.

Keller, G.R., C. Prodehl, J. Mechie, K. Fucks, M.A. Khan, P.K.H. Maguire, W.D. Mooney, U. Achauer, P.M. Davis, R.P. Meyer, L.W. Braile, I.O. Nyambok, and G.A. Thompson, The East African rift system in the light of KRISP 90, *Tectonophysics, 236*, 465-483, 1994.

King, D.W., and G. Calcagnile, P wave velocities in the upper mantle beneath Fennoscandia and western Russia, *Geophys. J. R. Astron. Soc., 46*, 407-432, 1976.

Krisp Working Party, Large-scale variation in lithospheric structure structure along and across the Kenya Rift, *Nature, 354*, 223-227, 1991.

Langston, C.A., Barker, J.S., and G.B. Pavlin, Point-source inversion techniques, *Phys. Earth Planet. Inter., 30*, 228-241, 1982.

LeFever, L.V., and D.V. Helmberger, Upper mantle P velocity structure of the Canadian shield, *J. Geophys. Res., 94*, 17749-17765, 1989.

Nyblade, A.A., and S.W. Robinson, The African Superswell, *Geophys. Res. Lett., 21*, 765-768, 1994.

Nyblade, A.A., and H.N. Pollack, A global analysis of heat flow from Precambrian terrains: Implications for the thermal structure of Archean and Proterozoic lithosphere, *J. Geophys. Res., 98*, 12207-12218, 1993a.

Shaw, P., and J. Orcutt, Propagation of PL and implications for the structure of Tibet, *J. Geophys. Res., 89*, 3135-3152, 1984.

Slack, P.D., P.M. Davis, KRISP Teleseismic working group, Attenuation and velocity of P-waves in the mantle beneath the East African Rift, Kenya, *Tectonophysics, 236*, 331-358, 1994.

Su, W. R.L. Woodward, and A.M. Dziewonski, Degree 12 model of shear velocity heterogeneity in the mantle, *J. Geophys. Res., 99*, 6945-6980, 1994.

Wallace, T.C., Long period regional body waves, Ph.D. thesis, Calif. Inst. of Technol., Pasadena, 1983.

Wohlenberg, J., The structure of the lithosphere beneath the East African Rift zones from interpretation of Bouguer anomalies, in *Afar Depression of Ethiopia*, 2, edited by A. Pilger and A. Rosler, Schweizerbart, Stuttgart, pp. 125-130, 1975.

Woodward, R.L., and G. Masters, Global upper mantle structure from long-period differential travel times, *J. Geophys. Res., 96*, 6351-6377, 1991.

Table 1. Earthquake Parameters.

Event	Date	Strike	Dip	Rake	m_b	M_0 (10^{24} dyne-cm)	Depth (km)
1	6/29/86	191.4	81.1	-72.0	5.0	2.9	36
2	9/29/69	123.5	89.4	-0.58	5.6	37.6	4
3	5/15/68	49.1	39.8	263.2	5.7	3.32	28
4	12/2/68	20.3	40.2	264.8	5.9	4.38	6

Table 2. Starting Velocity Model.

V_p (km/s)	V_s (km/s)	ρ (g/cm^3)	Q_p	Q_s	Thickness (km)
6.10	3.52	2.72	1000	440	15
6.25	3.61	2.77	1000	440	10
6.65	3.84	2.90	1000	440	15
8.05	4.64	3.35	500	220	half-space

Figure 2. Data (top bold trace) and synthetics for Event 1; (a) vertical component, (b) radial component. Traces are aligned on the first upswing (P_n) and have been low-passed filtered at 0.3 Hz. The top number to the right of each trace gives the maximum amplitude in microns and the bottom number is the P_n/PL amplitude ratio. A reference line (dashed) aligned on the first large downswing of the PL phase illustrates the arrival time of PL relative to P_n.

Figure 1. Map of the southern African subcontinent showing the Precambrian tectonic framework (after Hartnady et al., 1985), the northern boundary of the African superswell, and the location of seismic stations (solid triangles) and earthquakes (solid stars) used in this study. Archean cratons are shaded, the boundaries of the Proterozoic mobile belts are delineated with dashed lines, and the Congo Basin is shown with a stippled pattern.

277

Figure 3. Radially symmetric velocity models used to construct synthetics for Event 1; (a) crustal models, (b) upper mantle models.
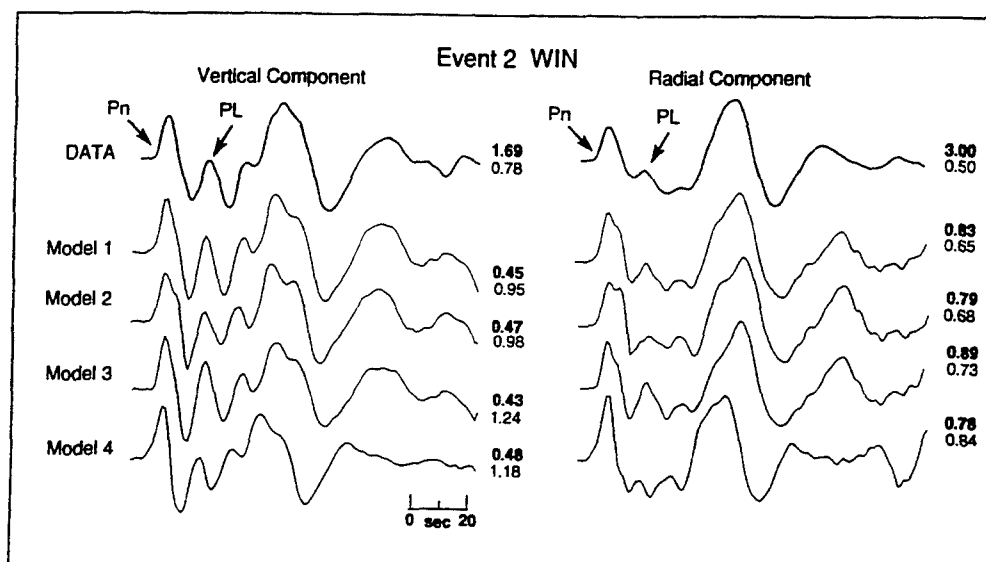
Figure 4. Data (top bold trace) and synthetics for Event 2. Traces are aligned on the first large upswing (P$_n$). Numbers to the right of each trace are the same as in Figure 2.
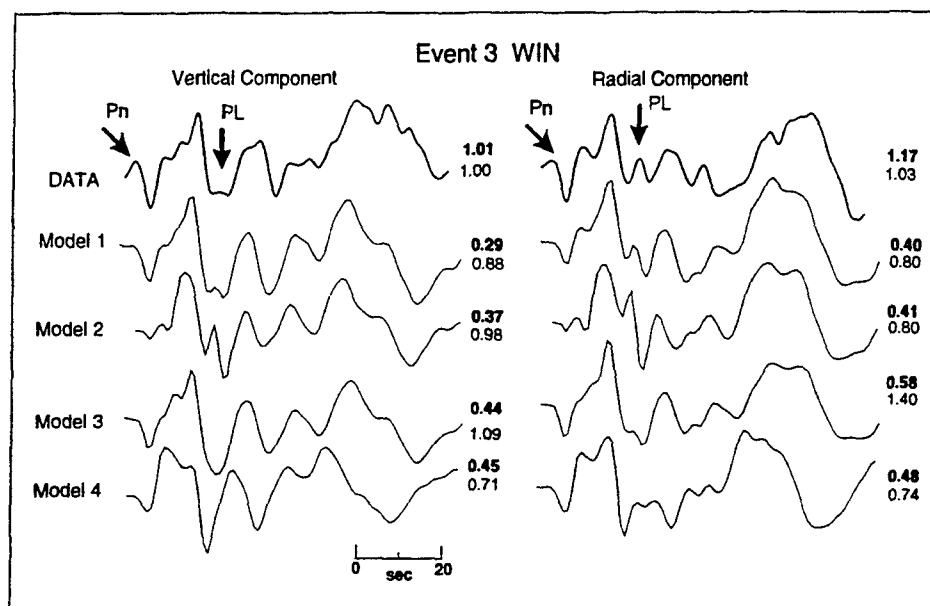
Figure 5. Data (top bold trace) and synthetics for Event 3. Traces are aligned on the first large downswing (P_n). Numbers to the right of each trace are the same as in Figure 2.
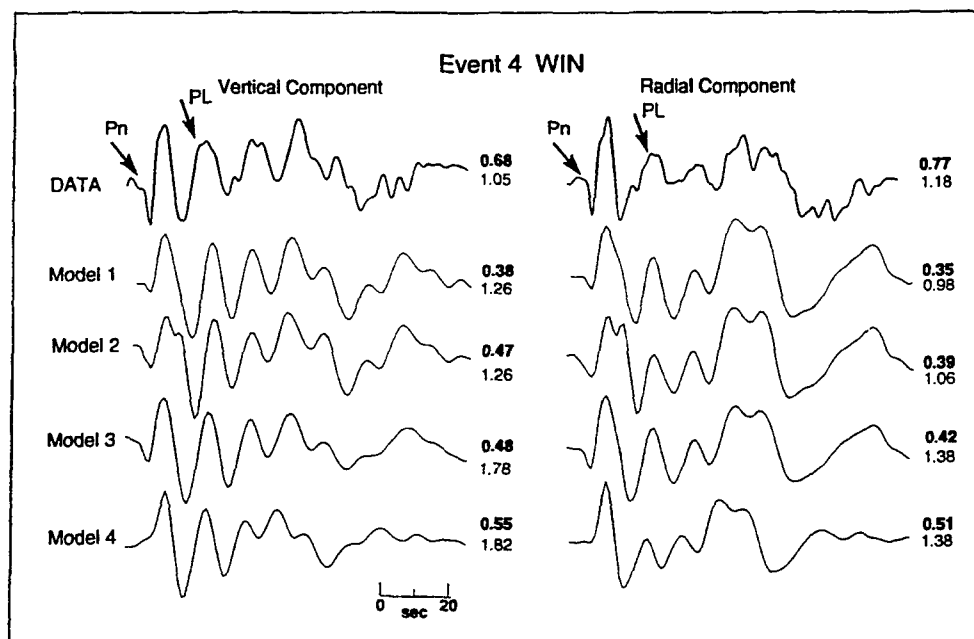
Figure 6. Data (top bold trace) and synthetics for Event 4. Traces are aligned on the first large downswing (P_n). Numbers to the right of each trace are the same as in Figure 2.

279
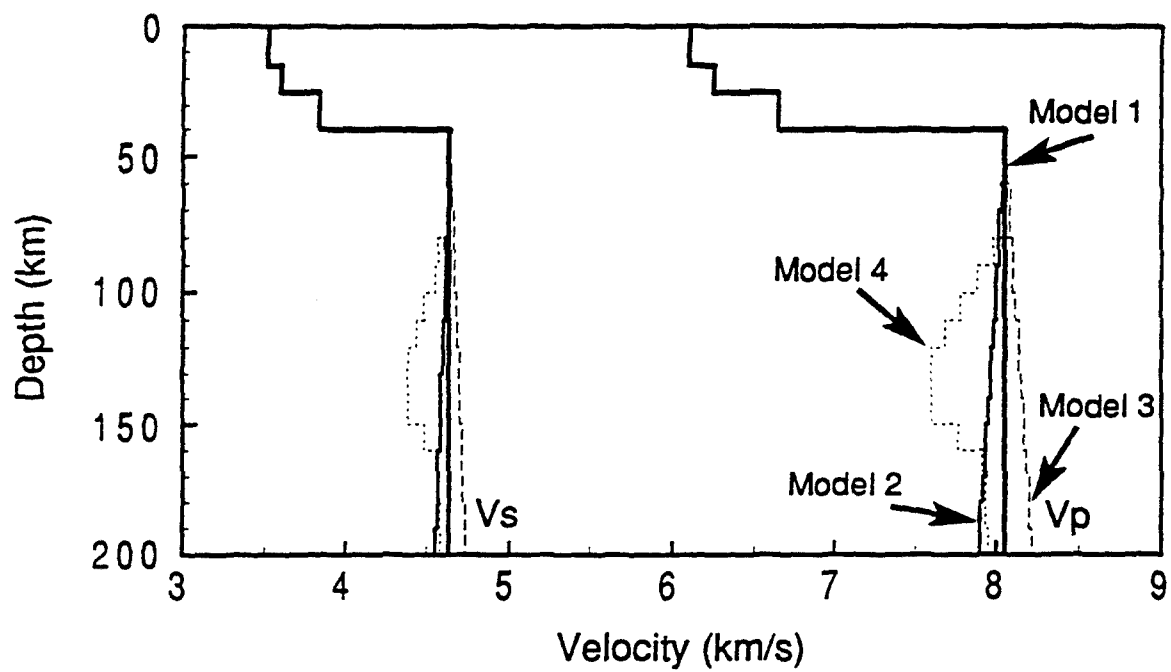
Figure 7. Velocity models used to construct the synthetics in Figures 4, 5, and 6.

Regional Wave Propagation in and around the Tibetan Plateau

T.J. Owens, H.P. Crotwell, D.E. McNamara‡, G.E. Randall†

Department of Geological Sciences
University of South Carolina
Columbia, SC 29208

ABSTRACT

The Tibetan Plateau is a dominant structural feature influencing seismic wave propagation in Central Asia. Using data from the 1991-92 Tibetan Plateau Seismic Experiment deployment of broadband PASSCAL sensors, we are studying the effects of the Tibetan Plateau on a variety of regional phases propagating within the plateau and crossing its boundaries. In this report, we summarize results from two such studies. First, the propagation and attenuation characteristics of *Lg* are used to document that *Lg* can propagate within the thickened crust of the Tibetan Plateau and to confirm previous studies showing that all boundaries of the plateau are effective barriers to *Lg* propagation. Our results further indicate that attenuation of *Lg* within the plateau is relatively high, comparable to areas of active tectonics, such as the Basin and Range Province. The second study involves waveform modeling of *Pn* and *Sn* waveforms from regional events of moderate magnitude. Source mechanisms for these events have been recently published, providing the necessary constraints to begin detailed structural modeling. It has been known for a decade that there are significant lateral variations in *Sn* propagation within the plateau, specifically that the central northern Tibetan Plateau blocks the propagation of high-frequency *Sn* phases. Using broadband regional seismograms from events within the plateau, we document that this blockage is strongly frequency-dependent. The available station spacing allows us to observe a rapid loss of high frequencies as regional *S* phases cross into the northern plateau while frequencies below 0.05Hz propagate throughout the plateau. Variations in the displacement pulse-shapes through the transition into the northern plateau are more easily explained by a changes in Poisson's ratio with depth than by simply rapid changes in the attenuation structure.

† Now at: Los Alamos National Laboratory
‡ Now at: Lawrence Livermore National Laboratory

Keywords: regional phase propagation, Tibetan Plateau, Lg, Pn, Sn

OBJECTIVE

One approach to calibrating areas of nonproliferation concern is the use of mobile arrays of new generation, high dynamic range, broadband digital seismic instruments. This project uses existing data from a variety of seismic deployments to assess the utility of this approach and to develop strategies for using temporary deployments to gather data relevant to seismic monitoring concerns. We focus on regional structure and wave propagation studies of importance to understanding wave propagation in Central Asia using a large scale lithospheric profile (The 1991-92 Tibetan Plateau Broadband Seismic Experiment). Another aspect of our contract, the characterization of lithospheric heterogeneities and their influence on regional wave propagation is addressed in an accompanying paper by Greg Wagner.

PRELIMINARY RESEARCH RESULTS

We review results from two related studies intended to better define the characteristics of regional phase propagation in and around the Tibetan Plateau. The first is a completed study of *Lg* propagation and attenuation (McNamara et al, 1995a) and the second is an ongoing study of the lateral variations in *Pn* and *Sn* propagation.

Lg Propagation within the Tibetan Plateau. The propagation of *Lg* has been observed across most of Asia and the Indian Shield, however, *Lg* has not been observed for paths crossing through the Tibetan Plateau (e.g. Ruzaikin et al., 1977; Ni and Barazangi, 1983) This effect has been attributed to either scattering due to a change in the crustal thickness and/or structural discontinuities at the boundaries of the plateau or an unusual velocity structure or high attenuation within the plateau. Previous studies were limited since they had to rely on stations outside of the Tibetan Plateau. They were only able to observe *Lg* for paths that cross the boundaries of the plateau. Consequently, they were not able to distinguish between the effects that the interior of the plateau versus its boundaries may have on *Lg* amplitudes.

We study the nature of *Lg* propagation and attenuation in two parts. First, we attempt to qualitatively analyze *Lg* attenuation and blockage by visually inspecting *Lg* amplitudes for paths crossing through the Tibetan Plateau and surrounding regions (Figure 1). Second, we invert *Lg* amplitudes, from paths restricted to the Tibetan Plateau, for frequency dependent attenuation (Figure 2).

The most significant new observations from our dataset is that *Lg* propagates within the Tibetan Plateau and that both the northern and southern boundaries of the plateau effectively block *Lg* propagation. We have observed strong *Lg* at every station from events with epicenters within the plateau. Though *Lg* is generated on the plateau, for our data set (Mb=3.7-5.5), we find that energy is quickly attenuated for event/station paths within the plateau that are greater than about 600-700 km. Events to the north of the Tibetan Plateau do not have observable *Lg* energy at recording stations within the Tibetan Plateau. This suggests that the northern boundary of the plateau blocks *Lg* transmission. We do, however, observe *Lg* at our stations at the northern edge of the plateau for long paths (> 700 km) from these same events north of the plateau, suggesting that the Tarim and Qaidam Basins allow for more efficient propagation of *Lg* than the Tibetan Plateau. We also confirm previous observations that the southern boundary of the Tibetan Plateau blocks *Lg* propagation (Ruzaikin et al., 1977; Ni and Barazangi, 1983).

In order to quantify our inferred high attenuation, we have examined the amplitudes of *Lg* arrivals from events within the Tibetan Plateau for apparent Q. This may provide information to compare our observed *Lg* propagation to other regions throughout the world. Details of this analysis can be found in McNamara et al (1995a).

The inversion was performed over five octaves with center frequencies of 0.75, 1.5, 3, 6 and 12 Hz. Figure 2a shows *Lg* amplitude data with the source and receiver contributions removed. As is often observed, Q increases with increasing frequency. However, our measured Q for the Tibetan Plateau is low relative to other continental regions (Benz et al., 1994). A least squares fit to the plateau data is shown in Figure 2b and gives:

$$Q(f) = (279 \pm 39.5)f^{(0.53 \pm 0.09)} \quad (0.5 \le f \le 16Hz).$$

Using Figure 2b, it is possible to compare our value of Lg $Q(f)$ with other tectonic regions. The highest values for Q_0 are for stable continental paths. Low Q values are generally observed in tectonically active regions. Comparison of our results with regions in North America suggest that Lg Q_0 within the Tibetan Plateau is well below the eastern and central US and only slightly above the Basin and Range values. This suggests that the Tibetan Plateau is more similar to a tectonically active region than a stable continental interior or passive margin. However, a complicating factor in making these comparisons is the role of the thickened crust in the Tibetan Plateau in the development and propagation of Lg. If the thickened crust leads to an increase in the thickness of the Lg waveguide, then the intrinsic Q of the plateau could be higher while the Q estimated from Lg would remain low due to the energy lost in a thickened waveguide. Additional analysis is needed to understand this potential trade-off.

Lateral Variations in Sn Propagation in the Tibetan Plateau. It has been known since the early 1980's from the work of Ni and Barazangi that high-frequency Sn waves do not propagate across the northern Tibetan Plateau. We use broadband regional seismograms recorded during the 1991-92 Tibetan Plateau Seismic Experiment to analyze this phenomena over a much broader frequency band. The long-range goal of this study is to identify one or more causal mechanisms for the observed propagation effect and to constrain the physical state of the upper mantle beneath the Tibetan Plateau.

Spectral and spatial variations in regional S-wave propagation within the Tibetan Plateau were analyzed using highpass filtered, regional, broadband displacement seismograms. Then, these seismograms from regional events were examined to uncover variations in waveforms of Pn and Sn that might be related to the anomalous region. Lastly, we calculated complete regional synthetic seismograms using the reflectivity method to examine the effects of velocity gradients and attenuation on Pn and Sn waveforms.

High pass filters were applied to the regional data set with corners at 1, 0.2, 0.1, and 0.02 Hz. For each station event pair, we calculated the $Pcoda$ to Sn amplitude ratio using filtered displacement seismograms. The Sn amplitudes were measured for a window around the expected Sn arrival time on the tangential component while the $Pcoda$ amplitudes were measured for a window before the Sn arrival on the vertical component. $Pcoda$ amplitudes were measured in the vertical component due to its relatively small dependence on source mechanism while the Sn amplitudes were measured in the tangential component because this was generally the strongest arrival. $Pcoda$ to Sn ratios below 1.0 indicate that Sn is clearly visible while $Pcoda$ to Sn ratios greater than 2.0 indicate that Sn is absent. Many intermediate values were obtained, but we display the end-members since they most clearly illustrate the spatial and frequency dependence of the data.

When the results of this analysis are summarized by plotting each ray path with a line intensity indexed to the $Pcoda$ to Sn ratio, the spatial and spectral variation becomes clear (Figure 3). For frequencies above 1 Hz, there is a clearly defined region of inefficient Sn propagation in the northern plateau. We found it to be somewhat larger than the region defined by Ni and Barazangi (McNamara et al, 1995b). However, as longer period Sn energy is included in the ratio measure, Sn propagates in an increasingly larger portion of the plateau. At the longest periods measured, Sn propagates efficiently throughout the entire plateau.

In addition to the spectral and spatial variation, there are other observations that can be seen from this analysis. First, Sn is attenuated over distances of less than 200 kilometers as it enters the northern plateau. There are several conveniently located events that show clear Sn energy at stations just outside of the zone of inefficient Sn propagation and little to no Sn energy at nearby stations just inside of the zone. Secondly, the longest regional paths for events located in the far western plateau occasionally have visible S-wave energy after passing through the anomalous zone. Since these paths are nearly 20° long, the energy is unlikely to be Sn. However, it does suggest that there is a depth limit to the zone that attenuates S-waves.

Figure 4 displays several views of broadband displacement seismograms for event 92.095.17.42.50 (see inset for location). Paths for this event propagate nearly parallel to our network, thus eliminating the need to consider source mechanism in these displays. The path to AMDO does not enter the northern plateau anomalous zone, while the paths to WNDO, ERDO, and BUDO represent increasing path lengths within the zone. There are only minor variations in the *Pn* waveforms along the line (Figure 4). However, there are significant variations in *Sn* waveforms (Figure 4). For example, there is a dramatic change in frequency content between AMDO and WNDO that marks the boundary of the anomalous region. In Figure 4, the traces for *Sn* waveforms and *Pn* waveforms for the same station-event pair are displayed. Amplitudes are normalized for each trace to allow easy comparisons. Note the change in waveform shape as *Sn* propagates into the northern plateau. At AMDO (top left), the *Pn* and *Sn* waveforms are similar in shape. The *Sn* waveform begins to broaden at WNDO and has become significantly wider than the *Pn* waveform at ERDO, within the anomalous zone. At BUDO, the *Sn* waveform is essentially a broad step, significantly different from the more pulse-like *Pn* waveform. This difference is consistent with the loss of high-frequency *Sn* within this region.

Complete reflectivity modeling was used to compare the effects of attenuation and gradients on the shape of waveforms (Randall, 1994; Kennett, 1983). In our simplified modeling efforts, we did not attempt to compute seismograms for specific source mechanisms, but rather, we used the vertical component of the Green's function for the moment tensor source Mxx for *Pn* and the tangential component for *Sn*. The Mxx source is chosen purely for illustrative purposes and is clearly not physically reasonable. Also, source depth and crustal thickness are not intended to be realistic for the Tibetan Plateau. The modeling is only intended to explore the sensitivity of *Pn* and *Sn* waveforms to upper mantle velocity parameters. Comparisons between the Q models and the negative velocity gradient models are emphasized because these models show characteristics that are consistent with our observations. The positive velocity gradients show nearly constant pulse-like *Pn* and *Sn* waveforms. In addition, McNamara et al (1995b) found little evidence for positive velocity gradients in the regional P-wave data.

To begin to analyze the unusual waveform variations in our data, we used the reflectivity method to generate synthetic seismograms for three simple models. In each case a constant velocity crust with a thickness of 40 kilometers exists above the upper mantle. Within this upper mantle a velocity gradient exists for the upper 60 kilometers and a constant velocity half space exists below that. All variations in velocity and Q occurred in this upper mantle layer. The velocity models are radially symmetric, and so an earth-flattening transformation is applied before the reflectivity synthetics are calculated.

The first type of model was a positive velocity gradient below the Moho. The range of gradients was from .001 to .004 km/s/km in P-wave velocity. Poisson's ratio was held constant throughout the model. The second type of model was a negative velocity gradients below the Moho. The range in gradients is from -0.001 to -0.004 km/s/km in P-wave velocity and again, Poisson's ratio was held constant throughout the model. The third type of model was a variable Q structure within the upper mantle. In this case, no velocity gradients were used. A constant Qp to Qs ratio of 2 was assumed with Qp values of 2000, 1000, 500, 250 and 124.

Analysis of the maximum envelope of negative gradients and Qs with distance showed that, in general, negative velocity gradient models show faster amplitude decays with distance than the Q models tested. In addition, there is little variation in the decay curves for *Pn* and *Sn* phases. In order to observe the frequency variation, we looked at the waveshape variation for the negative gradient and Q models (Figure 5). Two critical observations were made here. First, negative gradient models always produce a broader, more step-like waveshape than do the Q models. Second, the *Sn* and *Pn* waveshapes are similar whether Q or the gradient is being varied. Our modeling to date is clearly preliminary. However, the results show considerable promise and allow some speculation as to the cause of the anomalous *Sn* zone. We have observed that *Sn* waveforms broaden quickly in the northern plateau and become step-like within a few hundred kilometers. However, *Pn* waveforms maintain a more pulse-like waveform within the northern plateau. Our modeling suggests that negative velocity gradients can most efficiently produce a step-like waveform. Very low Q structures can also produce step-like waveshapes, but would require long path lengths with seemingly unrealistic Q values. Finally, neither negative gradient models nor low Q models can produce different *Pn* and *Sn* waveshapes with constant Qp:Qs and Vp:Vs ratios.

Based on these results, we believe a defensible hypothesis for continuing analysis is that the *Sn* waveform distortion within the northern plateau is the result of a negative velocity gradient in the upper mantle. Since the *Pn* waveshape is not modified in this region, it is unlikely that a significant negative velocity gradient exists for *Pn* in the upper mantle. This would imply that Poisson's ratio varies in the upper mantle beneath the northern Tibetan Plateau. This variation may be the result of a high geothermal gradient and/or the existence of partial melt in the upper mantle. Similar phenomena has been suggested to explain differences in *Pn* and *Sn* seismograms at higher frequncies in other areas (Gajewski et al, 1990). Our continuing analysis involves waveform modeling of specific events to verify if the suggested phenomena can explain the observed lateral variations in *Sn* and *Pn* propagation in this region.

CONCLUSIONS AND RECOMMENDATIONS

Temporary broadband networks are clearly an advantage to efforts to calibrate relatively unknown regions. Our results demonstrate the type of information that can be determined with this type of data. Our *Lg* results have clarified a long-standing debate about the cause of *Lg* blockage by the Tibetan Plateau. Understanding the nature of this blockage is critical to understanding the effect it has on common discriminants that utilize *Lg* . Our preliminary calculations (McNamara et al, 1995a) indicate that *P/Lg* ratio discriminants would not be effective for events crossing a plateau boundary, but the existence of *Lg* within the plateau suggests that it may still be useful for certain paths. The unusual propagation characteristics of *Sn* also lead to anomalous waveforms that need to be understood before regional waveforms from this area can be confidently used for seismic monitoring measurements. In the future, we will continue to investigate the structure of the Tibetan Plateau utilizing this unique data set. The suggestion that a depth-varying Poisson's ratio is a reasonable mechanism for explaining our observed waveform behavior will be studied in detail as will the correlation of the anomalous *Sn* zone with a low *Pn* velocity region in the northern plateau. In addition, using the sources (Randall et al, 1995) and structural information derived in our work, we will be compiling common discriminant measurements for many regional events in the plateau to better document the influence the unusual regional structure may have on event discrimination in Central Asia.

REFERENCES

Benz, H. M., R. Buland, and A. Frankel (1994). Source and structure studies using the U. S. national seismographic network (abstract), *Sixth annual IRIS workshop*, 7.

Gajewski, D., R. Stangl, K. Fuchs, and K.J. Sandmeier, (1990). A new constraint on the composition of the topmost continental mantle-anomalously different depth increases of P and S velocity, *Geophys. J. Int.*, 103, 497-507.

Kennett, B.L.N. (1983). Seismic Wave Propagation in Stratified Media, Cambridge University Press, Cambridge, England, 342 pages.

McNamara, D. E., T. J. Owens, and W. R. Walter (1995a). Propagation characteristics of Lg across the Tibetan Plateau, *Bull. Seis. Soc. Am* , submitted 1995.

McNamara, D. E., T. J. Owens, and W. R. Walter (1995b). Observations of regional phase propagation across the Tibetan Plateau, *J. Geophys. Res.*, in press.

Ni, J. and M. Barazangi (1983). High frequency seismic wave propagation beneath the Indian shield, Himalayan arc, Tibetan Plateau and surrounding regions: high uppermost mantle velocities and efficient propagation beneath Tibet, *Geophys. J. R. Astr. Soc.*, 72, 665-689.

Randall, G.E. (1994). Efficient calculation of complete differential seismograms for laterally homogeneous earth models, *Geophys. J. Int.*, 118, 245-254.

Randall, G.E., C.J. Ammon, and T.J. Owens (1995). Moment-tensor estimation using regional seismograms from portable network deployments, *Geophys. Res. Lett.*, July 1 issue.

Ruzaikin, A., I. Nersesov, V. Khalturin, and P. Molnar (1977). Propagation of *Lg* and lateral variations in crustal structure in Asia, *J. Geophys. Res.*, 82, 307-316.

Please refer to McNamara et al (1995a) for a complete list of references for Figure 2b.

A: Paths with Lg
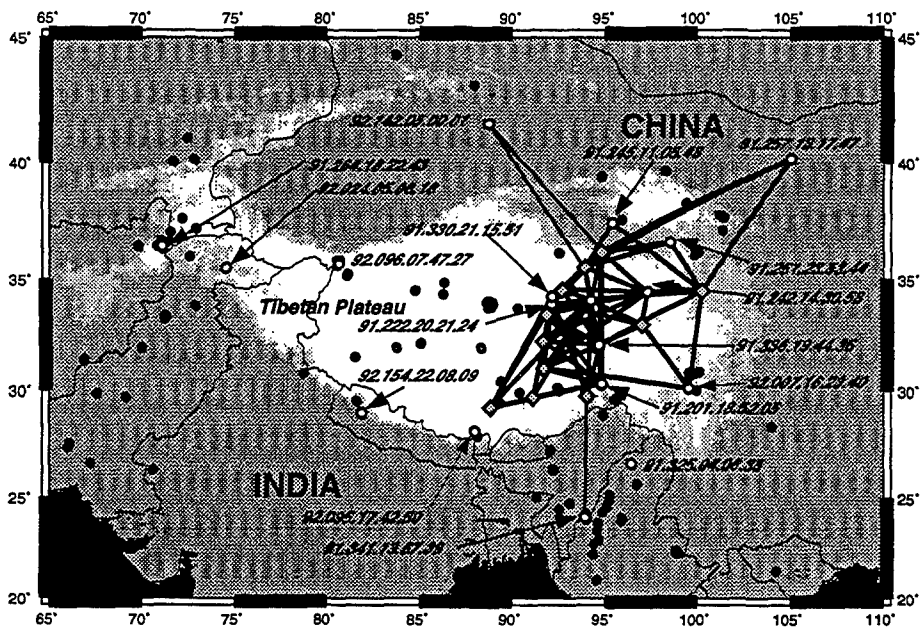
B: Paths without Lg
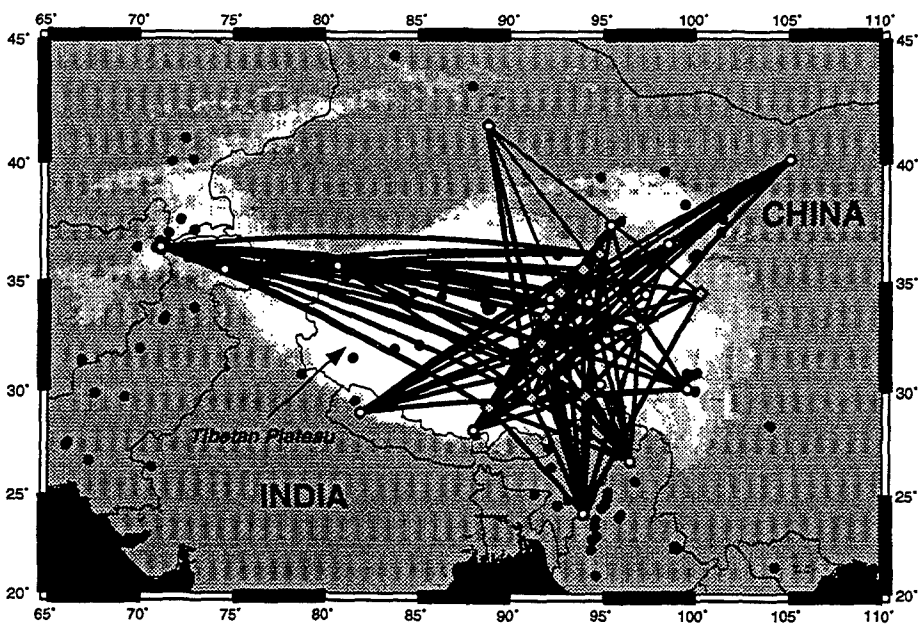
Figure 1. Representative paths showing the variation of Lg propagation within the Tibetan Plateau. Paths showing observable Lg (Top Frame) are restricted to paths in the eastern plateau, generally less than 700km in length. Paths without observable Lg (Bottom Frame) include those that cross the plateau boundaries and a few long paths from the western plateau.

286
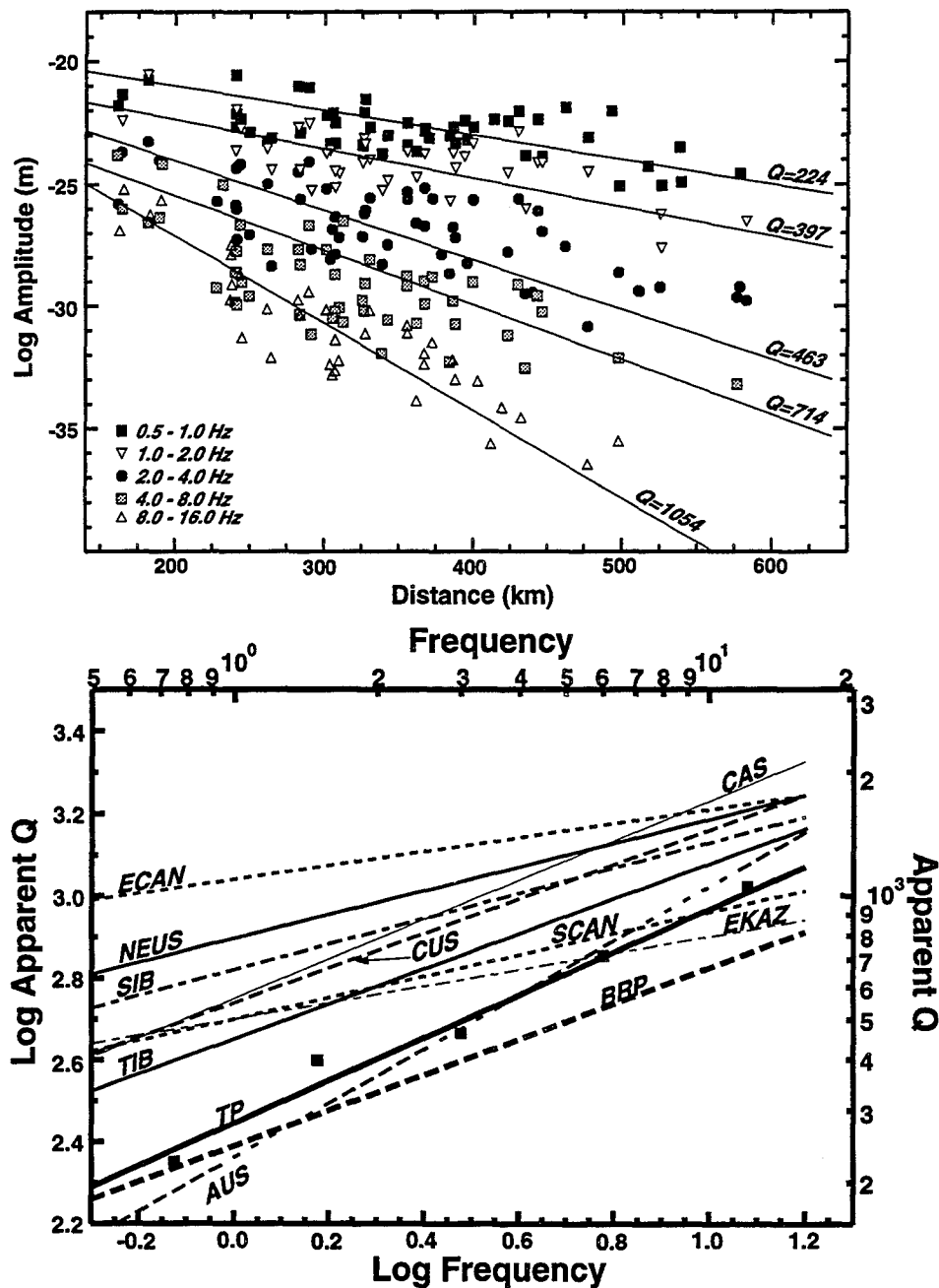
Figure 2. (Top) Lg amplitude versus distance for 5 octaves in frequency from 0.5 to 16 Hz. (Bottom) Apparent Q versus frequency for the Tibetan Plateau (Line Labeled TP) compared to worldwide observations including the northeastern United States (NEUS), central United States (CUS), Basin and Range province of North America (BRP) (Benz et al., 1994), Russian explosion recorded in central Asia (CAS) and stations in Siberia (SIB) (Xie, 1993), eastern Canada (ECAN) (Atkinson, 1989), eastern Kazakstan (EKAZ) (Sereno, 1990), Scandinavia (SCAN) (Sereno et al., 1988), Australia (AUS) (Bowman and Kennett, 1991), and a previously determined value for the Tibetan Plateau (TIB) (Shih et al., 1994). Axes are displayed as both frequency versus apparent Q and log frequency versus log apparent Q. Q(f) was determined assuming a geometric spreading term of 0.5.
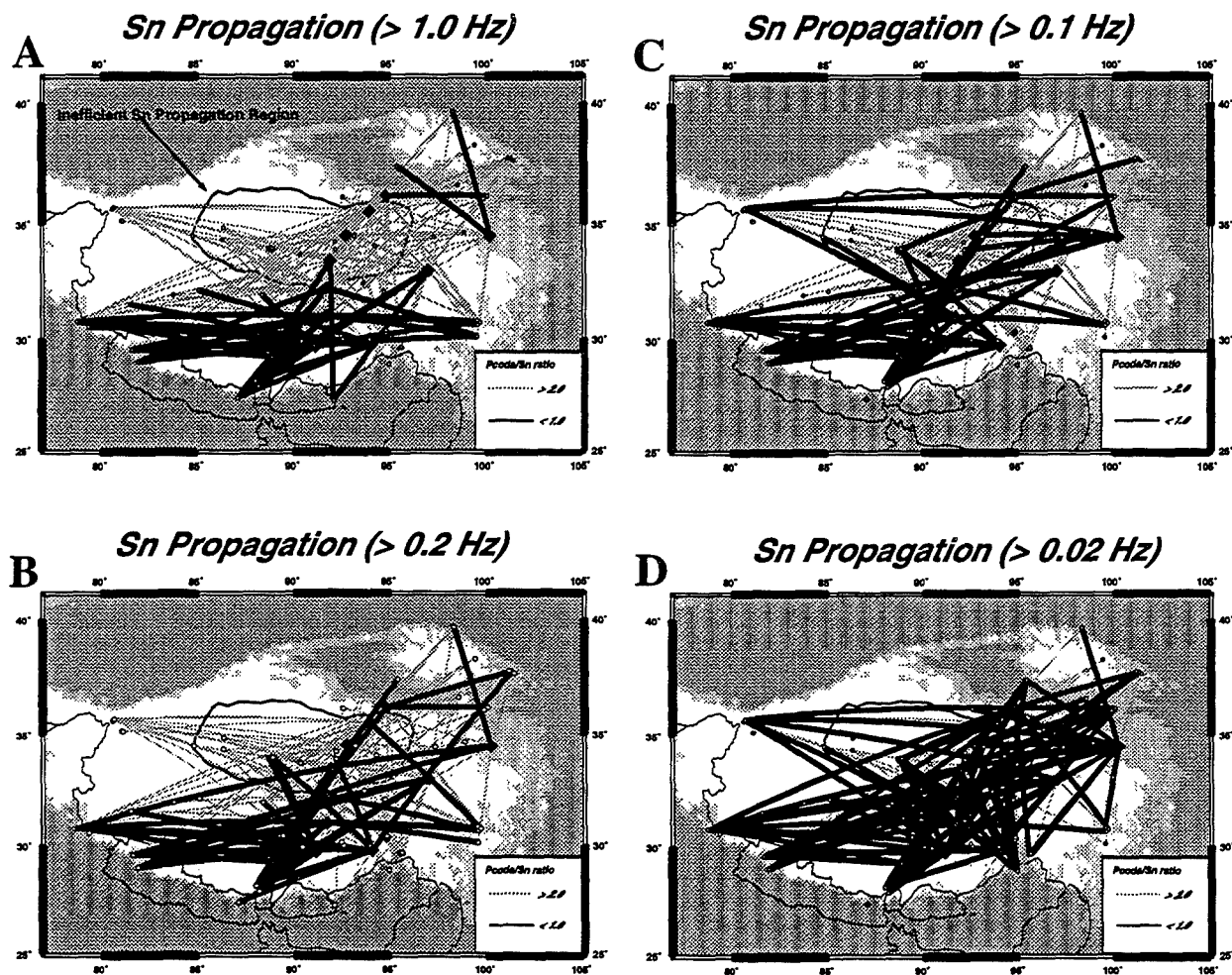
Figure 3. Four passbands illustrating the variation in Sn propagation efficiency spatially and with frequency. In each passband, the tangential Sn amplitude is compared to the Pcoda amplitude on the vertical component. This gives a stable measure of the "existence" of Sn energy in that passband. Gray colored paths indicate paths for which the Pcoda energy was more than twice the Sn energy. Black paths are where Pcoda energy is less than Sn energy. The region of the north-central plateau that is known to block high-frequency Sn is clearly visible in the higher frequencies, but disappears at longer periods.

AMDO
Distance 578 km
Azimuth 37.2

ERDO
Distance 837 km
Azimuth 31.3

WNDO
Distance 697 km
Azimuth 31.6

BUDO
Distance 992 km
Azimuth 32.9

——— **P waveform**
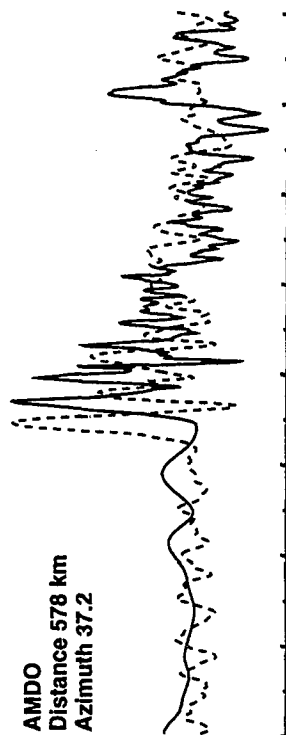
------- **S waveform**

Pn and Sn Waveform Comparison for Event 95.095.17.42.50
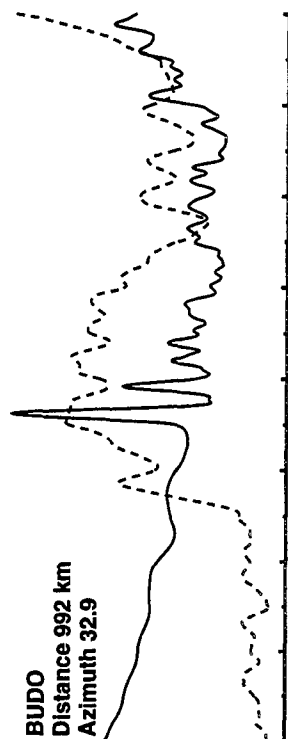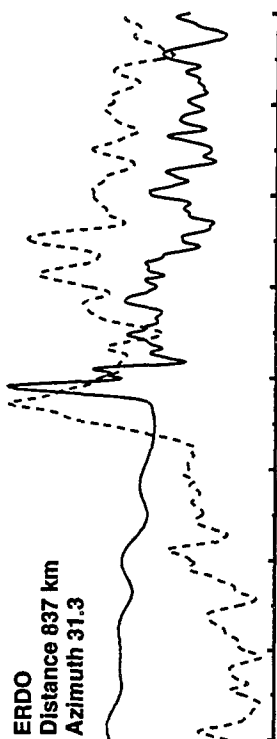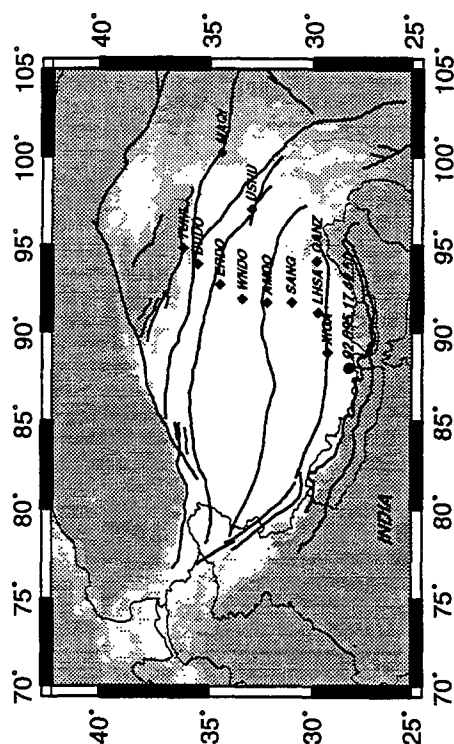
Figure 4. Variations in Pn and Sn waveforms across the Tibetan Plateau. Event 95.095.17.42.50 is located south of the network (see reference map), so energy propagates nearly in-line with the network. In each frame, the solid line is the Pn broadband displacement waveform and the dashed line is the Sn broadband displacement waveform. At AMDO, before the attenuating zone, the Pn and Sn waveforms are similar in shape. As the energy propagates to the north, the Pn waveform is relatively unchanged while the Sn waveform loses high frequencies and becomes a broad step in displacement.

289

**Pn Waveform for Different Radial Gradients
and Q for a Two Layer Model**

Key:
— No Grad, Qs = 1000
— − − −0.002 km/s/km P Grad, Qs = 1000
— −0.004 km/s/km P Grad, Qs = 1000
− − − No Grad, Qs = 250
− − − No Grad, Qs = 62

Pn Amplitude (centimeters x 10⁻⁹) vs Time (seconds)

**Sn Waveform for Different Radial Gradients
and Q for a Two Layer Model**

Key:
— No Grad, Qs = 1000
— − − −0.002 km/s/km P Grad, Qs = 1000
— −0.004 km/s/km P Grad, Qs = 1000
− − − No Grad, Qs = 250
− − − No Grad, Qs = 62

Sn Amplitude (centimeters x 10⁻⁸) vs Time (seconds)

Figure 5. Synthetic analysis of the effects of negative velocity gradients and Q. Key in the upper left of each frame identifies the parameters of the models. The general observations are: 1) Sn and Pn waveshapes for a given model are roughly the same (this does not match the data), 2) Negative velocity gradients are more effective at broadening the Sn waveform than Q for reasonable values of each. A possible explanation is that the P-velocity and S-velocity may vary independently to produce the effects observed in the data, which suggests a depth-varying Poisson's ratio.

290

The Spatial Stability of Rayleigh Wave Amplitudes and Path Dependent Propagation Characteristics of Central Asia

Gary L. Pavlis, Dept. of Geological Sciences, Indiana Univ., Bloomington, IN 47405
Hanan Mahdi, Dept. of Geosciences, Southeast Missouri State Univ.,
One University Plaza, Cape Girardeau, MO 63701
Grant F49620-94-1-0039

Abstract
We analyzed Rayleigh waves from eleven regional events with pure continental paths recorded by the Kyrghystan broadband network (KNET) located in the northern Tien Shan mountains of central Asia. We utilized the frequency variable filter technique to isolate fundamental mode Rayleigh waves and extract stable surface wave amplitude spectra in the 10-40 s period band. We found a strong azimuthal dependence in the amount of variability of observed amplitudes across the 150 km aperture of KNET. Rayleigh waves from northerly azimuths that have propagated across the Kazakh shield show little difference in amplitudes. At the opposite extreme are Rayleigh waves from nuclear tests at Lop Nor which propagate across KNET from east to west. Lop Nor amplitude spectra vary by approximately a factor of 8 in the 10 to 30 s period band. Other paths generally show small variation in amplitude at periods above 20 s, but variation comparable to the Lop Nor path at periods less than 20 s. We also utilized KNET as an array to construct a suite of beams. We then used the frequency variable filter to extract amplitude spectra from the beam signals as we did for the single station data. Comparison of the results demonstrates that amplitude spectra variability correlates directly with stacking coherence. As a result, the performance of KNET as a long-period array for analyzing Rayleigh waves is highly dependent on azimuth. Events to the north and west can be expected to be stacked reliably to 10 s period or possibly less, while events to the east and south can not be stacked reliably for periods shorter than 20 s. We argue that our observations are explained by radical differences in the Rayleigh wave scattering properties of the crust in the tectonically active region to the south and east compared to the more stable crust of to the north and west. (Keywords: Rayleigh waves, magnitude, discrimination, Asia)

Objectives
We are working to utilize data from broadband, three-component seismic arrays to improve estimates of surface-wave magnitudes from small events observed at regional distances. This work is highly relevant since the M_s-m_b discriminant remains the most robust discrimination technique. However, this discriminant is known to not work as well for low yield explosions for reasons that are not fully understood. Our long-term goal is to understand why this happens and what alternative methods might be designed to provide more robust discriminates for small magnitude events. The focus of this paper is improved understanding of how surface waves propagate in the real earth. Our approach here is largely observational. We have utilized array processing in conjunction with state-of-the-art signal processing methods to examine the stability of observed spectral amplitudes of Rayleigh waves recorded by a broadband seismic array. The results provide new insights into surface wave propagation along pure continental paths.

Research Accomplished
Data
For this study we have utilized data from the IRIS Joint Seismic Program broadband array in Kyrghystan, which we will refer to as KNET (Figure 1). KNET is a ten element array that began operation in the summer of 1991 and remains operational as of the date of this report. The aperture of this array is approximately 150 km with nominal station spacings of 20-30 km. It is equipped with STS-2 broadband sensors and utilizes digital telemetry to provide a dynamic range of 120 dB. The system also records two separate data streams: (1) a 100 sps triggered mode using a network trigger algorithm; and (2) 20 sps continuous recording. Most of this work is based on signals extracted from the 20 sps stream because the 100 sps records commonly turn off before or during

Date(D/M/Y)	Julian Day	Origin Time	Latitude	Longitude	Depth (km)	m_b	Region
22/9/1991	265	06:32:37.3	49.64N	156.55E	30	5.5	Kuril Island
27/10/1991	300	07:01:23.2	40.19N	63.05E	39	5.0	Uzbekistan
08/11/1991	312	15:13:43.8	26.28N	70.58E	22	5.6	India-Pakistan
26/11/1991	330	19:40:48.5	42.05N	142.52E	56	6.1	Japan
24/4/1992	115	07:07:23.9	27.55N	66.07E	25	5.9	Pakistan
21/5/1992	142	04:59:57.5	41.60N	88.81E	0	6.5	Lop Nor
27/6/1992	179	13:21:20.9	35.14N	81.13E	33	5.0	s.XinJiang, China
11/27/1992	332	21:09:16.67	37.47N	59.86E	24	5.1	Turkmenistan
5/10/1993	278	01:59:56.2	41.65N	88.68E	0	5.9	Lop Nor
7/10/1994	280	03:25:58	41.55N	89.07E	0	5.9	Lop Nor
15/5/1995	135	04:05:57.9	41.59N	88.74E	0	6.1	Lop Nor

Table 1. Source parameters of events used in this study.
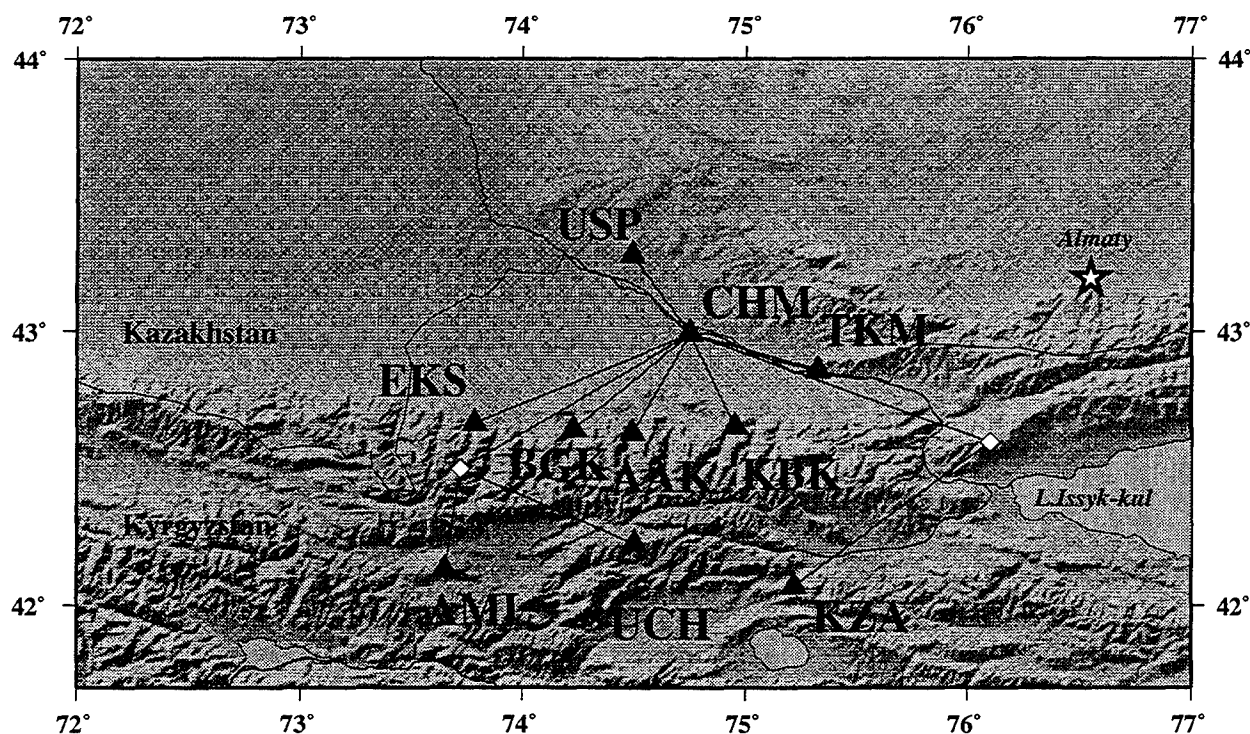
Figure 1. Map of KNET broadband array. Triangles are station locations. Diamonds are radio repeater sites and lines illustrate radio transmission links. Background is a shaded relief map of topography. Location of this array in central Asia is illustrated in Figure 2.

the surface wave arrivals.

To date we have fully studied Rayleigh wave data from eleven events whose source parameters are given in Table 1. This data set consists of seven earthquakes and four nuclear explosions from the Chinese test site at Lop Nor. These events were selected from the larger data set based on three major criteria:

(1)   We looked at all available data from nuclear explosions.

(2)   Earthquakes were selected to span as wide a range of azimuths as feasible.

(3)   We considered only pure continental paths. The Kuril Island and Japan events (Figure 2) actually propagate across a back-arc basin, but because the back-arc is near the source and only a small fraction of the path we consider these "pure" to all intents and purposes.

(4)   We focused on events at regional distances (5 to 20 degrees). For more northerly azimuth, however, we were forced to use more distant events (Figure 2).

The distribution of paths we have been able to study with available data recorded by KNET are shown in Figure 2. Notice that there is a gap in azimuth of approach of nearly 180 degrees to the north and west of KNET. We may be able to eventually fill the gap to the west with events from the Aegean, but significant events with pure continental paths from the north are unlikely unless Russia resumes nuclear testing.
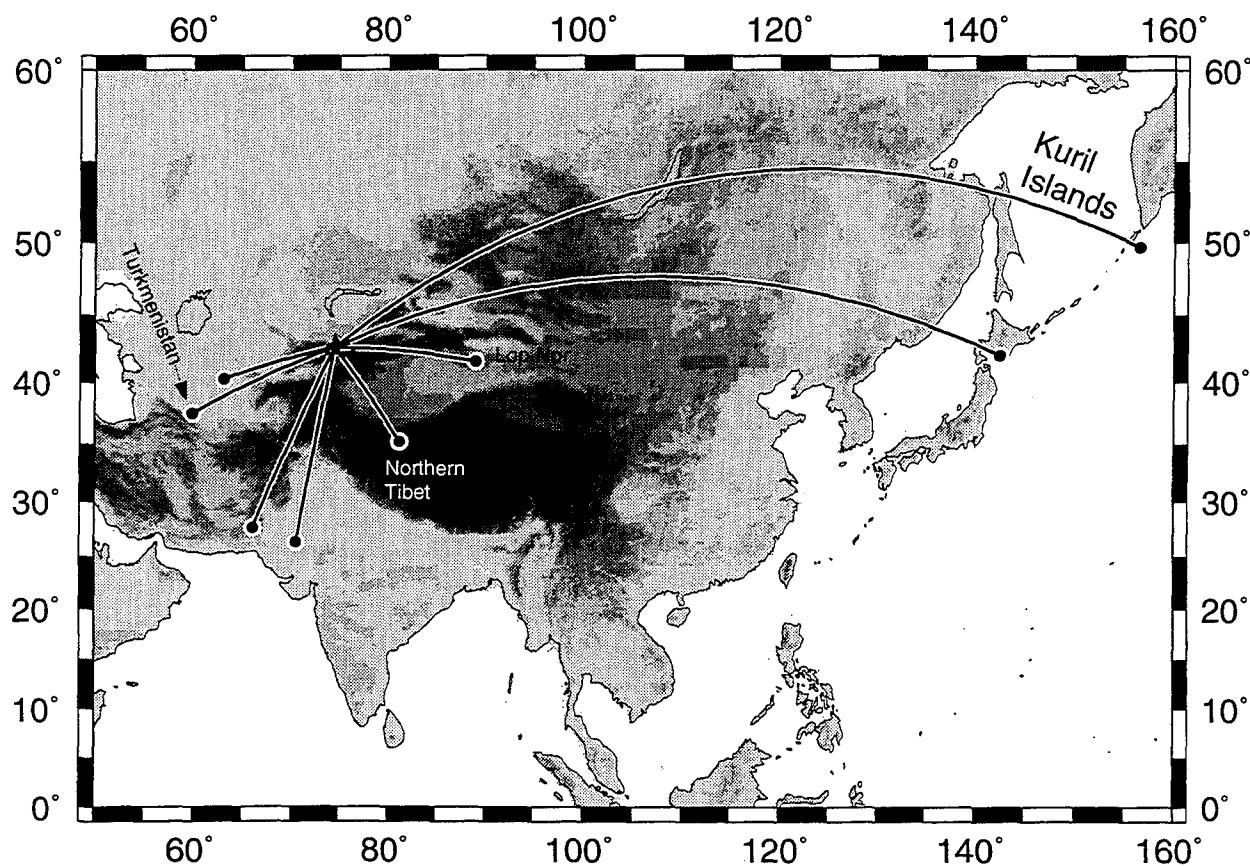
Figure 2. Map showing great circle paths of surface waves analyzed in this study. Black circles mark locations of each source. All events were recorded by the broadband network (KNET) in Kyrghystan. Background is grey scale topography with elevations over 5000 m black. Events for which results are presented in Figure 3 are labelled.

293

Methods

We are utilizing a mix of single station surface wave and array processing techniques. The array processing we used is one of the simplest methods possible. We use KNET as a long-period array, and compute a series of simple slant-stack array beams. In a recently completed paper (Pavlis and Mahdi, 1995) we conducted a more comprehensive array analysis of three regional events recorded by KNET. We found strong evidence for extensive multipathing and scattering along two of the three paths. Multipathing and scattering have an affect on array processing of surface waves that is somewhat different than a nondispersive signal like a P wave. In array processing of impulse signals, it is common practice to construct a "best beam" defined by f-k analysis. That is, f-k analysis is used to define the stacking velocity and back azimuth that will yield the maximum power in the beam. The resulting velocity and back azimuth are then used to define the "best beam" for that phase. In the presence of multipathing and scattering, the "best beam" for a surface wave become an ill defined quantity. The reason is that the "best beam" is frequency dependent because the dominate energy at one period may have a significantly different azimuth and velocity than the "best beam" at a different period. One could, in principle, process a range of beams that span the range of feasible "best beams". However, to make this manageable we limited our analysis to beams directed along the great circle path back azimuth and a fixed set of stacking velocities: 3.3, 3.5. 3.7, and 4.0 km/s. We made this choice for two reasons. First, it is the simplest model. Secondly, in our previous work (Pavlis and Mahdi, 1995) we found that the earliest parts of the surface wave packet was always the most coherent part of the surface wave group. This is consistent with what is expected from the geometry of forward scattering. That is, the initial surface wave arrival is a least time path, and as one moves later into the group the seismogram is the superposition of an ever expanding range of potential scattering points. One alternative we considered was to use the back azimuth obtained by f-k analysis of the front end of the Rayleigh wave signal as the "best beam" direction. However, up time for several KNET stations was marginal for the first two years of operation because of power and telemetry problems. As a result, reliable f-k azimuth estimates from a large fraction of the available data are not feasible. Thus, for consistency we decided it was preferable to use only the great circle path back azimuth.

For surface wave processing our goal is to extract the best possible estimate of the fundamental mode Rayleigh wave from a given signal. In our case this "signal" is either the seismogram recorded by a single station or an array beam. To accomplish this we used two basic tools. The first is an implementation of the multiple filter technique (MFT) of Dziewonski *et al.* (1969) by Herrmann (1973). We used the MFT to produce initial estimates of the dispersion curve and amplitude spectra of the fundamental mode signal.

Herrin and Goforth (1977) pioneered the use of phase-match filters (PMF) to isolate a mode of interest from a group of superimposed, multimode surface waves and to refine group and phase velocity measurements. They defined the phase-matched filter as a class of linear filters in which the Fourier phase spectrum of the filter is made equal to that of a given signal. This is done by removing the phase of the desired mode (In our case, we obtained this initial estimate from MFT analysis.) resulting in a zero-phase signal with energy concentrated about zero lag in the time domain. This dephased signal, which Russell *et al.* (1988) call a "pseudo-autocorrelation function", is windowed to isolate the mode of interest. When the effect of dispersion is restored, the resulting waveform is an estimate of the desired mode that reduces the effects of multipathing, other modes, and other forms of "noise". The principal enhancement introduced by Russell (1987) and Russell *et al.* (1988) was a more complex windowing scheme that combines the beneficial

294

aspects of Landisman *et al.*'s (1969) time variable filter with the PMF. This modified PMF method has been called the frequency variable filter. The principle advantage of the FVF is that it reduces the amplitude distortion (bias) of the PMF through the use of window functions that depend on frequency (Russell *et al.*, 1988). Because the focus of this study was on surface wave amplitude spectra, we used the FVF technique exclusively because of its superior capabilities in estimating amplitude spectra.

Results

Our major results are summarized in Figure 3. This figure displays estimates of fundamental mode Rayleigh wave amplitude spectra extracted by the FVF from four of the eleven events we have examined to date. The Lop Nor results presented are for the event on May 15, 1995. We present these four examples as representative of the larger data set. There are three important observational results that follow from figure 3 which we will now discuss.

1. There are dramatic variations in amplitude spectra of different stations within KNET and these variations are highly path dependent. The observed variations are of two flavors that need to be digested separately: (1) overall variability of the spectra from all the stations in the array viewed collectively; and (2) single station outliers like that from station AML in Figure 3d. First consider item 1. Notice that amplitude variability of the Kuril Islands event is almost negligible at all periods. Lop Nor is the opposite end member. There we find drastic variability of observed amplitudes at all periods. The other two events (ignoring for now the anomalous curve for AML) are intermediate. They tend to show quite large variability at periods shorter than about 20 s, but relatively small variations at longer periods. Results from the other events not presented in Figure 3 are consistent with this. That is, all Lop Nor explosions results show large amplitude variability, and results from similar azimuths are comparable. The Kuril Islands event shows the least variability of all the data.

Anomalous results like the spectrum for AML shown in Figure 3d are, we believe, a different issue. The result is particularly hard to explain because the observed amplitudes are anomalously low across the entire frequency band. We have similar examples of anomalous amplitude behavior of station CHM for two other events that are not shown in Figure 3. We are quite certain this is not an instrumentation problem for three reasons. First, high frequency signals do not show this anomalous behavior. Secondly, different stations show this anomalous type behavior for different events. Finally, gain codes are encoded in every transmitted packet and overall system responses are known very accurately. Pavlis and Mahdi (1995) demonstrated from particle motion analysis of the same event analyzed in Figure 3d that this anomalous amplitude is associated with a pronounced flattening of the Rayleigh wave elliptical particle motion. As a result we speculate that this type of anomalous amplitude response may result from a site effect related to 3-D structure of the crust and upper mantle beneath KNET at scale lengths less than a wavelength.

2. There is a general tendency for amplitude fluctuations to increase below 20 s period.

3. At periods of 20 s and above FVF filtering of the array beam from KNET provides a reasonably stable estimate of average amplitude of the single station measurements. Figure 3d shows that this remains true even in the presence of a relatively severe outlier like AML. Furthermore, this is relatively true even for the wildly variable results from Lop Nor. Below 20 s period there is a strong tendency for the beam to systematically underestimate the amplitude. This bias scales with the degree of amplitude fluctuation across the array. That is, for events like the Kuril Island event or the Turkmenistan event (ignoring AML) the amplitude bias is relatively small

295

Kuril Islands

Lop Nor

Northern Tibet

Turkmenistan
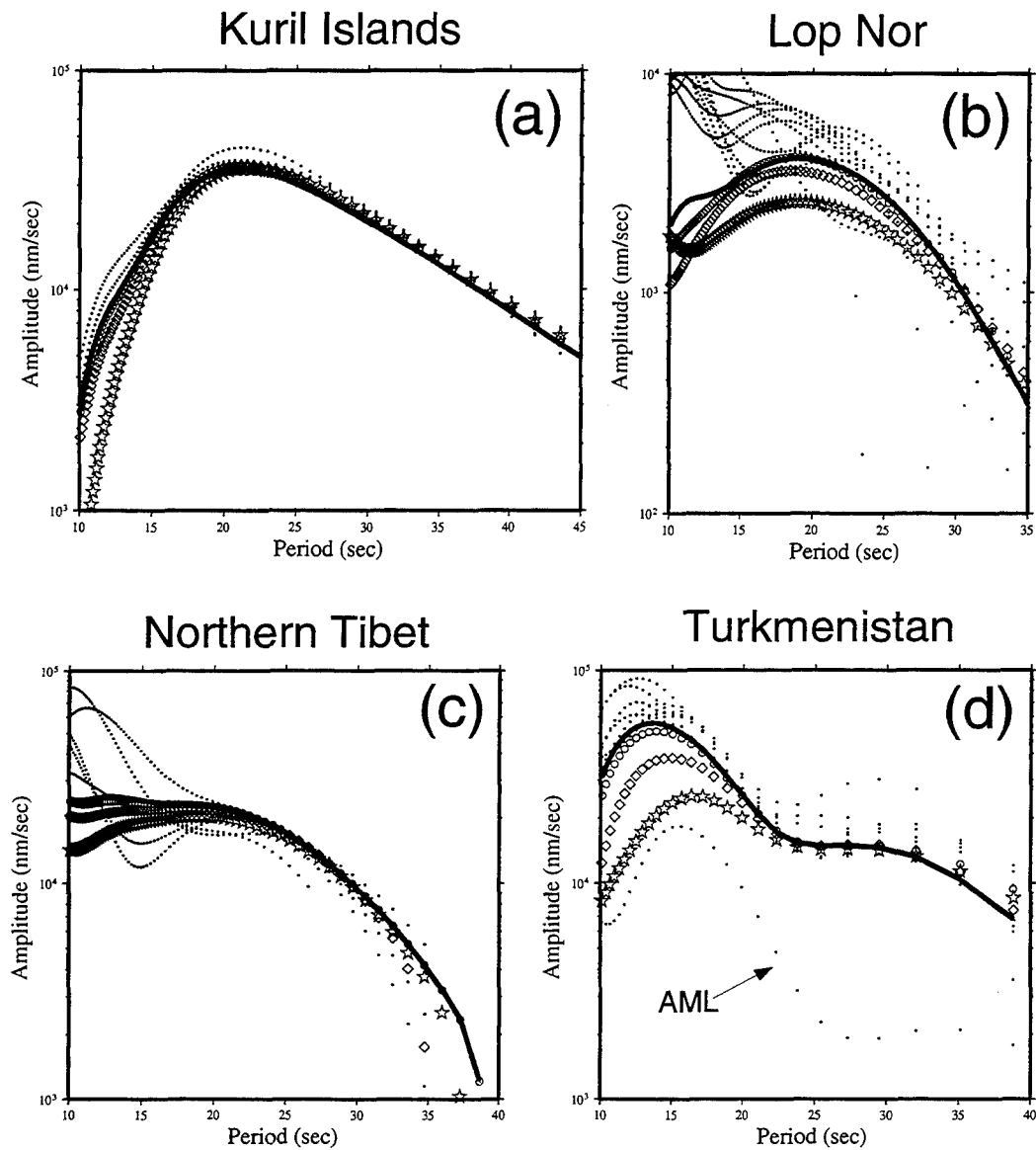
Figure 3. Amplitude versus period variations for different KNET stations and array beams. Results are presented here for four of the eight paths shown in Figure 2. Amplitudes spectra shown were, in all cases, obtained from the estimates produced by the frequency variable filter method of Russell *et. al* (1988). Dots show results from individual stations. Others are for different array beams constructed, in all cases, by pointing the array at the source back azimuth and stacking over different phase velocities. Stars are result using a velocity of 4.0 km/s; diamonds using 3.7 km/s; open circles used 3.5 km/s; and the solid line used 3.3 km/s.

while for Lop Nor the beam amplitude is more an order of magnitude smaller at 10 s periods.

To understand these three basic observations it is important to first grasp an issue of scale. The aperture of KNET is approximately 150 km. This means that for the range of periods analyzed in Figure 3, KNET spans a range of from around 1 to 5 wavelengths. This is why KNET is a functional long-period array for surface-waves in the band shown in Figure 3. It is well known that seismic arrays have difficulty yielding coherent stacks when the aperture of the array exceeds from 2 to 5 wavelengths. The loss of amplitude in the beam at periods less than about 20 s is a direct consequence of this. That is, at these shorter periods the signals do not stack. This is not a consequence of choosing the incorrect beam azimuth and slowness. Pavlis and Mahdi (1995) conducted moving window broadband f-k analysis on the October 1994 Lop Nor and the Turkmenistan events shown in Figure 3b. We found that for the Lop Nor path these shorter periods would not yield a coherent stack from any direction, while we could produce reasonable stacks at these periods for the Turkmenistan event. Thus, there is a strong azimuthal variation in the stacking capabilities of this array. For some azimuths (Figure 3a and 3d) KNET is a reasonable surface wave array for periods as short as 10 s, while for others (Lop Nor) is doesn't even work very well at 30 s period.

We would argue that these results are well explained by known large scale crustal structure of central Asia. The Kuril Islands path (Figure 2) traverses a stable shield region for all but the beginning and ending sections of the path. The lack of scattering along this path translates into almost negligible amplitude variations across the array. Paths from the southwest (Figure 3d) are relatively simple because these waves propagate primarily through a single crustal block which Zonenshain et al. (1990) call the Kara Kum-Tarim block and Sengor (1984) calls the Cimmerian subcontinent. This section of the crust seems to have been accretted onto Asia during the late Paleozoic, and forms the basement in an east-west band along the southern boundary of the former Soviet Union and into China in the Tarim basin (the almond shaped flat region within which the Lop Nor test site is located). This crustal block is relatively undeformed to the southwest. This appears to translate into relatively simple crustal structure and minimal scattering of 10-40 s Rayleigh waves. Surface waves from sources to the south and east of KNET, on the other hand, are strongly contaminated by extensive scattering and mulitpathing due to interaction with the complex geologic structures that characterize the crust in that region (Figure 2). An interesting preliminary observation is that propagation from the east (Lop Nor) is subject to greater amplitude fluctuations and inferred scattering than propagation from more southerly azimuths (e.g. Figure 3c). This may relate to the fact that the overall crustal fabric of this area of central Asia has a predominant east-west strike due to the predominant north-south compression that has thrown up the Tien Shan mountains.

A final result we note is that these results confirm an assertion we made previously (Pavlis and Mahdi, 1995) that in stacking surface wave data from an array like KNET, it is preferable to tune the beam to the highest frequency of interest. In all cases except Lop Nor the results are essentially identical for the full range of stacking velocities we used at periods longer than about 20 s. This occurs because the phasing errors induced by an inappropriate phase velocity have a negligible impact at the longer periods. Thus the best overall results are obtain by using the slowest phase velocity, which is appropriate for the shortest periods.

Conclusions and Recommendations

Regional earthquake monitoring networks equipped with broadband sensors and modern digital recording systems can double as highly functional long-period arrays. It is apparent to us

that regional earthquake monitoring networks throughout the world will evolve to this level of technology in the future. We assert that regional networks with this level of technology can play a critical role in the future in monitoring a CTBT by providing auxiliary data to discriminate questionable events. We recommend that CTBT negotiations should give careful consideration to the potential role of upgraded regional networks as a global monitoring resource.

Our work demonstrates that networks like KNET are highly useful tools for stacking data to obtain more reliable estimates of M_s than what would be possible with a single broadband station. On the other hand, we see that a network like KNET, which is located in an active tectonic zone defined by a major mountain belt, has highly variable utility in stacking surface waves. Our current working hypothesis to explain the observed differences in amplitude and frequency dependent stacking capabilities for the array is that we are seeing the interference effects of distinct multipaths and/or pervasive scattering of surface waves that characterize complex paths like that from Lop Nor into KNET.

Finally, we claim our work demonstrates although 20 s Rayleigh waves are the backbone of the most robust discrimination method presently known, there is a considerable lack of knowledge on the basic mode by which these waves propagate. The amplitude variations and stacking characteristics we observe are not consistent with layered earth structures commonly used to model this kind of data. Additional careful analysis of surface waves using arrays of three-component, broadband sensors will be necessary to fully understand the phenomena we have observed here.

References

Dziewonski, A. M., S. Bloch, and M. Landisman (1969). A technique for the analysis of transient seismic signals, *Bull. Seism. Soc. Am.*, 59, 427-444.

Herrin, E. and T. Goforth (1977). Phase-matched filters: application to the study of Rayleigh waves, *Bull. Seism. Soc. Amer.*, 67, 1259-1275.

Herrmann, R. B. (1973). Some aspects of band-pass filtering of surface waves, *Bull. Seism. Soc. Amer.*, 63, 663-671.

Landisman, M. A. Dziewonski, and Y. Sato (1969). Recent improvements in the analysis of surface wave observations, *Geophys. J. R. Astron. Soc.*, 4, 369-403.

Pavlis, G. L. and H. Mahdi (1995). Surface wave propagation in central Asia: Observations of scattering and multipathing with the Kyrgystan broadband array, *J. Geophys. Res.*, in review.

Russell, D. R. (1987). *Multi-channel processing of dispersed surface waves*, PhD dissertation, St. Louis University.

Russell, D. R., R. B. Herrmann, and H. J. Hwang (1988). Application of frequency variable filters to surface-wave amplitude analysis, *Bull. Seism. Soc. Amer.*, 78, 339-354

Sengor, A. M. C. (1984). *The Cimmeride orogenic system and the tectonics of Eurasia, Geological Society of America Special Paper, 195,* Boulder, CO, Geological Society of America.

Zonenshain, L. P., M. L. Kuzmin, and L. M. Natapav, *Geology of the USSR: A plate-tectonic synthesis, Geodynamics Series, 21,* ed. B. M. Page, American Geophysical Union, Washington, DC.

Regional Characterization of Western China

G.E. Randall, T.A. Weaver, H.E. Hartse, S.R. Taylor, R.G. Warren,
and A.H. Cogbill
Geophysics Group EES-3, Los Alamos National Laboratory

ABSTRACT

Geological, geophysical, and seismic data are being assembled and organized into a knowledge base for Western China as part of the CTBT Research and Development regional characterization effort. We have begun our analysis using data from the station WMQ of the Chinese Digital Seismic Network (CDSN). Regional seismograms are being analyzed to construct travel time curves, velocity models, attenuation characteristics, and to quantify regional propagation effects such as phase blockages. Using locations from the USGS Preliminary Determination of Epicenters (PDE) we have identified Pn, Pg, Sn, and Lg phases, constructed travel time curves, and estimated apparent velocities using linear regression. Surface wave group velocities will be measured and inverted for regional structure. Preliminary noise spectra for WMQ have been obtained from the IRIS DMC. Chinese seismicity catalogs from the USGS and SSB are being used to identify and obtain seismic data (including mine seismicity) and information for lower magnitude events. We have identified the locations of nearly 500 mines in China for inclusion in the knowledge base. Future work will involve expanding the data collection and analysis efforts to a larger region using data from additional CDSN, IRIS and portable stations.

OBJECTIVE

We are characterizing regional excitation and propagation of seismic waves in Western China with sufficient accuracy to explain observed seismic data, and to detect, locate, and discriminate seismic events for the verification of a Comprehensive Test Ban Treaty (CTBT). Our primary source of seismic data for the initial effort has been the station WMQ of the Chinese Digital Seismic Network (CDSN) using events located by the USGS Preliminary Determination of Epicenters (PDE). Using seismic waveforms from WMQ and event locations from the PDE, we have identified Pn, Pg, Sn, Lg, Love and Rayleigh phases and picked arrival times for the body waves. The picks have been used with the PDE locations to compute preliminary travel time tables. We have also collected detailed Chinese seismicity catalogs that are complete to lower magnitudes than the PDE and will allow us to identify and study smaller events in the future. Noise spectra for WMQ have been obtained, and will allow a signal to noise detection threshold to be estimated based on the regional amplitude of various phases. We are compiling basic geologic and geophysical information for China including maps for surficial, basement, tectonic and structural geology which will prove useful for the interpretation of special events and forming estimates of seismic propagation characteristics in regions where we are unable to obtain observational data. Analysis of mining activity in China and an attempt to correlate the Chinese seismicity catalogs with mining operations are underway to provide information for geographic location and reference waveforms for discriminating mine explosions from earthquakes and nuclear explosions. We are working closely with the research efforts in discrimination at LANL to avoid redundant efforts and insure the effectiveness of the regional characterization results.

RESEARCH ACCOMPLISHED

Geologic and Geophysical Reference Data Compilation: As part of our effort to compile available geologic and geophysical reference information, Los Alamos is having the US Geological Survey (Flagstaff) construct digital geologic maps for basement, surficial, tectonic and structural geology for Southern Asia, beginning with China. These maps will be online reference material for natural and cultural seismic sources such as major faulting, mining and mineralized areas, and determination of bedrock under reservoirs, construction areas, mines, etc. The digital maps are scheduled for incremental completion, beginning with the basement geology of China in January 1996. We have recently received an additional geologic reference summary (Matzko, 1995) that will prove to be extremely useful in our compilation.

Seismicity Data (Natural, Explosion and Cultural combined): We have initially used the USGS Preliminary Determination of Epicenters for identifying the seismicity of Western China. For more detailed seismicity with a lower magnitude threshold we have obtained historical and contemporary seismicity catalogs for China to identify the characteristic regions and rates of observed seismicity. Historic catalogs are biased by population distributions (Lee et al. 1976, 1978) and the quality of the contemporary catalogs is unknown. The Chinese seismicity catalogs have no indication of the source type so we do not know if explosions from mining and construction operations have been included or deleted from the catalogs. Figure 1 shows the PDE seismicity for the study region for the years 1989 through 1994.

A preliminary analysis of mining and blasting in China is scheduled for completion in August 1995. In addition to identifying and describing the major mining areas of China, the paper will report on the state of blasting technology used in mining (and other fields such as civil engineering) in China. This report will be updated in about a year for final inclusion into the reference library for the China Regionalization results and inclusion into the knowledge base.

We have a contract with the University of Arizona to study regional seismicity catalogs for western China and correlate the mining sites to identify mining explosions and related seismicity in

the catalogs. This will allow us to build a database of reference waveforms for Chinese mining operations and identify mining events for discrimination analysis.

Seismic Waveforms for Data Analysis and Reference Event Library: We have obtained broadband seismic recordings from CDSN station WMQ for events identified and located by the PDE for regionalization and discrimination analysis as well as for permanent archival as reference event waveforms. Station WMQ was chosen because it is close to source regions of interest and it has been operating since 1988 with data easily accessed from the IRIS DMC. In Figure 2 we present a 3 component recording of an earthquake 633 km from WMQ with the horizontals rotated from North and East to radial and tangential. The figure shows both the broadband velocity and the instrument corrected displacement seismogram showing the effective frequency range covering both body and surface waves. McNamara (1995) has shown in Tibet that Sn can have significant long period propagation even when the high frequency Sn phase is not observed, demonstrating the effectiveness of broadband data for complete regional characterization. Data analysis from seismograms recorded at WMQ will establish the excitation of specific seismic phases in the region of interest, and future analysis of longer paths using other CDSN and IRIS stations will allow us to study path specific effects at distances that may be closer to operational distances for regional monitoring of a CTBT.

Preliminary Phase Identification from Seismograms: Phase identification from 3 component broadband seismograms for regional events with known locations has been relatively easy for recordings from WMQ. Using approximate travel times and expected polarizations, seismologists can easily identify the phases Pn, Pg, Sn, and Lg on the majority of the well recorded events and pick arrival times. Figure 2 presents an example and shows the utility of using both velocity and displacement representation of broadband seismograms to emphasize various phases. We have established the excitation and propagation of these phases in the region around WMQ and need to examine longer paths and other stations to establish the attenuation or blockage or any of these phases. We have located some attenuation results (Jin, 1988) and are awaiting the completion of a manuscript by J. Xie (personal comm., 1995). As we collect data for longer paths and multiple stations we will assess the attenuation models.

Travel Time Tables (Pn, Pg, Sn, Lg, L, R): For events recorded at WMQ and locations from the USGS PDE, we have picked arrival times for Pn, Pg, Sn, and Lg when the signal is clear and estimated preliminary travel times for these phases with linear regression. Figure 3 shows the arrival times and the linear regression fits for Pn, Pg, Lg, and Sn. In Figure 4 we show the residuals after removing the regression estimate from the observed arrival times. There is significant scatter in the residuals, and we will need to examine the residuals to determine if there are any significant source region time corrections for WMQ. If depth estimates for the events can be refined by waveform modeling, we will correct the travel times for source depth. As we acquire data from more stations we will also need to determine station corrections. We will need to examine the arrival times for more distant events to expand the regional coverage of travel time tables, and carefully study the regional variations in travel times. We will measure the dispersion for Rayleigh and Love wave fundamental modes. Surface wave tomography results will be available after the completion of a contract with University California, Santa Cruz. We will study the correlation of the larger events that are located by the USGS and the Chinese seismicity catalogs to assess the location accuracy.

Noise Statistics for Seismic Station WMQ: Seismic noise level at the recording stations will be an critical item for establishing expected station detection performance based on signal to noise levels. We have obtained plots of the seismic noise at WMQ from the IRIS DMC for both annual average broad band noise level as well as the diurnal and seasonal variation for mid and long period noise. The noise power spectra are for acceleration $(m^2 / s^4 / Hz)$ and were obtained with a Petersen high and low noise model for reference. These serve as a preliminary noise model

and we can obtain similar noise studies for IRIS stations. We will need to form similar noise spectral estimates for other stations as they become available.

RECOMMENDATIONS AND FUTURE PLANS

We will continue the assembly of regional information, and begin the validation of models by comparing synthetics with real data. Waveform modeling for seismic source and event depth characterization will be attempted. We will continue the collaboration with the discrimination efforts to identify propagation issues and details relevant to discrimination, obtain smaller events identified from regional seismicity catalogs, and mining related events identified from correlation of catalogs with mining. Results we be organized in a form suitable for use by AFTAC in their routine processing and special event studies.

REFERENCES

Hu, P. and Y. Hu, Advances in reservoir induced seismicity in China, *Tectonophysics, 209,* 331-337, 1992.

Jigang, X, A review of seismic monitoring and earthquake prediction in China, *Tectonophysics, 209,* 325-329, 1992.

Jin, A. and K. Aki, Spatial and temporal correlation between coda Q and seismicity in China, *Bull. Seis. Soc. Am., 78,* 741-769, 1988.

Lee, W.H.K., F.T. Wu, and C. Jacobsen, A catalog of historical earthquakes in China compiled from recent Chinese publications, *Bull. Seis. Soc. Am., 66,* 2003-2016, 1976.

Lee, W.H.K., F.T. Wu, and S.C. Wang, A catalog of instrumentally determined earthquakes in China (Magnitude $\geq$ 6) compiled from various sources, *Bull. Seis. Soc. Am., 68,* 383-398, 1978.

McNamara, D.E., T.J. Owens, and W.R. Walter, Observation of regional phase propagation across the Tibetan Plateau, *J. Geophys. Res.* in press, 1995.

Matzko, J.R., Geologic Factors Affecting Seismic Monitoring in China, *USGS Open File Report 95-562,* 44pp, 1995.
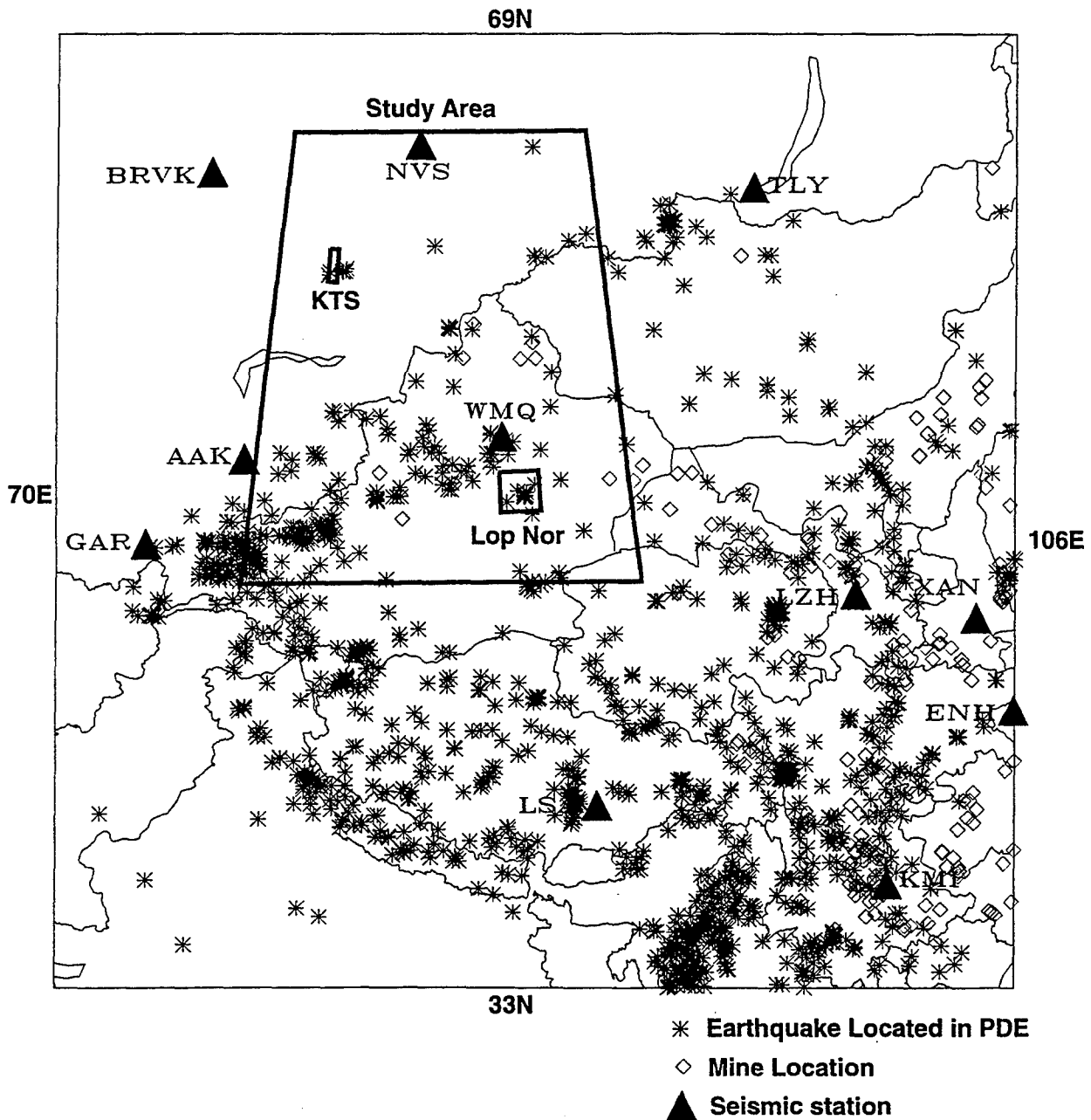
Figure 1. Map of Western China and surrounding areas. The study area, Lop Nor and the Kazakh Test site are outlined in bold borders. The map symbol key for earthquakes, mine locations, and seismic stations is shown at the lower right below the map. The seismicity is from the USGS PDE for the period 1989 through 1994.
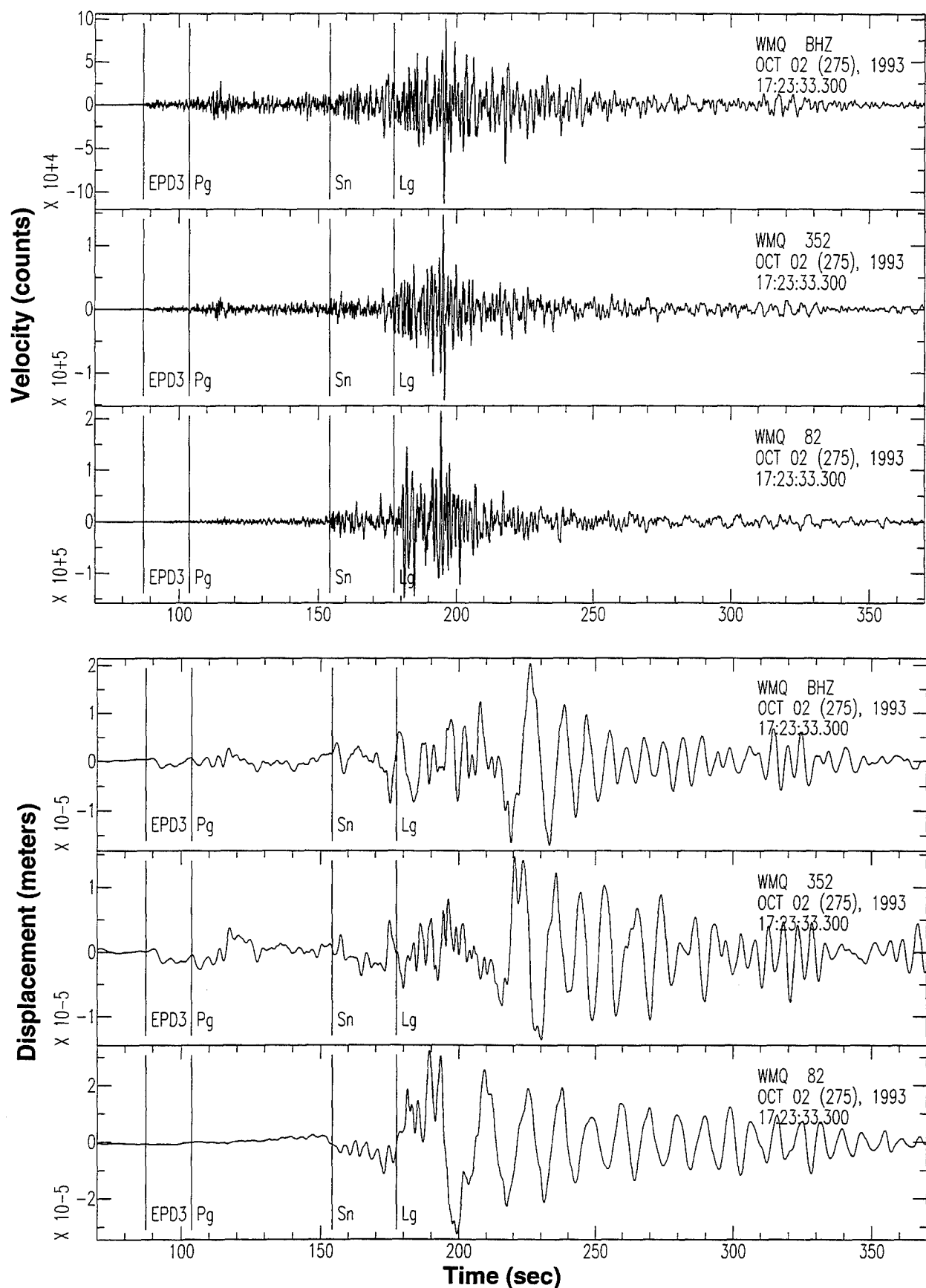
Figure 2. Seismograms for and earthquake 633 km from WMQ. The top traces are raw broadband velocity and the bottom traces are instrument corrected displacement low pass filtered at 0.2 Hz. In both plots the horizontal components are rotated to radial and tangential directions. The displacement shows the dispersed surface wave energy, not visible in the velocity version.
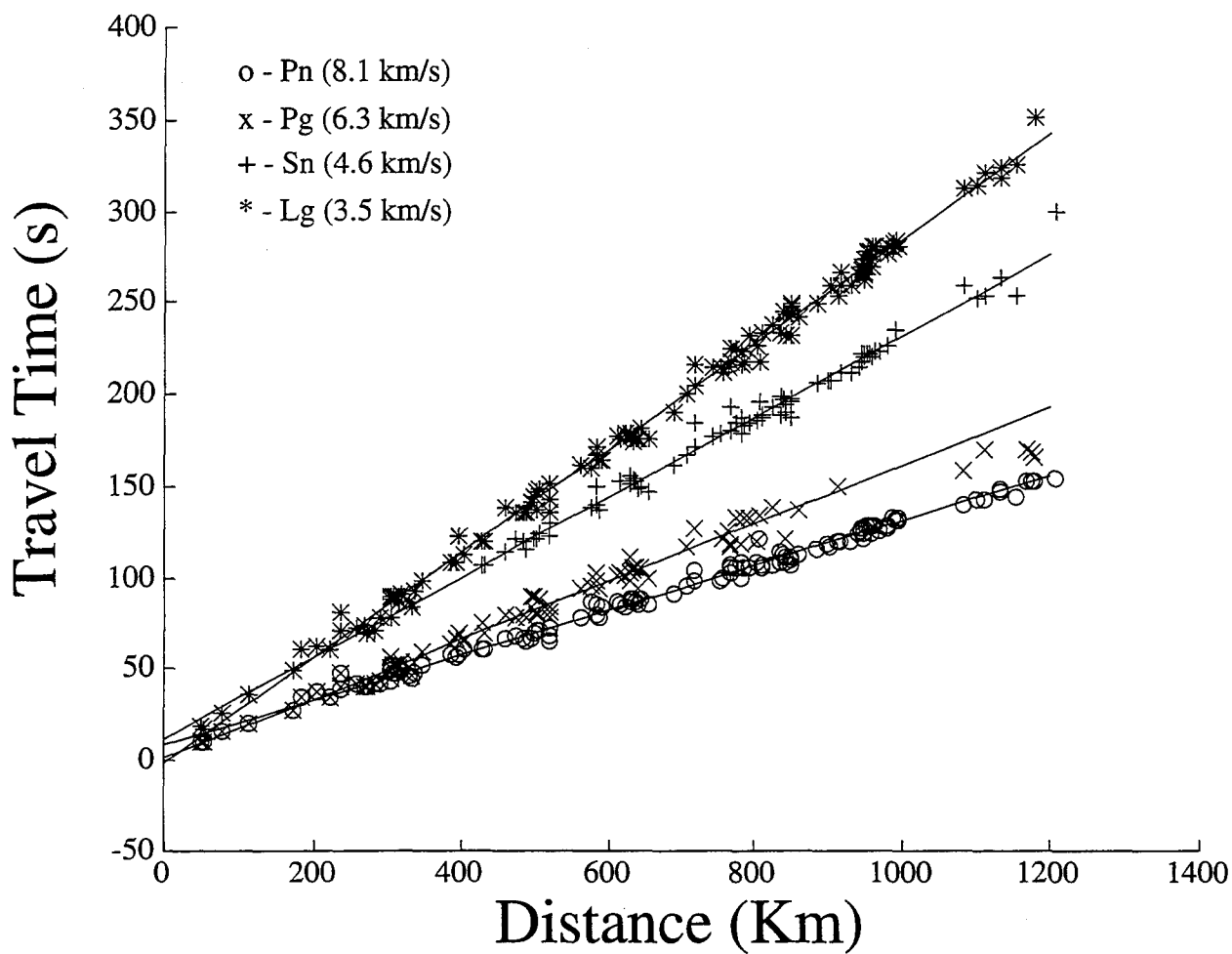
Figure 3. Travel times for Pn, Pg, Sn, and Lg for earthquakes recorded at WMQ. Lines show the linear regression results and estimated velocities for each phase are shown in the symbol key in the upper left hand corner.
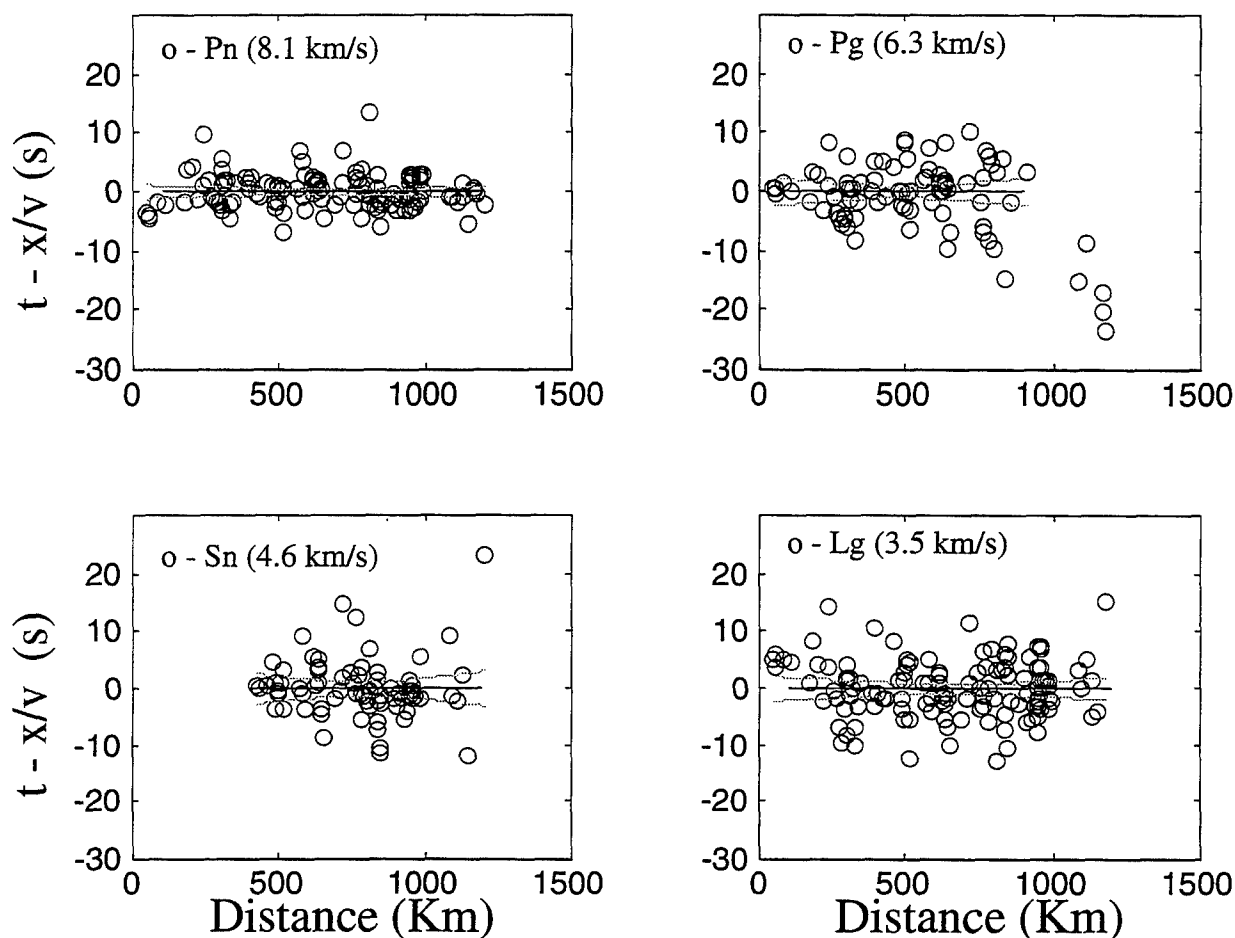
Figure 4. Reduced travel times and linear regression results from the earthquake travel times for events recorded at WMQ shown in Figure 3. The results for Pn, Pg, Sn, and Lg are shown on a common scale for comparison. The residuals for the later phases show more scatter about the regression line and the 95% confidence region (dashed lines) is broader. The velocity estimated from the regression is shown in the upper left hand corner for each phase. For Pg the regression only used arrivals out to 1000 km in order to avoid the more distant arrivals that appear to be from another phase.

DOE Program on Seismic Characterization for Regions of Interest to CTBT Monitoring

Alan S. Ryall[1] and Thomas A. Weaver[2]

1) Earth Sciences Division, Lawrence Livermore National Laboratory
2) Geophysics Group, Los Alamos National Laboratory

ABSTRACT

The November 1993 transfer of responsibility to the Department of Energy (DOE) for part of the Defense Department's research in support of a Comprehensive Test Ban Treaty (CTBT) has led to a significant reorientation of the DOE seismic research effort, with significant new efforts on Geophysical Characterization of the Middle East-North Africa (ME-NA) and Southern Asia (SA) regions, respectively guided by Lawrence Livermore National Laboratory (LLNL) and Los Alamos National Laboratory (LANL). These programs will provide detailed regional calibrations that can be used to improve seismic phase identification, association, event location and event identification. Parameters and other information generated by these efforts will be incorporated into the knowledge bases of the Prototype National Data Center (PNDC) operated by the Air Force Technical Applications Center (AFTAC), and the Prototype International Data Center (PIDC) being developed by the Advanced Research Projects Agency (ARPA).

Knowledge required for improved automated data processing by the PNDC and PIDC includes detailed, region-specific parameter sets related to traveltime, attenuation and frequency content of the various seismic phases that record at regional distances, plus information on seismicity, location and blasting practices of operating mines, structure of the lithosphere, topography and other data. For stations of the primary CTBT monitoring network, this information will be path-specific, with calibration parameters determined for the receiver sites, the source-receiver paths to potential source areas around the station, and the source areas. Insofar as possible these data will be formatted for direct incorporation into the knowledge base system of the data centers.

The DOE approach to characterization of the ME-NA and SA regions will be evolutionary -- initially building on the geophysical literature and experience that is being acquired during the current Conference on Disarmament, Group of Scientific Experts Third Technical Test (GSETT-3), then developing geophysical models to predict observables (traveltimes, amplitudes, etc.), checking the predictions against observations in the areas of interest, and fine-tuning this procedure as needed to produce an accurate knowledge base for the region. Both efforts, but in particular that of LLNL, will be aided by an external research program consisting of contracts with universities and industrial research groups. Deliverables on these contracts will be primarily in the form of scientific reports and/or waveform data sets -- LLNL and LANL will act as *integrators*, collecting region-specific data from the contractors and using the data to prepare input for the PNDC and PIDC knowledge base systems. Updates of the knowledge bases will occur through periodic synthesis of the results of network operations and investigation of "special events" or outliers -- events that fail to locate or discriminate during routine processing. The program is also intended to generate a prescription for calibrating other regions with which the U.S. has had little or no previous monitoring experience.

Introduction

The primary goal of the DOE programs on Geophysical Characterization of 1) the Middle East and North Africa (ME-NA) and 2) Southern Asia (SA) is to provide the Air Force Technical Applications Center (AFTAC) with the analytic tools and knowledge base to permit effective verification of Comprehensive Test Ban Treaty (CTBT) compliance in those regions. The program also aims at using these regionalizations as models for the development of a detailed prescription for seismic calibration and knowledge base compilation in areas where the U.S. has had little or no previous monitoring experience.

For automated data processing systems of the Prototype National Data Center (PNDC, operated by AFTAC) and the Prototype International Data Center (PIDC, operated by ARPA) to be effective, a knowledge base is needed that contains specific information to calibrate the seismic analysis procedures -- *phase detection, phase identification, association, location (including depth determination) and identification.* Because CTBT monitoring will focus on small seismic events, often detected by only a few stations at regional distance ranges, U.S. capability to effectively monitor the treaty will depend critically upon accurate information on the velocity structure, scattering, attenuation and wave blockage of the earth's crust and upper mantle in regions of interest, as well as knowledge of the signal characteristics of different types of events (earthquakes, mine explosions, small decoupled nuclear tests, mine tremors, rockbursts, etc.).

In any given region, the CTBT seismic monitoring system will depend heavily on a few key arrays and/or three-component stations, and it will be important to know as much as possible about the physical properties of the earth's crust and upper mantle: 1) in the vicinity of these stations, 2) in areas of potential earthquake activity or commercial blasting in the region containing the stations, and 3) along the propagation path from the sources to the stations. To be able to discriminate between various source types, we will also need to know how well the various event characterization techniques perform when they are transported from one tectonic or geologic environment to another.

The Department of Energy's CTBT R&D program plan (DOE, 1994), which includes the ME-NA and SA characterization programs, incorporates an iterative process that combines field experiments, computer modeling and data analysis for the development, testing, evaluation and modification of data processing algorithms as appropriate to achieve specific U.S. monitoring objectives. This process will be applied to seismic event detection, location and identification.

An external research program to support and complement these tasks has been funded by DOE, using the Air Force Phillips Laboratory (PL) as its contracting agent. Through a Broad Agency Announcement in June 1994 PL advertised the research areas of interest to the ME-NA and SA programs, and in November 1994 a number of proposals were selected for funding. Under the current plan, LLNL and LANL will be responsible for integrating results of the ME-NA and SA research programs, respectively, into algorithms for the PNDC system and parameter sets to be installed in the PNDC and PIDC knowledge bases.

Regional Calibration Data Needed by the PNDC and PIDC

The PNDC will require specific types of regional calibration data for areas of particular monitoring concern, and AFTAC desires that the data be in formats that will be appropriate for direct incorporation into the Knowledge Base System of the PNDC. The types of data required, illustrated in Table 1, will also be needed by the PIDC.

For *phase detection and phase identification* the system will need information on the phase velocity and frequency content of regional and teleseismic signals from events in areas of interest, together with information on seismic propagation characteristics for various azimuth and distance ranges around primary and key secondary stations.

Phase Detection/Identification	Association	Location	Identification
Sta. Noise	Traveltime curves	Traveltime corrections	mb, Ms corr'ns
Inst. Calibration	Azimuth	Expected phases	Topography
Beam Settings	Amplitude	Earth model	Regional tectonics
Filter Modes	Det. Probability	Lithosph. structure	Seismicity
Detection threshold		Reference events	Mine loc'ns
Phase velocity, freq			Reference events
Attenuation, scattering, phase blockage			Expected frequency content
			Expected amplitude ratio

Table 1. Examples of information needed by the PNDC and the PIDC for phase detection, phase identification, association and event location, and by the PNDC for event identification.

COUNTRY	ALG	EGP	IRN	IRQ	ISR	JRD	KWT	LBN	LIB	MRC	ARB	SYR	TUN	TRK	YMN
TRAVELTIME CURVES			BFI		B	B			L	B	BI	B		FI	
DEPTH TO BASEMENT		B	■	■	■	■	■	■		B	■	■			
DEPTH TO MOHO		■	BF	B	B	B	B	B	L	■	BI	B	B	F	
STRUCTURE			AFJ		D				L	■				AFJ	
SP ATTENUATION			A									I		AJ	
Lg, LP ATTENUATION		H	H		H	H	H	H	L	H	■ HI	H	H	H	
EQ CATALOG	■	■	■	■	■	■	■	■	■	■	■	■	■	■	■
GAMMA DATA		E			BD	BE		B	L	■		B		E	B
GEOLOGY/TECTONICS	B	B	B	B	B	B	B	B	BL	B	B	B	B	B	B
TOPOGRAPHY	■	■	■	■	■	■	■	■	■	■	■	■	■	■	■
GRAVITY	B	B	B	B	B	B	B	B	L	B	B	B	B		
LANDSAT IMAGERY	B			B	B			B		B		B	B		
M-T FOCAL MECH.	B	B	B	B	B	B	B	B	B	B	B	B	B	B	B
DISCRIMINATION		CG	A		CDG	CG				CG	CG			ACG	
MINE LOCATIONS	▼	E	▼	K	E	BE			▼	BE	BE	BE			

Table 2. Expected data products from the ME-NA Characterization external program. Key to contractor designations is given below. Country designations: ALG -- Algeria, EGP -- Egypt, IRN -- Iran, IRQ -- Iraq, ISR -- Israel, JRD -- Jordan, KWT -- Kuwait, LBN -- Lebanon, LIB -- Libya, MRC -- Morocco, ARB -- Saudi Arabia, SYR -- Syria, TUN -- Tunisia, TRK -- Turkey, YMN -- Yemen. "GAMMA DATA" -- waveform or bulletin data from local and/or national networks.

■ Cornell U. (Barazangi) — Cornell U. GIS already contains this information

▼ U.S. Bureau of Mines — Survey of Mining Activity in Algeria and Libya - completed

A Cambridge U. (Priestley) — Lithospheric Structure and Discrimination in MidEast

B Cornell U. (Barazangi) — Geophysical Information System for ME-NA

C ENSCO (Baumgardt) — Transportability of Regional Discriminants

D IPRG (Shapira) — Discrimination Using the Israeli Seismic Network

E Multimax (Grant) — Ground-Truth Database for Identification Research

F New Mexico (Ni) — Regional Propagation in ME and Southern Asia

G Radix (Pulli) — Transportable Seismic Discriminants

H St. Louis U. (Mitchell) — Efficiency of Regional Wave Propagation in ME

I UC San Diego (Berger) — Broadband Seismic Field Study of the Arabian Shield

J UC Santa Cruz (Rogers) — Waveguide Effects on Broadband Signals in ME

K U.S. Bureau of Mines — Survey of Mining Activity in Iran and Iraq

L U. Texas El Paso (Doser) — Lithospheric Structure of North Africa

Table 2. Expected data products from the ME-NA characterization external program. Key to contractor designations is given below the table. Country designations are: ALG - Algeria; EGP - Egypt, IRN - Iran, IRQ - Iraq, ISR - Israel, JRD - Jordan, KWT - Kuwait, LBN - Lebanon, LIB - Libya, MRC - Morocco, ARB - Saudi Arabia, SYR - Syria, TUN - Tunisia, TRK - Turkey, YMN - Yemen. The term "GAMMA DATA" refers to waveform or bulletin data from local and/or national earthquake monitoring networks.

Association of detected arrivals with events will require a determination of the probability that a given station detected a particular event, and this in turn will depend on the event size, station noise level at various frequencies, and attenuation of regional seismic phases for particular source-receiver paths. To make such a determination requires knowledge of scattering, attenuation and blockage of particular phases due to structure along the path. Association will also require detailed knowledge of regional and teleseismic traveltimes for particular source-receiver paths.

Accurate *event location* will be even more dependent on detailed knowledge of path-specific corrections to traveltimes and azimuths, and these should be empirically determined using "ground truth" data from local or national networks in the ME-NA region, or based on models of the lithosphere along particular source-receiver paths. A library of reference events will be useful for locating repeated events in mining districts or in known earthquake source areas.

Event identification will require most of the knowledge listed above, with particular importance attached to an accurate picture of attenuation of the various regional phases as a function of distance and frequency. In addition, information will be needed on source/spectral characteristics of earthquakes and explosions in the areas of interest, location of mines, seismicity, geologic/tectonic features. For most regions of the world, the signature to be expected from nuclear tests under various assumptions relative to coupling will have to be simulated by waveform modeling techniques. These techniques will be extrapolated from U.S. and Russian experience, based on an improved understanding of the dependence of seismic propagation parameters on regional structure and other properties to be defined under the various elements of this program. For earthquakes, mine explosions and mine collapses, a library of waveforms for known event types in the areas of interest will be invaluable to the discrimination process.

The reader should note that in the above listing there is a progression, in terms of amount and detail of the knowledge required, for succeeding stages of the data processing. It should also be noted that to the maximum extent possible, the PNDC and PIDC will need datasets in a form that can be directly incorporated into system knowledge bases -- e.g., tables of traveltime and amplitude corrections to standard curves, calculated for each of a large number of grid points distributed over a range of azimuths and distances around the station locations. It will be a primary goal of the LANL and LLNL programs to collect data -- from the literature, historic waveform archives, the PNDC and PIDC databases, local and regional networks in the ME-NA and SA regions, and from contractor reports and datasets -- to convert these data into the parameters needed for the knowledge bases of the PNDC and PIDC, and to deliver the parameter sets to AFTAC and ARPA. In many, or perhaps most cases this conversion will not be straightforward, but will require extensive data interpretation, modeling, testing and evaluation by Laboratory seismologists to insure that the parameters and algorithms delivered to AFTAC will actually improve AFTAC's capability to monitor the regions of interest.

Elements of the LLNL Research Program

The Middle East and North Africa (ME-NA) comprise a unique natural laboratory that will be exploited by LLNL for the development of a seismological knowledge base and new data processing algorithms needed by the PNDC and PIDC for improved phase identification, association, location and event discrimination. A major objective of the ME-NA program will be to demonstrate that over a relatively short period of time both the tools and the knowledge can be acquired for effective CTBT verification in a region that has not previously been a major focus of U.S. monitoring efforts.

Tectonically, the ME-NA region is as complex as any on earth, with major features including a stable platform (Arabian plate), sea-floor spreading (Red Sea, Gulf of Aden, Afar region, western Arabia), continental collision zone (Zagros Mountain fold belt), recent volcanism (western margin of Arabian plate), and transform faulting (Dead Sea, Anatolian fault zone in Turkey). Significant seismicity is observed in many of these zones, and mining activity is ubiquitous -- at least some

mining is conducted in most or all of the countries, and large explosions are regularly detonated in potash mines in Morocco, Jordan and Syria; in addition, numerous offshore explosions and earthquakes have been reported off the coast of Israel. Short-period earthquake monitoring networks are common to most of the countries and now include more than 300 stations for the whole ME-NA region. Some countries have deployed digital, broadband, wide dynamic-range stations at key locations. New regional seismic arrays have been or will be deployed at a number of sites within regional distance ranges from ME-NA seismic source areas, including arrays in Turkey, Egypt, Pakistan, Israel, Spain, Turkmenistan and the Caucausus. Taken together, the geophysical/tectonic features and the potentially excellent seismic coverage make this region ideal for research and experimentation aimed at developing methods and algorithms for network data processing, as well as a prescription for the timely acquisition of calibration information in other regions with which the U.S. has had little previous monitoring experience.

Figure 1 shows elements of the LLNL external program, with data collected from seismic stations and arrays in the ME-NA region being used for the extraction of data products, which are used in turn for research to improve location and identification of events recorded in that region. The data products will also be used to produce deliverables for the AFTAC knowledge base: improved velocity structure of the earth's crust and upper mantle in the ME-NA, improved traveltime curves for regional distance ranges, maps of seismicity, and tabulated estimates of background seismic noise at station sites. A second set of deliverables will consist of calibration parameters to improve event locations in the ME-NA region, and these locations will in turn be used in discrimination research to produce improved methods for event identification in the region. The collected data and data products will also be used for comparison with synthetic waveforms, developed to model regional wave propagation effects and source phenomenology.
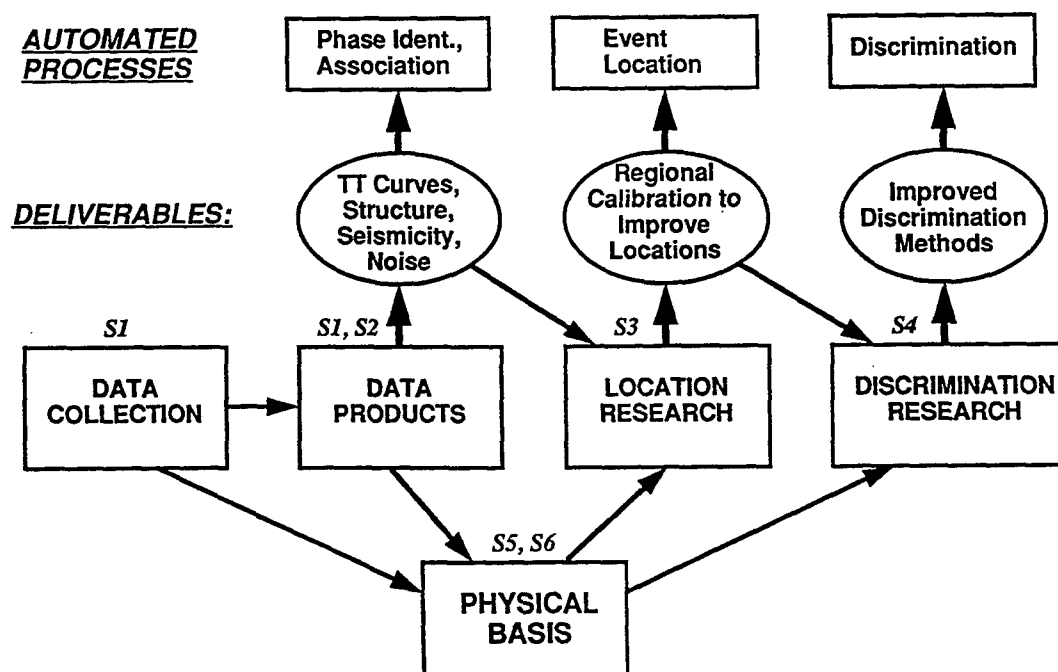
Figure 1. Elements of the LLNL *Middle East-North Africa Geophysical Characterization Program*. Labels *S1*, *S2*... correspond to designations in DOE R&D plan (DOE, 1994).

In the following sections we describe the individual contractor efforts in four of the eight task areas cited in the DOE R&D plan (DOE, 1994). Deliverables on these contracts are categorized in chart form in Table 2, above.

Data Collection (S1)

A key contract in the data collection element of the ME-NA program is the continuation with DOE support of Cornell University's effort to develop a Geophysical Information System (GIS) for the ME-NA region. The objective of the Cornell effort is to collect and organize seismological, geophysical and geological datasets for the ME-NA region. These datasets are incorporated into a digital information system that is accessible via the Internet, and can be used by the National and International Data Centers (PNDC, PIDC) and by other researchers in the nuclear monitoring research community. Previous work by the Cornell group produced digital datasets for Eurasia containing depth to Moho and to basement, crustal velocity and density structure, and other geophysical information and considerable progress has already been made in compiling a variety of datasets for Egypt, Iran, Iraq, Israel, Jordan, Syria, Lebanon and Saudi Arabia. All data are stored in Cornell's Arc/Info Geographic Information System (GIS). A comprehensive bibliography of all relevant references is maintained in a computer database. Preliminary versions of these databases are being released in different forms, including a Web page available over the Internet.
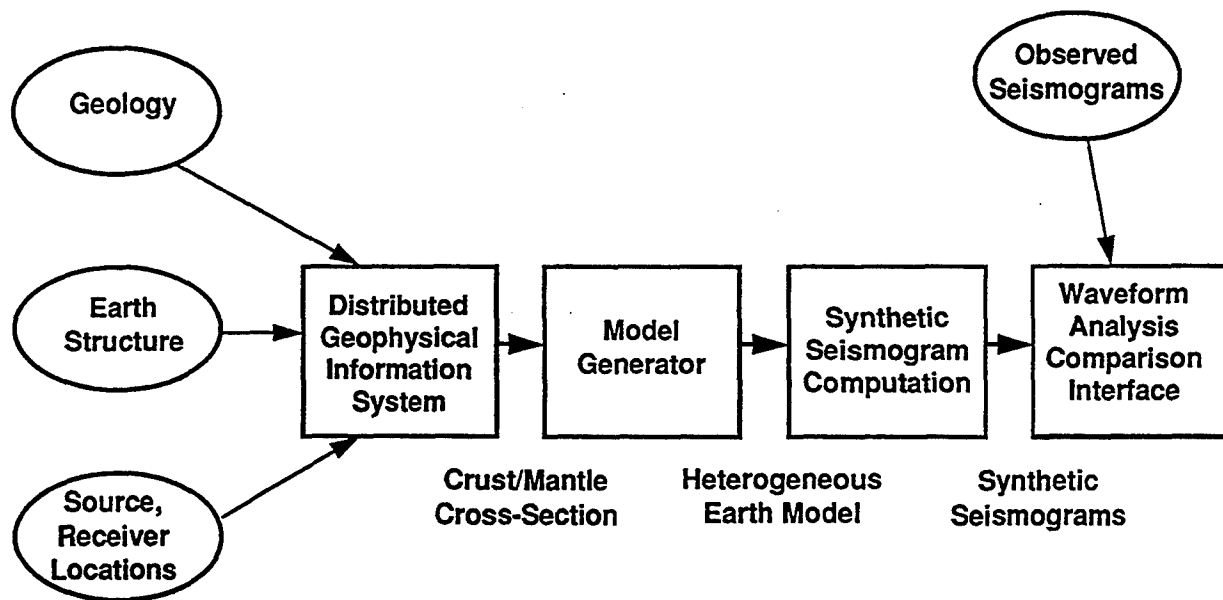
Figure 2. Geophysical information system, earth model generator and synthetic seismogram computation modules for characterizing seismic propagation paths

The Cornell GIS will be used in a distributed system, illustrated by Figure 2, in which tabulated information on geology, earth structure, seismicity and other information is accessed through the system. The system will also have the capability to generate crust-mantle cross-sections, and to synthesize heterogeneous earth models based on the cross-sections. The third block of the system shown on Figure 2 is a "user-friendly" environment for the generation of synthetic

seismograms. This module will be developed under a separate contract with S-Cubed, discussed below under task S5. Together, the GIS, model generator and synthetic seismogram computation programs will allow researchers to examine tradeoffs in structure as these tradeoffs affect seismic wave propagation. Synthetic seismograms generated by the system will be compared with actual recordings from the ME-NA region to validate or reject the structural models being tested.

A second project under the data collection element will be the compilation, by Multimax, Inc., of a "ground-truth" database (GTDB) for regional identification research. This effort will begin with the collection of in-country seismic bulletins, and other contractors will be contacted to determine the availability of older data from the Iranian Long-Period Array (ILPA) and other deployments. Later, as new arrays become operational in Turkey, Egypt, Pakistan and other ME-NA countries, continuous data from those arrays will be scanned to select "interesting" events from the viewpoint regional characterization and/or event identification research, and supplemental data will be requested from earthquake networks already operating in the region. Particular attention will be paid to the collection of ground truth data for source areas where, based on the GSETT and national earthquake bulletins, events tend to cluster -- e.g., repeated events in known mining districts, earthquake aftershock zones, etc. As the database is developed, it will be ported to an archive at LLNL, for use by Laboratory researchers for investigations to improve event location and identification capability. The data will also be accessible over the Internet to authorized researchers within the CTBT R&D Program.

Several other contracts in the ME-NA program are aimed at collecting data from that region. In a joint effort, the University of California San Diego (UCSD), Boise State University and King Saud University will undertake during the fall of 1995 a field program in Saudi Arabia. This experiment involves the deployment of six portable broadband seismic stations along three profiles on the Arabian Shield, for a recording period of about a year. During this period the team will collect a suite of broadband seismic waveform data and the associated parametric data describing the sources (event location, depth, magnitude and type) of events recorded by the field stations. Data will also be collected from other broadband stations operated by IRIS, GEOSCOPE and MEDNET in the ME-NA region. Most of the events recorded will be in tectonically active areas of Iran and Turkey to the northeast. The main objectives of the investigation will be to study seismic propagation, seismicity and crustal structure of the Arabian Shield, and to characterize potential sites for permanent seismic stations in the region. When archived at LLNL and combined with recordings of the same events from new arrays in Turkey, Egypt and possibly Pakistan, these data will be a valuable resource for studies to improve event location and discrimination capability. Supplementary information on at least some of the recorded events can be obtained from seismic bulletins distributed by various national networks in the region.

Under another contract, workers at the University of Texas El Paso will construct a model of the North African lithosphere, via an integrated analysis of seismic, potential field and geologic data. Particular emphasis in this research will be on the construction of two-dimensional models from known earthquake source regions to key seismic monitoring stations in the region. The principal investigators on this project have had over ten years' experience working in Libya, and have supervised a number of graduate thesis projects by Libyan students. An outgrowth of this effort will be a database of geological and geophysical information that will enhance the GIS development being pursued by Cornell University.

A project being conducted by Cambridge University is aimed at determining the structure of the Iranian Plateau, characterizing regional seismic propagation (in particular the amplitude and frequency characteristics of seismic phases Pn, Pg, Sn and Lg), and testing the effectiveness of regional discriminants for that region. The Cambridge group now operates three-component broadband digital seismic stations at six sites around the South Caspian Sea and in the republics of Turkmenistan and Azerbaijan, and these stations will be operated until the end of 1995.

Under a previous Department of Defense (DoD) contract, seismologists at the New Mexico State University (NMSU) initiated a study of the lithospheric structure of the Turkish-Iranian plateau, using Pn tomography, Sn attenuation and Lg propagation, and have published two papers describing

313

their results. During the next two years they will extend this study for DOE, to focus on amplitude measurements of regional phases and regionalization of seismic propagation characteristics for the Middle East and southern Asia. Data for these investigations will include data from an array (ILPA) operated in Iran during the 1970's (recordings of more than a hundred regional events are already on hand), the IRIS Caucausus Network (CNET), ten stations in Kyrgystan (KNET), the Chinese Digital Seismic Network (CDSN) and nine stations operated briefly in Pakistan (over 800 local and regional events were recorded). Data collected for this project will be accessible to LLNL and other nuclear monitoring researchers in CSS database format.

A contract with the geophysics group at St. Louis University has as its goal characterization of regional variations in attenuation of regional seismic phases across a broad region of the Middle East and southern Asia. This work will be complementary to the NMSU project just described, as it will be based initially on analysis of long-period (5-50 seconds) Rayleigh waves, primarily recorded at pairs of stations, to determine S-wave attenuation models for the earth's crust in regions of interest. With the velocity and S-wave attenuation models they will then use waveform synthesis to predict the ground motion of Lg and other phases. Similar to work done by this group for Eurasia, products of this research will include maps of shear-wave Q, Lg Q and Lg coda Q for the region from India to the eastern Mediterranean.

One additional contract with the U.S. Bureau of Mines, Minerals Availability Field Office (MAFO) is supported with LLNL discretionary funds. The MAFO group is drawing from numerous sources to identify active mining operations in Algeria, Iran, Iraq and Lybia, and to estimate probable amounts of explosives used in operations at those mines. Final reports on mining operations in Algeria and Lybia have been delivered to LLNL, and the reports on Iran and Iraq are due by September 1995.

Empirical Discriminants (S4)

While work in this area emphasizes the development and testing of discriminants, rather than regional characterization *per se,* the contractors will be developing software tools for automatically extracting "features" from the data and for comparing those features and discriminants based on them (amplitude and spectral ratios, etc.) with features and discriminants predicted from theoretical modeling. For example, under a key DOE-funded effort ENSCO, Inc. will implement its Intelligent Seismic Event Identification System (ISEIS) at LLNL, and will work with Laboratory staff to test and improve this system as a tool to study regional waveform discriminants. ISEIS, developed under DoD support and used by ENSCO to test the portability of regional discriminants, has expert system capabilities as well as interactive features that permit it to be used as a testbed for the development of both rule-based and case-based event identification procedures.

A second discrimination research project by Radix, Inc. will utilize existing GTDB's for northern Europe as well as new GTDB's for the western U.S. and the ME-NA region to test a new cross-band spectral discriminant. The contractor will also work on optimizing feature extraction from seismic data with the goal of reducing discriminant variance from region to region, and thereby reducing the necessity of compiling GTDB's in regions that are relatively uncalibrated.

A contract with the Institute for Petroleum Research in Geophysics (IPRG) in Israel will focus on discrimination of seismic sources using the Israeli seismic network. This project will also provide nuclear monitoring researchers access to data from the Israel Seismic Monitoring Systems.

An effort by the University of California Santa Cruz (UCSC) will focus on the partitioning of seismic energy between the various regional phases as a function of crustal structure. This work will utilize new data from broadband stations in the ME-NA region as well as older data from the Iranian Long-Period Array (ILPA). This study will be a follow-on effort to work already completed for the Iranian region by UCSC.

<u>Physical Basis for Regional Propagation and Discrimination (S5, S6)</u>

It is anticipated that the LLNL research staff will provide most of the effort to develop models leading to a better physical understanding of regional propagation effects, factors that affect event location and discrimination, and the behavior of particular discriminants in different geologic or tectonic environments. A few of the DOE-supported contracts have been selected for their potential to fill in gaps in the program, and in one case to add new software tools to those now available for the modeling effort. In the latter case, a contract with S-Cubed, Inc., is for the development of a user-friendly interface for the efficient computation of synthetic waveforms, and for the archiving and retrieval of a library of syntheticwaveforms that can be used to test various concepts related to the regional characterization effort. The contractor will also investigate effects due to scattering and lateral heterogeneity in the crust and upper mantle -- both important for accurate event location and identification. The software developed under this contract, as well as synthetic waveforms for a wide range of source and path conditions, will be extremely useful to the LLNL staff in comparing the observed behavior of seismic signals in the ME-NA region with effects predicted from theoretical considerations, based in turn on earth models obtained from various sources -- published literature, surface-wave dispersion, field experiments, etc.

Elements of the Los Alamos Regional Characterization Research Program

To better integrate all CTBT Seismic R&D tasks, LANL has chosen to perform onsite most of the tasks related to characterization of the southern Asia region, using the regionalization effort as the primary data collection, processing and preliminary interpretation task for the Southern Asia region. Like LLNL, LANL's regional characterization task will be striving to fill in all of the needs of the KBS for Southern Asia (seismic, geophysical, geological, and cultural databases and models). We have begun with China and will be expanding to the area South of China and Mongolia late in FY 1996.

To assist with primary seismic data collection, processing and interpretation, LANL has let the following subcontracts to universities for support analyses of seismic data

1) University of South Carolina - Acquisition and analysis of data from the PASCAL deployment across central Tibet.

2) University of Arizona - Seismicity in the Region around the Lop Nor Test Site. This project involves obtaining seismicity catalogs from the State Seismological Bureau in Urumuqi to identify pockets of seismicity that may be associated with mine activity. SPOT photos will then be used to locate the mines and triggered IRIS data from WMQ will be obtained for mining explosions.

3) UC - Santa Cruz - Crustal and Lithospheric Structure in China: Waveguide Effects on Regional Phases Used in Nuclear Test Monitoring. Regional surface wave tomography will be conducted across China (having lateral resolution of 100 - 500 km). The velocity models will be combined with other geologic information to examine waveguide effects on regional phases used for seismic monitoring.

A larger contract was let to the US Geological Survey in Flagstaff, Arizona, to construct digital geologic maps (basement geology, surficial geology, and tectonic and structural features) of the Southern Asia region, beginning with China. These maps will serve as three of the GIS (Geographic Information System) planes for on-line source term analysis. Other GIS planes will include, among others, seismicity, topography, depth to Moho, depth to basement, mines and mineral deposits, Q, geographic information (roads, towns, etc.) and other seismic noise sources.

LANL is also conducting special studies on mining and blasting practices, explosions of interest, and tectonic/geologic features of interest (salt domes, soluble media layers, etc.). In addition, Los Alamos is exploring for an appropriate three-dimensional database management system to build

3-D models of various aspects of the geology, seismic parameters and ancillary information. Data generated at Los Alamos will soon be available to researchers in the program on a worldwide web server at Los Alamos. Access to this information will be through the future Sandia InfoWeb center.

A more detailed description of the initial LANL efforts on the regional characterization effort for Southern Asia can be found in the poster session "Regional Characterization of Western China" (this volume).

Discussion

Because monitoring small seismic events is essentially a regional problem, the DOE seismic characterization program will focus most of its effort on seismic monitoring at regional distance ranges, out to about 2,000 km. The program has begun with a literature search to obtain first-order regional traveltime and amplitude-distance relationships for the ME-NA and SA regions, with LANL and LLNL staff working with Cornell University and other DOE contractors to gather data and generate derivative products on a country-by-country basis. This search will result in a series of summary reports, and a computer database containing the references and key data (e.g., traveltime curves, amplitude-distance relationships, lithospheric models). Copies of national seismic bulletins are being requested from those countries that issue such bulletins, and these will be used, after consistency checking, as a source of ground truth information on event locations and, as a basis for requesting waveform data from national earthquake networks and the GSETT-3 global network. Reports and data products from contractors in the DOE external research program will be collected as they become available and integrated with information collected by the Laboratories. The research database that results from this process will be used to generate higher-order models of the lithosphere and improved knowledge of signal propagation in the regions of interest, and both the models and empirical data will be analyzed, compared and interpreted to produce specified parameter sets for incorporation into the knowledge bases of the PNDC and PIDC. This iterative process is illustrated by Figure 3 and described in more detail in the remainder of this section.
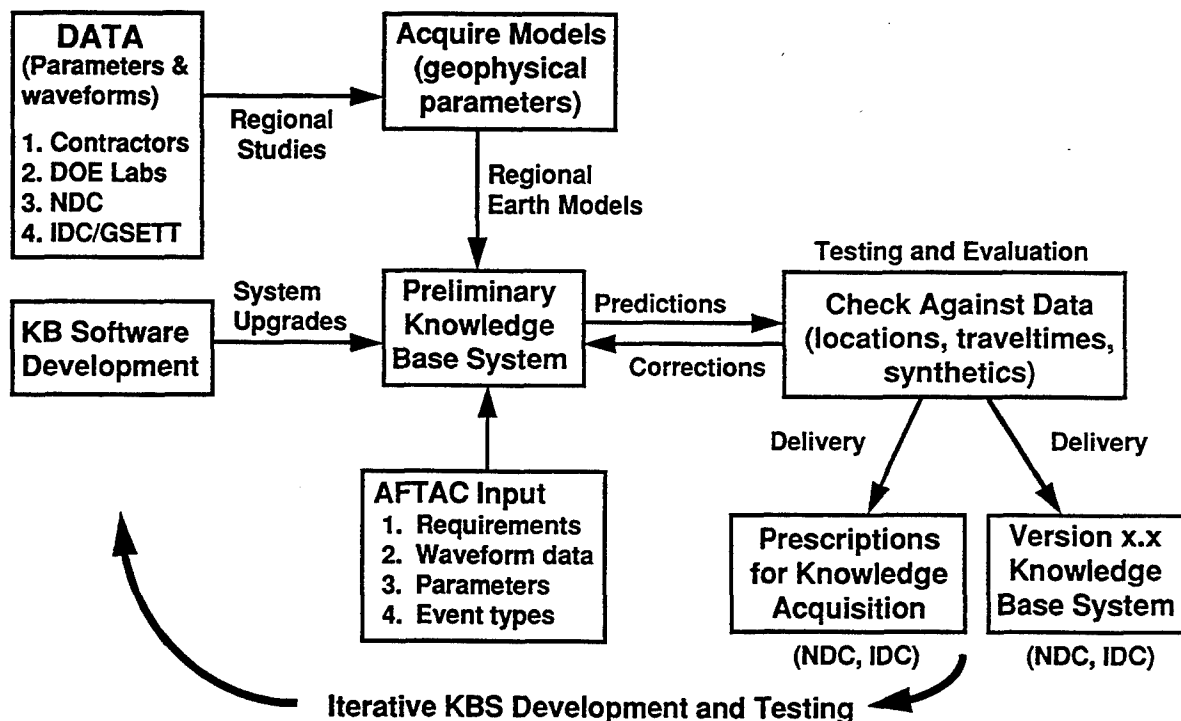
Figure 3. Elements of the DOE program for regional characterization and knowledge base system development, testing and evaluation.

Under the external research contracts described in previous sections of this report, U.S. seismologists will be collaborating with in-country scientists to develop models of the lithosphere, study attenuation of regional seismic waves, etc. In the course of these investigations it is anticipated that a considerable amount of data will be accumulated, including waveform data and information on chemical explosions and earthquake hypocenters determined by local and national networks. LLNL and LANL will be responsible for collecting this data, subjecting it to quality assurance procedures and archiving it in databases that will be used for detailed studies, e.g., of regional traveltime and amplitude corrections. As waveform data become available from the ME-NA and SA regions -- either data from arrays and stations of the GSETT-3 network or data that may in the future be supplied by local and regional earthquake monitoring networks in the region -- these data will be collected and archived in the research databases, including the Ground Truth Database for those events for which independent confirmation can be obtained on event location, depth and source type.

Within the Laboratories' internal research programs a number of additional investigations are planned or in progress that will complement and strengthen the regionalization effort. For example, field studies are under way in Nevada and Colorado that will lead to new insights into source characteristics of mine explosions and mine tremors. Theoretical waveform modeling calculations are being conducted to develop a better better understanding of the various types of sources (earthquakes, mine explosions, rockbursts, mine tremors) that may be observed in the regionsof interest, and to develop a comprehensive picture of tradeoffs between effects due to event type, depth, size, structure along the path, and other factors. Because it will not be possible to acquire data from most areas within the ME-NA or SA regions for direct application to the problem of identifying nuclear explosions in those areas, every effort is being made to save the information that is now available for nuclear tests conducted in Nevada and elsewhere, and to make those data available to the research community. Synthetic data may be the only means of evaluating nuclear explosion signals in structures typical of those in a particular region, and synthetic data will be generated under varying assumptions as to coupling, depth, source medium, etc.

As the various datasets are compiled, they will be interpreted by LANL and LLNL researchers in terms of the parameters needed for improved phase identification, association, event location and discrimination, and the parameter sets will be entered into the knowledge base of a testbed system being operated at the PNDC. Assessment of improvements in monitoring capability due to these parameters will be done by reanalysis of data for events with known location, magnitude and event type (i.e., events in the Ground Truth Database), using the testbed system with the new sets of corrections and other parameters. This process will be both evolutionary and iterative, with future updates to the knowledge base tied to results obtained during operation of the PNDC, as well as to results of investigations of "special events" (i.e., those events that fail to locate or discriminate during automated processing of the monitoring network data).

While developing and testing the corrections and other parameters needed by the automated processing systems, the DOE Laboratories will also have the opportunity to independently test and evaluate the algorithms used for the PNDC operations illustrated in Table 1, and will develop improved algorithms when new or revised procedures are needed to improve system performance. To avoid duplication of effort this development will build on experience that has been gained with the PNDC and the PIDC systems, and those technologies, datasets and formats that are found to perform satisfactorily and are technically sound will not be changed.

Within the DOE program the overall design of the KBS will be a responsibility of Sandia National Laboratory, but this design will be driven in large part by seismological considerations based on the regional characterization efforts of LANL and LLNL. The final knowledge base must contain traveltime corrections and other parameters that will be specific to regions of interest to CTBT monitoring, and in many cases specific to source-receiver paths around stations of the primary monitoring network and key stations of the secondary network. Parameters tabulated in the knowledge base must be appropriate for routine automated processing of network data, and must also be available for analyst-intensive work on "special" events. For efficient automated data processing the KBS will appear to the user as a hierarchical system containing global, regional and local

parameter sets, with the various algorithms incorporating "inheritance," in the sense that the local features inherit those of the regional model, and the regional parameters inherit features of the global model. Thus, lacking local corrections, automated data processing routines will default to the regional database, and if the latter do not exist global features will be used.

In all cases, the relationships between the performance of algorithms and the properties of the databases must be explicit and well understood. In addition, for the KBS and its datasets to be usable by AFTAC the algorithms and databases must be system-ready, thoroughly tested, and demonstrated to be effective for monitoring seismic events in the regions of interest. To accomplish these goals will require close coordination between all participants in this program -- the DOE Laboratory teams, the DOE contractors, AFTAC, ARPA and contractors involved in developing, testing and operating system components.

References

U.S. Department of Energy (1994). *Comprehensive Test Ban Treaty Research and Development FY95-96 Program Plan*, DOE/NN-0003, November 1994, 60 pp.

For a list of references on geophysics of the ME-NA region, the reader is referred to a database that has been compiled by workers at Cornell University. This database can be accessed via the Internet under the World Wide Web address:

http://www.geo.cornell.edu/geology/me_na/main.html

CALIBRATION STUDIES AT TXAR

Ileana Tibuleac, Eugene Herrin, Paul Golden
Department of Geological Sciences
Southern Methodist University
Dallas, Texas
1 August 1995

ABSTRACT

This poster presents some of the results of calibration studies at TXAR. Well over 100 regional and teleseismic events that were located by the USGS were used in this study. A time domain correlation method was used to process the TXAR data and obtain estimates of phase velocity and back azimuth for these events. A magnitude scale and an azimuth correction table was then constructed for TXAR.

Keywords: array, TXAR, phase velocity, back azimuth, calibration, magnitude

OBJECTIVE:
Provide sufficient calibration information such that TXAR can provide reliable single-array locations and magnitudes of seismic events.

RESEARCH RESULTS:
Calibration is generally required in order to reduce bias in location and magnitude determinations at regional to near-teleseismic distances using seismic array data. Calibration is particularly important at TXAR because the array is located near the boundary between two geophysically different regions, the Mid-continent and the Basin and Range Provinces. A modified version of the correlation method described by Cansi, Plantet and Massinon was used to estimate azimuth and horizontal phase velocity of 36 events recorded at TXAR for which we had USGS m_b values. Modifications to the correlation method include Fourier interpolation of the data by a factor of 8 to obtain a virtual sample rate of 320/sec, use of an L-1 technique (least absolute deviation) to obtain estimates of azimuth and phase velocity, and a moving window display to indicate those portions of the waveform that show strongest correlation across the array.

Figures 1-4 show the estimates of phase velocity and azimuth for the four events. For some azimuths (Oklahoma event) the estimated azimuth is within a couple of degrees of the USGS back azimuth from TXAR, but for other events (Western Texas), the estimated azimuth is off by 16 degrees. This bias in estimated azimuth results from crustal structure under TXAR and must be corrected before making a single array location. Figure 5 shows the azimuth bias more than 100 events. In addition, at some azimuths the first arrivals from regional events had phase velocities normally associated with Pn (less than 8.6 km/sec) but to the northwest beyond about 1600 km the first arrival was always an upper mantle refraction with phase velocity greater than 8.6 km/sec. Phase identification is essential in order to select a suitable magnitude scale.

Array Data Processing Outline

❖ Digital array data were loaded.

❖ Data from excessively noisy channels were discarded.

❖ Data were band-pass filtered between 0.75 and 10 Hz with the exception of two events. (Oklahoma, 1-3 Hz and Wyoming, 0.5 - 5 Hz).

❖ A 3.2 second window was selected.

❖ Data were Fourier interpolated by a factor of 8 to obtain a virtual sampling rate of 320/sec.

❖ A complete correlation matrix was computed.

❖ A complete lag matrix was computed by calculating the lag-times of the maxima of the cross-correlation functions. This matrix must be skew-symmetric.

❖ The lag matrix was corrected for differences in station elevations within the array.

❖ In the absence of noise and computational errors, the lag matrix is Toeplitz.

❖ Median values were used to estimate the elements of the Toeplitz matrix.

❖ An iterative L-1 method (minimum absolute deviation) was used to estimate azimuth and horizontal phase velocity using the elements of the estimated matrix.

❖ The 3.2 second window was advanced 5 data points (125 millisec) and the correlation process repeated.

❖ Estimates of phase velocity and azimuth and the normalized sum of the absolute errors of fit were plotted as a function of window start time.

❖ A "best" window was selected based on stability of estimates and minimum estimation error.

❖ The array beam was computed based on estimates from the "best" window.

Explanation Of Figures

Subplot 1   Shows the filtered beam and the 3.2 seconds window used to estimate azimuth and phase velocity.

Subplot 2, 3   Shows the waveforms parameters, velocity and azimuth, as a function of the start time of successive 3.2 second windows. The dotted line shows the accepted estimates.

Subplot 4   Shows the normalized sum of the time residuals as a function of the start time of the 3.2 second windows.

Northridge, 01/17/1994, (8.603 km/s, 291.2 deg)
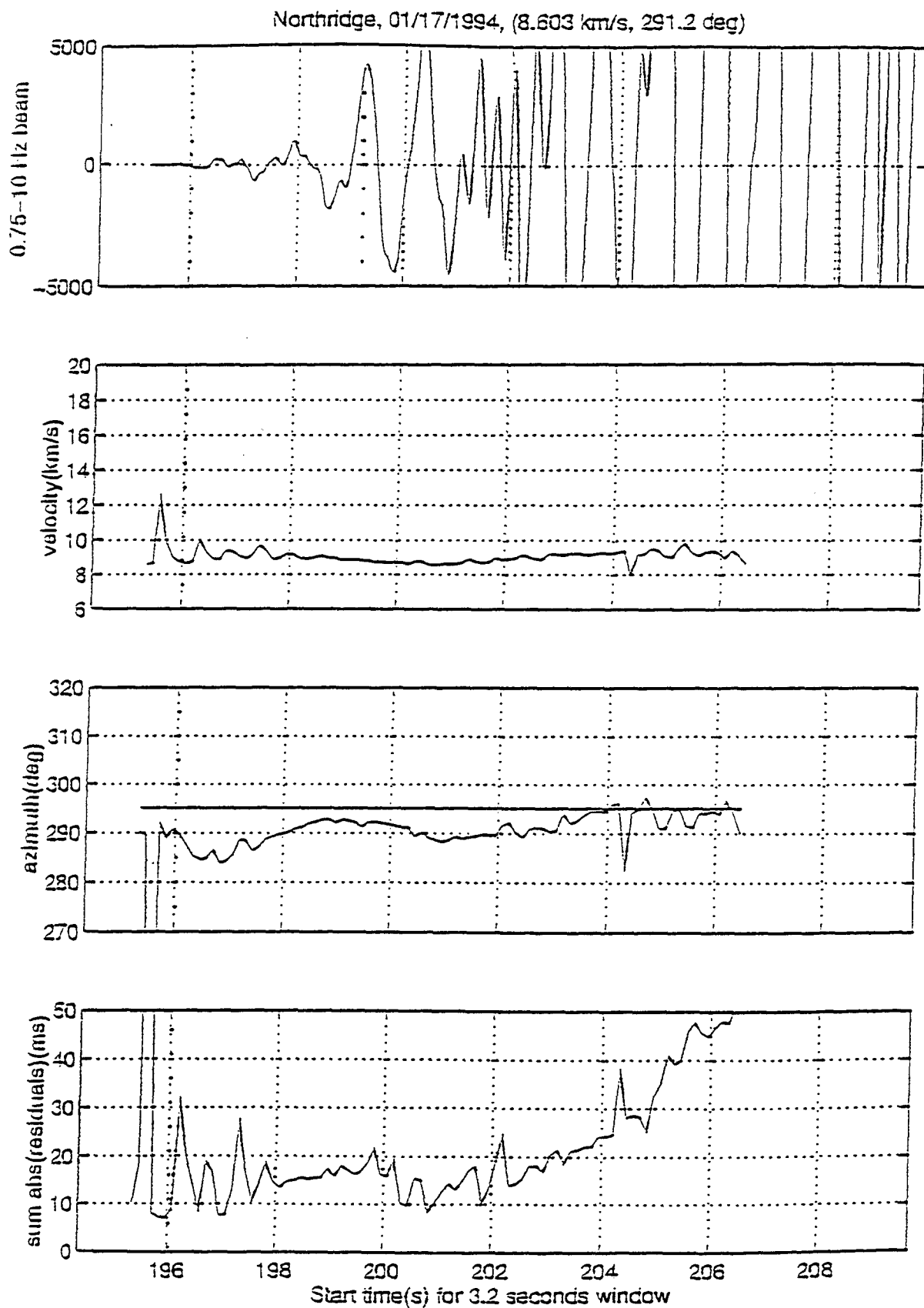
NORTHRIDGE mb 6.4

Origin Time: 01/17/94   12:30:55.3
Distance: 1505 km   Azimuth: 295°

Oklahoma, 01/18/1995, (8.485 km/s, 44.67 deg)
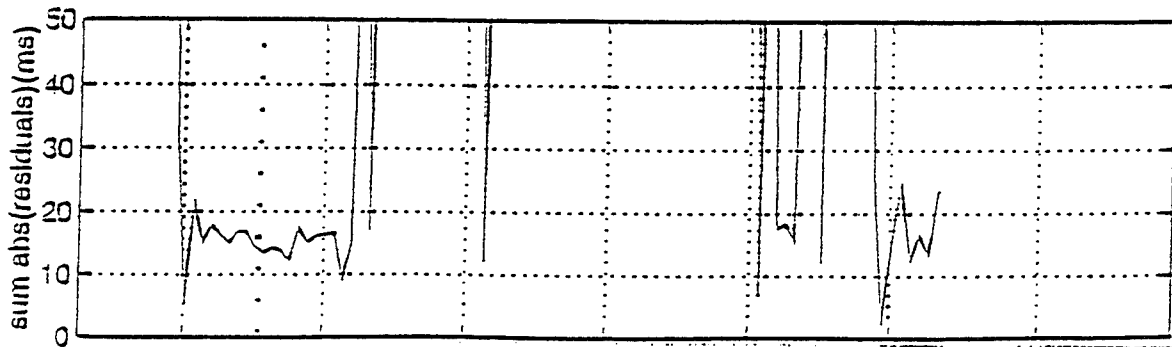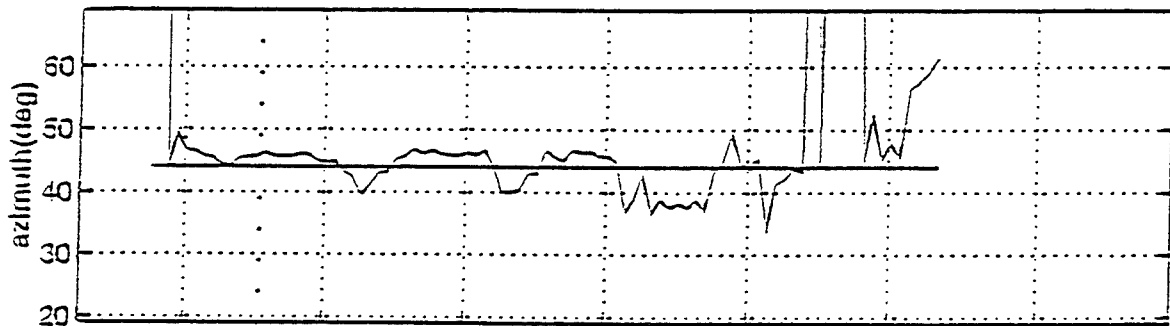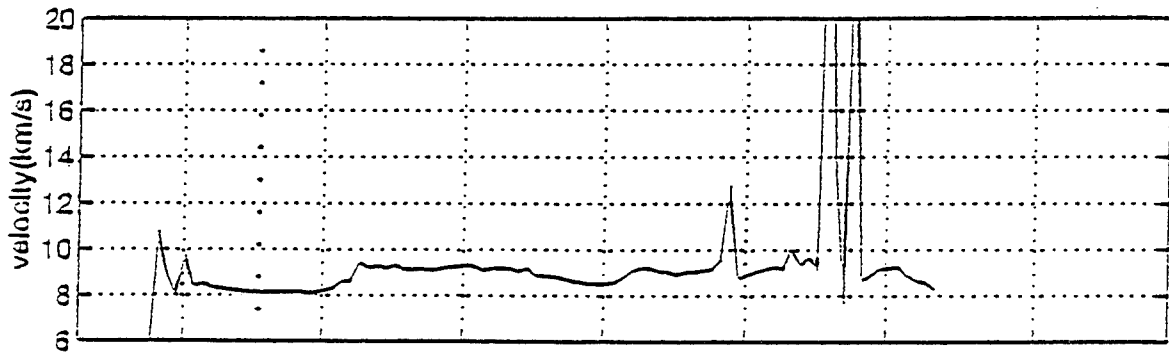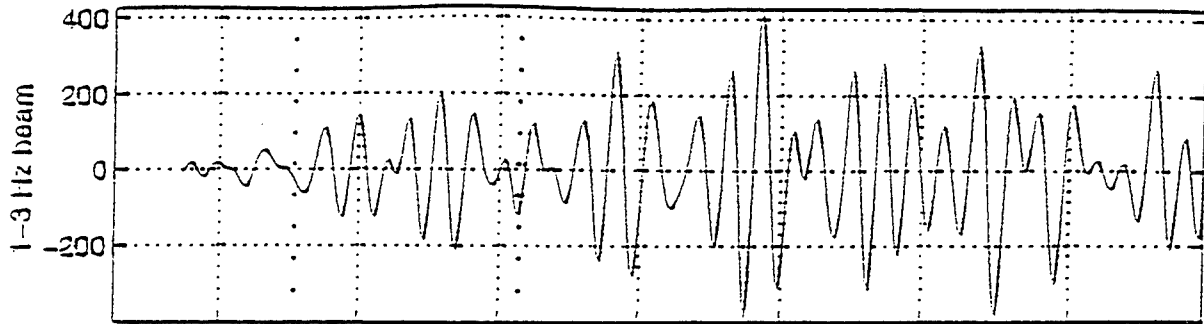
OKLAHOMA   mb 4.0 (mb Lg)

Origin Time: 01/18/95   15:51:37
Distance: 819 km   Azimuth: 44°

Western Texas, 04/14/1995, (7.139 km/s, 4.035 deg)
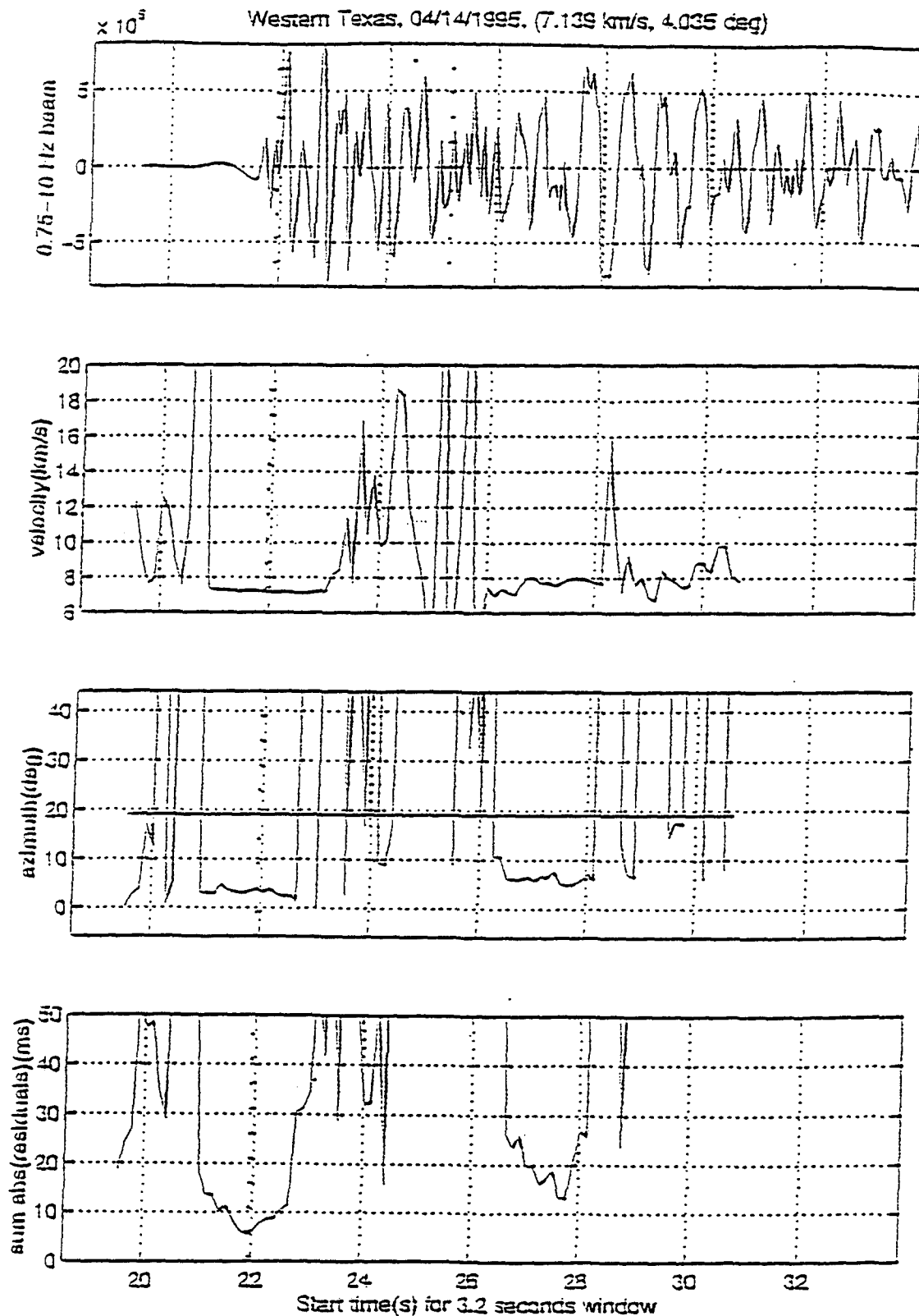
WESTERN TEXAS m_W 5.8

Origin Time: 04/14/95 00:32:54
Distance: 107 km Azimuth: 19°
The correlation method works well with digitally clipped data.

Wyoming, 02/03/1995, (10.5 km/s, 343 deg)
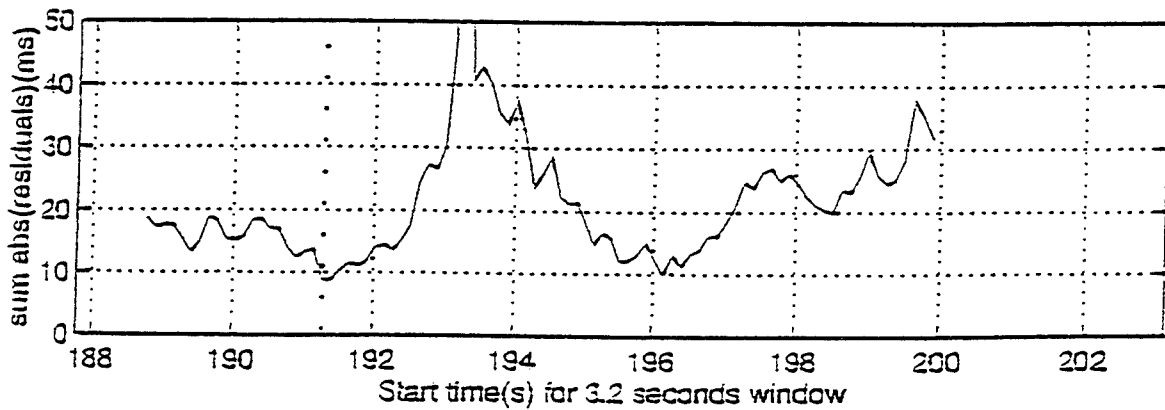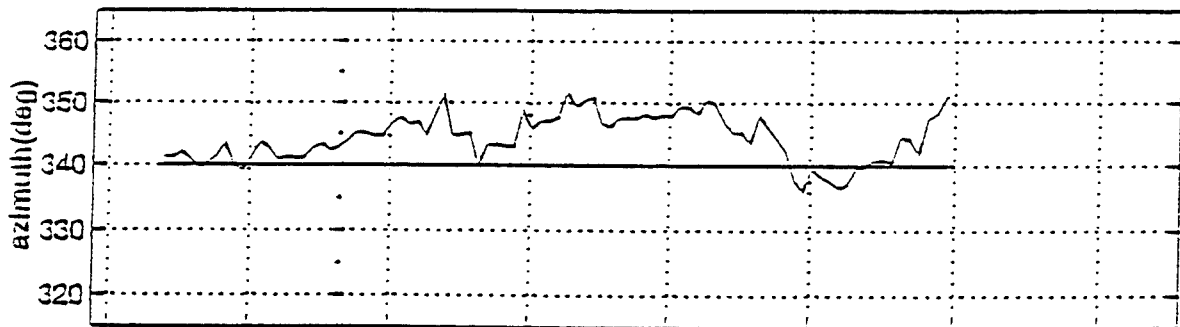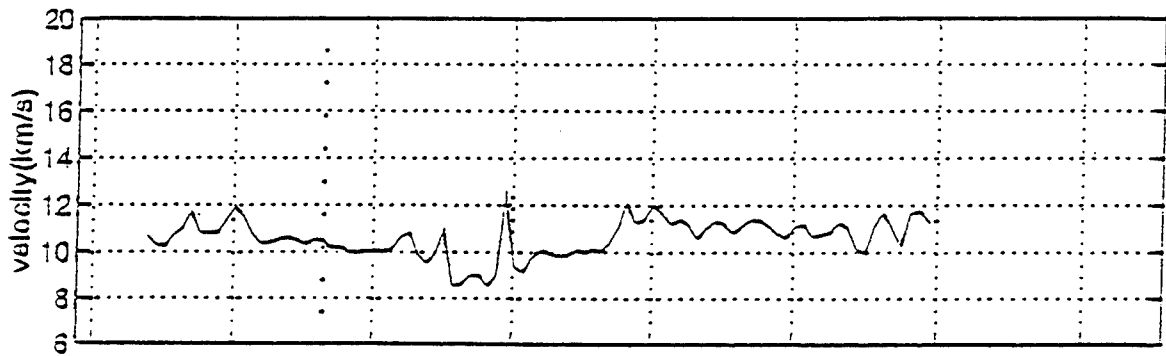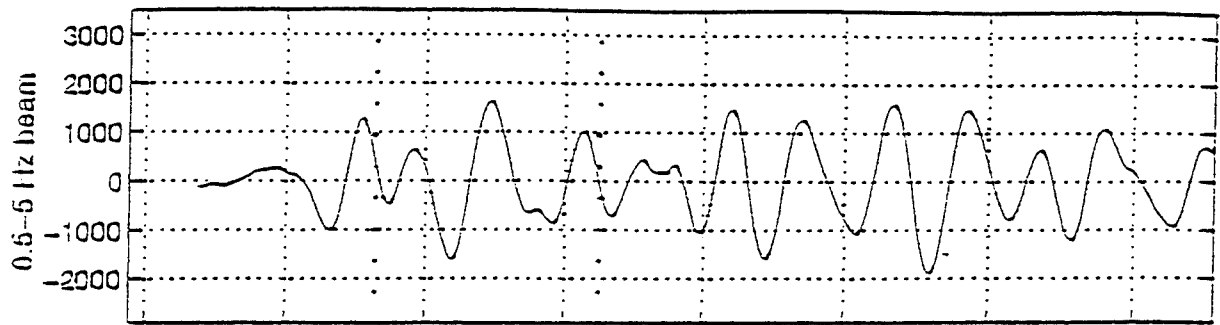
WYOMING   mb 5.4

Origin Time: 02/03/95   15:26:11
Distance: 1468 km   Azimuth: 340°

326

Location of the events relative to TXAR
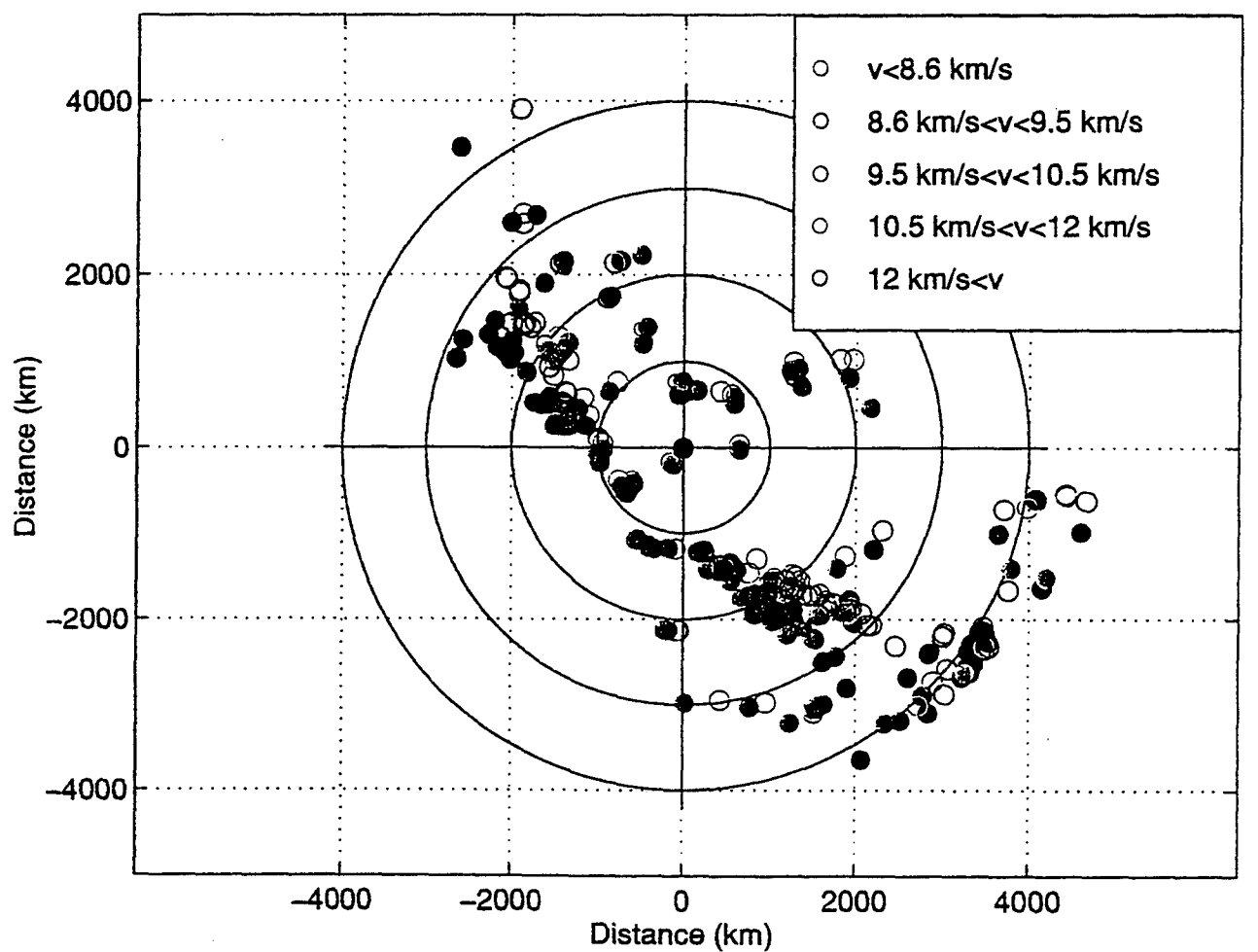
True azimuth (USGS) – open circles
Calculated azimuth (TXAR) – solid circles

(Original in color)

327

Magnitude Estimation at TXAR

Various magnitude estimates were made for the first 35 events analyzed and compared with USGS m_b. The most reliable estimates were those that used the Denny, Taylor and Vergino formula as follows.

For horizontal phase velocity less than 8.6 km/sec:

$$m_b(D) = \log A + 2.4(\log \Delta) - 3.95 + C$$
$$\text{with } C = -0.35$$

For horizontal phase velocity greater than 8.6 km/sec:

$$m_b(D) = \log A + 2.4(\log \Delta) - 3.95 + C$$
$$\text{with } C = -0.05$$

where A is zero to peak amplitude in nanometers and Δ is epicentral distance in km.

CONCLUSIONS AND RECOMMENDATIONS

We now have adequate calibration data to locate and determine the magnitude of regional events that are not seen at PDAR or any other GSETT 3 primary station, but may be observed at secondary stations such as Tucson and Albuquerque. Studies of these events should allow us to determine the effectiveness of single array detection.

Broadband Seismic Characterization
of the
Arabian Shield

Dr. Frank Vernon, Scripps Institution of Oceanography, UCSD

Dr. Jon Berger, Scripps Institution of Oceanography, UCSD

Dr. James Zollweg, Boise State University

Professor Abdullah Al-Amri, King Saud University

Abstract

We propose to carry out a field program in the Kingdom of Saudi Arabia to collect a suite of broadband seismic waveform data and the associated parametric data describing the sources. We plan to deploy 6 portable broadband seismic stations along 3 profiles on the Arabia Shield and record over a period of about a year. Most of the regional seismic sources will be in the tectonically active area of Iran and Turkey to the northeast. Other areas of seismic activity include the Red Sea Rift bordering the Shield to the southwest, and the Dead Sea Transform fault zone to the north.

In addition to data recorded at the portable stations, we will also utilize other broadband data sources in the region including GSETT-3 stations, GSN stations, and other seismic facilities in Central Asia. All data collected in the course of this program will be organized in version 3.0 CSS databases and be available for distribution.

The main research objectives of the proposed program are:

1. to study the propagation of regional phases across the Arabian Shield over a broad band of frequencies,

2. to study the crustal structure and seismicity of the Arabian Shield, and

3. to characterize potential sites for permanent seismic facility installation

Background and Collaboration

The Arabian Peninsula presents several interesting seismological problems. On the west, rifting in the Red Sea has split a large Precambrian shield, the Arabian Shield, into two distinct parts (see Figure 1). The geometry of the Arabian Plate is well-outlined by teleseismic epicenters (see Figure 2). Active rifting is responsible for the geometry of the plate margins in the west, and southwest. To the south, similar rifting running in a more east-west direction through the Gulf of Aden has separated the Arabian Peninsula from Africa. In the northwest, the Gulf of Aqaba forms the southernmost continuation of the Dead Sea transform. The northern and northeastern boundaries of the Arabian Plate are areas of continental collision, with the Arabian Plate colliding with the Persian Plate. The overall lack of seismicity in the interior of the Arabian Plate, though not as absolute as might be thought from Figure 2, suggests that little internal deformation of the plate is presently occurring.

There has only been a modest amount of earthquake seismological work done in the Arabian Peninsula. Several countries either on or surrounding the Peninsula have seismograph stations, but most stations are equipped only with short-period vertical seismometers. In any event, the networks are sparse and often are poorly situated with respect to active areas. Surface wave dispersion studies and explosion studies have defined crustal structure in the oil-producing areas adjacent to the Persian Gulf and along a transect of the southern part of the Arabian Shield, but only gross features of crustal structure are known in most of the Peninsula. Broadband data required for analysis of teleseismic receiver functions are almost wholly lacking. Regional wave propagation from earthquakes and seismic wave attenuation have not been studied. Microseismicity is known to occur in many areas of the Peninsula, but the existing network of stations is inadequate for accurately defining spatial characteristics or determining focal mechanisms.

We propose to address several of these problems by a program of broadband seismic monitoring in Saudi Arabia, in cooperation with Saudi scientists. For many years the Kingdom has been very "closed" to all but a few joint projects. In fact, one cannot even visit the country without written invitation by a Saudi official. We are very fortunate in having obtained Saudi government permission for this field program from Dr. Mohammed Al- Suwaiyel, the Vice President for Research of the King Abdul Aziz City for Science and Technology (KACST), the government agency responsible, by Royal decree, for seismological studies in the Kingdom. This will be the first joint US-Saudi field program in seismology for many years and, we hope, represents a new openness of the Kingdom for such joint works. This joint program will be carried out under the aegis of the King Saud University (KSU).

Structure of the Arabian Shield

The Arabian Shield consists of a large outcrop of Precambrian rocks in the western Arabian Peninsula (see Figure 2). The Red Sea rift has separated similar rocks which outcrop in Egypt and the Sudan. Rocks of the shield are highly variegated (U. S. Geological Survey and Arabian American Oil Company, 1963). Although granite and gneiss do not dominate the exposed rocks, there are large outcrop areas of both. Cenozoic basalts overly shield rocks in some areas (Figure 2). On the west, shield rocks are bordered by Cenozoic deposits of the Red Sea coastal plain, including volcanics from a number of late Quaternary vents. On the east, shield rocks are bordered by sedimentary rocks of the Arabian platform. Three principal Precambrian tectonic provinces have been

distinguished in the area of the shield lying generally south of latitude 24 degrees North (Greenwood et al., 1980).

A USGS velocity profile was run across the Arabian Shield from near Riyadh to the Red Sea in 1978 (Mooney et al., 1985). To first order, the Arabian shield consists of two layers, each about 20 km thick. Average velocities are 6.3 and 7.0 km/sec, respectively. The depth to the Moho averages about 40 km, thinning slightly from northwest to southeast. The upper mantle velocity is 8.0 - 8.2 km/sec. Based on surface wave dispersion studies using regional WWSSN-type stations, the Mooney et al. model is a reasonable approximation to crustal structure throughout the Arabian Shield (Mokhtar et al., 1992).

Mooney et al. suggest that the geology and velocity structure of the shield can be explained by a model in which the shield developed in the Precambrian by suturing of island arcs. Mooney et al. interpret the boundary between the eastern shield and the Arabian Platform as a suture zone between crustal blocks of differing composition. Prodehl (1985) noted that the upper crust of the eastern shield appears to be more uniform than that of the western shield. Mooney et al. note that mapped gneiss domes correlate with high velocity bodies in the upper crust.

The record sections shown by Mooney et al. (1985) and their interpretations indicate that crustal phases such as P_n and P_mP are well-recorded to distances of at least 300 km. Intracrustal reflectors were also observed, which were interpreted as coming off the tops of bodies of mafic intrusives.

There is differing information on the attenuation structure of shield rocks. Short-period Rayleigh waves along the USGS line suggest Q of 400 to 700 for the upper igneous rocks at depths of 500 m or so (Mokhtar et al., 1988). Badri (1989), from the P waves recorded on the USGS profile, found that Q_p for P_g ranges from 50 to 850 in the shield. Qp for the Pn phase averaged 1075. On the other hand, H. Ghalib's studies of regional attenuation of the L_g phase suggest much lower values of Q, around 150-250 (personal communication, 1992). Shield areas of most parts of the world are associated with generally high Q values, and the interpreted velocities from the refraction profile would also suggest that Q should be moderate to high. All studies that could distinguish between Arabian Shield and Arabian Platform propagation paths found that velocities were lower and attenuation higher in the platform.

Seismo-tectonics of the Arabian Peninsula

Dead Sea Transform

The Dead Sea transform system connects active spreading centers of the Red Sea to the area where the Arabian plate is converging in southern Turkey (see, e. g., Dewey et al., 1973). The transform fault system dates from the Middle Cenozoic and is primarily a left-lateral feature (Nur and Ben-Avraham, 1978). Over 100 km of sinistral motion is estimated to have occurred on the system (Quennel, 1958; Freund et al., 1970). The southern portion of the rift system is the Gulf of Aqaba. Both strike-slip and normal faulting occur in the Gulf of Aqaba in connection with the formation of en-echelon rhombic-shaped grabens (Al-amri et al., 1991).

Seismicity of the Dead Sea transform is moderately high. A magnitude 6 1/4 earthquake occurred in Jordan in 1927. About 800 events of magnitude 1.5 to 4.6 have been located in the Gulf of Aqaba by the King Saud University seismic network between October

1986 and March 1990 (Dr. Abdullah Al-amri, personal communication, 1994). More recently, magnitude 6.0 and 5.7 events occurred on 3 August 1993.

Red Sea Rift

The Red Sea Rift is the dominant tectonic feature of western Arabia. The Red Sea's axial rift developed in the Pliocene in a pre-existing depression (Girdler and Styles, 1974). It connects the Dead Sea transform to the Afar triple rift junction in eastern Africa. Continued active rifting is indicated by the high rate of seismicity in the Red Sea. A magnitude 7.1 event occurred in the northernmost Red Sea near the mouth of the Gulf of Aqaba in 1969, and a magnitude 5.8 event occurred on 13 March 1993 in the central Red Sea, south of Jiddah. There are many NE-trending transform faults along the Red Sea (Whiteman, 1970) and some of these may extend into the western Arabian Peninsula.

Gulf of Aden

The plate boundary extends east-northeast from the Afar region through the Gulf of Aden and into the Arabian Sea. The boundary is clearly delineated by teleseismic epicenters (Figure 2), although there are fewer epicenters bounding the eastern third of the Arabian Plate south of Oman.

The Zagros Folded Belt

The Arabian Plate is bounded along its entire northeastern length by the Zagros folded belt, a continental collision zone with the Persian Plate. Most seismicity appears to occur in the crustal part of the Arabian Plate beneath the Zagros folded belt (Jackson and Fitch, 1981). The Zagros is a prolific source of large magnitude earthquakes, with numerous magnitude 7+ events occurring in the last few decades.

Arabian Plate Interior

The interior of the Arabian Plate is generally marked by very low levels of seismicity. This is not merely an effect of poor network coverage; operation of the King Saud University seismic network indicates that microearthquake activity generally originates in the same areas as the teleseismically-located events. In the western Peninsula, however, there are some areas of enhanced seismicity that are unquestionably on land. The 1982 North Yemen earthquake (Langer et al., 1987) is the best-known recent earthquake to occur on the Arabian Peninsula, having resulted in about 3,000 fatalities. This magnitude 6 event was caused by normal faulting (Choy and Kind, 1987). At least 3 other magnitude 5 1/2 to 6 1/4 events are known from the Asir region of southwestern Saudi Arabia between 1941 and 1965. Microearthquake investigations have demonstrated seismicity in the Asir area (Merghelani and Gallanthine, 1980), and the King Saud University telemetry network has occasionally located events there (Altan Necioglu, personal communication, 1993). Farther to the north along the Red Sea, on-land seismicity is known from the Yanbu region of northwestern Saudi Arabia (Merghelani, 1981) and in the Makkah-Taif region (Merghelani et al., 1981). Seismicity in the Makkah-Taif region may be associated with a northeast-trending mapped fault.

The causes of this intraplate seismicity are not well understood. There is widespread Quaternary volcanism along the Red Sea coast, with at least one documented historical eruption in 1256 A. D. Some seismicity was associated with that eruption. Seismicity may also be related to transform faults in the Red Sea continuing onto land, as well as other causes. To date, few on-land epicenters are accurately located and there are few focal mechanisms available.

A large earthquake (magnitude 6.6) is shown on the seismicity map (Figure 2) in the plate interior along the Iraq-Saudi Arabia border. This earthquake occurred in 1953, but we know little about it.

Deployment Plan

We have a plan to operate 6 portable broadband seismographs at a minimum of 9 sites in the Arabian Shield. Our planned deployment is shown in Figure 3. The triangular pattern will insure that seismic wave characteristics over a large area of the Shield will be assessed for a wide variety of sources, and that there will be a tie-in to previous refraction seismology studies in the shield.

The first deployment will consist of 3 seismographs in the area of the proposed GSN station at Ar Rayn near Riyadh. The remaining 3 units will be deployed at existing sites along an east-west profile from Daharan through Riyadh to Makkah.

We then plan to move the 3 units deployed around Ar Rayn along the 1978 USGS profile line, running from just west of Riyadh to Asir Province near the Red Sea Coast in the southwest. The profile's long axis is pointed in the direction of high seismicity in the Zagros. These earthquakes are occurring in the Arabian Plate where it is colliding with Persian Plate (Jackson and Fitch, 1981). Seismic wave ray paths along this profile from Zagros events should therefore have entirely intra-plate paths. Stations will be between 900 and 1500 km from the nearest Zagros sources, although existing broadband and long-period stations not located on the Arabian Shield are closer (350 to 700 km). Events in the highly active area of the Afar triple junction in Africa are also generally aligned with the deployment.

The array deployments will allow sampling of regional wave characteristics over a broad area, from very numerous source regions. It is reasonable to expect that ray paths traversing virtually every area of the shield will be recorded, given the high seismicity rates characteristic of most of the active areas around the shield. We expect from experience operating portable seismographs in some parts of the shield that most sites will have very low noise levels, so a variety of teleseismic signals suitable for receiver function analysis should also be obtained.

Instrumentation and Installation Methods

Each station will have a Streckeisen STS-2 broadband seismometer which has a pass band between 0.008 Hz and 100 Hz. Each seismometer will be heavily insulated to protect it from the daily changes in temperature. We have successfully run STS-2 seismometers in a desert environment during the summer of 1992. These sensors were deployed for the Landers earthquake aftershock experiment in the Mojave Desert in southern California. Each sensor will be attached to bedrock outcrops whenever possible.

The output of the STS-2 will normally be recorded at a sample rate of 40 sps by a 24-bit REFTEK RT72A-08 datalogger. At the station the data will be stored on a 1 Gbyte SCSI disk. To take advantage of the copious amounts of sunshine available in Saudi Arabia, we will use solar panels to charge car batteries. Timing to the station will be provided by a local GPS clock. This will avoid the problem of any potential leap second changes. Data will be retrieved by exchanging disks at each site during service runs. Each site will need to be visited on a monthly basis.

RESEARCH PRODUCTS

CSS Databases

Operating at 40 samples/second continuously, each station will collect 41.5 Mbytes of waveform data per day. Thus, about 250 Mbytes per day for the 6 stations will have to be processed. Assuming that there will be the equivalent of about 300 network-days of operation during the experiment, the total data produced will be on the order of 75 Gbytes.

All data gathered from the portable stations (and some data from other sources) will "packaged" into a version 3.0 CSS databases. These databases will include one containing all waveforms with the continuous data segmented into some convenient epochal length and the associated station descriptive data will be stored in the *site, sitechan, sensor,* and *instrument* relations. Another database will contain segmented waveforms containing seismic signals and information on these signals and their sources, stored in the *origin, assoc,* and *arrival* relations. These databases will be available for distribution with the final report.

REFERENCES

Al-Amri, A. M., F. R. Schult, and C. G. Bufe, Seismicity and aeromagnetic features of the Gulf of Aqaba (Elat) region, *Journal of Geophysical Research*, 96 (1991) 20179-20185.

Badri, M., Qp and velocity crustal structure of central Saudi Arabia, *KACST project final report* 09-006 (1989), 135 p.

Choy, G. L., and R. Kind, Rupture complexity of a moderate-sized (mb 6.0) earthquake: Broadband body-wave analysis of the North Yemen earthquake of 13 December 1982, *Bulletin of the Seismological Society of America*, 77 (1987), 28-46.

Dewey, J. F., W. C. Pitman, W. B. F. Ryan, and J. Bonnin, Plate tectonics and the evolution of the Alpine system, *Bulletin of the Geological Society of America*, 84 (1973), 3137-3180.

Freund, R., Z. Garfunkel, I. Zak, M. Goldberg, T. Weissbrod, and B. Devin, The shear along the Dead Sea Rift, *Philosophical Transactions of the Royal Society of London, Series A*, 267 (1970), 107-130.

Greenwood, W. R., R. E. Anderson, R. J. Fleck, and R. J. Roberts, Precambrian geologic history and plate tectonic evolution of the Arabian Shield, Saudi Arabia, Director General of Mineral Resources Bulletin, 24 (1980), 34 p.

Jackson, J., and T. Fitch, Basement faulting and the focal depths of the larger earthquakes in the Zagros mountains (Iran), *Geophysical Journal of the Royal Astronomical Society*, 64 (1981), 561-586.

Langer, C. J., G. A Bollinger, and H. M. Merghelani, Aftershocks of the 13 December 1982 North Yemen earthquake: Conjugate normal faulting in an extensional setting, *Bulletin of the Seismological Society of America*, 77 (1987), 2038-2055.

Merghelani, H. M., Seismicity of the Yanbu region, Kingdom of Saudi Arabia, *U. S. Geological Survey Saudi Arabian Mission, Technical Record* 16 (1981), Jiddah, Saudi Arabia, 32 p.

Merghelani, H. M., and S. K. Gallanthine, Microearthquakes in the Tihamat-Asir region of Saudi Arabia, *Bulletin of the Seismological Society of America*, 70 (1980), 2291-2293.

Merghelani, H. M., A. R. Kinkar, and M. W. As-Sawwaf, Seismicity studies in Saudi Arabia: Microearthquakes in the Jeddah area, *Open-File Report DGMR-OF-01-08* (1981), 33 p.

Milkereit, B and E.R. Fluh. Saudi Arabian refraction profile: crustal structure of the Red Sea-Arabian Shield transition. *Tectonophysics*, 111 (1985) 283-298.

Mokhtar, T. A., R. B. Herrmann, and D. R. Russell, Seismic velocity and Q model for the shallow structure of the Arabian Shield from short-period Rayleigh waves, *Geophysics*. 53 (1988), 1379-1387.

Mokhtar, T. A., M. Maamoun, and A. M. Al-amri, Seismic structure of the Arabian Peninsula from surface waves, *KACST project final report* 10-48 (1992), 259 p.

Mooney, W.D., M.E. Gettings, H.R. Blank, and J.H. Healy. Saudi Arabian seismic-refraction profile: a traveltime intrepatation of crustal and upper mantle structure. *Tectonophysics*, 111 (1985) 173-246.

Nur, A., and Z. Ben-Avraham, The eastern Mediterranean and the Levant: Tectonics of continental collision, *Tectonophysics*, 46 (1978), 297-311.

Petroconsultants, Ltd., Tectonic Map of the Middle East, (1970), Dublin, Ireland, 1 sheet.

Prodehl, C. Intrepretation of a seismic-refraction survey across the Arabian Shield in western Saudi Arabia. *Tctonophysics*, 111 (1985) 247-282.

Quennell, A. M., The structural and geopmorphic evolution of the Dead Sea rift, *Quaternary Journal Geological Society of London*, 114 (1958), 1-24.

U. S. Geological Survey and Arabian American Oil Company, Geologic Map of the Arabian Peninsula, *Miscellaneous Investigations Map MI-I-270a* (1963), 1 sheet.

Whiteman, A. J., The existence of transform faults in the Red Sea depression, *Philosophical Transactions of the Royal Society of London, Series A*, 267 (1970), 407-408.

Figure 1. Map of the Arabian Peninsula area, adapted from tectonic map produced by Petroconsultants (1977). Lightly stippled area shows extent of Precambrian shield rocks on both sides of the Red Sea. Darkly stippled areas are shield areas covered by Quaternary basalts.

Mb >= 4.0 Events at Regional Distances from Saudi Arabia
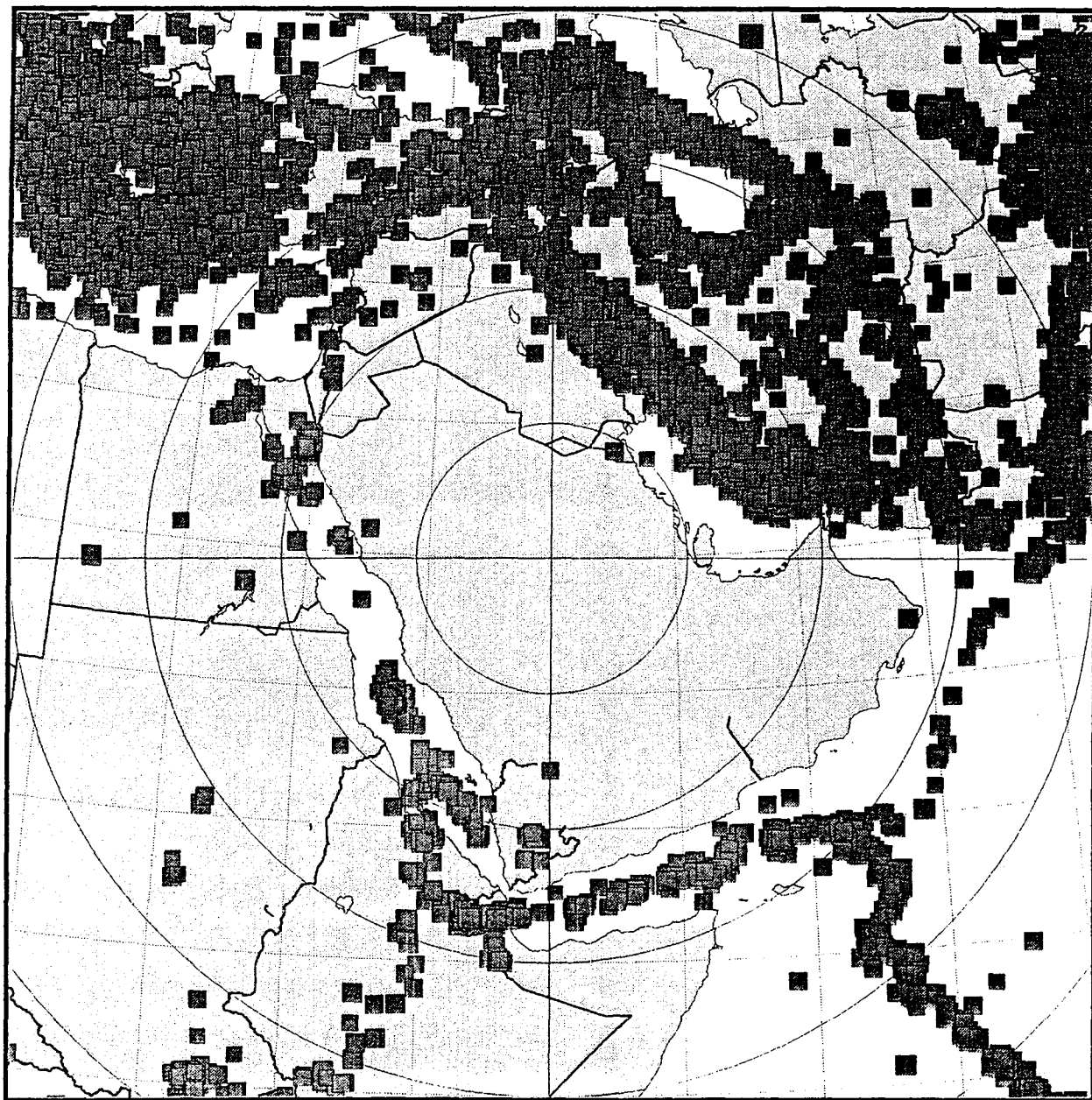
Figure 2. Seismicity of the Arabian Peninsula area, taken from the PDE data base. Map shows events with magnitude greater than 4.0 since 1966.
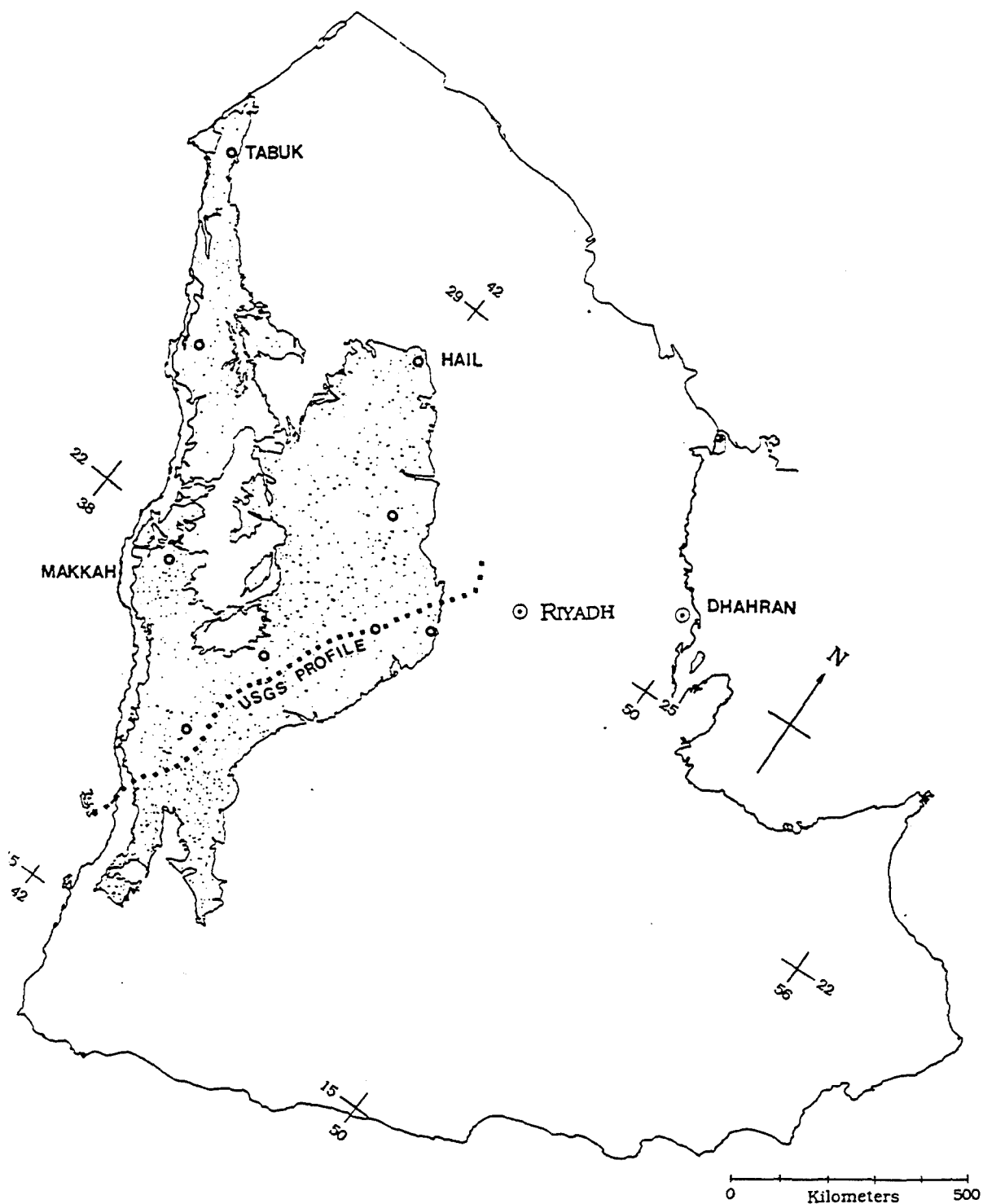
Figure 3. Planned broadband station deployment (small circles). Lightly stippled area is Arabian Shield; Quaternary lava cover within the shield is not stippled. In the first phase of our deployment, the four stations along the USGS profile and at Hail and Makkah would be operated. In the second phase, the four stations along the Red Sea coast and the 4 running along the northeast edge of the shield would be occupied. 6-component stations exist at Riyadh.

338

Loss of High Frequency Upon Propagation Through Shock-Damaged Rock

Thomas J. Ahrens and Cangli Liu
Seismological Laboratory,
California Institute of Technology, Pasadena, CA 91125

ABSTRACT: The attenuation of stress waves in samples of gabbroic rock subjected to shock loading up to 11 GPa is studied. We determine the attenuation coefficients, α_p, for samples with different damage parameters under dynamic strains of 2×10^{-7} and at frequencies around 2 MHz using the ultrasonic pulse-echo method. A fit to the data yields the P-wave spatial attenuation coefficient versus damage parameter: $\alpha_p = 40.9 \, D_p - 30.5 \, D_p^2$ (db/cm). Basing on O'Connell-Budiansky theory a relation between attenuation coefficient and crack density is derived. The predictions of α_p and Q from Walsh's theory agrees well with the experiment results for the samples with different damage deficits and the Q's we measure are in the range of 10 to 20. These very low values give rise to the sharp decrease in high frequency seismic energy, as the stress-wave from an explosion leaves the source region.

Key Words:

attenuation
shock-damage

OBJECTIVE:

The attenuation of stress waves in rocks is largely caused by internal friction between crack surfaces. When a stress-wave propagates in rock this induces differential motion along the usually present cracks [Born, 1941; Walsh, 1966]. Generally, attenuation depends on stress amplitude and frequency, as well as, pressure, temperature and fluid saturation.

Experimental measurements of attenuation of stress waves in several rocks have been extensively studied since the 1940's in the laboratory using different techniques over a wide-frequency range [Born, 1941; Toksoz et al., 1979; Winkler and Plona, 1982]. All these studies concentrated on the relations between attenuation and parameters other than crack density induced velocity deficits. Because attenuation is directly related to crack density, research on influence of crack density on attenuation can provide detailed information about the mechanism of attenuation. The present study presents the first experimental data of the P-wave attenuation of gabbroic rocks (San Marcos, CA) which are pre-damaged by shock waves.

EXPERIMENTAL TECHNIQUE:

Sample Preparation

The rock studied was San Marcos gabbro which has been studied previously [Ahrens and Rubin, 1993; Rubin and Ahrens, 1991] The density of San Marcos gabbro is 2.87 g/cm^3, and there is very low initial crack density.

Initially a large gabbro target with dimensions 200x200x150 mm was impacted by a lead projectile at a velocity of 1.2 km/s, the projectile had a diameter of 7 mm and mass of 3 gm. The pressure of the shock wave in the target was estimated to be about 11 GPa at a radius of 0.35 cm and about 0.1 GPa at radius of 8 cm from the impact site along the center-line of the impact using a power-decay relation and impedance match method [Ahrens, 1987; Ahrens and Johnson, 1995].

The recovered target was cut into 1 cm cubes with two surfaces being perpendicular to the impact axis. The 1 cm cubes were polished to ± 0.03 mm. Prior to measurement, the samples were dried in an oven under normal pressure at 100° C for 24 hours.

Damage Parameter for P-wave

For the damage parameter, we follow the definition used in Grady et al. [1987] and Ahrens et al. [1995] which gives

$$D_p = 1 - \left(\frac{C_p}{C_{p0}}\right)^2 \tag{1}$$

where D_p is the damage parameter for a P-wave, C_p is the P-wave velocity measured for the damaged samples and C_{p0} is the intrinsic P-wave velocity for initial samples.

Attenuation Coefficient

The ultrasonic experimental apparatus used in this work is similar to that developed by Winkler et al. [1982] for attenuation coefficient measurements (Fig. (1)).
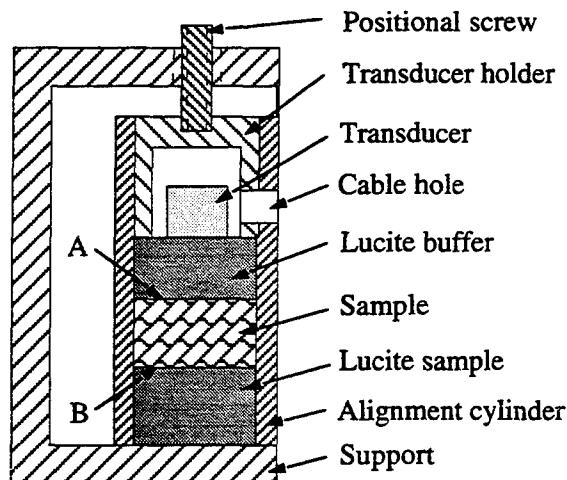
Fig. 1 Measurement system

Suppose that the reflecting and transmission coefficients of the surfaces between the buffer and sample are equal to that for plane-wave incidence as in Winkler et al. [1982], the changing amplitude of the wave is then totally from intrinsic attenuation. Let R be reflection coefficient for the interface between the coupling buffer and sample and L/2 be sample thickness, A(f) and B(f) be the frequency-dependent amplitudes of the pulses reflected from the surface A and B (in Fig. 1) of the sample, respectively. The attenuation coefficient obtained from the two reflected stress waves is expressed as [Winkler and Plona, 1982]

$$\alpha(f) = \frac{8.686}{L} \ln\left[\frac{A(f)}{B(f)}(1 - R^2)\right] \tag{2}$$

where the unit of $\alpha(f)$ is db/cm when the unit of L is cm and R is expressed as

$$R = \frac{C_p \rho - C_{pc} \rho_c}{C_p \rho + C_{pc} \rho_c} \tag{3}$$

where C_p and ρ are the P-wave velocity and the density of the gabbro sample measured, respectively. C_{pc} and ρ_c are the P-wave velocity and density of the coupling buffer (Lucite). From ultrasonic measurements, C_{pc} is 2.68 km/s and ρ_c is 1.19 g/cm^3.

A piezoelectric transducer (Panametrics, Model 102) is used as the pulse generator and the receiver. The transducer's driver is a Panametrics 505UA pulser/receiver. The recorded signals are used to calculate the magnitude of each frequency component of each pulse using a Fast Fourier Transformation (FFT).

PRELIMINARY RESEARCH RESULTS AND ANALYSIS:

A typical signal recorded for the attenuation measurement is shown in Fig. 2, in which the first signal is reflected from the surface A of the sample and the second from the surface B, and T_1 and T_2 are the data length used in FFT. We also measured the strain in the rock produced by the ultrasonic transducer. The strain level is 10^{-7} and,

341

the present data are taken in the ultrasonic region, the results are also applicable to seismic frequencies.
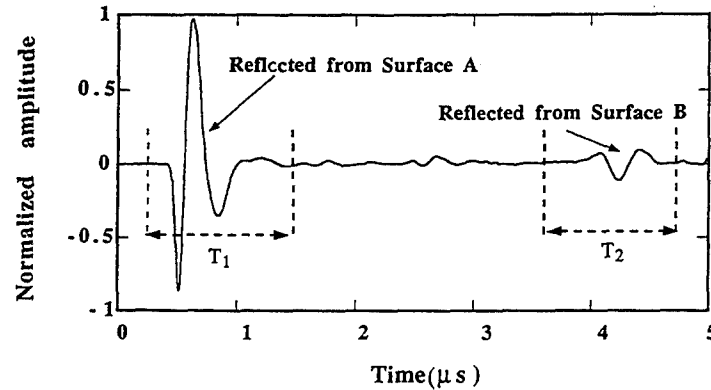
Fig. 2 Typical ultrasonic record

A typical result of spectral analysis is shown in Fig. 3, it is found that most of energy of the stress wave generated by the transducer is concentrated in the frequency range between 1.5 and 3.5 MHz. Using Eq. (2), the attenuation coefficients for the samples with differential damage parameters have been evaluated as shown in Figs. (4) (5) and (6). From Fig. (4), we can see that the attenuation coefficients for samples with different damage parameters increase approximately linearly with frequency. From Fig. (5), the relation between attenuation coefficient and damage parameters for 2 MHz are fitted as

$$\alpha_p (db/cm) = 40.9 D_p - 30.5 D_p^2 \tag{4}$$
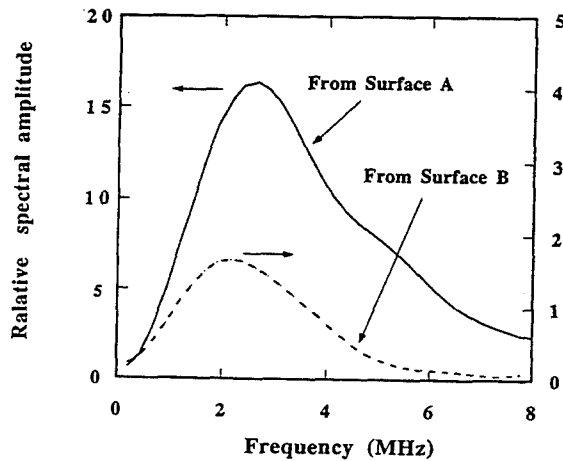
Fig. 3 Typical spectral amplitude of signals
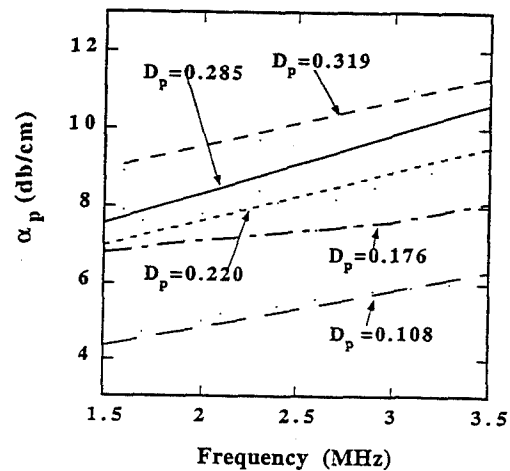
Fig. 4 Experiment results of attenuation coefficient with frequency for samples with different damage parameters
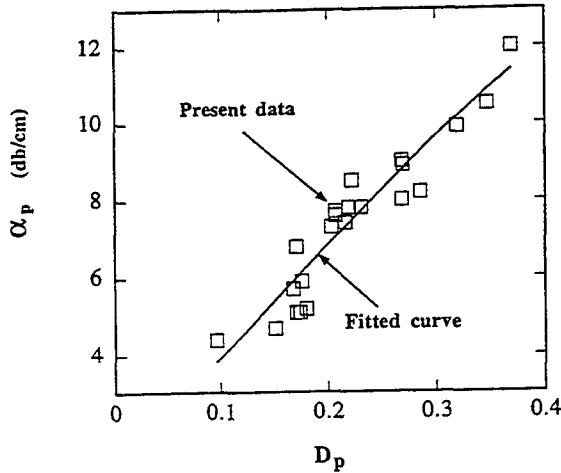
Fig. 5 Relation between damage deficits and attenuation coefficient
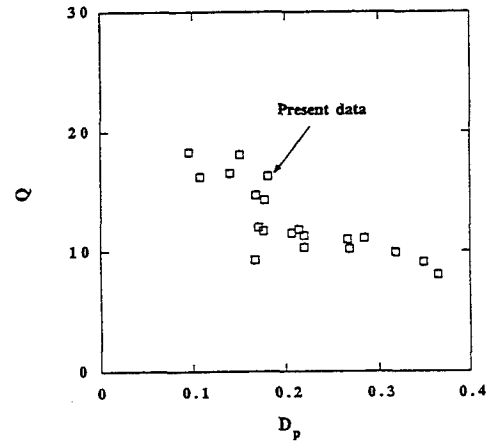
Fig. 6 Quality factor versus damage deficits

O'Connell and Budiansky [1974] established the relation between velocity and crack density follows as

$$\left(\frac{C_p}{C_{p0}}\right)^2 = \frac{(1-v)(1+v_0)}{(1+v)(1-v_0)}\left(1-\frac{16(1-v^2)\varepsilon}{9(1-2v)}\right) \tag{5}$$

$$\frac{v}{v_0} = 1 - \frac{16\varepsilon}{9} \tag{6}$$

where v and v_0 are effective and intrinsic Poisson's ratio, respectively. ε is crack density which is defined as

$$\varepsilon \equiv N < a^3 > \tag{7}$$

where N is the number of cracks per unit volume and a is the half-length of cracks.

From the definition of damage parameter, Eq. (1), and the relation between velocity and crack density, Eqs. (5), (6) and (7), the relation between D_p and ε is approximately

$$D_p = 2.4\varepsilon - 1.2\varepsilon^2 \tag{8}$$

From Eqs. (4) and (8), an approximate expression relating α_p to ε is

$$\alpha_p = 96.1\varepsilon\left(1 - 2.2\varepsilon + 1.69\varepsilon^2 - 0.4\varepsilon^3\right) \tag{9}$$

Figure 7 presents experimental results of attenuation versus crack density and the fitted curve. It can seem that increasing rate of attenuation coefficient versus crack density decreases with crack density. This can be explained using the relations among attenuation coefficient, crack density and half-length. From the definitions of the

343

attenuation coefficient and crack density, the attenuation coefficient is related to the area of crack surface, this means $\alpha_p \propto a^2$, therefore, from the definition of crack density, we have

$$\frac{\alpha_p}{\varepsilon} = \frac{b}{a} \qquad (10)$$

where b is a constant. Therefore, the ratio, $\dfrac{\alpha_p}{\varepsilon}$, must decrease with increasing of crack density. This is shown by the experimental results of Fig. 7. Moreover, in Fig. 6 we suppose b is a constant, the average half-length of cracks can be estimated as shown in Fig. 8.
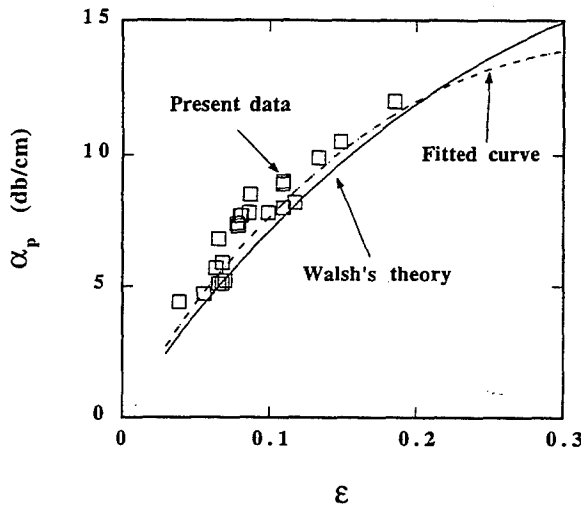
Fig. 7 Relation between attenuation coefficient and crack density
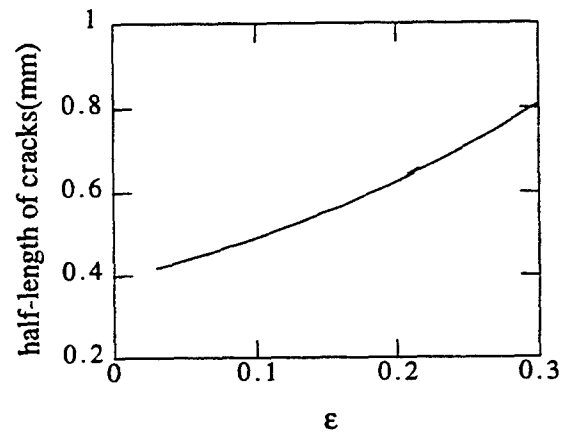
Fig. 8 Estimated average half-length of cracks versus crack density parameter

Basing on the concept that frictional dissipation at crack surfaces in-contact slide relative to one another during the passing of stress wave, Walsh [1966] developed an expression for the attenuation coefficient that can approximately be expressed as

$$\alpha_p = Hf\varepsilon \frac{K(1-v)(1-2v)}{K_0(1-2v)(1-2v_0)} \qquad (11)$$

where H is considered to be a constant and f is frequency. Only one parameter, H, needs to be determined. If let $\varepsilon = 0.1$, from Eqs. (6), (8), the relation between K and K_0 [O'Connell and Budiansky, 1974] and experimental results of attenuation coefficient, H is evaluated to be 60.7db/cm for f = 2 MHz.

The calculated results from Eq. (11) is shown in Fig. 7. It is obvious that the form of Walsh's theory is in good agreement with the experimental results and the relation between α_p and ε is not linear. This result demonstrates that Walsh's theory can be used to evaluate attenuation coefficient in rocks with high crack densities such as occur in the very close vicinity of contained explosions.

CONCLUSIONS AND RECOMMENDATIONS:

Some 20 samples of San Marcos gabbro cut from a shock loaded target are used to measure attenuation coefficients for different damage levels experimentally using the ultrasonic method. We used O'Connell and Budiansky's theory for relating crack density to elastic constant with various damage parameters. Walsh's theory [1966] was used to predict the attenuation coefficients of the samples with different crack density. Our main conclusions are:

(1) The P-wave attenuation coefficient and the damage parameters are given by Eq. (4).

(2) Based on the O'Connell and Budiansky's theory, the relation between the crack density and attenuation coefficient can be expressed approximately as Eq. (9).

(3) Basing on Walsh's theory, we evaluated the attenuation coefficient. The predictions of attenuation coefficient fit experimental results as shown in Fig. (7). Moreover, the Q's of damaged rocks are low, 10-20. This gives rise to the very strong attenuation of the high frequency portions of the seismic signals from contained explosions.

REFERENCES:

Ahrens, T. J., Shock wave techniques for geophysics and planetary physics, in *Methods of Experimental Physics*, vol. 24, part A, edited by C. G. Sammis and T. L. Henyey, pp. 185-235, Academic Press, New York, 1987.

Ahrens, T. J., and M. L. Johnson, Shock wave data for rocks, in *Mineral Physics and Crystallography, A Handbook of Physical Constants*, vol. 3, edited by T. J. Ahrens, pp. 35 - 44, Amer. Geophys. Union, Washington, D. C., 1995.

Ahrens, T. J., and A. M. Rubin, Impact-induced tensional failure in rock, *J. Geophys. Res.*, *98*, 1185-1203, 1993.

Born, W. T., The attenuation constant of earth material, *Geophysics*, *6*, 132-148, 1941.

Grady, D. E., and M. E. Kipp, Dynamic rock fragmentation, in *Fracture of Mechanics of Rock*, edited by B. K. Atkinson, pp. 429-475, Academic, San Diego, 1987.

O'Connell, R. J., and B. Budiansky, Seismic velocities in dry and saturated cracked solids, *J. Geophys. Res.*, *79*, 5412-5426, 1974.

Rubin, A. M., and T. J. Ahrens, Dynamic tensile failure induced velocity deficits in rock, *Geophys. Res. Lett.*, *18*, 219-222, 1991.

Toksoz, M. N., D. H. Johnston, and A. Timur, Attenuation of seismic waves in dry and saturated rocks: laboratory measurements, *J. Geophysics*, *44*, 681-690, 1979.

Walsh, J. B., Seismic wave attenuation in rock due to friction, *J. Geophys. Res.*, *71*, 2591-2599, 1966.

Winkler, K. W., and T. J. Plona, Technique for measuring ultrasonic velocity and attenuation spectra in rocks under pressure, *J. Geophys. Res.*, *87*, 10776-10780, 1982.

Lg Site Amplification Calibration for Isolation of Lg Propagation Effects

G. Eli Baker
J. Bernard Minster
Contract no. F49620-93-1-0508
University of California, San Diego

Abstract

We observe geographically clustered variations in Lg/Pg amplitude ratios of regional earthquakes and NTS events, using southern California seismic network (SCSN) recordings. These variations can occur abruptly over length scales on the order of ten kilometers and are the cause of significant errors in discrimination of regional earthquakes from nuclear explosions. Observations from events at different distances and azimuths suggest that variations are not due to distance effects, very near receiver or source effects, or source radiation, and so we conclude that the variations are largely due to the effects of propagation along the different source-receiver paths.

Our goal is determine which measurable path parameters, if any, (e.g. topographic roughness, waveguide thickness, waveguide thickness variation, attenuation) correlate with variations in the crustal phases. To avoid ambiguity over which phase varies, Lg or Pg, we will estimate the Lg site amplification at each station using the *diffuse* (near receiver scattered) component of teleseismic coda. Near receiver scattered coda and Lg can both be described in terms of surface waves, and measurements using a temporary array indicate that for the same passbands, Lg and diffuse teleseismic coda have similar phase velocities. The array measurements also indicate that the incoming directions of arrival of energy in diffuse coda are fairly evenly distributed. By beamforming, using all SCSN records for a given event, we make an estimate of the *coherent* (near source scattered) component of teleseismic coda, which we remove from each individual coda record. We find, in agreement with previous researchers, that the deep teleseismic coda is almost entirely composed of near receiver scattered energy while 10% to 60% of the shallow teleseismic coda may be composed of near source scattered energy. The removal of the coherent coda appears to be very effective and so lets us use shallow earthquakes as well as deep ones, for better azimuthal coverage of teleseismic events.

Objective:

The objective of this research is to better understand the propagation of regional phases important to discrimination. Specifically, we want to test whether spatial variations in regional Lg to Pg amplitude ratios exist and are strong enough to effect discrimination. Then, to separate Lg amplitude variations from Pg amplitude variations, in order to reduce ambiguity in any interpretation, we want to estimate Lg site amplifications at the recording stations using the diffuse component of teleseismic coda. Finally, we want to test whether the Lg or Lg/Pg anplitude variations may be be predicted by topography, gravity, or other easily measurable geophysical parameters.

Preliminary Research Results:

The Lg phase is very important in regional discrimination.The Lg/Pg amplitude ratio is the best performing regional discriminant, and spectral ratios of Lg are more effective discriminants than those of Pn or Pg (Taylor et. al., 1989). Lg is also important in estimating earthquake magnitude or yield of explosions, but frequency-dependent attenuation causes significant variation in scaling slopes between different paths (Xie and Lay, 1995). There is, however, significant error associated with the Lg/Pg amplitude ratio discriminant (figure 1).
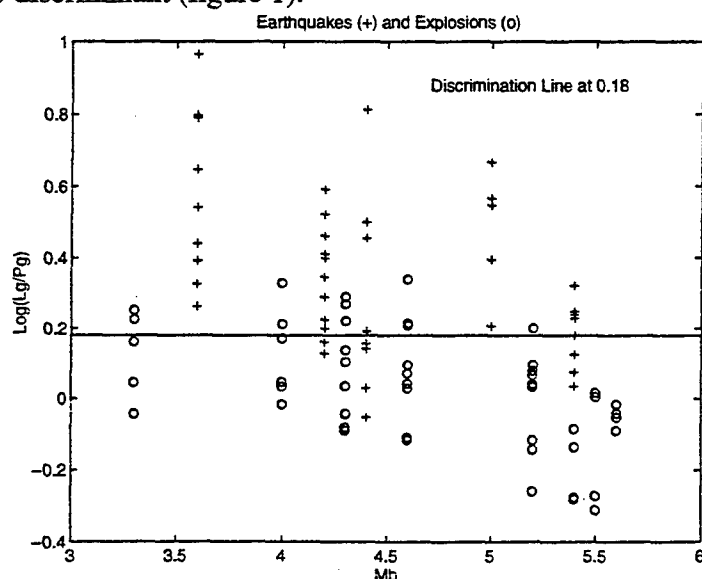
Figure 1: The discriminant Ln(lg/Pg) vs. magnitude for NTS explosions (plusses) and regional earthquakes (circles), divided by a discrimination line at 0.18 (very similar to that found by Taylor et. al., (1989), for the western U.S.). Note that many events of both types would be misclassified at some stations.

To improve discrimination, we would like to know whether the events misclassified in figure 1 have anything in common. Previous research (e.g. Baumgardt, 1985; Zhang et. al., 1994) has shown correlations of Lg amplitude variation with features along the propagation path. Thus it is reasonable to expect some systematic geographic variation in the amplitude ratios. Indeed, this is observed in southern California (see figure 2). That source radiation or near source scattering is not the primary cause of the variation is indicated in figures 2 and 3. We also see no correlation between nodes in the P radiation pattern (either predicted by known mechanisms or observed in first arrival polarizations) and maxima in Lg/Pg ratios, suggesting that the source radiation pattern does not dominate the observed geographical distribution. Figure 4 indicates that variations in the Lg/Pg amplitude ratio are neither due to a simple distance effect nor are they due to near station scattering or site effects. Similar ob-

347

servations for regional earthquakes at different distances and azimuths remain consistent with these findings. By elimination of other possibilities, we conclude that geographic variations in Lg/Pg amplitude ratios are due to effects along the path of propagation.
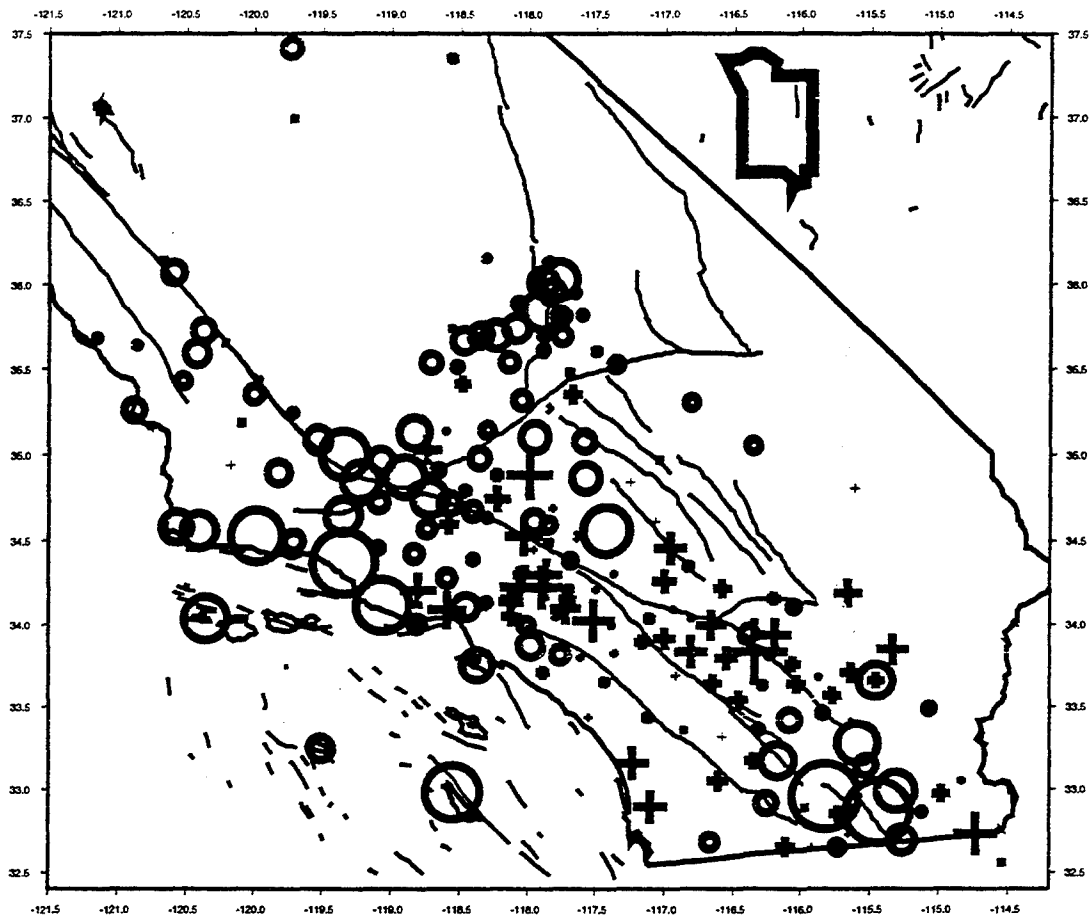
Figure 2: The symbol at each southern California seismic network station represents the typical Lg/Pg amplitude ratio at that site relative to the rest of the network, determined by averaging normalized Log(Lg/Pg) amplitude ratios for 10 NTS explosions. The symbols are as in figure 1, and are scaled by distance from the discrimination line. As these are normalized, a plus at some station does not necessarily mean that the event would necessarily have been misclassified as an earthquake, only that it appears more "earthquake-like" at that station than at other locations. The important point of this plot is the consistent very distinct geographic clustering of like symbols over many explosions with source locations separated by as much as 50 km. This suggests that near source scattering does not cause the geographic variation.

Lg amplitude variations (usually relative to the amplitude of one of a variety of other phases) have been related to other geophysical parameters that can be independently measured or estimated (e.g.Mitchell et. al. 1995, Zhang et. al, 1994, Zhang and Lay, 1994). This has laid the groundwork for the calculation of path corrections for regional discriminants. The broadband data available for those studies was limited, however, to between 7 and 10 stations spread over several thousand kilometers. The southern California seismic network (SCSN), with several hundred stations spread over a few hundred kilometers has station spacing on the order of 10 to 15 km. Such fine spatial sampling in such

a heavily studied region should permit more precise correlation of Lg amplitude variations with path structure.
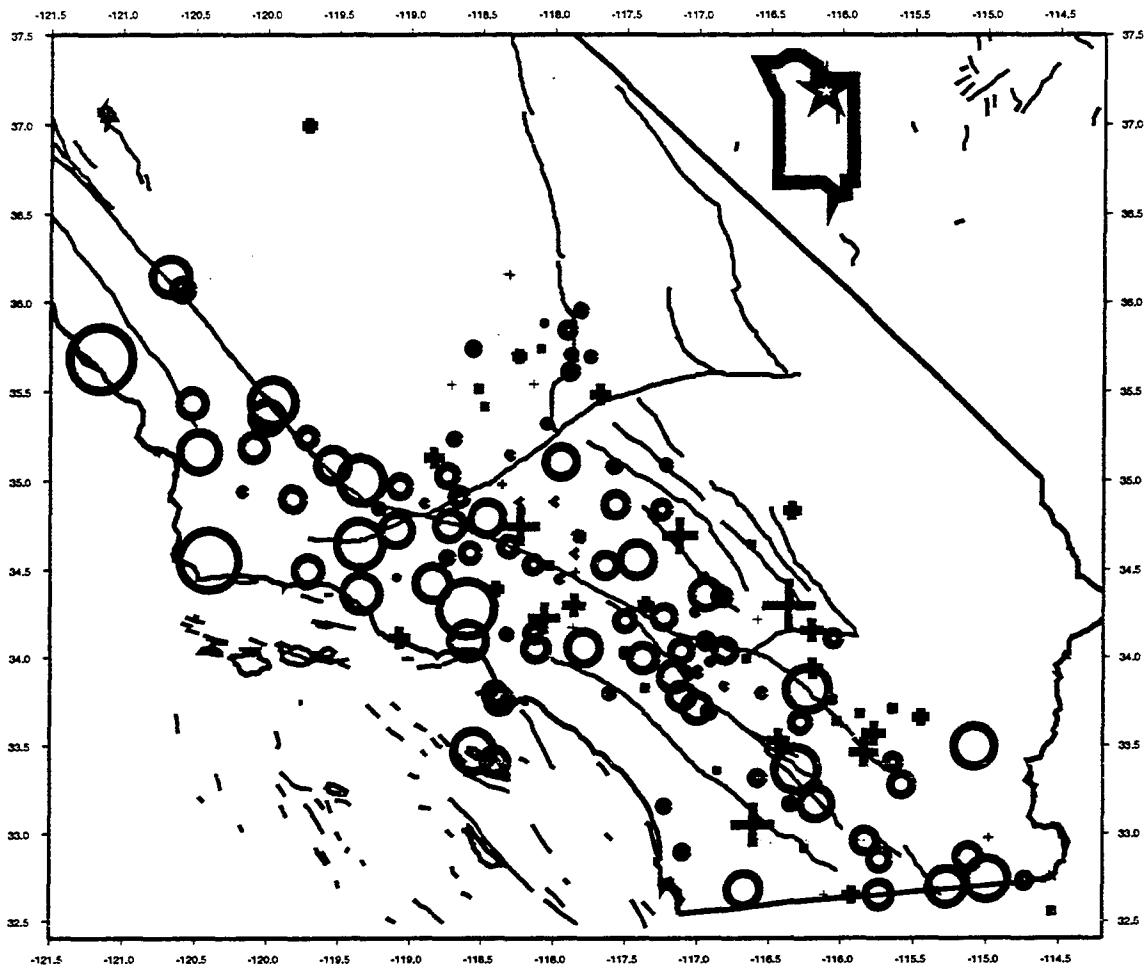
Figure 3: Classification as an earthquake or explosion, by station, of a shallow earthquake within NTS (star symbol indicates earthquake location). Note that the pattern of symbols is similar to that in figure 2, with more plusses in the central part of the network. This suggests that the source radiation pattern plays only a minor role, and provides further evidence that near source scattering may not be important.

The geographic variation of amplitude ratios could be due to either Lg or Pg amplitude variations, or both. To prevent this ambiguity from clouding any interpretation, we would like to calibrate the amplification of each site so we can obtain estimates of amplitude variations for single phases. Note that when we use amplitude ratios, we implicitly assume that site amplifications are the same for both phases used, a possible source of error if differences exist and are mapped into path corrections. Barker et.al. (1980), however, found that for recordings of events with very similar paths to adjacent stations on very different geological structures, the Lg to Pg amplitude ratios were the same. They also distinguished no azimuthal effect.

We propose to use the near receiver scattered component of teleseismic coda as an azimuthally evenly distributed source of Lg-like energy. The nature of both Lg and near-station scattered coda in the frequencies of interest merits further discussion. We must also ask how effectively we can isolate the

349

near-station component of teleseismic coda.
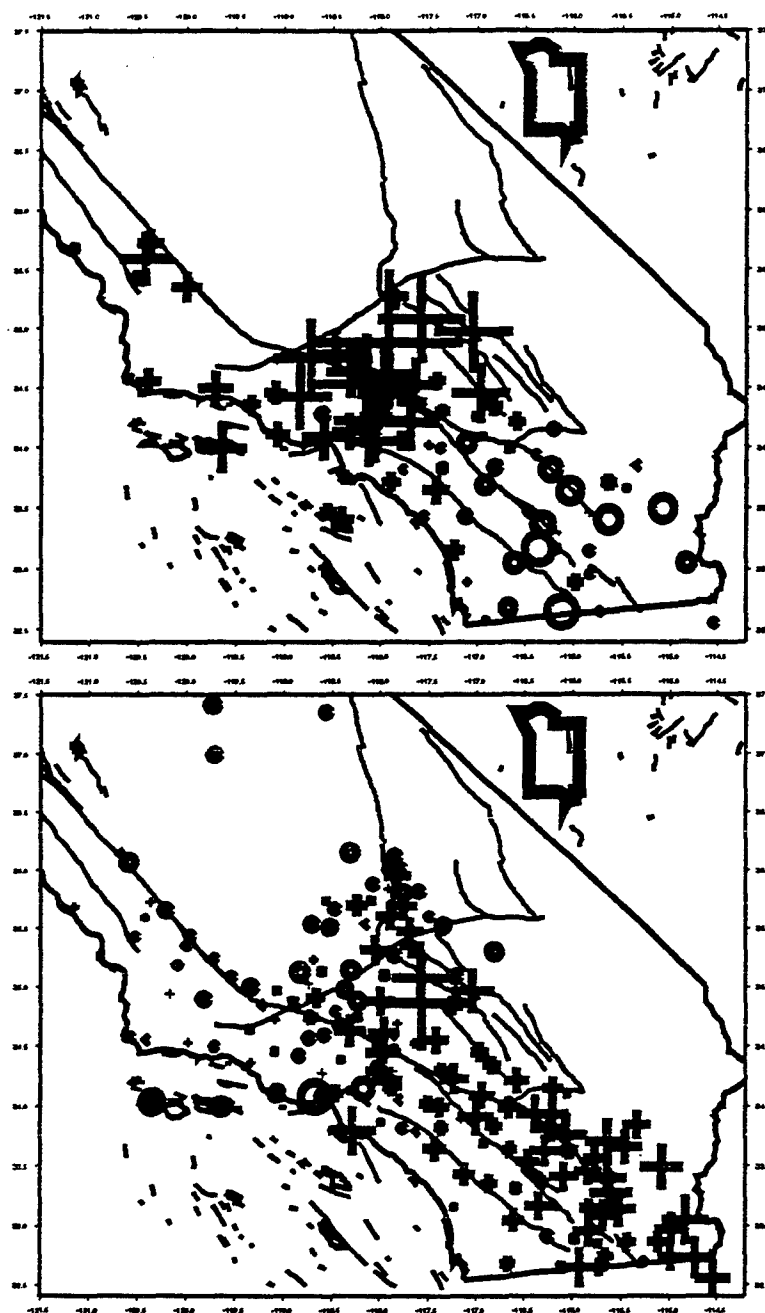
Figure 4: Symbols are as in all previous figures. Above are the classifications for an earthquake in the southern Sierra Nevada. Below are classifications for an earthquake near Cape Mendocino. In the first case, the most distant stations are misclassified as explosions, while in the second case, it is the nearest stations that would misclassify the event. This suggests that the pattern of misclassification is not a near station effect or a distance effect.

Lg is commonly thought to consist of higher mode surface waves (e.g. Båth, 1954). These phases do not remain coherent over even short distances (e.g.. Baumgardt, 1985) due to their sensitivity to variations in crustal structure and so should be especially short lived in a tectonically young region as

southern California, with its rapid spatial variations in crustal thickness and velocities (e.g. Magistrale, 1992). Nonetheless, Cara et. al (1981) found that peaks in phase and group velocity measured in southern California for 2 to 5 second period data were consistent with higher mode Rayleigh waves predicted from appropriate velocity models. More recently, Wagner (1995) used 3 component array analysis to identify specific high frequency Rayleigh and Love waves (1.8 and 2.5 Hz. peak frequencies respectively) in the most prominent part of a nuclear explosion Lg wavetrain.

Teleseismic coda is generally understood to consist of the sum of near-source and near-receiver scattered energy (e.g. Langston, 1989). Energy scattered near the source, into P, travels along nearly the same path as the initial P wave, and is referred to as the *coherent* part of the coda (Dainty, 1990). The *diffuse* component of coda, that is, energy scattered near the receiver from the incoming P wave, travels with much lower phase velocity, 3.3-3.4 km/sec near NORESS. Dainty (1990) notes that this is "*typical of shear waves propagating sufficiently close to horizontal to be trapped in the crustal waveguide (Lg) or surface waves*", and suggests that those are the major components of diffuse coda. The teleseismic coda of deep focus earthquakes has been shown to consist largely of diffuse coda (e.g. Dainty, 1990), and so may provide the multi-azimuthal source of energy appropriate for Lg site calibration.

Individual very near receiver scatterers have been identified, usually by stacking large data sets in some way to enhance an image. As noted by Revenaugh (1995b), identification of individual scatterers associated with topography has been limited to those with vertical scale lengths on the order of half the seismic wavelength. Revenaugh (1995a,b) uses the southern California seismic network (SCSN) to investigate the contribution of P to P, P to S, and P to Rg scattering to teleseismic coda and finds significant scattering over large areas. Using migration, he obtains the sharpest image of Rg scattering efficiency at a group velocity of 2.9 km/sec. This is not proof that most of the energy travels at that group velocity, but only that the most coherent energy does. Revenaugh (1995a,b) finds both topographic and upper mantle scatterers, although nearly twice as many events are required to produce an image of an upper mantle scatterer. For site calibration, we will use much later coda windows than those used for identification of single scatterers, or even those used for scattering efficiency, in an effort to reduce any potential bias from nearby strong scatterers or strong scattering regions.

Another strong argument for the use of teleseismic coda for Lg site amplification calibration is found in an explanation for the existence of Lg in explosion seismograms. Patton and Taylor (1995), using synthetic modeling and a comparison of Lg and Pg spectral ratios with the strength of spall, argue that scattering of Rg into Lg at the surface is the main source of Lg energy at around 1 hz. If this mechanism works at the surface near a shallow source, it should also work for Rg generated at the surface by scattering from teleseismic P waves. This is consistent with the well known observation that high frequency Rayleigh waves suffer rapid attenuation in areas of sharp topography and complicated velocity structure (e.g. Kafka, 1990).

The phase velocities of Lg, measured for 2 regional earthquakes and one nuclear explosion at a temporary array at PFO, are similar to the phase velocities of the energy in the diffuse component of teleseismic coda, measured at the same array for 2 earthquakes (figure 5). Lg generally has a slightly higher peak phase velocity and somewhat more energy at higher phase velocity, possibly due to the contribution of P coda or to a higher percentage of higher mode Rayleigh waves in the Lg. We interpret the result as further evidence of the appropriateness of teleseismic coda for calibration of Lg.

The separation of the coherent and diffuse components of the teleseismic coda at the array merits some discussion. We used this technique on the SCSN network data, partly to test our assumption that the teleseismic coda of deep events consists mostly of near receiver scattered energy. The time lag between any near-source scattered energy and the initial P arrival should be nearly constant across the

network. We will return to this point when we discuss the network data. For the array, of 6 km diameter, we will accept that assumption. To estimate the coherent portion of the coda, we simply align the seismograms on the first arrival and stack them. All near-source scattered energy should stack coherently and near-receiver scattered energy should be incoherent. We then remove the coherent coda from each individual record by subtracting the estimate of the coherent coda (the "beam") from the coda of each individual record. Before subtraction, the beam is scaled by its cross-correlation with the individual trace, to maximize the removal of energy. The result is an estimate of the diffuse coda at each station. In fact, a judicious choice must be made of which array elements to use in forming the beam. The array has closely spaced stations in its inner rings, for which much locally scattered energy will stack coherently. Synthetic tests have confirmed that we can avoid the inclusion of the lower phase velocity diffuse coda in the beam by using only very widely spaced stations for the beamforming, and so we use a subset of the array with a minimum interstation spacing of nearly 1 km. We verify, by inspecting the array response (Aki and Richards, 1980), that the station coverage is not so thin that sidelobes of the beam pattern overlap the slownesses of interest in our estimates.
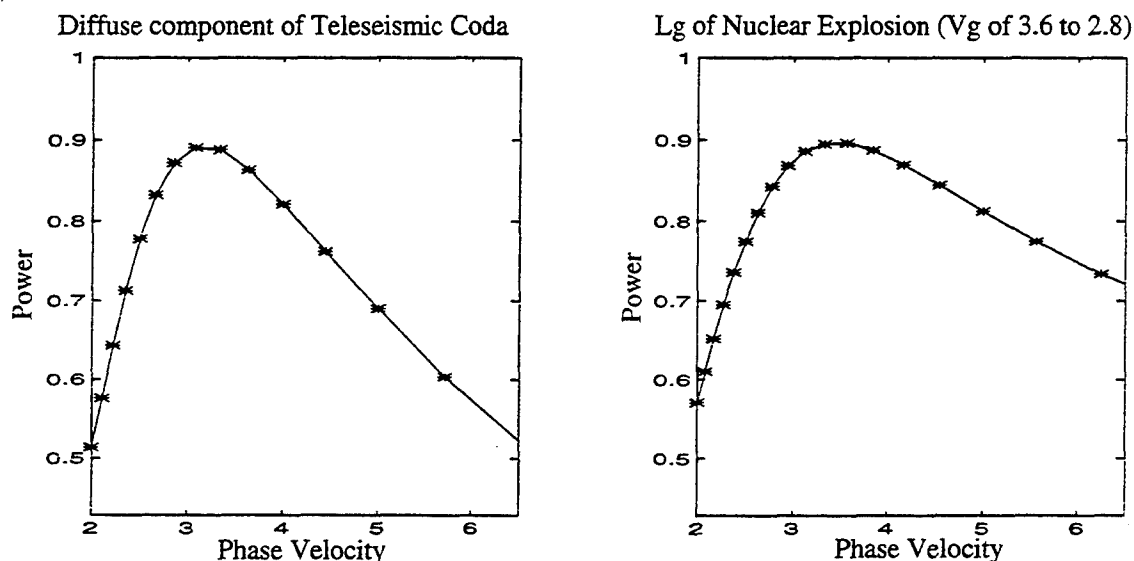
Figure 5: Power vs. phase velocity for the diffuse component of teleseismic coda (left) and Lg of an NTS explosionat 400 km distance (right).

For data collected across the SCSN, the same technique is used. For this data set, we must carefully test the assumption that all near source scattered energy will stack coherently. If scattering at several degrees distance from the source were to contribute to the coherent component of coda, the time lag between the initial P arrival and that scattered energy would not be constant over the several hundred kilometers spanned by the network and so that contribution to the *coherent* coda would not stack coherently. For example, for a source 50 degrees from the network, at 600 km depth, and a scatterer 3 degrees from the source at the same depth (to maximize the variation in ray parameter), the difference in time lag between the direct and scattered P wave for stations 0.1 degrees apart in the plane of the ray would be 0.02 seconds. For stations 1 degree apart, the difference in time lags would be 0.19 second, and so the coherence of the scattered phase would be degraded, as energy in the signal peaks at approximately one hz. For stations 3 degrees apart in the propagation direction, the difference in direct and scattered P times would be 0.6 seconds, and so when stacked, aligned on the initial P arrivals, the scattered arrivals would be nearly 180^0 out of phase and would largely cancel. As we want to use only energy traveling laterally in the crust to estimate Lg amplification, we are concerned about

how much steeply incident energy may exist that is not removed by subtraction of the beam. In a situation as described above, where the change in wavenumber across the network of some scattered energy in the coherent coda is significantly different from the change in the initial arrival wavenumber across the network, the correlation coefficient between coda records should vary with station spacing. Figure 6 shows the correlation coefficients of coda windows for all SCSN station pairs plotted vs. distance for a deep earthquake. Before beam removal (top), the least-squares fit line to the points is virtually horizontal, with a slope of -5×10^{-5}. The mean value is 0.0354. Hence, while some non-zero coherence is apparent, it does not vary significantly with distance from the source. That the coherent portion of the coda is effectively removed by beam subtraction is illustrated in the lower half of the figure. There, the mean value is effectively zero. We obtained similar results for shallow earthquakes, with much larger initial values of mean coherence, but effectively zero coherence after beam removal, indicating effective separation of the coherent from the diffuse coda even for shallow earthquakes. This result has allowed us to improve our azimuthal coverage of teleseismic sources..
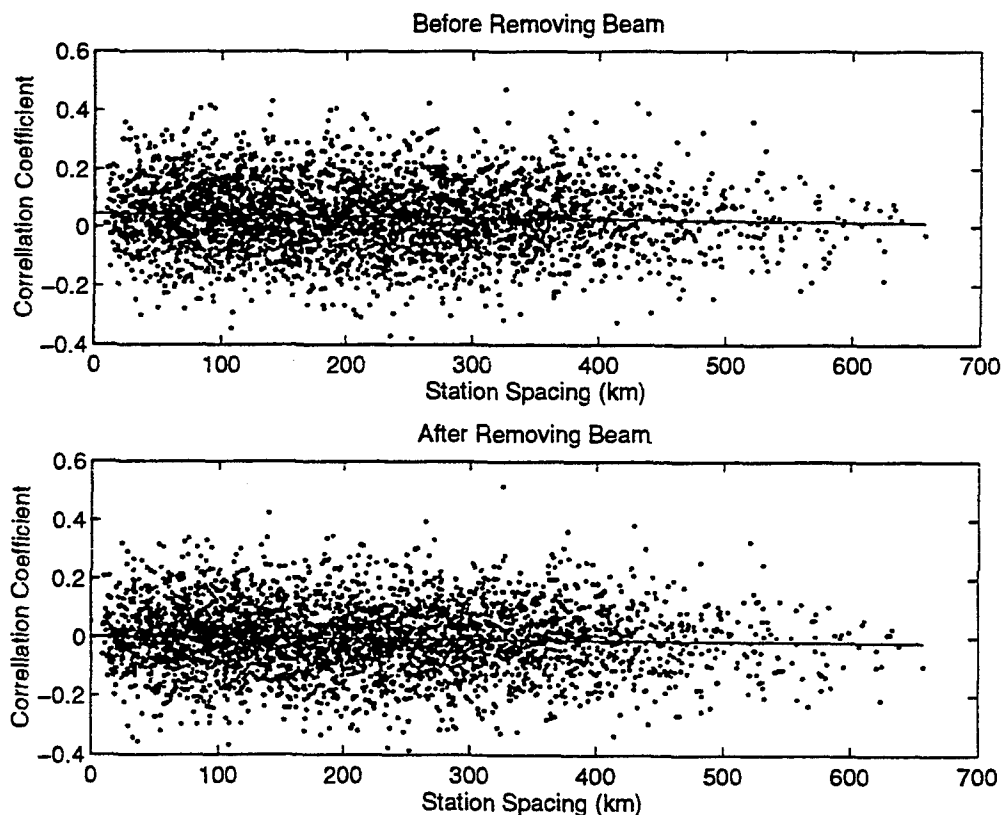
Figure 6: The correlation coefficient of the teleseismic coda records for the same time window after the initial P, at each pair of stations, for one deep event recorded at the SCSN, plotted vs. interstation spacing. (top) before beam removal and (bottom) after beam removal.

The mean ratio of energy in coherent to diffuse coda for 10 deep events was 0.05. The ratio for 9 shallow events varied from 0.12 to 1.18. It also was necessary to calculate instrument calibrations (Wald et. al., 1994), even though the magnification could have been absorbed into the site response. This is so we could take into account the times when calibrations changed. It also will permit a comparison with site amplifications determined from local S-wave coda (Su F. and K. Aki, 1995) once our site response calculations are completed.

353

For the actual calculation of site amplifications, we will need to take into account the censoring of the data. That is, at certain stations, records are clipped for large signals, and at others the amplitudes remain below the pre-event noise level for small signals. Ignoring those facts would lead to biases in the estimates of amplitudes over the whole network, downward for large signals and upward for small signals. Following Ringdal (1977) and Blandford (1982). we can write

$$A_{i,j} = E_j \times S_i \qquad (1)$$

where, $A_{i,j}$ is the measured amplitude of event j at station i, E_j is the mean amplitude of the coda averaged over the network for the chosen window for event j, and S_i is the site amplification at station i. We take the natural log of equation 1, to get

$$a_{i,j} = e_j + s_i, \qquad (2)$$

where $a_{i,j}$ is $\ln(A_{i,j})$, e_j is $\ln(E_j)$, and s_i is $\ln(S_i)$.

The likelihood function for our amplitude observations is then,

$$L(a_{1,1}, a_{1,2}, \ldots, a_{i,j}, \ldots, a_{n,m} \mid e_1, e_2, \ldots, e_m, s_1, s_2, \ldots s_1) =$$

$$\prod_{i,j \in \mathcal{D}} \phi_{i,j}(a_{i,j}) \prod_{k,l \in \mathcal{N}} \Phi_{k,l}(_1 t_{k,l}) \prod_{p,q \in C} \Phi_{p,q}(_2 t_{p,q})$$

where ϕ and Φ are the normal and cumulative normal distribution functions, $\mathcal{D}$ is the set of measured amplitudes, $\mathcal{N}$ is the set of observations in which the signal was below the noise level, and C is the set of clipped records. For the latter 2 sets, $_1 t_{k,l}$ and $_2 t_{p,q}$ are the estimated threshold values. So we find

$$\frac{\delta}{\delta e_j} \ln(L) = \sum_{i,j \in \mathcal{D}} \frac{1}{\sigma_{i,j}^2}(a_{i,j} - e_j - s_i) + \sum_{k,l \in \mathcal{N}} \frac{1}{\sigma_{k,l}^2} \frac{\phi_{k,l}(_1 t_{k,l})}{\Phi_{k,l}(_1 t_{k,l})} + \sum_{p,q \in C} \frac{1}{\sigma_{p,q}^2} \frac{\phi_{p,q}(_2 t_{p,q})}{\Phi_{p,q}(t_p^{(2)})} \qquad (3)$$

where

$$\phi_{i,j}(a_{i,j}) = \frac{1}{\sigma_{i,j}} \phi\left(\frac{a_{i,j} - e_j - s_i}{\sigma_{i,j}}\right), \text{ and}$$

$$\Phi_{i,j}(t) = \int_{-\infty}^{t} \phi_{i,j}(x_i) \delta x_i$$

Setting the right side of equation 3 equal to 0 provides the set of equations we must solve numerically to obtain station corrections.

Recommendations and Future Plans:

We have concluded that propagation effects cause variations in Lg/Pg amplitude ratios of sufficient size to affect discrimination significantly. Once station calibrations have been computed from diffuse teleseismic coda, they will be applied to Lg of regional earthquake and explosion records for all possible azimuths (such as those shown in figures 2-4). Mitchell et. al. (1995) distinguish the effects of intrinsic from scattering attenuation in Eurasia by comparing Lg Q and Lg coda Q. A similar approach with the very dense data set in southern California may provide good results. If scattering is very important to Lg amplitude variation in southern California, it should also prove useful to compare variations in Lg amplitude with changes in path parameters in the direction of propagation.

Having a measure of absolute Lg amplitude variation will permit a comparison with Lg/Pg amplitude ratio variation, and so determination of which phase varies. Hence, in addition to furthering our basic understanding of Lg propagation, we should be able to bring our results to bear on the development of path corrections for the Lg/Pg regional discriminant.

Bibliography:

Aki, K. and P. Richards, (1980), *Quantitative Seismology: Theory and Methods*, Vol. 2, 630-633

Barker, B., Z. Der, and C. Mrazek, (1981), The effect of crustal structure on the regional phases Pg and Lg at the Nevada Test Site, *J. Geophys. Res.*, **86**, 1686-1700

Båth, M., (1954), The elastic waves Lg and Rg along Eurasiatic paths, *Arkiv för Geofysik*, 295-325

Baumgardt, D., 1985, Comparative analysis of teleseismic P coda and Lg waves from underground nuclear explosions in Eurasia, *Bull. Seism. Soc. Am.*, **75**, 1413-1433

Blandford, R., and R. Shumway, (1982) Magnitude:yield for nuclear explosions in granite at the Nevada Test Site and Algeria: joint determination with station effects and with data containing clipped and low-amplitude signals, *Teledyne Geotech Report*, VSC-TR-82-12

Cara, M., J.B. Minster, and R. Le Bras, Multi-mode analysis of Rayleigh-type Lg. Part 2. Application to southern California and the northwestern Sierra Nevada, *Bull. Seism. Soc. Am.*, **71**, 985-1002

Dainty, A. (1990), Studies of coda using array and 3-component processing, *Pageoph*, **132**, 221-244

Kafka, A., (1990) Rg as a depth discriminant for earthquakes and explosions: A case study in New England, *Bull. Seism. Soc. Am.* **80**, 373-394

Langston, C.A., (1989) Scattering of teleseismic body waves under Pasadena, California, *J. Geophys. Res*, **94**, 1935-1951

Magistrale, H., H. Kanamori, and C. Jones, (1992), Forward and inverse 3-dimensional P-wave velocity models of the southern California crust, *J. Geophys. Res.*,**97**, 14,115-14,135

Mitchell, B., J. Xie, and Y. Pan, (1995), Attenuation and blockage of Lg in Eurasia, *NATO ASI series E, Verification of a test ban treaty*, ed. Husebye, E. and A. Dainty

Patton, H., and S. Taylor, (1995) Analysis of Lg spectral ratios from NTS explosions: Implications for the source mechanisms of spall and the generation of Lg waves, *Bull. Seism. Soc. Am.* **85**, 220-236

Revenaugh, J., (1995a), The contribution of topographic scattering to teleseismic coda in southern California, *Geophys. Res. Lett.*, **22**, 543-546

Revenaugh, J., (1995b), A scattered-wave image of subduction beneath the Transverse Ranges, *Science*, **pp.** 1888-1892

Ringdal, F. (1977) Maximum likelihood estimation of seismic event magnitude, *Bull. Seism. Soc. Am.* **67**, 789-802

Su F. and K. Aki, (1995), Site amplification factors in central and southern California determined from coda waves, submitted to *Bull. Seism. Soc. Am*

Taylor, S.R., M. Denny, E. Vergino, and R. Glaser (1989), Regional discrimination between NTS explosions and western U.S. earthquakes, *Bull. Seism. Soc. Am.* **79**, 1142-1176

Wagner, G. (1995), Regional wavefield analysis using 3-component seismic array data, *Proceedings 17th Annual Seismic Research Symposium,* PL-TR-95-2108

Wald, L., S. Perry-Huston, and D. Given, (1993), The southern California network bulletin January-December 1993, *USGS Open-File Report 94-199*

Xie X.B., and T. Lay, (1995), The log (rms Lg)-Mb scaling law slope, *Bull. Seism. Soc. Am.* **85**, 834-844

Zhang, T., S. Schwartz, and T. Lay, (1994), Multivariate analysis of waveguide effects on short-period regional wave propagation in Eurasia and its application to seismic discrimination, *J. Geophys. Res.*, **99**, 21,929-21,945

Zhang, T. and T. Lay, (1994), Analysis of short-period regional phase path effects associated with topography in Eurasia, *Bull. Seism. Soc. Am.*, 84, 119-132

A Dynamic Linear Model For Three-Component Seismic Waveforms

Don Simone Daly, Kevin Anderson
Alan Rohay, Wes Nicholson
Pacific Northwest Laboratory

Abstract

A three-component waveform is modeled as a sum of trigonometric functions using Dynamic Linear Modeling (DLM), a statistical extension of Kalman filtering. The DLM method converts a waveform into a multivariate time series of amplitude and phase-angle estimates. This time series is then transformed into a multivariate time series of descriptive features such as magnitude, direction-of-travel and dimensionality which are more closely related to the underlying seismic phases. There are many possible transformations, and several are considered here. This paper also explores the expected behavior of the dimensionality, magnitude and direction-of-travel time series over the duration of a phase. Dynamic Linear Modeling and parameter transformation is illustrated with an artificial waveform having compressional and Rayleigh phases.

Key words: Dynamic Linear Model, Kalman filter, waveform characterization, eigenanalysis.

Objective

The object of this study is to apply a trigonometric-based dynamic linear model (Kalman filter model)to a three-component seismic waveform in order to derive a set of descriptive features useful for CTBT discrimination.

Preliminary Research Results

Discriminating between a natural or manmade source of seismic activity begins with the extraction of descriptive features from a seismic waveform. Our approach to this extraction is straightforward. First, for a selected set of frequencies, model a three-component waveform as a sum of trigonometric functions with time-varying amplitude and phase-angle parameters. Then, transform the amplitude and phase-angle time series into a multivariate time series of features (e.g. dimensionality, direction-of-travel, magnitude) that are more descriptive of the underlying seismic phases. Next, analyze these descriptive series to identify and characterize the seismic phases and, to distill from them a set of statistics that summarize the discriminating information for a three-component waveform.

Three-component seismic waveforms have been described using a trigonometric-based Dynamic Linear Model(DLM), a statistical extension of the Kalman filter which is well-suited to the transient, nonstationary nature of seismic time series. In the DLM state space model, the estimates of time-varying amplitude and phase-angle parameters are strongly influenced by a three-component waveform's evolving cross-component and temporal covariance structure. Fitting the Dynamic Linear Model produces time series of parameter estimates and both cross-component and temporal covariance matrices.

One set of transformations of parameter estimates to time series of more relevant features involves the eigenanalysis of frequency-specific cross-component covariance matrices at each time step. More descriptive features (e.g. direction-of-travel, dimensionality and magnitude) are calculated from the eigenvalues and eigenvectors of each covariance matrix generating a multivariate time series of descriptive features.

The stability, or lack thereof, of the multivariate time series of descriptive features is directly related to the character of the underlying seismic phases. For example, the arrival of a P phase results in a sharp increase in eigenvalue magnitudes for the higher-frequency covariance matrices but minimal change in eigenvalue magnitudes for the lower-frequency covariance matrices. Related dimensionality and direction-of-travel time series remain relatively constant over the duration of the phase.

A Conceptual Model for a Seismic Waveform

Let us assume that a three-component seismic waveform results from the superposition of transient seismic phases and background noise. Let us further assume that the superpositioned waveform can be decomposed into a set of limited-frequency, three-component waveforms. For our purposes, a limited-frequency waveform has a waveshape whose frequency may vary over time in a band about a dominant frequency. Variation in frequency and amplitude of this waveshape is influenced by the arrival, direction-of-travel, dimensionality, polarity, magnitude and duration of certain underlying seismic phases; namely those seismic phases whose frequency content falls within the frequency band of the limited-frequency waveform. Therefore, the stability, or lack thereof, of the waveshape's frequency and amplitude are indicative of the underlying phase.

A Seismic State Space Model

Let $\Theta_\omega(t)$ represent the state, at time t, of one wave in the set of the f limited-frequency waves whose sum produces one component of a three-component waveform. For ω in the frequency set Ω, let the state of the limited-frequency wave be defined by

$$\Theta_\omega(t) = A_\omega(t)\{\sin[\omega t + \phi_\omega(t)] + i\cos[\omega t + \phi_\omega(t)]\}$$

The state of the wave $\Theta_\omega(t)$ at time t is summarized by the two parameters $A_\omega(t)$ and $\phi_\omega(t)$. Note that the amplitude and phase-angle parameters are allowed to vary with time. Hence, a small set of limited-frequency waves can adapt to fit the superpositioned wave.

Derivations follow more easily if the state of the wave, $\Theta_\omega(t)$, is expressed in matrix format. Let $\alpha_\omega(t) = \text{Re}[\Theta_\omega(t)]$ and $\beta_\omega(t) = \text{Im}[\Theta_\omega(t)]$. Then,

$$\Theta_\omega(t) = \begin{bmatrix} \alpha_\omega(t) \\ \beta_\omega(t) \end{bmatrix} . \tag{1}$$

Note that the amplitude $A_\omega(t)$ and phase-angle $\phi_\omega(t)$ can be determined from the real and imaginary parts of $\Theta_\omega(t)$ by

$$A_\omega(t) = \sqrt{\alpha_\omega^2(t) + \beta_\omega^2(t)} ,$$
$$\phi_\omega(t) = \tan^{-1}\left(\frac{\alpha_\omega(t)}{\beta_\omega(t)}\right) - \omega t .$$

Through a series of applications of trigonometric identities, $\Theta_\omega(t)$ can be defined as a recursive linear function of $\Theta_\omega(t-1)$. Namely,

$$\Theta_\omega(t) = \mathbf{G}_\omega \Theta_\omega(t-1)$$

where

$$\mathbf{G}_\omega = \begin{bmatrix} \cos(\omega) & \sin(\omega) \\ -\sin(\omega) & \cos(\omega) \end{bmatrix} .$$

Using the representation $\Theta_\omega(t)$ for each state, the set of states of the f limited-frequency waves can be represented by a $2f \times 1$ matrix

$$\Theta'(t) = [\Theta'_{\omega_1}(t) \cdots \Theta'_{\omega_f}(t)] .$$

Letting $\mathbf{G}$ be a $2f \times 2f$ block-diagonal matrix with one block equal to G_ω for each ω in Ω, the recursive definition can be extended to include $\Theta(t)$

$$\Theta(t) = \mathbf{G}\Theta(t-1) .$$

Finally, the model, $\Theta(t)$, describing one component of a three-component waveform, is extended to accomodate three components by adding one column for each component to $\Theta(t)$ so that equation 1 becomes

$$\Theta_\omega(t) = \begin{bmatrix} \alpha_{\omega,n}(t) & \alpha_{\omega,e}(t) & \alpha_{\omega,v}(t) \\ \beta_{\omega,n}(t) & \beta_{\omega,e}(t) & \beta_{\omega,v}(t) \end{bmatrix}$$

where the subscripts n, e and v refer to the north, east and vertical components, respectively. The results listed above for the one component model apply directly to the three-component model.

Incorporating Stochastic Elements

In practice, $\Theta(t)$ is a function of its previous states plus any additional effects introduced by new phase arrivals, environmental factors, and/or random perturbations. Further, only sums of the real parts of the set of states $\Theta(t)$, say $\mathbf{Y}(t)$, are observed and these are accompanied by some observational error. The model can accomodate these elements with two equations; a system equation to describe the evolution of $\Theta(t)$ and an observation equation to describe the measurement of $\mathbf{Y}(t)$. These are

$$\Theta(t) = \mathbf{G}\Theta(t-1) + \Psi(t)$$
$$\mathbf{Y}(t) = \mathbf{F}'\Theta(t) + \nu(t) ,$$

where $\mathbf{F}' = [1\ 0\ \dots\ 1\ 0]$ sums the real parts of $\Theta(t)$; $\nu(t) \sim N(0, v\Sigma(t))$ accounts for the observation error; and $\Psi(t) \sim MVN(0, \Gamma(t), \Sigma(t))$ allows for environmental uncertainties.

By choosing Normal and MultiVariate Normal distributions to model the uncertainties, we are assuming

358

that the uncertainties are as likely to be positive as negative, and, more likely near zero than not. We also assume that the uncertainties from time to time are independent, and that observation errors are independent of environmental uncertainties.

Fitting the Stochastic Model

The set of amplitude and phase-angle parameters, and the two covariance matrices at each time t are estimated by Dynamic Linear Modeling (Kalman filtering); a Bayesian approach is taken wherein the estimates at time t depend on the estimates at time $t-1$ and, to a lesser degree, on the estimates at times $t-2, t-3, \ldots$ [WH89, MS83]. The estimation procedure makes extensive use of the temporal and cross-component associations in a waveform; associations induced by the underlying seismic phases. Further, under the Bayesian formulation, the parameter set at each time t has a joint probability distribution. Therefore, it is possible to make statements about the precision of the parameter estimates and, hence, about the estimates of phase characteristics derived from the parameters.

Eigenanalysis and Time Series of Descriptive Statistics

One set of transformations of amplitude and phase-angle estimates into statistics more closely related to seismic phase characteristics begins with the definition of limited-frequency signal covariance matrices and their decomposition into eigenvectors and eigenvalues. The definition of relevant cross-covariance matrices followed by eigenanalysis is common to waveform characterizations proposed by several authors [BRAN94, Jur88, SH91, Tak91, Vid86]. Time series of dimensionality, polarity and magnitude measures are derived from the eigenvalues. Direction-of-travel (incidence angle and azimuth) time series are derived from the eigenvectors.

Let $\widehat{\alpha}_\omega(t)$ denote the three-component estimate $\widehat{Y}_\omega(t) = [\widehat{\alpha}_{\omega,n}(t) \quad \widehat{\alpha}_{\omega,e}(t) \quad \widehat{\alpha}_{\omega,v}(t)]$. The vector $\widehat{\alpha}_\omega(t)$ is an estimate of the real parts of $\Theta_\omega(t)$ and a row from the seismic state space matrix $\Theta(t)$. For time t and frequency $\omega \in \Omega$, define the cross-component covariance $\Sigma_\omega(t)$ as a weighted average of $\Sigma_\omega(t-1)$ and the outer product of $\widehat{\alpha}_\omega(t)$,

$$\Sigma_\omega(t) = \frac{\mathrm{w}\Sigma_\omega(t-1) + \widehat{\alpha}_\omega(t)\widehat{\alpha}'_\omega(t)}{\mathrm{w}+1}.$$

Frequency-specific measures of waveform dimensionality, spatial magnitude and direction-of-travel for each time t can be calculated from the eigen-values and eigenvectors of $\Sigma_\omega(t)$. For instance, waveform dimensionality can be estimated by comparing the magnitudes of the eigenvalues $\lambda_\omega(t)$. If one eigen-value, say $\lambda_{\omega,1}(t)$, is significantly larger than the other two over a period of time, then the limited-frequency wave Θ_ω is linear during that interval, and characteristic of a compressional wave. The size of the eigenvalues $\lambda_\omega(t)$ is related to the energy in $\Theta_\omega(t)$ and, hence, to the magnitude of the underlying seismic phases which contribute to the composite wave at that frequency. One measure of magnitude is the logarithm of a weighted geometric mean of the eigenvalues. This measure is an extension of the M_b and M_s measures.

Direction-of-travel can be estimated from direction cosines, the entries in an orthonormal eigenvector. For the appropriate frequency and eigenvector, the arc cosine of the entry associated with the vertical component is a measure of the incidence angle. The arc tangent of the ratio of the east to north elements provides an estimate of the azimuth.

Though the value of these statistics at any time t can be interesting, it is the behavior of the time series of these statistics that is most informative. For instance, a significant change in the magnitudes of the eigenvalues should occur with the arrival of a P phase. Over its duration, the related dimensionality measure should be stable indicating linearity. Further, the appropriate direction-of-travel time series should also be stable during this period.

An Example

Application of seismic eigenanalysis to the DLM cross-frequency, cross-components covariance time series was reported earlier [BRAN94]. The DLM was fit to artificial waveforms, Little Skull Mountain earthquake aftershock waveforms, and NTS explosion waveforms recorded at Goldstone, California. Paralleling the by-

359

frequency eigenanalysis described in the previous paragraph, the cross-frequency covariance time series were transformed into sets of derived time series corresponding to waveform dimensionality, magnitude, incidence angle, and azimuth. The effectiveness of the DLM approach was then illustrated using these derivative time series. A highlight of the report was the introduction of a novel ternary plot to visualize a waveform's evolving dimensionality. The distinct dimensionality of different phases (Pn+Pg, P-coda and S-coda) was apparent using the ternary plotting technique.

The cross-frequency analysis [BRAN94] could not accurately extract phase-specific characteristics. Our current emphasis on frequency-dependent analysis is in response to this shortcoming. We have defined frequency-specific covariance matrices and are now re-analyzing the aforementioned waveforms. We have improved the selection of model frequencies, initialization parameter values and model-evolution constants. Preliminary results show that characteristics of individual phases are identified more easily using this modified frequency-specific eigenanalysis.

Artificial waveforms featuring compressional, shear and Rayleigh wave characteristics in combination with background noise were generated to tune and test the DLM methodology. A composite waveform with compressional and Rayleigh phases is presented in Figure 1. This figure also shows the DLM decomposition of the composite waveform into five limited-frequency three-component waveforms.

The compressional phase of the combination waveform is a series of seven impulsive spikes. The spikes were inclined from vertical 20, 20, 20, 20, 20, 30 and 20 degrees, respectively; and had azimuths of 290, 280, 290, 300, 290, 290 and 290 degrees, respectively. The Rayleigh phase is a low-frequency surface wave having a vertical component 90 degrees out of phase with the horizontal components and an azimuth of polarization set at 45 degrees.

A subset of the feature time series derived from the DLM fit to the artificial composite waveform is shown in Figures 2, 3 and 4. These figures illustrate the variety of useful information about seismic phases that can be extracted using the DLM model. In particular, the stability of certain properties is revealed. The sharp change in the feature time series with the arrival of phases is also apparent.

The DLM successfully separates, by frequency, the compressional and Rayleigh phases in the composite waveform, Figure 1. The Rayleigh waveform is apparent in the 1 Hz DLM reconstruction, while the compressional waveform is apparent in the the 2, 4, and 8 Hz DLM reconstructions.

An eigenanalysis of the frequency-specific cross-component covariances indicates elliptical dimensionality for the lowest frequencies (two co-dominant eigenvalues) and linear dimensionality for the higher frequencies (one dominant eigenvalue) — which is consistent with two-dimensional Rayleigh and one-dimensional compressional waveforms, respectively, as shown in Figure 2. The relationship between phase arrival and the frequency-specific eigenvalues is illustrated by the sharp increases in the 2, 4, and 8 Hz dominant eigenvalues with the arrival of the compressional pulses.

Incidence angles and azimuths can be derived from the direction cosines that make up the frequency-specific eigenvectors. The angles and azimuths derived from the 4 Hz eigenvectors relate to the compressional wave, Figure 3. Note the stability of the incidence angle and azimuth measures, and how well they track the true angles for the compressional phase (Note that the azimuth angles, 280, 290, and 300 degrees, are equivalent to -80, -70 and -60 degrees, as shown in Figure 3).

For a planar wave such as a Rayleigh wave, the plane of motion is defined by the eigenvectors associated with the two largest eigenvalues. These fluctuate over time. The normal to this plane is defined by the eigenvector associated with the smallest eigenvalue. This eigenvector is stable over time. Figure 4 presents the incidence angle and azimuth time series corresponding to the smallest 1 Hz eigenvalue and, hence, the normal to the Rayleigh plane of motion. These graphs show the most stable estimates related to the incidence angle and azimuth of the Rayleigh wave. The estimate of incidence angle of the normal is approximately 90 degrees indicating that the incidence angle of the Rayleigh plane is nearly vertical. The estimated azimuth of the normal is approximately 135 degrees indicating that the azimuth of the Rayleigh wave is 45 or 225 (135 +/- 90) degrees. Both these estimates agree with the parameters of the artificial Rayleigh phase.

Conclusions and Future Plans

For simple artificial waveforms, trigonometric-based Dynamic Linear Models effectively capture the spectral and dimensional characteristics of three-component waveforms in time series of amplitude and phase-angle

estimates. These time series are readily transformed into time series of descriptive statistics closely related to the underlying seismic phases. Graphs of these descriptive series display distinguishing features related to the type of underlying phase. For instance, over the duration of a P phase, the dimensionality time series for the appropriate frequency is stable, and indicates a linear form whil the related time series of azimuths is nearly constant. Several of the descriptive time series contain sharp change points indicating a change in underlying phase (Figure 2). The DLM approach appears well suited to characterizing properties of seismic phases that are stable.

The next phase of our research will build upon the knowledge we have gained from the development and analysis efforts to date. We plan to address DLM adaptations, improvements, and developments in several areas:

- develop DLM modeling diagnostics to improve the DLM fit.
- develop user guidelines to aid implementation and interpretation of the DLM.
- develop guidelines for parameter initialization and frequency selection.
- extend classical methods to use the extensive information in the time series of coefficient and covariance estimates.
- derive statistical measures of precision/quality to accompany DLM-based phase characteristic estimates.
- improve DLM visualization tools.

References

[BRAN94] D.K. Blough, A.C. Rohay, K.K. Anderson, and W.L. Nicholson. Dynamic Bayesian Filtering For Real-Time Seismic Analyses. In M.D. Denny, editor, *Symposium on the Non-Proliferation Experiment Results and Implications*, Livermore, CA, 1994. Lawrence Livermore National Laboratory. CONF-9404100.

[Jur88] A. Jurkevics. Polarization Analysis of Three–Component Array Data. *Bulletin of the Seismological Society of America*, 78(5):1725–1743, 1988.

[MS83] R.J. Meinhold and N.D. Singpurwalla. Understanding the Kalman Filter. *The American Statistician*, 37:123–127, 1983.

[SH91] A. Suteau-Henson. Three–Component Analysis of Regional Phases at Noress and Arcess: Polarization and Phase Identification. *Bulletin of the Seismological Society of America*, 81(6):2419–2440, 1991.

[Tak91] T. Takanami. A Study of Detection and Extraction Methods for Microearthquake Waves by Autoregressive Methods. *Journal of the Faculty of Science, Hokkaido University*, 9(1):67–196, 1991.

[Vid86] J.E. Vidale. Complex polarization analysis of particle motion. *Bulletin of the Seismological Society of America*, 76(5):1393–1405, 1986.

[WH89] M. West and J. Harrison. *Bayesian Forecasting and Dynamic Models*. Statistics. Springer-Verlag New York Inc., New York, New York, 1989.
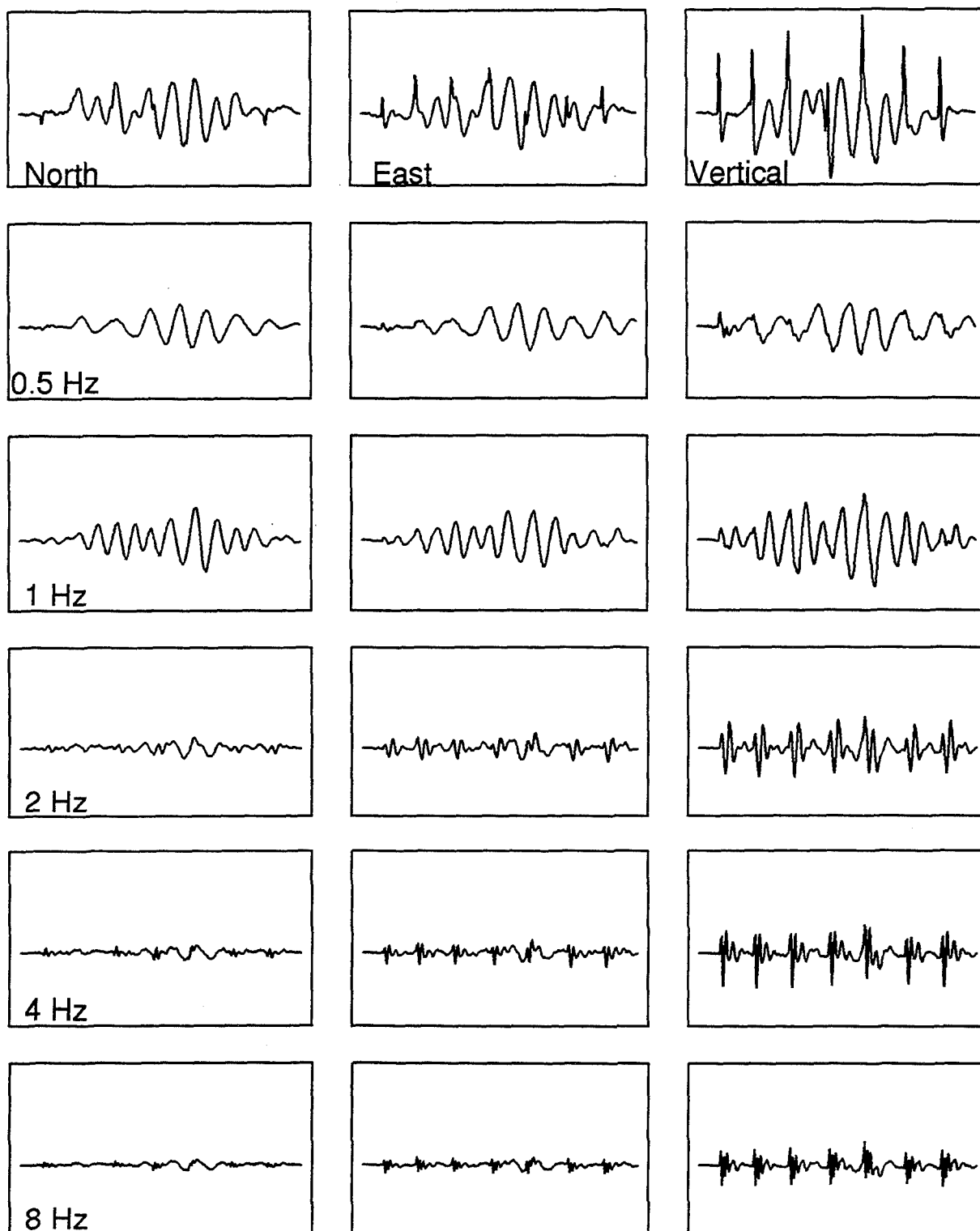
Figure 1: Artificial Three-component Waveform and DLM-reconstructed Components. Row 1 shows the north, east and vertical components of the artificial compressional and Rayleigh waveform. Rows 2 thru 6 show the separation of phases by frequency and waveform component achieved using a five-frequency DLM. The extracted Rayleigh phase is apparent in the 0.5 and 1 Hz panels, while the extracted compressional phase dominates the 2, 4, and 8 Hz panels.

362
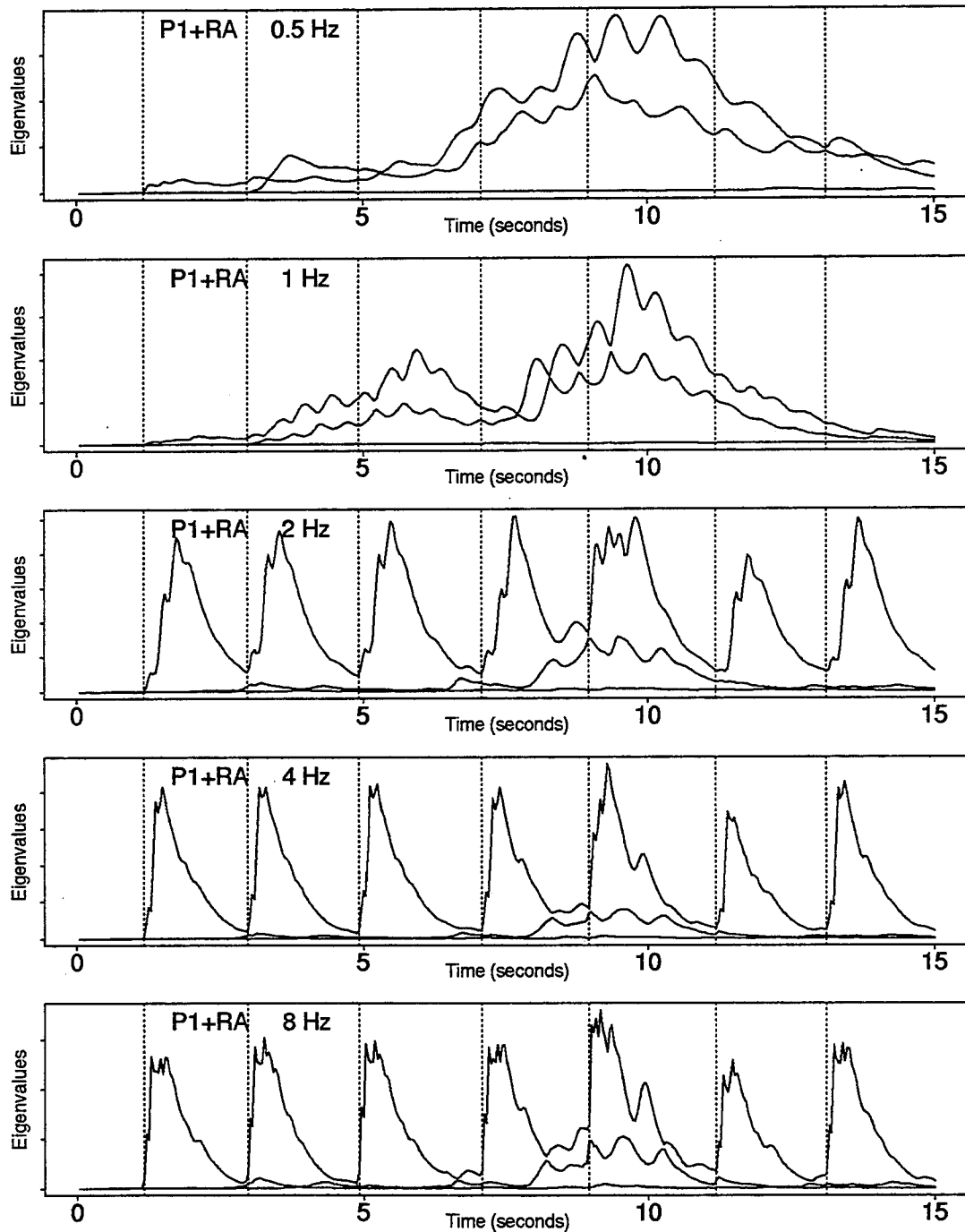
Figure 2: Time series of frequency-specific eigenvalues extracted from the DLM fit of the artificial composite waveform. At the lowest frequencies (top panels), the parallel profiles are consistent with the elliptical dimensionality expected with a Rayleigh wave. The bottom panels associated with the higher frequencies show the dominance of one eigenvalue, indicating linear dimensionality and a compressional wave. The sharp rise in the eigenvalue profiles in the lower panels is associated with the arrival of compressional waves. Note that the eigenvalue axis in each plot was scaled to aid visual comparison of within-plot profiles, so eigenvalue magnitudes are not comparable across plots.
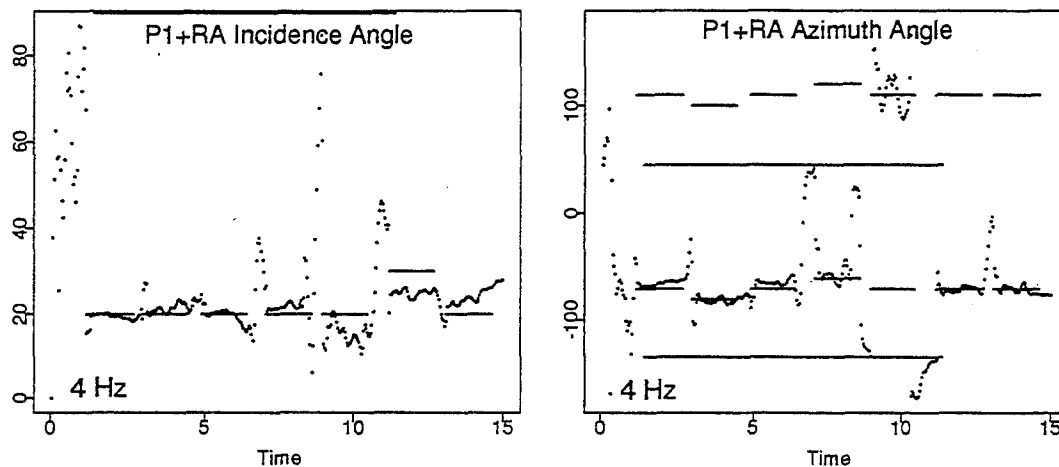
Figure 3: Time series of estimated incidence angles and azimuths for the "P1+RA" waveform, from the 4 Hz output of the DLM. The short and long horizontal bars denote approximately the known arrival times and durations of the compressional pulses and Rayleigh waveform, respectively. The rows of plots, top to bottom, are associated with the largest to smallest eigenvalues. At this frequency, the first row of graphs pertains to the one-dimensional compressional waveforms. The paired horizontal bars shown in the azimuth panels reflect the ambiguity in the eigenanalysis, which can resolve azimuths only to the angle plus or minus 180 degrees.
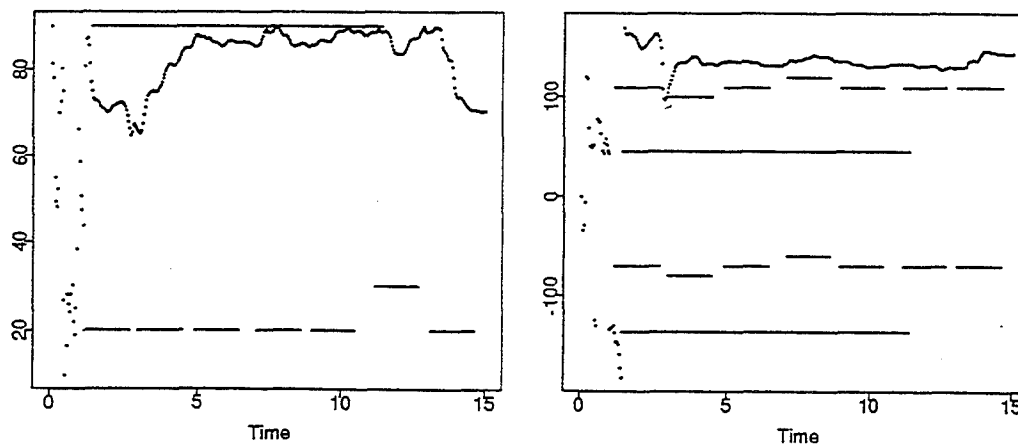
Figure 4: Time series of estimated "P1+RA" incidence angles (left) and azimuths (right) from the 1 Hz output of the DLM. The short and long horizontal bars denote approximately the known arrival times and durations of the compressional pulses and Rayleigh waveform, respectively. The rows of plots, top to bottom, are associated with the largest to smallest eigenvalues. At this frequency, the third row of graphs pertains to the dimension normal to the plane featuring the Rayleigh waveform. Note the stability of the features in these two panels. The incidence angle of the Rayleigh plane is nearly vertical, since this plane is orthogonal to the normal. Similarly, the azimuth is 45 degrees (90 degrees from the azimuth of the normal). The paired horizontal bars shown in the azimuth panels reflect the ambiguity in the eigenanalysis, which can resolve azimuths only to the angle plus or minus 180 degrees.

364

SEISMIC WAVE PROPAGATION IN SOUTH AMERICA

Lawrence A. Drake, Estela Minaya and Jorge Loa
Observatorio San Calixto
Casilla 12656, La Paz, BOLIVIA
adrake@osc.bo

Abstract

The Comprehensive Test Ban Treaty, at present being negotiated in the Conference on Disarmament, requires an International Seismic Monitoring System and On-Site Inspections. Harjes has recalled three lessons learned from previous Group of Scientific Experts Technical Tests: 1. The International Seismic Monitoring System needs to be calibrated with respect to standard travel-time curves and amplitude-distance relations. 2. Provision of adequate surface wave detection and reporting should be included in the design of the International Seismic Monitoring System. 3. To detect and locate small events, the observation of the seismic wavefield at regional distances is essential. On-Site Inspection requires the location of events, whether earthquakes or explosions, to plus or minus 5 km. In the highly irregular region of northern and western South America, we cannot simply use uncorrected partial derivatives from standard travel-time curves. We have found the response curves of the seismographs that operated at La Paz from the years 1913 to 1962, thus revealing a considerable amount about South American seismicity. We have observed at La Paz that L_g waves of periods of 1.5 and 1.6 s arrive from the Caribbean Sea, north of northwestern Colombia, but not from the Chilean trench to the west of La Paz. We have constructed models of the structure below Iquique, Chile, and of structure below the oceanic trench off the coast from Iquique. For the model of the structure below the oceanic trench off the coast of Iquique, the modes of the shorter periods travel practically entirely in the sediments in the trench (assumed to be of thickness 1 km), while the mode of period 10 s travels predominantly in the low velocity zone at a depth of approxi-mately 110 km. The phase velocities of these modes in the model of the structure below Iquique are between 3.06 and 4.14 km/s; the phase velocities of the Love modes of shorter period (1.9 s to 3.7 s) in the model of the structure below the trench are between 0.51 s and 0.57 s. There is practically no coupling between the Love modes below the oceanic trench and the modes below Iquique. At present we are considering the relation between the Love and Rayleigh modes of short period in our various models and the L_g and the R_g phases. For Colombia, we have constructed models of the regions below Quibdó, below Barranquilla and below the Caribbean Sea northwest of Barranquilla. The Caribe plate motion near Mérida, western Venezuela, suggests, together with right hand strike-slip motion, a substantial portion of thrust. We are at present analyzing by the finite element method the propagation of Love and Rayleigh waves across these regions.

Key Words: Andes Mountains, seismograph response, Love waves, Lg waves, finite element method

Objective

The Comprehensive Test Ban Treaty, at present being negotiated in the Conference on Disarmament (Alewine, 1995; Conferencia de Desarme, 1994a; 1994b), requires an International Seismic Monitoring System and On-Site Inspections. Harjes (1995), discussing the International Seismic Monitoring System, has observed that the use of modern technology does not necessarily improve the seismological results. He has recalled, among other lessons, three principal lessons learned from previous Group of Scientific Experts Technical Tests: 1. The International Seismic Monitoring System needs to be calibrated with respect to standard travel-time curves and amplitude-distance relations. 2. Provision of adequate surface wave detection and reporting should be included in the design of the International Seismic Monitoring System. 3. To detect and locate small events, the observation of the seismic wavefield at regional distances is essential. Kennett (1993) has noted that the seismic source imposes a distinctive pattern on the radiated seismic wavefield, but this pattern is profoundly modified on passing through an irregular region. The crustally guided wave L_g is useful in the discrimination of seismic sources. However, even from a single source, amplitude ratios of short period waves like L_g can vary significantly. On-Site Inspection requires the location of events, whether earthquakes or explosions, to plus or minus 5 km (for an inspection area of 100 km^2). In the highly irregular region of northern and western South America, we cannot simply use uncorrected partial derivatives from standard travel-time curves (to change inconsistencies in arrival times to a change in the position of the event). Eisenberg and his coworkers (1989) located with local seismograph stations aftershocks of the 1985 Chile earthquake and some 1981 earthquakes; they found that almost 10 percent of the National Earthquake Information Service locations of these earthquakes differed by more than 65 km from the locations found from the local stations. We need to understand the structure of the Andean Cordillera and we need to model the ground motion of waves passing across it in order to locate events accurately, to discriminate between them and to estimate correctly their magnitude. The task of the International Monitoring System is considerable. An explosion of 10 kt, fully decoupled in salt, has a magnitude of approximately 3.5 (Sykes, 1995). There are, on average, 57 events of magnitude 3.5 in the world each day; 21,000, each year (Conferencia de Desarme, 1994a). A considerable proportion of these events occur in South America; difficulties of location, discrimination and magnitude estimation need to be reduced.

Preliminary Research Results

We have found the response curves of the seismographs that operated at La Paz from the years 1913 to 1962, thus revealing a considerable amount about world, and especially South American, seismicity. "Data for the southern hemisphere were much improved by the establishment of the station at Riverview (near Sydney), Australia, beginning March 18, 1909.... A further improvement followed the installation at La Paz (Bolivia), with reports beginning May 1, 1913. La Paz at once became, and still remains, the most important single seismological station of the world. This is a consequence of its isolated location, the sensitive instruments, and the great care with which records were interpreted and reports issued under the direction of Father Descotes" (Gutenberg and Richter, 1954, p.6; in 1962, the World-Wide Standard Seismograph Network became operational). For the three seismographs recording on smoked paper, dynamic magnification equals $V/D^{1/2}$, where V is static magnification and

$$D = [1 - (\frac{T}{T_o})^2]^2 + \frac{4 \ln^2 \epsilon}{\pi^2 + \ln^2 \epsilon} (\frac{T}{T_o})^2$$

T being the ground period, T_o the period of the seismometer, ϵ the damping ratio and ln the logarithm to the base e. V, T_o and ϵ are given in the La Paz Boletín Sísmico; r/T_o^2, the solid (or pen) friction, is also given, but its effect, except for very large pen movement, is included in the damping ratio ϵ (Sohon, 1932, p. 63 ; Byerly, 1933; 1942, p. 110). At a period of 12 s, the dynamic magnification of the two horizontal seismographs recording on smoked paper was approximately 500 (Fig. 1). For the Galitzin-Wilip seismographs, dynamic magnification equals $T/C'UD^{1/2}$, where C' is $\pi L/AK$, L is the distance from the hinge to the center of oscillation of the pendulum, A is the optical lever arm of the galvanometer, K is Galitzin's 'transfer factor', U is $1+(T/T_g)^2$, T_g is the period of the galvanometer, μ^2 is $1-\zeta^2$, ζ is the fraction of critical damping of the seismometer and

$$D = (1 + (T/T_o)^2)^2 - 16\mu^2(T/T_o)^2$$

(Galitzin, 1911, p.266). T_o, T_g, μ^2 and log C' are given in the La Paz Boletín Sísmico. At a period of 8 s, the dynamic magnification of the Galitzin-Wilip seismographs at La Paz was approximately 2000 (Fig. 2).

In northern Bolivia, the Andean Cordillera forms the Cordillera Occidental, at the border with Chile, and, 250 km northeast, the Cordillera Real. These two branches of the Cordillera are separated by Lago Titicaca and the Altiplano. In central Bolivia, on account of the Arica 'elbow' of the western South American coastline, the Nazca plate is forced to spread and change its strike from approximately NW-SE to approximately N-S (Omarini et al., 1991; Dorbath et al., 1993; Baby et al., 1993; Lamb et al., 1993). We have observed at La Paz that L_g waves of periods of 1.5 and 1.6 s arrive from the Caribbean Sea, north of northwestern Colombia,
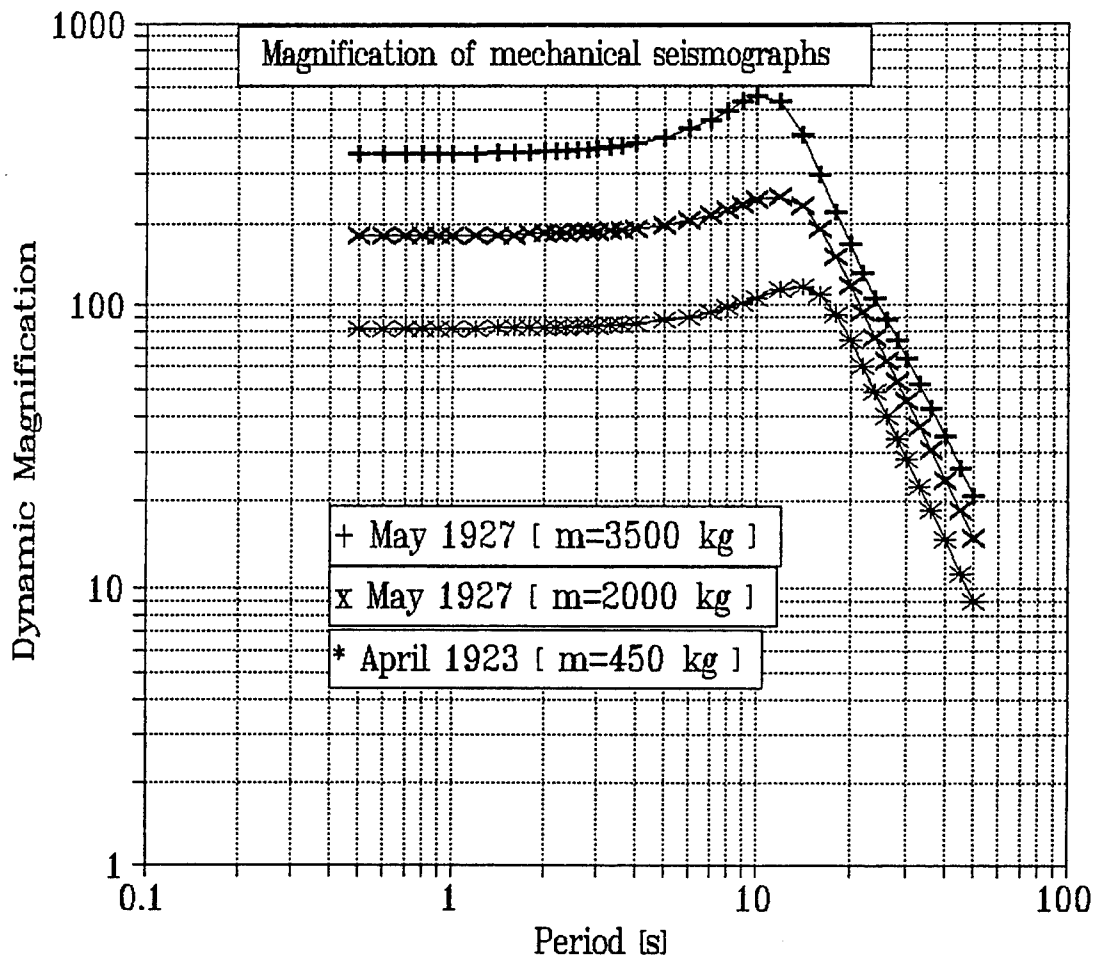
Fig. 1. Examples of the dynamic magnification of the mechanical
seismographs recording on smoked paper at La Paz: E-W (3500 kg),
May, 1927; N-S (2000 kg), May, 1927; E-W (450 kg), April, 1923.

but not from the Chilean trench to the west of La Paz. We have
constructed models of the structure below Iquique, Chile (20°13'S,
70°10'W), and of structure below the oceanic trench off the coast
from Iquique (Tables 1 and 2; Wigger et al., 1994; Dziewonski et
al., 1975; Dziewonski and Anderson, 1981; Drake, 1989). The
variation of displacement with depth of the fundamental Love modes
of periods 0.7 s, 1.5 s, 5.0 s and 10.0 s for the model of the
structure below Iquique are shown in Fig. 3; the modes are
normalized so that the energy they transmit is proportional to the
product of their angular frequency and wavenumber (Lysmer and
Drake, 1972). The variation of displacement with depth of the
fundamental Love modes of these periods for the model of the
structure below the oceanic trench off the coast of Iquique cannot
be conveniently shown, because the modes of the shorter periods
travel practically entirely in the sediments in the trench (assumed
to be of thickness 1 km), while the mode of period 10 s travels
predominantly in the low velocity zone at a depth of approximately
110 km (Drake and Bolt, 1980). The phase velocities of these modes
in the model of the structure below Iquique are between 3.06 and
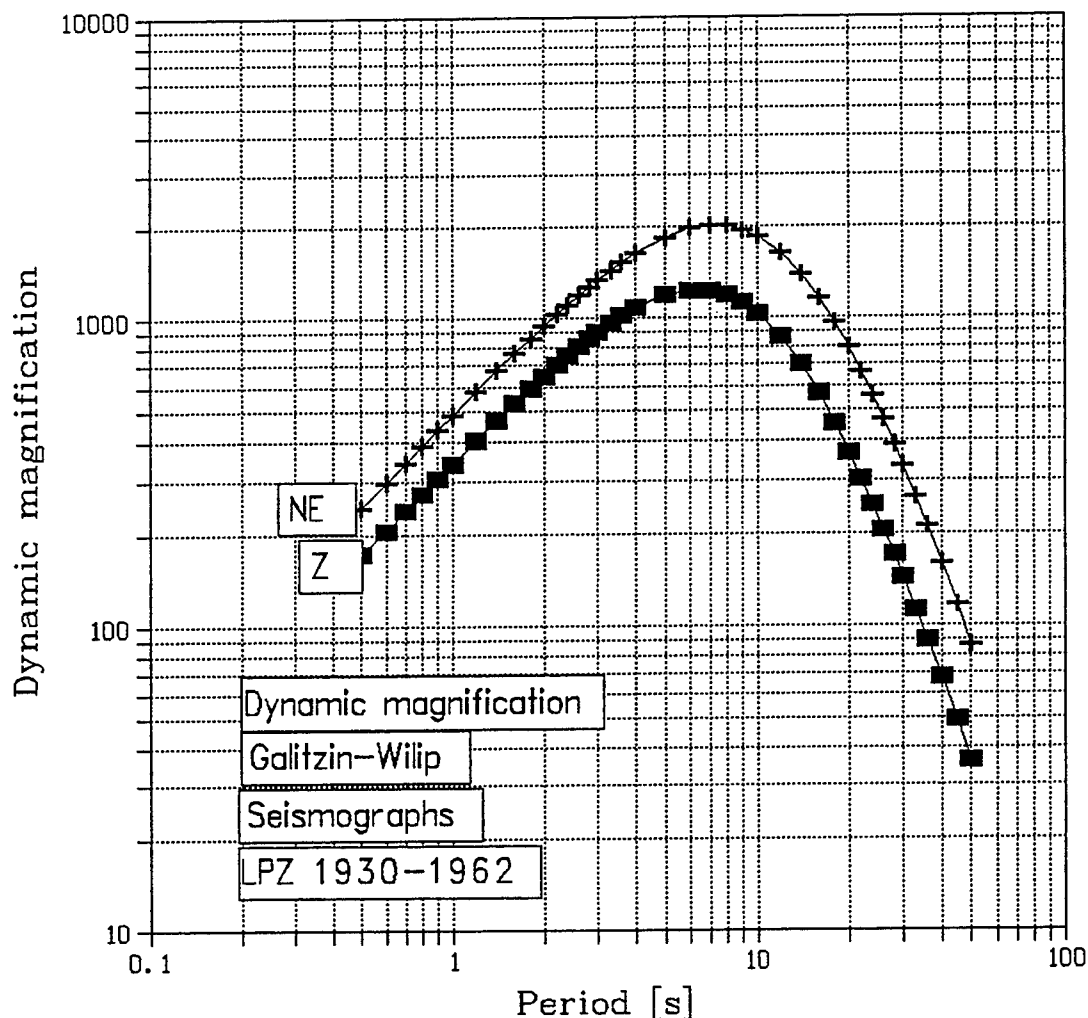
Fig. 2. Examples of the dynamic magnification of the Galitzin-Wilip
seismographs operating at La Paz: N-S and Z for 1960; E-W is very
similar to N-S.

4.14 km/s; the phase velocities of the Love modes of shorter period
(1.9 s to 3.7 s) in the model of the structure below the trench are
between 0.51 s and 0.57 s. There is no need to analyze a two-
dimensional finite element model to see that there is practically
no coupling between the Love modes below the oceanic trench and the
modes below Iquique. In 1957, Ewing, Jardetzky and Press (p. 219)
noted that as little as 2° of intervening ocean is enough to
eliminate the L_g phase entirely. At present we are considering the
relation between the Love and Rayleigh modes of short period in our
various models and the L_g and the R_g phases (Press and Ewing, 1952;
Nuttli, 1986). For Colombia, we have constructed models of the
regions below Quibdó (05°42'N, 76°40'W; Flüh et al., 1981), below
Barranquilla (10°59'N, 74°48'W) and below the Caribbean Sea
northwest of Barranquilla. We have also constructed models of the
regions below the Coastal Cordillera, east of Iquique, below the
Cordillera Occidental, below the Altiplano, below La Paz and below
the Cordillera Oriental. We are at present analyzing by the finite
element method the propagation of Love and Rayleigh waves across

369

these regions.

TABLE 1. MODEL OF IQUIQUE TO A DEPTH OF 220 KM

Layer thickness km	Compressional velocity km/s	Shear velocity km/s	Density g/cm³	Poisson's ratio	Quality factor Q
0.3	3.80	2.28	2.35	0.219	20
1.5	5.50	3.30	2.63	0.219	20
1.8	5.90	3.51	2.68	0.227	20
10.4	6.30	3.74	2.75	0.227	30
6.0	6.80	3.98	2.83	0.240	40
8.8	7.00	4.09	2.86	0.240	60
13.6	7.40	4.27	3.14	0.250	80
9.0	8.20	4.80	3.30	0.240	400
22.6	8.02	4.69	3.35	0.240	400
23.0	8.02	4.69	3.36	0.240	400
23.0	8.02	4.69	3.37	0.240	400
20.0	7.85	4.46	3.38	0.262	80
20.0	7.85	4.46	3.39	0.262	80
20.0	7.85	4.46	3.40	0.262	80
20.0	7.85	4.46	3.41	0.262	80
20.0	7.85	4.46	3.43	0.262	80

TABLE 2. MODEL OF IQUIQUE TRENCH TO A DEPTH OF 220 KM

Layer thickness km	Compressional velocity km/s	Shear velocity km/s	Density g/cm³	Poisson's ratio	Quality factor Q
6.0	1.52	0.001	1.03	0.500	500
1.0	2.15	0.50	1.80	0.471	20
1.0	4.70	2.50	2.50	0.303	40
5.0	6.80	3.80	2.90	0.273	60
20.0	8.20	4.70	3.31	0.255	400
27.0	8.20	4.70	3.33	0.255	400
20.0	7.90	4.34	3.34	0.284	80
20.0	7.90	4.34	3.36	0.284	80
20.0	7.90	4.34	3.37	0.284	80
20.0	7.90	4.34	3.38	0.284	80
20.0	7.90	4.34	3.39	0.284	80
20.0	7.90	4.34	3.40	0.284	80
20.0	7.90	4.34	3.41	0.284	80
20.0	7.90	4.34	3.43	0.284	80

Recommendations and Future Plans

We have recently obtained the Mapa Neotectónico de Venezuela (Beltran, 1993), which includes the faults of much of eastern Columbia and their directions of movement. Also, we have obtained a recent estimation of plate motions and boundaries (Gordon, 1995). The general motion near Cumaná, in eastern Venezuela

Love wave displacement
Depth variation 0.3, 1.5, 5.0, 10.0 s
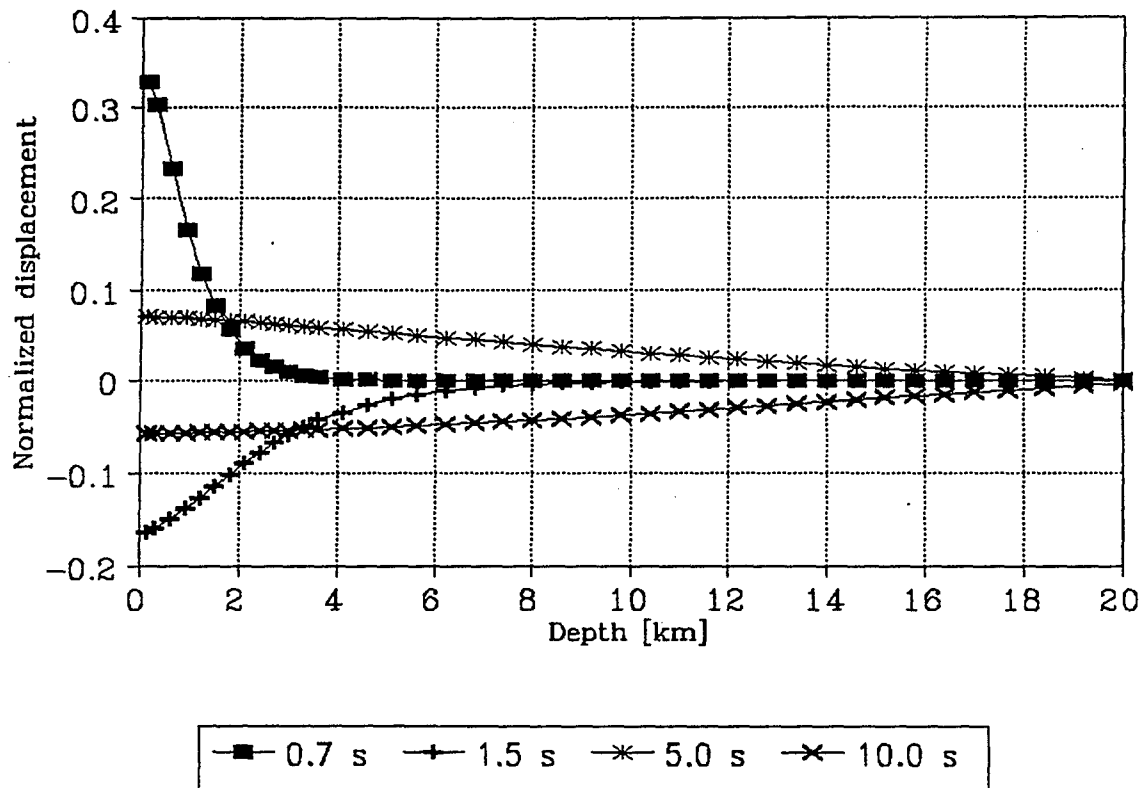
Fig. 3. The normalized variation of displacement with depth of the fundamental Love modes of periods 0.7 s, 1.5 s, 5.0 s and 10.0 s for the model of the structure below Iquique.

(10°28'N, 64°10'W) is clearly right-hand strike-slip, but the right-hand strike-slip motion near Mérida, in western Venezuela (08°36'N, 71°08'W), if we assume approximately rigid Caribe and South American plates, must include a substantial portion of thrust. Bueno and his coworkers (1993) consider the Lake Maracaibo region in western Venezuela to be part of the South American plate. However, it appears that much of Colombia is part of neither the South American plate nor the Caribe plate, but is part of the bloque Andino (Ramírez, 1977; Pennington, 1981). We plan to continue to model by the two-dimensional finite element method the propagation of Love and Rayleigh waves, considering also L_g and R_g phases, across Bolivia, Chile and Colombia. Also, with improved models of these regions, we can consider the more accurate location of events.

References

Alewine, R.W. (1995). Global CTBT monitoring - an overview. In Monitoring a Comprehensive Test Ban Treaty (E. Husebye, Director), NATO Advanced Study Institute, Alvor, Algarve, Portugal (Abstract). Baby, P., B. Guiller, J. Oller, G. Herail, G. Montemurro D.

Zubietta and M. Specht (1993). Structural synthesis of the Bolivian Subandean zone. In Andean Geodynamics (Extended Abstracts), L'Institut Français de Recherche Scientifique pour le Développement en Coopération, Paris.

Beltran, C. (1993). Mapa Neotectónico de Venezuela. Fundación Venezolana de Investigaciones Sismológicas (FUNVISIS), Departamento de Ciencias de la Tierra, Caracas.

Bueno, E., A. Chirinos, J. Pinto and J. Moreno (1993). Structural interpretation of Ceuta Field, Lake Maracaibo, Venezuela. In Andean Geodynamics (Extended Abstracts), L'Institut Français de Recherche Scientifique pour le Développement en Coopération, Paris.

Byerly, P. (1933). Reduction of trace amplitudes. Bulletin of the National Research Council 90, 198-205.

Byerly, P. (1942). Seismology, Prentice-Hall, New York.

Conferencia de Desarme (1994a). Informe del Grupo ad Hoc de Expertos Científicos Encargado de Examinar las Medidas de Cooperación Internacional para Detectar e Identificar Fenómenos Sísmicos al Cómite ad Hoc sobre la Prohibición de los Ensayos Nucleares acerca de la Vigilancia Sismológica Internacional y el Experimento ETGEC-3. CD/1254, Ginebra.

Conferencia de Desarme (1994b). Informe a la Conferencia de Desarme sobre los Trabajos Realizados por el Grupo ad Hoc de Expertos Científicos Encargado de Examinar las Medidas de Cooperación Internacional para Detectar e Identificar Fenómenos Sísmicos. CD/1270, Ginebra.

Dorbath, C., M. Granet, G. Poupinet and C. Martinez (1993). A teleseismic study of the Altiplano and the Eastern Cordillera in northern Bolivia: new constraints on a lithospheric model. J. Geophys. Res. 98, 9825-9844.

Drake, L.A. (1989). Love and Rayleigh waves in irregular structures. In Observatory Seismology (J.J. Litehiser, ed.), University of California Press, Berkeley, pp. 333-346.

Drake, L.A. and B.A. Bolt (1980). Love waves normally incident at a continental boundary. Bull. Seism. Soc. Am. 70, 1103-1123.

Dziewonski, A.M. and Anderson, D.L. (1981). Preliminary Earth reference model. Phys. Earth planet. Interiors 25, 297-356.

Dziewonski, A.M., Hales, A.L. and Lapwood, E.R. (1975). Parametrically simple Earth models consistent with geophysical data. Phys. Earth planet. Interiors 10, 12-48.

Eisenberg, A., D. Comte and M. Pardo (1989). The need for local arrays in mapping the lithosphere. In Observatory Seismology (J.J. Litehiser, ed.), University of California Press, Berkeley, pp. 187-198.

Ewing, W.M., W.S. Jardetzky and F. Press (1957). Elastic Waves in Layered Media, McGraw-Hill, New York.

Flüh, E.R., B. Milkereit, R. Meissner, R.P. Meyer, J.E. Ramírez, J. del C. Quintero and A. Udías (1981). Observaciones de refracción sísmica en el noroeste Colombiano en la latitud 5.5°N. In Investigaciones Geofísicas sobre las Estructuras Océano-Continentales del Occidente Colombiano (J.R. Goberna, ed.), Instituto Geofísico, Universidad Javierana, Bogotá, Colombia, pp. 83-95.

Galitzin, B. (1911). Seismometrische Tabellen: Nachtrag zu der Abhandlung: über ein Neues Aperiodisches Horizontalpendel mit

Instituto Geofísico, Universidad Javierana, Bogotá, Colombia, pp. 83-95.

Galitzin, B. (1911). Seismometrische Tabellen: Nachtrag zu der Abhandlung: über ein Neues Aperiodisches Horizontalpendel mit Galvanometrischer Fernregistrierungen. Comp. Rend. Commission Sismique Permanente, St. Petersburg, 4.

Gordon, R.G. (1995). Present plate motions and plate boundaries. In Global Earth Geophysics: a Handbook of Physical Constants (T.J. Ahrens, ed.), American Geophysical Union Reference Shelf 1, pp. 66-87.

Gutenberg, B. and C.F. Richter (1954). Seismicity of the Earth (2nd ed.), Princeton University Press, New Jersey.

Harjes, H-.P. (1995). Towards a global seismic monitoring system - lessons learned from the Geneva experiments. In Monitoring a Comprehensive Test Ban Treaty (E. Husebye, Director), NATO Advanced Study Institute, Alvor, Algarve, Portugal (Abstract).

Kennett, B.L.N. (1993). The distance dependence of regional phase discriminants. Bull. Seism. Soc. Am. 83, 1155-1166.

Lamb, S., L. Kennan and L. Hoke (1993). Tectonic evolution of the Central Andes since the Cretaceous. In Andean Geodynamics (Extended Abstracts), L'Institut Français de Recherche Scientifique pour le Développement en Coopération, Paris.

Lysmer, J. and L.A. Drake (1972). A finite element method for seismology. In Methods in Computational Physics (B.A. Bolt, ed.), Academic Press, New York, pp. 181-216.

Nuttli, O.W. (1986). Yield estimates of Nevada Test Site explosions obtained from seismic L_g waves. J. Geophys. Res. 91, 2137-2151.

Omarini, R., K. Reutter and T. Bogdanic (1991). Geological development and structures. In Central Andean Transect, Nazca Plate to Chaco Plains: Southeastern Pacific Ocean, Northern Chile and Northern Argentina, Global Geosience Transect 6 (R. Omarini and H.-J. Goetze, eds.), American Geophysical Union, Washington, pp. 5-12.

Pennington (1981). Subduction of the Eastern Panama Basin and seismotectonics of northwestern South America. J. Geophys. Res. 86, 10753-10770.

Press, F. and M. Ewing (1952). Two slow surface waves across North America. Bull. Seism. Soc. Am. 42, 219-228.

Ramírez, J.E. (1977). Panorama geológico y geofísico de Colombia. In La Transición Océano-Continente en el Suroeste de Colombia (J.E. Ramírez and L.T. Aldich, eds), Instituto Geofísico, Universidad Javeriana, Bogotá, pp. 43-46.

Sykes, L.R. (1995). Dealing with decoupled nuclear explosions under a Comprehensive Test Ban Treaty. In Monitoring a Comprehensive Test Ban Treaty (E. Husebye, Director), NATO Advanced Study Institute, Alvor, Algarve, Portugal.

Wigger, P.J., M. Schmitz, M. Araneda, G. Asch, S. Baldzuhn, P. Giese, W.-D. Heinsohn, E. Martínez, E. Ricaldi, P. Roewer and J. Viramonte (1994). Variation in the crustal structure of the southern Central Andes deduced from seismic refraction investigations. In Tectonics of the Southern Central Andes (K.-J. Reutter, E. Scheuber and P.J. Wigger, eds), Springer-Verlag, Berlin, pp. 23-48.

SEISMIC SOURCES AND WAVE PROPAGATION IN 3-D: RADIATION FROM CYLINDRICAL CAVITIES

R. L. Gibson, Jr., M. N. Toksöz, and W. Dong

Earth Resources Laboratory
Department of Earth, Atmospheric, and Planetary Sciences
Massachusetts Institute of Technology, Cambridge, MA 02139

ABSTRACT

We apply the boundary element method (BEM) to study seismic wave radiation from explosions in cylindrical cavities. This approach simulates wave propagation by replacing the boundary between the cavity wall and the surrounding formation by a distribution of fictitious sources that produce the same composite wavefield as the original model. The cavity wall is discretized into elements in the numerical implementation, and the fictitious source amplitudes on each element are determined by solving boundary condition equations. In order to accomplish this, the interactions of all elements must be computed as well as the wavefields radiating from the sources to the receiver positions. A parallel computer implementation of the algorithm is therefore advantageous, since the frequency domain computations are easily parallelized for rapid solution of the problem. We also compute discrete wavenumber synthetic seismograms at regional distances from the cavity source, using an equivalent moment tensor model of the explosion in the cylindrical cavity.

Results for the radiation patterns show that at large aspect ratios (the ratio of cavity length to cavity diameter), the source has a strong variation in signal strength at high frequency. However, at lower frequencies typical of regional wave propagation, the P-wave radiation pattern is more nearly isotropic, and the S-wave amplitude is not so large. In addition, we find the interesting result that the radiation pattern of a large aspect ratio cavity in a transversely isotropic medium can be more like a classical point source than an a similar isotropic example. Incorporation of the cavity source into simulations of regional wave propagation using discrete wavenumber techniques shows that even though the shear wave is relatively weak at the source, it can still lead to the generation of a significant transverse component Lg wave at regional distances.

OBJECTIVE

The primary goal of the work reported in this paper is to examine the influence of source cavity geometry on radiation of seismic waves at regional distances. Specifically, by examining radiation patterns of these sources, we seek to determine whether or not these sources can explain variations in S and P-wave energy observed in field data, and whether or not they can generate significant SH-waves. We therefore simulate the radiation patterns of explosion sources located in cylindrical cavities that model tunnels using the boundary element method (BEM). In addition, we examine the behavior of such sources in representative models of the earth's crust using the discrete wavenumber method and have computed results for these sources in 3-D earth models using finite difference methods. Results from these numerical experiments show that the radiation patterns from explosion sources located in tunnels may not produce significantly strong shear waves. If the rock formations surrounding the borehole are transversely isotropic (axis of symmetry parallel to the cavity axis), the BEM results show that the quasi-shear wave produced in this case can actually be weaker than in the isotropic case. Discrete wavenumber seismograms show that even though the shear wave is somewhat weaker than the compressional wave at the source, it still produces a strong *Lg* wave at regional distances with some amplitude variations as a function of observation azimuth.

RESEARCH ACCOMPLISHED

Introduction

The radiation patterns of seismic sources are very important in utilizing seismic signals to distinguish between nuclear explosions and natural earthquake events. The standard model of the nuclear explosion source, the spherically symmetric pressure field corresponding to a moment tensor model with three equal, mutually perpendicular dipoles, generates only an isotropic compressional wave disturbance. However, any deviation from this ideal configuration can significantly change the radiation pattern of the source. For example, Zhao and Harkrider (1992) show that when the source is located off-center in a spherical cavity it will generate significant shear wave energy. Their work considers a source located in a spherical solid, which is in turn embedded within another infinite solid, representing a fully tamped explosion.

Another way of altering the radiation of the source is to change the shape of the cavity. Glenn et al. (1985, 1986), Rial and Moran (1986) and Glenn and Rial (1987) considered the radiation patterns of sources located in ellipsoidal and cylindrical cavities. Using a combination of analytical and numerical methods, they obtained results suggesting that the P-wave radiation pattern would be strongest perpendicular to the cavity axis and that a strong shear wave would be generated as cavity aspect ratio (ratio of length to diameter) became large. However, Stevens *et al.* (1991) performed non-linear numerical simulations that suggested that at lower frequencies more typical of regional wave propagation, the compressional wave radiation pattern from a cylindrical cavity would be relatively isotropic and only a small S-wave would be generated. More recently, Ben-Menahem and Mikhailov (1995) derived approximate analytic solutions for radiation from cylindrical cavities. In contrast to the results of Stevens *et al.* (1991), they predict a comparatively large S-wave amplitude for low frequencies. Hence, there are significantly different results for cylindrical cavity radiation patterns available in the literature.

We therefore continue this line of investigation by applying the boundary element method

375

(BEM) to simulate the radiation of seismic waves from a cylindrical cavity representing a source located in a vertical shaft or a horizontal tunnel. The BEM is well suited to problems such as this, where the model combines small features (the cavity) with large features (propagation distances on the order of 10 km or more) (Bouchon, 1993; Dong, 1993; Dong et al., 1995; Dong and Toksöz, 1995). After a brief description of this method, we show radiation patterns obtained with the BEM that are similar to those obtained by Stevens et al. (1991). They show a weak variation of P-wave amplitude with direction and a comparatively small shear wave at frequencies characteristic of regional wave propagation. After presenting these results and demonstrating the effects of locating the cavity in a transversely isotropic medium, we consider the effects of such a source in a plane layered model of the earth. The source is applied in a discrete wavenumber code by developing an equivalent moment tensor representation of the source. Synthetic seismograms at regional distances show that the effect of the cavity, though subtle, will generated SH-wave motion and may still be distinguishable in terms of an azimuthal variation in amplitudes.

Method

The BEM has recently been applied to synthesize borehole wave propagation in experimental configurations typical of exploration geophysics applications (Bouchon, 1993; Dong, 1993; Dong et al., 1995; Dong and Toksöz, 1995). One model considered in this earlier work is a semi-infinite borehole, where the seismic source is applied at or near the end of the borehole. A straightforward, logical extension of this approach is to model a cylindrical cavity of finite length, such as the source cavities that might be utilized in testing nuclear devices. Like the exploration simulations, we model the interior of the cavity as an acoustic medium and also assume symmetry about the cavity axis.

The essence of the method is that the effects of the diffracting boundary between the source cavity and the surrounding medium can be reproduced by a discrete set of fictitious secondary sources (Bouchon, 1993). Hence, implementation of the algorithm begins by discretizing the wall, both the cylindrical portion and the flat ends capping the cavity. The magnitudes of the fictitious sources are determined by enforcing boundary conditions at the cavity wall (continuity of radial displacement and stress, vanishing of shear stress). These three boundary conditions are sufficient to determine the sources, since for each element there is a volume injection source radiating energy into the acoustic material in the cavity, and a vertical and radial force generating elastic waves in the rock formation outside the source region. The determination of source magnitudes is accomplished by computing the displacement field generated by each element incident on the other elements using a discrete wavenumber method to evaluate the integrals over horizontal wavenumber. Given the intense computation that must be performed in order to obtain these quantities, it is advantageous to implement the algorithm on a parallel computer. The computations for each frequency are independent, so we assign each processor on an nCUBE-2 computer the work for a different frequency.

In order to solve the resulting matrix of boundary condition equations, we must also specify the initial field generated by the true, primary source. A straightforward model of this field, when there is complete decoupling of the explosion, is to assume that the explosion instantaneously pressurizes the cavity. In computing our frequency domain results, we therefore model the source condition as a step function of constant pressure applied to the cylindrical cavity wall. Earlier versions of this work (Gibson et al., 1994) instead used a volume injection point
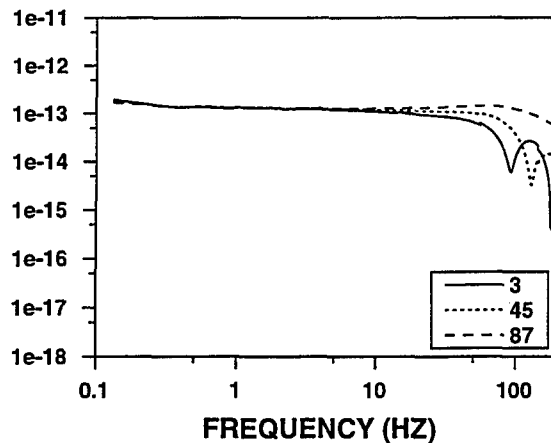
Figure 1: P-wave amplitude spectra of the seismic wavefields radiated by a source in a cylindrical cavity of aspect ratio 5. Spectra are presented for three different propagation directions relative to the cavity axis, where 0° is parallel to the axis. The directions corresponding to 3° and 87° were used instead of 0 and 90° to avoid some numerical problems associated with computations for these directions.

source located on the axis of the cavity. The differences from the results we show below are caused by the different definition of the initial wavefields. Although for relatively small cavity, the incident wavefield generated by the point source will strike the cavity wall essentially simultaneously, the amplitude of the incident field will decay with distance. This change in amplitude alters radiation patterns somewhat and makes the patterns sensitive to the location of the source within the cavity.

Results

Isotropic medium

We applied the BEM to a cavity with aspect ratio 5 located in a medium with a P-wave velocity of 4000 m/s, S-wave velocity 2200 m/s and density 2.2 gm/cm^3. These parameters will show the behavior of the source in a hard rock site. Spectra for observation directions of 3°, 45°, and 87° (0° is along the axis of the cylindrical cavity, 90° is perpendicular to it) show that the corner frequency of the wavefields depends on this direction (Figure 1). Specifically, the corner frequency is higher for observation directions perpendicular to the cavity. These results are similar to those of Glenn et al. (1985, 1986) and Stevens et al. (1991).

However, most of the amplitude difference in these wavefields does occur at high frequencies. To test the effects that might be seen in regional seismograms, we computed radiation patterns at lower frequencies. Radiation patterns of both P and S-waves were obtained by first computing synthetic seismograms for a set of observation points at a constant distance of 10000 m from the source and convolving the frequency domain results with a Ricker wavelet of 1 Hz.

In Figure 2, we show the resulting radiation patterns for cavities 80 m long with varying aspect ratio. In general, the changes in these radiation patterns are relatively subtle, but some variations are evident. As aspect ratio decreases from 5 to values near 1, the amplitude of the

377

ASPECT RATIO 5

ASPECT RATIO 2.5

ASPECT RATIO 1.25
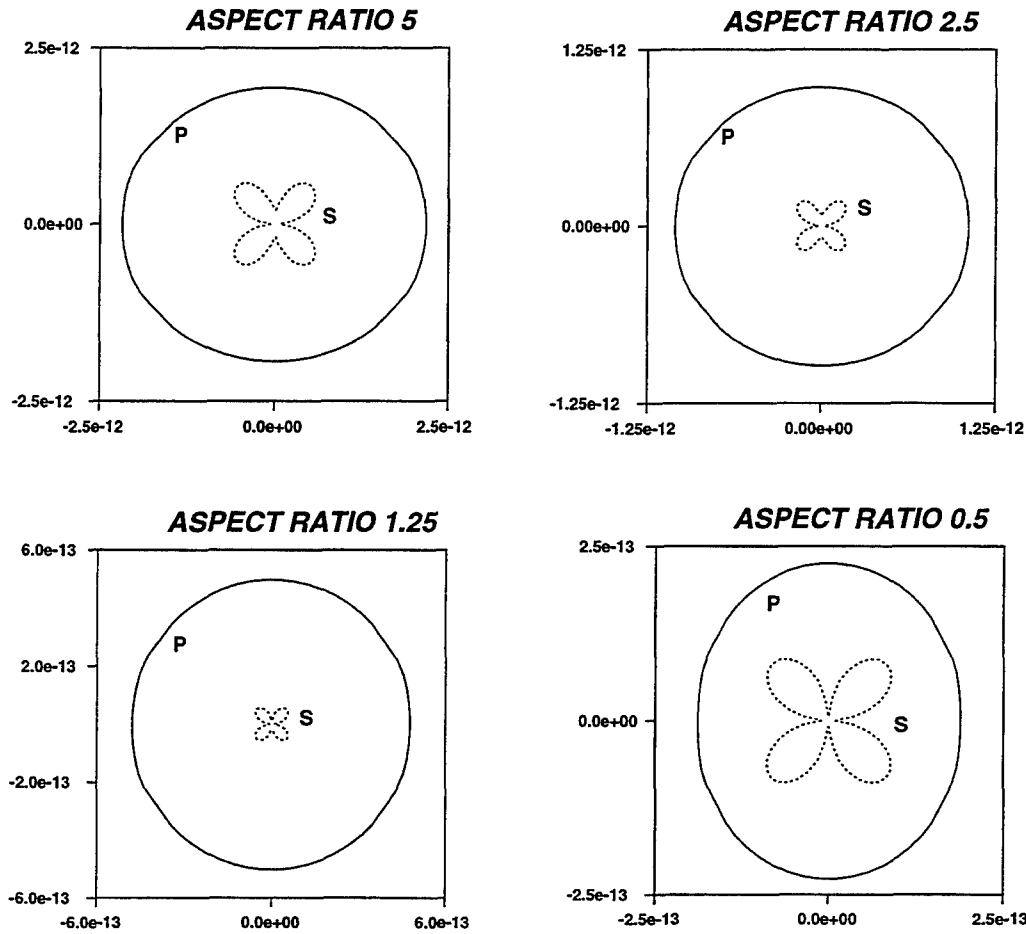
ASPECT RATIO 0.5

Figure 2: Radiation patterns for explosion sources in a hard rock formation (velocities specified in the text). Results are shown for several values of the cavity aspect ratio to demonstrate the effect of variations in cavity shape on far-field seismic wave radiation.

shear wave decreases relative to the compressional wave, and the compressional wave pattern becomes more isotropic. When the aspect ratio is less than one, the shear wave amplitude increases once again. In the end however, the changes suggest that the shear wave amplitude will be less than the P-wave at frequencies representative of regional seismic wave propagation, a conclusion also reached by Stevens *et al.* (1991). Ben-Menahem and Mikhailov (1995), on the other hand, find a much larger S-wave amplitude using an approximate analytic solution that maps the cylindrical cavity surface onto an equivalent spherical cavity. The differences in results may be caused by this mapping for a cylindrical cavity, which is not very sphere-like.

Transversely isotropic formation

The implementation of the BEM simulation assumes axial symmetry of both the cavity model and the wave propagation. A transversely isotropic medium can be incorporated into the modeling as long as the axis of symmetry of the formation is parallel to the axis of symmetry of the cylindrical cavity. An example of this situation would be a medium containing aligned
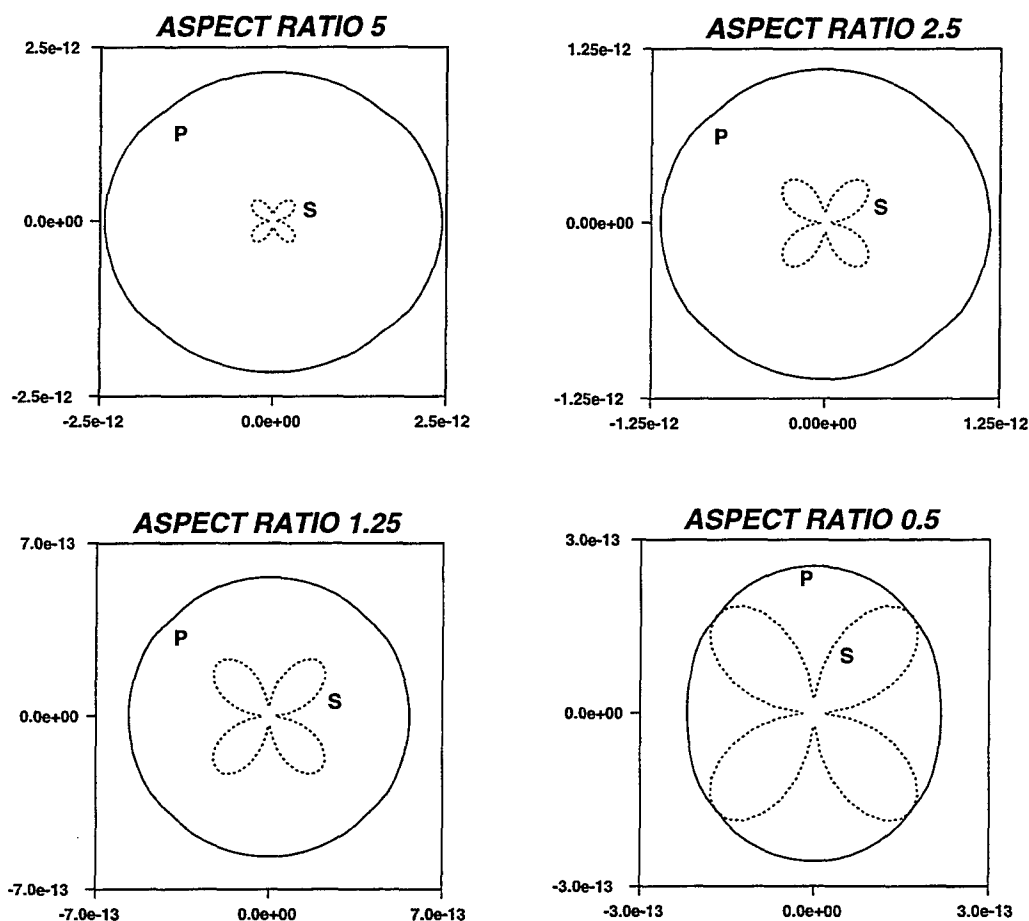
Figure 3: Radiation patterns for explosion sources in a fractured hard rock formation. This medium, with elastic constants shown in Table 1, contains cracks aligned perpendicular to the cavity axis. It is therefore transversely isotropic. At large aspect ratio, the S-wave radiation is weaker than in the isotropic formation (Figure 2).

vertical cracks, a material that is effectively anisotropic with a horizontal axis of symmetry (e.g., Crampin, 1981). If the axis of a tunnel is horizontal and is oriented perpendicular to the vertical cracks in such a transversely isotropic medium, we can model the radiation patterns with the current implementation of the BEM. The elastic moduli of the medium can be computed using the theory of Hudson (1980, 1981). We take the elastic properties of the uncracked rock to be the same as the isotropic formation considered above and set the crack density to $\xi = na^3 = 0.05$ (n=number density of cracks, a=radius of the penny-shaped cracks). We also assume that the cracks are dry (empty). Table 1 displays the elastic constants of both the isotropic material and the composite medium with aligned cracks.

Radiation patterns for the cylindrical cavities in this formation are displayed in Figure 3. The results are somewhat surprising in that the shear waves are somewhat *weaker* than in the isotropic medium for cavities with large aspect ratio. Theoretical results show that a point source in an anisotropic material can have generate a very large shear wave (e.g., Ben-Menahem *et al.*, 1991). Since the ideal point source explosion in an isotropic medium will generate no shear waves at all, this is a dramatic change, and our initial intuition might suggest that shear

waves should also be large for the cavity sources. However, our results show that when the explosion is located in the cylindrical cavity, the shape of the cavity alters the effective moment tensor corresponding to the source in such a way that the resulting wave field resembles the classic isotropic explosion more than the cylindrical cavity source in an isotropic medium!

Regional synthetic seismograms

Although the radiation patterns show that the amplitude of the shear wave is not too large (Figures 2, 3), the effects of these sources at regional distances is not necessarily obvious. In order to more directly predict the effects of such source within layered models of the crust, we computed discrete wavenumber synthetic seismograms (e.g., Bouchon, 1982). The layer thickness and velocities are shown in Table 2. The receivers were located on the free surface at a distance of 500 km from the explosion source, and the full range of azimuths was considered to see how displacement fields would depend on propagation direction relative to the cavity axis. The explosion source itself was incorporated within the modeling by estimating the moment tensor producing the radiation pattern for the aspect ratio 5 cavity in Figure 2 (tests show that the moment tensor representation does not depend too much on the velocity outside the cavity).

The seismograms show that the vertical component seismograms do not change much with azimuth, and they look essentially the same as the seismograms computed for an explosion point source. However, unlike the classical explosion model, this cylindrical cavity source does generate SH-wave energy that has a strong azimuthal amplitude variation (Figure 4). Hence, even though the S-wave is not too strong at the source, the development of the *Lg* wavetrain is still efficient enough that the cavity shape has a detectable influence at regional distances. We have also computed 3-D finite difference synthetic seismograms for an earth model essentially the same as the one described in Table 2, except with a randomly irregular Moho. In this case, the effect of the cavity shape still is more effective in generated a transverse component signal than is the Moho roughness.

CONCLUSIONS AND RECOMMENDATIONS

The BEM provides a useful means of simulating the seismic wavefields generated by explosion sources in cylindrical cavities. Unlike the finite difference method, which requires a discretization of the entire earth model, an implementation of the BEM requires only that the boundary and the cavity be divided into elements, allowing an efficient simulation of the elastic waves at large distances from the source cavity. Results for cavities in a hard rock situation show that though there are significant variations in amplitudes of P-waves at very high frequencies (e.g., 150 Hz), at frequencies more typical of regional wave propagation, only a modest change in amplitude is predicted. Likewise, only a relatively small shear wave is predicted. An explosion source located in a cylindrical cavity in a transversely isotropic formation can have shear wave amplitudes even lower than in similar isotropic media. Incorporation of these explosion sources into discrete wavenumber models of regional propagation suggest that there still will be some azimuthal variation of *Lg* wave amplitude depending on propagation direction relative to the cavity axis (when the cavity is horizontal).

Future work should include further testing of these theoretical predictions against observed field data. The best scenario would be tests against data collected where a source cavity
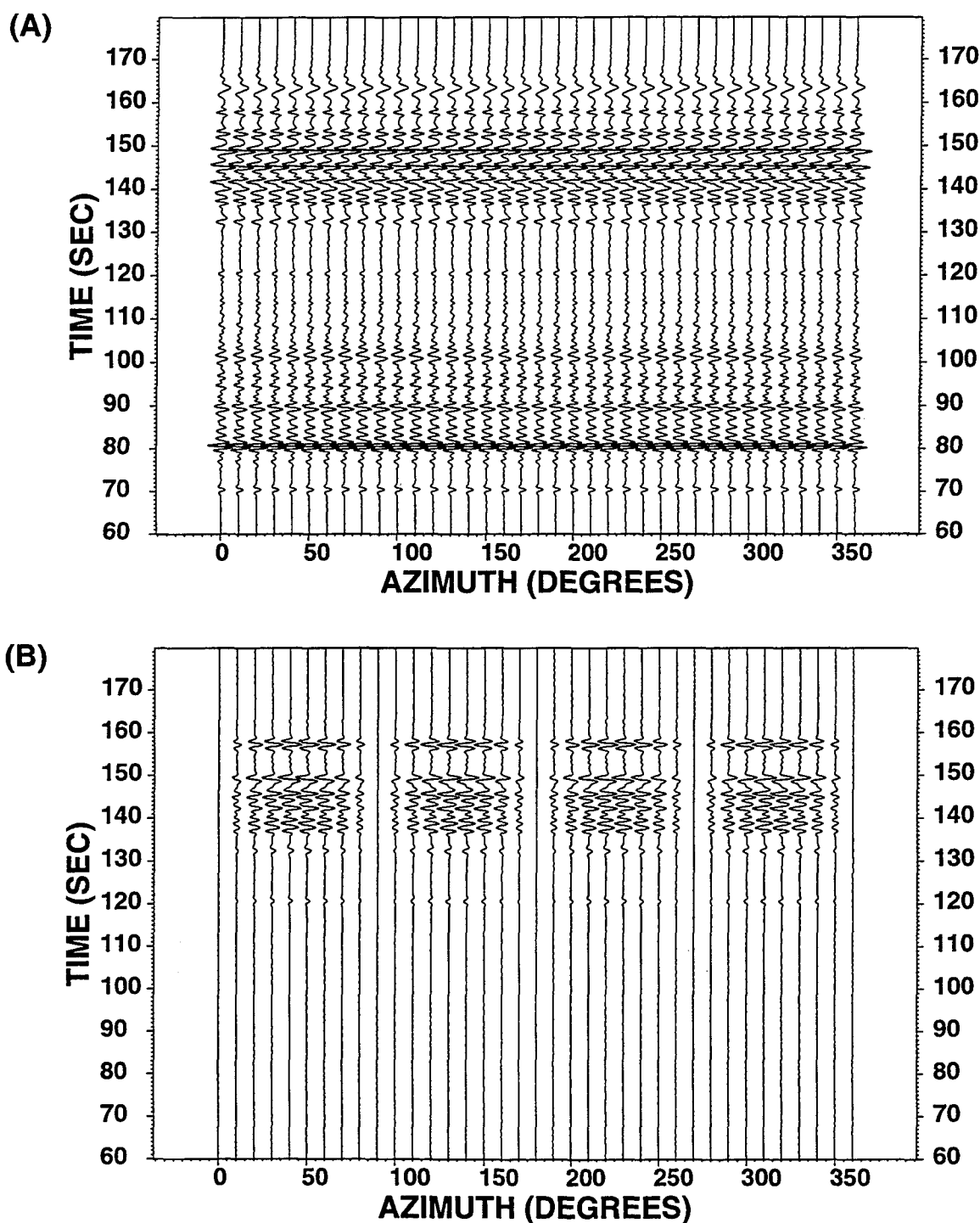
Figure 4: Synthetic seismograms computed for the earth model described in Table 2. Receivers were located at a constant offset of 500 km and cover the full range of azimuth to show the effect of a source located in a cylindrical cavity on regional wave propagation. Both component plots have the same plotting gain applied for direct comparison of amplitudes. The cavity axis direction corresponds to 0°. (A) Vertical component. (B) Transverse component.

orientation and approximate shape is known, as well as the location of the source within the cavity. Another valuable task is further consideration of simulations where we include equivalent moment tensors in simulation of regional wave propagation in order to explore the effects of the explosion sources on such features as *Lg* wave amplitude. The overall goal is to better develop our understanding of near source effects in order to better understand the influence on regional seismic wave propagation.

REFERENCES

Ben-Menahem, A., R.L. Gibson, Jr. and A.G. Sena, 1991. Green's tensor and radiation patterns of point sources in general anisotropic inhomogeneous elastic media, *Geophys. J. Int. 107*, 297–308.

Ben-Menahem, A. and Mikhailov, O., 1995. Multipole radiation of seismic waves from explosions in nonspherical cavities and its application to signal identification, *J. Acoust. Soc. Amer.*, *97*, 2675–2698.

Bouchon, M., 1982. The complete synthesis of seismic crustal phases at regional distances, *J. Geophys. Res.*, **82**, 1735–1741.

Bouchon, M., 1993. A numerical simulation of the acoustic and elastic wavefields radiated by a source in a fluid-filled borehole embedded in a layered medium, *Geophysics, 58*, 475–481.

Crampin, S., 1981. A review of wave motion in anisotropic and cracked elastic-media, *Wave Motion, 3*, 343–391.

Dong, W., 1993. Elastic wave radiation from borehole seismic sources in anisotropic media, Ph.D. thesis, Massachusetts Institute of Technology.

Dong, W., M. Bouchon, and M. N., Toksöz, 1995. Borehole seismic source radiation in layered isotropic and anisotropic media: boundary element modeling, *Geophysics, 60*, 735–747.

Dong, W., and M. N., Toksöz, 1995. Borehole seismic source radiation in layered isotropic and anisotropic media: real data analysis, *Geophysics, 60*, 748–757.

Gibson, Jr., R.L., M.N. Toksöz, and W. Dong, 1994. Radiation from seismic sources in cylindrical cavities, *in* J.J. Cipar, J.F. Lewkowicz, and J.M. McPhetres, Proceedings of the 16th Annual Seismic Research Symposium, PL-TR-94-2217, Phillips Laboratory, Hanscom AFB, Massachusetts. ADA284667

Glenn, L. A., A. J. C. Ladd, B. Moran and K. A. Wilson, 1985. Elastic radiation from explosively-loaded ellipsoidal cavities in an unbounded medium, *Geophys. J. R. astr. Soc., 81*, 231-241.

Glenn, L.A., B. Moran, A.J.C. Ladd, K. Wilson, J.A. Rial, 1986. Elastic radiation from explosively-loaded axisymmetric cavities, *Geophys. J. R. astr. Soc.,, 86*, 119–136.

Glenn, L.A. and J.A. Rial, 1987. Blast wave effects on decoupling with axisymmetric cavities, *Geophys. J.R. astr. Soc.* **91**, 229–239.

Hudson, J.A., 1980. Overall properties of a cracked solid, *Math. Proc. Camb. Phil. Soc.* **88**, 371–384.

Hudson, J.A., 1981. Wave speeds and attenuation of elastic waves in material containing cracks, *Geophys. J. R. astr. Soc.* **64**, 133–150.

Rial, J. A. and B. Moran, 1986. Radiation patterns for explosively-loaded axisymmetric cavities in an elastic medium: analytic approximations and numerical results, *Geophys. J. R. astr. Soc., 86*, 855-862.

Stevens, J.L., N Rimer., J. Murphy, T.G. Barker, E. Bailey, E.J. Halda, W.J. Proffer, S.H.

Rogers and B. Shkoller, 1991. Simulation of seismic signals from partially coupled nuclear explosions in spherical and ellipsoidal cavities, MAXWELL S-CUBED Division, SSS-FR-91-12735, Final Report on Contract No. 90-N3039000-000.

Zhao, L., and Harkrider, D.G., 1992. Wavefields from an off-center explosion in an embedded solid sphere, *Bull. Seis. Soc. Amer.*, *82*, 1927–1955.

Parameter	Background Value (GPa)	Perturbed Value (GPa)
C_{11}	35.2 GPa	33.8 GPa
C_{33}	35.2	26.0
C_{13}	13.9	10.3
C_{44}	10.6	9.53
C_{66}	10.6	10.6
ρ	2.2 g/cm^3	2.2

Table 1: Elastic constants for the background medium and a medium with aligned cracks computed using the theory of Hudson (1980, 1981). The background parameters correspond to P and S-wave velocities of 4000 m/s and 2200 m/s, respectively, and the perturbed values were obtained using a crack density of 0.05.

Layer thickness	V_p	V_s	Density
1 km	5.3 km/sec	3.1 km/sec	2.4 g/cm^3
12	6.1	3.5	2.6
22	6.6	3.8	2.7
(half space)	8.1	4.7	2.8

Table 2: Crustal velocity model used to compute the synthetic seismograms in Figure 4.

HIGH FREQUENCY S-WAVE SCALING TO 500 KM

R. B. Herrmann
Department of Earth and Atmospheric Sciences
Saint Louis University
Email: rbh@eas.slu.edu
TEL: 314/977-3131, FAX: 314/977-3117

ABSTRACT

A systematic effort at understanding high frequency ground motion of regional S and Lg phases is undertaken to develop stable, transportable methods for regional magnitude scale calibration. Aspects of the study are as follow:

a) an evaluation of the limitations of the coda normalization technique as a robust method of reducing effects of unknown source and site and instrument effects in determining the distance dependence of peak ground motion with distance,

b) the simultaneous determination of source, site and distance function,

c) an evaluation of the relation between the coda Q parameter and the frequency dependent peak motion distance function,

d) empirical determination of the relation between coda excitation and peak motion excitation, and

e) an attempt at modeling observations of peak motions in terms of wave propagation in crustal models, with the corresponding determination of the necessary detail of those models.

The results of studying ground motion in the 1 - 16 Hz frequency band in the New Madrid region of the central, and the Southern Great Basin regions of the United States show that significant regionally dependent crustal structure control of the distance dependence occurs in the 0-200 km range. Since this will affect the quantification of source properties from distant observations, one must worry about more than variations in average crustal Q. Crustal and upper mantle structure are also very important. Data processing of other data sets is beginning since the necessary software has been validated.

OBJECTIVE

This study addresses the problem of defining the scaling of high frequency S-wave ground motion with distance by using recordings of regional earthquakes and explosions. The methodology assumes as little as possible about the underlying functional form of the distance dependence because such assumptions may mask important, but unappreciated, affects of local earth structure.

The overall purpose of the study is to develop a methodology for defining a transportable seismic source size estimator for regional phases.

RESEARCH ACCOMPLISHED

In a region of low level seismicity, there is always a question of the scaling of ground motion with distance in order to correctly assign a magnitude to an event or to define proper ground motion levels for earthquake resistant design. In addition to low levels of observed ground motion, the task may be complicated by the lack of proper instrument calibration and unknown site effects. So how can one address unknown source, site and instrument effects?

Source - Site - Distance Separation

Peak ground motion of the S wave may be modeled as the separable effects of source, site and propagation

$$a(r,f) = Src_S(f)\,Site_S(f)\,d(r,f)$$

or after applying logarithms

$$PEAK = SRC_S(f) + SITE_S(f) + D(r,f)$$

For a large data set such that a) each site observes earthquakes at many distances, and b) all sites do not share a common character, separability works. In order to use the technique, constraints must be applied, e.g., forcing $D(r,f) = 0$ at some reference distance, and constraining some or all site terms, often by $\sum SITE_i = 0$. This last condition forces common site effects into all source terms.

If the data are not sufficient for this separation, then a coda normalization technique introduced by Aki (980) and used by Frankel *et al.* (1990) can be applied to obtain a first order estimate of D(r,f). The coda can be described by an rms (root mean square) function of lapse time as a function of source and site terms and a shape function depending upon the scattering environment. In the logarithmic domain, the separation of a bandpass filtered signal becomes:

$$RMS(f,t) = SRC_C(f) + SITE_C(f) + CODA(f,t)$$

If we assume that $SRC_C = a_1 SRC_S$ and $SITE_C = a_2 SITE_S$, then

$$D(r,f) = PEAK - RMS(f,t_{ref}) - CODA(f,t_{ref}) + K.$$

is a first order estimator of the $D(r,f)$ function if the assumptions are valid.

There are some important considerations based on recent work to keep in mind:
• It is now recognized (Atkinson and Boore, 1995) that actual ground motion scaling

in the 70 - 150 km range is not simple, because of changes in signal duration and amplitude due to S waves supercritically reflected at the crust mantle interface.

• Site effects can be very large and very significant. A recent study by Boore, Joyner and Fumal (1994) demonstrates a very strong correlation between observed peak ground motions and shallow S-wave velocity (30 m).

Data Processing

The data used are from regional seismic networks in the New Madrid and Southern Great Basin regions of the central and western United States, respectively. The are from similar 1-Hz seismometers digitized at 100 Hz using a 12-bit A/D. All observed data are deconvolved to yield vertical component ground velocity in the 0.5 - 30 Hz band. Next each observed trace is passed through band pass filters composed of a cascade of an 8 pole low pass and an 8 pole high pass Butterworth filter with respective corner frequencies of 1.414 f_n and 0.707 f_n, where the f_n are 1, 2, 3, 4, 6, 8, 10, 12, 14 and 16 Hz. For each filtered trace, the peak value is noted, and an RMS trace is computed using overlapping 5 second windows. In addition each RMS value has a flag indicating whether the value is prior to P, between P and S, after S, and into the coda (defined as twice the S wave travel time). The signal duration is estimated, and random process theory estimates of peak amplitudes are made.

Following this, the coda shape function, $CODA(f, t)$, is determined. Next and initial estimate of $D(r)$ is made, which is followed by an iterative regression for source, site and improved distance terms. The functional dependence of $CODA(f, t)$ and $D(r, f)$ is assumed to be piecewise linear, with a 2nd derivative smoothing constraint. For $D(r, f)$ distance nodes in the interpolation function are placed at 10, 15, 20, 30, 40, 50, 75, 90, 105, 120, 135, 150, 175, 200, 250, 300, 400 and 500 km. The time nodes for $CODA(f, t)$ are placed at 10, 20, 30, 40, 55, 70, 85, 105, 125, 145, 175, 210, 250, 290, and 330 seconds. Constraints that $D(40, f) = 0$, $CODA(f, 10)$, $\sum SITE_S = 0$ and $\sum SITE_C = 0$ are applied.

Figure 1 shows the empirically determined coda shape for 2 Hz filtered data for the Southern Great Basin. Figure 2 shows the peak amplitude data for the same frequency. The coda normalization technique, top panel, yields a good estimate of the $D(r, f)$ term, which is very obvious at higher frequencies, which have fewer observations.

Figure 3 compares the $D(r, f)$ functions for the Southern Great Basin and New Madrid. Interpretation of the frequency dependence of each figure in terms of Q is not simple because of lack of knowledge of the underlying geometrical spreading function. However, regional differences are obvious in the levels of high frequency ground motion at large distances. In addition there appear to be differences in the ground motions in the 70 - 200 km, which are due to supercritical arrivals from the Moho and upper mantle.

The distance scaling for New Madrid differs significantly from a current model proposed for Eastern North America (Atkinson and Boore, 1995) at distances greater than 150 km. The New Madrid data requires a flattening of low frequency motion beyond this distance to 250 km whereas their model does not. This can only be understood in terms of differences in earth structure affecting the Lg. Figure 4 shows the an model, *modl.ham*, resulting from a waveform inversion of a broadband
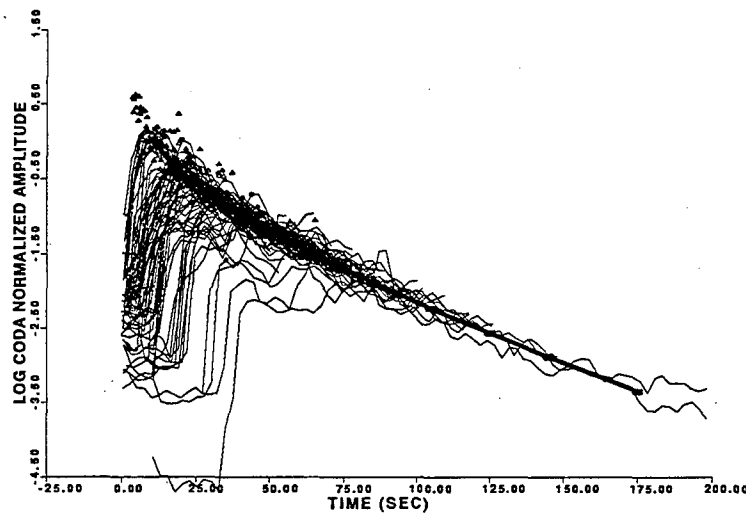
Fig. 1. Signal envelopes for 2 Hz filtered data. The shades of gray indicate signal prior to P, used for noise level, signal between P and S, signal between S and twice the travel time, and finally the signal in the stable coda. The heavy line is the coda shape function used in the coda normalization technique. The smaller symbols indicate the largest value of the RMS envelope, as well as the adjusted peak motion.

signal 175 km from a magnitude 4.4 Missouri earthquake of September 26, 1990. This earth model was required to align the high frequency S-arrivals in time, and also to improve the agreement in peak amplitudes. The waveform match requires a positive gradient in the upper mantle shear-wave velocity, which may be the explanation for larger high frequency amplitudes in the New Madrid region at this distance.
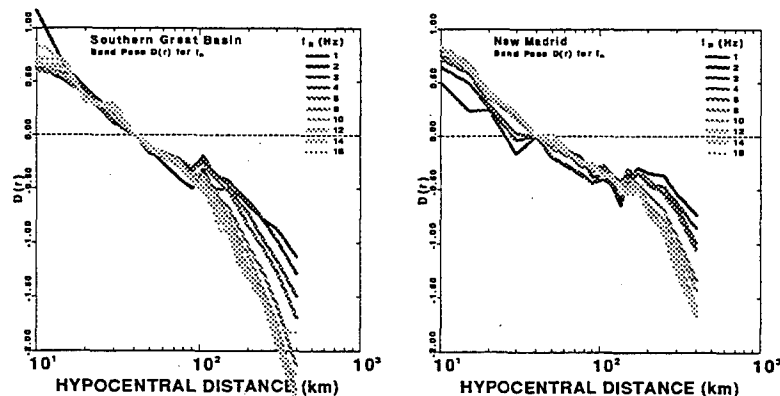
Fig. 3. Comparison of the empirically determined $D(r, f)$ terms for Southern Great Basin and New Madrid.

References

Aki, K. (1980). Attenuation of shear waves in the lithosphere for frequencies from 0.05 to 25 Hz, *Phys. Earth Planet. Inter.* **21**, 50-60.
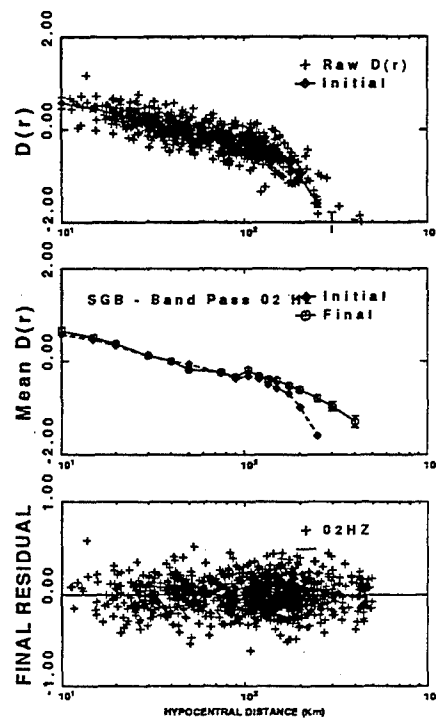
Fig. 2. Peak amplitudes and D(r,f). Bottom part. Residuals following the source, site and distance regression. The purpose is to demonstrate the independence of residual distribution with distance. Center panel, final distance dependence term (light gray) compared to initial estimate using coda normalization (darker with diamonds). Top panel, raw data of peak amplitude after coda normalization, together with the least square first estimate of D(r), shown more clearly in the center panel. Because of limited data lengths, the coda normalization could not be applied at large distances. The peak amplitude data filled in the large distance information.

Atkinson, G. M., and D. M. Boore (1995). Ground-motion relations for eastern North America, *Bull. Seism. Soc. Am.* **85,** 17-30.

Boore, D. M., W. B. Joyner, and T. E. Fumal (1994). Estimation of response spectra and peak accelerations from western North American earthquakes: An interim report Part 2., *U. S. Geological Survey Open-File Report 94-127,* 40 pp.

Frankel, A., A. McGarr, J. Bicknell, J. Mori, L. Seeber and E. Cranswick (1990). Attenuation of high-frequency shear waves in the crust: measurements from New York state, South Africa, and southern California, *J. Geophys. Res.* **95,** 17,441-17,457.

RECOMMENDATIONS AND FUTURE PLANS

A processing methodology has been developed for examining high frequency ground motions. The coda normalization technique is very useful. Initial data sets indicate the need for detailed knowledge of the crust-mantle transition to understand high-frequency shear-wave ground motion.

Future work will consider other regions, and will attempt to explain observations by combining high frequency ray theory, Q and random process theory. It is assumed that the velocity structure required to understand amplitude versus distance must be more detailed than that used for location.

Wavefield synthetics in 3D and fully automatic event locations

Eystein S. Husebye and Bent O. Ruud
Institute of Solid Earth Physics, University of Bergen, Norway

Abstract

The research under this contract have mainly been along two directions: **(1)** three-dimensional (3D) finite difference (FD) modeling of scattering from free surface topography, and **(2)** near real time event location using only seismogram envelopes from local networks. In **(1)** we have simulated scattering from teleseismic P-waves using a plan vertical incident P-wave and real topography from a 40 × 40 km area centered at the NORESS array in south-eastern Norway. Snapshots and synthetic seismograms of the wavefield show clear conversion from P to R_g (short period fundamental mode Rayleigh) waves in an area of rough topography approximately 10 km east of NORESS. This result is consistent with numerous observations.

In **(2)** a new method is described for automatic epicenter locations in near real time using short period z-component data from local seismograph networks. The original waveform data is bandpass filtered, 'STA envelope' parameterized and then resampled at a rate of 2 Hz. The physical principle invoked for epicenter determinations is that of constructing the space-time image of a source in the gridded network area on the basis of P- and S-wavelet intensities. Since such intensities for a stratified half space is almost model independent we did not bother to use local travel time tables nor crustal models. The latter information is naturally needed for precise origin time estimates. The method is robust because and to our surprise, P- and S-intensities (low frequency wavelets) vary smoothly (1D) with distances at least out to 700 km. Compared to conventional event location approaches, we bypassed tasks like signal detection, phase identification and phase association - in essence we aim for joint *event* detection and location. The method has been very convincingly tested on Italian, German and Norwegian network data off-line but has not been adapted to a real time operational environment nor attempted extended to teleseismic recordings. In the former case we see no principal problems and besides computational requirements can be handled by a PC machine. The essence of our automatic epicenter location scheme is the potential for fast (3-4 min), effective and low-cost exploitation of CTBT relevant monitoring information from the very many local networks deployed in most continental areas. In the future we foresee that local network Hubs may inform the IDC of a CTBT treaty about incoming P-waves at teleseismic located stations and arrays from specific sources at given locations. Also, the ever increasing use of Internet for seismic data exchange may at least partly move CTBT seismic monitoring into the seismological community sphere and perhaps partly into the public domain.
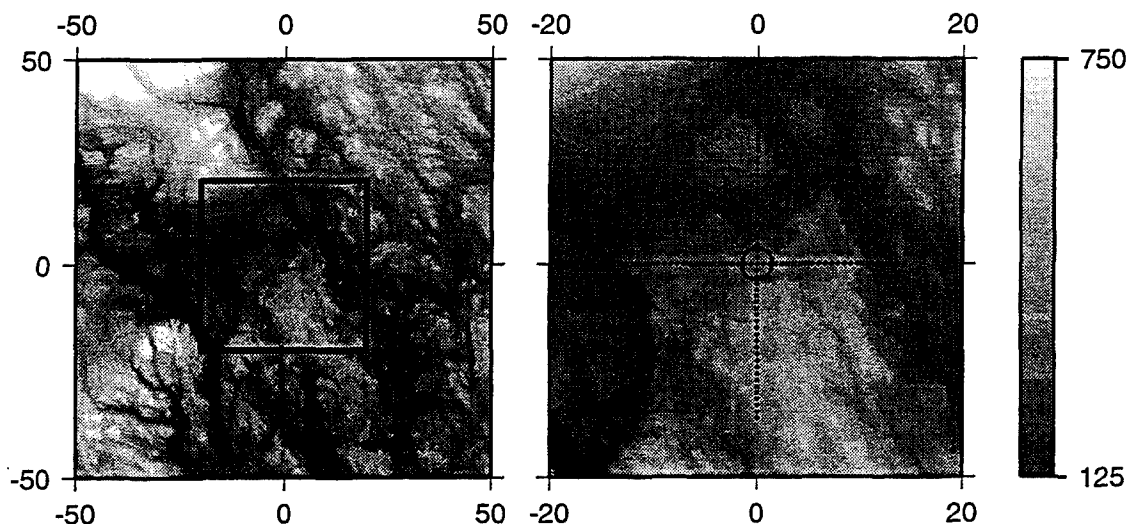
Figure 1: Leftmost section shows the topography in an 100 × 100 km area centered at the NORESS array. The innermost 40 × 40 km was used in the modeling experiment. The dotted lines shows the positions of the receivers in the two profiles and the circle outlines the NORESS array. Labels are in kilometers and elevations are in meters above mean sea level. The black area is Lake Mjøsa (123 m above sea level).

1 Objective

The main goal of the basic seismological research performed under this contract is to improve our understanding of wave propagation and scattering phenomena for local and regional distance travel paths. The tool used here is numerical simulations through the very general and powerful, but computationally demanding, finite difference technique.

Another research goal is aimed at exploiting the information potential of local network recordings in the context of CTBT monitoring. the first step here is the development of a fast, cost-efficient method for automatic event locations using such network data. To ensure robustness, conventional analysis tasks like signal detection, phase identification and association were avoided.

2 Basic research results (B.O.Ruud and S.Hestholm)

2.1 3D FD modeling of scattering from topographic relief

The scattering of teleseismic P wave energy into R_g have been extensively studied and documented using data from the NORESS array in south-eastern Norway (Bannister et al, 1990; Gupta et al, 1993; Hedlin et al, 1991, 1994). For our 3D FD modeling experiments we have obtained digital elevation data for an area of 100 × 100 km centered on the NORESS array (Fig. 1). Due to the huge computer memory requirements of 3D FD methods, we have so far been restricted to a model of size 40 × 40 × 35 km with 0.2 km sampling.

390
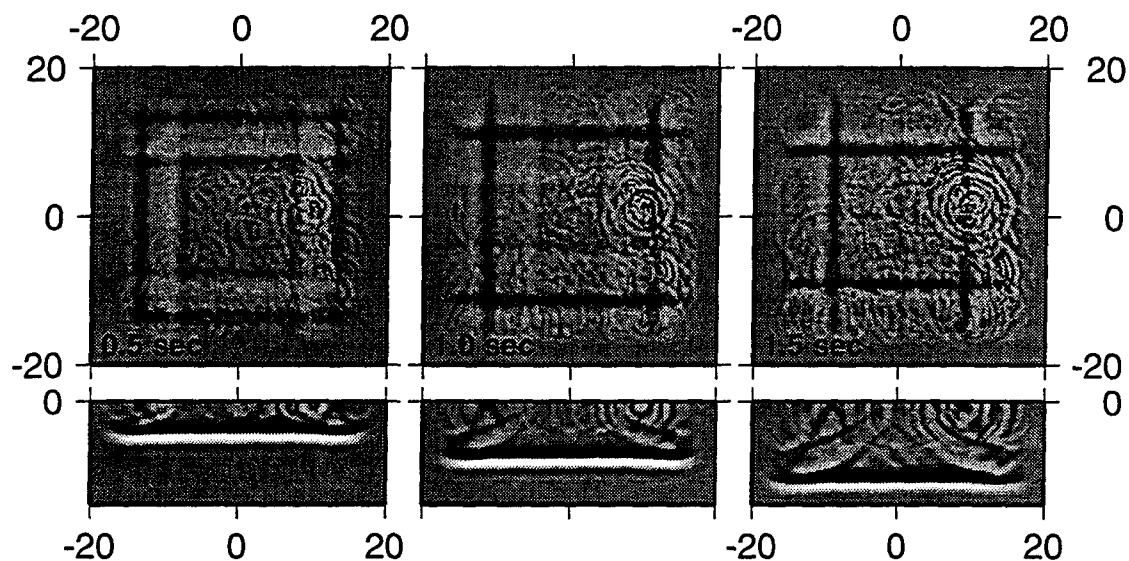
Figure 2: Snapshots of the vertical component of the particle velocity. The upper snapshots are horizontal sections at the free surface and the lower snapshots are vertical sections along a west-east profile through the center of the model. The time in the lower left corner of each horizontal section is the time from when the plane vertical incident P-wave was reflected from the surface. The straight wavefronts parallel to the model boundaries are artificial reflections from the absorbing boundaries. These artificial reflections are seen also in the vertical sections. Note the strong scattering source located at Bronkeberget (2 km N, 10 km E) which is also highly prominent in real record analysis (Bannister et al, 1990).

The method used to implement free surface topography in the 3D FD code is an extension of the 2D method described by Hestholm and Ruud (1994). In all the examples shown here the incoming wave is a vertical incident plane P-wave simulating a teleseismic short period P-phase. The center frequency of the Ricker wavelet is 2.5 Hz, the P-wave velocity of the homogeneous medium is 6.0 km/s and the Poisson's ratio is 0.25. The absorbing boundary condition used along the sides and bottom of the model is the so called 'exponential damping' technique.

The main problem encountered in our test runs was instabilities which started near the surface in areas of steep and rough topography. The instabilities appear as surface waves of exponentially increasing energy which slowly propagate out from the starting points. The first modeling attempt with unsmoothed real topography gave very unstable results (infinite amplitude) within a second after the wave front reached the surface. In our next attempt the elevations were first multiplied by 0.5 in order to reduce the topography. The results were stable and this is also consistent with previous 2D FD modeling results. Also in the latter case an west-east profile running through NORESS was unstable with real topography but stable with half elevations. Snapshots of the wavefield (vertical component of the particle velocity) are shown in Fig. 2. A dominant feature of the snapshots is the low-frequency/long-wavelength artificial reflections from the absorbing boundaries. Although the exponential damping technique is the most efficient absorbing boundary method we have tested, the case of an wave incident at an angle of 90° with the boundary is the most difficult one. Fortunately, the artificial reflections are frequency dependent, with longer wavelengths than most of the surface waves scattered by the topography, and can therefore be
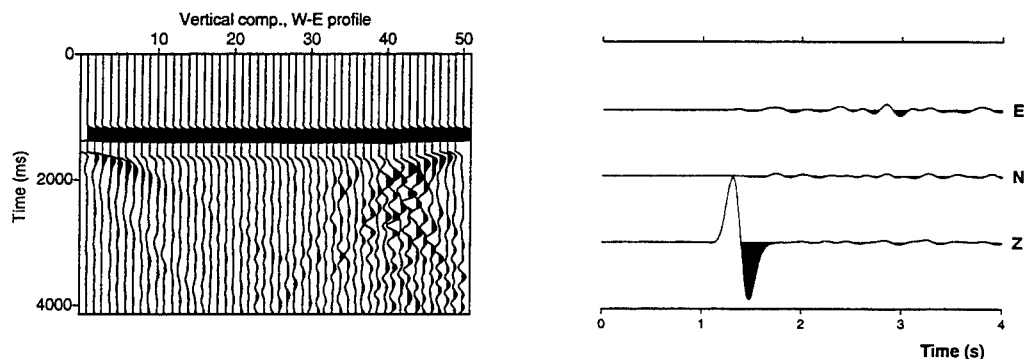
Figure 3: Seismograms extracted at the free surface of the model. Left section shows the vertical component of the particle velocity along a 30 km long west-east profile through the center of the model. The right section shows 3-component seismograms from a receiver 3.6 km east of the center.

removed by filtering and image processing techniques. As seen from Fig. 2 the scattered surface waves appear to radiate out from secondary point sources which coincide with areas of high topographic gradients (Fig. 1). The dominant scattering points are along the steep valley side east of 'Bronkeberget' about 10 km east of NORESS (Bannister at al., 1990). Also in seismograms from the west-east profile the P-to-R_g scattering from this area is clearly seen (Fig. 3).

2.2 Recommendations and future plans - 3D FD synthetics

Even for small scale experiments 3D FD synthetic wavefield analysis provide, as demonstrated here, improved insight and a better understanding of surface scattering phenomenon. We find it particularly gratifying that the strong P-to-R_g scattering from the Bronkeberget hill, observed by Bannister et al. (1990) through analysis of NORESS recordings, can be realistically synthesized. Another interesting feature is that for certain spatial low-frequency variants of the local NORESS topography the R_g wave propagation seems to change abruptly over relatively small distances. Probably, this is due to strong directionality dependence of the scattering from some topographic features. Such wavefield characteristics are sometimes observed in NORESS and GERESS recordings – at some sensors the R_g-phase is prominent while hardly visible at nearby sensors less than a kilometer away. In other words, also small scale crustal features may contribute to blocking effects as often observed for R_g- and L_g-phases. Many of such wave field phenomena are out of range for 2D FD synthetic experiments hence our emphasize on continuous research efforts on 3D synthetic simulation of crustal wave field propagation.

Recently, we have modified the code to run on parallel computers and we are now in the testing stage. Future directions of our research will be to increase the model size to also include the scattering areas SE of Lake Mjøsa. Furthermore, in order to compare directly with NORESS recordings it is necessary to allow for non-vertical incident waves and to use source time functions derived from teleseismic P beams. Although the physical dimensions of 3D models still will be quite small compared with 2D FD models, the use of parallel computer technology opens new avenues to study of 3D scattering phenomena in fields like random media and corrugated interface scattering.

3 Automatic event location using local network data

(G.A. Ryzhikov, M.S. Biryulina and E.S. Husebye)

As a preamble to deciding on a local event location strategy we attempted to formulate sort of 'boundary conditions' for approach. Firstly, to tie the analysis to the parameterized waveforms make sense also scientifically because signal waveforms are dissimilar for station separations exceeding a few kilometers. Likewise, an approach in principle similar to conventional ones including signal detection, phase identification and phase association was rated unattractive because corresponding parameters extraction in an automatic mode is unlikely to be robust (Ruud et al, 1993). Finally, for local events there is no need to ignore a priori information embedded in the event records namely the presence of the two P- and S-wave modes and with the latter being relatively energetic. Incorporating amplitude information would naturally reduce the severity of the phase association problem due to fast signal amplitude decay with epicenter distance.

From the above considerations, we formulated the following epicenter location strategy:

1. Analysis restricted to parameterized waveform data say tied to rms or to the STA detector parameter definition (sampling rate 0.5-1.0 sec)

2. Extraction of 1D (distance dependence only) signal attributes to ensure robustness of analysis.

3. A grid search approach giving an option for including a priori information in on-line analysis.

4. Epicenter location criteria based in minimizing differences between observed and expected seismic signal attribute features.

5. 'Expected' attributes to be anchored in seismic wave propagation theory.

3.1 Theory - event localization strategy realization

Out of the various task listed above, that of transforming the original waveforms or parameterized waveform records in such a manner that distinct signal attributes could be extracted reliably, proved difficult to realize in practise. In particular the increasing scattering contribution to the observed wavefield with time tend to obscure distinct signal features for larger ($\Delta > 300$ km) epicenter distances. With the failure of our empirical experiments in minimizing distinct signal attributes, we examined many works on wave propagation in stratified media for a clue to this problem (e.g., see Brekhovskikh 1960, Aki and Richards 1981, Kennett 1983, Flatte et al, 1979). On this, presumably adequate theoretical basis, we proceeded in a manner reminiscent of Chap.3 and 4 in the Aki and Richards book. In other words, the starting point being the far field displacement for a time-space distributed source in an inhomogeneous media expressible as:

$$\varphi_i(\mathbf{x}, t) = G_{ij}(\mathbf{x}, \mathbf{x}'; t - \tau)s_i(\mathbf{x}', t) \tag{1}$$

where φ_i is the ith displacement component at location $\mathbf{x}$ ($\mathbf{x} = \{x_1, x_2, x_3\} \stackrel{\text{def}}{=} \{\mathbf{r}, z\}$), $\mathbf{r}$ being the free surface location and z is depth) and time t; G_{ij} is the Green operator (tensor function) and s_i is the body force equivalent at position $\mathbf{x}'$ and time τ. The Green function is complicated, depending essentially on an infinite number of medium parameters and as such not attractive in

393

a real time analysis environment. Hence we rewrite eq. (1) for an isotropic stratified medium in the following form:

$$\varphi^0 = G^0 s \qquad (2)$$

with index zero signifying the simplified medium. We may rewrite the general Green function in terms of that for the simplified media, namely

$$G = G^0 + \delta G \qquad (3)$$

where $G^0 = G^0(|\mathbf{x} - \mathbf{x}'|; t - \tau)$. Introducing the Lamé operator L on G:

$$LG = \delta(\mathbf{x} - \mathbf{x}')\delta(t - \tau) \qquad (4)$$

where the L-operator in time-frequency representation is of the form:

$$L = -\rho\omega^2 \delta_{ik} - \partial_j [c_{ijkl}\partial_l] \qquad (5)$$

with $\rho=$ density, $\delta =$ Kronecker delta, $\omega =$ angular frequency and $c =$ elasticity tensor. Using the L-operator, we have for δG (eq. 3):

$$\delta G = -G^0(L - L^0)G = G^0 V G \qquad (6)$$

where the potential $V = L^0 - L$. Obviously, seismic waveforms vary rapidly between stations so preferences are for wavefield intensity or amplitude square measures, that is

$$\varphi\varphi^* = GG^* ss* \qquad (7)$$

where G^* stands for the operator being adjoint to G. Inserting eqs.(2), (3), and (6) in eq. (7) we get

$$\overline{\varphi\varphi^*} = \overline{\varphi^0\varphi^{0*}} + G^0 G^{0*} \overline{VV^*} \overline{\varphi\varphi^*} \qquad (8)$$

where the overline imply averaging over two separate recording positions and operator $\overline{VV^*}$ is supposed to be essentially nonlocal. Note that equation (8) describes wavefield intensities taking into account that we have omitted the expression $\delta(\mathbf{x}_1 - \mathbf{x}_2)\delta(t_1 - t_2)$ for equation (8); all terms should be multiplied by the expression.

Now, recalling, that our 'target zone' is the free surface we are interested in describing of energy flux in lateral direction, with G^0 describing the propagation in a stratified halfspace with smooth perturbations. V can be modeled as an ensemble of random functions with *lateral* radius of correlation being dominant, which gives the wave propagation in terms of adiabatically perturbed normal modes. This means that propagation in lateral direction $\mathbf{r} - \mathbf{r}^*$ ($\mathbf{r}^*$ is epicenter) can be treated in terms of a parabolic wave equation, and eq. (8) can be treated as an equation of evolution of intensity $w \overset{\text{def}}{=} \overline{\varphi\varphi^*}\delta(\mathbf{x}_1 - \mathbf{x}_2)\delta(t_1 - t_2)$. Physically, we have at this stage a simplified expression for wavefield intensity with the term $\overline{\varphi^0\varphi^{0*}}$ being the energy flux in an isotropic medium and the $\overline{VV^*}$- term giving diffusion of energy during propagation. Note, the propagation of an *impulse* signal in isotropic stratified half space has two main wavefield intensity components in a vicinity of the free surface: *P-primary*, or '3D-mode' and *S-secondary*, or principal '2D-mode', having specific group velocities, which are defined for the P-mode by turning points at depth $z > 0$ and for S-mode is caused by a turning point at depth $z = 0$ (Kennett, 1983). Now the difference $\Delta w = w - w^0$ between intensities in an inhomogeneous half space w and in an isotropic stratified one has to satisfy the diffusion equation:

$$\frac{\partial \Delta w(r,t)}{\partial r} = a^2 \frac{\partial^2 \Delta w(r,t)}{\partial t^2} \qquad (9)$$

where a is the diffusion coefficient. Equation (9) gives the distance dependence of wavefield intensity for localized (point) source function.

Observationally, seismogram intensity may be of form of the STA detector (Ruud et al,1993), and we want to minimize the differences between observed u and modeled w wavefield intensities, namely to find w such that

$$\mathcal{M} = \langle u - w | u - w \rangle \rightarrow \min \tag{10}$$

where $u = \{u(\mathbf{r}_n, z = 0; t) = u(\mathbf{r}_n, t) = u_n | n = 1, 2, \dots, N\}$, where $\mathbf{r}_n$ is the n-th station, N is number of stations and $w = w(|\mathbf{r} - \mathbf{r}'|, z = 0; t - \tau)$, and

$$\langle u | w \rangle \stackrel{\text{def}}{=} \frac{1}{N} \sum_{n=1}^{N} \int_{\Delta t} u(\mathbf{r}_i, t) w(\mathbf{r}_i, t) dt$$

We may write a model for observations u_i on the base of modeled w (eq.(8)) in an approximate manner by assuming linearity in terms of intensities, that is:

$$w_n = w_n^0 + \delta w_n = Wf + \delta w_n \tag{11}$$

where $W = G^0 G^{0^*}(|\mathbf{r}_n - \mathbf{r}'|, z = 0; t - \tau))$, $f = f(\mathbf{r}', t)$ is source function squared; $\delta w_n = \delta w(\mathbf{r}_n, t)$ is an error term, which can be interpreted as a random realization of Δw with covariance operator $C_w = \overline{\delta w_n \delta w_n} = \exp\{a^2 r_n \partial_t^2\}$ (eq.(9)). The equation $w_n^0 = Wf$ is similar to eq.(1) except that displacement is replaced by wavefield intensity and at that in a simplified manner. From eq.(11) we can estimate the source intensity $f(\mathbf{r}', t)$:

$$\hat{f} = (W^* C_w^{-1} W + \alpha \mathrm{I})^{-1} W^* C_w^{-1} u \tag{12}$$

where α is positive parameter of regularization. Using a RT-approximation (Ryzhikov and Troyan 1992 a,b) and presuming linearity of w with respect to f, we may rewrite eq.(11) for dimensionless values $\tilde{f} = f/f_{\max}$ and $\tilde{u} = u/u_{\max}$ in the following form:

$$\tilde{f}(\mathbf{r}', \tau) = \frac{\langle W\tilde{\mathbf{r}'}_{,\tau} | \mathcal{F}\tilde{u} \rangle}{\langle W_{\mathbf{r}',\tau} | W_{\mathbf{r}',\tau} \rangle + \alpha} \tag{13}$$

where observed data $\tilde{u}$ are filtered by operator $\mathcal{F} = exp\{-(1/2)a^2 r_n \partial_t^2\}$ (Fig. 4c) and the unit intensity source response $W\tilde{\mathbf{r}'}_{,\tau} = W(|\mathbf{r} - \mathbf{r}''|, t - t')\delta(\mathbf{r}'' - \mathbf{r}')\delta(t' - \tau)$ (an eq.(1) analogy). Albeit $\hat{f}$ may be used as an event magnitude measure, we prefer to work with normalized observational data. This ensures that corresponding source intensity function $\tilde{f}$ varies between 0 to 1.0 and plays the role of correlation between the real and virtual source intensity functions. It allows us to introduce the *source image* function:

$$\psi(\mathbf{r}', \tau) = \exp\{\sigma^{-2}[\tilde{f}(\mathbf{r}', \tau) - 1]\} \tag{14}$$

where $\tilde{f}(\mathbf{r}', \tau)$ is the normalized value of f in eq.(13). The entropy of source image contrast (EnIC), defined by Biryulina and Ryzhikov (1995) is :

$$\mathcal{E}_\psi(\tau) = - \int_\Omega \mu(\mathbf{r}', \tau)) \ln \mu(\mathbf{r}', \tau)) d\mathbf{r}' \tag{15}$$

via a pseudo-probability density function $\mu(\mathbf{r}', t) = (\partial_{\mathbf{r}'} \psi)^2(\mathbf{r}', \tau) / \int_\Omega (\partial_{\mathbf{r}'} \psi)^2 d\mathbf{r}'$. The attractive feature of the EnIC is that of beig a very good measure for detecting a single impulse-like seismic event. A more detailed theoretical basis of this epicenter location scheme is given by Ryzhikov, Biryulina and Husebye (1995, in preparation)
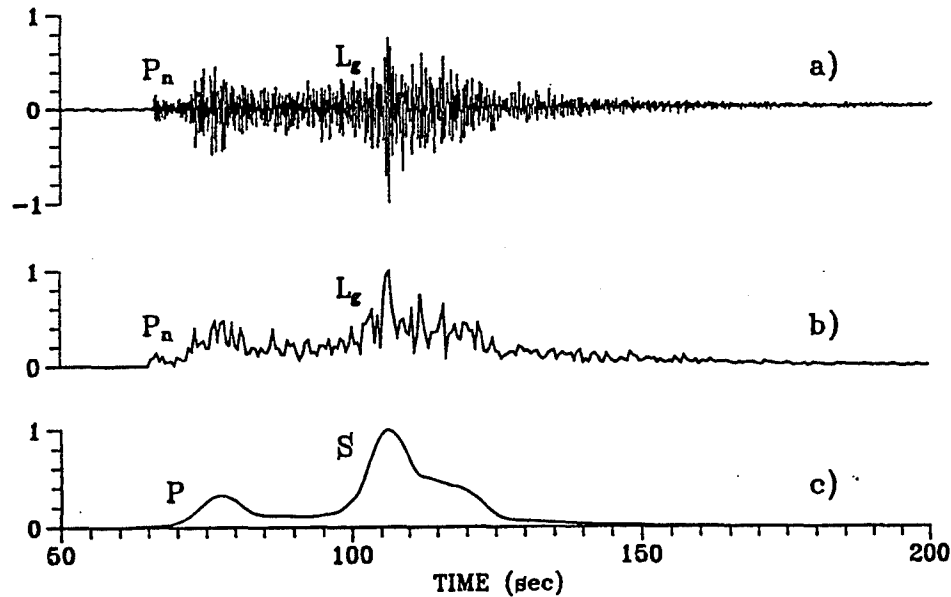
Figure 4: Local event record for the Italian station FVI at an epicenter distance of 240 km (date 11/02/95 - Table 1). a) Original waveforms after 2 - 4 Hz bandpass filtering; sampling rate is 50 Hz. b) Parameterized version of the (a) waveform subjected to a simple non-overlapping short-term-average 'envelope' transform; sampling rate is 2 Hz. c) P- and S-intensity wavelets derived from the parameterized waveforms shown in (b). The peak of these wavelets as a function of distance (Fig. 5) are the only information used in our automatic location scheme. Basic seismic network traces used in analysis is the (b)-type parameterized waveforms which are easily produced in situ. Note, we have for convenience used the classical P- *primary* and S-*secondary* notations for the intensity wavelets in (c) and *with no relation* to corresponding analyst phase notations. The wavefield counterparts of the P- and S-intensity wavelets are given in eq.8.

3.2 Event location exercise using Italian, German and Norwegian data

We requested short period (z-component) STA transformed data from 3 local networks and in this respect as implied above did not bother about instrument responses, local travel time tables, and crustal models. In case of the German data we only had at hand station coordinates and the corresponding recordings. The various analysis steps were as follow:

1. Band pass filtering; 2-4 Hz pass band for SNR enhancement. The initial STA-transforms of waveforms was (sampling rate 0.5 sec, no overlap): $STA^2 = \frac{1}{K} \sum_k \varphi_k^2$

2. Derive model for P- and S- mode intensity as a function of distance. Analysis step (1 and 2) is illustrated in Figures 4 and 5. Initially we used Fig. 5a for Germany.

3. Estimating minimum of entropy of source image contrast in time (see Fig. 6 for visualization)

4. Knowing the minimum of entropy time we searched the grid for the most probable location - our choice of epicenter locations (Fig. 7). In Table 1 we list reference epicenter locations (bulletins) and relative positions of our automatic locations.

The following comments apply; our location scheme is tied to epicenter determinations from which we could accurately compute origin time for a preset focal depth and local travel time tables. Event and magnitudes are easily derived from the STA-parameters using the Mendi and Husebye (1994) method.

396
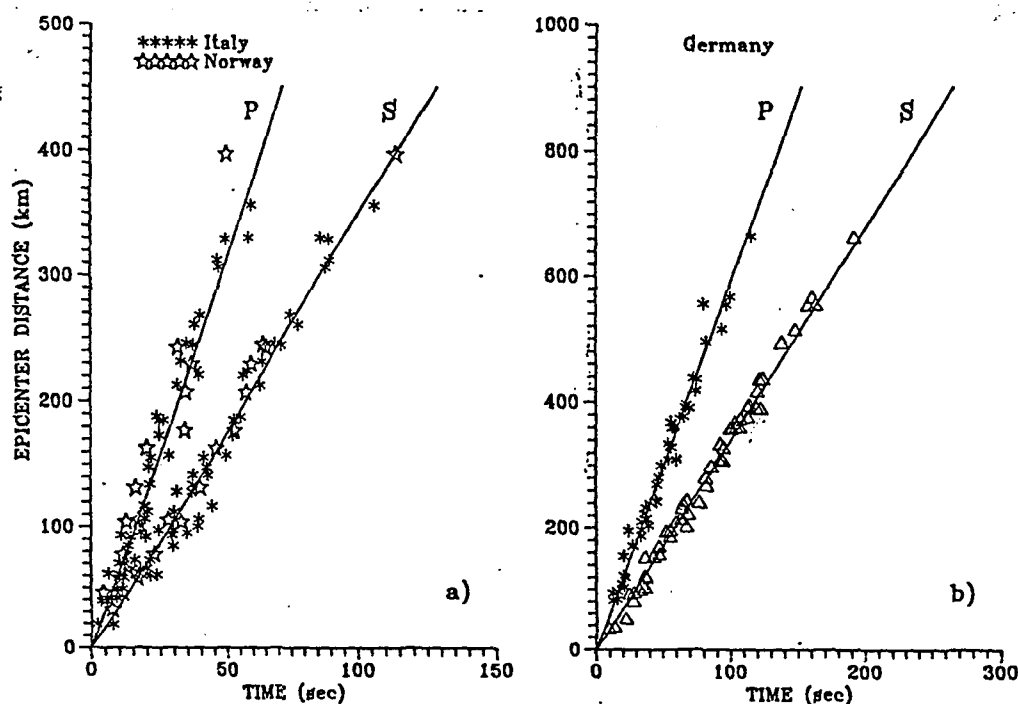
Figure 5: P- and S-intensity wavelet travel times for Italian, Norwegian (a) and German (b) network recordings. The corresponding wavelet velocities are 6.3 km/s and 3.5 km/s for (a) and 5.9 km/s and 3.4 km/s respectively for (b).
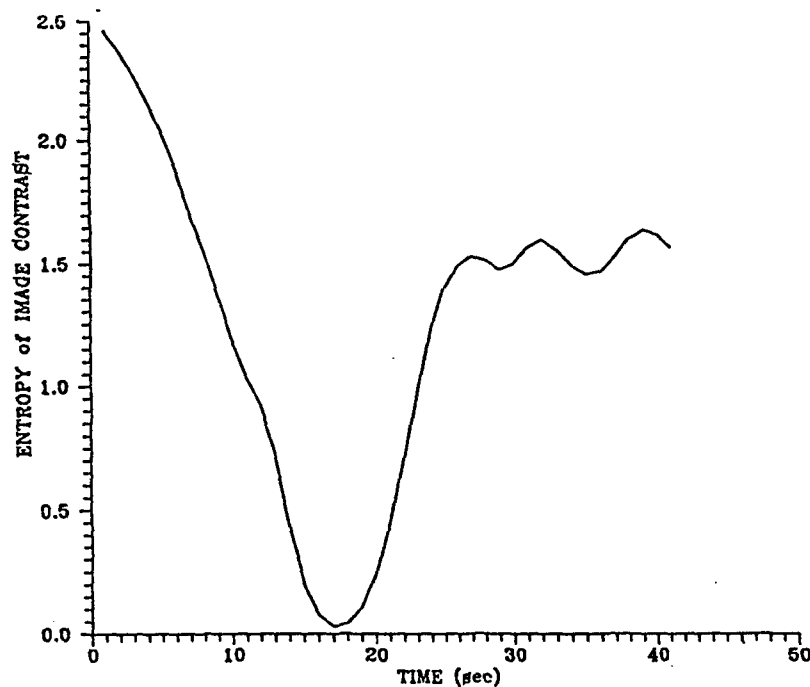
Figure 6: Entropy of source image contrast as a function of time (eq.15) for the Italian event of 11/02/95 (Table 1). Note the clear functional minimum at 17 sec being typical of real event detections. The corresponding spatial distribution of the source image function over the spatial sampling area is shown in Fig.7 .

397
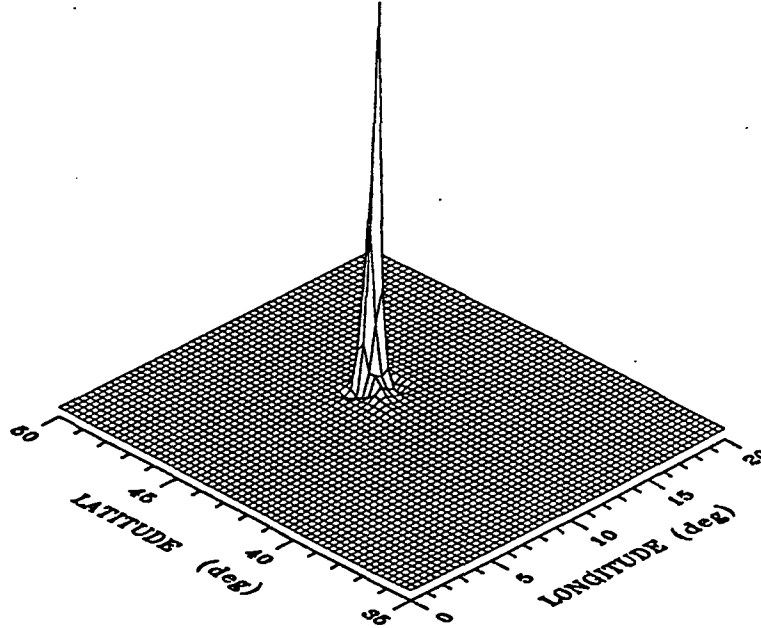
Figure 7: The spatial distribution of the source image function for the Italian event of 11/02/95 at time 17 sec coinciding with the entropy minimum in Fig. 6. The spatial position of the functional maximum in eq.(14) is taken as the epicenter coordinates (see listings in Table 1, where comparisons are made with bulletin locations).

Date	Bulletin data		Deviation		Date	Bulletin data		Deviation	
d/m/y	LatN	LonE	ΔLat	Δ Lon	d/m/y/	LatN	LonE	ΔLat	Δ Lon
GERMANY					ITALY				
30/07/94	51.45	11.43	0.06	0.02	11/12/94	37.81	15.61	-0.01	-0.27
17/09/94	51.45	10.50	0.08	0.13	02/01/95	40.82	15.34	-0.15	-0.10
04/12/94	50.25	12.44	0.23	-0.12	04/01/95	44.87	7.36	-0.11	-0.26
16/01/95	50.83	6.35	-0.05	0.11	11/02/95	44.28	11.50	0.01	-0.16
22/01/95	48.18	8.75	-0.11	-0.13	18/02/95	39.14	16.45	0.11	-0.23
10/03/95	50.79	6.35	0.01	0.04	26/02/95	44.49	12.08	-0.05	0.12
24/03/95	47.79	8.83	-0.36	-0.64	NORWAY				
30/03/95	51.46	10.40	-0.29	0.39	26/08/93	59.05	5.77	0.02	0.24
03/06/95	51.49	16.20	0.18	-0.16	26/08/93	61.11	4.07	-0.10	0.18
07/06/95	51.48	16.20	0.22	-0.12	13/09/93	66.34	5.67	-0.34	0.68

Table 1: Comparisons between event locations as reported in local bulletins and those obtained using our automatic location scheme - differences are mostly small. The few exceptions in this regard are events located outside or on the periphery of the German (ca 8 stations used) and Norwegian (ca 6 stations used) network areas where the epicenter resolution is relatively poor for any location method. (ca 20 stations used from Italian network area)

3.3 Research accomplished

An automatic and robust method for event location using local network data has been developed. It is easily adapted to any local network area - no need for overly detailed structural information. It is economical on two accounts; (i) In situ sampling rate is 0.5 sec or lower so minimal data transfer costs (ii) Analyst interference with finalized event solutions is likely to be minimal since we bypass conventional not so robust analysis steps like signal detection, phase identification and phase association. Event detectability, not excessively tested, is likely to be good as the method 'focuses' on maximum P-and S-wave- mode intensities and not often weak phase onsets (Fig. 4)

3.4 Recommendations and future plans

The main recommendation is that the information potential of local seismograph networks in the context of CTBT monitoring should be exploited to an extent far greater than currently under consideration. The novel method of event location presented provides one avenue for achieving a better, faster and more effective monitoring environment. Note, our approach is based on existing network instrumentation and perhaps most important does not incure excessive data transmission costs.

Options for further method refinements are by no means exhausted; future research topics are better handling of short distance records (P/S interference/overlap), interfering events and naturally method adaptation to a real time operational environment. Future plans also include efforts to extend methodology to teleseismic recordings and most challenging if source type identification estimates can be included for earthquake magnitudes above 3 and naturally for the many stationary mining and quarry sites.

References

Aki, K. and Richards, P.G., 1980. *Quantitative Seismology: Theory and Methods*, Vol. 1, W.H. Freeman, San Francisco.

Biryulina, M. and Ryzhikov, G., 1995. Rytov-Born decomposition in 3-D reflection seismics, in *Extended Abstracts of EAEG and EAPG 57th Conference and Technical Exhibition*, Vol.1, EAGE, Glasgow.

Brekhovskikh, L.M., 1960. *Waves in Layered Media*, Academic Press, New York.

Bannister, S.C., Husebye, E.S., and Ruud, B.O., 1990. Teleseismic P-coda analyzed by three-component and array techniques – deterministic location of topographic P-to-R_g scattering near the NORESS array, *Bull. Seism. Soc. Am.*, 80, 1969-1986.

Flatte, S.M., Dashen, R., Munk, W.H., Watson, K.M. and Zachariasen, F.,1979. *Sound Transmission Through a Fluctuating Ocean*, Cambridge University Press, New York.

Gupta, I.N., Lynnes, C.S., and Wagner, R.A., 1993. An array study of the effects of a known local scatterers on regional phases, *Bull. Seism. Soc. Am.*, 83, 53-63.

Hedlin, M.A., Minster, J.B. and Orcutt, J.A., 1991. Beam-stack imaging using a small aperture array, *Geophys. Res. Lett.*, 18, 1771-1774.

Hedlin, M.A., Minster, J.B., and Orcutt, J.A., 1994. Resolution of prominent crustal scatterers near the NORESS small-aperture array, *Geophys. J. Int.*, **119**, 101-115.

Hestholm, S.O. and Ruud, B.O, 1994. 2D finite difference elastic wave modeling including surface topography, *Geophysical Prospecting*, **42**, 371-390.

Kennett, B.L.N.,1983. *Seismic Wave Propagation in Stratified Media*, Cambridge University Press, Cambridge.

Mendi, C.D. and Husebye, E.S., 1994. Near real time estimation of magnitudes and moments for local seismic events, *Annali di Geofisica*, **37**, 365-382.

Ruud, B.O., Lindholm, C.D. and Husebye E.S., 1993. An exercise in automating seismic record analysis and network bulletin production, *Bull.Seism.Soc.Am*, **83**, 660-679.

Ryzhikov, G.A. and Troyan, V.N., 1992a. Diffraction tomography. Part 1: Construction and interpretation of tomography functionals, in *Proceedings of Russian - Norwegian Oil Exploration Workshop II*, Voss, Published by Norsk Hydro A/S, Bergen, Norway.

Ryzhikov, G.A. and Troyan, V.N., 1992b. Diffraction tomography. Part 2: Reconstruction algorithm with statistical regularization, in *Proceedings of Russian - Norwegian Oil Exploration Workshop II*, Voss, Published by Norsk Hydro A/S, Bergen, Norway.

Ryzhikov, G.A., Biryulina, M.S. and Husebye E.S., 1995. Automatic local event location excluding signal detection, phase identification and association, *in preparation*.

Numerical Investigation of Relative Contributions of R_g
Scattering and Incomplete Dissipation to L_g Excitation[1]

Rong-Song Jih

Phillips Laboratory, PL/GPE

Hanscom AFB, MA 01731-3010

Abstract

Numerous mechanisms have been proposed over the years to explain how the regional L_g phase can be generated by nuclear explosions. Commonly quoted mechanisms include trapped pS phase, non-geometrical S^*, spall, multiple reflections of initial P rays, anisotropy, and various near-source, near-surface scattering processes. Recent observational studies (*e.g.*, Patton and Taylor, 1995) indicate that R_g plays an important role in L_g excitation for Yucca Flat explosions. Numerical experiments by Jih and McLaughlin (1995) readily demonstrate that rough topography and random heterogeneity can scatter significant R_g energy into body waves. In this study, an additional R_g–to–L_g conversion mechanism is presented and the relative effectiveness and importance of all three R_g–related mechanisms are examined.

It might be anticipated intuitively that the net effect of anelasticity in the surface layers is solely to reduce the amplitude of incident seismic waves. R_g wave is particularly susceptible to such a mechanism since it is confined in the uppermost crustal layers. If the anelastic attenuating layer is only thick enough to dissipate the retrograde rolling near the surface, then the free surface would behave asymptotically like a fixed point. Beyond certain distance, the fundamental mode can no longer be sustained by such a waveguide, and accordingly any undissipated R_g energy would have to propagate in other wave types or modes. Linear finite-difference calculations show that this process couples the undissipated R_g energy into pure shear waves or higher modes, depending on the complexity of the structure. In terms of R_g–to–S to R_g–to–P ratio, this process appears to be more efficient than other near-surface R_g scattering mechanisms. Furthermore, in this process, the R_g spectrum is naturally imprinted onto the converted S waves, which could help to explain some recently observed spectral characteristics of L_g waves.

For models embedded with shallow random heterogeneity, the RMS velocity fluctuation correlates very well with the R_g transmission coefficient. For 1 Hz R_g, a 2%–5% variation in the velocity leads to an equivalent spatial Q value of several hundreds or larger, regardless which of the three commonly used random media is embedded. Rough topography typically results in a Q value ranging from 10 to 100, which is approximately equivalent to a random medium with a 10% (or larger) velocity variation. Incomplete dissipation of R_g waves produces a very simple wave field, with almost all of the undissipated energy continues to propagate laterally towards the forward, and hence postcritical, directions. On the other hand, the scattering by shallow heterogeneity or rough topography would generate a rather complicated wave field, with a significant fraction of the scattered energy going downward steeply. Whichever of the three mechanisms is invoked, the S waves converted from R_g always dominate the whole scattered field. The uppermost crust is highly heterogeneous, and in many places very attenuative and hilly as well. All of the three R_g-related mechanisms should therefore contribute to L_g and coda excitation.

Project Objective

The long-term objective of this project is to improve the fundamental understanding of seismic wave excitation and propagation. The full potential of linear finite-difference [LFD] method and other techniques shall be exploited in modeling various seismological problems directly related to a CTBT monitoring.

Research Accomplished

The first task of this project is to improve the capability of modeling L_g, R_g, P_n, P_g, and S_n in complex geological / geophysical environments, using LFD or hybrid modeling tools. Following the LFD implementation of a pure L_g wave packet (Jih, 1994), which is an ideal tool for investigating certain wave propagation phenomena (such as L_g blockage), our research effort under this project has been re-directed to several subtasks:

[1] Use synthetic waveforms as an analysis aid to improve the phase-identification capability.[2]

[2] Explore the physical basis of high-frequency shear wave excitation in the vicinity of explosions due to cracking or pre-existing cracks.[3]

[3] Continue to investigate mechanisms responsible for explosion L_g excitation.

This paper summarizes our results obtained to date under subtask [3], with emphasis placed on topics related to R_g. A new R_g –to–L_g conversion mechanism is presented, and the relative effectiveness and importance of all three R_g –related mechanisms are reviewed.

Numerous mechanisms have been proposed over the years to explain how the regional L_g phase can be generated by nuclear explosions. Commonly quoted mechanisms include trapped pS phase, non-geometrical S^*, spall, multiple reflections of initial P rays, anisotropy, and various near-source, near-surface scattering processes. Recent observational studies (*e.g.*, Patton and Taylor, 1995) indicate that R_g plays an important role in L_g excitation for Yucca Flat explosions. Numerical studies conducted at Teledyne Geotech and Phillips Laboratory (*e.g.*, McLaughlin and Jih, 1986, 1987; Jih, 1993ac, 1994) readily demonstrate that rough topography and random heterogeneity can scatter significant R_g energy into body waves. However, in several cases only a fraction of the scattered energy would be favorably trapped in the crust as L_g or L_g coda, with more scattered energy lost to steeply going directions. In reality some additional R_g -to-S mechanisms may have contributed to the observed L_g signal as well.

It might be anticipated intuitively that the net effect of anelasticity in the surface layers is solely to reduce the amplitude of incident seismic waves. R_g wave is particularly susceptible to such a mechanism since it is confined in the uppermost crustal layers. If the anelastic attenuating layer is only thick enough to dissipate the retrograde rolling near the surface, then the free surface would behave asymptotically like a fixed point. Beyond certain distance, the fundamental mode can no longer be sustained by such a waveguide, and accordingly any undissipated R_g energy would have to propagate in other wave types or modes. Linear finite-difference calculations show that this process couples the undissipated R_g energy into pure shear waves or higher modes, depends on the complexity of the structure (Figure 1). In terms of R_g –to–S to R_g –to–P ratio, this process appears to be far more efficient than other near-surface R_g scattering mechanisms (Figure 5). Furthermore, in this process, the R_g spectrum is

---

[2] See Kadinsky, Jih, Dainty, and Cipar (1995) of this issue.

[3] In progress with collaboration from A. Dainty and R. Blandford.

naturally imprinted onto the converted S waves, which could help to explain some recently observed spectral characteristics of L_g waves. Figure 2 compares the propagation of R_g waves incident upon an elastic and an attenuative basin models with identical velocity structures. Both the wave field snapshots (Figure 2) and the synthetic seismograms (Figure 3) clearly illustrate that R_g–to–L_g conversion can be enhanced if the sedimentary rocks are shallow and strongly attenuative.

For the R_g waves, rough topography could still be the strongest means of scattering (Jih, 1993abc). Scattering by random heterogeneity in the upper crust (*cf.* McLaughlin and Jih, 1987, and Jih, 1993b), is important in that random variations of velocity are virtually present in any type of crustal structure. McLaughlin and Jih (1987) made a comparison with Greenfield's (1971) P-coda observations (at teleseismic distance), and it was concluded that self-similar or Gaussian models with RMS velocity fluctuation between 7% and 15% in the uppermost 3 km of the crust can produce the observed P-coda/P power levels reported in Greenfield (1971). With the emphases of treaty-monitoring seismic research shifted to regional phases, R_g scattering by shallow random heterogeneity needs to be re-examined in order to evaluate its importance and efficiency, with respect to other mechanisms, in exciting L_g waves from explosions. In this study, a suite of forty five models embedded with shallow self-similar heterogeneous layer of varying randomness and thickness have been tested with LFD. Table 1 summarizes the propagation statistics we measured. Within 15% of velocity variation, the transmission, reflection, and the scattering loss all exhibit a linear relationship with the RMS velocity fluctuation. Models with thicker heterogeneities certainly associated with a stronger scattering and reflection, as well as a weaker transmission, as expected. However, the thickness appears to be less relevant than the RMS velocity variation (See Figure 4), primarily because R_g scattering in the top 1 km is more important. These observations are also valid for random media with Gaussian or exponential correlations (see Frankel and Clayton, 1986, for the definitions of various random models).

Conclusions and Recommendations

There are at least three R_g–to–SV(L_g) mechanisms: [A] scattering by shallow, random heterogeneity, [B] scattering by rough surface topography, and [C] incomplete dissipation by anelastic attenuation. Under this project, forward modeling is used to gain a better understanding of these three mechanisms. It is shown that, through extensive LFD modeling, each of these mechanisms can contribute to L_g and coda waves from explosions. In terms of $R_g \rightarrow$S / $R_g \rightarrow$P power ratio, [C] is the most efficient one, followed by [B] and then [A]. R_g–to–S conversion systematically dominates the scattered wave field. In terms of equivalent spatial Q's, rough surface topography typically corresponds to a Q_0 in the range between 10 and 100 (Jih, 1993c), which is approximately equivalent to a self-similar random medium with 10% (or larger) RMS variation in the velocity. An RMS velocity fluctuation between 5% and 10% would correspond to a Q_0 value between 100 and 450 (Table 1). Stable shield regions have been reported to have an RMS velocity fluctuation less than 5%, which would yield a Q_0 larger than a few hundreds, regardless which type of random heterogeneity is considered. For all three types of random media that are commonly used in numerical studies with RMS velocity variation below 15%, all four measurable R_g propagation statistics correlate extremely well with the RMS velocity fluctuation. Incomplete dissipation of R_g waves produces a very simple wave field, with almost all of the undissipated energy continues to propagate laterally towards the forward, and hence postcritical, directions. On the other hand, the scattering by shallow heterogeneity or rough topography would generate a rather complicated wave field, with a significant fraction of the scattered energy going downward steeply.

An accurate prediction of the regional phases in areas of high proliferation concern requires a decent understanding of the attenuation/scattering mechanisms along the propagation paths. Synthetic seismograms are particularly useful for regions where earthquake or explosion data are not available. 2D numerical experiments, as described herein and in our previous studies, demonstrate that R_g can be a significant contributor to the formation of L_g and coda waves, in support of several observational studies. It would seem reasonable that, as 3D structure is taken into account, R_g's possible role in L_g excitation would only become more important. On a long term, however, extending 2D modeling capability to 3D is definitely useful, as it would add an extra level of realism and complexity to the earth's structures that we need to model. In particular, in order to quantify 3D effects of surface topographic irregularities, the operational 2D formulations of Neumann boundary conditions (Jih *et al.*, 1988) need to be expanded to a 3D version.

References

Frankel, A. and R. W. Clayton (1986), Finite-difference simulation of seismic scattering: implications for the propagation of short-period seismic waves in the crust and models of crustal heterogeneity, *J. Geophy. Res.,* **91,** 6465-6489.

Greenfield, R. J. (1971). Short-period *P*–wave generation by Rayleigh-wave scattering at Novaya Zemlya, *J. Geophys. Res.,* **76,** 7988-8002.

Jih, R.-S. (1993a). Directional excitation of R_g due to ripple-fired explosions: a 2-dimensional finite-difference calculation, in *Proceedings of Numerical Modeling for Underground Nuclear Test Monitoring Symposium* (S. Taylor and J. Kamm, eds.), *Los Alsmos National Laboratory Report No. LAUR-93-3839.*

Jih, R.-S. (1993b). User's manual of FD2: a software package for modeling seismological problems with 2-dimensional linear finite-difference method, *Report TGAL-93-06,* Teledyne Geotech, Alexandria, VA.

Jih, R.-S. (1993c). Statistical characterization of rugged propagation paths with application to R_g scattering study, *Report TGAL-93-07,* Teledyne Geotech, Alexandria, VA.

Jih, R.-S. (1994). Numerical modeling of crustal phase propagation in irregular waveguides, in *Proceedings of 16th PL/AFOSR Seismic Research Symposium* (J. Cipar, J. Lewkowicz, and J. McPhetres, eds.), *Report PL-TR-94-2217,* Phillips Laboratory, Hanscom AFB, MA, pp. 173-181 (ADA284667).

Jih, R.-S., K. L. McLaughlin and Z. A. Der (1988). Free boundary conditions of arbitrary polygonal topography in a 2-D explicit elastic finite difference scheme, *Geophysics,* **53,** 1045-1055.

McLaughlin, K. L. and R.-S. Jih (1986). Finite-difference simulations of Rayleigh wave scattering by 2-D rough topography, *Report AFGL-TR-86-0269,* Air Force Geophysics Laboratory, Hanscom AFB, MA (ADA179190).

McLaughlin, K. L. and R.-S. Jih (1987). Finite-difference simulations of Rayleigh wave scattering by shallow heterogeneity. *Report AFGL-TR-87-0322,* Air Force Geophysics Laboratory, Hanscom AFB, MA (ADA194961).

Patton, H. J. and S. R. Taylor (1995). Analysis of L_g spectral ratios from NTS explosions: implications for the source mechanisms of spall and the generation of L_g waves, *Bull. Seism. Soc. Am.,* **85,** 220-236.

Table 1. Transmission/Reflection/Scattering Statistics of Self-Similar Models					
Model	T(1Hz)	R(1Hz)	1-T-R	Q(1Hz)	γ
1km, 2%	0.99	0.01	0.01	10172	0.000
2km, 2%	0.98	0.01	0.01	8018	0.000
5km, 2%	0.98	0.01	0.01	6710	0.000
10km, 2%	0.98	0.01	0.01	6179	0.000
1km, 3%	0.96	0.02	0.03	2000	0.001
2km, 3%	0.95	0.02	0.03	1788	0.001
5km, 3%	0.95	0.02	0.04	1646	0.001
1km, 4%	0.92	0.03	0.06	931	0.001
1km, 5%	0.86	0.04	0.10	548	0.002
2km, 5%	0.85	0.04	0.11	502	0.002
5km, 5%	0.84	0.04	0.12	473	0.002
10km, 5%	0.84	0.04	0.12	457	0.002
15km, 5%	0.83	0.04	0.12	451	0.002
1km, 6%	0.80	0.06	0.14	363	0.003
1km, 7%	0.73	0.07	0.20	258	0.004
1km, 8%	0.66	0.09	0.25	192	0.005
1km, 9%	0.58	0.10	0.31	147	0.007
1km, 10%	0.51	0.12	0.38	116	0.009
2km, 10%	0.47	0.11	0.42	105	0.009
5km, 10%	0.45	0.11	0.44	99	0.010
10km, 10%	0.45	0.11	0.44	99	0.010
15km, 10%	0.45	0.11	0.44	98	0.010
1km, 11%	0.43	0.13	0.44	92	0.011
1km, 12%	0.35	0.14	0.50	75	0.013
1km, 13%	0.28	0.16	0.56	61	0.016
1km, 14%	0.22	0.17	0.61	51	0.020
1km, 15%	0.16	0.18	0.66	42	0.024
2km, 15%	0.13	0.17	0.71	37	0.027
5km, 15%	0.12	0.17	0.72	36	0.028
10km, 15%	0.13	0.16	0.71	38	0.026
15km, 15%	0.13	0.16	0.71	38	0.026
1km, 16%	0.11	0.19	0.70	35	0.028
1km, 17%	0.08	0.20	0.72	30	0.034
1km, 18%	0.05	0.21	0.74	25	0.040
1km, 19%	0.03	0.22	0.76	21	0.048
1km, 20%	0.01	0.22	0.76	17	0.058
2km, 20%	0.01	0.23	0.76	15	0.066
5km, 20%	0.01	0.23	0.77	14	0.069
10km, 20%	0.01	0.23	0.76	15	0.066
15km, 20%	0.01	0.24	0.75	17	0.060
1km, 21%	0.01	0.23	0.77	14	0.070
1km, 22%	0.00	0.23	0.76	12	0.081
1km, 23%	0.00	0.24	0.76	11	0.088
1km, 24%	0.00	0.24	0.76	11	0.091
1km, 25%	0.00	0.24	0.76	10	0.097

T: transmitted power, R: reflected power, 1-T-R: scattering loss, γ : attenuation coefficient.
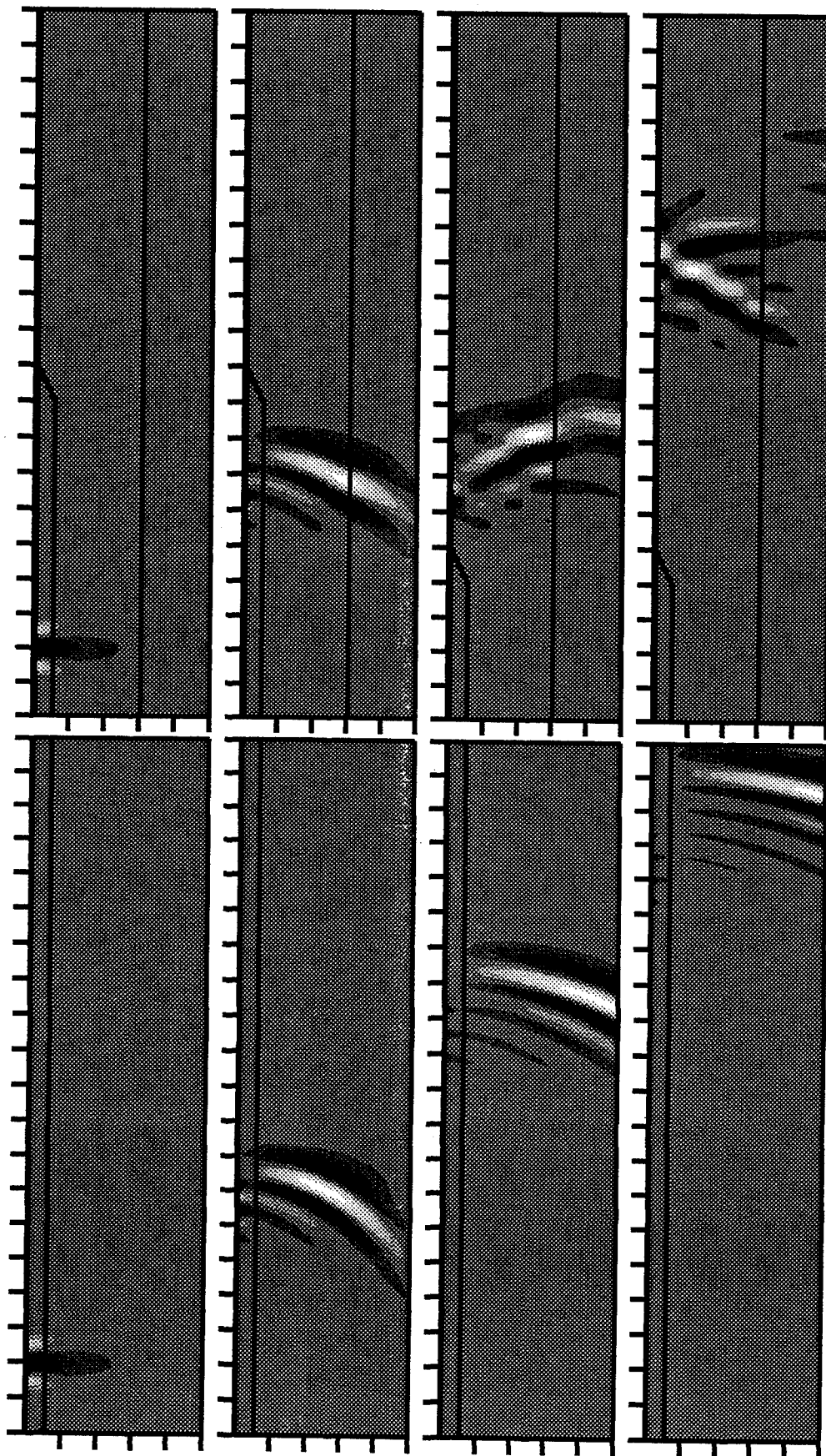
Figure 1. Snapshots of vertical wavefield of planar R_g incident upon simple attenuative structures. In the case of an elastic half space overlain by a strong, shallow attenuative layer (left), the retrograde rolling near the surface is dissipated after certain distance. With the free surface behaves asymptotically like a fixed point, this waveguide could no longer support the fundamental mode. As a result, most of the undissipated R_g energy is forced to propagate (in the forward direction) as shear waves. As the structure becomes more complex, the converted shear waves can easily couple into higher modes and contribute to L_g and L_g coda. Shown on the right is a model with a terminating attenuative layer on the top. Adding an extra layer (of higher velocity) to the model helps to trap the converted shear waves in the waveguide.
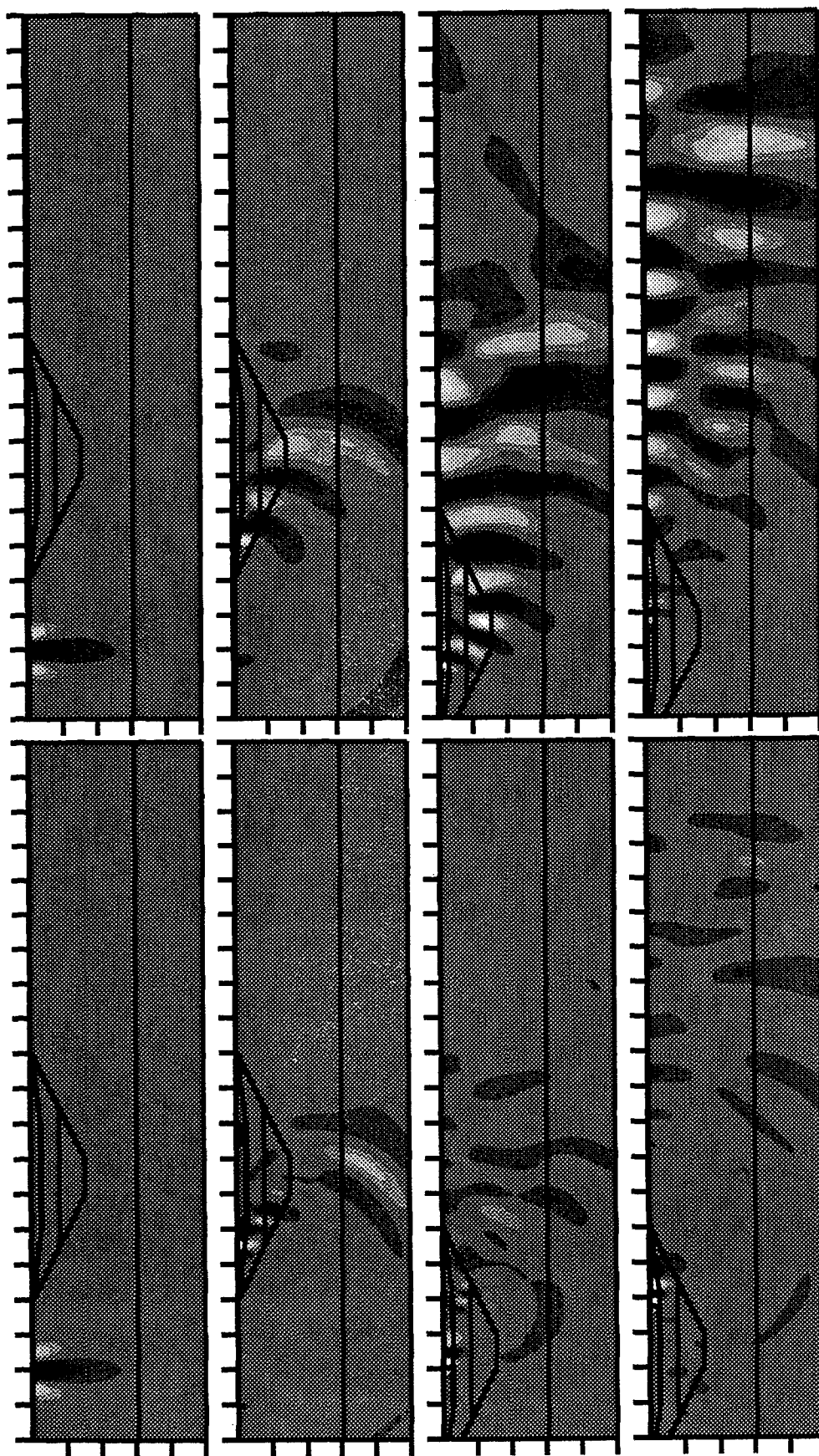
Figure 2. Snapshots of planar R_g incident upon contained basin structures. In the elastic basin model (left), the low-velocity basin slows down the fundamental mode. Although the scattering at the basin edges removes some energy from the R_g wave packet, the fundamental mode still retains the largest amplitude (See Figure 3). When the basin is replaced with depth-dependent low-Q materials (with the velocity unchanged), the fundamental mode is broken up, with the energy that tunneling through the deeper portion of the basin dominates the wavefield. This energy propagates as higher modes after passing through the basin.

407
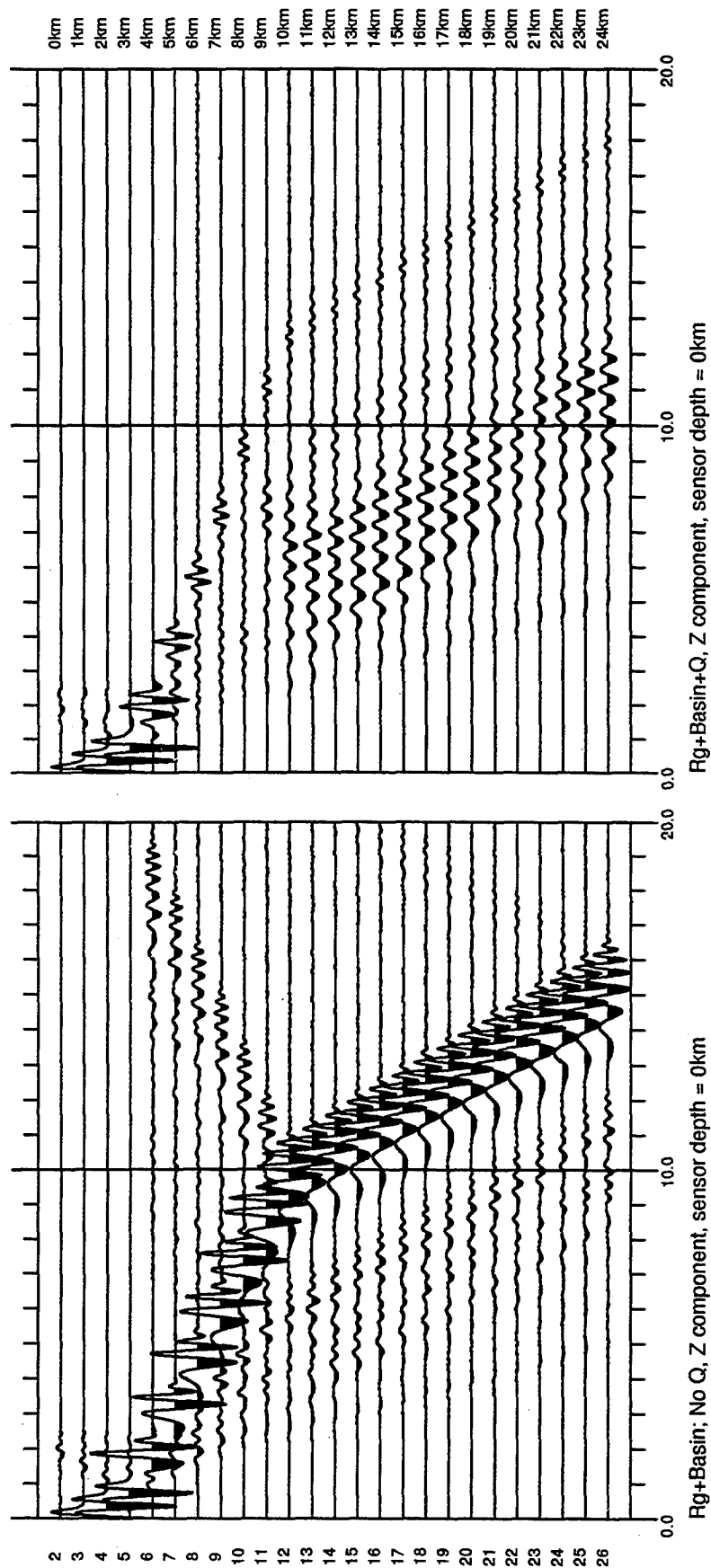
Figure 3. Synthetic seismograms, plotted in the same scale, for the two models shown in Figure 2. In the elastic basin model (left), the low-velocity sedimentary layers slow down the fundamental mode and cause significant backscattering at the basin edge. A fraction of the energy tunnels through (and under) the deeper layers of the basin and becomes higher modes, which travels ahead of the dominating fundamental mode. A little R_g–to–P conversion is also visible. When the basin is replaced with depth-dependent low-Q material (with the velocities unchanged), the R_g amplitude is reduced dramatically The higher modes become the dominant phase in the transmitted wave train. Forward R_g–to–P conversion becomes negligible (in this scale).
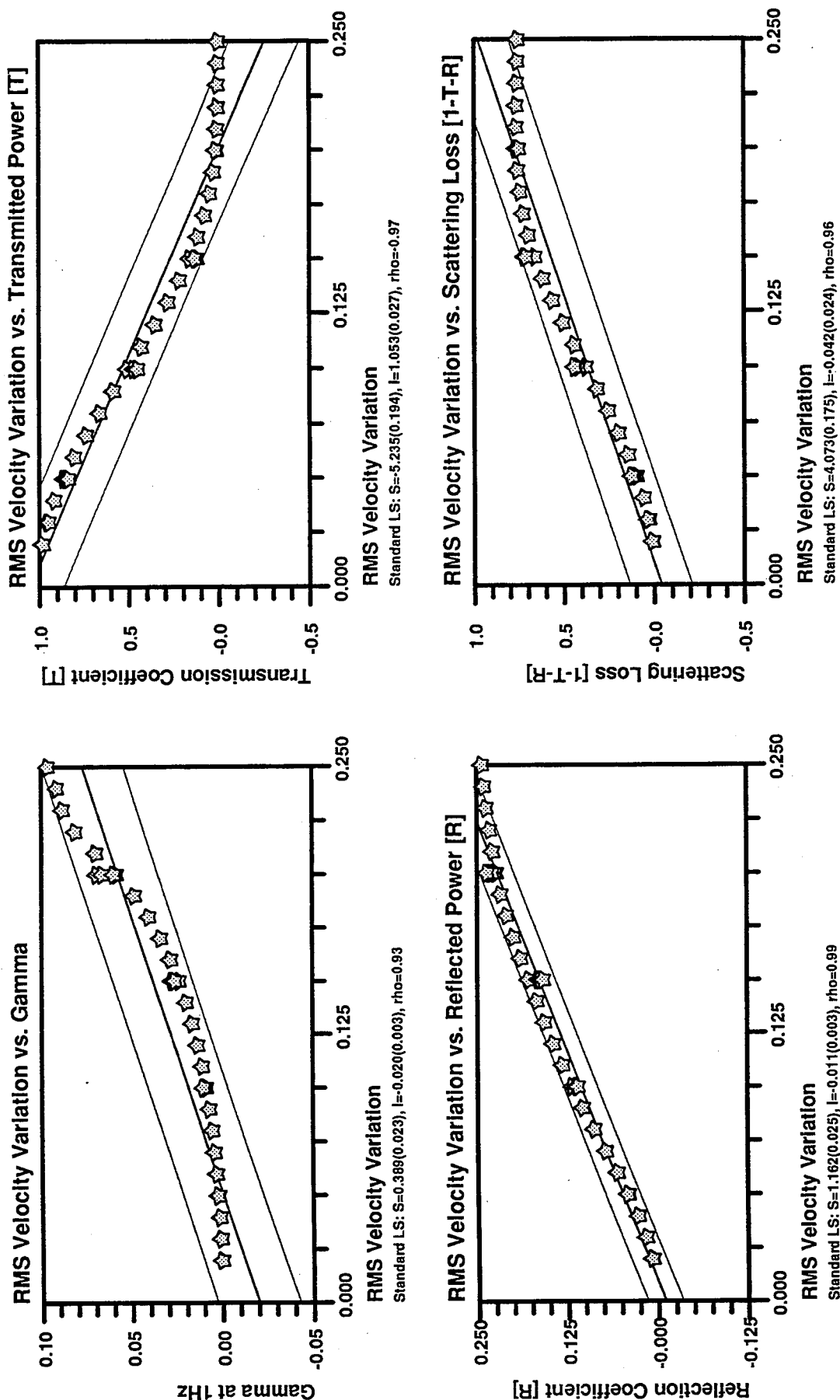
Figure 4. Regressing the attenuation coefficients [γ] (top left), transmitted power [T] (top right), reflected power [R] (bottom left), and scattering loss [1-T-R] (bottom right), respectively, on the RMS velocity fluctuation, σ, of 45 models with the thickness of the embedded self-similar shallow heterogeneous layer ranges from 1km to 5km. A 2%–5% variation in the velocity leads to an equivalent spatial Q value of 400 or larger for 1Hz R_g phase. Models with stronger heterogeneities have larger γ's, stronger reflection, and smaller T's, as expected. The excellent linear fit (for up to 15%) suggests that general propagation statistics can be predicted with the RMS velocity variation alone.

409
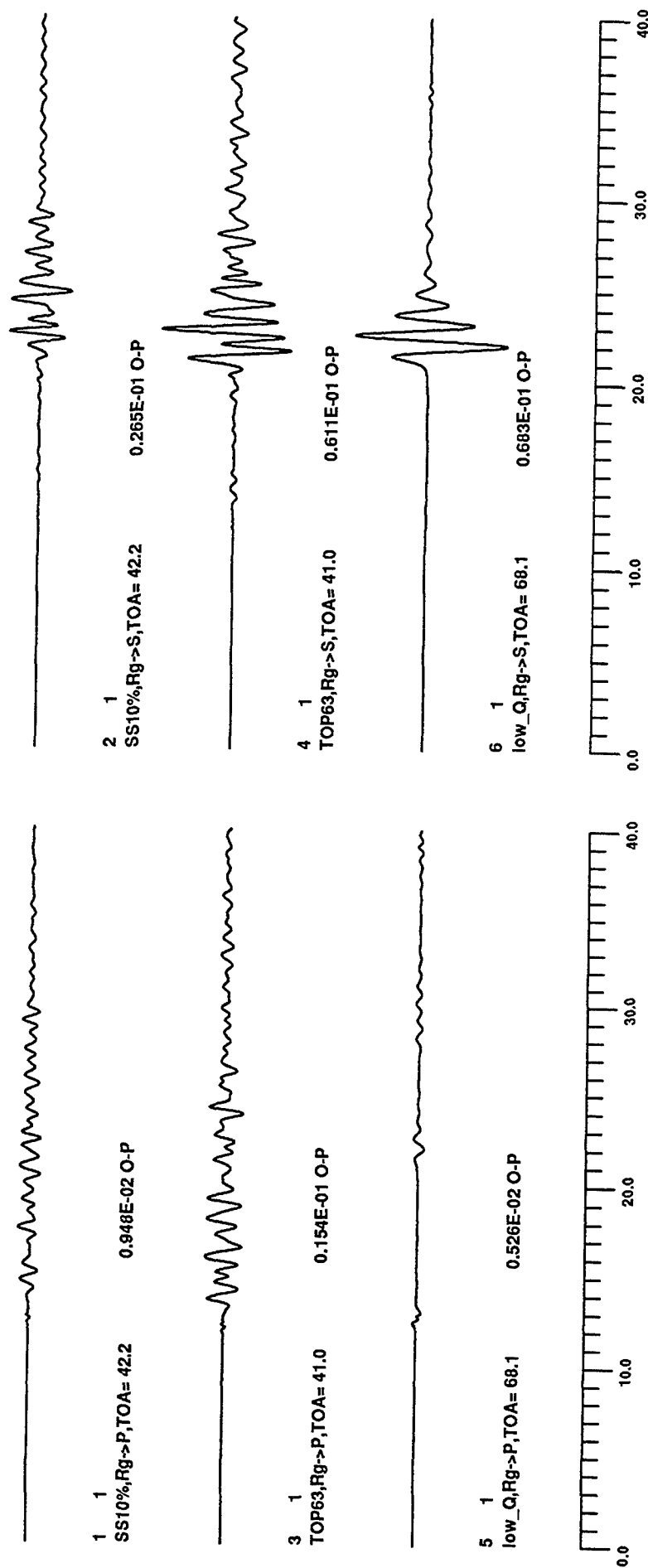
Figure 5. Comparison of LFD synthetic displacement seismograms of scattered body waves converted from R_g due to three different mechanisms. Shown on the left and right are the converted P and S waves, respectively, recorded at a depth of 5 km. The take-off angle and the peak amplitude of the scattered rays are shown under each trace. The three heterogeneous structures being compared are (from top) [1] a half-space model embedded with self-similar shallow heterogeneity with 10% velocity fluctuation, [2] a half-space model overlain by a rough topographic profile, and [3] a half-space model overlain by a strongly attenuative layer. A pure R_g wave packet was injected into the homogeneous portion of the grid to trigger the LFD calculations. In addition to the identical initial condition, other parameters (such as the grid size, the grid spacing, and the material properties of the bedrock) were also identical in these LFD simulations. Controlled numerical experiments using LFD are particularly convenient in isolating the effect of different mechanisms on R_g (or other phases). In terms of $R_g \rightarrow S$ / $R_g \rightarrow P$ ratio or peak S-wave amplitude, incomplete dissipation of R_g waves appears to be more efficient than the two scattering processes. Scattering by topography or heterogeneity would generate a much longer coda, however. For each of the three R_g mechanisms investigated so far, $R_g \rightarrow S$ conversion is univocally stronger than that of $R_g \rightarrow P$.

410

Simultaneous Inversion of Event m_{Lg} and Path Attenuation Coefficient with Application to a Transportable L_g Magnitude Scaling[1]

Rong-Song Jih   R. Baumstark, and R. Wagner
Phillips Laboratory, PL/GPE   Seismic Operations Support (Florida & Virginia)
Hanscom AFB, MA 01731-3010   Teledyne Brown Engineering

Abstract

A simple, consistent, and transportable magnitude scale for regional phases is useful and often required in order to (A) improve the source discrimination capability, (B) determine the station detection threshold, and (C) estimate the explosive yield. A convenient, and hence recommended, magnitude formula for L_g phase is:[2]

$$m_{L_g} \equiv 4.0272 - \text{Bias} + \log A(\Delta) + \frac{1}{3}\log(\Delta(\text{km})) + \frac{1}{2}\log[\sin(\frac{\Delta(\text{km})}{111.1(\text{km/deg})})] + \frac{\gamma(\Delta - 10\text{km})}{\ln(10)} , \quad [1]$$

where the "bias" term is meant to account for the different L_g excitation relative to m_b. For instance, a bias of approximately 0.39 magnitude unit for Iranian Plateau has been suggested by Nuttli.[3]

Given a suite of events with L_g phases recorded at a seismic network, we present an iterative procedure to simultaneously invert for the path γ and the event m_{L_g} values in Equation [1] without using a priori path γ information. Independently derived γ (or Q) values, if available, can be utilized to further constrain the trade-off between the bias term in [1] and the resulting γ values. Other constraints can be easily incorporated into this iterative inversion scheme as well. The procedure is less sensitive to rounding errors, and hence it is numerically more accurate than those direct methods based on matrix factorization or Gaussian elimination. When the number of equations becomes large, the iterative approach is often the only practical means to tackle the inversion. This joint inversion scheme is a natural extension to crustal phases of the one we previously used in the teleseismic analyses.[4]

The proposed joint inversion scheme has been tested with Pahute Mesa and Novaya Zemlya explosions, and the $m_b - L_g$ bias at these two sites are inferred to be -0.34 and -0.26 magnitude unit, respectively. These bias estimates are "optimal" in that the resulting path Q_0 values, which are the by-product of this inversion exercise, would be in best agreement with those derived by the coda-Q method.[5][6][7] This exercise yields twenty and eleven stations calibrated for L_g phase from Pahute Mesa and Novaya Zemlya regions, respectively.

---

[2] Jih, R.-S. and C. S. Lynnes (1993). Studies of regional phase propagation in Eurasia. *Report PL-TR-93-2003 (=TGAL-93-01)*, Phillips Laboratory, Hanscom AFB, MA (ADA262801).

[3] Nuttli, O. W. (1980). The excitation and attenuation of seismic crustal phases in Iran, *Bull. Seism. Soc. Am.*, 70, 469-485.

[4] Jih, R.-S. and R. R. Baumstark (1994). Maximum-likelihood network magnitude estimates of low-yield underground explosions, *Report TBE-4617-3 / TGAL-94-02*, Teledyne Brown Engineering, Arlington, VA.

[5] Nuttli, O. W. (1986a). Yield estimates of Nevada Test Site explosions obtained from seismic L_g waves, *J. Geophys. Res.*, 91, 2137-2151.

[6] Nuttli, O. W. (1988). L_g magnitudes and yield estimates for underground Novaya Zemlya nuclear explosions, *Bull. Seism. Soc. Am.*, 78, 873-884.

[7] Patton, H. J. (1988). Application of Nuttli's method to estimate yield of Nevada Test Site explosions recorded on Lawrence Livermore National Laboratory's digital seismic system, *Bull. Seism. Soc. Am.*, 78, 1759-1772.

Project Objective

Develop simple, transportable magnitude scales for miscellaneous regional phases. Review and improve inversion techniques currently in use. Some anticipated products/payoffs include:
[1] a more consistent way of calibrating a suite of propagation paths,
[2] refined event magnitudes which have immediate or potential use in (a) source discrimination study, (b) determination of station detection threshold, and (c) yield estimation.

Research Accomplished

To date the absolute L_g magnitude scale is defined on a region-by-region basis. For Eastern U.S., Nuttli's (1986ab) two-step formulae are equivalent to the following one-step procedure (Jih and Lynnes, 1993):

$$m_{L_g} \equiv 4.0272 + \log A(\Delta) + \frac{1}{3}\log(\Delta(\text{km})) + \frac{1}{2}\log[\sin(\frac{\Delta(\text{km})}{111.1(\text{km/deg})})] + \frac{\gamma(\Delta - 10\text{km})}{\ln(10)} . \quad [1]$$

This formula defines a magnitude scale such that a seismic source with 1-sec L_g amplitude of 110 μm at 10 km (extrapolated) epicentral distance would correspond to a m_{L_g} of 4.0272 + 2.0414 + 0.3333 - 1.4019 + 0.0000 = 5.000, which was suggested to be appropriate for both eastern North America and Semipalatinsk. That is to say, a seismic source in these two regions with m_b 5.0 would have a m_{L_g} approximately the same.

For Iranian Plateau, Nuttli (1980) reported that seismic sources with the ISC bulletin m_b 5.0 excite L_g amplitudes approximately 270 microns at a 10-km extrapolated distance. If m_{L_g} scale is to be "normalized" to m_b scale at m_b = 5.0, then Equation [1] would have to be revised for Iran as:

$$m_{L_g} \equiv 4.0272 - \text{Bias} + \log A(\Delta) + \frac{1}{3}\log(\Delta(\text{km})) + \frac{1}{2}\log[\sin(\frac{\Delta(\text{km})}{111.1(\text{km/deg})})] + \frac{\gamma(\Delta - 10\text{km})}{\ln(10)} , \quad [2]$$

where a "bias" of approximately 0.39 magnitude unit [m.u.] is added to account for the different L_g excitation (relative to m_b) observed in Iranian Plateau. Two fundamental issues arise immediately:

[A] If we accept Equation [2] as the general definition of m_{L_g} scale, what is the "bias" term appropriate for other places, say western North America (such as NTS) or Novaya Zemlya regions?

[B] The path anelastic attenuation coefficient, γ, is assumed to be known before Equation [1] (or [2]) can be applied. How should the path attenuation coefficient, γ, be determined for regions like Novaya Zemlya where L_g might be blocked rather than absorbed through the intrinsic attenuation? Would the coda-Q method still be applicable to those blocked paths?

Using L_g amplitudes collected under a recently completed AFTAC contract F08606-91-C-0005 (Baumstark and Wagner, 1994), these two issues are partially examined with an inversion algorithm which simultaneously determines the event sizes, the bias term, and the path corrections without utilizing any *a priori* path γ information. The original formulation of this iterative inversion procedure was first presented in Jih (1992), and it was tested with some quasi-synthetic data. Its updated version is briefly described in the Appendix below.

Given a postulated bias value, a system of linear equations (based on Equation [2]) can be solved for the event m_{L_g} and path γ values. If the path attenuation coefficients are readily available from other studies independently, then such extra information can be used to further constrain the bias term for the

most probable solution. This is exactly the approach to be used in the following exercises.

1. Novaya Zemlya Results

For Novaya Zemlya test site, there are 24 explosions recorded at 13 stations, totaling 92 L_g paths. The average m_G of these 24 events is 5.88, based on the path-corrected / station-corrected m_G reported in Jih and Baumstark (1994) (*cf*. pages 27-28). This value was used to constrain the inversion. The Q_0 and η values associated with each of five postulated bias terms ranging from 0.0 to 0.40 m.u. are listed in Table 1. It turns out that adopting a bias of 0.26 m.u. in Equation [2] would lead to the best agreement between the resulting Q_0 values and those measured by Nuttli (1988) with the coda-Q method.

Table 1. Q_0, η of Novaya Zemlya – WWSSN Paths						
Station	Nuttli	Postulated $L_g - m_b$ Bias and Resulting Q_0				
Code	BSSA 1988	.00	.10	.20	.26*	.40
COP	633 0.4	802 0.86	745 0.87	697 0.89	670 0.89	615 0.91
DAG	— —	290 0.68	279 0.69	268 0.71	262 0.71	249 0.73
ESK	— —	499 0.67	481 0.69	463 0.70	454 0.71	433 0.73
IST	— —	592 0.71	569 0.72	547 0.73	536 0.74	509 0.75
KBS	315 0.5	— —	— —	— —	— —	— —
KEV	252 0.6	314 0.50	292 0.52	274 0.54	263 0.55	242 0.57
KON	496 0.5	— —	454 0.04	433 0.10	421 0.13	396 0.20
NOR	— —	243 0.47	235 0.49	228 0.51	223 0.53	213 0.55
NUR	420 0.5	512 0.64	479 0.66	450 0.67	434 0.68	401 0.70
STU	531 0.5	603 0.62	577 0.64	553 0.65	540 0.66	512 0.68
TRI	— —	521 0.48	502 0.51	485 0.52	475 0.54	454 0.56
UME	391 0.5	456 0.87	427 0.88	401 0.89	386 0.89	358 0.90

2. Pahute Mesa Results

For Pahute Mesa explosions, a $L_g - m_b$ bias of 0.34 m.u. (Table 2) appears to give Q_0 values most consistent with those Nuttli (1986a) and Patton (1988) obtained. 225 L_g signals recorded at 21 Eurasian stations were used in this inversion. The 47 Pahute Mesa events have an average m_G of 5.51 (*cf*. pages 17-18 of Jih and Baumstark, 1994).

Table 2. Q_0, η of Pahute Mesa – WWSSN Paths						
Station	Nuttli+Patton	Postulated L_g–m_b Bias and Resulting Q_0				
Code	BSSA 86, 88	.00	.10	.20	.34*	.40
AAM	— —	904 1.11	838 1.11	782 1.10	714 1.10	689 1.10
ALQ	— —	264 0.86	247 0.87	231 0.88	212 0.89	205 0.90
ATL	— —	— —	360 0.01	352 0.07	340 0.14	336 0.17
BKS	139 0.6	180 0.88	166 0.89	153 0.89	139 0.90	133 0.90
BLA	— —	560 0.38	537 0.42	515 0.45	488 0.48	476 0.50
CMB	— —	138 0.36	125 0.43	115 0.49	102 0.56	98 0.59
COR	— —	203 0.26	193 0.30	184 0.35	173 0.39	168 0.41
ELK	150 0.5	287 0.47	243 0.52	211 0.56	179 0.60	168 0.61
FVM	— —	373 0.12	359 0.17	346 0.21	328 0.26	321 0.28
GOL	— —	234 0.53	221 0.56	209 0.58	195 0.61	190 0.62
JAS	— —	149 0.66	134 0.69	123 0.71	109 0.74	104 0.75
JCT	— —	456 0.72	428 0.74	402 0.76	371 0.78	359 0.79
KNB	142 0.4	218 0.79	181 0.81	157 0.82	132 0.82	124 0.83
LAC	097 0.7	189 0.53	164 0.59	145 0.65	124 0.71	117 0.73
LON	— —	202 0.58	194 0.60	186 0.62	176 0.65	172 0.66
LUB	— —	423 1.57	393 1.55	367 1.52	337 1.49	325 1.48
MNV	093 0.6	— —	— —	140 0.24	110 0.45	100 0.52
OGD	— —	664 0.48	637 0.52	611 0.55	577 0.58	564 0.59
SCP	— —	520 0.04	514 0.13	506 0.20	491 0.29	484 0.32
WES	— —	1205 1.02	1114 1.01	1035 1.01	942 1.00	908 1.00

Conclusions and Recommendations

For Pahute Mesa, where the Q_0 (and η) values derived by the coda-Q method are believed to be appropriate to account for the path attenuation, the L_g–m_b bias is estimated as 0.34 m.u. This value happens to be in agreement with the published m_b bias caused by the different upper mantle absorption in the eastern and western U.S. Thus this Pahute Mesa exercise might be in support of Nuttli's assertion that the same absolute L_g magnitude scale can be used for both eastern and western U.S. However, this is probably an exception rather than a general rule.

Previously only a handful number of stations was analyzed by Nuttli (1986a) and Patton (1988) with the coda-Q method. We now have 20 "calibrated" stations for L_g phases from Pahute Mesa. However, the proposed calibration is subject to the choice of the "bias" parameter which is not quite obvious to decide. This indeterminacy of L_g absolute magnitude scale could be a persistent issue encountered in every attempt of using seismic phases like L_g which is not as transportable as M_S. A (new) feature of this simultaneous inversion code is that it offers a suite of solutions to choose from. If only a "relative" L_g scale is of interest, then setting the bias to an arbitrary value, say 0, would suffice. In any case, the simultaneous inversion can calibrate a suite of stations in a more consistent manner, which is the typical advantage of GLM inversion schemes.

The same procedure gives a L_g–m_b bias of 0.26 m.u. for northern Novaya Zemlya explosions. Since it is known that L_g blockage does occur for paths crossing the Barents Shelf, there remains a question whether it is appropriate to use Nuttli's Q_0 values to constrain our selection of the bias term.

Based on the t^* study, it has been suggested that the upper mantle of Novaya Zemlya is similar to that of Semipalatinsk. Thus 0.26 m.u. is expected to be the "upper bound" of the bias term. It seems that, however, the Q_0 values based on the coda-Q method can provide a Q map which is qualitatively consistent with that based on the time-domain computation. The L_g blockage at Barents Shelf could have caused the predominant frequency of L_g waves to shift in a way very similar to that due to a stronger anelastic attenuation. Consequently, Nuttli's Q_0 values may be biased low, yielding an over-compensation of the attenuation effect in computing his Novaya Zemlya m_{L_g}. This conjecture can be tested with numerical modeling experiments using LFD method (*e.g.*, Jih, 1994).

If many stations are deployed along the same azimuth from the shot, *i.e.*, if a profile is available, then the coda-Q results can be verified independently using the inter-station spectral ratios. This could be included in future field experiments.

References

Baumstark, R. R. and R. A. Wagner (1994). Measurements and statistics of underground nuclear explosions, *Report TBE-4617-1 / TGAL-94-01*, Teledyne Brown Engineering, Arlington, VA.

Blandford, R. R., and R. H. Shumway (1982). Magnitude:yield for nuclear explosions in granite at the Nevada Test Site and Algeria: joint determination with station effects and with data containing clipped and low-amplitude signals, *Report VSC-TR-82-12*, Teledyne Geotech, Alexandria, VA.

Bunch, J. R. and D. J. Rose (eds.) (1976). *Sparse Matrix Computations*, Academic Press, New York, N.Y.

Dempster, A. P., N. M. Laird, and D. B. Rubin (1977). Maximum-likelihood estimation from incomplete data via the EM algorithm, *J. Roy. Statist. Soc. B.*, **39**, 1-38.

Forsythe, G. E., M. A. Malcolm, and C. B. Moler (1977). *Computer Methods for Mathematical Computations*, Prentice Hall, Englewood Cliffs, NJ.

Golub, G. H. and C. F. Van Loan (1983). *Matrix Computations*, John Hopkins University Press, Baltimore, MD.

Jih, R.-S. (1992). Simultaneous inversion of explosion size and path attenuation coefficient with crustal phases. *Report TGAL-92-11*, Teledyne Geotech, Alexandria, VA.

Jih, R.-S. (1994). Numerical modeling of crustal phase propagation in irregular waveguides, in *Proceedings of 16th PL/AFOSR Seismic Research Symposium* (J. Cipar, J. Lewkowicz, and J. McPhetres eds.), *Report PL-TR-94-2217*, Phillips Laboratory, Hanscom AFB, MA, pp. 173-181 (ADA284667).

Jih, R.-S. and R. R. Baumstark (1994). Maximum-likelihood network magnitude estimates of low-yield underground explosions, *Report TBE-4617-3 / TGAL-94-02*, Teledyne Brown Engineering, Arlington, VA.

Jih, R.-S. and C. S. Lynnes (1993). Studies of regional phase propagation in Eurasia. *Report PL-TR-93-2003 (=TGAL-93-01)*, Phillips Laboratory, Hanscom AFB, MA (ADA262801).

Jih, R.-S. and R. H. Shumway (1989). Iterative network magnitude estimation and uncertainty assessment with noisy and clipped data, *Bull. Seism. Soc. Am.*, **79**, 1122-1141.

Nuttli, O. W. (1980). The excitation and attenuation of seismic crustal phases in Iran, *Bull. Seism. Soc. Am.*, **70**, 469-485.

Nuttli, O. W. (1986a). Yield estimates of Nevada Test Site explosions obtained from seismic L_g waves,

J. Geophys. Res., **91**, 2137-2151.

Nuttli, O. W. (1986b). L$_g$ magnitudes of selected East Kazakhstan underground explosions, *Bull. Seism. Soc. Am.,* **76,** 1241-1251.

Nuttli, O. W. (1988). L$_g$ magnitudes and yield estimates for underground Novaya Zemlya nuclear explosions, *Bull. Seism. Soc. Am.,* **78,** 873-884.

Patton, H. J. (1988). Application of Nuttli's method to estimate yield of Nevada Test Site explosions recorded on Lawrence Livermore National Laboratory's digital seismic system, *Bull. Seism. Soc. Am.,* **78,** 1759-1772.

Spedicato, E. ed. (1991). *Computer Algorithm for Solving Linear Algebraic Equations: the State of the Art, NATO ASI Series,* Springer-Verlag, Berlin, Germany.

Tewarson, R. P. (1973). *Sparse Matrices,* Academic Press, New York, NY.

Appendix A. Joint Inversion Method: Basic Concepts

Consider the case of m explosions recorded at some or all of n stations. For simplicity, we assume that these m explosions are detonated in the same test site for the moment. The case of multiple test sites will be discussed later. The linear model for L_g phases can then be written as

$$E(i) - \gamma(j)(\Delta(i,j)-10km)/\ln(10) + \varepsilon(i,j) = Y(i,j) ,$$ [3]

$$\text{where } Y(i,j) \equiv 4.0272 - \text{Bias} + \log A(i,j) + \frac{1}{3}\log(\Delta(i,j)) + \frac{1}{2}\log[\sin(\frac{\Delta(i,j)}{111.1(km/deg)})] .$$

Once the amplitudes and the locations of the events (and hence the epicentral distances, Δ) are available, Y would be completely known. Only the event sizes (E) and the path-specific coefficients of anelastic attenuation (γ) are the unknown parameters to be determined. The obscuring errors ε are assumed to be uncorrelated and to belong to the same probability distribution, namely a common Gaussian distribution with zero mean and variance σ^2.

If all the events are clustered in a small region, then the epicentral distances $\Delta(i,j)$ would be almost identical for a given station j. In this case, our model (Equation [3]) is a special case of a more general linear system:

$$E(i) + S(j) + \varepsilon(i,j) = Y(i,j) , \text{ for } i = 1,..., m ; j = 1,..., n .$$ [4]

which can be expressed in a matrix formulation:

$$H X + e = Y ,$$ [5]

where **H** is the design (or observation) matrix. X and Y are the column vectors of unknowns and observations, respectively. The standard least-squares [LS] solution (viz, the one that minimizes the *residual sum of squares:* RSS $\equiv (Y - H\hat{X})' (Y - H\hat{X}))$ to *any* linear system with a general form like Equation [5] is

$$\hat{X}_{LS} \equiv (H'H)^{-1}H'Y ,$$ [6]

where H' is the transpose of **H**. This least-squares estimator has many optimality properties. For instance, it is unbiased, and it gives minimum variance within the class of linear unbiased estimators. Furthermore, $\hat{X}_{LS}$ is also the *Maximum-Likelihood Estimate* [MLE] under the Gaussian assumption. It is straightforward to compute the uncertainty by using Var$[\hat{X}_{LS}] \equiv$ the diagonal of $\sigma^2(H'H)^{-1}$, which is simply

scaling the variance of the random perturbations by the number of observations associated with each unknown.

In our case, however, the matrix $H'H$ in Equation [6] is singular, and hence the least-squares theory can not be applied immediately unless the linear system of [4] is modified somewhat. Perhaps the easiest way to illustrate the indeterminacy due to the singularity of the matrix $H'H$ is that given any set of solution to [4], we can always obtain yet another set of solution by adding a constant to all event magnitudes, $E(i)$, $i = 1,..., m$, and subtracting the same constant from each station term $S(j)$ (Jih and Shumway, 1989). Alternatively, we can verify that the matrix $H'H$ has zero determinant with linear algebra packages such as LINPACK, EISPACK, or LAPACK. In this study, however, a formal proof is presented below. Without loss of generality, we can assume that each of the m events is fully recorded at all n stations, then

$$X \equiv [E_1, E_2, E_3, \ldots, E_m, S_1, S_2, \ldots, S_n]', \quad H'H = \begin{bmatrix} n \cdot I_m & 1_{mxn} \\ 1_{nxm} & m \cdot I_n \end{bmatrix}$$

where I_m is the identity matrix of order m, and all elements of the m-by-n matrix 1_{mxn} are 1. For instance, if $m = 3$ and $n = 2$, then

$$H'H = \begin{bmatrix} 2 & 0 & 0 & 1 & 1 \\ 0 & 2 & 0 & 1 & 1 \\ 0 & 0 & 2 & 1 & 1 \\ 1 & 1 & 1 & 3 & 0 \\ 1 & 1 & 1 & 0 & 3 \end{bmatrix}$$

which is a *doubly-bordered band diagonal* sparse matrix (Tewarson, 1973; Press *et al.*, 1988). After exactly n row operations eliminating the lower-left submatrix, 1_{nxm}, the determinant of $H'H$ can be computed (up to a multiplicative constant) as that of

$$\begin{bmatrix} I_m & (\frac{1}{n})_{nxm} \\ 0_{nxm} & P_n \end{bmatrix} \qquad\qquad [7]$$

where P_n is a square matrix of order n with $\frac{-m}{n}(n-1)$ on the diagonal and $\frac{-m}{n}$ elsewhere. For $m = 3$ and $n = 2$, [7] becomes

$$\begin{bmatrix} 1 & 0 & 0 & 0.5 & 0.5 \\ 0 & 1 & 0 & 0.5 & 0.5 \\ 0 & 0 & 1 & 0.5 & 0.5 \\ 0 & 0 & 0 & 1.5 & -1.5 \\ 0 & 0 & 0 & -1.5 & 1.5 \end{bmatrix}$$

It suffices to examine the determinant of this P_n, or, equivalently, to check the determinant of a square matrix of order n with n-1 on the diagonal and -1 elsewhere:

$$\begin{bmatrix} n-1 & -1 & -1 & \cdot & -1 \\ -1 & n-1 & -1 & \cdot & -1 \\ -1 & -1 & n-1 & \cdot & -1 \\ \cdot & \cdot & \cdot & \cdot & \cdot \\ -1 & -1 & -1 & \cdot & n-1 \end{bmatrix}$$

It is straightforward to prove that, by *mathematical induction,* this matrix has zero determinant for any n ≥ 2. Thus the matrix $H'H$ in our linear model is always singular regardless how good the observed amplitudes/magnitudes, Y, might be. We therefore need an extra boundary condition to constrain our linear model for a unique solution. The most commonly adopted approach in teleseismic magnitude

determination is to have all station terms sum up to zero. This implies that larger events would tend to be unchanged whether we apply the station corrections or not, and hence the bulletin magnitudes of larger events published by ISC and NEIC can be regarded as more or less unbiased. This extra constraint can be incorporated into [4] by replacing all S(n) by $-\sum_{j=1}^{n-1} S(j)$. It not only reduces the number of unknowns by one, but, more importantly, regularizes the whole linear system to make H′H invertible. However, this is not the only plausible constraint. We can impose the extra constraint on E(i) instead, or, even impose the constraint on *some* selected stations.

A first glance of Equation [4] might lead to a conclusion that the inversion scheme for crustal phases is identical to that for teleseismic phase, and hence the algorithms and the constraints suitable for the teleseismic data reduction would be appropriate for the regional case as well. This is not the case. There are generally fewer regional stations available for inversions with crustal phases. The implicit assumption that the recording stations are evenly (and randomly) distributed may not be valid. Some S(j) terms may carry more weight due to the larger corresponding $\Delta(\cdot,j)$. This implies that the zero-sum assumption on the S terms may not be appropriate for the L_g inversion. In fact, the S term in Equation [4], by definition, can not have zero sum across the network because both γ and Δ in Equation [3] are always non-negative.

Appendix B. Joint Inversion Method: The Iterative Procedure

Once a constraint has been chosen, the inverse matrix of H′H in Equation [6] can be computed with matrix factorization (such as *Singular Value Decomposition,* [SVD]) or *Gaussian elimination* method. Numerical algorithms of these types are called *direct methods.* Direct methods can be impractical if H′H is large. In that case, iterative methods are often the only possible method of solution, as well as being faster and more accurate than Gaussian elimination and matrix factorization. The largest area for the application of iterative methods is that of the linear systems arising in the numerical solution of partial differential equations. Systems of orders 10,000 to 100,000 are not unusual in aerospace sciences, although the majority of the coefficients of the systems are typically zeros.

The basic idea of iterative methods is that one starts with a trial solution vector $X^{(0)}$ and carries out some process using H, Y, and $X^{(0)}$ to get a new vector $X^{(1)}$. Then one repeats. At the k stage, one uses the iterative process to get $X^{(k)}$ from H (or H′H), Y, and $X^{(k-1)}$. The specific algorithm for our problem is summarized in five steps:

Step 0
    Set initial value of $\gamma(j)$ for j = 1,..., n.
Step 1
    Compute event m_{L_g} , E(i), for i = 1,..., m:

$$E(i) = \frac{1}{\#(j)} \sum_j [Y(i,j) + \gamma(j)[\Delta(i,j) - 10km]/\ln(10)] \,,$$

where #(j) is the number of stations used in the summation.
Step 2
    Adjust E(i), i = 1,..., m, with the desired boundary condition.
Step 3
    Compute the path-specific coefficient of anelastic attenuation, $\gamma(j)$, for j=1,..., n:

$$\gamma(j) = \ln(10)\sum_i [\ E(i) - Y(i,j)\ ]/\sum_i [\Delta(i,j) - 10 km]\ .$$

Step 4

Fill in missing paths (i,j) with predicted pseudo-observations:

$$Y(i,j) \equiv E(i) - \gamma(j)(\Delta(i,j) - 10 km)/\ln(10)\ .$$

Step 5

Repeat steps [1]-[4] to update E and γ till convergence.

Although an arbitrary guess of γ will do at Step 0, picking an initial γ close to the average across the whole area of interest would speed up the convergence. The choice of the extra boundary condition (at Step 2) is very flexible. Constraining the mean of all event m_{L_g} seems to perform extraordinarily well, however. Note that the pseudo-observations predicted at Step 4 are treated as "good" observations at steps 1 and 3 except during the first iteration loop.

The iterative procedure described above is a special case of a general algorithm known variously as the *Gaussian-Seidel* method, the *Liebmann process,* or the *method of successive displacements* (Bunch and Rose, 1976; Forsythe *et al.*, 1977; Golub and Van Loan, 1983; Spedicato, 1991). The major difference between this method and that of *Gaussian-Jacobi (viz.,* the *simultaneous displacement* method) is that we solve for one component (viz, E(i) or $\gamma(j)$) of the new vector X using for each other component of X its most recently computed value, whereas Gaussian-Jacobi method updates all unknown parameters simultaneously at the end of each iteration loop. In our case, Gaussian-Seidel method converges faster than does Gaussian-Jacobi method. The first application of this iterative technique to the magnitude determination problem was Blandford and Shumway (1982), although the methodology was identified as the E-M [Expectation-Maximization] algorithm (Dempster *et al.*, 1977) following the convention in the statistical community.

The advantage of our multi-event joint inversion scheme, as compared to the simple network averaging for each individual event that Nuttli (1986ab, 1988) used, is that we can have a more consistent network for all events. By "consistent" it means that the joint inversion procedure provides the best approximation to the network-averaged values that would have been obtained if all the events were recorded at every station in the network. This advantage may not be very obvious in using direct methods such as SVD or Gaussian elimination. However, it would become quite natural as revealed by Step 4 of our iteration scheme.

High-Frequency Shear Wave Generation at Pre-existing Cracks[1]

R.-S. Jih and A. M. Dainty

Phillips Laboratory, PL/GPE

Hanscom AFB, MA 01731-3010

Recent observational studies indicate that, relative to decoupled explosions, tamped explosions tend to have a larger high-frequency L_g /P ratio. Discrimination using such ratios is promising, and yet little is known about the basis for this discriminant. Improved fundamental understanding of the reasons this discriminant may be successful is desired. A plausible explanation offered by Blandford (1995) is that tamped explosions generate more high-frequency S waves due to the cracks in the source region.
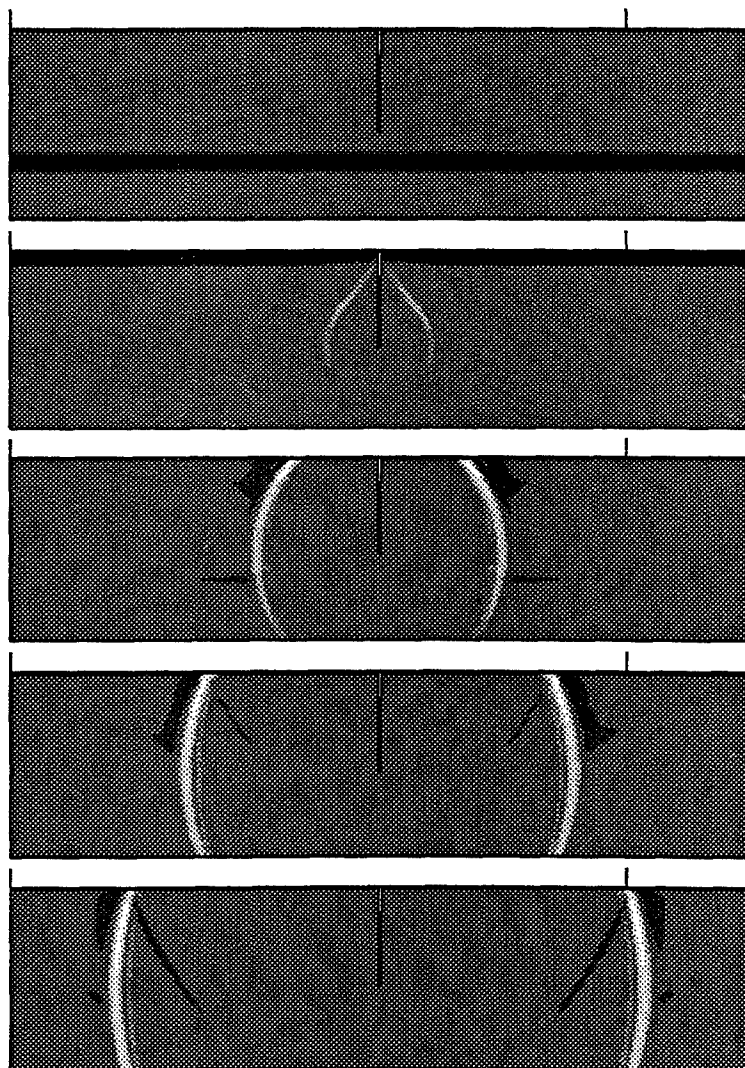
Simple linear finite-difference [LFD] calculations have been conducted to test the hypothesis whether a non-growing radial fracture can cause strong P-to-S scattering in the source region. In this experiment, the free-surface boundary (*i.e.*, von Neumann) conditions (*cf.*, Jih *et al.*, 1988) were actually applied to the crack walls. The needle tip radiates S waves as if it was a point shear source. Thus the *"cracking theory"* seems to be able to provide a physical justification for the discrimination using high-frequency S/P ratios. Follow-up research shall utilize both linear and non-linear calculations to explore the seismic coupling near the source, where pre-existing cracks nucleate new fractures which granulate the rock. Results obtained under several federally funded projects shall be integrated as well.

THE EFFECT OF NEAR-RECEIVER SCATTERING ON SEISMOGRAMS

Lane R. Johnson

Center for Computational Seismology, Lawrence Berkeley Laboratory,
and Seismographic Station, University of California,
Berkeley, California 94720

ABSTRACT

In the study of physical processes involved in the generation and propagation of seismic waves at near and regional distances, it is important to distinguish those features on the seismogram which contain primary information concerning the source and those features which are due to noise. In this study the data recorded from the Non-Proliferation Experiment (NPE) are used to study the possibility that signal generated noise caused by scattering of elastic waves near the receiver may contribute significantly to the recorded waveforms of the direct P wave. Two different examples of anomalous waveforms, the vertical component of free-field recordings and the transverse component of surface recordings are investigated.

The results of this study indicate that elastic wave scattering near seismic receivers can have a significant effect upon recorded waveforms, with effects as large as 50% of the primary wave easily achieved. The scattering effect is complex, with strong directional, frequency, and near-field effects. A better understanding of these scattering effects could lead to improved methods of siting seismic receivers for the purposes of reducing the signal-generated noise on seismograms.

OBJECTIVE

The general objective of this research effort is the detection and discrimination of underground explosions through the study of radiated seismic waves. Particular emphasis is on the study of physical processes in the source region through the development of improved models for the generation and propagation of elastic waves. Such models are tested by the collection and analysis of broad-band seismic data at near and regional distances. The present paper reports on one phase of the research effort which is concerned with the reliability of source parameters which are inferred from the analysis of waveform data. The near-source seismic data from the Non Proliferation Experiment (NPE) provide an opportunity to check one aspect of this general problem.

RESEARCH ACCOMPLISHED

Introduction

The ability to extract useful information about seismic sources from seismic waveform data is limited by the amplitude and characteristics of the noise present on the seismograms. A type of noise which is particularly treacherous in this respect is that which is signal generated, as it typically has the transient character and frequency content which can easily be mis-interpreted as due to some property of the source.

This study is concerned with the signal generated noise which is contributed by scattering of elastic waves near the receiver. Such scattering will occur whenever the waves encounter lateral heterogeneity in earth properties, and, unfortunately, the shallow crust of the earth where most seismic receivers are located is a region of strong heterogeneity. The question to be investigated is whether the amplitude and frequency content of these scattered waves are sufficient to represent a significant source of noise on the seismograms used to study seismic sources.

Characteristics of seismic scattering

The existence of scattered energy on seismograms is well established and provides evidence of earth heterogeneity on a broad range of length scales. The codas on seismograms are the most obvious examples of scattering and also the most commonly analyzed effects of scattering. However, it is apparent that energy represented by codas was originally derived from primary waves, and thus these primary waves must also be affected by the scattering. The present study is primarily concerned with the effects of scattering upon these primary waves.

While the effects of scattering are typically analyzed by treating the scattering as a stochastic process, the objectives of the present study require a more deterministic approach. This causes a considerable increase in the difficulty of the analysis, as several different types of effects have to be considered simultaneously. These effects are discussed in considerable detail in the papers by Korneev and Johnson (1993a, 1993b), and Gritto et al. (1995), so they will only be briefly summarized here. The strong directional effects of scattering are usually illustrated by scattering diagrams, which show, depending upon frequency, various combinations of forward scattering, backward scattering, and scattering at oblique angles. The strong frequency dependence of scattering is usually illustrated by scattering cross-sections and can be classified in terms of ranges where Rayleigh, Mie, and ray scattering are dominant. Scattering is a very efficient method of converting wave types, with P to S conversions generally stronger than S to P conversions. Finally, it is important to recognize that scatterers can be viewed as secondary sources in the sense that they have different radiation patterns and different distance dependencies for far-field and near-field parts of the scattered field.

In the analysis of scattering effects there is a choice between using exact solutions for approximate geometries and using approximate solutions for more realistic geometries. The first choice has been selected in the present study, where the canonical problem of scattering from a spherical inclusion is used to illustrate some of the effects of scattering. It is important to point

out that the objective of the study is not to solve an inverse problem for the determination of the location and strength of the heterogeneities causing the scattering, as the amount of available data are insufficient for this purpose. Rather, the intent is to investigate whether the scattering effects of credible heterogeneities are consistent with some of the anomalous effects observed on seismograms.

Source of data

The Non-Proliferation Experiment (NPE) provided an excellent data set with which to test some of the critical issues concerning the effects of near-receiver scattering. This experiment consisted of detonating 1.1 kt of chemical explosive at a depth of 389 meters within Rainier Mesa at the Nevada Test Site in September of 1993. The resulting ground motions were well recorded by a large number of instruments, including free-field gauges in the distance range of 100 to 1100 meters at shot level and surface gauges at epicentral distances of 600 to 2200 meters. The data analyzed in this study came from several different sources, including the Lawrence Livermore National Laboratory, the Los Alamos National Laboratory, Southern Methodist University, the Lawrence Berkeley National Laboratory, the University of California at Berkeley, and the Defense Nuclear Agency.

The fact that the NPE was a very well-controlled experiment which produced large amounts of high-quality seismic data provides an opportunity to isolate some of the scattering effects. Good estimates of both the source function and the velocity structure of the surrounding region are available, making it possible to model most of the primary features that were recorded on the seismograms. However, there are a few features of the seismograms which are not easily explained by simple source and propagation effects, and it is these features which have been investigated in terms of their possible scattering origin.

Analysis of free-field data

Figure 1 shows part of the tunnel complex which was used to emplace and record the NPE explosion. The tunnels are horse-shoe shaped and the larger ones have a nominal diameter of about 6 meters. Free-field recordings of ground motion were obtained with three-component accelerometers grouted into small drilled holes at about 1 tunnel diameter below the tunnel floor. Given the facts that the geological layers are approximately horizontal and relatively homogeneous (Baldwin et al., 1994) and that major discontinuities such as the free surface and basement are some distance away, it would appear that these instruments should produce accurate recordings of the free-field displacements caused by the explosion. However, it remains to be determined whether elastic waves scattered from the tunnel could have a significant effect upon the recorded seismograms.

Figure 2 illustrates the three components of ground motion recorded at station TM07 at a horizontal distance of 228 meters and about 5 meters below the center of the NPE explosion. Based solely upon this geometry, one would expect the ground motion to be almost entirely radial, which is clearly not the case. This study has concentrated upon explaining the anomalous motion on the vertical component, which for station TM07 is about 37% of the radial motion. Two possible explanations have been considered, one being the refraction of the direct P wave by a velocity gradient near the depth of the explosion, and the other being the scattering of the direct P wave by the tunnel.

The proper method of modeling the tunnel complex shown in Figure 1 for the purposes of the scattering calculations is not obvious. Station TM07 was chosen for analysis primarily because the relationship between the source, receiver, and tunnel complex appeared to be the most simple for this station. However, even in this case it is clear that a single infinite cylinder is not a good approximation to the situation at station TM07. Instead, the tunnels near station TM07 have been modeled by summing the effects of a series of overlapping spheres, with 13 different spheres
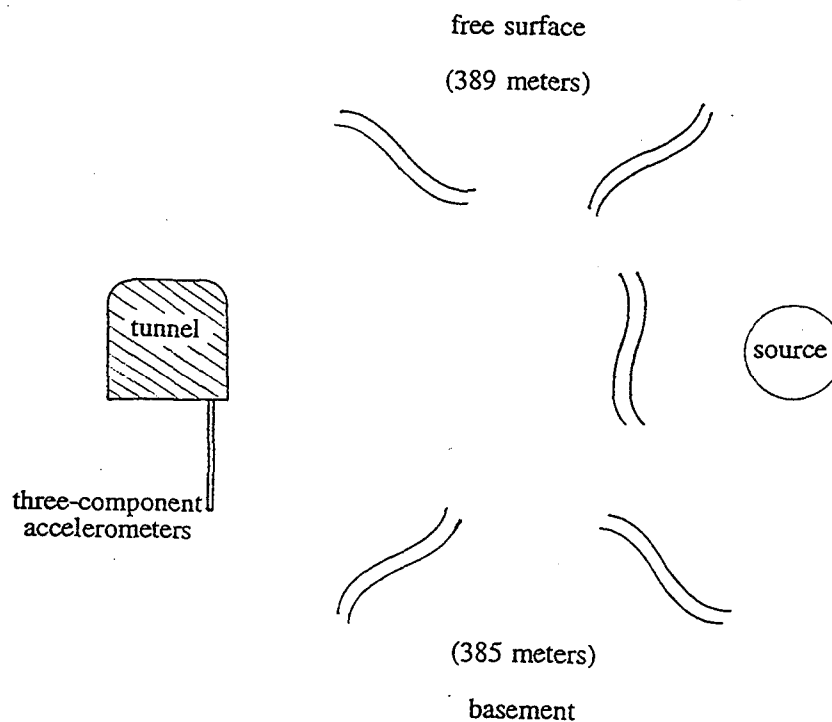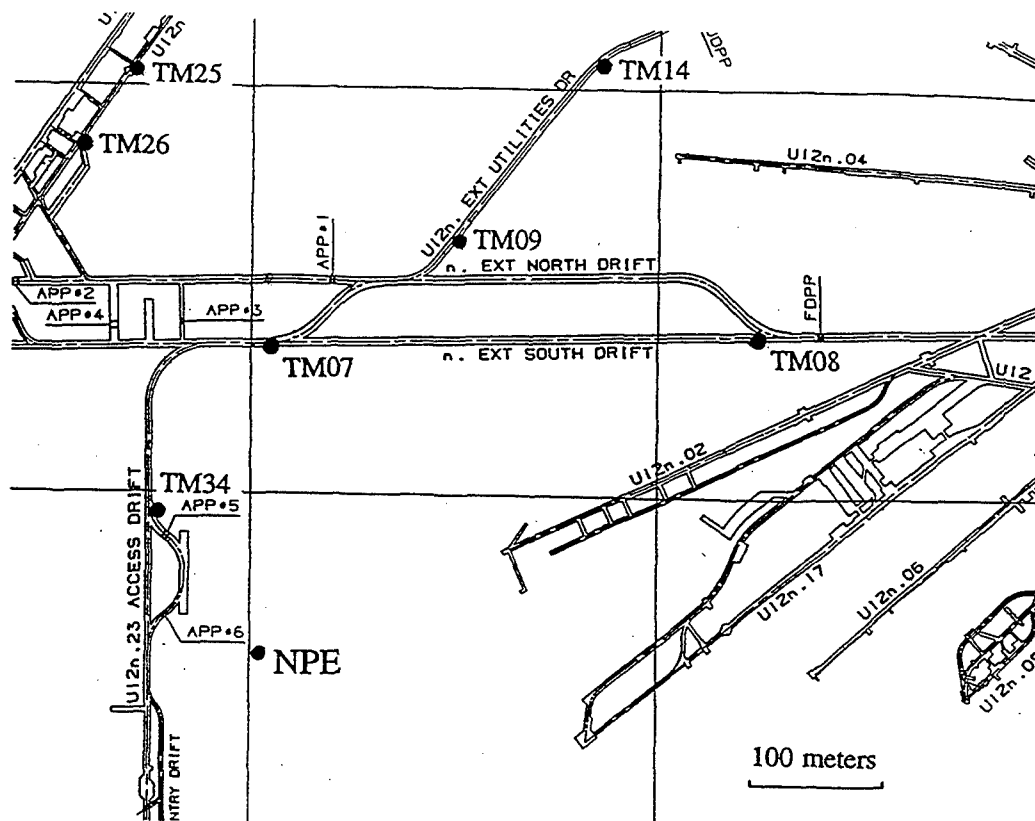
Figure 1. The emplacement geometry for the free-field part of the NPE experiment. The upper part of the figure shows the tunnel complex at a depth of about 390 meters in the vicinity of the NPE explosion. The lower part is a sketch of how the gauges were placed in holes drilled from the bottom of the tunnels.

424

used to model the three tunnel elements within about 20 meters of the station. With this approximation it is assumed that more distant parts of the tunnel complex do not have a significant effect and that multiple scattering between the spheres is not important. Some preliminary numerical calculations indicated that these approximations are reasonable, but more work on this aspect of the problem is definitely required.

The middle and lower parts of Figure 2 show the comparison between the observed and calculated seismograms for station TM07. The traces labeled "structure" were obtained by assuming a model for velocity structure that had a positive velocity gradient of approximately 4 km/sec/km for the P velocity in the depth range of the explosion. While this is a strong velocity gradient, it is not completely inconsistent with the available information concerning the geological structure of Pahute Mesa. The traces labeled "scattering" were obtained by only considering the scattering effects of the tunnel complex, as outlined in the previous paragraph. The structure and scattering calculations both produce results for an impulse source and thus must be convolved with a source time function in order to compare with the observational data. Here it was assumed that the radial component of motion was a reasonable approximation to the free field motion, and so the time function on this component was used as the source time function. Thus the agreement in Figure 2 for the radial accelerations is to be expected, although the structure calculations do not agree as well as do the scattering calculations. The results for the vertical accelerations in Figure 2 are the primary interest, as they illustrate that both structure and scattering have the potential to explain an appreciable amount of the anomalous motion on this component, with the maximum being 46% of the observed for the structure and 80% for the scattering. As far as agreement in waveforms, the structure result appears to have a generally lower frequency content than the observed, while the scattering result has somewhat higher frequencies.

Figure 3 illustrates another method of investigating the relative contributions of structure and scattering. The ratio of vertical to radial components in the frequency domain for the structure calculations is larger at low frequencies and smaller at high frequencies than the observed ratio. This ratio for the scattering calculations agrees quite well with the general trend of an increase with frequency which is contained in the observed data, providing strong evidence that scattering effects are a significant part of the anomalous motion observed on the vertical component.

The results in Figure 3 show that the scattering effect of the tunnel can be significant for instruments that are emplaced only one tunnel diameter away from the tunnel. It is worth noting that if the effective size of the tunnel were actually greater than that used in the scattering calculations, then the amplitude of the scattered wave on the vertical component would be increased and its frequency content decreased, producing a better agreement with the observations. This could possibly be due to the fact that the total lengths of the tunnels were not completely modeled or that the excavation of the tunnel has caused a change in material properties in its immediate vicinity. It is should also be noted that the most likely explanation is a combination of structure and scattering effects, but this is a much more complicated calculation because scattering effects have to be calculated for a variety of waves arriving at the recording site.

Analysis of surface data

Another example of features on seismograms which are not easily explained by simple source and propagation effects was produced by recordings of the NPE at the surface. Figure 4 shows the radial and transverse components of ground acceleration which were observed at a north-south linear array which was located about 600 meters west of the NPE epicenter. The spacing between the recording sites was about 100 meters. The instruments were buried in soil about 0.3 meters below the surface of Rainier Mesa. The vertical component is not shown here, but its general appearance is very similar to the vertical with slightly smaller amplitudes, indicating waves arriving at an angle of about 45 degrees with respect to the surface normal. The radial accelerations in Figure 4 show a general similarity across the array for the initial waveform, as
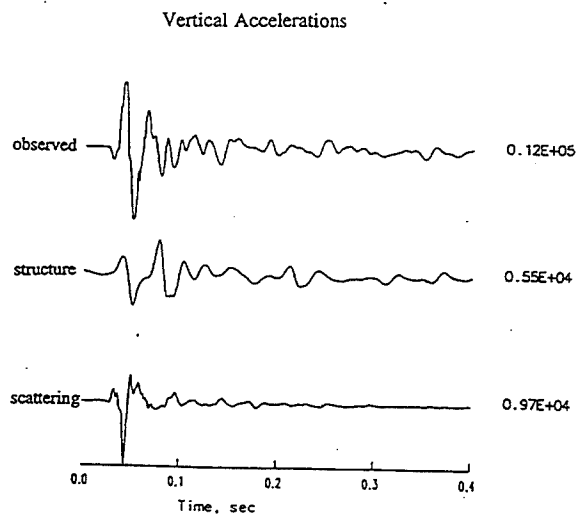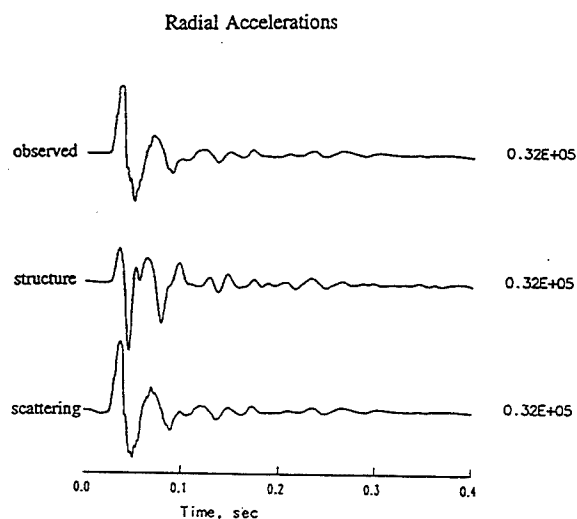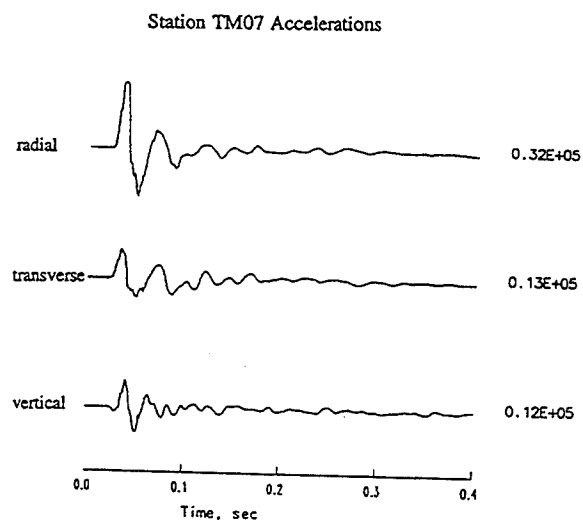
Figure 2. The results of the analysis for the free-field data recorded at station TM07 at a distance of 228 meters from the NPE explosion. The top panel shows the observed accelerations, with the numbers on the right being maximum accelerations in units of cm/sec^2. The middle and bottom panels show a comparison between observed and calculated accelerations for the radial and vertical components, with the structure calculation representing the effects of a velocity gradient in the vicinity of the explosion and the scattering calculation representing the effects of scattering from the tunnel.
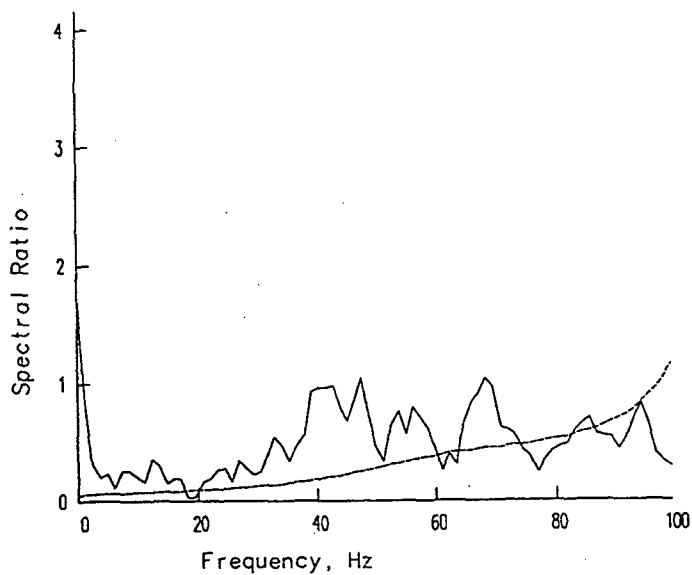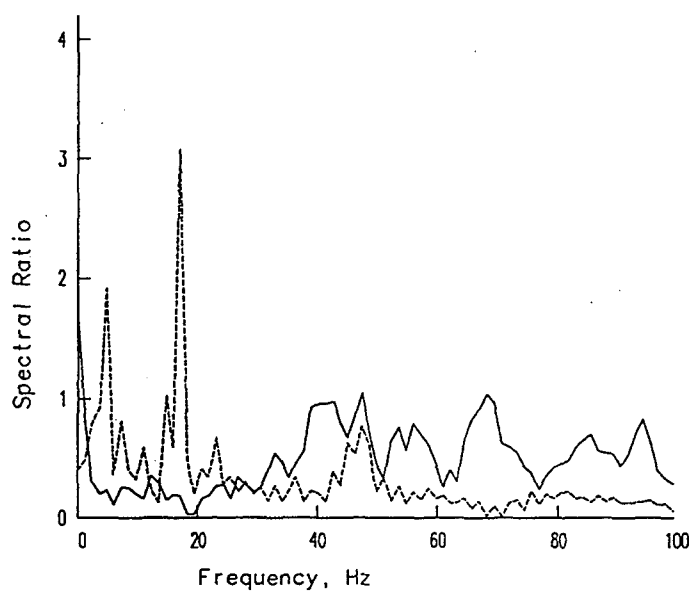
Figure 3. Spectral ratios of the vertical to radial components for the free-field station TM07. In both the upper and lower parts the solid line is for the observed data, while the dashed line is the calculated ratio for the effects of structure in the upper part and for the effects of scattering from the tunnel in the lower part.

one would expect for these closely spaced recording sites. However, the transverse components of acceleration are rather anomalous, as there should be no high-frequency transverse components of motion arriving with the P velocity from an explosive source. Also note that these transverse motions can change considerably over distances of 100 meters, which is quite different from the situation with the radial and vertical components.

The upper part of Figure 5 shows the three components of acceleration recorded at station UCB120. The maximum acceleration on the transverse component is 60% of that on the radial component and the frequency component on the transverse component appears to be significantly higher than on the other components. This higher frequency content is suggestive of a scattering origin, so the possibility that the motion on this transverse component was due to scattering was investigated. The fact that the motion on the transverse component begins simultaneously with that on the radial and vertical components suggests that the scattering object must be near the receiver. However, the precise location and properties of the scattering object or objects can not be determined with the available data, so only calculations for plausible situations are possible. The surface of Rainier Mesa is a relatively flat tuff unit partially covered by weathered rock and soil. It was hypothesized that the scattering was caused by an interface between rock and soil and modeled by a spherical boulder of unweathered rock 30 meters in radius surrounded by soil. While a spherical boulder was used for the calculations, this could also be considered as an approximation to an uneven boundary between weathered and unweathered material or to a topographic protrusion of unweathered material. Free surface effects were not included in these calculations.

The middle and lower parts of Figure 5 show the results of such scattering calculations for station UCB120 with the boulder placed 26 meters from the station. As with the free-field calculations, the waveform on the radial component was used as the source time function to be convolved with the results of the scattering calculations. The maximum amplitude on the transverse component for this scattering calculation is about 50% that which was observed, but the frequency content and general appearance of the records is quite similar. The amplitude of the scattered wave on the transverse component is somewhat arbitrary, as it depends strongly upon the distance to the scatterer. This is illustrated by similar calculations that were were performed for station UCB140, which has its observed waveforms displayed in Figure 6. The scattering calculations are shown in the middle and lower parts of Figure 6, where the scatterer is now located only 10 meters away from the station. The maximum amplitude on the transverse component contributed by the scattering is now even larger than observed, with the same good agreement with respect to waveforms and frequency content that was noted in Figure 5. It should be pointed out these results were obtained for a single scatterer, whereas a more realistic situation would be a number of scatterers having different properties and located at different distances. While these calculations were performed for a geometry which is likely to be a gross over-simplification of the actual situation that exists on Rainier Mesa, it seems clear that scattering of elastic waves near the receiver is capable of explaining the anomalous arrivals on the transverse component which arrive at the time of the direct P wave.

Radial Accelerations

UCB100

UCB120

UCB140

UCB160

UCB180

UCB200

AVERAGE

] 1 g

0   1   2   3   4

Time, sec

Transverse Accelerations

UCB100

UCB120

UCB140

UCB160

UCB180

UCB200

AVERAGE

] 1 g

0   1   2   3   4

Time, sec
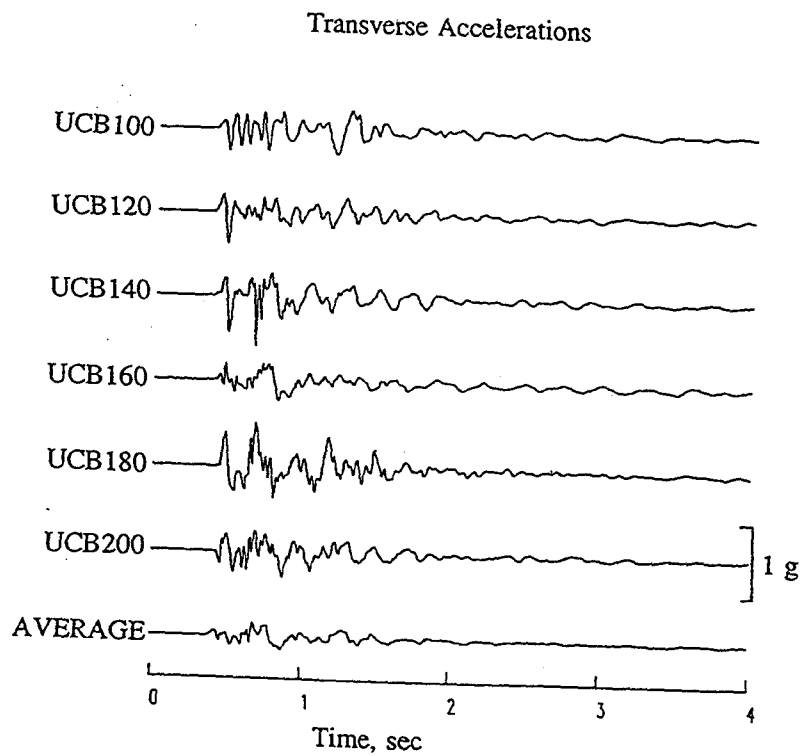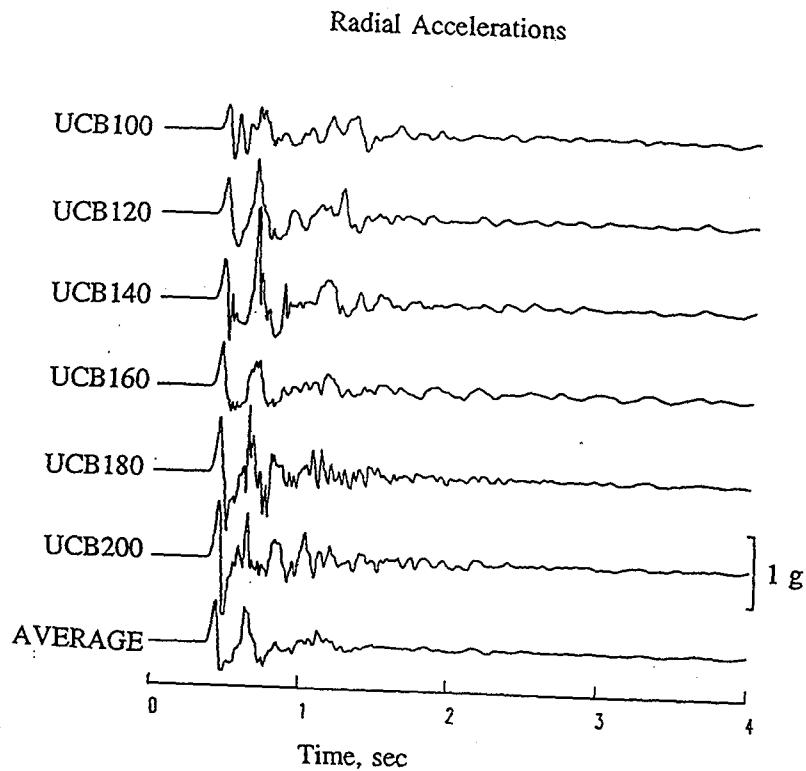
Figure 4. Accelerations recorded on the surface of Rainier Mesa from the NPE explosion on a linear north-south array located about 600 meters west of the epicenter.

radial

0.79E+03

transverse

0.47E+03

vertical

0.66E+03

Time, sec

Radial Accelerations

observed

0.79E+03

scattering

0.79E+03

Time, sec

Transverse Accelerations

observed

0.47E+03

scattering

0.24E+03

Time, sec
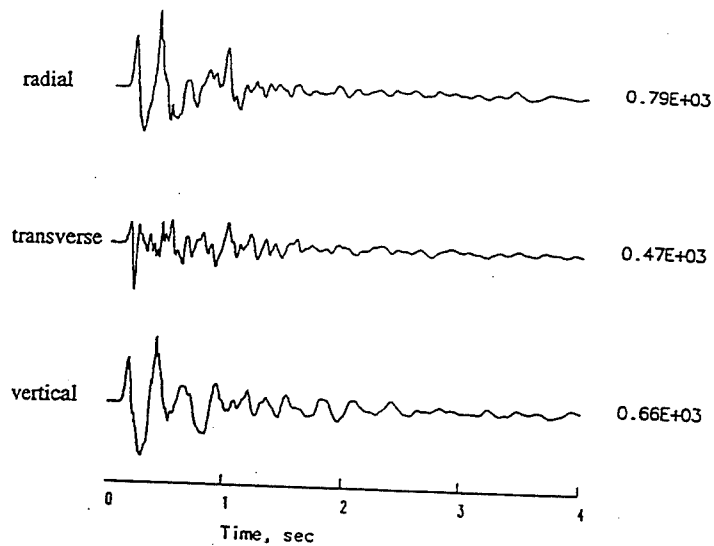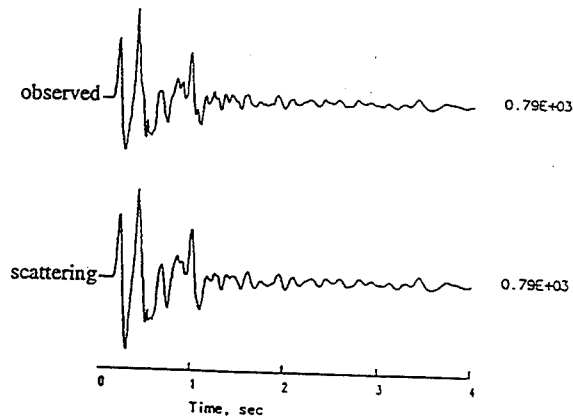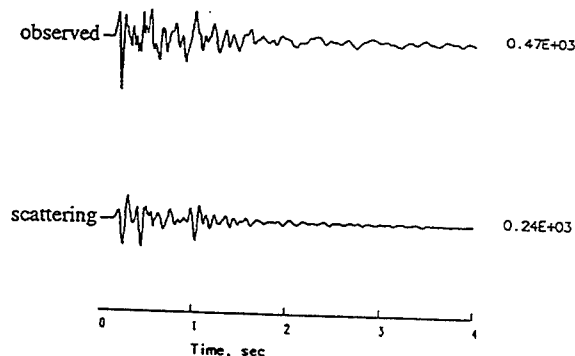
Figure 5. The results of the analysis for the surface data recorded at station UCB120 at an epi-central distance of 662 meters from the NPE explosion. The top panel shows the observed accelerations, with the numbers on the right being maximum accelerations in units of *cm/sec²*. The middle and bottom panels show a comparison between observed and calculated accelerations for the radial and transverse components. In this case the scattering is from a high-velocity obsta-cle 30 meters in radius located 26 meters from the station.
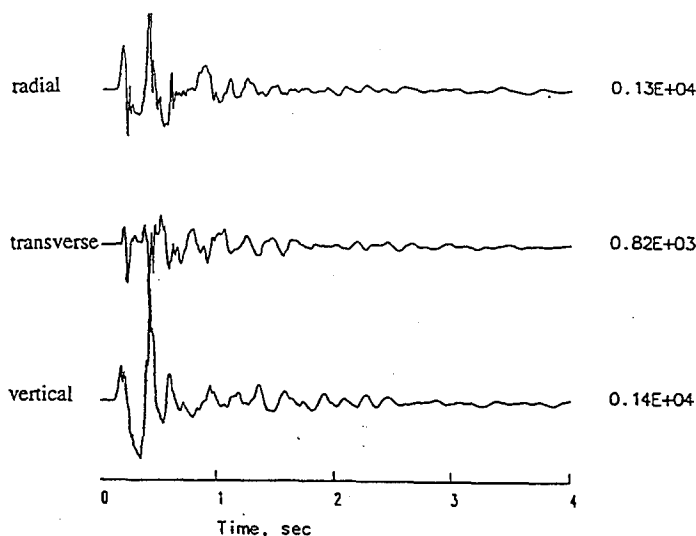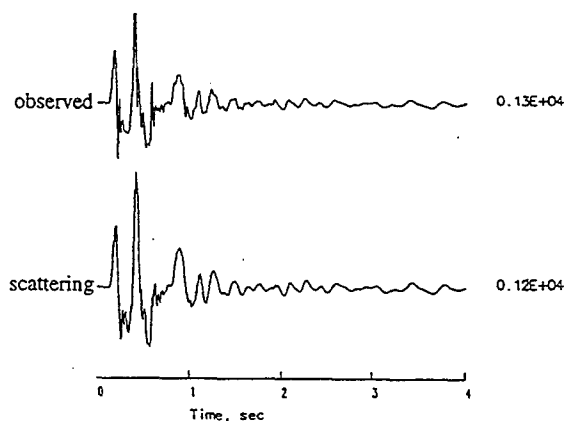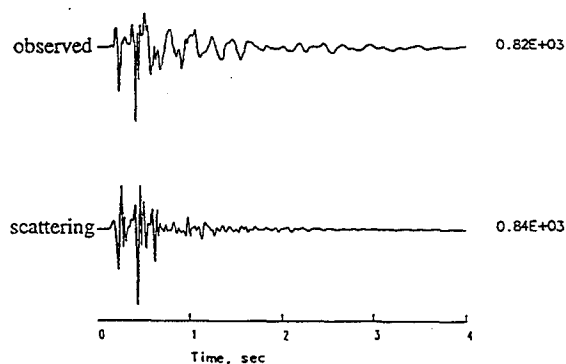
Figure 6. The results of the analysis for the surface data recorded at station UCB140 at an epicentral distance of 596 meters from the NPE explosion. The top panel shows the observed accelerations, with the numbers on the right being maximum accelerations in units of cm/sec^2. The middle and bottom panels show a comparison between observed and calculated accelerations for the radial and transverse components. In this case the scattering is from a high-velocity obstacle 30 meters in radius located 10 meters from the station.

431

CONCLUSIONS AND RECOMMENDATIONS

The seismic data provided by the NPE have allowed an investigation of some features of the seismic data which are somewhat anomalous and difficult to explain with simple source and propagation effects. The investigation of scattering as a possible cause of these features has led to the following preliminary conclusions:

- Elastic wave scattering near seismic receivers can have a significant effect upon recorded waveforms.

- Scatterers act as secondary sources, with near-field terms and strong directional effects.

- Scattering is effective in changing the wave type and direction of particle motion, so it often causes anomalous components of motion.

- Scattering effects tend to increase with frequency, which may serve as a diagnostic tool.

- Scattering effects are enhanced in low velocity materials, so near surface regions are especially prone to this phenomenon.

A better understanding of some of the possible effects of scattering may lead to methods of mitigating such effects, and this lead to the following general recommendation.

- The consideration of scattering effects in the siting of seismic receivers could help reduce the signal-generated noise on seismograms.

References

Baldwin, M. J., R. P. Bradford, S. P. Hopkins, D. R. Townsend, and B. L. Harris-West, Geologic characteristics of the NPE site in the U12n.25 drift of N-tunnel, Nevada Test Site, in Proceedings of the Symposium on the Non-Proliferation Experiment Results and Implications, M. D. Denny et al. (eds), Lawrence Livermore National Laboratory, Livermore, CA, CONF-9404100, 1994.

Gritto, R., V. A. Korneev, and L. R. Johnson, Low-frequency elastic-wave scattering by an inclusion: limits of applications, Geophys. J. Int., 120, 677-692, 1995.

Korneev, V. A., and L. R. Johnson, Scattering of elastic waves by a spherical inclusion - I. Theory and numerical results, Geophys. J. Int., 115, 230-250, 1993a.

Korneev, V. A., and L. R. Johnson, Scattering of elastic waves by a spherical inclusion - I. Limitations of asymptotic solutions, Geophys. J. Int., 115, 251-263, 1993b.

Stochastic Modeling of Small-Scale, Anisotropic Structures in the Continental Upper Mantle

THOMAS H. JORDAN AND JAMES B. GAHERTY

Department of Earth, Atmospheric and Planetary Sciences
Massachusetts Institute of Technology, Cambridge, MA 02139

Abstract

New methods for the analysis of three-component seismograms have been applied to data from both continental and oceanic regions. Polarization anisotropy, manifested as the splitting of surface, guided, and shear body waves, has been observed in all regions, but no significant azimuthal anisotropy has been detected. This is expected if the local orientation of olivine crystals in the upper mantle is incoherent on the scale of the path lengths used in these experiments ($\Delta = 35°$–$50°$). From a detailed study of trans-Australia paths, we have shown that the shear-wave anisotropy in the western Australia craton averages 3-4% in the uppermost mantle, but it terminates abruptly at a Lehmann (L) discontinuity near a depth of 250 km. Our physical interpretation is that the L discontinuity beneath the ancient continental cratons marks the transition from an anisotropic mechanical boundary layer to a more isotropic region of a thick continental tectosphere. Above L, the temperatures have evidently remained cold enough to freeze-in the small-scale anisotropic structures and tectonic fabrics generated in episodes of orogenic compression associated with tectospheric stabilization. Below L, such structures were either never generated or were annealed out subsequent to their formation. These hypotheses about subcontinental structure have considerable bearing on a diverse set of geological and geodynamical problems, ranging from formation of the cratons to kimberlite vulcanism.

To provide additional quantitative tests of these hypotheses, we have formulated stochastic models that specify the small-scale heterogeneity of the continental upper mantle as samples of Gaussian random fields with self-affine (fractal) scaling at high wavenumbers. We approximate the spatial variations in elasticity $C(x)$ as a hexagonal tensor field with a local axis of symmetry given by a unit vector field $\hat{s}(x)$. We impose the structure of a stationary Gaussian random field on $s(x)$ and, from a deterministic functional relationship between C and s, calculate the ensemble averages of $C(x)$ that are needed to describe low-frequency wave propagation. Solving forward problems of this type allows us to set up quantitative inverse problems for the parameters of the stochastic distributions. In the modeling discussed here, s is assumed to have transversely isotropic stochastic symmetry and to be specified by four statistical parameters: an aspect ratio of the anisotropy, ξ, a characteristic horizontal wavenumber of the heterogeneity, k, an aspect ratio of the heterogeneity, η, and a fractal dimension, D. For $\xi = 1$, the distribution of $\hat{s}$ is isotropic in all three directions; in the limit $\xi \to \infty$, s_3 equals zero with probability one, and $\hat{s}$ is isotropically distributed in the horizontal plane. We show that the upper-mantle anisotropy in Gaherty and Jordan's [1995] model AU3 is consistent with Voigt averages given by $\xi \approx 2$-3. We discuss how better approximations to the effective elastic tensor can be obtained from a self-consistent, second-order Born approximation.

Objectives

The technologies of nuclear-monitoring seismology are built, in part, on studies of wave propagation at regional distances (< 2000 km). One poorly understood aspect of regional propagation is the forward scattering of high-frequency signals by small inhomogeneities. The objectives of this research are threefold: (1) to formulate parameterized stochastic models of small-scale heterogeneity that are suitable for assessing scattering effects at regional distances, (2) to constrain the model parameters using broadband seismic data, and (3) to assess the implications of these models for regional wave propagation related to nuclear monitoring.

Research Accomplishments: Observations and Modeling of Seismic Corridors

Our approach is to model small-scale heterogeneity by a bootstrap from low to high frequencies [Jordan and Gaherty, 1994]. In the first phase of this program, we have used low-frequency (< .05 Hz), phase-coherent waves to derive anisotropic, path-averaged models of crustal and upper-mantle structure. We have developed methods for extracting phase delays and amplitudes from three-component seismograms that have delivered new information about impedance discontinuities and velocity gradients in the upper mantle [Revenaugh and Jordan, 1991; Gee and Jordan, 1992], and we have applied them to data from both continental [Gaherty and Jordan, 1995] and oceanic [Gaherty et al., 1995] regions. Polarization anisotropy, manifested as the splitting of surface, guided, and shear body waves, has been observed in all regions, but no significant azimuthal anisotropy has been detected. This is expected if the local orientation of olivine crystals in the upper mantle is incoherent on the scale of the path lengths used in these studies ($\Delta = 35°-50°$). We have therefore modeled the splitting in terms of radially anisotropic, but transversely isotropic, elasticity. From a detailed study of trans-Australia paths [Gaherty and Jordan, 1995], we have shown that the shear-wave anisotropy in the western Australia craton averages 3-4% in the uppermost mantle, but it terminates abruptly at a Lehmann (L) discontinuity near a depth of 250 km. At the L transition, which occurs over a depth range of less than 30 km, the average SV wavespeed increases and the average SH wavespeed decreases, obtaining nearly equal values in the mantle layer between L and the 410-km discontinuity.

Our physical interpretation is that the L discontinuity beneath the ancient continental cratons marks the transition from an anisotropic mechanical boundary layer to a more isotropic region of a thick continental tectosphere [Revenaugh and Jordan, 1991; Gaherty and Jordan, 1995]. Above L, the temperatures have evidently remained cold enough to freeze-in the small-scale anisotropic structures and tectonic fabrics generated in episodes of orogenic compression associated with tectospheric stabilization [Jordan, 1988; Silver and Chan, 1991]. Below L, such structures were either never generated, perhaps because L coincides with a transition from dislocation to diffusion creep [Karato, 1992], or were annealed out subsequent to their formation. These hypotheses about subcontinental structure have considerable bearing on a diverse set of geological and geodynamical problems, ranging from formation of the cratons to kimberlite vulcanism [Gaherty and Jordan, 1995].

Research Accomplishments: Stochastic Modeling of Fine-Scale Anisotropic Structures

In the current phase of our research program, we are focusing on the interpretation of polarization anisotropy in terms of heterogeneity at subwavelength scales. We have formulated stochastic models that specify the small-scale heterogeneity of the continental upper mantle as samples of Gaussian random fields with self-affine (fractal) scaling at high wavenumbers, and we have derived expressions relating the parameters of these models to the speeds of low-frequency seismic waves. This report presents some of these results and outlines future research activity related to this modeling.

We consider a medium governed by a linear stress-strain relation $\sigma_{ij} = C_{ijkl}\varepsilon_{kl}$, where the elasticity tensor $\mathbf{C}$ has Cartesian components $\{C_{ijkl}(\mathbf{x}): i,j,k,l = 1,2,3\}$ that are functions of three-dimensional position vector $\mathbf{x}$. Theoretical calculations [Estey and Douglas, 1986] and measurements on kimberlite xenoliths [Mainprice and Silver, 1993; Christensen, 1994] indicate that the elasticity of upper-mantle peridotites has quasi-hexagonal symmetry on the hand-sample scale. Therefore, it is reasonable to approximate $\mathbf{C}(\mathbf{x})$ as a hexagonal tensor field with a local axis of symmetry given by the unit vector $\hat{\mathbf{s}}(\mathbf{x}) = \mathbf{s}(\mathbf{x})/|\mathbf{s}(\mathbf{x})|$. This can be accomplished by restricting the tensor field to be a functional of a vector field $\mathbf{s}(\mathbf{x})$: $\mathbf{C}(\mathbf{x}) = \mathbf{C}(\mathbf{s}(\mathbf{x}))$. In petrological terms, $\hat{\mathbf{s}}(\mathbf{x})$ is largely determined by the local average orientation of the a axis of olivine, which is aligned by mantle deformation [Estey and Douglas, 1986]. Our strategy is to impose the structure of a Gaussian random field on $\mathbf{s}(\mathbf{x})$ and, from the functional relationship $\mathbf{C}(\mathbf{s})$, to calculate the ensemble averages of $\mathbf{C}(\mathbf{x})$ that are needed to describe low-frequency wave propagation. Solving this forward problem will allow us to assess the applicability of the stochastic models to the continental upper mantle and, if justified, to set up quantitative inverse problems for the parameters of the stochastic distributions.

Specification of the Vector Field. Within some region of the upper mantle, the Gaussian random field $\mathbf{s}(\mathbf{x})$ is assumed to be stationary with zero mean, $\langle \mathbf{s}(\mathbf{x}) \rangle = 0$, and thus specified by its autocovariance matrix, $C_{ss}(\mathbf{x}) = \langle \mathbf{s}(\mathbf{x}')\mathbf{s}^{\mathrm{T}}(\mathbf{x}'+\mathbf{x}) \rangle$. C_{ss} is symmetric and positive definite and admits the zero-lag eigenvector expansion

$$C_{ss}(0) \equiv \mathbf{S}_0^2 = \sum_{n=1}^{3} \sigma_n^2 \hat{\mathbf{e}}_n \hat{\mathbf{e}}_n^{\mathrm{T}} . \tag{1}$$

We specialize this matrix in the following way: its last eigenvector is assumed to be vertical, $\hat{\mathbf{e}}_3 = \hat{\mathbf{z}}$, with dimensionless variance ξ^2, and the variances of the other two eigenvectors are set equal to unity. Hence, the $\mathbf{s}$ field is required to be statistically isotropic in the xy plane, with principal components having root-mean-square (r.m.s.) variations given by

$$\sigma_1 = \sigma_2 = \xi \sigma_3 = 1. \tag{2}$$

We will call the dimensionless parameter ξ the *aspect ratio of the anisotropy*. In terms of the coordinates $s_1 = s \sin\theta \cos\varphi$, $s_2 = s \sin\theta \sin\varphi$, $s_3 = s \cos\theta$, the three-dimensional probability density element (p.d.e.) for $\mathbf{s}$ can be written

$$p(\mathbf{s})dV(\mathbf{s}) = \frac{\xi}{(2\pi)^{3/2}} e^{-\frac{1}{2}(s_1^2 + s_2^2 + \xi^2 s_3^2)} ds_1\, ds_2\, ds_3$$

$$= \frac{\xi}{(2\pi)^{3/2}} e^{-s^2/2}\, e^{\kappa(s)\cos^2\theta}\, s^2 ds \sin\theta\, d\theta\, d\varphi, \qquad \kappa(s) \equiv \frac{1}{2}s^2(1-\xi^2). \tag{3}$$

From this expression, it can be seen that the p.d.f. on a sphere of radius s corresponds to a Watson distribution with dispersion parameter $\kappa(s)$ [Fisher et al., 1987]. For $\xi = 1$, the distribution of $\hat{\mathbf{s}}$ is isotropic in all three directions. Where $\xi < 1$, the probability of $\hat{\mathbf{s}}$ is concentrated towards the vertical axis (bipolar distribution, $\kappa > 0$); where $\xi > 1$, it is concentrated towards the equatorial plane (girdle distribution, $\kappa < 0$). In the limit $\xi \to \infty$, s_3 equals zero with probability one, and $\hat{\mathbf{s}}$ is isotropically distributed in the xy plane. For fixed ξ, the conditional distribution $p(\hat{\mathbf{s}} \mid s)$ becomes more isotropic as $s \to 0$.

To specify the spatial correlation of the $\mathbf{s}$ field, we define the Riemannian length,

$$r^2(\mathbf{x}) = \mathbf{x}^T \mathbf{Q}\, \mathbf{x}, \tag{4}$$

$\mathbf{Q}$ is a symmetric positive-definite matrix chosen, like $\mathbf{S}_0$, to be transversely isotropic; i.e., to have eigenvectors $\{\hat{\mathbf{e}}_1, \hat{\mathbf{e}}_2, \hat{\mathbf{e}}_3 = \hat{\mathbf{z}}\}$ and eigenvalues

$$k_1^2 = k_2^2 = \eta^2 k_3^2 \equiv k^2. \tag{5}$$

We adopt an autocovariance matrix of the form

$$C_{\mathbf{ss}}(\mathbf{x}) = S_0^2\, \rho(r(\mathbf{x})), \tag{6}$$

where $\rho(r)$ is a scalar-valued autocorrelation function such that $\rho(0) = 1$ and $\lim\limits_{r \to \infty} \rho(r) = 0$. A convenient and useful function with these properties is

$$\rho(r) = 2^{-(v+1)} r^v K_v(r) / \Gamma(v), \qquad 0 \le r < \infty,\ 0 \le v < 1 \tag{7}$$

Here $K_v(r)$ is the modified Bessel function of the second kind and $\Gamma(v)$ is the gamma function. This anisotropic autocorrelation function was introduced as a stochastic representation of seafloor roughness by Goff and Jordan [1988], who describe many of its properties. A three-dimensional Fourier transform yields the power spectrum:

$$P(\mathbf{k}) = \int \rho(r(\mathbf{x})) e^{-i\mathbf{k}^T \mathbf{x}}\, dV(\mathbf{x}) = 8\pi^{3/2} \frac{\Gamma(v+3/2)}{\Gamma(v)} |\mathbf{Q}|^{-1/2} [\mathbf{k}^T \mathbf{Q}^{-1}\mathbf{k} + 1]^{-(v+3/2)} \tag{8}$$

This spectral density has principal axes $\hat{\mathbf{e}}_1, \hat{\mathbf{e}}_2, \hat{\mathbf{e}}_3$ with corner wavenumbers $k, k, \eta k$; it is flat below these corners and rolls off above them at an asymptotic rate of $-(2v + 3)$. Realizations of this Gaussian field are thus characterized by two outer scales: k^{-1} in the xy plane, and $(\eta k)^{-1}$ in the z direction. The dimensionless parameter η is termed the *aspect ratio of the heterogeneity*. At scales much smaller than $(\eta k)^{-1}$, the field is statistically self-affine with scaling parameter v, and it has a Hausdorff (fractal) dimension of

$$D = 4 - v \tag{9}$$

(see the appendix of Goff and Jordan [1988] for definitions and proofs). The special case $v = 1/2$ corresponds to the exponential correlation function, $\rho(r) = e^{-r}$, that has been commonly used in theoretical studies of wave scattering [e.g., Chernov, 1960].

In summary, we have constructed a dimensionless vector field s that has a transversely isotropic stochastic symmetry. Its statistics are described by a single dimensionalized parameter, the characteristic horizontal wavenumber of the heterogeneity k, ($[k] = length^{-1}$), and three dimensionless numbers: the aspect ratio of the anisotropy ξ, the aspect ratio of the heterogeneity η, and the fractal dimension D. Figures 1 and 2 illustrate sections taken through some realizations of this Gaussian random field for $k^{-1} = 200$ km, D = 3.2, and several values of ξ and η.

100 km
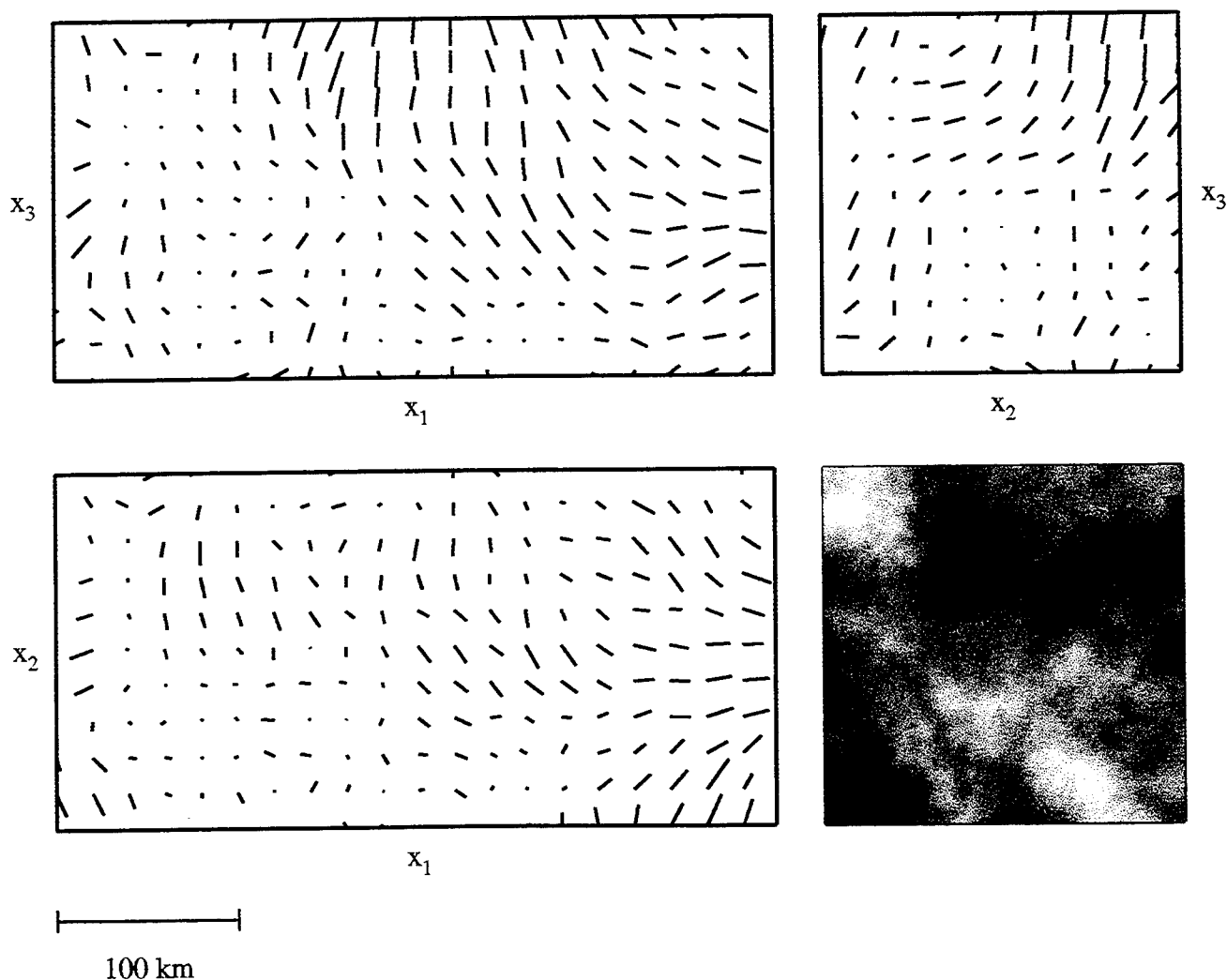
Figure 1. A realization of the vector field s for $k^{-1} = 200$ km, D = 3.2, and $\xi = \eta = 1$. The vectors are calculated on a 20 km × 20 km grid and displayed as their projections onto the sides of a 500 km × 200 km × 200 km rectangular domain. Lower right panel is a grayshade plot of the x_2 coordinate of s in the x_2-x_3 plane, showing the structure of the field at higher resolution than the vector sampling. In this case, the field is statistically isotropic in all directions in both the vector orientation and the heterogeneity.

437
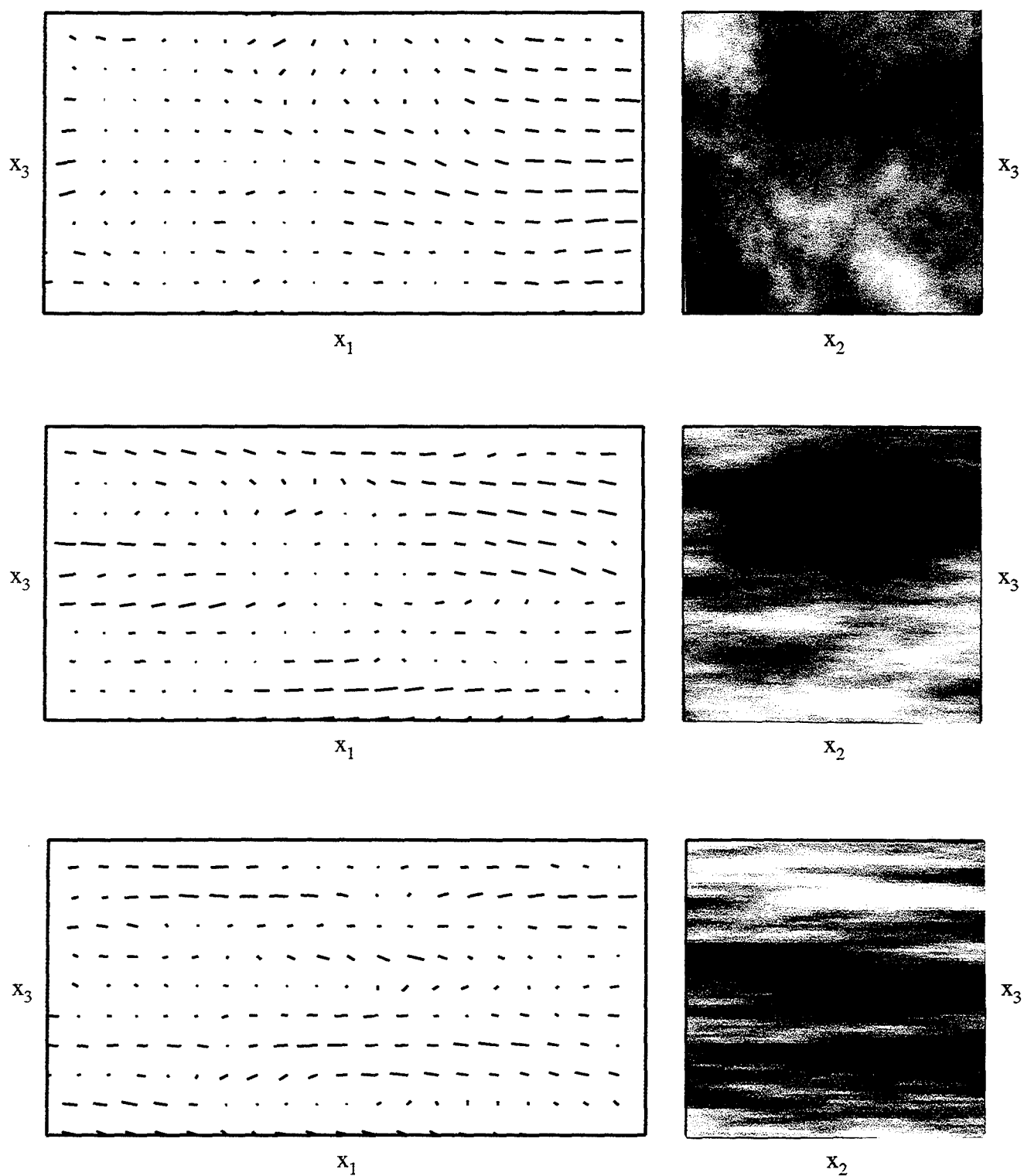
Figure 2. Realizations of the vector field s for $k^{-1} = 200$ km, $D = 3.2$, and $\xi = 5$, and values of the heterogeneity aspect ratio η equal to 1 (*top*), 5 (*middle*), and 10 (*lower*). In each case, the left and right panels are plotted with the same conventions as the upper-left and lower-right panels of Figure 1, respectively. The field in the top panel has statistically isotropic heterogeneity but anisotropic vector orientation. The field in the lower panel corresponds to an anisotropic stochastic laminate ($\eta \gg 1$). All realizations are isotropic in the x_1-x_2 plane.

438

<u>Representation of the Elasticity Field</u>. The Gaussian random field structure of $s(\mathbf{x})$ is mapped onto the elasticity tensor field $\mathbf{C}(\mathbf{x})$ through a deterministic functional relationship $\mathbf{C}(s)$. If $\mathbf{C}$ is a functional of s, then it must be hexagonal with symmetry axis $\hat{s}$. Any hexagonally symmetric elasticity tensor with components C_{ijkl} can be represented by six elastic parameters, which are taken here to be

$$C_{1111} = c_{11} = a, \qquad C_{1122} = c_{12} = b, \qquad C_{3333} = c_{33} = c,$$

$$C_{1133} = c_{13} = f, \qquad C_{1212} = c_{44} = m, \qquad C_{1313} = c_{55} = l. \qquad (10)$$

Only five of these parameters are independent, because the symmetry requires

$$b = a - 2m. \qquad (11)$$

An alternative and analytically convenient representation is the Backus [1970] harmonic decomposition:

$$C_{ijkl} = \mathfrak{D}_{ijkl}^{(4)} H^{(4)} + \mathfrak{D}_{ijkl}^{(2)} H^{(2)} + \mathfrak{D}_{ijkl}^{(0)} H^{(0)} + d_{ijkl}^{(2)} h^{(2)} + d_{ijkl}^{(0)} h^{(0)}. \qquad (12)$$

Here $H^{(\ell)}$ and $h^{(\ell)}$ are harmonic polynomials of degree ℓ, and $\mathfrak{D}_{ijkl}^{(\ell)}$ and $d_{ijkl}^{(\ell)}$ are the ℓ th -order differential operators (δ_{ij} is the Kronecker delta),

$$\mathfrak{D}_{ijkl}^{(4)} = \frac{1}{4!} \partial_i \partial_j \partial_k \partial_l, \qquad (13a)$$

$$\mathfrak{D}_{ijkl}^{(2)} = \frac{1}{2!}(\delta_{ij}\partial_k\partial_l + \delta_{kl}\partial_i\partial_j + \delta_{ik}\partial_j\partial_l + \delta_{jl}\partial_i\partial_k + \delta_{il}\partial_j\partial_k + \delta_{jk}\partial_i\partial_l), \qquad (13b)$$

$$\mathfrak{D}_{ijkl}^{(0)} = \delta_{ij}\delta_{kl} + \delta_{ik}\delta_{jl} + \delta_{il}\delta_{jk}, \qquad (13c)$$

$$d_{ijkl}^{(2)} = \frac{1}{2!}(\delta_{ij}\partial_k\partial_l + \delta_{kl}\partial_i\partial_j - \frac{1}{2}\delta_{ik}\partial_j\partial_l - \frac{1}{2}\delta_{jl}\partial_i\partial_k - \frac{1}{2}\delta_{il}\partial_j\partial_k - \frac{1}{2}\delta_{jk}\partial_i\partial_l), \qquad (13d)$$

$$d_{ijkl}^{(0)} = \delta_{ij}\delta_{kl} - \frac{1}{2}\delta_{ik}\delta_{jl} - \frac{1}{2}\delta_{il}\delta_{jk}. \qquad (13e)$$

For a hexagonal fourth-order tensor with symmetry axis $\hat{s}$, the harmonic polynomials are

$$H^{(4)}(\mathbf{r}) = 8H_4 r^4 P_4(\hat{s}^T\hat{r}), \qquad (14a)$$

$$H^{(2)}(\mathbf{r}) = -2H_2 r^2 P_2(\hat{s}^T\hat{r}), \qquad (14b)$$

$$H^{(0)}(\mathbf{r}) = H_0, \qquad (14c)$$

$$h^{(2)}(\mathbf{r}) = -2h_2 r^2 P_2(\hat{s}^T\hat{r}), \qquad (14d)$$

$$h^{(0)}(\mathbf{r}) = h_0, \qquad (14e)$$

where $P_\ell(\cos\Delta)$ is the Legendre polynomial of order ℓ and $\Delta = \mathrm{acos}(\hat{\mathbf{s}}^T \hat{\mathbf{r}})$ is the angle between $\mathbf{r}$ and $\mathbf{s}$. As shown by Backus [1970], the three polynomials $\{ H^{(\ell)} : \ell = 0,2,4 \}$ represent the totally symmetric part of $\mathbf{C}$, whereas the two polynomials $\{ h^{(\ell)} : \ell = 0,2 \}$ represent its antisymmetric part. The elastic constants in (10) are related to the coefficients H_ℓ and h_ℓ by

$$a = 3H_4 + 6H_2 + 3H_0, \tag{15a}$$

$$b = H_4 + 2H_2 + H_0 + 2h_2 + h_0, \tag{15b}$$

$$c = 8H_4 - 12H_2 + 3H_0, \tag{15c}$$

$$f = -4H_4 - H_2 + H_0 - h_2 + h_0, \tag{15d}$$

$$l = -4H_4 - H_2 + H_0 + \frac{1}{2}h_2 - \frac{1}{2}h_0, \tag{15e}$$

$$m = H_4 + 2H_2 + H_0 - h_2 - \frac{1}{2}h_0. \tag{15f}$$

(Here we have corrected some errors in equation (34) of Backus [1970].)

To complete the functional relationship between $\mathbf{C}$ and $\mathbf{s}$, we specify the elastic parameters to be monomials in the vector length s:

$$H_\ell(\mathbf{s}) = \hat{H}_\ell s^n, \quad h_\ell(\mathbf{s}) = \hat{h}_\ell s^n, \tag{16}$$

where n is a non-negative integer that is constant for all ℓ. We call this additional model parameter *the strength exponent*. In the case $n = 0$, the harmonic coefficients are independent of position, and $C_{ijkl}(\mathbf{x})$ is a constant tensor rotated to have an axis of symmetry $\hat{\mathbf{s}}(\mathbf{x})$.

Voigt Average. The Voigt average is the expected value of the elasticity tensor, $\overline{C}_{ijkl} = \langle C_{ijkl}(\mathbf{x}) \rangle$, which can be calculated directly from the expected values of the harmonic polynomials. The latter can be expressed as sums over the integrals

$$\int s^n P_\ell(\cos\Delta(\hat{\mathbf{s}})) p(\mathbf{s}) dV(\mathbf{s}). \tag{17}$$

Integrating the Legendre polynomials term-by-term yields

$$\overline{H}^{(4)}(\mathbf{r}) = \hat{H}_4(35 I_4^n - 30 I_2^n + 3 I_0^n) r^4 P_4(\hat{\mathbf{z}}^T\hat{\mathbf{r}}), \tag{18a}$$

$$\overline{H}^{(2)}(\mathbf{r}) = -\hat{H}_2(3 I_2^n - I_0^n) r^2 P_2(\hat{\mathbf{z}}^T\hat{\mathbf{r}}), \tag{18b}$$

$$\overline{H}^{(0)}(\mathbf{r}) = \hat{H}_0 I_0^n, \tag{18c}$$

$$\overline{h}^{(2)}(\mathbf{r}) = -\hat{h}_2(3 I_2^n - I_0^n) r^2 P_2(\hat{\mathbf{z}}^T\hat{\mathbf{r}}), \tag{18d}$$

440

$$h^{(0)}(\mathbf{r}) = h_0.$$ (18e)

Hence, the Voigt average is transversely isotropic with a vertical symmetry axis, as expected for a random medium whose statistics have this symmetry. The integrals appearing in (18) are

$$I_\ell^n(\xi) = \int_0^1 \frac{\xi\, x^\ell}{[1 + (\xi^2 - 1)x^2]^{(n+3)/2}}\, dx$$ (19)

We give explicit forms for $n = 0, 1$:

$$I_0^0 = 1,$$ (20a)

$$I_2^0 = \frac{1}{\xi^2 - 1}\left(\frac{\xi}{\sqrt{\xi^2 - 1}}\, \mathrm{asinh}\sqrt{\xi^2 - 1} - 1\right),$$ (20b)

$$I_4^0 = \frac{1}{2(\xi^2 - 1)}\left(1 - 3I_2^0\right),$$ (20c)

$$I_0^1 = \frac{\xi}{\sqrt{\xi^2 - 1}}\, \mathrm{atan}\sqrt{\xi^2 - 1},$$ (21a)

$$I_2^1 = \frac{1}{\xi^2 - 1}\left(I_0^1 - \frac{1}{3}\right),$$ (21b)

$$I_4^1 = \frac{1}{\xi^2 - 1}\left(\frac{1}{\xi} - 3I_2^1\right).$$ (21c)

Application to the Upper Mantle. We have applied this theory to the interpretion of the anisotropy observed by Gaherty and Jordan [1995]. Their model AU3 has a radially anisotropic region extending from the M discontinuity at 30 km depth to the L discontinuity at 252 km depth. The magnitude of the anisotropy in such a transversely isotropic model is measured by an S-wave anisotropy ratio, $(v_{SH} - v_{SV})/v_{SV}$, and a similar ratio for P wavespeeds. At the base of the AU3 anisotropic region, these ratios are both about 4%. In comparison, the anisotropy ratios calculated for a pyrolite mineralogy in which the olivine and pyroxene crystals have been completely aligned by shear deformation in the horizontal plane (but randomly oriented within that plane) is about 7% [Estey and Douglas, 1986]. Within the context of our stochastic model, this type of average corresponds to $\xi = \infty$, describing the (geologically unexpected) situation where all the s vectors are horizontal. As ξ decreases, the anisotropy ratios decrease, achieving values comparable to AU3 for $\xi \approx 2$-3. Figure 3 shows this behavior for the Voigt average in the case where $n = 0$. An anisotropy aspect ratio of this magnitude is geologically reasonable, although it must be admitted that not much is known from direct observation about what ξ should be. The results in Figure 3 at least suggests that our approach to the stochastic modeling of fine-scale upper-mantle structure might be on the right track.
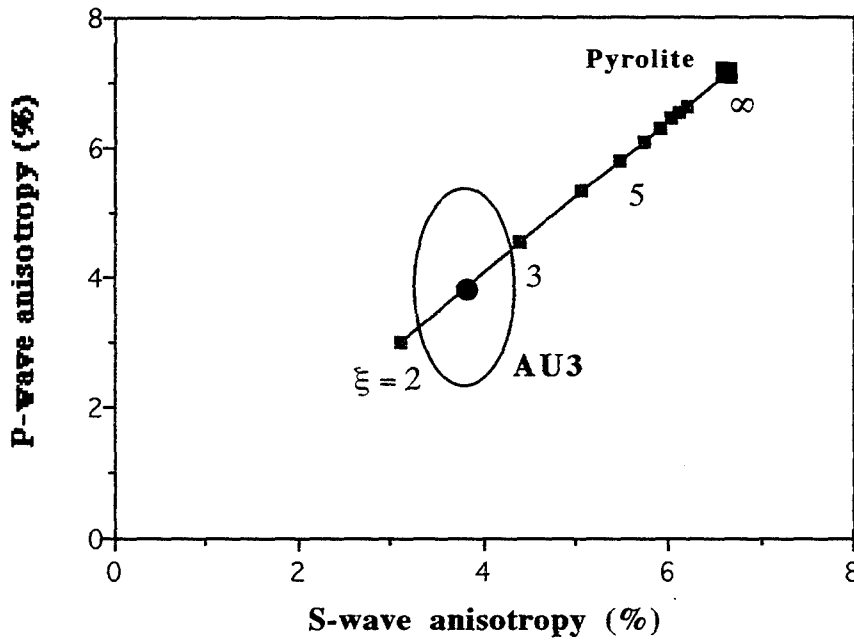
Figure 3. Plot of the P-wave anisotropy, $(v_{PH} - v_{PV}) / v_{PV}$, versus the S-wave anisotropy, $(v_{SH} - v_{SV}) / v_{SV}$. The point with the 1-$\sigma$ error ellipse is the upper-mantle value from model AU3 of Gaherty and Jordan [1995]. The large square is the value calculated by Voigt averaging the hexagonally symmetric pyrolite model of Estey and Douglas [1986] assuming complete crystallographic alignment in the horizontal plane ($\xi = \infty$). The small squares are Voigt averages for a strength exponent $n = 0$ at integer values of the anisotropy aspect ratio ξ, showing how the apparent anisotropy decreases as the local orientation becomes statistically more isotropic. This calculation suggests that the value of ξ appropriate for the Australian upper mantle is on the order of 2 or 3.

Our analysis is not complete, however. The one-point probability density $p(s)$ is independent of the two-point correlation parameters; hence, the Voigt average depends only on the aspect ratio of the anisotropy ξ and the strength exponent n. On the other hand, the effective anisotropy sensed by low-frequency waves must also be dependent on the aspect ratio of the heterogeneity η. This illustrates the well known fact that the Voigt average can be a poor approximation to the effective elasticity tensor governing low-frequency wave propagation [Backus, 1962; Berryman, 1994].

Self-Consistent Effective Media Theory: The Second-Order Born Approximation. Better approximations can be obtained from self-consistent theories of effective media based on an integral-equation formulation of the scattering problem. This technique was developed and first applied to polycrystalline aggregates by Korringa[1973], and Zeller and Dederichs [1973]; see reviews by Gubernatis and Krumhansl [1975], Domany et al. [1975], and Berryman [1994]. In the long-wavelength limit, the time derivatives of the dynamic displacement field commute with ensemble averaging, so that the effective elasticity tensor

$$\tilde{C}_{ijkl} = \langle \sigma_{ij} \rangle \langle \varepsilon_{kl} \rangle^{-1} \tag{22}$$

can be calculated from the static problem. The development of these theories begins by expressing $C_{ijkl}(\mathbf{x})$ as the sum of a constant tensor C_{ijkl}^0 and a perturbation $\delta C_{ijkl}(\mathbf{x})$; then, the condition for static equilibrium can be put in the form of a Lippman-Schwinger equation

$$\varepsilon_{ij}(\mathbf{x}) = \varepsilon_{ij}^0(\mathbf{x}) + \int G_{ijkl}(\mathbf{x},\mathbf{x}')\delta C_{klmn}(\mathbf{x}')\varepsilon_{mn}(\mathbf{x}')dV(\mathbf{x}'). \tag{23}$$

G_{ijkl} is the strain Green's function corresponding to $C_{ijkl}(\mathbf{x})$. In operator notation, this equation can be written as $\varepsilon = \varepsilon^0 + \mathbf{G}\,\delta\mathbf{C}\,\varepsilon$ and solved iteratively via a Born series. The series can be summed to obtain

$$\varepsilon = \varepsilon^0 + \mathbf{G}\mathbf{T}\varepsilon^0, \tag{24}$$

$$\mathbf{T} \equiv \delta\mathbf{C}(\mathbf{I} - \mathbf{G}\,\delta\mathbf{C})^{-1} = \delta\mathbf{C} + \delta\mathbf{C}\mathbf{G}\,\delta\mathbf{C} + \delta\mathbf{C}\mathbf{G}\,\delta\mathbf{C}\mathbf{G}\,\delta\mathbf{C} + \cdots. \tag{25}$$

The fourth-order tensor defined in (25) is equivalent to the T matrix of quantum mechanics, and the nth-order term in its series (Born) expansion expresses the scattering process of order $n-1$. Using (24) in (22) yields the exact solution

$$\tilde{\mathbf{C}} = \mathbf{C}^0 + (\mathbf{I} - \langle\mathbf{G}\mathbf{T}\rangle)^{-1}\langle\mathbf{T}\rangle. \tag{26}$$

Because the exact evaluation of the second term in (26) is infeasible (e.g., $\mathbf{G}$ must be calculated for $\mathbf{C}(\mathbf{x})$), we resort to a self-consistent approximation: $\mathbf{C}^0$, which has thus far been arbitrary, is chosen to equal $\tilde{\mathbf{C}}$, so that (26) is recovered if $\langle\tilde{\mathbf{T}}\rangle = 0$. Substituting the Born expansion in (25) generates a sum in which the nth term is a contraction of the $(n$-$1)$th outer product of $\tilde{\mathbf{G}}$ against the n-point moment of $\delta\mathbf{C}$.

Truncating the Born series at first order yields the Voigt average, $\tilde{\mathbf{C}} \approx \overline{\mathbf{C}}$. To obtain a better approximation, we have carried the expansion to second order. Since $\tilde{\mathbf{C}} - \overline{\mathbf{C}} \sim O(\delta\mathbf{C})$, the second-order Born approximation takes the form of an implicit integral equation,

$$\tilde{C}_{ijkl} \approx \overline{C}_{ijkl} + \int \tilde{G}_{pqrs}(\mathbf{x})\mathcal{V}_{ijpqrskl}(\mathbf{x})dV(\mathbf{x}), \tag{27}$$

where $\tilde{G}_{pqrs}$ is the strain Green's function for a transversely isotropic medium with a constant elasticity tensor $\tilde{C}_{ijkl}$, and $\mathcal{V}_{ijklpqrs}$ are the components of the eighth-order, spatially stationary covariance tensor $\mathcal{V}(\mathbf{x}) \equiv C_{\mathbf{C}\mathbf{C}}(\mathbf{x})$,

$$\mathcal{V}_{ijklpqrs}(\mathbf{x}) = \langle[C_{ijkl}(\mathbf{x}') - \overline{C}_{ijkl}][C_{pqrs}(\mathbf{x}'+\mathbf{x}) - \overline{C}_{pqrs}]\rangle. \tag{28}$$

$\mathcal{V}(\mathbf{x})$ can be evaluated from the Backus harmonic decomposition (12) by integrating two-point products of the harmonic polynomials against the joint p.d.f. $p(s',s'+s)$. This allows us to fully exploit the transversely isotropic stochastic symmetry of the $\mathbf{C}$ field. Moreover, we can obtain considerable simplifications by rewriting the second term in (27) as an integral over the wavevector $\mathbf{k}$; e.g., the 3D Fourier transform of $\tilde{\mathbf{G}}(\mathbf{x})$ depends only on $\hat{\mathbf{k}}$, and the spatial derivatives in (12) reduce to multiplications by k_i. We are currently developing an iterative method for calculating (27) using this approach.

443

References

Backus, G. E., Long-wave elastic anisotropy produced by horizontal layering, *J. Geophys. Res.*, *67*, 4427-4440, 1962.

Backus, G. E., A geometrical picture of anisotropic elastic tensors, *Rev. Geophys. Space Phys.*, *8*, 633-671, 1970.

Berryman, J. G., Mixture theories for rock properties, in *Rock Physics and Phase Relations*, AGU Reference Shelf #3, American Geophysical Union, Washington, D.C., 1994.

Chernov, L. A., *Wave Propagation in a Random Medium*, McGraw-Hill, New York, 1960.

Christensen, N. I., Seismic properties of mantle xenoliths: clues to the interpretation of deep seismic observations beneath the kimberlite province of Yakutsia, unpublished manuscript, January, 1994.

Domany, E., J. E. Gubernatis, and J. A. Krumhansl, The elasticity of polycrystals and rocks, *J. Geophys. Res.*, *80*, 4851-4856, 1975.

Estey, L. H., and B. J. Douglas, Upper-mantle anisotropy: a preliminary model, *J. Geophys. Res.*, *91*, 11393-11406, 1986.

Fisher, N. I., T. Lewis, and B. J. J. Embleton, *Statistical Analysis of Spherical Data*, Cambridge University Press, Cambridge, 329 pp., 1987.

Gaherty, J. B., and T. H. Jordan, Lehmann discontinuity as the base of an anisotropic layer beneath continents, *Science*, *268*, 1468-1471, 1995.

Gaherty, J. B., T. H. Jordan, and L. S. Gee, Seismic structure of the upper mantle in a western Pacific corridor, *J. Geophys. Res.*, submitted, August, 1995.

Gee, L. S., and T. H. Jordan, Polarization anisotropy and fine-scale structure of the Eurasian upper mantle, *Geophys. Res. Lett.*, *15*, 824-827, 1988.

Gee, L. S., and T. H. Jordan, Generalized seismological data functionals, *Geophys. J. Int.*, *111*, 363-390, 1992.

Goff, J., and T. H. Jordan, Stochastic modeling of seafloor morphology: inversion of Sea Beam data for second-order statistics, *J. Geophys. Res.*, *93*, 13589-13608, 1988.

Gubernatis, J. E., and J. A. Krumhansl, Macroscopic engineering properties of polycrystalline materials: elastic properties, *J. Appl. Phys.*, *46*, 1875-1883, 1975.

Karato, S., On the Lehmann discontinuity, *Geophys. Res. Lett.*, *19*, 2255-2258, 1992.

Korringa, J., Theory of eslastic constants of heterogeneous media, *J. Math. Phys.*, *14*, 509-513, 1973.

Jordan, T. H., Structure and formation of the continental tectosphere, *J. Petrology Special Lithosphere Issue*, 11-37, 1988.

Jordan, T. H., and J. B. Gaherty, Polarization anisotropy and small-scale structure of the continental upper mantle, *Proceedings of the 16th Annual Seismic Research Symposium*, PL-TR-94-2217, Phillips Laboratory, Massachusetts, pp. 189-195, 1994. ADA284667

Mainprice, D., and P. Silver, *Phys. Earth Planet. Inter.*, *78*, 257, 1993.

Revenaugh, J.R. and T.H. Jordan, Mantle layering from *ScS* reverberations, 3, The upper mantle, *J. Geophys. Res.*, *96*, 19,781-19,810, 1991.

Silver, P.G. and W.W. Chan, Shear-wave splitting and subcontinental mantle deformation, *J. Geophys. Res.*, *96*, 16,429-16,454, 1991.

Zeller, R., and P. H. Dederichs, Elastic constants of polycrystals, *Phys. Status Solidi (b)*, *55*, 831-842, 1973.

The influence of 3-D structure on seismic wave propagation at regional and teleseismic distances

B.L.N. Kennett
Research School of Earth Sciences, Australian National University,
Canberra ACT 0200, Australia

Abstract

Three-dimensional heterogeneity is pervasive in the Earth on a wide variety of scales. The aim of this project is to improve understanding of the influence of lateral variations in structure in the upper mantle on wave propagation at regional to far-regional and teleseismic distances.

At regional scales we have investigated how to map the seismic velocity structure of a region exploiting records from natural events as a model for upgrading the knowledge base for verification studies. The primary focus of this aspect of the work is on the use of waveform inversion for surface waves (including higher modes) to determine three-dimensional shear wave structure, but receiver function studies of crustal structure and P wave tomography can be achieved with the same data. A set of deployments of portable broadband instruments in Australia have demonstrated how detailed knowledge of crustal and lithospheric structure can be built up by combining specific experiments (of about 6 months duration) with information available from permanent seismic stations.

For global studies we have parametrized heterogeneous structures using a flexible interpolation scheme based on Delaunay tetrahedra. This approach is being applied to the construction of regionalized models of the upper mantle by inversion of travel times from selected events. The resultant three-dimensional model will be suitable for the prediction of wave propagation characteristics,such as travel time corrections for a wide range of seismic phases.

These studies are designed to contribute to the support of a verification regime for a CTBT by providing improved knowledge of regional structure in different tectonic environments and developing representations of 3-D structure which can be used to aid in, for example, improved event location and characterisation.

Keywords

Regional structure, surface wave inversion, mantle heterogeneity, travel times.

The influence of 3-D structure on seismic wave propagation at regional and teleseismic distances

1 OBJECTIVE

Three-dimensional heterogeneity is pervasive in the Earth on a wide variety of scales. The objective of this project is to understand the influence of lateral variations in structure in the upper mantle on wave propagation at regional to far-regional and teleseismic distances.

There are two main facets to the research. The first is an exploration of how to map the seismic velocity structure of a region exploiting records from natural events. The primary focus of this aspect of the work is on the use of waveform inversion for surface waves (including higher modes) to determine three-dimensional shear wave structure. The second class of work is the construction of regionalized models of the upper mantle which are suitable for the prediction of wave propagation characteristics, for example travel time corrections for a wide range of seismic phases.

These studies are designed to contribute to the support of a verification regime for a CTBT by providing improved knowledge of regional structure in different tectonic environments and developing representations of 3-D structure which can be used to aid in, for example, improved event location and characterisation.

2 RESEARCH ACCOMPLISHED

Although radial earth models provide a good description of the major features of wave propagation through the lower mantle and core, the level of lateral heterogeneity in the upper mantle requires region specific information.

2.1 Determination of regional structure

For natural events recorded on broad-band systems the largest arrivals for distances of 10° or more are the S waves and surface waves. For the frequency band between 0.01 Hz and 0.03 Hz the characteristics of the S portion of waveform (for multiple S waves such as SS, SSS etc and surface waves) can be well matched using a radial model which represents the path average along the great-circle path between source and receiver, once the source mechanism is known. When such one-dimensional models are constructed for many paths it is possible to extract the three-dimensional S wave structure by a linear inversion of the multiple constraints provided by the various path averages. This partitioned waveform scheme (Nolet 1990) has been previously applied to determining structure in Central Asia using data from permanent seismic observatories. This application required careful allowance for the strong variation in crustal thickness across the region.

In this period we have applied the same waveform inversion procedure to record from
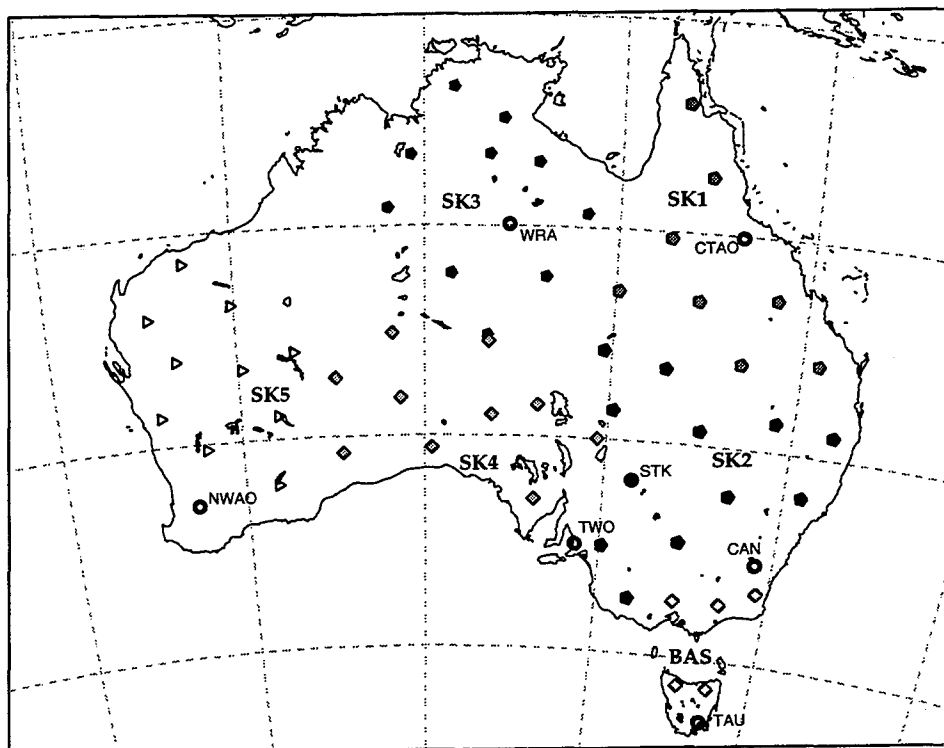
Figure 1. Configuration of array of portable broadband seismic stations and permanent broadband stations in Australia.

an array of portable broadband seismic recorders deployed in northeastern Australia with an inter-station spacing of about 400 km. The array spans the contact between the exposures of Precambrian and Phanerozoic rocks (figure 1). The deployment of the broadband instruments was for 5 months which was long enough to provide sufficient path control to dramatically improve regional coverage compared with the available data for the few permanent broadband stations on the continent. The available path coverage from the experiment is illustrated in figure 2a.

A cross-section through the three-dimensional shear velocity structure determined by partitioned waveform inversion at a depth of 140 km is illustrated in figure 2b. The strong contrast in structure between the high velocities below the craton of central Australia and the lower velocities beneath most of the younger exposure is striking. However, there are unexpected features such as the high shear velocities at depth beneath the New England block. The low velocities along the Queensland coast may be related to the Quaternary volcanism in this area.

This study demonstrates that a limited deployment of broadband instruments in a areal array can provide strong constraints on structure in a region using natural sources. The details of crustal structure can be augmented by the analysis of quarry blasts to provide an improved characterisation of the Pg, Lg propagation at shorter distances. The broadband records obtained in the experiment provide a wealth of other information which can also be used to improve knowledge of regional structure. Thus, P wave residuals at the stations can provide constraints on three-dimensional P wave

-220m/s ▭ +220m/s
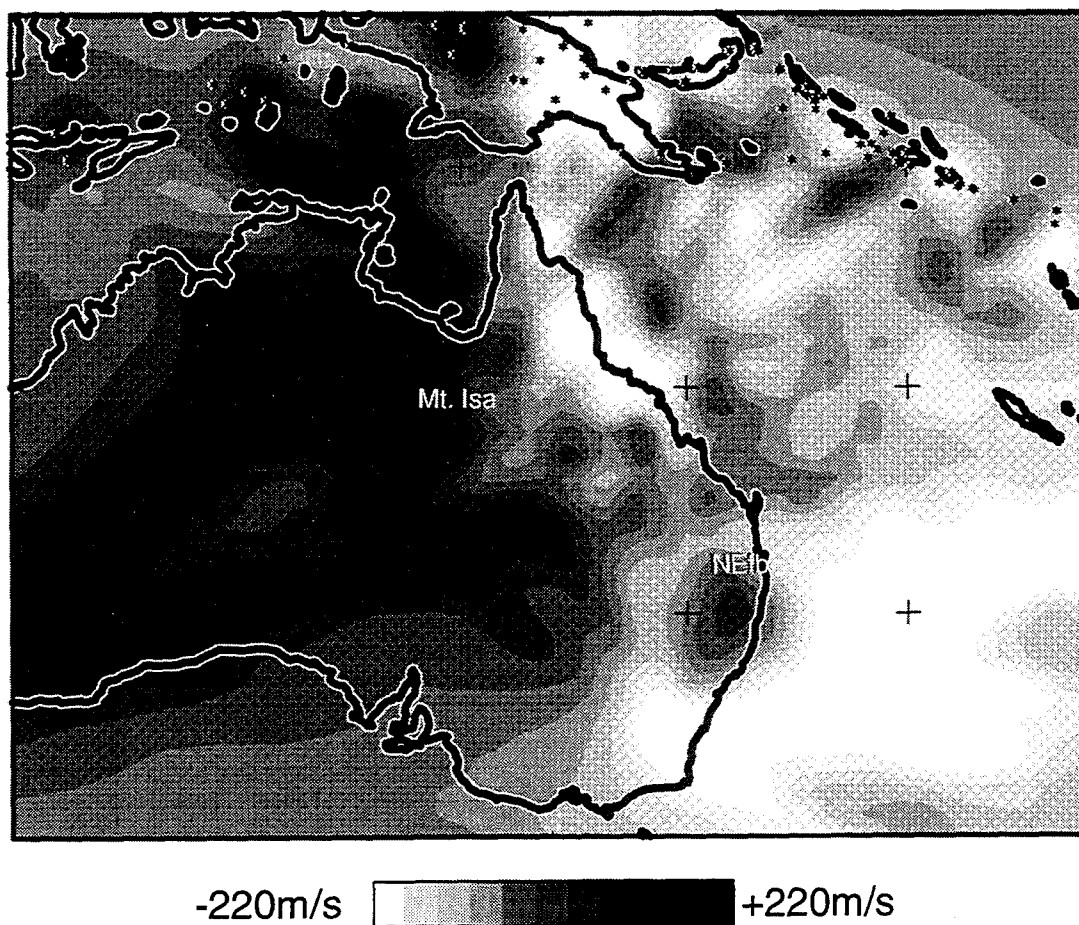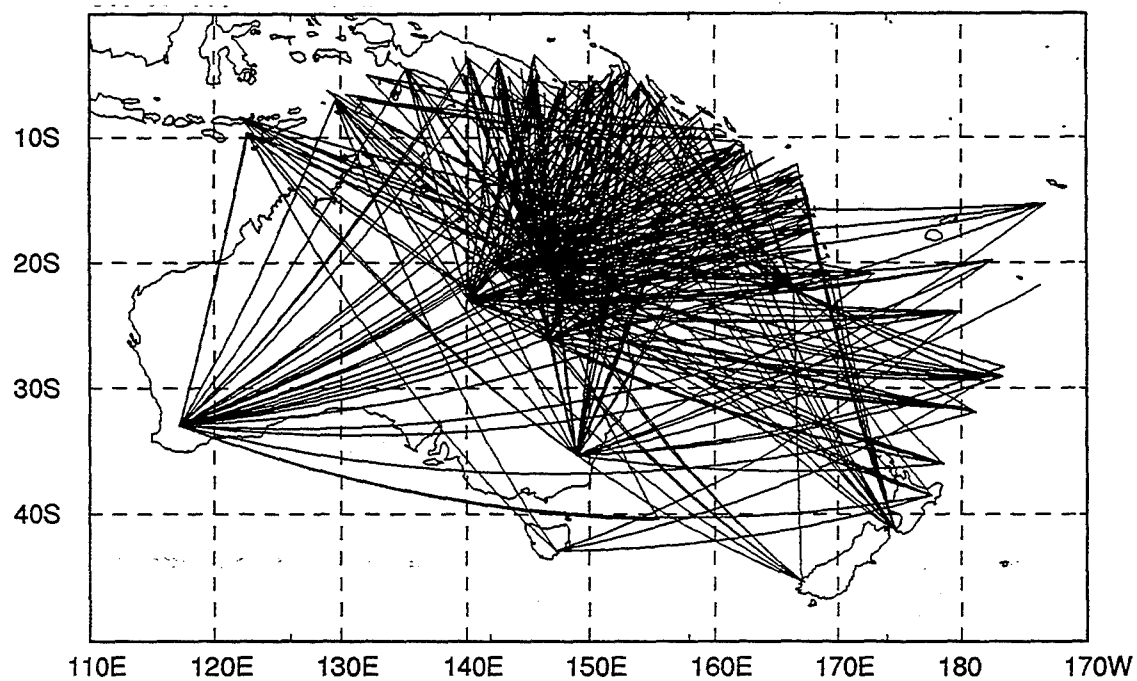
Figure 2. (a) Path coverage for waveform analysis of surface waves from both the portable and broadband station, (b) Section through three-dimensional shear wave model derived by partitioned waveform inversion at 140 km depth.

structure via tomographic inversion. The inclusion of a limited number of additional short-period stations can markedly improve the resolution of P wave structure.

2.2   Regionalisation of Earth structure

Although global coverage of the deep earth is quite good, detailed knowledge of upper mantle structure is rather limited. It is therefore desirable to devise a scheme which can incorporate well-determined structure where this is available, but which can provide a rational extrapolation where structural control is more limited.

2.2.1   Parametrization of 3-D models

In inverse problems like seismic tomography a region of the Earth is usually divided into rectangular 'cells' and the value of the (constant) seismic velocity in each cell is an unknown to be fund in the inversion. In 3-D this can often lead to a very large number of cells, only a small proportion of which are well sampled by criss-crossing raypaths. Ideally, we would like to avoid using many cells in areas where the data constraint is poor. In global tomography, the scale lengths of seismic structures (e.g. subduction zones) can be small compared to the volume of the Earth sampled by the data (e.g. the whole mantle), and so a regular cellular parametrization would lead to an enormous number of unknowns.

A powerful mechanism has been developed for overcoming these difficulties which retains the advantage of a flexible local parametrization. The new approach uses some sophisticated methods from the field of computational geometry to divide a region into irregularly sized Delaunay triangles in 2-D or tetrahedra in 3-D. This tessellation of the medium may be produced from an arbitrary set of 'nodes' or 'reference points', the distribution of which is completely controlled by the user and can therefore be concentrated in the parts of the model well constrained by the data. An important property of the resulting tessellation is that although the sizes of the triangles (or tetrahedra) are highly irregular, their shapes are regular in the sense that they are 'as least long and thin as possible'. This makes them very useful as an irregular parametrization in inverse problems or numerical modelling methods.

The Delaunay tessellation in 3-D also provides an ideal basis for the local interpolation of irregularly distributed data when combined with another method also derived from the field of computational geometry, known as 'natural neighbour' interpolation. This method is based on the Delaunay tetrahedra and may be applied to any irregular distribution of 3-D data in a procedure which provides smooth, accurate and efficient interpolation of arbitrarily distributed irregular information.

2.2.2   Building an upper mantle model

The results of upper-mantle tomography reveal the ancient cores of the continents to have high seismic velocities, while beneath the oceans the seismic wavespeeds become lower with decreasing age of the sea floor. A tectonic subdivision of the globe can therefore be a useful basis for the parametrization of an upper mantle model. Since the tectonic regions of the globe are odd shapes and sizes, the Delaunay tessellation in an ideal tool to handle such an irregular parametrization.

Figure 3(a) shows the Earth's surface divided into regions of 8 tectonic types - as

a)

- young ocean (0-25 Myr)
- intermediate ocean (25-100 Myr)
- old ocean (>100 Myr)
- tectonic regions
- island arcs
- continental rifts
- young stable continent Phanerozoic
- old stable continent Precambrian basement
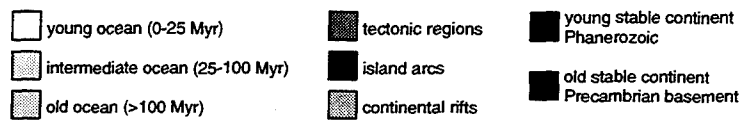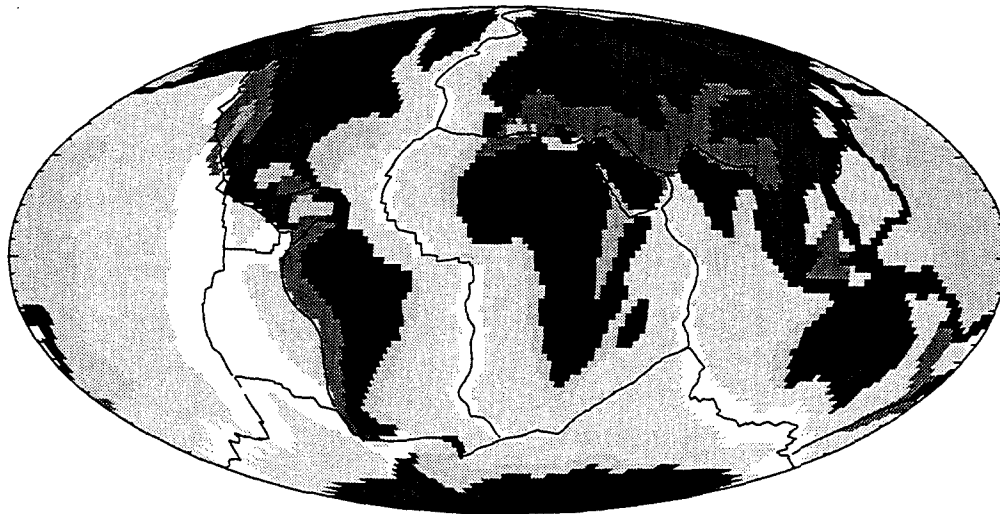
b)
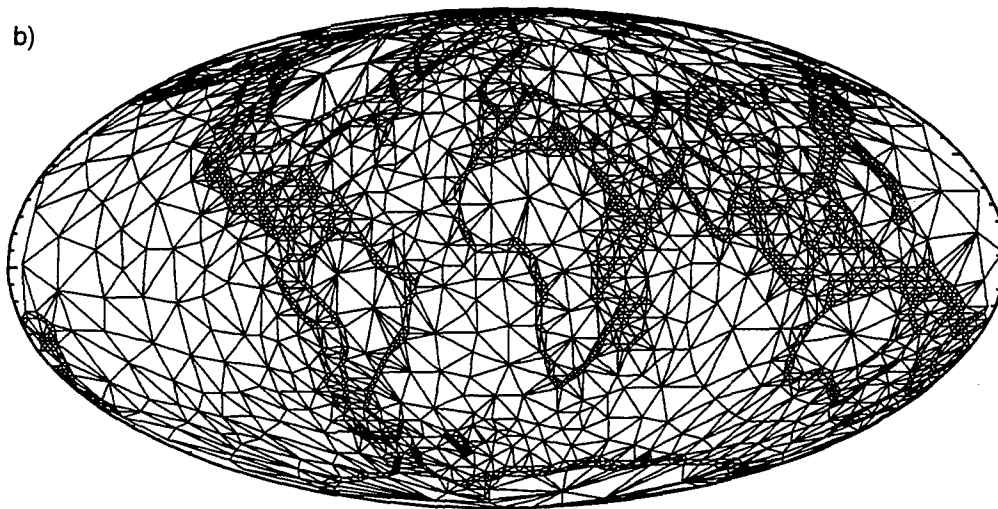
Figure 3. (a) A detailed tectonic regularisation of the surface of the Earth and (b) a Delaunay tessellation between nodes chosen to give a detailed parametrization of the transition from one region to another. This representation is proposed as suitable for a global inversion of travel times for an upper mantle model.

450

indicated in the legend. These tectonic regions are then subdivided into 97 geographical regions. Nodes are selected in each region so that the boundaries are parametrised in detail (resolution about 200km). A total of 2601 nodes are used to form the Delaunay tessellation on the surface of the globe as shown in figure 3(b). The tessellation can be carried into three dimensions to allow the representation of the rather complex behaviour of subduction zones.

A velocity perturbation at each of these nodes, with all nodes within the same region at a particular level constrained to be equal, represents a highly irregular parametrization of an Earth model. The parametrization allows for detail or sharp transition in structure where we this might be expected. The representation economically avoids over-parametrization in regions of uniform surface signature. A each level the maximum number of degrees of freedom allowed by this parametrization in 97, which is about the same as is resolved in global tomography.

This parametrization is being applied to global inversion on the basis of selected high quality travel times. Such an inversion allows the construction of regionalised one-dimensional velocity models of the upper mantle which can then be used to correct travel times for the effects of 3-D structure in a simple and efficient manner. Such corrections is crucial to removing the biases imposed by heterogeneity within the Earth on the location of seismic events (earthquakes and nuclear tests).

3 FUTURE PRIORITIES

The next stage of building realistic models for the upper mantle is to incorporate the results from detailed tomographic models for subduction zones into the global representation to compensate for strongest lateral heterogeneity. Such detailed models are available for the major subduction zones of the western Pacific margin and the Indonesian region. There is a considerable challenge to convert the tomographic images into suitable velocity models for integration into the Delaunay tessellation scheme.

It is desirable to make an extension of waveform analysis procedures for surface waves to try to exploit a wider frequency band to improve resolution of crustal and uppermost mantle structure - to improve regional representation. Higher frequency surface waves are quite sensitive to three-dimensional structure (Kennett 1995) but once the larger scale structure has been determined it should be possible to introduce path corrections to compensate for such structure

References

Kennett B.L.N. 1995. Approximations for surface wave propagation in laterally varying media, *Geophys. J. Int*, in press

Nolet G., 1990. Partitioned waveform inversion and two-dimensional structure under the Network of Autonomously Recording Seismographs, *J. geophys. Res*, 95, 8499-

Advances in Modeling Wave Propagation

Keith Lynn McLaughlin
(scatter@scubed.com)
S-CUBED Division of Maxwell Laboratories
POB 1620 La Jolla CA   92038
(http://www.scubed.com/products/geop)
VOICE 619-587-8436, FAX 619-755-0474

The statistics of regional seismograms as a function of source type, depth, distance, and frequency are not generally available for regions of the world where seismic and human activity has not provided an historic database of earthquakes, nuclear explosions, large industrial blasts, mine bumps, and rockbursts. Therefore, it is expected that future seismic discrimination practice may rely in part upon theoretical transportation of discriminants tested in regions of the world where various source types are historically available. In order to perform such a theoretical transport of a discriminant, we require an understanding of the discriminant's statistics for all source types in both the old and the new crustal structures.

In this talk we review numerical efforts to model regional seismograms in CTBT research. We categorize these methods as procedures that attempt to model the average 1D layered crustal structure, 2D crustal sections as approximations to lateral heterogeneity, and methods that attempt to model propagation in 3D lateral heterogeneity. The relative merits of the various proposed synthesis methods will be discussed regarding efficiency, completeness, and accuracy. A list of research topics and questions will be presented with examples from some recent work by CTBT researchers.

Key Words: CTBT, Synthetic Seismograms, Seismic Discrimination

Efficient Calculation of Regional Synthetic Seismograms

K. L. McLaughlin (scatter@scubed.com)
S-CUBED, POB 1620 La Jolla, CA 92038
(http://www.scubed.com/)
Contract No. F-19628-95-C-0207
Sponsored by DoE

The general behavior of regional seismograms as a function of source type, depth, distance, and frequency is not generally available in many regions of the world where seismic and human activity has not previously provided an empirical base of earthquakes, nuclear explosions, industrial blasts, mine bumps, and rockbursts. Under these circumstances, it is expected that discrimination practice may rely in part on theoretical transportation of discriminants tested in other regions of the world. In order to perform such a theoretical transport of an empirical discriminant, we must have a theoretical understanding of the behavior of that regional discriminant for both regional crustal structures. This work is intended to serve two objectives; provide more accurate and efficient means to compute, store, and retrieve synthetic regional seismograms for reference layered Earth structures and examine limitations to using layered Earth structures to model principal features of regional seismograms in the presence of lateral heterogeneity.

The project will provide means to efficiently compute wavenumber integration regional Green 92s functions on networks of UNIX workstations for layered Earth structures and then evaluate the use of layered Earth structures in discrimination research and practice. A system of programs including a user interface, a numerical seismogram generation module, and a database storage and retrieval interface will be developed. The Parallel Virtual Machine (PVM) library will be used to distribute the numerical load over a network of UNIX workstations. Wavenumber integration is an ideal candidate for parallel computing. Initial tests suggest that nearly linear improvement in calculation efficiency can be accomplished networks of CPU 92s using PVM. Improvements to existing wavenumber integration algorithms will include frequency dependent intrinsic attenuation, $Q(f)$.

Using 3D finite differences and layered Earth Green 92s functions, near-source and regional scattering will be simulated and implications for regional discrimination will be investigated. The intend of this research is to test scattering hypotheses for generation of regional waveform complexity, coda, and scattering attenuation while suggesting simple models to predict statistics of regional seismograms. Calculations will be performed using Tres3D with recursive grid refinement (RGR). This multigrid method makes efficient use of computer memory and CPU-cycles to maximize bandwidth of the finite difference calculation by placing small zones where there are low-velocity zones in the model and larger zones in regions of high-velocity in the model. Additional information on the RGR multigrid method may be found on the World Wide Web at the URL:
http://www.scubed.com/products/tres3d/Tres3D.intro.html

Regional Seismic Wavefield Modeling
with a Generalized Pseudospectral Method

Jeffrey Orrey and Charles Archambeau
Dept. of Physics, TAGG
University of Colorado
Boulder, CO 80309-0583

ABSTRACT

In this study we apply a numerical modeling method to predict and analyze discriminatory seismic signals in realistic models of the crust and to characterize wave propagation effects as functions of source and medium characteristics. The numerical method we use is the recently-developed generalized Fourier method (GFM). Based on the standard Fourier pseudospectral method, the generalized method exhibits optimal gridpoint-per-minimum-wavelength sampling and no numerical dispersion from spatial approximations. In addition, the highly accurate interface boundary condition approximations in GFM makes the method very useful for the study of the regional propagation of the discriminatory phase Lg and the effects of source and structure characteristics on the relative strengths of Lg and Rg, as well as crustal body wave phases. Furthermore, the method's computational efficiency, from the standpoint of machine storage requirements, makes possible relatively broadband simulations, relative to lower-order finite difference and finite element simulations, in both two and three dimensions.

Numerical simulations are performed to systematically determine the effects of random (small scale) and coherent (large scale) heterogeneities, anelasticity (without a weak attenuation limitation), and irregular layer topography on the energy partitioning between important seismic phases, such as Pg, Lg, and Rg. We find that Rg scattering to Lg is the dominant mechanism determining the relative amplitudes of these phases, and our results suggest the necessity of using fully-heterogeneous 3-D simulations to quantitatively assess the causes and effects of scattering in the crust.

Regional Seismic Wavefield Modeling
with a Generalized Pseudospectral Method

Objective

In this study we apply a numerical modeling method to predict and analyze discriminatory seismic signals in realistic models of the crust and to characterize wave propagation effects as functions of source and medium characteristics. The numerical method we use is the recently-developed generalized Fourier method (Orrey [3], Orrey *et al.* [4]). Based on the standard Fourier pseudospectral method (Fornberg [2]), the generalized Fourier method (GFM) exhibits optimal gridpoint-per-minimum-wavelength sampling and no numerical dispersion from spatial approximations. In addition, the unusual accuracy of interface boundary condition approximations in GFM makes the method very useful for the study of the regional propagation of the discriminatory phase L_g and the effects of source and structure characteristics on the relative strengths of L_g and R_g, as well as crustal body wave phases. Furthermore, the method's computational efficiency, from the standpoint of machine storage requirements, makes possible relatively broadband simulations, relative to lower-order finite difference and finite element simulations, in both two and three dimensions.

The objective of this study is (1) to increase the bandwidth of current 2-D and 3-D wavefield simulations in complicated, laterally-varying earth structures, (2) to systematically determine the effects of random (small scale) and coherent (large scale) heterogeneities, anelasticity, and irregular layer topography on the energy partitioning of important discriminatory signals in the crust, and (3) to quantitatively characterize discriminant dependence on differences in seismic sources, such as those from earthquakes of various types, tamped and decoupled nuclear explosions, and large industrial explosions.

Research Accomplished

A series of GFM wavefield simulations were performed for 2-D Earth models which contain complexities typical of the Earth's crust. The examples given illustrate the method's capabilities for studies of the effects of medium complexity on seismic signals and suggest directions of further study for simulations in media with three-dimensional variations in structure. All of the complicated Earth models considered in this paper are obtained by increasing the complexity of a layered crustal model containing nine layers. We examine the

wavefield propagation effects of randomization, attenuation and coherent lateral variations of this structure.

The first structural complexity we consider is the addition of random variations to the velocity values of the layered structure. In this regard, Figure 1 illustrates the effects of random spatial variations in the velocity values about mean values within a layered model, where the randomization is in both the vertical and lateral directions. In particular, Figure 1(a) shows the GPM synthetic seismograms for an explosion at 1 km depth in a layered crustal model with nine layers, and Figure 1(b) shows the seismograms in the same model with 10% rms variability imposed on the (mean) P and S wave velocities. Clearly there are major differences, in that the R_g phase is reduced as a function of distance from the source and the L_g and P_g phases are considerably increased and more complex. Since this effect is generally observed, we conclude that random fluctuations are responsible for the relatively large L_g observed relative to R_g at greater distances from the source. In this case the L_g energy is largely derived from scattering from R_g, with an associated rapid attenuation of R_g with distance and a relative growth of L_g amplitudes.

Figure 2(a), again for an explosion source at 1 km depth and a lateral position of 30 km, shows the effects of vertically and laterally discontinuous changes in the randomization, where the rms percentage of randomization changes from layer to layer in depth (with decreasing fluctuations with depth) and also decreases within lateral zones at greater distances from the explosion source. The randomization model is given in Table 1. For this model, the

Table 1: Randomization model used for the simulations of Figures 2(a) and 2(b). Each zone is 100 km in lateral extent.

depth range (km)	rms fluctuations (%)			
	zone 1	zone 2	zone 3	zone 4
$0 \leq z \leq 5$	25	20	15	10
$5 < z \leq 10$	20	15	10	5
$10 < z \leq 15$	15	11	7	3
$15 < z \leq 30$	10	7	5	3
$30 < z$	5	4	3	3

L_g is larger and the R_g smaller than was the case for the results in Figure 1(b), which had the same average velocity values. This change is largely due to the larger fluctuations in near-surface P and S velocities for the model used for Figure 2(a) compared to the structure model for Figure 1(b) (25% compared to 10% in the upper 1 km near the source). These large random velocity variations, of 25% and greater, are commonly observed from well logs and can persist to depths of at least 5 km in most areas. Therefore, the structure model used in Figure 2(a) is not extreme and, indeed, is probably conservative with respect to velocity fluctuations, particularly in tectonic areas. Furthermore, the synthetic seismograms in 2(a) are yet closer approximations to those commonly observed, compared to those in Figure 1(b).
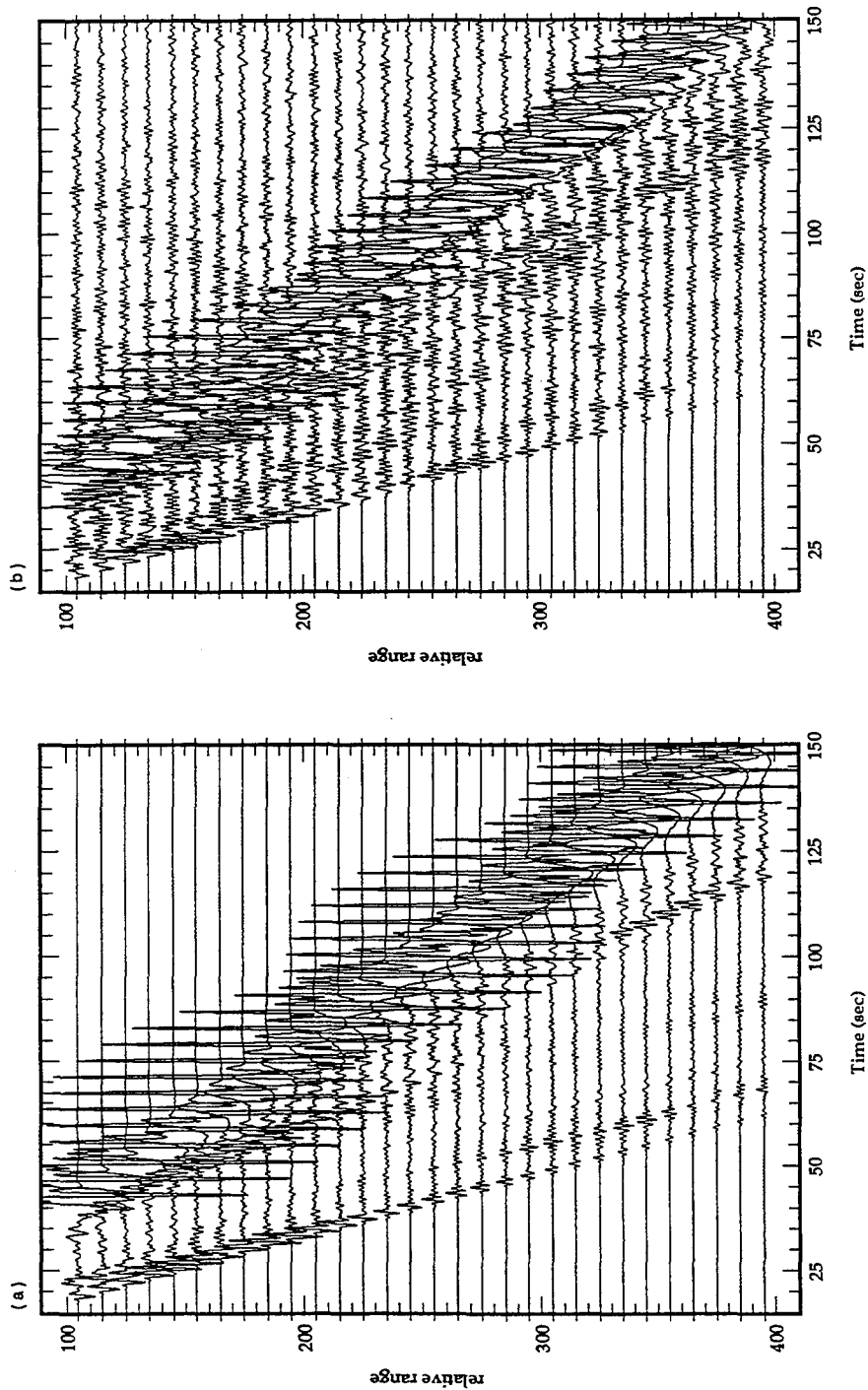
Figure 1: Comparison of GFM generated seismograms at different regional distances (in km) from an explosive source at 1 km depth in (a) the layered crustal structure and (b) the layered structure with 10 % random fluctuations in the elastic velocities. No anelastic attenuation was included in either simulation. Note in (b) the much lower levels of the R_g surface wave at larger distances and the larger amplitudes of P_g and L_g relative to the results in (a), showing the transfer of energy from the fundamental mode (R_g) to the higher modes making up P_g and L_g. This effect increases as random fluctuations increase in magnitude.

Figure 2(b) shows seismograms for a simple double couple source at a depth of 5 km in the same structure model used in Figure 2(a). In this simulation, the short period R_g excitation is lower, relative to the explosion in (5a), in part due to its greater source depth. and the P, P_g and L_g waves are also different for the two source types. However, in order to quantify the relative differences, it will be necessary to account for radiation pattern effects in a full 3-D, azimuthally-variable simulation.

Figures 3(a) and 3(b) show the effects of anelastic attenuation when compared to the simulations in Figure 2(a). In particular, the structure and explosive source used for the elastic simulation in 2(a) are also used for the simulations in Figures 3(a) and 3(b). However, in the latter simulations anelastic effects were included by the introduction of a space-dependent Q using the attenuation method of Emmerich and Korn [1]. Thus the results in Figure 2(a) are for an elastic medium (infinite Q), while those in Figures 3(a) and 3(b) include different levels of dissipation. The results in Figure 3(a) were produced with a depth-dependent Q, with a Q value of 150 near the free surface and increasing Q with depth, while those in Figure 3(b) are for a (low) Q value of 25 near the surface that also increases with depth. Comparing Figures 2(a) and 3(a) indicates a modest decrease in R_g and L_g due to moderate anelastic attenuation, while comparison of the results for the low Q case in Figure 3(b) with the elastic or moderate Q cases shows a dramatic reduction in both the R_g and L_g energy with distance while the P waves remain relatively unaffected. We note that a low near-surface Q model will always have a rather drastic effect on the short period R_g and L_g surface wave modes and that in comparison to actual data this is not typically the case. That is, while R_g decreases rapidly with distance, L_g does not, and in fact the L_g coda tends to increase in duration and magnitude in many areas. This suggests that R_g scattering to L_g is the dominant mechanism and that results like those in Figure 3(a), with a moderate Q, are appropriate in the general case.

In the final example, we show the effect on crustal phases of the large-scale lateral variation in structure illustrated in Figure 4. This structure is intended to approximate the occurrence of a sedimentary basin along the source-receiver path. Figure 5 shows the seismograms obtained from a simulation through the structure of Figure 4. These results should be compared to those in Figure 2(a) since the model used contained no anelastic dissipation and the velocity structure was the same for both simulations, except for the presence of the basin in the results in Figure 5. Clearly the R_g phase is strongly affected by the basin structure, with reduced amplitudes upon emergence from the basin, and the L_g is also reduced. Thus, this large-scale structure had the effect of "blocking" both R_g and L_g while not affecting the P and P_g phases very much.

Conclusions

To some extent, even with the small sampling of simulations presented here, it is possible to infer specific effects of structure variations on the important discriminatory signals. These examples suggest the similarity of the results of the numerical simulations to observed seismograms. Realistic synthetic data can be analyzed in precisely the way field observations would be analyzed to form various discriminatory measures (e.g. modified m_b vs. M_s at
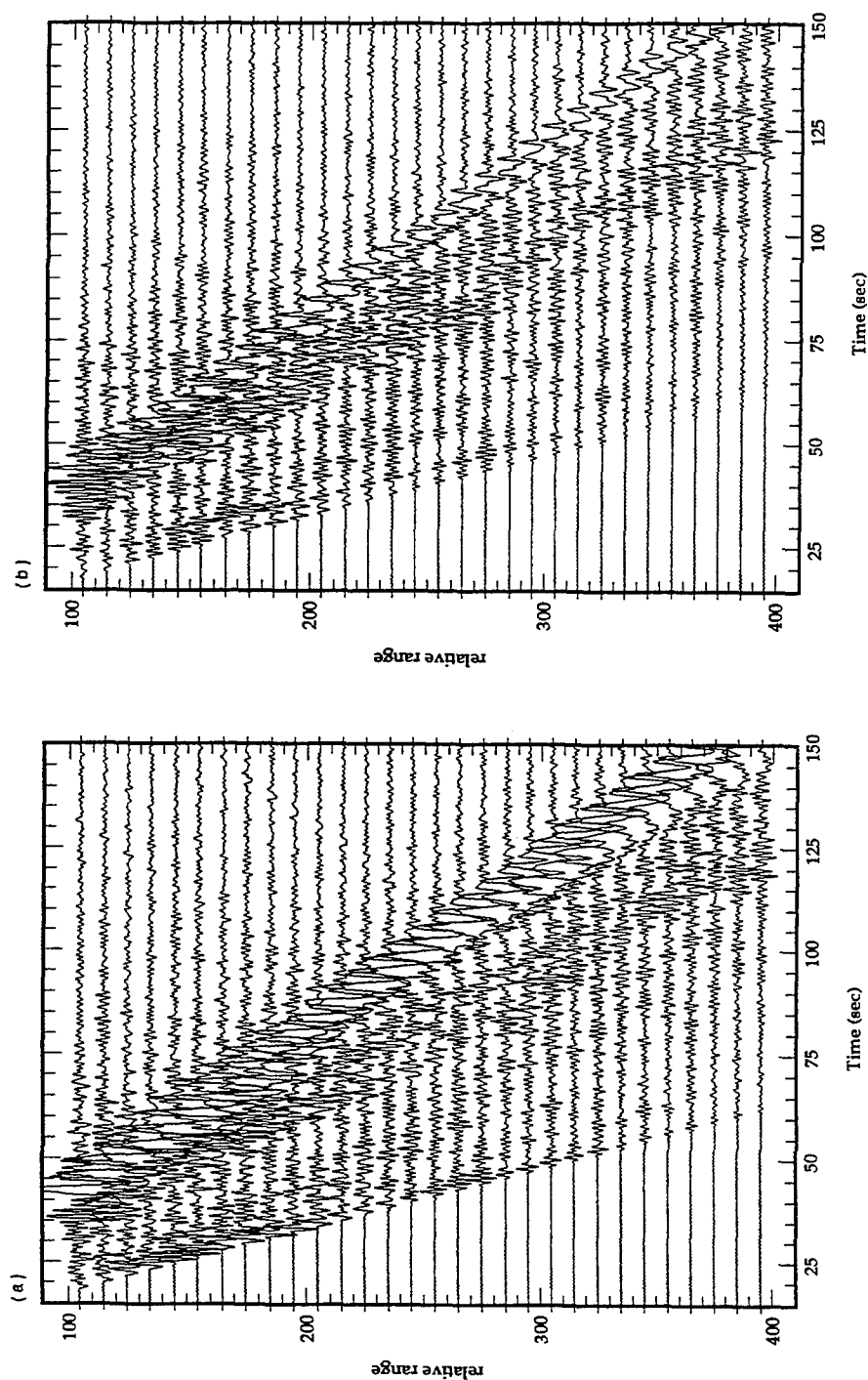
Figure 2: GFM generated seismograms in the layered structure with strong, random elastic velocity fluctuations and no anelastic attenuation. The strongest fluctuations are 25 % rms, and the fluctuations decrease with distance from the source. The source in (a) was an explosion at 1 km depth, and the source in (b) was a double couple at a depth of 5 km with the fault plane oriented at 45 degrees from the vertical.
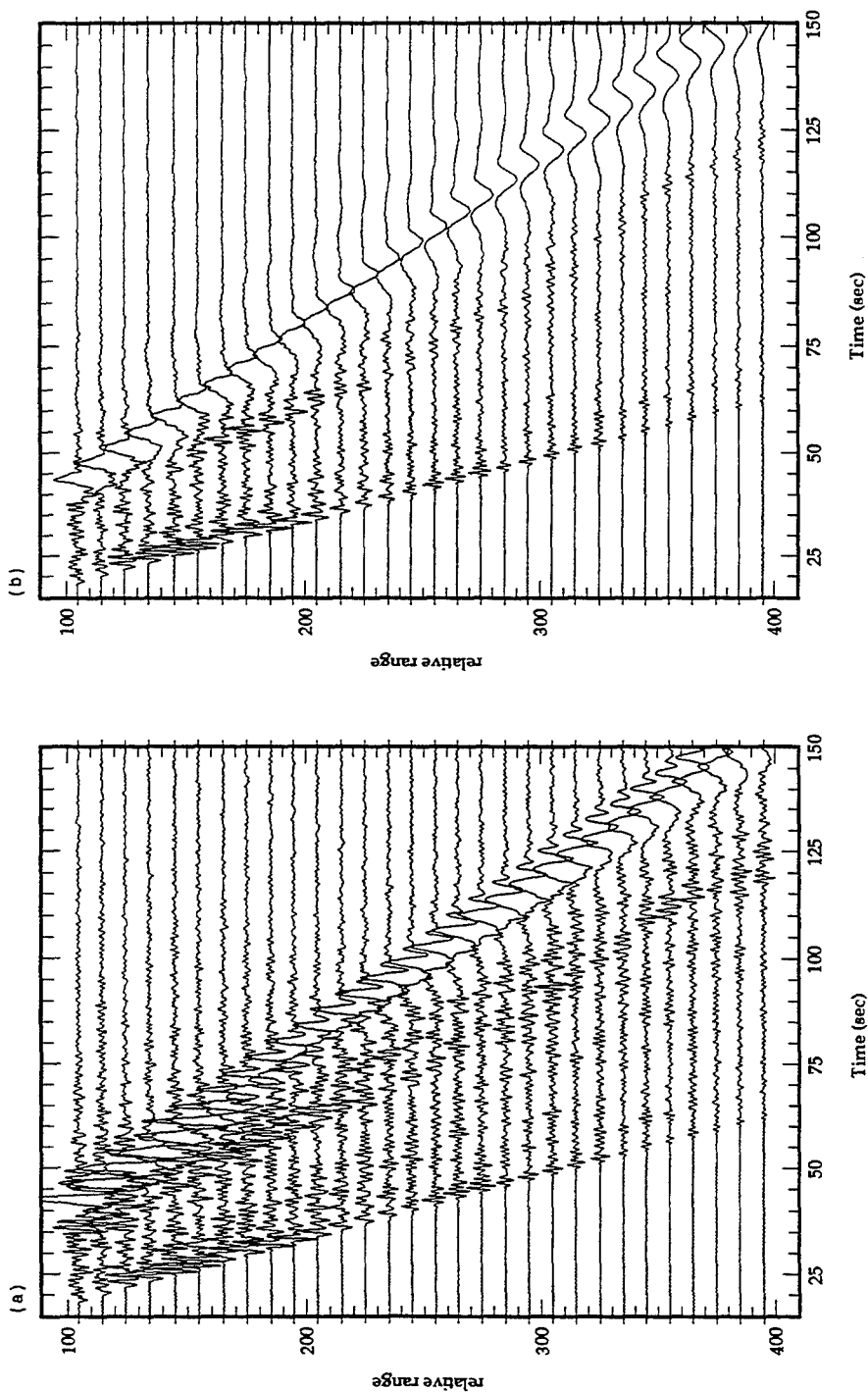
Figure 3: GFM generated seismograms in the same structure used for the simulations of Figure 2 except these models contain anelastic dissipation effects. The Q values are depth-dependent, with the Q increasing with depth. In (a), the minimum Q value is 150 near the free surface. In (b), the Q values are much lower, with a minimum Q value of 25 near the free surface.
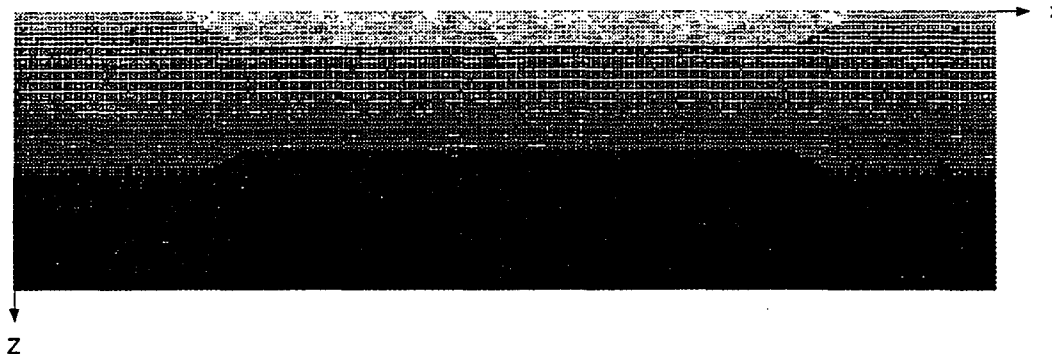
Figure 4: Randomized basin structure used to generate the seismograms in Figure 5. Light shades indicate low velocities and dark shades indicate high velocities. The basin and its associated mantle uplift span a source-receiver range (x) of 70 km to 270 km, and the basin extends to a depth (z) of 10 km and contains stronger (30 % rms) near-surface velocity fluctuations than exist in the surrounding structure.

different frequencies, spectral ratios, etc.) in order to infer their physical basis, robustness, variability and any structure-induced anomalies.

References

[1] H. Emmerich and M. Korn. Incorporation of attenuation into time-domain computations of seismic wave fields. *Geophysics*, 52(9):1252–1264, September 1987.

[2] B. Fornberg. The pseudospectral method: Comparisons with finite differences for the elastic wave equation. *Geophysics*, 52(4):483–501, April 1987.

[3] J. L. Orrey. *A Generalized Fourier Pseudospectral Method for Elastodynamics*. PhD thesis, University of Colorado, Boulder, 1995.

[4] J. L. Orrey, C. B. Archambeau, and G. A. Frazier. Complete elastic wavefield synthesis with a pseudospectral method: The Generalized Fourier Method. Submitted to *Geophys. J. Int.*
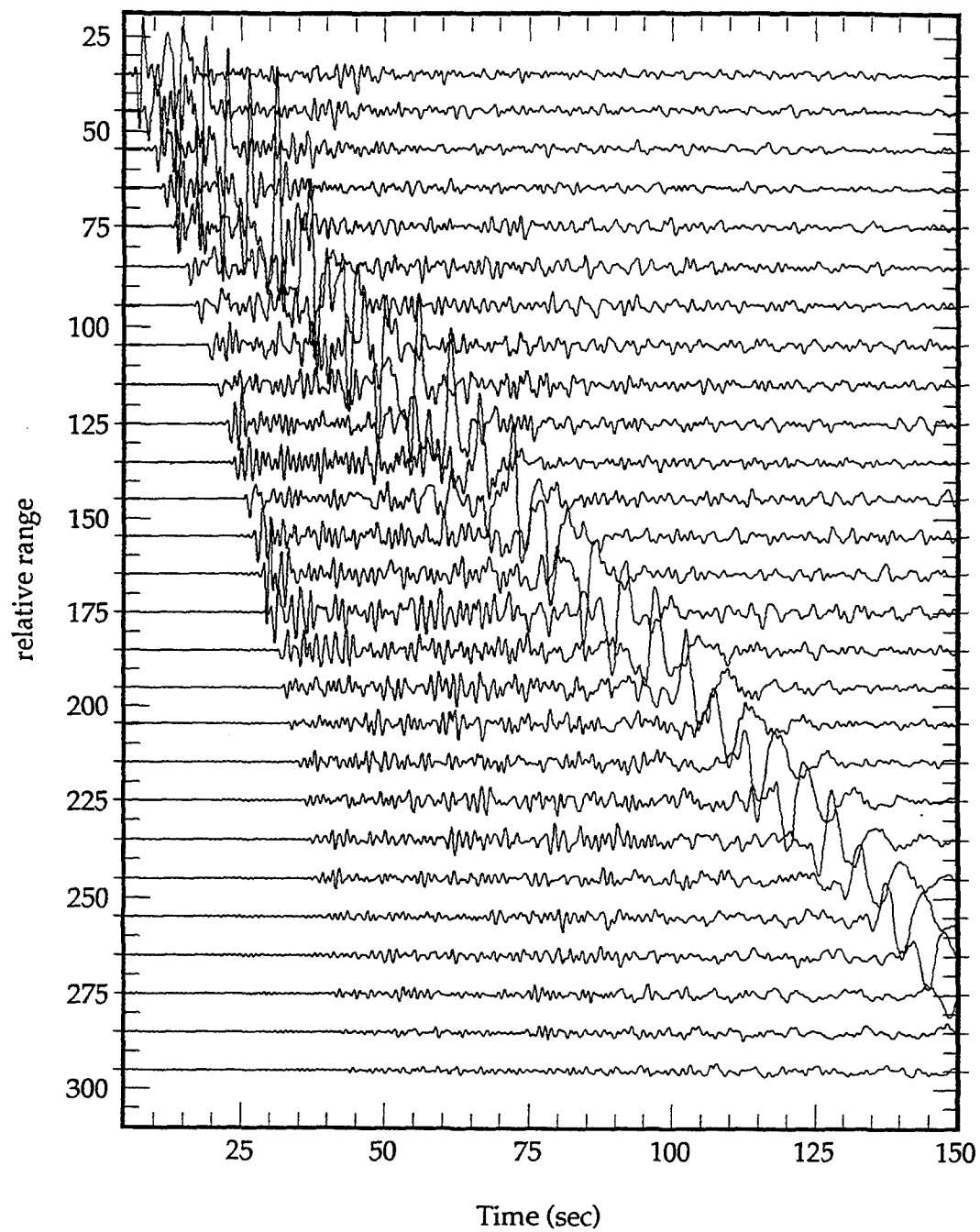
Figure 5: GFM generated seismograms from an explosive source at 1 km depth in the layered, randomized basin structure of Figure 4.

TITLE: The Effects of Anisotropy on Regional Seismic Wave Propagation

PRINCIPAL INVESTIGATOR: Jeffrey Park
Co-WORKERS: Liqiang Su, Jonathan Lilly
AFFILIATION: Department of Geology and Geophysics, Box 208109
Yale University, New Haven, CT 06520-8109
AFOSR contract: F49620-94-1-0043

August 3, 1995

ABSTRACT

We have examined the effect of seismic anisotropy on the scattering of surface waves in actively-deforming continental regions, many of which occur in areas of nonproliferation concern. We have approached the problem from three angles, 1) we have developed waveform inversion methods for Love-Rayleigh coupling in seismic data from the Tibetan Plateau and Tien Shan region, 2) we have developed a flat-layered surface wave code to study the effect of crust and upper-mantle anisotropy on crustal resonances, and 3) we have advanced wavelet-based signal processing methods to estimate the polarization of coherent seismic energy across a broadband seismic array. In data from the recent portable broadband PASSCAL deployment in Tibet, we found clear evidence of long-period Love-to-Rayleigh scattering that is best explained by lateral gradients of anisotropy in the upper mantle, developed in the course of the compression and uplift of the plateau. We developed a modal summation technique for waveform perturbations that allowed us to infer that *both* S and P wave anisotropy, with a ratio consistent with the mineral alignment of sheared peridotite, in the depth range 100–300 km are necessary to fit the observed data. Using a plane-layered geometry, we are investigating the effect of crust and upper mantle anisotropy on Love-Rayleigh coupling in the 5-30 second period range. Most previous studies have posited a horizontal or vertical axis of symmetry for seismic anisotropy, but our code can incorporate a tilted axis of symmetry, which enhances coupling and scattering effects. Such dipping geometries could develop in the crust as a result of thrust ramps in compressive tectonic regimes, either in the form of oriented crystals in shear zones or fine-layering of isotropic material. We have developed a multiple-station wavelet-based method for detecting frequency-dependent polarization in noisy seismic data. The wavelet method, unlike the moving-window Fourier transform, scales the time interval analysed to the period of the presumed signal. We have applied this method successfully thusfar to Terrascope data from Southern California, and have documented a strong refraction of intermediate-period surface waves along the "big-bend" portion of the San Andreas Fault.

463

OBJECTIVE

We wish to determine the effect of seismic anisotropy, within the crust and uppermost mantle, on surface waves with periods between 10 and 30 seconds. In particular, we wish to characterize the scattering caused by lateral variations in anisotropy in regions of past and present lithospheric deformation. This path-dependent scattering can distort seismic waveforms, and make more difficult the discrimination of explosions from earthquakes. We plan to identify regions of the Earth where scattering associated with lithospheric anisotropy is important. Data from regional networks and arrays located in Eurasia and the US will also be used in experiments to extract 'scattered' waveforms from the principal Love and Rayleigh wavepackets. In addition to standard stacking/beamforming techniques, we will develop a frequency-dependent variant of the MUSIC algorithm to identify coherent surface waves that traverse an array. We plan to test, in selected areas, whether anisotropy inferred from the 'splitting' of 1-20 second shear waves is sufficient to explain observed Love to Rayleigh scattering.

TECHNICAL PROPOSAL: RESEARCH ACCOMPLISHED

We have developed codes for the dispersion characteristics of crustal surface waves in a 1-D anisotropic media, with anisotropy that is hexagonally symmetric, but with an axis of symmetry that is arbitrary. Previous investigators have restricted attention to symmetry axes that are either vertical or horizontal, but a tilted axis of symmetry is plausible in the uppermost crust and perhaps near the Moho, where thrusting and extension involves a combination of vertical and horizontal deformation. A modification of this code can be used to examine the behavior of teleseismic body waves that propagate upward through an anisotropic crustal structure. Enhanced coupling between P-SV and the SH particle motion occurs for waves that have significantly non-vertical incidence, in particular between P and SH motion.

We would like to express the interaction of upgoing and downgoing plane waves in a weakly anisotropic layered medium with hexagonal symmetry. Hexagonal symmetry implies a stress-strain relation that possesses an axis of symmetry $\hat{w}$. Elastic properties are constant within each of a stack of layers over a uniform halfspace, but the axis of symmetry can vary among the layers. We express the elastic properties as a function of depth as $\Lambda(r)$, where Λ_{ijkl} is the fourth-order stress-strain tensor. If the axis of symmetry is horizontal, we can express the azimuthal dependence of the squared P and SV velocities for horizontal propagation in terms of the angle ξ from $\hat{w}$, according to formulas similar to the head-wave formulas of *Backus*, [1965], *Crampin* [1977] and *Park* [1993]:

$$\rho\alpha^2(\xi) = A + B\cos 2\xi + C\cos 4\xi$$
$$\rho\beta^2(\xi) = D + E\cos 2\xi. \tag{1}$$

If density perturbations are neglected, knowledge of A, B, C, D, E is sufficient to determine the stress-strain tensor [*Shearer and Orcutt*, 1986]. *Park* [1993] showed how these azimuthal relations generalize to other orientations of $\hat{w}$. We assume a flat earth, $z = 0$ at the free surface, and z increasing downward. We assume a plane-wave solution of the form $U(x, t) =$

464

$\mathbf{u}(\mathbf{x})e^{i(\mathbf{k}\cdot\mathbf{x}-\omega t)}$. The strain tensor

$$\epsilon = \frac{1}{2}(\nabla\mathbf{u} + (\nabla\mathbf{u})^T) = \frac{i}{2}(\mathbf{k}\otimes\mathbf{u} + \mathbf{u}\otimes\mathbf{k})e^{i(\mathbf{k}\cdot\mathbf{x}-\omega t)}$$

In each layer, the elastic tensor can be expressed

$$\Lambda = A\Lambda_A + B\Lambda_B + C\Lambda_C + D\Lambda_D + E\Lambda_E, \tag{2}$$

where

$$
\begin{aligned}
\Lambda_A &= \mathbf{I}\otimes\mathbf{I} \\
\Lambda_B &= \mathbf{W}\otimes\mathbf{I} + \mathbf{I}\otimes\mathbf{W} \\
\Lambda_C &= 8\mathbf{W}\otimes\mathbf{W} - \mathbf{I}\otimes\mathbf{I} \\
\Lambda_D &= (\mathit{13})\mathbf{I}\otimes\mathbf{I} + (\mathit{14})\mathbf{I}\otimes\mathbf{I} - 2\mathbf{I}\otimes\mathbf{I} \\
\Lambda_E &= 2[(\mathit{13})\Lambda_B + (\mathit{14})\Lambda_B - 2\Lambda_B] + \Lambda_D,
\end{aligned}
\tag{3}
$$

where '$\otimes$' is the tensor product operation, and $\mathbf{W} = \hat{\mathbf{w}}\otimes\hat{\mathbf{w}} - \frac{1}{2}\mathbf{I}$, where $\mathbf{I}$ is the identity tensor. The permutation (ij) indicates the interchange of the ith and jth tensor index e.g., $\{(\mathit{13})\mathbf{I}\otimes\mathbf{I}\}_{ijkl} = \delta_{kj}\delta_{il}$. An isotropic elastic tensor $\Lambda^{(0)}$ contains only terms proportional to the isotropic tensors Λ_A and Λ_D, as neither depends on $\hat{\mathbf{w}}$.

Because P, SV and SH motion can couple at all interfaces in a layered anisotropic structure with general axis of symmetry $\hat{\mathbf{w}}$, all interacting upgoing and downgoing plane waves share the same horizontal wavenumber. Let $\frac{\mathbf{k}}{\omega} = p\hat{\mathbf{x}} + \nu\hat{\mathbf{z}}$, where p and ν are the horizontal and vertical slownesses, respectively. In a general anisotropic medium, there are three upgoing and three downgoing plane waves. For fixed p, the Christoffel relations lead to six possible solutions for ν, as determined by the quadratic eigenvalue problem

$$(p^2\mathbf{T} - \rho\mathbf{I} + \nu p\mathbf{S} + \nu^2\mathbf{R})\cdot\mathbf{u} = 0 \tag{4}$$

where

$$
\begin{aligned}
\mathbf{T} &= (A - B + C - D + E)\hat{\mathbf{x}}\otimes\hat{\mathbf{x}} + (D + (2w_x^2 - 1)E)\mathbf{I} + (8w_x^2 C + 2E)\hat{\mathbf{w}}\otimes\hat{\mathbf{w}} \\
&\quad + (B - 4C - 2E)w_x(\hat{\mathbf{w}}\otimes\hat{\mathbf{x}} + \hat{\mathbf{x}}\otimes\hat{\mathbf{w}}) \\
\mathbf{S} &= (A - B + C - D + E)(\hat{\mathbf{x}}\otimes\hat{\mathbf{z}} + \hat{\mathbf{z}}\otimes\hat{\mathbf{x}}) + 4w_x w_z E\mathbf{I} + 16w_x w_z C\hat{\mathbf{w}}\otimes\hat{\mathbf{w}} \\
&\quad + (B - 4C - 2E)[w_z(\hat{\mathbf{w}}\otimes\hat{\mathbf{x}} + \hat{\mathbf{x}}\otimes\hat{\mathbf{w}}) + w_x(\hat{\mathbf{w}}\otimes\hat{\mathbf{z}} + \hat{\mathbf{z}}\otimes\hat{\mathbf{w}})] \\
\mathbf{R} &= (A - B + C - D + E)\hat{\mathbf{z}}\otimes\hat{\mathbf{z}} + (D + (2w_z^2 - 1)E)\mathbf{I} + (8w_z^2 C + 2E)\hat{\mathbf{w}}\otimes\hat{\mathbf{w}} \\
&\quad + (B - 4C - 2E)w_z(\hat{\mathbf{w}}\otimes\hat{\mathbf{z}} + \hat{\mathbf{z}}\otimes\hat{\mathbf{w}})
\end{aligned}
\tag{5}
$$

To transform (8) into a linear 6×6 eigenproblem, define $\tilde{\mathbf{T}} = \mathbf{R}^{-1}\cdot(p^2\mathbf{T} - \rho\mathbf{I})$ and $\tilde{\mathbf{S}} = p\mathbf{R}^{-1}\cdot\mathbf{S}$ to obtain $(\tilde{\mathbf{T}} + \nu\tilde{\mathbf{S}} + \nu^2\mathbf{I})\cdot\mathbf{u} = 0$. This 3×3 system can be solved with the 6×6 system

$$(\mathcal{T} - \nu\mathcal{I})\cdot\mathcal{U} = \left(\begin{bmatrix} -\tilde{\mathbf{S}} & -\tilde{\mathbf{T}} \\ \mathbf{I} & 0 \end{bmatrix} - \nu\begin{bmatrix} \mathbf{I} & 0 \\ 0 & \mathbf{I} \end{bmatrix}\right)\cdot\begin{bmatrix} \nu\mathbf{u} \\ \mathbf{u} \end{bmatrix} = 0 \tag{6}$$

Solving (6) will obtain three upgoing and three downgoing waves, aside from exceptional cases e.g., if p equals the P or S slowness in a layer and the associated wave travels horizontally. (In this case the matrix system is formally defective.) To solve the equation of motion

465

in a stack of constant-property layers, one matches boundary conditions for traction and displacement continuity for these six waves at each interface. We obtain surface-wave modes by forcing an evanescent condition in the halfspace, propagating the stress-displacement vector to the free surface, and enforcing a zero-traction condition. There are several schemes for doing this. We have adapted the computational algorithm of *Chen* [1993], which forces all evanescent waves to "decay" away from interfaces to decrease roundoff error. At a fixed frequency, the algorithm searches the allowable interval of horizontal slowness for roots to the secular function that describes free-surface traction. The computational formulas are quite similar to the Rayleigh-wave formulas of *Chen* [1993], except that the reflection and transmission matrices are 3×3, rather than 2×2. The numerical application is complicated by the need to separate travelling modes that are closely spaced in phase velocity. To keep track of solutions, we use the group velocity of a mode at a frequency f to predict a phase-velocity "window" in which a solution should be found at frequency $f + \delta f$. This also reduces the number of propagator-evaluations of the surface traction condition, each of which requires solution of a 6×6 eigenvector system in each layer. This type of interpolator is not always successful, unfortunately, because the coupling of Rayleigh and Love motion can cause "bow-ties" in the dispersion curves where surface-wave modes mix in near-equal amounts - see Figure 1.

We have developed and coded a path-integral formalism to invert Love-to-Rayleigh and Rayleigh-to-Love scattered waveforms. Although we plan to apply these techniques to flat-layer geometry for crustal/lithospheric surface waves, our earlier work made natural the initial development of a spherical-earth formalism using coupled free oscillations. A problem when calculating coupled-mode synthetics in a 3-D earth model is the sum over all singlets associated with spherical harmonic multiplets. By using the summation theorem of spherical harmonics, we sum the singlets analytically and calculate the synthetics by summing multiplets rather than singlets. We expand the elastic tensor to a general 6×6 matrix to handle arbitrary orientations of the anisotropic fast axis. This technique enables us not only to calculate synthetics quickly in a 3-D anisotropic structure but also to establish an inverse algorithm because of the linear property of differential seismograms. These synthetics compare well with 3-D strong Born synthetics, which implies that, for the models we have considered, Love-Rayleigh scattering occurs primarily along the great-circle path. We use the great-circle technique to fit waveforms recorded in a recent broadband PASSCAL experiment in Tibet (Figure 2). We find that the observed waveform anomalies in the southern part of the Plateau can be well explained with a strong anisotropic gradient zone beneath the central Plateau. An additional anisotropic zone in central Alaska can be used to fit details in the Tibet data better. The presence of such an anisotropic zone is supported by a quasi-Love wave, observed at College, Alaska, in data from the 1/16/95 Kobe, Japan earthquake.

We have also extended the multiple wavelet polarization method to apply to three-component array data. We have been testing this method on data from the Terrascope broadband regional network in Southern California. The wavelet method enables the user to pick apart the time-frequency behavior of seismic data, and the SVD-polarization code enables the user to correlate motion between stations, preserving the small time shifts and amplitude/polarization variability that would be averaged out in simple beamforming. For surface waves in the 40-100 sec period range, there is considerable variability in amplitude and polarization within the roughly 250 km aperture of the Terrascope network. There is also evidence for significant Love-to-Rayleigh forward scattering in the 40-100 sec period
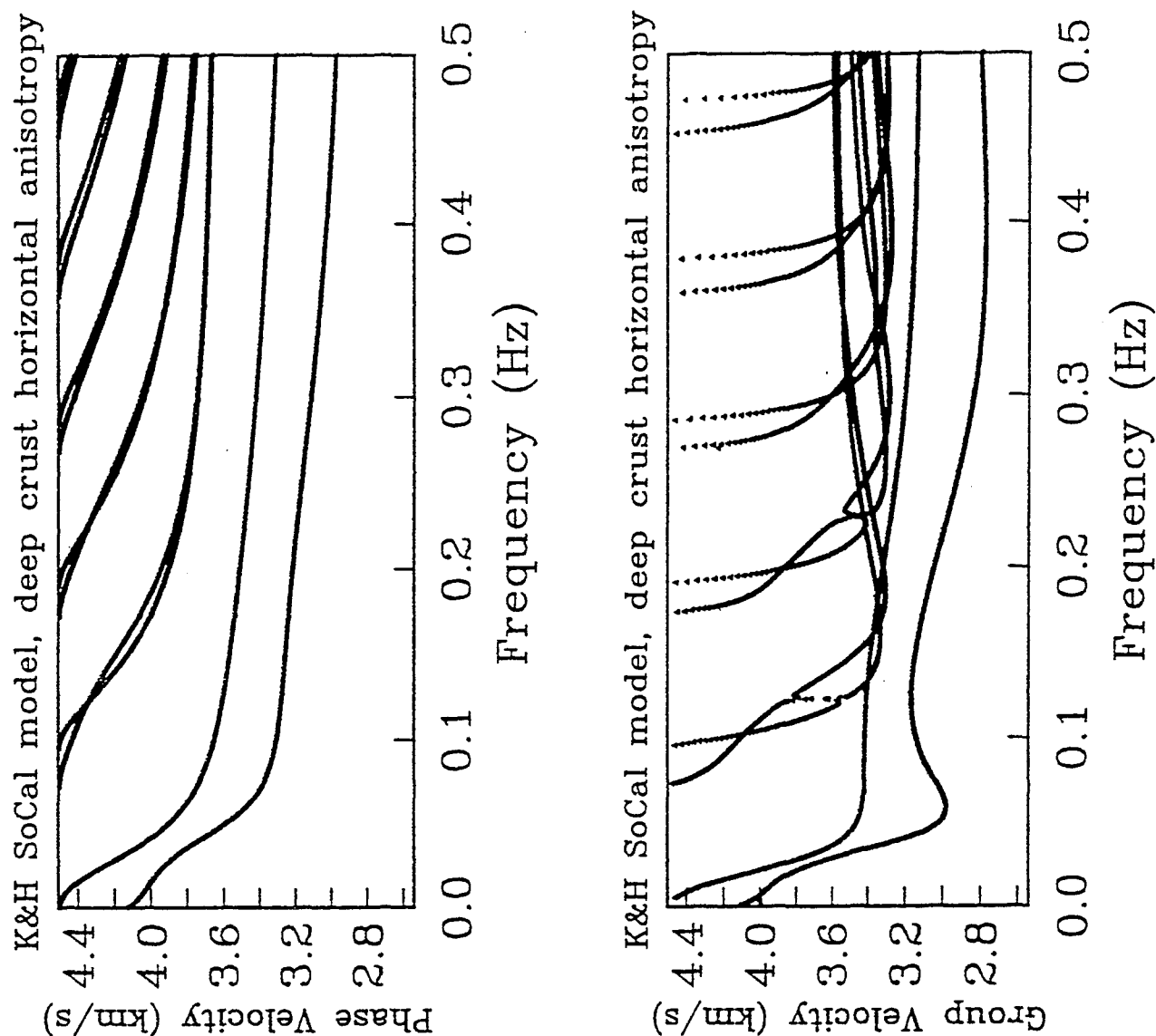
Figure 1. Dispersion curves for hybrid Love-Rayleigh surface waves in an anisotropic crustal waveguide. The velocity model is a modified form of the one-dimensional velocity model used to locate earthquakes in Southern California. Anisotropy with a horizontal axis of symmetry at 45° angle to the propagation is assumed, with 4% peak-to-peak variation in P-velocity and 2% peak-to-peak variation in S-velocity, both with sin 2θ azimuthal dependence. The anisotropy is prescribed only in a 5-km thick layer at the base of the crust, consistent with the crustal extension common in the western US. The Love and Rayleigh dispersion curves tend to couple strongly where they cross in the phase-velocity graph, making "bridges" between pairs of group velocity curves. The eigenfunctions for these dispersion branches (not shown) exhibit significant mixing of Love and Rayleigh particle motion, even far from these crossing points.
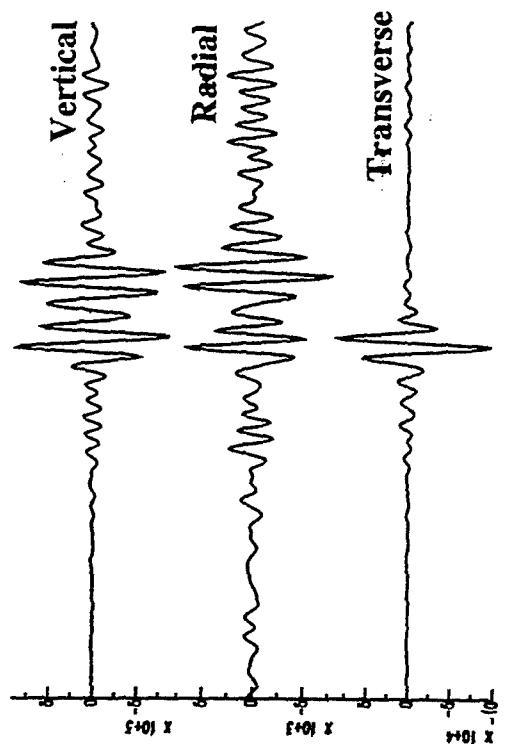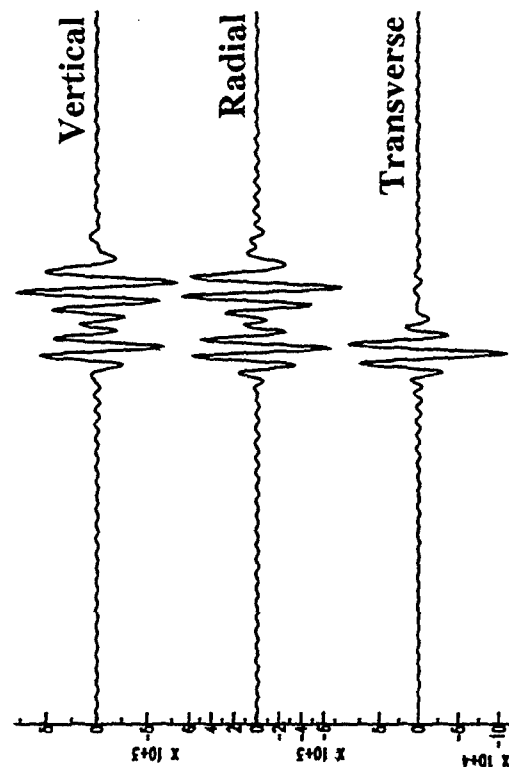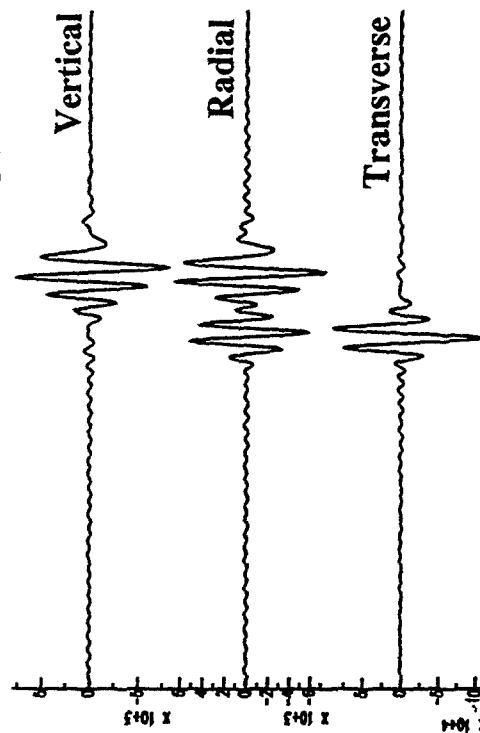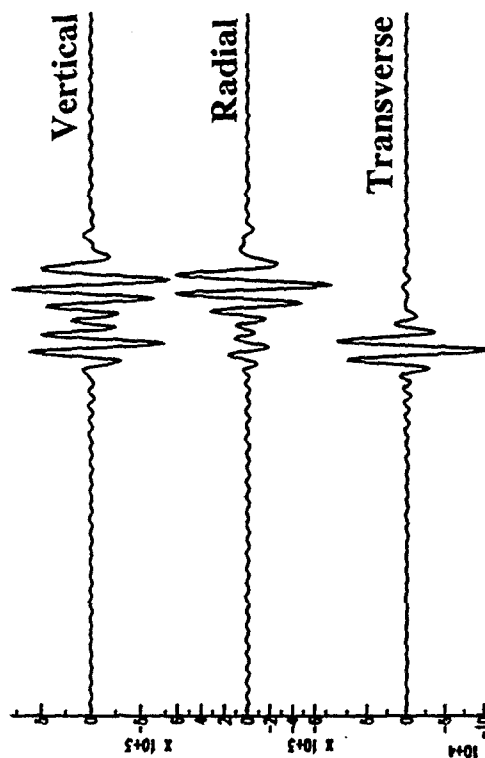
Figure 2. The upper right panel shows broadband data from 28 June 1992 Landers, California event, recorded at CDSN station LSA (Lhasa, Tibet). The lower right panel shows the coupled-mode-sum synthetics with only S wave (2%) anisotropy, with an east-west horizontal symmetry axis, at 100-300 km depth, consistent with lithospheric compression beneath the Tanggula Shan mountain range in southern Tibet. The lower left panel shows the synthetics with only P wave (6%) anisotropy. The upper left panel shows the synthetics combined with 6% P anisotropy and 2% S anisotropy.

range, which indicates lithospheric, perhaps crustal, scattering. Although rough isotropic lateral structure can scatter Love to Rayleigh motion, significant scattering usually involves a strong deflection of the wave. Anisotropic structure is a better model for forward scattering, as the spatial distortion of the stress-strain relation better couples the Love and Rayleigh particle-motion polarizations.

We have looked at seismic data recorded by Terrascope from Pacific earthquakes in a broad azimuthal range, to examine forward-scattering across the array. For the 24 May 1994 strike-slip earthquake in Taiwan (M_S=6.6, depth=33 km), surface waves intersect the California coastline at a low angle to the North-America/Pacific plate boundary, and so are susceptible to severe multipathing and scattering. At the inland station GSC (Goldstone, CA) the wavelet transform of the three components (vertical, radial, transverse) reveals significant radial-component energy for the Love wave, and transverse-component energy for the Rayleigh wave. A clear quasi-Love scattered wave follows the Love wave closely on the vertical component, in the period range 40-100 seconds. Wavelet polarization analysis of the GSC record (Figure 3) shows that, though long-period (> 100 sec) Love polarization is undisturbed, the intermediate-period polarization suffers refraction and some elliptical motion on the horizontals. The projection of correlated motion onto the radial-vertical plane shows low-amplitude elliptical motion, consistent with the quasi-Love wave's "Rayleigh" nature. The first pulse of Rayleigh energy is strongly refracted at intermediate frequencies, by roughly 45 degrees!

We have solved for polarized signals that are correlated network-wide using a singular value decomposition (SVD) of a matrix of complex-valued "wavelet coefficients," very much like the complex values of a standard discrete Fourier transform, or DFT. There are two aspects of this that differ from standard array-stacking techniques, and which justify the extra processing of the SVD. First, the SVD looks for a signal expressed as a linear combination of wavelet coefficients. Since these are complex valued, relative time shifts between stations can be accommodated by the algorithm as phase shifts in the wavelet coefficients. In principle, the SVD-decomposition could solve for the proper stacking velocity of a pulse, and could capture the non-plane-wave nature of a wave scattered within or close to the sensors. Similarly, the distortion of the wavefront across the seismic sensors can be captured by the SVD algorithm, which does not prescribe a uniform polarization at all stations. For Terrascope data, application of the SVD algorithm reveals that strong refraction of surface waves, usually attributed to the continent-ocean boundary, appears to occur most strongly inland of the Los Angeles Basin along the San Andreas Fault (Figure 4). Similarly, we observe that Love-to-Rayleigh scattered waves tend to be stronger for inland, relative to coastal, Terrascope stations. This suggest that, from the point of view of forward scattering, the strongest lateral gradients of material properties in the upper mantle beneath Southern California are associated with the plate boundary, not the coastline.

The following papers have been supported by this contract thusfar:

Yu, Y., J. Park & Wu, F., 1995. Mantle anisotropy beneath the Tibetan Plateau: evidence from long-period surface waves, *Phys. Earth and Planet. Int.*, , *87*, 231–246.

Lees, J., and J. Park, 1995. Multiple-taper spectral analysis: A standalone C-subroutine, *Computers and Geosciences, 21,* 199–236.

Park, J., 1995. Seismic wave propagation studies in the US: 1991-1994, US National Report to the IUGG, *Reviews of Geophysics Supplement, 33,* 335–340.

Lilly, J. and J. Park, 1995. Multiwavelet spectral and polarization analysis of seismic records.

GOLDSTONE - GSC
Seismic Data

Time (second)

← RADIAL VS. TRANSVERSE ↓

← RADIAL VS. VERTICAL ↑
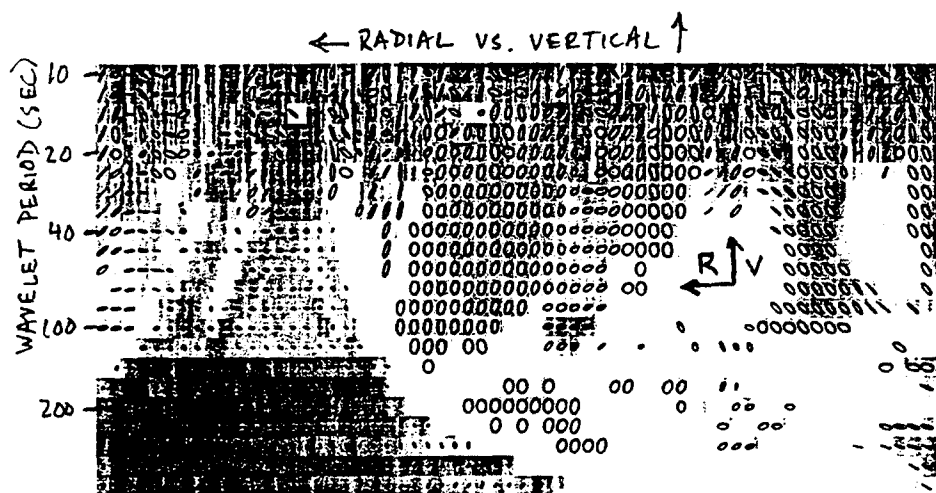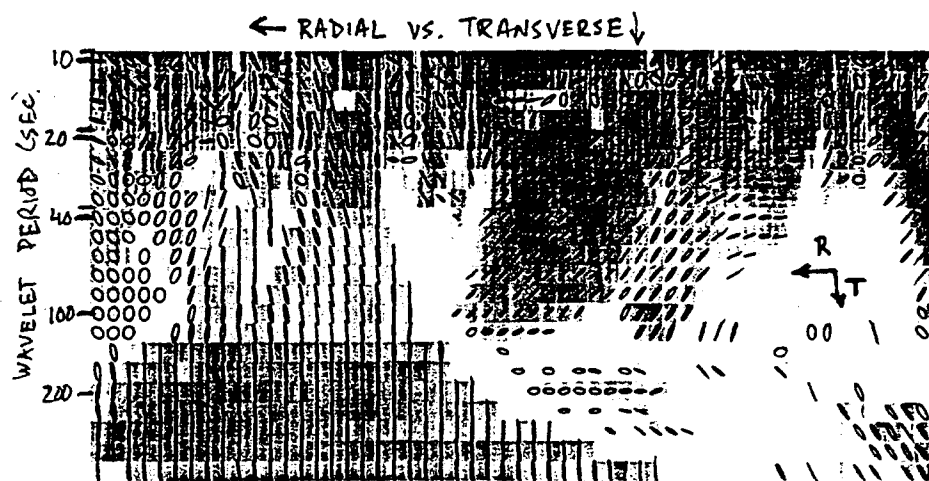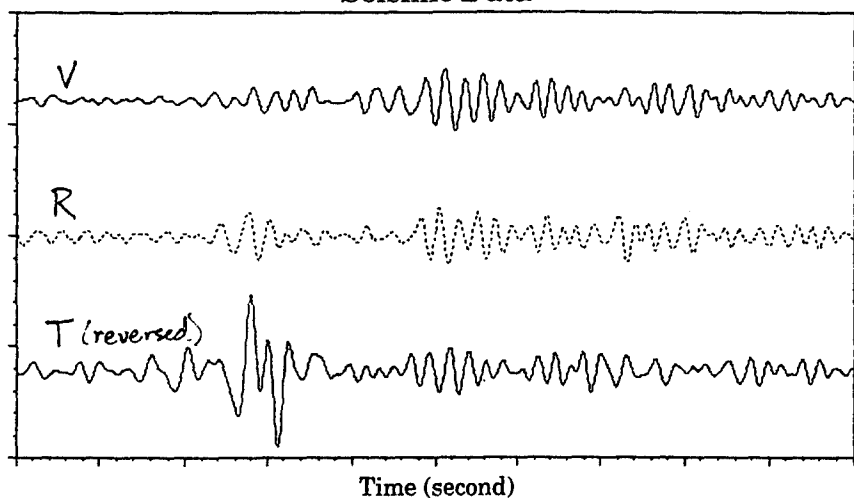
Figure 3. Multiwavelet polarization analysis of the 24 May 1994 Taiwan event recorded at GSC (Goldstone, CA). Our analysis uses three complex Slepian wavelets with $p = 2.5$, $p_c = 3.0$. The data is plotted in the upper panel, with horizontals rotated to radial and transverse directions. In the lower panels the normalized first singular value d_1 of the multiwavelet transform matrix M is shaded where it exceeds 90% confidence for nonrandomness. The center panel shows particle motion in the horizontal plane, with radial component oriented right-left, and the transverse component oriented up-down. The lower panel shows particle motion in the radial-vertical plane, with radial component oriented right-left, and the vertical component oriented up-down.

470

Propagation Direction of Rayleigh Wave
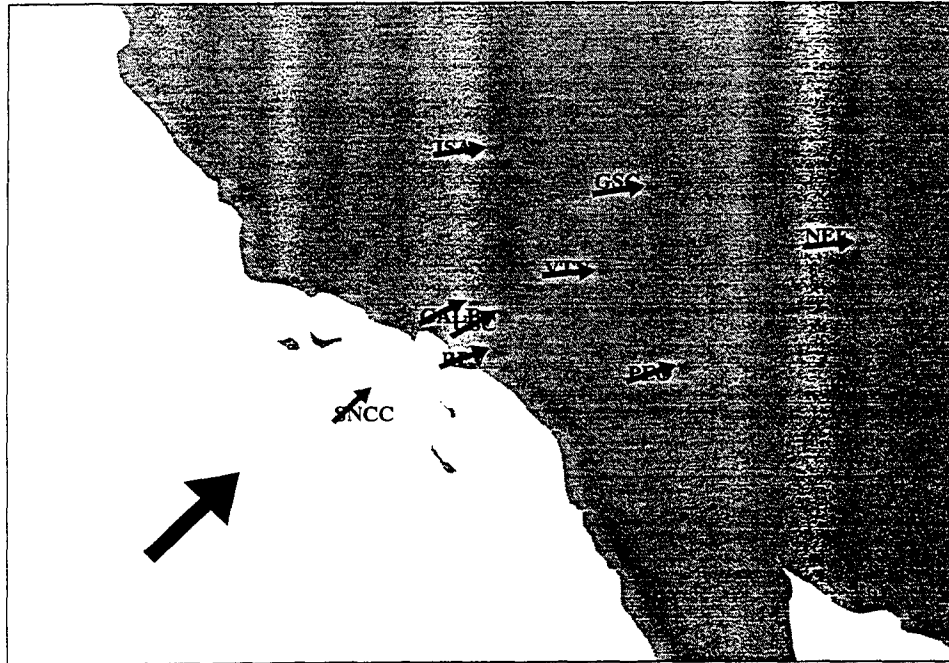
Propagation Direction of Love Wave
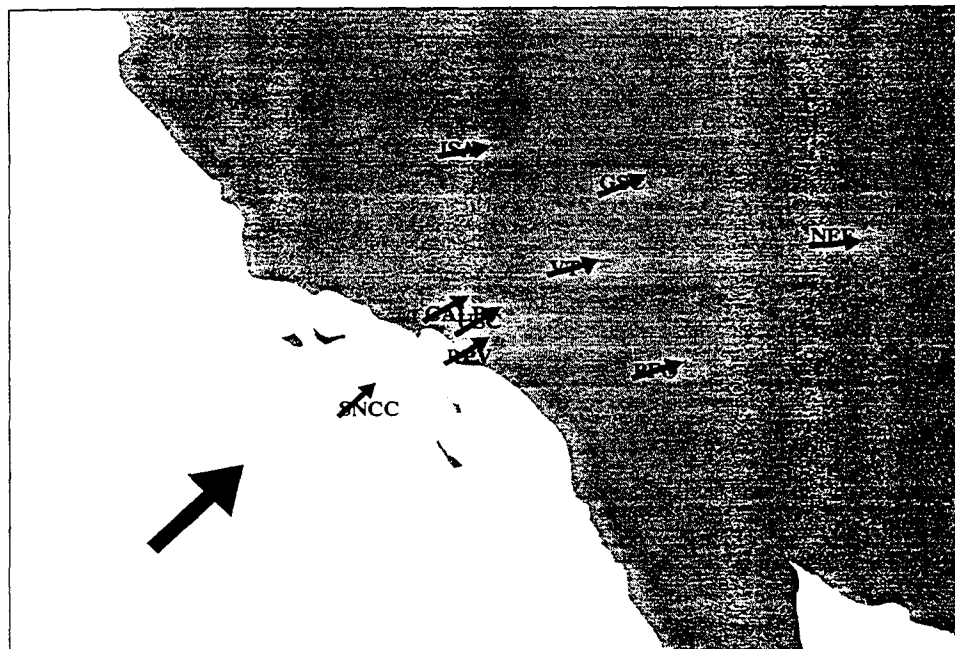
Figure 4. Wavelet polarization for 50 second surface waves across the Terrascope network in Southern California. The large arrow indicates the great-circle azimuth from the earthquake source, off the north island of New Zealand. Stations near the coast, including SNCC, RPV, CALB and USC, show little deflection of particle motion, but large deflections are apparent at inland stations ISA, GSC, NEF, VTV and PFO, all within or beyond the San Andreas deformation zone.

Geophys. J. Int., in press.

Su, L., and J. Park, Asymptotic path integral synthetics using the strong Born approximation, *Geophys. J. Int.*, in review.

RECOMMENDATIONS AND FUTURE PLANS

By the end of the year, we anticipate submitting manuscripts for publication in three areas. In particular, we plan to submit manuscripts 1) on the array-version of the multiple-wavelet transform, comparing crustal surface wave data from the Terrascope and Kyrghyzstan regional networks; 2) on the hybridization of Love and Rayleigh waves in 1-D anisotropic structures; 3) on the effect of receiver-side 1-D anisotropy, with an arbitrary symmetry axis, on upgoing body waves e.g. split shear waves and the shear-coupled PL wave.

Additional areas to explore:

1) We would like to apply the multiple-wavelet processing to an array with smaller aperture, like the broadband Pinon Flat experiment or the Geyocha array in Turkmenistan, and to go beyond a general study of wavefield properties to test the detection enhancement of wavelet-based techniques on surface waves at low signal-to-noise ratios.

2) We would like to examine the coupling of anisotropic crustal waveguide modes more fully, and compare theory with data in a more systematic manner. We anticipate using data from convergent-tectonic regions, like the broadband PASSCAL deployment in Tibet (we are familiar with this dataset, and have noted how Love-to-Rayleigh scattering becomes complex as periods decline from 100 to 50 seconds, as surface waves sample the mantle less and sample the crust more. Data from the broadband Kyrghyzstan network is also applicable in this context. We plan to test the behavior at some US stations where active-source seismic profiling has revealed a highly reflective lower crust e.g., within the Basin and Range Province. Some crustal seismologists have attributed this reflectivity to thin anisotropic layers, which would develop as a result of extensional thinning of the crust. It would be interesting to see if coupled-mode crustal surface waves can be used to confirm or deny this model.

REFERENCES

Backus, G. E., Possible forms of seismic anisotropy of the uppermost mantle under oceans, *J. Geophys. Res.*, *70*, 3429–3439, 1965.

Chen, X., 1993. A systematic and efficient method of computing normal modes for multi-layered half-space, *Geophys. J. Int.*, *115*, 391–409.

Crampin, S., A review of the effects of anisotropic layering on the propagation of seismic waves, *Geophys. J. Roy. astron. Soc.*, *49*, 9–27, 1977.

Park, J., 1993. The sensitivity of seismic free oscillations to upper mantle anisotropy I: Zonal symmetry, *J. Geophys. Res.*, *98*, 19933-19949.

Shearer, P. M., and J. A. Orcutt, Compressional and shear wave anisotropy in the oceanic lithosphere - the Ngendie seismic refraction experiment, *Geophys. J. Roy. astron. Soc.*, *87*, 967–1003, 1986.

Scattering Attenuation in Fractally Homogeneous Random Media

C. Reese, J. Ni, and T. Hearn
New Mexico State University, Department of Physics
Las Cruces, NM 88003

Abstract

Much of seismic nuclear monitoring depends on a proper understanding of attenuation and scattering of regional seismic waves. This report seeks to characterize wave scattering from both an observational and theoretical approach. A theory of wave propagation in fractally homogeneous random media is developed and applied to southern Tibet in order to quantify the analytical and statistical properties of crust and upper lithosphere heterogeneity. Seismic velocity heterogeneity is modeled by a self-affine band limited random fractal. An approximation to multiple scattering theory yields a relationship between the exponent of the frequency dependent scattering quality factor Q and the fractal dimension of velocity iso-surfaces. In this study, the attenuation quality factor of P-waves, Q_P, is calculated for southern Tibet and the implications for the fractal dimension of the velocity field are discussed. In addition, the topic of intermittent heterogeneity is introduced. The generalization of the model to fractally homogeneous media implies that scattering attenuation measurements are characterized by two fractal dimensions: one related to the self-affinity of the velocity field and the other related to the metric of the space which the field occupies.

Within a fractal random media model, the attenuation calculation for southern Tibet yields a fractal dimension of velocity iso-surfaces of $D = 9/4$ which implies the existence of complex large-scale structure in the upper lithosphere. For the more general case of fractally homogeneous heterogeneity, the frequency dependence of the scattering quality factor is a function of two parameters D and another fractal dimension $\bar{D}$. The predicted frequency exponent can differ from the homogeneous case by as much as 2/3 for reasonable choices of the parameters D and $\bar{D}$. However, the relative contributions of topological disorder and intermittency are inextricably linked and cannot be isolated by scattering attenuation measurements. Continued investigation of wave propagation in fractally homogeneous media may further quantify the statistical properties of crustal heterogeneity.

keywords: scattering attenuation, quality factor, crustal heterogeneity, fractal

473

Scattering Attenuation in Fractally Homogeneous Random Media

Objectives

Much of seismic nuclear monitoring depends on an understanding of the attenuation and scattering characteristics of regional seismic phases. The objective of this report is to quantify the nature of heterogeneity in the crust and upper lithosphere in southern Tibet and to show that for wave propagation in general fractally homogeneous media, the frequency dependence of the scattering attenuation quality factor Q is a function of two parameters related to the geometry of the velocity field. Following Wu and Aki, seismic velocity heterogeneity is modeled by a band limited random fractal (Wu and Aki, 1985). An approximation to multiple scattering theory in such media yields a relationship between the exponent of the frequency dependent quality factor and the fractal dimension of velocity iso-surfaces (Wu, 1982). In this study, the attenuation quality factor of P-waves, Q_P, is calculated for southern Tibet and the implications for the fractal dimension of the velocity field are discussed. In addition, the topic of intermittent heterogeneity is introduced. The generalization of the model to fractally homogeneous media implies that scattering attenuation measurements are characterized by two fractal dimensions: one related to the self-affinity of the velocity field and the other related to the metric of the space which the field occupies.

Research Accomplished

Model Random Media

The model random media is defined by a position dependent velocity $c(\vec{r}) = c_0 + \delta c(\vec{r})$ where the fluctuating part $\delta c(\vec{r})$ is a zero-mean, isotropic, random funtion. For

the purposes of this study the fluctuation is taken to be a fractional Brownian function $\delta c(\vec{r}) = B_H(\vec{r})$ (Mandelbrot, 1977). The fractional Brownian function $B_H(\vec{r})$ is defined through a variance or structure function,

$$F(r) = <(B_H(\vec{r'} + \vec{r}) - B_H(\vec{r'}))^2> = r^{2H}. \tag{1}$$

For the value of the parameter $H = 1/2$, the function $B_H(r)$ along any line in space is a Brownian walk whose variance scales linearly with sample size. Mandelbrot has shown that the fractal dimension of the iso-surfaces of such a field is $D = 3 - H$ (Mandelbrot, 1975). Thus, if the fluctuations are characterized by a root mean square variation γ, the structure function can be written as $F(r) = \gamma^2 r^{2(3-D)}$. The value of $F(r)$ characterizes the intensity of fluctuations with length scale smaller than or on the order of r. The one-dimensional spectral density is related to the structure function through an integral transform (Tatarski, 1960). One finds that the spectral density is given by,

$$\Phi(k) = \frac{\Gamma(1 + 2(3-D)) \sin(\pi(3-D))}{2\pi} \gamma^2 k^{-(2(3-D)+1)}. \tag{2}$$

Of course any real medium posseses some outer scale of heterogeneity such that the power law spectrum is truncated at some point. A spectrum that corresponds to Eq. (2) in the high frequency limit and includes a characteristic length is the von Karman spectrum,

$$\Phi(k) = \frac{\gamma^2 \Gamma(3 - D + 1/2)}{\sqrt{\pi} \Gamma(3 - D)} \frac{a}{(1 + k^2 a^2)^{(D-3+1/2)}}, \tag{3}$$

where a is the outer length scale of the inhomogeneity. Wu (Wu, 1982) has shown that within a cumulative-forward, single-backscatter approximation to multiple scattering theory, the inverse of the scattering quality factor

$$Q^{-1} = 2k_0\{\Phi(\sqrt{2}k_0) - \Phi(2k_0)\}, \tag{4}$$

where k_0 is the wavenumber in a homogeneous medium of velocity c_0. Thus, substituting for the spectral density Φ, in the high frequency regime the model yields a frequency dependent quality factor,

$$Q^{-1} \sim k^{-2(3-D)}. \tag{5}$$

If the fractal dimension of constant velocity surfaces D lies between $2 < D < 3$, then $Q^{-1} \sim k^{-\beta}$ where $0 < \beta < 2$. Thus, observations of smaller β correspond to larger amplitudes of high frequency spectral harmonics and smaller amplitudes of low frequency components. This implies the existence of small scale field structure and the absence of large scale structure. This is illustrated in Figure 1 for two approximations to two-dimensional fractional Brownian functions. As the value of D increases from two to three the surfaces become more erratic and small scale detail is increased. This fact is the underlying geometrical basis for the observed correlation between degree of frequency dependence of Q and crustal stability (Aki, 1980).

Southern Tibet

A three-component broadband array in southern Tibet was deployed from May 2, 1994 to October 23, 1994. The INDEPTH-II passive source experiment used both short period and broadband seismometers to record about 120 teleseismic and 80 local and regional earthquakes. The broadband seismometers used in the deployment were Guralp CMG-3T's. The data were continuously recorded by Reftek 72-06 24 bit digital recorders using 50 samples per second.

The quality factor Q_P was estimated for southern Tibet by computing spectral ratios of thirty seconds of P-wave train in narrow frequency bands for five local earthquakes. Figure 2 shows seismograms for a local event recorded at two epicentral distances along with the correpsonding spectra for the P-wave coda. The results of the attenuation calculation are shown in Figure 3. The theoretical curve correspds to a model random medium with $\gamma = 0.2$, background velocity $c_0 = 7.5$ km/sec, correlation length $a = 1.0$ km, and fractal dimension $D = 9/4$. Accordingly the high frequency dependence of Q_P^{-1} is

$$Q_P^{-1} \sim k^{-3/2}, \tag{6}$$

The seemingly large value of γ could be reduced by including intrinsic attenuation in the calculation.

Intermittent Inhomogeneity

Intermittency, as defined by Mandelbrot, is the fact that in natural turbulence dissipation is not distributed uniformly in space (Mandelbrot, 1977). Likewise, there is no *a priori* reason to believe that seismic velocity heterogeneity is homogeneously distributed in three dimensional Euclidean space. Instead, some crustal regions may be very heterogeneous while others are devoid of velocity impedence. Furthermore, the region where the scalar field quantity concentrates may sufficiently tortured and convoluted such that the geometry is appropriately described by a fractal. The case of homogeneous turbulence concentrated in a space of dimension $\bar{D} < 3$ has been called fractally homogeneous turbulence by Mandelbrot (Mandelbrot, 1976). Likewise the case of seismic velocity fluctuations concentrated on a fractal may be called fractally homogeneous inhomogeneity. Thus there are two dimensions which describe general fractally homogeneous fields. The dimension $\bar{D}$ describes the way the field is spread around while the dimension D describes the way the field is connected. An important result of intermittency is that the spectra of fluctuations is altered by a factor related to the dimension of the support of the fluctuations. The support of a function is the set of values of the argument for which the function is non-zero. For example, in the case of fluid turbulence where the structure function goes like $r^{2/3}$, the spectrum is proportional to $k^{-(5/3+B)}$ where B is related to a function that describes the process of 'curdling' which concentrates the inhomogeneity (Mandelbrot,1976). Likewise

476

for fields with structure functions like $r^{2(3-D)}$, the spectral exponent is $-(2(3-D)+B+1)$ so that within an intermittent version of the model described above the scattering attenuation quality factor,

$$Q^{-1} \sim k^{-(2(3-D)+B)}. \tag{7}$$

In the case of absolute curdling, the support of the field is a closed set and the parameter

$$B = -(3-\bar{D})(2(3-D)-1). \tag{8}$$

If the dimension of the support $\bar{D}$ lies between $2 < \bar{D} < 3$ then $0 < B < 2/3(2(3-D)-1)$. As an example, consider a random fractal medium with $D = 2.25$ which has curdled into a support with fractal dimension $\bar{D} = 2.5$. One finds that $B = -1/4$ and

$$Q^{-1} \sim k^{-5/4}. \tag{9}$$

In general, if the model velocity field is indeed intermittent ($\bar{D} < 3$) and and the iso-surfaces have dimension $D > 2.5$, the factor B is positive. This implies that if the observed frequency dependence of scattering Q is attributed totally to homogeneous inhomogeneity, the amount by which the iso-surface dimension exceeds two would be overestimated. On the other hand, if $D < 2.5$ the factor B is negative and homogeneous theory yields an underestimate of the dimension D of constant velocity surfaces.

Several studies of coda wave attenuation have yielded frequency dependent quality factors Q_c. Some results are summarized below as a function of tectonic region. The value of the iso-surface dimension D is given for three different dimensions of support $\bar{D}$.

Region	β	$D(\bar{D}=3)$	$D(\bar{D}=2.75)$	$D(\bar{D}=2.5)$
Western U.S. (Singh and Hermann, 1983)	0.7	2.65	2.70	2.80
Garwhal Himalaya (Gupta et. al., 1995)	0.9	2.55	2.57	2.60
Western Anatolia (Akinci et. al., 1994)	1.0	2.5	2.5	2.5
Southern Tibet (Q_P) (This study)	1.5	2.25	2.17	2.0

Interestingly, when $\beta = 1$ intermittency has no effect on the fractal dimension D.

Conclusions and Recommendations

Scattering attenuation measurements provide an effective means to constrain the analytical and geometrical properties of seismic media with random velocity perturbations. Within a fractal random media model, the attenuation calculation for southern Tibet yields a fractal dimension of velocity iso-surfaces of $D = 9/4$ which implies the existence of complex large-scale structure in the upper lithosphere. For the more general case of fractally

homogeneous heterogeneity, the frequency dependence of the scattering quality factor is a function of two parameters D and $\bar{D}$. The predicted frequency exponent can differ from the homogeneous case by as much as 2/3 for reasonable choices of the parameters D and $\bar{D}$. However, the relative contributions of topological disorder and intermittency are inextricably linked and cannot be isolated by scattering attenuation measurements. Continued investigation of wave propagation in fractally homogeneous media may further quantify the statistical properties of crustal heterogeneity.

References

Aki, K., Scattering and Attenuation of Shear Waves in the Lithosphere, *J. Geophys. Res.*, *85*, 6496-6504 (1980).

Akinci, A., Taktak, A.G., and Ergintav, S., Attenuation of coda waves in Western Anatolia, *Phys. Earth Planet. Int.*, *121*, 155-165 (1994).

Gupta, S.C., Singh, V.N., and Kumar, A., Attenuation of coda waves in the Garwhal Himalaya, India, *Phys. Earth Planet. Int.*, *87*, 247-253 (1995).

Mandelbrot, B.B., On the geometry of homogeneous turbulence, with stress on the fractal dimension of the iso-surfaces of scalars, *J. Fluid Mech.*, *72*, 401-416, (1975).

Mandelbrot, B.B., *Proceedings: Turbulence and Navier Stokes Equations* ed. R. Temam (Springer-Verlag, Berlin, 1976).

Mandelbrot, B.B., *Fractals, Form, Chance, and Dimension.* (W.H. Freeman and Company, San Francisco, 1977).

Singh, S. and Herrmann, R.B., Regionalization of Crustal Coda Q in the Continental United States, *J. Geophys. Res.*, *88*, 527-538, (1983).

Tatarski, V.I., *Wave Propagation in a Turbulent Medium* (McGraw-Hill, NY, 1960).

Wu, R.S., Attenuation of Short Period Seismic Waves Due to Scattering, *Geophys. Res. Lett.*, *9*, 9-12, (1982).

Wu, R.S. and Aki, K., The Fractal Nature of the Inhomogeneities in the Lithosphere Evidenced from Seismic Wave Scattering, *Pure Appl. Geophys.*, *88*, 805-818, (1985).
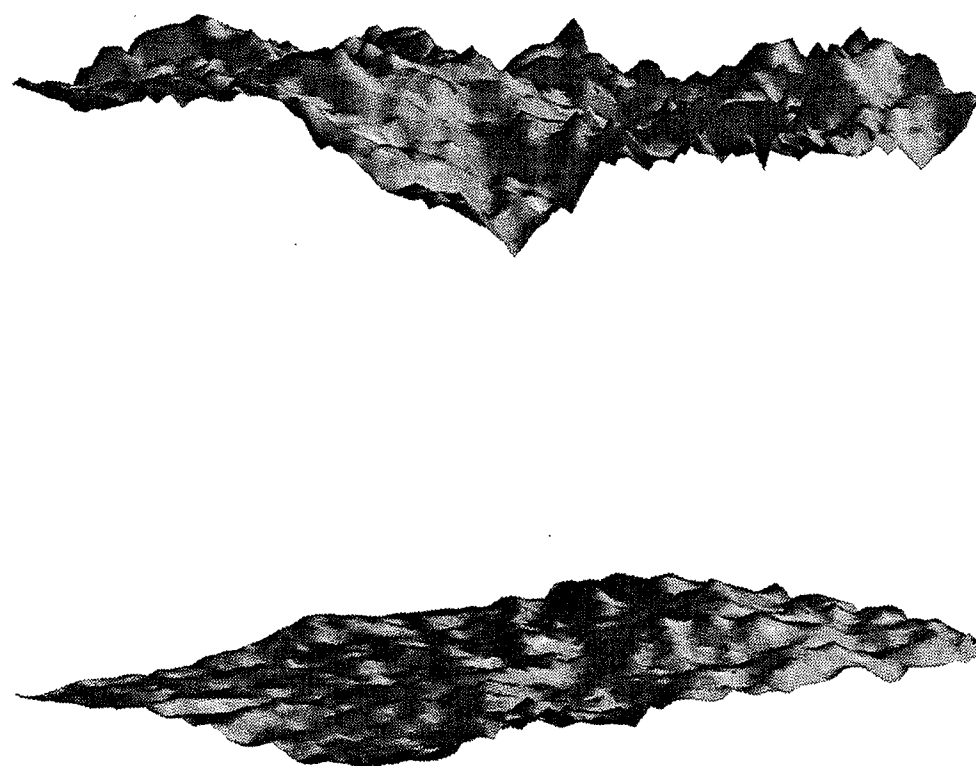
Figure 1. Two dimensional approximations to fractional Brownian functions. The fractal dimension of the top figure is D=9/4=2.25 while the fractal dimension of the bottom figure is D=8/3=2.66. In general, as D increases from two to three the small scale structure of the surfaces is enhanced.
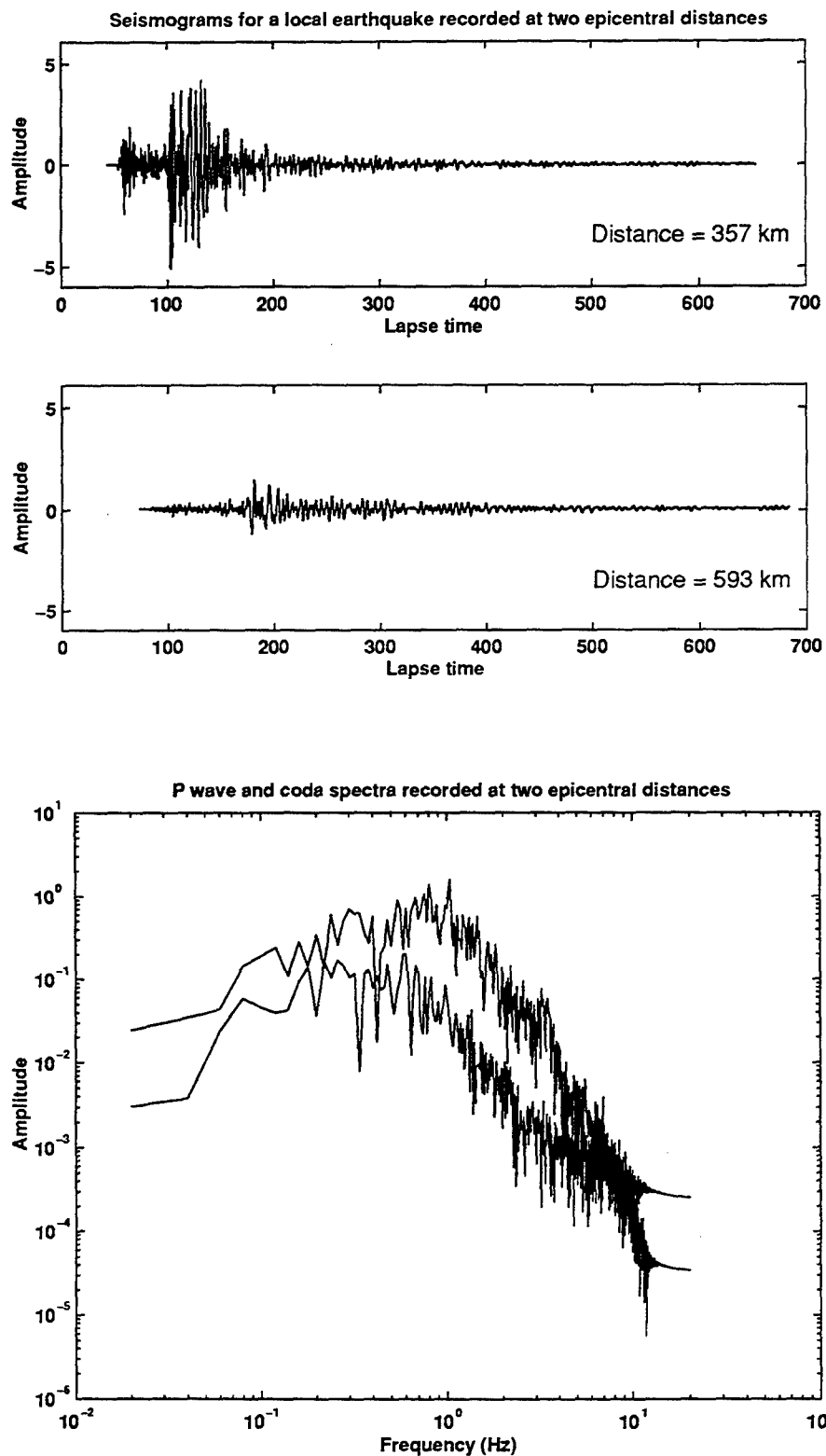
Figure 2. Vertical traces for a local event of magnitude 4.7 recorded at two epicentral distances. The corresponding P-wave coda spectra are plotted on the bottom demonstrating the frequency dependent attenuation.

480
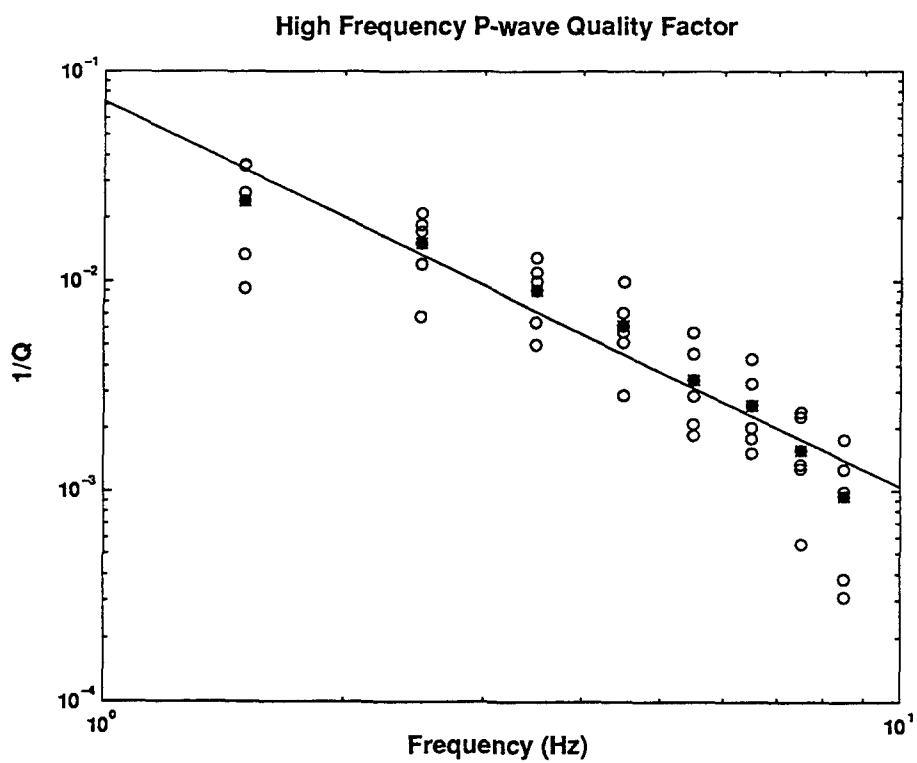
Figure 3. Observed quality factor Q for P-wave coda. All the data for five local earthquakes in Tibet are plotted as open circles. The mean in each frequency band is plotted as an asterisk and the straight line is fit in the least squares sense. The frequency dependence is $Q \sim f^{1.5}$

MAKING ACCURATE CONTINENTAL BROADBAND SURFACE WAVE MEASUREMENTS

M. H. Ritzwoller, A. L. Levshin, S. S. Smith, and C. S. Lee

Department of Physics, University of Colorado, Boulder

Abstract

Described herein are methods designed to obtain accurate broadband surface wave dispersion measurements on two spatial/frequency scales: continent-wide (Eurasia; 20 - 300 s) and regional (Central Asia, within 20^0 of KNET; 5 - 50 s). These methods are based on well developed frequency-time and floating-filter analyses, and are included within procedures that utilize relational parametric and waveform database structures with rapid graphics, which allow measurements to be made quickly on relatively large volumes of data from a variety of source regions recorded on heterogeneous networks. These methods are currently being applied systematically to GSN/CDSN/GEOSCOPE/MEDNET data and Kyrghyz Telemetered Seismic Network (KNET) data to yield Rayleigh and Love wave group velocity, phase velocity, polarization, and amplitude measurements.

The complexity of Eurasian structure implies that the crucial problem is to extract the desired signals, related to nearly directly arriving waves that can be interpreted deterministically, from the essentially stochastic interfering multipaths and coda. Continent-wide, 200 events have been processed yielding dispersion measurements for more than 3000 paths to date (Levshin et al., 1995). Regionally, data from KNET's continuous channels have been accumulated for future analysis. All waveform (including 'cleaned' waveforms) and parametric data (including dispersion measurements and frequency-time images) are stored in CSS v. 3.0 (with appropriate extensions).

In the near future, experiments will be performed to automate this method, which currently depends critically on human interaction. The resulting measurements and cleaned waveforms will be used as follows. (1) Group and phase velocity measurements are being inverted for 2D maps of group (Levshin et al., 1995) and phase velocities. (2) These maps will be inverted for lithospheric shear velocity structure which should provide significantly higher resolution than previous models, especially in Central Asia. (3) The cleaned waveforms are ideal targets for surface waveform fitting, which augments and complements the dispersion measurements. (4) Higher resolution phase velocity maps in Central Asia will be used to develop surface wave stacking/array processing methods for regional broadband arrays located in geologically complex settings, such as KNET. Such methods must incorporate differences in the dispersion characteristics among stations in the array.

key words: Eurasia, surface wave propagation, Love waves, Rayleigh waves, group velocity, phase velocity, polarization

Objective

Because approximately two-thirds of Eurasia is surrounded by seismically active regions (some of which extend well into the continent), in principle Eurasia provides the Earth's best laboratory for studying continental wave propagation and for the use of seismic wave characteristics to map crustal and upper mantle structures on a variety of length scales. The development of seismic networks (e.g., GSN, CDSN, GEOSCOPE, KNET) in the Former Soviet Union, China, and the countries of Southern Asia hold out the promise to realize aspects of this potential.

There are two main objectives of the studies described herein. (1) The first objective is to apply well established methods of surface wave analysis to a continent-wide broadband network (GSN, GEOSCOPE, CDSN, MEDNET) and to a broadband regional array (KNET; Kyrghyz Telemetered Seismic Network) to yield Rayleigh and Love wave group velocity, phase velocity, polarization, and amplitude measurements on two spatial scales and frequency bands: continent-wide (Eurasia; 20 - 300 s) and regional (Central Asia, within 20^0 of KNET; 5 - 50 s). These measurements will be used in the future to invert for more sharply focused lithospheric models on these two spatial scales. (2) The second objective is to use the estimated regional phase velocity maps to develop surface wave stacking/array processing methods for large-scale broadband arrays in complex geological settings, such as KNET, to attempt to reduce the magnitude threshold for the analysis of intermediate period (5 - 30 sec) surface waves. To date, preliminary research results have been achieved only for the first objective.

Preliminary Research Results

Measurement Procedures

Problems associated with the estimation of accurate surface wave characteristics (wave velocities, amplitudes, polarizations) do not change in nature with the spatial scale or frequency band of interest, although they do change in magnitude. The most significant issues concern the accrual of high quality data, the identification and extraction of unwanted signals, and the measurement of the signals of interest.

Data quality on both continental (GSN/GEOSCOPE/CDSN/MEDNET) and regional (KNET) scales is quite good, as exemplified by the record sections shown in Figure 1. The main problem to be faced is that continents are complicated. This not only makes interpretation in terms of structural models difficult, but also greatly complicates measurements; or more accurately complicates the identification of the aspects of the waveforms on which measurements are to be applied. Our aim, then, is to extract the signals we desire, related to nearly directly arriving waves that can be interpreted deterministically, from the potentially interfering multipaths and coda that are essentially stochastic in nature. Figures 2 and 3 demonstrate the analysis procedure, in which unwanted signals, in particular surface wave coda, overtones, and body waves are greatly reduced in the filtered seismogram on which measurements are obtained.

The basic characteristics of the current measurement procedure is based on a long history of development of surface wave analysis (e.g., Dziewonski *et al.* 1969, 1972; Levshin *et al.*, 1972, 1989, 1992, 1994; Cara, 1973; Russell *et al.*, 1988). The recent innovation is that code has been developed which allows measurements to be made rapidly on relatively large volumes of data from heterogeneous networks and a variety of source regions. The innovations have required the development of rational parametric and waveform database structures (more on below) and the development of relatively rapid graphical routines for human interaction with the data.

The general form of the measurement procedure is as follows. Group velocity - period diagrams for the vertical, radial, and transverse components are constructed. An analyst manually traces the apparent group velocity curve for the Rayleigh wave (on the vertical and radial components) and the Love wave (on the transverse component). Time-variable filters are applied around the selected curve to separate the desired signal from the 'noise'. This results in filtered group velocity - period diagrams for which contamination from interfering signals should be reduced. Group velocity, phase velocity, amplitude, and polarization measurements are automatically obtained on the filtered images. Figures 2a and 3a attempt to display this procedure.

An unfortunate, but currently still necessary, characteristic of this procedure, is that it depends crucially on direct human interaction with potentially large volumes of seismic waveform data. The success of this method is based on the analyst accurately identifying the main dispersion ridge of the fundamental modes, separating the 'direct arrival' from surface wave coda at periods below about 30 seconds, inspecting interpolation near spectral holes, and truncating the measurements appropriately at long periods as the signals weaken. This interaction limits the speed with which the method can be applied, and, therefore, the volume of data that can be processed.

To date, the method has been applied to waveform data from approximately 200 events surrounding Eurasia. The analysis of significantly larger volumes of data will require the automation of the technique. Attempts at automation will be based on initial continent-wide group and phase velocity maps which are currently under development (Levshin et al., 1995). This will increase the volume of data that can be processed and should result in improved resolution of the group/phase velocity maps and the resulting structural models.

Measurements on a Continental Scale

Due to the high, average efficiency of surface wave propagation across Eurasia, surface wave measurements can be made at periods up to 100 - 150 seconds for earthquakes as small as $M_s = 5.0$ that propagate across the entire continent. Of course, measurements can be extended to longer periods for substantially larger events. To date, event volumes have been accumulated for GSN/GEOSCOPE/CDSN/MEDNET data from approximately 300 events occurring between 1988 and 1995. Of these events, shown in Figure 4a, approximately 200 have been completely processed, yielding measurements on more than 3000 paths (Levshin et al., 1995).

As an example, group velocity measurements for a single station (KEVO, Finland) for one event (Kuril event, 10/9/94, $M_s = 7.0$) are shown in Figure 3b for the Rayleigh wave (measured on the vertical and radial components) at periods between about 20 and 300 seconds and for the Love wave at periods between about 30 and 250 seconds. Predictions for the spherical model PREM (Dziewonski and Anderson, 1980) are shown for comparison.

A useful by-product of these analyses are 'cleaned' or 'filtered seismograms'. Figure 3b shows a comparison between the raw and filtered seismograms for a single station:event pair. Surface wave coda, overtones and body waves have been greatly diminished from the cleaned seismograms, making them an ideal target for surface wave fitting techniques during a later stage of this research.

Measurements on a Regional Scale

On a regional scale at shorter periods, smaller events ($M_s < 5.0$) can be analyzed similarly. KNET, situated in a complex tectonic setting in Central Asia surrounded to the East, West and South by significant seismicity, is a natural site to focus studies of regional scale measurements. To date, approximately 200 events (Figure 4b) with $M_s > 4.0$ within approximately 20 degrees of

484

KNET have been extracted from KNET's continuous channels. Analyses of these data are just beginning.

Figure 3b presents an example the analysis of these data. Seven KNET stations were operating during the passage of surface waves from an event in the Qinghai Province, China on 1/17/94 ($\Delta \approx 16$ degrees, $M_s = 4.8$). Rayleigh and Love wave group velocity measurements are shown in Figure 3b. Rayleigh wave measurements are quite similar across the array above about 20 seconds period and for Love waves above about 30 seconds period at this azimuth. Variations across the array at shorter periods result both from real differences along the various wave paths near the network and also from Rayleigh - Love interference, which can be significant since the group velocities of the two wave types are similar in this period range. Cleaned and raw waveforms are presented in Figure 3c.

Data Base Structure

All waveform and parametric data as well as surface wave measurements are stored in the CSS v. 3.0 relational database (Anderson *et al.*, 1990) plus extensions. This data base will be delivered to the funding agents upon completion of the contracts. The standard relations (affiliation, event, gregion, instrument, network, origin, sensor, site, sitechan, sregion, wfdisc) are augmented with two event relations modified slightly from CSS v. 2.8 (centryd, moment) and three extensions (disp, ftdisc, wfedit). The wfedit relation contains information about the time, duration and nature of waveform problems (e.g., clips, gaps, nonlinearities, interfering events, etc.). The disp and ftdisc relations point to dispersion measurements and group velocity - period images, respectively. For each station:event pair, raw and filtered group velocity images are output and pointed to by the ftdisc relation. Dispersion measurements (group velocity, phase velocity, spectral amplitude, polarization) are output and pointed to by the disp relation. Cleaned or filtered waveforms are output and pointed to by a cleaned wfdisc relation.

Conclusions and Future Plans

The ability to make relatively rapid and accurate surface wave measurements (phase and group velocities, amplitudes, polarizations) on fairly large volumes of data has allowed us to begin to process systematically surface waves propagating across Eurasia. Dispersion measurements have been made for approximately 200 events on a continental scale recorded at GSN, GEOSCOPE, CDSN, and MEDNET stations. Data from continuous channels of KNET have been accumulated and are just beginning to be processed in support of a regional scale study of Central Asia. These developing data sets should provide significantly higher resolution than represented in previous models, which promises more accurate lithospheric models.

Future developments will be along three lines.

- To increase the rate of surface wave processing, measurement methods must be automated. This will be based on the use of preliminary group and phase velocity maps resulting from the continental scale study. See Levshin *et al.* (1995) for preliminary group velocity maps.

- Filtered seismograms will be used for surface waveform fitting, which augments and complements current measurement procedures.

- Higher resolution phase velocity maps in Central Asia will be used to develop surface wave stacking/array processing methods for regional broadband arrays located in a geologically complex setting, such as KNET. Such methods must incorporate differences in the dispersion characteristics among stations in the stack.

485

References

Anderson, J., W. E. Farrell, K. Garcia, J. Given, H. Swanger, Center for Seismic Studies Version 3 Database: Schema Reference Manual, CSS Technical Report C90-01, September, 1990.

Cara, M., 1973. Filtering of dispersed wave trains, *Geophys. J. R. astr. Soc.*, **33**, 65 - 80.

Dziewonski, A. M., Bloch, S., and M. Landisman, 1969. A technique for the analysis of transient seismic signals, *Bull. seism. Soc. Am.*, **59**, 427 - 444, 1969.

Dziewonski, A. M., J. Mills, and S. Bloch, 1972. Residual dispersion measurements: a new method of surface wave analysis, *Bull. seism. Soc. Am.*, **62**, 129 - 139.

Dziewonski, A. M. and D. L. Anderson, Preliminary Reference Earth Model, *Phys. Earth Planet. Int.*, **25**, 297-356, 1981.

Levshin, A. L., Pisarenko, V. F., and G. A. Pogrebinsky, 1972. On a frequency-time analysis of oscillations, *Ann. Geophys.*, **28**, 211 - 218.

Levshin, A. L., T. B. Yanovskaya, A. V. Lander, B. G. Bukchin, M. P. Barmin, L. I. Ratnikova, and E. N. Its, 1989. *Seismic surface waves in a laterally inhomogeneous Earth*, (ed. V. I. Keilis-Borok), Kluwer Publ., Dordrecht.

Levshin, A. L., L. Ratnikova, and J. Berger, 1992. Peculiarities of surface wave propagation across Central Eurasia, *Bull. seism. Soc. Am.*, **82**, 2464 - 2493.

Levshin, A. L., M. H. Ritzwoller, and L. I. Ratnikova, 1994. The nature and cause of polarization anomalies of surface waves crossing northern and central Eurasia. *Geophys. J. Int.*, 117, 577-590.

Levshin, A. L. and M. H. Ritzwoller, 1995. Characteristics of surface waves generated by events on and near the Chinese nuclear test site, *Geophys. J. Int.*, in press.

Russell, D. W., R. B. Herrman, and H. Hwang, 1988. Application of frequency-variable filters to surface wave amplitude analysis, *Bull. seism. Soc. Am.*, **78**, 339 - 354.
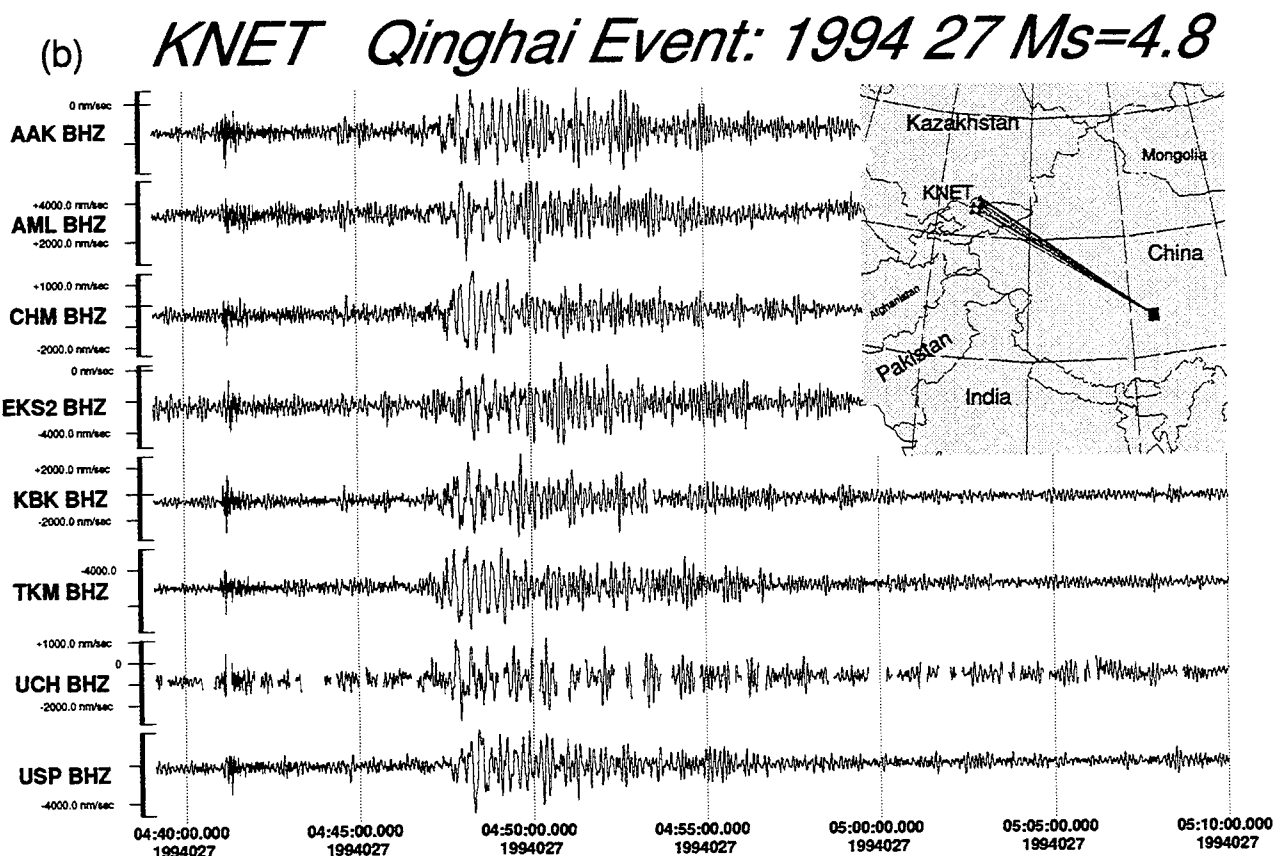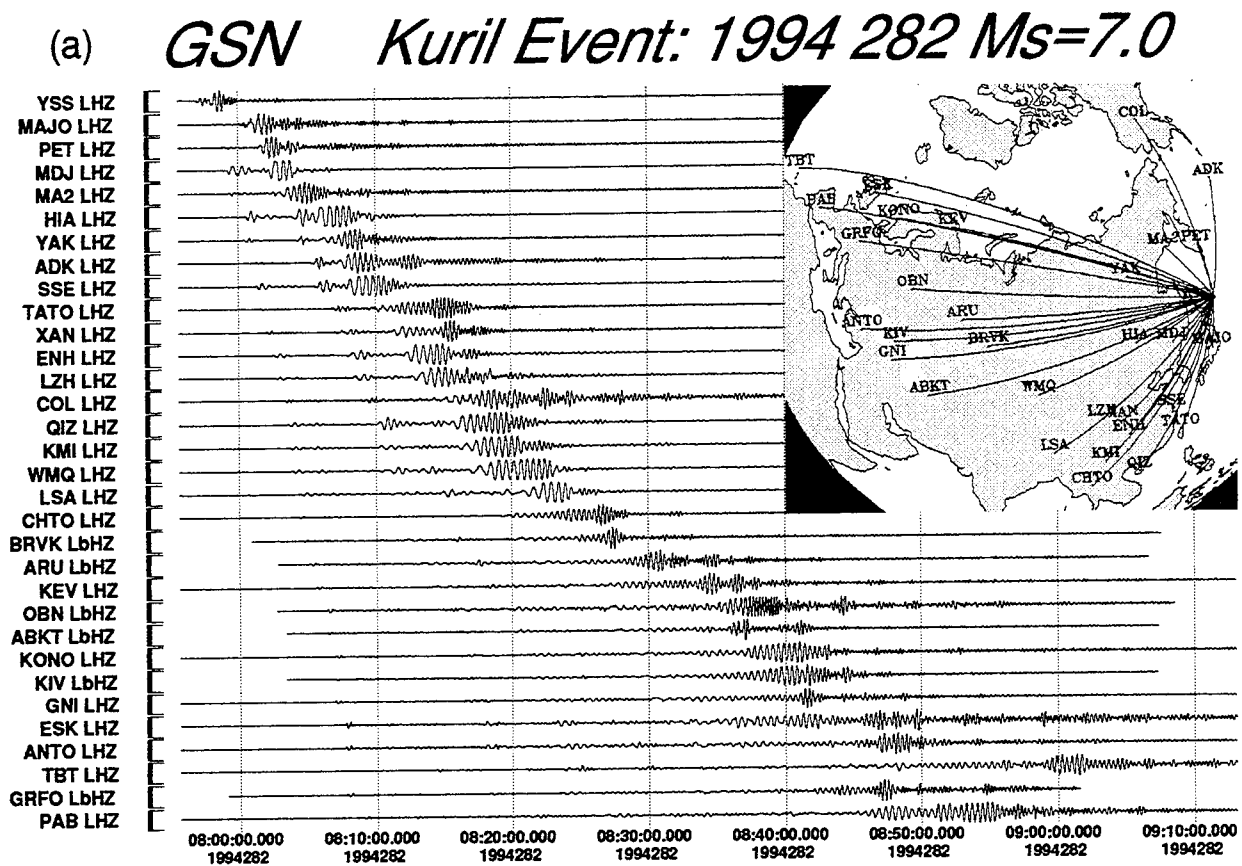
Figure 1. (a) Record section of IRIS/GSN vertical waveforms recorded for the Kuril event of 10/9/95 (Ms = 7.0). Waveforms have been low pass filtered with a lower corner of 20 seconds period. Raypaths are inset. (b) Record section of KNET vertical waveforms recorded for the Qinghai, China Event of 1/27/94 (Ms = 4.8).
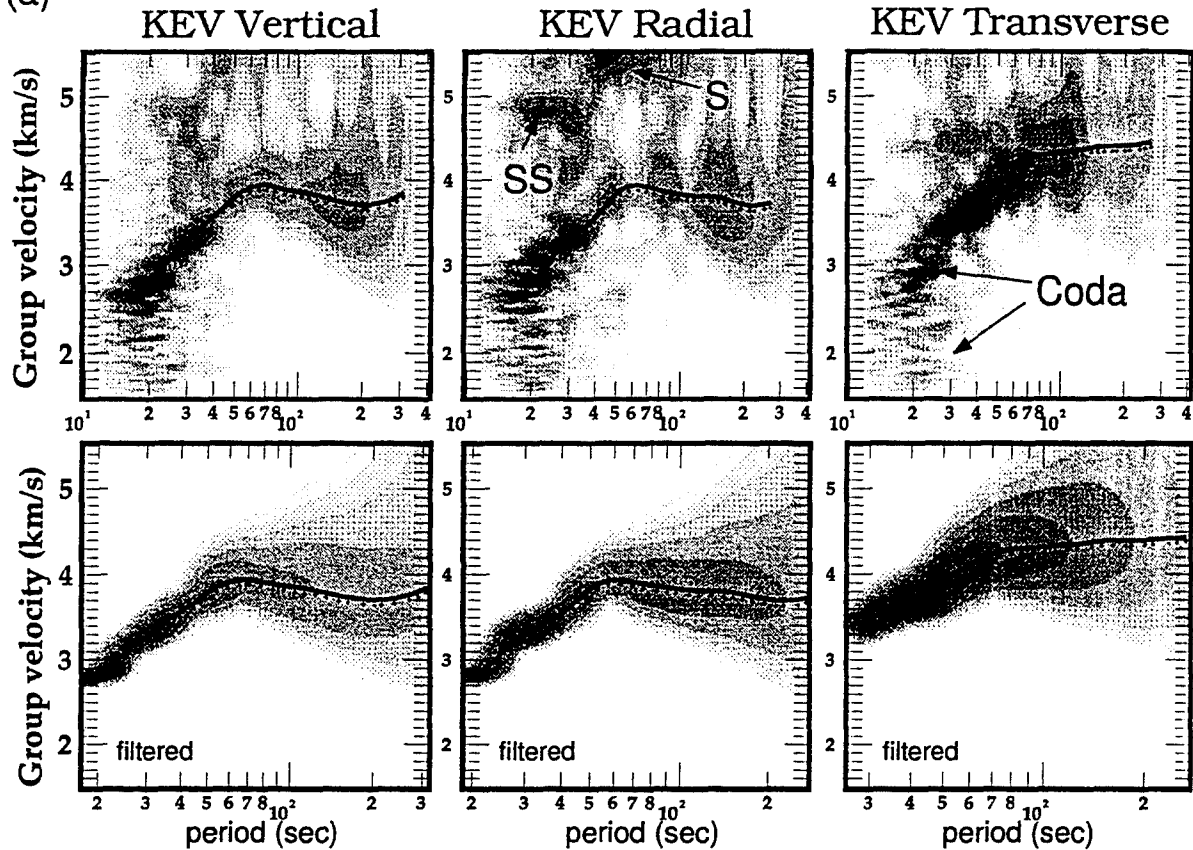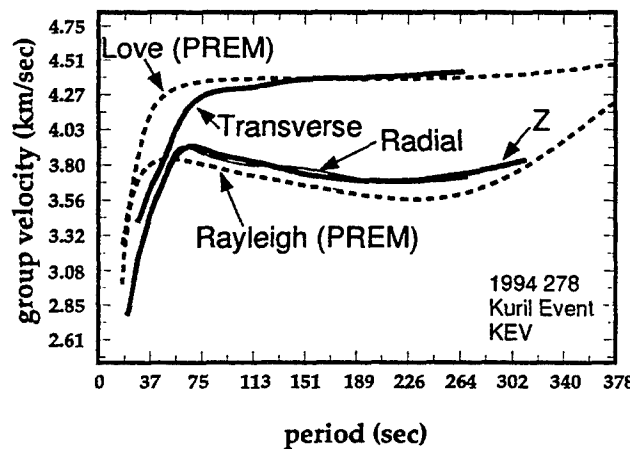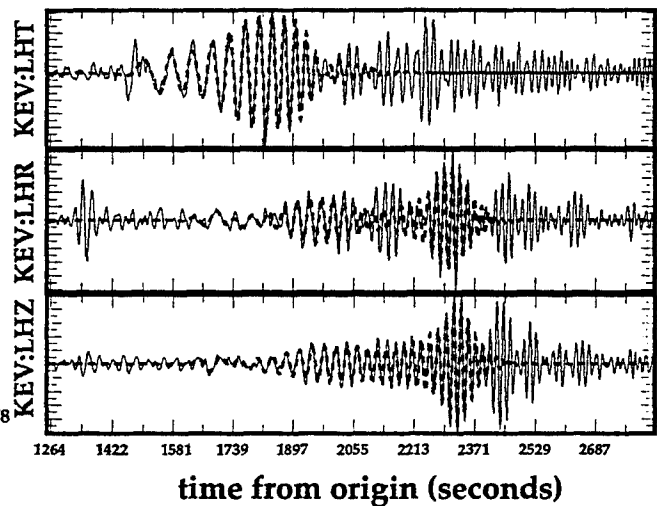
Figure 2. (a) Group velocity - period diagrams for the vertical, radial, and transverse components recorded at the GSN station at Kevo, Finland for an event in the Kurils (10/9/94, Ms = 7.0, Δ = 58.5 degrees). Estimated group velocity curves are shown. (b) Rayleigh and Love wave group velocity measurements compared with predictions from PREM. (c) Raw (thin solid) and filtered (bold dashed lines) waveforms for KEV.

488
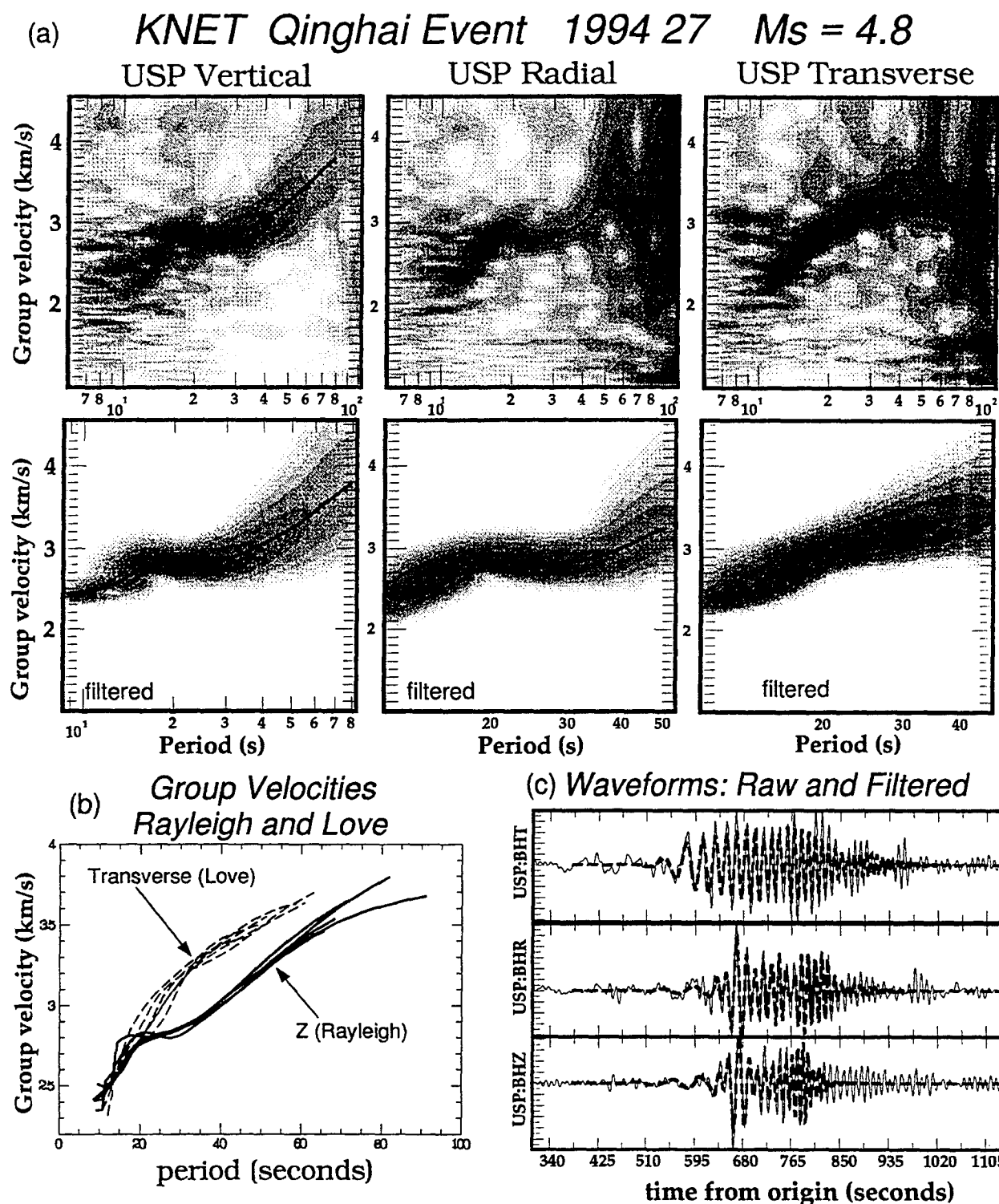
Figure 3. (a) Group velocity - period diagrams for the vertical, radial, and transverse components recorded at the KNET station USP for an event in the Qinghai Province (1/27/94, Ms = 4.8, Δ = 16 degrees). Estimated group velocity curves are shown. (b) Rayleigh and Love wave group velocities measured across the array for the same event. (c) Raw and filtered waveforms for the station USP.

KNET Events 1992 - 1995

Mb = 2.0
Mb = 3.0
Mb = 4.0
Mb = 5.0

Figure 4b. Distribution of sources (squares) and KNET receivers (triangles) to be analyzed in the regional scale surface wave study of Central Asia. Source symbol sizes are scaled linearly by body wave magnitude.

Eurasian Tomography 1988 - 1995

Ms = 5.0
Ms = 5.5
Ms = 6.0
Ms = 6.5
Ms = 7.0

Figure 4a. Distribution of sources (squares) and receivers (triangles) used in the continental scale surface wave study of Eurasia. Source symbol sizes are scaled linearly by surface wave magnitude.

STRESS-STRAIN MODELING IN THE DAMAGE REGIME

CHARLES G. SAMMIS
DEPARTMENT OF GEOLOGICAL SCIENCES
UNIVERSITY OF SOUTHERN CALIFORNIA
LOS ANGELES, CA 90089-0740

ABSTRACT

The micromechanical damage mechanics developed by Ashby and Sammis allows calculation of the failure surface of a brittle solid containing a known density of initial flaws of known size. However, inclusions of damage mechanics into numerical simulations of underground explosions also requires the effective elastic modulus as a function of damage. If the damage is not changed during a stress increment, then the theoretical results of O'Connell and Budianski (O&B) can be used. However, if the stress increment results in an increase in damage, then the effective elastic modulus will be lower than that given by the O&B theory due to the extra energy associated with crack propagation. Because this is a cumbersome calculation not suitable for implementation in numerical simulation codes, we have adopted the empirical approach of lowering the modulus by an additional factor during crack growth, and have evaluated this factor using stress strain data on Barre granite.

key words: seismic coupling, source modeling, rock mechanics, damage mechanics.

STRESS-STRAIN MODELING IN THE DAMAGE REGIME

OBJECTIVE

The objective of this research is to develop a simplified semi-empirical version of the damage mechanics developed by Ashby and Sammis (1990) which is suitable for inclusion in the numerical codes used to simulate underground nuclear explosions. This work is motivated by discrepancies between theoretical and observed seismic waveforms produced by explosions in crystalline rock which have tentatively been ascribed to the extensive fracturing and granulation of the rock in the non-linear source region. It is also possible that such fracturing in an initially anisotropic medium will generate significant S wave energy.

RESEARCH ACCOMPLISHED

The most computationally difficult part of this task has been the evaluation of the effective elastic modulus during damage accumulation. We have decided to handle this problem empirically by fitting stress-strain curves measured in Barre granite in collaboration with Greg Boitnott at New England Research.

In the absence of damage accumulation, Young's modulus decreases with damage according to (O'Connell and Budianski, 1974)

$$E = E_0 [1 - 1.25D]   \qquad (1)$$

where damage D is defined as

$$D = (4/3)\pi N_V(L + \alpha a)^3   \qquad (2)$$

N_V is the number of cracks of length 2a per unit volume and L is the crack growth as shown in Figure 1.
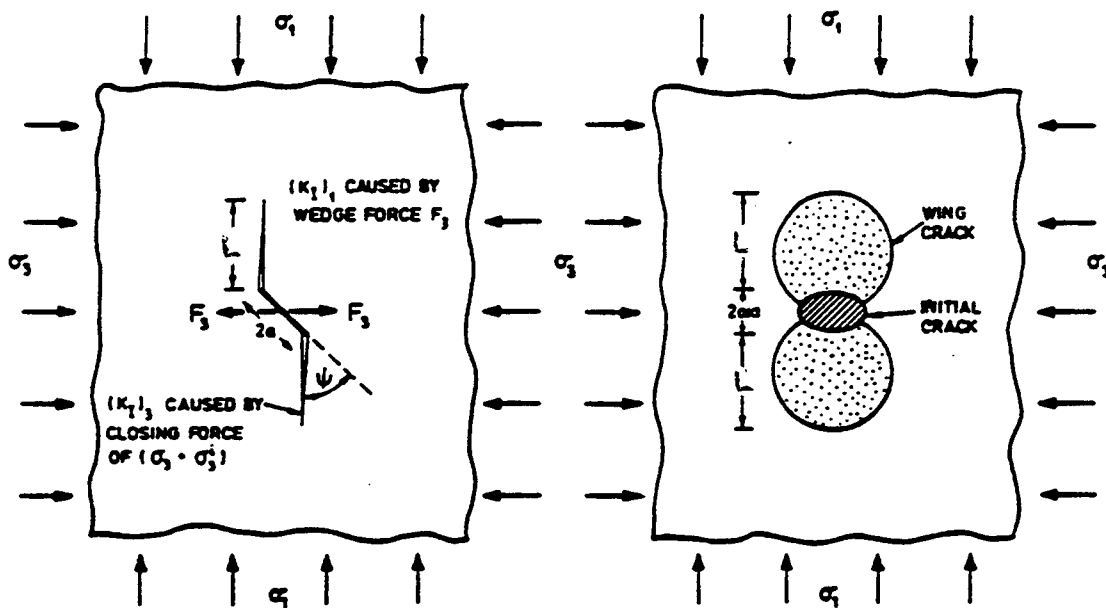
Figure 1 Growth of wing cracks from preexisting inclined cracks in the damage mechanics model developed by Ashby and Sammis (1990).

However, eqn. (1) is only applicable if L does not change during a stress increment. If L increases, then the effective E will be smaller. We represent this effect by introducing an empirical factor ζ into eqn. (1)

$$E = E_0[1 - (1.25 + \zeta)D]$$ (3)

and evaluate ζ by fitting experimental stress-strain curves.

Figure 2 shows the fit for two cases for which ζ was found to be $\zeta = 0.55$ and $\zeta = 0.50$ respectively. The positive curvature of the data at low stresses is due to crack closure and was not modeled. The curvature at high stresses is well described by eqn. (3). We are still working to analyze the hysteresis loops.
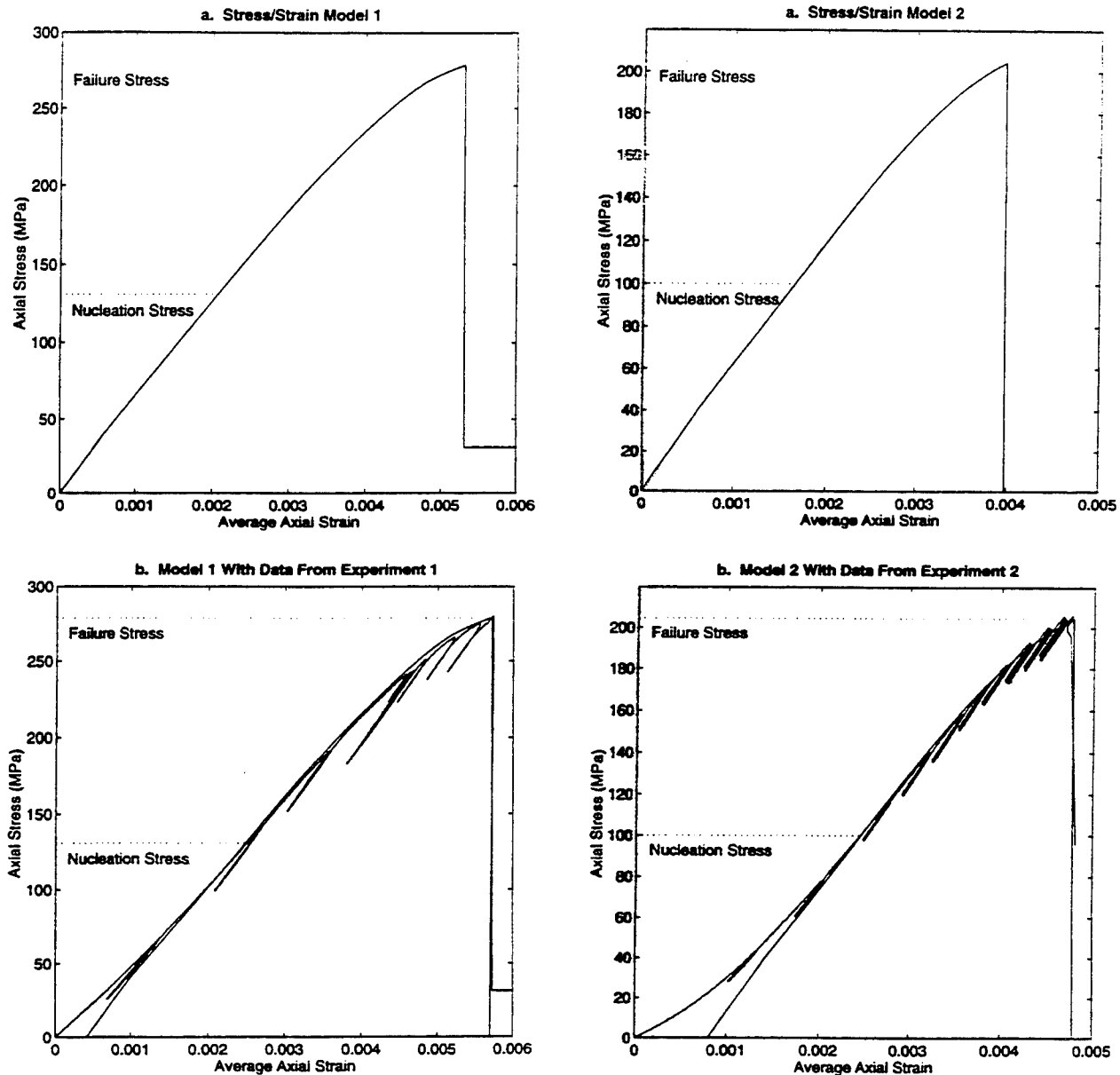
Figure 2 Stress-strain curves fit to two experiments in Barre granite in order to find the empirical factor ζ. For experiment 1 on the left, $\zeta=0.55$. For experiment 2 on the right, $\zeta=0.50$

CONCLUSIONS AND RECOMMENDATIONS

The empirical approach reproduces stress-strain curves measured in the laboratory and have established the approximate value of the empirical parameter ζ. The next step is implementation in a source code.

REFERENCES

Ashby, M.F., and C.G. Sammis, The damage mechanics of brittle solids in compression, PAGEOPH, 133, 489-521, 1990.

O'Connell, R.J. and B. Budianski, Seismic velocities in dry and saturated cracked solids, J. Geophys. res., 79, 5412-5426, 1974.

A SPECTRAL SCHEME FOR VISCOELASTIC SEISMIC MODELING

James C. Schatzman and Zhaobo Meng

Department of Mathematics, University of Wyoming, P.O. Box 3036, Laramie, WY 82071
(307) 766-3208; jcs@uwyo.edu

ABSTRACT

The pseudospectral method is especially valuable for seismic modeling because of its high accuracy compared to other numerical techniques. The method can be regarded as a limit of finite difference of increasing orders, and a process of trigonometric interpolation, thus it exhibits high accuracy. Stability of the method is also favorable. Fourier polynomials are especially efficient but have the disadvantage of forcing periodicity, and Chebyshev polynomials are somewhat less efficient but are more flexible in application of boundary conditions. We have used a Fourier pseudospectral method in the horizontal direction and Chebychev polynomials in the vertical direction. Curved grids conforming to the surface topography and major interfaces are made possible by coordinate transformations. A full viscoelastic formulation permits convenient implementation of attenuating layers to reduce wrap-around in the horizontal direction. The result is an efficient method for 2- and 3-D linear viscoelastic wave propagation.

Key Words viscoelastic, wave propagation, seismic modeling

1. Objective

1.1. Introduction

Anelasticity and anisotropy of the earth play important roles in wave propagation, especially when waves travel long distances. Finite difference and finite element methods suffer from inaccuracies in the form of numerical dispersion and attenuation that make it difficult to simulate wave propagation over hundreds to thousands of wavelengths. The pseudospectral method exhibits very striking features of very low grid density and high efficiency, compared to the standard Cartesian discrete methods. The goal here is to simulate wave propagation in a region of about 2,000 km in azimuth and 100-200 km in depth; source frequencies are 0.5-10 Hz. Since wavelengths range from 120-4,000 meters, this represents propagation of about 500-20,000 wavelengths. Most FD or FE schemes either exhibit excessive numerical artifacts or are very inefficient for such problems.

Due to space limitations, we describe only the isotropic 2-D formulation. However, the anisotropic 3-D case is a straightforward extension and a detailed analysis is available from the authors.

1.2. 2-D Viscoelastic Wave Equations

When we talk about viscoelasticity, there are mainly two different ways to describe the strain–stress relationship, i.e. Voigt's model or Maxwell's model, each corresponding to connections of the elastic and viscous behavior in parallel and series. For computational consideration, Voigt's model is highly recommended because of its simplicity and generality.

For an isotropic-elastic medium the stress-strain relation is

$$\sigma_{ii} = \overline{\lambda}\Delta + 2\overline{\mu}\varepsilon_{ii}, \quad i = 1, 2, 3, \tag{1}$$

$$\sigma_{ij} = \overline{\mu}\varepsilon_{ij}, \quad i \neq j, \ i,j = 1,2,3, \tag{2}$$

where $\overline{\lambda} = \lambda + \lambda'\frac{\partial}{\partial t}$ and $\overline{\mu} = \mu + \mu'\frac{\partial}{\partial t}$. It is beyond the scope of this paper to include a derivation, but we find that λ' and μ' are related to the Q for P- and S-wave propagation by

$$Q_p = \frac{\sqrt{(\lambda + 2\mu)^2 + k^2(\lambda' + 2\mu')^2 v_p^2} + \lambda + 2\mu}{2(\lambda' + 2\mu')k v_p}. \tag{3}$$

$$Q_s = \frac{\sqrt{\mu^2 + k^2\mu'^2 v_s^2} + \mu}{2\mu' k v_s}. \tag{4}$$

We see that in this model, Q_p and Q_s are not constant but are functions of wavenumber. The viscoelastic equations of motion are

$$\rho\frac{\partial^2 u_i}{\partial t^2} = \frac{\partial}{\partial x_i}[(\overline{\lambda} + \overline{\mu})\theta] + \nabla \cdot (\overline{\mu}\nabla u_i) + f_i, \quad i = 1, 2, 3, \tag{5}$$

where $\mathbf{f} = (f_1, f_2, f_3)^T$ is the applied force.

If in a region the medium is partially homogeneous (μ and μ' are constants), then in this region we have

$$\rho\frac{\partial^2\theta}{\partial t^2} = (\overline{\lambda} + 2\overline{\mu})\Delta\theta, \tag{6}$$

and

$$\rho\frac{\partial^2\omega}{\partial t^2} = \overline{\mu}\Delta\omega. \tag{7}$$

where $\theta = \nabla \cdot \mathbf{u}$ and $\omega = \nabla \times \mathbf{u}$. Thus we see that even in viscoelastic media the dilation wave equation is similar to a "pure" P-wave equation and the rotational wave equations coincides in form with the "pure" S-wave equation.

1.3. 2-D Isotropic Viscoelastic Wave Equations

For a 2-D isotropic viscoelastic medium, we have

$$\rho\frac{\partial^2 u_1}{\partial t^2} = \frac{\partial}{\partial x_1}\left[\left(\overline{\lambda}+\overline{\mu}\right)\left(\frac{\partial u_1}{\partial x_1}+\frac{\partial u_3}{\partial x_3}\right)\right] + \frac{\partial}{\partial x_1}\left(\overline{\mu}\frac{\partial u_1}{\partial x_1}\right) + \frac{\partial}{\partial x_3}\left(\overline{\mu}\frac{\partial u_1}{\partial x_3}\right) + f_1,\tag{8}$$

and

$$\rho\frac{\partial^2 u_3}{\partial t^2} = \frac{\partial}{\partial x_3}\left[\left(\overline{\lambda}+\overline{\mu}\right)\left(\frac{\partial u_1}{\partial x_1}+\frac{\partial u_3}{\partial x_3}\right)\right] + \frac{\partial}{\partial x_1}\left(\overline{\mu}\frac{\partial u_3}{\partial x_1}\right) + \frac{\partial}{\partial x_3}\left(\overline{\mu}\frac{\partial u_3}{\partial x_3}\right) + f_3.\tag{9}$$

We then rewrite these equations as a system of four first order equations:

$$\frac{\partial u_1}{\partial t} = v_1,\tag{10}$$

$$\frac{\partial u_3}{\partial t} = v_3,\tag{11}$$

$$\rho\frac{\partial v_1}{\partial t} = \frac{\partial}{\partial x_1}\left[\left(\lambda+\mu\right)\left(\frac{\partial u_1}{\partial x_1}+\frac{\partial u_3}{\partial x_3}\right)\right] + \frac{\partial}{\partial x_1}\left(\mu\frac{\partial u_1}{\partial x_1}\right) + \frac{\partial}{\partial x_3}\left(\mu\frac{\partial u_1}{\partial x_3}\right)$$
$$+ \frac{\partial}{\partial x_1}\left[\left(\lambda'+\mu'\right)\left(\frac{\partial v_1}{\partial x_1}+\frac{\partial v_3}{\partial x_3}\right)\right] + \frac{\partial}{\partial x_1}\left(\mu'\frac{\partial v_1}{\partial x_1}\right) + \frac{\partial}{\partial x_3}\left(\mu'\frac{\partial v_1}{\partial x_3}\right) + f_1,\tag{12}$$

$$\rho\frac{\partial v_3}{\partial t} = \frac{\partial}{\partial x_3}\left[\left(\lambda+\mu\right)\left(\frac{\partial u_1}{\partial x_1}+\frac{\partial u_3}{\partial x_3}\right)\right] + \frac{\partial}{\partial x_1}\left(\mu\frac{\partial u_3}{\partial x_1}\right) + \frac{\partial}{\partial x_3}\left(\mu\frac{\partial u_3}{\partial x_3}\right)$$
$$+ \frac{\partial}{\partial x_3}\left[\left(\lambda'+\mu'\right)\left(\frac{\partial v_1}{\partial x_1}+\frac{\partial v_3}{\partial x_3}\right)\right] + \frac{\partial}{\partial x_1}\left(\mu'\frac{\partial v_3}{\partial x_1}\right) + \frac{\partial}{\partial x_3}\left(\mu'\frac{\partial v_3}{\partial x_3}\right) + f_3,\tag{13}$$

The 2-D forward modeling problem consists of solving equations (24–27) in rectangular domains with a free surface on $x_3 = X_S(x_1)$. The equations for zero normal and tangential surface stress are respectively:

$$(\lambda+2\mu)\frac{\partial u_3}{\partial x_3} + \lambda\frac{\partial u_1}{\partial x_1} + (\lambda'+2\mu')\frac{\partial v_3}{\partial x_3} + \lambda'\frac{\partial v_1}{\partial x_1} = 0,\tag{14}$$

$$\mu\left(\frac{\partial u_1}{\partial x_3}+\frac{\partial u_3}{\partial x_1}\right) + \mu'\left(\frac{\partial v_1}{\partial x_3}+\frac{\partial v_3}{\partial x_1}\right) = 0.\tag{15}$$

We choose radiation boundary conditions at the bottom:

$$\prod_{a=p,s}\prod_{j=1}^{J}\left[\alpha_a(x_1,x_3) + \cos\phi_j^a(x_1,x_3)\frac{\partial}{\partial x_1} + \sin\phi_j^a(x_1,x_3)\frac{\partial}{\partial x_3} + n\frac{1}{v_a(x_1,x_3)}\frac{\partial}{\partial t}\right]\left(\begin{array}{c}u_1\\u_3\end{array}\right) = 0,\tag{16}$$

where $|\phi_j| < \pi/2, j = 1, 2, \cdots, J$. The radiation boundary conditions (30) are imposed such that the wave motions from the interior of the domain to pass through the boundary $x_3 = X_B(x_1)$ without being reflected. In general it is not possible to find practical boundary conditions that do the above task perfectly, however, the artificial reflections can be substantially reduced. Any linear combination of plane waves traveling out of the boundary $x_3 = X_B(x_1)$ at angles of incidence $\pm\phi_1, \pm\phi_2, \cdots, \pm\phi_J$ with speed v_a satisfies these boundary conditions (Higdon, 1987), where the absorption coefficients (Meng et al., 1989) are

$$\alpha_p = \frac{(\lambda+2\mu)'_s}{2(\lambda+2\mu)} + \frac{\omega^2\sqrt{\rho}(\lambda'+2\mu')}{2(\lambda+2\mu)^{3/2}},\tag{17}$$

$$\alpha_s = \frac{\mu'_s}{2\mu} + \frac{\omega^2\mu'\sqrt{\rho}}{2\mu^{3/2}},\tag{18}$$

No explicit boundary conditions are use on the sides. The natural (periodic) conditions are employed for Fourier polynomials. Absorption is accomplished by using hin absorbing layers with μ' and λ' gradually increasing towards the boundaries.

To obtain a rectangular geometry for a problem with an irregular top and bottom (due to surface topography and curvature of the earth) we employ a transformation from (x_1, x_3) to (x_1, η), where $\eta = \eta(x_1, x_3)$ (Fig. 1). The equations of motion then become

$$\frac{\partial u_1}{\partial t} = v_1, \tag{19}$$

$$\frac{\partial u_3}{\partial t} = v_3, \tag{20}$$

$$\rho \frac{\partial v_1}{\partial t} = \left(\frac{\partial}{\partial x_1} + \eta_{x_1} \frac{\partial}{\partial \eta} \right) \left[(\lambda + \mu) \left(\frac{\partial u_1}{\partial x_1} + \eta_{x_1} \frac{\partial u_1}{\partial \eta} + \eta_{x_3} \frac{\partial u_3}{\partial \eta} \right) \right]$$

$$+ \left(\frac{\partial}{\partial x_1} + \eta_{x_1} \frac{\partial}{\partial \eta} \right) \left[\mu \left(\frac{\partial u_1}{\partial x_1} + \eta_{x_1} \frac{\partial u_1}{\partial \eta} \right) \right] + \left(\eta_{x_3} \frac{\partial}{\partial \eta} \right) \left[\mu \left(\eta_{x_3} \frac{\partial u_1}{\partial \eta} \right) \right]$$

$$+ \left(\frac{\partial}{\partial x_1} + \eta_{x_1} \frac{\partial}{\partial \eta} \right) \left[(\lambda' + \mu') \left(\frac{\partial v_1}{\partial x_1} + \eta_{x_1} \frac{\partial v_1}{\partial \eta} + \eta_{x_3} \frac{\partial v_3}{\partial \eta} \right) \right]$$

$$+ \left(\frac{\partial}{\partial x_1} + \eta_{x_1} \frac{\partial}{\partial \eta} \right) \left[\mu' \left(\frac{\partial v_1}{\partial x_1} + \eta_{x_1} \frac{\partial v_1}{\partial \eta} \right) \right] + \left(\eta_{x_3} \frac{\partial}{\partial \eta} \right) \left[\mu' \left(\eta_{x_3} \frac{\partial v_1}{\partial \eta} \right) \right] + f_1 \tag{21}$$

$$\rho \frac{\partial v_3}{\partial t} = \left(\eta_{x_3} \frac{\partial}{\partial \eta} \right) \left[(\lambda + \mu) \left(\frac{\partial u_1}{\partial x_1} + \eta_{x_1} \frac{\partial u_1}{\partial \eta} + \eta_{x_3} \frac{\partial u_3}{\partial \eta} \right) \right]$$

$$+ \left(\frac{\partial}{\partial x_1} + \eta_{x_1} \frac{\partial}{\partial \eta} \right) \left[\mu \left(\frac{\partial u_3}{\partial x_1} + \eta_{x_1} \frac{\partial u_3}{\partial \eta} \right) \right] + \left(\eta_{x_3} \frac{\partial}{\partial \eta} \right) \left[\mu \left(\eta_{x_3} \frac{\partial u_3}{\partial \eta} \right) \right]$$

$$+ \left(\eta_{x_3} \frac{\partial}{\partial \eta} \right) \left[(\lambda' + \mu') \left(\frac{\partial v_1}{\partial x_1} + \eta_{x_1} \frac{\partial v_1}{\partial \eta} + \eta_{x_3} \frac{\partial v_3}{\partial \eta} \right) \right]$$

$$+ \left(\frac{\partial}{\partial x_1} + \eta_{x_1} \frac{\partial}{\partial \eta} \right) \left[\mu' \left(\frac{\partial v_3}{\partial x_1} + \eta_{x_1} \frac{\partial v_3}{\partial \eta} \right) \right] + \left(\eta_{x_3} \frac{\partial}{\partial \eta} \right) \left[\mu' \left(\eta_{x_3} \frac{\partial v_3}{\partial \eta} \right) \right] + f_3 \tag{22}$$

The free surface boundary conditions at the top become:

$$(\lambda + 2\mu) \left(\eta_{x_3} \frac{\partial u_3}{\partial \eta} \right) + \lambda \left(\frac{\partial u_1}{\partial x_1} + \eta_{x_1} \frac{\partial u_1}{\partial \eta} \right) + (\lambda' + 2\mu') \left(\eta_{x_3} \frac{\partial v_3}{\partial \eta} \right) + \lambda' \left(\frac{\partial v_1}{\partial x_1} + \eta_{x_1} \frac{\partial v_1}{\partial \eta} \right) = 0 \tag{23}$$

$$\mu \left(\eta_{x_3} \frac{\partial u_1}{\partial \eta} + \frac{\partial u_3}{\partial x_1} + \eta_{x_1} \frac{\partial u_3}{\partial \eta} \right) + \mu' \left(\eta_{x_3} \frac{\partial v_1}{\partial \eta} + \frac{\partial v_3}{\partial x_1} + \eta_{x_1} \frac{\partial v_3}{\partial \eta} \right) = 0 \tag{24}$$

The radiation boundary conditions at the bottom take the form

$$\alpha_1 + \cos \phi \left(\frac{\partial u_1}{\partial x_1} + \eta_{x_1} \frac{\partial u_1}{\partial \eta} \right) + \sin \phi \left(\eta_{x_3} \frac{\partial u_1}{\partial \eta} \right) + \frac{v_1}{v} = 0, \tag{25}$$

$$\alpha(x_1, x_3) u_3 + \cos \phi(x_1, x_3) \left(\frac{\partial u_3}{\partial x_1} + \eta_{x_1} \frac{\partial u_3}{\partial \eta} \right) + \sin \phi(x_1, x_3) \left(\eta_{x_3} \frac{\partial u_3}{\partial \eta} \right) + \frac{v_3}{v(x_1, x_3)} = 0. \tag{26}$$

These equations are to be approximated through collocation and quadrature (we use fourth order Runge-Kutta). The solutions are represented as 2-D discrete Fourier-Chebyshev transforms in (x_1, η). Differentiations with respect to x_1 and η are carried out in the usual way. The η derivatives of u_1, u_3, v_1 and v_1 result in four unknowns per k_x value: the $4N_x$ highest Chebyshev modes are lost in the differentiation process. In principal, these are to be determined by the $4N_x$ top and bottom boundary conditions. Due to the higher derivatives in the equations of motion, there are actually a total of $14N_x$ unknown highest Chebyshev modes. The highest modes in the equations are irrelevant and are ignored. Instead, the highest modes in the $4N_x$ unknowns are updated according to the $4N_x$ top and bottom boundary conditions.

Stability of Runge-Kutta for this problem has been studied. Details are available from the authors.

499

1.4. About the Grids

The strategy adopted for choosing the mapping function η is to flatten the surface and major contours. "Major contours" are those interfaces, typically the basement and moho, that are continuous across the section. Fig. 1 shows one of a set of "deep sedimentary basin" models that are being tested. Fig. 2 shows a model, derived from seismic data, for a trans-Urals DSS path.

Once the "major contours" are identified, the average travel time between the contours is computed (p-waves have been used so far), and constant values of η are assigned to the major contours so that the differences in η are proportional to the travel time. In this way, increments of constant $\Delta\eta$ correspond roughly to equal increments of travel time. This is done so as to improve the stability properties of the time integration.

1.5. Preliminary Results

Preliminary calculations indicate that it is practical to simulate wave propagation for 2-D models of about 2,000 by 200 km. Such simulations require several days of compuation on a SGI Power Challenge (300 MFlops).

We are in the process of quantifying the effects of particular types of crustal features on regional waveforms. Features under study include deep sedimentary basins (see Fig. 1), moho uplift and lateral variation in surface features. Also, some realistic models (such as the Soviet DSS model in Fig. 2) are currently being tested.

2. Recommendations and Future Plans

Other authors have performed simulations for particular models (e.g., Jih (1994) uses a finite difference method); there is not yet completed a comprehensive and quantitative study of the effects of crustal features. Our plan is to use a series of models, for example the deep sedimentary basin models, varying the size and elastic parameters of the basin, to determine how the effects of such basins on crustal wave propagation, such as attenuation of L_g, depend on the parameters of the basin. Additionally, we will study the effects of moho uplift, combined basin and uplift, and surface topographical roughness and other surface features.

One weakness of this method is that, because of its 2-D nature, amplitudes and decay times are not correct, and relative amplitudes of differing phases are not readily obtainable. Although the method described in this paper can readily be applied to the 3-D problem, it is apparent that elastic wavefield computations in a region of 2,000 by 2,000 by 200 km are not practical with any computer available to the authors. However, two acceleration techniques may be employed when solving the problem of wave propagation between two points (source and receiver):

1. Model only a narrow channel between the source and receiver (see Fig. 3). Use absorbing boundary conditions on the lateral boundaries to avoid reflections or wrap-around.
2. Use smaller tracking grids that follows the major wave fronts. A full simulation would then require several runs, each to capture the modes with essentially different paths, but each run would be much quicker than a global computation.

1. Bayliss, A., Jordan, K. E., Lemesurier, B. J. and Turkel, E., 1986, A fourth-order accurate finite-difference scheme for the computation of elastic waves: *Bulletin of the Seismological Society of America*, **76**, pp. 1115–1132.
2. Carcione, J. M., 1992, Modeling anelastic singular surface waves in the earth: *Geophysics*, **57**, pp. 781–792.
3. Carcione, J. M., Kosloff, D. and Kosloff, R., 1988, Wave propagation simulation in an elastic anisotropic (transversely isotropic) solid: *Q. J. Mech. Appl. Math.*, **41**, pp. 319–415.
4. Carcione, J. M., Kosloff, D., Behle, A. and Serian, G., 1992, A spectral scheme for wave propagation simulation in 3-D elastic-anisotropic media: *Geophysics*, **57**, pp. 1593–1607.
5. Fornberg, B., 1988, The pseudospectural method: Accurate representation of interfaces in elastic wave calculations: *Geophysics*, **53**, pp. 625–637.
6. Fornberg, B., 1987, The pseudospectrul method: Comparisons with finite difference for the elastic wave equation: *Geophysics*, **52**, pp. 483–501.
7. Fornberg, B. and Sloan, D. M., 1994, A review of pseudospectral methods for solving partial differential equations: *Acta Numerica*, pp. 203–267.
8. Gottlieb, D., Gunzburger, M. and Turkel, E., 1982, On numerical boundary treatment of hyperbolic systems for finite difference and finite element methods: *SIAM Journal of Numerical Analysis*, **19**, pp. 671–682.
9. R.-D. Jih, 1994, Numerical Modeling of Crustal Phase Propagation in Irregular Waveguides, 16th PL/AFOSR Seismic Symposium, pp. 173-81.

PL-TR-94-2217, ADA284667

10. Nielsen, P., Flemming, I, Berg, P. and Skovgaard O., 1994, Using the pseudospectrual technique on curved grids for 2D acoustic forward modeling: *Geophysical Prospecting*, **42**, pp. 321–341.

11. Kosloff, D., Kessler, D., Filho, A. Q., Tessmer, E., Behle, A. and Strahilevitz, R., 1990, Solution of the equations of dynamic elasticity by a Chebychev spectral method: *Geophysics*, **55**, pp.734–748.

12. Kindelan, M., Kamel, A. and Sguazzero, P., 1990, On the construction and efficiency of staggered numerical differentiators for the wave equation: *Geophysics*, **55**, pp. 107–110.

13. Sheriff, R. E., and Geldart, L. P., 1982, *Exploration Seismology*, Vol. 1:*History, Theory and Data Acquisition*, Cambridge, Cambridge University Press.

14. Sheriff, R. E. and Geldart, L. P., 1983, *Exploration Seismology*, Vol. 2: *Data-processing and Interpretation*, Cambridge, Cambridge University Press.

15. Tessmer, E. and Kosloff, D., 1994, 3-D elastic modeling with surface topography by a Chebyshev spectral method: *Geophysics*, **59**, pp. 464–473.

16. Tessmer, E., Kosloff, D. and Behle, A., 1992, Elastic wave propagation simulation in the presence of surface topography: *Geophysical Journal International*, **108**, pp. 620–632.

17. Meng, Z., Feng, Y. and Fan, Z., 1992, Radiation boundary conditions for complicated wave propagations: *Chinese Journal of Geophysics*, **34**, pp.509–516.

18. Fan, Z. and Teng, Y., 1988, Numerical simulations of viscoelastic waves: *Acta Geophysica Sinica*, **31**, pp. 198–209.
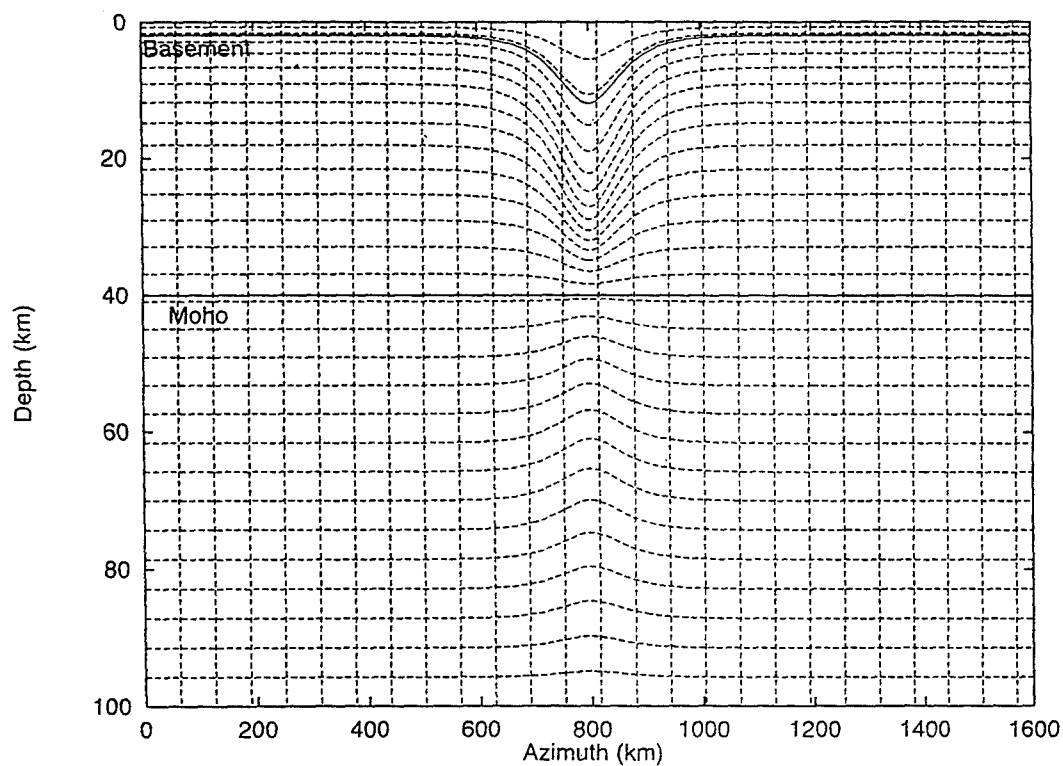
Fig. 1. Deep sedimentary basin model, showing eta grid lines conforming to the major contours, and eta spacing proportional to travel time.
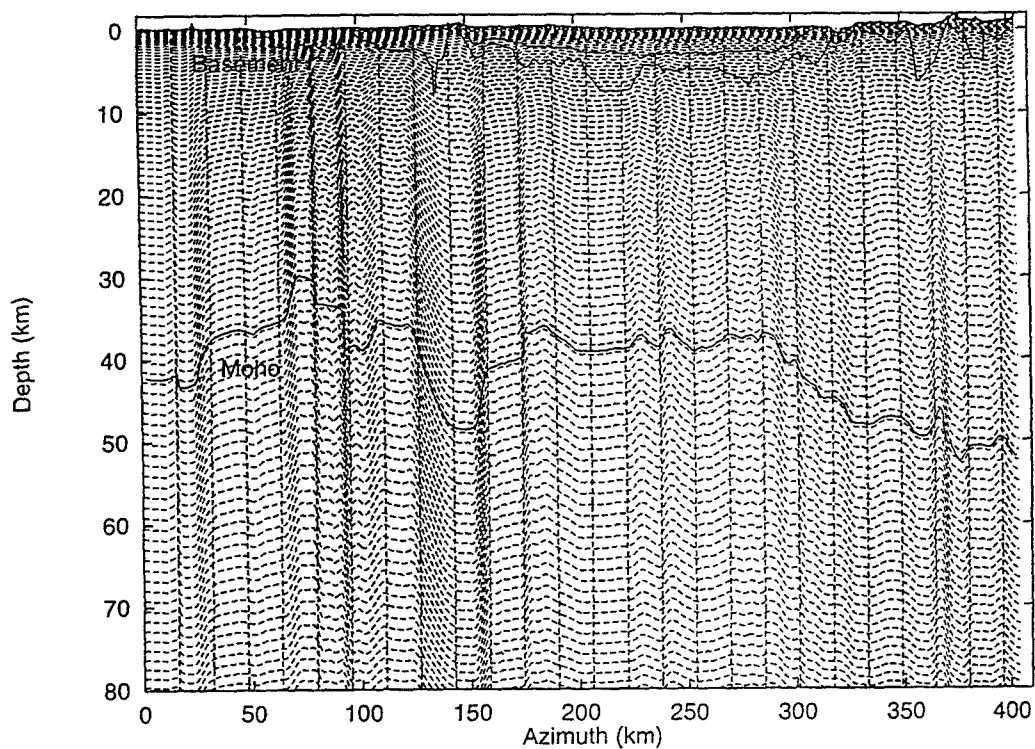
Fig. 2. Trans-Urals Soviet DSS model.
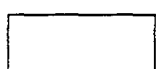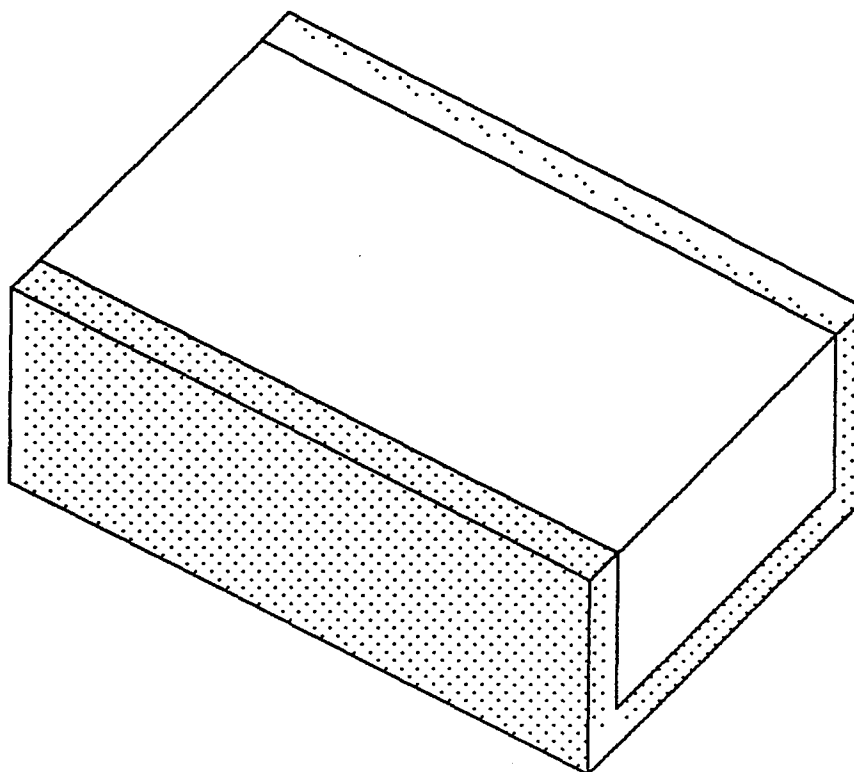
Active Computational Region
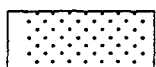
Attenuating Layer

Figure 3. Sketch of three-dimensional computational domain showing attenuating layers at bottom and sides.

Wave Propagation Modeling Capabilities at LLNL: Applications to Regional Discrimination

C. A. Schultz, S.C. Larsen, P. Goldstein, S.D. Ruppert

Earth Sciences Division, Lawrence Livermore National Laboratory
University of California

ABSTRACT

The numerical synthesis of regional seismograms has become an integral part of Lawrence Livermore National Laboratory's (LLNL) seismic discrimination program. In this paper, we summarize our fundamental approaches to numerical modeling. Our capabilities currently include reflectivity, normal mode, boundary integral, and finite-difference modeling, along with hybrid approaches which utilize two or more of these techniques together. We apply these capabilities to the discriminant variability along three different arrays deployed during the Non-Proliferation Experiment (NPE). Phase amplitudes have been calculated for the approximately three hundred regional stations which recorded the NPE. The majority of these recordings were to the west of the NPE, along one profile of the Southern Sierra Continental Dynamics (SSCD) refraction profile. Based on the three profiles which made up the SSCD refraction experiment, traveltime tomography was utilized to develop a well constrained 3D velocity model across a profile which extends from the Basin and Range, through the southern Sierra Nevada range, the Great Valley, to the San Andreas fault zone in the coastal ranges. The western array of the NPE regional deployment consisted of 285 stations coincident with this SSCD profile. This resulted in phase and discriminant coverage along one of the most well constrained velocity profiles in the western United states. Our analysis shows that although there is amplification of Pg and Lg, Pn has some of the most dramatic variations in amplitude. In California, these amplifications coincide with the western flank of the Sierra Nevada, the eastern quarter of the Great Valley, and the coastal ranges. In Nevada, a dramatic amplification occurred in the Broken Hills volcanic region. To the east, along the Arizona-Utah border, amplification occurred along the transition between the Basin and Range and the Colorado Plateau. The amplification of Pn in these regions resulted in a considerable deviation in 6-8 Hz Pn/Lg ratios. However, we find that the Pn/Lg slope was considerably more stable, showing less variation as a function of distance from the NPE. Numerical modeling with the reflectivity shows that when material contrasts are large enough, a local plane layered structure can result in significant Pn amplification. Boundary integral modeling shows that site resonances due to local 2D structure and topography can account for the dramatic amplification and time duration of Pn observed in Broken Hills. Finite-difference modeling shows that crustal thickening along the Colorado Plateau can result in focusing which may explain much of the amplification in the 0.5 to 10 Hz frequency band which appears at distances of 200 and 280 km.

OBJECTIVES

A primary goal of our research at LLNL has been to develop an assemblage of the most promising numerical techniques for simulating regional wave propagation through complex media. These numerical capabilities will be an integral part of our approach to regional characterization in both the Middle East and North Africa. In this paper, we focus on demonstrating and validating our current modeling capabilities, which include reflectivity, boundary integral, finite-difference, along with hybrid forms of these approaches. We use the boundary integral and finite-difference techniques to provide better understanding of regional discriminant variability along three arrays which were deployed to record regional signals from the NPE. These arrays extend west, northwest, and east from NTS, with the western line coinciding with one of three Southern Sierra Continental Dynamics (SSCD) refraction experiment profiles (Ruppert et al., in press; Fliedner et al., in press). This gives detailed coverage of regional phases along one of the most well constrained crustal profiles in the western United States. Phase amplitudes and the resulting discriminant variability are presented. This "ground truth" dataset will then act as the basis for the future validation of our numerical codes concurrent with our regionalization of the Middle East and North Africa.

RESEARCH ACCOMPLISHED

Current Capabilities

Synthetic modeling of seismic wave propagation in elastic media is an integral part of LLNL's seismic discrimination program. The purpose of our research is to apply a collection of validated wave propagation codes to the Middle East and Northern Africa for discriminant phase analysis. This includes discriminant development, the interpretation of discriminant results, and regional characterization. Our current numerical capabilities for seismic wave propagation include a generalized 1D reflectivity algorithm (Randall, 1994) and a 2D boundary integral algorithm, which generalizes the reflectivity approach to irregular boundaries (Schultz and Toksöz, 1994; Bouchon et al. 1989). Our current finite-difference capabilities consist of a highly optimized 2D/3D wave propagation code, ELAS3D (Levander, 1988; Larsen and Harris, 1993; Larsen, 1995) for modeling full elastic wave propagation in a complex media.

In general, the boundary integral techniques form a very accurate approach to modeling the propagation of P and S waves in an irregularly layered media, allowing for the simple inclusion of free surface topography, irregular boundaries separating homogeneous layers, and attenuation. Unfortunately, the boundary integral techniques are somewhat limited with respect to regional propagation, since the algorithm quickly becomes computationally intensive as the boundary conditions along each interface must be solved with a full general matrix at each independent frequency. Bouchon et al. (in press) have recently shown that the biconjugate gradient approach combined with a threshold cutoff in the matrix can greatly accelerate these algorithms. However, these approaches are still prohibitively large for modeling high frequency responses ($f > 1$ Hz) at regional distances. We, therefore, implement the boundary integral approach more as a site tool for modeling the response of local structure to incident seismic energy. In addition, this code has proven extremely useful for benchmarking the validity of recently developed wave propagation techniques for complex media.

Using the boundary integral technique as a benchmarking tool, we have placed a major emphasis on making finite-difference an accurate and viable tool for modeling wave propagation at regional distances. ELAS3D has become a highly optimized 2D/3D finite-difference algorithm which is fourth-order accurate in space and second order accurate in time. This code has a run-time visualization feature and post-processing capabilities. A variable density grid has been implemented, yielding significant savings in computer speed and memory. We have incorporated both active grid and a propagating envelope algorithms. These speed up the code by eliminating calculations in regions which are void of "interesting" seismic energy. In addition, we have implemented a very efficient scheme for modeling

505

the response of free surface topography in the 2D portion of the code. This implementation is currently undergoing rigorous testing.

We have ported ELAS3D to several platforms including the Sun workstations, SGI, IBM 2000, and the Cray Y-MP, giving us the ability to model wave propagation at regional distances. Since numerical dispersion resulting from coarse grid sampling is the greatest limitation to propagation at larger distances, we have started implementing ELAS3D on a massively parallel processor to increase the spatial sampling rate. We have since ported a simpler acoustic version of the code to LLNL's 256-processor Meiko CS-2 where we observed a speed of 28 GFLOPS. Initial tests show that the parallelized version of the full elastic code will dramatically decrease the current run-time while significantly increasing the available memory. The largest predicted 2D model is 300 x 3000 kilometers at 10 Hz, given a constant P-wave velocity of 5 km/s. The time to compute a full seismogram on this grid is on the order of a week. Considering a typical regional propagation distance to be on the order of 50 x 500 km, there is ample memory to increase the sampling rate above the minimum limit of ten points per wavelength, thereby reducing numerical dispersion considerably. In the 3D case, the largest possible model is 25 x 25 x 25 kilometers at 10 Hz given the constant P-wave velocity of 5 km/s. The time to compute a whole seismogram is on the order of only a few hours.

Application to Discriminant variability
An improved understanding of the variability of regional seismic phases with distance is needed to improve the performance and transportability of regional seismic discriminants. Numerous studies, in a number of regions, have observed large variations in each of the dominant regional phases. Studies have shown large variations in *Pn*, *Sn*, and *Lg* over relatively short distances (e.g. Keller et al., 1994; Kadinsky-Cade et al., 1981; Ni and Barazangi, 1983). An improved understanding of these variations has been gained from numerous empirical studies (e.g. Chavez and Priestley, 1986; Zhang et al., 1994) and theoretical studies (e.g. Campillo, 1990; Kennett, 1993). The numerical approaches discussed in the section above, give us the tools to compliment these previous studies and gain physical insight into the propagation of phases, thereby allowing us to better understand the transportability of discriminants.

As part of our efforts to develop procedures for regional geophysical characterization, we have been making and assembling empirical observations of regional phase propagation. At the same time, we have been interpreting these observations with our numerical modeling to describe the observed phenomena. Examples include measurements and modeling of the variability of regional *Pn*, *Pg*, and *Lg* signals from the NPE along lines to the east, west, and northwest. Figure 1 shows the three arrays deployed to record regional phases propagating from the NPE. The 330 km long Nevada array extends from the NPE northward through the Basin and Range province of northwestern Nevada. The 300 km Arizona array extends eastward from the Basin and Range crossing over to the Colorado plateau, while the Sierra array is a 460 km profile which extends across one of the most rugged profiles in the western United States. This profile crosses Owen's Valley, the Sierra Nevada Ranges, the Great Valley, and finally terminates just short of the San Andreas fault zone. The average station separation along the Sierra line is less than 2 kilometers, giving excellent station coverage of regional phases.

Observations and modeling of variations in regional phases, both with distance and from region to region, are important because the detection, location, and identification of small magnitude events rely heavily on observation of these phases. For example, one of the most popular regional discriminants is based on the ratio of high-frequency (e.g. 6-8 Hz) *Pn* to *Lg* spectral amplitudes. If one of these phases is more sensitive to variations in structure such as Moho depth or topography, we would expect to observe significant variations from station to station, or at a single station for events from different azimuths. Figure 2 shows recordings of the NPE along the line that extends across the Sierra Nevada Range and Figure 3a demonstrates the variability in the discriminants. We find that large variations in *Pn* map

directly into the 6-8 Hz *Pn/Lg* spectral amplitude ratio. Variations do exist in *Lg*, although they tend to be much smaller than those in *Pn*. If such variations are due to systematic changes in features like crustal thickness or topography, they would be very sensitive to source-receiver distance or azimuth, potentially introducing large variability into discriminants such as *Pn/Lg* spectral ratios. Based on the SSCD refraction experiment (Ruppert et al., in press; Fliedner et al., in press), travel time tomography has been used to attain a 3D "ground truth" velocity model for both the crust and mantle in this region using data from 24 shots and three profiles. We are utilizing this profile for code validation as we try to better define our ability to predict observed variations in regional phases. This testing will continue and improvements will be made concurrent with our efforts of regional characterization in the Middle East and North Africa.

The 6-8 Hz spectral amplitude of the three most dominant regional phases is plotted as a function of position on Figure 1. There is a substantial amount of variation in the amplitude of the regional phases, the most dramatic variations being in the *Pn* phase while both the *Pg* and *Lg* phases have less variation with distance. Although variability of these three regional phases are minimal as they pass through northwestern Nevada, there is an order of magnitude amplification at the Broken Hills site near Fallon, Nevada. *Pn* is amplified by almost an order of magnitude relative to the surrounding stations, while *Pg* and *Lg* are amplified by only a factor of two. Figure 4 shows two proposed structures based on the little that we know of the geology at this site (Vitaliano, 1957) and the observation that much of the amplification consists of a 6 Hz resonance. Modeling with reflectivity shows that although the spectral shape and the drawn out time domain signal can be generated with two low velocity volcanic layers, one at the surface and the other a few hundred meters deep, at most only a four time amplification factor is predicted. Boundary integral modeling of a basin consisting of hydrothermally altered low-velocity volcanics with local topography demonstrates that 2D site structure can extend the time duration of the *Pn* signal and provide the additional amplification observed at the site.

The Arizona line also shows a large variation in *Pn* with distance, while *Lg* again tends to be more stable in spectral amplitude at 6-8 Hz. However, the oblique polarization of *Pn* at the site of amplification strongly suggests that the source of this amplification is a deeper focusing mechanism. Zandt (1995) has shown that raytracing combined with geologic and geophysical control along this profile predict crustal thickening along the transition between the Basin and Range and the Colorado Plateau, resulting in two consecutive Moho steps and significant lateral velocity variations. This model predicts focusing at the stations where *Pn* appears amplified in Figure 1. Finite-difference synthetics, shown in Figure 5, predict a similar amplification of *Pn* at the corresponding regional distances. Utilizing the broadband nature of this finite-difference modeling, this step is over a large enough distance that, in addition to the observed amplification at 6 Hz, significant amplification occurs over the full 0.5 to 10 Hz range typically utilized in regional discriminant analysis.

CONCLUSIONS AND RECOMMENDATIONS

LLNL will continue to develop a numerical foundation for the synthesis of seismograms at regional distances. We have developed a "ground truth" database across the southern Sierra Nevadas which will be used for the continued validation of our numerical modeling capabilities. In addition, future enhancements will be made to ELAS3D which include 3D implementations of attenuation, topography, and variable density grids, along with a 2.5D axial-symmetric option. This code will be made available on a number of additional platforms including workstation clusters.

Integrating these numerical algorithms with our empirical study of phase and discriminant variability in the southwestern United States, we have demonstrated the great variability of *Pn* due to crustal thickening and local site resonances, especially as observed in regions containing low-velocity layers. Examples include the crustal thickening of the Colorado Plateau and Sierra Nevada range and near surface low velocity structure in the Great Valley and Broken Hills region. The low velocity resonances

507

tend to amplify *Pn* both due to the resonance itself and the vertical polarization of *Pn*. Even though *Lg* is amplified by these low velocities it becomes radially polarized, significantly reducing the amplitude on the vertical component. Therefore, the vertical component shows an anomalously large *Pn/Lg* ratio, potentially introducing the risk of false alarms. This emphasizes the importance of three-component analysis when transporting these discriminants to different regions. One example where numerical calculations can lead to insights about discriminant performance is the *Pn/Lg* slope discriminant (Goldstein, 1995). This discriminant may be more stable than taking a *Pn/Lg* ratio in a narrow frequency band because of the inherent averaging that occurs over narrow band resonances.

References

Bouchon, M., M. Campillo, & S. Gaffet, 1989, A boundary integral equation-discrete wavenumber representation method to study wave propagation in multilayered media having irregular interfaces, *Geophysics*, **54**, 1134-1140.

Bouchon, M., C. A. Schultz, & M. N. Toksöz, 1995, A fast implementation of boundary integral equation methods to calculate the propagation of seismic waves in laterally-varying media, *Bull. Seism. Soc. Am.*, submitted.

Campillo, M., 1990, Propagation and attenuation characteristics of the crustal phase *Lg*, *Pure Appl. Geophys.*, **13**, 1-19.

Chavez, D. A. & K.F. Priestley, 1986, Measurement of frequency dependent *Lg* attenuation in the Great Basin, *Geophys. Res. Lett.*, **13**, 551-554.

Fliedner, M. & S. D. Ruppert, Three-dimensional crustal structure of the southern Sierra from seismic fan profiles and gravity modeling, *Geol.*, in press.

Goldstein, P., 1995, Slopes of P- to S-wave spectral ratios: a broadband regional seismic discriminant and a physical model, UCRL-JC-121223.

Kadinsky-Cade, K., M. Barazangi, J. Oliver, & B. Isacks, 1981, Lateral variations of high-frequency seismic wave propagation at regional distances across the Turkish and Iranian plateaus, *J. Geophys. Res.*, **86**, 9377-9369.

Keller, G. R., P. E. Malin, & S. D. Ruppert, 1994, Southern Sierra Nevada Continental Dynamics Project: 1993 field observations of the NPE, *DOE symposium on the Non-Proliferation Experiment, April 19-21*, Rockville Maryland.

Kennett, B. L., 1993, The distance dependence of regional phase discriminants, *Bull. Seism. Soc. Am.*, **83**, 1155-1166.

Larsen, S.C., 1995, 3D MPP simulations in the earth sciences: seismic applications, LLNL Symposium on Distributed Computing and Massively Parallel Processing.

Larsen, S.C. & D.B. Harris, 1993, Seismic wave propagation through a low velocity nuclear rubble zone, UCRL-ID-115729.

Levander, A., R., 1988, Fourth-order finite-difference P-SV seismograms, *Geophys.*, **53**, 1425-1436.

Ni, J. & Barazangi, High-frequency seismic wave propagation beneath the Indian Shield, Himalayan Arc, Tibetan Plateau and surrounding regions: high uppermost mantle velocities and efficient Sn propagation beneath Tibet, *Geophys. J. Roy. Astr. Soc.*, **72**, 665-689.

Randall, G.E., 1994, Efficient calculation of complete differential seismograms for lateral homogeneous earth models, *Geophys. J. Int.*, **118**, 245-254.

Ruppert, S. D. & Fliedner, M., Crustal structure and thickness of the southern Sierra Nevada from seismic refraction profiles, *Geol.*, submitted.

Schultz, C. A. & M. N. Toksöz, 1994, Enhanced backscattering of seismic waves from a highly irregular, random interface: P-SV case, *Geophys. J. Int.*, **117**, 783-810.

Vitaliano, C.J., 1957, Wall-rock alteration in the Broken Hills Range, Nevada, *J. Geol.*, **65**, 167-77.

Zandt, G., 1995, Crust and mantle structure across the Basin and Range-Colorado Plateau boundary at 37N latitude and implications for Cenozoic extensional mechanism, *J. Geophys. Res.*, **100**, 10529-548.

Zhang, T.R., S.Y. Schwartz, & T. Lay, Multivariate analysis of waveguide effects on short-period regional wave propagation in Eurasia and its application in seismic discrimination, *J. Geophys. Res.*, **99**, 21929-945.
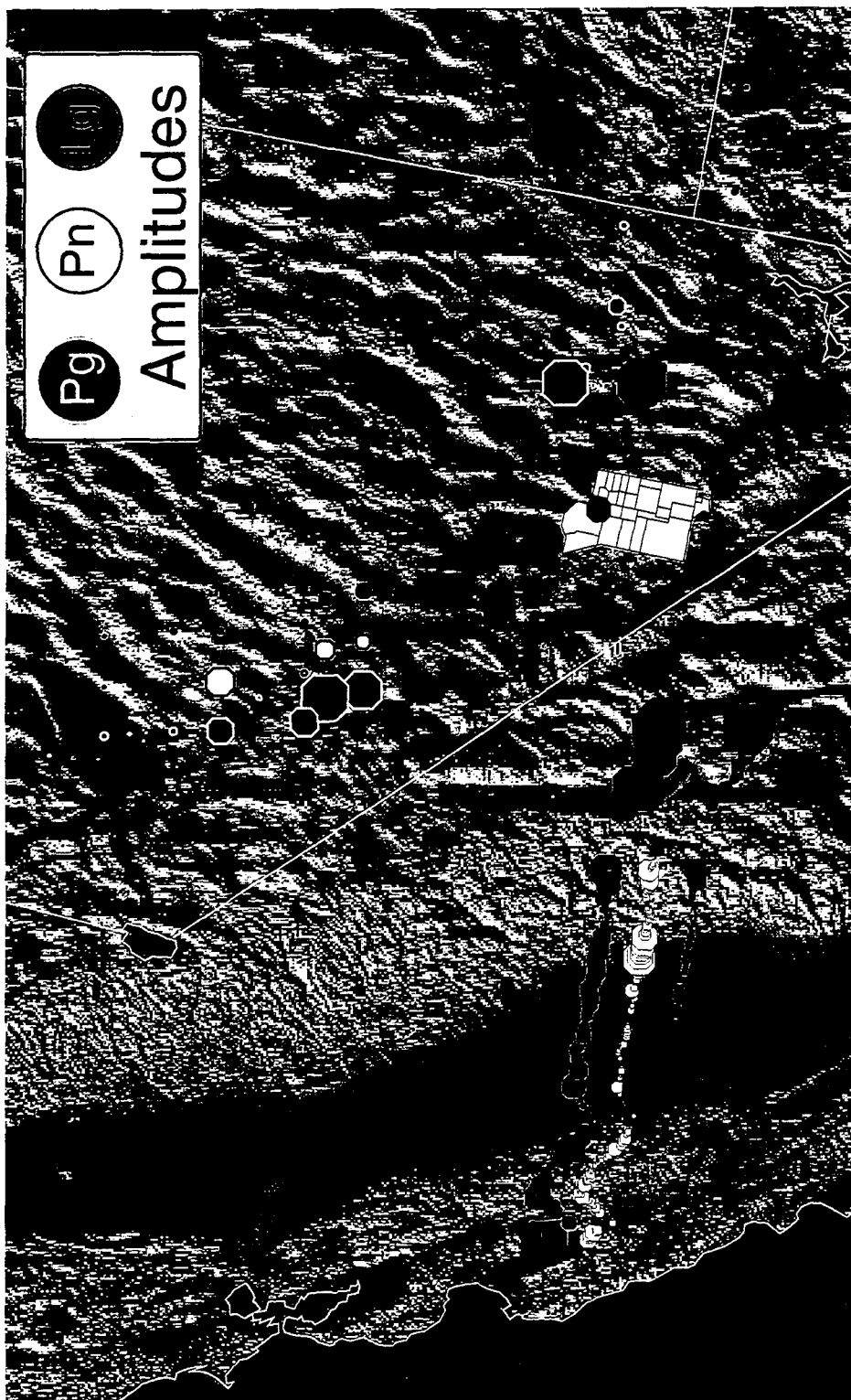
Figure 1: Spectral amplitude in the 6-8 Hz range for *Pn*, *Pg*, and *Lg* phases along each of the three arrays deployed during the NPE. The three phase amplitudes are plotted side by side along each array so that *Pn* is plotted over the actual station location and *Pg* and *Lg* are plotted to each side of the station location. Data is normalized for each independent array to the single largest phase amplitude recorded at a station along the array. A distance correction has not been applied to this data.
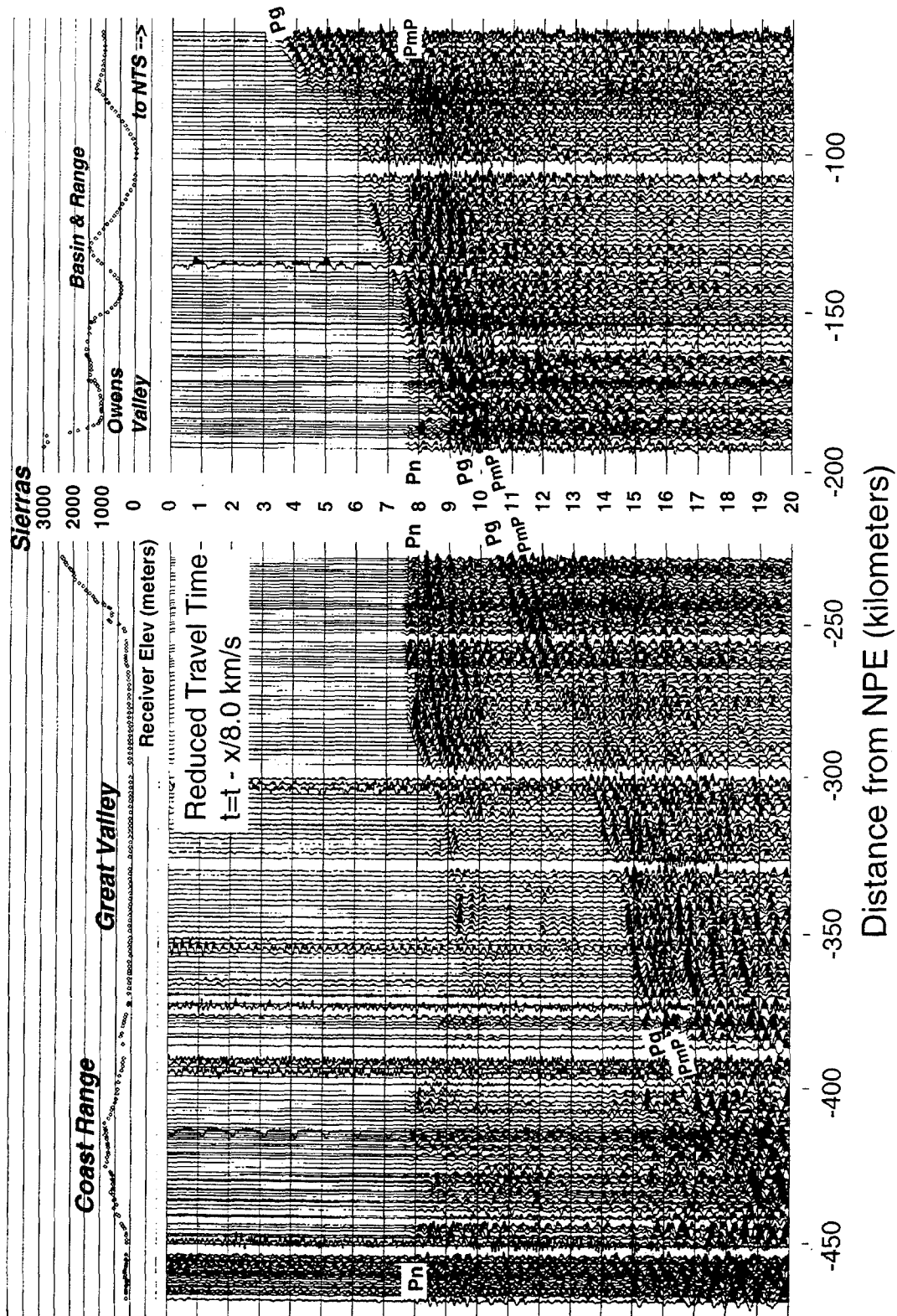
Figure 2: Plot of the regional seismograms recorded along the western array. Data is trace normalized to emphasize phases at the larger offsets. Lg arrives outside the time window shown.
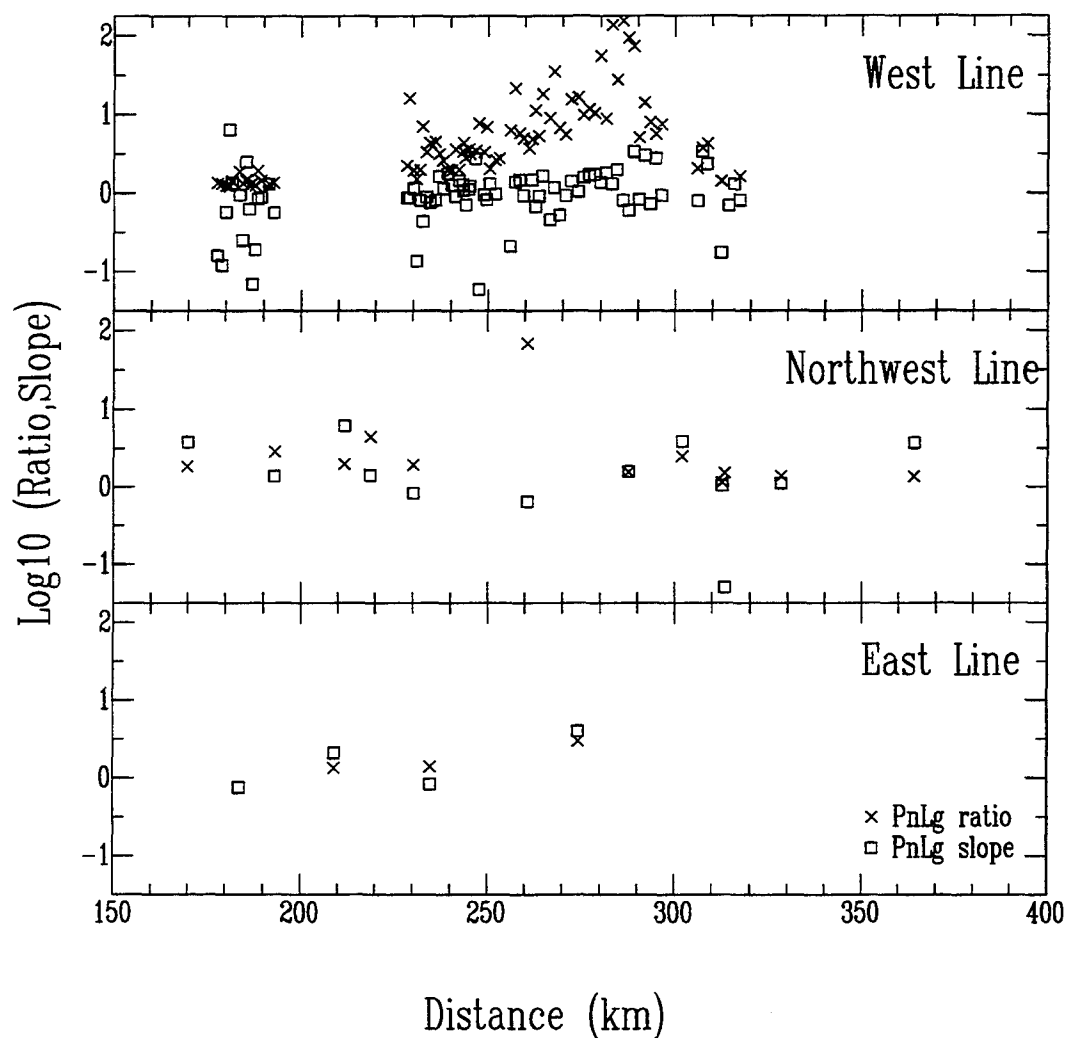
Figure 3: Two commonly used discriminants, the *Pn/Lg* ratio in the 6-8 Hz band and *Pn/Lg* slope over the full spectral range, calculated along the three seismic lines deployed for the NPE. We have applied a preliminary distance correction to this data. The lower outliers in the *Pn/Lg* slope are partially due to a low signal-to-noise criterion.

511
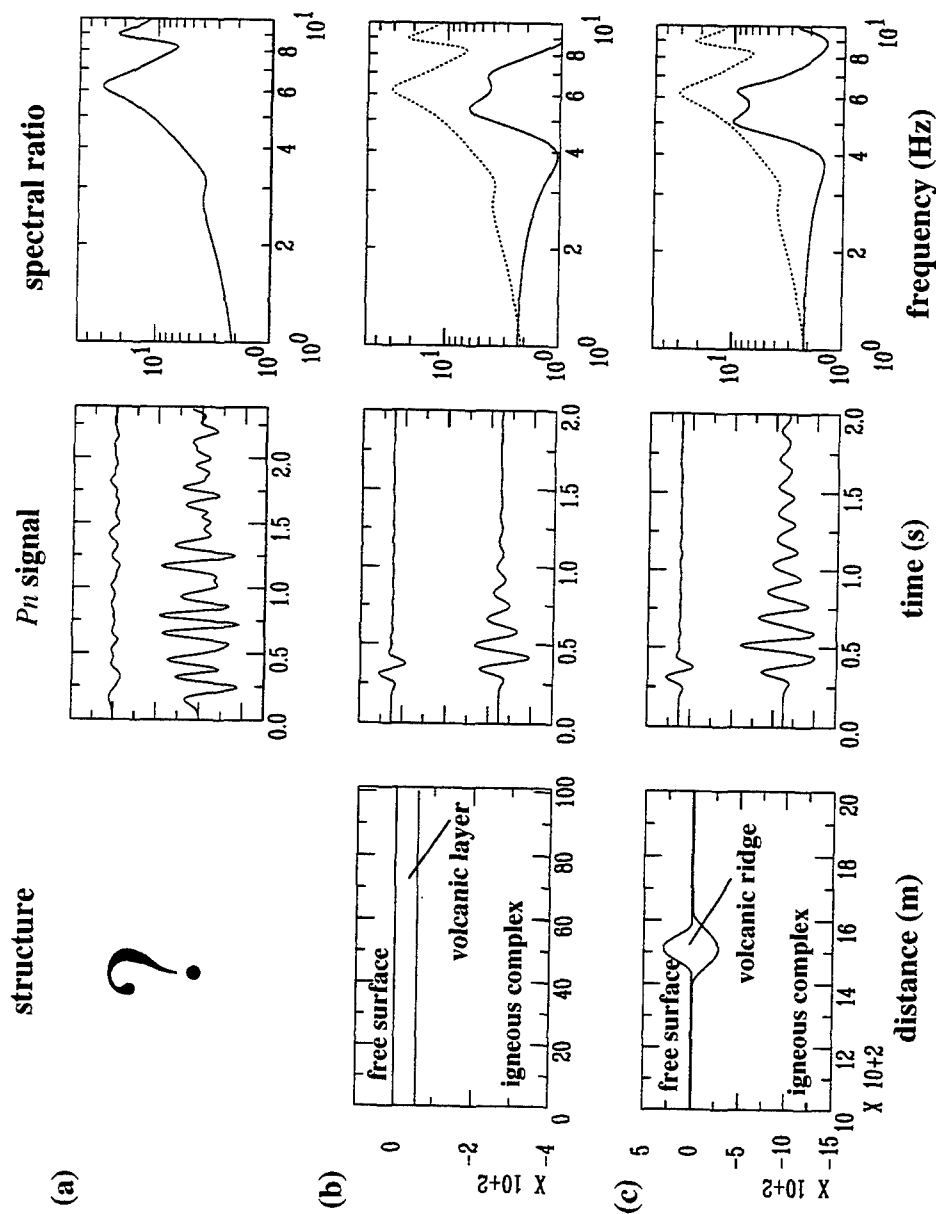
Figure 4: Comparison of (a) the anomalous *Pn* phase observed along the northwest line with an adjacent station approximately 20 km away. The dramatic 6 Hz amplification can be seen at this site. This *Pn* amplification is modeled with an igneous body covered by (b) a low velocity volcanic layer and (c) a low velocity volcanic ridge. A reference case corresponding to the response of a homogeneous igneous body is also given on the same plot. In all cases, the spectral ratios are given to show the general site amplification. The observed spectral ratio is shown for reference in the synthetic results.
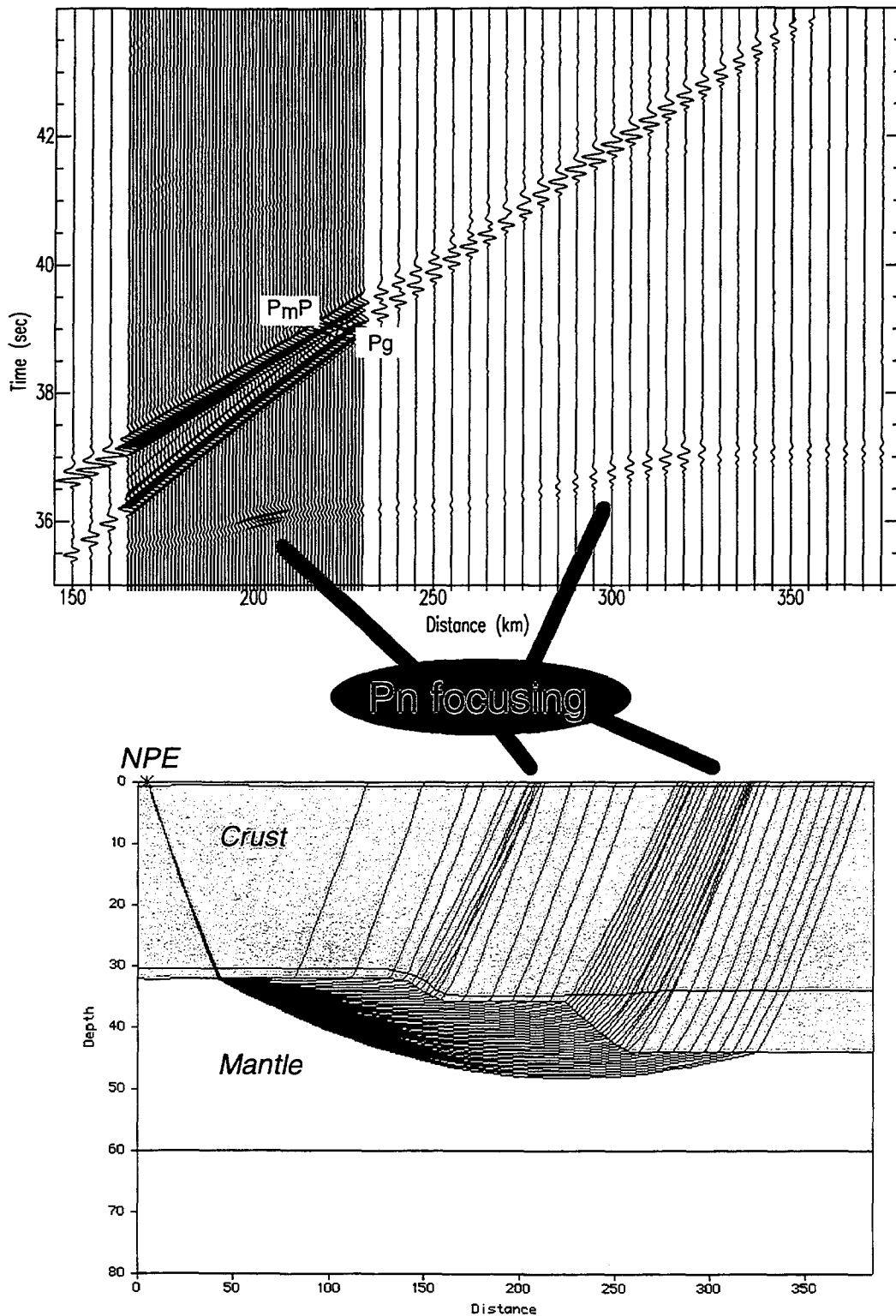
Figure 5: Finite-difference synthetics showing the response of the *Pn* and *Pg* phases to crustal thickening along the transition between the Basin and Range and the Colorado Plateau. At 200 km the *Pn* is amplified by approximately a factor of three due to focusing from a Moho step.

513

REGIONAL WAVEFIELD ANALYSIS USING
THREE-COMPONENT SEISMIC ARRAY DATA

Gregory S. Wagner & Thomas J. Owens
Department of Geological Sciences
University of South Carolina
Columbia, SC 29208

Abstract

An example of regional wavefield analysis using three-component seismic array data is presented. We examine the high-frequency (0.5–5.0 Hz) wavefields from three events that occurred in or near the Nevada Test Site (NTS), two underground nuclear tests and one earthquake, observed at the IRIS Joint Seismic Program three-component array located approximately 400 km to the south at Piñon Flat Observatory (PFO). The three-component array data are first displayed as broadband bearing-time records (BTR) which provide a time history of the propagation direction of coherent direct and scattered signals crossing the array; these displays are used primarily as a guide for further analysis. The BTRs reveal significant differences in the three wavefields. These differences are somewhat surprising in light of the fact that these data have essentially sampled the same terrain between NTS and PFO. The BTRs show that the P and S codas, and the L_g wavetrains for these three events contain a considerable amount of forward scattered/multipathed energy. It is only with the arrival of surface waves (apparent velocity approximately 3 km/s) that the coda becomes more random in nature. The fact that much of this later coda cannot be modeled as plane waves suggests that it is not scattered from distant sources.

The L_g wavetrain for one event is examined in detail. A spectogram, and P-SV, SH BTRs computed using the three-component array data reveal that the early portion of this particular L_g wavetrain is comprised of two linearly polarized SH/Love waves and a Rayleigh wave. The most prominent arrival in this L_g wavetrain is examined in more detail. When plotted in three-dimensions, the tangential and elliptical components of particle motion are more pronounced. High-resolution frequency-wavenumber analysis reveals that this section of this particular L_g is comprised of simultaneously arriving PSV_z (principal-component in the P-SV plane with predominantly vertical motion) and SH/Love modes with different frequencies, wavenumbers, and slightly different apparent velocities. The nearly identical radial and Hilbert-transformed vertical component waveform data provide further evidence that the P-SV energy is a Rayleigh as opposed to a shallow incidence angle SV wave.

key words: *array, polarization, seismic phase identification, regional wave propagation, scattering, multipathing, seismic coda.*

• Objective

The objective of our research is to: *(i)* improve event detection, phase identification and parameter and waveform estimation, *(ii)* provide an improved understanding of regional wave propagation, and *(iii)* to aid in the characterization of lithospheric heterogeneities. These goals are addressed by combining analysis of observed three-component array data and numerical simulations of elastic wave propagation in realistic earth structures.

• Preliminary Research Results

For this report we examine three events that occurred in the Nevada Test Site area (NTS); two are underground nuclear tests and one an earthquake. These data were collected as part of the Incorporated Research Institutions for Seismology (IRIS) consortium's Joint Seismic Program at Piñon Flat, California (PFO) (Al-Shukri *et al.*, 1991). The upper part of Figure 1 shows the PFO array geometry and a regional seismicity map (from CALNET and CALTECH catalogs, $M_L > 3$) for the three-month PFO experiment. The locations of NTS and PFO are shown on the seismicity map. The lower part of Figure 1 shows the broadband and 0.5–5.0 Hz bandpass filtered data for the three events examined for this report. These waveforms are event-wise normalized with amplitudes relative to the maximum in the broadband and bandpass filtered data, respectively, listed with each trace. Table 1 lists the origin times, locations, *etc.*, for the three events examined for this report.

• *Processing Approach*

The bandpass filtered (0.5–5.0 Hz) three-component array data are analyzed using the approach discussed in Wagner & Owens (1995b). Briefly, the magnitude of the multidimensional enhanced minimum-variance (EMV) spectrum is the inverse of the minimum eigenvalue, $\lambda_3(\theta, \omega, c)$, of the matrix

$$\mathbf{C}(\theta, \omega, c) = \mathbf{E}^\dagger(\theta, \omega, c) \ \mathbf{U}_\mathcal{N}(\omega) \ \mathbf{\Lambda}_\mathcal{N}(\omega) \ \mathbf{U}_\mathcal{N}^\dagger(\omega) \ \mathbf{E}(\theta, \omega, c) \tag{1}$$

where $\dagger$ denotes conjugate transpose, $\mathbf{U}_\mathcal{N}(\omega)$ is the unitary matrix whose columns are the [eigen]vectors that span the signal subspace's (Owsley, 1978) orthogonal complement, $\mathbf{\Lambda}_\mathcal{N}(\omega)$ is the diagonal matrix containing the associated eigenvalues, and

$$\mathbf{E}(\theta, \omega, c) = \begin{bmatrix} \uparrow & \uparrow & \uparrow \\ \mathbf{e}_\mathrm{Z}(\theta, \omega, c) & \mathbf{e}_\mathrm{NS}(\theta, \omega, c) & \mathbf{e}_\mathrm{EW}(\theta, \omega, c) \\ \downarrow & \downarrow & \downarrow \end{bmatrix} \tag{2}$$

where the $\mathbf{e}_i(\theta, \omega, c)$ are mutually orthogonal steering vectors for Z,NS,EW polarized plane waves traveling in direction θ with apparent velocity c. The eigenvector associated with the minimum eigenvalue, $\mathbf{p}_3(\theta, \omega, c)$, is in general complex and parameterizes the component-wise amplitude and phase relations. The mode vector for the ω frequency component is

$$\mathbf{e}(\theta, \omega, c, \mathbf{p}_3) = \mathbf{E}(\theta, \omega, c) \ \mathbf{p}_3(\theta, \omega, c) \tag{3}$$

Note that Equation 3 merely provides high-resolution estimates of the mode vectors. Waveform estimates are obtained by projecting the $\mathbf{e}(\theta, \omega, c, \mathbf{p}_3)$ onto the signal subspace (Gething, 1971)

$$\mathbf{w}(\theta, \omega, c, \mathbf{p}_3) = \mathbf{\Lambda}_\mathcal{S}^{1/2}(\omega) \ \mathbf{e}^\dagger(\theta, \omega, c, \mathbf{p}_3) \ \mathbf{U}_\mathcal{S}(\omega) \tag{4}$$
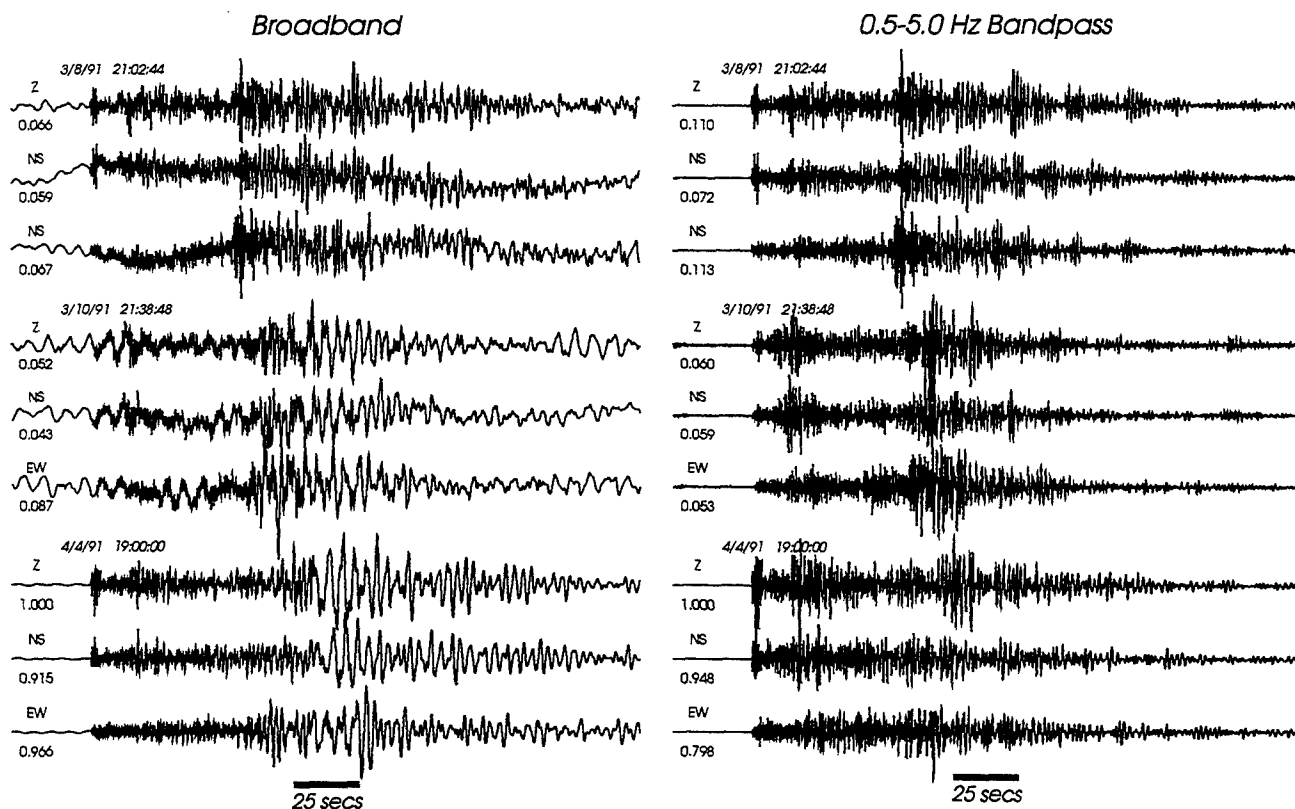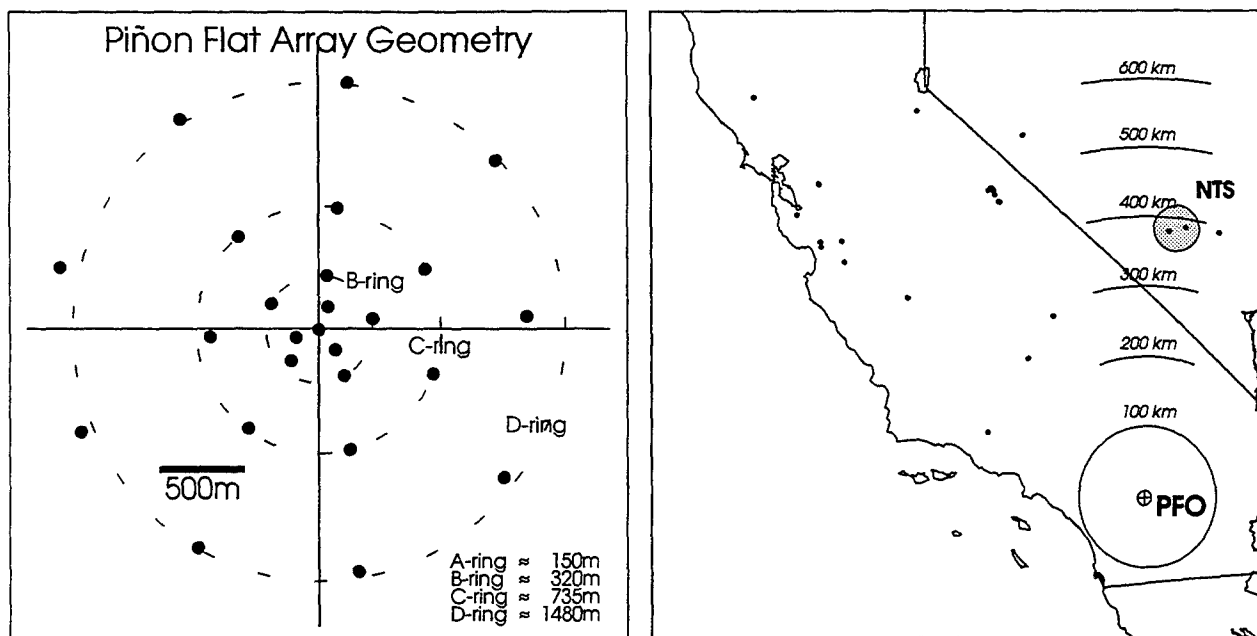
Figure 1: Top, the PFO array geometry and regional seismicity ($M_L > 3$) that occurred during the three-month PFO experiment. Bottom, the broadband and 0.5–5.0 Hz bandpass filtered data for the three events examined for this report. The waveforms are event-wise normalized with amplitudes relative to the maximum in the broadband and bandpass filtered data, respectively, listed with each trace See Table 1 for origin times, locations, etc..

date	hr:mn:sec	lat° (N)	lon° (E)	z (m)	M_L	delta°	BAZ°
03/08/91	21:02:45.40	37.104	-116.074	475	4.6	3.49	5.04
03/10/91	21:38:47.51	37.110	-115.232	5,000	4.0	3.63	15.67
04/04/91	19:00:00.00	37.296	-116.313	629	5.4	3.67	3.01

Table 1: Origin times, latitudes, longitudes, depths (meters), magnitudes, distances, and back azimuths from PFO for the three events examined in this report.

where $\mathbf{U}_S(\omega)$ is the unitary matrix whose columns are the [eigen]vectors that span the signal subspace, and $\mathbf{\Lambda}_S^{1/2}(\omega)$ is the diagonal matrix containing the square roots of the associated eigenvalues. Knowing the direction of energy flux, θ, the wavetype can be determined based on the particle motion parameterized by $\mathbf{p}_3(\theta, \omega, c)$. The associated power flux density is

$$\mathcal{P}(\theta, \omega, c, \mathbf{p}_3) = \mathbf{e}^\dagger(\theta, \omega, c, \mathbf{p}_3) \; \mathbf{U}_S(\omega) \; \mathbf{\Lambda}_S(\omega) \; \mathbf{U}_S^\dagger(\omega) \; \mathbf{e}(\theta, \omega, c, \mathbf{p}_3) \; . \tag{5}$$

The following section provides an outline of the analysis procedure using this approach.

- *Data Analysis*

Our analysis typically begins by computing broadband bearing-time records (BTR) of the three-component array data (Wagner & Owens, 1995a). BTRs provide a time history of the propagation direction of the coherent direct and scattered arrivals crossing the array. The BTRs serve primarily as a guide to further analysis. Figure 2 shows the broadband (0.5–5.0 Hz) EMV BTRs for the three events shown in Figure 1. Also calculated but not displayed in Figure 2 are the component-wise amplitude and phase relations for the coherent modes (*i.e.* the $\mathbf{p}_3(\theta, \omega, c)$). It is this information, combined with the direction-of-arrival (DOA) information, that allows us to identify the wavetype. Apparent velocity information is, unfortunately, lost with this particular broadband implementation.

Figure 2 raises several questions of particular interest for regional monitoring. First, the increased interest in regional characterization is both motivated by and based on the assumption that events that occur in the same region and sample the same terrain will be similarly affected by the structure, and that this effect occurs independent of source magnitude. One might expect, therefore, that the wavefields for these three events would exhibit similar characteristic. This is, however, not the case. The second observation is that the P and S codas, and the L_g wavetrains contain considerable amounts of forward scattered/multipathed energy. It is only with the arrival of the surface wave energy (apparent velocity of approximately 3 km/s) that the coda begins to exhibit more varied/random DOAs. The fact that much of this later coda cannot be modeled as plane waves suggests that it is not the product of scattering from distant sources.

Of the three events examined for this report, the event that occurred on 3/8/91 has the best developed L_g wavetrain. Because L_g is of considerable interest in CTBT monitoring and regional wave propagation in general, we conducted detailed analysis of the L_g wavetrain for this event. Figure 3 shows the spectogram (Equation 5 as a function of time) for the 4–3 km/s apparent velocity window. The Z,NS,EW data are plotted with the spectogram to help provide insight into the way each of the components contributes to the total field (note that these data are essentially naturally rotated). Similar plots showing the relative magnitudes of the Z,R,T components of $\mathbf{p}_3(\theta, \omega, c)$ as red, blue, green can be used to help identify wavetypes. Figure 3 shows the higher frequency L_g wavetrain proceeding and superimposed on the lower frequency S-coda and surface wave energy. The early L_g (11–16 secs in Figure 3) is comprised of three distinct phases with two simultaneous

517
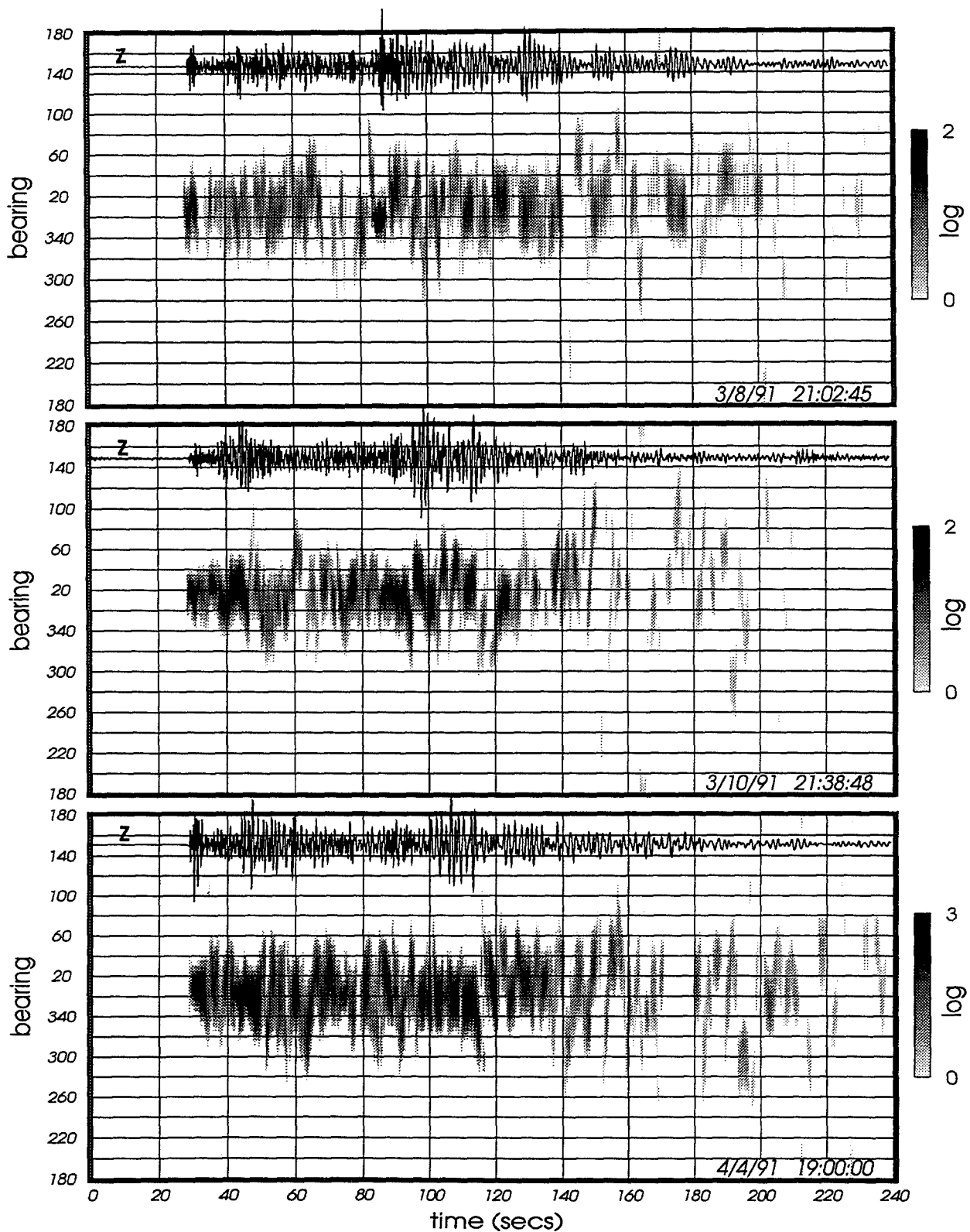
Figure 2: Three-component, broadband (0.5–5.0 Hz) bearing-time records for the three events listed in Table 1.
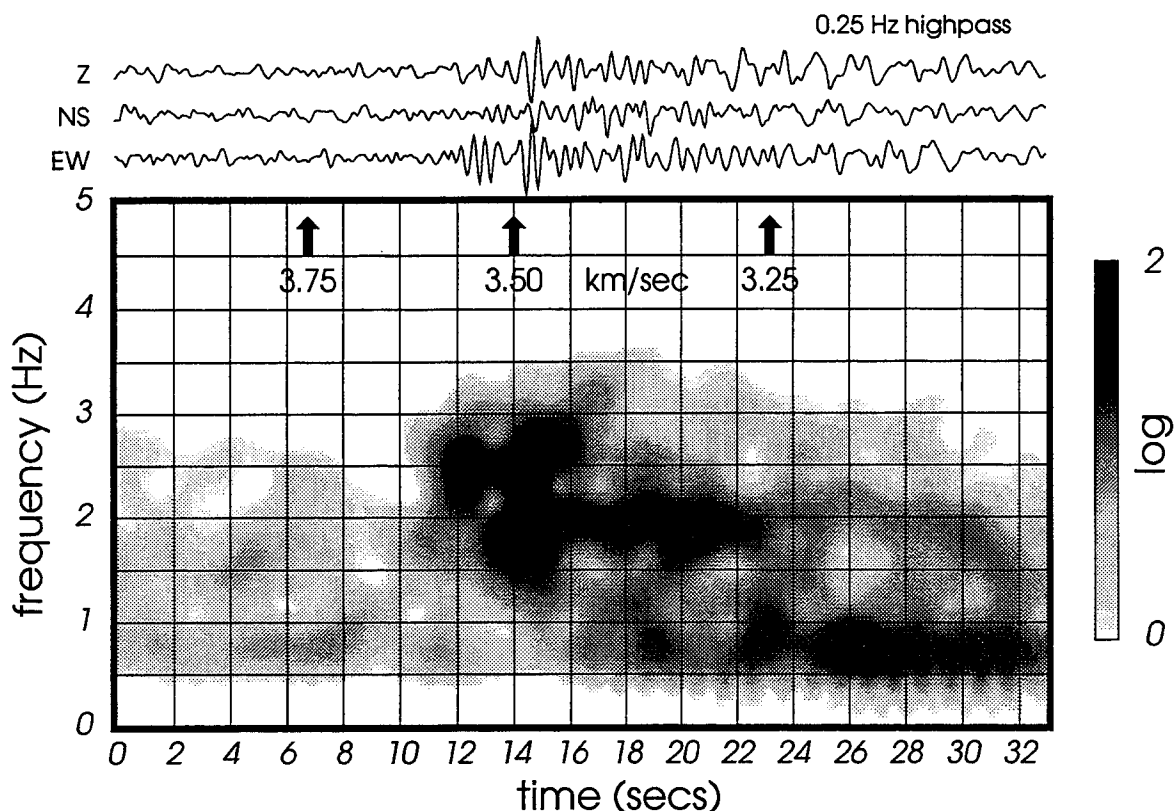
Figure 3: Spectogram for the 4–3 km/s apparent velocity window for event 3/8/91.

arrivals at approximately 14.5 secs. Based on $p_3(\theta, \omega, c)$, these two phases are identified as linearly polarized Love/SH and Rayleigh waves with peak frequencies of approximately 2.5 and 1.8 Hz, respectively. Figure 4 shows the BTRs for the total field, and the field decomposed into P-SV and SH components (Wagner & Owens, 1993). These P-SV, SH component BTRs reveal the characteristic simultaneously-arriving mixed-mode nature of L_g.

Further analysis was conducted on the most prominent arrival in the L_g wavetrain for this event (3/8/91). The top part of Figure 5 (part A) shows the three-dimensional particle motion for the 1 sec window containing the largest arrival in the L_g wavetrain. When viewed from the NNW and ENE, the tangential and elliptical components of particle motion are more pronounced. The middle part of Figure 5 (part B) shows the EMV frequency-wavenumber (ω-k) spectra for the PSV_z, PSV_r and SH components (Wagner & Owens, 1993). The ω-k spectra were computed (using the complex analytic signal) for the beam steered in the direction indicated by the BTRs. The ω-k analysis reveals that this data window contains simultaneously arriving PSV_z (principal-component in P-SV plane with predominantly vertical motion) and SH/Love modes with different frequencies, wavenumbers, and slightly different apparent velocities. The bottom part of Figure 5 (part C) shows the vertical- and radial-component waveforms (left), and the radial- and Hilbert-transformed ($\mathcal{H}$) vertical-component waveforms (right). The elliptical particle motion (part A) and the nearly identical $\mathcal{H}(Z)$ and R waveforms concur with the component-wise phase relations parameterized by $p_3(\theta, \omega, c)$, all of which suggest that the arrival isolated on the PSV_z spectrum is a Rayleigh as opposed to a shallow incidence angle SV wave.
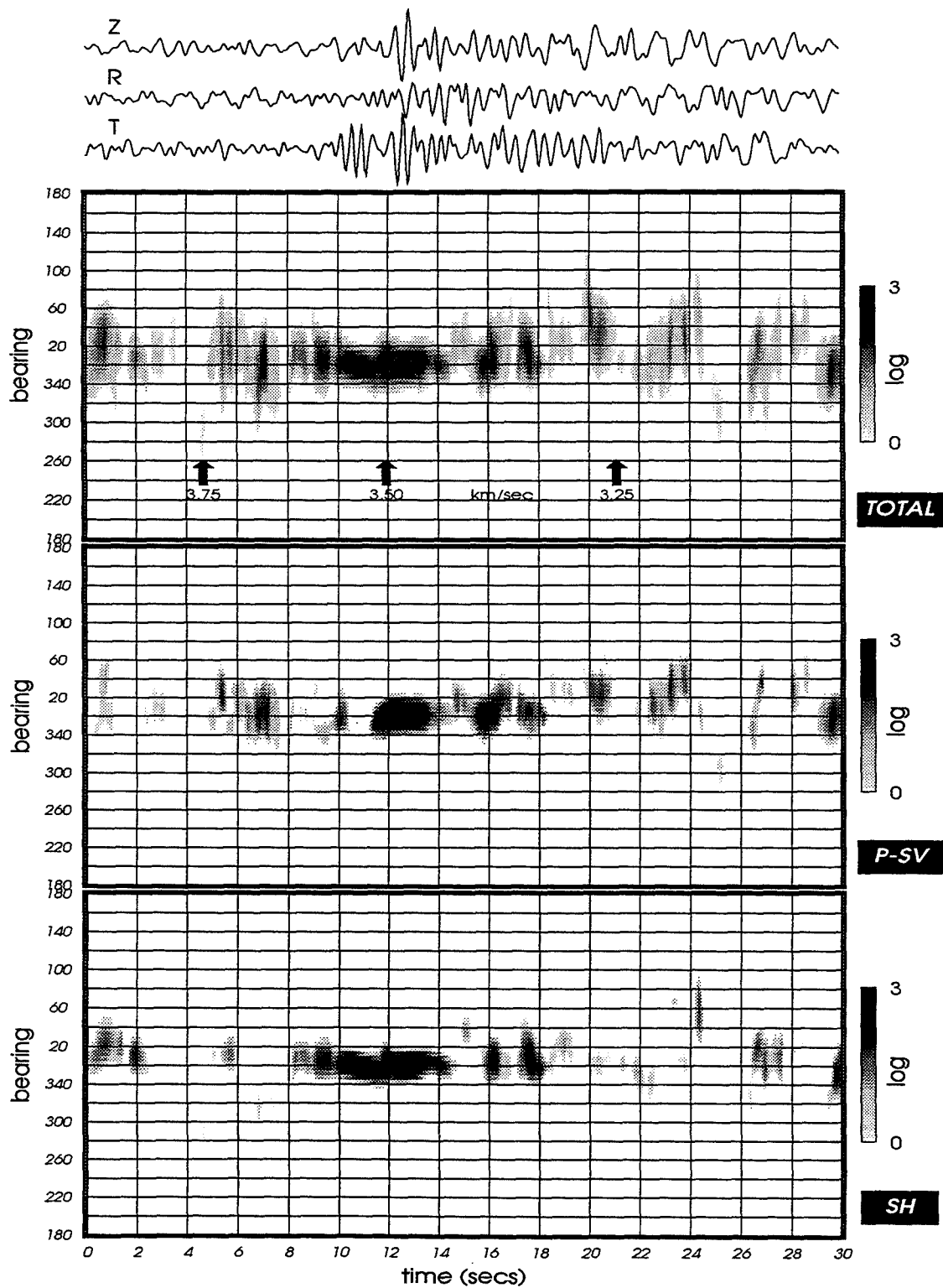
Figure 4: Total field, *P-SV*, and *SH* bearing-time records for the 0.5–5.0 Hz passband, 4–3 km/s apparent velocity window for the event that occured on 3/8/91 (see Table 1 for origin times, location, *etc.*).
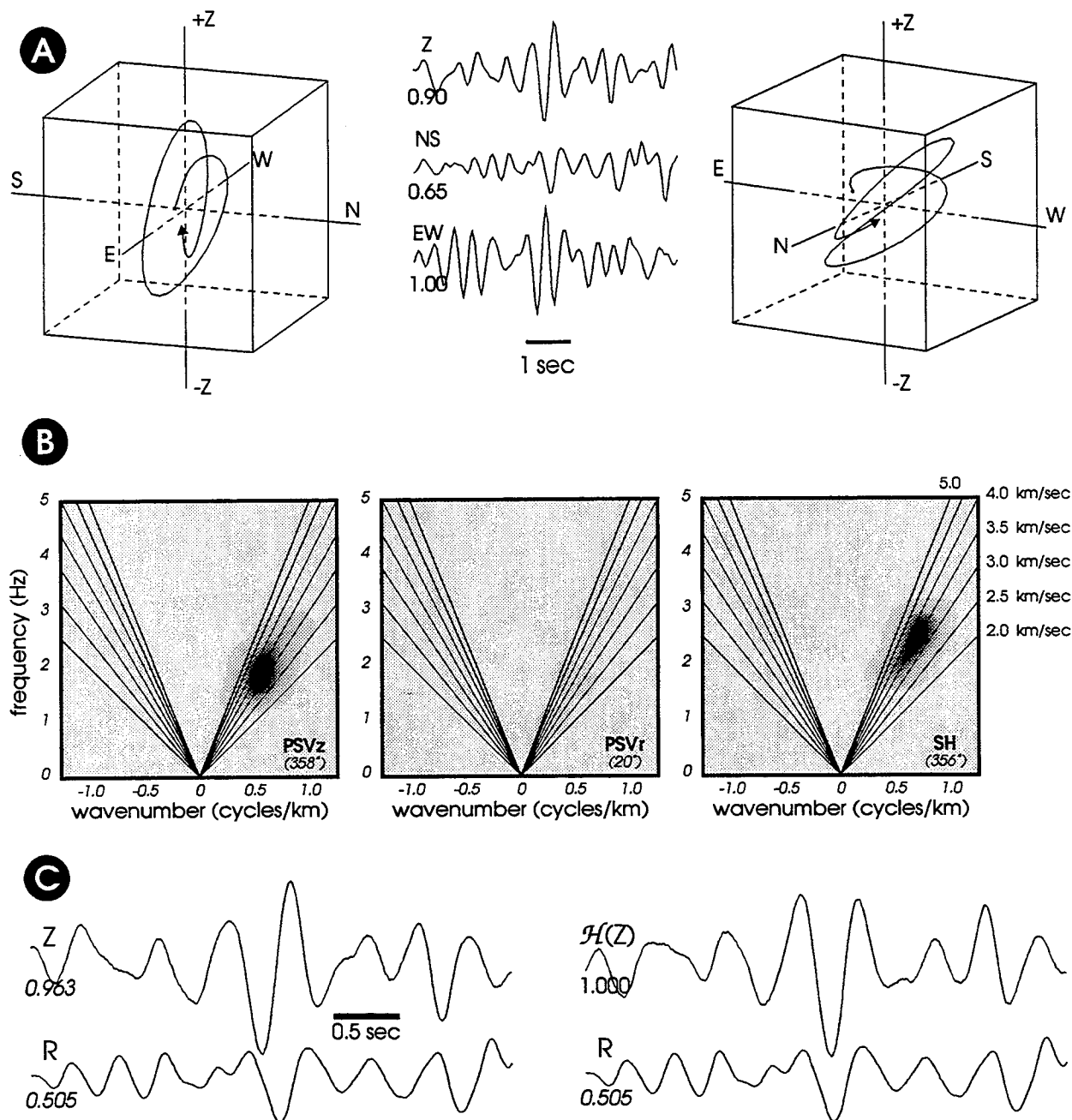
Figure 5: Top (A), three-dimensional particle motion, viewed from the ENE (left) and NNW (right), for the 1 sec window containing the most prominant arrival in the L_g wavetrain for event 3/8/91. Middle (B), PSV_z, PSV_r, SH frequency-wavenumber spectra for the most prominant L_g arrival; the three spectra are plotted using the same amplitude sacle. Bottom (C), the vertical- and radial-component waveforms, and the radial- and Hilbert-transformed vertical-component waveforms of the early L_g.

- **Conclusions, Recommendations & Future Plans**

This report provides an example of analysis of the regional wavefield using three-component seismic array data. Our analysis of L_g provides an example of the wealth of information provided by the elastic wavefield and three-component array data. Vertical-component array data provide no information about the SH/Love component of the seismic wavefield, and reduce our ability to detect, identify, and obtain truly representative waveform estimate for P, SV and Rayleigh waves. Elastic wavefield decomposition using single-site three-component data requires additional information (*i.e.* wavetype, propagation direction) that may not be available in a realistic monitoring situation. Three-component array data do not restrict our analysis to the vertically polarized component of the wavefield, and allow us to resolve the numerous problems and ambiguities inherent in elastic wavefield decomposition using data form isolated three-component sensors.

The complex problems we are faced with in monitoring a CTBT are exacerbated by not taking full advantage of the wealth of information provided by the elastic wavefield. Elastic waveform data provide the best and sometimes our only source of information about source processes and earth structure. Regional waveform data play a vital role in CTBT monitoring by providing information about smaller events that may not be observed at teleseismic distances. Broadband three-component array data provide a multidimensional, spatially and temporally unaliased sampling of the regional wavefield that permits a nearly comprehensive decomposition of the elastic wavefield. These data allow us to address and answer fundamental questions about seismic wave propagation that simply cannot be answered conclusively using data from vertical-component arrays or networks of isolated single- and/or three-component sensors. The availability of broadband three-component array data collected in regions around the globe would provide a unique and invaluable resource to the entire community.

Future plans are to continue analysis of these data to provide an improved understanding of regional wave propagation, to improve event detection, phase identification and waveform estimation, and to aid in the characterization of lithospheric heterogeneities. Our analysis is limited somewhat by the availability of three-component array data from different regions. Without data from other regions it is not possible to ascertain which of the characteristics observed in PFO data are unique to this region in particular, and which are true for regional wave propagation in general.

References

Al-Shukri, H., Owens, T., Pavlis, G., Roecker, S., Vernon, F., and Wagner, G., 1991. Data report for the 1991 Piñon Flat broadband array experiment *IRIS/PASSCAL Data Report*, pp. 27.

Gething, P. J. D., 1971. Analysis of multicomponent wavefields, *Proc. IEE*, **118**(10), 1333–1338.

Owsley, N. L., 1978. Adaptive data orthogonalization, *Proc. IEEE Int. Conf. Acoust., Speech, Signal Processing*, 109–112.

Wagner, G. S. and Owens, T. J., 1993. Broadband bearing-time records of three-component seismic array data and their application to the study of local earthquake coda, *Geophys. Res. Letters*, **20**(17), 1823–1826.

Wagner, G. S. and Owens, T. J., 1995a. Broadband eigen-analysis for three-component seismic array data, *IEEE Trans. on Signal Processing*, **43**(7), 1738–1741.

Wagner, G. S. and Owens, T. J., 1995b. A processing approach for three-component seismic array data, submitted to *Geophysical Journal International*, January, 1995.

NUMERICAL SIMULATIONS OF REGIONAL WAVE PROPAGATION IN REALISTIC EARTH MODELS

Gregory S. Wagner & Thomas J. Owens
Department of Geological Sciences
University of South Carolina
Columbia, SC 29208

Abstract

Preliminary results for numerical simulations of regional propagation in realistic earth models are presented. The modeling is motivated in part by three-component array observations which show that the P and S codas, and L_g wavetrains for regional sources are comprised of substantial amounts of forward scattered/multipathed energy, and in part by results from numerical simulations of teleseismic wave propagation which suggest a correlation between the coda level and rate of decay and the aspect ratio of lithospheric heterogeneities. Numerical simulations are conducted using a two-dimensional, fourth order accurate, P-SV finite difference routine. The models consist of a heterogeneous layer over a homogeneous half-space. Perturbations are in velocity and parameterized using a gaussian correlation function.

The wavefields generated using models containing high aspect ratio heterogeneities (ANISO) exhibit several characteristic consistent with regional array observations. First, the Pg wavetrain and coda consists of forward scattered, coherent plane wave energy trapped in the crustal waveguide. Models containing isotropic heterogeneities (ISO) inhibit the extent to which energy is trapped in the crustal waveguide and produce codas dominated by randomly scattered energy. Waveforms generated using models containing ANISO heterogeneities exhibit another feature commonly observed in regional array data. That is, that detailed features in waveforms observed at adjacent sensors exhibit a high degree of coherence, while those observed at sensors separated by distances on the order of a wavelength exhibit a somewhat surprising loss of coherence. Waveforms generated using models containing ISO heterogeneities exhibit a degree of incoherence inconsistent with regional array observations.

The modeling results presented in this report add to the growing body of evidence illustrating the important role spatially anisotropic heterogeneities play in seismic wave propagation and scattering. An important but overlooked implication inherent in parameterizing heterogeneities with spatially anisotropic correlation functions is that the dimensionless normalized wavenumber ka commonly used to categorize the scattering regime looses its meaning. Estimates of the effective scattering cross section and the associated scattering radiation pattern need include the vector quantity $\mathbf{k}$-$\mathbf{a}$ to reflect the fact that the nature of scattering depends not only on the (scalar) ratio of the "size" of the heterogeneities to the wavelength of the incident wavefield, but also on the spatial relation/orientation of the incident wavefield and heterogeneities.

key words: *regional wave propagation, scattering, seismic coda, spatially anisotropic heterogeneities, heterogeneity aspect ratio.*

• Objective

The main objective of our research is to provide an improved understanding of regional wave propagation and to aid in the characterization of lithospheric heterogeneities by combining analysis of observed three-component array data and numerical simulations of elastic wave propagation in realistic earth structures.

• Preliminary Research Results

This report provides preliminary results from numerical simulations of regional wave propagation in realistic earth structures. The modeling is motivated in part by three-component array observations which show that the P and S codas, and L_g wavetrains for regional sources are comprised of a considerable amount of forward scattered/multipathed energy (Wagner & Owens, 1993,1995a,b; Dainty & Schultz, 1995), and in part by results from numerical simulations of teleseismic wave propagation which suggest a correlation between the coda level and rate of decay and the aspect ratio of lithospheric heterogeneities (Wagner & Langston, 1992). The results presented in this report are simply an extension of the teleseismic modeling to the regional problem in an effort to determine the types of structure required to produce wavefields that exhibit the same characteristics observed in regional array data.

The basic model used in our investigation is a heterogeneous layer (*i.e.* lithosphere) over a homogeneous half-space (*i.e.* mantle). The use of this general model for both teleseismic and regional simulations is motivated by the assumption that small scale heterogeneities are generally confined to the lithosphere. The heterogeneities are parameterized using a gaussian correlation function (space domain $\leftrightarrow$ wavenumber domain)

$$\exp\left[-(x^2 + z^2)/(a_x^2 + a_z^2)\right] \quad \longleftrightarrow \quad \frac{(a_x^2 + a_z^2)}{2} \exp\left[-(k_x^2 a_x^2 + k_z^2 a_z^2)/4\right] \qquad (1)$$

where a_x, a_z are the horizontal and vertical correlation distances, respectively. The two end members of this model parameterization scheme are models with isotropic heterogeneities (ISO) and models with homogeneous plane layers. As the aspect ratio (a_x/a_z) increases, the heterogeneities are stretched in the horizontal direction. Heterogeneities with higher aspect ratios (ANISO) mimic plane layers of varying lateral extent. These types of models are intuitively appealing because they agree with geologic models where layers do not have infinite lateral extent but are truncated by faulting, pinch outs, *etc.*. Figure 1 shows examples of ISO and ANISO models; the correlation distances are $a_x=a_z=5$ km for the ISO model, and $a_x=50$ km, $a_z=5$ km for the ANISO model.

The results presented in this report are for models whose heterogeneities consist of correlated P and S velocity perturbations. The mean P and S velocities are, respectively, 5.25 and 3.03 km/s in the layer, and 7.50 and 4.33 km/s in the half-space. The standard deviation of the P and S velocity perturbations is 5% of their respective background means. The density is 2.5 kg/m^3 for both the layer and the half-space. No intrinsic attenuation is included in the model.

Numerical methods are currently the only methods available to compute waveforms in a medium whose properties vary both laterally and vertically in a random manner. Simulations were performed using a two-dimensional, fourth-order accurate, displacement, *P-SV* finite difference (FD) routine. Because our main objective was to identify models that will produce predominantly forward as opposed to back scattered codas, it was crucial that we use a numerical approach capable of modeling both the forward and back-scattered components of the wavefield. Absorbing boundary conditions (Clayton & Engquist, 1977) are used on the sides and bottom of the model, and
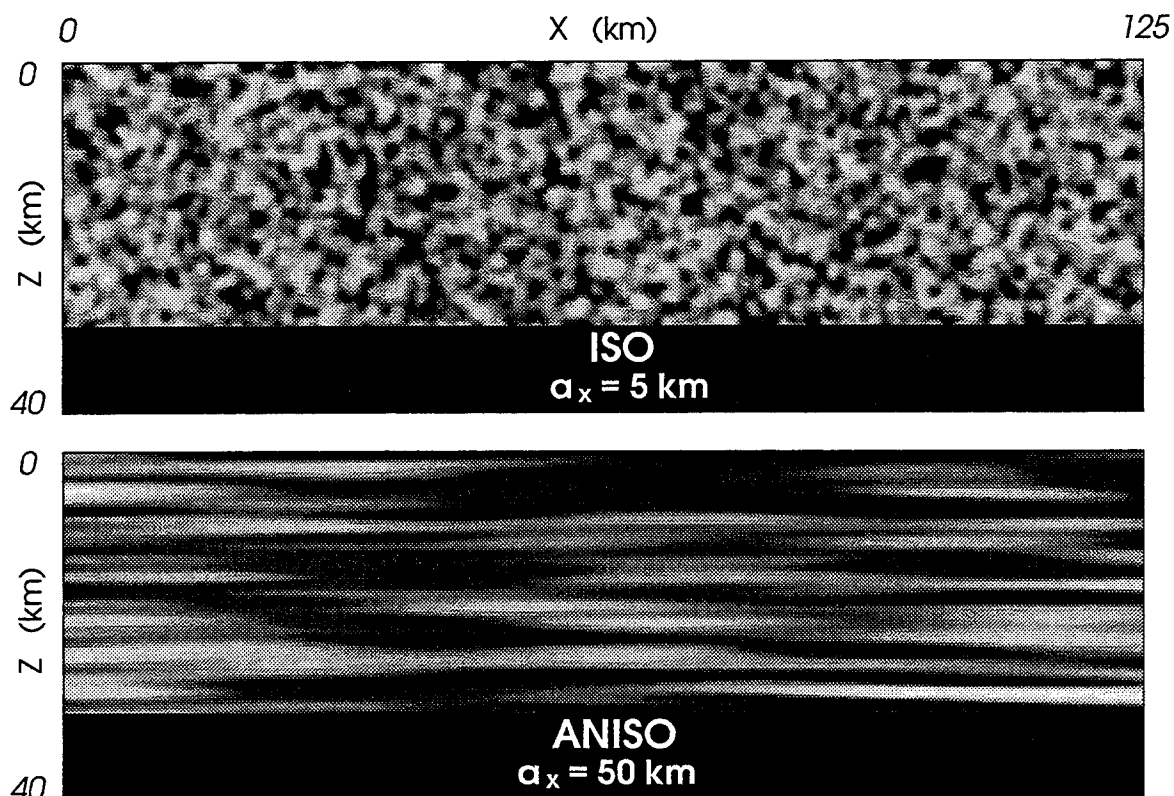
Figure 1: Examples of models with spatially isotropic (ISO) and spatially anisotropic (ANISO) heterogeneities. The perturbations are parameterized using a gaussian correlation function. The ISO model (top) has spatially isotropic heterogeneities with a correlation distance of 5 km. The ANISO model (bottom) has spatially anisotropic heterogeneities with vertical and horizontal correlation distances of 5 km and 50 km, respectively.

stress-free boundary conditions (Ilan & Loewenthal, 1976) at the surface. The source is an isotropic gaussian at a depth of 5 km.

Figures 2 and 3 show the vertical and horizontal component snap-shots for the ANISO and ISO models, respectively (note that each frame is normalized to its respective maximum; time in seconds is listed to the right). While Figures 2 and 3 do not show propagation to regional distances (only to 125 km here), it is clear that the salient wavefield features are established at this early stage. Figures 2 and 3 illustrate two important differences in the wavefields associated with these two models. First, the wavefield generated using the ANISO model is consistent with regional array observations in that it consists largely of forward scattered, coherent plane wave energy (note also the coherent plane wave nature of the energy entering the "mantle"). The wavefield generated using the ISO model is, conversely, dominated by randomly scattered energy. The few plane waves generated in the ISO model are the direct, and the P and P-to-SV converted waves reflected/refracted at the layer/half-space interface and the free surface. While we certainly would not suggest that the ISO model represents a reasonable model for lithospheric structure, it is clear that models with ISO heterogeneities inhibit the development of wavefields with characteristics consistent with observed array data. The heterogeneity aspect ratio appears to play the key role in determining the extent to which energy is forward scattered and, consequently, trapped in the crustal waveguide.
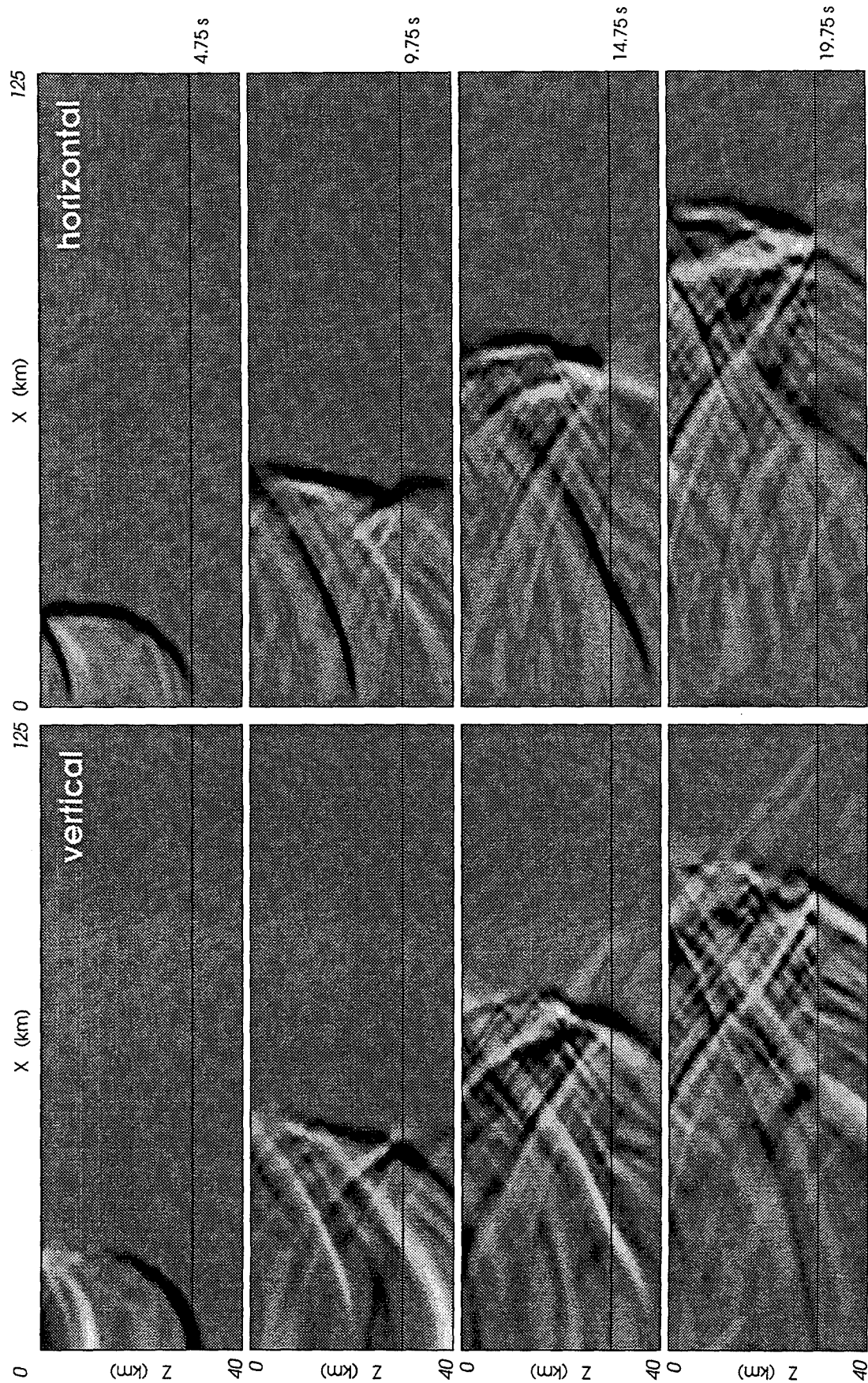
Figure 2: Vertical (left) and horizontal (right) component snap-shots for propagation through the model with spatially anisotropic heterogeneities (see Figure 1). Each frame is normalized to its respective maximum. Time, in seconds, is listed to the right. Note that the P-coda is dominated by coherent, forward scattered plane waves, a characteristic feature observed in both local and regional array data.
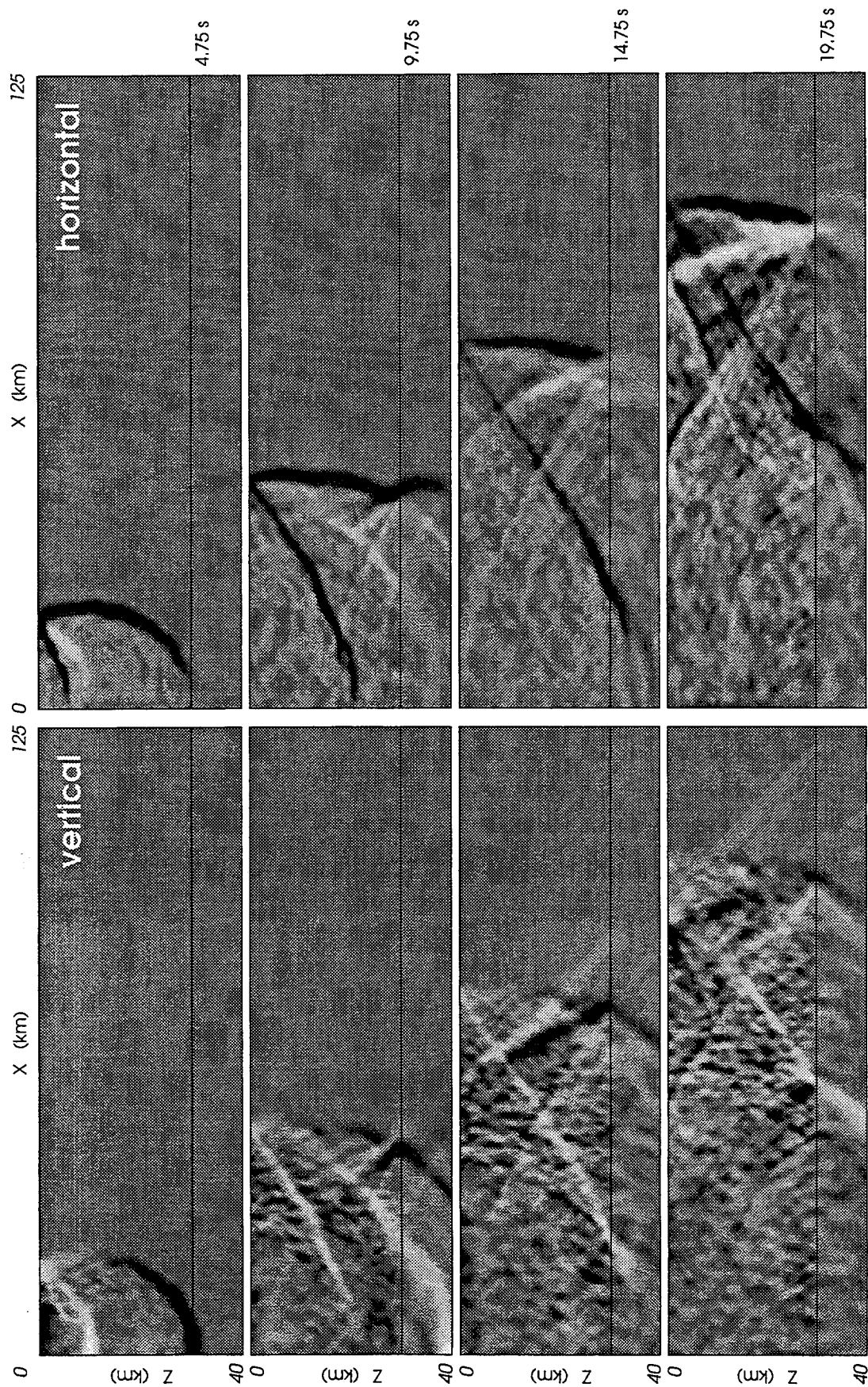
Figure 3: Vertical (left) and horizontal (right) component snap-shots for propagation through the model with spatially isotropic heterogeneities (see Figure 1). Each frame is normalized to its respective maximum. Time, in seconds, is listed to the right. Note that the P-coda is dominated by randomly scattered energy, this feature is inconsistent with array observations for both local and regional sources.

527
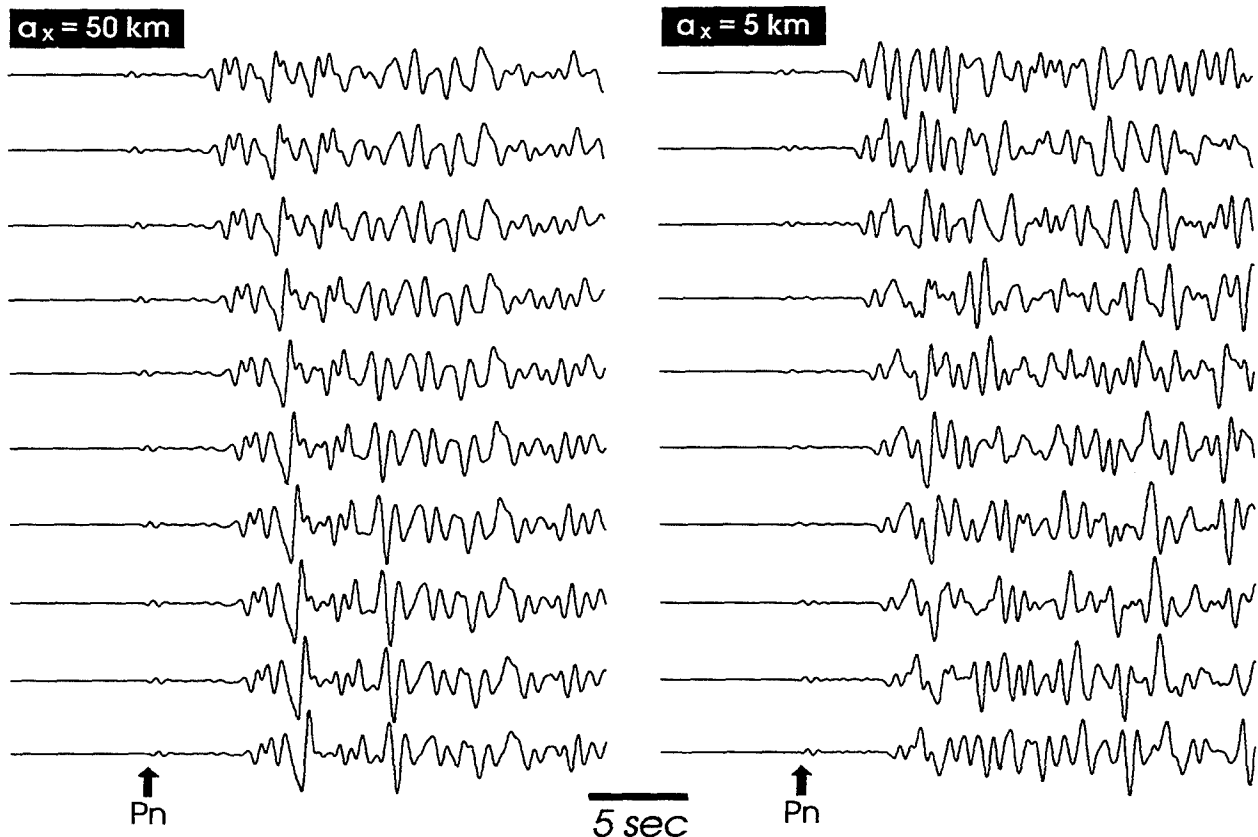
Figure 4: Vertical component (velocity) P_n, P_g and P_g-coda waveforms generated using the ANISO (left) and ISO models (right) shown in Figure 1. Sensor spacing is 1 km. Source distance increases from top (250 km) to bottom (260 km).

The second significant difference illustrated in Figures 2 and 3 is that the ANISO model facilitates the excitation of considerable source zone reverberations. This feature coupled with other structural effects, such as scattering from topographic features, could conceivably result in enhanced contributions to the regional wavefield from source zone scattering (Greenfield, 1971).

Figure 4 shows the vertical component (velocity) waveforms generated using the ANISO (left) and ISO models (right) observed at 250–260 km. Because we used a P source we limit attention to the P_n and P_g wavetrains and codas. The P_n for both models are similar and rather nondescript. P_n coda is not readily produced in either of the models, both of which have homogeneous "mantles". The implication here is that P_n coda is not the product of P_n scattering in the crust, but P_n scattering that occurs in the upper mantle. Presumably, therefore, the addition of ANISO heterogeneities to the upper-mantle would be needed to generate forward scattered P_n coda.

The P_g wavetrain and coda generated using the ANISO model exhibit several characteristics observed in regional array data. First is simply the extended coherent nature of P_g. There is no one distinct P_g arrival but several equal amplitude arrivals, some of which may be a direct result of the aforementioned source zone reverberations, that have traveled slightly different crustal paths from source to receiver (Kennett, 1989). The second similarity between the ANISO and observed array data is that subtle feature in waveforms observed at adjacent sensors exhibit a high degree of coherence, while those observed at sensors separated by distances on the order of a wavelength exhibit an unexpected reduction in correlation, and those observed at sensors separated by several

wavelengths are seemingly unrelated. The waveforms generated using the ISO model exhibit a degree of sensor-wise incoherence inconsistent with regional array observations. In fact, the P_g wavetrain generated using the ISO model exhibits almost no coherent coda. Both the extended nature and slow spatial evolution of the ANISO model's P_g wavetrain result from the interaction and interference of the numerous forward scattered plane waves generated by scattering from the spatially anisotropic heterogeneities and trapped in the crustal waveguide and, potentially, the numerous smaller waveguides bound by the spatially anisotropic heterogeneities.

• Conclusions & Future Plans

The FD modeling outlined in this report was conducted in an effort to determine the type of structures capable of producing regional wavefields with characteristics consistent with those observed in regional three-component array data. Namely, wavefields whose P and S codas, and L_g wavetrains contain significant amounts of forward scattered/multipathed energy. The use of models with spatially anisotropic heterogeneities was motivated by previous results from simulations of teleseismic wave propagation. For the teleseismic case, the heterogeneity aspect ratio appears to play an important role in determining the coda level and rate of decay by controlling the extent to which vertically propagating energy is scattered into the horizontal direction. The modeling results presented in this report suggest that for the regional case, the heterogeneity aspect ratio plays an important role in determining the extent to which energy is forward scattered and, consequently, trapped in the crustal waveguide. It is this feature, the presence of waves such as P_g and L_g comprised of energy trapped in the crustal waveguide, that differentiates the regional wavefield from local and teleseismic wavefields. Models with spatially anisotropic heterogeneities not only produce wavefields consistent with array observations, but also provide a physically and intuitively appealing way to parameterize earth structure.

The modeling results presented in this report add to the growing body of evidence illustrating the important role spatially anisotropic heterogeneities play in seismic wave propagation and scattering (cf. Wagner & Langston, 1992; Hestholm et al., 1994; Hoshiba, 1995). An important but overlooked implication inherent in parameterizing heterogeneities with spatially anisotropic correlation functions is that the dimensionless normalized wavenumber ka commonly used to categorize the scattering regime (i.e. Rayleigh, Mie, Fresnel) looses its meaning. Clearly, spatially anisotropic heterogeneities can not be treated as point scatterers. The effective scattering cross section and associated scattering radiation pattern for ANISO heterogeneities depend not only on the physical properties of the heterogeneity (Wu & Aki, 1985), but also need include the vector quantity $\mathbf{k} \cdot \mathbf{a}$ to reflect the fact that the scattering depends not simply on the scalar ratio of the "size" of the heterogeneities to the wavelength of the incident wavefield, but also on the spatial relation/orientation of the incident wavefieldfield and heterogeneities.

In future modeling, ANISO heterogeneities with varying aspect ratios, standard deviations, physical properties, etc., will be incorporated into models with various background structures such as low velocity surface layers, and surface and layer/half-space boundary topography. Our modeling has also highlighted the limitations of using a two-dimensional routine to investigate what is truly a three-dimensional phenomena. Future modeling will be three-dimensional and include heterogeneities with $a_x \approx a_y > a_z$.

References

Clayton, R. and Engquist, B., 1977. Absorbing boundary conditions for acoustic and elastic wave equations, *Bull. Seis. Soc. Am.*, **67**(6), 1529–1540.

Ilan, A. and Loewenthal, D., 1976. Instability of finite difference schemes due to boundary conditions in elastic media, *Geophys. Prosp.*, **24**, 431–453.

Dainty, A. M. and Schultz, C. A., 1995. Crustal reflections and the nature of regional P coda, *Bull. Seis. Soc. Am.*, **85**(3), 851–858.

Greenfield, R. J., 1971. Short-period P-wave generation by Rayleigh-wave scattering at Novaya Zemyla, *J. Geophys. Res.*, **76**(32), 7988–8001.

Hestholm, S. O., Husebye, E. S., and Ruud, B. O., 1994. Seismic wave propagation in complex crust-upper mantle media using 2-D finite-difference synthetics, *Geophys. J. Int.*, **118**, 643–670.

Hoshiba, M., 1995. Estimation of nonisotropic scattering in western Japan using coda wave envelopes: application of a multiple nonisotropic scattering model, *J. Gephys. Res.*, **100**(B1), 645–657.

Kennett, B. L. N., 1989. On the nature of regional seismic phases—I. phase representations for P_n, P_g, S_n, L_g, *Geophys. J. R. astr. Soc.*, **98**, 447–456.

Wagner, G. S. and Langston, C. A., 1992. A numerical investigation of scattering effects for teleseismic plane wave propagation in a heterogeneous layer over a homogeneous half-space, *Geophys. J. Int.*, **110**, 486–500.

Wagner, G. S. and Owens, T. J., 1993. Broadband bearing-time records of three-component seismic array data and their application to the study of local earthquake coda, *Geophys. Res. Letters*, **20**(17), 1823–1826.

Wagner, G. S. and Owens, T. J., 1995a. Broadband eigen-analysis for three-component seismic array data, *IEEE Trans. on Signal Processing*, **43**(7), 1738–1741.

Wagner, G. S. and Owens, T. J., 1995b. Regional wavefield analysis using three-component seismic array data, *Proceedings 17th Annual Seismic Research Symposium.* PL-TR-95-2108

Wu, R-S. and Aki, K., 1985. Scattering characteristics of elastic waves by an elastic heterogeneity, *Geophysics*, **50**(4), 582–595.

Synthetic Seismograms in Heterogeneous Media and Study of Formation and Propagation of Regional Phases

Ru-Shan Wu, Thorne Lay, Xiao-Bi Xie and Lian-Jie Huang

University of California, Santa Cruz

Abstract

The object of this project is aimed at development and application of a new 3D wave propagation and modeling method in complex heterogeneous media using one-way wave approximation to study many outstanding problems of regional wave propagation in the context of nuclear test monitoring. The great advantages of one-way propagation methods are the fast speed of computation, often by several orders of magnitudes faster than finite difference and finite element methods, and the huge saving in internal memory. The first year's effort is concentrated on developing theory and techniques for fast calculation of reflected or backscattered waves, namely methods of synthetic seismograms using the concept of one-way wave propagation and single interaction. The research effort supported by this contract has produced the following results regarding the backscattered field modeling. Wu and Huang (1995a, b) has introduced a wide-angle modeling method for acoustic waves using the De Wolf approximation and phase-screen propagator. Xie and Wu (1995) introduced a complex screen method for the calculation of backscattered elastic waves under small-angle approximation. Wu (1995) extended the wide-angle method to the case of elastic waves, and derived the relation between the wide-angle method and the screen approximation for the acoustic case. Numerical examples showed excellent results of the method. Comparison of angular dependence of reflection coefficients calculated from synthetic seismograms by this method with the theoretical curves showed good agreement between theory and synthetics. The wide-angle version of the method can even model the critical and post-critical reflections. From the comparison of synthetic seismograms made by this fast method and by finite difference calculations the validy and applicability of the method has been demonstrated. Even the screen approximation method which involves a small-angle approximation for the medium-wave interaction, can produce satisfactory synthetic seismograms for many practical cases. The wide-angle version of the method, though more computationally intensive than the screen method, will have a wide range of applications. The next year's effort will be concentrated on solving the free surface and Moho reflections and applying the method to the synthetic seismograms of regional phases.

1 Objective

The new task for monitoring a Comprehensive Test Ban Treaty and the current Nuclear Non-Proliferation Treaty presents a great challenge to the existing methods using regional phases. This is because the nature and properties of regional phases remain unclear due to the lack of theory and efficient methods for computing synthetic seismograms in complex environments. The object of this project is aimed at development and application of a new 3D wave propagation and modeling method in complex heterogeneous media using one-way wave approximation to study many outstanding problems of regional wave propagation in the context of nuclear test monitoring. The great advantages of one-way propagation methods are the fast speed of computation, often by several orders of magnitudes faster than finite difference and finite element methods, and the huge saving in internal memory. The new project will take the advantages of the recent progress in elastic one-way wave propagation theory (Wu, 1994) and continue to develop the theory and method for the purpose of regional wave synthetic seismograms. The major effort for the new project will be to solve the problems of backscattering calculation and free-surface/Moho reflections so that the one-way wave theory and method can be applied to the regional waveguide environment. Then the influence of upper and lower crustal small-scale heterogeneities to Lg propagation and attenuation, and other path effects will be examined by numerical simulations using the new method. The development of the theoretical model will be combined with analysis of the Eurasian regional phase observations to extract quantitative information from regional phases.

2 Research Accomplished

The recent successful extension and applications of one-way elastic wave propagation methods, e.g. the complex screen method (Wu, 1994; Wu and Xie, 1994), stimulated the research interest in developing similar theory and techniques for reflected or backscattered wave calculation, namely methods of synthetic seismograms using the concept of one-way wave propagation and single interaction. The research effort supported by this contract has produced the following results regarding the backscattered field modeling. Wu and Huang (1995a, b) has introduced a wide-angle modeling method for acoustic waves using the De Wolf approximation and phase-screen propagator. Xie and Wu (1995) introduced a complex screen method for the calculation of backscattered elastic waves under small-angle approximation. Wu (1995) extended the wide-angle method to the case of elastic waves, and derived the relation between the wide-angle method and the screen approximation for the acoustic case. The validity of the method and the wide-angle capability for the dual-domain implementation are demonstrated by numerical examples.

2.1 Synthetic Seismograms in Heterogeneous Media By One-Return Approximation

A new method based on multiple-forescattering single-backscattering (MFSB) approximation, i.e. the one-return approximation (the De Wolf approximation) for calculating backscattered fields was introduced (Wu and Huang, 1995a, b; Wu, 1995). When discontinuities inside a medium are not very sharp or parameter perturbations of heterogeneities are not very strong, reverberations between heterogeneities or resonance scattering may be neglected. However, accumulated effect of forward scattering usually can not be neglected. In such cases, the Born approximation is not valid but the De Wolf approximation can be applied.

The Lipmann-Schwinger equation has a formal solution of multiple scattering Born series. The widely used Born approximation is the leading term of the series. After renormalization of the multiple

scattering series, De Wolf (1971, 1985) derived a MFSB approximation given by

$$p(\mathbf{x}) = p^f(\mathbf{x}) + k^2 \int_v d^3\mathbf{x}' g^f(\mathbf{x}; \mathbf{x}') F(\mathbf{x}') p^f(\mathbf{x}') , \qquad (1)$$

where p^f and g^f are the renormalized, multiple forescattered field and Green's function, respectively, F is the perturbation function or equivalent force which is a scalar function in the case of scalar media, but involves vector operators, such as gradient and divergence operators, and tensor operators, such as the strain operators and double divergence operator, in the case of acoustic and elastic media, respectively. The renormalized p^f and g^f will be calculated using the phase-screen or complex-screen propagator.

To speed up the calculation of backscattered fields, the local Born approximation can be used within a thin-slab (cf. Fig. 1). This means that the forescattered field p^f can be kept unperturbed and g^f can be replaced by a constant medium Green's function within the slab. Assume z' and z_1 as the slab entrance (top) and exit (bottom) respectively (cf. Fig. 1), and Fourier-transform above equation with respect to $\mathbf{x}_T$, we get a dual-domain expression for the calculation of scattered fields. In the case of scalar media, the dual-domain expression is

$$P(\mathbf{K}_T, z^*) = \frac{i}{2\gamma} k^2 \int_{z'}^{z_1} dz e^{i\gamma|z^* - z|} \iint d^2\mathbf{x}_T e^{-i\mathbf{K}_T \cdot \mathbf{x}_T} [F(\mathbf{x}_T, z) p^f(\mathbf{x}_T, z)] . \qquad (2)$$

where z^* is the receiver depth, x_T is the horizontal coordinates, K_T is the horizontal spatial frequency, and $\gamma = \sqrt{k^2 - K_T^2}$. Note that the two dimensional inner integral is a 2-D Fourier transform. Therefore, the dual-domain technique can be used to implement the equation.

For the case of acoustic media, the dual-domain formulation is

$$P(\mathbf{K}_T, z^*) = \frac{i}{2\gamma} k^2 \int_{z'}^{z_1} dz e^{i\gamma|z^* - z|} \left\{ \int d^2\mathbf{x}_T e^{-i\mathbf{K}_T \cdot \mathbf{x}_T} [\varepsilon_\kappa(\mathbf{x}_T, z) p^f(\mathbf{x}_T, z)] \right.$$
$$\left. + \frac{i}{k} \hat{k} \cdot \int d^2\mathbf{x}_T e^{-i\mathbf{K}_T \cdot \mathbf{x}_T} [\varepsilon_\rho(\mathbf{x}_T, z) \nabla p^f(\mathbf{x}_T, z)] \right\} , \qquad (3)$$

where $\varepsilon_\kappa(\mathbf{x}) = \kappa_0/\kappa(\mathbf{x}) - 1$, $\varepsilon_\rho(\mathbf{x}) = \rho_0/\rho(\mathbf{x}) - 1$, and $\hat{k} = \frac{1}{k}(\mathbf{K}_T, k_z)$, with $k_z = \pm\gamma$ for forescattering and backscattering, respectively. When the receiving level is at the bottom of the thin-slab (forescattering), $z^* = z_1$; while $z^* = z'$ is for the backscattered field at the top of the thin-slab. The total transmitted filed at the slab bottom can be calculated as the sum of the forescattered field and the primary field.

The dual-domain expressions for the case of elastic media is more complicated and involved tensor operations. Readers are referred to Wu (1995).

2.2 The screen approximation

For some special applications, the synthetics only involve small-angle backscattering. In this case the screen approximation can be applied to accelerate the computation.

Under small-angle scattering approximation, we can compress the thin-slab into an equivalent screen and therefore change the 3-D spectrum into a 2-D spectrum. Dual-domain implementation of the screen approximation will make the modeling of backscattering very efficient. In the following the case of acoustic media will be shown as an example. For the screen approximation in the case of elastic media, readers are referred to Xie and Wu (1995) and the forthcoming publications.

With the screen approximation, scattered field can be calculated as

$$P(\mathbf{K}_T, z^*) \approx i\frac{k^2}{2\gamma} e^{ik_z(z^* - z')} \iint d\mathbf{x}_T e^{-i\mathbf{K}_T \cdot \mathbf{x}_T} S(\mathbf{x}_T) p^0(\mathbf{x}_T) \qquad (4)$$

where

$$S(\mathbf{x}_T) = S_V(\mathbf{x}_T) = \int_0^{\Delta z} dz[\varepsilon_\kappa(\mathbf{x}_T, z) - \varepsilon_\rho(\mathbf{x}_T, z)] \quad for\ forescattering \tag{5}$$

is the velocity screen and

$$S(\mathbf{x}_T) = S_I(\mathbf{x}_T) = \int_0^{\Delta z} dz e^{i2kz}[\varepsilon_\kappa(\mathbf{x}_T, z) + \varepsilon_\rho(\mathbf{x}_T, z)] \quad for\ backscattering \tag{6}$$

is the impedance screen.

2.3 Numerical examples

First we compare the calculated reflection coefficients by the one-return method with the theoretical ones for plan wave incidences. The model is shown in Fig. 2, where a plane interface between two layers is located at the depth of 500m. The model is defined on a 2048×300 rectangular grid. The grid spacing in the horizontal direction is 8m and that in the vertical direction is 5m. A pressure point source is applied at the center of the upper border of the model. The velocity and density of the upper layer are 2000m/s and 1.0 g/cm^3, respectively. The frequency range used in the calculation is from 14.6Hz to 19.5Hz with 11 frequency components. We calculate the reflection coefficient for each frequency component and take an average over the 11 frequencies.

Fig. 3a shows the results for 10% of velocity and density perturbations in the lower layer and Fig. 3b is for 20%. In both figures, the dashed lines are theoretically predicted reflection coefficients of plane wave incidence and the solid curves are calculated results. We can see the good agreement between the theoretical ones and the synthetics when the incidence angles are smaller than the critical angles. When the incidence angles are near and beyond the critical angles, the numerical results deviate from the theoretical curves. This may be due to several reasons such as the curved wavefronts of waves from the point source, the wavenumber filtering in the process of forward propagation which reduces the amplitudes of large-angle scattered waves, and the effect of finite layer thickness. When the velocity and density perturbations of the lower layer are -10% and -20%, the corresponding results are given in Fig. 4a and 4b, respectively. We see from these figures that the synthetic reflection coefficients agree well with the theoretical results when the incidence angles are smaller than approximately 70°. For larger incidence angles, the amplitudes of reflection coefficients decrease because of the wavenumber filtering.

The next two examples is for the test of screen approximation for synthetic seismograms. Fig. 5 shows the model space for scalar wave modeling. A high velocity cylinder with 10% perturbation is situated at the middle of the model space. A plane wave is incident vertically down to the model space. The source time function is a Gaussian first derivative with the dominant frequency of $30Hz$. The screen interval is 10 m inside the cylinder; while the horizontal grid spacing is 3.125m. Fig. 6a shows the comparison of synthetic seismograms calculated by the screen approximation and by the finite difference method. In the figure only the transversal components are shown. We see good agreement between the results of finite difference calculations and this method.

The model for the elastic wave scattering is similar to that in Fig. 5. The parameters for the background media are $\alpha = 3500m/s$, $\beta = 2050m/s$ and $\rho = 2200kg/m^3$. The inclusions have a 5% perturbation for both P- and S-wave velocities. The diameter of the elastic cylinder is 300m. A plane P-wave is incident on the cylinder. Fig. 6b gives the synthetic seismograms from a receiver array 700m away from the center of the cylinder. The synthetics marked with "SCREEN" is from the complex-screen method while with "FD", from the finite-difference method. The upper panel is for $x-$component (transverse component) and the lower panel is for $z-$component (longitudinal component). Shown in the figure are two P-arrivals and two S-arrivals which are reflections from both the upper and lower

boundaries of the cylinder. The results show general agreements in both amplitude and arrival time. Since the receiver array is only 550m from the border of the cylinder, the receiving profile spans a rather wide range of scattering angle. That means that even the small angle approximation can give satisfactory results in many cases.

3   Conclusions and Recommendations

We have made significant progress in modeling backscattering. Synthetic seismograms showed good agreement with finite difference calculations in our numerical examples. Next year's effort will be concentrated on solving the problems of free surface and Moho reflections and applying the method to simulate regional wave propagations

References

[1] De Wolf, D.A., 1971. Electromagnetic reflection from an extended turbulent medium: cumulative forward-scatter single-backscatter approximation, *IEEE trans. Ant. and Propag.*, **AP-19**, 254-262.

[2] De Wolf, D.A., 1985. Renormalization of EM fields in application to large-angle scattering from randomly continuous media and sparse particle distributions, *IEEE trans. Ant. and Propag.*, **AP-33**, 608-615.

[3] Wu, R.S., 1994, Wide-angle elastic wave one-way propagation in heterogeneous media and an elastic wave complex-screen method, *J. Geophys. Res., 99*, 751-766.

[4] Wu, R.S., 1995, Synthetic seismograms in heterogeneous media by one-return approximation, submitted to Phys. Earth & Planet. Inter..

[5] Wu, R.S. and Huang, L.J., 1992. Scattered field calculation in heterogeneous media using phase-screen propagator. Expanded Abstracts of the Technical Program, SEG 62th Annual Meeting: 1289-1292.

[6] Wu, R.S. and Huang, L.J., 1995. Reflected wave modeling in heterogeneous acoustic media using the De Wolf approximation. to be appeared in "Mathematical methods in geophysical imaging III".

[7] Wu, R.S., Huang, L.J. and X.B. Xie, 1995. Backscattered wave calculation using the De Wolf approximation and a phase-screen propagator. submitted to Expanded Abstracts of the Technical Program, SEG 65th Annual Meeting.

[8] Wu, R.S. and X.B. Xie, 1994. Multi-screen backpropagator for fast 3D elastic prestack migration. Mathematical Methods in Geophysical Imaging II, SPIE vol. 2301: 181-193.

[9] Xie, X.B. and Wu, R.S., 1995. A Complex-Screen Method for Modeling Elastic Wave Reflections. submitted to Expanded Abstracts of the Technical Program, SEG 65th Annual Meeting.

Figure 1: Geometry of the thin-slab formulation.
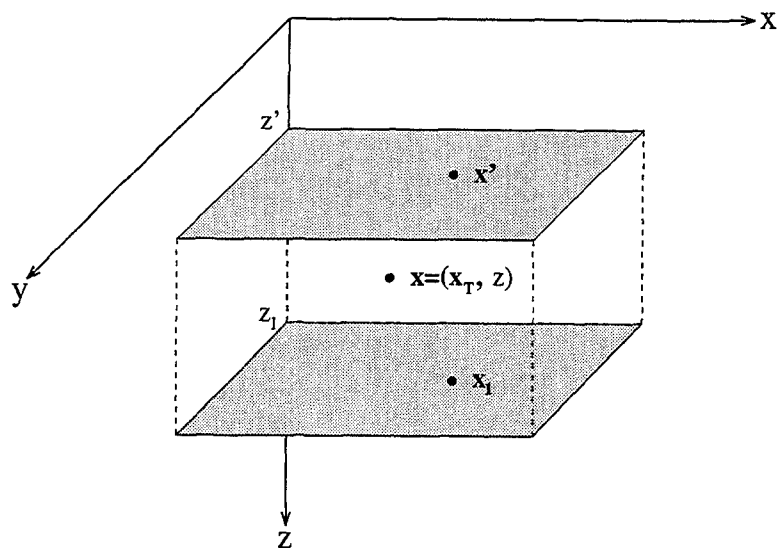
Figure 2: The layered model used in the numerical simulation.
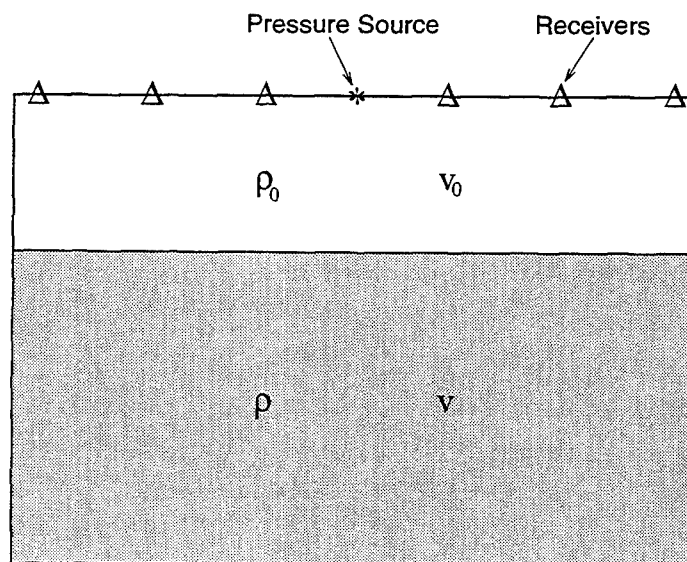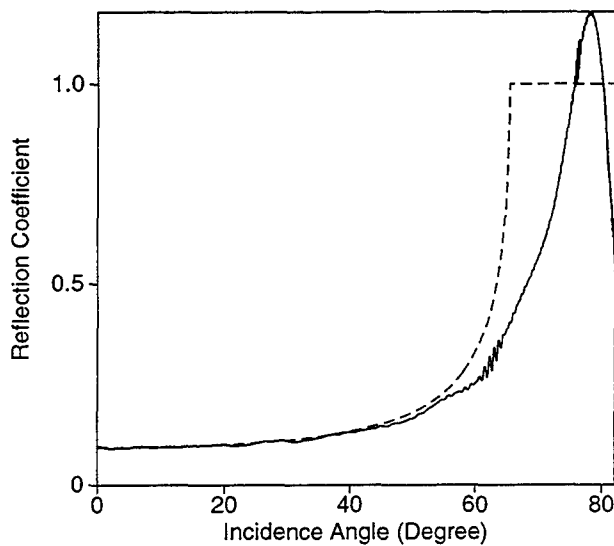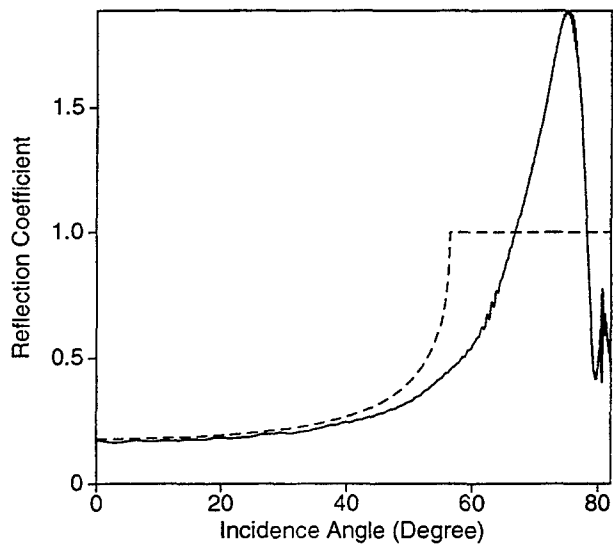
Figure 3: Comparison between theoretical and simulated reflection coefficients for a high-velocity 'half-space' shown in Figure 2 when the velocity and density perturbations of the lower 'half-space' are (a) 10% and (b) 20%. Dashed lines represent the theoretical reflection coefficients and the solid curves, the simulated results.
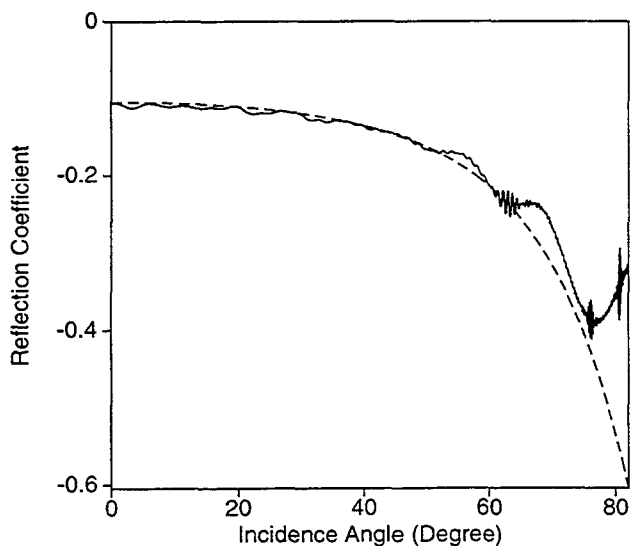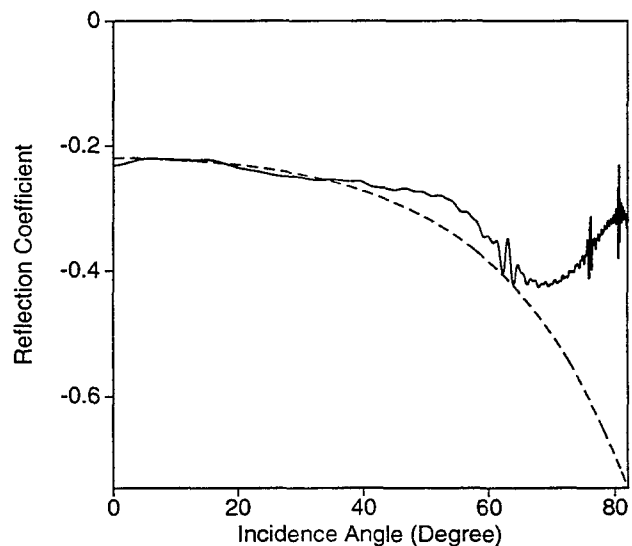
Figure 4: Comparison between theoretical and simulated reflection coefficients for a low-velocity 'half-space' shown in Figure 2 when the velocity and density perturbations of the lower 'half-space' are (a) -10% and (b) -20%. Dashed lines represent the theoretical reflection coefficients and the solid curves, the simulated results.
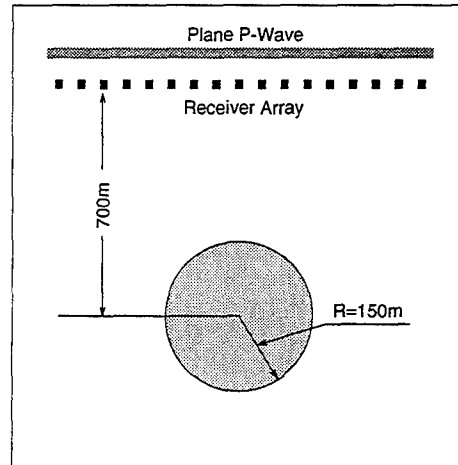
Figure 5: A model used to compare the screen approximation method with a FD method.

(a)

(b)
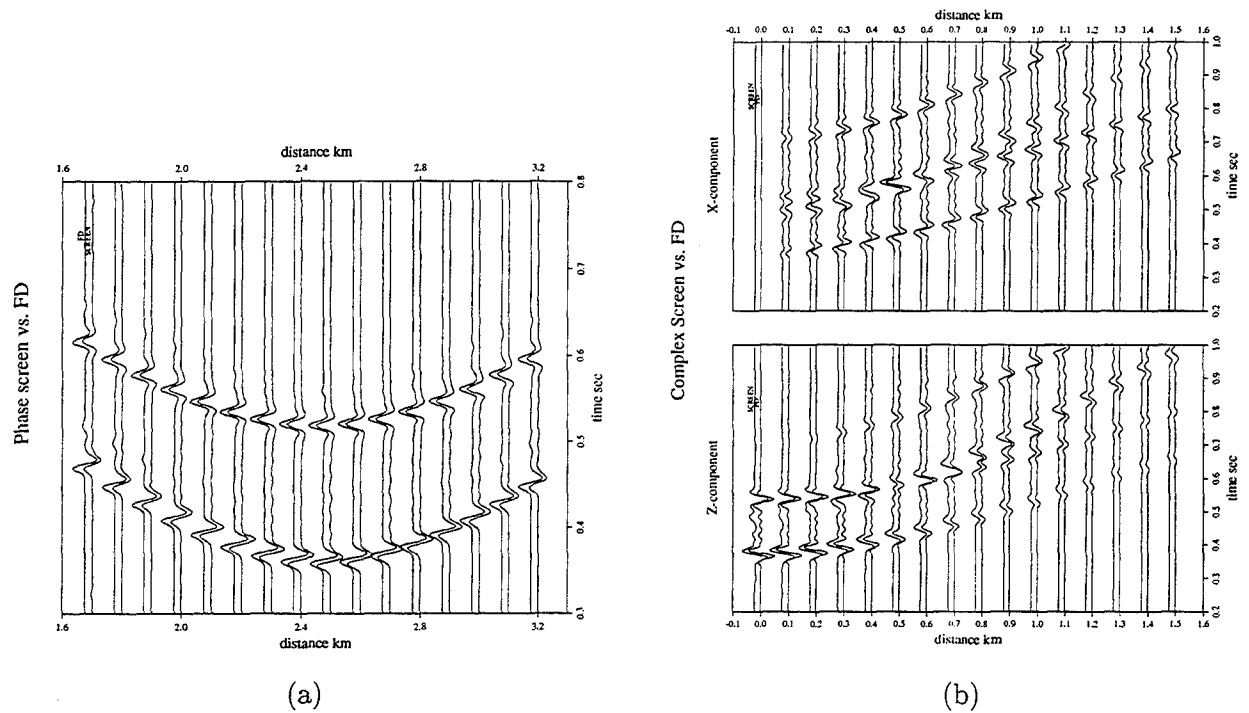
Figure 6: Comparison between the results of the screen method and the FD method for scalar waves (a) and elastic waves (b).

Physical Mechanisms of Quarry Blast Sources

T.G. Barker, K.L. McLaughlin and J.L. Stevens

S-CUBED, a Division of Maxwell Laboratories
Contract F19628-95-C-0112 (DoE)

ABSTRACT

Quarry mining practices vary considerably within the United States and worldwide, the variations reflecting the materials that are to mined, the means for removing and processing the materials, operator preferences, safety considerations and constraints imposed by nearby population and structures. Models of quarry blasts that can be used to develop efficient and robust methods for discriminating quarry blasts from other source must reflect the varied practices. Development of models for quarry blasts was the subject of work done at S-CUBED under a previous contract to ARPA. Under a new contract to DoE (which has not been initiated), we will validate and extend the models using using near-source and regional data. Our objective will be to use the models to determine the sensitivity of proposed regional discriminants to varied mining practices.

OBJECTIVE

The objective of the work to be undertaken is to develop an understanding of the physical processes of quarry blast sources as they affect discriminants using regional signals. We will build on previous modeling studies at S-CUBED, incorporating realistic and varied practices from mines in regions of CTBT interest. These models will be used to determine the sensitivity of discriminants to features of quarry blasts. This modeling will include 1D, 2D and 3D calculations.

RESULTS of MODELING RESEARCH

The objective of the previous project was to provide a theoretical basis for the discrimination of quarry blasts from earthquakes and nuclear tests, and to evaluate an evasion scenario of simultaneously exploding a nuclear test beneath a quarry. The quarry blast source models incorporated the effects of ripple fired sources, the finite size and duration of the source, the horizontal and vertical movement of spalled material, the relative excitation of the explosive charges and the spall process, and the bench topography.

From the calculations, we made the following conclusions. Conclusions 1 through 7 are the result of the relative excitation of the explosive and spall components of the source and the relatively long duration of the quarry blast. Conclusions 8 through 11 are the result of the quarry geometry.

(1) The quarry blast source is a band-limited signal compared to the overburied bomb.

(2) Pg spectral values rise in the band from 0.5 to 3.5 hz for a bomb, but decay in that band for the quarry blast.

(3) Spall strongly affects the quarry blast source. Peak Pg and Lg amplitudes from spall and from the explosive charges are comparable.

(4) Quarry blast spectral scallops are primarily due to the finite size of the source and are insensitive to the details of ripple firing.

(5) In simultaneous explosion and quarry blast, the explosion will dominate if the explosion yield (tamped or equivalent decoupled) exceeds approximately 10 percent of the quarry blast yield.

(6) Seismic amplitudes are insensitive to the direction of spall as long as there is minimal elevation change.

(7) An elevation change (the spalled face falling to a lower level) can significantly increase seismic amplitudes from quarry blasts. An elevation change of 10 meters can increase the signal by as much as a factor of 5 in the 2-5 Hz band.

(8) Two-dimensional simulations show that seismic signals from point explosion (dilatational) sources located behind the quarry face can be reduced substantially in amplitude, while seismic waves from sources on the quarry floor may be amplified. Seismic signals from point forces are affected very little by proximity to the quarry face. The source amplitude variations occur for sources within about one bench height of the quarry face.

(9) An extended source in the standard configuration averages these variations leading to a source that is reduced slightly in amplitude relative to a source in a half space.

(10) Results (8) and (9) are nearly independent of the takeoff angle of the seismic signal.

(11) Three-dimensional simulations show that the quarry creates a shadow for signals exiting the the quarry on the side opposite the bench.

RECOMMENDATIONS AND FUTURE PLANS

The primary focus of future work will be to test the models described above against observations, incorporate world wide blasting practices and evaluate identification procedures for quarry blast sources.

Seismic Characteristics and Mechanisms of Rockbursts

T. J. Bennett, M. E. Marshall, K. L McLaughlin, B. W. Barker and J. R. Murphy
S-CUBED
11800 Sunrise Valley Dr., Suite 1212
Reston, Virginia 22091

Abstract

Rockbursts and related mining-induced seismicity present several interesting problems for seismic monitoring of potential underground nuclear explosion tests. Such events occur in mining areas throughout the world and may be quite frequent at levels currently of interest for CTBT. The shallow focal depths of rockbursts prevent their discrimination from nuclear tests on the basis of depth identification. Many rockbursts also appear to be inefficient in excitation of long-period surface waves which negates the effectiveness of the traditional M_S-vs-m_b discriminant. This research project is aimed at finding alternative ways to identify rockbursts or related mine tremors. One additional aspect of interest is that mine tremors may be deliberately triggered, which could provide an evasion opportunity if timing of such events can be accurately predicted. Our investigations have focussed primarily on regional seismic signal characteristics and source mechanisms which may distinguish mine tremors from other source types.

Over the past year or two, there have been several rockbursts in widely different tectonic environments. We have taken a close look at some of these events, including the February 3, 1995 (M = 5.2) mine collapse in southwestern Wyoming, the January 5, 1995 (M = 4.4) rockburst in the central Ural mountains, the October 30, 1994 (M = 5.6) mine tremor in South Africa, the March 11, 1995 (M = 4.0) mine bump in eastern Kentucky, and the March 12, 1994 (M = 3.6) mine collapse in northern New York. A consistent feature of the regional signals from all of these events appears to be relatively large S/P or L_g/P ratios. This behavior is similar to that seen in many earthquakes. The regional signals for rockbursts also often appear more complex than those from other source types. For the Wyoming event ground truth from the mine indicates collapse over a large area. Such collapses often have a strong implosional component distinct from the double-couple mechanisms seen in earthquakes.

Key Words: Seismic, Discrimination, Mechanism, Rockbursts, Earthquakes, Explosions, Regional, South Africa, Europe, North America, Evasion.

Objective

Rockbursts and related mine tremors present an unique challenge for seismic discrimination. Unlike earthquakes, which often occur at focal depths well below those normally associated with underground nuclear explosion tests, rockbursts are located in approximately the same depth range as nuclear tests; and, therefore, standard discriminants based on focal depth are not useful. Observations from several rockbursts suggest relatively weak long-period surface waves which could significantly reduce the effectiveness of the M_S-vs-m_b discriminant often used to distinguish between earthquakes and explosions. Therefore, the frequent occurrence of rockbursts and related events in mining regions throughout the world poses a potential problem for seismic monitoring at the levels currently considered of interest for the CTBT. Our principal objective is to identify and test regional discriminants which can help facilitate the identification of these numerous rockbursts. For this purpose we are pursuing analyses of empirical data from rockbursts in a variety of different mining, tectonic, and propagation environments. We are also investigating theoretical techniques for modeling several of the varied rockburst mechanisms and their associated regional seismic signals in an effort to better characterize those types of rockbursts which are likely to be problematic for seismic discrimination. Finally, there is evidence in mining case histories that activation of rockbursts might be deliberately triggered, thereby providing an opportunity to conceal a clandestine nuclear test if the timing and size can be adequately predicted. We are continuing to seek historical evidence supporting this predictive capability, and we also plan to use the results of theoretical model studies to further assess mining conditions which might be required to effect such evasion scenarios.

Research Accomplished

Interest in rockbursts or related mine tremors has been increasing over the past few years. This is only partially due to the recognition of the potential problem which they pose for seismic discrimination. The increased prominence for such events is due mainly to the occurrence within the past year or two of several large, destructive mine tremors which have drawn public attention because of the damage and, in some cases, fatalities which were caused by these events. The focus of our initial empirical investigations under this research program has been the characteristics of the seismic signals generated by several of these recent rockbursts. Some of these events occurred in tectonic regions different from those for which we had previously investigated the characteristics of regional seismic signals from rockbursts. Among the mining-induced events investigated for this study are the February 3, 1995 (M = 5.2) mine collapse in southwestern Wyoming, the January 5, 1995 (M = 4.4) rockburst in the central Ural mountains, the October 30, 1994 (M = 5.6) mine tremor in South Africa, the March 11, 1995 (M = 4.0) mine bump in eastern Kentucky, and the March 12, 1994 (M = 3.6) mine collapse in northern New York. For each of these events we have been attempting to compile a database of regional seismograms and performing a variety of time-domain amplitude comparisons and spectral measures of the regional phase signals. Where the data permit we have compared and contrasted the characteristics of the regional signals from these mine tremors with those from similar and alternate source types including events from the same and different tectonic regions.

The February 3, 1995 mine collapse in southwestern Wyoming is particularly interesting because it is one of the largest rockbursts historically to have occurred in

North America. The event produced extensive damage, numerous injuries, and resulted in a fatality. The epicenter of the event was located by the PDE at 41.5 N 109.8 W; and, assuming the source to be at the approximate depth of the mine, the focal depth is at about 0.5 km. The Wyoming mine collapse shows many similarities to the 1989 Völkerhausen, Germany rockburst which we analyzed in detail in a previously published report (Bennett et al., 1994) and which we have described at prior PL review meetings. In particular, both events produced dilatational P-wave first motions at nearly all regional and far-regional stations at all azimuths, which is indicative of a strong implosional component. Slumping above the Wyoming mine associated with the collapse reached a maximum of 0.9 m and averaged 0.6 m over a rectangular area of 1 km by 2 km. This is quite similar to the slumping seen above the German mine which averaged 0.9 - 1 m over an area extending 2 - 3 km laterally over the mine. The cause and mechanism for this event are currently being carefully scrutinized by the U.S. Bureau of Mines, and Pechmann et al. (1995) have already produced a scientific report describing background information on seismological parameters and seismic mechanism for the event. It appears from these initial studies that this event is likely to become one of the most carefully investigated mining-induced tremors and should ultimately have a very precisely defined source mechanism for use in improving understanding of the coupling of source energy into the radiated seismic field. The radiated seismic field in this case includes observations of signals at numerous regional and far-regional stations throughout North America. We have collected seismic waveform data for most of these stations from the Wyoming mine collapse. Our analysis here focusses on the signals recorded at the array station at Lajitas, Texas (R ≈ 1470 km; cf. Figure 1). For comparison purposes we have selected several additional events of different source types which are located at comparable epicentral distances from the Lajitas station. These include an earthquake with magnitude 4.1 m_b in western Colorado (R ≈ 1300 km), the NTS nuclear test JUNCTION (R ≈ 1470 km) with magnitude 5.5 m_b, and the Little Skull Mountain earthquake of 06/29/92 in the southwestern part of NTS (R ≈ 1435 km) with magnitude 5.6 m_b. The regional waveforms from each of these latter events were provided by SMU. In addition, we have analyzed the regional signals recorded by the Pinedale, Wyoming array station from the earthquake of 04/14/95 in southwest Texas (R ≈ 1500 km) which provides a nearly reciprocal propagation path to the Wyoming mine collapse recorded at Lajitas.

We performed narrow bandpass filter analyses on the vertical component waveforms for each of the events. Figure 2 shows the results of the filter analysis for the Wyoming mine collapse. In all filter passbands the far-regional P phase appears very emergent. Ignoring apparent noise contamination at later times in the high-frequency bands (3-6 Hz and above) and in the vicinity of the P_g window in the 2-4 Hz band, L_g/P ratios appear to be generally well above one in all frequency bands for the mine collapse. There is also an indication of a long-period Rayleigh wave on the low-frequency (0.05-0.1 Hz passband) trace, but the amplitude is very low and near the level of the low-frequency background noise. The amplitude of the Rayleigh wave in this low-frequency band is only about one-twentieth that of the P wave in the 0.1-3 Hz passbands. In comparison, similar bandpass filter analyses for the northern Colorado earthquake and the reciprocal Texas earthquake showed slightly more impulsive regional P. The L_g/P ratios for the Texas earthquake were well above one in all frequency bands, while L_g/P ratios for the northern Colorado earthquake were well above one at lower frequencies and near one in higher frequency bands. Long-period
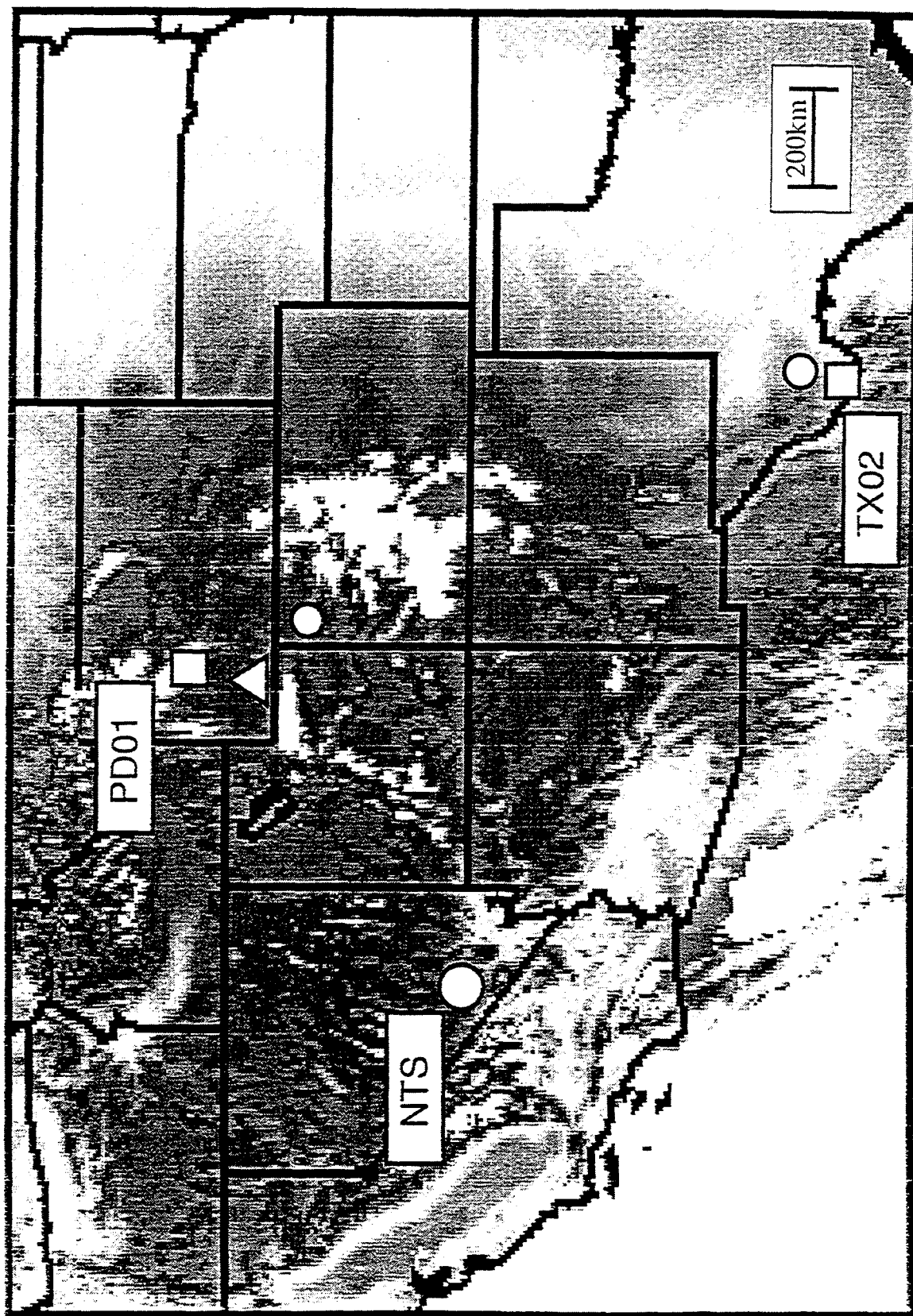
Figure 1. Locations of southwestern Wyoming rockburst of February 3, 1995 (△), earthquakes used in comparisons (◯) and regional seismic stations (□).
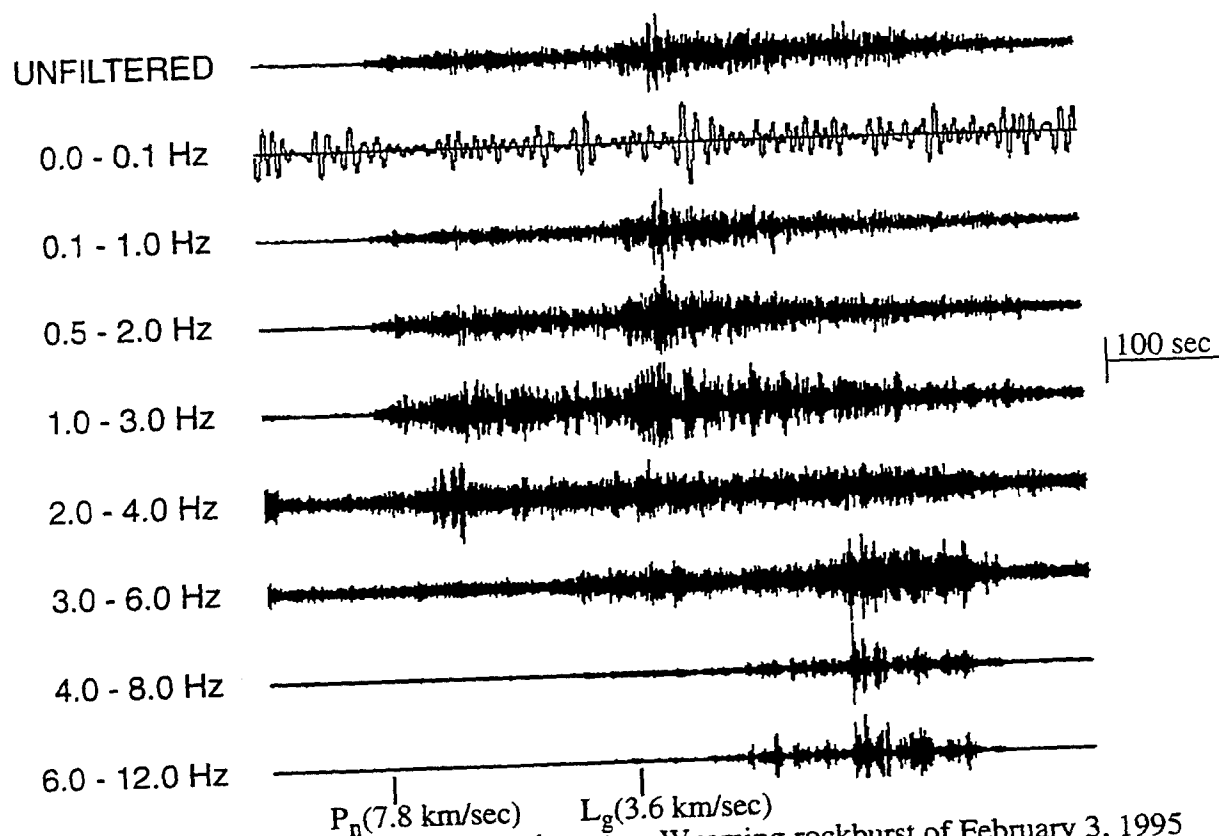
Figure 2. Bandpass filter analysis of southwestern Wyoming rockburst of February 3, 1995 recorded at Texas array (R = 1470 km). Note emergent P and large L_g/P ratio.
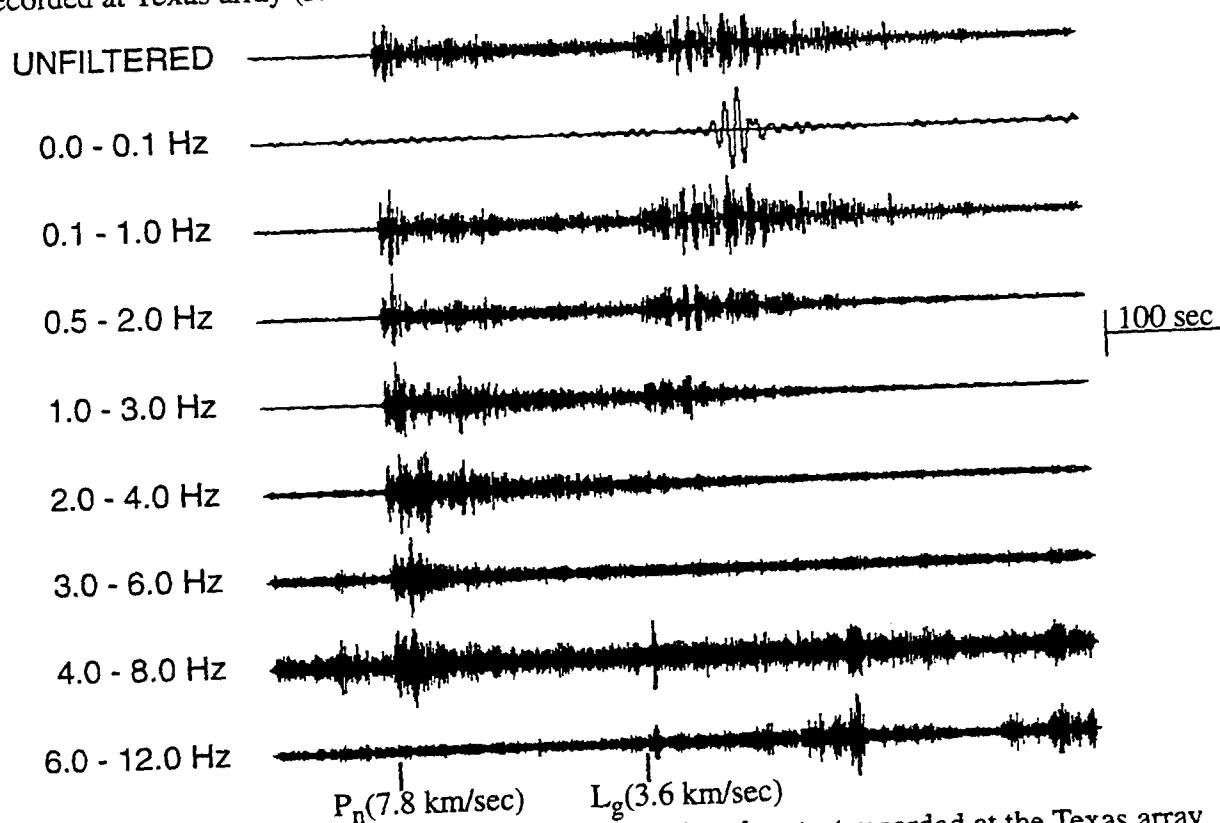
Figure 3. Bandpass filter analysis of the JUNCTION nuclear test recorded at the Texas array (R = 1470 km). Note sharp onset of P.

546

Rayleigh wave signals in the low-frequency passband were relatively large for the southern Texas earthquake but at or below the noise level for the Colorado earthquake. Perhaps the most interesting comparison from the standpoint of regional discrimination is to the band-pass filter results from the JUNCTION nuclear test. Figure 3 shows that analysis. The regional P phase is most prominent and has a clear onset at nearly all the high-frequency passbands from 0.1 to 6 Hz. The L_g/P ratio is near one at low frequencies (0.1-1.0 Hz) but falls off to well below one at high frequencies. It is also interesting that the passband 0.05-0.1 Hz shows a fairly strong long-period Rayleigh wave for the nuclear explosion about one-fortieth the size of the P in the 0.1-3 Hz passbands. The filter analysis of the Little Skull Mountain earthquake in southern Nevada revealed an even more prominent long-period Rayleigh signal with an amplitude in the 0.05-0.1 Hz band about two-thirds that of the regional P in the 0.1-3 Hz bands. These observations appear to be consistent with the report by Pechmann et al. (1995) that the surface-wave magnitude and moment magnitude for the Wyoming mine collapse were at least half a magnitude unit lower than m_b and M_L, which make these differences more like those typically seen for nuclear explosions than for earthquakes. The relatively large L_g/P ratios over a range in frequencies is also consistent with the behavior which we have seen for rockbursts in several other tectonic regions (cf. Bennett et al., 1994).

The South African mine tremor of 10/30/94 occurred in the Orange Free State mining district and was well recorded by the broad-band digital station at Boshof, South Africa (R ≈ 155 km). In spite of the large magnitude of the event (viz. 5.6 m_b) and the proximity of the station, the regional signals are well recorded and on scale. The recorded waveforms provide an excellent opportunity to study the close-range behavior of the regional phase signals from South African tremors. We have also retrieved data for several mine tremors from other South African mining districts in the vicinity of Johannesburg at somewhat larger regional distances from the Boshof station which could be useful for investigating source variability and propagation effects. Figure 4 shows a bandpass filter analysis of the vertical-component record for the 10/30/94 mine tremor. The records show a strong R_g phase which is most prominent in the 0.5-2.0 Hz passband and clearly indicates the shallow focus of the source. S/P ratios are greater than one in each of the passbands. Finally, there is an indication on the trace corresponding to the 0.05-0.1 Hz passband of a fairly strong long-period surface wave. The amplitude of this surface wave is only about one-tenth the amplitude of the regional P signal in the 0.1-3 Hz passbands; however, it is difficult to draw implications from this observation since we have not compensated for the instrument response and we do not have available direct comparisons with other source types. Nevertheless, it should be noted that we have previously observed that South African mine tremors often produce M_S magnitudes at teleseismic stations which are up to one magnitude unit lower than the corresponding m_b (cf. Bennett et al., 1994). Similar long-period surface wave measurements at Boshof and other near-regional stations could provide a valuable link to understanding this surface-wave anomaly for rockburst sources.

With regard to the seismic source mechanism of rockbursts, six distinct models for mining-induced events were described by Hasegawa et al. (1989). These models are schematically illustrated in Figure 5. The various source models produce different seismic radiation, and we would expect this to be represented in differences in the regional signals which may be observed. Some rockburst mechanisms may simply correspond to the individual models shown in Figure 5, but others may be more
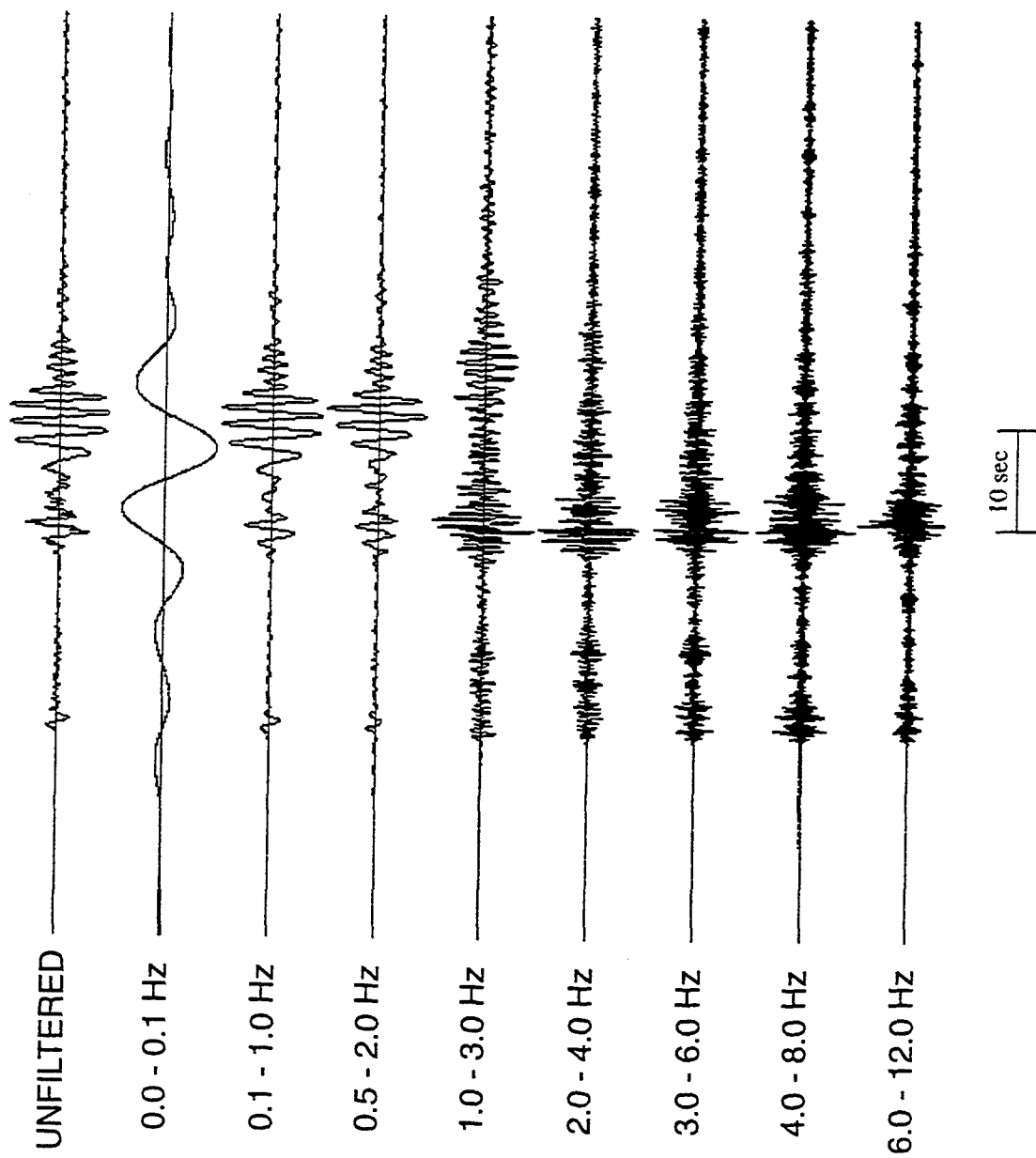
Figure 4. Bandpass filter analysis of large South African rockburst of October 30, 1994 recorded at station BOSA (R = 155 km). Note long-period surface wave, strong R_g and large L_g/P ratio.
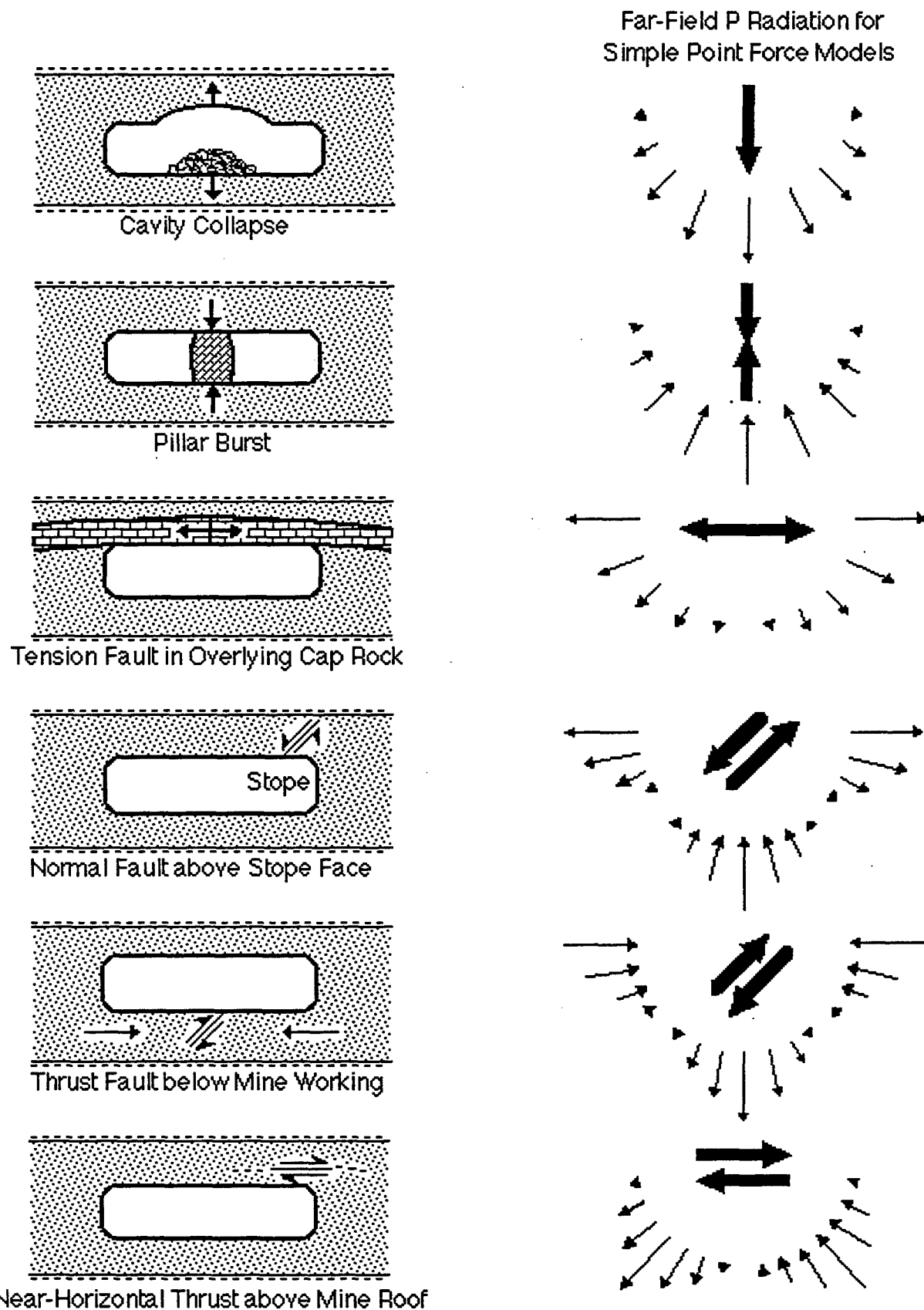
Figure 5. Simplified models of six rockburst mechanisms and corresponding P-wave radiation patterns (adapted from Hasegawa et al., 1989).

549

complex and represent combined effects of more than one model. In South Africa many large rockbursts are associated with shear failure on faults or zones of weakness near the excavation. These events often have double-couple mechanisms similar to those found in earthquakes and may draw some of their energy from the ambient regional tectonic stress field. Because South African rockbursts have been large, frequent, catastrophic, and studied for many years, that experience tends to dominate global understanding of rockburst behavior. However, the occurrence of some of the larger events in recent years in other tectonic regions (as described above) has suggested that some of the other models may also be significant and may sometimes produce more complex, non-earthquake mechanisms. Such anomalous mechanisms could present problems for seismic discrimination.

Some of the clearest examples of non-double-couple mechanisms appear to be mine collapse events. Simple calculations suggest that the gravitational potential energy released by dropping of the rock mass above the mine is adequate to account for the seismic energy in the 1989 Völkershausen, Germany event (cf. Bennett et al., 1994) and in the 1995 Wyoming event (cf. Pechmann, 1995). In the latter study the collapse was modeled as a horizontally oriented tension crack which closes by vertical motion. It was found that such a model generates dilatational first motions at all regional stations and fits the observed regional waveforms better than pure implosional or double-couple models. We believe that such a model can also explain the explosion-like M_S-m_b differences seen in many rockbursts of this type. Rockbursts which can be represented as closure of tension cracks would be expected to have low M_S because the Rayleigh waves for the shallow sources draw their principal energy from the M_{xx} and M_{yy} components of the moment tensor. The M_S-vs-m_b excitation will also depend to some extent on the rate of closure of the crack. If the collapse occurs more rapidly, the rockburst is more likely to appear explosion-like. However, a slower collapse or a rockburst associated with shear motion adjacent to the mine opening might be more likely to appear earthquake-like. Depending on the details of their mechanisms, rockbursts are likely to cover a broad range in M_S-vs-m_b and corner frequency dependence which overlaps explosion and earthquake behavior.

Conclusions and Recommendations

Rockbursts and related mine tremors pose some unique problems for seismic discrimination under a CTBT. They occur in mining areas throughout the world and are frequent in some areas. Because rockbursts are shallow, depth discriminants will not be effective. Observations from events in several different regions indicate a relatively low excitation of long-period Rayleigh waves in rockburst events. This behavior tends to make some rockburst events appear explosion-like with respect to the traditional M_S-vs-m_b discriminant. Regional phase signals observed from rockbursts or mine tremors in several regions show consistently large S/P or L_g/P ratios, which is analogous to the behavior seen in many earthquakes. Regional signal observations for some events also suggest greater complexity in the rockburst sources. Several of the larger recent rockbursts which have occurred in different parts of the world are known to have been associated with large-scale collapse in mine workings. Such collapses have a strong implosional component and may tend to be weak exciters of long-period Rayleigh waves. We are continuing to investigate the implications of different rockburst mechanisms for various regional discrimination methods.

References

Bennett, T. J., M. E. Marshall, B. W. Barker, and J. R. Murphy (1994). "Characteristics of Rockbursts for Use in Seismic Discrimination," PL-TR-94-2269. ADA290881

Hasegawa, H. S., R. J. Wetmiller, and D. J. Gendzwill (1989). "Induced Seismicity in Mines in Canada - An Overview," Pageoph 129, pp. 423 - 453.

Pechmann, J. C., W. R. Walter, S. J. Nava, and W. J. Arabasz (1995). "The February 3, 1995, M_L 5.1 Seismic Event in the Trona Mining District of Southwestern Wyoming," Seismological Research Letters 66, pp. 25 - 33.

STATISTICS ON MINE BLASTING AND BLASTING SIGNALS IN DIFFERENT REGIONS: PRELIMINARY RESULTS FROM RUSSIA AND KAZAKHSTAN

Vitaly I. Khalturin, Tatyana G. Rautian, and Paul G. Richards[1]
Lamont-Doherty Earth Observatory of Columbia University
([1]also, Dept. of Geological Sciences), Palisades, NY 10964

ABSTRACT

We have recently begun a project to document the numbers of mine blasts that will be detected teleseismically, and at regional distances, by seismograph networks used to monitor compliance with a Comprehensive Test Ban Treaty. We plan to study blasting in the United States, in countries of the former Soviet Union, and in Australia, Canada, China, and Korea. Knowledge of mine blast statistics is needed in order to plan efforts in discrimination, recognizing that in general it is more difficult to tell the difference, from seismic data, between underground nuclear and chemical explosions, than between underground nuclear explosions and earthquakes. If the number of large mine blast signals is large, the effort to analyse such signals could swamp discrimination programs.

So far we have acquired and analysed mine blast data from eight different areas of the former Soviet Union. We have established as a total for all these regions that only on the order of 30 blasting events per year have K (energy class) value of 9 or greater – corresponding to m_b around 3.35 or greater. Also, the slope of the frequency-magnitude relation is much steeper for mine blasting signals, than for earthquakes (the b-value is greater than 2 for blasting, and around unity for earthquakes). This latter result is good from the perspective of concern over very large blasts – because it implies there are very few such events. It also indicates that the number of blast signals rises very rapidly as one considers events with magnitude below about m_b 3.25.

Keywords: mine blasting, seismic discrimination, CTBT monitoring

OBJECTIVE

Our goal is to document the rates of occurrence of chemical explosions of different sizes, in as many mining regions as possible, but with a focus on the observability of blasting signals originating in the former Soviet Union, Australia, Canada, possibly China, Korea, and the U.S.

The size of a chemical explosion is expressed commonly in terms of charge size. But we shall be more interested in size expressed in terms of seismic magnitude, whether local, regional, or teleseismic, since our concern is with the observability of blasting activity. We shall be particularly interested in estimating the numbers of chemical explosions that occur in different regions and that are detected teleseismically with $m_b > 3$. Underlying our work, is the fact that mine blast signals are less easily discriminated from nuclear explosion signals, than are earthquake signals, so mine blast signals may require more sophisticated analysis in programs of CTBT verification. Therefore, large numbers of detectable mining blasts would represent a problem for those who must routinely identify the nature of seismic sources (earthquake, mining blast, underground nuclear explosion). Our project will help estimate the extent of this problem, by making surveys of the observability of mine blast signals of various sizes.

RESEARCH ACCOMPLISHED

Prior to starting this project in June 1995, we had preliminary indications for the U.S. that, in practice, only around 10 to 30 mine blasts appeared to be detectable teleseismically with $m_b > 3$. This number was surprisingly low, since, using magnitude-yield relationships for contained single-fired tamped explosions, one would expect from knowledge of the amounts of chemical explosives used, that thousands of U.S. blasts would be teleseismically detectable each year by sensitive arrays (Richards *et al*, 1992; Richards, 1995). For the first six months of GSETT-3, it has turned out (Eric Bergman, personal communication) that about one U.S. blast each week has been reported in the Reviewed Event Bulletin – and that such events are detected and located mainly on the basis of regional, not teleseismic, signals. The REB therefore confirms our preliminary indications for the U.S., on the low numbers of observable blast events.

The reason for the low numbers in the case of the U.S., is that it is inappropriate to apply magnitude-yield relationships for contained single-fired tamped explosions to the problem of estimating the seismic magnitude of a commercial blast of known charge size. Commercial blasts are inefficient at exciting impulsive body-wave signals, compared to tamped single-fired explosions, because virtually all mine blasts in the U.S. are ripple fired. Commercial blasts are also poorly coupled (another way of saying they are inefficient at exciting signals), because the purpose of commercial blasting is almost always to break rock into fragments of predetermined size, and, to this end, commercial blasts are usually not fully contained.

To carry out our surveys for different mining regions around the world, we have begun with acquisition of six different types of information, as follows:

- coordinates of active quarries and mines, in the different regions we shall study;
- lists of times at which representative blasts, and large blasts, occurred;

- information on total charge size, and, if possible, of blasting patterns
  (numbers of holes, charge size and timing of delays);
- regional magnitudes for mining blasts;
- information on the teleseismic observability of mining blasts; and
- pertinent seismograms, for our own analysis.

We are particularly interested in blasts that are detected teleseismically with $m_b > 3$, and/or are detected by regional signals out to distances of 1000 km or more, since such blasts may well be reported routinely by global networks organized for CTBT monitoring. As part of our analysis, we have an interest in comparing various regional magnitude scales and duration magnitude scales, preferably against the teleseismic (m_b) scale. Comparison of magnitudes against charge size is also of interest, though substantial scatter is to be expected. We shall also study the relation between the regional Russian K scale and teleseismic m_b for underground nuclear explosions, mine blasts, and earthquakes in different regions.

Our contract began in June 1995, and to date our preliminary results are for some of the countries of the former Soviet Union. In the remainder of this section, we first list the types of data we have acquired for several different regions; and then we give four Figures that summarize the main features of blasting that we have been able to document so far in this project.

Kazakhstan: southeastern region (Northern Tien-Shan, 42–46°N, 75–80°E)

We have a list of blast dates and times, and charge sizes, for several tens of events in 1994. For several of these events, we have been able to find waveform data at the Kurchatov 21-element array, operated since the summer of 1994 by Lamont (under IRIS's Joint Seismic Program) on the former Semipalatinsk Test Site.

We have a longer blast list, handwritten for 5399 events, for the period 1979 – 1994, used to prepare parts of Figures 1 and 3 (discussed further, below).

We also have all relevant information (date, time, K value, duration magnitude, charge size, and quarry locations) for more than 120 blasts during 1972 – 1976 in the area around the capital city of Almaty.

Kazakhstan: south central region around Dzhambul (41.5–44°N, 68–74°E)

We have a list of about 2130 blasts with known date (during June 1988 to December 1991), time of day, and signal strength.

Russia: Lake Baikal region

We have a map and a listing of quarry/mine locations.

Russia: Caucasus region around Anapa (N.W. Caucasus, 44.1–45.7°N, 36.1–38.3°E).
Also the Caucasus region to the south around Kislovodsk

We have quarry/mine locations, catalogs of blasts for several years, and a catalog of

earthquakes (the basis for parts of Figures 3 and 4, discussed below). In the southern Caucasus around Kislovodsk, Lamont operated a regional network during 1991 – 1992 under IRIS's Joint Seismic Program, and the resulting waveform data have been worked up (for example in Vigen Aharonian's 1994 master's paper at Lamont/Columbia University) for numerous small blasts and earthquakes.

Russia: Kuzbass region (southeast of Novosibirsk)

We have a map and a listing of quarry/mine locations. We have identified waveforms for several large events from this region, recorded at a distance of approximately 700 km with high signal-to-noise, at the Kurchatov array operated by Lamont.

Russia: Central Urals

We have a list of quarry/mine names, their location, and distance from the IRIS/GSN/GSETT-3 station at Arti (ARU) in the Urals.

Russia: Far East region ("Primorye", 43.5–56°N, 123.5–138.5°E)

We have a map and a listing of quarry/mine locations, and lists of blast times and blast signal strength.

Ukraine

We have the location of 24 major quarries and mines active in the years 1986 – 1990, and 23 examples of blasts of known latitude, longitude, origin time, and total charge size.

Complete details on the above data, and additional data, will be supplied in future technical reports. In this paper there is space to give only a brief account of two aspects of our newly acquired data. Thus, we have examined:

(1) the distribution of the sizes of seismic signals resulting from blasting, and have compared this distribution to the results for earthquakes in the same region, paying particular attention to the size of the largest blasting events (largest, in terms of seismic signal strength); and

(2) the time distribution (time-of-day) of blasting signals.

Russian and other CIS countries routinely report the strength of seismic sources using the K value, which was designed originally to be an estimate of the logarithm of the total energy, in joules, of radiated seismic waves. The relationship between K value and values of seismic magnitude, on scales commonly used by western seismologists, will be examined at a later stage in our project. Sufficient here to say, that the approximate relationship is

$$K = 9 + 2.32 * [m_b - (3.35 \pm 0.25)].$$

It follows that the K value of blasts of a size likely to be of interest in the context of CTBT monitoring, is around 9 and greater. In some cases there may be interest in blasts with K somewhat less than 9.

It is clear from Table 1 that blasting activity in Kazakhstan is currently much reduced from levels reached during Soviet era. We believe this reduction is likely also to have occurred in Russia and Ukraine. Much of our data comes from the years of greater activity, prior to 1992.

Table 1. Annual numbers of quarry blasts in southeastern Kazakhstan during 1985 - 1994.

| Year | Total | Ranges of K – values | | |
		8.5-8.9	9.0-9.4	>9.4
1985	405			4
1986	371			4
1987	431			5
1988	551	14	9	2
1989	461	21	3	1
1990	489	10	2	2
1991	476	8	2	1
1992	324	2	0	1
1993	136	1	0	0
1994	89	1	0	0

Figure 1 shows the numbers of events (blasts, and earthquakes), in each unit of energy class K, for more than 5000 blasts in a region of southeast Kazakhstan that includes the capital city, Almaty. This display is similar to a typical magnitude-frequency relation, plotted with an incremental rather than a cumulative frequency. Note from the straight-line fit to the earthquake data, that the detection capability of the network used to prepare this Figure is good down to at least K = 7. The blast data do not follow a straight line at lower values of K. The fall-off of blasts with signal strength above K = 8 is much faster than the fall-off for earthquakes. There are very few blasts events with K ≥ 9.

Figure 2 shows the numbers of blasting events at four specific mines/quarries in the same region covered in Figure 1, and again we see the rapid fall-off of events with seismic energy class K ≥ 8, and the paucity of events with K ≥ 9. These two features are found for all regions of the former Soviet Union for which we have so far acquired data. Whereas the *b*-value in the usual magnitude-frequency relation is about unity for earthquakes, the *b*-value for blasting is greater than 2 in all the regions we have studied so far.

Figure 3 gives the numbers of events per hour-of-day, using GMT, for four different mining areas. The Figure shows that blasting activity is concentrated at certain times, namely during the hours at the end of the regular working day. This feature of blast activity is interesting, in view of the similar type of plot shown in Figure 4, which is supposedly the numbers of earthquakes per hour-of-day, using GMT, for the Caucasus region. Reasons for the departure from uniformity include a variable noise level (so that more events are detected during quiet times), and failure to eliminate all the blasts. The latter explanation seems more likely as an explanation of the peak in activity shown at 1230 hours GMT, and the similar peak for the top left panel of Figure 3. The peak at around 2000 to 2200 hours GMT is not explained.

RECOMMENDATIONS AND FUTURE PLANS

This project is only 5 weeks old at this time of writing. We expect to acquire further lists of blasting events, and associated information on charge size and signal strength, for different regions including the former Soviet Union, Australia, Canada, China, Korea, and the U.S. We shall document the observability of these events, paying particular attention to any blasts observed teleseismically, and for them we shall compare values of magnitude assigned on different scales.

We also have begun a project to document large single-fired chemical explosions, several of which occurred in the nuclear weapons program of the former Soviet Union. These shots were conducted during 1959 – 1961, in order to gain experience, with chemical explosions, that would assist with the later underground nuclear explosions that began in 1961. These unusual chemical explosions were very similar to the U.S. "chemical kiloton" shot of September 1993.

ACKNOWLEDGEMENTS

We appreciate the assistance Dr. Natalya N. Mikhailova from the Institute of Seismology of the Kazakhstan Academy of Sciences, and Dr. Anna A. Godzikovskaya from the Hydroproject Institute in Moscow.

REFERENCES

Paul G. Richards, Douglas Anderson, and David Simpson, A Survey of Blasting Activity in the United States, *Bulletin of the Seismological Society of America*, **82**, 1416–1433, June 1992.

Paul G. Richards, Blasting Activity of the Mining Industry in the United States, in *Proceedings of a Symposium on the Non-Proliferation Experiment: Results and Implications for Test Ban Treaties*, sponsored by LLNL/Department of Energy, CONF-9404100, pp. 2-16 to 2-35, April 1994, Rockville, Maryland, ed. M.D. Denny, 1995.
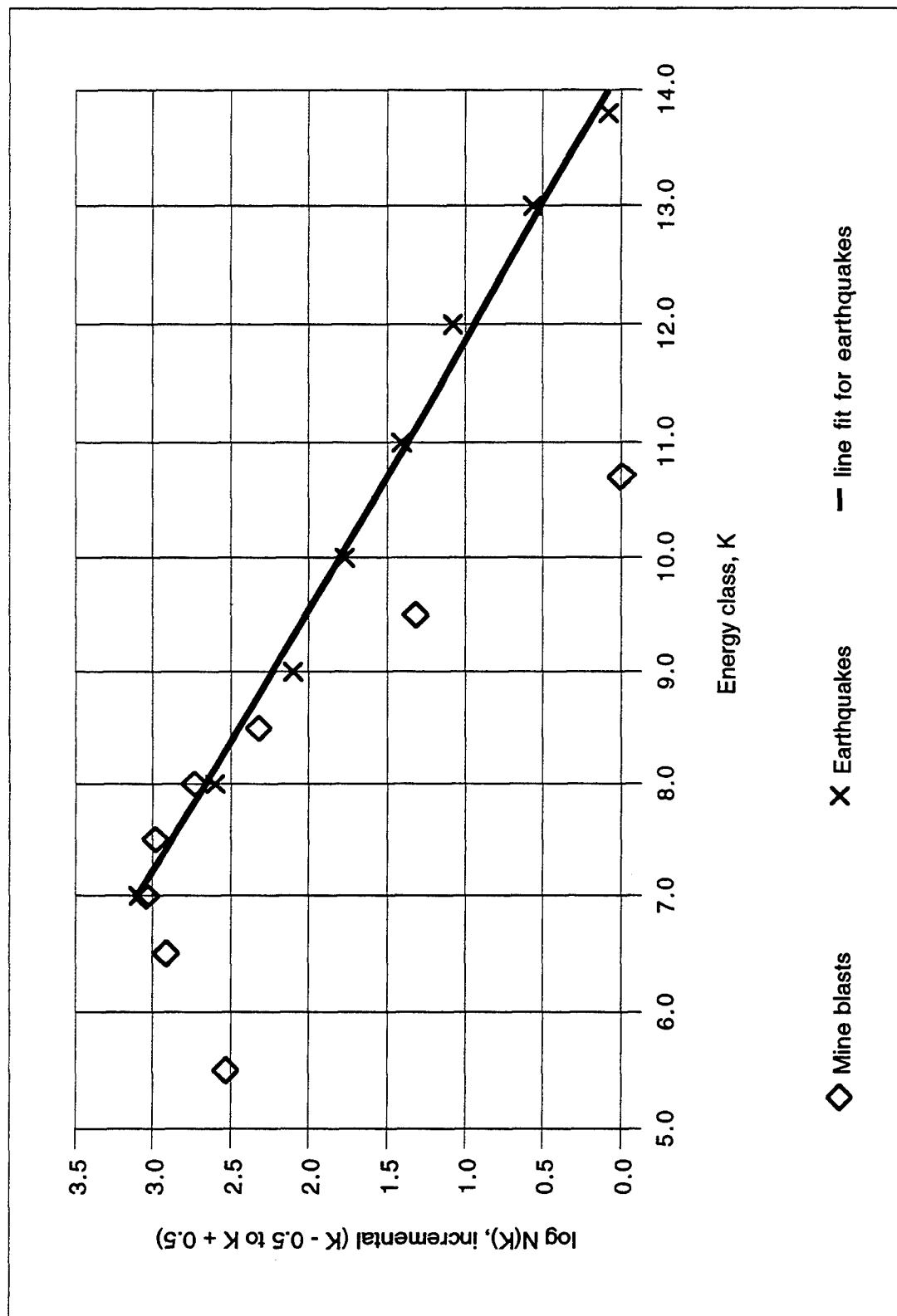
Figure 1. Comparison of recurrence curves for earthquakes and mine blasts in Southeast Kazakhstan (Northern Tien-Shan, 42 – 46° N, 75 – 80° E). The curve for blasts is based upon 5399 such events reported in the bulletin prepared by the Institute for Seismology, Kazakhstan, for the period 1988 – 1994. The slope for earthquakes is 0.43, corresponding to d(log N)/d(mb) = – 1.0, and the bulletin appears to be complete down to K = 7. The slope for mine blasts corresponds to d(log N)/d(mb) = – 2.3. There are very few blasts at the level K = 9 and greater (that is, mb around 3 – 3.5).
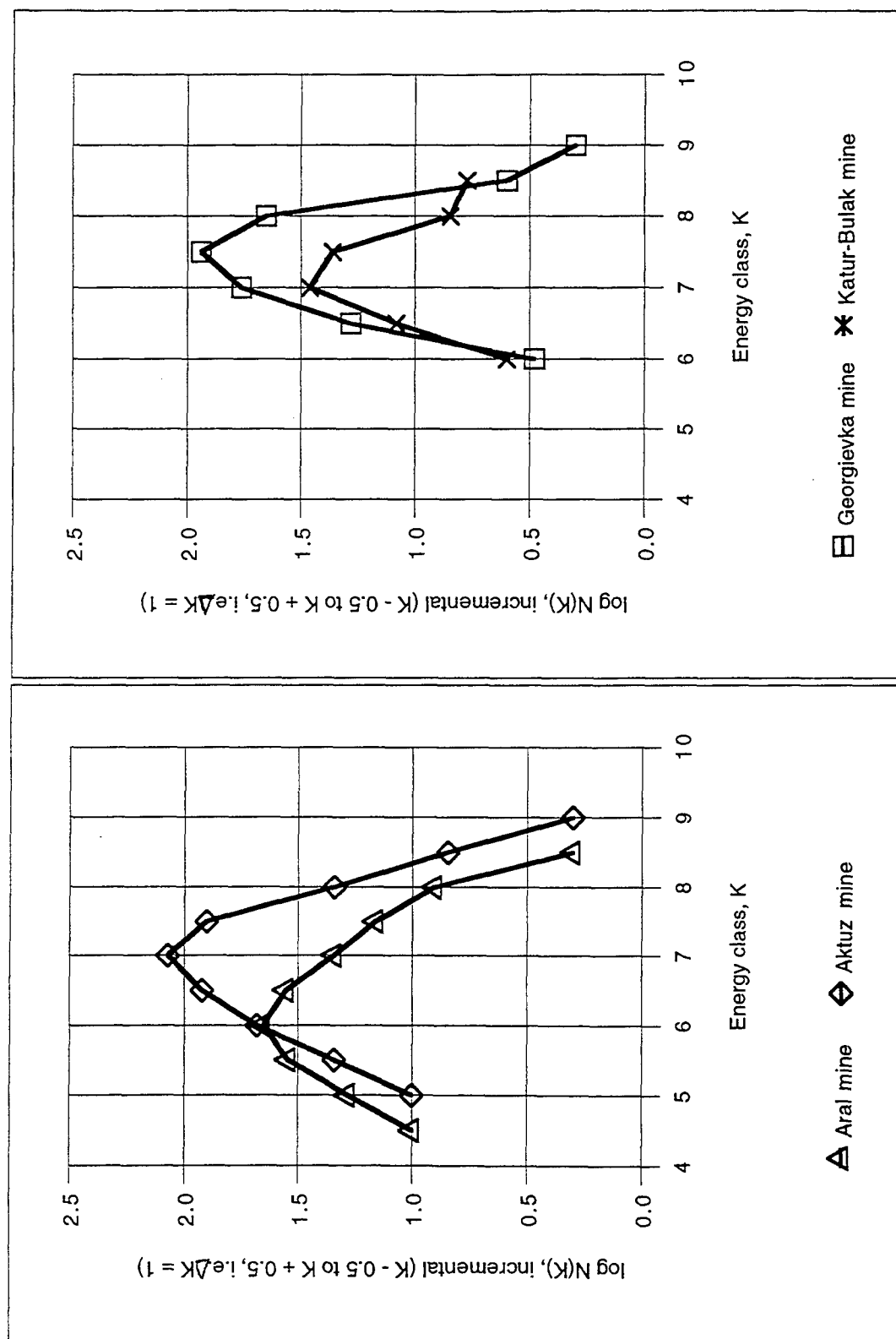
Figure 2. The recurrence curves of blasting signals from four mines in southeastern Kazakhstan during 1988 – 1994, all showing a strong decline in number of blasts with K class increasing above 7; and all showing few if any blasts with K = 9 (corresponding to mb 3 – 3.5). On the left, are curves for the Aral and Aktuz mines. On the right, are curves for the Georgievka and Katur-Bulak mines.
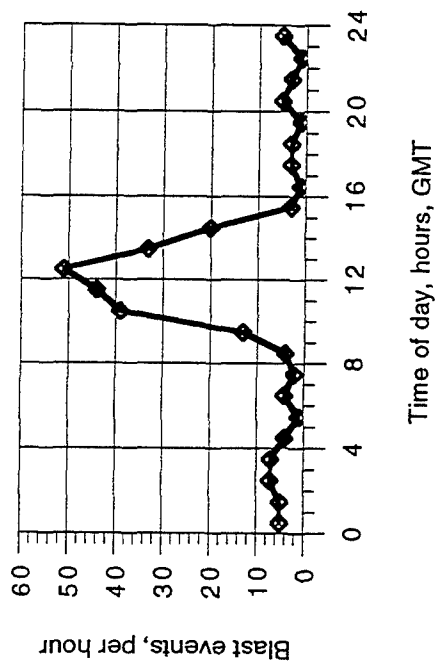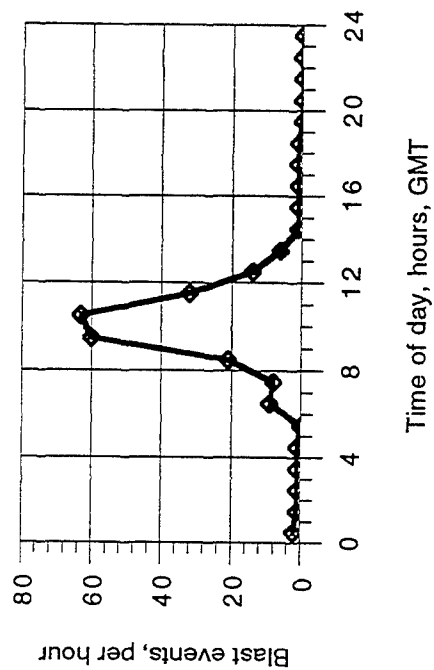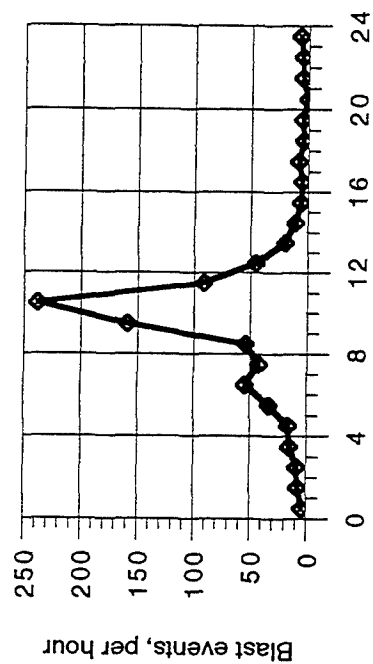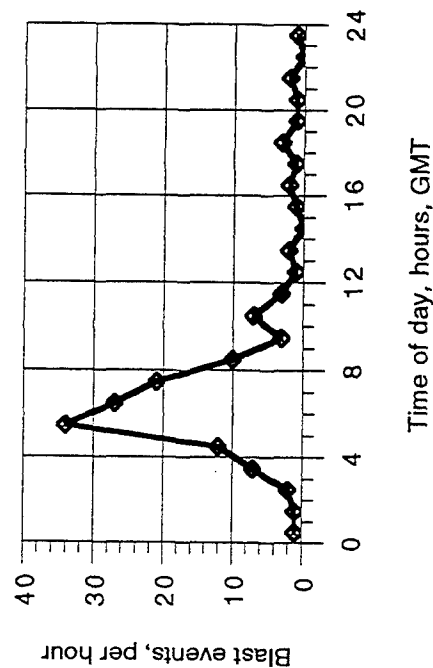
Figure 3. The distribution of mine blasts throughout the day, for four different regions in the former Soviet Union. For the North Caucasus (see top left), the maximum rate occurs at noon GMT, corresponding to 15 – 16 hours local time (the end of the work day). The maximum is shifted with respect to the Caucasus for the two Kazakhstan examples, and for the Russian Far East (see bottom right), but in each case the maximum occurs at a local time corresponding to the end of the work day.
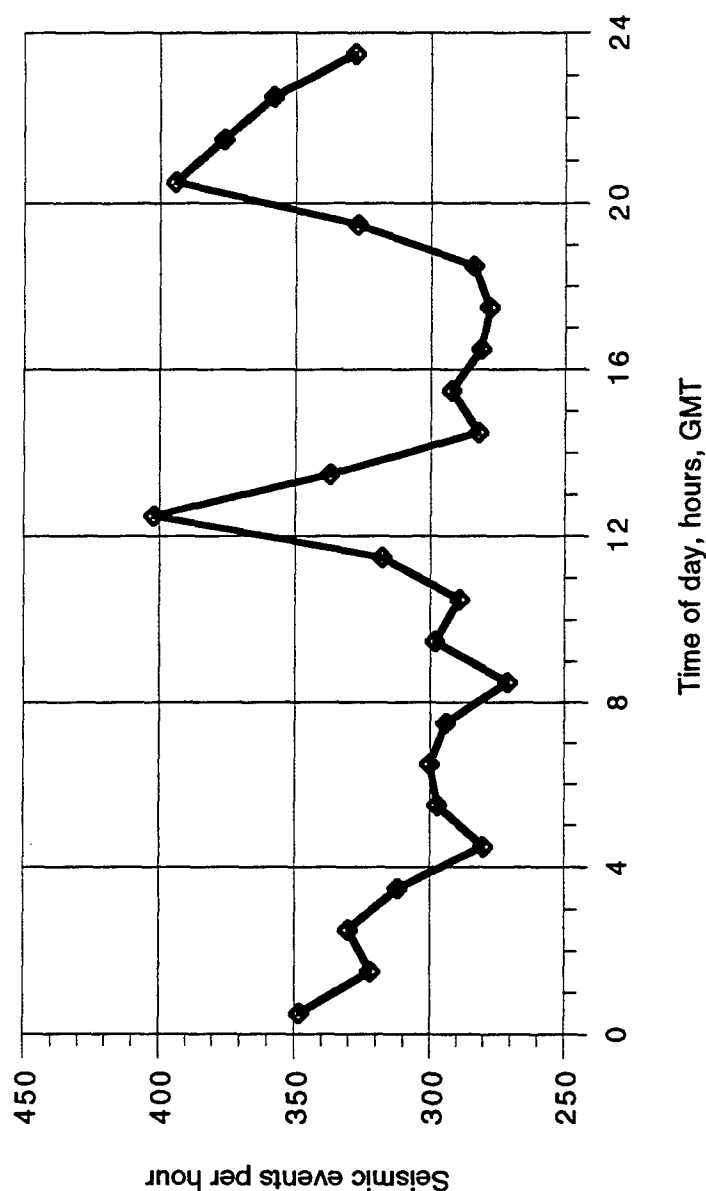
Figure 4. The distribution with respect to time of day (GMT), for events in the official Caucasus catalogue of earthquakes, taken for the years 1962 – 1986 from "Earthquakes in the USSR", published annually by the Institute of Physics of the Earth. From the presence of a strong maximum near 1230 hours, it appears that some blasts remain in this catalogue (compare with Figure 3, top left).

561

THE LANL / LLNL / AFTAC BLACK THUNDER MINE REGIONAL MINING BLAST EXPERIMENT

D. C. Pearson, B. W. Stump
D. F. Baker and C. L. Edwards
Los Alamos National Laboratory

ABSTRACT

Cast blasting operations associated with near surface coal recovery provide relatively large explosive sources that generate regional seismograms of interest in monitoring a CTBT. This paper describes preliminary results of a series of experiments currently being conducted at the Black Thunder Coal Mine in northeast Wyoming as part of the DOE CTBT Research and Development Program. These experiments are intended to provide an integrated set of near-source and regional seismic data for the purposes of quantifying the coupling and source characterization of the explosions. The focus of this paper is on the types of data being recovered with some preliminary implications. A companion paper (Stump, 1995) discusses the mining practices in this mine and the Powder River Basin in general where the mine is located.

The Black Thunder experiments are designed to assess three major questions:

A. *How many mining explosions produce seismograms at regional distances that will have to be detected, located and ultimately identified by the National Data Center and what are the waveform characteristics of these particular mining explosions?*

B. *Can discrimination techniques based on empirical studies be placed on a firm physical basis so that they can be applied to other regions where we have little monitoring experience?*

C. *Can large scale chemical explosions (possibly mining explosions) be used to calibrate source and propagation path effects to regional stations? Can source depth of burial and decoupling effects be studied in such a controlled environment?*

With these key questions in mind and given the cooperation of the Black Thunder Mine, a suite of experiments have been and are currently being conducted. This paper will describe the experiments and their relevance to CTBT issues.

EXPERIMENTAL PURPOSE

As discussed by Stump (1995), the Black Thunder Mine conducts large cast blasts with explosive loads on the order of 2,000,000 to 5,000,000 lb. on an interval of between two and four weeks. In addition, explosive shots are conducted on a daily basis in the coal in order to fracture the material at approximately a factor of ten smaller total charge. An experimental plan was developed to: (1) Quantify the amplitude and spectral differences of the cast and fracturing blasts; (2) Document the development of the seismic wavefield from close-in to the explosion at high bandwidth to regional distances at lower bandwidth; (3) Determine possible azimuthal effects that may result from the blasting geometry and affect regional observations which often sparsely sample the wavefield; (4) Investigate the utility of a small, high frequency array within a mine for monitoring blasting activity in the mine and at other mines in the region and (5) Characterize the differences in seismograms from these mining sources and single fired concentrated charges.

An array was deployed in and around the Black Thunder Mine for approximately a three month time period in order to address the above issues. These data are being combined with regional signals for the same events cataloged at the Pinedale Seismic Research Facility (PSRF, 360 km to the SW) and the US National Network Station RSSD (150 km to the northeast). In addition three portable deployments of regional stations were completed by LLNL personnel.

The near-source array consisted of three component velocity instruments with natural frequency of 1 Hz. A 16 station azimuthal array with a radius of approximately 2.5 km was fielded for a large cast blast on 16 June, 1995. These data are being used to quantify the radiation pattern induced by the mine and the blasting practices (3). Two linear arrays of 3 stations each at ranges of 1, 2.5, and 5 km were deployed in the directions of PSRF and RSSD. These stations, in conjunction with three additional portable regional stations, provided the data for quantifying the transition of the wavefield from close-in to distances typical of CTBT monitoring (2). Eleven additional stations were deployed on mine property to form a regional array with interstation spacings ranging from 40 m to 15 km. Each data acquisition system was continuously locked to its GPS clock to provide the necessary timing accuracy for array processing. The purpose of this last component of the experiment was to quantify blasting activity inside the mine as well as provide data for quantifying explosions at other mines in the Powder River Basin (4).

During the three months of the deployment the mine is conductng many explosions so the effects of different blasting practices can be quantified (1). An example of the activity are two casting shots in the south pit conducted on 16 and 23 June 1995. Individual explosive columns in the casting shots range from 3000 to 5000 lb with some holes loaded to as much as 10,000 lb per hole. Borehole diameters are predominately 10.625 inches with some boreholes drilled at 12.25 inches diameter. Typical overburden casting patterns consist of 700 to 1500 individual holes. Timing delays currently used are 100-200 ms between rows with 17 or 35 ms delays between holes in a row. Down hole delays of up to 1400 ms are used to prevent premature disconnection of the firing system at the surface.

A set of explosive product test holes will be detonated in the near future in close proximity to the two production cast shots described above. These test holes will be fired simultaneously to provide an impulsive source for the CTBT mining blast wave propagation experiments (5) while providing the mine personnel with valuable information concerning explosive performance. The total amount of explosive emplaced in the test hole shot is expected to be in on the order of 100,000 lb.

LOCATION OF THE EXPERIMENT

The Black Thunder Mine is located in the Powder River Basin approximately 50 miles south-southeast of Gillette, Wyoming (see Stump, 1995 for a discussion of the Powder River Basin). The mine is operated by the Thunder Basin Coal Company, a subsidiary of ARCO. Experimental design and implementation has been facilitated by the excellent support of Mr. Bob Martin, Drilling and Blasting Manager and other personnel at the mine. Martin and King (1995) report that the mining operation is recovering coal from a 68 foot thick seam located under up to 120 feet of overburden. Cast blast explosions are used to remove the overburden which consists of weathered sandstone and mudstone.

An aerial photograph acquired on 11/23/94 is overlain on the land map provided by the Black Thunder Mine in Figure 1. Station locations, primary and secondary roads, and the locations of overburden cast shots and future single detonated test shots are also depicted in Figure 1.

QUANTIFICATION OF MAGNITUDE-YIELD RELATION AND BLASTING PRACTICES (1&2)

The Black Thunder Mine shoots cast shots about every two to four weeks. They operate out of four pits with different geographical orientations (Figure 2). Some of the recent cast blasts demonstrate the size and frequency of the blasting operation: 2 Dec 94 (3,000,000 lb.); 15 Dec 94 (3,500,000 lb.,); and 25 Jan 95 (2,000,000 lb.). In addition to these types of explosions, they typically shoot in the coal to break the material. The 14 Dec 94 Coal Shot was 68,890 lb. These coal shots can be quite large as exemplified by the 20 January 95 coal shot which was 700,000 lb. The frequency and variety of these explosions coupled with the fact that even the smallest of the above explosions was observed at the PSRF makes this blasting program ideal for identifying magnitude-yield relations in a controlled environment.

The near source and regional stations will be used to quantify the generation and evolution of the regional signals with range. The data gathered from this integrated experiment will provide a basis for assessing not only the size and nature of the regional signals at different ranges but possible variations in magnitudes from such events. We anticipate recovering data from approximately six overburden cast shots and as many as 50 coal fragmentation shots during this long term deployment phase of the study. The analysis of the regional signals from these events will be coordinated with AFTAC.

AZIMUTHAL RADIATION EFFECTS AND GENERATION OF REGIONAL SIGNALS (3)

This portion of the Regional Mining Blast Wave Propagation experiment is designed to quantify the azimuthal variation in the seismic radiation in the near-source region and then link these observations with those at regional distances. Utilizing the motion field estimated from the 15 Dec 94 Cast Shot, the near-source azimuthal array described earlier was deployed (Figure 1). Sixteen near-source velocity gauges, all located within the mine property, were fielded with interstation spacing of 22.5 degrees at a range of approximately 2.5 km from the center of a large cast shot in the south pit. Figures 3, 4, and 5 depict the vertical, radial and transverse velocity seismograms recorded for the 16 June 1995 south pit cast blast. Time increases from the outer portion of the plot toward the middle with constant time demarcations every 5 seconds. The center of the figures shows a representation of the spatial extent of the cast shot and indicates the direction of propagation of the delay firing system. It is interesting to note that the largest amplitudes propagate at directions sub perpendicular to the free face of the pit which faces north. Instruments located in the northern half of the mine on previously mined and reclaimed surfaces show significantly smaller peak amplitudes and poorly developed surface wave components.

NEAR-REGIONAL SEISMIC ARRAY (4)

There are twenty-two active coal mines in the Powder River Basin, several of which utilize cast blasting. This is the type of region that has been suggested for special instrumentation under a CTBT monitoring regime. As an example of the frequency of blasting in the region on 27 January 95 two explosions (one from the Black Thunder Mine) occurred within 5 minutes of one another in different mines (Vindell Hsu, personal communication).

Hsu reports that the first of these events had a m_b of 2.3 and the second 3.1. An unmanned deployment of a near-regional, high-frequency array in the Powder River Basin has been implemented. As noted earlier, the 17 element array provides a range of scale lengths from 40 m to 15 km. A recent maintenance trip to the array indicates that an average of 3-4 mining blast events per day are being detected. Work is in progress to locate the events and characterize them. This array of stations will remain deployed until after completion of a contained shot of approximately 100,000 lb. scheduled for late August 1995.

FULLY CONTAINED EXPLOSION (5)

Comparison of the near-source waveforms from the Black Thunder Cast Shot and the NPE (Stump, 1995) suggests that at low frequencies the well coupled NPE is approximately an order of magnitude larger with the Cast Shot having more energy at high frequencies. This result is consistent with the magnitude estimates for the two sources. Unfortunately the NPE is in a different media, detonated in well saturated materials, and so the comparison cannot be relied upon for anything more than inference. The fact that the 14 Dec 94 Coal Shot (68,890 lb.) was recorded at PSRF suggests that a moderate size, contained, singly detonated, chemical explosion could be used to quantify similarities and differences between the delay fired cast shot and a

fully contained explosion. The success in modeling the NPE and the NPE CAL (Stump, Pearson and Reinke, 1995) further supports the use of the moderate size contained explosion.

Detonation of a moderate size (>50,000 lb.), singly detonated contained explosion has been explored with the mine. A target of opportunity has been identified since the mine is planning to conduct a series of explosive performance tests. They have agreed to fire all the explosive columns in each of two tests simultaneously, providing the CTBT Field Experiment with two large, contained shots. The depth of such an explosion would most likely be conducted at normal burial depths for an overburden cast shot (70 ft explosive column with 30 ft of stemming).

REFERENCES

Martin, Robert L. and Marlyn G. King, 1995. The Efficiencies of Cast Blasting in Wide Pits, Proceedings of the Twenty-first Annual Conference on Explosives and Blasting Technique, Volume 2, Int. Soc. of Explosives Engineers.

Stump, Brian W., D. Craig Pearson and Robert E. Reinke, 1994. Source Comparison Between Nuclear and Chemical Explosions Detonated at the Nevada Test Site, LAUR-94-4073, Los Alamos National Laboratory.

Stump, B. W., 1995. Practical Observations of US Mining Practices and Implications for CTBT Monitoring, PL-TR-95-2108
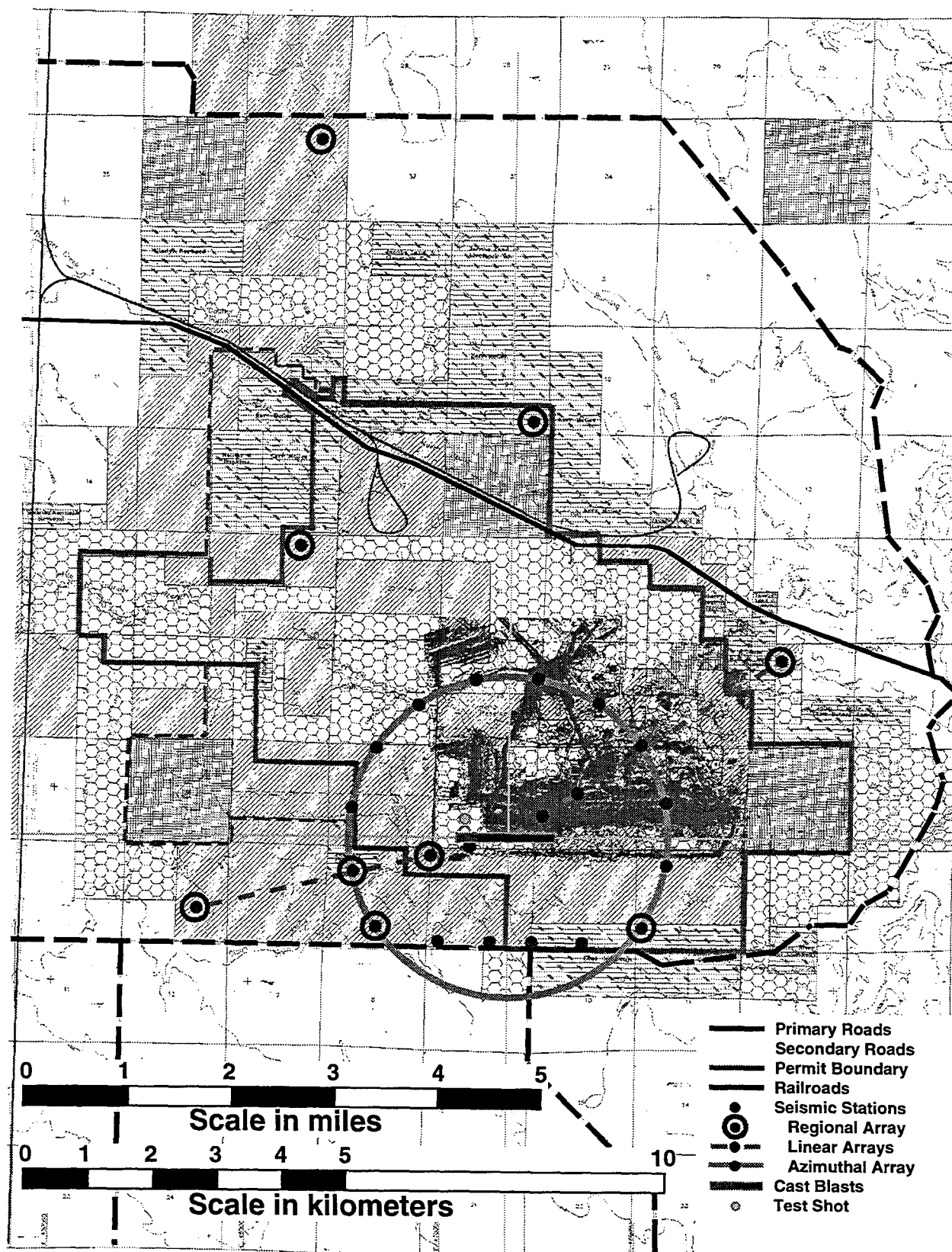
Figure 1. Experimental design for the azimuthal study. Seismic instruments were deployed in an azimuthal array on a 2.5 km radius circle centered on the first of the two overburden cast shots. Two linear arrays were deployed in the directions of Pinedale, Wyoming and RSSD in northwest South Dakota. A nine station regional array is shown, however, a total of 17 stations comprise the regional array which is being operated throughout the summer of 1995.
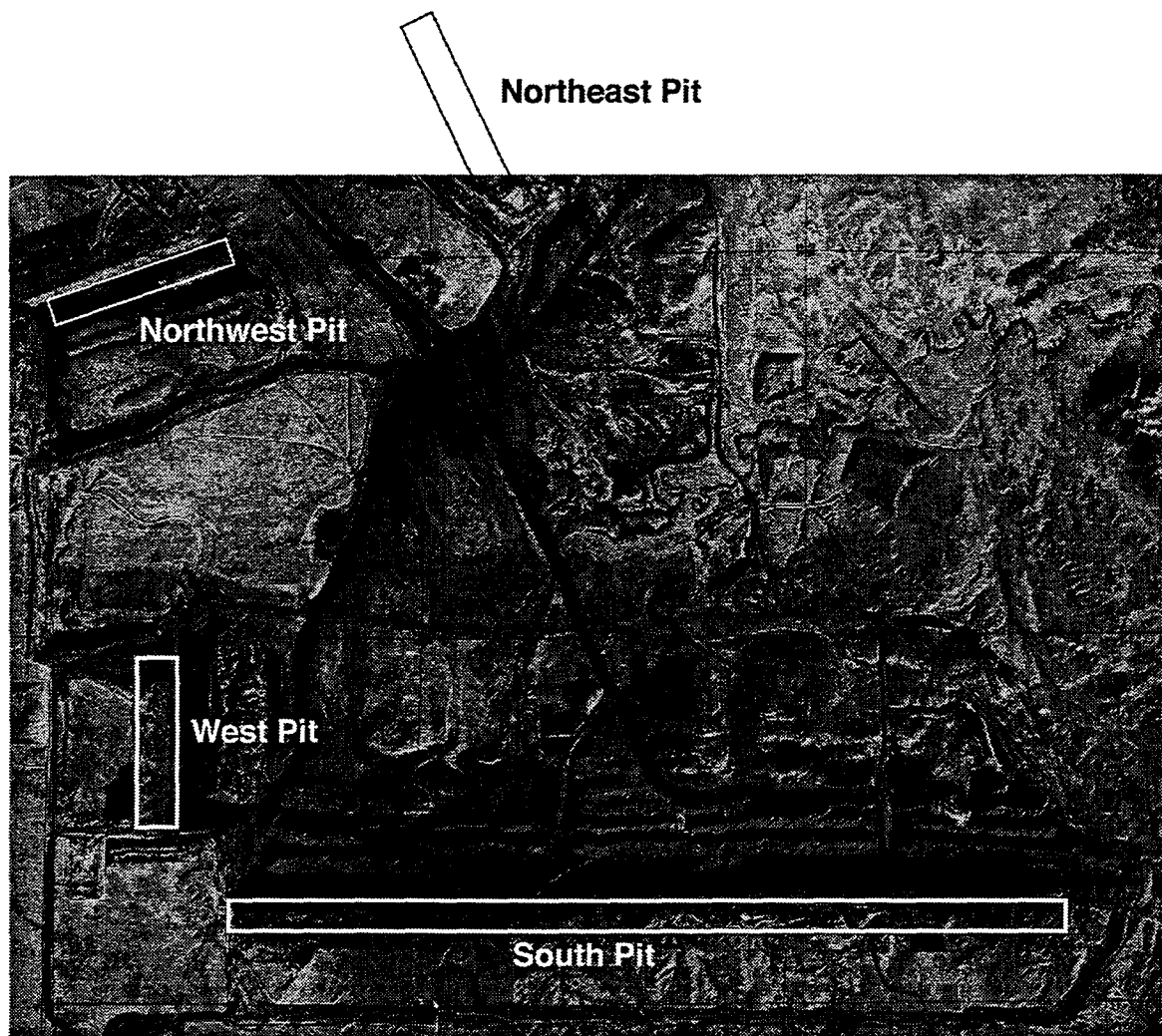
Figure 2. An overhead aerial photograph of a portion of the Black Thunder Mine in November, 1994. Outlines of the active pits in the mine show the variability of the strikes of the pits and indicate that azimuthal variation of the blasts radiation pattern could complicate regional locations and magnitude estimates.

Black Thunder Cast Shot 16 June 1995; Azimuthal Array Z Component
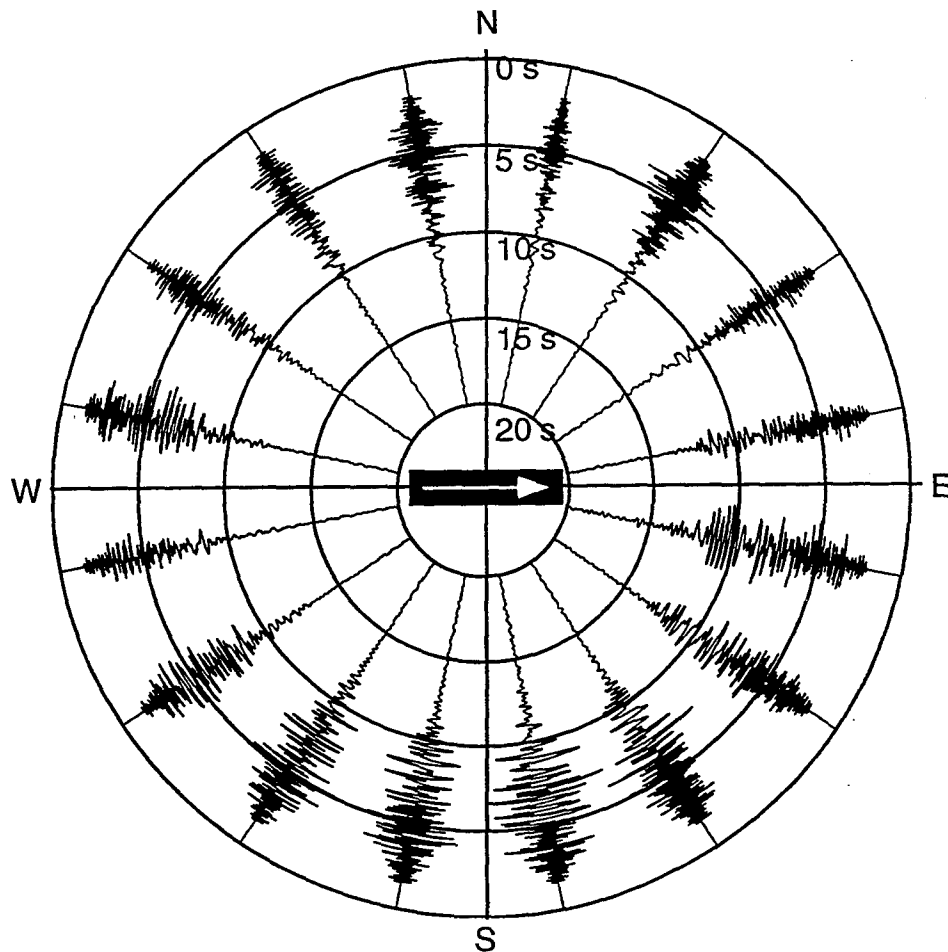
Figure 3. Vertical velocity seismograms centered on a 4.7 Mlb cast shot at the Black Thunder Mine on 16 June 1995. The orientation and shooting direction of the cast shot are indicated in the center of the figure.

Black Thunder Cast Shot 16 June 1995; Azimuthal Array R Component
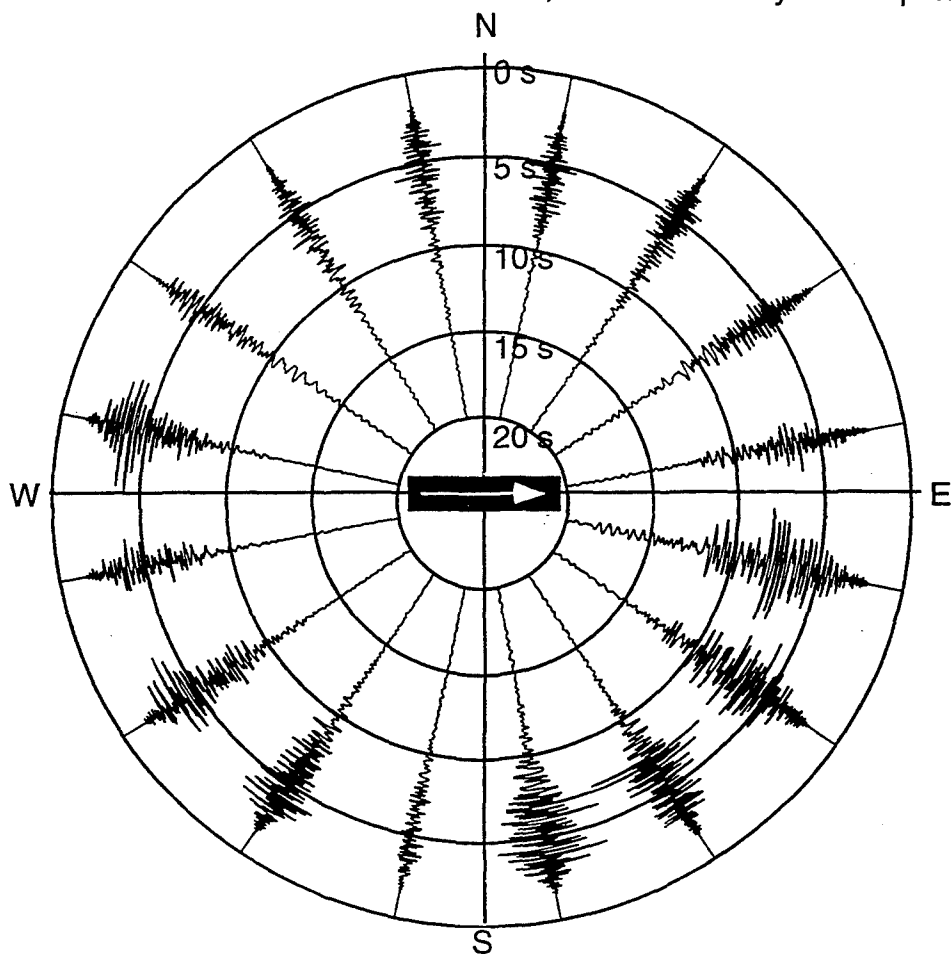
Figure 4. Radial velocity seismograms centered on a 4.7 Mlb cast shot at the Black Thunder Mine on 16 June 1995. The orientation and shooting direction of the cast shot are indicated in the center of the figure.

Black Thunder Cast Shot 16 June 1995; Azimuthal Array T Component
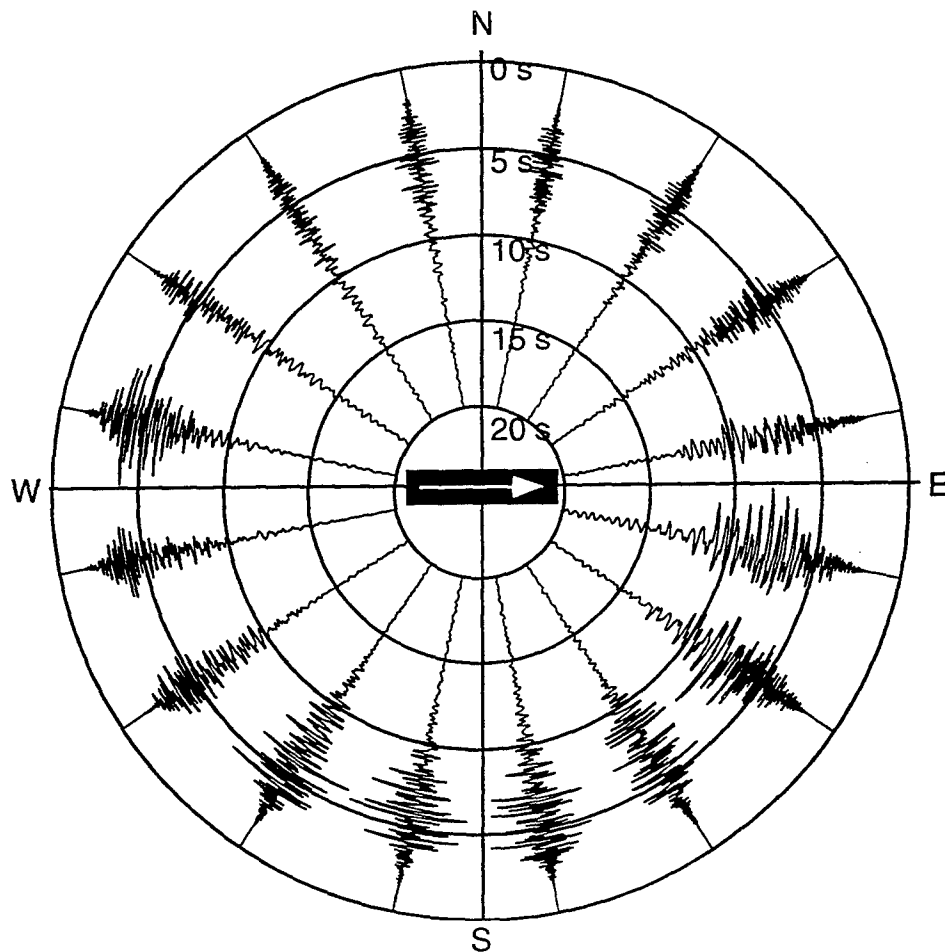
Figure 5. Transverse velocity seismograms centered on a 4.7 Mlb
cast shot at the Black Thunder Mine on 16 June 1995. The orientation
and shooting direction of the cast shot are indicated in the center of
the figure.

A Study of Mine Blasts and Rockbursts in the Pacific Northwest

Alan Rohay and Shannon Goodwin
Pacific Northwest Laboratory
Richland, Washington, 99352

Abstract

We have collected regional broad-band and densely-spaced short-period data for nearly 40 mining explosions from the Centralia mine, from two rockbursts in northern Idaho, and from several other explosions in the Columbia River Basalt and elsewhere in Washington state. These recordings, for events with magnitude 2.5 or larger, are being analyzed to determine the characteristics of the seismic signals that identify these events as explosions or rockbursts.

The type of delayed blasting at the Centralia mine may not be conducive to the detection of spectral scalloping or nulling, and this effect has not been clearly observed in preliminary spectral analyses of the regional seismic signals. However, these and other blasts generate relatively high-amplitude Rayleigh waves (Rg) that allow their identification as explosions at close distances. We are planning to make near-field deployments using broad-band, high-frequency seismic systems to characterize the effect of the delay pattern and charge sizes on the generation of regional seismic phases from the explosions at Centralia.

Rockbursts from the northern Idaho region are due to implosional and fault-slip mechanisms, as determined from in-mine seismic systems. Such events are often triggered by the failure of pillars, in some cases during de-stressing operations. Such events may be of particular interest to discrimination researchers.

We are preparing to arrange for the recording of Centralia coal mine blasts on a USGS refraction line in September. Several hundred portable recorders will be operated along a 400 km profile that passes within 20 km of the Centralia mine. This will provide a comparison of the delay-fired mine blasts to the single-shot USGS explosions.

We are currently in the process of integrating the broad-band stations of the USGS National Seismic System, the Canadian Digital Seismic Network, and the broad-band elements of the Pacific Northwest Seismograph Network, and Pacific Northwest Laboratory's own broad-band recordings into the data base.We have established cooperative relationships with other regional seismic arrays and mine operators to exchange data on the mining explosions and the Idaho rockbursts. In the future, we will compare these mine seismic signals with recordings of shallow earthquakes located in the same regions as the mines.

Objective

The objective of the field study is to collect and characterize the seismic signals from large mine and quarry blasts, mining-induced earthquakes or rockbursts, and shallow earthquakes. These signals will be used to test regional seismic discrimination methods, utilizing a combination of pre-existing, permanent short-period and broad-band seismic networks, and near-source recordings made with portable, broad-band, high-frequency systems.

The focus of the field study is the Pacific Northwest (Washington, Oregon, Idaho, and southern British Columbia, Canada) in areas of active mining and industrial blasting. Of particular interest are blasts registering greater than magnitude 2.5. These blasts are routinely recorded, located, and identified as blasts using the data from a regional seismographic network throughout Washington and Oregon. In addition to mine blasting, seismic events induced by deep mining activities in northern Idaho occasionally exceed magnitude 2.5 as determined on regional seismic networks in Washington, northern Idaho, and western Montana.

In some areas, mining explosions have a characteristic frequency-amplitude distribution that reflects the shot pattern. A pattern of constructive and destructive interference between the shot holes can sometimes generate a frequency spectrum with a "scalloped" appearance, with spectral nulls resulting from the destructive interference at an evenly-spaced set of frequencies (Baumgardt and Ziegler, 1988; Hedlin et al., 1990, Smith, 1989). However, this is not clearly evident in the seismic signals recorded on the regional networks, possibly because they can only be observed at short distances, or alternatively because the pattern of delayed detonations is not systematic enough to create the interference pattern.

Preliminary Research Results

Figure 1 shows the locations of short-period stations that comprise the Pacific Northwest Seismograph Network (PNSN). The regional seismic networks are comprised of short-period (1 Hz) seismometers, only a few of which record three-component motion, which generally record ground motions in the frequency range of 1-30 Hz. Figure 1 also shows the locations of broad-band stations that have been operated in the region in recent years. We examined the PNSN catalog of explosions to identify the primary areas in which explosions have been located. Figure 2 shows the locations of explosions that occurred in 1994 and 1995, and Figure 3 shows the locations of earthquakes with depth less than 5 km for the same time period.

Centralia Coal Mine. The predominant site of large explosions is currently and has for many years been a large coal mining operation at Centralia, Washington. At the Centralia mine, daily blasting routinely generates seismic events with magnitudes in excess of 2.5. Up to 600 ft. of overburden (a relatively soft sandstone) is removed during the mining at Centralia to expose the main coal seam, which is 60 ft. thick. Cast blasting is not employed at the Centralia mine (cast blasting throws or casts the overburden off of the underlying layers); the overburden is simply broken up with explosives and removed using a drag line. The coal bed itself is not usually shot. Shot holes are 9 in. diameter and are drilled vertically to a depth of approximately 60 ft. A slurry blend of ANFO explosive is usually pumped into the holes, although bags of ANFO are sometimes used in wet conditions. The top 15 ft. are filled with stemming material, and each

hole contains approximately 1000 lbs. of ANFO. Holes are drilled with a 25 ft. spacing, generally 5 to 6 rows and 10 to 40 holes/row in a rectangular pattern. The largest explosions at the mine occasionally include as much as 260,000 total pounds of explosive.

The explosions are delay fired using non-electric, or "pyrotechnic", delay systems. The delay pattern consists of a 25 ms (millisecond) delay along the spacing of each row (parallel to the free face), and a row-to-row (or "burden") delay of 84 ms. The spacing and burden delays are arranged across the surface of the area to be blasted, and an additional 500 ms down-hole delay is located at the bottom of each shot hole. In this way, each of the shots has been first delayed from hole-to-hole and row-to-row by the surface delays, and is then additionally delayed by the larger 500 ms down-hole delay. The spacing, row (burden), and down-hole delays are provided by devices manufactured in a variety of preset time lengths. Measurements made at the Centralia mine indicate that for the 500 ms delay mechanisms, there is a total variation of plus or minus 3.5 ms, and that this 1.5% variation is expected to also affect the 25 ms and 84 ms delays at the surface.

The Centralia mine staff are currently in the process of providing detailed maps of a selection of blasts recorded by the regional seismic network. These maps and descriptions provide exact locations of at least 4 of the shot holes (generally the corners) and the delay pattern that was used and the amount of explosive in each hole.

There have been 37 explosions at the Centralia mine in 1995 that exceeded magnitude 2.5, and 13 of these equaled or exceeded magnitude 3. We have assembled waveform data for all blasts larger than 2.5 in 1994 and 1995, including recordings by four broadband stations in the region. Seismic signals from a set of 20 explosions in 1994 are shown for a nearby seismic station (LMW, approximately 30 km east of the mine) in Figure 4. Most of these explosions can be easily identified as explosions because of the large Rayleigh wave (Rg) they generate (e.g., Kafka, 1990), but the amplitude of the Rayleigh wave is highly variable. We hope to correlate the relative phase amplitudes and spectral characteristics of these blasts with the detailed information from the mine operators.

Black Diamond Mine. The only other coal mine in Washington is located near Black Diamond but the explosions at this mine have all been less than magnitude 2. At the Black Diamond mine, the shot geometry consists of 35 ft. deep holes, stemmed for the top 12 ft., with the holes spaced 15-16 ft. in both directions. There are generally 4-5 rows consisting of 8-10, 6 in. diameter holes. The delay pattern for these shot is 17 ms along the spacing of each row, and 42 ms between rows. Two down-hole delays are often used here with one placed near the bottom of the hole (175 ms), and a second placed near the mid-depth of the hole (200 ms). Each hole has from 200-300 lbs. of ANFO, and the total amount of explosives detonated during the shot infrequently exceeds 10,000 lbs.

Figure 5 shows the total amount of explosives used in each shot at the Black Diamond mine from August 1994 to June 1995, plotted versus the magnitude determined from the seismic array. Many of these shots were too small to trigger the seismic network recording, and these are shown as a magnitude of zero. The seismic network triggers on most of the larger charges, and progressively misses a greater number of smaller ones, as indicated by the increasing density of "magnitude 0" points at small charge sizes on this plot.

Other blasting areas. Large open-pit copper mines in southern British Columbia near Penticton (see Figure 2) blast an average of 200 times per year with typical blasts ranging from 25,000 lbs. to 270,000 lbs. of explosives per blast. All four mines blast use delayed shots, both down-hole and on the surface. Highland Valley Copper in Logan, B. C. consistently has the largest blasts, with mine personnel manufacturing and loading the bulk emulsion on site. We have also contacted the largest coal mines in southeastern British Columbia and southwestern Alberta to determine if their blasting activity might be of a sufficient scale to be of interest.

The most difficult type of explosion to identify is the occasional blast to obtain rock for road or railroad grade material, although these blasts seldom exceed magnitude 2.5. Many of these explosions are detected in the Columbia River Basalt of southeastern Washington, and the mining operation for railroad ballast near Connell (see Figure 2) has agreed to provide us with information on their blasting practices.

Northern Idaho Rockbursts. The northern Idaho silver mining district lies just to the east of the PNSN, and seismic events induced by the mine frequently exceed magnitude 2.5 and are recorded by the regional array. In addition to the PNSN, there are seismic arrays in northern Idaho and western Montana that also record events in this region. Figure 6 shows the location of seismic events in the region of the four rockburst-prone mines from 1983-1992 that have been derived from the catalogs from these regional seismic arrays. The precision of these event locations is relatively poor, on the order of 20 km, but it is clear that there is a concentration of seismic activity near the mines, although naturally occurring earthquakes also occur in the region. We have undertaken an effort to gather information from the mine operators and the U.S. Bureau of Mines, Spokane Research Office (USBM) on the characteristics of these mine-induced events, and to unambiguously separate actual rockbursts from natural background seismicity.

Several of these mines operate in-mine seismic systems that are used by the mine operators to detect and locate rockbursts. Two of these mines also operate a "macro-seismic", or "mine-wide" system provided by the USBM. These systems include 10-12 geophones or accelerometers in remote areas throughout the mined region. The spacing of these sensors can be as large as a few km, and the geometry is designed to provide three-dimensional coverage of events in the mine for focal mechanism studies by the USBM. The mine monitoring systems and the rockburst characteristics are described in a series of papers published by the USBM (Maleki, 1995)

The Lucky Friday mine has had a long history of rockbursts. In the early 1980's, rockbursts were often caused by the failure of pillars left between mined out areas. There are several instances when attempts to de-stress the remnant pillars resulted in rockbursts as large as magnitude 3. The largest event to occur since 1989 was a magnitude 4.1 event on August 16, 1994. This event caused 2 in. of closure in a mined-out area approximately 500 by 500 ft. at the deepest level of the mine, 5570 ft. below the surface. Recently, a magnitude 2.9 rockburst occurred on June 23, 1995. At the Lucky Friday mine, the larger rockbursts are not correlated with mining activities, although smaller events are correlated with the rate of material extraction, and events such as the pillar collapses during de-stressing or removal are clearly induced by mine activity.

Focal mechanism studies indicate that many of the smaller rockbursts and some of the larger

ones have an implosional mechanism. The larger events usually have a significant fault-slip component that would make the events more earthquake-like. We obtained a short list of the largest rockbursts in 1994 and 1995 from the mine, and later received a more extensive list from the staff of the USBM. We have begun collecting seismograms from the PNSN and other regional arrays in northern Idaho and western Montana, and also from broadband stations in the region (see Figure 1) for these events.

Examples of the waveforms collected from the August 16, 1994, magnitude 4.1 rockburst at the Lucky Friday mine are shown in Figure 7 for a selection of stations that form two profiles, one directed southwest from the mine through eastern Washington and into central Oregon, and another directed more westward across the Cascade mountains and into Puget Sound. There appears to be greater attenuation of the signals on the latter profile, possibly indicating topographic or geologic blockage of the waves (the distance range for both profiles is 100-600 km from the mine).

Recommendations and Future Plans

The second phase of the field study involves actively collecting three-component broad-band signals near the most significant blasting activities identified. We will deploy Guralp CMG-40T seismometers with REFTEK portable digital recorders at a variety of azimuths and ranges from the Centralia mine, to search for spectral modulation from the delay firing, and to characterize the generation of the Rayleigh waves that identify the shallow depth of explosions.

In September, 1995, the U.S. Geological Survey will be recording a series of 17 controlled explosions along a seismic refraction line from the Pacific coast to eastern Washington. This line will be occupied by approximately 250 USGS REFTEK seismic recording instruments and an additional 500 instruments of other types. The line passes 20 km to the south of the Centralia mine, as shown in Figure 8, and this provides an opportunity to further examine the evolution of the Rayleigh waves generated at the mine, and an opportunity to compare the delay-fired mining explosions with the simultaneously-fired USGS explosions. We are making arrangements to schedule the recorders to record one or two of the Centralia mine blasts.

References

Baumgardt, D. R. and K. A. Ziegler, Spectral evidence for source multiplicity in explosions: Application to regional discrimination of earthquakes and explosions, Bull. Seismol. Soc. Am., 78, 1773-1795, 1988.

Hedlin, M. A. H., J. B. Minster, and J. A. Orcutt, An automatic means to discriminate between earthquakes and quarry blasts, Bull. Seismol. Soc. Am., 80, 2143-2160, 1990.

Kafka, A. Rg as a depth discriminant for earthquakes and explosions: A case study in New England, Bull. Seismol. Soc. Am., 80, 373-394, 1990.

Maleki, H., P. F. Wopat, R. C. Repsher, and Robert J. Tuchman (eds.), Proceedings: Mechanics and Mitigation of Violent Failure in Coal and Hard-Rock Mines, Special Publication 01-95, U.S. Department of the Interior, Bureau of Mines, 1995.

Smith, A. T., High-frequency seismic observations and models of chemical explosions: Implications for the discrimination of ripple-fired mining blasts, Bull. Seismol. Soc. Am., 79, 1089-1110, 1989.
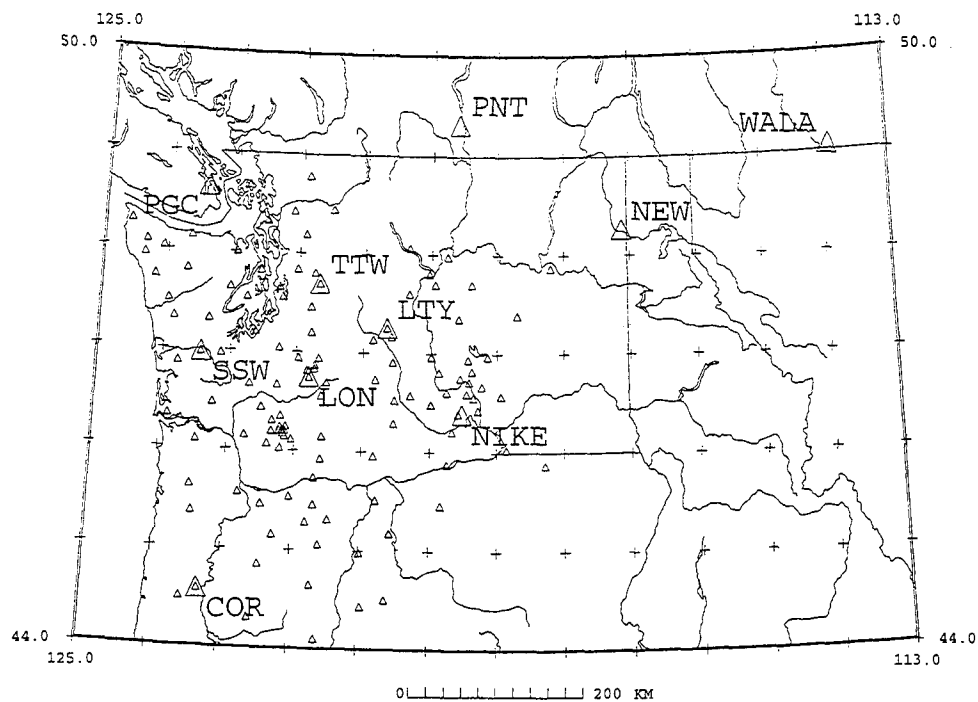
Figure 1. Location map of the Pacific Northwest Seismograph Network (small triangles), and regional broad-band seismic stations (large triangles with station names).
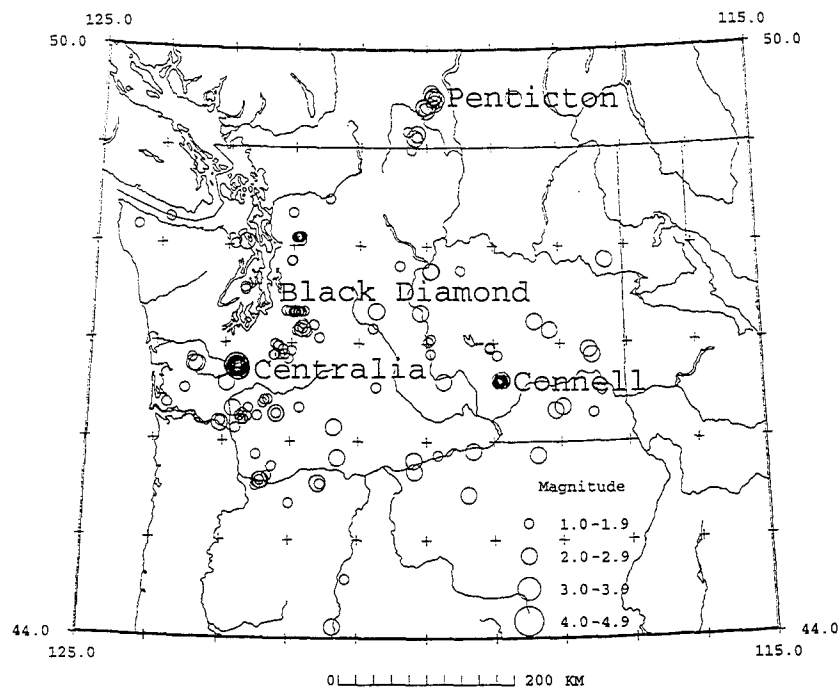
Figure 2. Location map of explosions 1994-1995 with coda-duration magnitudes larger than 1.5. Named sites are those we have obtained detailed blasting information from mine operators.
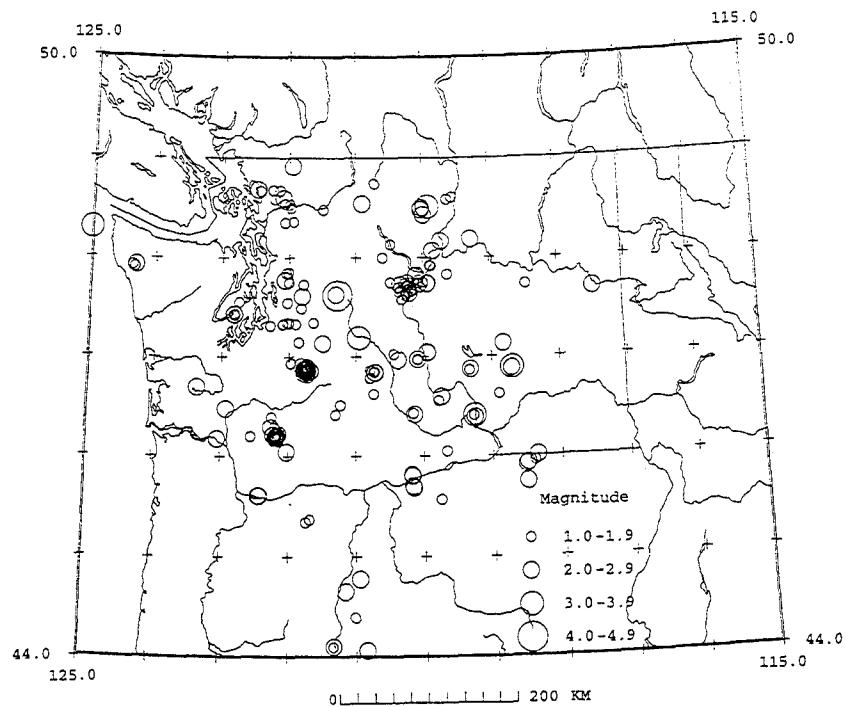
Figure 3. Locations of earthquakes 1994-1995 with coda-duration magnitudes larger than 1.5. Hypocenter depths for these events are less than 5 km.
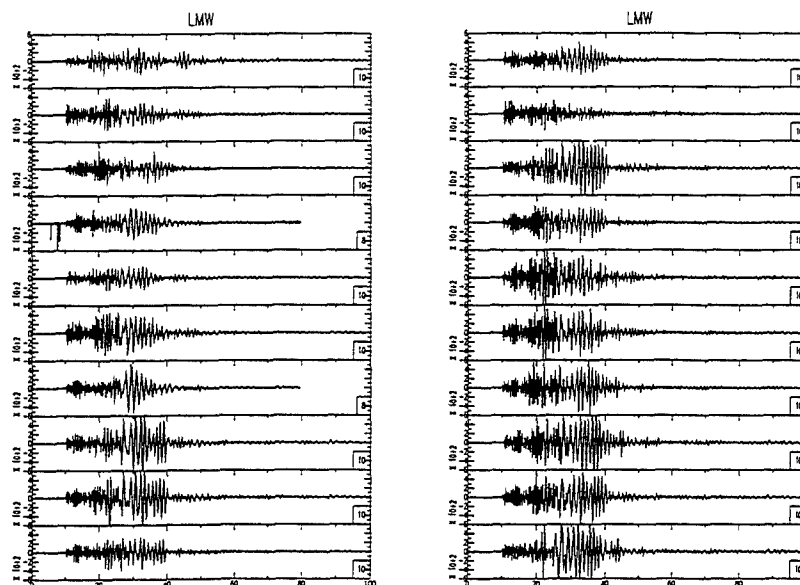
Figure 4. Seismic signals from the Centralia mine recorded at station LMW. The prominent, low-frequency signal on these traces is the Rg phase, indicating a shallow depth event.

Black Diamond Coal Mine
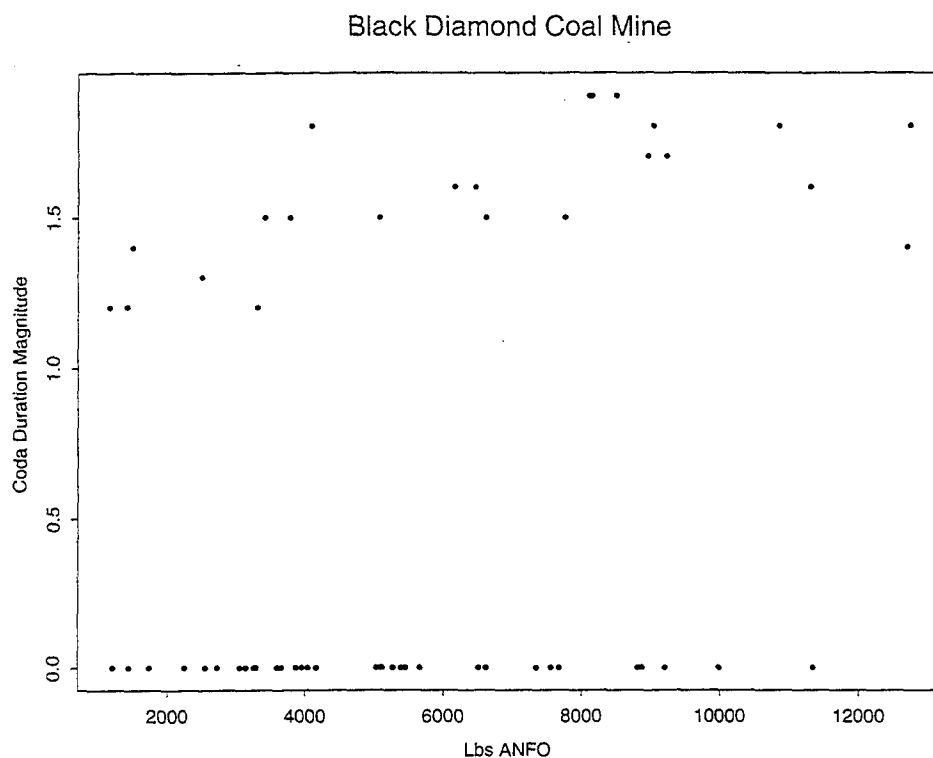
Figure 5. Relationship between total explosives used at the Black Diamond mine and the resultant coda-duration magnitude. Magnitudes of 0 indicate that the event was not located by the network.
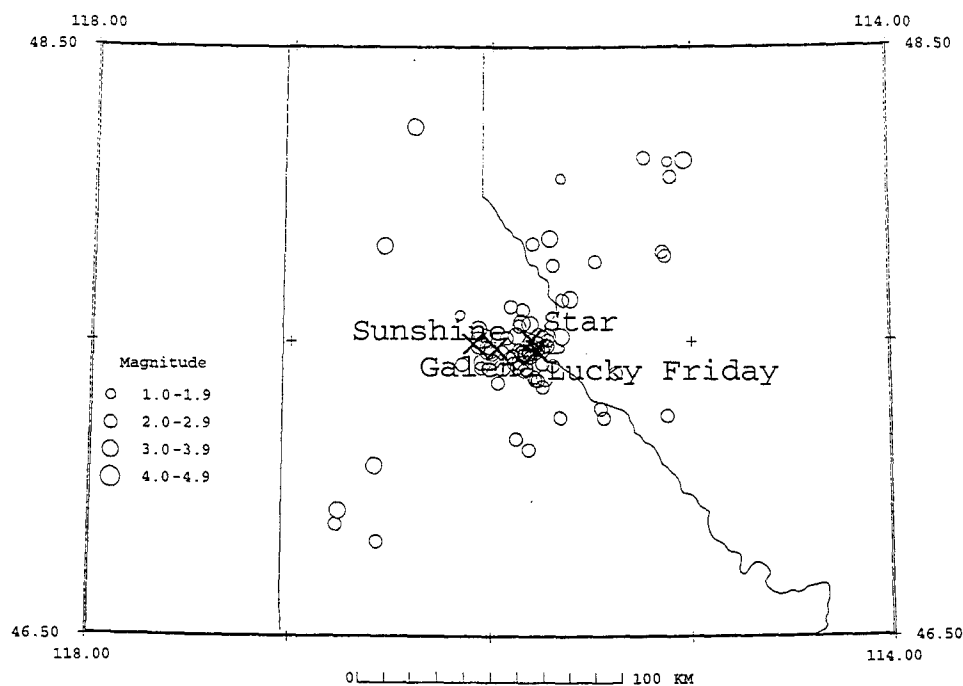
Figure 6. Location map of northern Idaho seismic events, 1983-1992. Most of the events in this region are triggered by the four deep silver mines indicated by the large crosses.

579
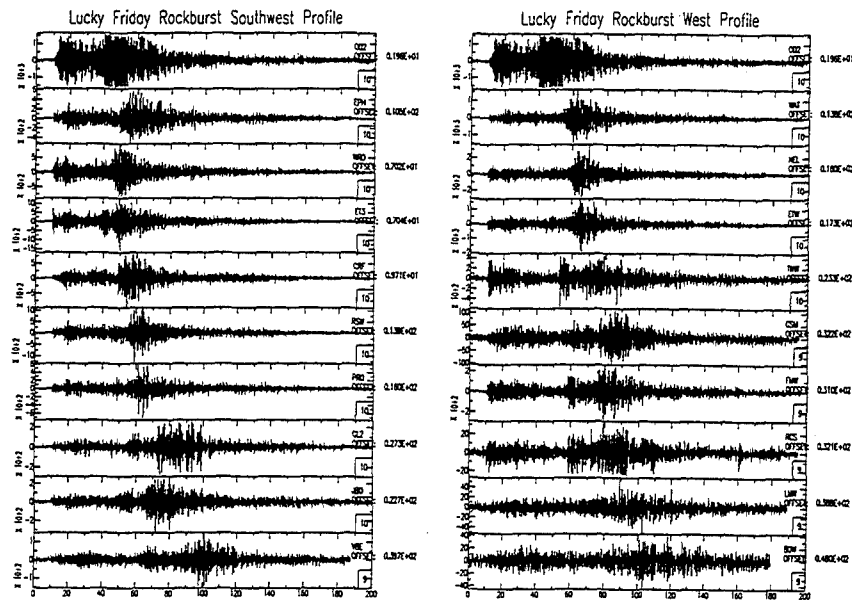
Figure 7. Seismograms from the August 16, 1994 Lucky Friday rockburst recorded from southwestern and western azimuths on the Pacific Northwest Seismograph Network.
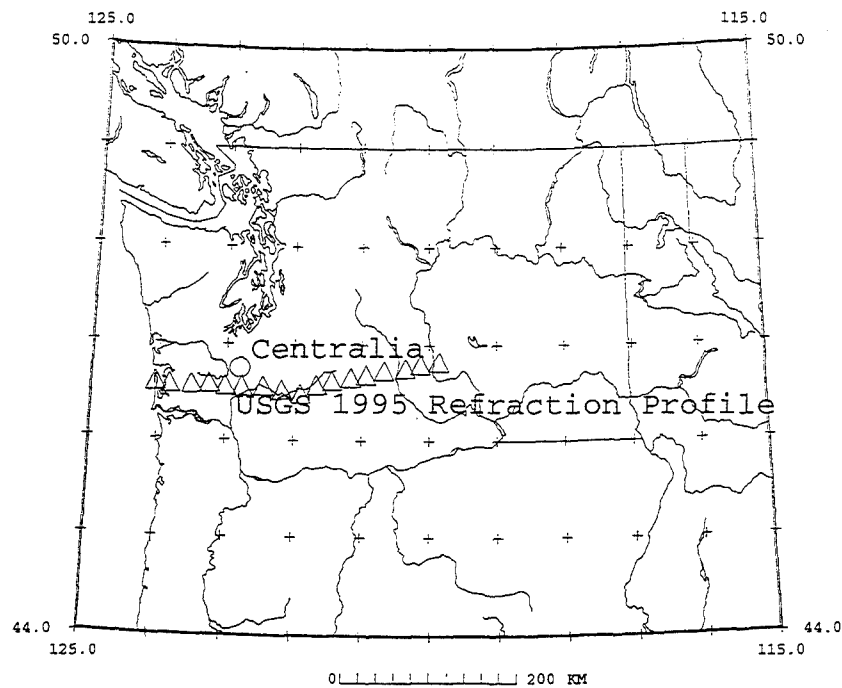
Figure 8. Planned U.S. Geological Survey refraction profile explosions and the location of the Centralia mine. The refraction line will be occupied by several hundred seismic recorders.

SEISMIC MONITORING OF ROCKBURSTS AND UNDERGROUND BLASTINGS FOR ASSESSING THE STABILITY OF DEEP MINE WORKINGS AT KOLAR GOLD FIELDS

C. Srinivasan,
Scientist & Head, Seismology Section,
National Institute of Rock Mechanics, INDIA.

ABSTRACT:

Rockbursts (RBs) are known to occur in and around deep mines like Kolar Gold Fields (KGF) in South India, since the beginning of this century. A rockburst is characterised by a sudden collapse of excavated region because of void created during the mining operation. At large depths the problem of RB is quite severe which is a major hazard not only to mining workers, but also to property, both on surface and underground.

In order to locate precisely the sources of RBs and also the blastings in the deep mines for investigation and assessment of stability of underground mine workings, current development in seismic recording technique has been used by establishing seismic network with 14 geophones and another microseismic network with 8 high frequency geophones at KGF. These systems have been providing accurate information of the strata stability and enabled the mining engineers to assess the safety of mines more reliably. This paper summarises the details of monitoring set-up, analysis of data together with some recent results.

Key words: Rockburst, Underground blast, Stability, Safety, Monitoring

INTRODUCTION:

One of the oldest mining areas in the world is KGF, where the mining activity reached a depth of 3.35 Kms. It is situated at 100 Kms east of Bangalore in South India bearing latitude 12° 57' and longitude 78° 16'. In this area, RBs due to sudden collapse of the underground workings have been a feature of mining operations since the very early days. Some major RBs have been recorded by various seismological stations in India and the magnitude of one of the largest RB in 1973 was 4.6 on Richter scale (Guha, et al 1981). Some such similar RBs of South African deep mines have disrupted the mining operations seriously and the same could be associated with large scale rock falls, rock slips in mining horizons (McGarr, 1971). Also the intense ground vibrations may, on the other hand, cause wide spread damages to residential and other structures in the mining area (Cook, 1976). To understand the phenomenon of a rockburst, considerable research has been carried out at KGF employing various techniques (Krishnamurthy, 1969). Seismic and microseismic investigations have been carried out since 1978 and 1983 respectively for assessing the day to day stability of mine workings and to forewarn the occurrence of a RB. This paper gives an over-view of the investigations carried out for monitoring RBs and the detection capabilitilites of the monitoring systems and its applications.

SEISMIC NETWORK:

For detailed knowledge of seismicity of the area, a seismic network was established with 14 geophones, 8 on the surface and 6 in the underground. The effective regional span covered by this network is 8 Km x 3 Km x 3 Km. The analogue data from these geophones are amplified and are continuously recorded on the 24-channel magnetic tape in the central recording laboratory located on the surface. The details are published by Subbaramu et al (1985) and Murthy et al (1980). The salient features of seismic instrumentation are given in Table-I.

Table - I

Salient Features of Seismic Instrumentation

Transducer	--	Geophone
Natural Frequency	--	7.5 Hz
Response Flat	--	Upto 400 Hz
Sensitivity	--	0.33 V/cm/sec at 0.6 critical damping
Coil resistance	--	380 Ohms
No. of field sensors	--	14 Nos.
Telemetry	--	Overhead cable with carrier frequency 540 Hz for F.M.
Cable specification	--	Four-core cable with mutual capacitance 0.055 microfarads/Km
Attenuation	--	1 dB/Km
Impedance	--	400 Ohms at 1 KHz
DC resistance	--	50 Ohms
Network dimension	--	6 Km x 3Km x 2 Km.
Electronic gain	--	80 dB
Data storage	--	1" mag.tape, 24 track
Tape speed	--	15.2 mm/sec
Mode of recording	--	FM analog recording with 540 Hz centre freq.deviation of 33.3 % for input ± 5V.
Pass band of replayed signal	--	5 ~ 170 Hz.

ANALYSIS OF SEISMIC DATA:

A visual helical recorder is hooked on to one of the geophones in the seismic network. Whenever an event is detected on helicorder, the relevant portion of the tape is replayed to obtain a hard copy of all channel data . From the time lag of arrival of signal at different locations, the source is located on the basis of least square error criteria.

ACCURACY OF SOURCE LOCATION:

The accuracy of source location depends on the reliable velocity model, set of geophones and the onset of seismic signals. The accuracy of onset obtained from seismograms is ±2 ms. A set of 8 geophones covering each area are selected and respective velocity models are used (Srinivasan, 1981). The accuracy of computed source location was verified with the actual co-ordinates of rockburst damage and blast locations. A comparison of computed location with actual location of known rockbursts showed that the two differ by about 30 meters in majority of the cases as can be seen in Table - II.

Table - II
Comparision of calculated and actual source locations
(Co-ordinates in feet)

No.	Date	Time	Computed Foci			Actual Foci		
			X	Y	Z	X	Y	Z
1.	25/12/90	19:49:06	21741	4212	8833	21871	4530	8859
2.	02/07/89	22:07:20	21735	4845	9115	21815	5008	8979
3.	07/06/89	19:55:30	21880	4830	9620	22120	4990	9203
4.	04/05/88	02:29:33	10724	5831	2976	10830	6252	3018
5.	03/05/88	04:00:08	10565	5742	3182	10730	6289	3112
6.	26/08/87	19:46:21	20287	4930	9225	20780	5075	9428
7.	09/07/86	11:32:29	11337	5882	3517	11357	6240	3594
8.	17/07/85	22:55:40	11554	5900	3938	11620	6205	3940
9.	27/05/85	00:15:50	21532	4240	9239	21807	4537	9545
10.	18/02/85	15:48:07	11573	5889	3825	11661	6204	3977
11.	16/02/84	04:09:22	17765	4721	9862	17850	5180	9825
12.	11/01/82	11:54:03	28028	4126	3040	28085	3939	2898

DEEP HOLE BLAST:

The deep hole blast has been carried out in the Champion reef mine at 113 level (3.35 Kms below surface) for improving the production. This blasting is different from other usual blastings carried out on a day-to-day basis. The maximum quantity of explosive used for this deep hole blast was 1000 kg. The signals picked up due to this blasting has been made use to obtain the velocity model. The results of improved source location due to velocity model in that region are shown in Table-III.

The seismic network has provided valuable data of rockbursts ever since it became operational. More than 11000 seismic events have been recorded and their sources located. They are now available in the form of a data base. The results of the study carried out so far can be summarised as follows:

1. Rockbursts could be located precisely with an accuracy of ±30 m and informed to the mine management for necessary precautionary measure.

2. Whenever rockburst occurred, special attention is being paid to the signals coming from that region to ensure that the affected region becomes relatively quiet.

3. Investigations have also given more insight for the better understanding of their causative mechanisms.

MICROSEISMIC NETWORK:

A network consisting of 8 high frequency geophones was installed at Osborne's shaft in the Champion Reef Mine in the vicinity of 300 meters from the stoping region which is highly stressed. This network has an aperture of 500 m X 300 m from 98 to 103 levels. The geophone response of this network extends upto 800 Hz with the natural frequency of geophones at 10 Hz. The specifications of the microseismic system is same as in Table-I with the only difference in the carrier frequency of 12 KHz (Subbaramu, et al.,1985) and (Nair, et al 1989).

ANALYSIS OF MICROSEISMIC DATA:

For overall assessment of strata stability during mining operations, one possible approach is to examine the rate of microseismic signals. For such study, the demodulated signals from the field are fed to an event detector. The threshold of event detection is set manually based on ambient background noise. Coincidence of event detection for any six channels is taken as a genuine event. It is found that a rockburst is likely to occur when the rate of microseismic event is low. The event rate is found to increase after a rockburst (Subbaramu et al, 1985).

Table - III

Results of Deep Hole Blast Experiment

Date & Time	Blast Location	Velocity (Old) Kms/sec	Computed Location	Velocity (New) Kms/sec	Computed Location
23.7.85	18500	6.2	18326	5.7	18417
20:18:57	5205	5.3	5061	5.5	5095
	10515	6.6	10325	5.95	10262
26.7.85	18500	6.2	18327	5.7	18420
14:42:25	5205	5.3	5005	5.5	5028
	10535	6.6	10562	5.95	10499
30.7.85	18500	6.2	18247	5.7	18339
20:10:01	5205	5.3	5040	5.5	5071
	10555	6.6	10668	5.95	10600

SOURCE LOCATION OF MICROSEISMIC EVENT:

The source location of microseismic event is an useful parameter for assessing the strata stability. To obtain quickly the location of microseismic event, a hardware unit has been installed which determines the arrival of signals by STA/LTA criteria. PDP 11/34 computer was installed for real time acquisition of event data and for on-line estimation of the event location and focal parameters of the event. The accuracy of source location is found to be $\pm$ 5 m.

Part of the analysis is based both on the location of the microseismic events and the rate at which they occur. Analysis of the microseismic events in the deeper level suggests that (Srinivasan et al, 1993).

(a) The area associated with the mine workings exhibits normal background microseismic activity

(b) Before the major rockbursts a distinct change takes place in the microseismic event which can be scaled in terms of microseismic precursor. Abnormal increase in the microseismic activity appears to be a reliable precursor of rockburst and

(c) The spatial distribution of microseismic events tend to cluster in the region of eventual failure.

DETECTION CAPABILITIES:

With the installation of different seismic and microseismic recording systems, the signals picked up by them are analysed to obtain the information regarding the signal charecteristics and detection capabilities of the recording systems. The details are discussed as case studies:

CASE STUDIES:

1. ROCKBURST ON 9.1.1984 AT 11:26:57 HRS:

The rockburst picked up by the geophones in the seismic network is shown in Figure-1. A clear seismogram where the signal to noise ratio is found to be high in all the cases except the 5th channel (Main shaft geophone). The hypocentre is 380 m from the first arrival. The signals show down or up (compression or dilatation) first motion at different geophones. It is interesting to note that the P and S wave signals are clearly distinguishable in the case of signals from G3, G4, G5 & G7 whereas in the other cases it is not very clear.

2. MICROSEISMIC EVENT ON 26.02.1984 AT 08:43:31 HRS:

This event has been picked up by 6 high frequency geophones and two geophones in seismic network as seen in the Figure-2. In the case of signals from the 98 level to 103 level geophones, high frequency signal content of 300 Hz to 500 Hz are observed, whereas the signals at 70th and 40th levels of Giffords shaft geophones are with low frequency signal content of 50 Hz to 100 Hz. The difference of first arrival P-wave signal to the farthest geophone in the microseismic network is found to be 16 ms. The time difference between first arrival to 70th and 40th levels geophones are 130 ms 280 ms respectively. The P and S waves arrival times are clearly distinguisable in the case of 70th and 40th geophone signals. This is due to long radial distance from the source of the event. In the case of high frequency signals P-wave signal is clear whereas S-wave signal is not clear. These high frequency geophones are very close to the source.

3. DEEP HOLE BLAST ON 15.5.1980 AT 22:16:06 HRS:

This blast was carried out at the extreme north of the seismic network at Golconda shaft. The quantity of explosive used was 1000 kg and the time delays were 125 ms. The seismogram as shown in the Figure-3 was run at a chartspeed of 100 mm/sec as against usual speed of 250 mm/sec for rockburst. One geophone was installed very close to the blast location and it responded first, but the signal quality is not good due to the ground being fractured nearby. The farthest geophone in the network G1 has also picked up the signal. The P-wave signals are found to be emersive (slow rise). The signals picked up at different geophones suggest that the wave has travelled in hetrogeneous medium. The onsets of this blast signal was made use to deduce velocity model in the Nundydroog mine area.

4. BLASTING ON 12.01.1984 AT 19:51:00 HRS:

A typical blasting signal obtained from microseismic monitoring system is shown in Figure-4. The signals due to normal blasting carried out very close to the geophone locations contain high frequency content from 200 - 300 Hz. First arrival and the last arrival time difference is around 16 ms. P-wave signals are clearly seen whereas S-wave signals are difficult to be identified. In the case of blasting in mines, different time delays are used due to which different P-wave signal arrivals are seen. The P-wave first motions are seen both upward and downward.

DISCUSSION:

The seismic network has picked up 373 earthquakes of different magnitude with epicentral distances ranging from 50 to 1500 Kms. The earthquake signal picked up by the geophones are found to be feeble and the difference in P & S wave signals is clearly reflected. In the case of rockbursts depending on the hypocentral distance the P & S waves can be seen. Here, only P-wave onset is used for computation of rockburst foci as S-wave onset is not clear. Microseismic event is very close to the source and it is very difficult to differenciate both the P & S-wave signals. Similarly in the case of normal blasting and deep hole blastings different P-wave arrivals are recorded due to different time delays used in blasting. The minimum and maximum detectable seismic and microseismic signal level are found to be 0.5 to 0.3 milli-micron and 500 and 300 milli-micron respectively. The discrimination of the source, whether it is a natural earthquake or a mine induced or a man made explosion is possible on the basis of the waveform and spectral energy distribution. Suitable recording system along with proper choice of sensor facilitates the recording of signals of different frequency for discrimination purposes. In the present case, the sensor and the recording sytem have been fabricated and installed to investigate exclusively mine induced seismic events. These signals are recorded in analogue mode.

APPLICATIONS:

From the voluminous data obtained from the seismic and microseismic network, they are further analysed for delineating high stress zones in mines and developed new approaches for long-range rockburst prediction and precursor pattern for short-range prediction of rockburst. The details are described (Srinivasan, 1993) and (Jha, et al, 1993).

In order to extend microseismic monitoring to other areas prone to RB in KGF, the most recent development in the data acquisition and analysis have been incorporated in a PC-386 based microseismic monitoring system, which has been installed in the Golconda shaft of Nundydroog mine. The system installed in the underground laboratory has the capability of detecting and processing upto 30 events per minute and has a facility for monitoring the source parameters including monitoring the waveforms and the FFT of events.

National Institute of Rock Mechanics has carried out microseismic investigation at Mochia mine of Hindustan Zinc Limited, India to monitor the induced microseismic activity with a view to evaluate overall ground stability for a safe deployment of workmen. This blast was one of the largest blast in the history of underground mining in India, where 145 tonnes of explosives were used in one go to extract around 0.55 million tonnes of high grade Lead-Zinc ore. Based on the energy release rate (ERR) of microseismic events monitored round the clock in the blasted area, the routine work operations were resumed in a phased manner after 13 days, by which time ERR in various levels started coming back to the normal background rate (Jha, et al, 1994).

FUTURE PLANS:

Seismic and microseismic investigations carried out in the KGF have provided extensive database. This data will be used to determine source parameters and focal mechanism of rockburst for understanding the rockburst phenomenon and to develop a suitable deformation model. Efforts are being put to improve upon the prediction algorithms for short range prediction. Fractal character of microseismic precursor to rockbursts will be studied in detail. The PC-based microseismic monitoring system could be extended to other mining areas, hydroelectric projects, nuclear power plant sites and other areas where ground control problems pose threats to regional stability.

REFERENCES

1. Cook, N.G.W., (1976) - Seismicity associated with mining, Engineering Geology Vol. 10., Nos 2-4, pp.99-122.

2. Guha, S.K., (1982) - Seismological study of the rockbursts at the Kolar Gold Field, India, Proc. IV Congress International Association of Engineering Geology, Vol.IV, New Delhi, India.

3. Jha, P.C., and Chouhan, R.K.S., (1994) - Long range rockburst prediction: A Seismological Approach. Int. J. Rock. Mech. Min. Sci & Geomech, Abstr. 31, No.1. Pp. 71-77.

4. Jha, P.C., et al (1994) - Blasting-induced seismo-acoustic anomalies as a measure of ground stability. Proc.Acoustic Emission Symposium NAWACE - 94 held at I.I.Sc., Bangalore.

5. Krishnamurthy, R., (1969) - Rockburst research in the Kolar Gold Fields. Proc. Symposium on use of Gauribidanur data for seismological research, Bhabha Atomic Research Centre, Seismic Arrary Station, Gauribidanur, pp.79-88.

6. Krishnamurthy, R., and Srinivasan, C., (1981) - Current seismic studies for the detection of rockburst in Kolar Gold Fields, Indo-German Workshop on Rock Mech., NGRI, Hyd'bad, INDIA.

7. McGarr, A., (1971) - Violent deformation of rock near deep level tabular excavations, seismic events, Bull. Seism.Soc.Am., Vol.61, No.5, pp.1453-1466.

8. Murthy, G.S., et al (1988) - Multichannel data acquisition and analysis system to monitor rockburst for assessing underground strata stability at Kolar Gold Fields. Proc. Vol.1, Int.Symp. on underground engineering.

9. Nair, G.J., (1989) - PDP 11/34 based microseismic monitoring system for Kolar Gold Fields, India, World meeting on Acoustic Emission, Journal of Acoustic Emission, S 266-267.

10. Nair, G.J., and Srinivasan, C., (1990) - Case study of microseismic data before and after major rockburst in Kolar Gold Fields - Implications to prediction and control. Proc. National Symposium on recent advances in Seismology and their applications, July 16-19.

11. Srinivasan, C., (1993) - Seismic and microseismic precursory signals for monitoring and prediction of rockbursts in Kolar Gold Fields, Ph.D. Thesis, Karnataka Regional Engineering College, Mangalore University, India (unpublished).

12. Subbaramu, K.R., et al (1985) - Seismic investigation of rockburst in the Kolar Gold Fields. Proc. 4th Conf. on AE/MS Activity in Geological structures and materials, Pennsylvania State University, USA, Oct 1985.

SENSITIVITY
4V \CM

GEOPHONE - 1

GEOPHONE - 2

GEOPHONE - 3

GEOPHONE - 4

GEOPHONE - 5

GEOPHONE - 6

←100 MS→

GEOPHONE - 7

FIGURE - 1 ROCKBURST ON 9TH JANUARY 1984 AT 11:26:57 HRS

TIME CODE

98 LEVEL   SENSITIVITY
           4V/CM

99 LEVEL   "

100 LEVEL   "

101 LEVEL   "

102 LEVEL   "

103 LEVEL   "

70 LEVEL   "

40 LEVEL   "

←100MS→

TYPICAL MICROSEISMIC SIGNAL ON 26-02-1984 AT 08:43:31 HRS

FIGURE 2

589

ONE SEC

GEOPHONE 1 SENSITIVITY 4V\CM

GEOPHONE 2 "

GEOPHONE 3 "

GEOPHONE 4 "

GEOPHONE 5 "

GEOPHONE 0 "

GEOPHONE 6 "

GEOPHONE 7 "

FIGURE-3 DEEP HOLE BLASTING ON 15-MAY-1980 AT 22:16:06 HRS

98 LEVEL SENSITIVITY 4V/CM.

99 LEVEL ,,

100 LEVEL ,,

101 LEVEL ,,

102 LEVEL ,,

103 LEVEL ,,

←100MS→

FIGURE - 4 BLASTING ON 12.1.84 AT 19:51:00 HRS.

PRACTICAL OBSERVATIONS OF US MINING PRACTICES AND IMPLICATIONS FOR CTBT MONITORING

Brian W. Stump, Geophysics Group, EES-3, Los Alamos National Laboratory

ABSTRACT

Man made and man induced seismic events associated with surface and underground mining operations produce seismic signals that might have to be identified when monitoring a Comprehensive Test Ban Treaty (CTBT). The importance of these sources to the monitoring process depend on the size of the seismic signal they generate and the degree of similarity these signals have to that expected from a contained nuclear explosion. Under the CTBT Research and Development Program sponsored by the DOE, an experimental task has been developed with the goal of identifying the seismological characteristics of sources associated with mining operations. The complete experimental program consists of three distinct components that include: (1) Characterization of mining explosions in hard and soft rock; (2) Investigation of source depth of burial effects; and (3) Characterization of rockbursts and collapses. Items 1 and 3 in this list relate directly to signals generated by mining and compose the topic of this review. Currently, seven experiments are planned under this program with initial results from a number of these reported in other presentations at this meeting (Pearson et al., 1995; Stump et al., 1995). This paper will focus on mining operations in one of the largest coal producing basins in the US, The Powder River Basin. This review is intended to illustrate the magnitude and complexity of mining operations that might produce seismic signals of large enough magnitude to be of interest to CTBT verification.

OBJECTIVE

Explosions associated with mining operations produce signals that will be detected by a world wide seismological monitoring system such as that currently being tested under GSETT-3. This point is illustrated in Figure 1 which is a summary of one of three explosions from the Powder River Basin that was detected on 11 Feb 95 and later located. The location (actual and calculated) of the largest event is illustrated in the figure with the associated error ellipse (which does not include the actual event location). This example demonstrates that to some degree these events will trigger the monitoring system and as such must be identified. This figure also illustrates that these types of events can provide useful practical information for calibration of the location capabilities of the monitoring system if we have ground truth.

Under the DOE CTBT Research and Development Program an experimental task . has been designed for quantifying and characterizing seismic signals that are generated by mining operations. This program is being conducted jointly by LLNL and LANL. The complete experimental program is more comprehensive including experiments associated with; (1) Mining explosions; (2) Depth of burial effects; and (3) Rockbursts/collapses. During FY95 seven experiments have been planned and are in various stages of implementation (Pearson et al., 1995; Stump et al., 1995; Jarpe et al., 1995). Data developed and cataloged under this program will provide the foundation for quantifying seismological effects from these different sources.

Implementation of this program has resulted in the development of close cooperative ties with the US mining industry. This cooperation has included input from companies such as The Thunder Basin Coal Company (ARCO), Newmont Gold Company, Cypress Amax Coal Company and Blasting Analysis International. As a result of this cooperation, much practical information has been gathered about US blasting practices and their contribution to the resulting seismic waves. This information can be used to assess the types of seismic signals expected from foreign mines.

The goal of this paper is to document some of the things learned in the initial phases of this program and indicate the direction of planned and ongoing experiments. The primary focus of this paper will be on blasting activities associated with the Powder River Basin for illustration.

RESEARCH ACCOMPLISHED

BASIN/MINE DESCRIPTION: The Powder River Basin is located in northeast Wyoming (Figure 1). It is a rich source of coal as well as oil and gas deposits. Within the Basin, which is approximately 60 km from east to west and 160 km from north to south, there are 22 active coal mines with an annual production each of over 5 million tons of coal (Jones, 1991). Figure 2 illustrates these mines, possible sites of explosive sources that one might have to monitor. The total coal production for the Basin in 1994 was estimated to be 225 million tons (Glass, 1995). Surface mining accounts for nearly all of the

coal recovery in this area because of the shallow depth of the coal. There are over 1 trillion tons of reserves that have been identified (Jones, 1991 and Glass, 1995). It is estimated by the local blasting community that between 300,000-400,000 tons of explosives are used annually in excavating the coal.

The Black Thunder Coal Mine is the largest in the region and is cooperating in the DOE field program. It provides an example of the types of blasting practices one might expect to find in a single mine. The southern portion of the mine with a dimension of 3.9 by 5.2 kilometers is displayed in Figure 3. Three of the four active pits in the mine are visible in this figure. The largest has a length of nearly 4 kilometers. The strike of the pits vary from east-west to north-south to northeast-southwest thus changing the orientation of the sources in these different pits to a fixed regional station. The coal seam that is mined in this region is buried at a depth between 33 and 49 m by weathered shales and sandstones and has a thickness of 18 m. The Pinedale Seismic Research Facility (PSRF) is 360 km to the southwest of the mine (Figure 1) and the US National Network Station, RSSD, is 150 km to the northeast.

BLASTING PRACTICES: Cast blasting is employed to remove a significant portion of the overburden above the coal. This process is followed by a drag line and bucket operation for coal recovery. The casting operation typically involves the largest explosions in the mine. Cast blasts with millisecond delays can contain between 2,000,000-5,400,000 lb. of explosives. These large explosions occur on the order of once every two to four weeks in this mine. Explosive emplacement holes for the cast blasting are as deep as 49 m and 27 cm in diameter. Each hole is loaded with ANFO/emulsion blends varying from 70/30 to 30/70 with approximately 5,000 lb. of explosives per hole. The holes are both top and bottom detonated.

As an example of a cast blast, a shot in the south pit is illustrated (Figure 3) that was recorded by the experimental program. In this case a total of nine rows were drilled in the pattern, each at 20 degrees from vertical which aids in free face stability. Blasting was completed with a non-electric system. The initiation of the system began on the west side of the front row and propagated to the east, front to back. Over 700 holes were detonated giving a total explosive weight of 3,500,000 lb.(1.75 ktons). The burden on the first row was 6.7 m with burdens between intervening rows as large as 11 m. The spacing between holes in a row was 9.8 m. The delays along one diagonal of the pattern were 125, 300, 500, 700, 900, 1000, 1200 and 1400 ms. Delays between individual charges in a row were 35 ms yielding a total source duration of over 4 seconds.

Coal shots, in contrast, are designed to fracture the coal after the overburden has been removed. These explosions as a result have shorter delay times, smaller total explosives and thus much shorter source duration. The coal shots occur on a daily basis within the mine with total explosive yield between 50,000 to 700,000 lb. With cast shots, coal shots and multiple pits a single mine can produce several different types of signals that can be observed at regional distances and thus must be identified. Both cast and coal shots are observed at the Pinedale Seismic Research Facility (personal communication Vindell Hsu).

SEISMOLOGICAL IMPLICATIONS: An example of possible implications of shooting practices on spectral amplitudes is given in Figure 4. The theoretical amplitude spectra of the impulse time series (design) for the example cast shot of 3,500,000 lb. (recorded during the experimental program) is displayed along with amplitude spectra for two theoretical shots, each with the same nine row pattern and 35 ms delay between charges in a row but with the total number of shots in each row halved (1,750,000 lb.) and halved again (875,000 lb.). The effect of total charge size is easily identified at the long period spectral levels below 0.2 Hz. It is interesting to focus on frequencies around 1 Hz where teleseismic body wave magnitude measurements are made. In this frequency band, the peak spectral amplitudes between the three shots of 1.75, 0.875 and 0.438 kilotons are nearly identical. This effect is a result of the shooting pattern used at the mine. With nine rows, very large delays are used in order to remove the burden prior to detonation of the later rows (the last row has a delay of 1400 ms). As the total number of explosions in a row are reduced, the total duration of the source does not decrease linearly but begins to be dominated by the large delays in the last row. This effect is illustrated by the total durations of the three shots in Figure 4 decreasing from 4320 to 2780 to 2010 ms.

The Non-Proliferation Experiment (NPE) was a fully contained (390 m depth of burial) single detonation of 2,850,000 lb. of an ANFO/emulsion mixture conducted at the Nevada Test Site (Denny and Zucca, 1994). The regional m_b for this event was 4.1, about a factor of 10 greater amplitude than typical Black Thunder cast blasts at regional stations if the observations were made along the same propagation path. Near-source observations like those made at the Black Thunder Mine were made for the NPE explosion as well. The expected surface velocities in the shales and weathered sandstones (~1800 m/sec) at Black Thunder are not significantly different from those where the surface measurements were made of the NPE. The NPE and the large Black Thunder Cast Shot provide observational data for making a qualitative comparison of a singly detonated, contained explosion representative of a nuclear shot and a typical cast shot.

Comparison of vertical acceleration time series and spectra is made in Figure 5. Near source observation from the cast shot was 450 m from the closest of the individual 5,000 lb. explosions and as far as 700 m. The near-source data from the NPE chosen for comparison is at a free surface range of 690 m (NPE at a much greater depth of burial). The four second duration of the cast shot is apparent in a comparison of the two time series. The effects of individual charges are seen in the waveform when the cast shot time series is expanded. The NPE waveform is quite impulsive and short in duration. The peak amplitude from the well coupled NPE explosion is slightly smaller than the peak amplitude recorded at later times in the cast shot when superposition and constructive interference of the individual charges begins to boost the amplitudes. The spectra from the two observations are compared in the bottom of Figure 5. The NPE has nearly an order of magnitude greater spectral amplitudes in the frequency band of 0.5 to 2 Hz, consistent with the regional m_b

differences. At the highest frequencies the mining shot has larger amplitudes. At the longest periods the two spectra converge although this is the region where the signal to noise ratio in the acceleration data for both data sets is decreasing. The convergence at the longest periods is consistent with the theoretical impulse spectra displayed in Figure 4 which argues that only periods longer than the total duration of the source will reflect the total charge size.

RECOMMENDATIONS AND FUTURE PLANS

Results from analysis of The Powder River Basin and The Black Thunder Mine illustrate the different types of explosive sources one might expect from a large cast blasting operation. The GSETT-3 detections on 11 Feb 95 indicates that in some circumstances, these sources will be detected in a monitoring regime. Comparison of cast blast waveforms with single shot data indicates that these cast blasts are deficient in long period energy resulting in reduced magnitudes relative to concentrated charges. The variety of blasting practices within the Black Thunder Mine indicates that multiple source types can be expected from a single mine. Within the Powder River Basin there are an additional 21 mines, many of which are also using explosives, complicating the identification process. Cooperative work with AFTAC is attempting to quantify relationships between the blasting practices in the mine and the resulting regional signals.

Additional experimental work associated with mine related seismicity includes blasting in hard rock as well as collapse events associated with underground operations. These parallel efforts will relate equivalent near-source physical processes in these other environments to the resulting regional seismic signals. This process will allow the assessment of monitoring challenges imposed by man made or man induced events.

REFERENCES

Denny, M. D. and J. J. Zucca, 1994. Introduction: DOE Non-Proliferation Experiment, *Arms Control and Nonproliferation Technologies, First Quarter 1994.*

Glass, G. B., 1995. Wyoming Geo-Notes, Wyoming State Geological Survey.

Jarpe, S. P., P. Goldstein, B. Moran and L. A. Glenn, 1995. Preliminary Report on the Implications of Mining Practices in an Open-Pit Gold Mine for Monitoring of a Comprehensive Test Ban Treaty, UCRL-ID-121228.

Jones, R. W., 1991. Coal Map Of Wyoming, State of Wyoming Map Series 34.

Pearson, D. C., B. W. Stump, D. F. Baker and C. L. Edwards, 1995. The LANL/LLNL/AFTAC Black Thunder Coal Mine Regional Mining Blast Experiment, PL-TR-95-2108

Stump, B. W., D. C. Pearson, C. L. Edwards, and D. F. Baker, 1995. The LANL Source Geometry Experiment, PL-TR-95-2108

Three Events Located by GSETT3 on 11 Feb

Largest Recorded Teleseismically

Error Ellipse Does Not Include the Mine

Explosion was 5,340,290 lb

No Magnitude Declared

Station	Dist	Phase(s)
PDAR	3.16	Pn,Lg
WALA	7.38	Pn
ULM	8.98	Pn,Lg
FCC	16.18	P
YKA	18.97	P,tx
WHY	23.87	P

Location error of ~75 km covering 1192 km².

Gillette

Mine

Scale in km
0   25   50

MONTANA

WYOMING

IDAHO

UTAH

COLORADO

NEBRASKA

SOUTH DAKOTA

RSSD (USGS)

Rapid City

Cheyenne

Casper

Rock Springs

Pinedale Seismic Research Facility

Powder River Basin

MINE

Scale in km
0   50 100   200

Figure 1: Powder River Basin with location of 11 Feb 95 GSETT-3 Event
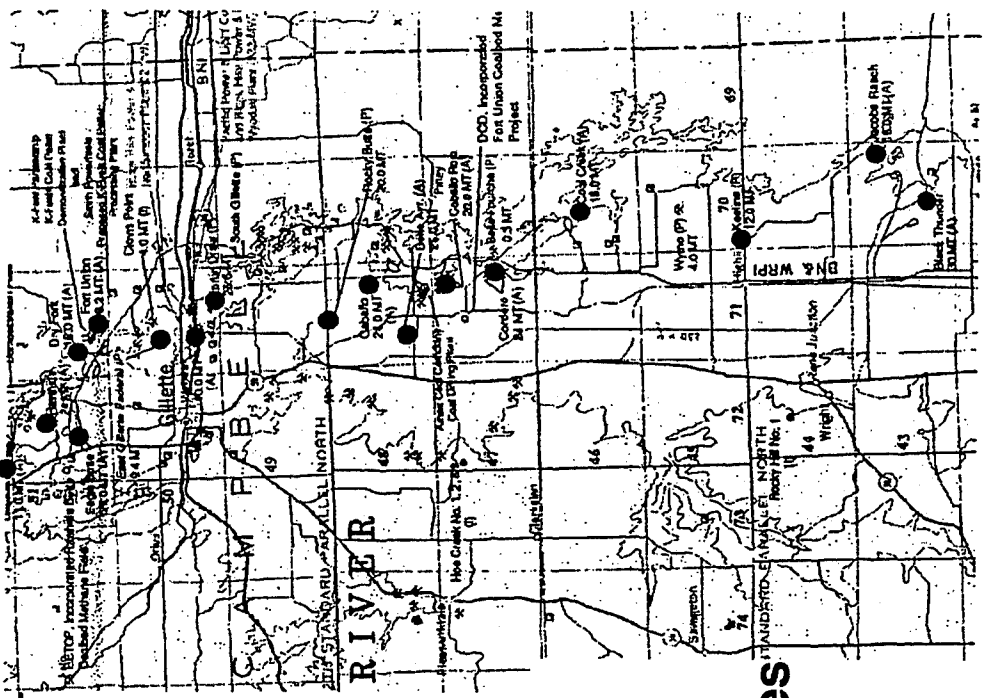
- ○ 225 MTons Coal in 94
- ○ 22 Mines > 5 MTons
- ○ 300-400,000 Tons Explosives
- ○ 99% SURFACE MINING
- ○ 1.46 Trillion Tons Reserve

Figure 2: Surface Coal Mining Operations in the Powder River Basin

Figure 3: Overhead image of the southern portion of the Black Thunder Mine.

Design Time Series
(15 Dec 94 Cast Shot)

Full, Half and Quarter Cast Array Response
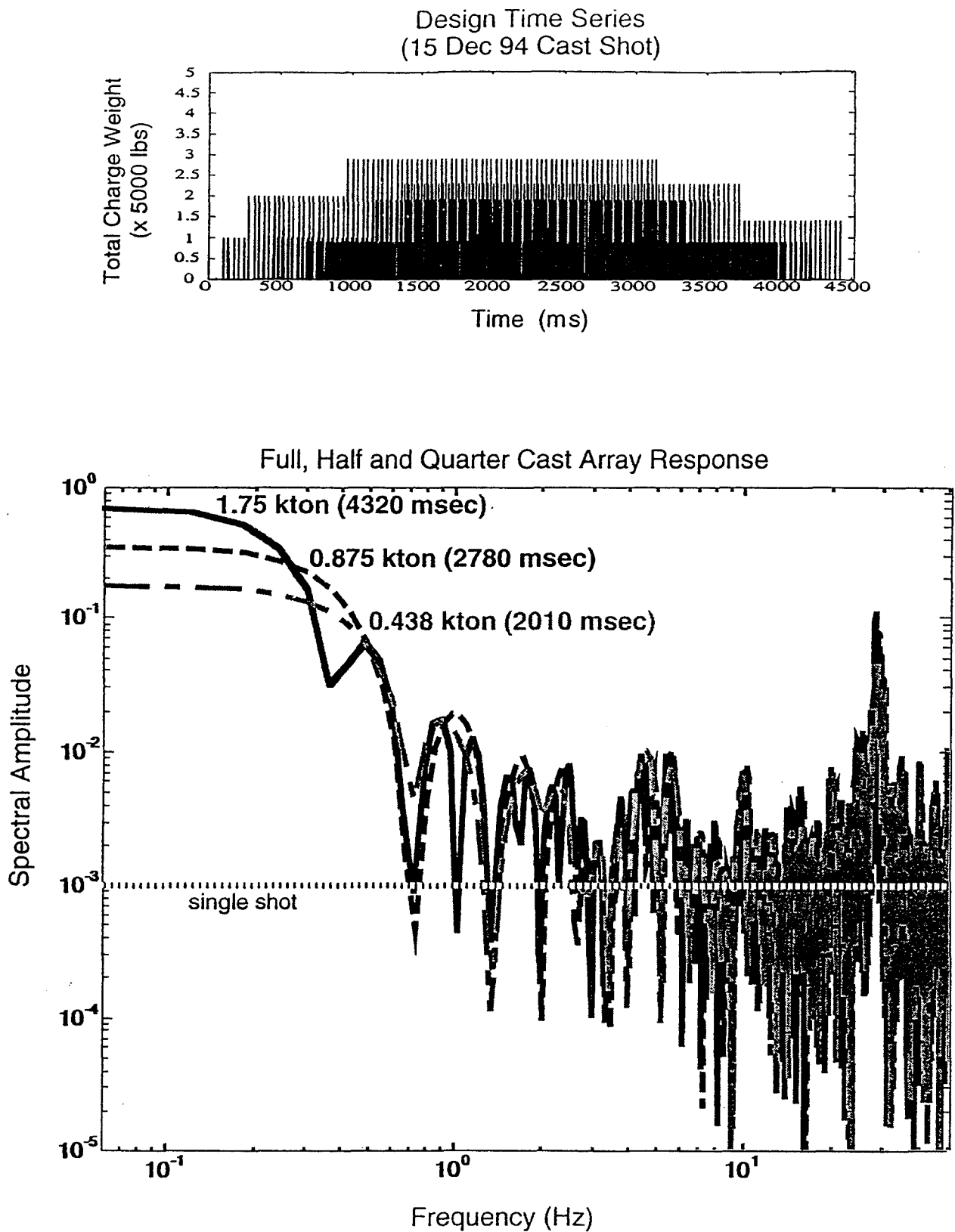
Figure 4: Impulse time series for the 1.75 kton cast blast (top) and spectra for this explosion (bottom) and two others each half the size.
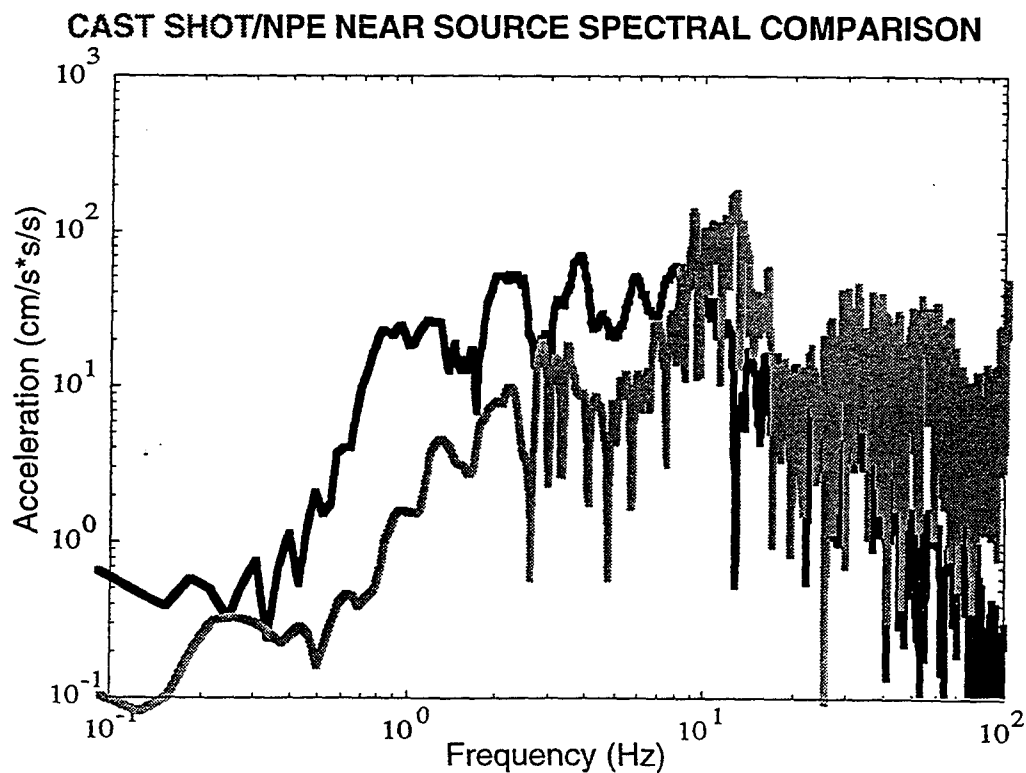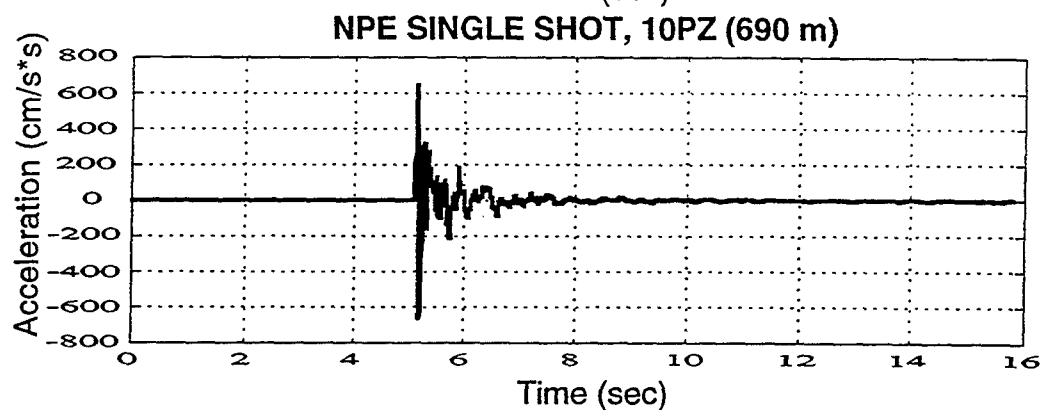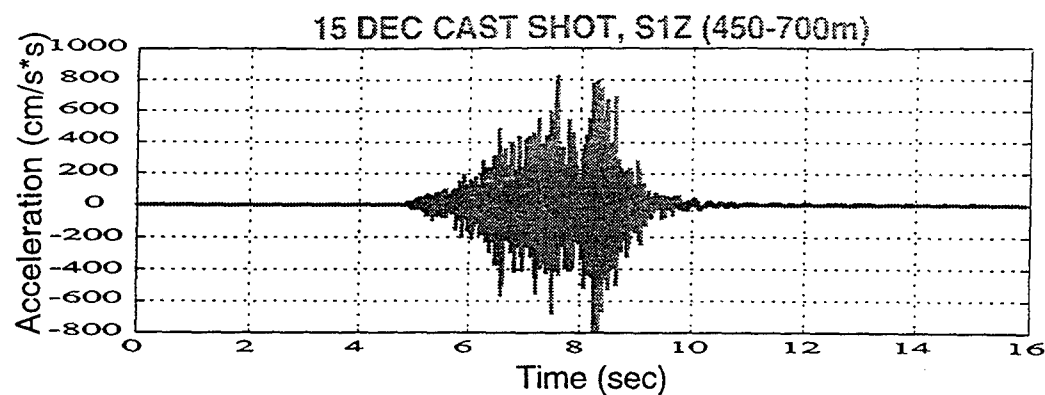
Figure 5: Comparison of near-source accelerations from a Cast Blast (top) and the NPE (bottom).

Seismic sources and structure in Iran and the Caucasus from Joint Seismic Program Array Data

G.A. Abers[1], W.-Y. Kim[2], and A. Lerner-Lam[2]
[1]Department of Geology, University of Kansas, Lawrence KS 66045
[2]Lamont-Doherty Earth Observatory of Columbia University, Palisades NY 10964

ABSTRACT

Amplitudes of seismic waves recorded at the Caucasus network, along the north flanks of the Greater Caucasus, are measured and analyzed for attenuation characteristics. From one year of observation, 96 events between 1° and 10° from the network provide stable measures of RMS *Pn*, *Sn*, *Lg*, and late coda amplitudes. Measurements were taken from seismograms filtered at several narrow frequency bands centered from 0.5 to 8.0 Hz, where signal levels are highest. Our results confirm previously-inferred spatial variations in *Sn* and *Lg* attenuation, that the Greater Caucasus marks an abrupt boundary between the high-*Q* Russian Platform and a region of exceedingly poor *Sn* and *Lg* propagation within the collision belt. Paths that cross large Quaternary volcanic provinces, along the Greater Caucasus, seem most affected. Amplitude ratios show the largest regional differences in the 1-2 Hz range and decrease at higher frequencies, and indicate complicated changes in the mechanism of attenuation between shield and tectonic paths.

For a given path the RMS amplitudes of the *Lg* group and late coda phases predict magnitudes as well as can be expected from *mb* uncertainties. However biases of 1.0-1.5 magnitude units are seen for RMS amplitudes along different paths, at frequencies higher than 1 Hz. Variation is much reduced by taking 3-component and network averages of amplitude measurements.

Keywords: attenuation, regional seismic waves, magnitudes, Caucasus region

This Page
Intentionally Blank

OBJECTIVE

We evaluate and characterize seismic data from digital network and array sites in and around the Former Soviet Union, in order to provide new constraints on seismic wave propagation characteristics in the Caucasus Ranges, Middle East and Iranian Plateau. Strong changes in the attenuation and velocity behavior of seismic waves are associated with the mountain belts here, and make it difficult to infer wave behavior from experiences gained within stable cratons. Seismograms from the JSP-Caucasus Seismic Network collected since 1991 include a large number of local and regional events in the region. These waveforms are used for assessing the amplitude and phase of major wave groups along regional paths, and constraining earth structure beneath the network. Results provide information on the behavior of common event discriminants and detection thresholds for regional paths.

RESEARCH ACCOMPLISHED

Severe changes in wave behavior are observed between paths that cross the Caucasus and other Alpine-Himalayan mountain belts, and those that do not (Figure 1). These changes represent substantial attenuation of phases often used to discriminate explosions from earthquakes and to estimate event size and type, such as Lg and other high-frequency surface-related phases. Work to date has concentrated on quantifying the behavior of seismic waves as they cross the Caucasus, mostly by examining phase amplitudes for events within 10° of the Caucasus Seismic Network (CNet). Other facilities, such as the Geyokcha, Turkmenistan array, the array in Garni, Armenia, and the Iran Long Period Array also provide digital seismograms that can give complementary information.

Caucasus Network

The Caucasus network was established in 1991 through the Joint Seismic Program, as a cooperative project between Lamont-Doherty and the OME-Obninsk group (Abers, 1994). The network, based in Kislovodsk (KIV), consists of 5-6 digitally telemetered 3-component sensors with 0.2 Hz natural periods, digitized at 60 sps. These stations are on the north side of the Greater Caucasus range, and straddle the transition from the Russian Shield to the Caucasus collisional zone. The northern stations lie on flat-lying, poorly consolidated Neogene sediments, while southern stations lie on tilted, well-lithified Mesozoic sediments. The response of the Kinemetrics SV/SH sensors are well-suited for analysis of local and regional seismic waves, although prior to mid-1993 triggering windows usually did not include S or Lg for events farther than 10-15° from the network. We are in the process of extracting seismograms from a continuously-recording backup system in order to produce a waveform data set suitable for these longer distances. Data for 1992 were picked and associated by the Joint Seismic Program Center (Harvey et al., 1994) and subsequent seismograms are distributed through IRIS. A total of 645 events were associated for 1992 (292 in the PDE), and 327 were associated with the PDE catalog in 1993 .

RMS Amplitudes of Regional Phases

We have measured RMS amplitudes of P-group, S-group, Lg and similar, and late coda from recordings of events 1-10° from CNet. Because the CNet time series contain occasional spikes and, at some stations, frequent telemetry gaps, spectral methods are often problematic. More robust amplitude estimates are made from RMS amplitudes of multiple-narrow-band signals. For each seismogram, a series of narrow-band filters are constructed and applied centered at 0.5, 1.0, 2.0, 4.0, and 8.0 Hz. For each channel and frequency, RMS amplitudes are made in several time windows: pre-event noise, Pn, Sn, Lg, and coda. Pn and Sn windows extend from 4 s before the predicted phase onsets to 0.25 times the $S-P$ time past the onset, up to 25 s in total length. The so-called Lg window covers the period in group velocity between 3.6 and 2.6 km/s; the range extends to slower than normal group velocities to include the dominant slow short-period surface phases observed for shield paths (Figure 1). The coda window is centered at twice the S travel time after
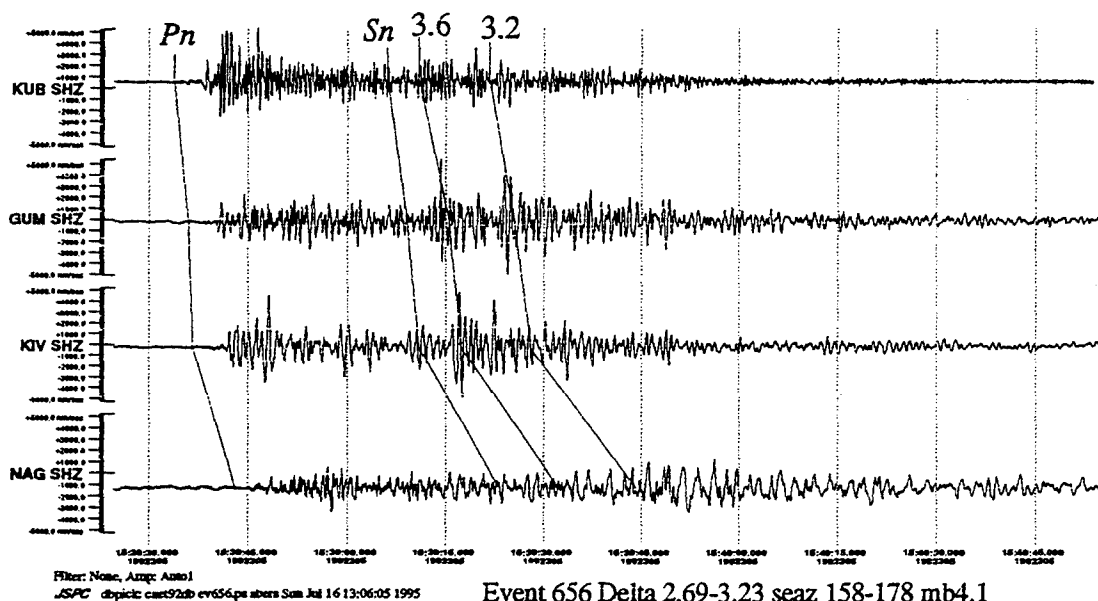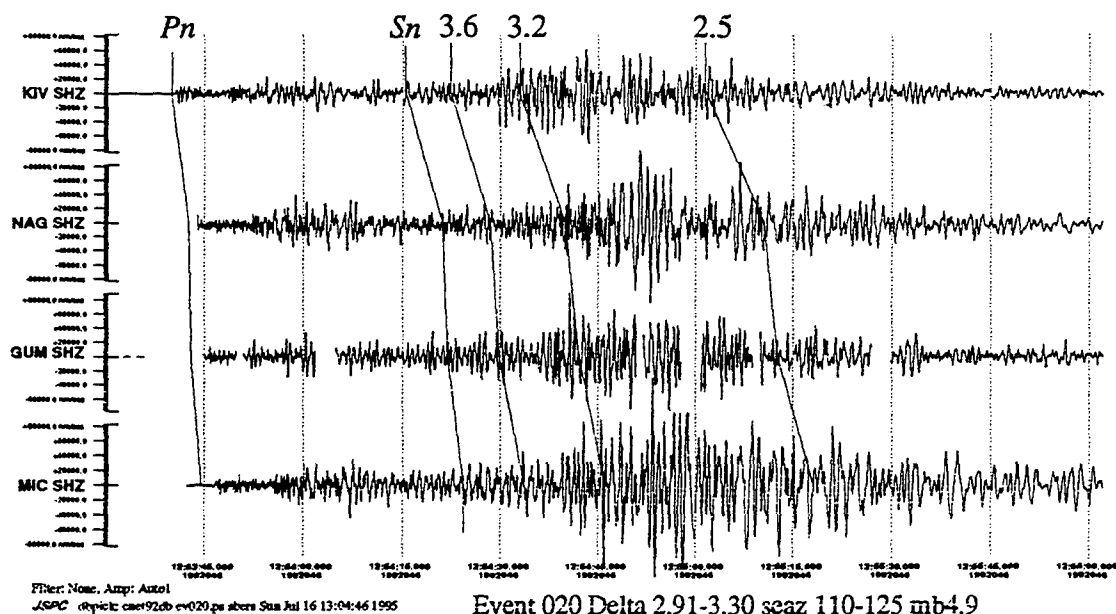
Figure 1. Records from two events from ~3° distance recorded at the Caucasus network. Waves for event 020 in Dagestan, top, travel largely on the Russian platform margin while waves for event 656, bottom, cross the Greater Caucasus and Kura basin. Seismograms are labeled by arrivals of *Pn*, *Sn*, and group velocities in km/s. Note absence of late-phase energy on lower traces, particularly in and after *Lg* window (after 3.6 km/s). Event 020 shows small *Pn* relative to *Sn* and late phases, and slow high-frequency surface waves (<3 km/s).
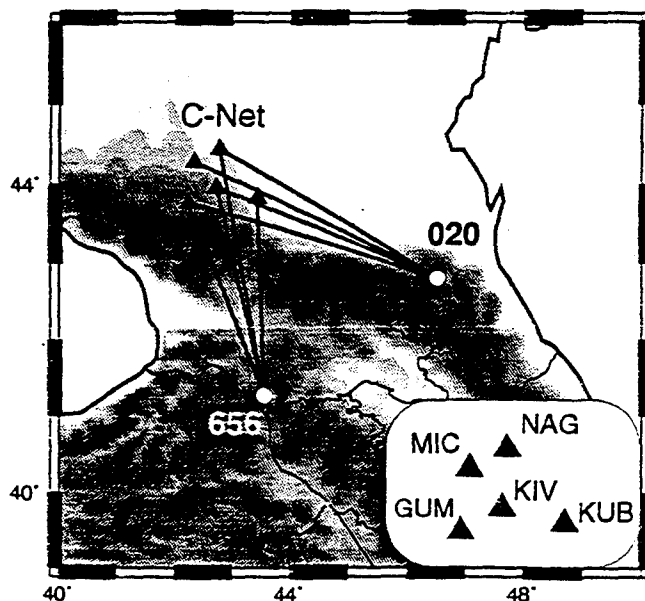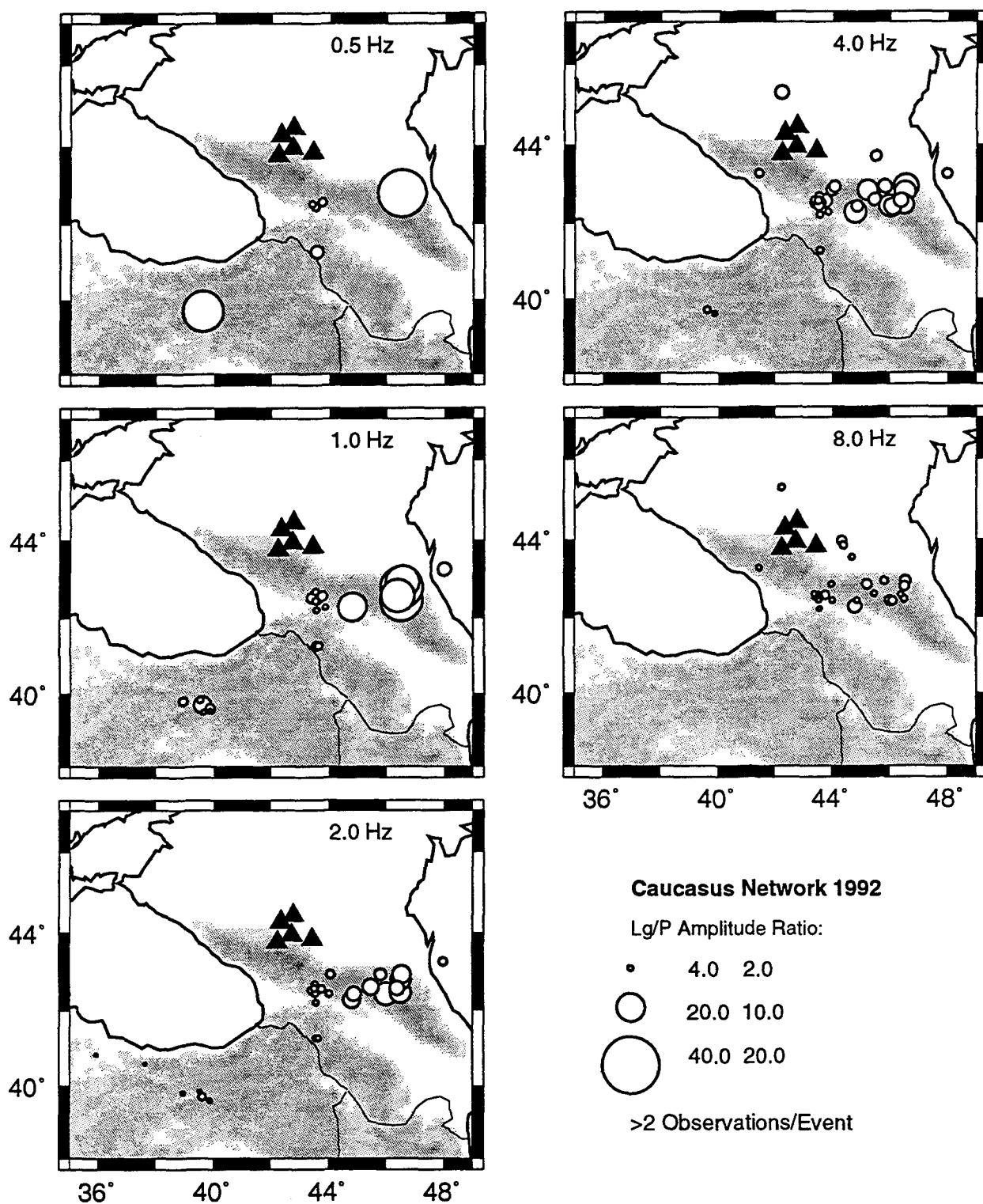
Figure 2. Ratios of RMS-Lg amplitude to P amplitude for events 1-10° from CNet, 1992. Each panel represents a different frequency seismogram, labelled top. Three-component RMS amplitudes are averaged over the network geometrically, and only shown when 3 or more stations are used. Symbols are centered on events. Size of symbols scales to amplitude ratios, as by key at lower right (left-hand and right-hand numbers are for left and right column of figure, respectively).

605

the origin time, and is 40 s in duration. Only segments that were more than 4 s long are used, and only those where dropouts constituted less than 10% of the time window. These requirements allow some data where short trigger-windows or occasional dropouts might be present, and because the RMS measurements are integrated quantities the measurements are still valid. All seismograms are visually culled for other, unusual problems.

An RMS combination is made of measurements from each 3-component seismogram set, for as many components as were usable. Signal-to-noise estimates are made on these combined sets, and records with low (<2) signal level signals are eliminated. Noise estimates are made from each filtered seismogram, where possible, or instead taken as the maximum observed RMS noise level for a particular channel and frequency. Amplitudes are corrected in an RMS sense for incoherent noise contamination. Finally, amplitudes are averaged geometrically across the network for each event (and across all events for each station) to give a network-average set of amplitude ratio estimates. Only averages of three more stations are kept. These averages were considerably less variable than single station estimates.

Results

In map view (Figure 2) large variations in amplitude ratios are seen between paths that cross the crest of the Greater Caucasus and those that do not, and indicate extensive *Lg* blockage and *Sn* attenuation throughout the actively deforming parts of the Caucasus belt. Such behavior was seen by Kadinsky-Cade et al. [1981], although they did not have access to stations north of the Caucasus and were limited to analog records. Using some of the same Caucasus Network data Rodgers et al. [1994] saw a region of poor *S* and *Lg* propagation beneath the Caucasus. Our results document the frequency dependence of this phenomenon, and (similar to Rodgers et al.) show that the boundary of the attenuative region is sharp and lies beneath the core of the Greater Caucasus. Results are most consistent for the *Lg* window although the *Sn* window behaves similarly. Differences are most pronounced at lower frequencies (Figure 3).
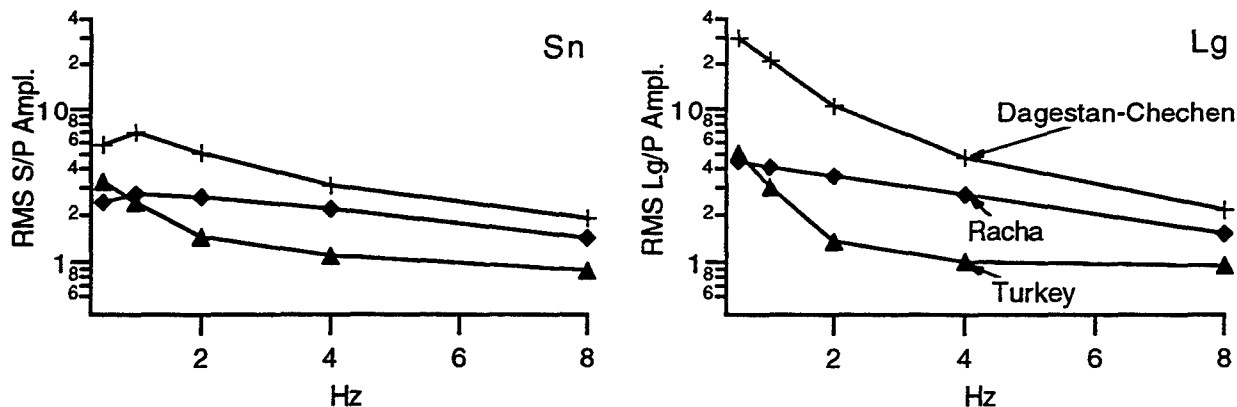
Figure 3. Variation in RMS amplitude ratios as a function of frequency for three regions. Regions on Figure 4.

Paths from events in the Dagestan-Chechnya region (DA, Figure 3,4) are roughly parallel to the strike of the ranges and follow the margin of the mountains and traverse thick foredeep sediments north of the Greater Caucasus. These paths are also characterized by slow (~2.9-3.0 km/s) high-frequency Rayleigh waves (Figure 1). Large amplitudes are seen most frequencies, particularly from 0.5 to 2 Hz, and may reflect the a layered, relatively undisrupted nature of the paths.

Paths that cross the Greater Caucasus show very low-amplitude *S* and *Lg*-related phases relative to the *P* arrivals, even for relatively short paths. Many events are roughly 200 km distant, near the 1991 Racha earthquake zone (Triep et al., 1995), yet show amplitude ratios 3-10 times lower than for Dagestan paths. Waves from these events traverse the active deformation front of the Greater Caucasus, and the region of Plio-Quaternary volcanism near Mt. Elbruz at the SE edge of the network. Paths from events farther south that traverse the Lesser Caucasus show very small-amplitude late phases.

Absolute RMS amplitudes for a given region correlate well with event size measures such as m_b (Figure 4) although the scaling parameters vary systematically between regions. The m_b values come from the PDE for region TU, and from the CNet Information Product for closer events (so that some coupling with RMS Pn is expected). In general correlation coefficients are 0.8-0.9 for each population between 1 and 4 Hz. Events from Turkey show RMS amplitudes of late phases a factor of 10-100 low at 2 Hz compared with shield paths, with the discrepancy increasing with frequency. Some of the best correlations (>0.9) come from late coda amplitudes, which have long been used for magnitude determination in the Caucasus (Rautian et al., 1979). The variation from region to region corresponds to biasses of 1.0-1.5 magnitude units in the ability of 2-Hz Lg, Sn, or coda to predict mb.

Variation is also seen between stations consistently for all events (not shown). The stations farthest onto the platform show consistently large Lg/Pn and Sn/Pn amplitude ratios by a factor of 1.7-2.5 relative to stations at high elevation, as well as the largest absolute amplitudes. The large amplitudes can be attributed to low velocities of Neogene near-surface sediments that lie beneath the platform stations.

CONCLUSIONS AND RECOMMENDATIONS

Reduction in high-frequency seismic wave amplitudes across Eurasian collision zones appears to be associated with a highly localized boundary that follows the northern margin of the Greater Caucasus. Events in the Racha region, on the southern flanks of the Greater Caucasus, show reduction in Lg/P and S/P amplitude ratios comparable to more distant events that cross the entire region. Although amplitude ratios seem stable for paths from individual regions, as evidenced by the good correlations with m_b, the attenuation effects are highly variable. A spatially-varying attenuation model for the region is necessary in order to utilize Lg/Pn and Sn/Pn discriminants as these amplitude ratios vary by over a factor of 5-20 between different paths. The amplitude reduction, seen throughout the 0.5-4 Hz band, suggests that signals will be small for small regional events in the Caucasus-Iranian Plateau region, relative to comparable paths along shield sites. Robust measurements seem to require both 3-component analysis and averaging over several nearby stations, both done here. Future work should include developing a data set of long seismograms appropriate to studying Lg and S-group energy at 10-20° distances, quantifying frequency-dependent Q in a way that can be used for path calibration, and adding complementary observations from other networks and arrays.

REFERENCES

Abers, G.A., The Caucasus Seismic Network, *IRIS Newsletter, 13*, 1994.

Harvey, D, and others, Caucasus Network Information Product Triggered events from January 1, 1992 to November 9, 1992, Version 1.0, IRIS-JSPC, 1994.

Kadinsky-Cade, K., M. Barazangi, J. Oliver, and B. Isacks, Lateral variations of high-frequency seismic wave propagation at regional distances across the Turkish and Iranian plateaux, *J. Geophys. Res., 86*, 9377-9396, 1981.

Rautian, TG, VI Khalturin, and IS Shengeliya, Seismic coda envelopes and assessment of earthquake magnitudes in the Caucasus, *Phys. Solid Earth, 15*, 393-398, 1979.

Rodgers AJ, TM Hearn, and JF Ni, Pn, Sn and Lg propagation in the Middle East, *EOS Trans AGU, 75(44)*, 463, Fall, 1994.

Triep, E., G.A. Abers, A. Lerner-Lam, V. Mishatkin, N. Zhacherenko, and O. Staravoit, Active thrust front at the south slope of the greater Caucasus: The 29 April, 1991 earthquake and its aftershock sequence, *J. Geophys. Res , 100*, 4011-4034, 1995.

2.00 Hz Event Averages
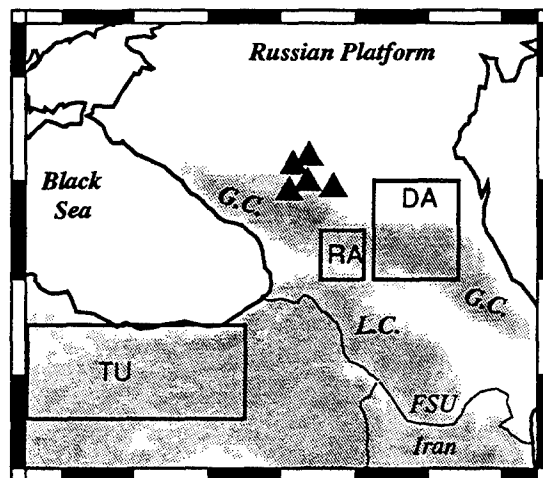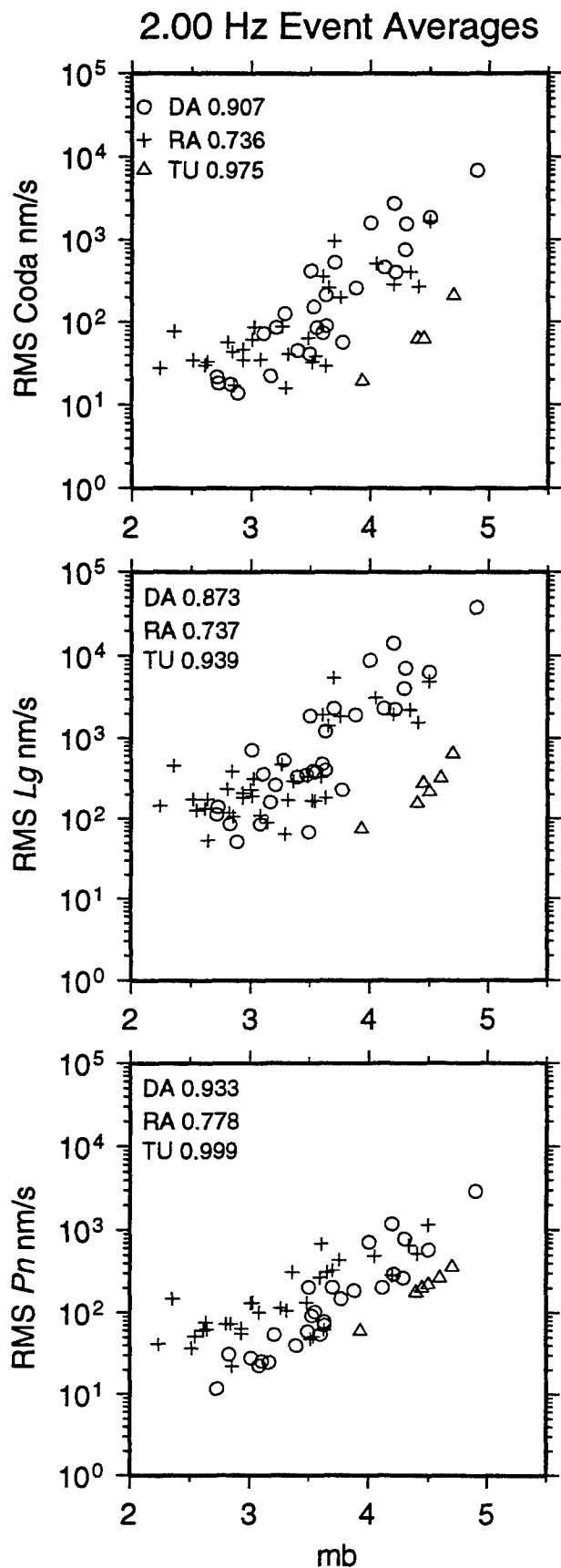
Figure 4. Right shows three-component RMS amplitudes of 2-Hz wavetrain vs. *mb* estimates. Coda is 15-30 s window centered at twice the *S* wave travel time, *Lg* window spans 3.6 to 2.6 km/s group velocity, and *Pn* window extends to 25% of *S-P* time. Signal-to-noise ratios exceed 2.0 for all measurements, and measurements are averaged over 3 or more network stations. Different symbols correspond to events from different regions as labelled: DA - Dagestan-Chechnya; RA-Racha aftershock zone; TU-Turkey. The *mb* value is taken from PDE for TU and from JSPC measurements on Caucasus events (Harvey et al. 1994) for closer regions. Correlation coefficients between log(amplitude) and *mb* are also shown in upper left of each plot. Correlations for individual paths are good although significant variations exist between regions. Amplitudes are corrected for cylindrical geometric spreading to nm/s at 100 km. Map, top right, shows region areas as well as: G.C. - Greater Caucasus, L.C. - Lesser Caucasus.

Examining Near-source Effects in the Far Field

F. N. App, R. J. Bos, T. N. Dey, E. M. Jones, J. R. Kamm, S. R. Taylor

EES Division, Los Alamos National Laboratory, Los Alamos NM 87545

Abstract

A fundamental objective of the S-6 (physical basis for discrimination) sub-task of the CTBT R&D Seismic Monitoring Program at Los Alamos is to analyze the sensitivity of the regional signal to source configuration, material properties, geologic layering and structure, along with complications along the path of the signal. Our approach is to combine the results of conventional analysis of field data from explosions and earthquakes with results of numerical models of actual and idealized situations. Existing first-principles, finite difference codes allow us to examine source effects in the non-linear regime; linking the results of these near-source calculations to finite difference, anelastic wave propagation codes allows us to examine the effect of various source region and propagation path characteristics on signals observed at regional distances. An investigation of discriminant differences for the DIVIDER and CORREO underground nuclear explosions is provided as an example of the approach used.

Objective

A fundamental objective of the S-6 (physical basis for discrimination) sub-task of the CTBT R&D Seismic Monitoring Program at Los Alamos is to analyze the sensitivity of the regional signal to source configuration, material properties, geologic layering and structure, along with complications along the path of the signal. Our approach is to combine the results of conventional analysis of field data from explosions and earthquakes with results of numerical models of actual and idealized situations. Existing first-principles, finite difference codes allow us to examine source effects in the non-linear regime; linking the results of these near-source calculations to finite difference, anelastic wave propagation codes allows us to examine the effect of various source region and propagation path characteristics on signals observed at regional distances. This report describes the progress thus far in the application of these capabilities.

Preliminary results

Our investigation of discriminant differences for the DIVIDER and CORREO underground nuclear tests provides one example of our approach. Our first efforts at generating regional synthetic seismograms from realistic source simulations involved linking the "strong motion" code TOODY (Swegle, 1978) to a LANL reflectivity code. This coupling approach was validated on a simple problem involving a purely elastic material (Taylor and App, 1994). We proceeded to calculate regional synthetics for actual underground nuclear tests conducted in Area 3 of the Nevada Test Site (NTS). The near-source geology for the selected events is relatively simple, except for one very well characterized fault scarp. Both close-in and regional seismic measurements are used in ground truthing the calculations.

Figure 1 shows a comparison between the regional signals recorded at the LLNL Kanab regional seismic station for the DIVIDER and CORREO underground nuclear tests, as well as synthetics generated from calculations of two highly idealized versions of these tests[1]. The events were conducted in similar rocks, with similar yields and explosion point depths. The paths from the two events to the Kanab station (approximately 250 km) are nearly equal: the total distance from CORREO is about 2 km greater than that from DIVIDER.

In both the calculations and measurements for the two events there are differences in the seismograms, most notably in the Pg to Lg ratio. This ratio, which is a promising discriminant between earthquakes and explosions (Taylor et al., 1989), is greater for DIVIDER than for CORREO, implying that DIVIDER has a more explosion-like signature than CORREO. The only known difference between the two sites is that DIVIDER is located in close proximity to the aforementioned fault scarp, whereas CORREO has no such nearby geologic complication.

Figure 2 is a geologic cross section of the DIVIDER site; the CORREO site is similar, but without the scarp. Both tests were conducted above a very large impedance discontinuity caused by Tertiary aged, porous tuffs overlying Paleozoic (Pz) aged limestone. Figure 3a is a snapshot from the idealized CORREO calculation, showing the velocity field at 1 s, with the lengths of the lines (vectors) being proportional to the amplitude of the particle motion and the directions indicating the direction of motion. From the strong transverse motion in the Pz, it is apparent that a very strong conversion

---

[1] By this we mean that we idealized certain specific test configurations to fit into a more manageable parameter study, but retained the important elements of the tests.

from primary compression (p) wave to shear (s) occurs at the tuff/Pz interface. Theory predicts that such conversions are maximized at angles of incidence between about 60 to 85 degrees[2]. Converted s-waves are believed to be strong contributors to Lg at regional distances, especially when the compressional velocity of the source material is low compared to the mantle shear wave velocity, as it is in this case (Xie and Lay, 1994). Figure 3b is the calculated velocity field for the idealized DIVIDER calculation, for which the picture is somewhat different. It appears that for DIVIDER more p-wave and less s-wave energy is transmitted into the Pz case than for CORREO, providing us with a working hypothesis for the observed differences at regional distances. For CORREO, the large expanse of Pz interface allows relatively more p-to-s conversion than for DIVIDER, for which the p-wave generated by the explosion has a higher angle of incidence at the Pz surface (due to the geometry); indeed, for DIVIDER there are no angles of incidence exceeding about 60 degrees, so that conversion to s-wave energy is less efficient, and transmission of p-waves more efficient. In the absence of strong effects elsewhere, it is plausible that DIVIDER should appear more explosion-like than CORREO.

It would be premature to conclude from this case that events conducted near large scarps generally would appear more explosion-like, and, therefore, that we need not worry about explosions being hidden near faults. The CORREO-DIVIDER case may be very special to the NTS. The calculations do suggest that events conducted in close proximity to a strong, near-horizontal discontinuity can generate sufficient shear close-in to influence regional waveforms, and thus cause such explosions to appear more earthquake-like. This effect may contribute to the observed reduced performance of the Pg/Lg discriminant for explosions at the NTS compared to other parts of the world.

The above example demonstrates one application of calculations to the discrimination task. These calculations, however, were two-dimensional; therefore, they are limited primarily to effects that can be described in two dimensions[3]. The remainder of this paper describes the other developments underway at LANL to address 3-D effects as well as to increase the flexibility to our current 2-D capabilities.

To investigate 3-D near-source effects, we have undertaken a series of calculations with the RAGE code. RAGE is an adaptive mesh refinement (AMR) "strong motion" code that provides state-of-the-art numerical treatments to reduce the number of computations in a 3-D model to a manageable number. RAGE was developed by SAIC and is being used at Los Alamos. Through SAIC, we are evaluating RAGE for use in modeling mining blasts, geologic structure, and other inherently 3-D configurations. Figure 4 shows the computational mesh from a test calculation involving a pressurized sphere in an elastic half-space. This problem is the same model mentioned above in connection with Taylor and App (1994). There are three main phases after reflection from the free surface: the main compressional-dilatational wave (p), the rarefaction from the surface (pP), and the converted shear wave (pS). As shown in this figure, the RAGE AMR algorithm refines the mesh where p and pP are strongest; the present algorithm requires further refinement to adequately capture the region about the pS shear wave.

---

[2] From the Zoeppritz equations, which express the partition of energy when a plane wave impinges on an acoustic-impedance contrast.

[3] Note that the case involving a scarp is inherently three-dimensional; however, auxiliary calculations were made to evaluate the influence of a conical vs. planar fault on shear conversions, and it was determined that in this instance we could tolerate such a geometric simplification. A complete description of the calculations is beyond the scope of this paper.

To address 3-D effects at regional distances, we have acquired the AFD-3D code. This elastic wave code, originally written by Ningya Cheng (1994), is fourth order in space and second order in time, making it relatively efficient to use in propagating close-in signals to regional distances (i.e., one can retain the desired frequency response with fewer computational zones and cycles). We are currently establishing linkages of our 2-D and 3-D strong motion codes to AFD-3D for generating regional synthetics. We have implemented the anelasticity model of Emmerich & Korn (1987) and are in the process of validating that methodology. Additionally, we have modified AFD-3D to perform 2-D cylindrically symmetric computations; this approach, an alternative to the reflectivity method, has the advantage that more complicated geologies can be simulated. We intend to incorporate a surface topography model into AFD-3D, with which we shall address the issue of topography-induced surface wave modification.

Recommendations and Future Plans

The computational investigations discussed above provide an avenue to deeper understanding of the physical processes involved in shaping the regional seismic signal. The application of properly validated codes to various source configurations will allow us to extrapolate to situations not amenable to experimentation. Such computational studies are an integral element of the CTBT R&D seismic monitoring effort, and provide a strong complement to the empirical studies.

In summary, we are successfully addressing issues and questions that arise out of current empirical discrimination. The DIVIDER-CORREO study is an example. In the longer term, we envision using synthetics generated from such simulations for testing and validating discrimination algorithms, investigating decoupling issues, and simulating complicated mining explosions.

References

Cheng, N., 1994. *Borehole Wave Propagation in Isotropic and Anisotropic Media: Three-Dimensional Finite Difference Approach*, Ph. D. thesis, MIT.

Emmerich, H. & Korn, M., 1987. Incorporation of attenuation into time-domain computations of seismic wave fields, *Geophysics, 52* (9), pp. 1252–1264.

Swegle, J. W., 1978. *TOODY IV - A computer program for two-dimensional wave propagation*, Sandia National Laboratory report SAND-78-0552.

Taylor, S. R. & App, F. N., 1994. *Representation theorem coupling of numerical and wave propagation codes for the generation of synthetic seismograms*, Los Alamos National Laboratory report LAUR-94-2194.

Taylor, S. R., Denny, M. D., Vergino, E. S. & Glaser, R. E., 1989. Regional discrimination between NTS explosions and western U.S. earthquakes, *Bull. Seism. Soc. Am., 79*, pp. 1142–1176.

Xie, X.-B. & Lay, T., 1994. The excitation of Lg waves by explosions: A finite difference investigation, *Bull. Seism. Soc. Am., 84*, pp. 324–342.
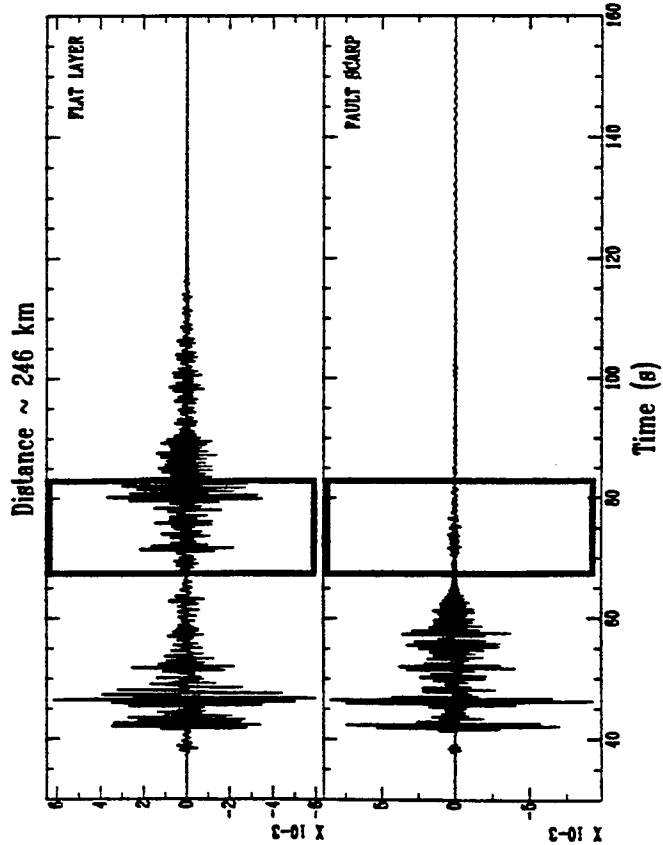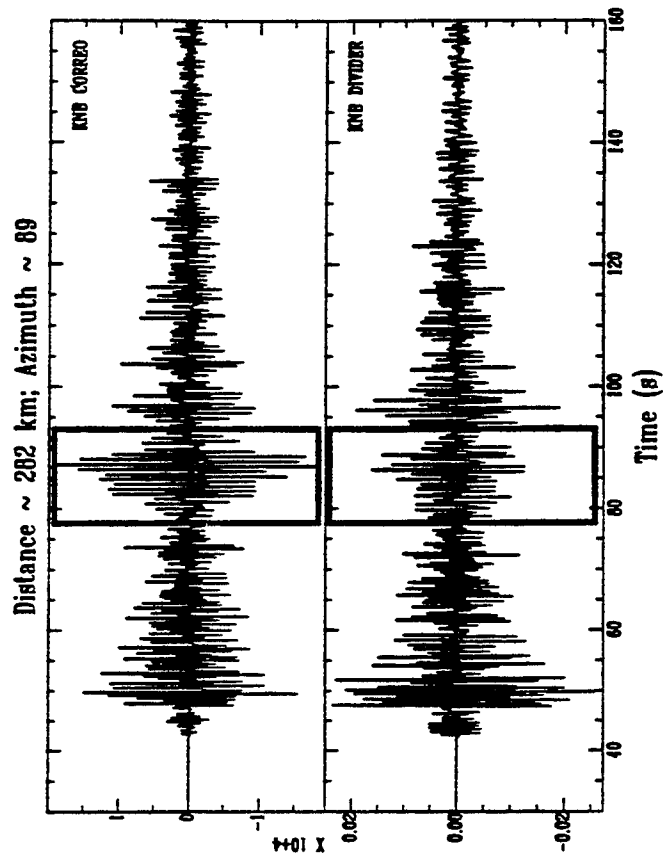
Figure 1. Comparison of the measured and calculated regional waveforms at LLNL Kanab recording station. The highlighted portions are the Lg phase. Early arrivals are the Pg phase. Calculations and observations suggest that the fault significantly affected the Lg wavetrain.

613
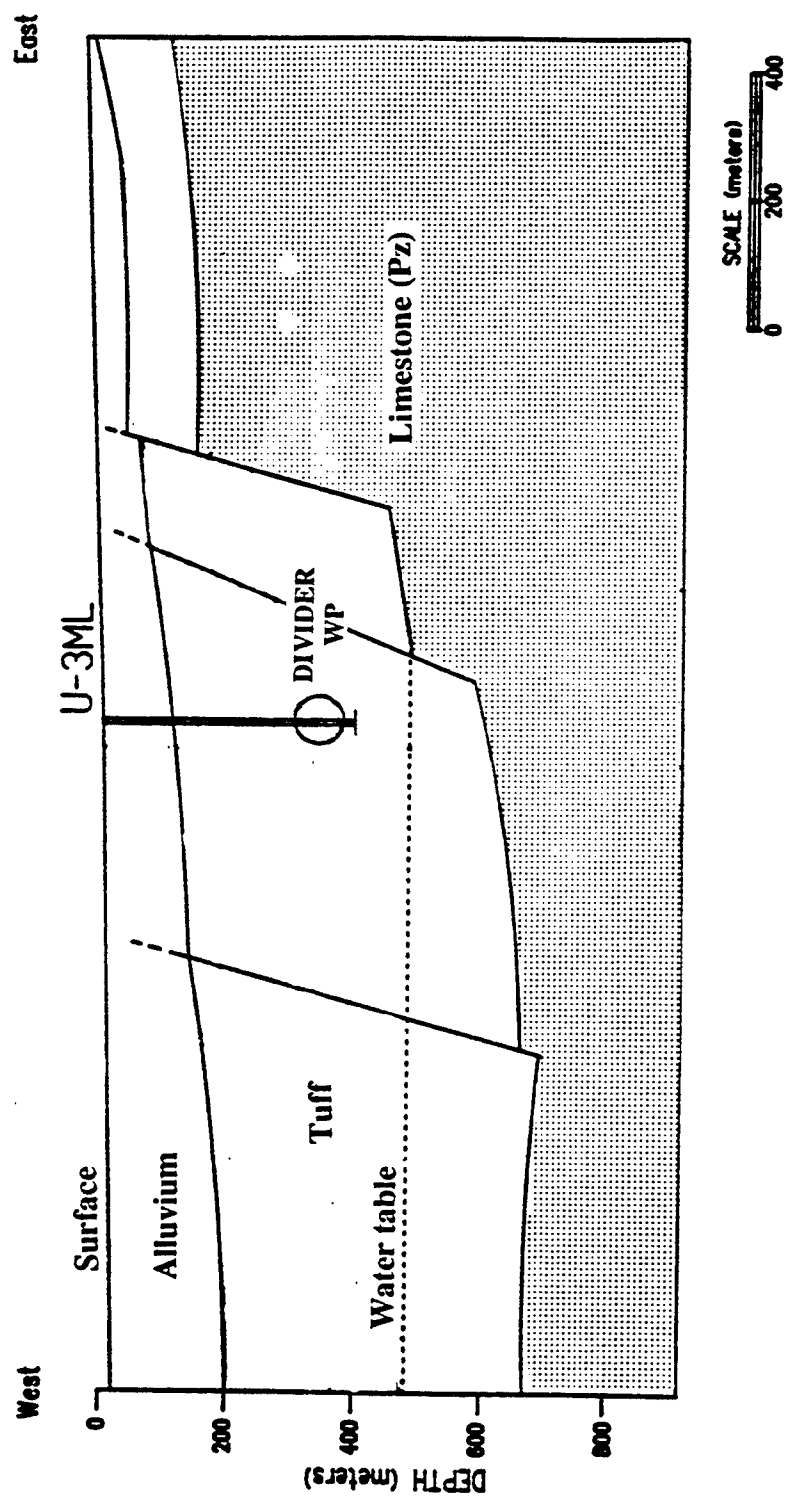
Figure 2. Geologic cross section across the DIVIDER event site. The stippled region is the Pz limestone. CORREO is similar but without the fault scarp.
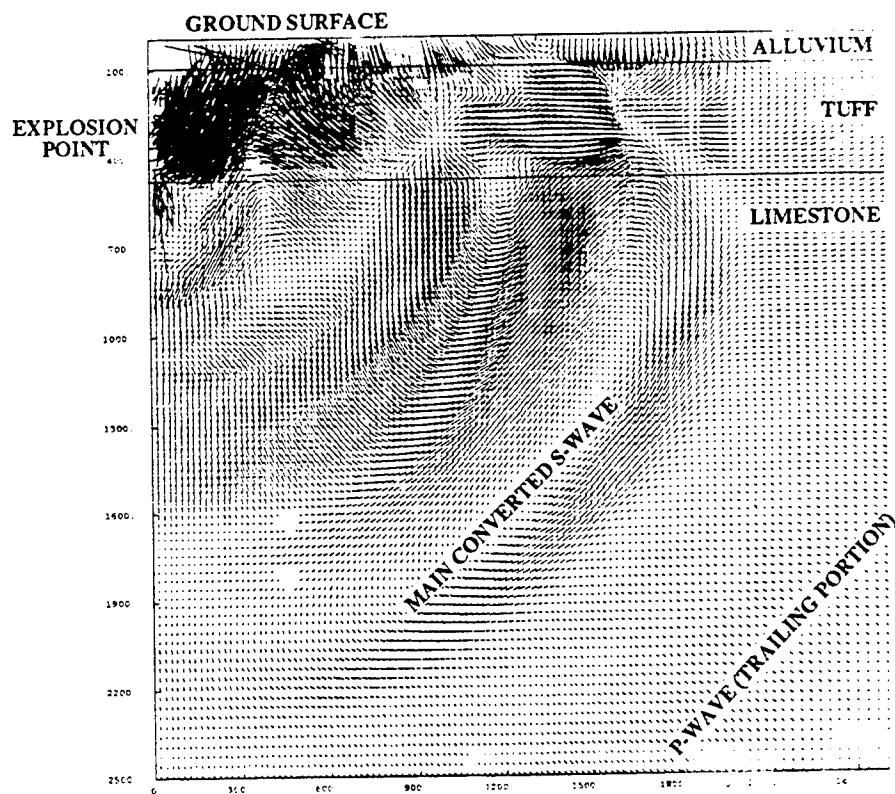
Figure 3a. Particle velocity field for the CORREO calculation at 1 sec.
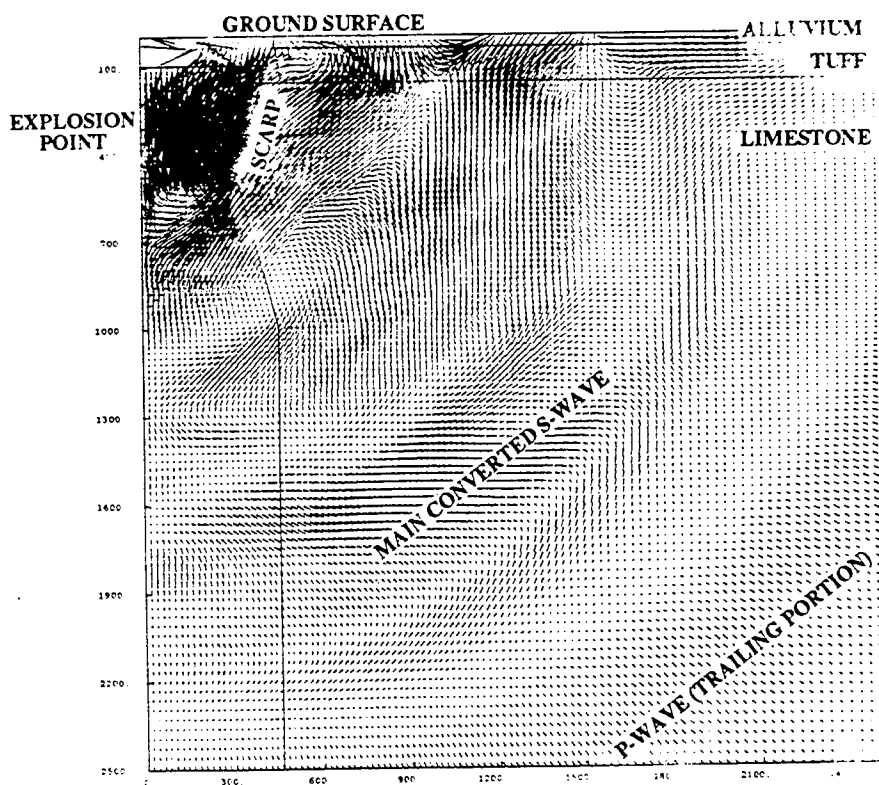
Figure 3b. Particle velocity field for the DIVIDER calculation at 1 sec.

615
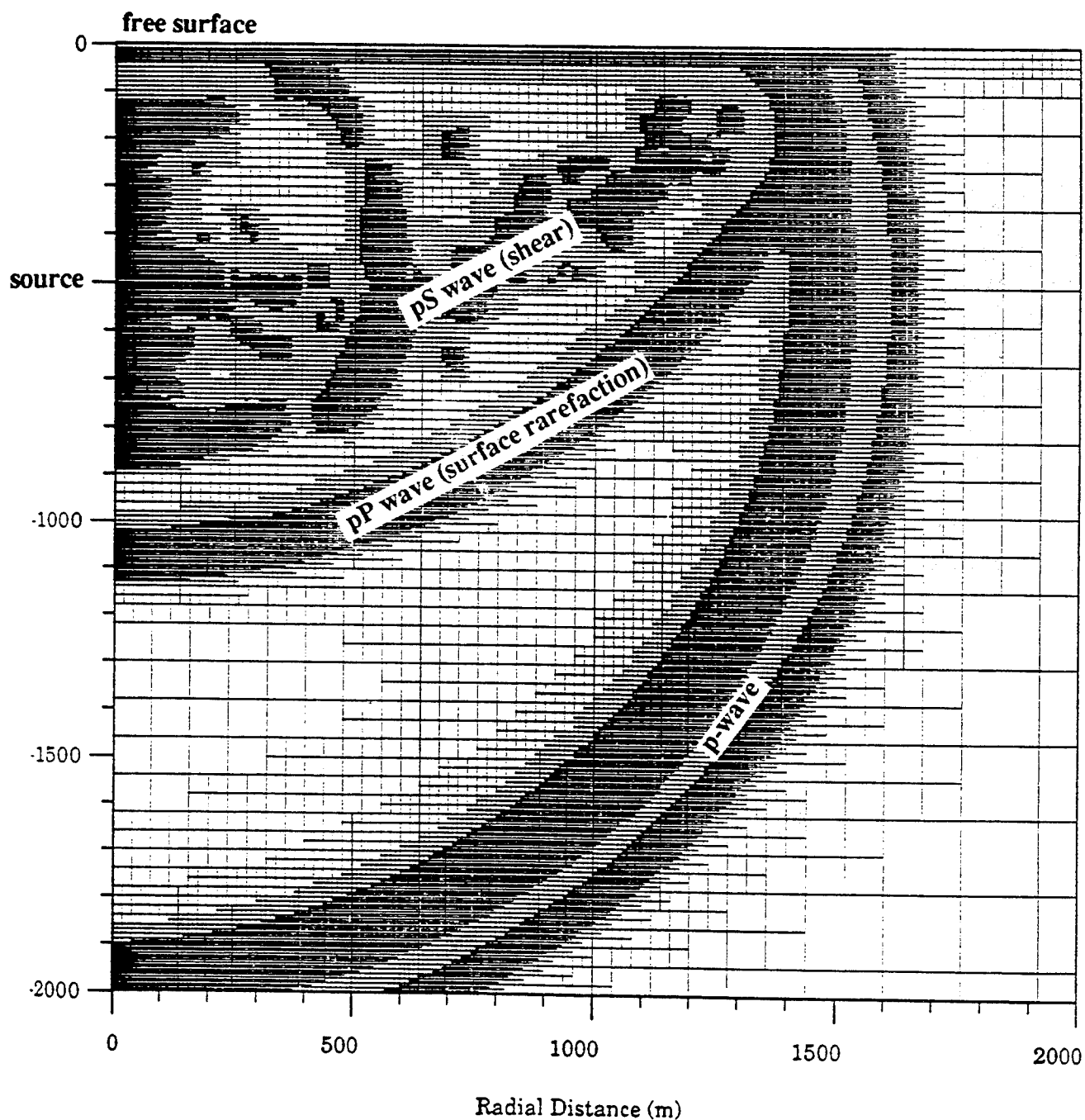
Figure 4. Plot of computational mesh for RAGE calculation at 500 ms. Stress waves produced by instant pressurization of sphere in an elastic half-space. The darkened regions are areas of very high zone resolution.

Elastic and Anelastic Structure Beneath Eurasia

Göran Ekström, Adam M. Dziewonski, Wei-jia Su and Gideon P. Smith

Department of Earth and Planetary Sciences
Harvard University
Cambridge, MA 02138

Abstract

We are collecting and analyzing large and diverse datasets of seismic waveforms, absolute and relative body wave traveltimes, and surface wave phase velocities and amplitudes. Our primary objective is to map the variations of elastic mantle properties beneath Eurasia over horizontal lengthscales of approximately 1000–1500 km and vertical lengthscales of 50–100 km. In comparison with recent Harvard global models, such as S12WM13, we have increased the horizontal resolution by expanding the global structure up to spherical harmonic degree $l = 20$, and we have adopted a radial parameterization which gives better vertical resolution in the upper mantle.

Using earlier and new datasets, we have derived a new whole mantle model, S20U7L5. The new model shows many of the same features seen in previous tomographic images, but with significantly sharper definition, in particular in the upper mantle. Lithospheric roots beneath the stable continental interiors are the most prominent feature in the uppermost mantle. The model is partially validated by comparisons with the earlier regional models SNA and TNA. While there is striking similarity in the velocity structure beneath a great variety of continental interiors, West Africa appears to overlie one of the fastest locations in the upper mantle, with faster than average velocities extending to 500 km depth.

Additional tasks to be completed before the new model is finalized is the incorporation of more accurate corrections for crustal thickness and structure, as well as the inclusion of an extensive dataset of recently measured teleseismic traveltimes.

Objective

We are adapting the seismic tomographic techniques developed in global scale studies to the regional scale problem of mapping the elastic and anelastic material properties beneath Eurasia. The main objective of this research is to obtain a tomographic seismic velocity model for the structure beneath Eurasia with a horizontal resolution corresponding to at least $l = 20$, consistent with the widest possible range of seismological observations. Related objectives are to evaluate the resulting model and its utility in event location algorithms.

Research Accomplished

In earlier reports (1993, 1994) we have presented results based on earlier whole mantle and preliminary upper mantle models, while also addressing the question of teleseismic event locations using heterogeneous mantle models. In this report we describe in greater detail the derivation of the new global mantle model S20U7L5. We discuss and compare some shallow mantel structures seen in this model with previously derived regional models, and point out some remaining problems/issues which we plan to address before producing the final version of the model.

A degree 20 model of the Mantle

Earlier tomographic models of the whole mantle, based on a variety of datasets, have provided descriptions of large, planetary-scale variations of P and S velocities in the mantle. With the goal of obtaining better resolution of structures, particularly for the upper mantle, we have collected and incorporated high-quality surface wave dispersion data with the previously developed, and now expanded, seismological datasets of travel times and body and mantle wave waveforms in the model inversion. The new model is parameterized to preferentially resolve smaller-scale structures in the upper mantle, while at the same time accounting for the dominantly large-scale structures in the lower mantle.

Parameterization

The parameterization and inversion approach are similar to those used for earlier Harvard mantle models, such as S12WM13 (Su *et al.*, 1993), with the following notable differences:

- We use a split parameterization for the mantle, and parameterize the radial variations in the upper mantle in terms of Chebyshev polynomials of degree 0–7. For the lower mantle we use Chebyshev polynomials of degree 0–5. This split parameterization, with more degrees of freedom in the upper mantle, reflects our goal of resolving primarily the shallow mantle structure, and the greater sensitivity of our data sets to heterogeneity in the upper mantle (see below).

- The spherical harmonic expansion is extended from degree 12 to degree 20. If we assume that we can resolve structures of dimensions that are approximately half the minimum wavelength of the highest harmonic, this implies a resolving length of ~1000 km. The new parameterization increases the number of parameters to be determined for each radial degree from 169 to 441, and the total number of unknown coefficients is $14 \times 441 = 6174$. While we do not expect to be able to resolve degree 20 structure in the deeper mantle, due to our data coverage, we do believe that this resolution is

achievable in the top several hundred kilometers of the upper mantle. We damp the spatial derivatives of the model in the inversions, and a higher damping is applied to the lower mantle.

- The data are corrected for crustal structure using a new compilation of crustal thicknesses by Mooney (1994). This is in contrast to previous models which were only corrected for average continental and oceanic crustal structure. The crustal correction is important for explaining phase velocities of shorter period surface waves.

Data Sources

Several types of data with sensitivity to velocity variations in different parts of the mantle are included. So far, the following data have been incorporated in the derivation of the new model, which we call S20U7L5 (spherical harmonic degree 20, degree 7 in the upper mantle and degree 5 in the lower mantle):

- Absolute and differential travel times measured from waveform data (S, SS, ScS, $SS-S$). These are the same data sets that were used in the development of S12WM13.

- Long-period body and mantle waveforms from 451 earthquakes recorded on the Global Seismic Network. This dataset is similar in coverage to the data that were used for S12WM13, but we use a more broadband spectral weighting in the waveform fitting.

- Dispersion measurements of Rayleigh waves at 140, 100, and 75 seconds (described below).

- Dispersion measurements of Love waves at 140, 100, 75, 60, and 50 seconds (described below).

The Love wave and Rayleigh wave dispersion datasets have not previously been used in inversions for mantle structure, and they are described in some detail in the next section.

Dispersion of Love and Rayleigh waves

The method developed by Ekström *et al.* (1993) matches an observed surface waves seismogram $o(t)$ with a model seismograms $m(t)$ through iterative adjustment of parameters which describe the dispersion and amplitude spectrum of the model waveform. A fundamental mode model waveform $m(t)$ is calculated using the JWKB expressions for surface waves, which reduce to

$$m(\omega) = A(\omega)\exp[i\Phi(\omega)]. \tag{1}$$

The propagation part of the phase is expressed as

$$\Phi_P(\omega) = \frac{\omega X}{c^\circ(\omega) + \delta c(\omega)} \tag{2}$$

where $\delta c(\omega)$ is the average phase velocity perturbation with respect to the PREM value c°. The amplitude function $A(\omega)$ and the phase velocity perturbation $\delta c(\omega)$ are parameterized as smooth B-spline functions of the period band of interest, 35–150 seconds. Since the adjustment of $m(t)$ to resemble $o(t)$ cannot be determined by direct linear inversion, an

iterative, non-linear algorithm was developed. The algorithm is based on two concepts: *Iterative Frequency Band Expansion*, and *Iterative Phase Isolation and Minimization of Residual Dispersion*, which are integrated in the following algorithm:

1. Spline parameters for surface wave dispersion and amplitudes are calculated for an initial Earth model, for example S12WM13, and a trial model seismogram is calculated.

2. Observed and model seismograms are filtered between 75–125 sec, the initial frequency window.

3. Dispersion and amplitudes are adjusted to maximize the fit in the current frequency window.

   - Observed and model seismograms are cross correlated, and the model seismogram is auto correlated.

   - An objective function is formed which reflects the difference between the cross- and autocorrelations.

   - Spline coefficients for $\delta c(\omega)$ and $A(\omega)$ are iteratively adjusted to minimize the objective function.

4. The frequency window is expanded to higher and lower frequencies.

5. Steps 3 and 4 are repeated until the whole frequency band of interest is included.

Ekström *et al.* (1993) automated this algorithm and applied it systematically to surface waves recorded on GSN, CDSN, GEOSCOPE, and MedNet stations. Moderate and large earthquakes over a 4-year-period have now been used, and more than 80,000 paths were analyzed, out of which approximately 10,000 Rayleigh and 8,000 Love waves were of high quality. Ekström *et al.* have reported on the derivation from these data of phase velocity maps, but in the derivation of S20U7L5, the raw phase anomalies were used and treated in the same way as travel times.

Inversion Results

The new model S20U7L5 shows many of the same features seen in previous tomographic images, but with significantly sharper definition. Figure 1 shows a comparison between the S velocity perturbations at 150 km depth beneath the Mediterranean and North Africa as imaged in S12WM13 (top) and in the new model S20U7L5 (bottom). Many features, such as the very fast West African craton and the slow velocities coincident with the Cameroon line are much clearer in the new model. The slow velocities associated with the Red Sea rift are also much better defined in S20U7L5. While the new model shows much greater lateral contrasts in the upper mantle, the low angular degree components of the new model in general agree very well with previous mantle models such as S12WM13.

On a global scale, the fast velocities beneath stable continental interiors is the most prominent anomaly in the top 300 km of the mantle. The very high velocities beneath the stable interior of West Africa continue even deeper, as can be seen in a velocity profile (Figure 2). The new model also shows that the slow velocity anomalies associated with ridges continue to great depth, in particular in the Indian Ocean. The Red Sea rift shows slow velocities

extending down to 400 km (Figure 2). Below 250 km, however, there are other slow features, not directly associated with surface tectonics, which predominate, in particular in the center of the Pacific Ocean.

Even though the tomographic models result from a formal inversion, damping and incomplete knowledge of data and model uncertainties make it difficult to assess the true resolution of our models. For example, a question which might be asked is whether the deep extent of fast velocities beneath West Africa is well resolved and imaged. If it is, the velocity structure beneath this shield is different from that seen beneath the Canadian shield (Grand and Helmberger, 1984), where faster than average velocities appear to terminate at 200–250 km depth.

One test which can be made is to see how Canadian shield structure is imaged in S20U7L5. Figure 3 shows a comparison between the vertical velocity profile SNA (Grand and Helmberger, 1984), representative for the Canadian shield, and S20U7L5 evaluated at a point just South of Hudson Bay. The agreement between the two is striking, both in terms of the overall amplitude of the perturbation, and the depth at which heterogeneity becomes small. Note that the velocity jump at 220 km is in our starting model (PREM), and that the smooth perturbations appear to counteract it. Also, there is agreement between SNA and S20U7L5 on the vertical gradient below 400 km, which disagrees with PREM.

A similar comparison can be made between the model TNA (Grand and Helmberger, 1984), and S20U7L5 (Figure 3). The agreement is not as striking as for the shield structure, which may in part be due to the fact that TNA was derived from data which sampled a variety of tectonic environments, including the East Pacific Rise, in addition to western US.

While the lithospheric root beneath West Africa extends deeper than that beneath the Canadian shield, the velocity structure beneath several other stable continental interiors are very similar to each other, as well as to SNA. Figures 4 shows a composite of six different velocity profiles which show similarities, not only in the upper few hundred kilometers, but also in the deepest part of the upper mantle.

Remaining Issues

The model S20U7L5 predicts all the datasets that went into its derivation well, indicating that the observations are compatible and complementary. Three concerns remain to be addressed before we finalize the model:

- Are the corrections for shallow structure (crustal thickness, etc.) adequate? While linearized corrections are adequate for longer period data (see Woodhouse and Dziewonski, 1984), we will investigate the effects of using more exact crustal corrections for the intermediate period surface waves.

- Is the lower upper mantle (250–600 km) well resolved? We have recently developed a new dataset of very long-period surface waves which we will include in the inversion. This should provide better constraints on the structure in this depth range.

- Are we damping the structure too much in the lower mantle? We will incorporate the additional datasets of all major teleseismic arrivals which we have been measuring from waveform data over the last two years. Several of these phases have sensitivity

primarily in the lower mantle, and incorporation of them will improve the resolution there.

Conclusions and Recommendations

Intermediate period surface waves provide excellent global coverage and sampling of shallow upper mantle structure. The inclusion of dispersion data for these waves in the derivation of the new model S20U7L5 has resulted in a higher resolution and better constrained model of the shear wave velocity in the upper mantle. Several interesting features are seen in the new model, including striking similarities of structure beneath continental cratons. In West Africa, however, fast velocities appear to extend to 500 km depth, while beneath the Canadian shield the fast structure terminates at around 300 km. Ridges also show a great variability in their expression at depth, with the Indian and Antarctic ridges having a distinct expression down to at least 200 km depth.

Lateral variations in S velocity in the upper 200 km of the mantle (as imaged in S20U7L5) are large, -5% – +7%. It is likely that in order to resolve heterogeneities on shorter lengthscales than those seen in S20U7L5, new tools have to be developed which take better account of wave propagation effects in heterogeneous media. In addition, improved corrections for crustal thickness and crustal structure will make it possible to better resolve mantle velocities just below the Moho. Incorporation of additional seismic data for regional distances (e.g. Pn, Sn) should also help to improve the resolution in the shallowest mantle.

By combining a large number of diverse seismological observations, we have made progress towards obtaining higher resolution tomographic images of the regional scale elastic structure globally and beneath Eurasia. Large and regional scale heterogeneity in the mantle has been shown to bias seismically derived event locations, and it appears likely that further improvements in locations can be achieved by correcting for better known elastic heterogeneity in the Earth's mantle.

References

Dziewonski, A. M., Mapping the lower mantle: Determination of lateral heterogeneity in P velocity up to degree and order 6, *J. Geophys. Res.*, **89**, 5929-5952, 1984.

Ekström, G., J. Tromp, and E. W. Larson, Measurements and models of global surface wave propagation (abstract), *EOS, Trans. Am. Geophys. Un.*, **74**, 438, 1993.

Grand, S. P., and D. V. Helmberger, Upper mantle shear structure of North America, *Geophys. J. R. Astron. Soc.*, **76**, 399–438, 1984.

Mooney, W. D., Global crustal structure, *EOS, Trans. Am. Geophys. Un.*, **75**, 57, 1994.

Su, W.-J., R. L. Woodward and A. M. Dziewonski, Degree-12 Model of Shear Velocity Heterogeneity in the Mantle, *J. Geophys. Res.*, **99**, 6945–6980, 1993.

Woodhouse, J. H., and A. M. Dziewonski, Mapping the upper mantle: three-dimensional modeling of Earth structure by inversion of seismic waveforms, *J. Geophys. Res.*, **89**, 5953-5986, 1984.
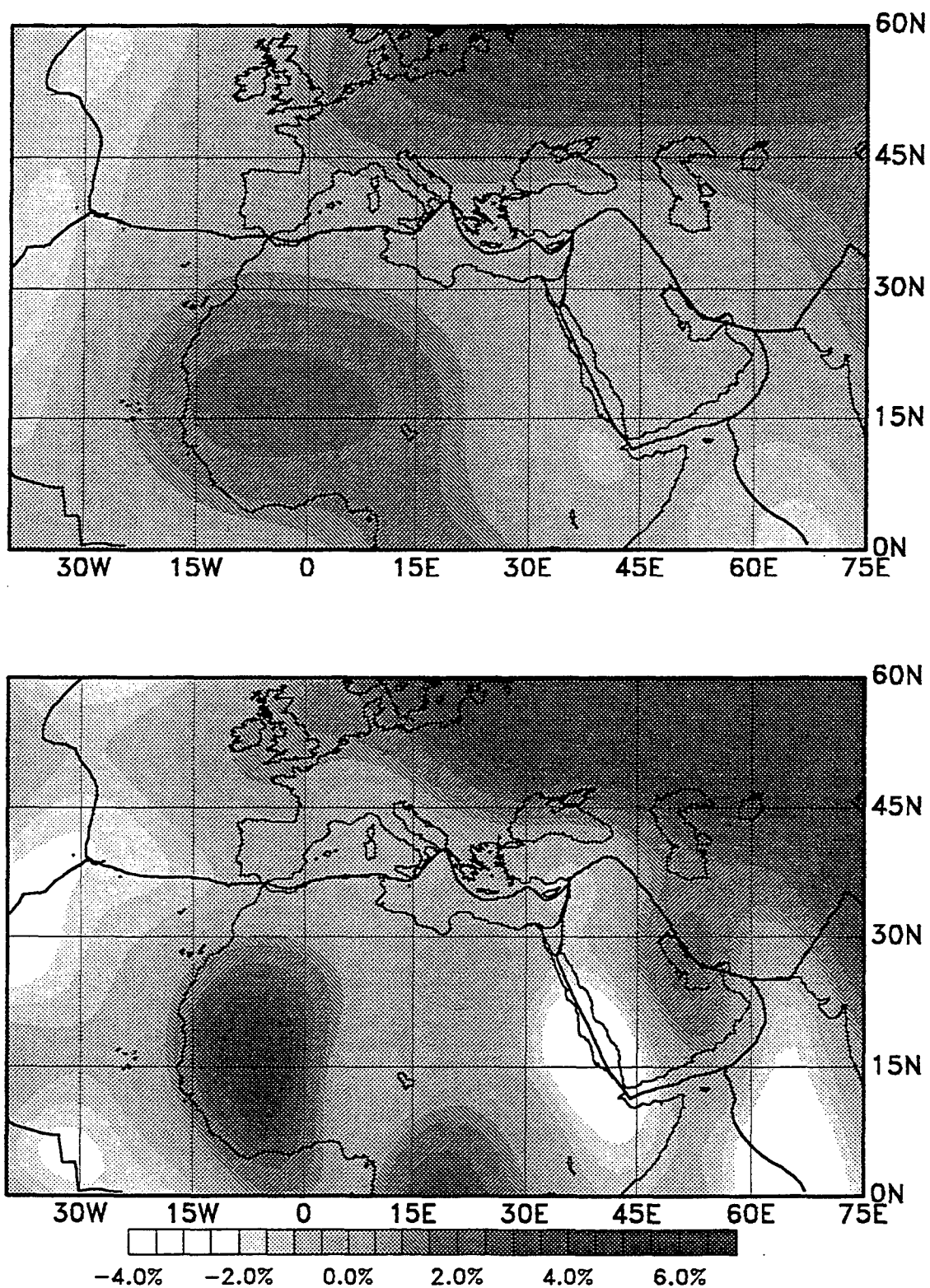
Figure 1 Top panel shows the velocity perturbations with respect to the global average at 150 km depth as seen in S12WM13 for the Mediterranean area. The bottom panel shows the same area, but for the model S20U7L5.

623
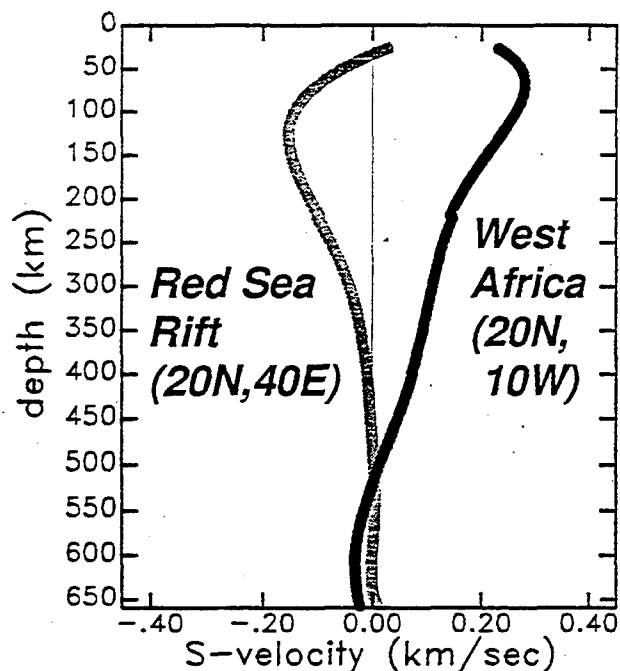
Figure 2 Vertical profiles of velocity perturbation with respect to the global average for two locations in Figure 1 associated with large velocity perturbations, West Africa and the Red Sea Rift. In the West African profile, fast velocities continue to 500 km depth, while the Red Sea Rift profile shows slow velocities down to 400 km depth.
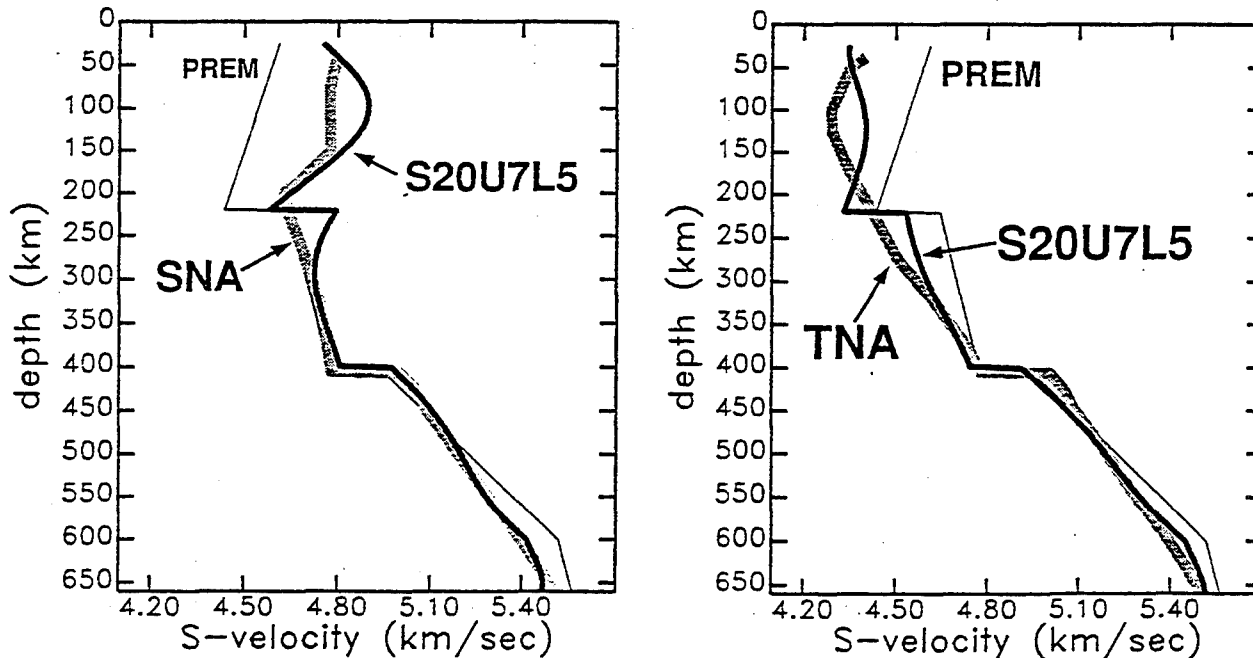
Figure 3 Vertical velocity profiles for two locations chosen to coincide with the regions analyzed by Grand and Helmberger (1984) in the development of the models SNA and TNA. Velocities for PREM, SNA, TNA, and S20U7L5 are shown with different line styles.

1. Baltic shield *(60N, 30E)*
2. Northeast Siberia *(60N, 120E)*
3. Northwest Africa *(20N, 10W)*
4. Western Australia *(30S, 120E)*
5. Guyana shield *(0, 60W)*
6. Canadian shield *(60N, 90W)*
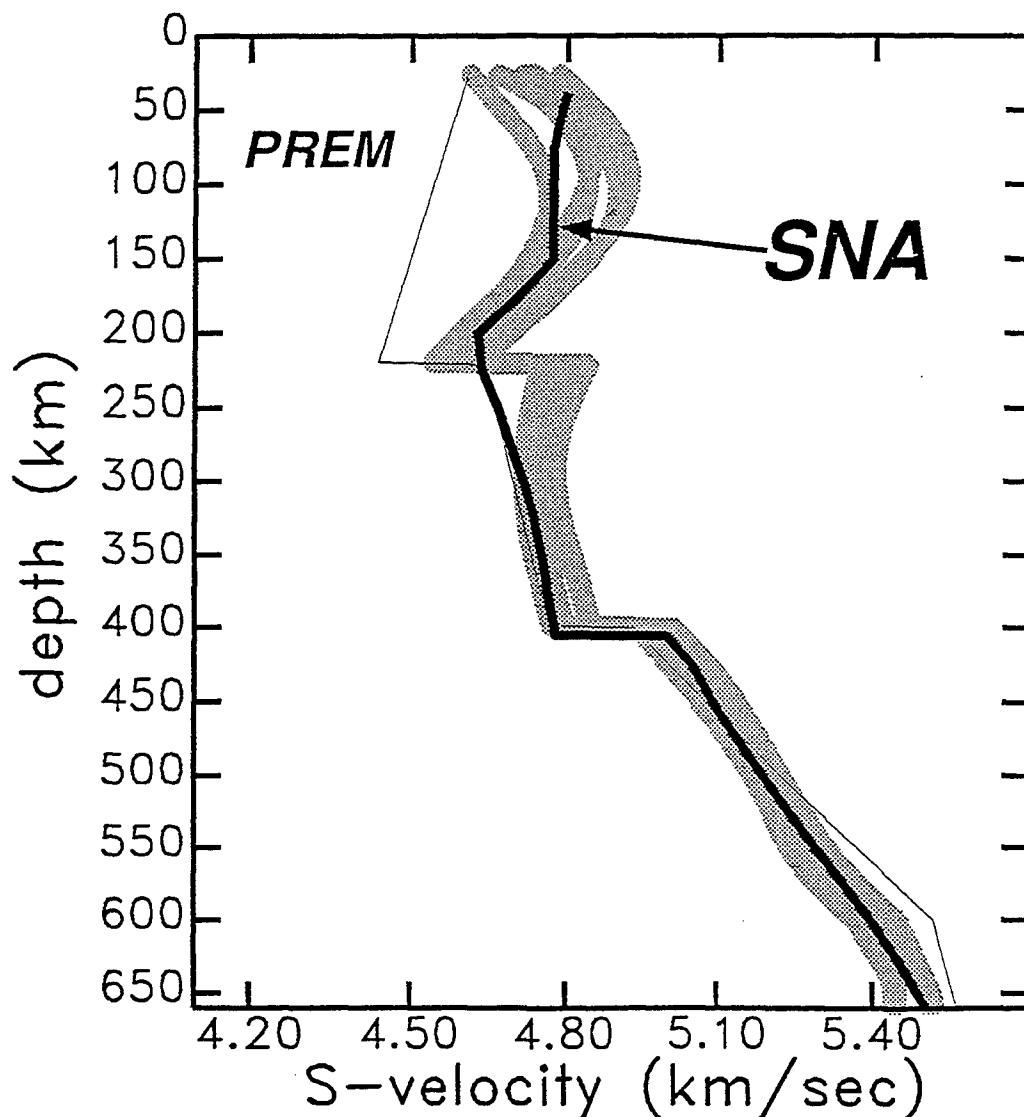
Figure 4 Vertical velocity profiles beneath six points located within stable continental interiors. Also shown, with the thick solid line, is the SNA structure. PREM is shown with the thin solid line.

Incorporating "sinuous connectivity" into stochastic models of crustal heterogeneity: Examples from the Lewisian gneiss complex, Scotland, the Francsican formation, California, and the Hafafit gneiss complex, Egypt.

John A. Goff, *Institute for Geophysics, University of Texas*
Alan Levander, *Rice University*

Abstract. Stochastic models are valuable and sometimes essential tools for investigating the behavior of complex phenomena. In seismology, stochastic models can be used to describe velocity heterogeneities that are too small or too numerous to be described deterministically. Where analytic approaches are often infeasible, synthetic realizations of such models can be used in conjunction with finite difference algorithms to systematically investigate the response of the seismic wavefield to complex heterogeneity. This paper represents a continuing effort at formulating a complete and robust stochastic model of lithologic heterogeneity within the crust, and the means of generating synthetic realizations; "complete" implies that the model is flexible enough to describe all types of random heterogeneity within the crust, while "robust" implies sufficiently constrained parameterization that an inversion problem may be well-posed. We use as a basis for investigation geologic maps of crustal exposures and petrophysically inferred velocities. Earlier efforts at stochastic modeling have focused on characterization of the univariate probability density function, which is typically modal (i.e., binary, ternary, etc.), and the covariance function, which is typically fit with a von Kármán function. Here we provide a means of characterizing the property of "sinuous connectivity" and for generating realizations that possess this property. Sinuous connectivity is the tendency for individual lithologic units to be continuous over long and highly contorted paths; there is no means in the earlier modeling of either characterizing or synthesizing this property. We first demonstrate that binary sinuously connective realizations can be generated by mapping alternating contour sets from a Gaussian-distributed surface (a "normal equivalent field") into the two values comprising the binary probability density. There is tremendous non-uniqueness in this operation, with wide classes of mapping functions and normal equivalent statistics resulting in model fields that are statistically identical. We infer from these observations that the property of sinuous connectivity can be represented by a simple binary yes-or-no parameter.

Keywords: lithospheric heterogeneity, sinuous connectivity, covariance modeling, stochastic models

I. Introduction

Investigations of the wavefield response to heterogeneous media (finite difference or otherwise) can be of a deterministic (i.e., the exact particulars) or stochastic (i.e., ensemble properties) nature. The choice of one or the other is a matter of scale, numbers, and resolution. The deterministic approach is typically used when the structures within the velocity field are few in number and large compared to the seismic wavelength. In such cases a well-posed inverse problem may be formulated to estimate the velocity field by, for example, matching a synthetic wavefield to the observed wavefield [e.g., *Jervis et al.*, 1995]. The stochastic approach is necessary when structures within the velocity field are numerous and/or small compared to the wavelength. Large numbers of scattering features tend to make the wavefield complex (i.e., deterministically unpredictable) through both single and multiple forward and backward scattering. Small scales make deterministic resolution of structures difficult or impossible. Recent studies have used finite difference algorithms to investigate the seismic wavefield response to synthetic realizations of stochastic velocity models [e.g., *Frankel and Clayton*, 1986; *Fisk et al.*, 1992; *Holliger et al.*, 1993; *Levander et al.*, 1994a,b]. So far these efforts have only been directed toward the forward problem, where a velocity model is assumed and the wavefield response computed. Qualitative comparisons of seismic data with finite-difference seismograms generated in a variety of realistic circumstances suggest that the seismogram is sensitive to variations in the stochastic character of the medium. Efforts are now being directed towards establishing quantitatively meaningful model/data comparisons to pose the inverse problem of estimating stochastic properties of a velocity field from observations of the seismic wavefield.

This report is one in a series of efforts to establish a "robust" and "complete" stochastic model for crustal heterogeneity through analysis of mapped crustal exposures. Though modified by the act of exhumation, crustal exposures represent our only direct multidimensional sampling of crustal rocks from depth. They provide invaluable information on lithologies and their spatial relationships. The principal goal of working with this data is not to establish precisely the stochastic nature of the crust, but rather to ascertain the types of stochastic models that are appropriate. By "robust" we intend a model with few-enough parameters that an inversion problem may be well-posed. By "complete" we intend a model that can reproduce, through synthetic realization, all the important physical properties of the field. There is a delicate balance between these two concerns. If we have too few parameters in the desire for robustness, then the model may not be flexible enough to characterize the variety of stochastic morphology observed. If we favor completeness we may require more parameters than we can ever hope to solve for in an inverse problem.

Previous work on mapped crustal exposures has focused on combined modeling of the covariance function and probability density function (PDF) of the velocity field (as inferred from petrophysical conversion of the lithographic field). The covariance function has often been successfully modeled using the *von Kármán* [1948] model [e.g., *Holliger et al.*, 1993; *Levander et al.*, 1994]. The PDF has often been modeled by a simple modal distribution (e.g., binary, ternary, etc.) [*Holliger et al.*, 1993; *Levander et al.*, 1994; *Goff et al.*, 1994], which reflects the observation that mapped crustal exposures, even morphologically complex ones, typically consist of a small number of distinct lithologic units of relatively constant velocity. Synthetic realizations generated from these models successfully reproduce many of the important physical properties of the observed field, including the modal PDF, characteristic scales, structural anisotropy, and fractal dimension. However, one property clearly seen on many of the crustal exposures has thus far remained beyond the grasp of stochastic characterization: "sinuous connectivity", the subject of this report.

Sinuous connectivity is a difficult property to define in words, but simple to demonstrate. Figure 1a is a digitized section of the Lewisian gneissic terrain (Scotland), an exposed section of the middle crust consisting primarily of amphibolite dikes (black) and gneiss (white) (gray = no data). The gneiss has a petrophysically inferred p-wave velocity of 6.2 km/sec, and the amphibolite 6.75 km/sec. *Levander et al.*, [1994a] formulated a stochastic model based on analysis of the PDF and covariance structure for the grid shown in Figure 1, and a synthetic realization from a refined version of this model is presented in Figure 1b. The grids shown in Figures 1a and 1b have essentially identical PDF and covariance, and those physical attributes characterized by those functions are well-matched; i.e., the percentage of gneiss and amphibolite, the characteristic scales, and the fractal dimension (the overall degree of roughness). Nevertheless the comparison is not satisfactory. The amphibolite in the geologic map is highly connected and sinuous, whereas in the synthetic field it is disconnected and blob-like.

In this paper we present a method for incorporating sinuous connectivity into stochastic models for lithologic (i.e., modal) heterogeneity, and the means by which to generate a sinuously connective synthetic realization that honors the covariance and PDF structure specified by the stochastic model. The success of this approach is demonstrated in Figure 1c, which displays a sinuously connective synthetic field with identical PDF and covariance structure to the synthetic shown in Figure 1b. The comparison between this synthetic to the Lewisian data in Figure 1a is clearly superior; we believe that this stochastic model, incorporating PDF (modal or otherwise), covariance, and sinuous connectivity characterization, represents as complete a model as might be necessary for characterizing seismic velocity heterogeneity within the earth. The robustness of this model, as applied to seismic inversion, will be the topic of future investigation.
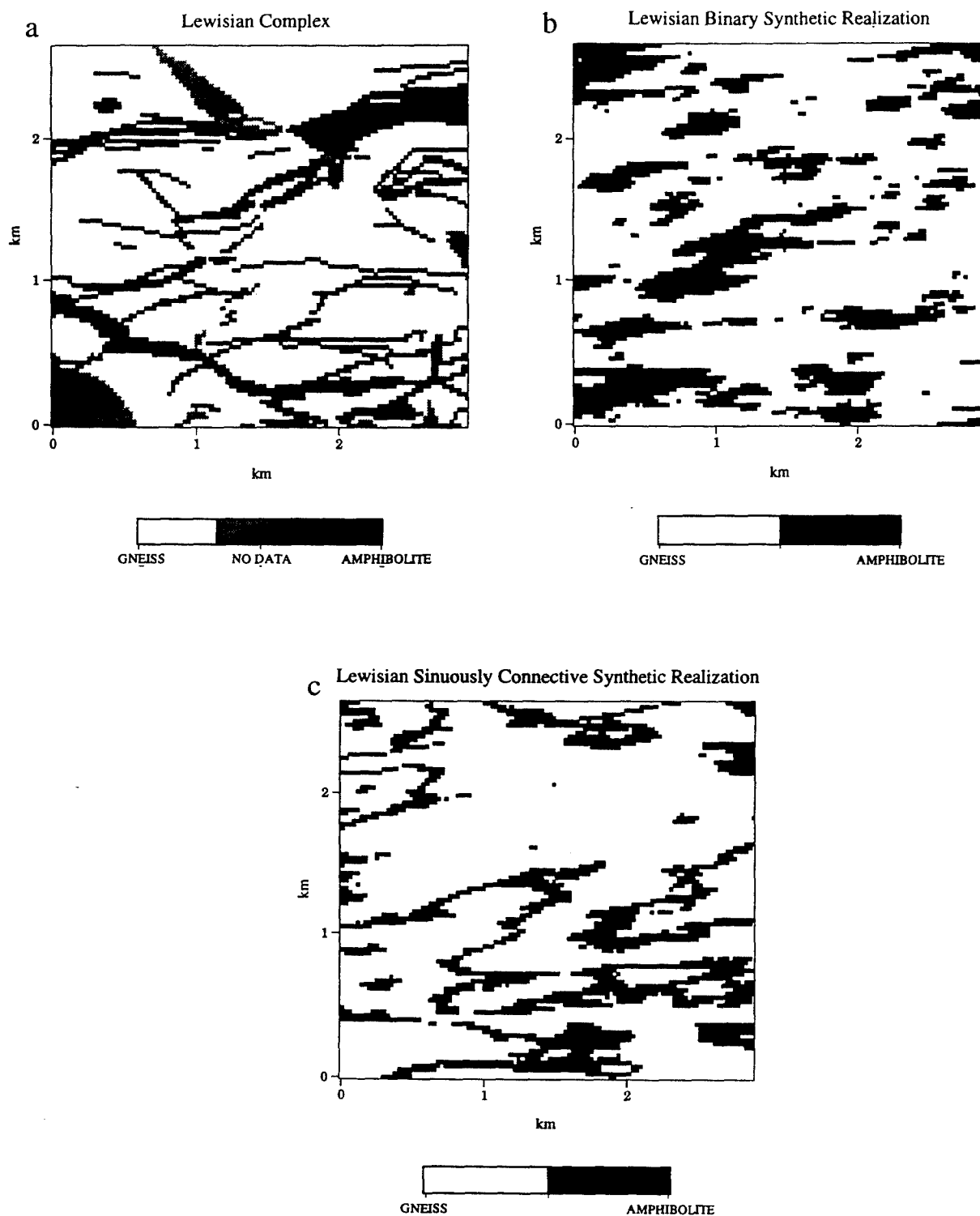
Figure 1. (a) Digitized map of the Lewisian gneiss complex, Scotland [*Levander et al.*, 1994]. Also mapped but not shown are intermediate schist, which comprise only 1% of the total and so were ignored as insubstantial. Map is 78% gneiss (6200 m/sec inferred p-wave velocity) and 22% amphibolite (6750 m/sec). The grid spacing is 0.0268 km, with 100 rows and 109 columns. (b) Synthetic realization based on PDF and covariance modeling of the Lewisian complex. (c) Synthetic realization based on PDF and covariance modeling of the Lewisian complex and including the property of sinuous connectivity.

II. PDF and Covariance Modeling and Synthetics

Details regarding PDF and covariance modeling based on crustal exposure maps are given in *Holliger et al.* [1993] and *Levander et al.* [1994a]. Heretofore covariance modeling has been accomplished by forward-model fitting of the von Kármán function to the data covariance. Here we apply the inversion algorithm of *Goff and Jordan* [1988] converted to use with gridded data. The method for generating synthetic realizations from such models is given in *Goff et al.* [1994]. In this section we provide a brief overview of the salient points from these references.

PDF Modeling

In the case of a modal field, modeling the PDF is robust and straightforward: the PDF simply describes the percentage of each unit present in the field. For example, in the Lewisian section described above, 78% of the map is gneiss, and the remaining 22% is amphibolite (Figure 2a).

Covariance Modeling

The covariance function, or its Fourier equivalent the power spectrum, represents our primary tool for characterizing spatial roughness properties. It is defined by:

$$C_{hh}(\mathbf{x}) = E[h(\mathbf{x}_1)h(\mathbf{x}_1 + \mathbf{x})], \qquad (1)$$

where $h(\mathbf{x}_1)$ is a zero-mean, homogeneous random field specified at vector location $\mathbf{x}_1$, and $E[\cdot]$ represents the expectation function [e.g., *Feller*, 1971]. The variable $\mathbf{x}$ is defined as the lag vector. Where h is sampled on a m by n grid specified by discrete (column,row) locations (i,j), the discrete covariance function $C_{hh}(k,l)$ can be estimated by

$$\tilde{C}_{hh}(k,l) = \frac{1}{(n-k)(m-l)} \sum_{i=1}^{n-k} \sum_{j=1}^{m-l} h_{i,j} h_{i+k,j+l}. \qquad (2)$$
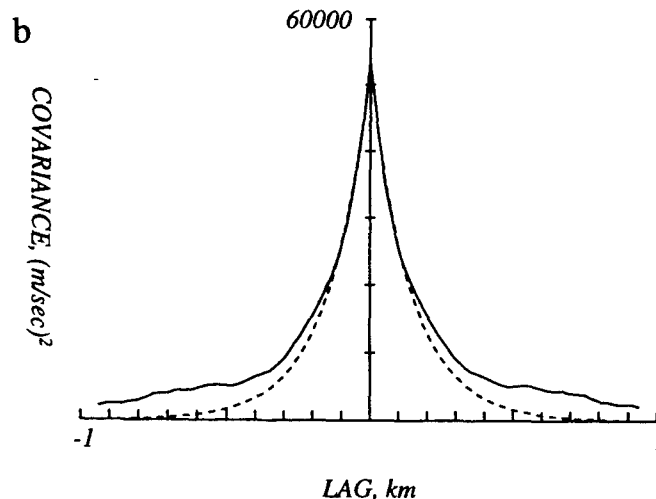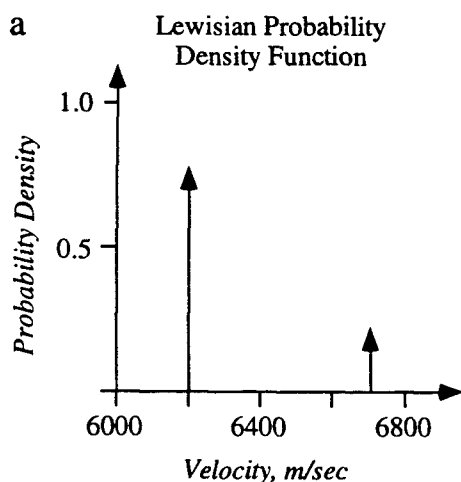
Covariance modeling is typically accomplished by fitting a parameterized functional model to the sample covariance estimated from the digital exposure map using forward modeling [e.g., *Holliger et al.*, 1993; *Levander et al.*, 1994a; *Holliger and Levander*, 1994] or a least-squares inversion [*Goff and Jordan*, 1988]. The *von Kármán* [1948] covariance model [e.g., *Wu and Aki*, 1985; *Frankel and Clayton*, 1986; *Fisk et al.*, 1992; *Holliger et al.*, 1993; *Levander et al.*, 1994a, *Holliger and Levander*, 1994] represents a class of monotonically decaying (i.e., aperiodic) functions, and includes as a subset the exponential form. The singular advantage of the von Kármán model is that it explicitly includes the fractal dimension as a variable. *Goff and Jordan* [1988] modified the von Kármán covariance function to account for structural anisotropy in 2-dimensions (easily expanded to 3-dimensions). The following parameters specify the 2-D anisotropic von Kármán model:

1. The rms velocity H is the average variation about the mean velocity.

2. The lineament orientation θ_S is strike of direction of maximum correlation; structures will tend to be oriented along this direction.

3. The scale parameter controls the rate of decay of the covariance. In one dimension the scale parameter is specified by k_0. In two dimensions there are two principal scale parameters: k_n in the normal-to-strike direction, and k_S in the along-strike direction; $k_n > k_S$.

4. The aspect ratio a is the characteristic planar shape of structures, defined by the ratio k_n/k_S.

5. The Hausdorff (fractal) dimension D is a measure of roughness.

An inversion procedure for parameter estimation also provides estimates of uncertainties. Estimated Lewisian model parameters are, with 1-σ uncertainties: $H = 234 \pm 4$ m/sec, $\theta_S = 85.0° \pm 0.4°$, $k_n = 24.5 \pm 1.0$ km^{-1}, $ks = 6.0 \pm 0.3$ km^{-1}, and $D = 2.54 \pm 0.04$. Figure 2b displays the best fit von Kármán model to the 1-D sample covariance in the row direction ($C_{hh}(i,0)$).

a Lewisian Probability Density Function

b

Figure 2. (a) PDF for the Lewisian stochastic model. (b) Comparison of Lewisian data (solid) and best-fit model (dashed) 1-D covariances for the row direction ($C_{hh}(i,0)$).

Synthetic Fields

Realizations of the stochastic model described above can be synthesized by first generating a Gaussian-distributed field, which we term a "normal equivalent" field, and then mapping it into a new field, the "model" field, that conforms to the PDF specified in the model. This algorithm includes the following steps [*Goff et al.*, 1994]:

1. A mapping function is created which specifies the conversion of a Gaussian PDF with zero mean and unit variance to the PDF $p(h)$ specified by the stochastic model. Specifically, for each possible value g sampled from a Gaussian PDF $p_G(g)$, we find a new value h such that:

$$\int_{-\infty}^{h} p(h')dh' = \int_{-\infty}^{g} p_G(g')dg' . \qquad (3)$$

For a simple binary field, where unit 1 has total probability ρ_1, and unit 2 has total probability $\rho_2 = 1 - \rho_1$, equation (3) is equivalent to identifying a cutoff Gaussian value g_c, where every value less than g_c is mapped to unit 1, and every value greater than g_c is mapped to unit 2, and

$$\rho_1 = \int_{-\infty}^{g_c} p_G(g')dg' . \qquad (4)$$

For the Lewisian PDF, $g_c = 0.75$. Hence, for the Lewisian model field, any Gaussian value less than 0.75 is mapped to gneiss, and everything else to amphibolite.

2. The covariance for the normal equivalent field, $C_{gg}(\mathbf{x})$, is determined such that when the PDF mapping described above is performed, the model field conforms to the model covariance $C_{hh}(\mathbf{x})$. Where both normal equivalent and model fields have zero mean and unit variance, the relationship is given by *Christakos* [1992; page 332, equation 3]. In general this equation must be solved by numerical integration.

3. Generate a synthetic normal equivalent realization $g(i,j)$ conforming to covariance $C_{gg}(k,l)$ by Fourier methods [e.g., *Goff and Jordan*, 1988; 1989a].

4. For each discrete value of the normal equivalent $g(i,j)$, determine the value of the model field $h(i,j)$ using the PDF mapping described in step 1.

The Lewisian Data/Synthetic Comparison, Take 1

The Lewisian 2-D stochastic model is summarized as follows: (1) The PDF is a binary distribution of 78% gneiss (6.2 km/s) and 22% amphibolite (6.75 km/s); (2) the covariance is modeled by a von Kármán function specified by parameters $k_n = 24.5$ km^{-1}, $k_s = 6.0$ km^{-1}, $\theta_s = 85.0°$ (where 0° represents vertical lineament orientation), and $D = 2.54$. Figure 1b displays a full two-dimensional synthetic realization of the stochastic model estimated from the

Lewisian map of Figure 1a. The covariance parameters for the normal equivalent field are: $k_n = 21.6$ km^{-1}, $k_s = 5.28$ km^{-1}, $\theta_s = 85.0°$, and $D = 2.00$.

As stated in the Introduction, comparison between Figures 1b, the synthetic realization of the stochastic model, and Figure 1a, the data from which the stochastic model is derived, indicates both successes and failures of the stochastic model. The success of the model is that it correctly describes the physical properties that it is designed to describe; i.e., probability of units, scales of structures, orientation, and roughness. The failure of the model is that it is not complete; i.e., it cannot reproduce the pattern which is visually obvious to the eye: the sinuous connectivity of the units.

III. Sinuous Connectivity Modeling and Synthetics

Till now we have employed a stochastic modeling technique which requires joint characterization of the PDF and covariance of the field of interest. A great advantage of this technique is that estimation of model parameters can be performed through direct inversion of sample data. An entirely equivalent, though indirect, stochastic modeling technique would be joint specification of a PDF mapping and the covariance function of a normal equivalent: i.e., the "recipe" for generating synthetic realizations. In the case of the Lewisian model discussed above, this type of stochastic model would be specified by the normal equivalent covariance parameters $k_n = 21.6$ km^{-1}, $k_s = 5.28$ km^{-1}, $\theta_s = 85.0°$, and $D = 2.00$, and the Gaussian-to-binary PDF mapping function with separation scale $g_c = 0.75$.

The rationale for adopting the latter approach to stochastic modeling is that it provides an added dimension to characterization not available in the former: the PDF mapping. The PDF mapping presented earlier is, in fact, only the simplest possible case of a Gaussian-to-binary mapping. The only real constraint that is placed on this mapping is that the total probability of unit 1 (gneiss) is 0.78, and the total probability of unit 2 (amphibolite) is 0.22. Instead of finding a single value g_c which separates the Gaussian PDF into regions of 0.78 and 0.22 probability, we can formulate a more complex mapping into alternating bands of unit 1 and unit 2, ensuring that the sum of all unit 1 probability is 0.78, and the sum of all unit 2 probability is 0.22. This operation will map the alternating units onto contour sets of the normal equivalent surface; we therefore apply the term "contour set mapping" to this type of PDF mapping. As anyone who has seen a contour map of topography will quickly intuit, contour set mapping should generate a binary surface possessing the property of sinuous connectivity.

Contour Set Mapping Synthetics

More formally, we specify a binary contour set mapping in the following way:

$$h(\mathbf{x}_1) = \begin{cases} & \cdot \\ & \cdot \\ H_2, & g_3 < g(\mathbf{x}_1) < g_4 \\ H_1, & g_2 < g(\mathbf{x}_1) < g_3 \\ H_2, & g_1 < g(\mathbf{x}_1) < g_2 \\ H_1, & g_0 = -\infty < g(\mathbf{x}_1) < g_1 \end{cases}, \qquad (5)$$

where H_1 and H_2 represent the values given to units 1 and 2 respectively. Each interval defined by the boundary values g_{i-1} to g_i is defined as a "contour set", and the difference $g_i - g_{i-1}$ is defined as the "contour set thickness". Total probabilities for each unit are computed by the following:

$$\rho_1 = \sum_{i \text{ odd}} \int_{g_{i-1}}^{g_i} p_G(g')dg',$$

$$\rho_2 = 1 - \rho_1 = \sum_{i \text{ even}} \int_{g_{i-1}}^{g_i} p_G(g')dg' \qquad (6)$$

The boundary values g_i must be chosen so that ρ_1 and ρ_2 satisfy our total probability constraints (for the Lewisian case, ρ_1 must equal 0.78 and ρ_2 must equal 0.22). Beyond that, however, the values of g_i are arbitrary, unfortunately resulting potentially in an infinite number of additional parameters to the model. Limitations on parameters will be discussed below.

While contour set mapping must satisfy total probability constraints, the covariance of the normal equivalent field must be chosen so that the model field corresponds to the model covariance. While we cannot at this time make formal statements of uniqueness, it is nevertheless clear from our experience in forward modeling that, for a given PDF mapping, this is a strong constraint.

Before presenting examples of synthetic realizations generated with contour set mappings, we must remark that von Kármán normal equivalent covariances do not strictly imply von Kármán model covariances, as was the case for simple Gaussian-to-binary mappings [*Goff et al.*, 1994]. This is particularly true where contour sets for either unit 1 or unit 2 or both are not of uniform thickness. Where unit 1 thickness are uniform and unit 2 thicknesses are uniform, the model covariance resulting from a von Kármán normal equivalent covariance can be reasonably approximated by a von Kármán function. The correspondence between the model covariance and a best-fitting von Kármán function in these cases is not always exact, but misfit, where it occurs, is concentrated at the larger lags where resolution of the covariance estimated from data is very poor (i.e., either will fit the data just as well). However, in some cases, two of which will be highlighted in the following section, the covariance estimated from the data field is not well-fit by the von Kármán function;

instead of a simple decay with increasing lag, the covariance of these fields exhibits two scales of decay. The flexibility allowed in the contour set mapping is instrumental in reproducing these more complicated covariance structures.

Figure 3 displays a series of four model fields generated using progressively thinner contour sets, labeled as model fields 1-4. The contour set mappings are also shown, displayed graphically as black and white areas below the Gaussian PDF. Each model field PDF and covariance correspond to the stochastic model described earlier for the Lewisian map (Figure 1a). Model field 1 is just a simple Gaussian-to-binary mapping presented earlier as Figure 1b. All the normal equivalent fields were generated with identical random phase spectra, which enhances visual recognition of structural similarities.

Our primary observation derived from Figure 3 is that contour set mappings successfully produce sinuous connectivity in the model field. In particular, model field 3 is identical to the synthetic realization in Figure 1c, which was compared to the data field (Figure 1a) in the Introduction. As noted earlier, this comparison is visually superior to the comparison of Figure 1b (simple Gaussian-to-binary mapping) to Figure 1a.

The Sinuous Connectivity Parameter

Now that we've established a method for characterizing and synthesizing fields that possess the property of sinuous connectivity, we ask ourselves if it is possible to quantify sinuous connectivity itself. In other words, might it possible to state that one field has more or less sinuous connectivity than another field? By stepping through progressively thinner contour set thicknesses, Figure 8 was designed to address this question. If sinuous connectivity were a quantifiable property, then we would expect a general increase in this property as we decrease in contour set thickness in the PDF mapping. However, this does not appear to be the case. While there is a strong contrast in character going from the model field 1 to model field 2 in Figure 3, beyond that there is little noticeable change in character with decreasing contour set thickness. The apparent invariance of sinuous connectivity characteristics is likely attributable to the self-similarity property of the fractal normal equivalent fields [e.g., *Mandelbrot*, 1981].

The important implication of the above observation is that wide classes of stochastic models based on contour set mappings and normal equivalent covariances are redundant, or non-unique. On the one hand this is problematic, since it implies that this technique for stochastic modeling will not be useful in an inversion problem. On the other hand, this observation is very powerful, because it vastly simplifies the parameterization that is necessary: the stochastic model is complete just by specifying its PDF, covariance, and whether or not it is sinuously connective.

631

Model Field 1
Normal Equivalent Parameters:
$k_n = 21.6$ km^{-1}, $k_s = 5.28$ km^{-1}, $D = 2.00$

Model Field 2
Normal Equivalent Parameters:
$k_n = 4.90$ km^{-1}, $ks = 1.20$ km^{-1}, $D = 2.04$

Model Field 3
Normal Equivalent Parameters:
$k_n = 1.89$ km^{-1}, $k_s = 0.46$ km^{-1}, $D = 2.10$

Model Field 4
Normal Equivalent Parameters:
$k_n = 0.82$ km^{-1}, $k_s = 0.20$ km^{-1}, $D = 2.10$
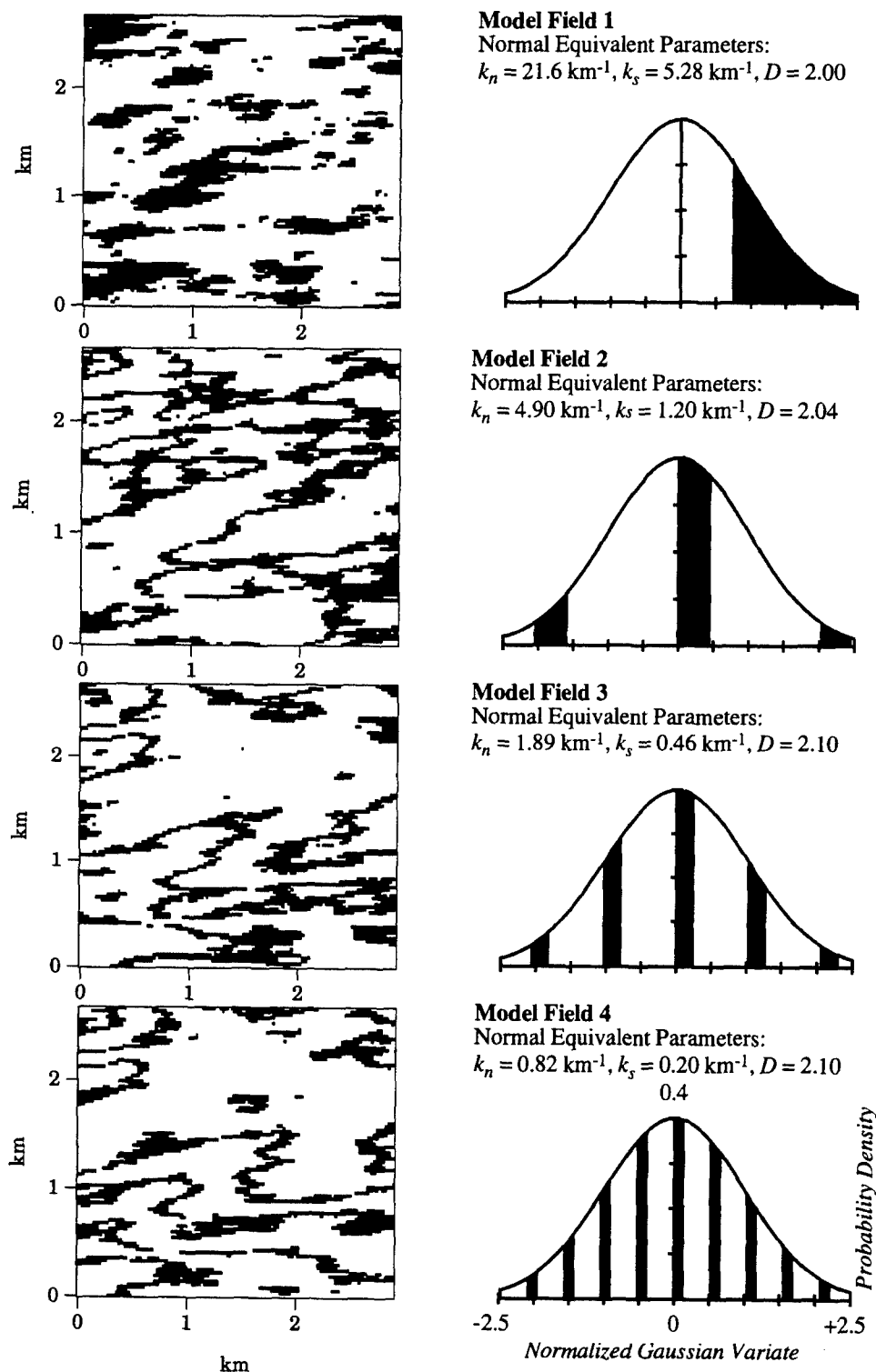
Figure 3. A series of 4 model fields, all with identical PDF and covariance (the Lewisian stochastic model), generated with contour set mappings of decreasing contour set thickness. To the right of each model field, normal equivalent covariance parameters are. All normal equivalent fields had identical H (1.0) and θs (85°). Also shown are to the right are graphical representations of the contour set mapping; any value sampled from the normal equivalent field that fell within the white regions was mapped to unit 1, and any sample that fell within the black regions was mapped to unit 2. In Model fields 2 through 4, the contour set thickness changes by a factor of 2 at each step. Model fields 1 and 3 are identical to model field presented in Figures 1a and 1b respectively.

632

a Franciscan Complex

b Franciscan Sinuously Connective Synthetic Realization

SANDSTONE NO DATA MELANGE

SANDSTONE MELANGE

c

Probability Density

0.4

-2.5 *0* *+2.5*

Normalized Gaussian Variate

d

COVARIANCE, (m/sec)²

1

-6 *LAG, km* *6*
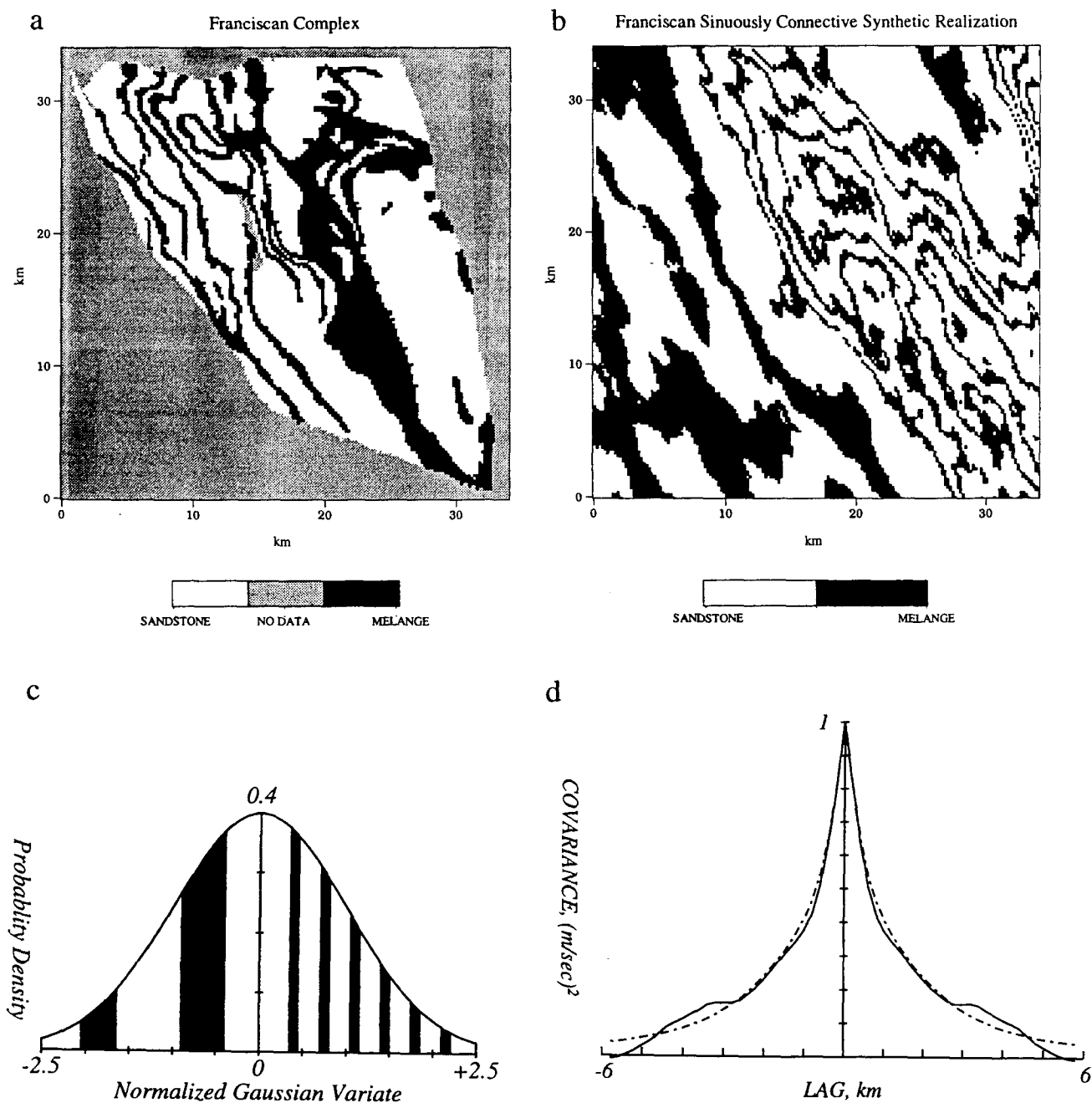
Figure 4. (a) Digitized map of the Franciscan complex, northern California (B.M. Page, 1994, unpublished). A small percentage of volcanic units within the map were ignored as insubstantial. Map is 66% sandstone and 34% melange. While sandstone will have a nearly uniform seismic velocity of ~5.8-5.9 km/s, melange is expected to exhibit a range of velocities from ~5.0-6.4 km/s. There are two problems in stochastic modeling associated with the Franciscan: the interaction between melange and sandstone, and the properties of the melange. For the present we concentrate on the former, and simply identify sandstone and melange with proxy values -1 and +1. (b) Synthetic realization based on PDF and covariance modeling of the Franciscan complex, including 2-scaled contour set mapping and the property of sinuous connectivity. Normal equivalent parameters are listed in text. (c) Graphical representation of the Franciscan contour set mapping; any value sampled from the normal equivalent field that fell within the white regions was mapped to unit 1 (sandstone), and any sample that fell within the black regions was mapped to unit 2 (melange). (d) Comparison of the Franciscan 1-D column-direction $(C_{hh}(0,j))$ data covariance (solid) with the model covariance (dashed) computed for the 2-scaled, sinuously connective field.

a

Hafafit Complex

GNEISSIC PSAMMITES OR   NO DATA   METAGABBRO
GNEISSIC GRANODIORITE

b

Hafafit Sinuously Connective Synthetic Realization

GNEISSIC PSAMMITES OR   METAGABBRO
GNEISSIC GRANODIORITE

c

Probablity Density

Normalized Gaussian Variate

d

COVARIANCE, (m/sec)²

LAG, km
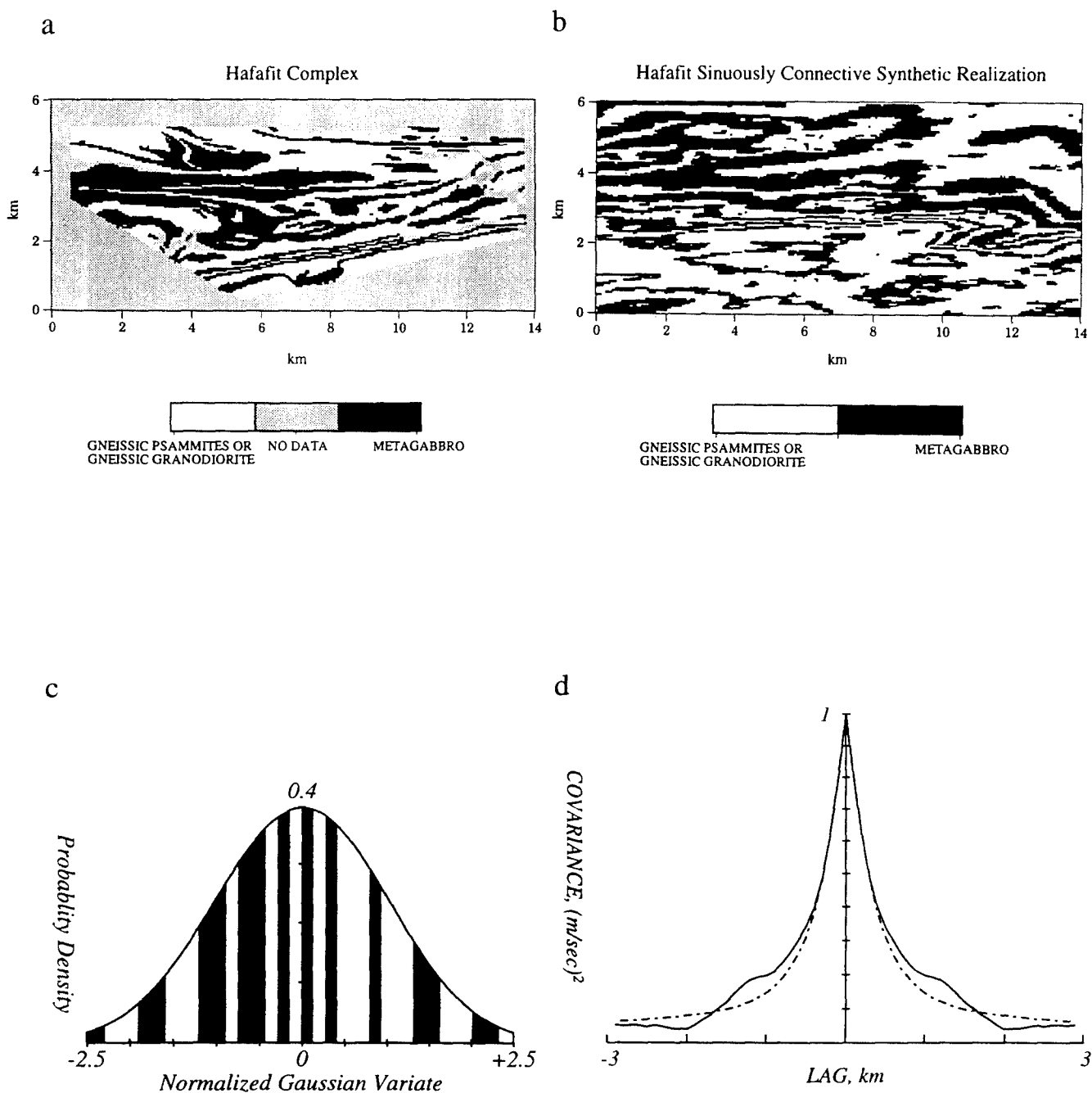
Figure 5. (a) Digitized map of the Hafafit complex, eastern Egypt [*Greiling and El-Ramly*, 1990; *Rashwan*, 1991]. The gneissic psammites and gneissic granodiorites have only incidental contact, and so were considered as one unit to increase coverage. A small percentage of granites were ignored as insubstantial. Where it was clearly obvious to do so, units were interpolated where covered by wadi alluvium. Map contains 50% gneiss and 50% metagabbro. Petrophysical data are not known, so proxy values of -1 and +1 were assigned respectively to the gneiss and metagabbro. It is certain, however, that the metagabbro will have a faster seismic velocity than the gneiss. (b) Synthetic realization based on PDF and covariance modeling of the Hafafit complex, including 2-scaled contour set mapping and the property of sinuous connectivity. Normal equivalent parameters are listed in text. (c) Graphical representation of the Hafafit contour set mapping; any value sampled from the normal equivalent field that fell within the white regions was mapped to unit 1 (gneiss), and any sample that fell within the black regions was mapped to unit 2 (metagabbro). (d) Comparison of the Hafafit 1-D row-direction ($C_{hh}(i,0)$) data covariance (solid) with the model covariance (dashed) computed for the 2-scaled, sinuously connective field.

634

IV. Complex Examples

Two more examples of sinuous connectivity modeling are presented in Figures 4 (Franciscan formation) and 5 (Hafafit gneiss complex). These examples are more complex than the Lewisian example because their covariance functions were not well-fit by a von Kármán model. In particular, we required two superposed scales of decay. This behavior can be matched, however, in the contour set mapping not by formulating a complex normal equivalent field, but rather by using complex combinations of contour thicknesses. Normal equivalent field parameters for the Franciscan are: k_n = 0.144 km^{-1}, k_s = 0.052 km^{-1}, θ_s = -26.3°, and D = 2.00. Normal equivalent field parameters for the Hafafit are: k_n = 0.43 km^{-1}, k_s = 0.080 km^{-1}, θ_s = 91.1°, and D = 2.10.

V. Conclusions

Previous work in stochastic modeling of lithologic heterogeneity has involved joint characterization of the PDF, which is usually modal (i.e., binary, ternary, etc.), and the covariance function, which is often well-represented by the von Kármán function. In this paper we have built upon that earlier work by incorporating, in addition to PDF and covariance characterization, a method for modeling fields that possess the property of sinuous connectivity. This method involves defining a Gaussian-to-binary contour set mapping and a normal equivalent field such that, when the normal equivalent field is mapped to the binary model field, the PDF and covariance of the model field honor the stochastic model. This modeling scheme also constitutes a recipe for generating sinuously connective synthetic realizations of the stochastic model.

An important observation derived from synthetic realizations is that, owing to the self similarity property of the fractal normal equivalent fields, sinuous connectivity modeling is highly non-unique. Wide classes of contour set mappings/normal equivalent fields will generate statistically identical model fields. It is suggested, therefore, that the property sinuous connectivity can be characterized by a binary parameter: either the field is sinuously connective or it is not.

Stochastic models and synthetic realizations of lithologic heterogeneity should play a critical role in modeling seismic wave propagation through a complex crust. The stochastic model presented here is the most realistic and complete representation of lithologic heterogeneity presented to date. We believe that this model is, in fact, sufficiently "complete" for application to the seismic problem; i.e., additional complexity or parameterization will probably not siginficantly affect the observed seismic wavefield. Our future plans center around investigating the response of the observed wavefield to parameters of the stochastic model.

References

Christakos, G., *Random field models in Earth sciences*, 474 pp., Academic Press, San Diego, 1992.

El-Ramly, M. F., and R. O. Greiling,*Wadi Hafafit Area*, 1988.

Feller, W., *An Introduction to Probability Theory and Its Applications*, vol. 2, 669 pp., John Wiley, New York, 1971.

Fisk, M. D., E. E. Charrette, and G. D McCartor, A comparison of phase screen and finite difference calculations for elastic waves in random media, *J. Geophys. Res.*, *97*, 12,409-12,423, 1992.

Frankel, A., and R.W. Clayton, Finite difference simulations of seismic scattering: Implications for the propagation of short-period seismic waves in the crust and models of crustal heterogeneity, *J. Geophys. Res.*, *91*, 6465-6489, 1986.

Goff, J. A., and T.H. Jordan, Stochastic modeling of seafloor morphology: Inversion of Sea Beam data for second-order statistics, *J. Geophys. Res.*, *93*, 13,589-13,608, 1988.

Goff, J. A., K. Holliger, and A. Levander, Modal fields: A new method for characterization of random seismic velocity heterogeneity, *Geophys. Res. Lett.*, *21*, 493-496, 1994.

Greiling, R.O., and M.F. El-Ramy, *Wadi Hafafit Area - Structural Geology*, Geologic map, German Ministry of Research and Technology, Technische Fachhochschule Berlin, Germany, 1990.

Holliger, K., A. Levander, and J. A. Goff, Stochastic modeling of the reflective lower crust: petrophysical and geological evidence from the Ivrea Zone (Northern Italy), *J. Geophys. Res.*, *98*, 11,967-11,980, 1993.

Holliger, K., and A. Levander, Seismic strcture of gneissic/granitic upper crust: geological and petrophysical evidence from the Strona-Ceneri zone (northern Italy) and implications for crustal seismic exploration, *Geophysical Journal International, 119*, 497-510, 1994.

Jervis, M., M. K. Sen, and P. L. Stoffa, Optimization methods in 2D migration velocity estimation, *Geophysics*, in press, 1995.

Levander, A., R.W. England, S.K. Smith, R.W. Hobbs, J.A. Goff, and K. Holliger, Stochastic characterization and seismic response of upper and middle crustal rocks based on the Lewisian gneiss complex, Scotland, *Geophys. J. Int.*, *119*, 243-259, 1994a.

Levander, A., S.K. Smith, R.W. Hobbs, R.W. England, D.B. Snyder, and K. Holliger, The Crust as a Heterogeneous "Optical" Medium, or "Crododiles in the Mist", *Tectonphysics, 232*, 281-297, 1994b.

Mandelbrot, B. B., *The Fractal Geometry of Nature*, 468 pp., W. H. Freeman, New York, 1983.

Rashwan, A.A., *Petrography, geochemistry and Petrogenesis of the Migif-Hafafit Gneisses at Hafafit Mine Area, Egypt*, Scientific Series of the International Bureau, 5, Forschungszentrum Julich GmbH, Germany, 1991.

von Kármán, T., Progress in the statistical theory of turbulence, *J. Mar. Res.*, *7*, 252-264, 1948.

Wu, R.-S., and K. Aki, The fractal nature of the inhomogeneities in the lithosphere evidenced from seismic wave scattering, *Pure Appl. Geophys.*, *123*, 805-818, 1985.

Simultaneous Inversion for Detailed Source and Structure Parameters Using Quarry Blast Data Recorded in Eastern Kazakhstan

Danny J. Harvey

University of Colorado

Abstract

We have completed a study aimed at the development of a full waveform joint structure-source inversion method. We used differential seismograms to represent the linearized structure effects and perturbed source terms to represent the source effects. We found it desirable to include unbalanced force terms, in addition to an arbitrary symmetric moment tensor, to represent the source. We also found it necessary to use exact expressions for computing the differential seismograms that did not involve eigenvalue-only approximations. We applied the inversion method to a dozen local quarry blasts recorded by the NRDC network in Kazakhstan in the 0.4 to 2.0 Hz frequency range. We found that it was possible to produce very good fits between the synthetic seismograms and the observed data on all three components simultaneously and for the P-wave, Rayleigh wave and Love wave. The inclusion of the unbalanced force terms significantly improved the fits for some of the events and resulted in more reasonable structure and source parameters than were obtained without the force terms. We interpreted some of the inverted source parameters as being characteristic of several different types of industrial surface mining operations.

Key Words
local events, waveform inversion, waveform modeling, industrial explosions

1. Objective

The objective was to obtain fundamental understanding of the source physics and local wave propagation characteristics associated with industrial explosions by attempting to match synthetic seismograms with real quarry blast data. In this report we will document a study in which we developed a technique for inverting full waveform data for both detailed source parameters and structure parameters. We used seismograms from a set of industrial explosions that were analyzed in a previous study as our data. These explosions took place in Eastern Kazakhstan and were recorded by the Natural Resources Defense Council seismic network that was in operation during 1987.

2. Research Accomplished

2.1 Inversion Procedure

We started using the structure inversion technique developed in a previous work[1] which we will refer to as Harvey (1993). In this study we developed a structure inversion method, using both dispersion and full waveform data, based upon the cylindrical geometry, laterally homogeneous, elastic wave propagation methods developed by Harvey[2] that uses a normal mode superposition approach for computing synthetic seismograms. The full waveform inversion method we developed is similar to the method described in Gomberg and Masters[3] and Walter and Ammon[4] and generally consists of the usual damped steepest descent approach that utilizes differential seismograms[5] for the determination of local performance function gradients. Although our method is most similar to that of Gomberg and Masters, since we use a normal mode as opposed to a reflectivity approach, we made some substantial changes to the method developed by Gomberg and Masters which we found necessary to insure rapid and accurate matching between the synthetic and real seismograms.

In our previous work, we essentially either constrained the source terms in the inversions, or inverted for a scalar source amplitude using a simple explosion source, or we employed a "seat-of-the-pants" method for obtaining more complicated source moment tensor solutions that did not involve the use of formal inversion for the source moment tensor. In this study we have developed a complete formal inversion method that allows us to infer both structural and source parameters simultaneously. We added unbalanced force terms to the standard symmetric moment tensor terms which we found to be desirable for modeling shallow industrial explosions.

---

[1] Harvey, D., 1993, Full waveform inversion for structure and source parameters using regional data recorded in Eastern Kazakhstan, Final Report, Report no. PL-TR-93-2078, Phillips Laboratory, Air Force Materiel Command. ADA266405

[2] Harvey, D. (1981). Seismogram synthesis using normal mode superposition: the locked mode approximation. *Geophys. J. R. Astr. Soc.* **66**, 37-61.

[3] Gomberg, J. and Masters, T., 1988, Waveform modelling using locked-mode synthetic and differential seismograms: application to determination of the structure of Mexico, *Geophys. J. R. Astr. Soc.*, **94**, 193-218.

[4] Walter, W. and Ammon, C., 1993, Complete regional seismic waveform inversion for crust and upper mantle structure: The September 14, 1988 JVE explosion, Kazakhstan, Eurasia, Preprint, Lawrence Livermore National Laboratory, Report no. UCRL-JC-112844

[5] Harvey, D., 1991, Studies of regional wave propagation using differential seismograms and randomized structural models, Final Report, Report no. PL-TR-91-2126, Phillips Laboratory, Air Force Systems Command, ADA247011.

2.1.1 Source Parameter Inversion

We follow the work of Stump[6] who describes the process of formulating a synthetic Green's function as a linear sum of a special set of synthetic seismograms weighted by terms that can be directly related to the symmetric moment tensor elements. We did our inversions in the time domain after applying a bandpass filter to both data and synthetics.

In addition to the ten synthetic Green's function components that are required to represent an arbitrary symmetric moment tensor (for laterally homogeneous structures), we added five more Green's function components that are required to represent an arbitrary unbalanced force vector. The resulting 15-component Green's function was combined with the 3-component data to form a 9x9 least squared inversion matrix for the 9 source parameters (6 moment tensor elements and 3 force elements). Standard singular value decomposition was used to form the inversions. The double-couple, dipole, explosion or force terms could be independently constrained in the source inversion.

2.1.2 Source-Structure Inversion Process

In order to simultaneously invert for both structure and source parameters, it is first necessary to expand the synthetic solution in terms of a linearized joint expression of both source terms and structural perturbations. If the source terms were small perturbations like the structural terms, then the linearized synthetic representation would be a simple expression involving both source and structure perturbations. However, in the case of the source inversion, the source terms are not small perturbations, but are the actual moment and force values and the linearized synthetic expression can be considered to be exact, to the extent that the linear elastic wave equation governs the overall physics of the wave propagation process. On the other hand, the linearized synthetic solution expressed as a function of the structural perturbations is definitely an approximation to the actual relationship between the synthetic waveforms and the structural parameters, which is highly non-linear even when using a linear form of the elastic wave equation. In this situation it is necessary that the structural perturbations remain small in order for the linearized synthetic waveforms to be valid and thus the inversion to remain stable.

We can write down an expression for the synthetic waveforms as a sum of the 15-component source Green's functions weighted by the source moment and force terms. Each of these Green's functions can then be expanded as a linear perturbation involving differential Green's functions and the structural perturbations. If we put these expanded Green's functions into the original representations for the synthetic waveforms we are left with expressions that are non-linear in the source and structure model parameters and are thus not suitable for linear inversion. One way around this problem is to assume that the source terms can be expanded into zeroth order terms plus small perturbations. Using this approach we can derive a set of synthetic waveform expressions with completely linearized dependences on small source and structure perturbations. However, we are still left with the determination of the zeroth order source parameters which will require source-only inversions.

Our joint source-structure inversion procedure is iterative in nature to account for the non-linear relationship between the synthetic waveforms and the structure parameters. We fix a set of layer thicknesses based upon the applicable wavelengths. We then make a zeroth order estimate of the structure velocities, densities and Q values using observed dispersion functions, travel times and any other constraints that we can

---

[6] Stump, B., Investigation of seismic sources by the linear inversion of seismograms, Ph.D. Thesis, University of California, Berkeley.

reasonable use. This initial estimate of the structure is one of the more tedious and difficult parts of the inversion. At this point we typically constrain the Q values and the densities.[7] We start the iterations by doing a source-only inversion to determine the zeroth order source parameters. Using these source parameters, we then do a simultaneous source-structure inversion for small source and structure perturbations. We add a small structure perturbation constraint to the performance function to stabilize the structure part of the inversion. We add the structural perturbations to the original model and we go on to the next iteration by doing another zeroth order source-only inversion.

Note that we do not add the inverted source perturbations to the zeroth order source parameters, but instead do another zeroth order source-only inversion. If the linearized synthetic expressions were exact, then there should be no difference between the two approaches, and in the case where the linearized synthetic expressions are inexact, redoing the source-only inversion acts to stabilize the inversion by removing the source perturbations that are produced as a result of inaccuracies in the linearized structure dependent parts of the expressions. One might ask why we bother to do the joint inversion at all if we are going to ignore the source perturbation results from the joint inversion. The answer to this is that it is desirable to allow the extra degrees of freedom when doing the structure inversion so that some amount of fit can be taken up in source terms as opposed to requiring structure perturbations only. This should cause the inversion to converge more rapidly than doing source-only, structure-only iterations.

2.2 Data and Observations

We used seismic data recorded as part of the NRDC program conducted during 1987. The NRDC network was operated by the University of California, San Diego and consisted of three stations that surrounded the Shagan River and Degelen Mountain areas of the Eastern Kazakhstan Soviet test site. Although there were three stations in the NRDC network, throughout most of the year only one or two stations were operational and the most consistent station was KKL (Karkaralinsk). All of the results in this study are based upon data collected at KKL. We used as our data source the NRDC Information Product which was compiled by IRIS' Joint Seismic Program Center and distributed through the IRIS Data Management Center.

The instrumentation at KKL consisted of a surface 1 Hz 3-component seismometer, a surface 0.2 Hz 3-component seismometer and a borehole 0.2 Hz 3-component seismometer all recording at two different gain levels (on 16-bit digitizers) and at 250 sps. The site was on granitic bedrock and generally exhibited low noise characteristics. The region around KKL is an active mining area with many shallow explosions and generally exhibits low natural seismicity. Most seismicity in the area is of the "induced" type and is associated with the large nuclear explosions at the former Soviet test site.

2.2.1 Data Characterization

A total of 12 events were used in this study. These events came from the results of Harvey (1993) and consist of presumed quarry blasts all within about 25 km of Karkaralinsk. Event epicenters were determined by using the S-P distances along with back azimuth estimates that were obtained from polarization analysis. We chose a set of events that were clustered and are presumably from a few different quarries.

---

[7] For this study we were able to assume elastic propagation throughout because of the short source-receiver distances and the relatively low frequencies.

Figure 1 shows the unfiltered KKL radial, transverse and vertical components for event number 521. The time is relative to the event origin time. The label on the left of the traces shows an event id for each event, along with the distance in km and the event to station azimuth in degrees. Figure 1 also shows the same event after passing through a 0.4 to 2.0 Hz Butterworth bandpass filter. The filtered traces show high signal to noise with strong Rg excitation. The transverse component shows strong Love wave excitation as well. In the high frequency band we can see that there must be a high degree of scattering of the P-wave into the transverse component which is likely due to 3-dimensional scattering. However, in the 0.4 to 2.0 Hz passband the transverse P-wave component is very small compared to the radial P-wave components. Also in the lower frequency band the P-wave to Rayleigh wave amplitude ratio is small.

We can see from Figure 1 that there is a strong low frequency Love wave. The relative amplitude of this Love wave varies considerably from event to event. At this distance and in this frequency band there can be no more than about 10 wave cycles for the lowest velocity waves at a frequency of 2 Hz. Given the observed variations in the Love wave relative amplitudes and the small number of wave cycles along the propagation path it is unlikely that the large Love waves are caused by lateral scattering, but instead are caused by direct source excitation.

The use of a simple explosion source will obviously produce none of the Love waves that we see in the data. We can use an arbitrary symmetric moment tensor to parameterize the source which will result in non-zero Love wave components. However, if we think about the physics associated with a large surface explosion, we can see that the use of a moment tensor to represent the source, which best characterizes completely contained explosions or other relaxation sources such as earthquakes, may not be adequate.

To start with, we assume that most large industrial explosions are intended to aid in the excavation of surface material and are thus designed to be uncontained. Completely contained explosions are usually used in underground mining operations and tend to be small to avoid damaging the mining infrastructure.[8] An explosion associated with a surface mining operation is designed to pulverize large amounts of rock and, in some cases, to move the pulverized material laterally. Regardless of whether or not the actual gases associated with the explosion are well contained, the rock material around the explosion will be broken up to the surface and there will be a disruption in the elastic integrity of the rock mass that originally surrounded the explosion which will result in an effective unconstrained source term. In addition, when significant quantities of rock material are moved laterally by the explosion, we would expect an unbalanced lateral thrust vector to be applied to the elastic material.

2.3 Inversion Results

Because of the large difference between the P-wave and Rg amplitudes we found it desirable to equalize these amplitudes through the application of a time-varying gain factor before performing the inversions. This was accomplished through the following steps for each event. First, we computed a time-varying rms average of the individual data components after rotating to radial and transverse components. These rms functions were then divided into the data to give amplitude equalized data functions (these are sometimes called AGC functions). We then used the same rms functions to equalize the amplitudes of the synthetic seismograms and each of the Green's function components and the differential seismograms. The inversions were then performed with these amplitude equalized traces. All data and synthetics were put through a 0.4 to 2.0 Hz bandpass filter before the inversion.

---

[8] The obvious exceptions to this are underground nuclear explosions.
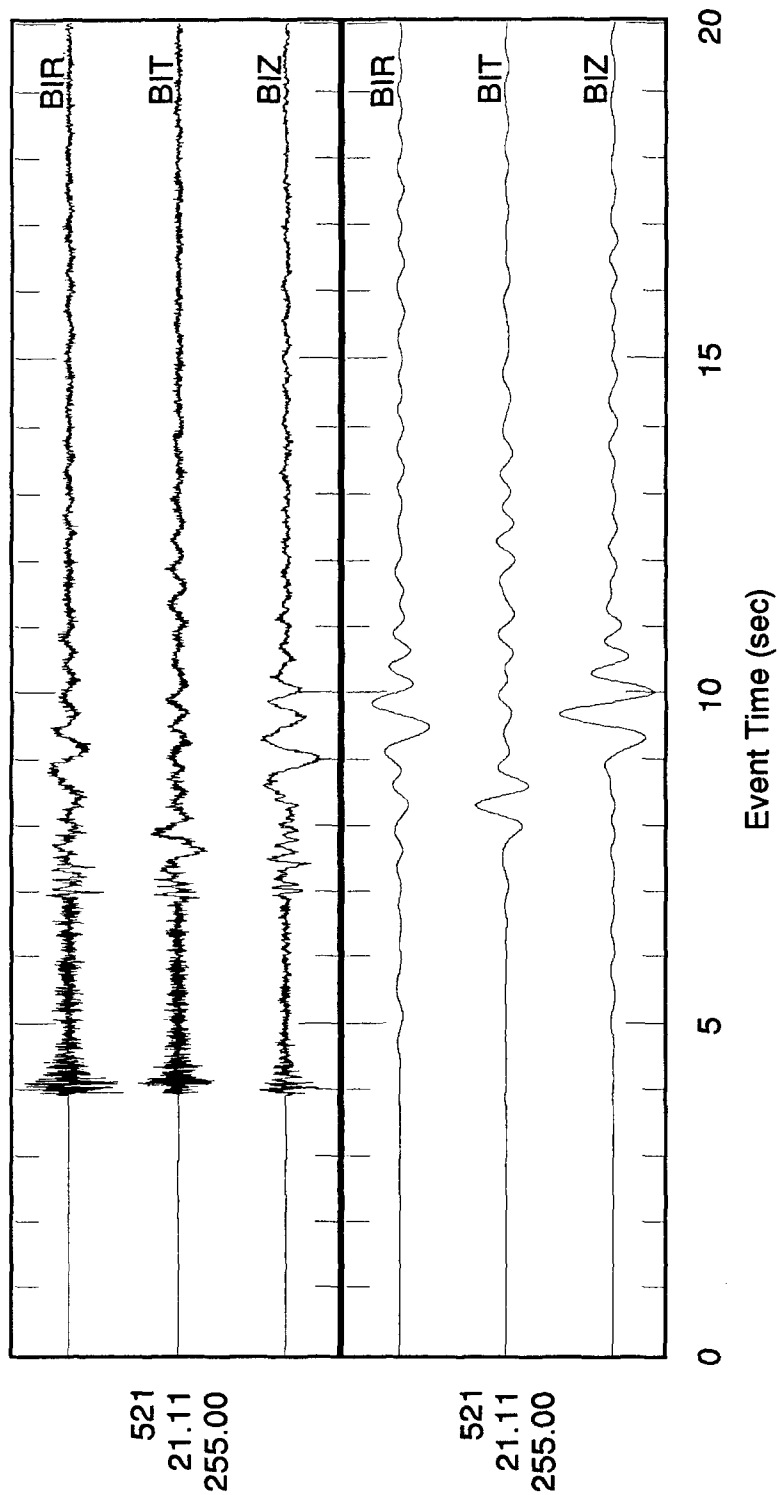
Figure 1. Unfiltered and filtered radial, transverse and vertical component seismograms for event number 521. The labels to the left refer to the event id, the distance in km and the event to station azimuth in degrees.

The results of simultaneous source-structure inversion of event number 521 are summarized in figure 2. At the bottom left hand corner are comparisons of the filtered and amplitude equalized radial, transverse and vertical component data traces and synthetic seismograms after the last inversion iteration. The data traces are shown as the thinner lines and the synthetic traces are shown as the thicker lines. At the upper left hand corner is a plot of the initial and final structure P and S velocity model. The initial model is shown with the light lines and the final model is shown with the thicker lines. At the center top is a display of the final moment tensor and force vector solution. The beachball is gray shaded according to the resulting particle motion with lighter shades representing dilitational motion and darker shades representing compressional motion. The right most panels show how the rms error and source terms changed with each inversion iteration. The panel labeled rms shows the auto scaled rms misfit error. The panel labeled mom0 shows the absolute value of the principle moment component with the bottom of the plot scaled to zero moment. The panel labeled percent shows the percentage of the moment term partitioned into explosion (darker shade), dipole (medium shade) and double-couple (lighter shade). In addition, a '+' or '-' character is put into each explosion and dipole bar to represent whether the term was compressional or dilitational in sign. The panel labeled force shows the absolute magnitude of the force vector with the bottom of the plot scaled to zero force. The panel labeled 'frc str/pl' shows the force strike and plunge angles. The force vector application angle is also shown on the beachball as the 'F' character.

We can see from this inversion that we have obtained a remarkably good fit between the data and synthetics for all three components and for the P-wave, the Rayleigh wave and the Love wave. Even more encouraging is that we obtained the fit after essentially five or six iterations. In our previous work (Harvey 1993) we found it necessary to perform as many as several hundred iterations to obtain a good fit and in some cases we were unable to adequately fit the data no matter how many iterations we performed.

In our initial attempt at fitting these events, we used the same inversion procedure as we used in our previous study (Harvey 1993) which is functionally equivalent to the procedure used by Gomberg and Masters (1988). In this approach the differential seismograms are approximated by using only the differential terms associated with eigenvalue derivatives of the modal expansion while ignoring the eigenfunction derivative terms. In another previous work (Harvey 1991), we had shown that these differential approximations broke down for body waves and that it was necessary to include the eigenfunction derivative terms to accurately compute the differential seismograms. However, we found that including the eigenfunction derivative computations increased the computer run times substantial and we decided to use the faster approximations instead. We reasoned that although the differential seismograms would not be strictly accurate, they would be good enough to move the inversion in the right direction and the use of the approximations would only effect the inversion by requiring more iterations to get to the ultimate results.

When we applied these approximations in the inversion of event 521 we found that although we could fit the Rayleigh and Love waves well, we were not able to fit the P-wave amplitudes no matter how many iterations we tried. When we put in the eigenfunction derivative terms we got the results shown in figure 4. Not only are we fitting the P-wave amplitudes well, but we are doing it in just a few iterations. We then realized that although we were able to fit the body phases in our previous study, we were doing so by adjusting Q values which directly effected the eigenvalue derivatives. In this study we are using elastic structural models and the only way we can match body wave amplitudes is through the elastic structural parameters (and the source terms). We can see that the use of eigenvalue based approximations for the differential seismograms can result in spurious Q values to overcome the inaccuracies in the differential seismogram computations.
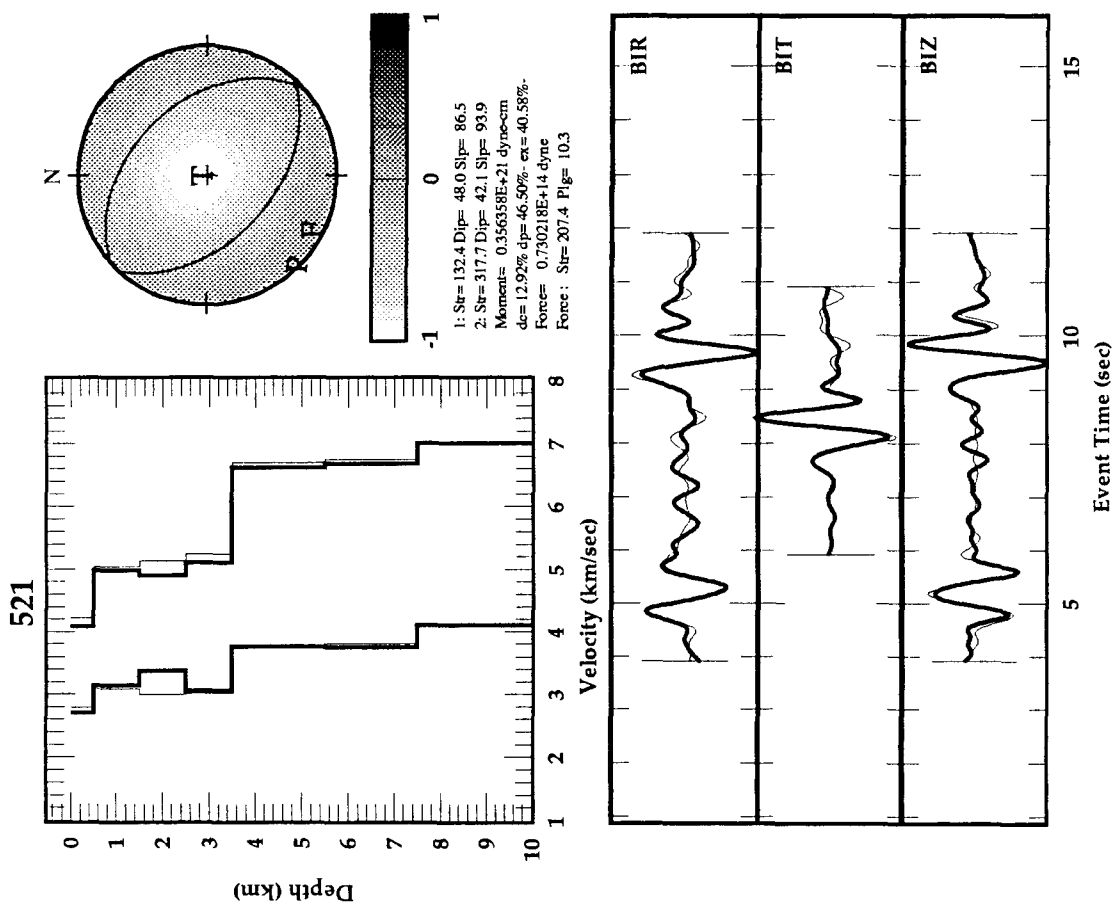
Figure 2. Summary results of full waveform inversion for source and structure parameters for event no. 521. All source terms were included in the inversion. The bold traces are the synthetic seismograms and the lighter traces are the real data.
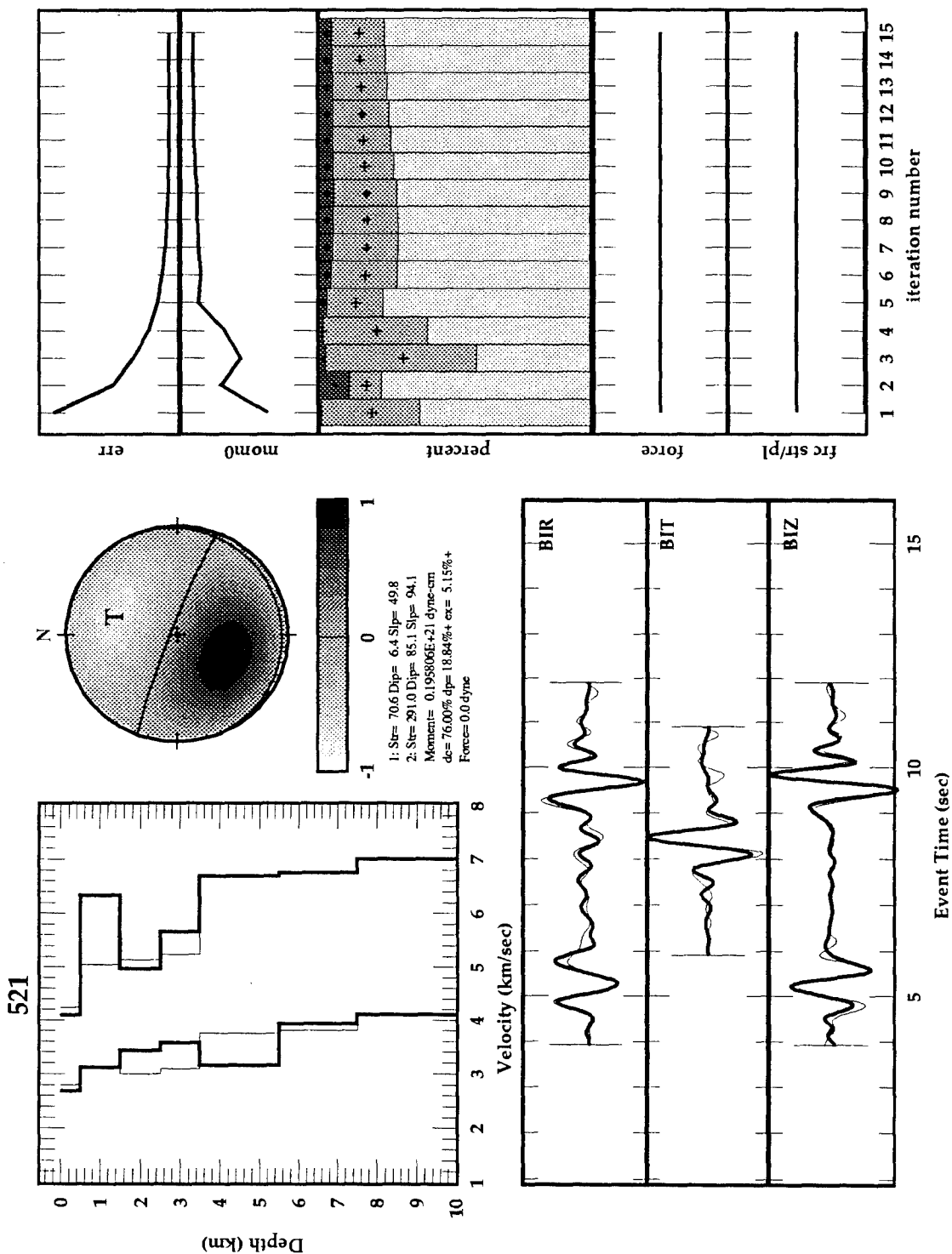
Figure 3. Summary results of full waveform inversion for source and structure parameters for event no. 521. Unbalanced force terms were excluded from the inversion. The bold traces are the synthetic seismograms and the lighter traces are the real data.

The inversion results summarized in figure 2 show a reasonable structural model that is not too much different from the starting model. Both the moment and force values would indicate a rather large explosion.[9] We can see that the moment is fundamentally implosive and vertical dilitational dipolar with a small residual amount of double-couple. The thrust vector is almost horizontal. We might expect these type of source terms for a cast shot type blast that ejects rock material laterally. The strong dilitational terms could be due to the rebound after removal of the ejected material.

In figure 3 we show the same inversion except we have constrained the source terms to only include the moment tensor (no force terms). We can see that the fit is not as good as in figure 3 especially for the Love wave. Also, the resulting structural model is less believable than the results from the original inversion. For this inversion we get a strong double-couple term which is probably necessary to fit the strong observed Love wave amplitude.

The same inversion proceedure was performed using data from the other events used in this study. The results for event 505 look very similar to those for 521. However for events 507, 510 and 509 we get somewhat opposite results in terms of the explosion and dipolar terms being compressional instead of dilitational. We suspect that some of these mines are coal mines that use surface strip mining operations to get at flat lying buried coal seams. A standard blasting technique in this case is to place charges over a horizontal spatial extent either within or slightly above the seams. The resulting blast is designed to break up the material above the seams for easy surface removal without moving it significantly. For an explosion of this type, we might expect the resulting moment tensor to be compressional due to the fact that no rebound due to removed material would occur combined with the effective gravity assisted confinement of the material above the blast.

The other events show a variety of source solutions, but we can say that in most cases the fits are very good and that in every case the resulting moment solutions are thrust fault or normal fault in nature. Also the resulting structures tend to cluster into two families; structures that look similar to the structure for event 521 and structures that show a low P-velocity zone from 1.5 to about 3.5 km depth. This may be indicative of two different quarries with slightly different average propagation characteristics.

When we compare the unconstrained with the constrained inversions, we see results similar to the comparisons of figures 2 and 3 except for event 510 in which case there appears to be no resolvable difference in the two inversions. For the other events the constrained inversions yield less believable structures and source terms that include large double-couple components to presumably fit the Love waves. We think that the inclusion of the unbalanced force terms provide realistic extra degrees of freedom in the source parameterization that generally produce more accurate inversions for the structure and moment parameters.

3. Conclusions and Future Plans

We have completed a study aimed at the development of a full waveform joint structure-source inversion method. We used differential seismograms to represent the linearized structure effects and perturbed source terms to represent the source effects. We found it desirable to include unbalanced force terms, in addition to an arbitrary symmetric moment tensor, to represent the source. We also found it necessary to use exact expressions for computing the differential seismograms that did not involve

---

[9] For comparison, a 10^{20} dyne-cm moment roughly corresponds to a $m_l = 2.5$ event in Southern California and a 10^{11} dyne force roughly corresponds to the thrust from a V-2 class rocket engine burning one ton of propellant over one second.

eigenvalue-only approximations.

We applied the inversion method to a dozen local quarry blasts recorded by the NRDC network in Kazakhstan in the 0.4 to 2.0 Hz frequency range. We found that it was possible to produce very good fits between the synthetic seismograms and the observed data on all three components simultaneously and for the P-wave, Rayleigh wave and Love wave. The inclusion of the unbalanced force terms significantly improved the fits for some of the events and resulted in more reasonable structure and source parameters than were obtained without the force terms. We interpreted some of the inverted source parameters as being characteristic of several different types of industrial surface mining operations.

The results documented in this report represent the successful conclusion of the first phase of our proposed research, as we listed in our original work statement. We found that although we obtain good fits using single station-event data, we suspect that many of the inversions are not well constrained and we expect that by combining multiple events and/or stations in simultaneous inversions we will significantly remove the ambiguities that we may have experienced in this study. In the next phase of this work, we will concentrate on doing joint inversions for several sources from the same area using a common structure and different source parameters. We have most of the tools to do this now. However, we will need to add the capability to invert for source location simultaneously with the other source parameters and the structure. This will be needed because mis-location errors could otherwise cause irreconcilable inconsistencies in the synthetic and real seismograms.

CRUSTAL HETEROGENEITY IN THE BASIN AND RANGE

A. LEVANDER, S.P. LARKIN, L.M. LA FLAME, S. PULLAMMANAPALLIL
RICE UNIVERSITY

J.A. GOFF
UNIVERSITY OF TEXAS INSTITUTE FOR GEOPHYSICS

ABSTRACT : We are investigating the fine-scale structure of the Earth's crust in order to understand its influence on high frequency (0.5-30 Hz) regional wave propagation. We have developed geologically based stochastic models of crustal heterogeneity for a number of different tectonic provinces and crustal levels. Here we have focused on examining geologic maps from extended terranes, and seismic data from the northern and southern Basin and Range. We have developed two different deterministic/stochastic velocity models which produce synthetic seismograms showing many of the reflectivity patterns and crustal events (Pg, PmP, Sg, SmS) observed in Basin and Range near-vertical and wide-angle seismic data. We also have developed several ways to measure the lateral heterogeneity scale length from unstacked seismic data, and have tested them on synthetic data with promising results.

Keywords : Fine-scale seismic velocity heterogeneity, stochastic models, Basin and Range.

OBJECTIVE : We are investigating the fine-scale seismic velocity heterogeneity of the Earth's crust over a broad range of scales (~0.025 to ~35km) in an effort to understand how wavelength scale heterogeneity affects seismic wave propagation in the the crust in the 0.5-30Hz band. We are approaching this problem in three ways. 1) Estimates of crustal velocity heterogeneity can be made from geologic maps and petrophysical data, and from seismic reflection data. Statistical analysis of geologic maps and petrophysical data, from which stochastic models for velocity heterogeneity are constructed. The stochastic models of different types of lithologies are then used to develop whole crustal models for which synthetic seismograms can be calculated. To improve the direct image of crustal velocity heterogeneity in the crustal column we are reprocessing COCORP reflection data from the Basin and Range. 2) Synthetic seismograms calculated for the stochastic models are compared to crustal reflection and refraction seismograms. 3) We are evaluating methods for estimating lateral heterogeneity scale lengths using several correlation measures on unstacked synthetic seismic data.

RESEARCH ACCOMPLISHED : *Reprocessing the COCORP 40°N Transect - Nevada Line 2.* Vertical incidence seismic data from the northern Basin and Range Province are often characterized by a transparent upper crust, a highly reflective midcrust, a slightly less reflective lower crust, and a strong reflection Moho up to a second in length. The COCORP 40°N transect - Nevada line 2 is part of a vibrator seismic survey that extends across the western Cordillera of the United States. Line 2, situated in the Basin and Range Province, has been processed and interpreted previously (Klemperer and others, 1986; Allmendinger and others, 1987: Hauge and others, 1987). A joint vertical-incidence to wide-angle reflection/refraction explosion experiment (known as the PASSCAL Basin and Range Experiment) was conducted over the same area in 1986.

Interpretations of these two datasets have produced somewhat contradictory models of the crust in the Basin and Range. One COCORP CMP section is a single fold near-trace CMP section, which shows a pair of bright reflectors at the base of the crust, whereas the stacked CMP stacked section shows a broad zone of reflectors from 9.5 - 10.5 s two-way-time (TWT), as opposed to two distinct bands of reflectivity. Neither section shows bright or continuous middle crustal reflectivity across the section, whereas a limited (~20km) dataset of densely recorded near vertical incidence explosion data shows pronounced reflectivity in the middle crust (at 4-7 s twt). The disparity between the stacked and single-fold vibrator and explosion images of the middle to lower crustal reflectors may be caused by inadequate seismic processing of the COCORP data. Surface related problems were pointed out by the original processors (Klemperer et al., 1986). It is our intention to use current processing capabilities to remove the near-surface effects and produce a better stacked image. Getting reliable consistent images of the middle crust, the Moho transition zone is crucial to estimating the parameters needed for stochastic models. We will then have a reflectivity/velocity model for the crust and mantle in an extended terrane which can be used to generate synthetic seismograms.

To reprocess COCORP Nevada Line 2 we followed the processing flow for Nevada line 2 outlined in Allmendinger and others, 1987, to reproduce the original COCORP image and give us a foundation on which to make improvements. Additional trace editing and careful muting removed some of the ground roll and extraneous noise later in the section. Velocity analysis was done interactively with a starting velocity model taken from the 1986 PASSCAL wide-angle survey of the same region (Holbrook, 1990). The stack produced after the velocity analysis showed incremental improvements. We further improved the section by calculating and applying refraction statics, which strip away some of the effects of the irregular topography and surface layers in the basins and ranges. The CMP stack following refraction statics and several iterations of velocity analysis show continuous Moho and middle crustal reflectors across the section. Additional processing will include residual statics and time and in depth migration.

The reprocessed image (Figure 1) appears much more consistent with the patterns seen in the limited explosion data, and thus suggests that we may be able to process the entire COCORP Basin and Range dataset to estimate crustal fabric across a regional scale.

Construction of stochastic model for the northern Basin and Range. Figure 2 displays our velocity model for the northern Basin and Range. The transparent upper crust is modeled as felsic intrusions into a gneissic basement terrane. The horizontal and vertical characteristic scales for the upper crustal zone are 963 m and 817 m respectively, with a fractal dimension of 2.5, and a binary probability density function (pdf) of 67% fast (avg 6.0 km/s) and 33% slow (avg 5.7 km/s). These statistics were obtained from outcrop maps within the Chocolate Mountains of southeastern California. (Although not within the northern Basin and Range Province, maps of this area show the effects of upper crustal Mesozoic plutonism). Seismic velocities are taken from laboratory measurements of rocks with similar compositions and are consistent with the bulk velocities determined from upper crustal refractions.

High heat flow and historical volcanism throughout the Basin and Range indicate that mafic intrusions are likely to exist at several levels in the crustal column. These intrusions provide the impedance contrasts required to produce high amplitude reflections. Rheological arguments suggest that these intrusions should have different orientations depending on their depth of emplacement, with horizontal intrusions prefering weak rheological boundaries, such as at the brittle/ductile transition and at the crust/mantle boundary (Parsons et al., 1992; Holliger and Levander, 1994). For these reasons we have developed a stochastic model of velocity heterogeneity consisting of either horizontally or vertically elongated high velocity bodies within a more felsic matrix. The zones having elongated horizontal bodies within the midcrust and at the Moho produce the observed high amplitude reflectivity. The mid and lower crust consists of dikes and sills with characteristic scales of 200 m and 800 m depending on orientation, a fractal dimension of 2.7, and a binary pdf of 5% fast (avg 6.8 km/s) and 95 % slow (avg 6.5 km/s). The fractal dimension is consistent with that measured from outcrop maps of the Ivrea Zone in northern Italy, an area believed to expose extended and intruded lower crust similar to that in the Basin and Range. Though we presently have no seismic constraints on the percentage of intrusion in the pdf, we have chosen a small extreme to emphasize the importance of orientation in producing reflectivity. Average crustal velocities and gradients were obtained by averaging the velocity models shown in Figure 3.

Construction of stochastic model for the southern Basin and Range in southeastern California. In contrast to the highly reflective crust prevalent in the northern Basin and Range, southeastern California north of the Chocolate Mountains exhibits a comparatively nonreflective seismic signature. We have therefore modeled this area without mafic intrusions, and instead have used the statistics derived from maps of Mesozoic plutons intruded into Proterozoic North American crust in the Chocolate Mountains (Figure 2, upper crust) as describing the entire crustal column. Average crustal velocities and gradients were obtained from the analysis of the PACE 92 refraction profile of this same area (Parsons and McCarthy, submitted to Journal of Tectonics).

Modeling PASSCAL 86 northern Basin and Range data and RISC 92 southern Basin and Range data. The two velocity models described above were used to generate 2-D visco-elastic finite-difference synthetic seismic sections. For the vertical incidence simulations, the models were 20 by 36km with 20 m grid spacing. The source pulse was a Ricker wavelet with an 18 Hz center frequency. For the wide-angle simulations, the models were 210 by 36 km with 60 m grid spacing. The source was a Ricker wavelet with a 5 Hz center frequency. The near-surface was modeled as a series of 2-D layered sedimentary basins. Average velocity within the near surface layer was 3.1 km/s with a gradient of 0.8 km/s/km and a Q of 50. Velocities were determined from travel time analysis; Q was determined from spectral ratios of the near-offset first arrival. Sedimentary layers were modeled as fractal tabular bodies with horizontal and vertical characteristic scales of 6000 m and 60 m, respectively, a fractal dimension of 2.5 (the smoothest possible binary fractal fabric), and a binary pdf of 50-50% high and low velocities with velocity contrasts of 0.4 km/s.

The results from the PASSCAL 86 northern Basin and Range simulations are shown in Figure 4. Figure 4a shows a shot record (Shotpoint 4B) from the 1986 PASSCAL seismic experiment, and Figure 4b shows our vertical incidence synthetic. Both show a reflective midcrust

649

and a 1 second thick Moho. No bulk changes in velocity occur at the onset of the reflective midcrust.

The results from the RISC 92 southern Basin and Range simulations are shown in Figures 5. The seismic section displayed in Figure 5a is a composite gather of a number of shots into a stationary recording spread near the Chocolate Mountains of southeastern California. The reverberatory nature of wide-angle PmP is reproduced remarkably well in the synthetics (Figure 5b) by a combination of crustal scattering and basin reverberation. Coda amplitude analysis has shown that the initial coda is dominated by near surface reverberation, but the later coda is due to body wave scattering and phase conversions. Crustal heterogeneity is also necessary to produce the strong SmS arrival observed in the data.

Statistical measures of crustal heterogeneity :   The Basin and Range data show that describing highly reflective zones within the crust as stochastic media can produce synthetic seismograms having many of the features seen in seismic reflection and refraction data. These crustal models are now based on the statistics derived from digitized maps of middle and lower crustal exposures. Synthetic seismograms generated through these models show that their fine-scaled features affect the propagation of seismic signals at and above 0.5 Hz frequency (Holliger and Levander, 1992; Holliger et al., 1993; Levander et al., 1993).

Our objective is to relate the statistics of the scattered wavefield, observed in the synthetic seismograms, to the statistics of the underlying medium. In the process, we explore the parameter space that determines the statistics of the medium. This includes modality, fractal dimension, velocity fluctuation, fabric anisotropy, and structure of the velocity pdf. The current work focuses on relating the statistics of the wavefield to the anisotropy of the stochastic medium, i.e. the ratio of the horizontal to vertical characteristic scale, a_X/a_Z. The stochastic models we use differ in their horizontal characteristic scales, and as a reference, the measurements are also done on a layered deterministic medium. The measurements are performed in the time-domain and take into account time-shifts in the traces caused by the small scale velocity fluctuations. Under the single scattering assumption, the lateral correlation function of the wavefield depends only on the corresponding lateral correlation function of the scattering medium. The stochastic model through which we generate the synthetic seismograms for our study is shown in Figure 6a. It is 40 km long and 10 km deep, with a grid spacing of 20 m. The scatterers are located in a 5 km thick ``target" zone, extending from a depth of 5 km to 10 km. The characteristic scale ratio (a_X/a_Z, with a_X horizontal and a_Z vertical characteristic scale) of the scatterers within the target zone is varied by changing a_X to observe the effect of heterogeneity anisotropy on the lateral coherence measure. A visco-elastic finite difference scheme was employed to generate synthetic seismograms. Our results show that changes in the correlation of the wavefield does correspond to changes in the lateral characteristics of the media, though the differences are not linear (Figure 6b). When the a_X/a_Z ratio of the velocity models change from 10 to 5 (a factor of 2), the correlation lag, corresponding to a correlation coefficient of 0.5, changes by a factor of 1.70. When the ratio (ax/ay) changes from 5 to 1, the correlation lag drops by a factor of approximately 2.20. This statistical measure was computed both in the shot-gather and common-offset domain and over time windows of 500, 1000, and 1500 milliseconds. The advantage of the latter domain are that normal-moveout (NMO) stretch can be avoided. Both analysis modes yield similar results over the different time windows, indicating the robustness of the measure.

Another measure we perform to discern the horizontal characteristic scale of the medium involved a wavenumber-time analysis. If the wavefield is influenced by the lateral characteristics of the medium, then a lateral wavenumber spectra should exhibit its effect. Comparison of the power spectra of the wavefield, after NMO correction, for our test models show that the corner wavenumber does vary in proportion to the horizontal characteristic scale of the medium (Figure 6c). The spectra of the traces from the media with ax/ay ratio of 10 has a corner wavenumber of 0.224 (1/km), while it is 0.430 for the ax/ay=5 model and 1.510 for the a_X/a_Z=1 model.

Ultimately we will apply these measures to the reprocessed COCORP and the PASSCAL datasets for the Basin and Range to estimate the lateral characteristic scales directly from the seismic data.

CONCLUSIONS AND RECOMMENDATIONS : The seismic modeling results show that a considerable fraction of the seismic wavefield observed in conventional seismic refraction profiles can be reproduced by scattering from wavelength scale seismic velocity heterogeneity. Moho reflections are modulated both by fine-scale fluctuations on the transmission path and by reverberation in the highly heterogeneous near-surface layers. The most pressing problem to address is the estimation of crustal heterogeneity from seismic data directly. We have developed two measures for estimating the lateral characteristic scale length from refraction and unstacked reflection data. Estimation of seismic velocity fabric from seismic data directly will permit utilization of the vast global seismic reflection/refraction database to quantitatively classify the Earth's crust according to heterogeneity type and fluctuation. The next issue to be resolved is the influence of complex overburden on the wave field reflected from deeper layers. Lastly we plan to model regional propagation (to ~2000 km) in realistic stochastic models of the crust, using the Basin and Range models as a starting point.

REFERENCES :

Allmendinger, R.W.,Hauge, T.A.,Hauser, E.C.,Potter, C.J.,Klemperer, S.L.,Nelson, K.D., Knuepfer, P., and Oliver, J., Overview of the COCORP 40°N Transect, western U.S.A.: The Fabric of an Orogenic Belt. *Geol. Soc. Am. Bulletin*, v.98, 308-319, 1987.
Hauge, T.A., Allmendinger, R.W., Caruso, C., Hauser, E.C., Klemperer, S.L., Opdyke, S., Potter, C.J., Sanford, W., Brown, L., Kaufman, S., Oliver, J., Crustal Structure of Western Nevada from COCORP Deep Seismic Reflection Data. *Geol. Soc. Am. Bulletin*, v.98, 320-329, 1987.
Holbrook, W.S., The Crustal Structure of the Northwestern Basin and Range Province, Nevada, from Wide-Angle Seismic Data. *J. Geophysical Research*, v.95, 21,843 - 21,869, 1991.
Holliger, K., and A. R. Levander, A stochastic view of the lower crust based on the Ivrea Zone, *Geophys. Res. Lett.*, *19*, 1153-1156, 1992.
Holliger, K., A. Levander, and J. A. Goff, Stochastic modeling of the reflective lowercrust: petrophysical and geological evidence from the Ivrea Zone (northern Italy), *J. Geophys. Res.*, *98*, 11967-11980, 1993.
Holliger, K., and A. Levander, Lower crustal reflectivity modeled by rheological controls on mafic intrusions, *Geology*, *22*, 367-370, 1994.
Klemperer, S.L., Hauge, T.A., Hauser, E.C., Oliver, J.E., and Potter, C.J., The Moho in the Northern Basin and Range Province, Nevada, along the COCORP 40°N Seismic Reflection Transect. *Geol. Soc. Am. Bulletin*, v. 97, 603-618, 1986.
Levander, A., R. W. Hobbs, S. K. Smith, R. W. England, D. B. Snyder, and K. Holliger, The crust as a heterogeneous "optical" medium, or "crocodiles in the mist",*Tectonophysics*, *232*, 281-287, 1993.
Parsons, T., Sleep, N.H., and Thompson, G.A., The role of magma overpressure in suppressing earthquakes and topography: Implications for understanding extending crust, *Tectonics*, *11*, 1348-1356, 1992.
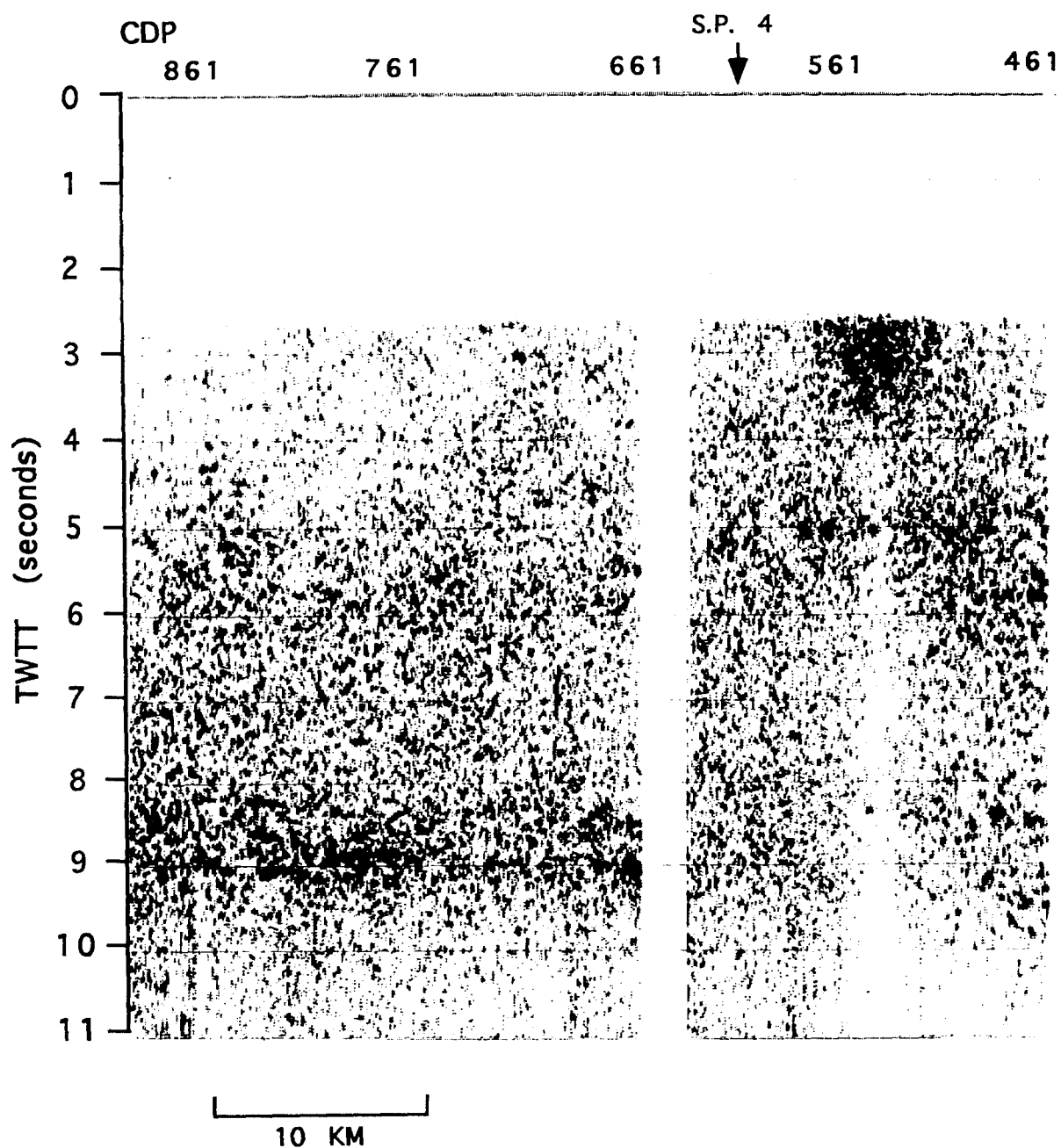
Figure 1 : Reprocessed COCORP Nevada Line 2, showing midcrustal (4-7 s twt) and Moho reflectivity (9-10s twt). The upper two seconds of the data are muted. Compare to the explosion shot record from Shotpoint 4B (Figure 4a). Reflectivity patterns are similar.

10 km

Basin (2.6-3.6 km/s)

Felsic Intrusions

5% Horizontal Intrusions

5% Vertical Intrusions

5% Horizontal Intrusions

Mantle (7.95 km/s)

0

30

Depth (km)
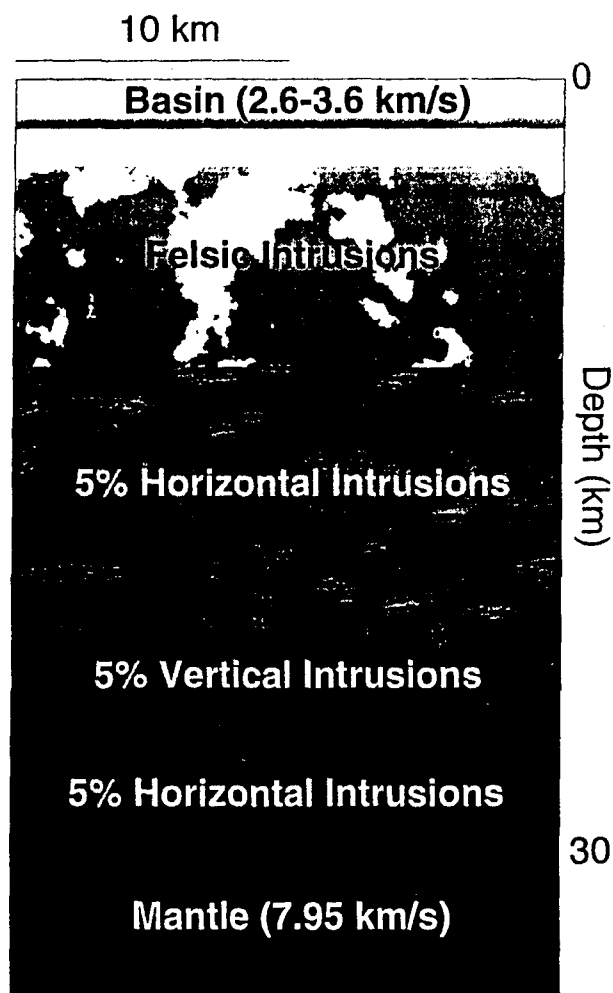
Northern Nevada Velocity Model

Figure 2

PASSCAL   Basin & Range 86
Refraction Velocity

Depth (km)

Benz 1
Benz 7
Holbrook 4
Zelt 4
Catchings 4

2 3 4 5 6 7 8 9

Compressional   Velocity   (km/sec

Figure 3

Figure 2 : Stochastic model for northern Basin and Range. There are no step changes in velocity within the crust above the Moho. **Figure 3** : 1-D P-wave velocity models derived from PASSCAL Basin and Range wide-aperture data by a variety of researchers. Note that the mean crustal velocity, the crustal thickness, and the velocity gradients are similar in all models, but the velocity steps within the crust are different. We model the crust with a 1-D deterministic velocity

(a)

NEVADA PASSCAL - SP4B

(b)
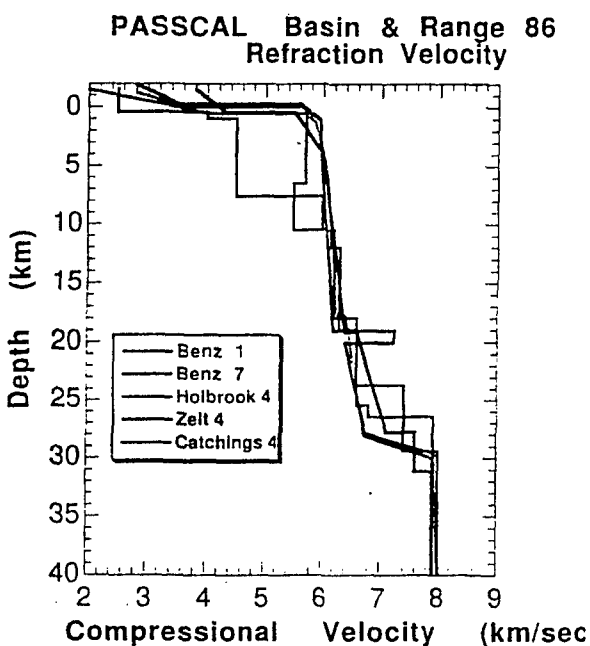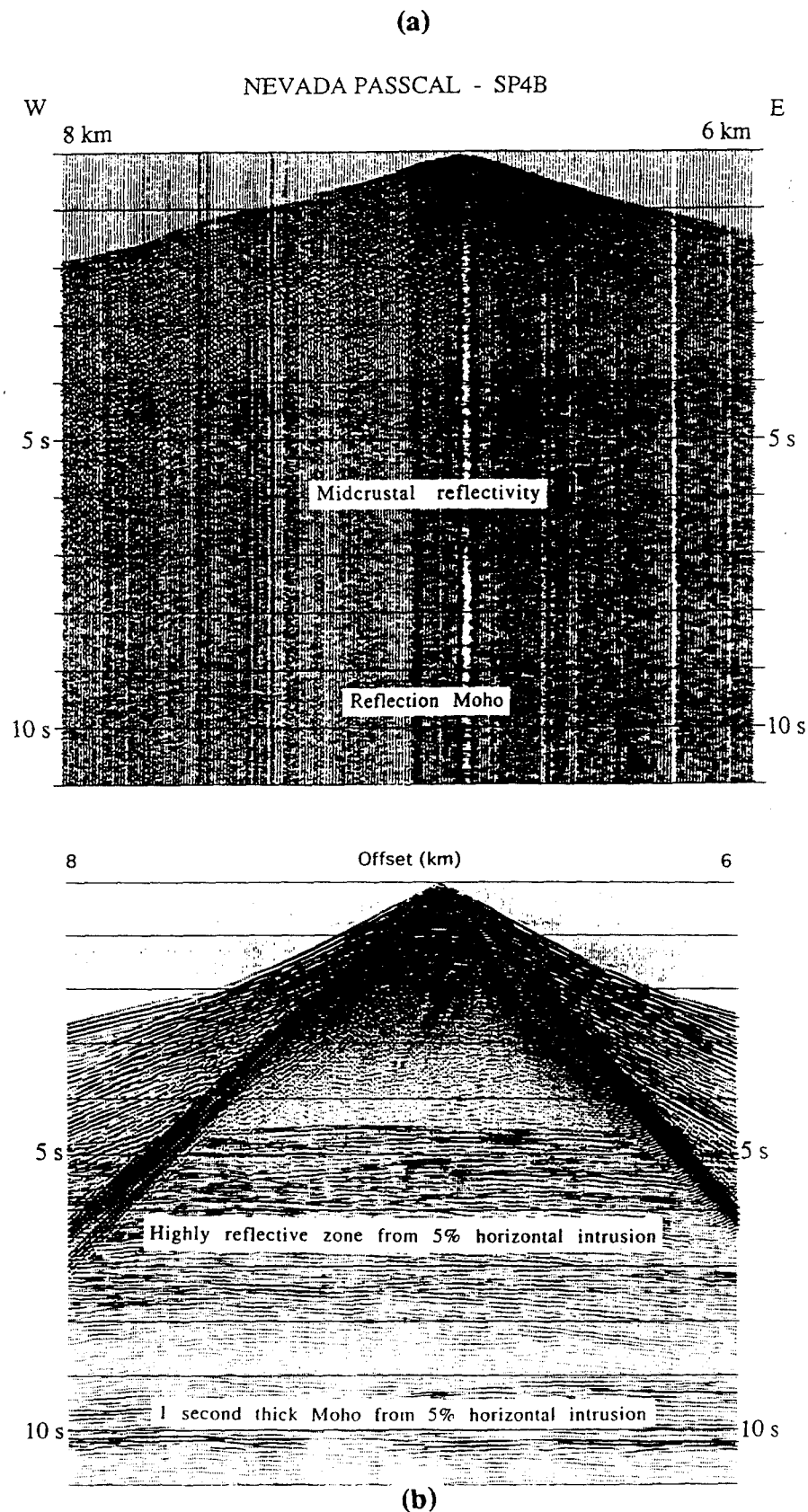
Figure 4 : a) Seismic shot record 4B from the PASSCAL Basin and Range experiment, recorded at 50m spacing. Note the bright reflectivity from 4-7 s twt, and at the Moho 9-10 s twt. b) Synthetic shot record for shot 4B from the velocity model in Figure 2. Note correspondence between reflective zones in the field record.

(a)

(b)
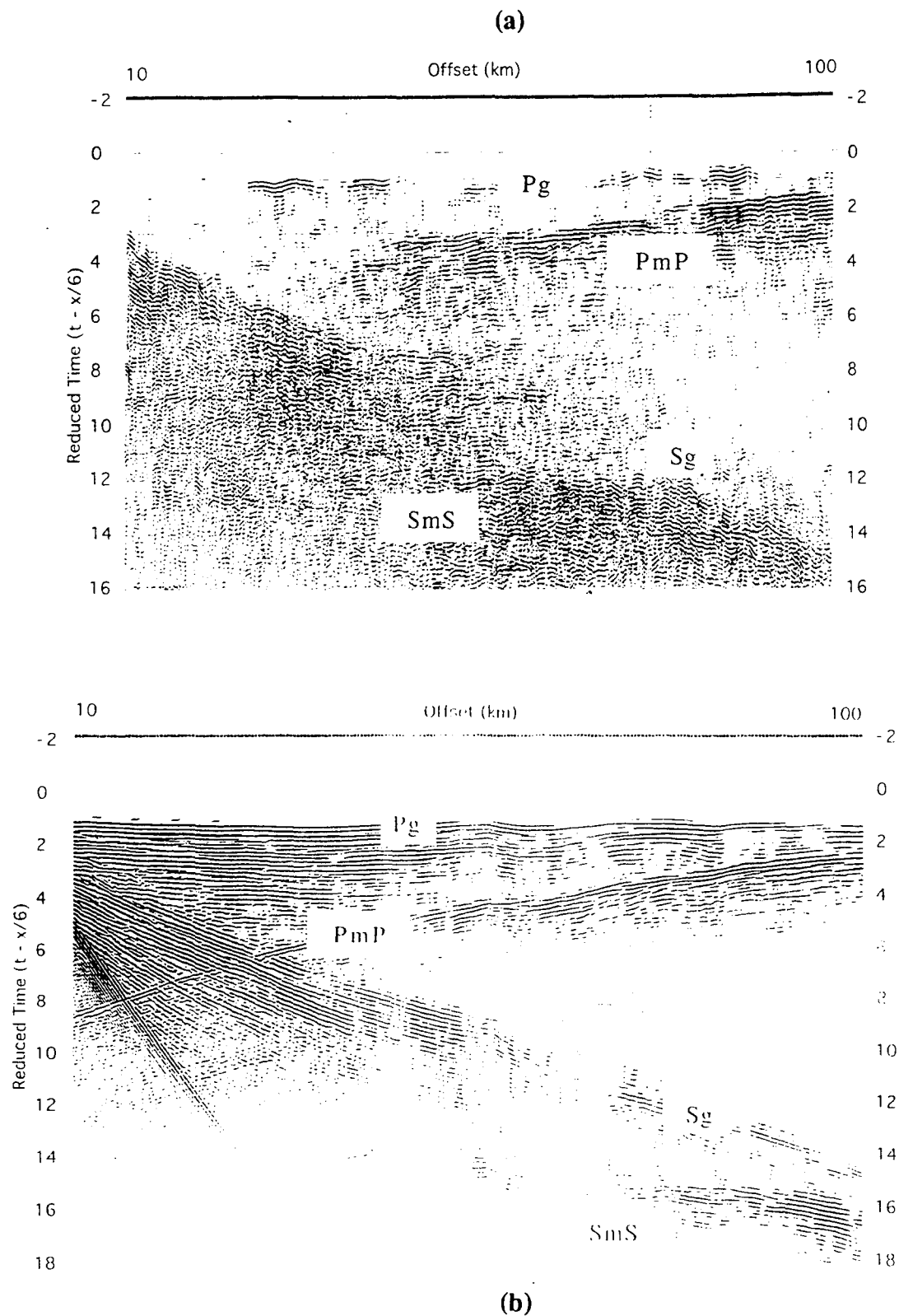
Figure 5 : a) Composite large offset shot record from southern Basin and Range RISC experiment. Note prominent crustal events. b) Synthetic shot record from a stochastic model consisting of flat sedimentary basins overlying a crust intruded by felsic rocks, similar to that at the top of the Figure 2. A uniform vertical velocity gradient has been used in the crust below the sediments.
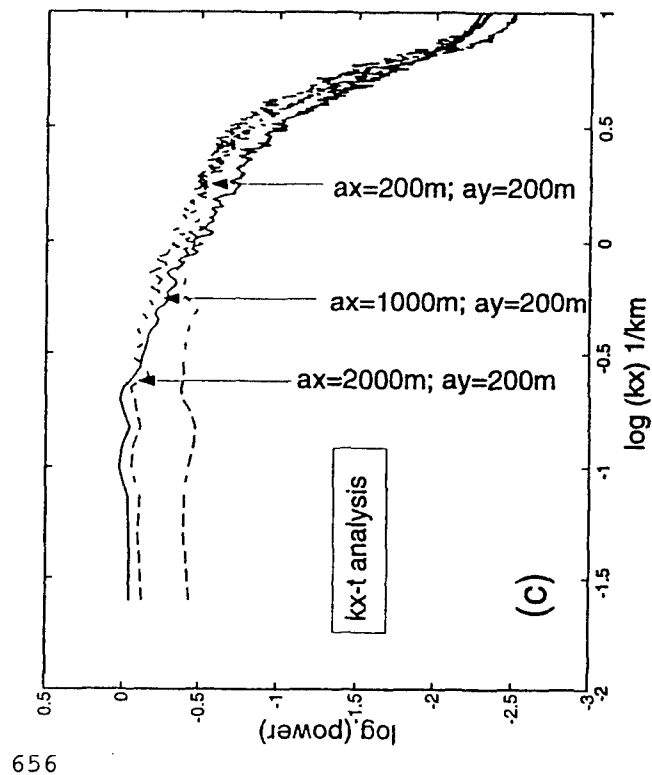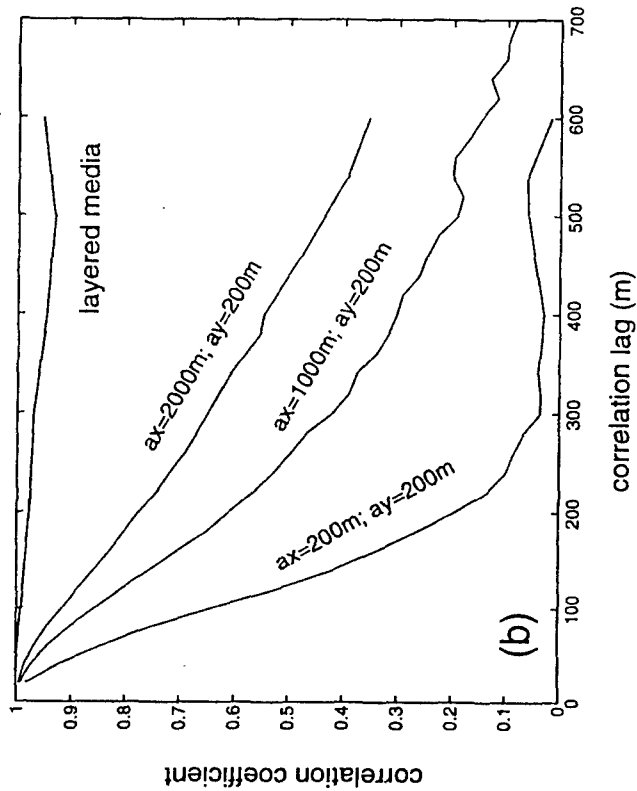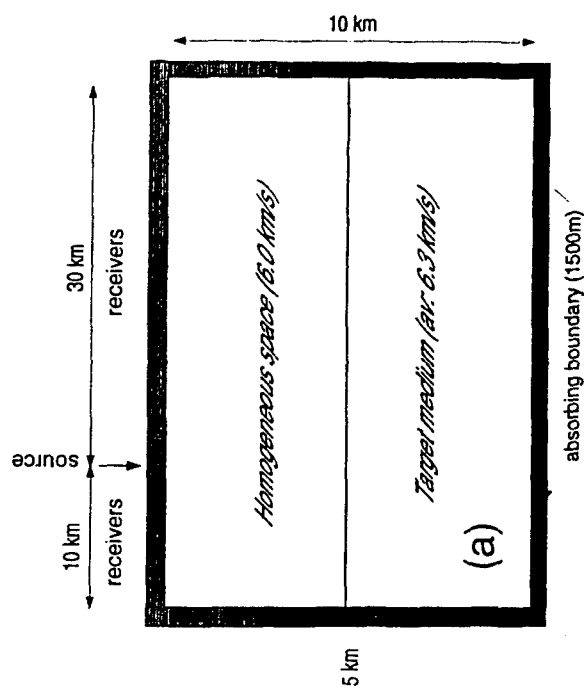
Figure 6. (a) Schematic representation of the model through which we generate the synthetic seismograms, using a finite-difference based visco-elastic code. (b) The lateral coherence measure for three models with different ax/ay ratios. For comparison, we also show the coherence measure for a layered media, where the reflectors extended across the model. (c) kx-t analysis on the NMO corrected seismograms through the three models. We note that the corner wavenumber increases in proportion to the decrease in the ax/ay ratio.

Two-dimensional crustal and upper-mantle velocity models from profile "Quartz", Russia

Igor Morozov, Werner Schueller, Elena Morozova,
and Scott Smithson

Department of Geology and Geophysics, University of Wyoming, PO Box 3006, Laramie, WY, 82071-3006.

ABSTRACT

We develop two-dimensional (2-D) P-wave velocity models for the crust and for the upper mantle along the ultra-long Deep Seismic Sounding profile (DSS) "Quartz". Two-dimensional effects play a principal role in Lg propagation and are directly related to the problem of quantitative modeling of Lg and its use as a seismic discriminant. The use of DSS profiles provides us with unique opportunities to study large-scale propagation effects of various seismic phases, and especially Lg, across geological and tectonic boundaries. The results of this study have a direct relevance to the calibration of seismic discriminants.

To develop our 2-D crustal model, we use the data obtained using 28 chemical explosions along the north-western half of the profile. It is the first attempt of using these data after they have been digitized and obtained in the West. Applying a travel-time tomographic inversion method, we develop a velocity model and estimates of its resolution. Two important resolved features of the model are: 1) high velocity block at the base of the crust under the Baltic Shield, 2) crustal roots under the Ural Mountains.

Using the data from 2 nuclear explosions in the same part of the profile we develop a preliminary 2-D upper mantle P-wave velocity model. The model supports the conclusion of the roots under the Urals, and suggests a south-east dipping low-velocity zone in the upper mantle. The latter, however, is to be supported by the analysis of the data from the third nuclear shot, which is now in the processing stage.

As a result of this work, we will obtain a comprehensive 2-D model of the crust and of the uppermost mantle, will obtain better estimates of obtained resolution of geological features. This knowledge would provide better means of calibration of the amplitudes of Lg and other phases for their use in CTBT applications.

INTRODUCTION

We report our progress in the digitization, processing and interpretation of the data from the profile "Quartz". Profile "Quartz" (also known as Murmansk-Kizil profile) acquired in 1984-87 is a part of the unique Deep Seismic Sounding (DSS) program carried out in the USSR during the past 25-30 years. The profile spans 3950 km from northwestern Russia to central Asia, crossing six major tectonic provinces (e.g., Zonenshain et al., 1990). 3 nuclear explosions (PNEs) were recorded by over 330 3-component instruments spaced at 10-16 km. The same instruments were used with 42 chemical explosions which were recorded at 200-300 km offsets (Figure 1).

Recent descriptions of the data were given by Mechie et al. (1993) and Morozova et al. (1994); a detailed overview of the Soviet DSS program can be found in Ryaboy (1989).

Here we present two-dimensional velocity models for the crust and for the upper mantle (depth range 0-200 km). It is the first attempt since the data have been digitized and obtained in the West to perform an analysis of the chemical shot records, and to obtain a two-dimensional velocity model of the mantle. The models are derived from the analysis of the northwestern part of the profile (Figure 1). The rest of the data were recently obtained and are in the processing stage.
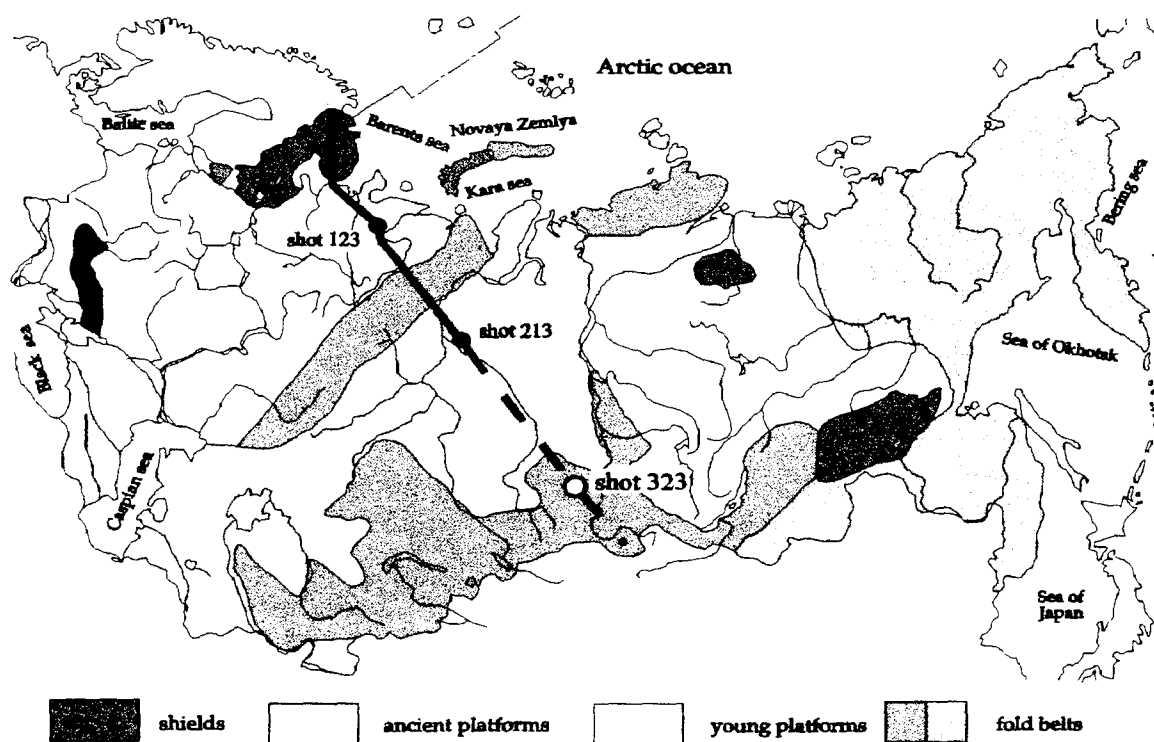
Figure 1. A generalized geologic map of the USSR. Profile "Quartz" is shown. *Solid line:* the part of the profile discussed in this paper. *Dashed line:* recently obtained remaining part of the profile.

OBJECTIVES

Ultra-long densely spaced DSS profiles using nuclear and chemical explosions provide unique opportunities to study wave propagation through complex lithospheric structures. This is particularly important in the context of the studies of the propagation of crustal-guided seismic phases, especially Lg. As we pointed out before (Morozova et al., 1994), existing crustal velocity models developed for the profile "Quartz" (Solodilov, 1994, personal communication) are not satisfactory for the purpose of the modeling of Lg propagation, which is recognized as one of the major issues for seismic calibration and monitoring. The profile also provides a substantial coverage of the upper mantle. One-dimensional models developed by several authors (Benz et al., 1992; Mechie et al., 1993) clearly show a number of features of prime importance (for example, prominent low-velocity zones), but are conceptually unacceptable for such a large-scale experiment (e.g. Ryaboy, 1989).

Our goals are first the development of comprehensive two-dimensional (2-D) velocity models for the crust and upper mantle using the data from both chemical and nuclear explosions. Our major concern is in the understanding of the obtained resolution of the velocity structure, and of its implications for the prediction of the propagation of seismic phases. The knowledge of the crustal P- and S- wave velocity is crucial the for understanding of Lg propagation of Lg. Depending on the scale of the problem, our specific objectives and corresponding methods of research (in approximate order of their priorities) are:

- To develop a <u>2-D P-wave crustal velocity model</u> and to estimate its spatial and velocity resolution using 2-D seismic travel-time tomography. Analysis of the To develop a <u>2-D P-wave crustal velocity model</u> and to estimate its spatial and resolution obtained and a comparison to earlier models of the crustal velocity structure.

- To obtain a <u>2-D P- and S-wave velocity model of the upper mantle</u> using the data from chemical shots for the uppermost part of the mantle, and 3 nuclear shots sampling the depth range of 0-400 km.

- To measure true <u>amplitudes of seismic phases</u> (especially those of P_n, S_n, Lg) along the profile, incorporating them into the travel-time inversion. To study their <u>amplitude ratios as potential seismic discriminants</u>.

- To establish constraints on the <u>2-D S-wave crustal velocity structure</u>.

- To investigate the possibility of using receiver function analysis to study <u>converted phases</u> in order to constrain S-wave velocity structure of the crust.

- To develop methods of analysis for the application to <u>the remaining part of the profile</u>.

- To model <u>Lg wave propagation</u> across laterally variable geological structures; to study the effects of the crustal P- and S- wave velocity structure on Lg wave propagation. Possibly to incorporate Lg into the travel-time crustal velocity inversion.

- As an integrating result, <u>calibration of regional seismic event discriminants</u>.

We have reported before our progress in the digitization, in basic processing, and in the measurement of vector and scalar amplitudes of the data from profile "Quartz" (Morozova et al., 1994, 1995). In this work we will discuss only problems related to the two-dimensional travel-time inversion of the data at two different scales - crustal, using the chemical shots, and upper mantle - using PNEs.

RESEARCH ACCOMPLISHED

2-D tomographic crustal velocity model

In the earlier velocity models developed in GEON[1] one of the most important processing steps was the "velocity filtering" (Ryaboy, 1989; Katz and Shubik, 1977), which is a nonlinear event-enhancing procedure. To our knowledge, the performance of the procedure in terms of the generation of spurious events has not been studied at all. The P-wave crustal velocity structure developed in GEON shows a large number of vertical and lateral velocity contrasts, with faults offsetting the Moho boundary (Figure 2). Such contrasts, if they are real, would greatly affect the propagation of crustal-guided waves and would be most important for our interpretation and modeling of Lg phase. A reliable crustal model is also necessary for the resolution of 2-D upper mantle structure. Therefore, a solution of problems of robust event detection and a critical reinterpretation of the crustal and upper mantle velocity models will be of crucial importance for this project. One of the immediate purposes of our study is to obtain a relevant P- and S-wave velocity model and to estimate its resolution. Seismic tomography provides one of the possible means to determine such a model.

A linearized tomographic inversion method based on the algorithm by White (1989) was applied to a part of the dataset including 28 chemical and 2 nuclear explosions at the northwestern part of the profile (Figure 1). The P-wave velocity model was defined on a uniform rectangular grid with horizontal spacing of the nodes 50 km and vertical spacing of 3 km. The values of velocity at the nodes were iteratively updated using a variant of conjugate gradient method (LSQR, Page and Saunders, 1982). LSQR method provides rapid solving of the sparse and large linear system of equations (common dimension of the system is about 10^3 x 10^3 elements. The disadvantage of this technique is in not providing an estimate for the model resolution.

A realistic starting model is important to generate a convergent solution. For our starting model we used a velocity/interface model obtained from a simplified and smoothed model produced in GEON. The data (travel time) root-mean-square (RMS) misfit for this model was 588 ms.

The first two iterations determined the uppermost crustal structure to the depth of about 9 km. Only rays refracted in the upper crust were used. No reflections from the top

---

[1] GEON - Center for Regional Geophysical and Geoecological Research (formerly the Special Geophysical Expedition) in Moscow, Russia, - the organization which had been in charge of the acquisitio, archiving, and processing of the data.

of the basement in the southern and central part of the study area could be identified. During the next iterations the uppermost velocity structure was maintained fixed, and P-wave refractions (Pg and Pn) and Moho reflections were included into the inversion. The velocities in the middle and lower crust, velocities in the uppermost mantle, and the depth of the Moho were obtained. The resulting velocity model is shown in Figure 2. Ray coverage (for refracted rays only) and the final travel time fit are shown in Figure 3. The RMS data misfit for this model was reduced to 252 ms, and could not be reduced further without introducing unrealistic model features. This misfit is close to the travel time picking errors for deeper events.

The most significant features of the resulting crustal model are the presence of the high velocity block at the base of the Baltic Shield and the crustal root beneath the Uralian foldbelt. The evidence for the root is quite clear. The model shows the depth of the Moho at about 46 km corresponding to low crustal velocities of 7.1 km/s and upper mantle velocities of 8.1 km.

The southeastern part of the profile is characterized by a thick sedimentary basin with velocities around 2.5-3.4 km/s and depth varying from 2 to 4.5 km. Crustal
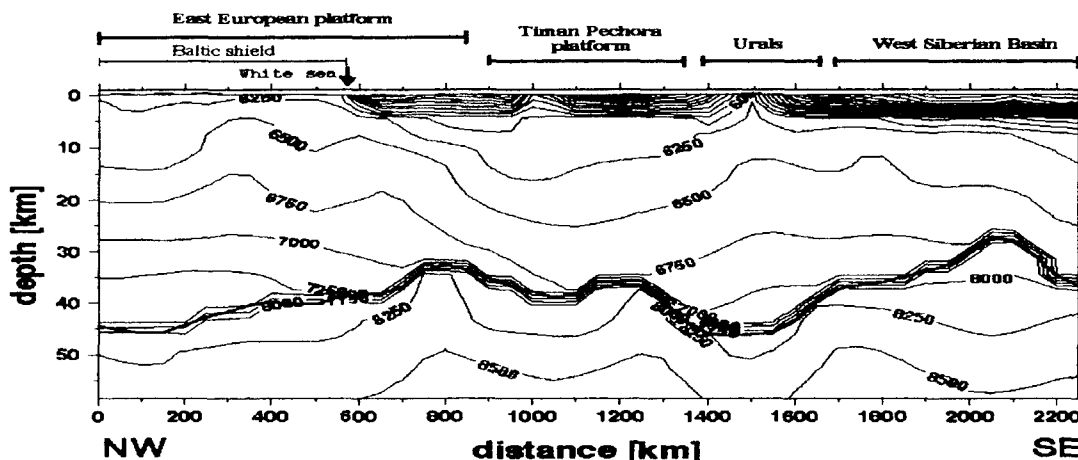
Figure 2. Crustal and uppermost mantle P-wave velocity model obtained using 2-D travel-time tomographic inversion.

basement velocities are below 6.9 km/s, upper mantle velocities range from 7.9 to 8.1 km/s. The tomographic inversion shows a prominent uplift in the Moho at about 2100 km along the profile. This feature is not supported by current geologic models and is not present in earlier interpretations. At present it is constrained only by three southern shot records. Additional data from the rest of the profile should allow us to verify the validity of this feature.

Following White (1989), we use singular value decomposition (SVD) to determine the resolution of the obtained velocity model. The resolution matrix $\mathbf{R} = \mathbf{V}_p \mathbf{V}_p^T$ is obtained from the SVD decomposition of the linear system $\mathbf{A} = \mathbf{U}\Lambda\mathbf{V}^T$, with $\mathbf{U}$ and $\mathbf{V}$ being the matrices of left and right singular vectors, and Λ a diagonal matrix of singular values of $\mathbf{A}$. The subscript p indicates the separation of the subspace corresponding to

non-zero singular values. A traditional way to illustrate the resolution to plot diagonal elements of the matrix **R** (top of Figure 4).
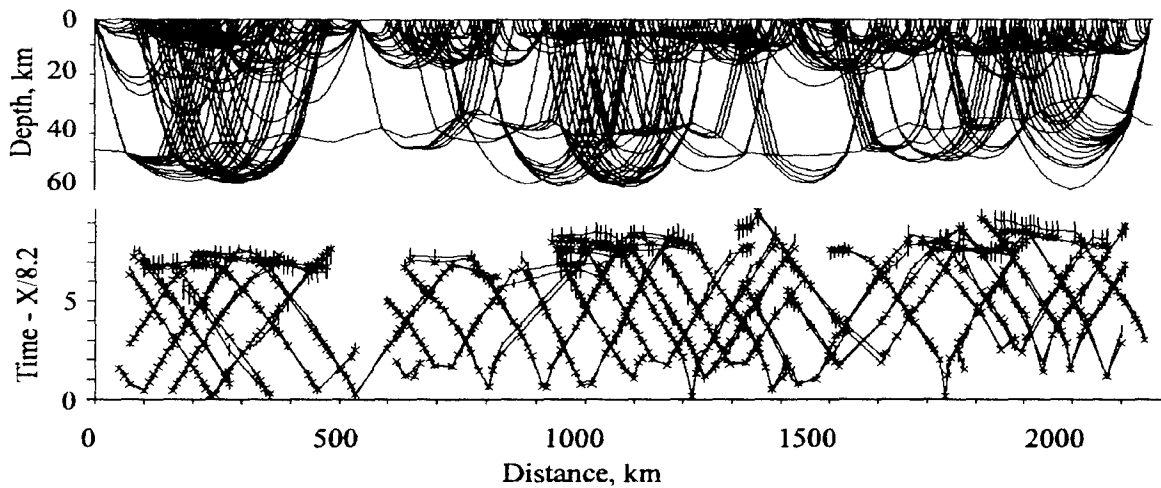
Figure 3. *Top:* refracted rays in the final tomographic velocity model. *Bottom:* travel time fit. The RMS misfit is 252 ms. Reduction velocity is 8.2 km/s.

The resulting resolution structure shows values near 1.0 in the upper crust along the northern and central part of the profile. The edges of the model and most areas of the upper mantle are only poorly resolved. The resolution is highest at the top 20 km of the and near the Moho (Figure 4). The latter is apparently due to additional coverage provided by the reflected waves.

Under the assumption that the uncertainties in the picked travel times are uncorrelated with uniform variance δ, the velocity model covariance matrix can be calculated as $\text{cov}(v) = \delta V_p \Lambda_p^{-2} V_p^T$. A plot of the velocity variance is shown at the bottom of Figure 4. This plot represents the estimated uncertainties in model velocities. These uncertainties, however, are interrelated with the uncertainties of the locations of various spatial features (e.g., Moho). This dependence does not lend itself easily to graphical representation, and thus the problem of the evaluation of the full spatial and velocity resolution is yet to be solved.

Preliminary 2-D upper mantle model from ray tracing

We used 2-D ray tracing to obtain a comprehensive upper mantle velocity structure along our part of the profile. For the crustal model, we used the same smoothed model that we used as a starting model for tomography. Adjusting mantle velocities to achieve a fit of the picked travel times of Pn and of the reflections from the top of the low-velocity zone (LVZ), we obtained a velocity model shown in Figure 5. In our inversion we intentionally tried to constrain only large-scale structures within the mantle. Below the LVZ our model is essentially one-dimensional, since this depth range is sampled only by the waves from the middle PNE (213). Two important 2-D features constrained by our model are: 1) the LVZ is dipping in a SE direction; 2) the ray tracing supports the relief of the Moho and lower upper-mantle velocities under the Ural Mountains obtained by the

Distance, km
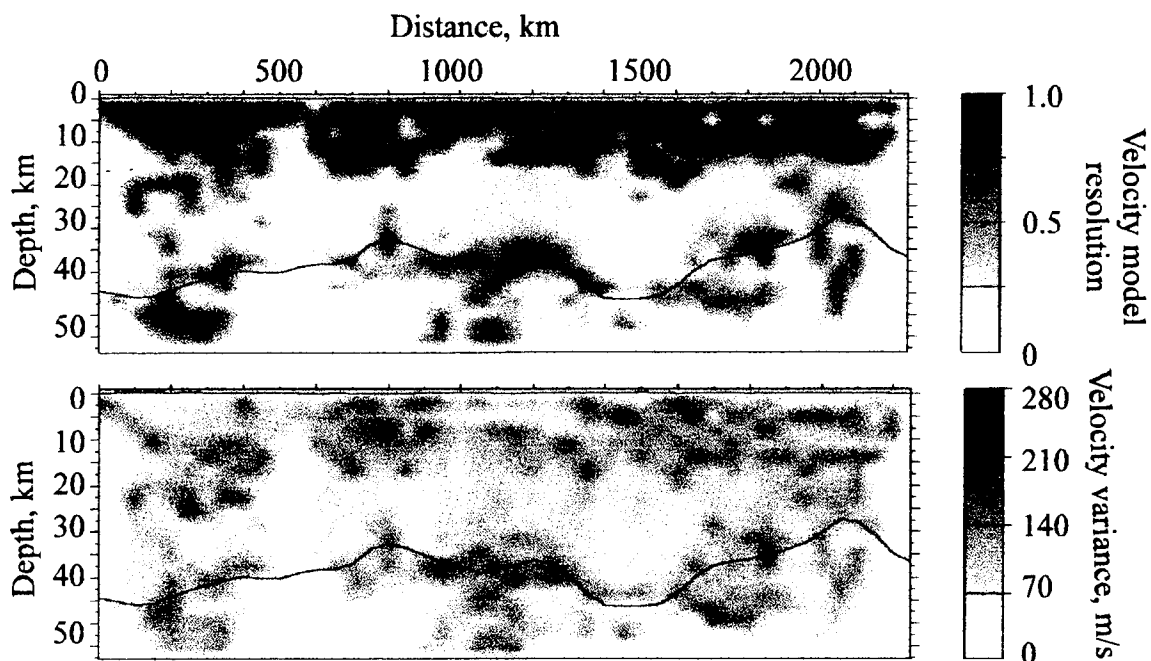
Figure 4. *Top:* diagonal elements of the velocity resolution matrix **R**. *Bottom:* estimated velocity variance. Location of the Moho interface obtained from tomographic inversion is also shown. Note that small velocity variance at the lower crust under the White Sea region (distance about 550 km) is rather due to insufficient ray coverage and low resolution.

Distance, km
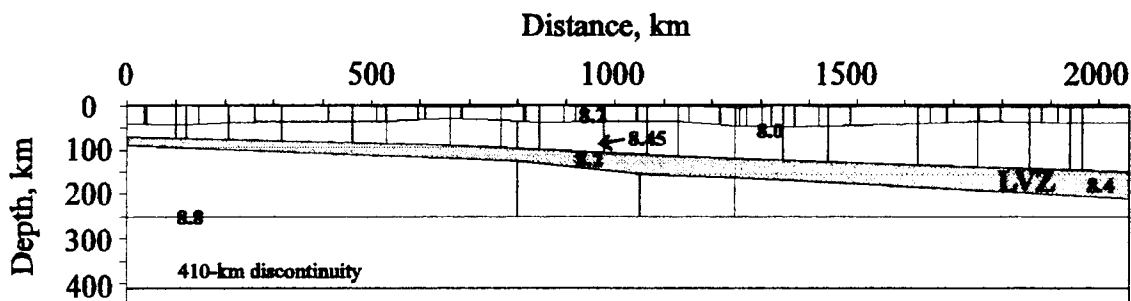
Figure 5. A preliminary (based on the data from 2 PNEs) upper-mantle velocity model. Note the roots under the Urals and the dipping in SE direction low-velocity zone in the upper mantle. Some P-wave velocity values are labeled in km/s.

tomographic inversion. These features can be related to the presence of roots under the Urals. We observe remarkable lateral variations of the P-wave velocities under the Moho boundary near the Urals: from about 8.2 km/s under the Timan Belt to the lowest for this profile values of 8.05-8.1 km/s under the Urals, and to higher velocities of 8.3-8.35 km/s under the West Siberian Platform.

<u>Receiver function analysis: converted phases</u>

The boundaries obtained in P-wave tomographic inversion may be completely different from the interfaces producing P-S conversions, which play a principal role in the formation of Lg. Careful examination of the first breaks of the "Quartz" data records shows that strong P-S converted phases (clearly observed in the horizontal components) are following the first breaks. To evaluate the time delays of these converted phases, we calculated receiver functions by rotating the horizontal components to their maximum amplitude and deconvolving the result from the vertical component (Figure 6). We use the receiver function normalization scheme proposed by Ammon (1991). Although the receiver functions are comparatively narrow-band, corrupted by noise, and difficult to interpret, three observations can be made: 1) there are no observable P-S conversions for the receivers located on the Baltic Shield; 2) the general patterns of the receiver function gathers are similar for shots 123 and 213 and follow the variations in the thickness of sedimentary rocks; 3) we do not see any conversions on the Moho: the delays of 0,3-1 s are smaller than expected for P-S conversions (3-4 s) on the Moho boundary.
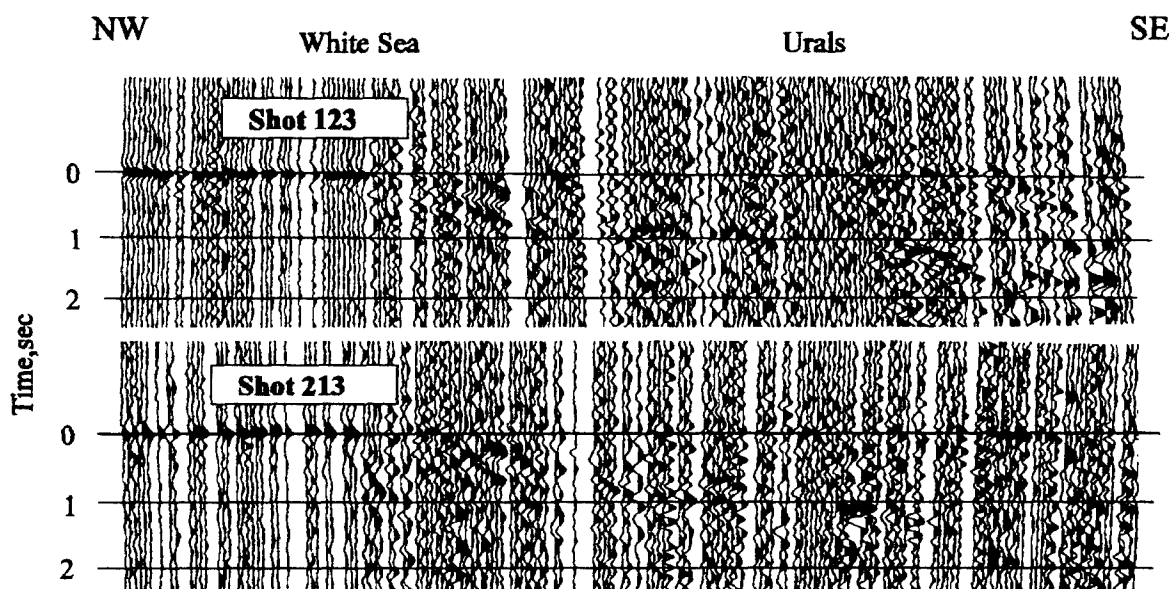
Figure 6. Receiver functions calculated for shots 123 (northern PNE) and 213 (middle PNE). Note the absence of conversions in the Baltic Shield area (left side of the gathers) and the correspondence of the pattern of receiver functions to the thickness of sediments (compare to Figure 2).

CONCLUSIONS AND RECOMMENDATIONS

Based on 600-sec digitization and processing of the data from long-range DSS profile "Quartz" we are able to detect a number of seismic phases refracted and reflected within the upper mantle and to analyze the propagation of crustal-guided waves (Pg and Lg) throughout the entire distance range (2000 km at present). Our analysis of the data shows that:

- The LVZ observed in the upper mantle before is dipping in a SE direction and is located at depths of about 100 km under Kola Peninsula and 200 km under the West Siberian Platform. The thickness of the LVZ increases from 20 km at the NW end of the profile to about 40 km at the SE end.

- Dipping Moho boundary relief and lower mantle velocities under the Urals can be associated with the roots of Ural foldbelt.

- as we pointed out before (Morozova et al., 1994) Lg phase is comparatively weak in the northern and middle PNE records. A preliminary examination of the data from the southern PNE shows that Lg phase is very prominent in these records, at least on the West Siberian basin.

- The Lg phase is much weaker than recorded on the Baltic Shield and appears to be blocked by Ural Mountains.

We observed P-S conversions on the top of the basement. These converted waves, however, cannot be Our work with these data is not, however, complete. Our major concern in future work is related to the improvement of the crustal and uppermost mantle P- and S-wave velocity models. The most important steps we will take are:

- we will complete the basic processing of the rest of the data (southern PNE, far-offset parts of the other 2 PNEs, and 12 chemical shots).

- we will complete our tomographic inversion of the crustal velocity structure.

- constraints of the S-wave velocity of the crust will be obtained from S-wave phases observed in chemical shot records, and possibly from the receiver function analysis.

- responsible for complex first break signatures.

- we will perform joint amplitude analysis of all three PNE records. The records from the southern PNE would yield new insight into the Lg blockage under Urals which we suggested before.

- 2-D modeling will be carried out for the entire "Quartz" profile, including the third PNE. This would strengthen our conclusions about the thickness and the shape of LVZ in the upper mantle.

- amplitude information needs to be included into the 2-D inversion of the upper mantle. This is necessary for the validation of the upper mantle velocity model (Ryaboy, 1989), and for the analysis of amplitude ratios, as seismic discriminants.

- based on the above, we will be able to perform a quantitative analysis and modeling of Lg phase propagation across the boundaries of various geological structures.

REFERENCES

Ammon, C., 1991, The isolation of receiver effects from teleseismic P waveforms, BSSA, 81, 2504-2510.

Benz, H. M., Unger, J. D., and Leith, M. S., 1992. Deep seismic sounding in northern Eurasia: interpretation of the Murmansk-Kizil ultra-long-range profile. In: Proc. of the 14th PL/DARPA Seismic Research Symposium. (Eds. Lewkowicz, J. F., McPhetres, J. M): 17 Aug. 1992. PL-TR-92-2210, ADA256711

Mechie, J., Egorkin, A. V., Fuchs, K., Ryberg, T., Solodilov, L. and Wenzel, F., 1993. P-wave mantle velocity structure beneath northern Eurasia from long-range recordings along the profile Quartz: Phys. of the Earth and Plan. Int., 79, 269-286.

Morozova, E. A., Morozov, I. B., Smithson, S. B., Shatzman, J. C., and Solodilov, L. N., 1994, Studies of P_n, S_n and L_g wave propagation across major crustal structures using PNEs. In: Proc. of the 16th PL/DARPA Seismic Research Symposium. (Eds. Lewkowicz, J. F., McPhetres, J. M.): Thornwood, Sept. 1994. PL-TR-94-2217, ADA284667

Morozova, E. A., Morozov, I. B., and Smithson, S. B., 1995, Evidence for upper mantle heterogeneities from the nuclear-shot sourced "Quartz" long seismic profile, Seismological Research Letters, 66, no. 2, 40.

Paige, and Saunders, 1982, ACM Trans. Math. Softw., 8, 43.

Ryaboy, V., 1989, Upper mantle structure studies by explosion seismology in the USSR, Delphic Assoc., Inc., Falls Church, VA.

White, D., 1989, Two dimensional seismic refraction tomography, Geophys., J., 97, 223.

Zonenshain, L. P., Kuzmin, M. I., and Natapov, L. M., 1990. Geology of the USSR: A Plate-Tectonic synthesis. In: B.M. Page (Ed.), Am. Geophys. Union Geodynamics Ser., 21; 242 pp.

Analyses of the Seismic Characteristics of U.S. and Russian Cavity Decoupled Explosions

J. R. Murphy, I. O. Kitov*, N. Rimer, D. D. Sultanov*,
B. W. Barker and J. L. Stevens

Maxwell Laboratories, Inc.,S-CUBED Division
11800 Sunrise Valley Dr., Suite 1212
Reston, Virginia 22091
Contract No. F19628-93-C-0126
Sponsored by Phillips Laboratory

Abstract

The cavity decoupling evasion scenario remains as the greatest challenge to effective seismic monitoring of any eventual CTBT. However, despite the fact that the feasibility of this evasion concept was experimentally established nearly 30 years ago by the U.S. STERLING test, a number of issues of importance with respect to seismic monitoring still remain unresolved. In an attempt to address some of these issues, we have been working with scientists from the Russian Institute For Dynamics of the Geospheres to integrate the limited U.S. and Russian data and modeling experience into a uniform database on cavity decoupling. During the past year, our research has centered on analyses of data recorded from an extensive series of Russian HE cavity decoupling tests conducted in Kirghizia in 1960 and on analyses of seismic data recorded from six Russian nuclear tests conducted in a water-filled cavity at Azgir.

The Kirghizia HE cavity decoupling series consisted of 10 tamped and 12 cavity tests in limestone, and included tests of the same yield in both spherical and nonspherical cavities of equal volume. Comparisons of near-field seismic data recorded from these tests indicate that the low frequency decoupling effectiveness is approximately independent of cavity shape for roughly cylindrical cavities with length to width ratios of 6 or more, in agreement with previous theoretical simulation results. Spectral analyses of waveform data recorded at the same distances from 1.0 ton tamped explosions and from a 1.0 ton decoupled test in a spherical cavity with a radius of 2.88 m indicate a maximum low frequency decoupling factor of about 25 for this test. Theoretical simulations conducted using a limestone model which is consistent with these observed seismic data predict a corresponding nuclear decoupling factor of about 60 for this yield/volume ratio.

During the period 1975 to 1979, the Russians conducted a series of nuclear tests at Azgir in the water-filled, approximately 30 m radius cavity created by the 27 kt tamped explosion of 7/01/68. Six nuclear explosions with yields ranging from 0.01 to 0.50 kt were subsequently detonated in this cavity and seismic data were recorded from these tests at fixed stations in the range from about 1 to 75 km. Spectral analyses of the seismic data recorded from these tests at near-field stations reveal a consistent and pronounced yield dependence to the cavity/tamped source spectral ratios. Detailed theoretical simulations of these spectral ratio data are currently being conducted in an attempt to develop improved equations of state for salt for use in theoretical simulations of various cavity decoupling evasion scenarios.

Key Words: Seismic, Cavity Decoupling, Kirghizia, Azgir

* Institute For Dynamics of the Geospheres, Russian Academy of Sciences

Objective

It has long been recognized that the most effective means for evading the detection of a clandestine underground nuclear test is to detonate the explosion in a cavity which is large enough to substantially decouple the radiated seismic signal. In this project we are working with scientists from the Russian Institute for Dynamics of the Geospheres (IDG) to integrate the U.S. and Russian data and modeling experience into a uniform database on cavity decoupling. The objective of the study program is to validate a quantitative prediction capability which can be used by the seismic verification community to evaluate the plausibility of various cavity decoupling evasion scenarios.

Research Accomplishments

During the past year, our research has continued to focus on analyses of data recorded from an extensive series of Russian HE decoupling tests and on analyses of seismic data recorded from six Russian nuclear tests conducted in a water-filled cavity at Azgir (Murphy et al., 1994). The HE decoupling tests consisted of a series of 22 tamped and cavity explosions conducted in a mine in the Tywya Mountains of Kirghizia in the summer of 1960. The tests were conducted in hard, homogeneous limestone in chambers excavated from alcoves constructed off the sides of the main access tunnel to the mine. The decoupled tests were conducted in spherical cavities having diameters ranging from about 3.5 to 10 m, as well as in nonspherical cavities with volumes of about $25m^3$. The test series was composed of 10 tamped and 12 decoupled explosions having yields of 0.1, 1.0 and 6.0 tons. The explosives consisted of ammonium nitrate, except for the two 6.0 ton tests which utilized a mix of TNT and ammonium nitrate. For the cavity tests, the explosives were suspended in the chambers and included cases in which the explosives were positioned off-center, near the cavity walls. The configurations of the various cavity tests are graphically summarized for each of the five test chambers in Figure 1.

Seismic data were recorded from these tests at locations in the mine over a distance range extending from about 10 to 250 m from the sources. Peak amplitudes of displacement and velocity have been reported for over 250 of these recording locations and about 60 of the corresponding seismograms have been digitized at IDG and prepared for detailed spectral analysis. Direct comparisons of the peak displacements recorded from cavity tests of the same yield provide good indications of the relative low frequency decoupling efficiencies of different cavity configurations. For example, Figure 2 shows comparisons of the peak displacement data observed from 0.1 ton decoupled tests in spherical and elongated cavities of the same volume (i.e. $25m^3$). The leftmost display in this

figure corresponds to a cylindrical cavity with length to width (L/W) ratio of about 3, while the other two displays are for tests in a nonsymmetrical cavity with dimensions of about 1m X 2m X 12m (i.e., L/W ≈ 6-12), one with the charge at the center (middle) and one with the charge near the end of the chamber (right). It can be seen that the peak displacement data observed from these various cavity configurations are all quite comparable, which suggests that the low frequency decoupling effectiveness is not very sensitive to cavity shape at this yield/volume ratio. The only notable anomaly in Figure 2 is for the case of the nonsymmetrical cavity with the charge at the end, for which the close-in displacement levels are somewhat higher than those observed from the spherical cavity of the same volume. However, this offset is fairly small and is not evident at distances which are large with respect to the cavity dimensions. This observed insensitivity to cavity shape is consistent with the theoretical simulation results previously reported by Stevens et al. (1991).

In order to make a fully quantitative assessment of decoupling effectiveness, it is necessary to carry out detailed spectral analyses of the complete waveform data. Such an analysis has been carried out using data recorded from the 1.0 ton decoupled test in the 2.88 m radius spherical cavity and the resulting estimated decoupling factor is shown as a function of frequency in Figure 3. It can be seen that these data indicate that a maximum low frequency decoupling factor of about 25 was achieved in this test. Also shown on this figure are the theoretical decoupling factors predicted for 1 ton HE and nuclear explosions in a 2.88 m radius cavity in limestone using our nonlinear finite difference code. It can be seen that although there are still some unexplained discrepancies in spectral shape over this band, the theoretical HE simulation does provide a fairly good description of the observed low frequency decoupling factor in this case. As has been noted previously by Glenn and Goldstein (1994) and others, the corresponding theoretical nuclear decoupling factor for this yield/volume ratio is predicted to be significantly larger, with a maximum low frequency value of about 60, roughly consistent with the value of 70 observed from the STERLING nuclear cavity test in salt.

During the period 1975 to 1979, the Russians conducted a series of nuclear tests at Azgir in the water-filled cavity created by the 27 kt tamped explosion of 7/01/68. The tamped explosion was detonated at a depth of 597 m and produced a nearly spherical cavity with a volume equal to that of a spherical cavity with a radius of 28.9 m. Six nuclear explosions with yields ranging from 0.01 to 0.50 kt were subsequently detonated in this cavity and seismic data were recorded from these tests at fixed stations in the range from about 1 to 75 km. Although these tests were not decoupled and, in fact, showed enhanced coupling in some frequency bands, their wide range in energy release at a fixed detonation point provides a unique opportunity to further investigate the seismic source characteristics of explosions in salt. Seismic data recorded from the tamped test which created the cavity, and from four of the water-filled cavity tests (i.e., 0.01,

0.08, 0.10 and 0.35 kt) have been digitized at IDG and subjected to detailed spectral analysis. Displacement spectra computed from the vertical component signals recorded from the tamped and four cavity tests at the station located at a range of 1.17 km are shown in Figure 4. Note that because of the dynamic range limitations of the hand-digitized data, the spectrum for the tamped 27 kt explosion, which is associated with a much lower corner frequency than those of the cavity tests, is only considered to be reliable below about 5 Hz, while the cavity test spectra are estimated out to 20 Hz. Assuming that propagation path effects on the spectra are of second order importance at these near-source distances, the observed tamped spectra were cube-root scaled to the yields of the cavity tests and cavity/tamped spectral ratios were computed using the data from stations at 1.17, 1.71 and 7.8 km. The resulting spectral ratios for a given explosion were found to be quite consistent at these three distances, suggesting that they represent useful approximations to the corresponding source spectral ratios. Consequently, the three spectral ratios for each cavity test were logarithmically averaged and the resulting estimates of the cavity/tamped source spectral ratios for the four cavity tests are shown in Figure 5. It can be concluded from this figure that the 0.35 kt water-filled cavity test shows enhanced low frequency coupling with respect to that expected from a tamped explosion of the same yield in salt, while the 0.10 kt and 0.08 kt cavity test sources appear to be very similar to those expected for tamped tests of comparable yield. The lowest yield 0.01 kt cavity test source, on the other hand, shows a pronounced resonance in the band around 10 Hz, where the overshoot of the low frequency level reaches a factor of 5 or more. Nonlinear finite difference simulations of this test indicate that this resonance is associated with reverberation of the explosive shock wave in the water-filled cavity. Detailed theoretical simulations of all these spectral ratio data are currently being conducted in an attempt to infer an improved equation of state for salt for use in the modeling of various cavity decoupling evasion scenarios.

Conclusions and Recommendations

Over the past several years, we have been working with scientists from the Russian Institute For Dynamics of the Geospheres (IDG) in an attempt to integrate the available U.S. and Russian data and modeling experience on cavity decoupling. Current research activities have been focusing on the analysis of data recorded from an extensive series of Russian HE decoupling tests and on an analysis of seismic data recorded from a series of nuclear tests conducted in a water-filled cavity in salt at Azgir. Comparisons of near-field seismic data recorded from the Kirghizia HE decoupling tests have indicated that the low frequency decoupling effectiveness is approximately independent of cavity shape for roughly cylindrical cavities with length to width ratios of 6 or more.

Furthermore, detailed spectral analyses of Kirghizia waveform data recorded from 1.0 ton HE tests indicate a maximum low frequency decoupling factor of about 25, and theoretical simulations suggest that this corresponds to a nuclear decoupling factor of about 60 for this yield/cavity volume ratio in limestone. Seismic data recorded from the Azgir water-filled cavity tests have been analyzed and a pronounced yield dependence has been identified in the resulting cavity/tamped source spectral ratios. Although these cavity tests were not decoupled and, in fact, show enhanced coupling in some frequency bands, their wide range in energy release at a common detonation point is providing a unique opportunity to further quantify the seismic source characteristics of explosions in salt.

References

Glenn, L. A. and P. Goldstein (1994), "Seismic Decoupling with Chemical and Nuclear Explosions in Salt," Journal of Geophysical Research, Vol. 99, No. B6, p. 11,723.

Murphy, J. R., I. O. Kitov, J. L. Stevens, D. D. Sultanov, B. W. Barker, N. Rimer and M. C. Friedman (1994), "Analyses of the Seismic Characteristics of U.S. and Russian Cavity Decoupled Explosions," S-CUBED Technical Report PL-TR-94-2295, ADA292881

Stevens, J. L., N. Rimer, J. R. Murphy and T. G. Barker (1991), "Simulation of Seismic Signals From Partially Coupled Nuclear Explosions in Spherical and Ellipsoidal Cavities," S-CUBED Technical Report SSS-FR-91-12735.
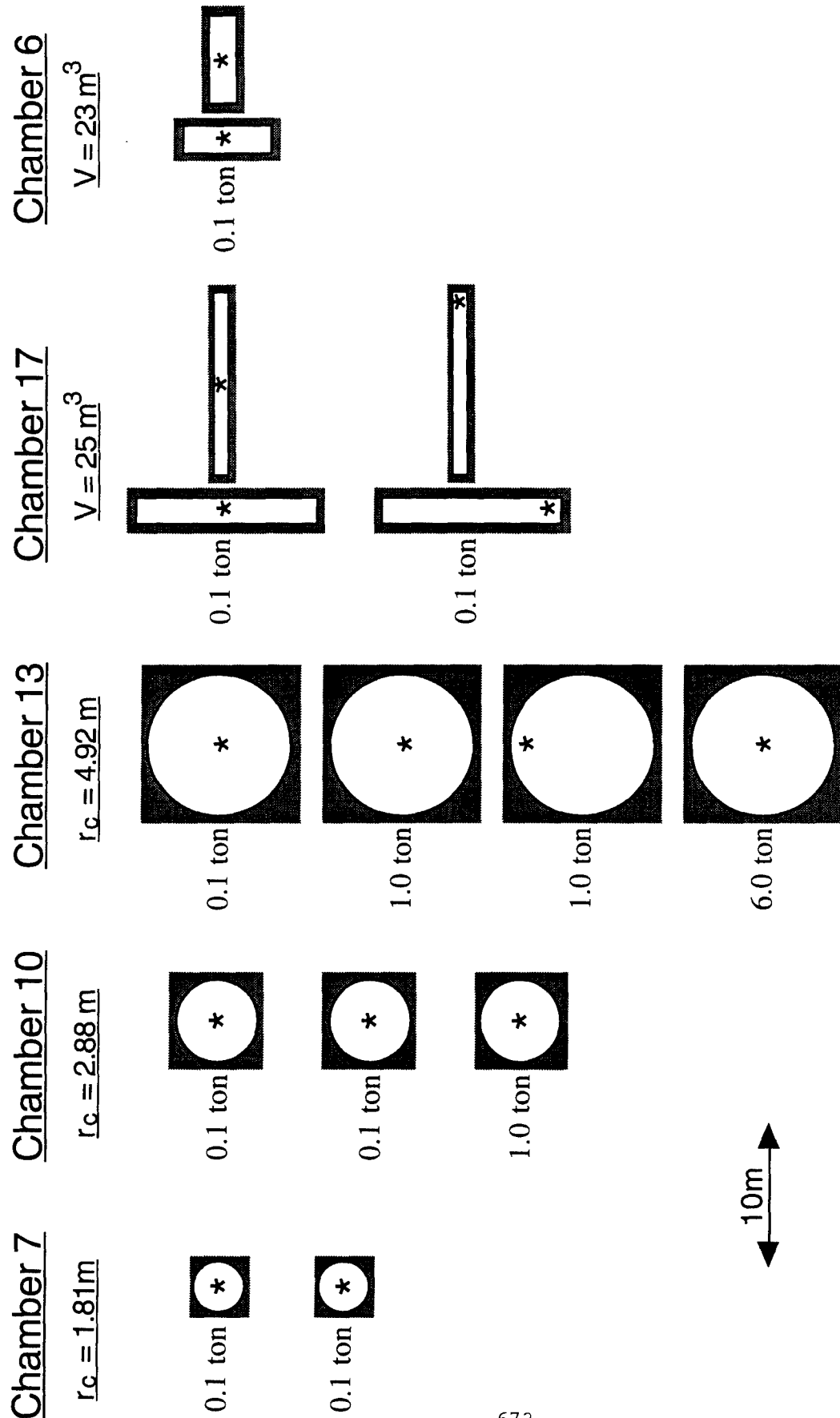
Figure 1. Graphical summary of the Kirghizia HE decoupling tests conducted in each of the excavated explosion chambers. The asterisk denotes the emplacement location of the charge within the chamber for each test. For the nonspherical cases, both horizontal (left) and vertical (right) sections through the chambers are displayed.
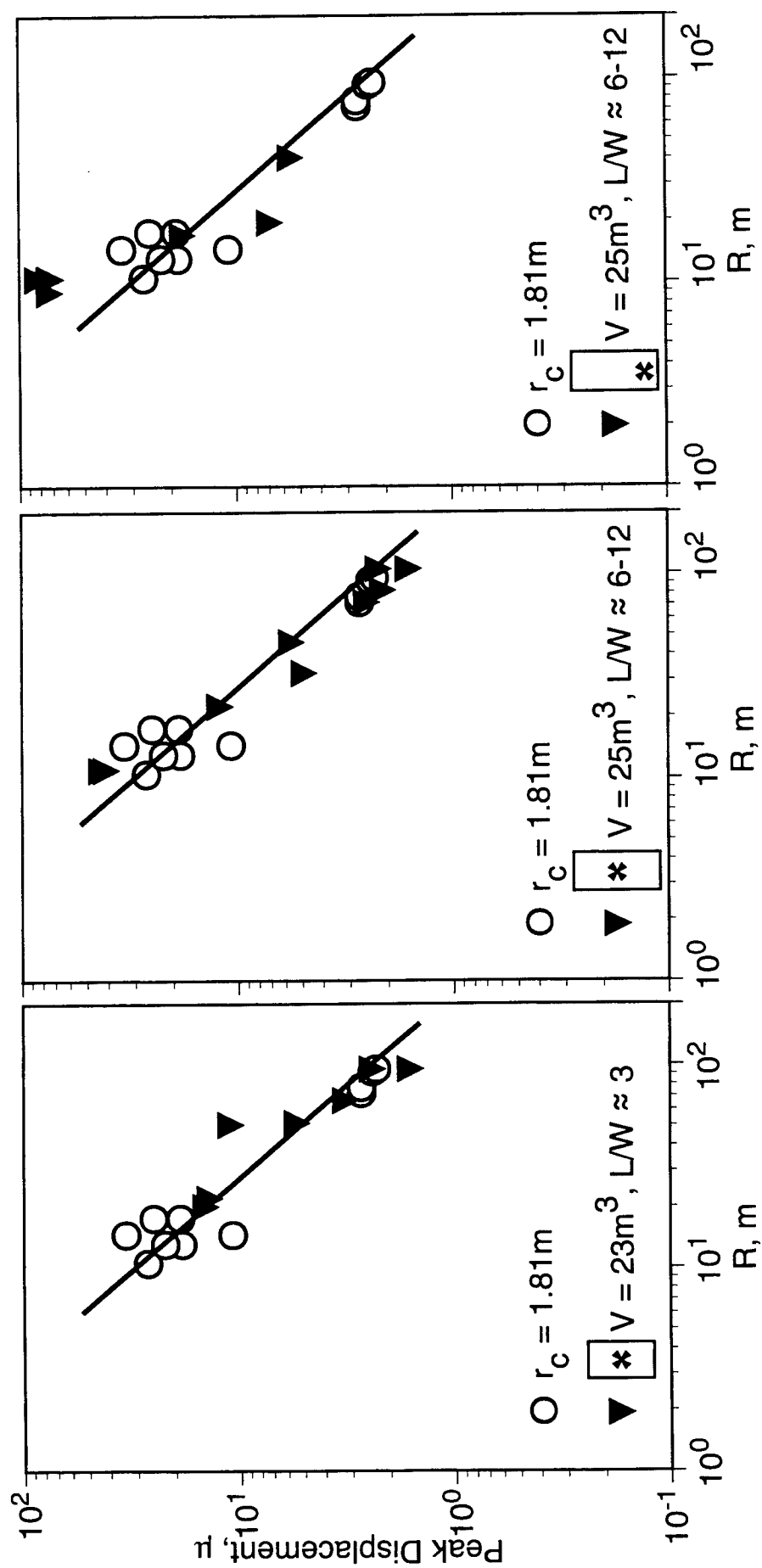
Figure 2. Comparison of peak displacement data observed from Kirghizia 0.1 ton decoupled tests in spherical and elongated cavities of comparable volume. For the nonspherical cavities, the asterisks denote the charge location.
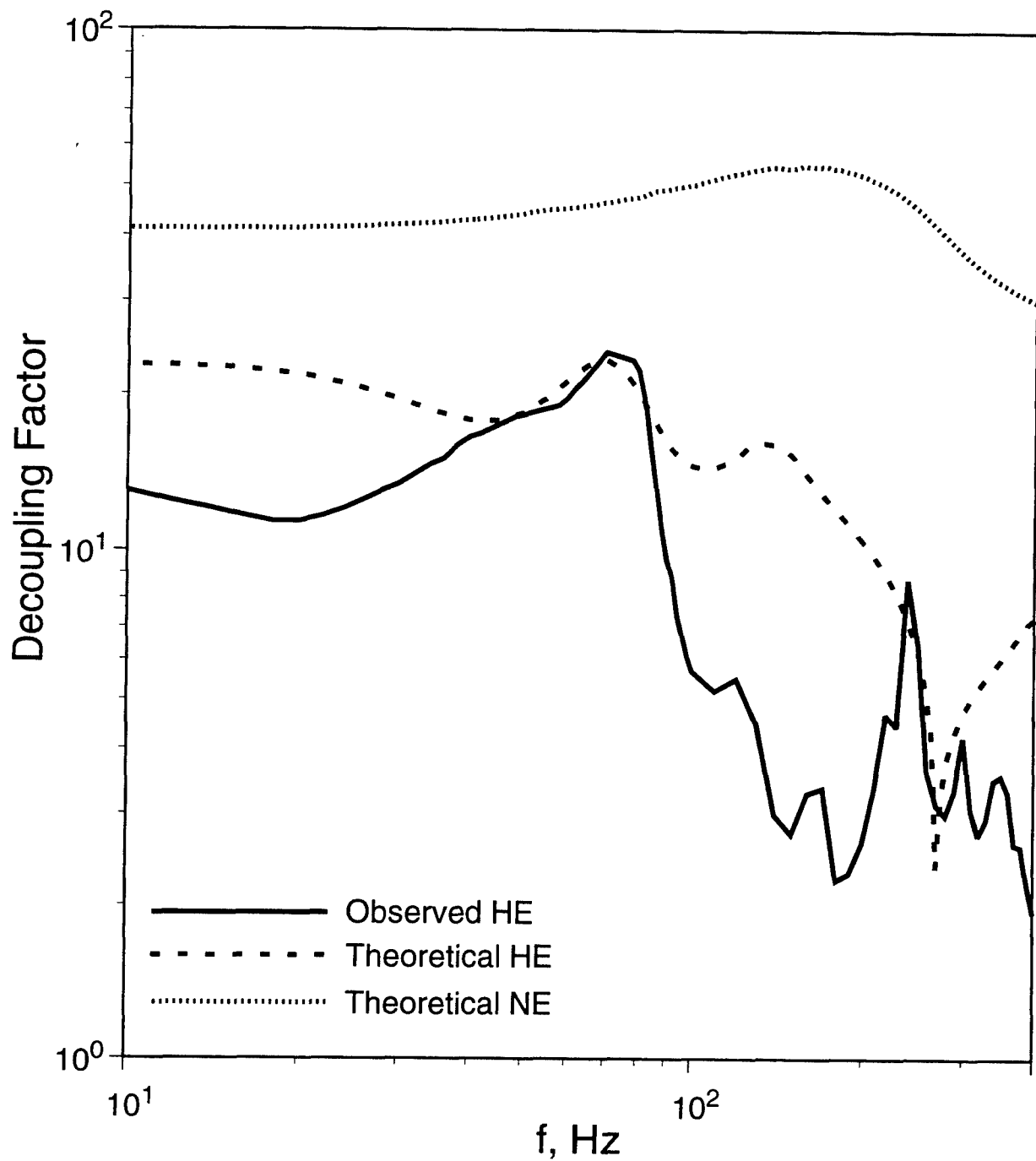
Figure 3. Comparison of observed and theoretical frequency dependent decoupling factors for 1 ton explosions in a 2.88m radius spherical cavity in Kirghizia limestone.

674
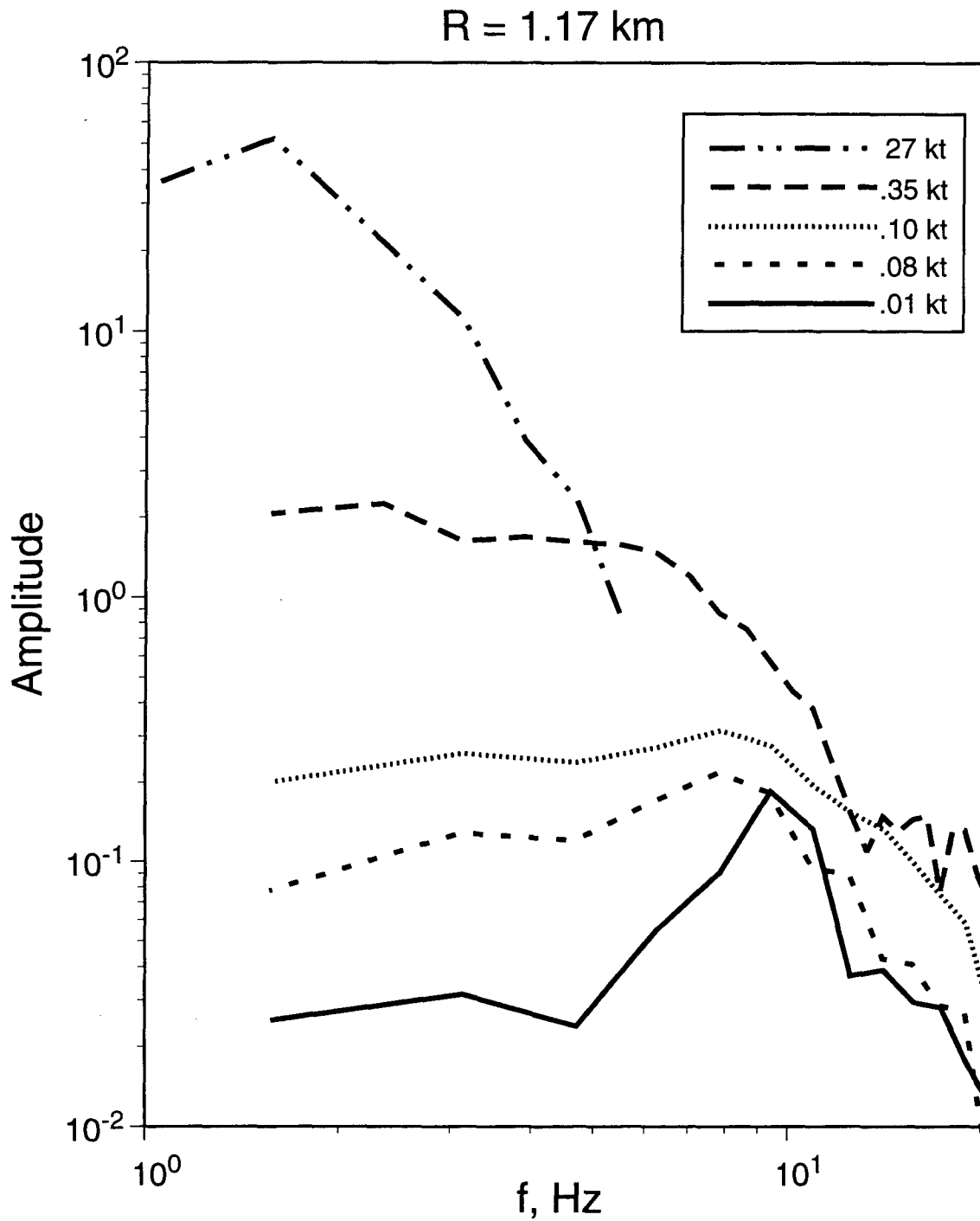
Figure 4. Comparison of displacement spectra computed from vertical component data recorded from the Azgir tamped and water-filled cavity tests at a range of 1.17 km.
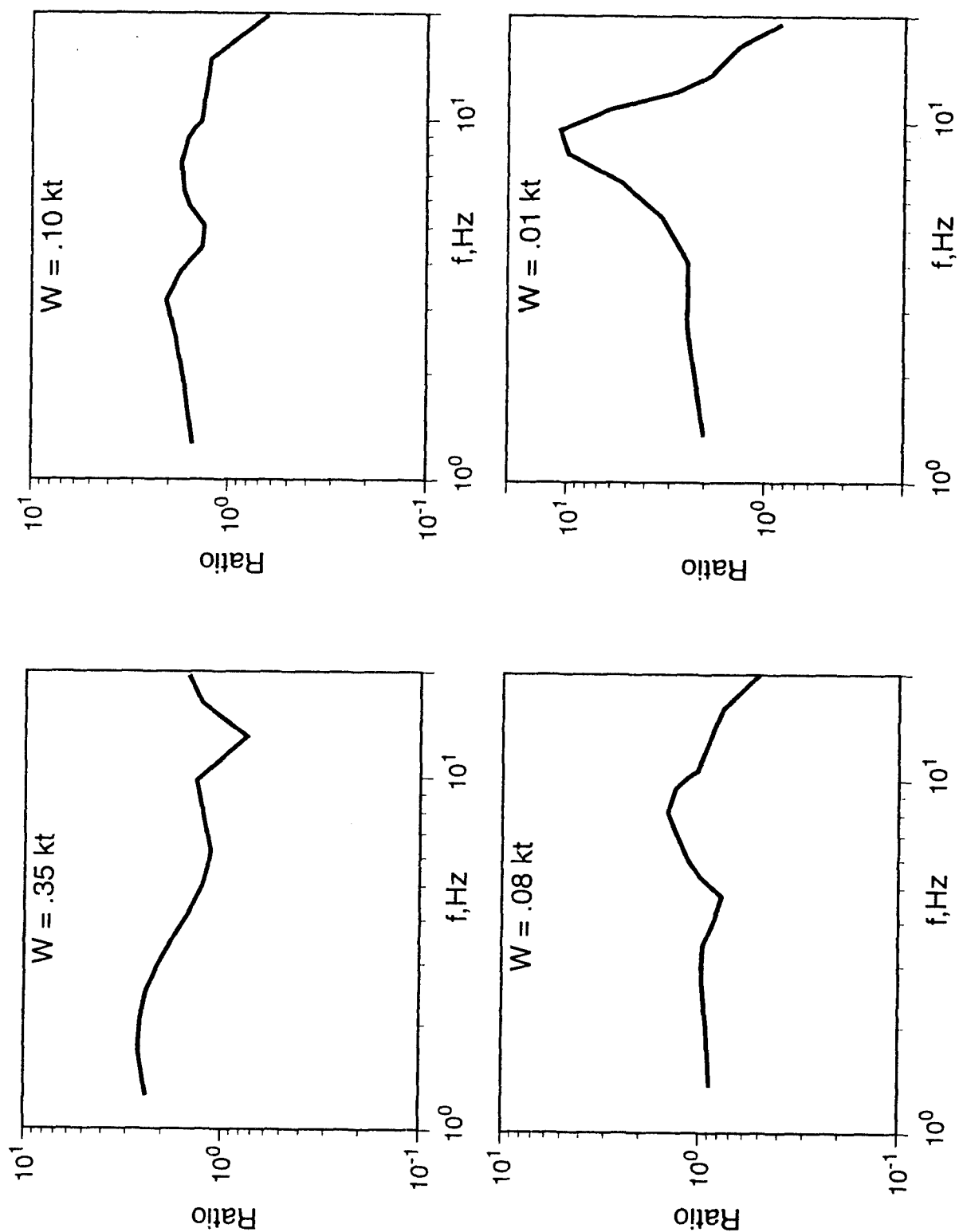
Figure 5. Average cavity/tamped source spectral ratios estimated from seismic data recorded from the Azgir tamped and selected water-filled cavity tests.

ASIAN UPPER MANTLE P-WAVE VELOCITY STRUCTURE FROM THE ANALYSIS OF BROADBAND WAVEFORMS

Arthur Rodgers and Susan Schwartz
Institute of Tectonics, University of California, Santa Cruz, CA, 95064
Contract # F49620-94-1-0050

Abstract

Upper mantle P-wave velocity structure beneath Asia was inferred by modelling high-quality broadband P and PP seismograms at distances 10° to 55°. Data were obtained from IRIS-GSN, CDSN and IRIS-PASSCAL instruments. We regionalized the Asian continent by fitting long-period filtered data to reflectivity synthetics computed for one-dimensional velocity models. Results show that major tectonic provinces can be characterized by single average regional velocity models. These average regional models reveal significant differences in crustal thickness, mantle lid, and low velocity zone properties, and thus will affect seismic discriminants. The data were then filtered less severely to model details of the broadband data and reveal lateral heterogeneity within a tectonic province. Structure of the Tibetan Plateau was studied in detail using regional data recorded at CDSN and GSN stations. Future work will include more broadband P- as well as S-wave modelling.

Key words: Asia, regionalization, crust and upper mantle structure

Objective

Seismic event discrimination methods, such as those relevant to CTBT monitoring, are strongly dependent on the structure of the crust and upper mantle. Thus, the transportability of discriminants is affected by regional differences in crust and upper mantle structures, particularly the nature of the mantle lid and possible low velocity zone (e.g. Beckers, Schwartz and Lay, 1993). The waveforms of P, PP, S and SS body-waves in the distance range 10° to 55° are very sensitive to the seismic velocity structure of the uppermost 200 km of the Earth (i.e. the crust and upper mantle lid and low velocity zone).

Recent deployments of IRIS-GSN, CDSN and IRIS-PASSCAL instrumentation in Asia and efforts by the IRIS-DMC to make these data available now make it possible to gather high-quality, modern data at these critical distances for many regions that were previously unsampled by historical data (e.g. WWSSN, SRO). The objective of this research is to determine one-dimensional crust and upper mantle structures that accurately predict the observed P, PP, S and SS waveforms. The Asian continent consists of many distinct tectonic units (figure 1). We regionalized Asia using the upper mantle velocity models shown in Figure 2. As the path density increases we will be able to infer laterally varying structures. The use of the new data will improve the regionalization of Asia. The impact of various upper mantle models on regional seismic wave propagation will be studied and related to discriminant analysis and transportablity.

Research Accomplished

1. Data and Modelling Strategy

Broadband three-component recordings of crustal events occurring within the Asian continent were extracted from IRIS-FARM products. We searched for moderately large (M_W = 5.5-6.8) events with known mechanisms and simple source-time functions. Instrument deconvolved displacement seismograms were previewed and judged for source complexity and good signal-to-noise. The source parameters (i.e. event depth, focal mechanism and source-time duration) were evaluated and possibly adjusted by modelling broadband waveforms of teleseismic P using WKBJ synthetics.

We modelled the observed waveforms for those events with well constrained source parameters. Synthetics were computed using the reflectivity method. It has been shown (Schwartz and Lay, 1991) that reflectivity is superior to ray-based methods for synthesizing the surface reflected PP phase, which consists of interfering multiple reflections and conversions (e.g. whispering gallery waves).

Synthetics were computed for each event-station pair for seven models of the upper mantle. These models (figure 2) represent a wide range of tectonic character from shield-like models (e.g S25, Lefevre and Helmberger, 1989; and K8, Given and Helmberger, 1980) to models for tectonically active regions (e.g. T7, Burdick and Helmberger, 1978 and WCH, Beckers et. al., 1994). Data and synthetics were convolved with a WWSSN long-period instrument response and compared by aligning the main P-wave arrival. The best fitting models were found by (subjectively) evaluating the relative timing and amplitude of the triplicated P or PP arrival, the PP-P differential time and the character of early coda.

2. Modelling Results: Regionalization of Asia

The Asian continent was regionalized based on the best-fitting model to the observed P and/or PP waveforms. The results are summarized for the distance range 8° to 26° in figure 3. (Results for PP in the distance range 26° to 50° will be shown in the poster.) The best-fitting models separate into the major tectonic provinces of Asia (compare with figure 1).

Specific regions and their upper mantle structures are described below:

The **Tibetan Plateau** (model TP) is characterized by a thick crust (65 km), high Pn velocity (8.23 km/s) and a strong low velocity zone.

Western China (model WCH), corresponding to the North China Fold System and parts of the Eastern Platforms, is characterized by moderately thick crust (50 km), moderately high Pn velocities (8.15 km/s) and a slight low velocity zone.

Siberia and Eurasia (models NCH and K8) are characterized by a more shield-like model: normal crustal thickness and normal to high Pn velocity (40 km and 8.0-8.2 km/s, respectively) and a positive lid gradient. This model also fits the PP path along the southern margin of the Tibetan Plateau (Indian Shield) and some paths through eastern China.

Eastern Asia (model CHE) is characterized by normal crustal thickness and Pn velocity (35 km and 8.12 km/s, respectively) and a constant lid velocity with no low velocity zone.

3. The Tibetan Plateau

Broadband three-component recordings of regional events in the Tibetan Plateau were extracted from IRIS-FARM products. The stations KMI, LZH, WMQ, XAN, ENH and CHTO are situated around the Plateau such that structure of the Tibetan Plateau and its margins can be studied using events that occurred within Tibet. In particular, the Pn velocity and velocity gradient of the mantle lid was investigated using data recorded at these stations from events in Southern Tibet.

Figure 4 shows the paths from three events to regional stations. We assumed a crustal thickness and velocity of 65 km and 6.4 km/s, respectively, and computed synthetics for a suite of upper mantle velocity models. Using four Pn velocities (8.05, 8.10, 8.15 and 8.20 km/s) and three mantle lid gradients (constant lid velocity, CLV; and positive lid gradients, PLG, of 0.001/s and 0.002/s), we computed reflectivity synthetics for the paths shown in figure 4. These Pn velocities are consistent with the range of velocities for this region inferred from Pn tomography by McNamara et. al. (1994).

Data for nearly all the paths were best fit by the low Pn velocity (8.05 km/s) and a constant lid velocity. The data for paths to KMI revealed differences in lid structure. The waveforms from the southern two events to KMI were best fit by a constant lid velocity (CLV) and Pn velocity of 8.05 km/s. The waveform from the northern event to KMI (shown as dashed line in figure 4) was best fit by a positive lid gradient (PLG) and a Pn velocity of 8.2 km/s. The southern paths sample the northern margin of the Indian Shield, while the northern path samples the southern margin of the Tibetan Plateau. The increased Pn velocity and mantle lid gradient of the northern path relative to the southern path probably results from the mantle responding to the additional load of material due to undertrusting of the Indian Plate or crustal shortening as previously inferred by Holt and Wallace (1980). These results, although preliminary, show that the modern data can be used to further investigate details of the mantle lid structure beneath Tibet.

Data from the IRIS-PASSCAL field experiment on the Tibetan Plateau are available in the IRIS-DMC TIPLT data product (Owens, et. al., 1993). We have only begun to work with the TIPLT data, however the recordings are of very high quality and promise to elucidate the crustal and upper mantle structure beneath the Plateau. A major advantage of these data over the GSN data is that the paths for regional Tibetan events to these stations all lie within the Plateau and do not cross tectonic boundaries. Preliminary results using these data will be presented at the poster.

Conclusions and Recommendations

Our preliminary results for the regionalization of Asia indicate that large areas can be characterized by single average regional upper mantle velocity models. The regions correspond fairly well with the known provinces of surface tectonics. The average regional models differ significantly in the uppermost 200 km and will affect event discrimination techniques. We have shown the results of processing only six (6) events. There are many more data to collect and process and future work will help fill in un-sampled areas.

S-wave data has been extracted and processed for many events, however modelling the data with synthetics has not yet been started. Future work will include S-wave modelling.

As the path density increases it may be possible to formulate a grid search and/or waveform inversion scheme in which the best-fitting average regional model to the long-period filtered data is used as a starting model. Along path average one-dimensional (1D) structure could be found for each path starting with the long-period filtered data, iterating through linearized inversions for 1D structure while gradually including shorter periods. Three-dimensional (3D) upper mantle structure could be inferred by projecting the best-fitting one-dimensional models onto three-dimensional space and solving for the best-fitting 3D model.

Finally, we plan on investigating the effects of our inferred upper mantle structures on regional seismic wave propagation. This will extend the previous work of Beckers et. al. (1993).

References

Beckers, J., Schwartz, S. and Lay, T., 1993. Analysis of the effects of Eurasian crustal and upper mantle structure on regional phases using broadband seiemic data, PL-TR-93-2131, Final Report for the Philips Laboratory, Hanscom Air Force Base, MA. ADA272446

Beckers, J., Schwartz, S. and Lay, T., 1994. The velocity structure of the crust and upper mantle under China from broad-band P and PP waveform analysis, *Geophys. J. Int.*, **119**, 574-594.

Burdick, L., and Helmberger, D., 1978. The upper mantle P velocity structure of the western United States, *J. Geophys. Res.*, **83**, 1699-1712.

Given, J. and Helmberger, D., 1980. Upper mantle structure of Northwestern Eurasia, *J. Geophys. Res.*, **85**, 7183-7194.

Holt, W. and Wallace, T., 1980. Crustal thickness and upper mantle velocities in the Tibetan Plateau region from the inversion of regional Pnl waveforms: evidence for a thick upper mantle lid beneath southern Tibet, *J. Geophys. Res.*, **95**, 12,499-12,525.

Lefevre, V. and Helmberger, D., 1989. Upper mantle P velocity of the Canadian Shield, *J. Geophys. Res.*, **94**, 17,749-17,765.

McNamara, D., Walter, W., Owen, T. and Ammon, C., 1995. Upper mantle velocity structure beneath the Tibetan Plateau from Pn travel time tomography, *LLNL-UCID*.

Owens, T., Randall, G., McNamara, D. and Wu, F., 1993. 1991-92 Tibetan Plateau Passive-source seismic experiment, PASSCAL Data Report 93-005, *IRIS-DMC*, Seattle, WA.

Schwartz, S. and Lay, T., 1993. Complete PP-waveform modelling for determining crust and upper mantle structure, *J. Geophys. Res.*, **112**, 210-224.

Figure 1. Tectonic Map of Asia.

NCKP=North China-Korean Platform

SP=Siberian Platform
TP=Tibetan Plateau
TB=Tarim Basin

ECP=Eastern China Platforms

IS=Indian Shield
IP=Iranian Plateau

SCFS=Southern China Fold System
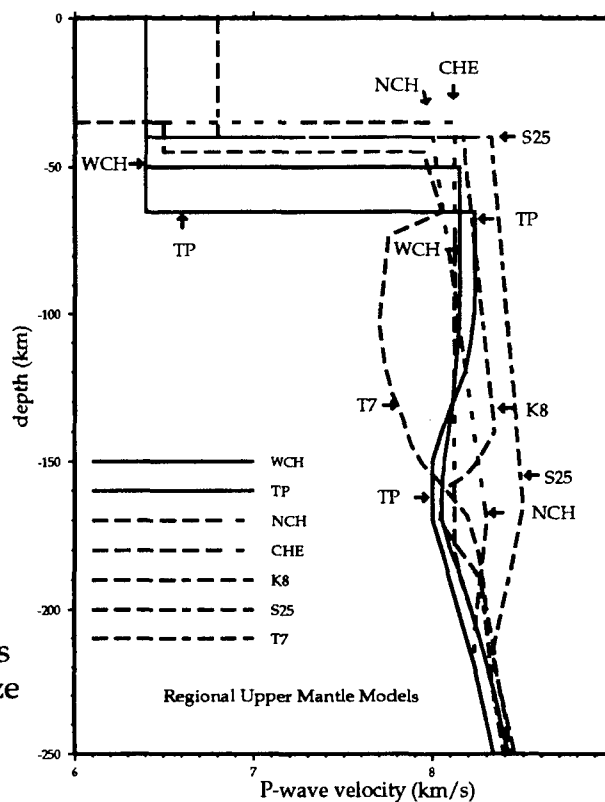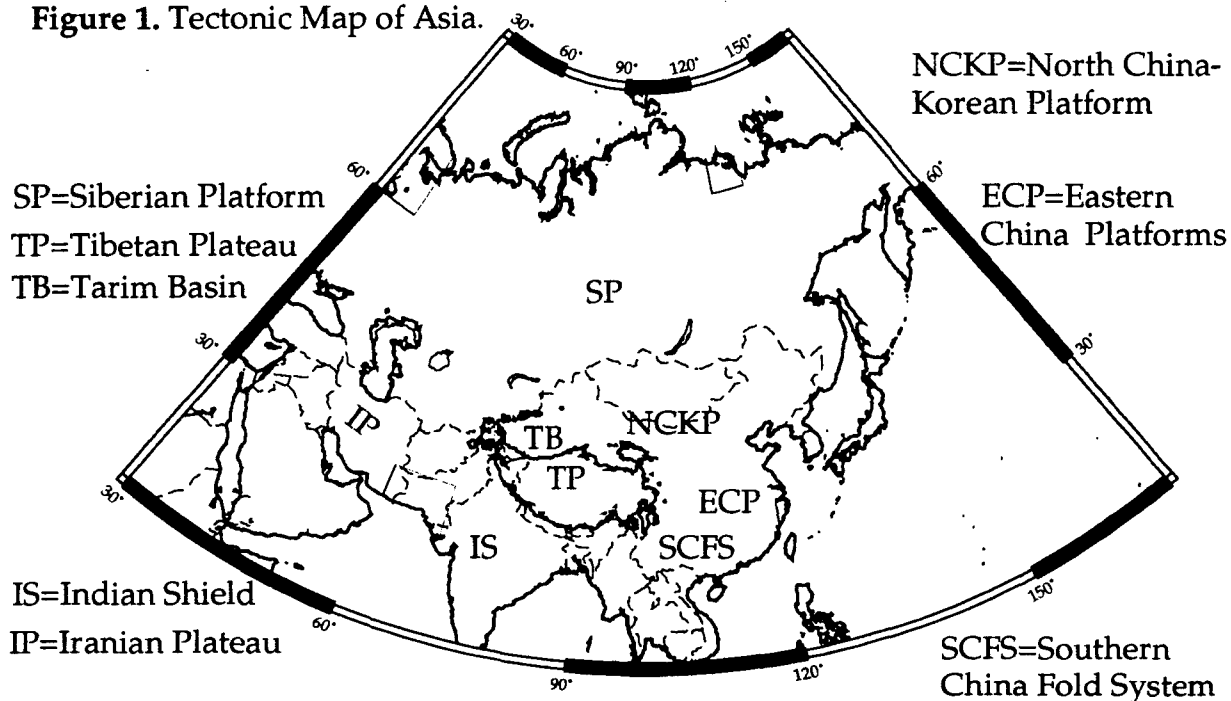
Figure 2. Upper mantle models used in this study to regionalize the Asian continent.

Regional Upper Mantle Models
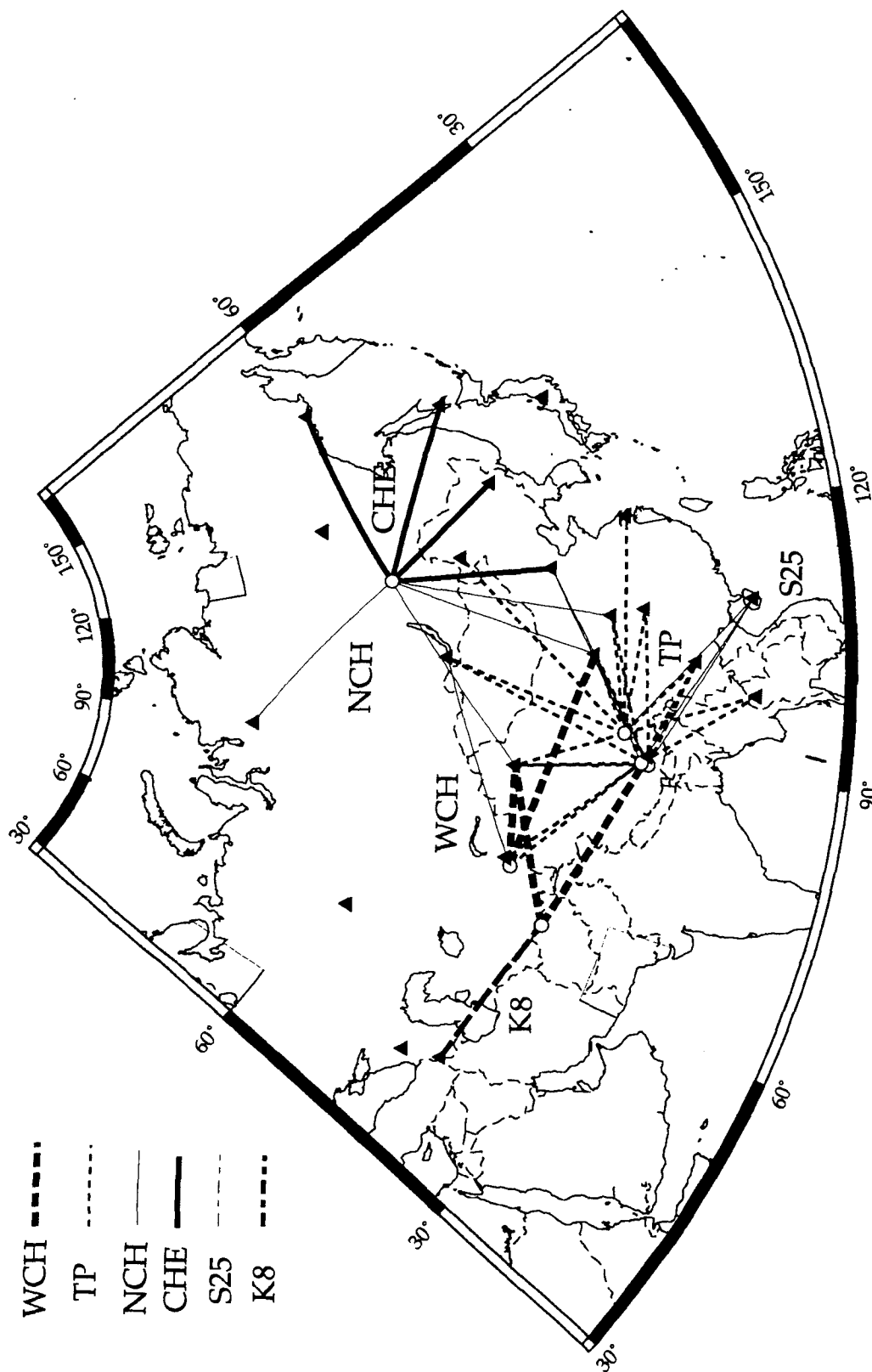
Figure 3. Best-fitting regional models for P, $\Delta = 8°\text{-}26°$
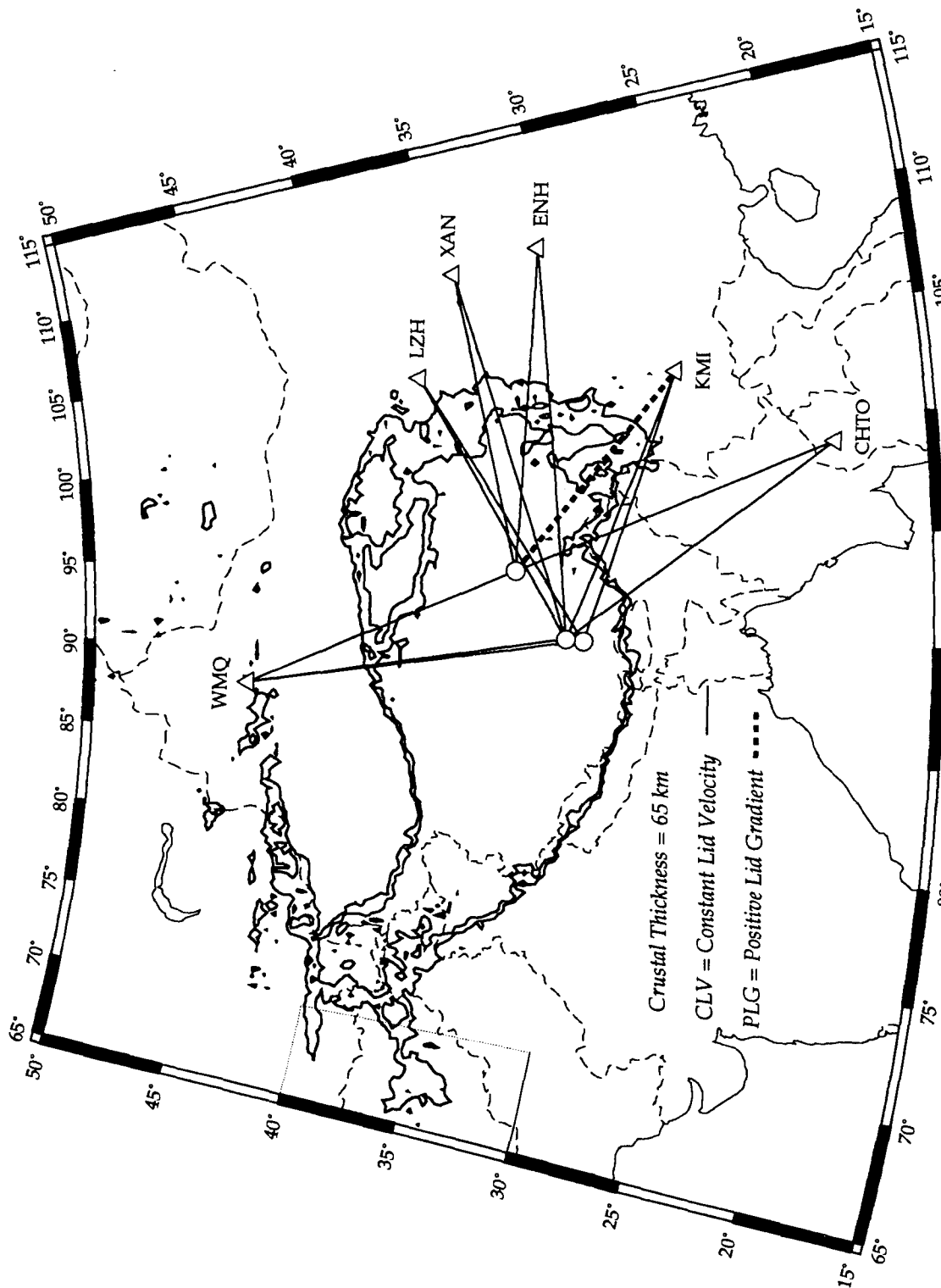
Figure 4. Tibet Events and Paths (3. & 4. km elevation contours shown)

Crustal Thickness = 65 km

CLV = Constant Lid Velocity

PLG = Positive Lid Gradient

683

THE LANL SOURCE GEOMETRY EXPERIMENT

B. W. Stump, D. C. Pearson,
C. L. Edwards and D. F. Baker
Los Alamos National Laboratory

ABSTRACT

The Source Geometry Experiment was successfully conducted over the time period 17 April to 7 May 95. Recording in the mine was conducted 24 April to 4 May 95. Five single sources were instrumented that included four cylindrical charges at different burdens (distance from the free face) and a pseudo-spherical charge. Nine production shots conducted during the two week visit to the mine were also recorded. Included in these production shots were a number of explosions designed to primarily bulk (no cast) the overburden and a number which cast material into the mine pit. Instrumentation was divided into six primary types: (1) Near-source accelerometers were deployed at distances of approximately 20 to 300 m [14, three-component 25 g/volt accelerometers and 16, three-component 1 g/volt accelerometers]; (2) Linear array of velocity gauges to quantify wave propagation effects [4-11 three component strong motion velocity gauges]; (3)Far-field velocity gages deployed in an azimuthal array around the mine at ranges from 500 to 2500 m [8, three component velocity gauges]; (4) High speed film and multiple camera video designed to quantify the two and three dimensional affects around the explosions [2 high speed cameras and 3 Hi-8 video cameras]; (5) Velocity of detonation and detonation time measurements of selected explosions [2 VODR systems]; and (6) Pre and post shot laser survey. Any one shot had as many as 154 channels of data. Although the complete data set is still being assembled, quality checked and analyzed, it appears that nearly 2,000 channels of data were successfully recovered during the experiment. Preliminary analysis of the data illustrates the: (1) Significant spall accompanied both the cylindrical and spherical single sources; (2) Similarity of waveforms from the cylindrical and spherical single sources; (3) Strong variations in the body and surface wave generation from the nine production shot. Regional data from some of the sources recorded during this field experiment have been recovered and will be included in the analysis allowing results and interpretations from the close-in data to be extrapolated to regional distances.

EXPERIMENTAL PURPOSE

The purpose of these experiments was focused on three primary issues. The first is directly linked to the efficiency of mining sources in the generation of both compressional and shear energy. This portion of the experiment produced data which can be used to develop a physical understanding of cylindrical explosive sources and the importance of the free-face which is failed in normal blasting practices. Single cylindrical sources, typical of the standard charges used in the multiple source production shots, were detonated at three different burdens. The first was that used in normal casting or fracturing shots. The second and third bridge the transition to a fully contained cylindrical source. The near-source and near-regional data spanning a number of azimuths gathered from these explosions will allow the quantification of energy coupling and the effect of the free-face in typical mining explosions.

The second issue to be addressed in this experimental series is the investigation of the charge shape, cylindrical in most mining applications, on the generation of seismic energy. A fully contained, pseudo-spherical, charge was designed, detonated and recorded using the same instrumentation array utilized in the cylindrical source study. This data will allow the cylindrical and spherical source geometry to be compared in a single geology. Extensive experience with spherical sources in a wide variety of geologies will allow this data to be extrapolated to other environments.

The final focus of this experimental study was the extension of the single, cylindrical source results to typical millisecond delay fired casting explosions. In this case multiple cylindrical explosions are detonated with millisecond delays between individual charges. The resulting waveforms are affected by the individual shot times as well as the interaction, possibly nonlinear, of the wavefield from each explosion. Nine, full production shots at the same mine and with the same cylindrical source configuration used in the single shot study were instrumented. Detonation times as well as velocity of detonation in the explosives for some of the holes in the explosive array were measured. This information along with the waveforms from the single cylindrical charges will allow a full assessment of both source interaction and timing effects.

In order to aid in the quantification of physical phenomena accompanying these explosions, multiple angle video and high speed photography accompanied the seismic measurements. This information will provide a quantification of two and three dimensional source processes and allow correlation with the resulting seismic measurements.

LOCATION OF THE EXPERIMENT

The mine is located outside of Terre Haute, Indiana. The mining operation is recovering coal from two seams, one at approximately 50 feet and the second near 100 feet. Explosions are used to remove this overburden which consists of a moderate to hard shale and lenticular sand units. Individual explosions in the casting shots range from 1000 to 4000 lbs. depending on whether 50 or 100 feet of overburden is removed in a single shot. Borehole diameters are 12 inches. Typical patterns consist of as many as 50 individual holes. Down hole delays are 700 milliseconds. These production casting or bulking shots are conducted approximately two out of every three days. There are homes and other structures near the mine requiring careful consideration of ground motions generated by the explosions. Aerial photography is completed by the mine on a frequent basis to assess progress. Figure 1 is an aerial view of the mine quantifying the size of the operation where we worked.

The areas where the experiments were conducted are high lighted in Figure 1. The source geometry experiments were completed in the east end of the pit where the first coal layer thins. Charge heights in this area of the pit are on the order of 100 feet with total explosive weight of 1800 to 3500 lbs. There is little surface topography in this portion of the mine and instrument installation was relatively easy, placing the surface installation in shallow holes that were backfilled with soil after leveling the instruments.

SHOT DESCRIPTIONS

Single Shots: Five single shot explosions were detonated during this experiment for the purpose of characterizing the single shot source and quantifying similarities and differences with a spherical explosion. As indicated in Figure 1, these explosions were conducted in the southeast corner of the mine. The characteristics of these five sources are summarized in Table 1.

Source Designation	Charge Size(lbs) ANFO/Emulsion	Bottom Hole depth (m)	Charge Height (m) 12" borehole	Overburden (m)
S1A	3381	30. 5	23	7.5
S2	3248 464/hole	18.3 , 2.7 m between holes	7 x 3 m	15.3
S3	3514	30.5	23	7.5
S4	1856	30.5	11.5	19
S5	2586	30.5	23	7.5

Table 1: Single Shot Characteristics

The emplacement borehole for each of the single sources is diagrammed in Figure 2. The variability in the charge sizes for the three full column cylinders (S1A, S3 and S5) reflect practical differences in drilling and loading the explosive emplacement holes. The first single borehole drilled and loaded (S1) did not detonate as a result of water and possible isolation of the detonator from the explosive charge in the hole and thus a second source S1A was drilled and fired slightly offset from the first.

The location and proximity of the individual charges to the free face of the mine pit of the five single charges (and Production Shot 9) are illustrated in Figure 3. S5 was drilled at the normal burden of approximately 10 m although a vertical hole was used where typical production shots are drilled at a 20° angle to match the slope of the vertical face in front of the charge. S3 is approximately 60 m behind S5 and S1A is 60 m further away. S4 is at the same burden as S3 but as noted in Table 1 is half the size with increased overburden.

The pseudo-spherical shot, S2, consisted of seven boreholes drilled in a hexagonal pattern with a charge in the center. This configuration results in 7 boreholes, each 2.7 m from the other. Each hole was filled with 3 m of explosive, ~494 lbs, intended to simulate a spherical explosive source taking advantage of typical drilling and explosive loading capabilities at the mine (Figure 2). The seven charges were simultaneously detonated and the detonation times were verified using NONEL tubing connected to the primer, brought to the surface and tied into a bow tie above each charge (shock propagation in the NONEL tubing is approximately 2000 m/s). High speed film of the shot is used to determine the time of detonation as represented by the surface flash of the NONEL tubing.

Production Shots: During the course of the experiment a total of 9 production shots were recorded. The first of the production shots began in the northwest part of the mine (Figure 1)

and then moved towards the single shot test area (Figure 3) culminating in Production Shot 9 which was conducted directly adjacent to S5. This sequence of production shots provided the opportunity to characterize variations in blasting practices across the mine and directly compare a production shot with the single shot results. Because of its proximity to the single shots, Production Shot 9 was the most heavily instrumented. Velocity of detonation measurements as well as NONEL tubing at the surface were used to quantify actual as opposed to design detonation times.

In the northwest part of the mine the coal that is being initially recovered is relatively shallow and charge boreholes are less than 50 feet deep. The production shots in this area of the mine are designed to primarily bulk the material with little or no cast. As one moves to the southeast, the coal that is recovered is at approximately 100 feet; therefore, the charge holes are deeper and the individual explosions in each shot are larger. The explosions in this region of the mine are designed to cast material into the pit. Table 2 characterizes the 9 production shots.

SHOT	DESCRIP-TION	DAY	DATE	TIME	CHARGE
Prod1	6x6 (1000 lbs/hole)	114	24 April 95	20:35	~36,000 lbs, No Cast
Prod2	6x6 (1000 lbs/hole)	115	25 April 95	19:36:09	~36,000 lbs, No Cast
Prod3	6x6 (1000 lbs/hole)	116	26 April 95	19:45:34	~36,000 lbs, No Cast
Prod4	6x6 (3000 lbs/hole)	118	28 April 95	19:24:32	~108,000 lbs, Cast
Prod5	6x6 (1000 lbs/hole)	118	28 April 95	19:27:12	~36,000 lbs, No Cast
Prod6	6x6 (3000 lbs/hole)	119	29 April 95	16:07:02	~108,000 lbs, Cast
Prod7	6x9 (3000 lbs/hole)	121	1 May 95	19:33:49	~162,000 lbs, Cast
Prod8	6x6 (3000 lbs/hole)	123	3 May 95	21:32:39	~99,000 lbs (three holes no fire), Cast
Prod9	6x4 (3000 lbs/hole)	124	4 May 95	16:00:47	~72,000 lbs (most diagnostic info on any production shot), Cast

Table 2: Single and Production Shot Characteristics

PRELIMINARY ANALYSIS

Analysis of a small portion of the data collected during the course of this experiment has been conducted to assess the quality and quantity of data. The analysis has focused on the far-field seismic data. Figure 4 compares the whole record spectra from the pseudo-spherical shot (Shot 2) and the two cylindrical shots with maximum burden (Shot 1 and 3) (Figure 2 and 3,

Table 2) as recorded at Stations 4 and 6 (Figure 1). In addition to the signal spectra displayed in each figure, a pre-event noise estimate is also plotted indicating the good signal to noise ratios from 0.5/1 to nearly 100 Hz. The cylindrical and spherical sources produced identical vertical component waveforms at these two stations.

Shot 4 (Table 1) had approximately half the cylindrical charge of Shot 1 and had significantly more overburden (Figure 2). The detonation of this charge resulted in little permanent surface displacement unlike the other cylindrical charges. Comparison of the vertical spectra from the far-field seismic station 4 are reproduced in Figure 5. Within the bandwidth of the data (0.5-100 Hz) the smaller, deeper charge has reduced spectral amplitudes out to approximately 10 Hz. The two spectra appear to merge at the higher frequencies. Definitive conclusions on this coupling issue awaits analysis of the complete data set.

Shot 5 (Table 1 and 2) was detonated at the standard burden from the free face (Figure 3). This charge was drilled with a straight borehole rather than the typical 20° slant hole typically used by the mine. There was only a small amount of degradation of the free face by the explosion. There was no formation of a retarc as observed for Shots 1 and 3. There were, however, a number of large cracks parallel to the free face that opened as a result of the explosion indicating the degree of interaction with the free face. The vertical velocity spectra from this shot and one of the fully contained cylindrical shots (Shot 1) are given in Figure 6. There is little difference between the two records except a decrease in high frequency energy (above 4-5 Hz) for the shot at the free face.

It is critical to understand propagation path effects in attempting to assess source signatures on seismograms. Figure 7 is a comparison plot of the vertical velocity spectra at all far-field stations (Figure 1) from Shot 5. There is more than an order of magnitude difference in spectral levels as well as significant interference hole differences resulting from the propagation paths to each of these stations. This figure illustrates the need to conduct single shots in the experimental program in order to quantify these propagation path differences.

Vertical velocity spectra (far-field Station 4) from the single shot at the free face (Shot 5) and Production Shot 8 and 9 that are on either side of the single shot are reproduced in Figure 8. Spectral scalloping from the two production shots is observed closely spaced in frequency relative to the single shot result which is dominated by propagation path effects. This data will be used to assess the effect of timing variations on the resulting seismograms and to determine coupling differences observed at smaller frequencies resulting from the interaction of the multiple sources.

Production shots in this mine are used to both cast material and to bulk material depending on the needs of the mining operation. Production Shot 4 was a typical cast shot which was followed within minutes by a bulking shot, Production Shot 5. Production Shot 5 was detonated directly behind Production Shot 4 and thus the differences in propagation paths from these two shots to the far-field stations was minimal. Figure 9 compares the vertical velocity spectra from these two shots at Station 4. There is as much as a factor of 5 difference in the amplitudes from these two explosions. Interpretation of this data utilizing the accompanying loading and shooting data will provide the opportunity to assess variations in seismic signals that might be expected from a single mine.

CONCLUSIONS AND PLANS

The LANL Source Geometry Experiment was successfully carried out over the time period of 24 April through 4 May 95 excluding travel and deployment. A great variety of data types that

are intended to give a complete characterization of the seismic sources for these explosions were collected. This data included near-source acceleration, strong motion velocity, far-field velocity, regional seismic, velocity of detonation, high speed film, digital video, still photography, refraction and pre and post shot surveys. This experiment could have only been conducted with the close cooperation of industry and the hard work of the people pictured in this report.

Preliminary analysis indicates that the cylindrical source configuration typical of the mining community generates significant spall in the near-source region. Quantification of this process with the high speed film, digital video and spall zone acceleration measurements will allow us to assess its contribution to the seismic source function. Strong spall was observed from the cylindrical and the spherical sources.

Comparisons of far-field vertical velocity spectra indicates little or no difference between the fully burdened spherical and cylindrical sources (S1,S2,S3). These empirical results indicate that there are little differences in the coupling of compressional energy from these different source geometries. They also indicate that a well contained cylindrical charge or charges may be useful for calibrating a site. The resulting seismograms from the well contained cylindrical charge could produce compressional signals like that expected from a contained spherical explosion. Analysis of the horizontal motions will allow an assessment of the shear energy from these different source types and thus a complete assessment of the similarities and differences of cylindrical and spherical sources.

Subtle yield effects were observed in comparing the large and small cylindrical sources (S1 and S4). The effect of the free-face on the waveform may be dominant at high frequencies based on the comparison of the normal burden shot S5 and S1.

Comparison of the seismograms recorded from the nine production shots conducted during the deployment indicates a great deal of variability in amplitudes as well as relative body and surface wave contribution. Quantification of these differences will include an analysis of source differences (charge size and timing) as well as propagation path effects. The variability in the seismograms from a single shot (Figure 7) illustrates the importance of conducting a single shot to calibrate propagation path effects in the mine prior to attempting to interpret source differences. Significant source differences are observed over and beyond these propagation path effects as indicated by the comparison of the cast and bulking production shots (Production Shot 4 and 5) recorded at the same station.

PARTICIPANTS

Figure 1. Aerial Photograph of the Chinook Mine with test areas and far-field seismic station locations.
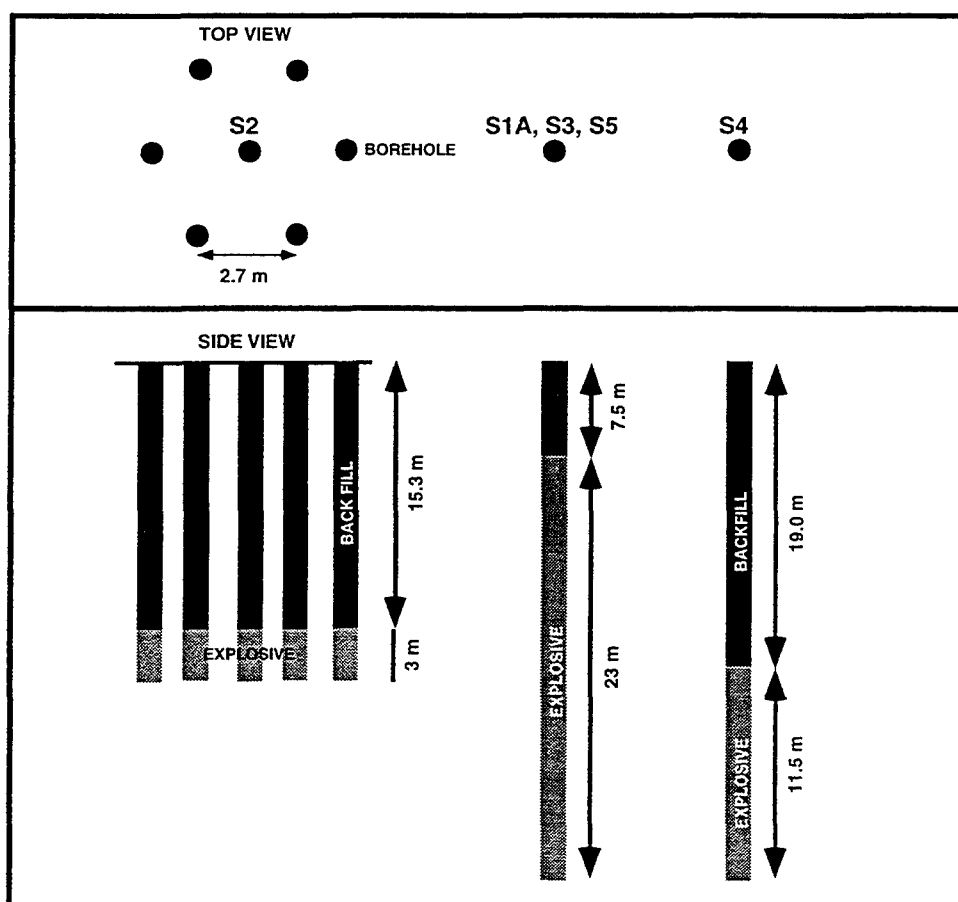
Fig 2. LANL Source Geometry Experiment, single shot configurations. Plan and side views of the three shot configurations used are shown.
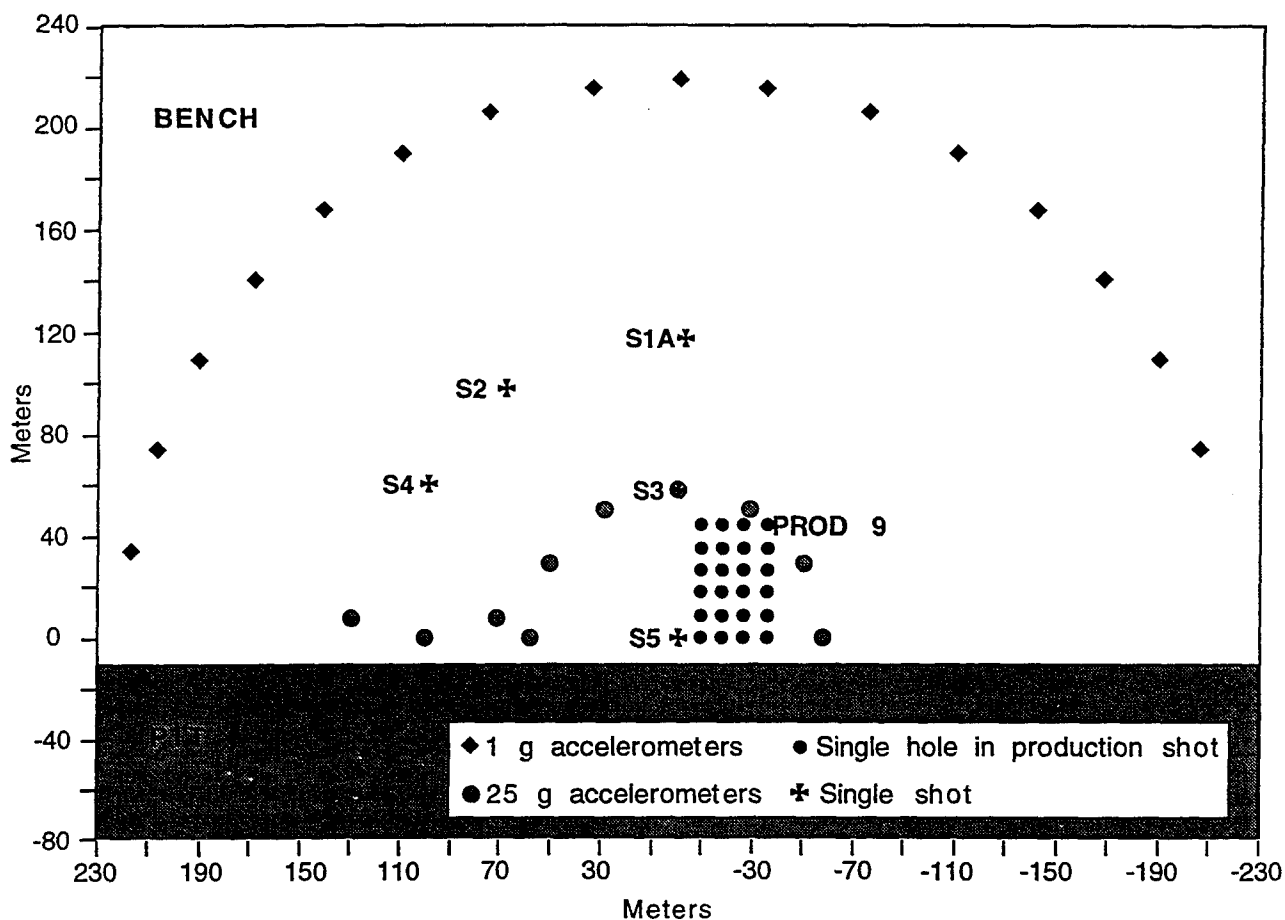
Fig 3: LANL Source Geometry Experiment, near source array deployment for shot S5.

SGE FFSTATION4Z
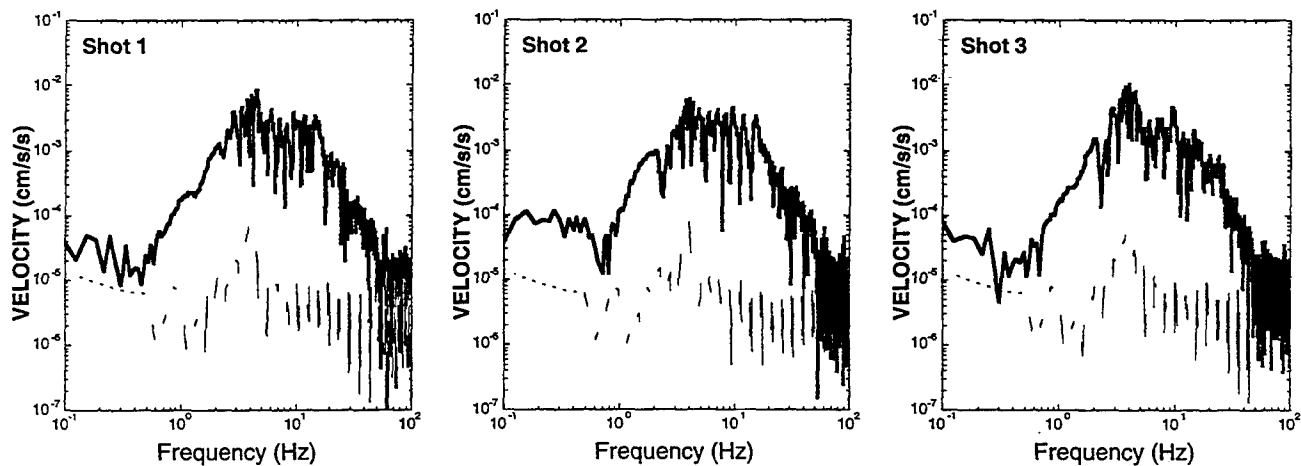
Fig 4: Vertical velocity spectra from Station 4 (Fig 2) for the two cylindrical charges (S1 & S3) and the spherical charge (S2).

SGE FFSTATION4Z
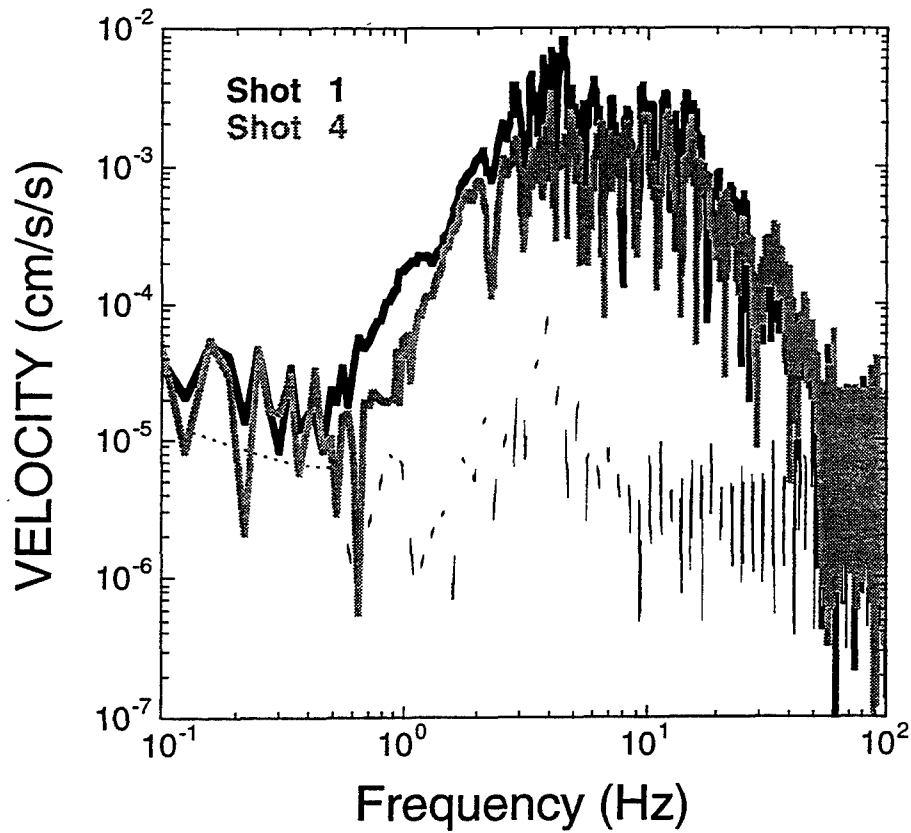
Fig 5: Vertical velocity spectra from Station 4(Fig 2) for the full cylindrical charge (S1) and the half cylindrical charge (S4). The noise estimate is plotted as a dashed line.

SGE FFSTATION4Z
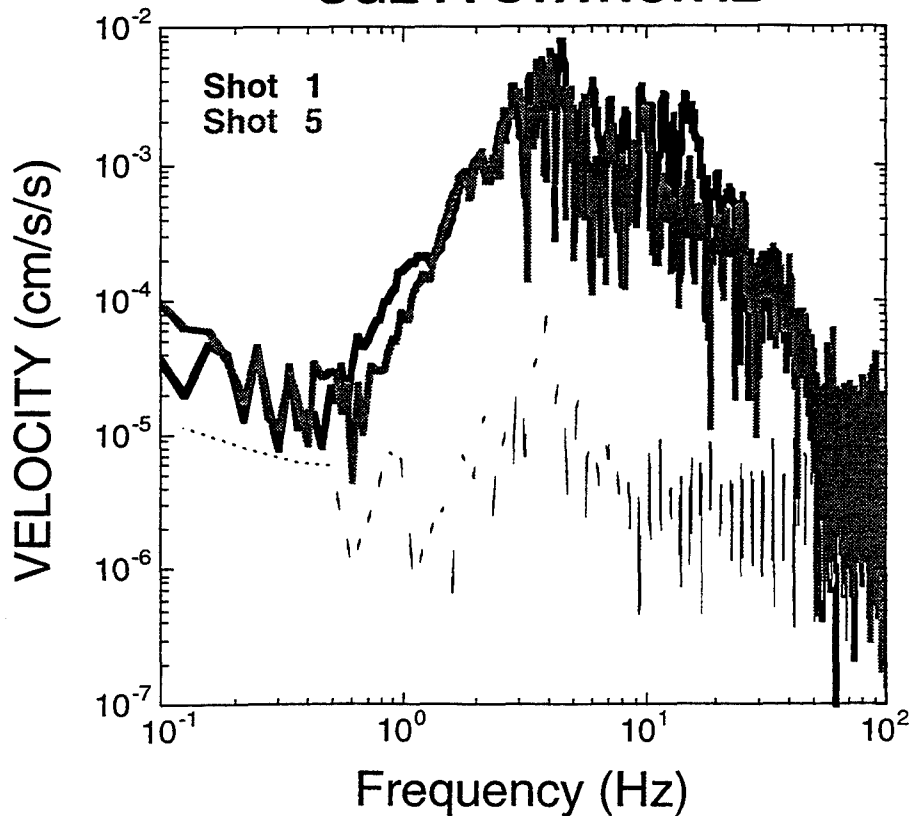
Fig 6: Vertical velocity spectra from Station 4 (Fig 2) for the fully burdened charge (S1) and the charge at the free face (S5). The noise estimate is plotted as a dashed line.

SGE FFSTATIONS SHOT 5
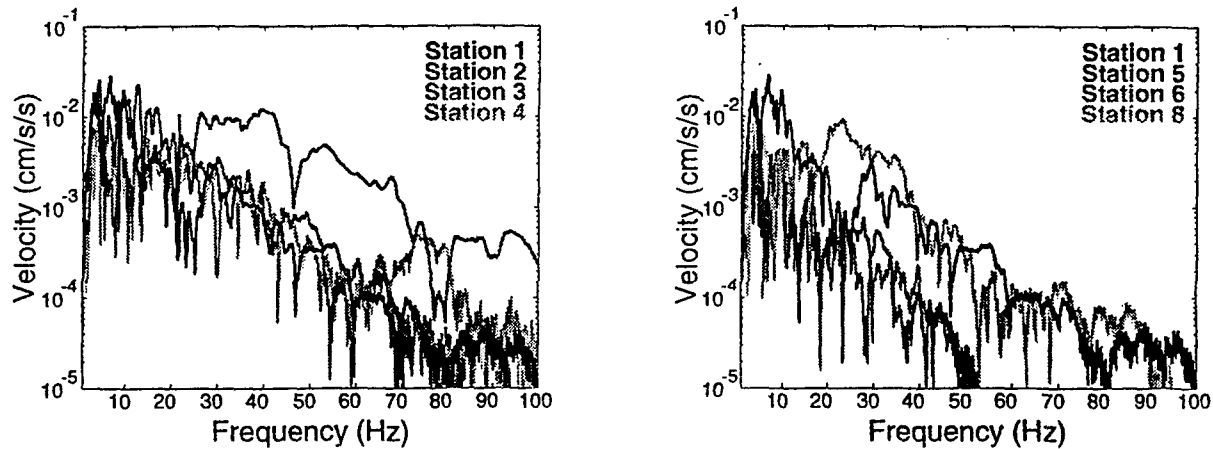
Fig 7: Vertical velocity spectra from all Far Field Stations for Shot 5 demonstrating the impact of propagation path effects. Plots are separated for clarity and the Station 1 spectrum is shown for reference in each plot.
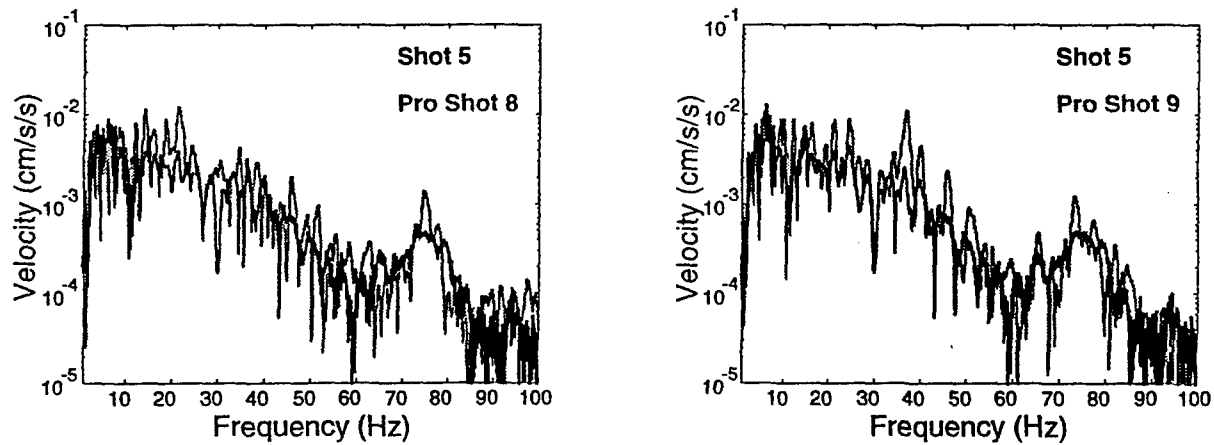
SGE FFStation4z

Fig 8: Vertical velocity spectra from Station 4 (Fig 2) for the single free face charge (S5) and the two near-by Production Shots 8 and 9. Plots are separated for clarity and the Shot 5 spectrum is shown for reference in each plot.

SGE FFStation4z
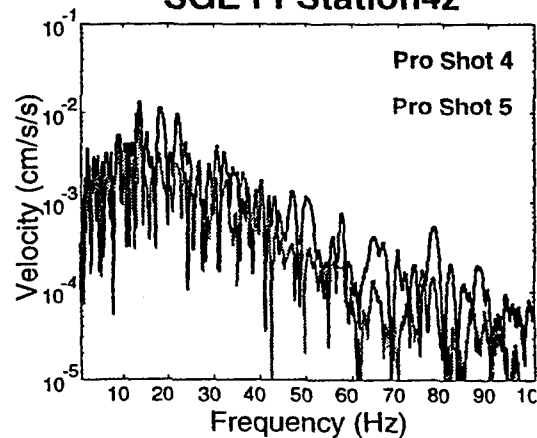
Fig 9: Vertical velocity spectra from Station 4 (Fig 2) for the two near-by explosions, Production Shot 4 which cast and Production Shot 5 which bulked.

693

Characterization of Seismic Source Using Short-Period Seismic Waves

Jiajun Zhang
Institute of Tectonics
University of California
Santa Cruz, CA 95064

ABSTRACT

A new algorithm is proposed for the reduction of the complexity of observed seismic waves in the 1-100 sec period band. The algorithm transforms the waveform for an event into a simplified form and is referred to as the Earth simplifying transformation (EST). The event is referred to as the primary event, for which properties of the source are to be determined. The EST algorithm uses data and synthetics for another event nearby, which is referred to as the secondary event. The synthetics are computed for a given Earth model using *a priori* source parameters for the secondary event. Data for the algorithm are regional or teleseismic seismograms, including surface waves and/or body waves. In this algorithm, data for the primary event are deconvolved with the residual waveform which is obtained from the deconvolution of data and synthetics for the secondary event. The residual waveform contains the effects of Earth's structure on seismic waves which are not predicted for the Earth model. The simplified waveform obtained from the algorithm is referred to as the EST seismogram. The EST seismogram represents the waveform which is expected for the seismic waves from the primary event for the Earth model. The source properties for the primary event can be determined from EST seismograms instead of original data, which contain not only the information on the source but also the effects of Earth's structure unpredictable for the model.

Several tests were made using data from earthquakes located in southern California recorded at Global Seismographic Network (GSN) stations, with the distance between the primary and secondary events being less than 100 km. These tests indicate that EST seismograms provide superior resolution power in the source characterization than original seismograms. The major limitation of the procedure is that *a priori* information on the source of the secondary event is required. This procedure can be applied to characterize an explosion source if source parameters for an event nearby are well known, with the secondary event being either an explosion or an earthquake. The application of this procedure may be useful for improving the regional monitoring and discrimination capability under a potential CTBT as well as basic seismological knowledge on source properties of explosions and earthquakes, including magnitude, location, mechanism, and source time functions.

Key words: source parameters, surface waves, nuclear test detection

OBJECTIVE

The objective of this study is to develop and apply new methods for the characterization of the source of explosions and earthquakes using short-period seismic waves, with improved resolution power on source properties, including magnitude, location, mechanism, and source time functions. The accurate characterization of the source with these parameters will improve the regional monitoring and discrimination capability under a potential CTBT as well as basic seismological knowledge on source processes involved in explosions and earthquakes.

RESEARCH ACCOMPLISHED

Our progress in the past year includes mainly two developments: (1) including Earth's aspherical corrections in the computation of synthetic seismograms and in the source determination using recently developed three-dimensional earth models; (2) developing a new procedure for the suppression of noise and unmodeled effects of Earth's structure on observed waveforms.

Although development (1) is of importance to this study, it is not much different from some techniques used elsewhere and thus is not discussed in this report. We will focus on (2), which involves a new data processing algorithm. This algorithm is referred to as the Earth simplifying transformation (EST), which allows us to reduce the complexity or to simplify observed waveforms but still retain the information relevant to the source determination.

Since seismic waves recorded at regional and teleseismic distances from the source are dominated by short-period surface waves in the 1-100 sec period band, it is desirable to use the short-period surface waves for the determination of source properties. However, this is hampered by the complexity of the waves due to the effects of Earth's lateral and radial heterogeneities.

Earth simplifying transformation. A procedure, which transforms a seismic signal into the simpliest form relative to a given earth model. The difference between the simplified waveform and the original signal corresponds to the effects of earth's structure which are not predicted for the earth model; and the signal in the simplified waveform corresponds to the effects that are predictable for the earth model and information on the properties of the source. This procedure enhances signal-to-noise ratio and thus improves the resolution power of short-period surface waves in the source characterization.

Method. According to Gilbert and Dziewonski [1975] the spectrum of a component of ground motion excited by a point source at angular frequency ω for a given earth model may be given by

$$u_k(x, \omega) = \sum_{i=1}^{6} \psi_{ki}(x, x_s, \omega) \, f_i(\omega). \qquad (1)$$

where u_k is the k-th record in a set of seismograms, with the receiver at position x and the source at x_s; ψ_{ki} are excitation kernels and f_i represent six independent components of the moment-rate tensor. For another event located at x_s' with moment-rate tensor f_i', the spectrum may be given by

$$u'_k(x, \omega) = \sum_{i=1}^{6} \psi_{ki}(x, x'_s, \omega)\, f'_i(\omega). \qquad (2)$$

Taking into account of our imperfect knowledge of the earth structure and noise generated from other sources, the spectra of observed ground motion for these events may be expressed as

$$U_k(x, \omega) = u_k(x, \omega)\, \alpha_k(x, \omega) + \varepsilon(x, \omega). \qquad (3a)$$

$$U'_k(x, \omega) = u'_k(x, \omega)\, \alpha'_k(x, \omega) + \varepsilon'(x, \omega). \qquad (3b)$$

where α and α' represent effects of the deviation of the earth's structure from the earth model. In the following analysis the noise terms (ε and ε') are ignored and the event at x_s is referred to as the primary event and the event at x'_s as the secondary event.

In the conventional algorithms the moment-rate tensor of the primary event, f_i, is determined from data for the event, U_k, by solving the following equation

$$U_k(x, \omega) = \sum_{i=1}^{6} \psi_{ki}(x, x_s, \omega)\, f_i(\omega), \qquad (4)$$

which is correct to the zeroth-order in terms of α, since implicit in the algorithms is the assumption

$$\alpha_k(x, \omega) = 1. \qquad (5)$$

The question that we shall address in this study is as follows. Given a set of seismograms from two events, U_k and U'_k, which are located at a close distance along with the synthetics for the secondary event, u'_k, predicted for a given earth model, is it possible to determine the moment-rate tensor of the primary event, f_i? For this purpose we define the following transformation

$$u_P^S(x, \omega) = u'_k(x, \omega)\, U_k(x, \omega)\, /\, U'_k(x, \omega). \qquad (6)$$

which is referred to as the earth simplifying transformation (EST) in the following analysis.

In general, α and α' in (3) are slowly varying functions of the source location and the moment-rate tensor, with the principle term of their Taylor expansion being independent of the source location and moment-rate tensor and the first and higher order terms much smaller than the principle term. Therefore we assume

$$\alpha_k(x, \omega) = \alpha'_k(x, \omega). \qquad (7)$$

Then the right hand side of (6) becomes $u_k(x, \omega)$, thus the spectrum of the EST seismogram may be expressed as

$$u_P^S(x, \omega) = \sum_{i=1}^{6} \psi_{ki}(x, x_s, \omega)\, f_i(\omega). \qquad (8)$$

which is correct to the first-order in terms of α and will be used to determine the moment-rate tensor (f_i). For the simplicity of our analysis we adopt a frequently used assumption: f_i are considered to be independent of frequency except for a correction for an assumed duration of the source and are regarded as the moment tensor.

696

Tests. Several tests were made using data from earthquakes located in southern California recorded at Global Seismographic Network (GSN) stations. Figure 1 shows the location of the primary event (event I: the January 17, 1994 Northridge mainshock, M_s 6.8) and secondary events (event II: an aftershock of the 1994 Northridge earthquake sequence, M_s 6.0; and event III: the June 28, 1991 Sierra Madre earthquake, M_s 5.2) along with source mechanisms for these events obtained previously by various investigators. For the primary event, three solutions of the source mechanism that are shown in Figure 1 are examined using EST seismograms.

Figure 2 shows the waveforms of ground motion recorded at station WMQ and synthetics, bandpass filtered between 7 and 30 mHz. There is considerable discrepancy between the observed waveforms (solid lines under the labels Z_I, R_I, and T_I) and the synthetics (dotted lines under the labels Z_I^{III}, R_I^{III}, and T_I^{II}) for the primary event. In clear contrast, the fit of the synthetics to the EST waveforms (solid lines under the labels Z_I^{III}, R_I^{III}, and T_I^{II}) is excellent.

Figure 3 shows the transverse components of the EST seismograms along with synthetics for the primary event computed for the three source mechanisms that are shown in Figure 1 for several stations in the azimuths between 3° and 12°. For each station, synthetics for different source mechanisms show larger differences in amplitudes. The amplitudes of the synthetics for the mechanism from the regional waveform inversions (B in Figure 3) are in the best agreement with the amplitudes of EST seismograms in comparison with other two mechanisms (A and C in Figure 3).

Figure 4 shows the vertical components of the EST seismograms along with synthetics computed for these source mechanisms for stations at various azimuths. The data shown here represent only a small portion of the whole data set; however, they are more sensitive to the source mechanisms discussed here and have higher signal-to-noise ratio than data for other stations. Analysis of these EST seismograms yields the same conclusion as our analysis of the transverse components: in general, the amplitudes of the synthetics for the mechanism from the regional waveform inversions are in the best agreement with the amplitudes of EST seismograms in comparison with other two mechanisms.

CONCLUSIONS AND RECOMMENDATIONS:

The EST seismograms provide superior resolution power in the source characterization than original seismograms. This method works better for stations at close distances from the source. It is desirable to apply this procedure to data from several underground nuclear explosions in Lop Nor, China, to characterize the source properties of the May 21, 1992 explosion. Another application is to examine the possibility to use earthquakes nearby as the secondary events to identify small explosions. The application may start with the examination of the seismicity near several nuclear test sites in the Central Asia, with both the earthquake and explosion being recorded at regional and/or teleseismic distances.
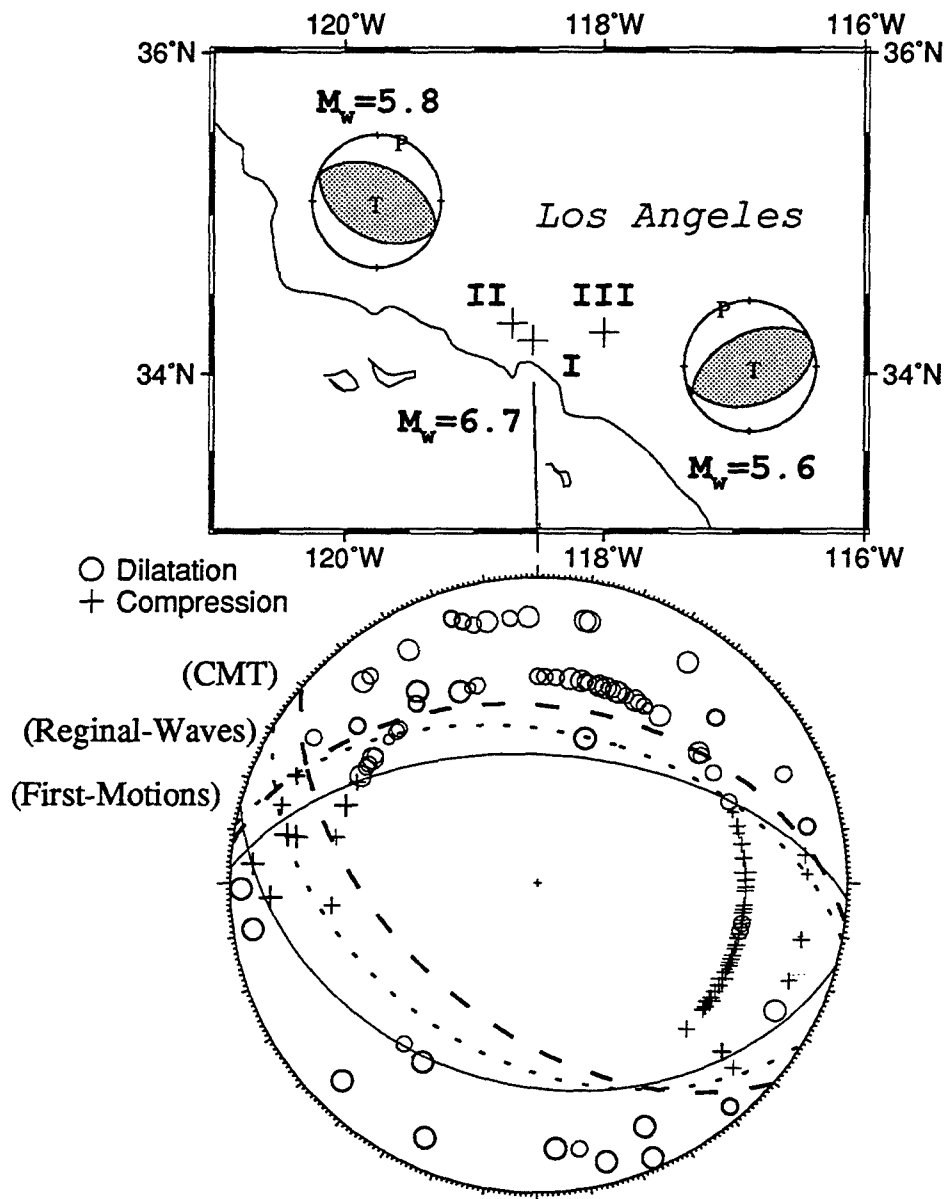
Fig. 1. Location (plusses) and mechanisms of the 1994 Northridge (I: mainshock, II: aftershock) and 1991 Sierra Madre (III) earthquakes. The mechanism for event II is shown for the solution from the regional wave inversions and for event III for the solution from P-wave first motions. Fist motion data are plotted with the uncertainty given by the size of each symbol.

WMQ ($\Delta=98°$, $\Phi=341°$)
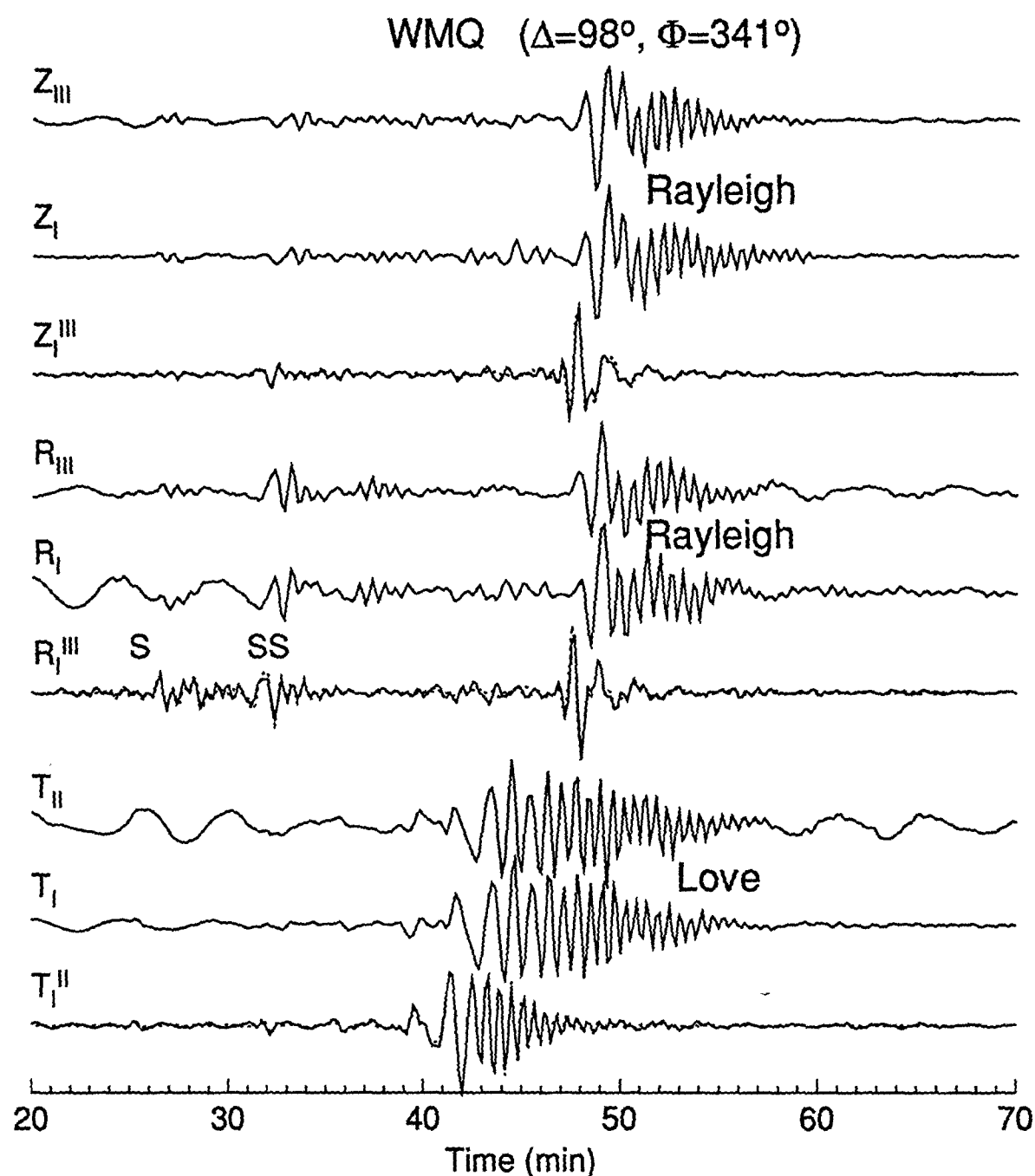
Fig. 2. Data and synthetics for station WMQ (Urumqi, China). Symbols Z, R, and T with subscripts I, II, and III indicate vertical (Z), radial (R), and transverse (T) components of ground displacements, respectively, from various events (subscripts I, II, and III identify the events). Symbols Z_I^{III} and R_I^{III} indicate the EST seismograms obtained using event III as the secondary event, with the synthetics for the event computed using the focal mechanism obtained from P-wave first motions. Symbol T_I^{II} indicates the EST seismograms obtained using event II as the secondary event, with the synthetics for the event computed using the focal mechanism from regional waveform inversions. Dotted lines indicate synthetics for the primary event computed using the focal mechanism from P-wave first motions. Amplitude is arbitrarily set to show waveform coherence. Time is measured from the origin time of the corresponding event.
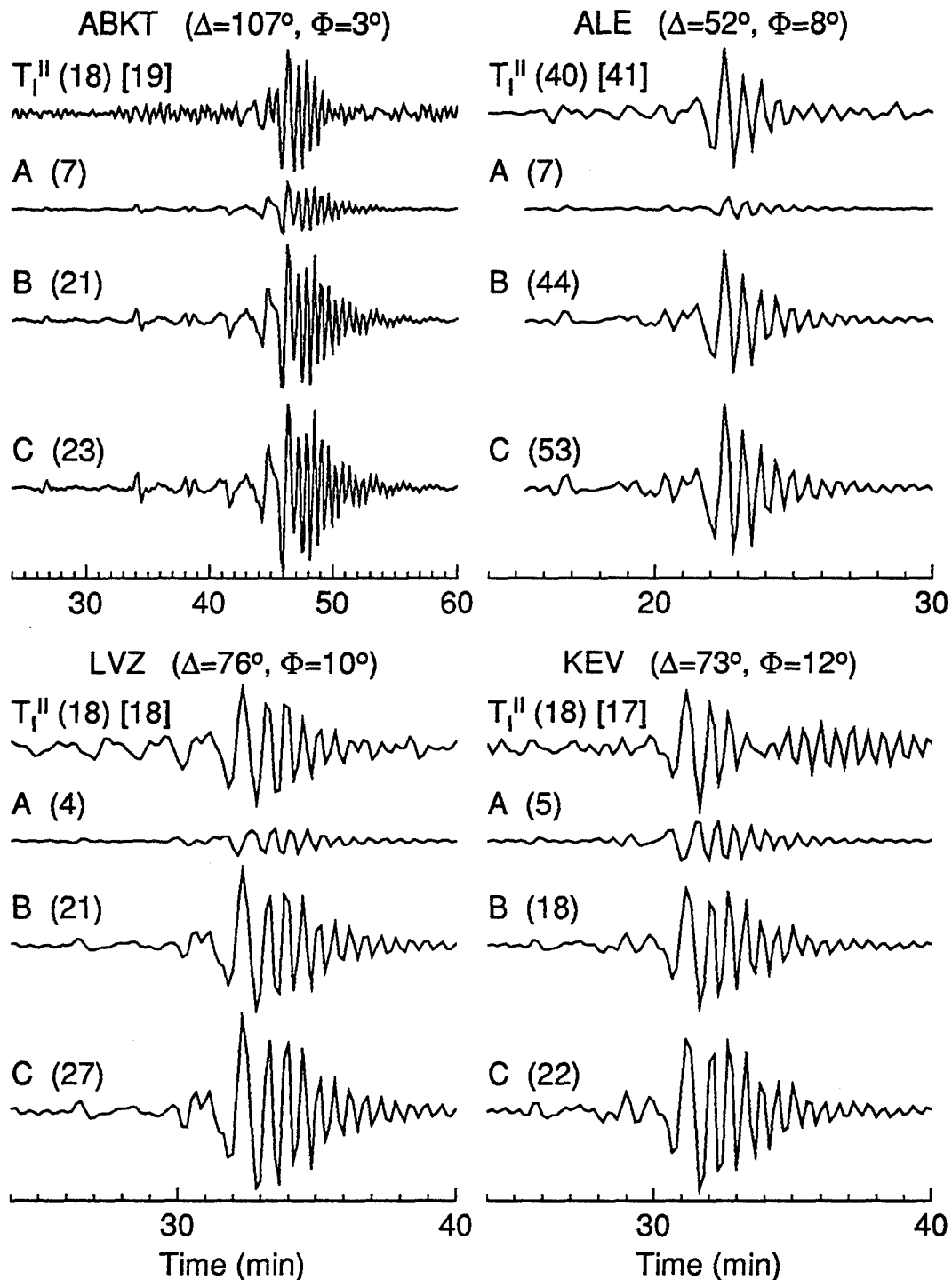
Fig. 3. Transverse components of EST seismograms (T_I^{II}) at various stations obtained with the synthetics for event II computed using the focal mechanism from the regional wave inversions, with amplitudes being given in parentheses in units of microns (amplitudes of T_I^{II} with the synthetics computed for event II using the focal mechanism from P-wave first motions are shown in brackets). Symbols A, B, and C indicate synthetics computed for the primary event using a seismic moment of 1.2×10^{19} Nm and various focal mechanisms: first-motion solution (A), regional-wave solution (B), and CMT solution (C).
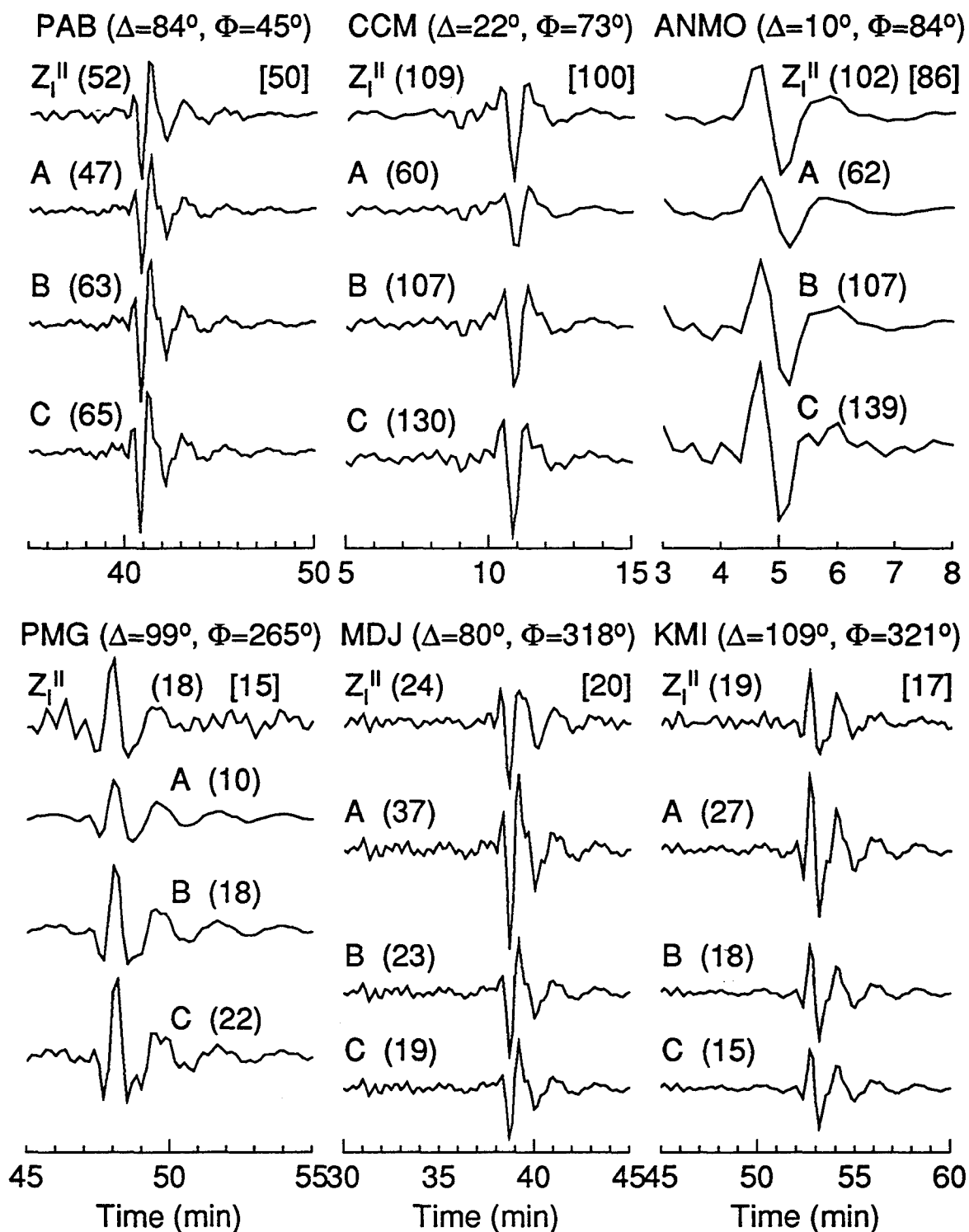
Fig. 4. Vertical components of EST seismograms for various stations. See caption to Figure 3 for symbol idetification.

Focal Mechanism Determination and Propagation Characteristics of High-frequency S-waves on the Tibetan Plateau

L. Zhu and D. V. Helmberger
California Institute of Technology
Contract No. F19628-95-C-0096

July 29, 1995

Abstract

One of the most useful regional discriminants is the ratio of short-period S/P energy, on the basis that nuclear explosions tend to have less S energy than earthquakes at high frequencies. However, the high-frequency S waves from earthquakes can also be easily blocked or attenuated during the propagation, especially along the boundaries between different tectonic regions and within tectonic active areas. So, an essential understanding of the regional crustal structures and associated wave propagation characteristics are needed before establishing effective discrimination methods for that area. In this report, we first determined the crustal structure of the Tibetan Plateau and the focal mechanisms of regional events recorded during the 1991-1992 Tibet passive recording experiment. In particular, we improve the source mechanism estimation technique proposed by Zhao and Helmberger (1994) by introducing a distance range scaling factor. This helps to constrain the source orientation by fully utilizing the radiation patterns contained in the different portions of the whole 3-component records. By apply the method to the regional events of the Tibet Plateau, we obtained the focal depths and mechanisms. Most events are found to be shallower than 20 km. However, we also identified 3 subcrustal events (at depth of 70-80 km) under the Himalayan Trust Belt and the Indus Zangbo suture zone. Their mechanisms are quite different from those of shallow events in the same region.

We find that the radiation pattern of P and S behave quite well as a function of frequency below 1 Hz. At frequencies above 3 Hz, the amplitudes vary strongly from station to station. High attenuation of short-period S waves is found for ray paths through the north-central plateau. This is consistent with previously observed inefficient propagation of high frequency Sn in this area. It also correlates with the young volcanisms and low crustal velocities and Pn velocities. The variation of energy ratio of short-period SH component vs. broadband SH component with distance range are modeled by reducing Q values in the lower crust. Combining with other observations, we suggest that there is a hot, possibly partially melted lower crust in the north-central Tibet.

Focal Mechanism Determination and Propagation Characteristics of High-frequency S-waves on the Tibetan Plateau

1 OBJECTIVE

Our objective is to investigate the propagation characteristics of broadband and high-frequency S-waves on the Tibetan Plateau. Regional crustal structure and the focal mechanisms are determined by analyzing broadband waveform data obtained during the 1991-1992 passive recording experiment (Owens et al., 1993). In particular, we improve the source mechanism estimation technique proposed by Zhao and Helmberger (1994) by introducing a distance range scaling factor. This helps to constrain the source orientation by fully utilizing the radiation patterns contained in the different portions of the whole 3-component records.

2 RESEARCH ACCOMPLISHED

2.1 Introduction

One of the most useful regional discriminants is the ratio of short-period S/P energy, on the basis that nuclear explosions tend to have less S energy than earthquakes at high frequencies. However, the high-frequency S waves from earthquakes can also be easily blocked or attenuated during the propagation, especially along the boundaries between different tectonic regions and within tectonic active areas. So, an essential understanding of the regional crustal structures and associated wave propagation characteristics are needed before establishing effective discrimination methods for that area.

The Tibetan Plateau is the youngest plateau in the world. It is estimated that the present elevation of much of the plateau was attained by about 8 million years ago (Harrison et al., 1992). The plateau is surrounded by several old platforms and shields with large-scale thrust faults and strike-slip faults serving as boundaries. Even within the plateau, structural heterogeneities exist. For example, by using the short-period records of shallow events of Tibet and vicinity at WSSN stations in India and Pakistan, Ni and Barazangi (1983) identified a zone of inefficient Sn propagation in the north-central Tibet. Together with the evidence of young volcanism found in the same area and the low crustal and upper-mantle velocities from surface wave dispersion analysis, Molnar suggests the existence of a partial melting uppermost mantle under north-central Tibet (Molnar, 1988).

Recent PASSCAL experiment on the Tibet Plateau (see Owens et al., 1993) provided a new data set in this area. For the first time, broadband regional waveforms are available with both the events and receivers inside the plateau. In this report, we use this data set to calibrate the regional crustal structure model, determine the focal depths and mechanisms of regional events, and investigate the propagation characteristics of high frequency S-waves on the plateau.

2.2 1-D Crustal model of the Tibetan Plateau

Several events occurred with the array (Figure 1) were used to calibrate the regional crustal model. From their broadband displacement records, major crustal phases such as Pn, Sn, PmP, SmS can be identified and provide constraints on the velocities of lower crust and uppermost mantle. Waveforms of regional Love wave are used to constrain the upper crustal velocity. Our best 1-D crustal model is shown in Table 1. It consists of a main crustal layer of 60 km thick with a 4 km layer on top of it. Note the lower crustal shear velocity (3.5 km/s) and higher crustal Vp/Vs ratio, which are also consistent with the teleseismic receiver function analysis (Zhu et al., 1993).

Table 1 Average velocity model of the Tibetan Plateau

layer	Thickness (km)	V_p (km/s)	V_s (km/s)
1	4	4.70	2.70
2	60	6.20	3.50
3	–	8.14	4.70
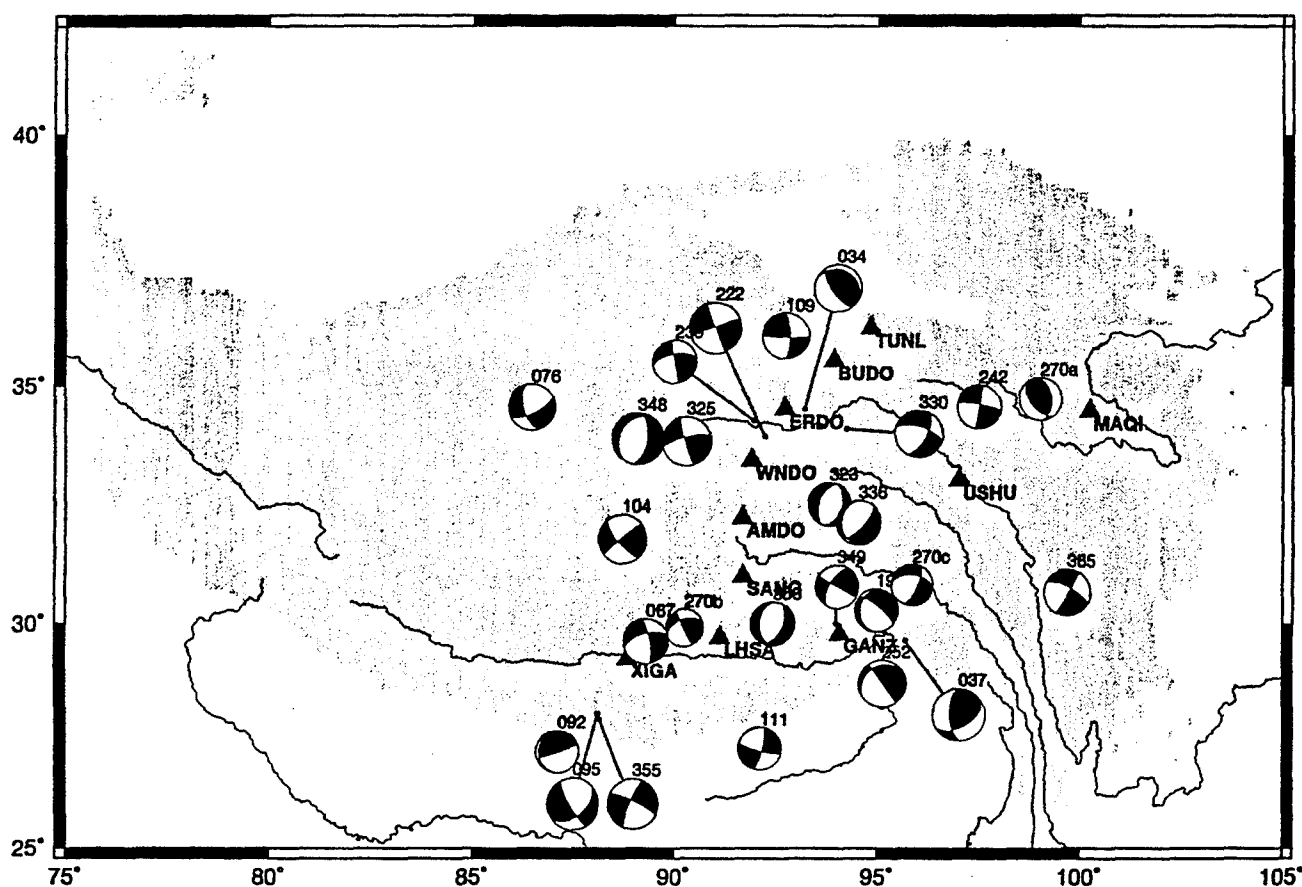
Figure 1: Broadband stations of 1991-1992 Tibet experiment. Shading indicates elevation above 3 km. Source mechanisms are determined from the broadband waveforms recorded at these stations (see text).

2.3 Improvement of source estimation technique

Zhao and Helmberger (1994) proposed a source mechanism estimation technique using regional broadband waveform data. The method applies a direct grid search in the source orientation parameter space for the minimum L1 and L2 norms of the difference between waveforms and synthetics. One of the advantages of

the method is that it desensitizes the timing between principal crustal arrivals by fitting portions of the waveforms independently, allowing some time shifts between the observation and synthetics. So, good source mechanism estimation can be obtained even when only imperfect Green's functions are available.

Since the Pnl portion of the waveform are much smaller in amplitude compared with the surface wave portion, and also because the procedure usually involves several station records at different distance ranges, the misfit error for each portion of the waveforms is defined as the norm of the discrepancy normalized by the norm of the data u and the synthetics f (Zhao and Helmberger, 1994):

$$e = \frac{\| u - f \|}{\| u \| \cdot \| f \|}, \tag{1}$$

such that all the portions of the data have similar weights in calculating the misfit between the observation and synthetics. However, in observations there are often some portions of the waveforms that are nodal. In that case, the grid search will fail since the norm of data and synthetic vanish. To overcome this problem, we introduce a distance range scaling factor and define the misfit error for record at distance range r as

$$e = \| (\frac{r}{r_0})^p \| \cdot \| f - u \|, \tag{2}$$

here p is a scaling factor to give the record at r the same weight as that at reference distance r_0. According to the propagation properties of the phases, an appropriate choice of p for body wave portion is $p = 1$, and for surface wave portion $p = 0.5$. The p-value could also be adjusted according to the actual amplitude attenuation in the studying area.

Figure 2a,b show the values of misfit errors defined by (1) and (2) as functions of the dip and rake of the source for a event in southern Tibet. The former one shows high peaks at the grids when synthetics is near nodal. The newly defined misfit error is much more well-behaved. It has the global minimum at ($strike = 315, dip = 85, rakke = 255$), but also shows three three local minimums (Figure 2b). In other words, the newly defined misfit error makes it easier to find the correct global minimum and estimate the uncertainties.

2.4   Focal mechanisms and depths of events in the plateau

We applied the improved source estimation technique to the regional events recorded during the one year experiment. The Green's functions are calculated using the 1D model (Table 1) at different depths. Figure 1 shows the low-hemisphere projection of focal mechanisms of the events we investigated. Randall et al (1995) estimated the moment tensors of most events from the long period waveforms of the same data set. Our results are similar theirs, although we analyzed 8 more events which are not included in Randall's solutions.

Most events are found to be shallower than 20 km. However, we also determined 3 events (event 355, 067, and 095 in Figure 1) to be deep, below the crust (Zhu and Helmberger, 1995). The existence of these intermediate depth events and their source mechanisms provided us important information about the temperature and stress in the upper mantle.

2.5   High frequency S-wave attenuation on the Tibet Plateau

The broadband waveform modeling shows that the radiation of P and S waves on the Tibet Plateau behaves quite well as a function of frequency below 1 Hz. Figure 3a shows tangential displacement records of event 222 compared to the synthetics. However, at frequencies above 3 Hz, the amplitudes vary strongly from station to station (Figure 3b). For example BUDO and AMDO are at similar distance ranges, but BUDO is located in the north-central plateau where high attenuation of high-frequency Sn were observed (Ni and Barazangi, 1983). Correspondingly, the high frequency amplitude at BUDO are much smaller than at AMDO. Same is true for station TUNL compared with SANG.

To characterize the propagation of high frequency S-waves within the plateau, we calculate the short-period S/P energy ratios for all the event-receiver paths within distance range between 320 to 1000 km. Figure 4 shows the results; the solid lines represent paths with a ratio of more than 0.6 and the dashed
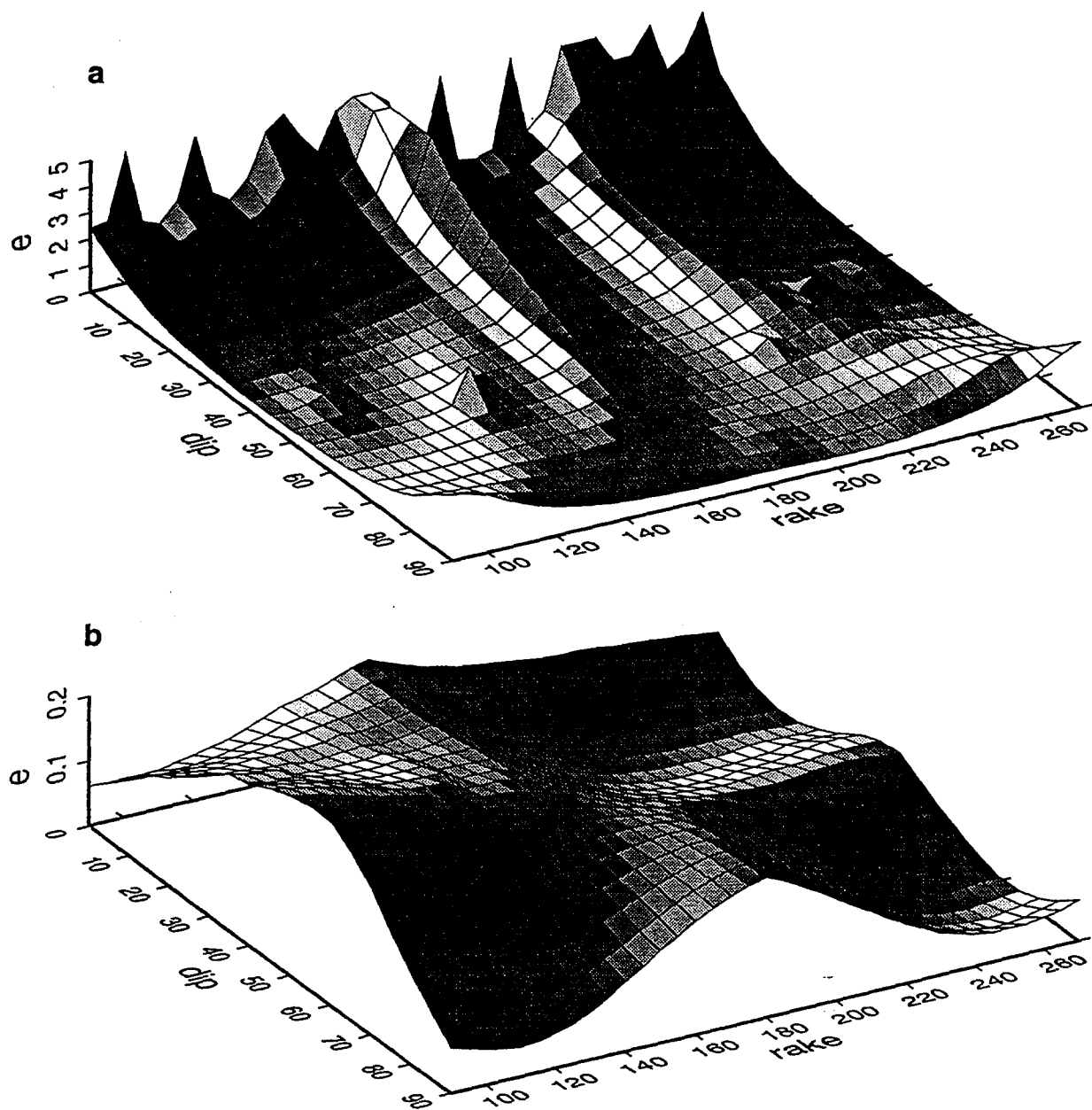
Figure 2: The waveform misfit errors as a function of dip and rake of the source orientation for one of the regional event (Event 199 in Figure 1). The strike is fixed at 315. a) The misfit error defined by Zhao and Helmberger (1994). b) Newly defined misfit error by introducing distance range scaling factor.
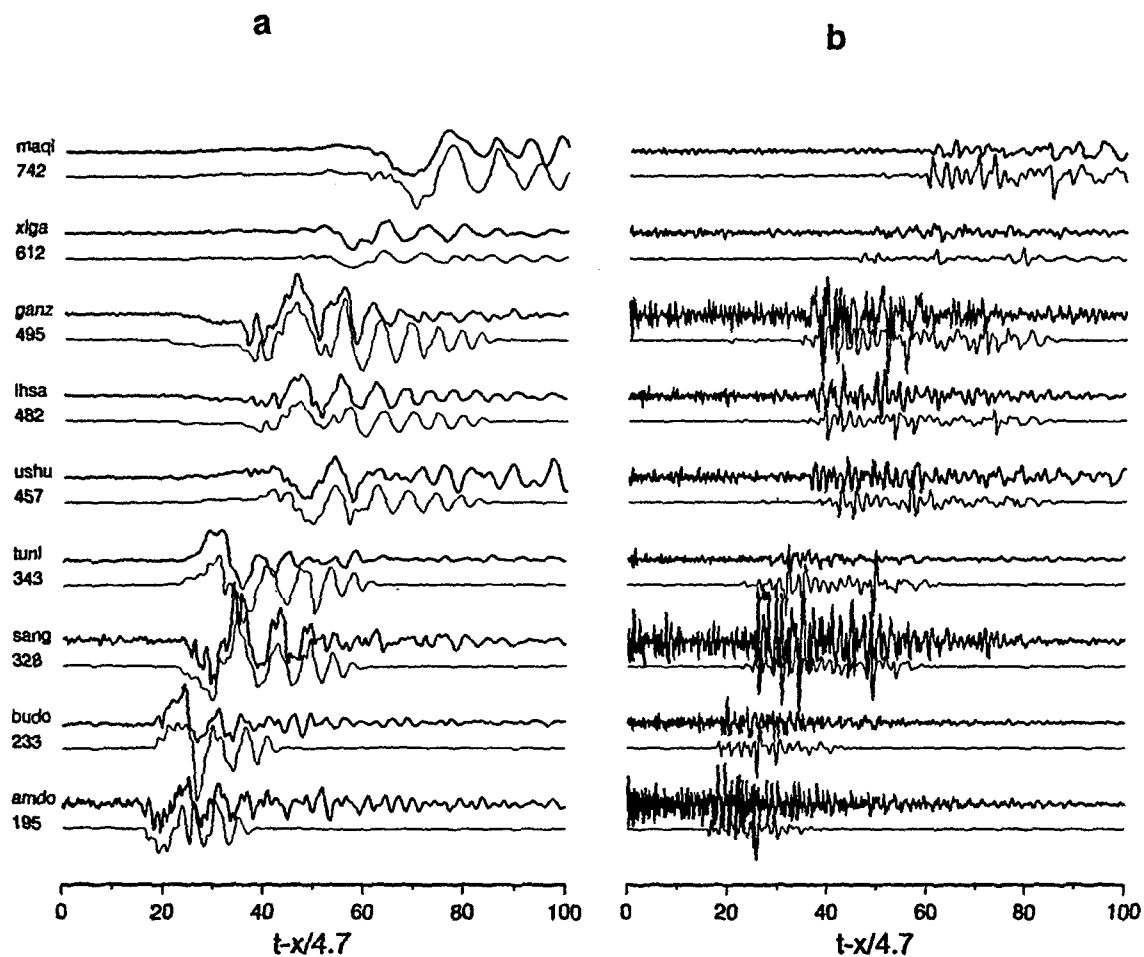
Figure 3: Broadband (a) and short-period (b) tangential displacements of event 222 (*focal depth at 10 km*). Thin lines are corresponding sythetics with source mechanisms obtained from the *grid search*. True amplitudes are plotted with distance range scaling factor $p = 0.5$ for (a) and $p = 2$ for (b)

lines correspond to paths with a ratio of less than 0.4. The high-frequency S-waves can propagate efficiently in southeastern Tibet and north of the Plateau, but have difficulty propagating through the north-central plateau.
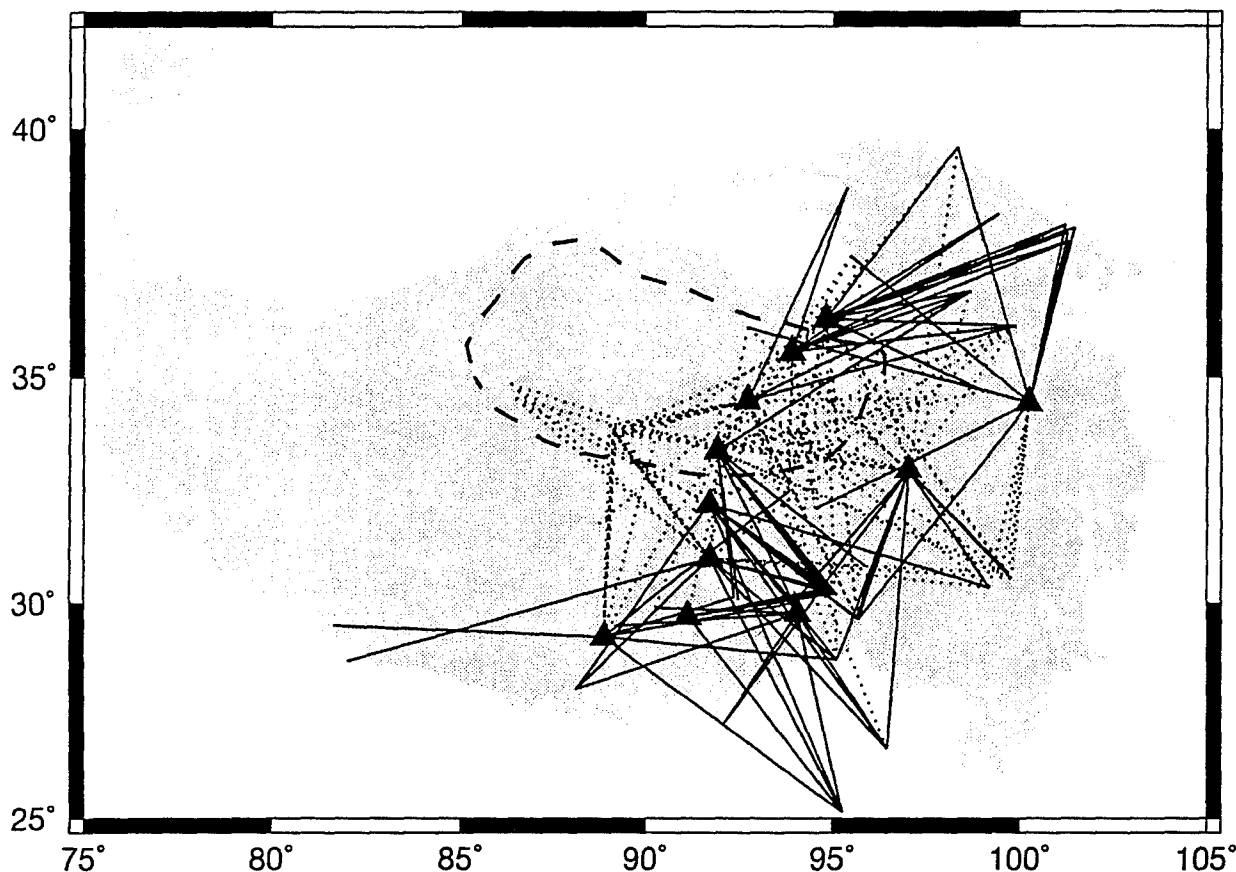
Figure 4: High-frequency S-waves propagation on the Tibet Plateau. Solid lines indicate efficent propagation paths(short-period S/P energy ratio > 0.6). Dashed lines indicate inefficent propagation paths (S/P ratio < 0.4).

The cause of the attenuation of high-frequency S-waves is not known. From the teleseimic receiver function analysis at 3 stations (TUNL, BUDO, and ERDO) located inside the attenuation zone, a mid-crustal low velocity layer is found (Zhu et al., 1995). A high Poisson's ratio was estimated in the crust under station WNDO from teleseimic P-to-S converted phase (Zhu, 1993). We suggest that there is a hot, possibly partially melted low crust in the north-central Tibet. The high attenuation of high-frequency S-waves is due to the low Q in the mid-lower crust. To demonstrate this, we plot the energy ratios of short period SH component vs. broadband SH component for all the paths within the attenuation zone and compare them with synthetic calculation for different lower crustal Q value (Figure 5). It is clear that the low Q curve (solid line in Figure 5, $Q_\beta = 300$) can fit the data better than high Q curve (dashed line, $Q_\beta = 600$).

As one more evidence for the low S-wave velocity and high attenuation in the north-central plateau, Figure 6 presents the tangential displacement records along with synthetics of one of the deep events in the southern Tibet (Event 095, Figure 1). Note that the observations at WNDO, ERDO, and BUDO are delayed about 3-5 sec relative to the synthetics. Their high-frequency amplitudes also drop compared to the stations located outside the attenuation zone (Figure 6b).
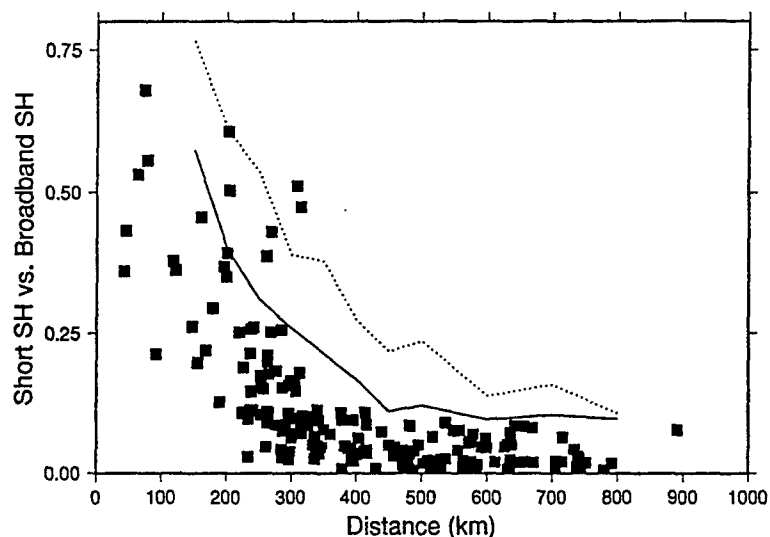
Figure 5: Energy ratios of short-period vesus broadband SH component for those ray-paths within the north-central plateau. Solid and dashed lines are theoretical calculations for crustal model listed in Table 1 with different Q values in the lower crust ($Q_\beta = 300$ for solid line, 600 for dashed line.
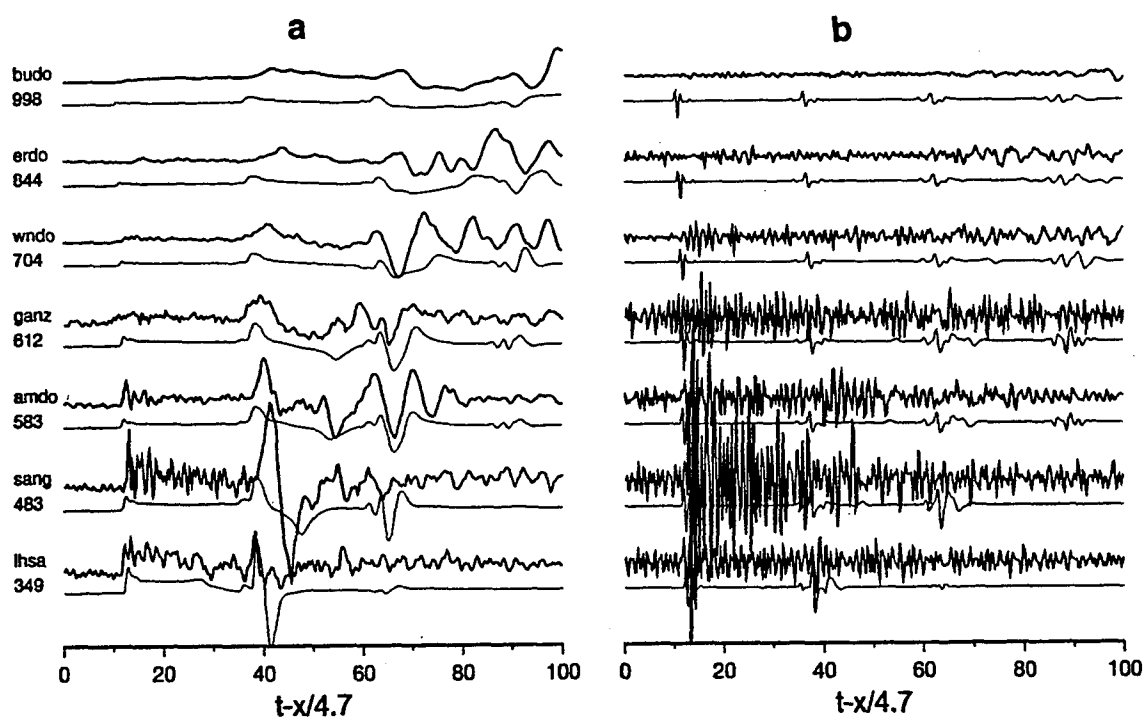
Figure 6: Broadband (a) and short-period (b) tangential displacements of event 095 (focal depth at 70 km). Traces are plotted in the same way as in Figure 3

3   CONCLUSION AND RECOMMENDATIONS

We have established an essentially good 1-D crustal model for the Tibetan Plateau. By applying improved source estimation technique to the regional events on the plateau, we have obtained their focal depths and mechanisms. Because the new method takes fully advantage of the source radiational information imbeded in the different portions of the waveforms, it will help to constrain the focal mechanisms even when only a few station records are available.

Strong variation of propagation efficiency of high-frequency S-waves exists through the plateau. In particular, there is a high attenuation zone in the north-central plateau. From the synthetic modeling and combining other evidences such as low crustal shear velocity and higher Poisson's ratio, it is suggested that the cause of the inefficient propagation of high-frequency S-wave in the north-central plateau is due to the low Q in the lower crust.

4   REFERENCES

Harison, T.M., P. Copeland, W.S.F. Kidd, and A. Yin, 1993, Raising Tibet, Science 255, 1663-1670

Molnar, P., 1988, A review of geophysical constraints on the deep structure of the Tibetan Plateau, The Himalaya and the Karakoram, and their tectonic implications, Phil. Trans. R. Soc. Lond. A326, 33-88.

Ni, J. and M. Barazangi (1983). High-frequency seismic-wave propagation beneath the Indian shield, Himalayan arc, Tibetan Plateau and surrounding regions – high uppermost mantle velocities and efficient Sn propagation beneath Tibet. JGR 72, 665-689.

Owens, T. J., G. E. Randall, F. T. Wu and R. S. Zeng, 1993, PASSCAL instrument performance during the Tibetan plateau passive seismic experiment, Bull. Seism. Soc. Am. 83, 1959-1970.

Zhao, L. and D. V. Helmberger, 1994, Source estimation from broadband regional seismograms, BSSA 84, 91-104.

Zhu, L., R. S. Zeng, F. T. Wu, T. J. Owens, and G. E. Randall, 1993, Preliminary study of crust-upper mantle structure of the Tibetan Plateau by using broadband teleseismic body waveforms, Acta Seism. Sinica 6, 305-315.

Zhu, L., 1993, Estimation of crustal thickness and Vp/Vs ratio beneath the Tibetan Plateau from teleseismic converted waves (abstract), EOS, Tran. 74.

Zhu, L., T.J. Owens, and G.E. Randall, 1995, Lateral Variation in Crustal Structure of the Northern Tibetan Plateau Inferred from Teleseismic Receiver Functions, BSSA, in press.

Zhu, L. and D.V. Helmberger, 1995, Intermediate Depth Earthquakes beneath the India-Tibet Collision Zone, submitted to Geophys. Res. Lett.

Advanced Systems for Assessing the Performance of Regional Networks

T.G. Barker, K.L. McLaughlin and J.L. Stevens

S-CUBED, a Division of Maxwell Laboratories
Contract F19628-95-C-0111 (DoE)

ABSTRACT

As studies are undertaken to collect information on factors affecting regional discrimination in various regions, it will be important to have available a tool for evaluating the performance of discriminants and the seismic networks being used. S-CUBED (under ARPA support) has developed an interactive computer system (called XNICE, for X windows program for Network Identification Capability Evaluation) for performing these assessments. We present detection and identification thresholds computed (under the ARPA contract) by XNICE for body and surface waves. We have focused on events occurring in Europe, Western U.S. and Tibet for which we have regional propagation data and previous regional discrimination studies. The propagation characteristics are calibrated to be compatible with observed magnitude-moment, distance decay rate and dispersion relations. We show identification results based on the ability of networks to determine location and depth, the ability to resolve spectral slopes of regional phases and the ability to find Ms:mb and Mw:ML ratios for earthquakes, overburied and normally buried explosions and quarry blasts. Under a new contract to DoE (which has not been initiated), we will extend both the capabilities and applications of the program beyond the scope of the current project. In particular, we will evaluate network (primarily GSETT stations) identification performance in regions that have been chosen for their relevance to monitoring a CTBT. The program will include an assessment of overall network performance and the performance of standard regional discriminants, as well as assessments of methodologies for extracting discrimination features, new developing discriminants and strategies for improving identification performance.

OBJECTIVE

The goal of this research to be undertaken is to formulate and apply techniques for making statistical descriptions of the performance of the tasks of detecting, locating and identifying seismic sources. These methods are to be applied to existing seismic networks and identification procedures, or to modifications.

RESULTS OF PREVIOUS RESEARCH

For this conference, we present results of work done under a previous ARPA contract. The results include the following:

1. We have developed models for regional source and propagation mechanisms (Barker, et al., 1994). The models of regional phases include the effects of non-linear processes, in particular, spall. We use kinematic models of spall to incorporate the effects of mass movements associated with nuclear explosions and quarry blast charges. These spall movements change the source spectra, generally causing the measured slope above 1 Hz to increase. We use models of source spectra and the relative excitation of the sources to account for the differences in regional phase excitation for the various source types. We apply discriminants based on the spectral slopes from 1 Hz to 10 Hz of Lg, Pg and Lg/Pg to the events generated by XNICE. The models predict that spectral slopes for Lg, Pg and Lg/Pg are least for earthquakes, are greater for normally buried explosions and are greatest for quarry blasts. Spectral slopes of Lg are closer to earthquakes for over-buried bombs, and can be indistinguishable at low magnitudes. These results are all consistent with numerous observations. We also show that network detection levels strongly influence these results.

2. We show global detection and identification thresholds for the Ms:mb and Lg spectral slope discriminants for proposed IDC stations. As a test of the XNICE program, we compare global detection contours with those from NetSim. As part of this exercise, a database of station characteristics and propagation parameters was established which the XNICE and NetSim programs share.

3. We show identification performance for source locations in central Europe for proposed alpha stations of the IDC networks and show the effects of including beta stations on identification thresholds. For these calculations, we focus on the Lg/P spectral ratio and Lg spectral slope discriminants.

4. We model the observations in Woods, et al., 1993, in which the ML:Mo discriminant for earthquakes and NTS explosions is investigated. We show that our regional models predict performance of this discriminant similar to the observations.

RECOMMENDATIONS AND FUTURE PLANS

The primary focus of future work will be the application of XNICE to regions of relevance to the CTBT. For the most part, these will be defined by the regions chosen for study which have recently been chosen for PL/AFOSR/DOE/AFTAC funding.

Micromachined Silicon Seismic Transducers

Carole Craig Barron, James G. Fleming, Jeffry J. Sniegowski, David L. Armour,
and R. Patrick Fleming

Sandia National Laboratories
P.O. Box 5800, Mail Stop 1080
Albuquerque, New Mexico, USA 87185-1080

ABSTRACT

Batch-fabricated silicon seismic transducers could revolutionize the discipline of CTBT monitoring by providing inexpensive, easily deployable sensor arrays. Although our goal is to fabricate seismic sensors that provide the same performance level as the current state-of-the-art "macro" systems, if necessary one could deploy a larger number of these small sensors at closer proximity to the location being monitored in order to compensate for lower performance. We have chosen a modified pendulum design and are manufacturing prototypes in two different silicon micromachining fabrication technologies. The first set of prototypes, fabricated in our advanced surface-micromachining technology, are currently being packaged for testing in servo circuits — we anticipate that these devices, which have masses in the 1-10 μg range, will resolve sub-mG signals. Concurrently, we are developing a novel "mold" micromachining technology that promises to make proof masses in the 1-10 mg range possible — our calculations indicate that devices made in this new technology will resolve down to at least sub-μG signals, and may even approach the 10^{-10} $G/\sqrt{Hz}$ acceleration levels found in the low-earth-noise model.

KEY WORDS

Silicon micromachining, microelectromechanical systems, bulk micromachining, surface micromachining, mold micromachining, seismic transducers, accelerometers, seismometers, CTBT.

1. INTRODUCTION AND OBJECTIVES

One of the principal factors inhibiting the effort to collect seismic data for CTBT monitoring is the sheer cost, including both the system cost and the deployment-cost, of current seismic transducers. Our motivation in pursuing microminiature silicon seismic transducers is twofold. First, such devices would be much less expensive to manufacture than current seismometers, since they could be batch-fabricated in much the same way that electronic integrated circuits are. Moreover their small size would make deployment easier and cheaper as well. Our goal is to fabricate seismic sensors that provide the same performance level as the current state-of-the-art "macro" systems, with adequate response, over a 0.01 to 100 Hz bandwidth, to the 10^{-10} $G/\sqrt{Hz}$ acceleration levels found in the low-earth-noise model. It may be possible, however, to relax the specification for the minimum resolvable signal — given the compactness of the micromachined sensor package we envision, it should be feasible to install the new sensors in much more proximate locations than can be attained with current systems.

We have calculated the best-case performance possible for a seismic acelerometer fabricated in Sandia's experimental "mold-micromachining" technology to be at or very near our most ambitious target specifications. Accordingly, we are pursuing development of this new micromachining technology. At the same time, we are manufacturing prototypes with more modest performance expectations in our much more mature "surface-micromachining" fabrication technology. These first prototypes, which have just recently been completed and have not yet

been characterized, will have nowhere near ideal performance (we expect mG resolution), but nonetheless do provide a starting point for further development of fabrication technology, mechanical designs, and servo circuits.

2. PROTOTYPE DESIGN

Because the principal axis of interest for seismic measurements is the vertical one, our basic accelerometer design consists of an unbalanced "teeter-totter" platform suspended on opposite sides by two small flexures (Figure 1). This design is a variation on the common "pendulum" design for existing seismic accelerometers, modified to allow differential capacitive pick-offs to be placed to either side of the flexures. We have chosen capacitive pick-offs rather than magnetic coil-based transducers because it is virtually impossible to make a coil in a micromachining process, while parallel-plate capacitors with very small, uniform gaps are a natural in this technology. We also discarded a third possibility, electron tunneling, which has been employed in sensitive accelerometer designs by another micromachining group,[1] because of reliability concerns and because of the 1/f noise which limits the performance of tunneling sensors at the very low frequencies which are of interest in seismic monitoring.

The signal-to-noise ratio for the motion of an accelerometer versus thermal-mechanical noise (electronic noise is not usually the limiting factor for seismic transducers) is given by

$$S / N = \sqrt{\frac{a_s^2 m Q}{4 k_B T \omega_o}} ,$$

where a_s is the acceleration signal, m the proof mass, Q the so-called "quality factor" (a measure of damping), k_B is Boltzmann's constant, T the absolute temperature in Kelvin, and $\omega_o = 2\pi f_o$ the natural frequency of the mechanical system.[2] If we insert 10^{-10} $G/\sqrt{Hz}$ for a_s, and the maximum possible Q of 30,000 (corresponding to the intrinsic material damping of a silicon device in an evacuated package), we obtain a set of pairs of $\{m, f_o\}$ which will give an adequate signal-to-noise ratio. From among these, a feasible pair is $m \geq 10$ mg and $f_o \leq 1$ Hz. In order to achieve these values, it will be necessary to develop a new silicon micromachining technology, as current technologies cannot deliver the combination of large (on this scale at least) proof mass and soft suspension. We have invented a novel fabrication process which may well address these issues — this new "mold" process is described below.
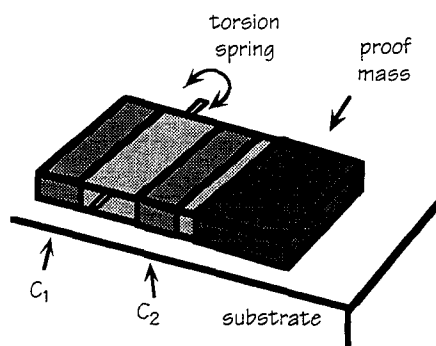
Figure 1. "Teeter-totter" seismic sensor concept.

3. SILICON MICROMACHINING TECHNOLOGIES

Silicon micromachining technologies can be divided into three categories — so-called "bulk," "surface," and "mold" micromachining. "Bulk" micromachining generally refers to processes involving wet chemical etching of structures formed out of the silicon substrate and so is limited to fairly large, crude structures. "Surface" micromachining allows patterning of thin films of polysilicon and other materials to form intricate but essentially two-dimensional layered parts (since the thickness of the parts is limited by the thickness of the deposited films). In "mold" micromachining, the mechanical part is formed by filling a mold which was defined by photo-lithographic means. Historically micromachining molds have been formed in some sort of pho-topolymer, be it with x-ray lithography ("LIGA") or more conventional UV lithography, with the aim of producing piece parts. Recently, however, several groups including ours at Sandia have independently come up with the idea of forming the mold for mechanical parts by etching into the silicon substrate itself. The following is a quick review of these three micromachining meth-ods intended to clarify the approaches we have taken in fabricating seismic sensor prototypes. Note that the references given here are only examples and are not by any means intended to be a complete survey of the literature.

3.1 Bulk micromachining

The term "bulk" micromachining literally refers to the process of making a mechanical structure out of the bulk material (i.e. the single-crystal silicon substrate). Generally the mechanical structure is formed either by doping-selective[3] or crystallogaphic[4] wet chemical etching. These processes are relatively large-scale and crude compared to the sub-micron photolithographic processes common in microelectronic fabrication, with dimensional variations on the microns to hundreds-of-microns scale. A subcategory of bulk micromachining which offers finer dimen-sional control is dry etching of mechanical structures — again, the part is formed from the sin-gle-crystal silicon substrate itself.[5] One of the major advantages of bulk micromachining is that it is relatively easy to fabricate large masses (for accelerometers, for example), but, on the other hand, delicate, sensitive suspensions are difficult to realize. Also, bulk micromachining pro-cesses are not particularly compatible with electronics, simply because they aren't planar.

We rejected bulk micromachining as a fabrication strategy for seismic sensors, even though the most sensitive silicon accelerometers to date have been made this way,[1] for several reasons. First, we do not have a mature bulk-micromachining technology at Sandia, and therefore mak-ing the prototypes using bulk processes would not leverage well with our other projects. Sec-ond, bulk micromachining does not lend itself to integration with electronics and we are convinced that integrated amplifiers and servo electronics will be necessary in order to achieve the sensitivities required for treaty monitoring.

3.2 Surface micromachining

Surface micromachining uses the planar fabrication techniques common to the microelectronic circuit fabrication industry to manufacture micromechanical devices. The standard building-block process consists of depositing and photolithographically patterning alternate layers of low-stress polycrystalline silicon and sacrificial silicon dioxide. As shown in Figure 2, holes etched through the sacrificial layers provide anchor points between the mechanical layers and to the substrate. At the completion of the process, the sacrificial layers, as their name suggests, are selectively etched away in hydrofluoric acid (HF), which does not attack the silicon layers. The result is a construction system consisting of one layer of polysilicon which provides electri-cal interconnection and one or more independent layers of mechanical polysilicon which can be used to form mechanical elements ranging from a simple cantilevered beam to complex systems of springs, linkages, mass elements, and joints. Because the entire process is based on stan-dard integrated-circuit fabrication technology, hundreds to thousands of devices can be batch-

fabricated on a single six-inch silicon substrate.

Because surface micromachining takes advantage of the advanced manufacturing processes developed in the microelectronics fabrication industry, it offers the same high degree of dimensional control found in electronic integated circuit fabrication, and is the micromachining method most compatible with integrated electronics.[7] The planarity which makes surface-micromachined parts relatively easy to integrate with microelectronics, however, is also the major limitation of surface micromachining — that is, surface-micromachined parts are essentially two-dimensional (since the thickness of the parts is limited by the thickness of the deposited films), and therefore relatively light and compliant. (Typical masses for surface-micromachined components are in the µg range and it is difficult to achieve natural frequencies below 1 kHz.)

Sandia's three-level polysilicon process is the world's most sophisticated surface-micromachining technology, and promises soon to offer integrated electronics as well as complex mechanical parts, so despite the difficulty of manufacturing a large proof mass in a surface process, we decided to begin by fabricating our initial seismic transducer prototypes in this surface-micromachining technology.

3.3 Mold micromachining

The principal advantage of all mold micromachining processes are that they make it possible to fabricate high-aspect-ratio parts (i.e. thick relative to surface dimensions). Mold micromachining has generally been used to manufacture piece parts (e.g. gears, etc.), although micromachined structures formed with thick photo-sensitive polymer molds have also been integrated with previously fabricated electronic circuits. Variations on the mold concept include, on the one hand, the well-known "LIGA" process, in which lithography is used directly to form a photoresist mold, and, on the other hand, silicon mold processes, in which the mold is formed by etching into the silicon substrate.

3.3.1 "LIGA" and "LIGA-like" processes

"LIGA" is a German acronym which refers to "lithography, electroplating, and injection molding". The original LIGA process, while it achieves impressive aspect ratios,[8] has only seen scat-
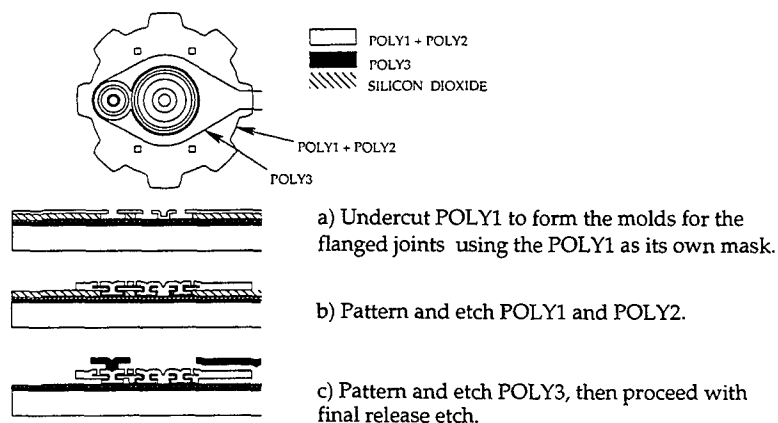
Figure 2: Example surface-micromachining process.[6] These are cross-sections through essential elements of the Sandia microengine gear and joints taken at three stages of completion.

717

- A deep mold is formed in the substrate with a silicon trench etch

- The mold is lined with sacrificial or etch stop layer

- Mold is filled with structural material to form the mechanical part
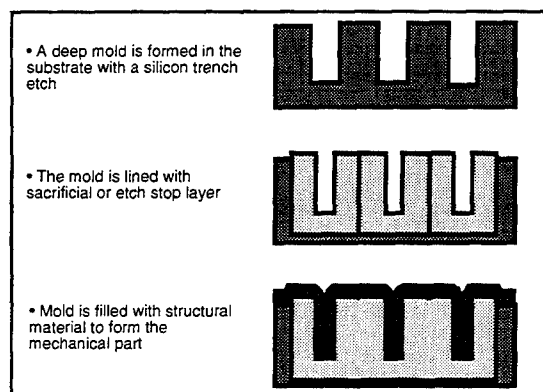
Figure 3. Generalized silicon mold process.

tered application because it requires specialized x-ray lithography equipment. "LIGA-like" processes include ones where the more common UV-exposed photoresist is used instead. These "LIGA-like" processes allow fabrication of thicker parts than can be made using surface micromachining, but are generally limited to much less extreme aspect ratios than the original LIGA process.[9] Both the original LIGA process and the "LIGA-like" processes lend themselves primarily to the fabrication of piece parts which require subsequent assembly into a microelectromechanical system.

3.3.2 Silicon mold processes

The basic concept behind silicon mold processes is that the mold for a micromechanical part is formed by etching into the silicon substrate (Figure 3). Silicon mold processes thus take advantage of the fact that, by etching a high-aspect-ratio mold (that is, one which is much deeper than it is wide) and filling it with a conformal thin film, one can form a mechanical structure that is much thicker than the maximum thickness of the deposited film itself. Our group at Sandia is one of three research groups which have independently conceived of the silicon mold idea and have been pursuing variants on the basic process.[10]

3.3.3 The Sandia mold micromachining process

The first step in the Sandia mold process is to etch the mold pattern into the substrate using a "deep trench" reactive-ion-etching process. The silicon pattern is then transformed into a mold in one of several ways. For example, if the structure will be formed of polysilicon and released in HF, the mold is oxidized at this point. It is also possible to remove the silicon mold by wet etching the silicon, in which case the mold is completed instead by depositing an etch stop layer. The commonality in both cases is that, in the end, the mold-micromachined parts are anchored to the substrate and released in place, like surface-micromachined parts — the mold is not reused. After the mold is formed, it can be filled with any of a number of materials, including most of the thin films common in the semiconductor industry (doped or undoped polysilicon, silicon nitride, CVD tungsten, etc.), as well as plated metals. The wafer is then planarized by an etchback or chemical-mechanical polish (CMP) process. At this point, assuming materials compatibility, it can be taken through a surface-micromachining or electronic integrated circuit fabrication process (or both). Once all the processing is complete, the mechanical parts are released so that they are free to move relative to the substrate.

This experimental process would be ideal for manufacturing seismic sensors because it offers

718
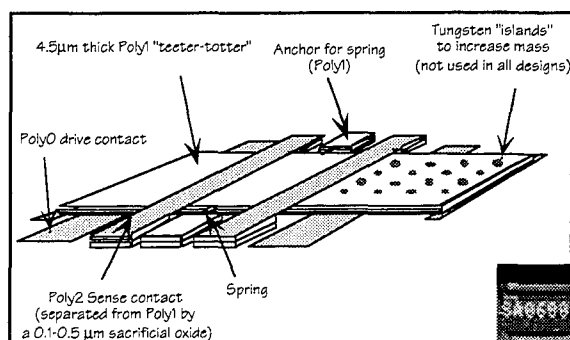
← Figure 4a. Conceptual sketch of surface-micromachined seismic sensor prototype.

→ Figure 4b. SEM photo of surface-micromachined seismic sensor prototype. These first prototypes have only one set of differential capacitive contacts, which will be used for both pick-off and forcing.
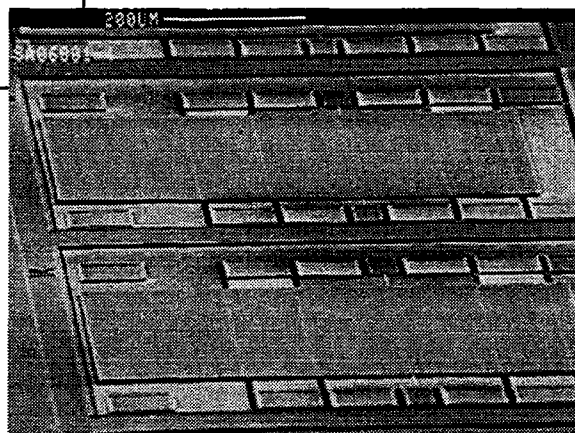
increased mass while retaining the ability to fabricate a compliant suspension. Accordingly, we are currently working on a version of the process which will provide a proof mass several orders of magnitude larger than is possible with surface micromachining and will also offer a compliant surface-micromachined suspension and the possibility of integration with electronics.

4. PRELIMINARY RESEARCH RESULTS: SURFACE-MICROMACHINED PROTOTYPE

We have designed and fabricated prototype seismic accelerometers in Sandia's state-of-the-art surface-micromachining process (see Figure 4 for a conceptual sketch and SEM photo). Again, this prototype design is a modified pendulum, in which differential capacitive sense pick-offs and forcers are positioned on either side of the torsional springs. The first lot of prototypes is completed, has passed basic functional testing, and is currently being packaged for insertion in a force-feedback circuit for more thorough testing. This first lot of prototypes has only one set of contacts (the lower set shown in Figure 4), and so will be tested using a charge-control servo circuit developed by Litton Guidance and Control Systems (Woodland Hills, CA), which uses one set of contacts for both signal pick-off and force-feedback. Subsequent prototypes will have separate pick-off and forcer contacts, so it will be possible to test them using modified Sandia voltage-control navigational servo circuits. We expect these surface-micromachined prototypes to resolve signals in the mG to μG range.

5. PRELIMINARY RESEARCH RESULTS: MOLD-MICROMACHINED PROTOTYPE

Concurrently with the surface-micromachined prototype fabrication effort, we are developing the capability to make heavier proof masses using the silicon mold technology described in Section 3 above. As a first attempt at a mold-micromachined seismic sensor prototype, we fabricated a molded tungsten proof mass by oxidizing a trench-etched silicon mold, and filling it with metal. Figure 5a shows the etched mold after oxidation. In order to form this mold, we used a $Cl_2/HBr/O_2$ etch chemistry in an electron cyclotron resonance (ECR) reactive-ion etcher to etch pillars roughly one micron in diameter and over twenty microns tall out of the silicon substrate. We then oxidized the wafer to an oxide thickness of 1.5 microns. Finally, we filled the mold with chemical-vapor deposited (CVD) tungsten and planarized the wafer with CMP. Figure 5b shows
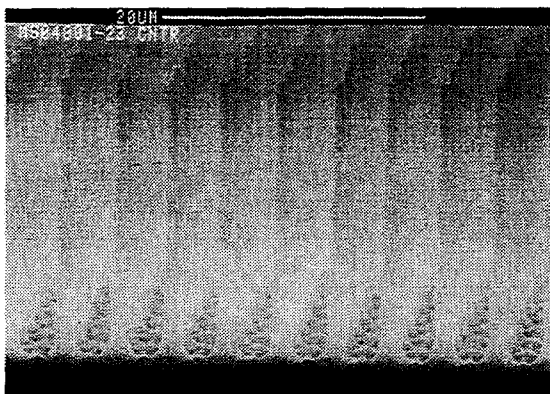
Figure 5a: Silicon dioxide mold for accelerometer proof mass.
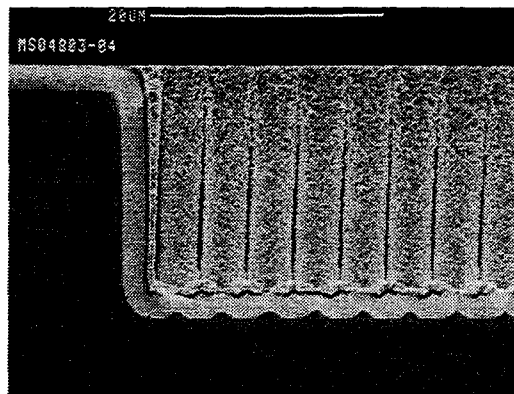
Figure 5b: Molded tungsten proof mass.

the finished proof mass ready to be integrated with surface-micromachined suspension springs and sense contacts before being released in a hydrofluoric acid etch.

6. FUTURE PLANS

Our future plans for the surface-micromachining prototype effort are to servo the present proto-types, and to continue improving the design, leading to more sensitive prototypes. Concur-rently, we plan to continue development of the silicon mold process — we expect that the mold process will ultimately yield stand-alone seismic sensor prototypes which, when servoed, will resolve better than 1 $\mu G/\sqrt{Hz}$ signals.

Once we have manufactured discrete sensors with good performance, we plan to turn to the challenge of integrating parts of the servo circuitry on-chip with the sensor. Integrated electron-ics will increase the performance of the sensor by reducing stray-capacitance problems, and will reduce the size of the overall system as well.

7. SIGNIFICANCE FOR CTBT

Inexpensive micromachined silicon seismic sensors could revolutionize the seismic data-gather-ing process. The cost savings realized by a micromachined design would result not only from the reduced cost of the sensor itself, but also from lower installation and maintenance costs. A borehole system using current sensor and electronics technologies can be as heavy as 200 pounds (90 kg) and its installation requires a drilling rig. The expense of installing and main-taining an array of such sensors often far outweighs the cost of the sensors themselves. A small, low-cost sensor could also make portable/disposable systems for both cooperative and non-cooperative seismic monitoring viable.

The capabilities and cost of the proposed seismic sensor would also make it attractive for related commercial applications such as low-cost, sensitive earthquake monitors and sensors for oil and gas exploration. The existence of large commercial markets for the sensor would drive manufacturing volumes up and costs down and would attract the interest of commercial sensor manufacturers. The CTBT community, which is in itself a relatively small market, would then benefit from association with these larger commercial applications.

NOTES AND REFERENCES

1. T. W. Kenny, S. B. Waltman, J. K. Reynolds, and W. J. Kaiser, "Micromachined silicon tunnel sensor for motion detection," Applied Physics Letters, Vol. 58, No. 1, Jan 1991, pp. 100-102.

2. T. B. Gabrielson, "Mechanical-Thermal Noise in Micromachined Acoustic and Vibration Sensors," IEEE Transactions on Electron Devices, Vol. 40, No. 5, May 1993, pp 903-909.

   This equation, strictly speaking, does not hold for the torsional motion of our device, but it turns out that the results one obtains by substituting in the torsional equivalents (moment of inertia for mass, etc.) are to the first order indistinguishable from the linear motion equation given here.

3. L. Spangler and K. D. Wise, "A New Silicon-on-glass Process for Integrated Sensors," IEEE Sensor and Actuator Workshop, Hilton Head, SC, pp. 140-142, June, 1988.

4. K. E. Petersen, "Silicon as a Mechanical Material," Proc. IEEE, vol. 70, no. 5, pp. 420-457, May, 1982.

5. Examples of bulk micromachining using dry etching:

   W.H. Juan and S. W. Pang, "A Novel Etch-Diffusion Process for Fabricating High Aspect Ratio Si Microstructures," 8th International Conference on Solid-State Senosrs and Actuators, Stockholm, Sweden, June 25-29, 1995, pp. 560-563.

   Y. Xu, S. A. Miller, and N. C. MacDonald, "Microelectromechanical Scanning Tunneling Microscope", 8th International Conference on Solid-State Senosrs and Actuators, Stockholm, Sweden, June 25-29, 1995, pp. 640-643.

   K. A. Shaw, Z. L. Zhang, and N. C. MacDonald, "SCREAM I: A single mask, single-crystal silicon process for microelectromechanical structures," Tech. Digest, IEEE Solid-State Sensor and Actuator Workshop, 1993.

6. The Sandia tri-level polysilicon surface-micromachining technology has been described in

   J. J. Sniegowski and E. J. Garcia, "Microfabricated Actuators and their Application to Optics," Proc. SPIE vol. 2383, pp. 46-64.

   For an earlier review of surface micromachining:

   R. T. Howe, "Surface micromachining for microsensors and microactuators," J. Vac. Sci. Technol. B, vol. 6, no. 6, pp. 1809-1813, 1988.

7. T. A. Core, W. K. Tsang, and S. J. Sherman, "Fabrication technology for an integrated surface-micromachined sensor," Solid State Technology, vol. 36, no. 10, pp. 39+, 1993.

6. H. Guckel, T. Earles, J. Klein, D. Zook, and T. Ohnstein, "Electromagnetic Linear Actuators with Inductive Position Sensing for Micro Relay, Micro Valve and Precision Positioning Applications," 8th International Conference on Solid-State Sensors and Actuators, Stockholm, Sweden, June 25-29, 1995, pp. 324-327.

E. W. Becker, W. Ehrfeld, P. Hagman, A. Maner, and D. Münchmeyer, Microelectronic Engineering, vol. 4,) pp. 35-56, 1986.

7. Examples of "LIGA-like" processes:

M. W. Putty and K. Najafi, "A Micromachined Vibrating Ring Gyroscope," 1994 Solid-State Sensor and Actuator Workshop, Hilton Head, SC June 13-16, 1994, pp. 213-220.

A. B. Frazier and M. G. Allen, "Uses of Electroplated Aluminum in Micromachining Applications," 1994 Solid-State Sensor and Actuator Workshop, Hilton Head, SC June 13-16, 1994, pp. 90-94.

10. Other examples of silicon mold micromachining:

C. G. Keller and R. T. Howe "Hexsil Bimorphs for Vertical Actuation," pp. 99-102, and "Nickel-Filled HEXSIL Thermally Actuated Tweezers," pp. 376-379, 8th International Conference on Solid-State Sensors and Actuators, Stockholm, Sweden, June 25-29, 1995.

C. Keller and M. Ferrari, "Milli-Scale Polysilicon Structures," 1994 Solid-State Sensor and Actuator Workshop, Hilton Head, SC June 13-16, 1994, pp. 132-137.

A. Selvakumar and K. Najafi, "High Density Vertical Comb Array Microactuators Fabricated Using a Novel Bulk/Polysilicon Trench Refill Technology," 1994 Solid-State Sensor and Actuator Workshop, Hilton Head, SC June 13-16, 1994, pp. 138-141.

Source Finiteness, Signal Decorrelation, Spectral Scalloping and Identification of Multiple Delayed Explosions.

by
Zoltan A. Der
and
Douglas R. Baumgardt

ENSCO Inc, 5400 Port Royal Rd, Springfield VA 22151.

ABSTRACT.

Our results show that a generalized model that includes propagation delays and signal decorrelation can reproduce numerous observed features in the spectral modulation patterns of regional phases from quarry blasts. Analyses of spectra associated with various regional arrivals of the same event revealed differences in modulation strength and apparent shifts in modulation patterns These may be associated with source finiteness, propagation delays and signal decorrelation. Potentially these features can be used to derive information with regards to the spatial extent and layout of shot arrays. Modulation patterns or the locations of first minima in the spectra are generally not determined solely by the time duration of the shot sequences as often claimed, but are complex functions of numerous factors. Lack of spectral modulation does not necessarily indicate a single explosion or the absence of ripple firing either. Since this project has just begun, the results presented here are relevant only a to a subset of the tasks to be performed under this contract.

Key Words

Discrimination

Mining practices

Quarry blasts

Seismic sources

OBJECTIVES.

The objective of this project is the implementation of various advanced time series processing techniques for small array data and their implementation in Geotool and, ultimately, various AFTAC systems for seismic monitoring. The project includes the implementation of site-specific automatic phase recognition algorithms, signal enhancement methods, and deconvolution algorithms combined with signal complexity discrimination.

RESEARCH ACCOMPLISHED.

Spectral modulation (scalloping) is an effective discriminant for distinguishing ordinary ripple-fired quarry blasts from large, single explosions and earthquakes. It cannot be used, however, to distinguish between single chemical explosions and small nuclear blasts, neither can it be used discriminate between ripple-fired quarry blasts and multiple large explosions, some of which could be nuclear. Thus as a discriminant, scalloping has limitations. Nevertheless spectral scalloping can provide information about the spatio-temporal structure of sources.

Data Analyses.

The regional phase spectra presented in this paper were produced by a uniform procedure. For a given event all traces were inspected and only the sensor outputs with uncompromised data quality were kept. All events analyzed also had very high signal-to-noise ratios with the even weakest arrivals (such as Pn), high above the background noise level. The various regional arrivals were windowed using the same chosen window length of 12.8 seconds for each type of arrival. The Parzen tapering function was used on each window which heavily tapered off both ends of each window. The position of the windows were chosen such that the arrival to be analyzed was close to the center of the window in order avoid reduction of its amplitude by the taper. After Fourier transforming and squaring the amplitude spectra of each sensor for a given arrival the resulting power spectra were smoothed by a 5 point moving average and averaged over all the chosen sensors of the array.

The most common modulation pattern observed in regional seismograms is nearly identical for the various phases in the seismogram (**Figure 1**). Such modulations can be easily seen in spectra computed for various time windows or continuous sonograms. When the causative time patterns of shots are simple, such as a pair of collocated explosions, we also can discern the time pattern in cepstral analyses. In some seismograms there are some finer observable spectral features that can be explained by source finiteness effects. These observable effects include phase-velocity dependent frequency shifts (or rescaling) in the spectral modulation patterns (**Figure 2**) and differences in the degree of modulation for the various regional seismic arrivals (**Figure 3**).

Theoretical Modelling of Spectral Modulation.

A common assumption made in various studies of spectral modulation is that the modulation patterns, especially the frequency of the first spectral minimum, are simple functions of source duration, i.e. the time length of the shot sequence. It is easy to show that this is not the case. The time delays between shots at quarries are generally much shorter than the digitizing time interval at most sensors of regional arrays (25 msec). Thus

the arrays essentially "see" a simplified time function which can be derived by smoothing the original time sequence with a sinc function and resampling it at a 25 msec sampling rate. One can easily verify that this procedure does not change the resulting spectra below the Nyquist frequency of 20 Hz. By generating shot time sequences that have the same duration but have different variations in charge sizes with time we show that the locations of the first spectral minimum can be shifted significantly. It is also easy to design ripple firing sequences with approximately Gaussian envelopes when smoothed and resampled at 40 Hz that would not display any modulation despite their finite duration. Thus the spectral modulation patterns are not simple functions of duration.

Obviously the model of linear superposition of shots with identical waveforms cannot fully explain the observations of differences in modulation of the various regional arrivals presented above. What is needed is a model that incorporates the effects of signal decorrelation and propagation delays. Descriptions of firing practices at some mines indicate the use of very large shot arrays with dimensions close to a kilometer and firing time delays of the order of seconds (Kim et al 1994). When a shot array is even moderately large, for instance, when its dimensions are of the order of hundreds of meters we can no longer assume that the waveforms of two widely separated shots are the same. The waveforms originated by the various charges are bound to be decorrelated, by invoking reciprocity arguments, in a way similar to waveform decorrelation observed at small arrays. The frequency-limited correlation coefficients (coherences) of waveforms at small arrays were found to be approximately exponentially dependent on the product of distance between two observation points and frequency.

Analyses of waveform decorrelation at NORESS indicated that the waveform decorrelation is stronger for for phases with low propagation velocities such as Sn and Lg compared to fast travelling phases such as Pn and Pg. The stronger decorrelation for Sn and Lg may also be related to the more complex mode-ray structures of these phases (Der and Baumgardt 1994). There are also indications that the rate of decorrelation may depend on the direction of the wave propagation relative to the direction chosen in the horizontal plane (Der et al 1988). For simplicity in this paper we shall ignore this directionality and will assume a decorrelation factor proportional to $exp(-\alpha fd)$, where α is a constant determining the rate of decorrelation f is frequency and d is the intersensor diatance. The rate of waveform decorrelation will obviously depend on the degree of heterogeneities in the local structure and path and thus will vary from place to place. The second factor that must be considered for large shot arrays is the propagation delay between pairs of charges which for shot patterns of the order of hundreds of meters are not negligible compared to the absolute time lags among shots. These delays will be added to the absolute time differences and produce essentially a Doppler effect. For nonsymmetrical space-time distributions of shots thus will give a directional dependence to the spectra of quarry blasts observed. Moreover, since the additive relative propagation delays depend on the dominant phase veocity of each arrival, the spectral modulations will not be the same for all phases. The formula that approximately describes the observed power spectra including all these factors is

$$Y(\omega) = \sum_{i=1}^{N} |X_i(\omega)|^2 + 2 \sum_{j=1}^{N} \sum_{k=j+1}^{N} |X_j(\omega) X_k(\omega) C(\omega, \Delta_{jk})| \cos \omega (\tau_j - \tau_k + d_{jk})$$

$$(1)$$

where the factor $C(\omega,\Delta)$ is the coherence between two waveforms corresponding to the angular frequency ω and the distance Δ, d_{jk} is the propagation delay for a phase between the two sensors j and k which can be computed using the average, dominant phase velocity of the phase in question (such as *Pn, Pg, Sn or Lg*). The formula states that the total observed spectrum is made up of the individual spectra of the sources plus all the cross-spectral contributions between all the possible distinct pairs of sensors. Given the fact that according to experience spectra of individual explosions are generally smooth, almost all of the modulation is caused by the cross spectral contributions, i.e. the second sum on the right side of (1).

In our simulations we have assumed, somewhat arbitrarily, the dominant phases velocities of 8.2, 6.0, 4.7 and 4.0 for Pn, Pg, Sn and Lg respectively. We have varied the decorrelation rates to study their effects for various types of geological situations. Seismic reciprocity as applied to regional signal decorrelation measurements at "small" arrays of a few km diameter implies that waveforms observed at a remote sensor from similar sources displaced over small distances will be similarly decorrelated. In order to optimize signal processing at regional arrays signal decorrelation was measured at the sites of small arrays in Scandinavia (Mykkeltveit et al. 1983). The results produced indicated that the degree of decorrelation increased in the order of Pn-Pg-Sn-Lg and that it also increased with increasing frequency.   In this paper we shall assume a decorrelation function of the direction-independent form of $exp(-\alpha f\Delta)$, where α is a constant, f is frequency and Δ is the distance. The costant α will undoubtedly depend on the local geological heterogeneity of the particular area where the sensor or shot array is located and thus will be varied.

Applying Equation (1) to a simulated linear array demonstates that the underlying model can reproduce both the relative displacement of the nulls and maxima of the modulation patterns and the differences in the strength (peak-valley contrast) of modulation for the various phases (**Figure 4**). The shifts in modulation patterns for this case are umambiguous and azimuth-dependent.

A more realistic areal pattern we have simulated consisted of 5 rows of ten shots which the firing in the successive rows overlapped (**Figure 5**). Patterns of this kind were described by Chapman et al (1991). Similarly to observed data, differences in the frequencies of various features in the modulation patterns are small in this example, but the strength of modulation decreases strongly from Pn to Lg. The two-dimensional layout of this shot pattern makes the Doppler shifts complex and hard to see. This figure provides an explanation why shifts in modulation patterns are rarely seen in real observations although most shot patterns are generally large enough to produce significant propagation delays compared to the absolute time delays in a pattern.

RECOMMENDATIONS AND FUTURE PLANS.

Obviously spectral modulation patterns in regional arrivals contain information about the spatio-temporal layout of the shot arrays used. This information can potentially be used, in conjunction of independent information, to assess the sizes of shot arrays and in discrimination. Observation of modulation patterns from various directions from the source may enable us to infer the spatial layout of the shotarrays. Since this inversion constitutes a complex nonlinear estimation problem combinatorial optimization methods (such as genetic algorithms) may be used advantageously in such applications.

We find this part of our investigation nearly complete, during the future work on this project we shall concentrate on the other tasks described above.

Selected References.

Anderson, D.P. and B. W. Stump (1994), Utilization of near-source video and ground motion in the assessment of seismic source functions from mining explosions (Abstract). 16-th Annual Research Symposium, Phillips Laboratory- Air Force Office of Scientific Research, Thornwood Conference Center, Thornwood, N.Y., 7-9 September, 1994

Barker, T.G., McLaughlin, K.L. and J.L. Stevens (1993), Numerical simulation of quarry blast sources. Maxwell Laboratories, S-Cubed, La Jolla, CA. Technical Report prepared for Phillips Laboratory, Kirtland AFB, NM.

Baumgardt, D.R. and K. A. Ziegler (1988). Spectral evidence for source multiplicity in explosions, application to regional discrimination of earthquakes and explosions, *Bull. Seism. Soc. Am.* **78**, 1773-1795.

Chapman, M.C., Bollinger, G.A. and M.S. Sibol (1991), Spectral studies of the ealstic wave radiation from Appalachian earthquakes and explosions - Explosion source spectra modeling using blaster's logs. Virginia Polytechnical Institute, PL-TR-91-2231. Prepared for the Phillips Laboratory, Air Force Systems Command, Hanscom AFB, MA. ADA243956

Der, Z.A., Shumway, R.H. and A.C. Lees (1988), frequency domain coherent processing of regional seismic signals at small arrays.*Bull. Seism. Soc. Am.*, **78**, 326-338.

Der, Z.A., Hirano, M.R., Ziegler, K.A. and R.H. Shumway (1991), Broadband studies of seismic sources at regional and teleseismic distances. PL-TR-91-2059 (1). ENSCO Inc. Prepared for Phillips Laboratory, Hanscom AFB. ADA239201

Der, Z.A., Baumgardt, D.R., and R.H. Shumway (1993), The nature of particle motion in regional seismograms and its utilization for phase identification. *Geophys. J. Intl.*, **115**, 1012-1024.

Der, Z.A. and D.R. Baumgardt (1994), Issues in regional monitoring and mining operations for the presence of hidden nuclear tests. 1994 *ARPA CTBT Monitoring Technologies Conference. San Diego CA.*

Gitterman, Y. and T. van Eck (1993), Spectra of quarry blasts and microearthquakes recorded at local distances in Israel. *Bull. Seism. Soc. Am.*, **83**, 1799-1812.

Goldberg, D.E. (1989). *Genetic Algorithms in Search, Optimization & Machine Learning,* Addison-Wesley Publishing Company.

Kim, W.Y., Simpson, D.W. and P.G. Richards (1994), High frequency spectra and regional phases from earthquakes and chemical explosions. *Bull. Seism. Soc. Am.*, **84**, 1365-1386.

Mykkeltveit, S., Astebol, K., Doornbos, K.J., and E.S. Husebye (1983), Array configuration optimization. *Bull. Seism. Soc. Am.*, **73**, 173-186.

Smith, A.T. (1993), Discrimination of explosions from simultaneous mining blasts. *Bull. Seism. Soc. Am.*, **83**, 160-179.
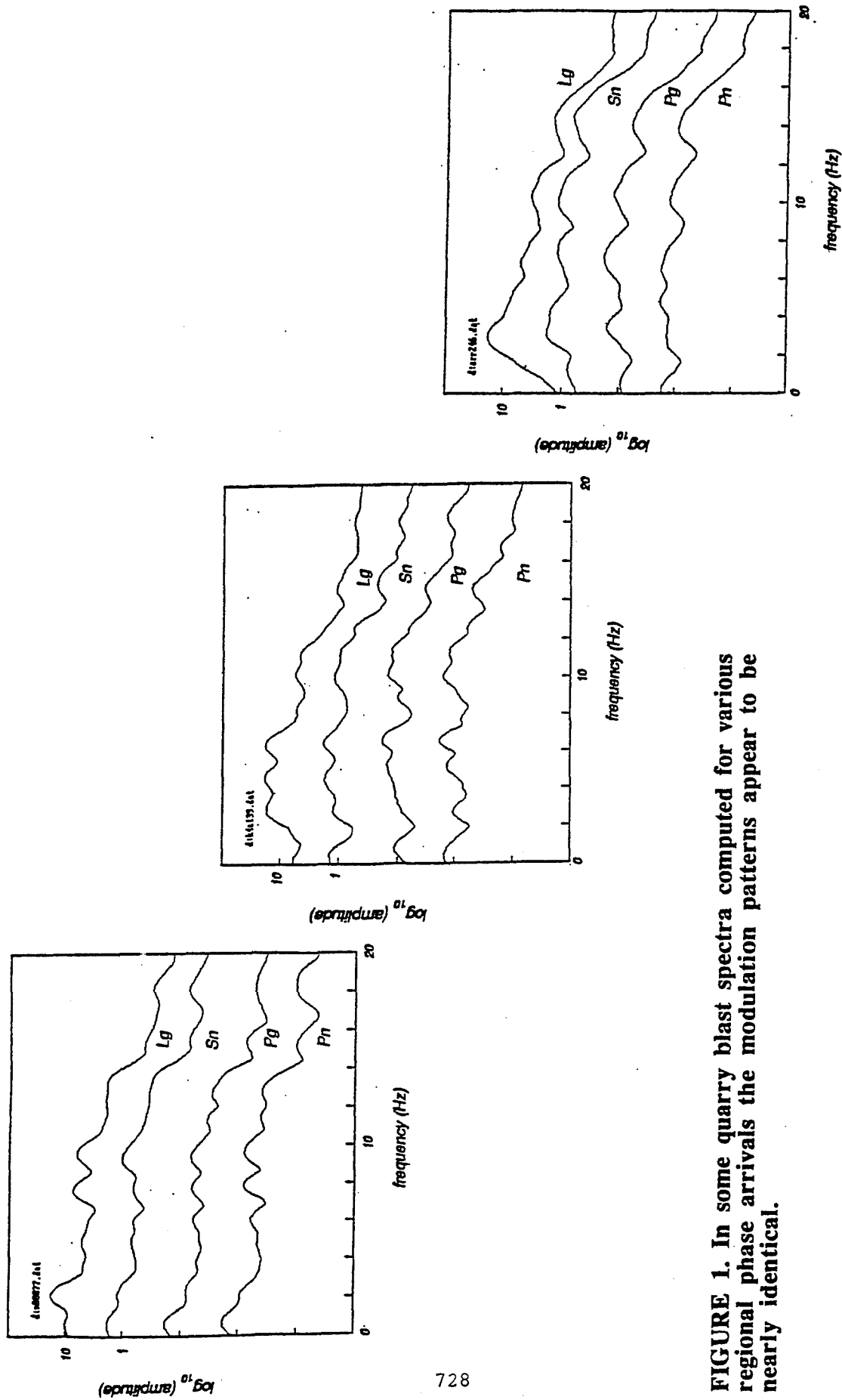
FIGURE 1. In some quarry blast spectra computed for various regional phase arrivals the modulation patterns appear to be nearly identical.
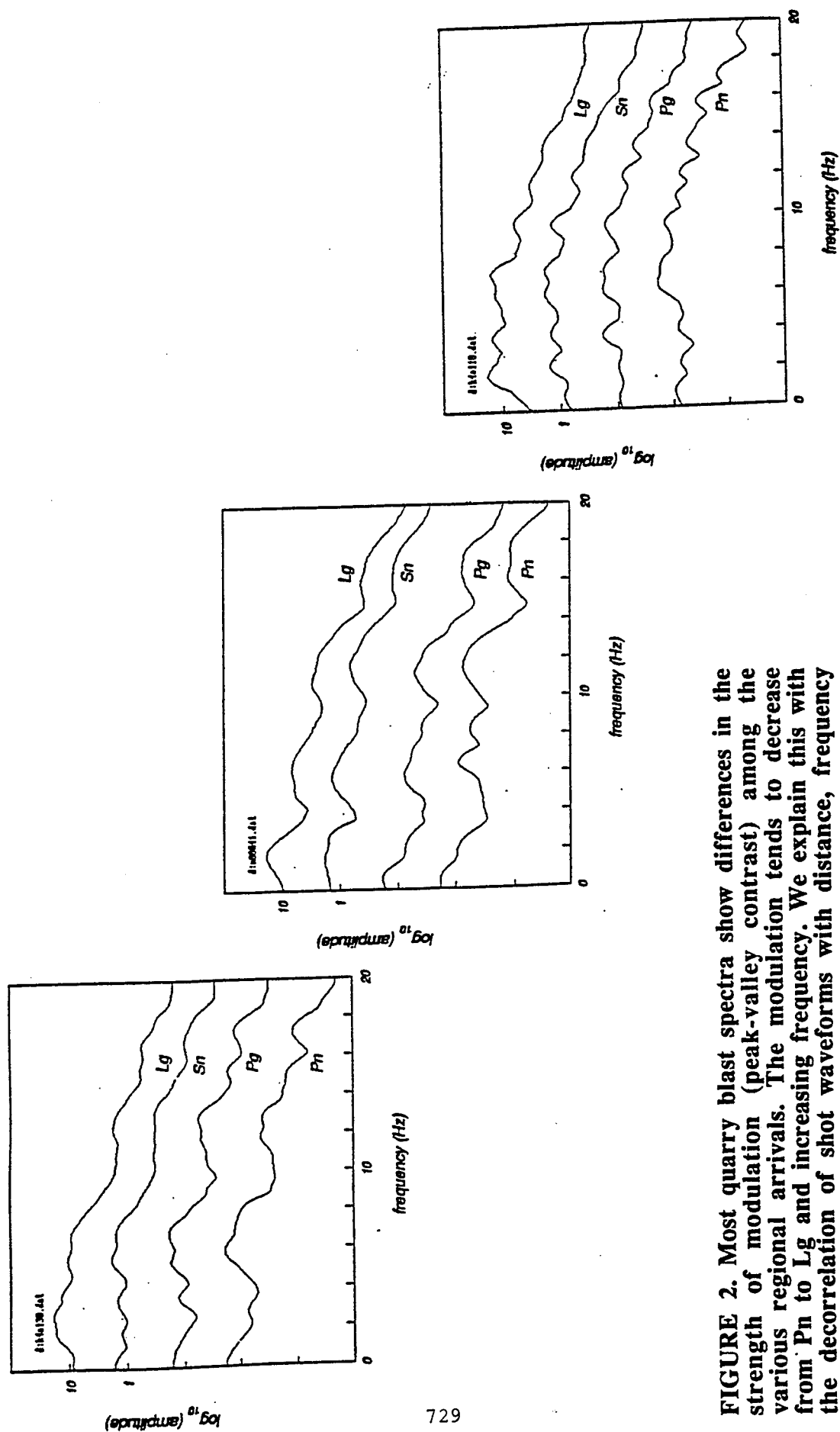
FIGURE 2. Most quarry blast spectra show differences in the strength of modulation (peak-valley contrast) among the various regional arrivals. The modulation tends to decrease from Pn to Lg and increasing frequency. We explain this with the decorrelation of shot waveforms with distance, frequency and the type of phase.
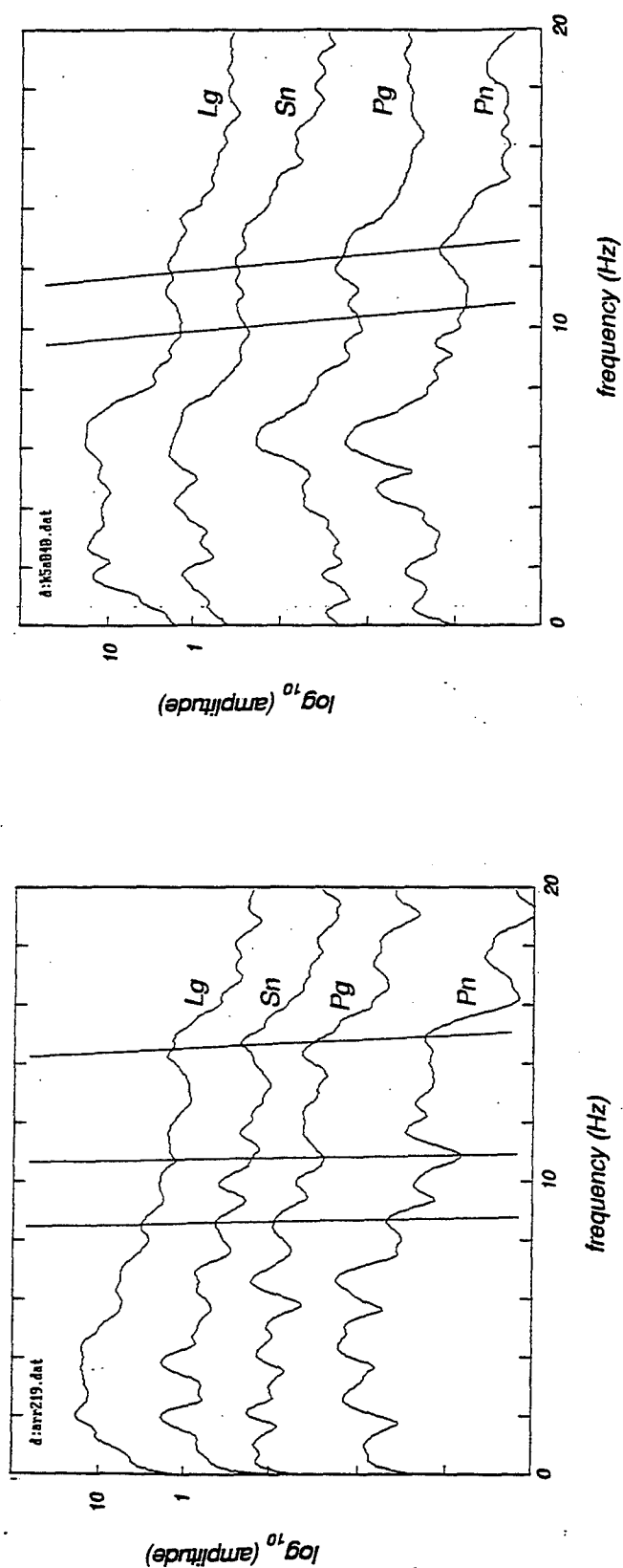
FIGURE 3. Some spectra show displacement (scaling) of modulation among the various phases as indicated by lines. Propagation delays (Doppler effect) are the probable explanation.
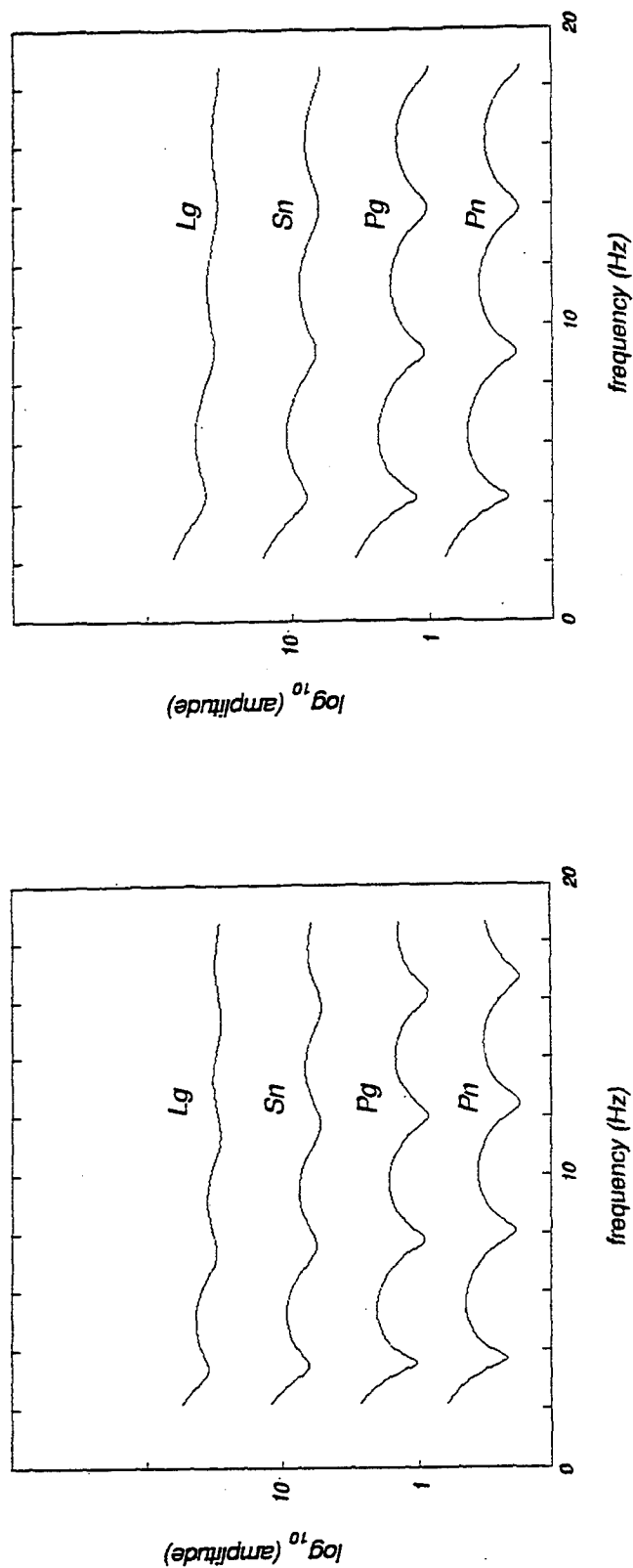
FIGURE 4. Simulated spectral modulation patterns for a 10 element linear shot array with spacings of 20 m and and intershot delays of .02 seconds. All spectra show a diminution of modulation intensity from Pn to Lg, but depending on the azimuth the features in the modulation shift to the left when the successive shots move away from the observer (left), and remain the same when the distances to the various shots are constant (right).
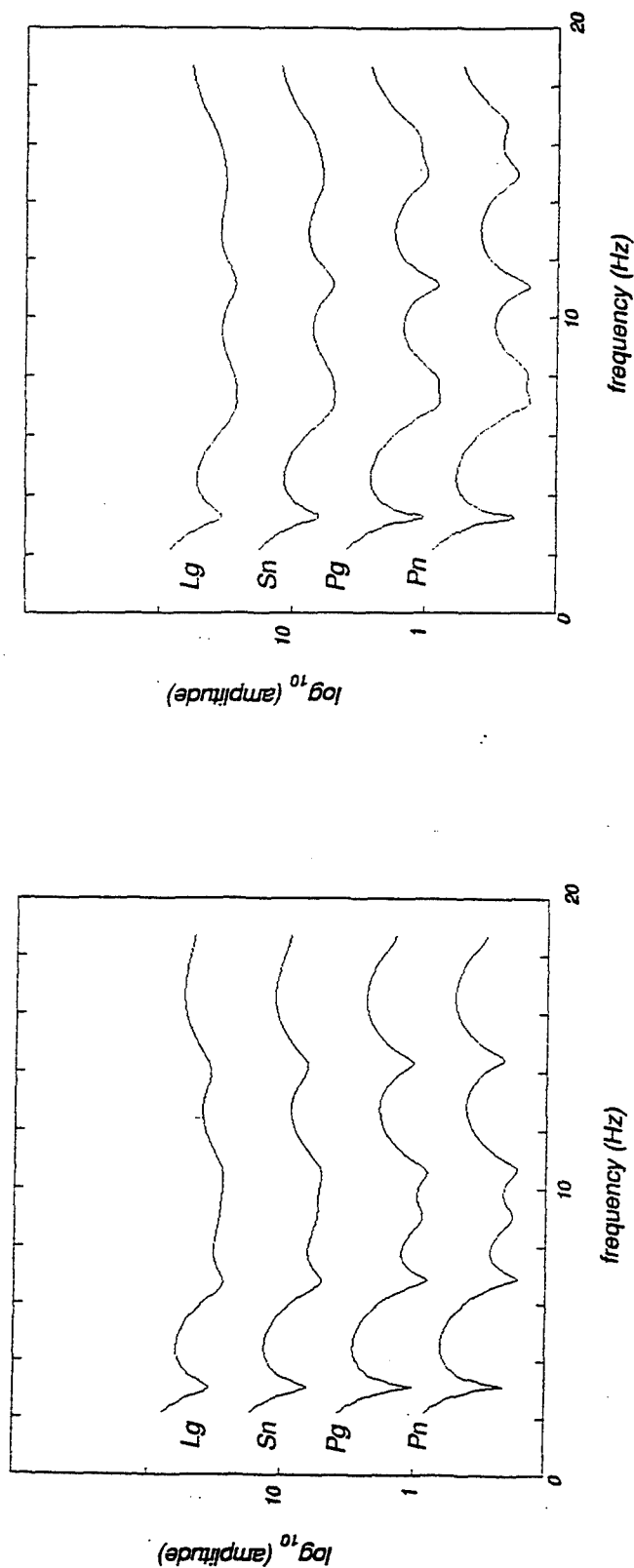
FIGURE 5. Simulated spectral modulation patterns for a 50 element areal shot array with row spacings of 10 m, 10 shots in a row spaced at 10 m. The intershot delays in each row are .01 seconds and the delay between rows is .05 seconds. All spectra show a diminution of modulation intensity from Pn to Lg, some of the modulation features show weak indications of small shifts. The left panel depicts spectra for the direction perpendicular to the rows, the right panel in the direction of the rows. The shooting sequences (of rows and columns respectively) move away from the observer. Shifts in features are weak or absent.

Automated Data Processing (ADP) Research and Development

Farid U. Dowla, Virgil N. Kohlhepp, and Richard R. Leach, Jr.

Earth Sciences Division, Lawrence Livermore National Laboratory

Abstract

Monitoring a comprehensive test ban treaty (CTBT) will require screening tens of thousands of seismic events each year. Reliable automated data analysis will be essential in keeping up with the continuous stream of events that a global monitoring network will detect. We are developing automated event location and identification algorithms by looking at the gaps and weaknesses in conventional ADP systems and by taking advantage of modern computational paradigms. Our research focus is on three areas: developing robust algorithms for signal feature extraction, integrating the analysis of critical measurements, and exploiting joint estimation techniques such as using data from acoustic, hydroacoustic, and seismic sensors. We identify several important problems for research and development; e.g., event location with approximate velocity models and event identification in the presence of outliers. We are employing both linear and nonlinear methods and advanced signal transform techniques to solve these event monitoring problems. Our goal is to increase event-interpretation throughput by employing the power and efficiency of modern computational techniques, and to improve the reliability of automated analysis by reducing the rates of false alarms and missed detections.

Key words: Automation, data fusion, event location, event identification, neural networks, self-organization, seismic networks, seismic arrays, signal processing, wavelets.

733

1. OBJECTIVES

Our primary objective is to develop efficient and reliable automated event location and identification algorithms. We are currently focusing on the problem of locating and identifying low-magnitude events. Only a small number of regional stations detect these events, but we must screen tens of thousands of such events each year. We emphasize three areas of research and development in the automatic processing of this data. First, how can we extract event features from full waveforms? Second, what is the best way to organize and integrate critical signal measurements? Finally, what improvements to seismic event detection can be realized by synergistic use of data from diverse sensors (e.g., seismic, hydroacoustic, infrasound, and satellite)? We must make progress on all these fronts to significantly improve the performance of the current monitoring systems in terms reduced rates of false alarms and missed detections.

2. PRELIMINARY RESEARCH RESULTS

2.1. Extraction of Features from Full Waveforms

2.1.1 Wavelet Analysis. The wavelet transform $W(a, \tau)$ of a signal, $s(t)$, such as a seismogram, is given by

$$W(a, \tau) = \frac{1}{\sqrt{a}} \int_{-\infty}^{\infty} s(t) \, h(\, [t - \tau]/a \,) \, dt,$$

where a represents the scale and τ time in the transform domain, and $h(t)$ is the analysis wavelet, which is localized in both time and frequency (Foufoula-Georgio and Kumar, 1994). It is well known that the most important features in a pattern are those that persist through different scales. Although computing the wavelet transform is somewhat similar to bandpass filtering, an appropriately designed wavelet brings out the concept of scale explicitly and it is particularly useful for transient analysis because of its constant-Q property. We have designed wavelets starting from real seismograms; Figure 1 shows example wavelet coefficients (in the transform domain) and bandpass filtering versions of a seismogram as a function of scale and time. The wavelet transform is an efficient representation of the seismogram and preserves the significant features in the waveform. We are developing noise-cancellation beamforming algorithms making use of this transform. The wavelet transform is an invertible transform meaning that the signal can be recovered perfectly from the wavelet coefficients. Note that unlike Fourier coefficients, wavelet coefficients preserve shape in the transform domain. Furthermore, while bandpass filtering represents each band of a N-point signal with another N-point signal, the discrete wavelet transform represents all scales with just one N-point set. Hence, the wavelet transform is more efficient than its corresponding filter bank representation.

2.1.2 High-Resolution Model Based Spectrograms. A spectrogram is simply a series of spectra computed by segmenting a long time series into many small and overlapping segments. We find that when the spectral estimation uses a high-resolution autoregressive model, spectrograms can play an important role in extracting the time-frequency features of the signal. The rapidly varying local features of the signal appear as functions of the frequency variable, and the slowly varying global trends of the signal appear as functions of the time variable. Finally, the large time-bandwidth product captured by a spectrogram helps in distinguishing the many different types of seismic events.

2.2 Organization and Integration of Signal Measurements

2.2.1 Event Identification with an Ill-Distributed Database. A rather stiff requirement on an ADP system is that it be able to detect and identify events from new source regions. This is a particularly difficult problem because we usually develop event identification systems using "recognition" or match-filtering techniques. In this section we discuss a solution to a slightly less difficult and related problem, where the number of explosions is much less than the number earthquakes in the training database, a realistic treaty-monitoring scenario.

Consider the problem of discriminating a nuclear explosion from an earthquake. Instead of attempting to solve a "binary" (i.e., earthquake=0, explosion=1) discrimination problem, suppose

we design an algorithm that can classify events by their various features; i.e., events are distinguished by depth, faulting mechanism, magnitude, and the like. We find that this type of n-ary discrimination algorithm is quite useful for outlier identification and might indeed be able to handle "new" or "unseen" event types because the projection of the "new" event ought to be poor on all the classes of events the method is able to recognize. A binary discrimination algorithm is forced to ignore differences that might exist among the events in a particular class. This results in its inability to distinguish outliers. Because there are many different types of earthquakes and explosions, we first employ self-organization of all the events in the database. This is followed by a match-filtering technique.

As shown in Figure 2-a, the identification system is a two-stage process. First, we allow all events in the database to self-organize into different cluster groups according to the similarity of the spectrograms. We use the self-organizing neural network to solve this clustering problem, although other clustering algorithms might work just as well. Members of some of these cluster groups will be purely earthquakes while other clusters might consist of just explosions; on the other hand, some clusters will consist of a mixture of earthquakes and explosions. In the second stage, we introduce a test event. If this test event has low correlation (poor match) with all cluster centroids or means, that event is an outlier. If the test event falls into one of the homogenous cluster groups with high correlation, there is no ambiguity about its class type. However, if a new event falls into a mixed class, we use only the members of that class and their identities to classify the test event. For example, the hierarchical clustering technique used by Israelsson (1991) might be quite appropriate at this stage because the number of events in any one cluster is reduced after the process of self-organization. We have completed a case study using earthquakes and explosion data from the NTS area. We used bootstrapping techniques and obtained results as function of the number of explosions in the training set. The results, shown in Figure 2-b, compare favorably against a standard Pg/Lg receiver operating curve.

2.2.2. Numerical Optimization and Global Search Techniques. The application of robust and fast numerical optimization techniques is essential with large volumes of high-dimensional data, a problem we face with seismic ADP. We developed optimization algorithms (Johansson et al., 1992; Altschuler et al., 1994) for nonlinear least-squares error minimization and for constrained global optimization techniques. We have successfully used these algorithms in many seismic event identification problems including discrimination and yield estimation (Dowla and Rogers, 1995). These methods will also be useful for event location applications, since location problems are solved by a global search method (Shearer, 1994).

2.3 Synergistic Use of Seismic, Acoustic, and Hydroacoustic Data

To improve our ability to verify adherence to treaties limiting or banning nuclear tests, we may need to combine seismic data with data from other types of sensors. Event identification that combines data from a diverse range of sensor types, such as seismic, hydroacoustic, infrasound, optical, or acoustic sensors, has been discussed recently. We are exploring the possibility of synergistic use of seismic, acoustic, and hydroacoustic data in event location and identification.

2.3.1 Acoustic and Seismic. One area of concern is the threat of clandestine nuclear testing under the guise of a normally operating mine. An inability to distinguish a nuclear test from a typical mining blast would constitute a serious problem in treaty monitoring. A potentially powerful approach to resolving these issues is to supplement seismic monitoring with acoustic analysis of mining blasts. Acoustic signals might be more noisy at low frequencies; for example, wind and storms often generate low frequency noise. However, for short distances, acoustic signals do not suffer from the strong attenuation of high frequency propagation of seismic signals. Combining both acoustic and seismic signals could improve the monitoring capability at a suspect mine. In addition, the cost of complementing seismic with acoustic monitoring is relatively low.

We are beginning to study seismic and acoustic signals recorded from two mining events that occurred in the Newmont Gold Company (NGC) gold quarry near Carlin, Nevada. A map of the quarry is shown in Figure 3. Example acoustic and seismic spectrograms are shown in Figures 4-a and 4-b.

Although seismic spectrogram analysis often works well in classifying mining events, there are instances for which this method becomes inadequate. One example is when ripple-fired, time-delayed detonations occur very close to each other (i.e., when mining operations use very short firing delays, on the order of 15 ms or so). These short delays result in higher frequencies at which spectral scalloping is observed. Because high-frequency signals are strongly attenuated, it becomes more and more difficult to identify the scalloping in the spectra of the recorded data. Depending on the geology, significant high frequency attenuation may occur even over short distances. In this situation, time-frequency features in the acoustic signal might be useful for source identification. In summary, ripple fire characteristics appear to be quite prominent in the spectrogram of the acoustic records and we think that the near source acoustic records are useful in the monitoring of mine shots.

2.3.2 Hydroacoustic and Seismic. Because wave propagation velocities are quite different for hydroacoustic and seismic signals, event location based on travel time analysis can be significantly more robust and accurate when travel time data are combined from the two types of signals. We are developing a database containing recordings from both hydroacoustic and seismic sensors for the same events. An example of a seismic event recorded using both types of sensors is shown in Figure 5. Since the source is the same for the two waveforms, similarities and differences between the two data can be useful in source characterization.

3. RECOMMENDATIONS AND FUTURE PLANS

Accurate event location for small magnitude events is a high priority problem for LLNL ADP research and development efforts. Some of the problems on which we are focusing are outlined in the following.

Given the fact that regional velocity models are not precisely known, we must develop location algorithms that are less sensitive to propagation models. While an *approximate* event hypocenter can be determined quite rapidly with a network of stations, *accurate* determination of a hypocenter is nontrivial (Herrmann, 1982; Veith, 1985; Palvis, 1986; Thurber, 1985; Wirth et al., 1976; Flinn 1965). Given arrivals at a number of stations and an approximate event location, the determination of the hypocenter estimate might be improved by judicial use of network travel time data and by extracting selected events from the database and performing station corrections based only on selected events and on the new event, thus minimizing uncertainties in event location. Fast global search algorithms must be developed both to select the events and to minimize arrival time residuals in determining event location. The feasibility of improving the velocity model while solving for the event location must be explored. Arrival time information from the secondary phases and bearing estimates from arrays and three-component stations should be incorporated into the algorithm. Finally, depth estimation with an optimal choice of stations might prove to be useful.

While location by waveform correlation has been proposed by many authors (Harris, 1991; Israelsson, 1990; Riviere-Barber, 1993; Thorbjarnardottir, 1987), there does not exist a robust algorithm that uses both waveform correlation and travel-time onset analysis and that converges to a consistent solution. Somewhat similar to the PMCC method (Cansi, 1995), it might be possible to systematically use stations of the network and to use advanced correlation techniques (Park et al., 1987; Duckworth, 1987) on full waveforms for improved location. We plan to explore the use of various error norms for outlier removal. In addressing the correlation estimation problem, the distance of the events from the stations makes the normalization issue an important one; i.e., normalized correlation (Neidell and Taner, 1971). Correlation as a function of frequency and scale (or wavelets) must to be studied.

Although a highly challenging problem, the location of events in an earthquake swarm or during mine related activities is important in CTBT monitoring. Very few studies have addressed this problem in depth in spite of the fact that treaty violations could easily go undetected if a test were performed in the midst of earthquake aftershocks or during quarry blasts and mine collapses. Joint use of bearing, amplitude, and travel time data might be necessary to develop location algorithms will exhibit robust performance.

Finally, use of reliable ground-truth data is important in developing better algorithms. For example, the CSS ground-truth database (Grant et al., 1993) can be of great use in this area. This database is a collection of regional events that have been reviewed, and some of the facts about the events (event type, location, depth, and origin time) are known with a high degree of confidence.

ACKNOWLEDGMENTS

REFERENCES

Altschuler, E., T. Williams, E. Ratner, F. Dowla, and F. Wooten (1994). Method of constrained global optimization. Physical Review Letters, Vol. 72, No. 17, pp. 2671-2674.

Cansi, Y. (1995). An automatic seismic event processing for detection and location: the PMCC method. Geophysical Research Letters, Vol. 22, No. 9, pp. 1021-1024.

Dowla, F. and L. Rogers (1995). Solving Problems in Environmental Engineering and Geosciences with Artificial Neural Networks, in press.

Duckworth, G. L. (1987). A robust algorithm for tracking of drifting acoustic arrays in the Arctic. Proceedings of the 21st Asilomar Conference on Signals, Systems, & Computers, IEEE Press, pp. 103-108.

Flinn, E. A. (1965). Confidence regions and error determinations for seismic event location. Reviews of Geophysics, Vol. 3, No. 1, pp. 157-185.

Foufoula-Georgio, E. and P. Kumar (Eds.) (1994). Wavelets in Geophysics, Academic Press, San Diego.

Grant, L., J. Coyne, and F. Ryall (1993). CSS Ground-Truth Database: Version 1 Handbook. Technical Report C93-05, SAIC, Arlington, VA.

Harris, D. B. and F. U. Dowla (1986). Seismic arrays for treaty verification. Energy and Technology Review, pp. 8-19.

Harris, D. B. (1991). A waveform correlation method for identifying quarry explosions. Bull. Seism. Soc. Am., Vol. 81, No. 6, pp. 2395-2418.

Herrmann, R. B. (1982). Digital processing of regional network data. Bull. Seism. Soc. Am., Vol. 72, No. 6, pp. S261-S276.

Hertz, H., Al Krough, and R. G. Palmer (1991). Introduction to the Theory of Neural Computation. Addison-Wesley Publishing Company, Redwood City, CA.

Israelsson, H. (1990). Correlation of waveforms from closely spaced regional events. Bull. Seism. Soc. Am., Vol. 80, No. 6, pp. 2177-2193.

Johansson, E., F. Dowla, and D. Goodman (1992). Backpropagation learning for multilayer feedforward neural networks using the conjugate gradient method. International Journal of Neural Systems, Vol. 2, No. 4, pp. 291-301.

Neidell, N. S. and M. T. Taner (1971). Semblance and other coherency measures for multichannel data. Geophysics, Vol. 36, No. 3, pp. 482-497.

Park, J., C. R. Lindberg, and F. L. Vernon (1987). Multitaper spectral analysis of high-frequency seismograms. Journal of Geophysical Research, Vol. 92, No. B12, pp. 12675-12684.

Pavlis, G. L. (1986). Appraising earthquake hypocenter location errors: a complete, practical approach for single-event locations. Bull. Seism. Soc. Am. Vol. 76, No. 6, pp. 1699-1717.

Riviere-Barbier, F. and L. T. Grant (1993). Identification and location of closely spaced mining events. Bull. Seism. Soc. Am., Vol. 83, No. 5, pp. 1527-1546.

Shearer, P. M. (1994). Global seismic event detection using a matched filter on long-period seismograms. Journal of Geophysical Research, Vol. 99, No. B7, pp. 13713-13725.

Thorbjarnardottir, B. S. and J. C. Pechmann (1987). Constraints on relative earthquake locations from cross-correlation of waveforms. Bull. Seism. Soc. Am., Vol. 77, No. 5, pp. 1626-1634.

Thurber, C. H. (1985). Nonlinear earthquake location: theory and examples. Bull. Seism. Soc. Am., Vol. 75, No. 3, pp. 779-790.

Veith, K. F. (1975). Refined hypocenters and accurate reliability estimates. Bull. Seism. Soc. Am., Vol. 65, No. 5, pp. 1199-1222.

Wirth, M. H., R. R. Blanford, and R. H. Shumway (1976). Automatic seismic array and network detection. Bull. Seism. Soc. Am., Vol. 66, No. 4, pp. 1375-1380.
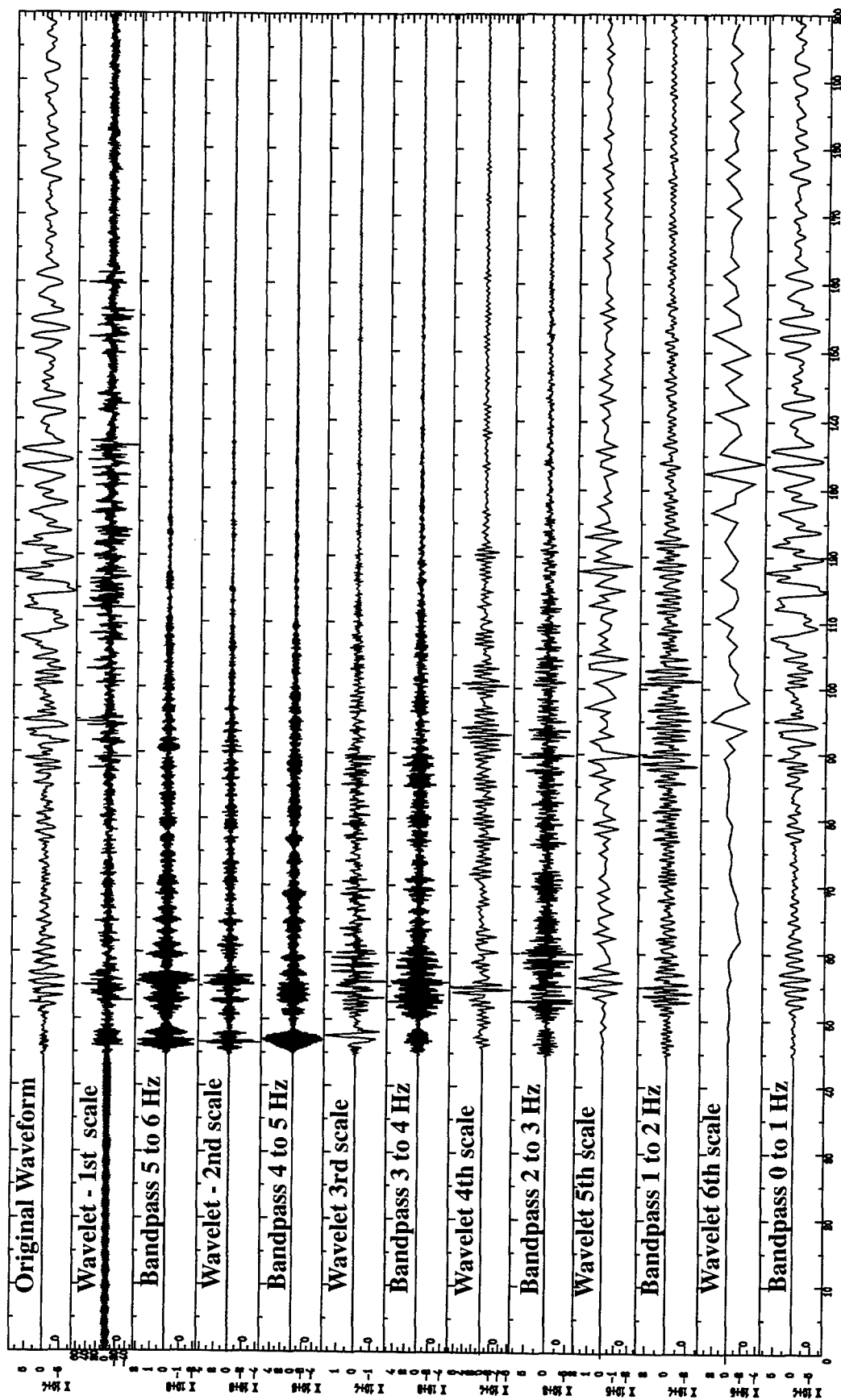
Figure 1. Comparison of wavelet coefficients and bandpass filtered seismograms of an explosion record at Landers. The top signal is the orginal raw waveform. The bottom traces are alternate wavelet and bandpass representations at different scales and frequencies. Since the relation between scale and frequency is nonlinear, it is difficult to make direct comparison of the two techniques.

(a) Method

(b) ROC at Kanab

(c) ROC at Mina
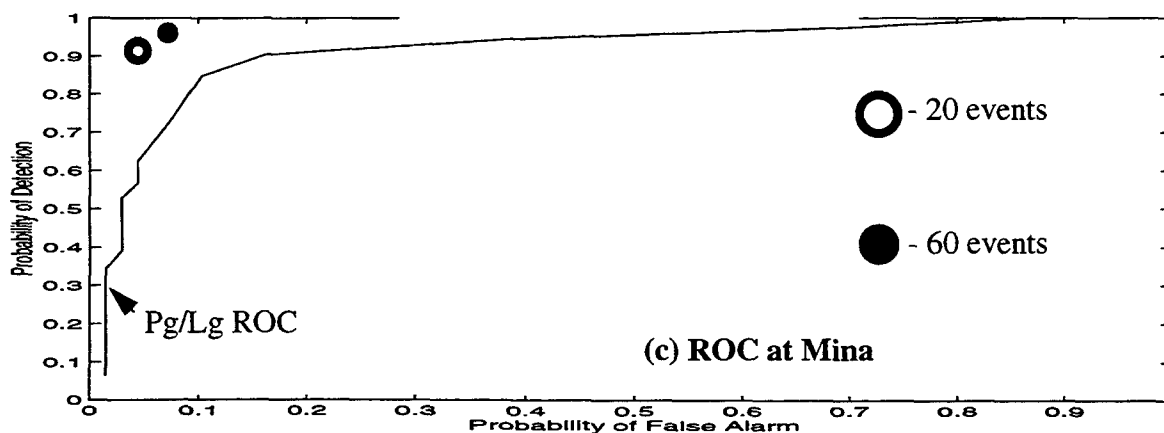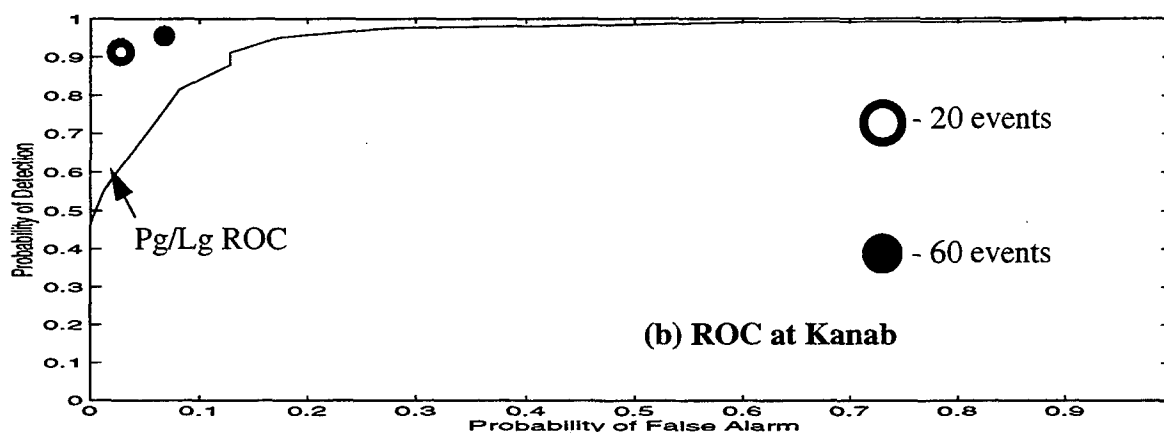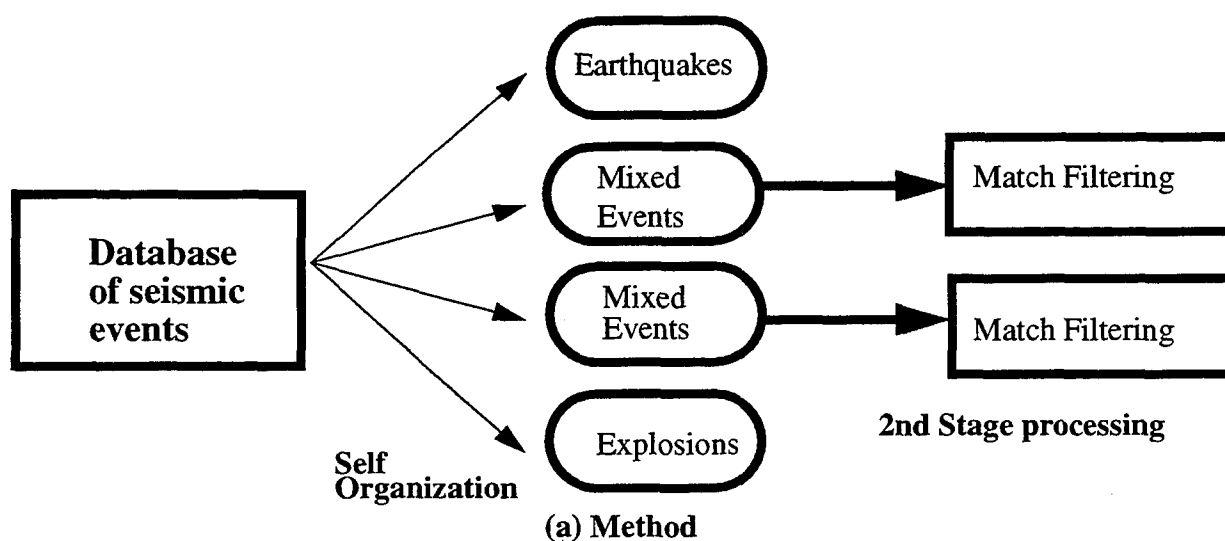
Figure 2. (a) The event discrimination algorithm described in the text is useful when there are many more earthquakes than explosions in the training database. (b) Performance comparison between the receiver operating characteristics (ROC) of a Pg/Lg discriminant and the self-organizing neural network with different number of explosions in the database at Kanab. (c) Same as (b) for the station Mina.

739
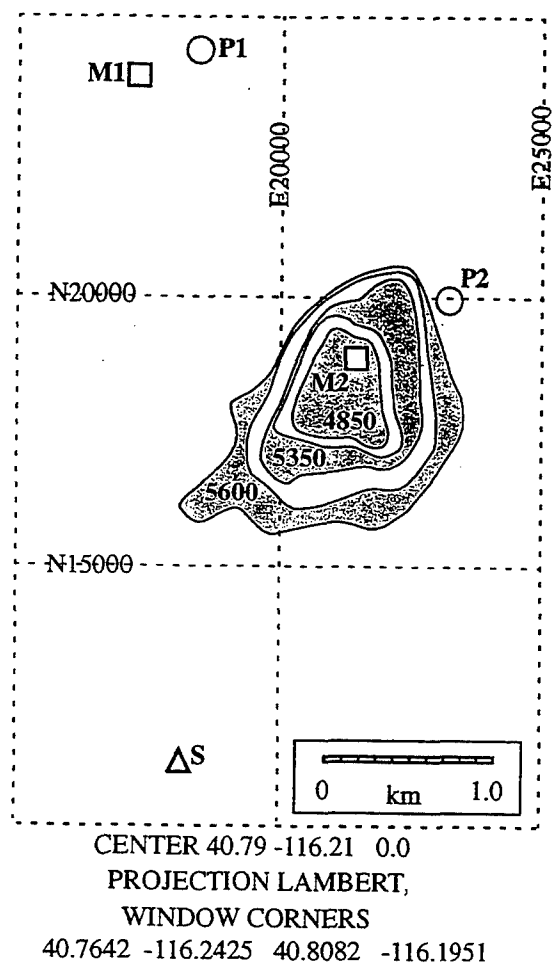
(a)
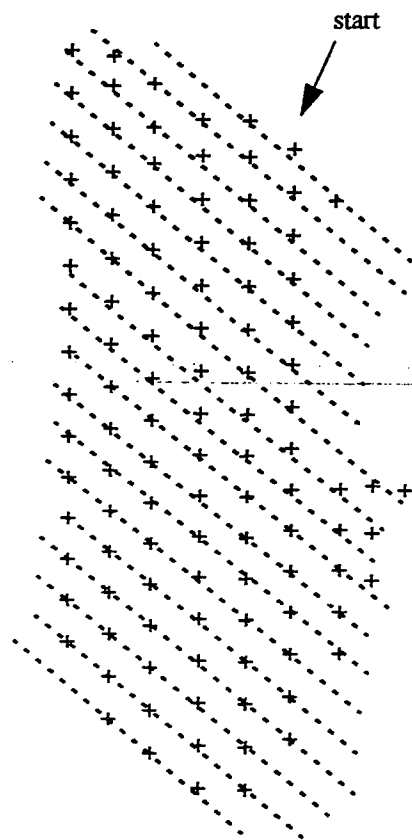
Firing pattern example

(b)

Figure 3. Map of the mining events recorded at the NGC gold quarry (left) showing the location of the April 14, 1995, explosion (M1) and the April 20, 1995, explosion (M2). Acoustic signals were recorded at P1 and P2 at a distance of about 0.3 km for events M1 and M2, respectively. Seismic signals were recorded at S for M1 and M2 at distances of 2.64 and 3.96 km. The shaded regions are the working levels in the Gold Quarry pit, which are at 4850-, 5350-, and 5600-ft elevations (above sea level). An example (not M1 or M2) firing pattern (right) shows the rows (dotted lines) and the individual explosion sites (+s). Delays between row detonations were approximately 50 ms for M1 and 65 ms for M2. Hole spacing for the individual explosions were 16x16 ft for M1 and 18x18 ft for M2.
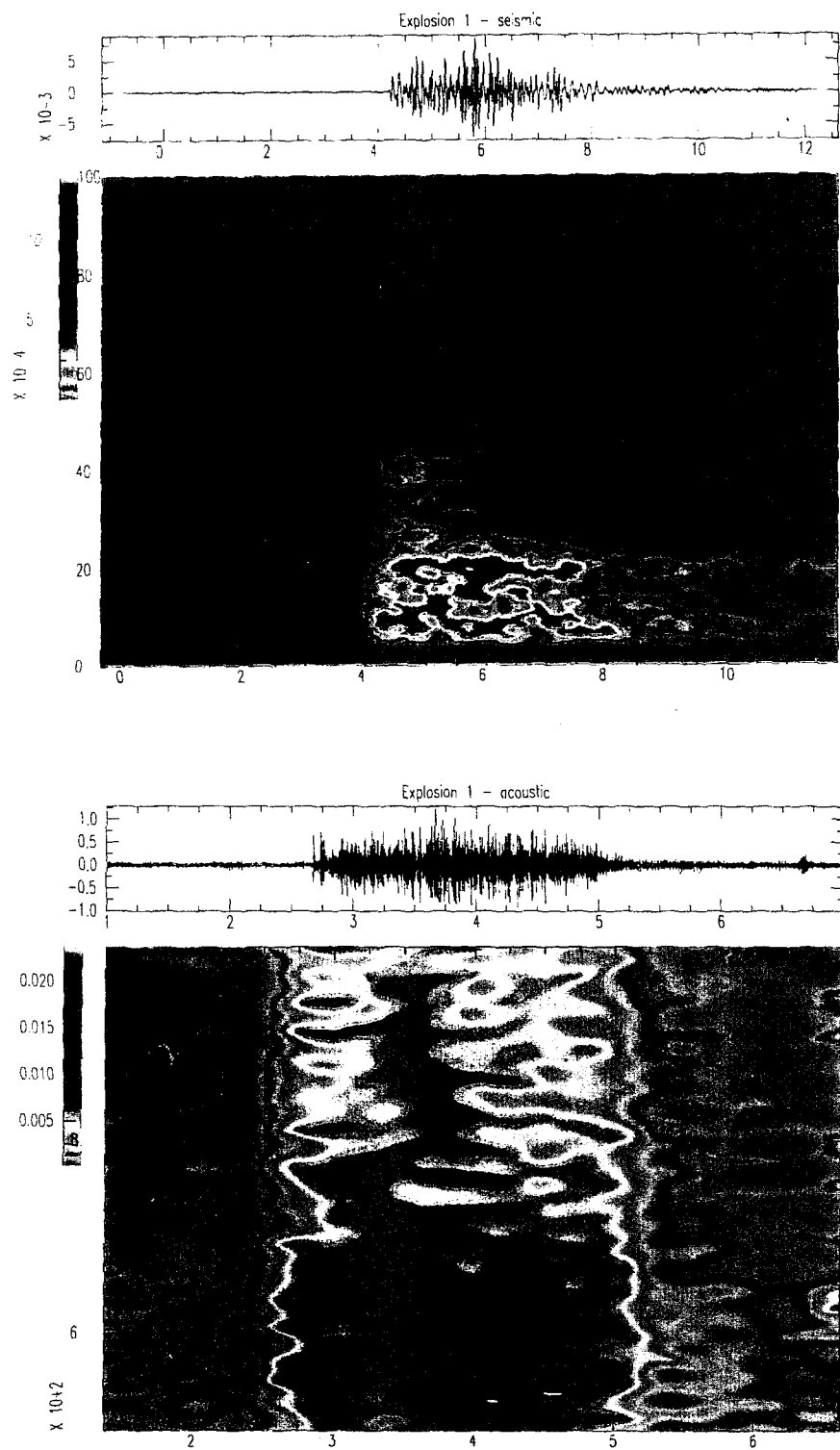
Figure 4. M1 mining explosion event showing filtered time series and resulting spectrogram for seismic signal (a) and for acoustic signal (b). All time series signals were bandpass filtered with a fourth order Butterworth filter. The seismic signal was bandpass limited from 1 to 100 Hz. The acoustic signal was bandpass limited from 500 to 1000 Hz.

741
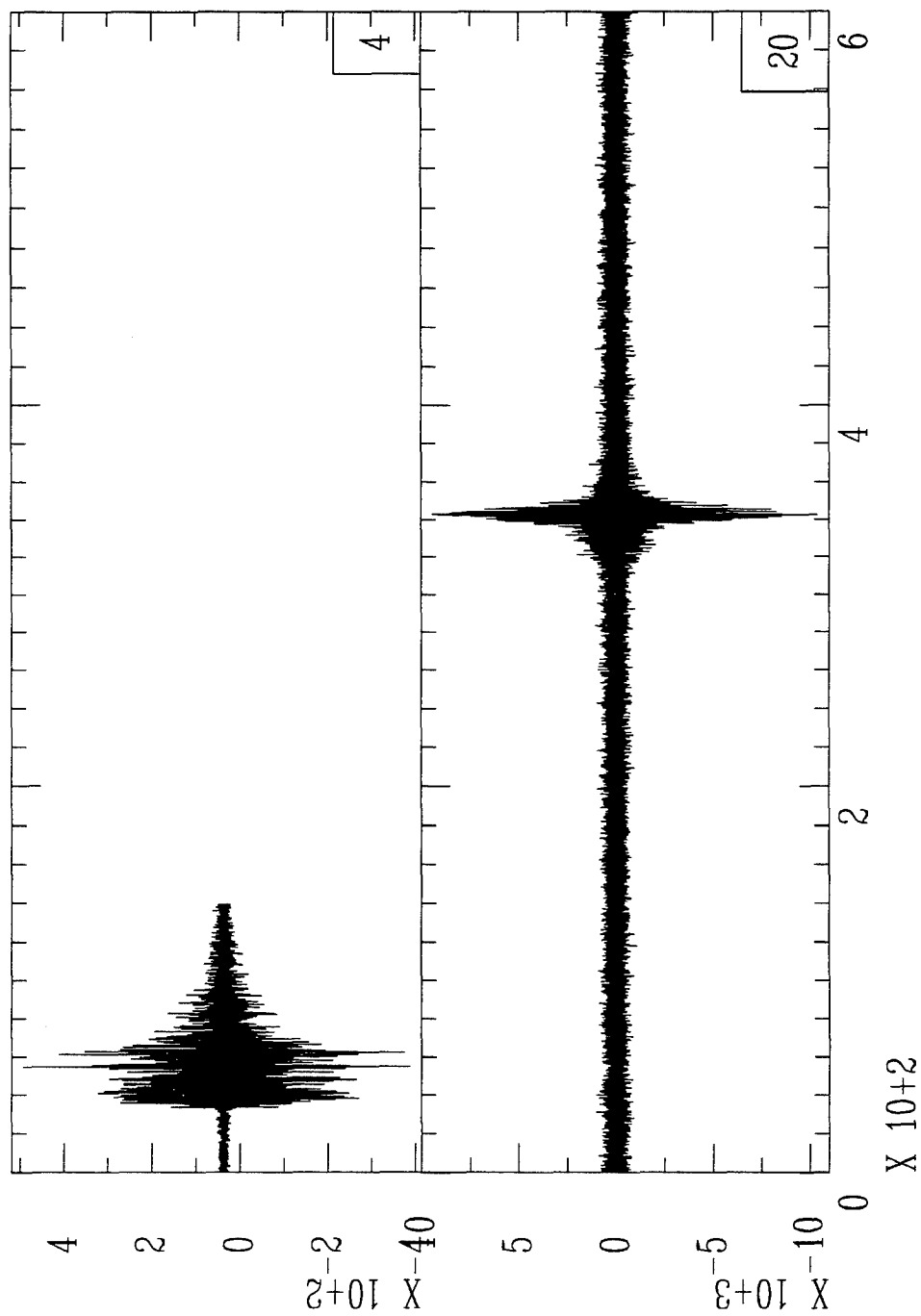
Figure 5. A qualitative comparison of seismic (top) and hydroacoustic (bottom) records for the same seismic event off the coast of southern California that occurred in 1994.

Evaluation of the Performance of Broadband Networks and Short Period Arrays in Global Monitoring

Douglas Dreger, Michael Pasyanos, and Barbara Romanowicz

University of California, Berkeley, Seismographic Station

Abstract

This study is a collaborative effort between the UC Berkeley Seismographic Station and the Lawrence Livermore National Laboratory to examine the performance of various seismographic systems in the regional monitoring of a Comprehensive Test Ban Treaty. Central California, with its abundant seismicity, regional broadband network (UCB BDSN), and dense short-period network (USGS NCSN) provides an ideal test-bed for the estimation of detection and location thresholds, source depth, and the seismic moment tensor of small events using sparse broadband network configurations. The objective is to investigate the importance of regional broadband stations in global monitoring. Together, the BDSN and NCSN networks provide the necessary data to construct a control catalog of very high quality event locations to a lower magnitude of approximately 1.8. We compare, against the control, catalogs obtained by inverting only BDSN data (both P only, and P and S waves), subsets of BDSN to test very sparse network configurations, as well as event detections and locations obtained from two regional short-period arrays located in Lajitas, TX and Pinedale, WY. In this manner we determine the detection and location threshold of each system and assess the resolving power of each. In particular, source depth resolution is investigated in the context of a traditional first motion location scheme, as well as the use of broadband waveforms recorded at regional distances. A component of this study will be the examination of path calibration to improve both source depth and seismic moment tensor determinations for small events recorded at regional distances. Improvements to the existing location algorithms will be examined to better constrain the BDSN and sparse network solutions. A goal of this research is to demonstrate how well a region may be monitored with a sparse broadband network given an optimal source-station geometry such as the case in central California. Hence this is a best case scenario. Another goal is to evaluate the performance of very sparse network configurations (using subsets of BDSN) such as will be the case in the monitoring of other regions.

Keywords: Detection, Location, Source Depth, Path Calibration

OBJECTIVE

The objectives of this study are related to better understanding the importance of broadband stations in global and regional monitoring. The primary objective is to investigate sparse broadband network and regional short-period array capabilities in the detection and location of seismic events in a region with very good control (Figure 1). One component of this study will provide an estimation of detection threshold for a best case scenario. The performance of the full compliment of BDSN stations, as well as subsets of stations to analyze the performance of very sparse configurations, will be examined. The performance of short-period arrays (TXAR and PDAR) in monitoring the same region are also compared. TXAR and PDAR are both located between 8° to 20° from central California (depending upon event location) and the analysis of these data will be representative of regional monitoring capabilities of these systems. The resolution of source depth from both traditional location techniques as well as full waveform techniques is also examined. Finally, path calibration to improve both source depth estimates and seismic moment tensor determinations for small events is investigated with the goal of developing procedures which may be ported to other regions of interest.

Research Plan and Preliminary Results

The research plan involves the construction of a number of event catalogs to assess the detection and location thresholds for various seismographic systems in the monitoring of central California seismicity. A control catalog of very high quality locations will be constructed for M>=3 events using BDSN P and S picks and the P picks from the NCSN network (Figure 1). The BDSN picks used in the control catalog are all human reviewed. The control catalog will be augmented with 1.8<M<3.0 events using only the NCSN phase picks. Test catalogs will be constructed from BDSN P only, BDSN P and S, and the Lajitas and Pinedale data set. We anticipate that the initial BDSN only locations will be rather poor depending upon event location and size, as discussed below. To improve the BDSN locations other information such as azimuth (obtained by vectoring the P-wave) will be incorporated in the location methodologies and compared against the control.

Although this project has just begun and we are still in the process of compiling the various catalogs, the following examples illustrate the type of information that we will use in the assessment of the performance of sparse broadband systems in regional monitoring. Figure 2 compares 8 solutions for a Mw4.0 event located near San Benito, CA (EVT_A, Figure 1). This particular earthquake was not reported in the GSETT-3 REB bulletin.

We compare the solutions in terms of origin time, magnitude, location and source depth. Solution 1 represents the control location obtained from hand timed P and S phases of the BDSN network and the automated P picks of the NCSN network. Readings which gave large residuals were culled from the phase file. Solution 2 is the location obtained from all of the available readings. In this case the two are very similar because the location of the event within both BDSN and NCSN provides a very good constraint on the location parameters. Solutions 3 and 4 are the culled and unculled BDSN P wave only inversions. Solutions 5 and 6 are the culled and unculled BDSN P and S wave inversions. Again in this case the culled inversions result in a relatively robust solutions and the unculled inversions show both the greatest uncertainty and mislocation. This implies that the inclusion of one or more bad picks in a sparse data set can lead to relatively large mislocations and location uncertainties. Solutions 7 and 8 are automated inversion results using BDSN P and NCSN, and BDSN P

only, respectively. Comparing 3 and 8 reveals that the human reviewed picks give both lower mislocation error and generally lower uncertainties. For this particular event the individual locations all fall within a circle with a 10 km diameter. Source depth is reasonably well constrained by inversions 1, 2, 3, and 5.

Figure 3 compares 7 solutions for a Mw4.1 event located near Quincy, CA (EVT_B, Figure 1). This event was also not reported in the GSETT-3 REB. As in Figure 2 the solutions are compared in terms of event origin time, magnitude, location and source depth. The solution numbers represent the same inversions that were performed in Figure 2 with the exception that solution 7 represents the automated solution using only raw BDSN P picks. The two most striking differences between Figures 2 and 3 are the magnitude of the mislocation errors and that depth is relatively poorly constrained for the Quincy event. Both result from the lack of close stations. In fact for the P wave only calculations, since the closest broadband station is 74 km away, the algorithm we use does not attempt to solve for depth and it is set to 5 km. When S waves are included the algorithm attempts to solve for source depth, however the uncertainties can be large.

Figure 4a illustrates the automated moment tensor (see Pasyanos et al., 1995) results for the Quincy event using the three closest BDSN stations in the frequency band from 0.02 to 0.05 Hz. This result is for a best fit depth of 11 km. The Green's functions in this calculation are computed for depth intervals of 3 km and therefore the depth resolution remains relatively poor. It is possible to use short-period regional phases as source depth indicators (e.g. Dreger and Helmberger, 1991, 1993; Zhao and Helmberger, 1994). Phases such as sPmP and sSmS etc. are examples of depth indicators at regional distances. It is possible to find other depth sensitive phases such as the SP free surface defraction for example. As Figure 4b illustrates, the SP phase is observed on the radial and vertical components of displacement recorded at ORV (74 km SW). Figure 4b shows that this particular phase is strongly source depth dependent, and following the assumption that the velocity structure used to compute the Green's functions is a reasonable approximation, it is possible to fine tune the depth to between 9 to 10 km.

CONCLUSIONS AND FUTURE PLANS

We have presented examples of the analysis that we intend to perform on 1993-present seismicity in central California. Our immediate plans are to compile the control and various test catalogs of past seismicity and to install the software necessary to update the catalogs with current seismicity. We have shown that sparse network solutions can have mislocations of several to tens of kilometers. It is anticipated that the very sparse calculations that will be performed will have initially poor results. We will therefore investigate modifications to our location routines to improve sparse network locations. One improvement which appears to be promising is the inclusion of azimuthal information contained in the P-wave. Source depth was also prone to large uncertainty, however utilizing secondary depth sensitive phases leads to improved source depth estimates. Whether or not the mislocation errors are acceptable depends upon the individual monitoring situations. The omission of both the Mw4.0 San Benito and Mw4.1 Quincy events from the GSETT-3 REB illustrates the need for regional broadband stations particularly in the monitoring of small events.

In conclusion, the results of this study are expected to provide important bounds on how well a region may be monitored with a relatively sparse broadband network. That is we will establish minimum detection and location thresholds for solutions using 1) the full compliment of BDSN stations, 2) very sparse BDSN network configurations, and 3) the Lajitas and Pinedale arrays.

REFERENCES

Dreger, D. S., and D. V. Helmberger, Source Parameters of the Sierra Madre Earthquake from Regional and Local Body Waves, *Geophys. Res. Lett.*,, 18, 2015-2018, 1991.

Dreger, D. S. and D. V. Helmberger, Determination of Source Parameters at Regional Distances with Single Station or Sparse Network Data, *J. Geophys. Res., 98,* 8107-8125, 1993.

Gee, L., D. Neuhauser, D. Dreger, M. Pasyanos, B. Romanowicz and R. Uhrhammer, The Rapid Earthquake Data Integration System, *submitted to Bull. Seism. Soc. Am.*, 1995.

Pasyanos, M. E., D. S. Dreger, and B. Romanowicz, Towards Realtime Determination of Regional Moment Tensors, *submitted to Bull. Seism. Soc. Am.*, 1995.

Zhao, L. S., and D. V. Helmberger, Source Estimation from Broadband Regional Seismograms, *Bull. Seism. Soc. Am., 84,* 91-104, 1994.
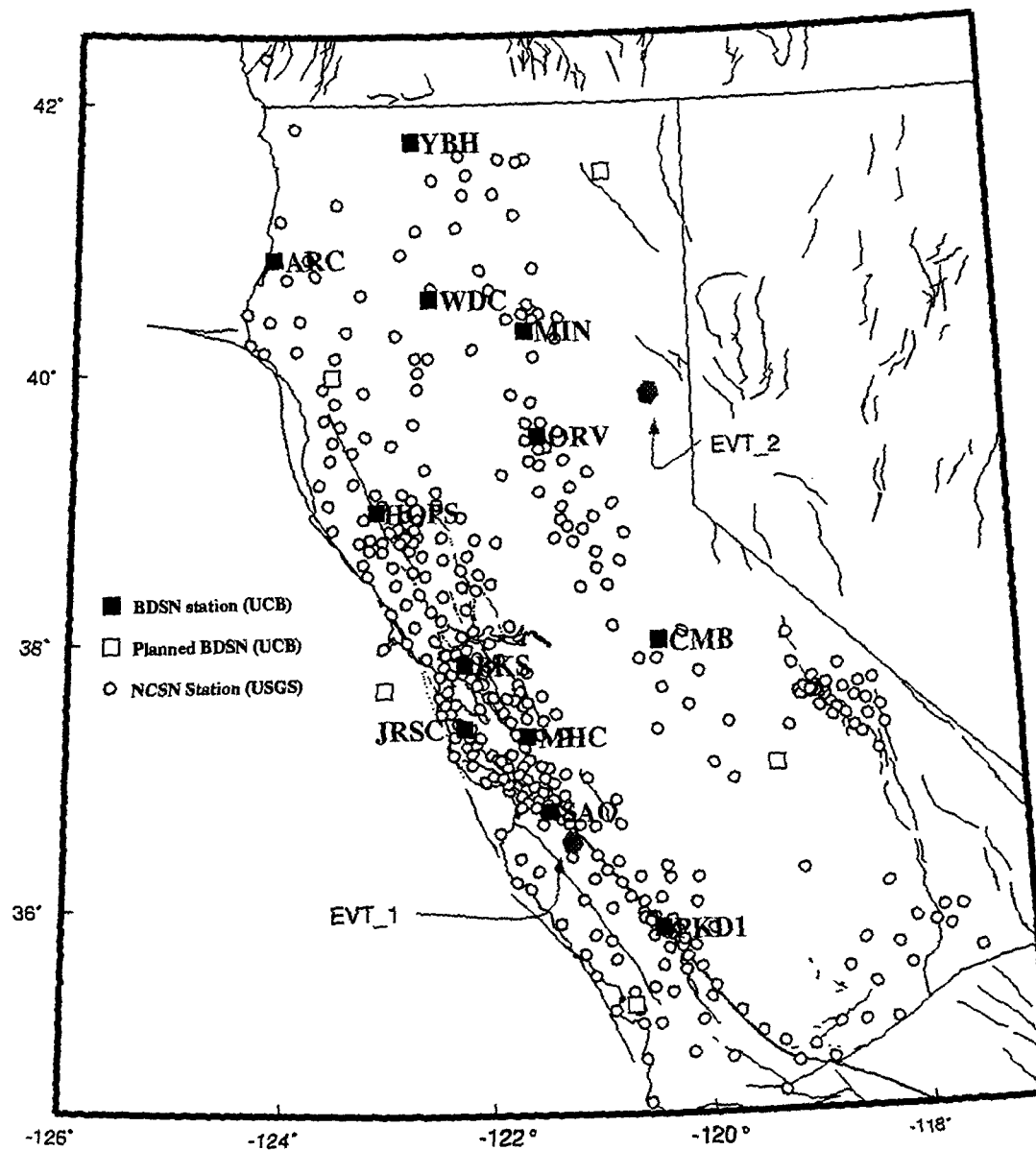
Figure 1. Map showing the locations of BDSN and NCSN stations. Two events discussed in detail in the text are labeled.

Figure 2. Comparison of event origin time (s), magnitude (ML), epicentral location and source depth for a number of different inversions. Inversion 1 refers to the control location obtained from human reviewed BDSN P and S and NCSN P phase picks. Stations with large residuals have been culled. Inversion 2 is the same as 1 except all of the data was used. Inversions 3 and 4 are BDSN P only inversions with large residual stations removed, and all of the available stations included, respectively. Inversions 5 and 6 are the same as 3 and 4 except that S waves were included. Inversions 7 and 8 are automated REDI (Gee et al., 1995) solutions using BDSN and NCSN autopicks.

Comparison of event locations
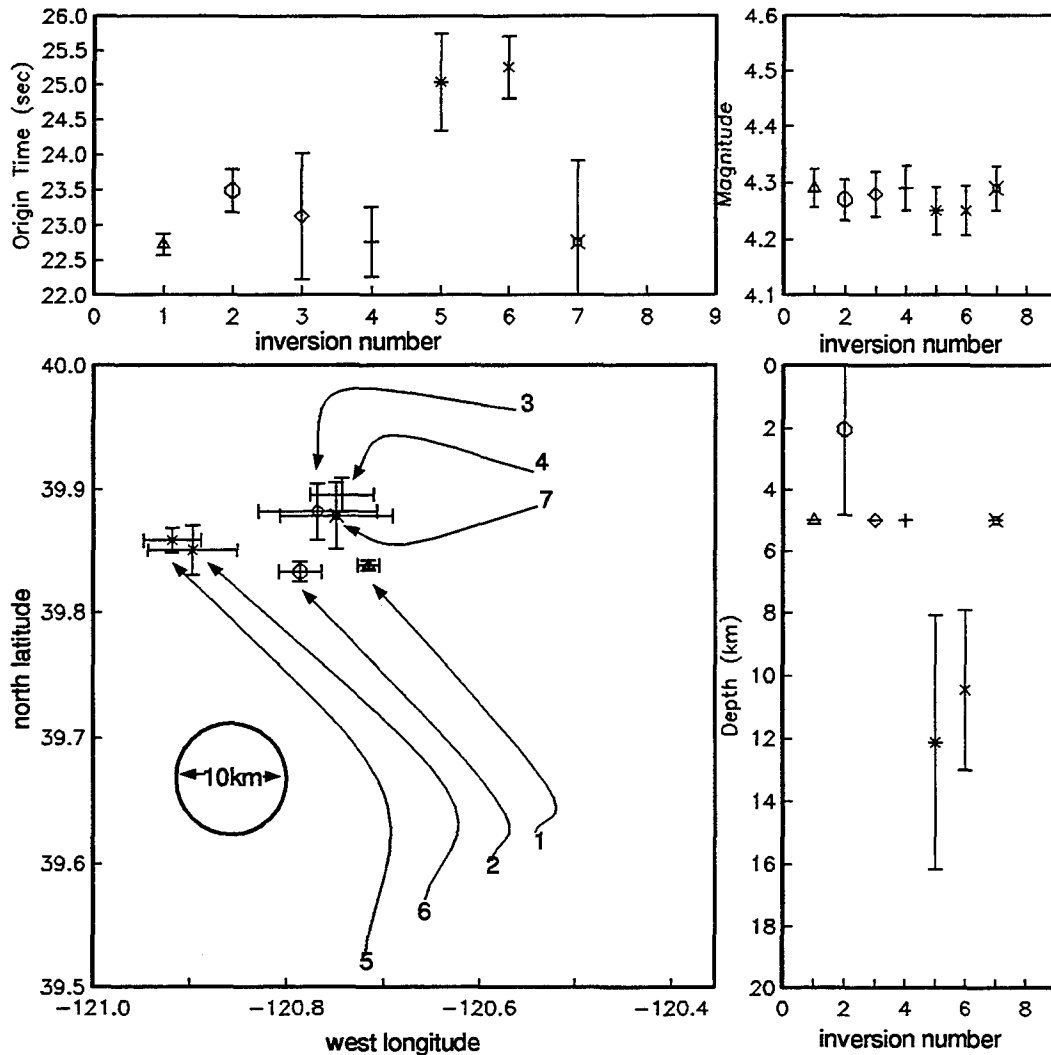
Figure 3. Comparison of event origin time (s), magnitude (ML), epicentral location and source depth for a number of different inversions. Inversion 1 refers to the control location obtained from human reviewed BDSN P and S and NCSN P phase picks. Stations with large residuals have been culled. Inversion 2 is the same as 1 except all of the data was used. Inversions 3 and 4 are BDSN P only inversions with large residual stations removed, and all of the available stations included, respectively. Inversions 5 and 6 are the same as 3 and 4 except that S waves were included. Inversion 7 is an automated REDI (Gee et al., 1995) solution using BDSN and NCSN autopicks.
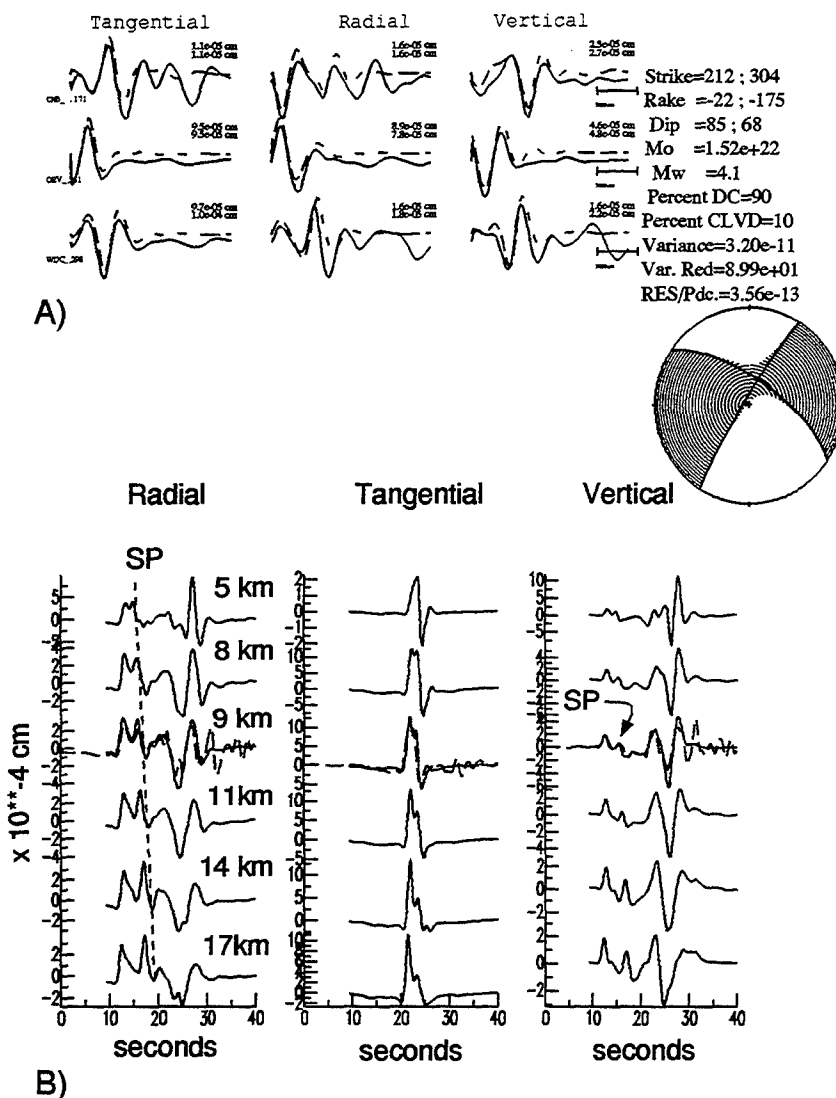
Figure 4. a) Moment tensor inversion of three-component displacement data (0.02 to 0.05 Hz) recorded at the three closest stations. The data are solid traces and the synthetics are dashed. The best fitting source depth was 11 km. b) Comparison of broadband (0.01 to 0.5 Hz) displacement synthetics (solid) with data recorded at the ORV station (dashed). The dashed line highlights the moveout of the SP phase.

CTBT INTEGRATED VERIFICATION SYSTEM EVALUATION MODEL (IVSEM)

Mike Edenburn, Senior Member of Technical Staff

and

Larry S. Walker, Manager, Seismic Verification

Sandia National Laboratories

DOE/NN-20, DOE/NN-40

ABSTRACT .

The CTBT Integrated Verification System Evaluation Model (IVSEM) is being developed to provide a tool for evaluation of the relative utility of candidate monitoring system concepts, for exploring opportunities for synergy among monitoring technologies, and to help define needed technology thrusts. The goal is to develop an affordable, portable, and easy to use and understand model which is flexible enough and fast enough to allow for near real time evaluation of the relative effectiveness of a wide spectrum of user-definable monitoring and test configurations. The emphasis is on moderate fidelity modeling of the capabilities of an integrated monitoring system which combines multiple sensor types, as opposed to high fidelity monitoring of the individual sensor types (breadth versus depth). In its current form, the model includes seismic, hydroacoustic, infrasound, and radionuclide sensors.and provides estimates of the detection effectiveness of a user-defined monitoring configuration against a user-defined test configuration (yield, location, altitude or depth and decoupling factor). Future efforts include incorporation of estimates of location and identification effectiveness plus validation of the model against more detailed single phenomenology models or experimental data. The model runs in near real-time on a PC or workstation platform.

OBJECTIVES:

The goal is to develop an affordable, portable, easy to use and understand model which is flexible enough and fast enough to allow for near real time evaluation of the relative effectiveness of a wide spectrum of user-definable CTBT monitoring and test configurations. It is envisioned that the model will be used to evaluate the relative utility of candidate monitoring system concepts, for exploring opportunities for synergy among monitoring technologies, and to help define needed technology research thrusts.

PRELIMINARY RESEARCH RESULTS:

Fig 1 depicts the major inputs to the model and the output products it provides. For each monitoring technology, the user can define the sensor locations, types, and noise levels and can enable or disable entire sensor types. This information can be input for immediate use or saved as "canned " files for later use. Previously generated input files can be edited in near real time. The user can also specify event parameters (test configurations) such as location, depth or altitude, and time, as well as other technical parameters such as coupling factors, required signal-to-noise ratios, fission fractions, etc. Finally, the user can define the criteria by which the effectiveness of the monitoring system is assessed. This definition can be in the form of specified criteria for what constitutes a "detected" event (e.g., four seismic responses, two seismics and two infrasounds, etc.) in which case the "system effectiveness" value assigned by the model is simply the probability of "detecting" the event. Alternately, the user can assign relative values of various combinations of station responses (e.g., two seismics are good, three seismics are better, three seismics and one infrasound are better yet, etc) in which case the "system effectiveness" value assigned by the model is a more qualitative, relative measure of goodness.

For a given set of input conditions, the model will calculate the probability of each station (sensor) responding and provides several output products. One of the output products is a map showing which stations responded. The model also provides a histogram representing the probability that a given number of each sensor type will respond. Using the user-defined scoring criteria, the system will calculate and plot a bar chart showing the "effectiveness" of each subsystem acting alone and of the combined system. Finally, the user can request that the system run the above calculations for each element of a grid of points across the globe (spaced at 7.5 degree intervals) and plot the combined results as a contour of system effective- ness. Single event calculations take a few seconds, the global contour calculations take about 10 minutes.

752

The heart of the model is that portion which takes the user defined inputs and operates on them to produce the output products. As shown in Fig 2, the model uses a generic set of processing steps, common to all monitoring technologies: First, based on the event specification, the model calculates the signal strength at the event in each of the relevant phenomenologies, then the model estimates the attenuation between the source and each station to arrive at a signal strength at each station. The signal is compared to the noise at each station to calculate the probability of response of each station, using the user specified criteria for response (e.g., signal to noise ratio). These individual station response probabilities are then operated on to generate the various displays and output products.
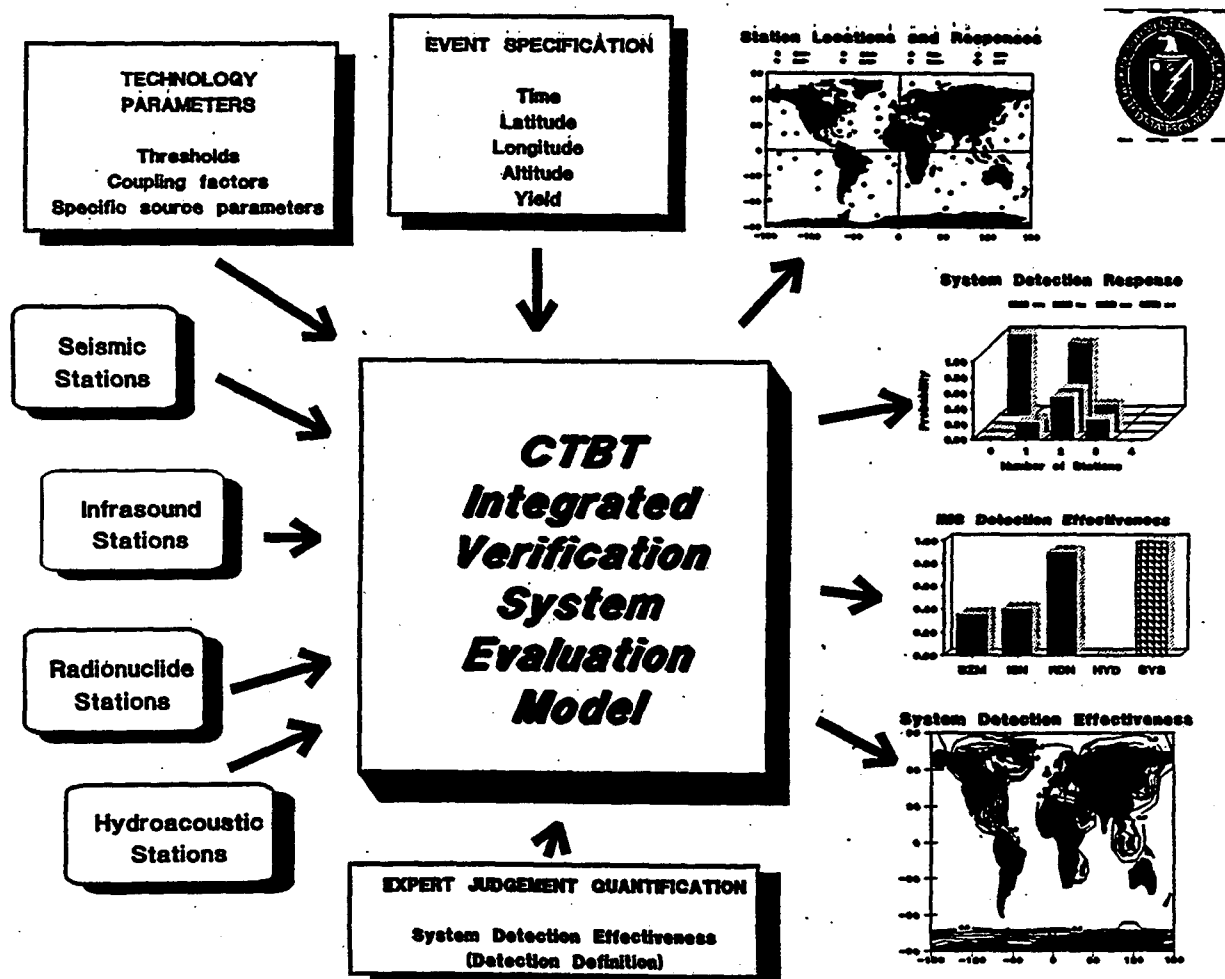
Figure 1

Subsystem Models Estimate the Probability that Individual Stations Respond to an Event
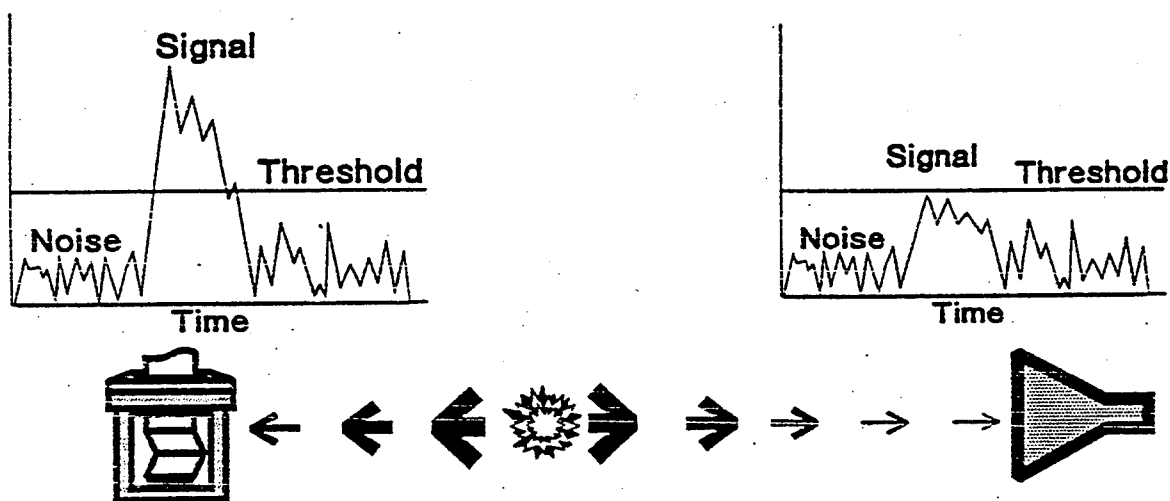
1. Signal Strength at Event
2. Attenuation and Propogation Effects
3. Signal Strength at Station
4. Noise and Signal Statistics
5. Probability that Station Responds

Figure 2

754

A conscious decision was made to emphasize breadth over depth in this model and to keep it simple, fast, and portable. Fig 3 summarizes the main simplifying assumptions made in association with these goals.

Simplifying Assumptions

What	Why	Effect
Seismic:		
P waves only (for detection)	Computation speed	Little on detection
Simple source and coupling	Facility, comp speed	Magnitude accuracy
No station corrections	Facility, no data	Small +- detection
Infrasound:		
No convergence zones	Facility, comp speed	Small +- signal
Hydroacoustic:		
Uniform bathymetry	Computation speed	+- signal, shadowing
Uniform sound velocity	Computation speed	Small +- signal
Radionuclide:		
Simple trajectory and cloud	Facility, comp speed	Not known presently
Xe-133g only (for detection)	Facility, comp speed	Little on detection

Figure 3

An obvious result of these simplifying assumptions is that the model does not provide the fidelity or capture all the nuances that individual phenomenology models can and this leaves open the question of the validity of the model. The proposed validation approach is not to try to defend the algorithms in terms of their ability to accurately model all the physics on a first-principles basis, but rather to benchmark the model against existing, generally accepted single phenomenology models and experimental data where available. Fig 4 summarizes the planned validation approach for each of the four subsystems.

CTBT Integrated Verification System Evaluation Model Validation

	Comparison to more Comprehensive Models	Comparison to Experimental data
Seismic	Preliminary comparison of detection probability vs. range and location accuracy with NETSIM	Defer to comparison of NETSIM results with experimental data
Infrasound	Pursuing comparison to LANL Normal Modes code	Preliminary comparison to NTS shot amplitudes at St. George & Bishop for different months
Radionuclide	Results presently being compared to PSR HYSPLIT results	Defer to PSR's comparison of HYSPLIT results to experimental data
Hydroacoustic	Will pursue comparison with Adiabatic Parabolic Equation Code at NRL and LLNL/NRL code when available	Will pursue comparison to Heard Island and other test data

Figure 4

Preliminary validation results for the seismic portion of the model are shown in Fig 5 which compares the probability of detection versus range for IVSEM versus the more detailed NETSIM model for a 1kt, fully coupled event using low noise, three axis stations.

Figure 5

There is as yet no well accepted, comprehensive single phenomenology model for infrasound, so the IVSEM model results have been compared against a set of experimental data as shown in Fig 6. There is a wide spread in the experimental data reflecting the effect of large wind variations. The model does however match the mean conditions fairly well.

Figure 6

RECOMMENDATIONS AND FUTURE PLANS:

Fig 7 summarizes the schedule for planned model development efforts, which include addition of location and identification capability predictions, plus model validation.

Model Development Schedule

Aug	Sept	Oct	Nov	Dec	Jan

Seismic
PKP added
Location details
Air-water-land coupling
Comparison to NETSIM
Identification Complete

Infrasound
100 km added
N-S 50 km wind
Noise Data Improved location
Comparison to LANL code
Comparison to test data
Identification complete

Hydroacoustic
Better bandwidth
Station noise
Better source-coupling
Improved location
Comparison to LLNL/NRL code
Identification complete

Radionuclide
Threshold
Venting Options
Background
Decay chains
Comparison to HYSPLIT
Identification Complete

General
New effectiveness table
Location integration
Complete graphics interface
User detection workshop
User location workshop
Identification integration
Identification workshop

Functional
Model
Version 0

7/19 Review
Improvements
Version 1.0

Location
Accuracy
Improvements
Version 1.1

Detection,
Location
Validation
Version 1.2

Identification
Added
Version 1.3

Figure 7

Ground-Truth Database for Regional Seismic Identification Research

Lori Grant

Claudia Carabajal*

Multimax, Inc., 331-C Forest Ave., Suite 3, Pacific Grove, CA, 93950

Abstract

The Ground-Truth Database (GTDB) provides a subset of the events necessary for seismic discrimination research: accurately located events with regional waveforms and known source type. While it is true that digital waveform data are easily exchanged through the Internet, the data are significantly more useful to discrimination research when event windows have been extracted from the continuous data and when additional documented information, such as source type, is associated with each event. Such a database, readily available and in a consistent format, minimizes the extensive efforts of data collection, organization, review and verification that are often the first phase of new research projects. Having this type of information is essential for development and assessment of algorithms for seismic event location and classification without having to assume the characteristics of the very events under investigation.

The Ground-Truth Database was introduced at the 14th Annual Seismic Research Symposium (Grant and Coyne, 1992) under an ARPA contract. By the time of the 15th Annual Seismic Research Symposium, 288 known events comprising 10 datasets in Western Europe and Scandinavia were available to the research community (Grant et al., 1993b). A large part of the success of the CSS GTDB was due to researchers who wanted to make data available to others by providing the results of their own data-collection efforts to the GTDB.

Two general methods were used to build these datasets. If the target events were the subject of a research study where ground-truth was published for a list of events, then we collected the associated waveforms. Another approach was to look at the regional seismicity bulletins produced by the IMS (Bache et al., 1990) and seek macroseismic information for significant clusters of events. In resuming the compilation of the GTDB we shall follow the model of the previous work but focus mainly on the Middle East and North Africa.

Keywords

Ground-Truth, Regional Waveforms, Discrimination, Database

---

*now at: State University of New York, Binghamton, NY 13902

Objective

The objective of this work is to compile a standardized database of regional waveforms from known events in a variety of tectonic regions and from a variety of seismic source types. We seek to bridge the gap between raw data and seismic events useful for regional seismic discrimination research by providing:

- event parameters— accurate event location and origin time, phase identifications and arrival times

- digital waveforms— preferably recorded at regional distance

- source type— known with a high degree of confidence, documented

Preliminary Research Results

Previous Effort

This work is a continuation of the Ground-Truth Database previously compiled under ARPA funding at the Center for Seismic Studies (CSS – now known as CMR- Center for Monitoring Research). Over a period of a year and a half, macroseismic information was gathered for waveforms residing in the IMS (Bache et al., 1990) and GSETT-2 (Bratt, 1992) databases.

The CSS GTDB comprises 10 distinct datasets totalling 288 known events as summarized in Table 1 and plotted in Figure 1. With the exception of Dataset 6, the events are grouped into clusters of between 10 and 31 events. Most of the waveforms are from the IMS Arrays ARCES, NORES, FINES and GERES. Some GSETT-2 data are also available for events occuring during that experiment (Bratt, 1992). Various methods were used in collecting ground-truth information: ground-truth data gathered as a part of a published study (Datasets 1,2,5,7,8,10); subsets of other databases (6); ground-truth acquired directly from in-country observers (3 and 4); and datasets where ground-truth information and waveform data were contributed together (9).

The CSS GTDB was released in two versions. Version 1, including datasets 1-3, is described in (Grant et al., 1993a). Version 2, including datasets 4-10, was described in a series of postings and e-mails distributed over the Internet. The data are no-longer on-line at CMR but are availble in CSS 3.0 format upon request to the authors. These datasets have been used in numerous CTBT-related research projects (see, for example the studies of (Pulli and Dysart, 1994; Baumgardt and Der, 1993; Fisk et al., 1993)).

New Effort

Our new data collection effort focuses on the Middle East and North Africa. Figure 2 gives an indication of the natural seismicity in the area of interest (10 to 50 degrees latitude and -30 to 75 degrees longitude). We have plotted all events with magnitude 4 or greater from the USGS database between January 1990 and June 1995. The great majority of these events are related to the tectonically active areas of the Mediterranean Sea, the Hindu Kush and

the Zagros fold belt. When we have access to seismological bulletins with accurate locations for smaller events, the seismicity patterns will presumably include events with other source types such as mining-related events.

The first priority for assembling waveform data from the area would be the high-frequency arrays which are planned in Egypt and Pakistan. As these stations are not yet operating, we will begin the work with other available data. Major networks that may record regional data in the area of interest are shown in Figure 3.

Future Plans

We are in the beginning stages of this project. The first step is to target events that have a chance of meeting the three criteria listed above and gather waveforms for those events. The next step is to verify the source type of the events.

After several datasets have been compiled, they will be carefully analysed for correct phase picks and consistency of event parameters. Following the model of the previous work, we shall work on several different datasets simultaneously. We plan to work closely with other contractors to provide the most useful datasets. One anticipated source of information is the World Wide Web page published at Cornell (Barazangi et al., 1995). Completed datasets will be announced on DOE's Web page, the URL for which is not yet available.

Acknowledgments

Maps were made using GMT (Wessel and Smith, 1991). We apologize for using outdated German and Czech borders.

References

Atakan, K., Lindholm, C. D., and Havskov, J. (1993). Earthquake swarm in Steigen, northern Norway: an unusual example of intraplate seismicity. *Terra Nova*.

Bache, T. C., Bratt, S. R., Wang, J., Fung, R. M., Kobryn, C., and Given, J. (1990). The Intelligent Monitoring System. *Bull. Seismol. Soc. Am.*, 80(6):1833–1851.

Barazangi, M., Seber, D., Vallve, M., Fielding, E., and Isacks, B. (1995). A geological and geophysical information system for Eurasia, the Middle East and North Africa: digital database development for the Middle East and North Africa. PL-TR-94-2092, Phillips Laboratory Scientific Report. ADA297018

Baumgardt, D. R. and Der, Z. (1993). Investigation of regional seismic discriminants using visualization and statistical analysis methods in the Intelligent Seismic Event Identification System. In Lewkowicz, J. F. and McPhetres, J. M., editors, *Proceedings of the 15th Annual Seismic Research Symposium, Vail, Colorado, 8-10 September, 1993*, PL-TR-93-2160, Phillips Laboratory, Hanscom AFB, MA. ADA271458

Bratt, S. R. (1992). GSETT-2: an experiment in rapid exchange and interpretation of seismic data. *EOS Trans. Amer. Geophys. U.*, 73(48).

Fisk, M. D., Gray, H. L., and McCartor, G. D. (1993). Applications of a robust statistical framework for seismic event identification. In Lewkowicz, J. F. and McPhetres, J. M., editors, *Proceedings of the 15th Annual Seismic Research Symposium, Vail, Colorado, 8-10 September, 1993*, PL-TR-93-2160, Phillips Laboratory, Hanscom AFB, MA. ADA271458

Gestermann, N., Harjes, H.-P., Jost, M., Schweitzer, J., and Wüster, J. (1992). GERESS: Monitoring natural and artificial seismicity in Central Europe. In Lewkowicz, J. F. and McPhetres, J. M., editors, *Proceedings of the 14th Annual Seismic Research Symposium, Tuscon, Arizona, 16-18 September, 1992*, PL-TR-92-2210, Phillips Laboratory, Hanscom AFB, MA. ADA256711

Grant, L. and Coyne, J. (1992). Ground-truth data for seismic discrimination research. In Lewkowicz, J. F. and McPhetres, J. M., editors, *Proceedings of the 14th Annual Seismic Research Symposium, Tuscon, Arizona, 16-18 September, 1992*, PL-TR-92-2210, Phillips Laboratory, Hanscom AFB, MA. ADA256711

Grant, L., Coyne, J., and Ryall, F. (1993a). CSS Ground-Truth Database: Version 1 Handbook. C93-05, Center for Seismic Studies Technical Report, Arlington, Virginia.

Grant, L., Ryall, F., and Coyne, J. (1993b). CSS Ground-Truth Database: Update and Case Study. In Lewkowicz, J. F. and McPhetres, J. M., editors, *Proceedings of the 15th Annual Seismic Research Symposium, Vail, Colorado, 8-10 September, 1993*, PL-TR-93-2160, Phillips Laboratory, Hanscom AFB, MA. ADA271458

Joswig, M. and Schulte-Theis, H. (1993). Master-event correlations of weak local earthquakes by dynamic waveform matching. *Geophysical Journal International*, 113.

Kradolfer, U. (1992). Recent seismicity in Switzerland as located by the Swiss network and the GERESS array. In *Proceedings of the GERESS Symposium, Waldkirchen, Germany, 22-24 June*.

Kremnetskaya, E. O. and Trjapitsin, V. M. (1992). Induced seismicity in the Khibiny Massif (Kola Peninsula). 1-92/93, NORSAR Scientific Report, Kjeller, Norway.

Kvaerna, T. (1993). Intelligent post-processing of seismic events— Part2. 2-92/93, NORSAR Scientific Report, Kjeller, Norway.

Mykkeltveit, S. (1993). Mining explosions in the Khibiny Massif (Kola Peninsula of Russia) recorded at the Apatity three-component station. 1-92/93, NORSAR Scientific Report, Kjeller, Norway.

Polish Academy of Sciences (1993). S. J. Gibowicz, personal communication.

Pulli, J. J. and Dysart, P. S. (1994). Two-dimensional signal processing for regional seismic event identification. PL-TR-94-2235, Phillips Laboratory Final Report. ADA292601

Wessel, P. and Smith, W. (1991). Free software helps display data. *EOS Trans. Amer. Geophys. U.*, 72:441,445–446.

Wüster, J. (1993). Discrimination of chemical explosions and earthquakes in Central Europe– a case study. *Bull. Seismol. Soc. Am.*, 83:1184–1212.

Table 1: Ten Datasets of the CSS GTDB

Dataset Name	Quake	Quarry Blast	Mine Tremor	Method	Publication
Version 1					
1: Vogtland	11	15	—	V*	(Wüster, 1993)
2: Steigen	25	—	—	V%	(Atakan et al., 1993)
3: Lubin	—	—	31	V#	(Polish Academy of Sciences, 1993)
Version 2					
4: Silesia	—	—	31	V#	(Polish Academy of Sciences, 1993)
5: Swiss Swarms	27	—	—	V*	(Kradolfer, 1992)
6: Gestermann	10	2	2	D	(Gestermann et al., 1992)
7: Ruhr Basin	—	—	13	*	(Joswig and Schulte-Theis, 1993)
8: Apa. Tremors	—	—	10	*	(Kremnetskaya and Trjapitsin, 1992)
9: Apa. Blasts	—	53	—	*	(Mykkeltveit, 1993)
10: Apa. Blasts	—	58	—	*	(Kvaerna, 1993)
Totals	73	127	88		

V	contact with original in-country source
%	locations from analysis of temp. seismic network
#	locations from mining seismic network
D	subset of another database
*	list of events from published report with ground-truth
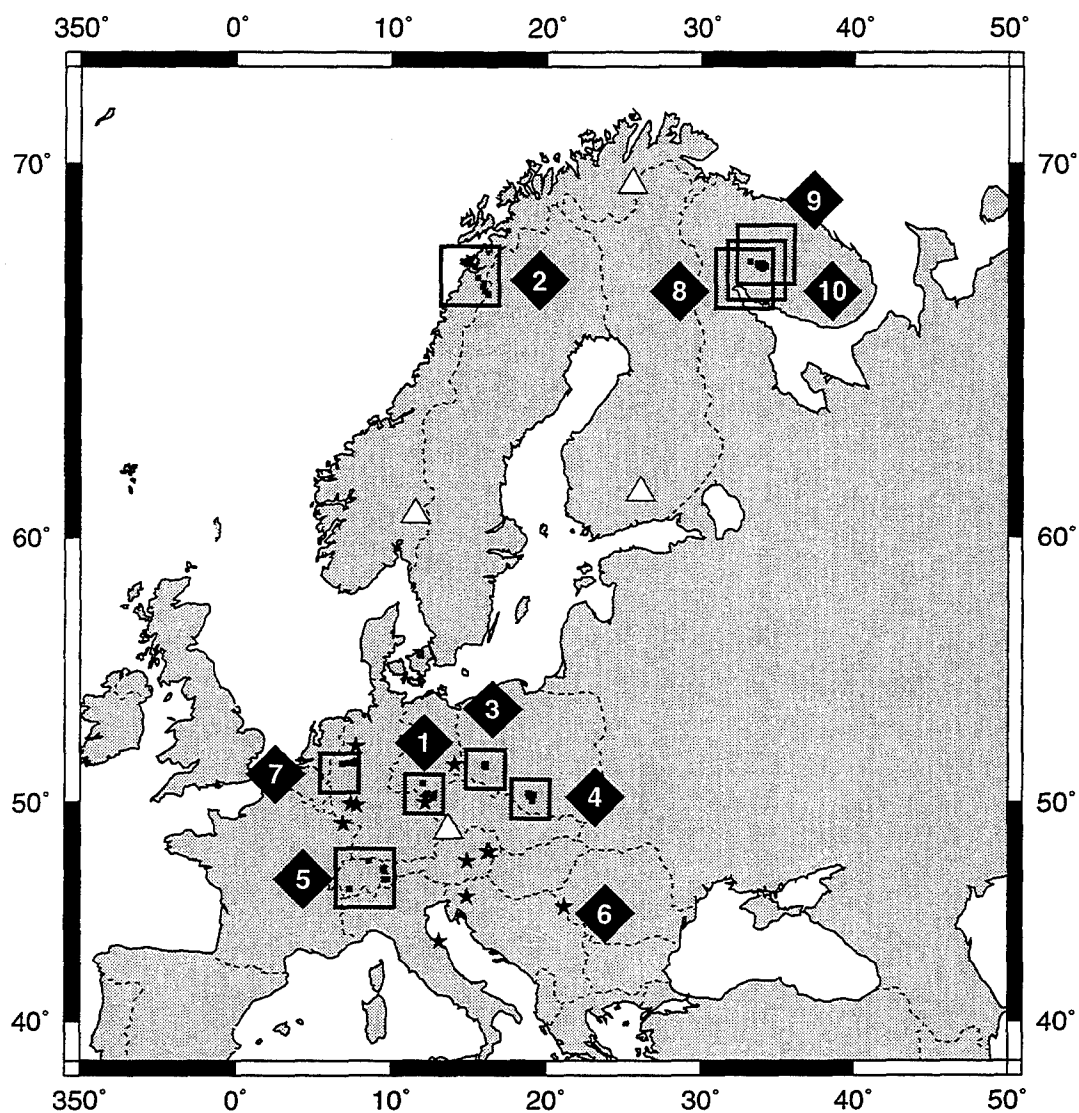
Figure 1. Ten Datasets of the CSS Ground-Truth Database. Open squares enclose clusters of events known as datasets 1-5 and 7-10 which are numbered by diamonds. Dataset 6 event locations are shown by stars. The majority of waveforms for these events comes from the high-frequency arrays ARCES, NORES, FINES and GERES, indicated by white triangles. Some waveform data from GSETT-2 stations are also available. See Table 1 for summary and text for details. This database is available from the authors (lori@es2.multimax.com).
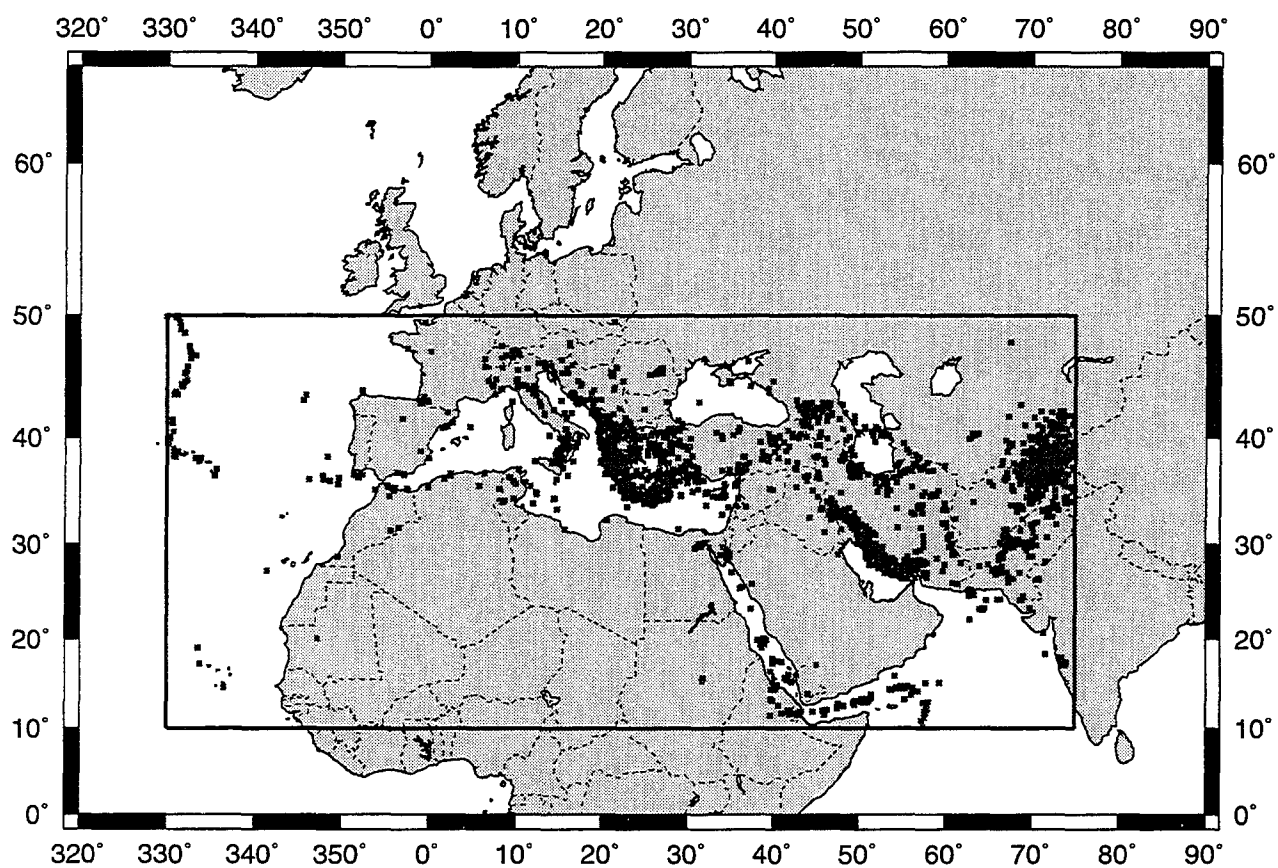
Figure 2. Seismicity in area of interest. USGS locations for all events with magnitude greater than 4 between January 1990 and May 1995.
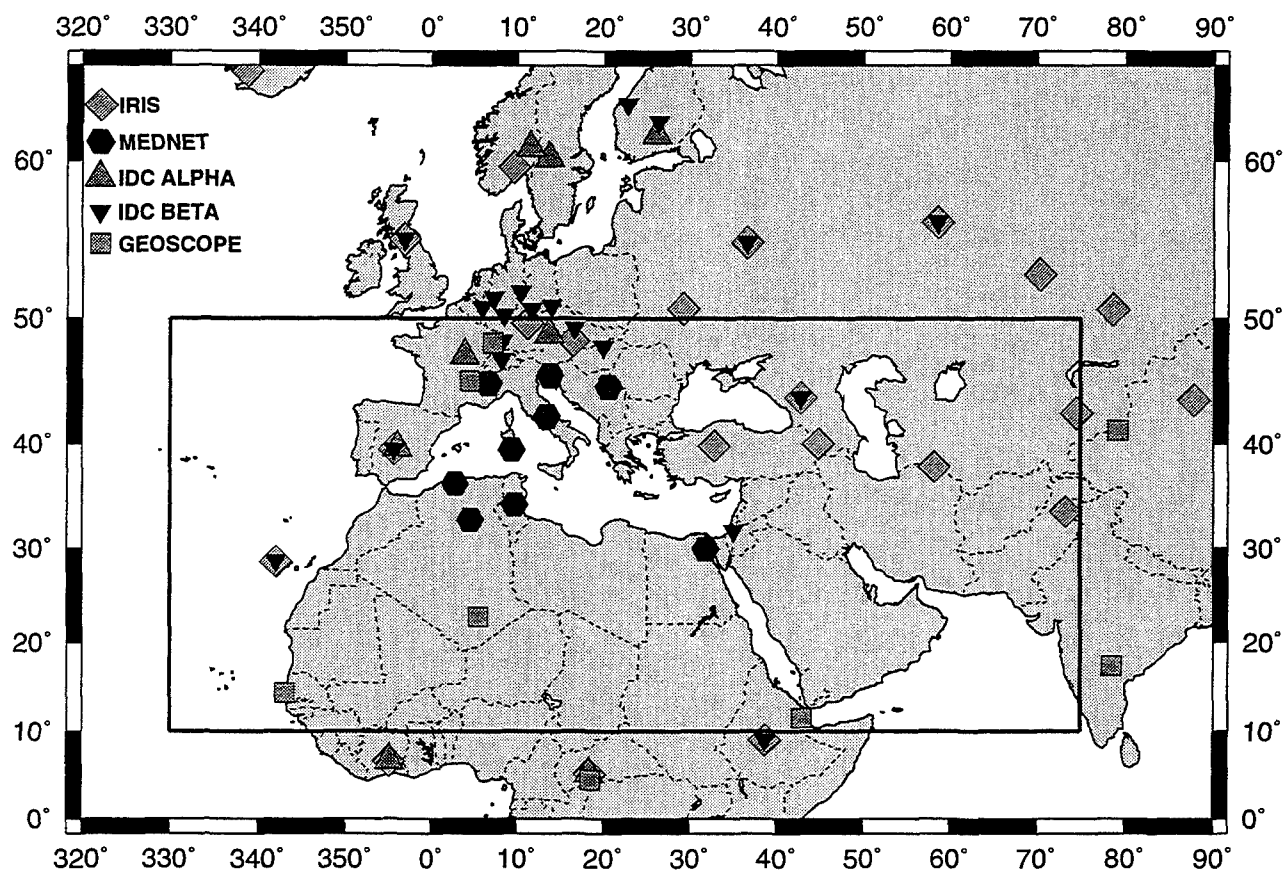
Figure 3. Networks that may record regional data in the area of interest. The IRIS network includes IRIS/USGS and IRIS/IDA stations. Many of the stations are affiliated with more than one of the networks listed. This is indicated on the map by overlapping symbols. An array is planned in Egypt appoximately 4 degrees southeast of the Mednet station KEG. The Pakistan array is planned at the same location as the current IRIS/IDA station NIL.

766

ADP Synthesis

Ralph G. Keyser
Senior Member of Technical Staff
Sandia National Laboratories
Albuquerque, New Mexico, USA

Larry S. Walker
Manager, Seismic Verification
Sandia National Laboratories
Albuquerque, New Mexico, USA

◆ Introduction

At the heart of the monitoring system for the Comprehensive Test Ban Treaty (CTBT) will be an Automated Data Processing (ADP) system charged with sorting through vast quantities of data from a world-wide network of sensors and providing distilled sets of information for decision makers. This system will evolve from the monitoring system prototypes in place today, but significant amounts of work remain to be done in order to complete this evolution.

This paper will address some of the challenges in the ADP area and the research efforts addressing those challenges. Efforts are underway at a number of agencies and organizations, aimed at successfully meeting the challenges presented by an automated data processing system for a CTBT. Successful synthesis or integration of these efforts will be necessary to the overall success of the CTBT monitoring efforts. Hopefully, the reader will come away with an appreciation for the wide variety of problems and approaches to solutions currently underway within the DOE program.

◆ Challenges in Data Processing for CTBT Verification

The verification of a CTBT presents some significant challenges in the Automated Data Processing (ADP) arena. These challenges are driven by the lower event thresholds required by the CTBT, and they cover a wide variety of problems that range from increases in data volumes and types to the complications added by trying to integrate new sensor technologies and techniques into the framework of existing verification data processing systems. This section will briefly touch on some of the challenges in the automated data processing research area.

Central among the challenges is the increase in data volumes brought on by the lowered thresholds required by the CTBT. In general terms, the raw data volumes are expected to increase by an order of magnitude over current monitoring systems to roughly 10 Gbytes of data every day. This increase in raw data volume ripples through the entire data processing pipeline since it implies an increase in the number of stations to process, the number of detections generated at each station, the number of events formed by the system, etc. In addition to the demands placed on physical resources such as disk space, network bandwidth, and I/O channels, this increased data load also impacts software algorithms since performance requirements prohibit the use of algorithms that are not efficient with large quantities of data. CTBT-level data volumes also have implications for the work done by human analysts in the processing sequence. The number of events and the number of stations capable of being used in event formation will both be several times greater than they are today. Since budgets are unlikely to allow an increase in staff size, the automated systems for CTBT monitoring must become more accurate, or the analysts must become more efficient, or both.

In addition to the increase in data volumes from lowered thresholds, the International Monitoring System (IMS) network will include data from multiple sensor sources such as infrasound and radionuclide sampling sensors. These additional technologies will mean new algorithms and new problems unique to processing data from these sensor systems when compared to existing seismic monitoring systems. It is expected that the experience with seismic systems can be leveraged to help with these additional technologies, but unique challenges will continue to arise from the integration of sensor data from multiple technologies. In addition, new display and analysis tools may be required to take full advantage of this integrated data set.

Integration of sensor technologies also allows opportunities for synergy between sensor systems. In the past, sensor systems were essentially dedicated to a particular domain for monitoring purposes. Under a CTBT, information will be used from multiple sensor systems to fully understand certain events and to defeat cer-

tain evasion scenarios. How to integrate and exploit this synergy between systems remains a significant challenge for researchers in automated data processing and other areas.

Another chief challenge in the ADP arena comes from the need to incorporate regional knowledge about the Earth in order to accurately detect, locate, and identify events at CTBT thresholds. The research to develop this regional knowledge is a significant part of the overall DOE research program, but once acquired, serious challenges exist in terms of organizing, storing, and making this data available to automated processing routines. This task is complicated by the fact that this knowledge is available at differing resolutions over the Earth, and it is also recognized that the types and level of knowledge will change over time.

Finally, all of the research done to meet the above challenges must be done with the goal of integrating the solutions into the existing prototypes being developed for the US National Data Center (NDC) and the International Data Center (IDC). These prototypes are complex, evolving systems in their own right, and integration of new algorithms and techniques must not interfere with the development of the centers. Both the IDC and NDC are establishing testbeds and procedures to facilitate the integration process, but the need for integration of prototypes into the NDC and/or IDC environment complicates the development of research prototypes.

◆ ADP as an Integrating Technology

Automated data processing technology acts as the focal point for the synthesis or integration of the various sensing technologies used to monitor a CTBT. It provides a vehicle for examining the similarities between technologies and the tools needed to process the data from those technologies. It provides leverage for bringing new sensing technologies on-line quickly due to the ability to reuse algorithms across technologies. These attributes make the ADP arena an ideal place to explore synergies between technologies and the application of existing techniques to new technologies, or the application of new techniques to existing technologies.

In addition to its key role of synthesis across technologies, ADP also acts as a bridge or migration route between research and operations. In many cases, research remains unused or under-used because the results are often reports or other outputs that are not directly suitable, or at least logically extensible, to the operational environment. Because of the need to integrate with the existing processing environment, a portion of the effort in the ADP area must focus on the

space between research and operations. Work in the ADP area is truly applied research, and as such, is ideally suited to aiding the transition of other research results into the operational arenas.

◆ ADP Research within the DOE's CTBT R&D Program

Although research applying to ADP problems is ongoing at a number of government agencies, universities, and commercial companies, this paper will focus on the work within the DOE sponsored CTBT R&D program. The work in this program is divided into three main areas; advanced processing technology, computer-human interface technology, and information systems technology. For each area, a general overview of the work in that area will be presented along with some examples of efforts in this area. ADP is a broad ranging task area, however, and this paper does not pretend to cover the topic in-depth. The reader is encouraged to examine the other papers and presentations at the symposium for more information.

⦿ Advanced Processing Technology

This task area focuses primarily on improvements to the automated engines that extract information from raw data. Within this task area, research is going into the development of new algorithms, the improvement of processing techniques using new computational technologies, and the exploration of cross-sensor synergies. As examples from within this area, the following paragraphs will briefly touch on research aimed at improving automated location capabilities, a method for doing full network event detection, and work being done to develop a high-level cross-sensor model of the overall CTBT network.

After careful consideration and consultation with the operational organizations, the decision has been made to place a priority on research into improved automated location techniques, especially those capable of improving depth estimation. Location is a strong indicator of event identity, and accurate locations are often a key to further processing necessary to refine an event. Several different directions are being investigated at the DOE labs to improve location capability. The first will focus on adaptive network locations that work to improve station corrections in regions with unknown velocity models. Another effort will address improving location capability by using a combination of travel time tables and waveform correlation techniques. Yet another effort will examine the problems associated with accurate location of individual events within a swarm. All of these efforts will result in new algorithms or techniques which can be applied to software in order to improve its capabilities.

Another area that has been the focus of considerable effort within the past few years is the issue of association of detections into events. A DOE-sponsored effort is underway to attempt direct event detection using the full data from a network of stations. This project (the Waveform Correlation Event Detection System - WCEDS) uses a uniform grid across the Earth's surface and into the subduction zones as search points. For each search point, the waveforms from all the stations are processed and aligned as if an event had happened at that point. The waveform pattern is then correlated with a master pattern for events at that location, and if the correlation exceeds the threshold, then an event is declared. This technique has the advantages of using all of the arrivals within the waveform to form the event, scaling well to larger numbers of stations, and being adaptable to distributed or parallel computer architectures. Early results in this effort have been promising, but this is clearly a longer term effort in order to produce a stable, reliable algorithm.

In a very different vein, work is also underway to develop a high-level model of the overall CTBT network. This model (the CTBT Integrated Verification System Evaluation Model - IVSEM) consists of integrated high-level models of seismic, hydroacoustic, infrasound, and radionuclide networks and can be used to evaluate the overall system performance of different numbers and types of sensors. It is intended as an affordable, portable model that is easy to use and understand, and it is envisioned as an aid for the treaty negotiation process. The model is designed to run on a portable 80486 or Pentium class machine, and it provides graphical outputs of its results as maps and charts. At this point, the model is capable of providing estimates of the network's ability to detect events, but future work will be aimed at adding the ability to estimate location and identification capability of the network.

● Computer-Human Interface Technology

While the Advanced Processing Technology efforts are focusing at improving the ability of the processing pipeline to automatically deal with the increasing number of events, the Computer-Human Interface efforts are aimed at making the analysts more productive as they deal with events. Both of the examples in this area are focused on exploring possible display methods that will improve the flow of information to an analyst, thereby allowing the analyst to make better decisions in a shorter period of time.

The first example is an effort at improving analyst efficiency by changing the approach used to evaluate events. Currently, event analysis starts with an analyst looking directly at the signal from a sensor, or at least a pre-processed version of that signal. The increasing number and types of sensors makes this an increasingly difficult method of event analysis. If, instead, the analyst were able to look

at a display that provided information about an event at the correct level of detail for the decisions being made about the event, then significant performance improvements might be realized. Work is underway to develop prototypes of such a level of detail display. This would act as a top end for the tools currently in use by analysts, so it would not replace them, but rather would allow the analyst to only examine those events which truly need human attention.

Another effort is aimed at providing very high dimensionality information to the analyst in an easily grasped format. Leveraging off of work done for the intelligence community, work is underway to use multi-dimensional clustering techniques to take a large number of relationships between elements of events and map them to a 2 or 3 dimensional space. By comparing the current event to a large population of other, well-known events, it is hoped that insights into the event's character can be discerned by the position of the event within the cluster of points representing other events. If this proves to be true, then the analysts will have a powerful tool that will allow them to assess in seconds a number of relationships between events that would today take many hours of the analysts time.

➡ Information Systems Technology

The third main area of the ADP portion of the CTBT R&D program is Information Systems Technology. This area focuses on the information handling and management infrastructure needed to allow the high-fidelity processing of the large volumes of data expected in a CTBT monitoring system. Examples in this area include the effort to develop a CTBT Knowledge Base to provide organized storage of the information needed by the ADP routines, and the efforts directed at data surety analysis.

A primary fallout of the move to lower thresholds in the CTBT environment is the need for detailed regional knowledge, such as travel time tables, to allow accurate locations for regional and local events. While this knowledge is being acquired in other portions of the CTBT R&D program, the task of developing a framework for the storing and retrieval of this knowledge is a task that falls within the ADP realm. The mechanism for providing this organized storage is the development of a CTBT Knowledge Base.

The Knowledge Base is envisioned as a storage area for the quasi-static parameters and geophysical data needed by the ADP routines. It will contain path-dependent information such as regional travel time tables, algorithmic information such as filter and beam sets, geophysical information for such as density and velocity models, and metadata to allow tracking of the knowledge both through time and the processing pipeline. One of the problems facing the monitoring sys-

tems today is the large number of ad-hoc mechanisms used to store knowledge today. This widely dispersed method of knowledge storage makes fine tuning of the system difficult, time consuming, and requires a great deal of familiarity with the whole system before a person can begin trying to fine tune. Another benefit of the Knowledge Base, therefore, will be its ability to consolidate the ad-hoc knowledge storage used by the current operations prototypes and improve the ease and accuracy of tuning the overall system.

The knowledge base is currently in the conceptual phase of development. A proposed Conceptual Requirements Document is available, and an effort is underway to fully identify the scope of the knowledge base and the types of data to be stored in it. That effort is expected to be complete soon, and the design process can then be undertaken.

Global monitoring systems clearly store a large quantity of information that would be a tempting target for tampering or destruction. Users place confidence in all types of data within the system from raw sensor data to knowledge base information and need confidence in its integrity and authenticity, so this data must be protected. At the same time, easy access to needed information is important for the participants. The efforts in the data surety area are balancing these requirements and making recommendations for future direction in this area.

◆ Summary

Monitoring a CTBT presents a number of significant challenges in the ADP area, and these challenges must be met with a variety of techniques and technologies. Success in the ADP area is crucial to the ability to monitor a CTBT, however, so successful synthesis of the various components within ADP should be a key goal for researchers everywhere.

PROPOSED CONCEPTUAL REQUIREMENTS

for the

CTBT KNOWLEDGE BASE

Ralph G. Keyser, Senior Member of Technical Staff
and
Hillary M. Armstrong, Member of Technical Staff

Sandia National Laboratories

July 31, 1995

ABSTRACT

The United States Government (USG) has indicated its support for a Comprehensive Test Ban Treaty (CTBT) by 1996, however, the existing verification systems will not provide monitoring capabilities at the level demanded by such a CTBT. Work is underway at the Department of Energy (DOE) and other agencies to improve the capabilities of the existing verification systems.

One area of research is focused on acquiring regional knowledge of the Earth to allow detection and identification the low magnitude events required by a CTBT. The problems associated with organizing, storing, and making this knowledge available to automated processing routines and human analysts are significant, and solving these problems is an essential step in ensuring that research results are smoothly transferred into the operational environment. The proposed knowledge base is an approach to solving the problems of knowledge storage in a CTBT system.

In addition to providing regional knowledge to automated processing routines, the knowledge base will also address the ad-hoc methods now used for knowledge storage. This will make the overall data processing system easier to maintain and tune since knowledge will be stored in a well defined location and not duplicated in multiple ad-hoc storage schemes.

The Proposed Conceptual Requirements Document for the CTBT Knowledge Base is a high-level requirements document intended to provide an overview of the scope and function of the knowledge base. In addition, the conceptual requirements document also provides examples of the data types envisioned for storage in the knowledge base. This conceptual requirements document is in a development phase and will continue to evolve along with other documents which will be developed during the analysis and design phases of this project.

Keywords: automated data processing, knowledge base, geophysical model, parameterized data

INTRODUCTION

The proposed knowledge base will be a vital part of CTBT verification analysis. It will be a centralized storage area for the ADP parameters and geophysical data. As a central storage area, it will facilitate the integration of and access to information. The major verification tasks in which this information will be used are: phase detection and identification, association of detected arrivals with events, event location, event identification, and special event analysis.

The need for regional geophysical information is apparent from the desire to lower the global monitoring threshold for CTBT purposes. The automated data processing (ADP) routines need parameterized data such as travel time tables and attenuation tables in a form that is useful for routine data processing functions.

Fig. 1: The Knowledge Base

The knowledge base will contain these regional parameters. The knowledge base will also need to manage underlying Earth model information for areas with no parameterized data, to allow refinement of existing parameterized data, and to support new algorithm development. Though both of these areas will be considered during analysis and design of the knowledge base, during implementation, first priority will be given to getting parameterized data into the knowledge base since that data is immediately useful to existing ADP routines.

The knowledge base will be a separate entity from the database containing the ADP processing results and the raw sensor data. An automated interface allowing the passage of parameters from the knowledge base to the ADP routines will be needed. The parametric data will also be available to the analysts and other users, so an interactive user interface will also be necessary (fig. 1). A data dictionary containing a preliminary list of these parameters can be found in Appendix 1.

The ADP results database changes almost constantly since it is continuously receiving new ADP processing results and sensor data. It is considered to be dynamic. By contrast, the knowledge base contents will change less frequently that of the ADP results database so it is considered to be quasi-static. Its parameters will be updated as the need arises. In order to make these updates, a maintenance interface will be needed (fig. 1).

This document discusses, at the conceptual level, the purpose of the knowledge base, who the customers are, where the knowledge base fits into the overall CTBT monitoring scheme, and the information and capabilities to be provided by the knowledge base. This document's primary purpose is one of initial content scoping in terms of data elements and functionality. This document is intentionally silent on the specific underlying hardware or software technologies that
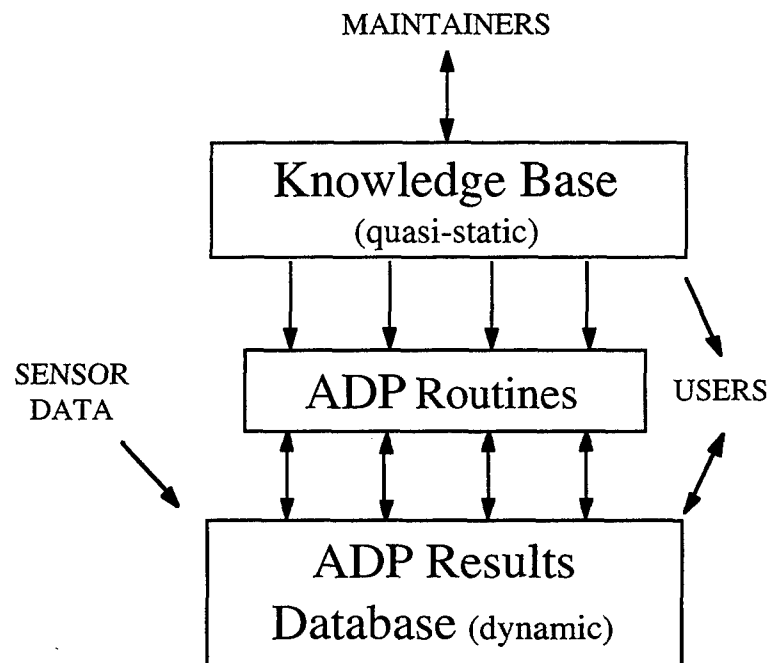
may be employed to support the knowledge base. (e.g., client server architecture, distributed database architecture, object oriented DBMS, relational DBMS, artificial intelligence, GIS, etc.) No inferences in the technology area are intended or implied. Furthermore, this document is not intended to be a functional requirements specification, a software requirements specification, a system design document, or an implementation plan. These will come later.

As discussed in the previous paragraph, this document provides the broad, high level scope of the knowledge base. Since its scope is necessarily broad, the knowledge base will need to have a phased implementation based on priority. The first priority will be to maximize performance in maintaining and providing the parameters to the ADP routines. Also high on the priority list is maintenance and provision of information currently used by the analysts and other users. Next on the list is maintenance and provision of parameters needed by ADP routines to be added in the near future. Following that is information which may be needed by the users in the future. Last on the implementation priority list is the storage of ancillary experimental data which may be of use in the future, but is currently not used in any algorithm.

Continued interaction with the customers (users) is vital to the success of any project. The Air Force Technical Applications Center (AFTAC) will be a primary user of the knowledge base. AFTAC is responsible for the development and operation of various US nuclear treaty monitoring systems including the prototype National Data Center (NDC), of which the knowledge base will be a part. The Advanced Research Projects Agency (ARPA) is another main knowledge base user. ARPA has a supporting responsibility to the Group of Scientific Experts (GSE). In that capacity, it is conducting the third Group of Scientific Experts Technical Trial (GSETT-3), which includes development of a prototype International Data Center (IDC), as well as detection and reporting capabilities to the Conference on Disarmament participants. The knowledge base will be an important source of regional information for the prototype IDC.

In addition to software development, the Department of Energy (DOE) Research and Development Laboratories are responsible for collection, integration, and synthesis of the information that will populate the knowledge base. DOE also has responsibility for research in support of CTBT monitoring efforts, so they will be users, as well as the developers, of the knowledge base. All of the expected CTBT technologies (i.e. seismic, hydroacoustic, radionuclide, infrasound, and on-site inspection) will be supported.

Another research and development user group is the community of organizations doing work on seismology and geosciences, such as the United States Geological Survey (USGS) and Incorporated Research Institutions for Seismology (IRIS). This community will both benefit from and contribute to information in the knowledge base. University and Industry research contractors comprise 2 large groups of users; the contractors under the joint agency Broad Area Announcement (BAA) managed by the Phillips Lab (PL), and the contractors working directly for AFTAC, ARPA, and the DOE Labs. Of particular note is Scientific Applications International Corporation (SAIC) which has a key programming / tool development role for both AFTAC (NDC) and ARPA (IDC).

ASSUMPTIONS

o   The constant stream of information which the ADP routines receive in near real time will increase in size, due to the anticipated increases in the number and type of sensors being used.

o   Lowering the minimum event threshold of interest, in order to meet U.S. Government detection goals, will increase the number of events to be examined.

o   Regional variations in the geophysical character of the earth now need to be considered in the Earth models used in CTBT verification. Thus, the system will evolve from primarily teleseismic to primarily regional analysis.

o   The knowledge base will need to cross traditional functional boundaries and be able to support all phases from detection through discrimination.

CONCEPTUAL REQUIREMENTS

o   **CONTENT SCOPING**

1. **provide the parameters to process raw sensor data used in CTBT detection location, and discrimination tasks**
The knowledge base must effectively manage and provide the necessary parametric data to process data from the following sensor types:
seismic
radionuclides
hydroacoustic
infrasound

2. **support information at a wide variety of resolutions and extents**
The knowledge base will need to process and manage geophysical, and other information at a wide variety of resolutions and extents. Resolution is the minimum distance between 2 adjacent objects, or the minimum size of an object, which can be detected (or resolved). Extent is the amount of space or surface area which something occupies (i.e. the size of the area of interest) Resolution and extent usually, but not necessarily, have an inverse relationship; as extent increases, resolution typically decreases. This is very application-dependent and occurs for a variety of reasons including the fact that applications which look at very large areas typically do not need as much detail as a more specialized application which requires much greater detail (i.e., macro vs. micro). Since detail is usually costly to acquire and maintain, the ideal is to have adequate resolution and extent for the particular application. It is interesting to note that this discussion also holds for temporal resolutions and extents. The following are examples of geographic resolution and extent. A diagram showing how the sensors are connected together in an array at a particular seismic station would probably have a high resolution and relatively small extent. Whereas, a map showing the location of global seismic arrays would probably not need to have as high a resolution, and would definitely have a larger extent. Another example of the wide range of resolutions and extents can be found in geophysical models. A local geophysical model of the immediate vicinity of an individual event site would probably have a high resolution and small extent. A geophysical model encompassing all known sites of interest in a particular country might have to be at a lower resolution, due to data storage and manipulation limitations, and would have a larger extent.

3. **provide regional geophysical information in a practical, usable form**
To carry out the major verification tasks effectively, the automated processing routines will require information for regional distances. A major development will be to incorporate new information about the geophysical characterization for regions of monitoring interest. This development will be driven by the need for algorithm-specific parameters, such as regional travel times, regional phase decay rates, array beam sets, etc., based on the following two considerations. First, that such parameters be derived as closely as possible from

seismic recordings for source regions, receiver sites, and propagation paths of monitoring interest. Second, that to address the initial demands on the knowledge base and the development of improved parameters for source regions in general, a parallel effort will be the synthesis of earth models from which parameters of present and future algorithms can be derived.

o **FUNCTIONALITY**

1. **provide a smooth transition path to knowledge base use, so as not to impact present verification capabilities**
Installation of the knowledge base, particularly the ADP interface, must be smooth so as not to impact the present verification capability. The existing interfaces and data structures should initially remain intact; there need not be any changes to existing software. The initial knowledge base ADP interface should be backward-compatible, working with a snapshot of the parameter files. The snapshot would be made at a designated time and interval (e.g., every night at 11:00 P.M.) and would contain all parameter files necessary to run any of the ADP routines (fig. 2). This is the most static scenario. The next step would be a more closely-coupled interface where the ADP routines would work with a parameter extract. This extract would be made at the startup of a program and would contain the parametric data necessary to run that program. Finally, the most closely-coupled interface would allow interactive queries of the knowledge base as the program needed the data. (e.g., program extracts path-dependent travel times during execution.) The last two interfaces could be used together to provide the most flexibility. Eventually, a combination of the last two interfaces will be implemented as the primary ADP interface to the knowledge base (fig. 3).
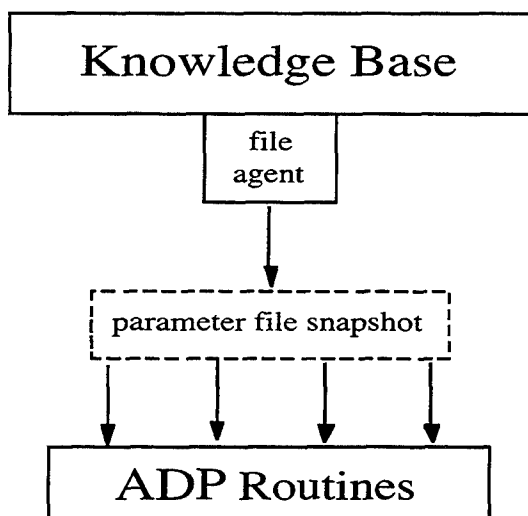
Fig. 2: Initial ADP Interface
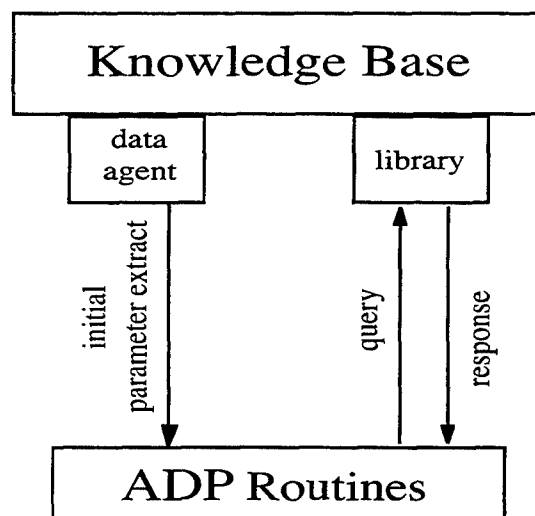
Fig. 3: Primary ADP Interface

2. **enhance the ADP environment through these automated interfaces**
The automated interfaces to the knowledge base (fig. 2 & 3). will help to improve the ADP environment by decreasing duplication of parameter data storage and standardizing parameter data access. Storing a parameter in one location only for a particular ADP routine will make the database easier to maintain and the changes easier to track. For example, it is critical to track what the value of a particular parameter was for a given run of

an ADP program. Having only one location of a parameter at a given time would make it easier to determine what the parameter value was at that time and, thus, what value was used for an ADP run at that time. The value of the parameter could be changed for subsequent runs, but would be time tagged and archived with other metadata to tie it to a particular run of the program. Development and eventual implementation of a standard way to access parameter data has the potential to improve program efficiency and make it easier to add new programs to the ADP environment. Given the assumption of an increase in the amounts and different types of raw sensor data to be handled by the ADP environment, this may prove to be a necessity.

3. **provide a user friendly, flexible, interface for accessing knowledge base contents**
The user interface to the knowledge base must be uncomplicated and easy to use, as it may need to operate in time critical situations. The analysts and other users need access to the same information as the ADP routines, as well as the models used to derive that information. The interface must also provide access to ancillary data necessary for special event analysis, that is, analysis of anomalous events which produced ambiguous results. The tools with which the users perform event analysis will have access to the necessary information in the knowledge base, however, development and maintenance of the tools themselves are explicitly out of scope of the knowledge base development project. The user interface to the database containing the ADP results and the raw sensor data is also out of scope.

o **MAINTENANCE AND DATA INTEGRITY**

1. **provide for creation, maintenance, and access to metadata**
Metadata is data about data. It provides the user with information about the origin, content, location, quality, condition, processing history and other characteristics of a given data element. The knowledge base needs to create, maintain, and make metadata easily accessible, as it is essential to preserving the integrity of the knowledge base. The following are some examples of how metadata would be used.

   o **determination of fitness for use**
   In order to determine which parametric data and models would be most appropriate to use for a particular event analysis, the analyst needs to know the accuracy (closeness to the truth) and precision (repeatability) at a given resolution and extent. For example, an algorithm may need to know the accuracy and precision of the various travel time computation options in order to decide which one to use.

   o **identification and description of raw sensor data source**
   Different Stations may have different equipment, sensor configuration, employee training level, data handling procedures, and communications protocol. Thus, the analyst will want to know which station the raw sensor data came from, the type and condition of the detection equipment, and other descriptive information about the station.

   o **identification and description of parametric data source**
   Metadata which identifies the source of models and parameters in the knowledge base are essential for maintaining a credible knowledge base with a verifiable scientific rationale. Metadata identifying the research report which generated a given parameter is one example of this.

o **knowledge base history**
There may be a need to be able to examine the state of the knowledge base at some time(s) in the past to help explain analysis results and conclusions. For example, it may be necessary to determine what parameters values were used by a particular run of an ADP program in order to explain a result that is in conflict with results from other sources. Additionally, it may be necessary to trace the entire processing history of an event. One way to do this is by examining an audit trail pieced together from automatically collected metadata. There may also be parameters which vary with time (i.e., wind speed), so what the value was at a given time needs to be tracked. In order to be able to do these things, changes to the parametric and geophysical model data stored in the knowledge base need to be tracked as to when, why, and by whom they were made. If a parameter has more than one value at a given time in the data base (i.e. for different runs of an ADP routine) then information associating a given parameter value to a given program run must also be collected. Note that this last example applies to the knowledge base testbed only, as the operational knowledge base parameters will probably not be that dynamic.

o **provide feedback on ADP results**
Metadata consisting of the error estimates for models and parameters in the knowledge base should be included for eventual use in error propagation calculations in the ADP algorithms. This will result in quantitative error analysis of results produced by the ADP algorithms that will aid the decision processes of later ADP algorithms, analysts, or other users.

2. **provide an extensible design**
The knowledge base design needs to support development of new algorithms on the NDC testbed. It must be able to easily accept new data types, data structures, and models as they are developed. It must also accommodate ancillary experimental data which may be of use in the future, but is currently not used in any algorithm. Thus the representation, storage, and maintenance of geophysical knowledge in both parametric equation and 3-D Earth model forms will be necessary in the knowledge base.

3. **provide a structured maintenance environment for the enhancement, or evolution, of the knowledge base**
Maintenance should follow established procedures in order to update and refine the knowledge base in an efficient, controlled, and organized way; configuration management is key here. A maintenance browser interface, with automated updating procedures and change recording capabilities may prove to be essential for this task. To assess the impact of updates and other maintenance tasks, system performance analyses will need to be regularly executed and archived (fig. 4). Note that although this is shown for the operational system only in fig. 4, there will be a similar feedback loop for the testbed system. The following are some of the maintenance tasks which may be required. In order to keep up with improving knowledge about the structure of the Earth, existing regional geophysical models will need to be replaced with new and improved models as they are developed. Additionally, newly created regional models will need to be integrated. In order to preserve knowledge base integrity, off-line Q.C. results will need to be incorporated according to some established procedures. Effective maintenance, together with metadata management, is essential to protect the integrity of the knowledge base and help to ensure that it remains a useful tool.
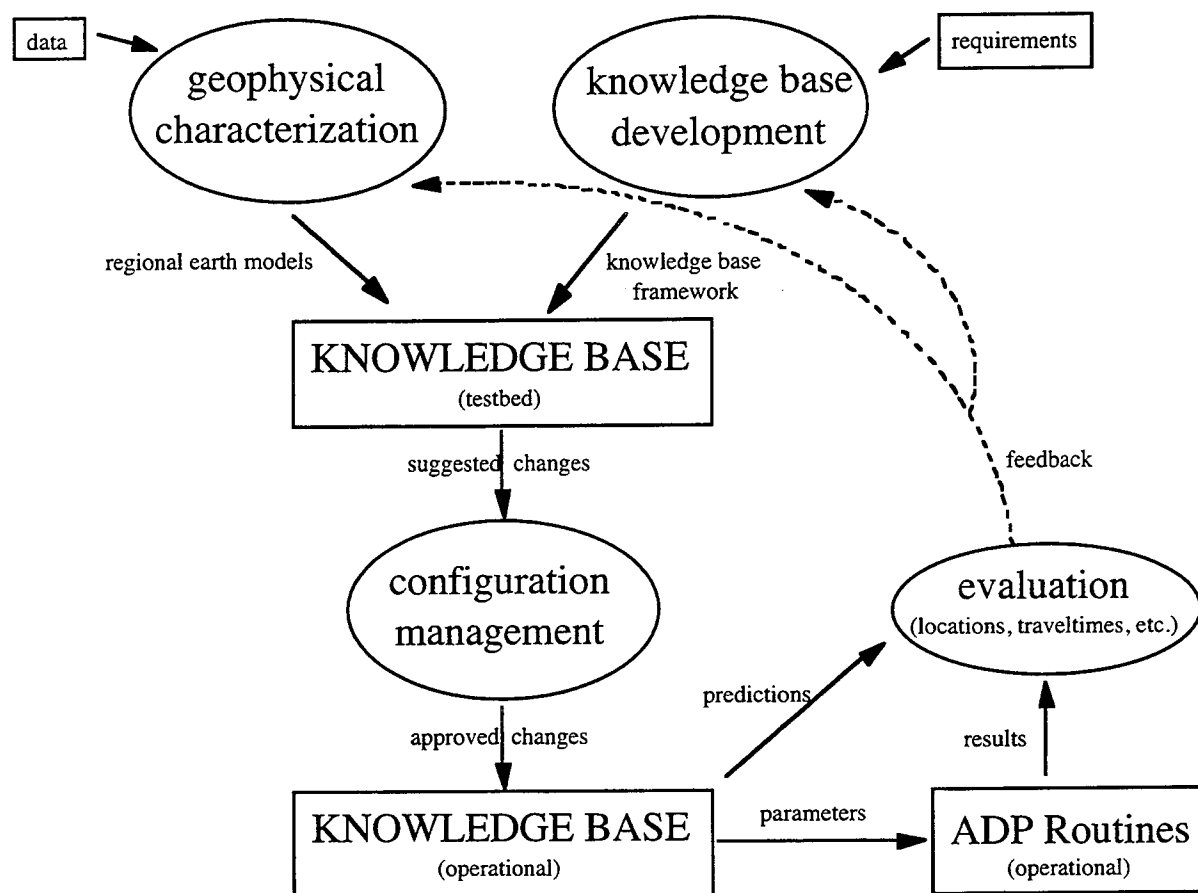
Fig. 4: Evolution of the Knowledge Base

Appendix 1

Knowledge Base Data Dictionary

July 31, 1995

At the heart of the CTBT Knowledge Base are the types of data to be included. This data dictionary is an attempt to list these data types and begin to group those data types into logical classes of data.

PATH-DEPENDENT INFORMATION

This class of information includes knowledge that depends on the path between a source event and the receiver. It will include information such as travel times and slowness along with correction factors for amplitudes, azimuths, etc. The knowledge base will support information at differing resolutions depending on the level of information available for the region. The knowledge base will also be able to support path specific information that varies by frequency or time.

Sample Data Types

1. Travel Time Table

2. Travel Time Corrections

3. Slowness Table

4. Slowness Corrections

5. Azimuth Corrections

6. Amplitude Corrections

7. Phase Blockage information

8. Discriminant Selection Information

ALGORITHMIC / PROGRAM-SPECIFIC PARAMETERS

This is information needed by a specific program or type of algorithm. It will support a wide variety of name-value pairs or vectors of name-value pairs that provide parameters for use by programs in storing information such as filter parameters, beam sets, signal detection parameters, measurement recipes, thresholds, etc.

Sample Data Types

1. Beam sets

2. Beam parameters

3. Signal Detection parameters

4. Channel sets

5. Filter sets

6. Filter parameters

7. Processing orders

8. Measurement recipes

9. Thresholds

10. Magnitude sets

11. Magnitude parameters

12. Noise measurement parameters

GEOPHYSICAL INFORMATION

This information class includes earth modeling information about a given point or region. It includes items such as tectonic region information, density and velocity data, knowledge about topography and geologic structure, and detailed data on seismicity in the region and its source.

Sample Data Types

1. Geographic Region

2. Tectonic Character

3. Density

4. Velocity

5. Q Information

6. Geologic Structure

7. Seismicity

8. Topography / Bathymetry

9. Depth to Moho

10. Depth to basement

11. Heat Flow

12. Gravity

13. Ocean Current

14. Reference Event Data including waveforms and event analysis

15. Sensor /Station Information

16. Wind

METADATA

This is "data about data". It provides the user with information about the origin, content, location, quality, condition, processing history and other characteristics of a given data element.

Sample Data Types

1. Quality

2. Origin

3. Processing history

GEOGRAPHIC INFORMATION

This information can be associated with a particular area of the earth. It may be useful as reference material.

Sample Information Types

1. Maps

2. Overhead Images

3. Mine Schedules

4. Demographics

5. Geopolitical

6. Cultural

7. Meteorological

LOW-FREQUENCY NOISE STUDY AND SURFACE WAVE ENHANCEMENT USING DATA FROM LARGE AND SMALL APERTURE ARRAYS

A.F.Kushnir*, A.Dainty**, A.I.Gashin***, B.M.Shoubik*

* *Moscow IRIS Data Analysis Center / SYNAPSE Science Center, Russia*
** *Air Force Phillips Laboratory, USA*
*** *International Institute of Earthquake Prediction Theory, Russian Academy of Science*

Abstract The detection and parameter estimation of surface waves originating from earthquakes and explosions are important procedures in nuclear test monitoring with seismic arrays, usually performed on a routine on-line basis. For small teleseismic and far regional events performing these procedures is often complicated because weak low-frequency surface waves from these events are as a rule registered against a background of temporally and spatially correlated seismic noise with a frequency spectrum overlapping that of the event surface waves. Low-frequency (LF) seismic noise has two explicit components: the first is transient and propagates as surface waves; the second has the features of a scattered field. The statistical properties of a LF noise field are affected by meteorological factors and vary in time.

In this work we investigated temporal and spatial features of the LF seismic noise below 0.5 Hz based on records of long period instruments of large and small aperture arrays: 6 z-componenl sensors of the NORSAR array, 11 similar sensors of the Grafenberg array, and 12 3-component very broad band sensors of the Geyokcha PASSCAL small aperture array. For assessment of noise field spatial correlation we evaluated noise coherence functions for array sensor pairs and implemented high resolution wide-band F-K analysis. The latter allows us to estimate azimuths and apparent velocities of the transient noise component of frequency (0.04-0.07) Hz which was observed at all the arrays and to confirm its origin as surface waves generated by sea shore surf. As an example, for the Geyokcha array the noise coherency for different sensors was to be greater than 0.8 in the frequency band (0.-1.) Hz. The transient LF noise component arrives at this array with apparent velocity about 4 km/sec and backazimuth pointing to the middle of the Caspian Sea. The LF noise component with a peak at frequencies about 0.2 Hz arrives at this array with very small incidence angles as scattered body waves.

The conventional beamforming method applied to LF array data for enhancement of weak teleseismic and far regional explosion surface waves sometimes failed to provide the expected increase in SNR. The reason is the noise coherence in the signal frequency band. This was the case for array data sets which we investigated. For example, for the Geyokcha array the beamforming did not give any noise suppression for frequencies below 0.8 Hz.

We have found that significant improvement in surface wave retrieval can be achieved by implementing adaptive group filtering (AGF) algorithms. We tested two versions of AGF: the optimal AGF (AOGF) which retains the signal waveform undistorted; and whitening AGF (AWGF) which distorts the signal but whitens residual noise and facilitates signal detection and onset time estimation. Both suppress the coherent noise component by taking into account the array noise matrix power spectral density (MPSD) estimated by multidimensional ARMA modeling.

Our experiments shows that AOGF and AWGF processing provides for 1-componnent large aperture arrays significant improvements of explosion surface wave SNR in comparison with beamforming. The improvement is due to suppression of the transient LF noise component at frequencies (0.04-0.07) Hz and is especially large if the explosion and noise arrival azimuths are well separated. For the small aperture 3-component VBB array the AGF procedures allows retrieval of surface waves with SNR = 0.1 by suppressing not only the transient but also the scattered LF noise components in the frequency range (0.-1.) Hz. We have found that the generalization of the AGF method for 3-component array data processing gives new potential for retrieving signals from noise and estimating their parameters.

Keywords Adaptive statistical processing of array data; optimal group filtering; high resolution F-K analysis; suppression of coherent noise; retrieval of surface waves from noise

OBJECTIVE: Seismic monitoring with arrays under strong noise conditions: algorithms, techniques, system design and experimental data processing.

PRELIMINARY RESEARCH RESULTS: Algorithms and software have been developed for adaptive statistical array data processing. Current noise features are taking into account in this processing by periodic estimation of the array noise matrix spectral density. A special programming shell was designed for SUN workstations, providing a convenient tool for running multichannel processing programs in interactive and real time modes.

RECOMMENDATIONS AND FUTURE PLANS: We recommend the wide use of VBB 3-component small aperture arrays, which are the most effective instruments for seismic monitoring. Our plan is to develop a modern adaptive statistical software for these array data processing.

Properties of low frequency noise fields. Detection and parameter estimation of surface waves originating from earthquakes and explosions are important procedures in nuclear test monitoring with seismic arrays, usually performed on a routine on-line basis. The effectiveness of these procedures impacts on the accuracy of small-events source location and on identification based on single array data[1]. Measurement of surface wave magnitudes is an effective means for the explosion yield evaluation [2].

For small teleseismic and far regional events, performing these procedures is often complicated, because weak low frequency surface waves from these events are, as a rule, being registered against a background of a temporally and spatially correlated seismic noise with a frequency spectrum overlapping that of the event surface waves. Low-frequency (LF) seismic noise has two explicit components with peaks at frequencies (0.04-0.07) and 0.2 Hz. The first is a transient propagating as a surface wave, the second is due to scattered noise field features. Both are assumed to originate from ocean storm activity but possess different mechanisms of transition to seismic energy. The serious nuisance for signal processing is that statistical properties of the LF noise field, namely temporal and spatial correlation features, are affected by meteorological factors and vary in time.

Optimal group filtering. The main procedures of conventional array data processing are beamforming and broad-band F-K analysis [3]. The first is implemented for refining from noise seismic phase waveforms that facilitate the subsequent phase parameter measurment, the second for estimating slowness vectors of signal waves. In practice these procedures do not provide the expected efficiency: for large aperture arrays, mainly due to the signal incoherence caused by medium inhomogenities; for small aperture arrays due to noise coherence (noise spatial correlation).

The generalized beamforming method [4] allows us to improve the signal waveform refinement in the case of coherent noise [5,6]. This method can be described as a group filtering of array data using the filter with the vector frequency response (VFR)

$$g^*(f,p) = h^*(f,p)\, F^{-1}(f)\, /\, [h^*(f,p)\, F^{-1}(f)\, h(f,p)],$$

where $h(f,p)$ is the vector of phase shift factors $h_j(f,p)=exp\{-i2\pi f\, p^*r_j\}$, $j=1,...,m$, which are determined by the array sensor coordinate vectors r_j and a signal wave slowness vector $p=(p_x,p_y)$;

* denotes the Hermitian conjugation. A group filter (GF) transforms a vector spectrum $x(f)$ of m-channel array time series into a spectrum $y(f)$ of output scalar time series by the equation $y(f) = g^*(f,p) x(f)$. The GF with the VFR $g(f,p)$ is the statistically optimal one (OGF) because it takes into account the array noise matrix power spectral density (MPSD) $F(f)$. Conventional beamforming can be treated as a group filtering with VFR $g(f,p)$, where $F(f) = I$, I is the identity matrix.

The optimal group filtering method can be extended for 3-component (3C) array data processing [7]. In this case $x(f)$ is a $3m$-dimensional vector spectrum of m 3C array traces, $F(f)$ is a MPSD of a 3C array noise, the vector $h(f,p)$ is composed of m 3C vectors $h^\circ_j(f,p) = h_j(f,p)b(p)$, where $b(p)$ depends on the type of a treated wave phase. In particular, for Raleigh surface waves, $b(p) = i \sin\psi (p_x, p_y, -i|p| ctg\psi)^*/|p|$, where ψ depends on the ellipticity of the Raleigh wave [8].

The efficiency of a practical application of the OGF is influenced by the method used for the estimation of the noise MPSD $F(f)$. For this purpose, we propose multidimensional ARMA modeling of array noise records preceding the event. The OGF with the VFR $g(f,p)$, containing such an estimated noise MPSD we call adaptive OGF (AOGF). Beamforming and AOGF are procedures that do not distort a signal waveform.

A useful modification of the AOGF is an adaptive noise whitening group filter (AWGF), which produces a white residual noise output and in many cases provides the highest output SNR, but distorts the signal [6]. The AWGF has the frequency response $w^*(f,p) = h^*(f,p) F^{-1}(f) /[h^*(f,p) F^{-1}(f) h(f,p)]^{1/2}$.

Estimation of wave apparent slowness. Coherent LF noise can sometimes be a significant hinderance for estimating slowness of weak surface waves by the conventional broad band F-K analysis. It is especially so if the number of sensors and/or the array aperture are small. We found that in this case, some improvement can be achieved if we use high resolution (HR) F-K analysis, which consists of mapping over slownesses (p_x, p_y) the function

$$ P(p) = [h^*(f_0,p) F^{-1}(f_0) h(f_0,p)]^{-1} , $$

where $F(f)$ is the ARMA estimate of a MPSD of array records. The vector p^* corresponding to a maximum of the map $P(p)$ represents the wave slowness estimate. The smoothness over frequency of an ARMA model (which in practice is calculated using low orders) implies that p^* is really a wide band estimate averaged over some frequency band around f_0.

There exist maximum likelihood (ML) algorithms for the slowness estimation of signal waves obscured by a spatially correlated noise. A ML algorithm derived under the assumption that nothing is known about a signal waveform consists of the evaluation of a vector p^* which maximizes the function

$$ Q(p) = \Sigma | h^*(f,p) F^{-1}(f) x(f)|^2 / [h^*(f,p) F^{-1}(f) h(f,p)], $$

where summation is made in f over an assigned frequency band around f_0 [7]. This theoretical formulation allows us to suggest an adaptive algorithm for wave slowness estimation under conditions of strong coherent noise. It consists of the mapping over slownesses (p_x, p_y) the

function $Q(p)$ where $x(f)$ are spectra of signal wave array records, $F(f)$ is the ARMA estimate of the noise MPSD calculated using preceding array noise observations.

Study of LP large aperture array records. We investigated characteristics of LF noise and efficiency of slowness estimation and SNR enhancement of surface waves using records of long period (LP) instruments of the large aperture NORSAR and Grafenberg arrays. Table 1 shows the characteristics of the analyzed data sets containing explosion surface wave seismograms and noise records at preceding and subsequent time intervals.

Table 1. Characteristics of LP array data sets

Data set	1	2	3	4
Array	NORSAR	NORSAR	NORSAR	GRAFENBERG
LP sensors	6 z-comp	6 z-comp	5 z-comp	11 z-comp
Day of observation	30.05.83	27.10.84	27.12.81	26.10.83
Wave azimuth (degrees)	78°	105°	75°	61°
Wave velocity (km/s)	3.5	3.6	3.6	3.7
Data interval (sec)	7200	5400	6000	2700
Signal onset time (sec)	4500	2700	3700	1300
Sampling rate (Hz)	1	1	1	1

Figs 1- 4 illustrate the processing results for these data sets. Fig. 1 shows the power spectral density (PSD) and coherence function of signals and noise registered at NORSAR. We see that, for all three records, taken in different seasons of the year, the noise PSD exhibits a strong peak at frequencies (0.04-0.06) Hz (Fig. 1,c), which overlaps with dominant frequencies of the surface wave signal (Fig. 1,d). This NORSAR noise component preserves rather strong coherence over the total array aperture (Fig. 1,e): for the sensors NA1 and NC4 having separation 47 km (Fig. 1,a), the coherence is above 0.6. The HR F-K analysis (Fig. 2,c and Fig. 3,d) shows that the NORSAR noise component in the frequency band around 0.05 can be treated as a transient propagating with apparent velocity about 3.5-4.0 km/sec, typical for surface waves. Note that the estimated propagation azimuths of these noise waves support the supposition that the waves are generated by surf at sea shores: at the Baltic Sea for data sets 1, 2 (Fig. 2,c) and at the North Sea for data set 3 (Fig. 3,d).

The noise component with peak frequency 0.2 Hz does not exhibit coherency (Fig. 1,e); this corresponds with its conventional representation as a scattered noise field. The explosion surface waves registered by NORSAR demonstrate rather good coherence: more than 0.8 over the total array aperture (Fig. 1,f).

Explosion surface waves in the data sets 1 and 2 have small SNR. For this reason, the signal processing was performed here after filtering the data in the frequency band (0.-0.1) Hz with the help of a high quality Chebyshev filter (Fig. 1,b). This increases SNR by suppressing the 0.2 Hz noise component. Note that signal processing of these data sets is also impeded by the small difference between the noise and signal wave arrival directions: noise azimuths in both cases are about 40-50° (Fig. 2,c), signal azimuths are 78° for event 1 and 105° for event 2.

Apparently for the above reasons, the F-K analysis of the signals does not provide a reliable estimation of the signal azimuths and apparent slownesses: the estimated values vary rather strongly with changes in the parameters of the HR F-K algorithm.

Figs 2,a and 2,b show the results of processing the data sets 1 and 2 with the help of beamforming (trace 1), AOGF (trace 2), and AWGF (trace 3) procedures. Trace 4 in each figure is a record of the first array sensor. Figs 2,d and 2,e show the PSDs of the traces mentioned. We see that, by taking into account the noise coherence, the AOGF provides in these examples a rather significant addition to the beamforming suppression of the transient noise in the frequency band (0.05-0.08) Hz. The AWGF traces demonstrate the potential of this method for enhancement of the accuracy of surface wave onset time estimation.

The data set 3 was processed in both initial (0.-0.5) Hz (Fig. 3,a) and LP-filtered (0-0.1) Hz (Fig. 3,b) frequency bands. For this data, signal and noise arrival directions are quite different (76° and 315°,) and the HR F-K analysis provides satisfactory accuracy and stability (Figs 3,c and 3,d). The adaptive group filtering performance (Figs 3,a; 3,b and 3,e) is also better than in the previous cases. It is seen from Fig. 3,e that the AOGF provides significant suppression of noise components in comparison with beamforming up to 0.2 Hz. After processing in the frequency band (0.-0.1) Hz, the Rayleigh phase waveform emerges explicitly in the AOGF trace and the low frequency start of the signal is emphasized in the AWGF trace, allowing exact estimation of the signal onset time.

Data set 4 contains records made at 11 long period sensors of the large aperture Grafenberg array. The array is located away from a sea shore, but the features of low frequency noise here are remarkably similar to those for NORSAR. One can clearly see this, if one compares the noise PSD in Fig. 4,e ('GR1' curve) with that in Fig. 1,e ('NA1-ev.3' curve) and the noise HR F-K diagram in Fig. 4,d with that in Fig. 3,d. From the signal and noise HR F-K maps (Figs 4,a and Fig. 4,B), arrival azimuths of the signal and transient noise are quite different for this data set (60° and 314 °). For this reason, the AOGF provides a significant addition to the beamforming enhancement of SNR in a wide frequency band (0.-0.5) Hz (Fig. 4,e). The greatest noise suppression is achieved for (0.05-0.08) Hz transient noise components, but some suppression is visible for scattered components around 0.2 Hz. In Figs 4,a and 4.b results of the AOGF and AWGF performance in the frequency bands (0.-0.5) Hz and (0.-0.1) Hz demonstrate that the method can be really useful for processing LF surface waves registered by large aperture arrays.

Study of VBB small aperture array records. The well-tested NORESS-type small aperture arrays are essentially oriented to regional seismic monitoring and are equipped with short period instruments recording seismic energy above 0.5 Hz. They contain only one central long period sensor. For this reason, there are not many studies of low-frequency noise field coherency in the limits of these array aperture. The α-stations of the International Monitoring Network currently being deployed could be designed as 3-component wide band small aperture arrays containing about ten very broad band (VBB) 3C sensors within an aperture about 1.5 - 3 km [9]. Prototypes of such stations have been tested in the framework of the PASSCAL program; for example, the VBB subarrays of the Pinyon Flat (USA) and Geyokcha (Turkmenia) experimental arrays can be treated as such prototypes. Fig. 5,d shows the configuration of the

VBB subarray of the Geyokcha array deployed not far from Turkmenia capital Ashgabad (latitude 37.93°, longitude 58.11°). It has been recording during 93 and 94. The array was situated on thick sedimentary rocks and hence was affected by intense seismic noise.

The typical PSD of the Geyokcha noise is shown in Fig. 5,e for the frequency range (0.-10.) Hz and in more detail in Fig. 5,f for the frequency range (0.-1.) Hz. We see that the PSD has four peaks at frequencies 0.07, 0.2, 1.5 and 4.5 Hz. In Fig. 5,e, the noise PSD for the central sensor Z-instrument is compared with the PSD of a beam composed from noise records of all 12 VBB Z-instruments. The beam is steered to surface waves originating from the Chinese Lop Nor Test Site (azimuth 71.7°, app. velocity 3.55 km/sec). We see that the noise below 1. Hz is not suppressed by the beamforming procedure. This indicates that the noise field is highly spatially correlated for these frequencies. Fig. 6,d shows noise coherence functions for two closely located (B32, C22) and two more widely spaced separated (NHB, SEH) Z-sensors of the array. We see that for the first case coherencies are very close to 1 over all the frequency band (0.-1.) Hz, and for the second case have values larger then 0.8 up to 0.3 Hz. The HR F-K analysis for the strongest spectral peak at 0.2 Hz (Fig. 5,a) revealed that this noise component can be regarded as composed of body waves arriving with very low incidence angles. In the light of the thick sedimentary layer beneath the array this does not contradict the description of this component as a scattered field. The HR F-K map for the other LF noise peak at (0.05-0.07) Hz (Fig. 5,b) shows that this noise component is composed of surface waves arriving from the Caspian Sea.

Due to the small aperture and the high correlation of noise for different sensors, one may erroneously conclude that the Geyokcha type VBB array is a bad instrument for analyzing teleseismic and far regional surface waves. Really, the beamforming method does not provide any improvement in SNR for these waves and their F-K analysis is hampered by the coherent LF noise. To demonstrate the applicability of the AOGF method for this case, we simulated explosion surface wave seismograms (in the form of Berlage pulses with mean frequency 0.06 Hz and duration of 150 sec shifted in time as if originating from the Lop Nor Test Site) and mixed them with real Z-component records of Geyokcha VBB array noise. This model mixture (with the power SNR=0.1) was processed by the AOGF in the frequency band (0.-1.) Hz. The results shown in Figs 5,c and 5,f allow us to assert that the AOGF has in this case great potential: the signal SNR was improved 40 times due to effective suppression of not only transient (0.06 Hz) but also scattered (0.2 Hz) noise components (Fig. 5,f).

Fig. 6 illustrates results of an implementation of the **3-component** version of the AOGF procedure for enhancing surface waves in seismograms of the Chinese nuclear test of 10.06.94. We had for experimental processing records of only six 3C STS-2 seismometers (marked in Fig. 5,c by crosses).

Fig. 6,c shows the noise PSDs for N, E, and Z components of the central VBB sensor. Interesting here is the similarity of all spectra for frequencies above 0.05 Hz and great differences between the spectra of the vertical and horizontal components below 0.05 Hz. The latter can be explained by the likely origination of this noise fraction from wind impact on the Earth's surface unevenness.

The 3C seismogram of the Lop Nor nuclear test is shown in Fig. 6,a. Figs 6,b, and 6,e exhibit the results of processing the six 3C explosion seismograms (18 channels) by the 3C

versions of the beamforming and AOGF procedures (for the band [0.-1.] Hz). We see that the beam steered to the azimuth and velocity of Lop Nor explosion surface waves does not enhance these waves and passes through the bulk of the P-wave energy. In contrast, the similarly steered AOGF remarkably extracts explosion surface waves and suppresses the P-wave and its coda. Note that the noise suppression is strongest for the (0.01-0.03) and (0.1-0.5) Hz bands.

The experiments made with the Geyokcha array LF signal and noise records allow us to assert that VBB small aperture arrays can serve not only as the best instruments for regional seismic monitoring but also as a good tool for measurements of surface wave parameters for teleseismic and far regional events.

References

1. S. Mykkeltveit, F. Ringdal, T. Kvarna and R. Alewine, 1990. Application of regional arrays in seismic verification. *Bull. Seism. Soc. Am., vol. 80, p.1777-1800.*

2. R.A. Hansen, F. Ringdal, P.G. Richards, 1990. The stability of RMS L-measurements and their potential for accurate estimation of the yields of Soviet underground nuclear explosions. *Seism. Soc. Am., vol. 80, p. 2106-2126*

3. S.Mykkeltveit and H. Bungam, 1984. Processing of regional events using data from small-aperture arrays. *Bull. Seism. Soc. Am., vol. 74. p. 2313- 2333.*

4. J. Capon, 1970. Application of space-time domain decision and estimation theory to antenna processing system design. *Proc. IEEE, vol. 58, p. 1170-1181.*

5. J.P. Claassen, 1992. The application of multiply constrained minimum variance adaptive beamforming to regional monitoring. *Bull. Seism. Soc. Am., vol. 82, p. 2191-2212.*

6. A.F. Kushnir, 1995. Algorithms for adaptive statistical processing of seismic array data. *Proceedings of NATO Advanced Study Institute on Monitoring of a Comprehensive Test Ban Treaty, Portugal 1995. Kluwer Pub. Comp., Amsterdam.*

7. A.F. Kushnir (ed.), 1995. Seismic monitoring with small aperture arrays under strong noise conditions: algorithms, technique, system design and experimental data processing. *Technical report on EOARD special project SPC-94-4039.*

8. K. Aki, P. Richards, 1980. Quantitative seismology. Theory and Methods, *Freeman and Co., San Francisco.*

9. Prototype Arrays Incorporate New Technologies and Reduce Costs, *The Monitor, Newsletter of the Nuclear Monitoring Research Office, ARPA, Vol. 4/No 2, 1994*
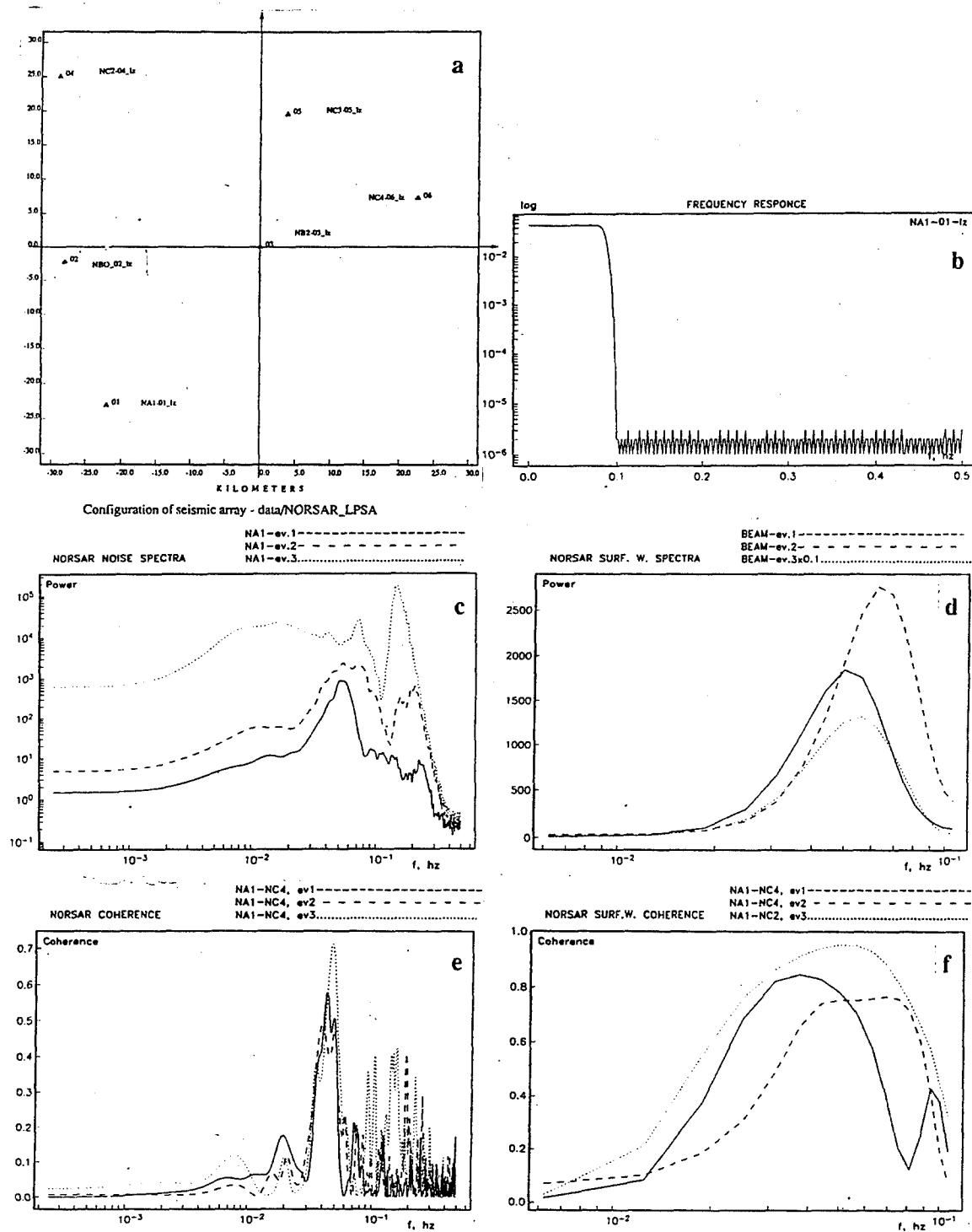
Fig. 1. NORSAR LP noise and signal characteristics: a) the location of NORSAR LP sensors;
b) the Chebyshev filter response; c) the PSD of NORSAR LP noise;
d) the PSD of explosion surface waves; e) the noise coherence functions;
e) the coherence functions of explosion surface waves.
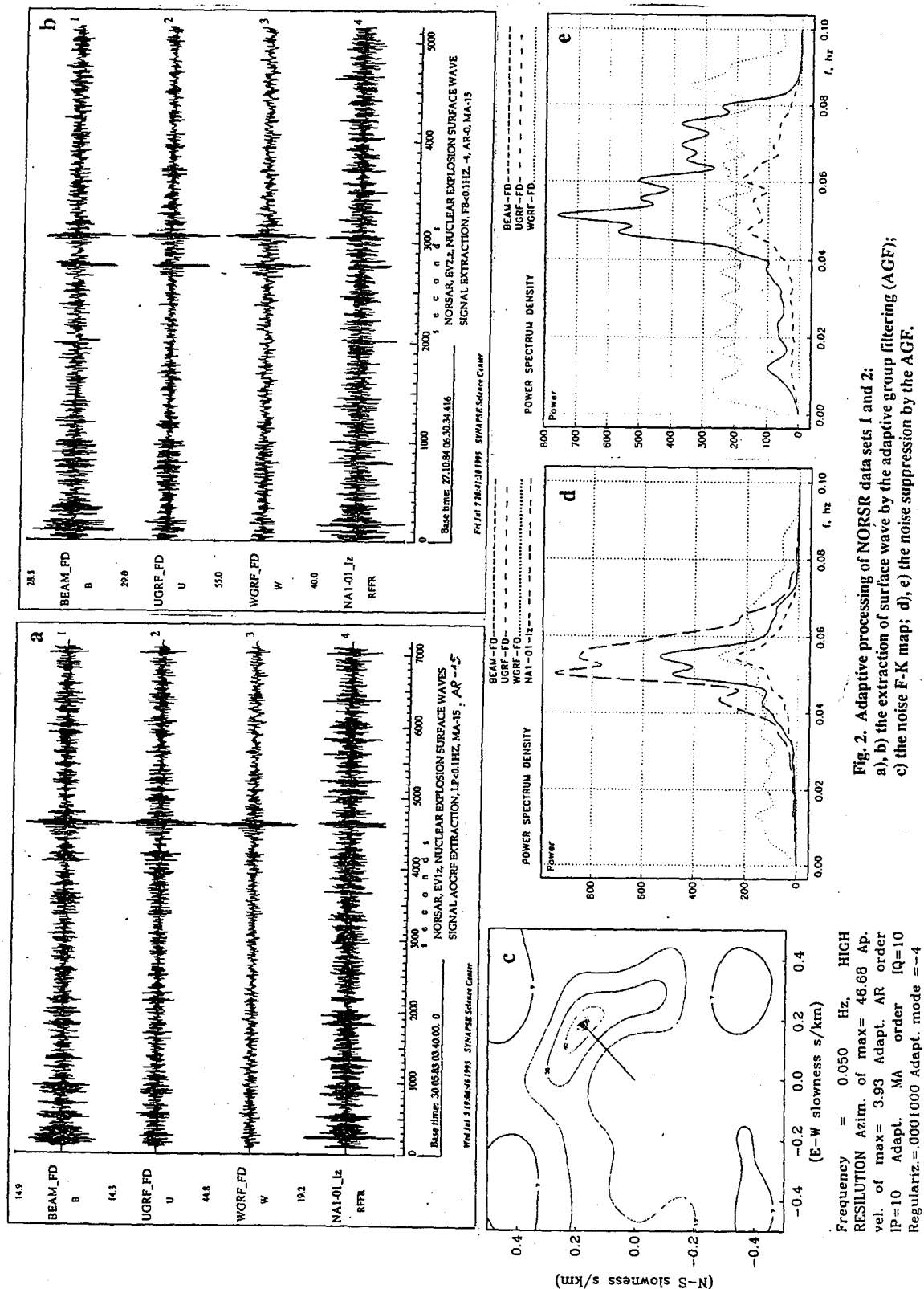
Fig. 2. Adaptive processing of NORSR data sets 1 and 2:
a), b) the extraction of surface wave by the adaptive group filtering (AGF);
c) the noise F-K map; d), e) the noise suppression by the AGF.

b

246.3 BEAM_FD B

289.5 UGRF_FD U

603.8 WGRF_FD W

227.1 NA1-01_1z RFFR

1 2 3 4

s e c o n d s

NORSAR. EV3, NUCLEAR EXPLOSION SURFACE WAVE
SIGNAL EXTRACTION, FB<0.1HZ, ARMA (15,15)

Base time: 26.10.83 02.48.21.786

Tue Jul 18 16:49:43 1995 SYNAPSE Science Center

a

288.8 BEAM_FD B

311.8 UGRF_FD U

134.0 WGRF_FD W

329.9 NA1-01_1z R

1 2 3 4

s e c o n d s

NORSAR. EV3, NUCLEAR EXPLOSION SURFACE WAVE
SIGNAL AOGRF EXTRACTION,<0.5, ARMA(15,15)

Base time: 26.10.83 02.48.16.420

Tue Jul 18 19:03:31 1995 SYNAPSE Science Center

e

POWER SPECTRUM DENSITY

Power

BEAM-FD
UGRF-FD
WGRF-FD
NA1-01-1z

f, hz

c

(N-S slowness s/km)

(E-W slowness s/km)

Frequency = 0.050 Hz, HIGH
RESILUTION Azim. of max= 76.52 Ap.
vel. of max= 3.74 Adapt. AR order
IP=15 Adapt. MA order IQ= 0
Regulariz.=.0001000 Adapt. mode =-2

d

(N-S slowness s/km)

(E-W slowness s/km)

Frequency = 0.040 Hz, HIGH
RESILUTION Azim. of max= 309.92 Ap.
vel. of max= 3.83 Adapt. AR order IQ=15
IP=15 Adapt. MA order
Regulariz.=.0001000 Adapt. mode =-4

Fig. 3. Adaptive processing of NORSAR data set 3:
a),b) the extraction of surface waves by the adaptive group filtering (AGF)
in the frequency ranges (0.-0.5) Hz and (0.-0.1) Hz;
c),d) the signal and noise F-K maps; e) the noise suppression by the AGF.
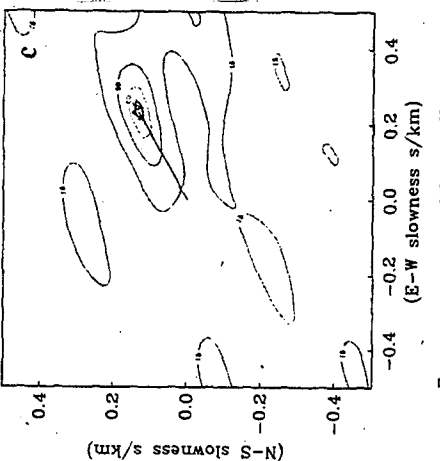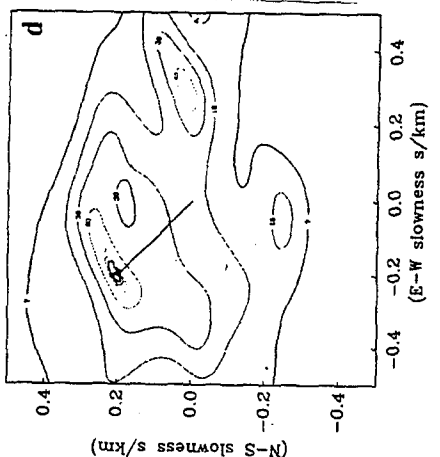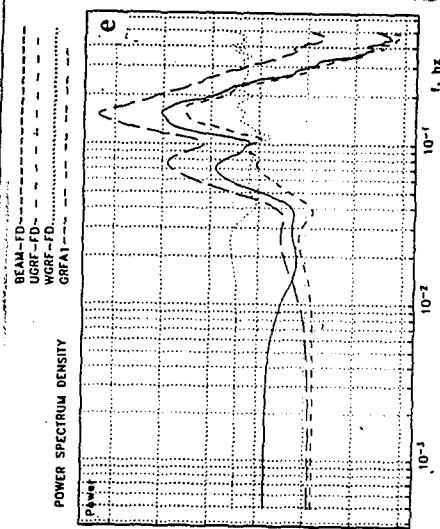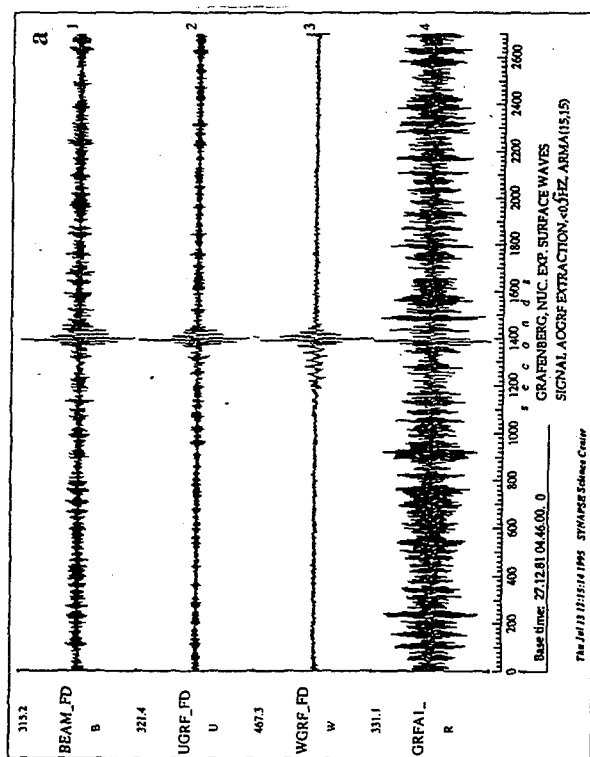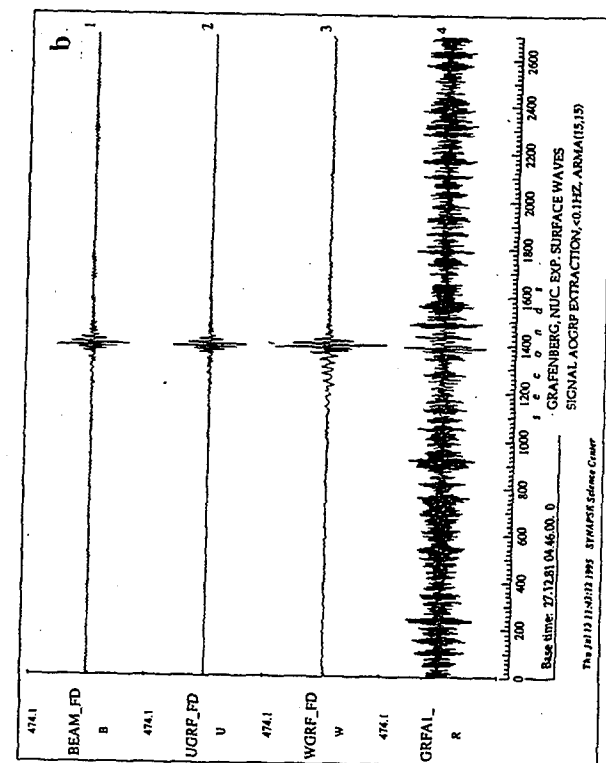
Fig. 4. Adaptive processing of the GRAFENBERG data set: a), b) the extraction of surface waves by the adaptive group filtering (AGF) in the frequency ranges (0.-0.5) Hz and (0.-0.1) Hz; c),d) the signal and noise F-K maps; e) the noise suppression by the AGF.

Fig. 5. GEYOKCHA LP noise characteristics: a) b) the F-K maps for different noise components; c) the extraction of simulated explosion surface waves from the real GEYOKCHA noise by the adaptive group filtering (AGF); d) the location of GEYOKCHA VBB sensors; e), f) the noise suppression by the beamforming and AGF in the frequency ranges (0.-10) Hz and (0.-1.) Hz;
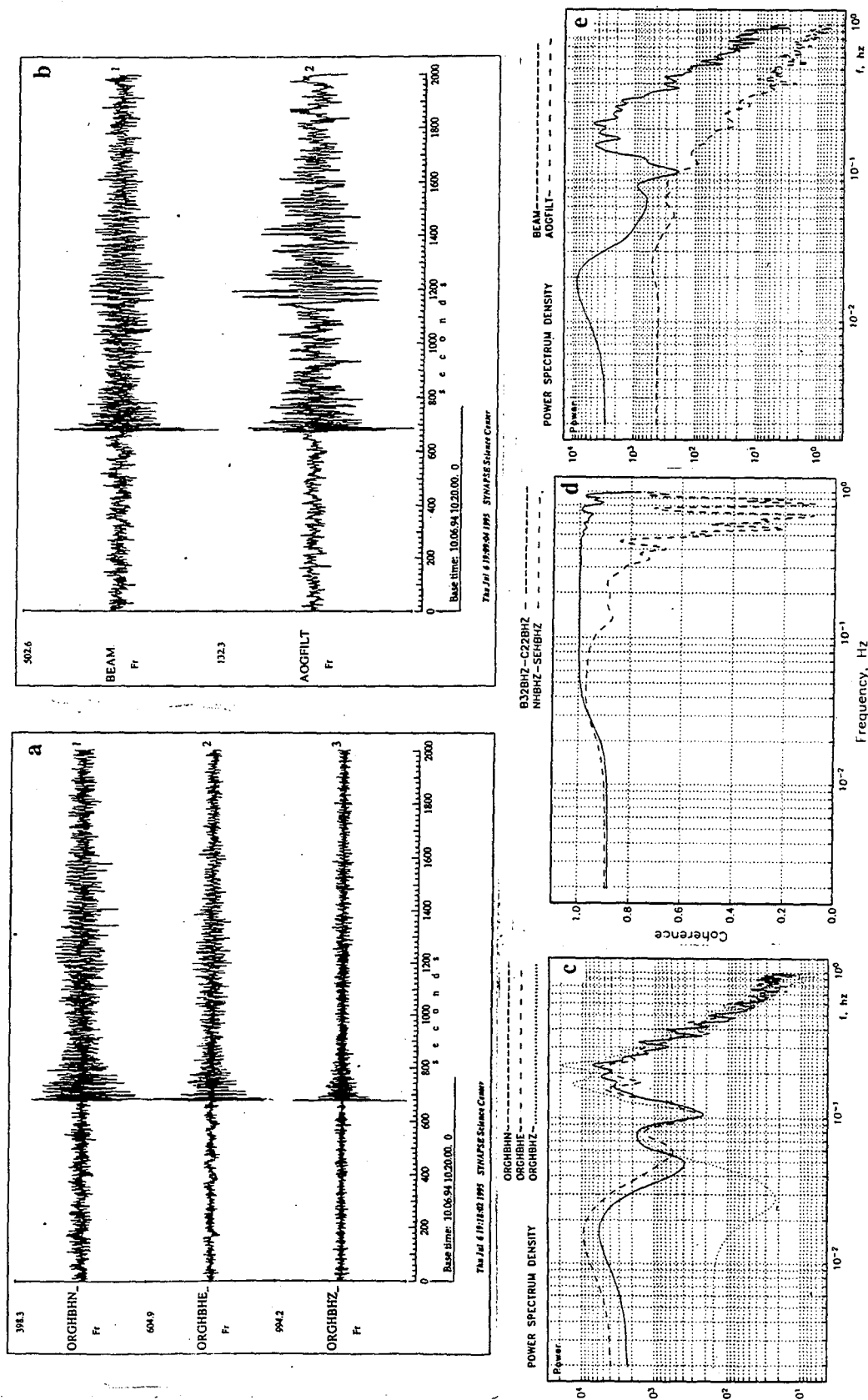
Fig. 6. Extraction of China explosion surface waves using GEYOKCHA VBB 3C records: a) the 3C seismograms of the China explosion; b) the extraction of surface waves by the adaptive group filtering (AGF); c) PSD of 3C noise; d) the noise coherent functions; e) the noise suppression by the AGF

A Geological and Geophysical Information System for the Middle East and North Africa

Dogan Seber, Eric Sandvol, Marisa Vallve and Muawia Barazangi

Institute for the Study of the Continents, Cornell University, Snee Hall, Ithaca, NY 14853

Abstract

We are collecting and organizing all available seismological, geophysical, topographical, geological, and satellite imagery datasets for the Middle East and North Africa into a digital information system that is quickly accessible via the Internet from Cornell and can be utilized in modeling and display programs. We are focusing our efforts on the Middle East and North Africa and locating and digitizing published crustal thickness, depth to basement, and crustal velocity and density structures, primarily as interpreted from seismic refraction and reflection, gravity and drill hole datasets. We have digitized some gravity maps and key geologic features for the Middle East. All data are being stored in ArcInfo Geographic Information System (GIS), the most widely used full-featured GIS. We are also maintaining a comprehensive bibliography of all the relevant references in a computer database. We are also developing new tools to extract and visualize the digitized databases. These new analysis tools will allow one easily to find and display any data and information in our database.

The databases being developed are essential for a successful global monitoring system, such as the International Data Center (IDC) and the GSETT-3 experiment. The final products, for example, will significantly contribute to accurate locations of seismic events, understanding high-frequency wave propagation at regional distances, and better characterization and calibration of seismic events in the region. The database, except the DMA topography, is accessible via the Internet from Cornell and can be accessed by ARPA/DOE/AFTAC/AFOSR researchers. Our Web address is: "http://www.geo.cornell.edu/geology/me_na/main.html".

Key words: Geographic Information System (GIS), digital databases, Middle East, North Africa

Objective

It is essential for the implementation and subsequent CTBT monitoring efforts that multidisciplinary information on any given region is readily available and accessible in a digital on-line format via electronic networks for use by concerned researchers and decision makers. New data, both seismological/geophysical and geological, are required to constrain advanced theoretical and modeling efforts in order to better understand the propagation of high-frequency seismic waves produced by very low yield events at regional distances. For these monitoring efforts to be successful, researchers must be able to detect, characterize, calibrate, discriminate, and verify any suspect event for most regions on earth. As important to the success of any monitoring strategy, such data must be swiftly accessible to researchers via networks in order to integrate with real-time recorded events to provide ground-truth for fast verification purposes. Our objectives are to collect and organize all available seismological, geophysical, topographical, and geological datasets for the Middle East and North Africa and to form a _digital_ information system that is accessible via the Internet (except the DMA topography) from Cornell.

In implementing these objectives, we are careful to focus on monitoring problems that are addressed or soon will be attacked by the different research groups. It is important that our digital, network-accessible information system is complete, comprehensive, multidisciplinary, unified, easy to update, and of direct relevance to monitor the negotiated CTBT or any other agreements. Because of the unique and considerable contacts between Cornell University and scientists and institutions in most of the countries of the Middle East and North Africa we are able to initiate contacts and assemble large data sets that need to be computerized to serve the ongoing and future work on monitoring the CTBT.

Research Accomplished

We have been focusing our efforts to develop and provide diversified databases on the Middle East and North Africa, including published results based on gravity, seismic refraction, and geologic/tectonic observations (e.g., Best et al., 1990; Seber et al., 1993; Barazangi et al., 1993). From available seismic refraction and gravity interpretation publications, we have digitized many of the crustal scale profiles available in the literature (Figure 1). This work has almost been completed. In addition to digitizing these profiles, we have written new tools that will make selection, identification and analyzing of these data quite easy. This eliminates potential problems that could have been faced when a user wanted to use the system without much ArcInfo knowledge. The new tool is all menu driven and requires no special training on ArcInfo to use it. We have put all the seismic refraction and gravity interpretations in one "coverage". The profile locations were digitized as accurately as possible. Then, the interpreted sections were digitized and "attached" to profiles locations. For refraction and gravity

profiles velocity and density information above and below each interface are recorded and saved in the coverage as attributes to the profile.

We have also complied a seismicity database from the USGS NEIC database. We extracted all the data (including explosions, mine blasts, rock bursts, etc.) for the Middle East and North Africa regions. This database is now a part of the databases at Cornell (Figure 2). We are developing menu driven tools that will make selection, search, and printing quite easy for an analyst or a researcher. We have also added to this database the Harvard CMT focal mechanism solutions of large earthquakes that occurred between 1977 and 1992 (Figure 2).

We have finished compiling a crustal scale Bouguer gravity data for Syria, Israel and Lebanon (Figure 3). This Bouguer gravity database is a part of our attempt to form a uniform grided Bouguer gravity data set for the entire Middle East, which then can be used along with previously interpreted seismic refraction profiles to obtain a Moho map for the whole Middle East. We are also compiling all available depth to Moho maps for the area. We digitized a map of Moho depth for Egypt (Figure 4), and Israel. These data sets will also be used in our efforts to map the Moho depth for the Middle East.

We have also developed a "profile maker" which runs under our World Wide Web (WWW) server (Figure 5). These tools, which are now under final testing, will allow any user to access our database through a client software (like Mosaic or Netscape) and make a crustal cross section for any region in Eurasia, including the Middle East and parts of North Africa. A user can define a profile from a computer screen and ask for the crustal cross section (which will include topography, basement, and Moho). The user can choose to use different data bases when available, and copy the graphics and/or ASCII files from our ftp server.

We still continue to build and expand our bibliographic database. References to books, journal articles, reports and other published literature are stored with the usual information on title, date, author, journal, page numbers, etc. and with searchable keywords on the content. This is becoming a comprehensive database of seismology, crustal structure, geology, and geophysics literature for the Middle East and North Africa. We will continue to update and add to this bibliographic database.

Conclusions and Recommendations

The data of our digital geological and geophysical information system will be useful for the interpretations of the seismic data in CTBT and nonproliferation monitoring. Geophysical and geological datasets can provide important ancillary information on the structure of the crust and upper mantle that may affect the

propagation of seismic phases through the continental lithosphere. In turn, this bears on the detection, discrimination, and yield estimation of nuclear explosions. The rapidly changing geopolitical situations in Eurasia, North Africa, and the Middle East make it imperative that databases are extended to areas outside the former Soviet test sites.

To monitor the anticipated multilateral comprehensive nuclear test ban and nonproliferation treaties, we recommend that multidisciplinary information on any given region be readily available and accessible in digital form via the Internet for use by concerned researchers and decision makers. New data, both seismological/ geophysical and geological, are required to constrain advanced theoretical and modeling efforts in order to better understand the propagation of seismic waves produced by very low magnitude events at regional distances. For these monitoring efforts to be successful, researchers must be able to detect, characterize, calibrate, discriminate, and verify any suspect event for most regions on earth. As important to the success of any monitoring strategy, such data must be swiftly accessible in digital form to researchers via networks in order to integrate with real-time recorded events to provide ground-truth for fast verification purposes.

References

Barazangi, M., Seber, D. , Chaimov, T. , Best, J. , Litak, R. , Al-saad, D. , and Sawaf, T. , 1993, Tectonic evolution of the northern Arabian plate in western Syria, in E. Boschi et al. (Eds), *Recent evolution and seismicity of the Mediterranean region*, p. 117-140.

Best, J.A., Barazangi, M., Al-Saad, D., Sawaf, T., and Gebran, A., 1990, Bouguer gravity trends and crustal structure of the Palmyride Mountain belt and surrounding northern Arabian platform in Syria, *Geology*, v. 18, p. 1235-1239.

Healy, J. H., Mooney, W. D., Blank, H. R., Gettings, M. E., Kohler, W. M., Lamson, R. J., and Leone, L. E., 1982, Saudi Arabian seismic deep-refraction profile: Final project report, *U. S. Geological Survey Open-File Report 02-37*, p 370.

Makris, J., R. Rihm, and A. Allam, 1987, Some geophysical aspects of the evolution and structure of the crust in Egypt, in, El-Gaby, S., and R.O., Greilings (Eds.), *The Pan-African Belt of Northeast Africa and Adjacent Areas*, Friedr. Vieweg & Sohn, Braunschweig, p. 345-369.

Seber, D., Barazangi, M., Chaimov, T., Al-Saad, D., Sawaf T., and Khaddour, M., 1993, Upper crustal velocity structure and basement morphology beneath intracontinental Palmyride fold-thrust belt and north Arabian platform in Syria, *Geophys. J. Int.*, v . 113, 752-766.
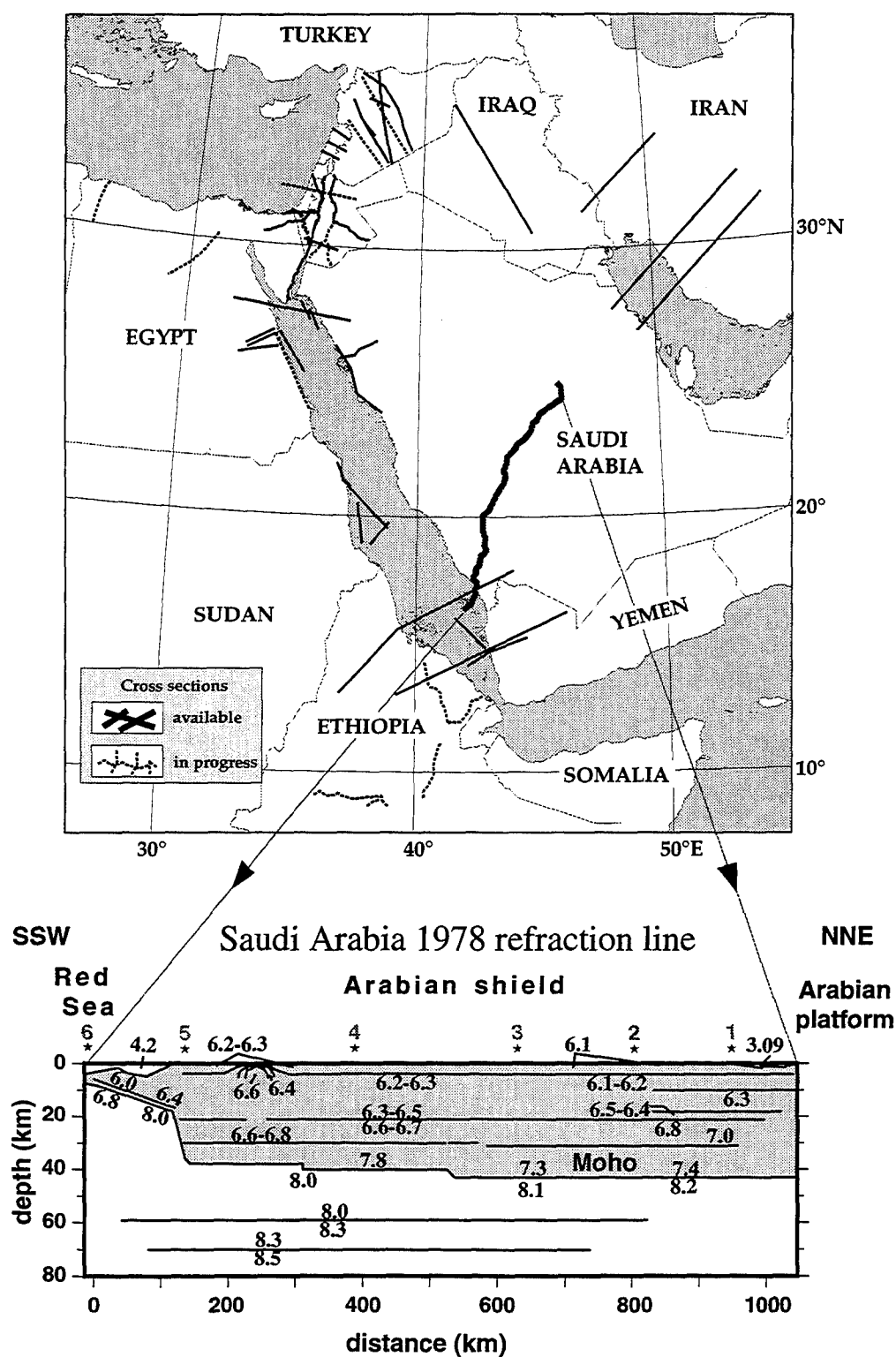
Figure 1. Map of the Middle East showing locations of crustal profiles. Both refraction and gravity profiles are shown as thick lines. The Saudi refraction profile (after Healy et al., 1982) is also shown as an example (shot points, stars, and velocity in km/s are shown).

Seismicity of the Middle East and North Africa (1960-1990)
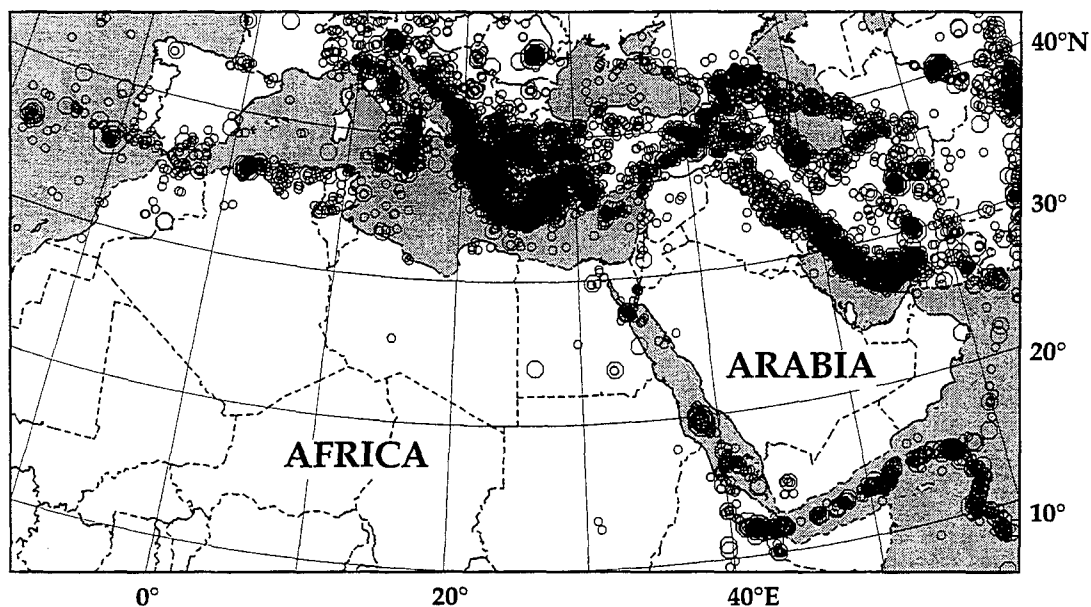
Focal Mechanism Solutions of the Middle East and North Africa (1977-1992)
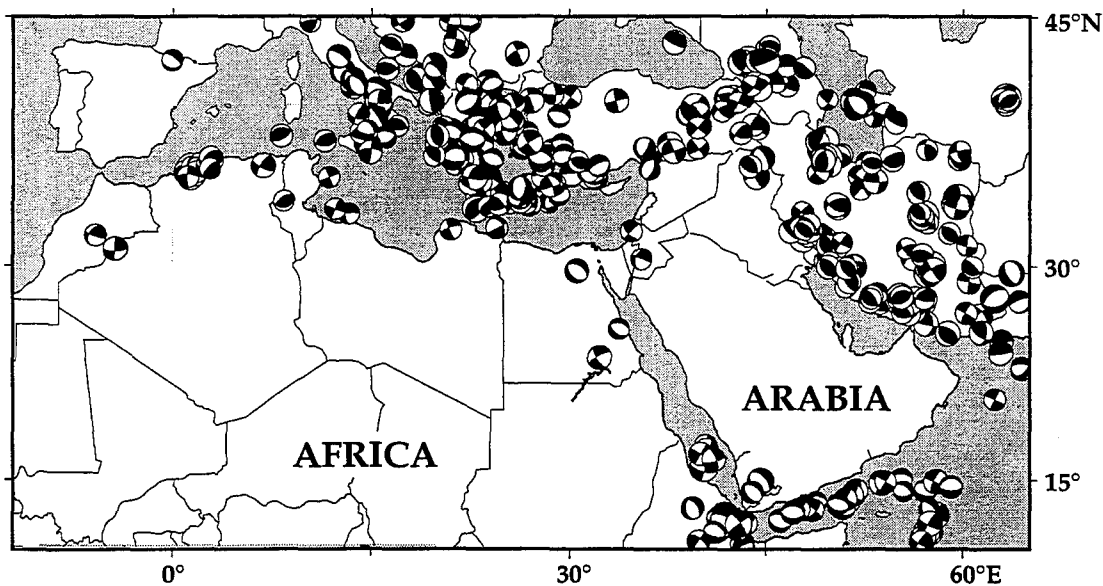
Figure 2. Seismicity and available focal mechanisms for the Middle East and North Africa.

Bouguer Gravity Map of Syria, Lebanon and Israel
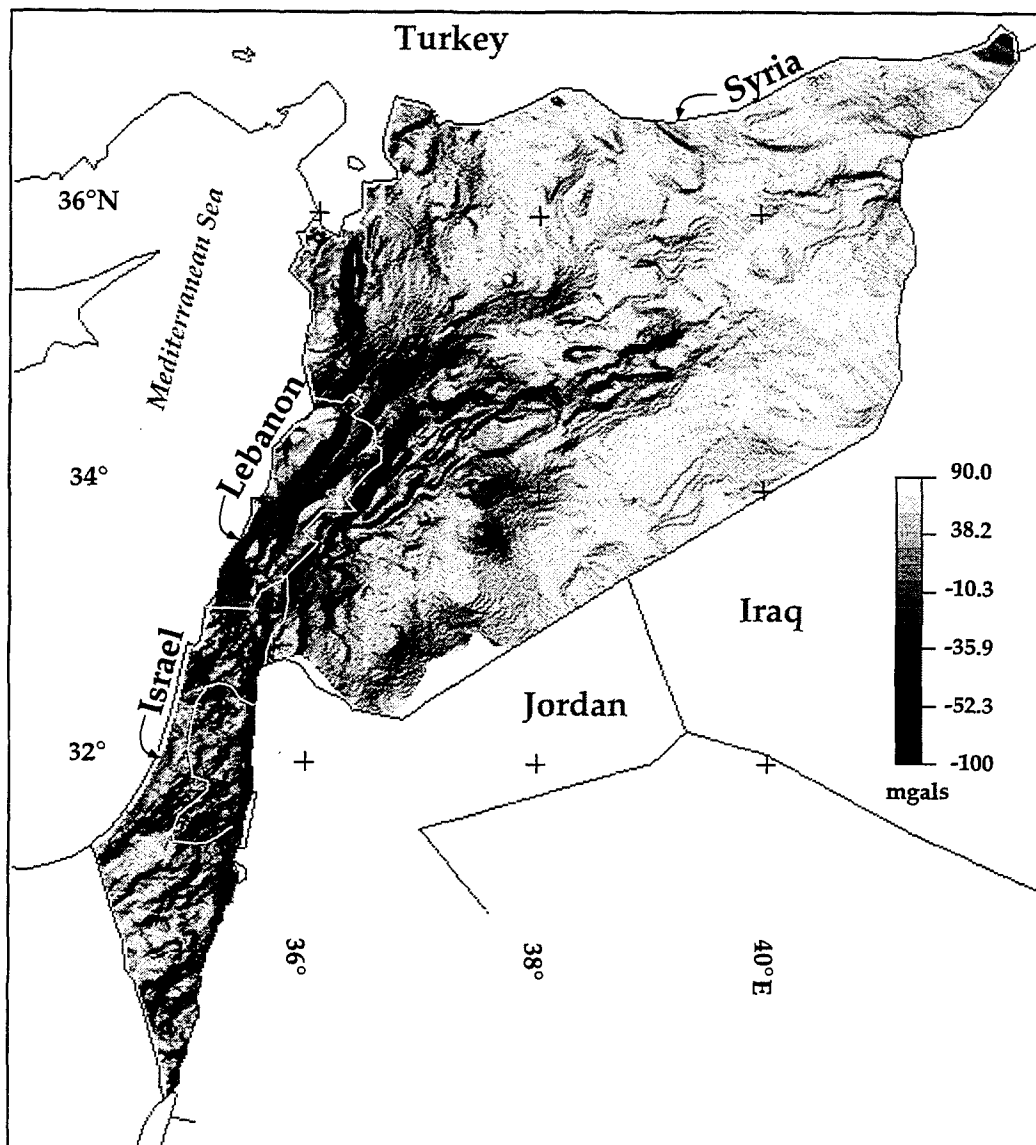
Figure 3. Shaded imsge of Bouguer gravity map of Syria, Lebanon, and Israel
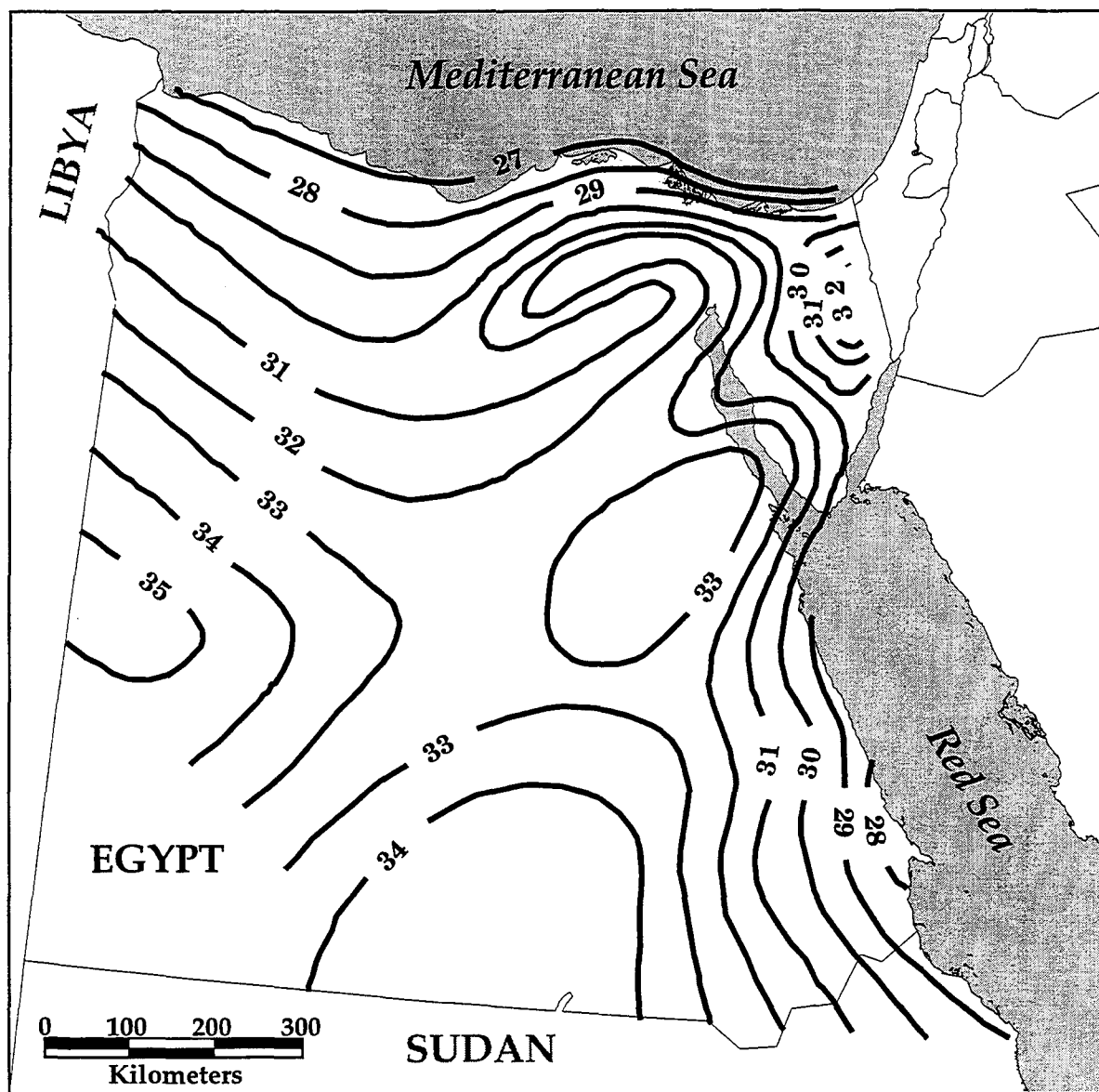
Figure 4. Contour map of depth to Moho in Egypt (after Makris et al., 1987).
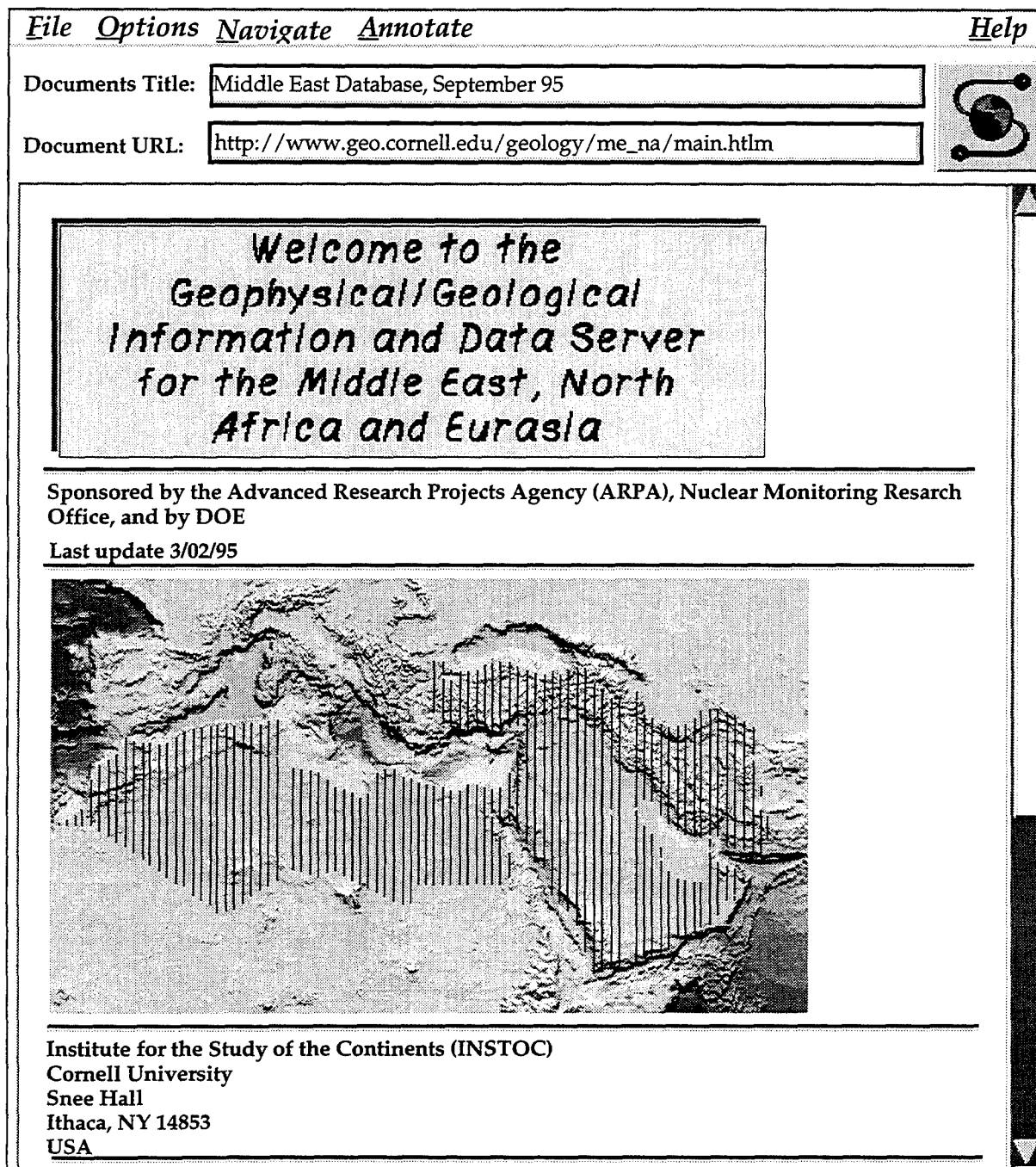
Figure 5. First page of our WWW server. Most of our data can be found in this server.

Broadband Signal Enhancement of Seismic Array Data: Application to Long-period Surface Waves and High-frequency Wavefields

Frank Vernon and Robert Mellors
IGPP, UCSD
La Jolla, California

David Thomson
ATT Bell Labs
Murray Hill, New Jersey

Abstract

We are developing a radically new approach to the problem of low signal-to-noise long-period surface waves using a newly developed approach that Thomson (1990) calls quadratic inverse theory. Analysis of surface wave dispersion requires precise measurements of relative phase. The double coherence estimate provides the the coherence and phase between different frequencies in the same signal. We tested the multitaper double-coherence technique with simple signals. The signals were designed to mimic the characteristics of idealized seismic data (both surface and body waves) but with defined frequency and amplitude. Initially, pure signals were processed and plotted. The signals were then degraded by adding random noise and plotted. We compared the results from the pure signals and the noisy signals to identify robust features in the coherence plots. Tests with real seismic data yield patterns similar to those seen in synthetic tests. We plan to conduct further tests with seismic data and investigate methods to further improve signal resolution.

ENHANCEMENT OF SURFACE WAVES WITH A BROADBAND ARRAY

The most successful technique yet devised for the discrimination of nuclear explosions and earthquakes is the now standard M_S versus m_b technique. Unfortunately, this technique fails for low-yield nuclear tests when the signal-to-noise of the long-period surface wave train drops to a low enough level to make measurement of M_S impossible. We are developing a radically new approach to this problem using a newly developed approach that Thomson (1990) calls quadratic inverse theory. Analysis of surface wave dispersion requires precise measurements of relative phase. However, a classical problem in time series analysis is that the standard methods of estimating spectra and autocorrelations loose phase information. Phase measurements using higher order statistics such as the bispectrum assume stationarity and typically have higher variances than second order methods. They are also much less robust than standard estimates and are more susceptable to noise.

The fundamental difference between stationary and non-stationary signals is that in a non-stationary signal energy at different frequencies are correlated. We are attempting to find the phase using some properties of non-stationary signals combined with some new estimation methods. The double coherence estimate provides the the coherence and phase between different frequencies in the same signal. We are testing this technique as a additional tool to refine dispersion curves for smaller events.

Multitaper double coherence

The double coherence technique uses spectral estimates derived from the multitaper method (Thomson, 1982; Park *et al*, 1987) to determine cross spectral coherences of two signals. Double coherence differs from standard estimates of coherence in that coherence is calculated between all the frequencies in the two signals rather than at one frequency.

The multitaper spectral estimates combines weighted spectral estimates from a number of differently tapered versions of a given signal to yield a high-resolution spectral estimate. The tapers are mutually orthogonal and are based on the prolate spheroidal tapers developed by Slepian (1983). Multitaper estimates have the advantage that they are optimized to minimize leakage from outside the desired band and provide statistically independent estimates of the spectra. Each spectral estimates (S_{ij}) is determined using:

$$S_{ij}(f) = \frac{A}{K} \frac{\sum_{k=0}^{K-1} \lambda_k d_k^2(f) y_{ik}(f) y_{jk}(f)^*}{\sum_{k=0}^{K-1} d_k^2(f)}$$

where d_k are the weights of each spectral estimate, λ_k are the eigenvalues associated with each taper, and y_k are the discrete Fourier transforms of the tapered data. A is determined using $A = \sum_{k=0}^{K-1} \lambda_k^{-1}$ and K is the number of tapers.

The multitaper double coherence $\gamma_{ij}^2(f)$ is calculated using

$$\gamma_{ij}^2(f_{1,2}) = \frac{|S_{ij}(f_1)S_{ij}(f_2)^*|}{S_{ii}(f_1)S_{jj}(f_2)}$$

This corresponds to standard coherence in the case where $f_1 = f_2$ which is the diagonal of the double coherence estimate. Since the numerator is in effect multiplying a signal by a time-delayed version of the frequency components of the other signal, this estimator is sensitive to dispersive signals.

Tests with synthetic data

We tested the multitaper double-coherence technique with simple signals. The signals were designed to mimic the characteristics of idealized seismic data (both surface and body waves) but with defined frequency and amplitude. Initially, pure signals were processed and plotted. The signals were then degraded by adding random noise and plotted. We compared the results from the pure signals and the noisy signals to identify robust features in the coherence plots.

The amplitude and phase coherence of these signals is plotted as two square matrices, with the frequencies (normalized to the Nyquist frequency) of one signal on the x axis and the frequencies of the other signal on the y axis. The intersection of each frequency shows the cross-spectral coherence of the two signals. The auto-coherence of white noise (generated by an random number generator), for example, shows a diagonal line on both the amplitude and phase plots since the coherence of a signal with itself at a given frequency is unity and zero-phase. We also plotted the cross-diagonal of the phase coherence plot to show the phase relationship between different frequencies.

Varying-frequency signals. A sine wave that varies in frequency, typical of dispersed surface waves, shows a clear and characteristic pattern (Figure 1). The pattern is dominated by a zone of high coherence very near the diagonal and a larger patch of high coherence located above the intersection of the two frequency ranges. A broad zone of low coherence, less visible on Figure 1, is present at the intersection of the two frequency ranges. This patch of low coherence is present where the energy in the frequency band is high but the sum of the signal multiplied with its conjugate is low, producing a low overall coherence amplitude. This zone of low coherence is

809

most resistant to the addition of noise, since noise reduces coherence but doesn't greatly change the energy level in that frequency band.

The plots of phase coherence were seriously degraded by the addition of noise. We also tested modulating the sweep signal to produce 'packets' of varying waves similar to the effects of multi-pathed surface waves. This had little effect on the results. Tests of sweep signals with varying ranges showed that the coherence decreased as the range of frequencies increased, as expected. The zone of high coherence was reduced was the addition of noise but a high amplitude zone remained. Coherence was also decreased by increasing the range of frequencies, as expected, since two closely matched frequencies are more coherent that two separate ones.

Impulsive signals. Several time-limited signals, intended to represent body waves, were tested. Figure 2 shows the results for a sinc-like function. The pure signal had a very high amplitude coherence across most frequencies except for a band near the center frequency of the sine function. Since the amplitudes of the off-center frequencies were very low, the addition of noise reduced the coherence. The addition of noise actually improved the contrast in coherency level and a diffuse patch of higher coherency is observed centered around the frequency of the sin function. A Ricker wavelet showed similar results. This signal produced an especially clear pattern in the phase spectrum, as the components of an impulse signal are closely related in phase. This pattern is obvious in the cross-diagonal plot. Noise decreased the phase coherence but the basic trend is still evident.

Tests with real data. We tested the algorithm with seismic data recorded by the Kyrgyzstan broadband seismic network. Figure 3 shows some of the preliminary results. The upper two plots show coherence and phase for a teleseismic P arrival (and following phases) from an event 28° away. Although the time domain appearance differs greatly, the signal yields a pronounced phase pattern similar to the impulsive sinc-like function in Figure 2, probably due to the time-limited nature of the signal. Coherence of surface waves from a small regional (250 km) event in southern Kyrgyzstan is shown in the lower part of Figure 3. The mixed frequency content of the signal creates a complicated pattern of coherence at higher frequencies and a band of low coherence at very low frequencies.

Conclusions. We demonstrate the use of double coherence algorithm to resolve synthetic representations of seismic signals in the presence of noise. Tests with real seismic data yield patterns similar to those seen in synthetic tests. We plan to conduct further tests with seismic data and investigate methods to further improve signal resolution.

References.

Park, J. J., F. L. Vernon III, and C. R. Lindberg, Multitaper spectral analysis of high-frequency seismograms, *J. Geophys. Res.*, **92**, 12,675-12,684, 1987.

Slepian, D., Some comments of Fourier analysis, uncertainty, and modeling, SIAM Rev., **25**, 379-393, 1983.

Thomson, D. J., Spectrum estimation and harmonic analysis, IEEE Proc.,**70**, 1055-1096, 1982.

Thomson, D. J., Quadratic-inverse spectrum estimates: application to palaeoclimatology, *Phil. Trans. R. Soc. Lond. A.*, **332**, 539-597, 1990.
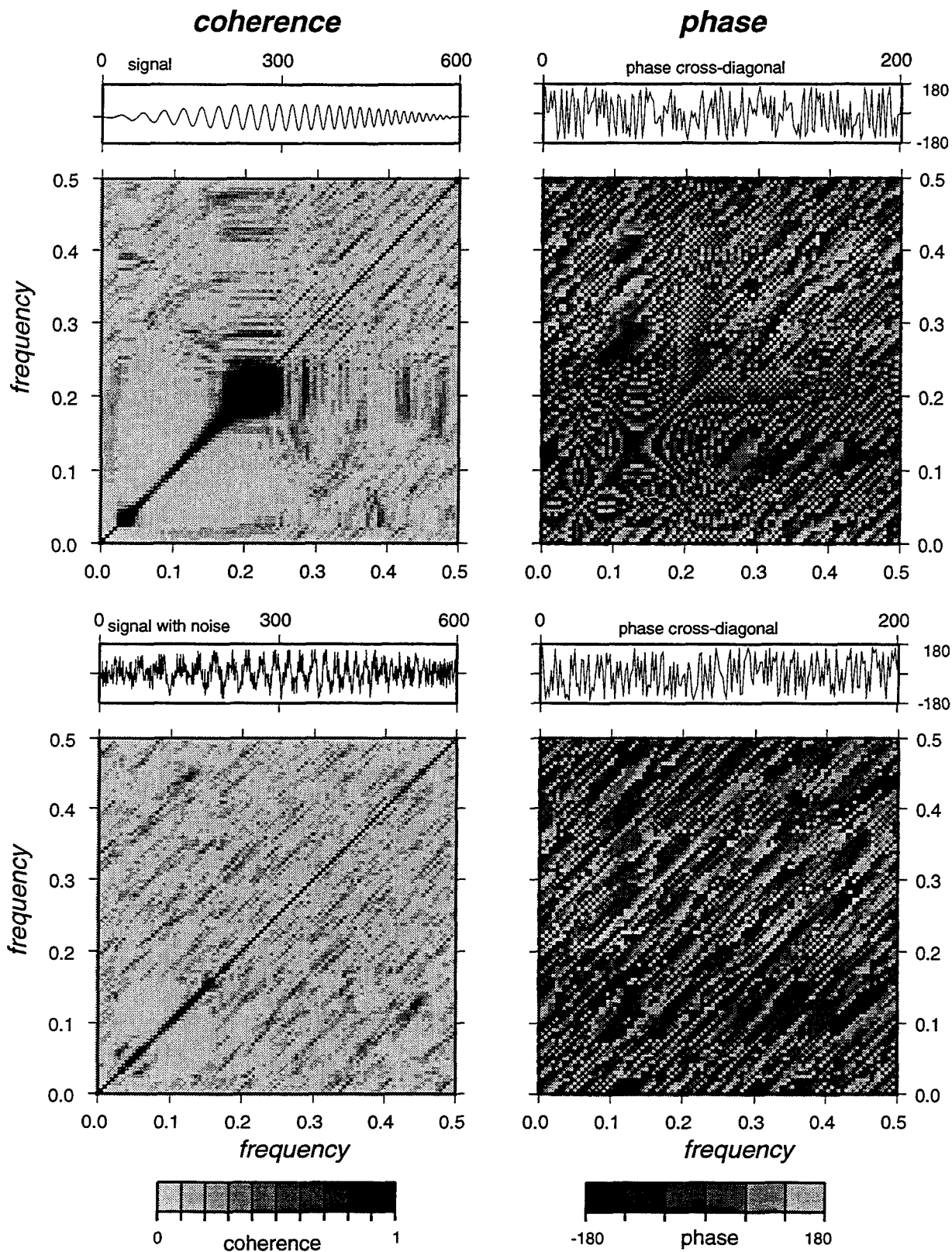
coherence

phase

Figure 1. Double coherence of a sweep signal ranging in frequency from 0.03 Nyquist to 0.2 Nyquist. Pure signal (top) and signal with noise (bottom) are shown. Signals are shown on left above corresponding matrix plots. Phase cross-diagonals are shown on left above matrix plots.
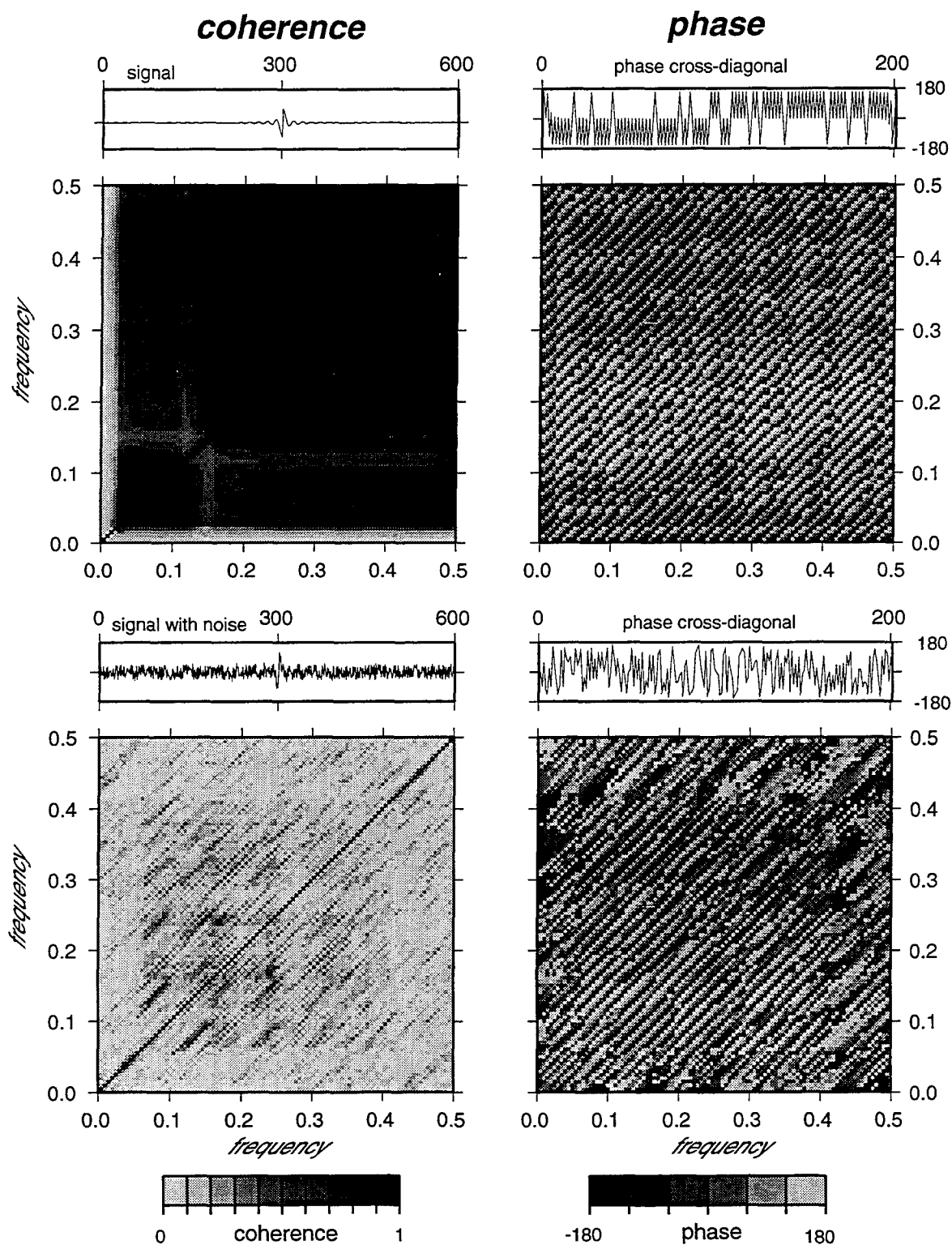
Figure 2. Double coherence and phase of a 0.15 Nyquist sinc-like function with and without noise. High coherence of the pure signal is greatly reduced by noise except at near the primary frequency. Note the clear phase relationship shown by the phase plots.
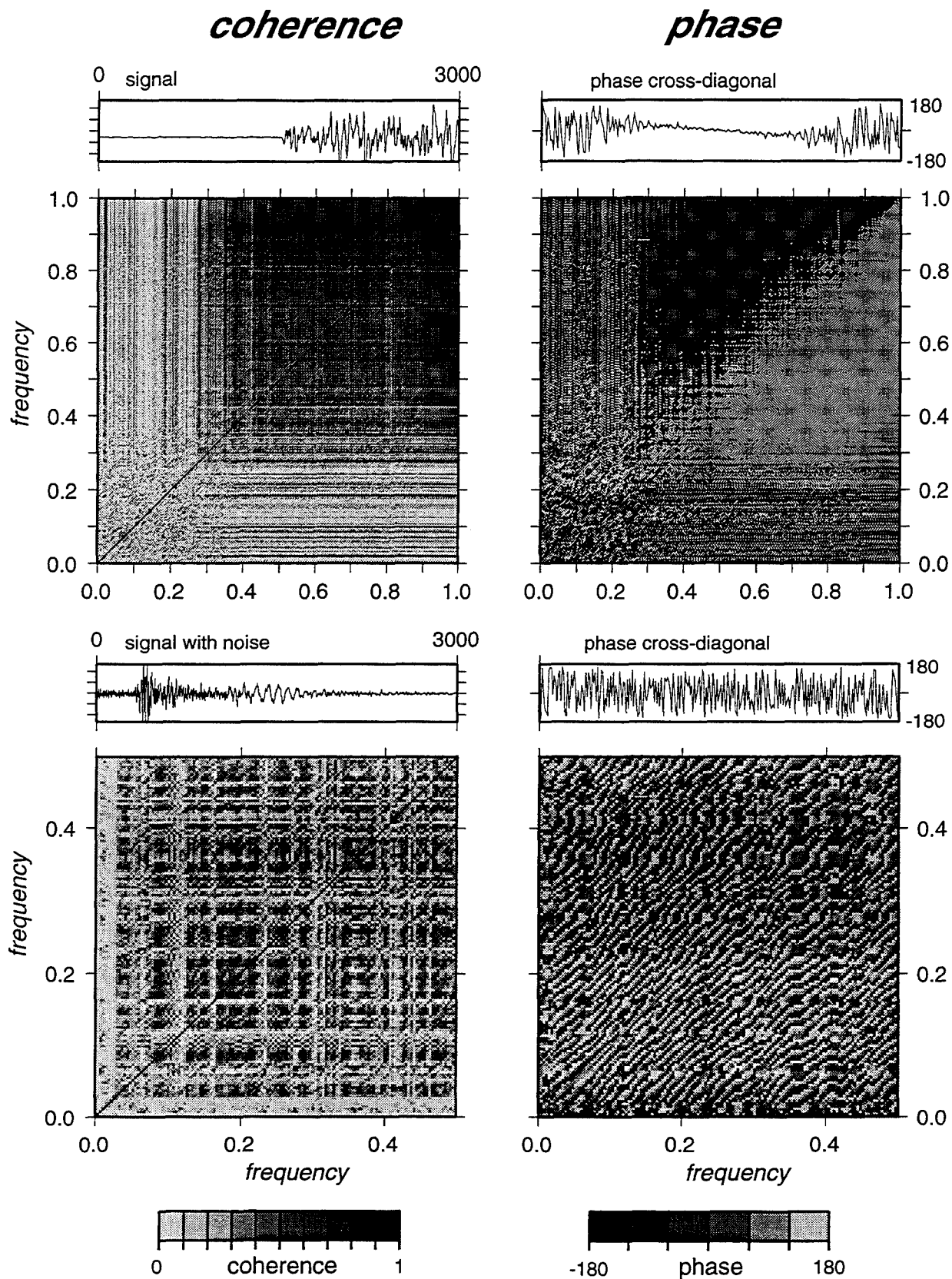
Figure 3. Double coherence for broadband seismic data recorded in Central Asia by the Kyrgyzstan broadband network. Event at top is teleseismic P wave and lower event is surface waves from a regional (300 km) earthquake. Note that the upper plots show full Nyquist frequency.

814

A Top-down Hierarchical Approach to the Display and Analysis of Seismic Data

Christopher J. Young, Constantine Pavlakos, Tony L. Edwards
Sandia National Laboratories
work completed under DOE ST485D

ABSTRACT

Seismic monitoring of a CTBT (Comprehensive Test Ban Treaty) will require analysts to review tens of events per hour recorded by networks of more than a hundred stations. Use of the traditional waveform display as the primary data display tool is incompatible with this requirement; traditional waveform displays are inefficient in their presentation of relevant data and place high demands on computer resources. Drawing on resident data visualization expertise and on our hands-on experience with the design and implementation of the ADSN (AFTAC Distributed Subsurface Network) system at AFTAC, we have designed a new system consisting of a hierarchical series of displays which present relevant information to the analyst in a more efficient manner. The displays are designed to be used in a top-down manner with the analyst starting with the most general display and proceeding to the most specific (the waveform display) only when it is needed. Testing to date has focussed on data from the GSETT2 (Group of Scientific Experts Technical Test #2) in 1991. Future efforts will be directed towards improved data sets from the ongoing GSETT3.

Keywords: data visualization, hierarchical, waveform display

INTRODUCTION

Full-time real-time monitoring for nuclear explosions implies high quality analysis done very quickly. Regardless of how well a monitoring system might meet one of these criteria, it cannot be used if it does not meet the other as well; thus seismic monitoring in general cannot be done on a system designed for research purposes. The entire job from signal detection to event discrimination was at one time done entirely by analysts, but a great deal of the work is now done by automatic systems. In fact, sophisticated systems such as the ADSN at AFTAC (AFTAC Distributed Subsurface Network) or the system at the IDC (International Data Center) start from the raw data and produce a complete listing of events without any analyst intervention. However, an analyst still must review all of the automatically built events and this can be very time consuming. Until a system can be developed which never misbuilds or misclassifies events, analysts will be important parts of seismic monitoring systems.

Despite the tremendous technological improvements of the last 30 years, the basic data display used by seismic analysts to review events has changed very little. Most analysts spend the majority of their time staring at some sort of display of the waveforms from the seismic stations in their network. For the research environment which emphasizes precision work on selected events, this approach still has many advantages, but as a standard method for examining the large number of events built by automatic systems, it is very inefficient. The situation will only be exacerbated as detection thresholds must be reduced for a Comprehensive Test Ban Treaty (CTBT).

The standard waveform display has several shortcomings. First, it is a poor way to display data from a large numbers of stations. For a handful of stations the display is acceptable, but for numbers of stations above 20 or so, either the waveforms must be reduced to a scale with very low resolution or the waveforms must be split into groups and viewed a screenful at a time. A second problem is that the amount of data required for the display (a waveform for each station) is large and consequently the time for such a display to be presented to the analyst is not trivial; in our own experience with the ADSN (AFTAC Distributed Subsurface Network) system at AFTAC, we have found that a significant portion of analysis time is taken up waiting for the waveform displays. Once the waveforms are displayed, an experienced analyst may need only a few seconds to decide whether an event is valid and should be refined or is bogus and should be broken; unfortunately, however, the decision generally cannot be made without going to the standard waveform display (other options are limited). Thus in theory the cost (in analyst time) of building false events should be relatively small, but in practice it can be quite large.

A third problem is that the standard display does not provide a convenient mode to display auxiliary information which may be of use to the analyst in working an event. For example, when evaluating the association (or lack thereof) of a particular station with an event, there are many parameters besides time that the analyst may use: e.g. observed distance (slowness) vs. predicted distance, observed azimuth vs. predicted azimuth, observed amplitude vs. predicted amplitude and/or amplitudes of other stations, background noise level, past recordings from known events in the same area, etc. All of this information is readily available and yet most of it is either not displayed or poorly displayed with traditional systems.

Some of these problems can be lessened by technological improvements -- multiple monitor systems can be used to display more waveforms simultaneously at acceptable resolution, and the wait for waveforms is bound to decrease as faster computers are developed -- but we believe it may be possible to achieve significant gains even with currently available resources by making a fundamental change in the way that data are presented to seismic analysts. The need for a better presentation method has never been clearer; as we move towards CTBT monitoring analysts may be faced with tens of events per hour and with networks of more than a hundred stations. To keep up, events must be dealt with very quickly, but this will be difficult given the potential number of stations to review. Routine

use of a waveform display for each event is impractical, and familiarity with the network on a station-by-station basis (a critical built-in assumption in many analysis schemes) is virtually impossible.

TOP-DOWN HIERARCHICAL DISPLAYS

A better system would present useful information to the analyst in a more efficient manner. At any given point in the analysis process, no more information should be displayed than is absolutely necessary for the analyst to complete their job. We have designed a system specifically to meet this requirement. Our system consists of a hierarchical series of displays underlain by access to all of the information available in a database populated by automatic and manual processing. The displays are meant to be accessed from the top down with the level of detail increasing as the hierarchical level decreases. The lowest level is the traditional waveform display, but it is hoped that for many events the analyst may not need it.

In designing the system, we have taken advantage of available Sandia expertise in the areas of computer visualization and seismic analysis systems (via the ADSN project). The former provides the tools for designing the interfaces while the latter provides the guidance to make them relevant. The resultant hierarchical design should not only streamline the process of analysis but it should also increase the quality of the product (i.e. an event bulletin) because the system will make the analyst better informed about network and event characteristics. The current generation of global monitoring systems (e.g. those at the IDC and at AFTAC) populate huge numbers of fields in database accounts with numerical measurements quantifying various parameters relevant to seismic analysis (phases, events, instrumentation at each station, noise levels, etc.) and yet much of this information is not presented to the analysts. This is doubly unfortunate because not only might the information be helpful, but typically access to it is much quicker than to the waveforms.

Our system presents the database information first, and then the waveforms if necessary; the underlying principal in the design of the new system is to present increasing levels of detailed only as they are needed. This is in direct contrast to traditional systems where the analyst frequently starts with the waveforms. Our current version of the system has three levels: a Global Event Summary Display, an Event Quality Display, and a traditional Waveform Display.

1. Global Event Summary

The Global Event Summary Display (GESD) provides a high level summary of the seismic activity and other relevant information (e.g. seismicity, known nuclear test locations, known mine locations, etc.) for a specified time period as determined by the analyst. The map portion of the display shows all of the events in the specified time period with certain (selectable) characteristics hilighted by visual cues (color, size, shape, etc.). In many cases the geographic location alone will decide the next course of action, but for other events the additional information displayed (e.g. depth, magnitude, number of

reporting stations, station locations, discriminations results, error ellipse, depth error) may considerably streamline subsequent analysis.

Main Display -- Global Event Summary
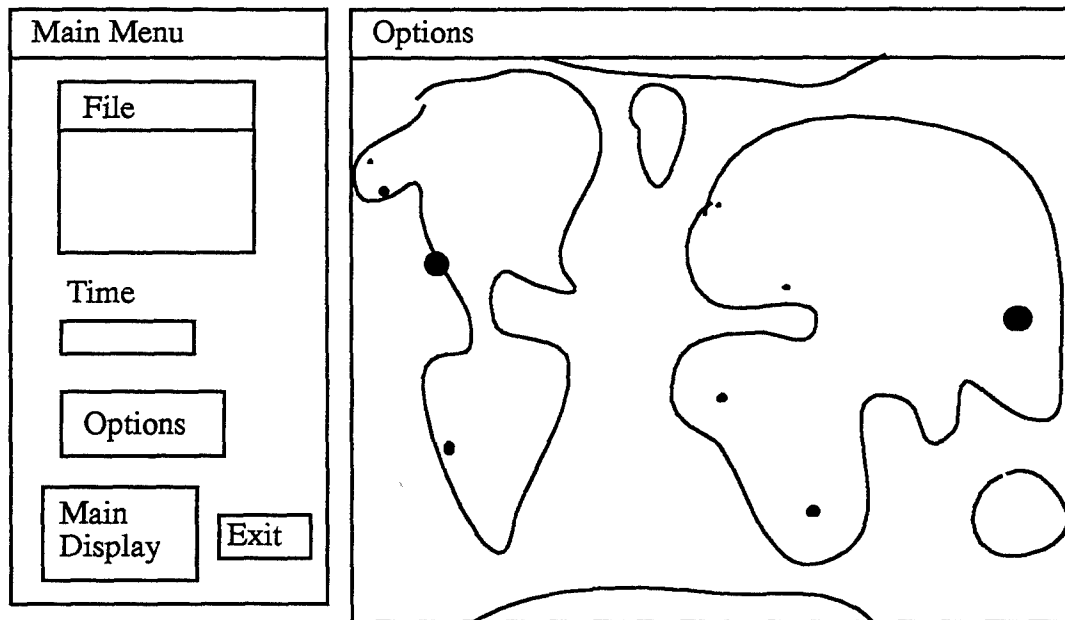
FIGURE 1. Cartoon of basic design for the GESD. The left side of the display contains various widgets (radio buttons, pull-down menus, text boxes) for specifying parameters to be displayed. The right side is a map with various superimposed objects representing relevant items such as events, stations, locations and types of known sources.

The GESD is linked to the next level, the Event Quality Display (EQD) by means of the events displayed in the GSED map: selecting an event will automatically bring up the EQD for that event.

2. Event Quality Display

The EQD provides a detailed view of the information relevant to a specific event. The basic information displayed includes the location of the event and the stations in the network, but a great amount of additional information can be projected onto these objects using visual cues. Potential parameters include:

- Event: depth, error information, number of defining stations, number of associated phases, magnitudes, discrimination results)

- Station: type of station (array, three component, etc.), noise level, signal-to-noise ratio, station magnitude, predicted amplitude, observed azimuth and slowness, theoretical azimuth and slowness

818

As much of the information as can be reasonably comprehended will be mapped via visual cues, but a complete summary of the relevant information is available in a text window as well.

Event Quality Display
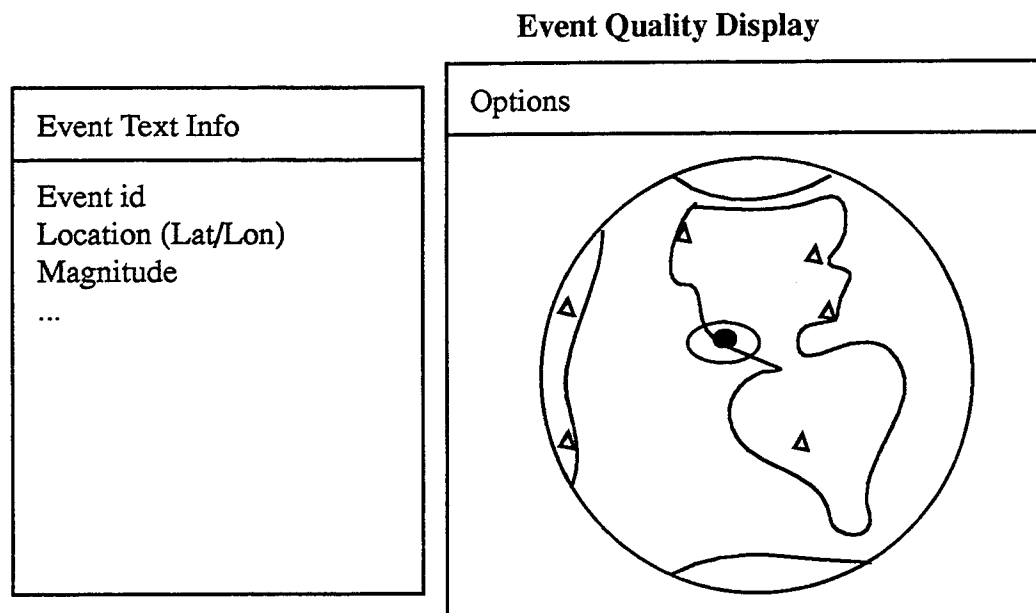
FIGURE 2. Cartoon of basic design for the EQD. The left side provides a (text) listing of information relevant to the event. The right side is a map display centered on the event with various other objects plotted which may be of use to the analyst. Parameters displayed and the visual cues (color, size, shape, etc.) used to highlight them can be set via pull-down menus.

The final display level, the traditional Waveform Display can be triggered either by clicking on stations (selected waveforms displayed) or on the event (all waveforms displayed).

3. Waveform Display

The waveform display provides the traditional times series and related displays (e.g. FK diagrams) used to analyze seismic data in detail. Rather than design a new waveform display, we plan to use one of the numerous available existing, mature packages (e.g. ARS, geotool, SAC).

PLATFORM AND DATA SET

The GESD and the EQD are being developed using the AVS/Express data visualization package running on an SGI Onyx. To date we have tested the displays using data from the GSETT2 (Group of Scientific Experts Technical Test #2) experiment in 1991 which are stored in a CSS3.0 format Oracle database.

FUTURE PLANS

Though useful for testing a prototype, the GSETT2 data set is limited: it contains only the final database account (after both the automatic system and the analyst have worked the data), the number of high quality stations is limited, and many of the database tables are not fully populated. In the near future we plan to begin to test our displays using information from the IDC database for the ongoing GSETT3. This data set is much more complete than that for GSETT2 and it contains several separate accounts which can be used to compare the value added by the automated system with that added by the analyst.

In particular we are interested in trying to provide visual cues which can help identify the events that are not common to both the automatic and analyst generated accounts. If

the proper combination of cues could make it possible to quickly identify bogus events (i.e. those rejected by the analysts in reviewing the output of the automated system) from either the GESD or the EQD, a significant amount of analysis time could be saved. Conversely, the proper use of visual cues for the events hand-built by the analysts might provide valuable guidance into the common features of those events which could then be fed back into the automatic system so that it could build them.

CONCLUSIONS

Although traditional waveform displays are still widely used, their inefficient presentation of relevant data and the high demands they place on computer resources make their replacement a priority for CTBT seismic monitoring. Drawing on in-house data visualization expertise and on our hands-on experience with the design and implementation of the ADSN system at AFTAC, we have designed a new system consisting of a hierarchical series of displays which present relevant information to the analyst in a much more efficient manner. The analyst starts with the most general display and proceeds to increasingly detailed displays only as they are needed. The traditional waveform display is the final level of detail and will still be used but only for events that require detailed analysis. So far all of our testing has been done on data from the GSETT2 in 1991, but in the near future we plan to start using the much more complete data set from the ongoing GSETT3.

NEW TECHNIQUES FOR ESTIMATING SOURCE DEPTH AND OTHER DIAGNOSTIC SOURCE CHARACTERISTICS OF SHALLOW EVENTS FROM REGIONAL OBSERVATIONS OF P, Lg, AND Rg SIGNALS

Shelton S. Alexander, Roy C. Hsu, and Sheri L. Karl (Penn State University)
Indra N. Gupta and David H. Salzberg (Multimax, Inc.)

ABSTRACT

As part of a broader study to develop effective regional discriminants for Iran (and other areas of interest) a new cepstral stacking method for estimating source depth from a single, short-period regional station has been developed and tested, and new insights have been gained on why high frequency Lg/P is a very good discriminant for different source regions while low-frequency (less than about 5 Hz) Lg/P is not.

It is shown that stacking (product or sum) of the cepstra of multiple sub-windows spanning the total P and P-coda time window enhances the depth phase delays, (pP - P) and (sP - P), with respect to other delay times from crustal phases, such that accurate depth determination can be made from a single, short-period regional signal. Further enhancement can be achieved by also stacking individual stacked cepstra over multiple regional stations. The stacked product of individual cepstra gives a better result than the stacked sum, because contributions from other delay times that are prominent in some sub-windows are more-effectively suppressed in the product. The method has been tested on regional events in Iran for which multiple teleseismic pP observations are available; on Soviet Test Site (STS) nuclear explosions and one STS earthquake recorded in Iran; and on synthetic regional signals. It appears that with reasonable signal bandwidth and signal-to-noise levels accuracies in depth of about 1 km or better can be achieved for crustal events using this method.

Observations and theoretical modelling suggest that the relatively high Lg/P ratios at frequencies around 1 Hz typical of many underground nuclear explosions are caused by scattering of Rg into S-waves near the source, which in turn contributes significantly to Lg amplitudes. Rg, the short-period fundamental-mode Rayleigh wave, is well-excited in the frequency band .5 to 2 Hz by very shallow crustal sources, whereas higher frequencies are poorly excited and are also subject to signifcant intrinsic attenuation as they propagate. Besides the contributions to Lg from explosion-generated Rg, there appears to be a significant CLVD excitation of Rg at a depth about one third the shot depth. This is inferred from the presence of spectral nulls in both Rg and Lg at the same frequency and theoretical modelling to show that a null is expected for a CLVD source at that depth. Regional data from three NTS explosions and one STS explosion all exhibit spectral nulls in Lg indicating a CLVD contribution at the two test sites, which have very different near-surface and deeper crustal structure. The fact that the CLVD contribution consistently appears to come from about one third the shot depth implies that spall or related tectonic-like effects would not lead to a misinterpretation of the Rg as being generated from a source deeper than the true shot depth.

OBJECTIVES

The overall objective of this study is to develop regional discriminants such as Lg/P, Ms (or moment) vs mb, and Rg or other depth indicators for Iran. Related objectives include the transportability of discriminants developed for different tectonic source regions, determination of regional variations in various discriminants within Iran, and event identification in near-real time. Obtaining reliable depth estimates from regional signals and understanding why in general Lg/P in the frequency band .5-5 Hz is a poor discriminant while Lg/P above about 5 Hz is one of the most-effective ones are the objectives addressed in more detail in this presentation.

RESEARCH ACCOMPLISHED

In addition to the findings described below, other results of this study can be found in Alexander, et. al. (1994), Gupta, et. al. (1995). Alexander, et. al. (1995), Hsu (1995) (PhD thesis), and Karl (1995) (B.S. thesis). Data from regional events recorded at MAIO and the ILPA array in Iran have been used in the study of various regional discriminants and compared with experience elsewhere.

A very promising new cepstral stacking method (CSM) for accurately estimating source depth from a single regional signal has been developed and tested in this study and applied to Iranian as well as other regional events. The method consists of stacking cepstra of sub-windows in the P and P-coda total signal window. The sub-windows all contain the same (pP - P) and (sP - P) delay times no matter how complicated the signal is, whereas delay times for different crustal phases appear in at most a few of the sub-windows; by stacking over the sub-windows the common, depth-phase delay times are enhanced while those for the distinct crustal phases are not. It was found that stacking using the product of individual sub-window cepstra is more effective than using the corresponding sum; this result most likely reflects the fact that a strong cepstral peak from crustal phase delay times present in a few of the sub-windows affects the product much less than the sum. Although arbitrary and not yet fully explored, it appears that overlapping the sub-windows by about 75 percent produces the best results. Further enhancement can be achieved by stacking these individual stacked cepstra over several regional stations, if more than one regional station records an event.

To assess the effectiveness of this new cepstral stacking method it was tested on different Iranian events that have several consistent and independent teleseismic pP arrival times listed in the ISC bulletin; on several known Soviet test site (STS) underground nuclear explosions and a nearby earthquake recorded regionally at MAIO in Iran; and on synthetic regional signals for earthquake and explosion sources at different depths. Figure 1 shows an example of an Iranian event recorded regionally at ILPA which had several independent pP arrivals in the ISC bulletin all giving a (pP - P) delay time of 7.1 seconds corresponding to a depth of approximately 21 km. The very prominent cepstral peak in Figure 1 gives almost exactly the same delay time. Figure 2 shows the result of stacking individual stacked cepstra over three stations in the ILPA array; one sees that the depth-phase peak at 7.1 seconds is further enhanced. Another important example is shown in Figure 3 for a known STS underground nuclear explosion at Degelen and a nearby earthquake of

nearly the same mb recorded at MAIO; the cepstral peak for the explosion occurs at a delay time of less than 1 second while that of the earthquake occurs at a delay time of approximately 3 seconds corresponding to a source depth of about 9 km. Because these events traveled virtually identical paths and were recorded by the same receiver, any differences must reflect only source differences, depth in this case. It should be noted that these events could also be discriminated on the basis of Lg/P differences observed at MAIO.

Based on the assessments of the CSM done so far, it appears to provide a powerful new tool for obtaining reliable source depths using only a single regional station or a very sparse regional network. While the emphasis here is on verification in particular areas of interest, in this case Iran, the method is applicable in general for estimating source depths of earthquakes or explosions anywhere.

Observations and a theoretical model suggesting that the low-frequency (.5 to 2 Hz) Lg from nuclear explosions is mainly due to the near-source scattering of explosion-generated Rg into S have been recently provided by Gupta *et al.* (1992). This mechanism has been supported by the analysis of regional data from several Yucca Flats, Nevada Test Site (NTS) explosions by Patton and Taylor (1995) who further argued that the prominent low-frequency spectral null in Lg is due to Rg from a CLVD source and is related to its depth. In this study, we examined the time-varying spectral characteristics of the observed seismic arrivals by narrow bandpass filtering (NBF) which provides amplitudes versus group velocity and period. NBF of synthetic seismograms generated using wavenumber integration shows the presence of a prominent spectral null for the CLVD source. For the Rainier Mesa (NTS) explosion, Mineral Quarry, data at several local and regional distances are available; NBF analyses show that the spectral null in the Rg-S wave-group at local distances is also observed in Lg at regional distances, indicating that the Rg spectrum is imprinted onto the scattered S waves (e.g. Figure 4). Similar analysis of regional data from two Yucca Flats (NTS) explosions at shot depths of 503 and 396 m, indicates prominent spectral nulls in Lg at periods of about 1.5 and 1.1 sec, respectively. Observations of a pronounced spectral null (at period about 0.7 sec) in regional data from a Soviet nuclear explosion (Figure 5) imply that the mechanism of generation of the low-frequency Lg at NTS and East Kazakh test sites, with completely different crustal structure and tectonics, is similar. Spectral nulls provide an estimate of depth of the CLVD source, which in our study appears to be nearly one-third of the depth of burial. These results together with other source information are summarized in Table 1.

TABLE 1
Observed Spectral Nulls and Source Information

Shot Name	Null T (sec)	DOB H (m)	Velocity (overburden) α (m/sec)	CLVD Depth $h = (\alpha T)/16$	h/H
Mineral Quarry	1.8	389	2200*	250 m	0.6
Texarkana	1.5	503	1720	160 m	0.3
Tulia	1.1	396	1530	110 m	0.3
Kazakh JVE	0.7	600 est	4600#	200 m	0.3

823

In summary, NBF analyses of data from Mineral Quarry show that, at the higher frequencies, Rg gradually scatters into body phases that travel with faster group velocities. The spectral null in Rg at local distances also appears in Lg at regional distances, indicating that the Rg spectrum is imprinted onto the scattered S waves. Regional data from three NTS shots and one East Kazakh test site indicate distinct spectral nulls in Lg, apparently due to the CLVD source associated with each explosion. This means that an effective CLVD source is present not only for explosions at the Yucca Flats (as demonstrated by Patton and Taylor, 1995) but also at other sites with considerably different near-surface and deeper crustal structure. Spectral nulls may provide estimates of the CLVD source depth which appears to be nearly one-third of the depth of burial for three out of four shots used in this study. Narrow band-pass filtering, combined with theory, may provide useful source and near-source information about underground nuclear explosions and improve our understanding of the generation of low-frequency Lg from underground explosions. There is clearly a need to further test and exploit these preliminary results by examining much more local and regional data from several latest sites.

REFERENCES

Alexander, S. S., C. Hsu, I. N. Gupta, and D. H. Salzburg, (1994). Development of discriminants and improved locations for regional events in Iran, Proc. 16th Annual Seis. Res. Symposium, 13-19. PL-TR-94-2217, ADA284667

Gupta, I. N., W. W. Chan, and R. A. Wagner (1992). A comparison of regional phases from underground nuclear explosions at East Kazakh and Nevada test sites, Bull. Seism. Soc. Am. 82, 352-382.

Gupta, I. N., D. H. Salzberg, and S. S. Alexander (1994). A study of regional discriminants for seismic events in Iran, EOS 75, no. 44, 428 (abstract).

Gupta, I. N. and D. H. Salzberg (1995). Observations of spectral null in Lg from underground explosions at the Nevada and Kazakh test sites, EOS 76, no. 17, S205 (abstract).

Hsu, C. (1995). Seismic Signal Pattern Recognition, Ph.D. Thesis, EE, The Pennsylvania State University, 185 pp.

Karl, S. L. (1995). Magnitude and source depth estimates for earthquake and explosions in Iran--regional observations, B.S. Thesis, Geosciences, The Pennsylvania State University, 79 pp.

Patton, H. J. and S. R. Taylor (1995). Analysis of Lg spectral ratios from NTS explosions: Implications for the source mechanisms of spall and the generation of Lg waves, Bull. Seism. Soc. Am. 85, 220-236.
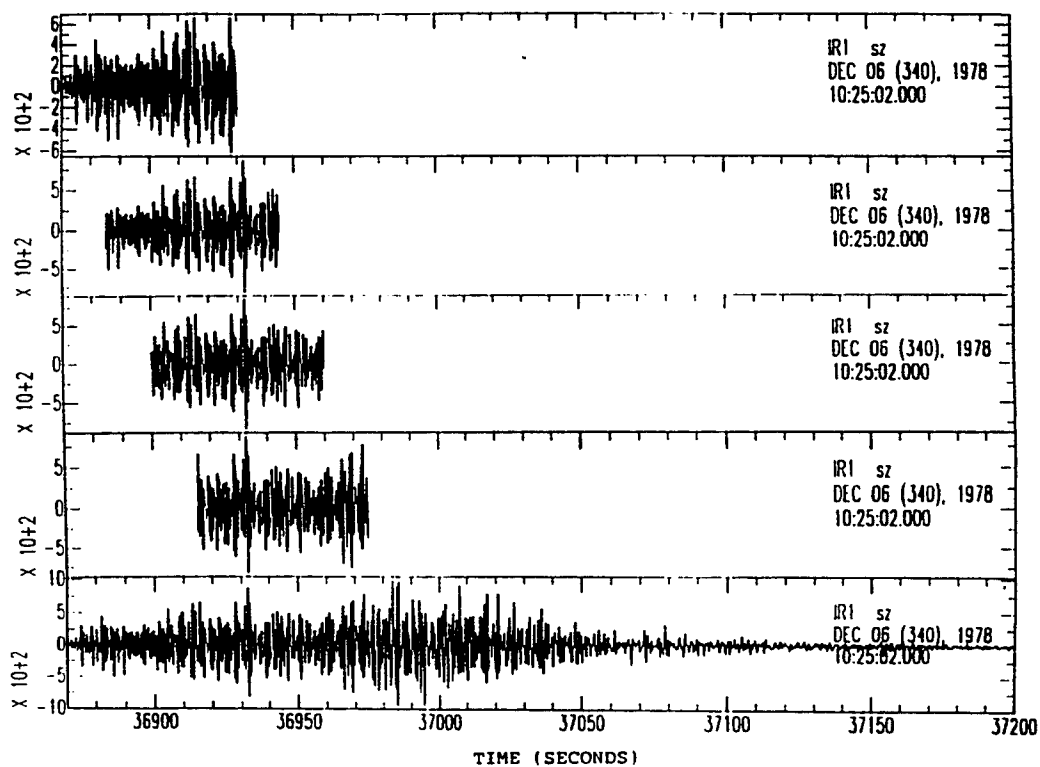
Figure 1a. Regional earthquake signal recorded at ILPA station IR1 and four sub-windows used for cepstral stacking. The epicentral distance is 638 km.
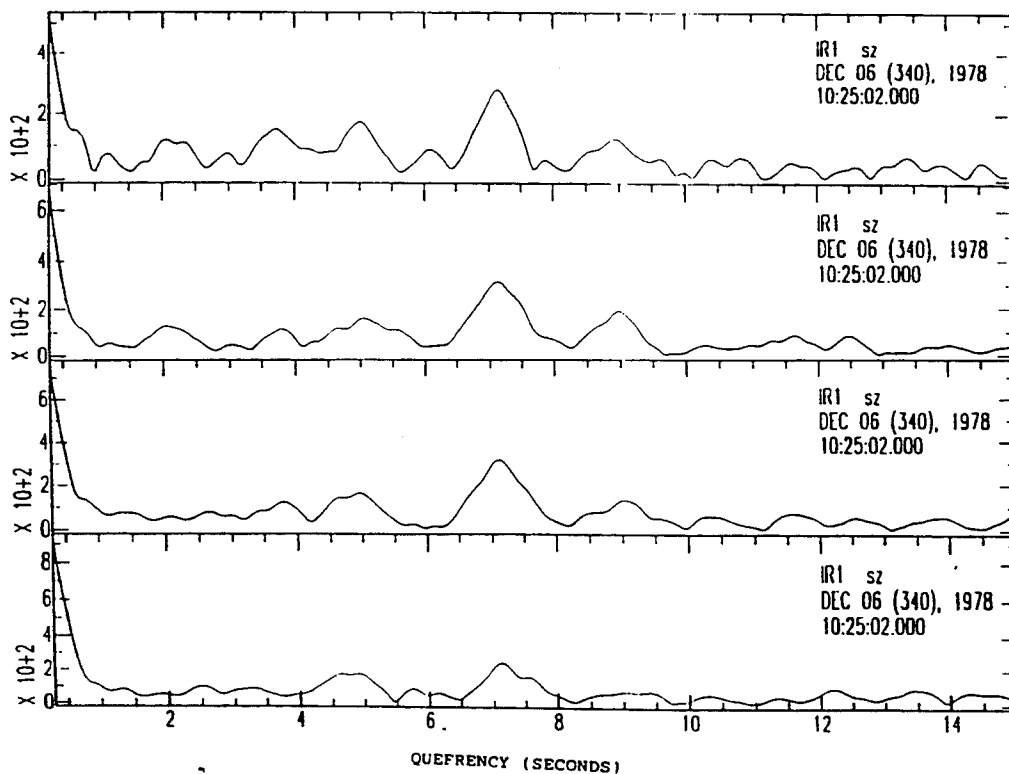
Figure 1b. Individual cepstra of sub-windows in Figure 1a.
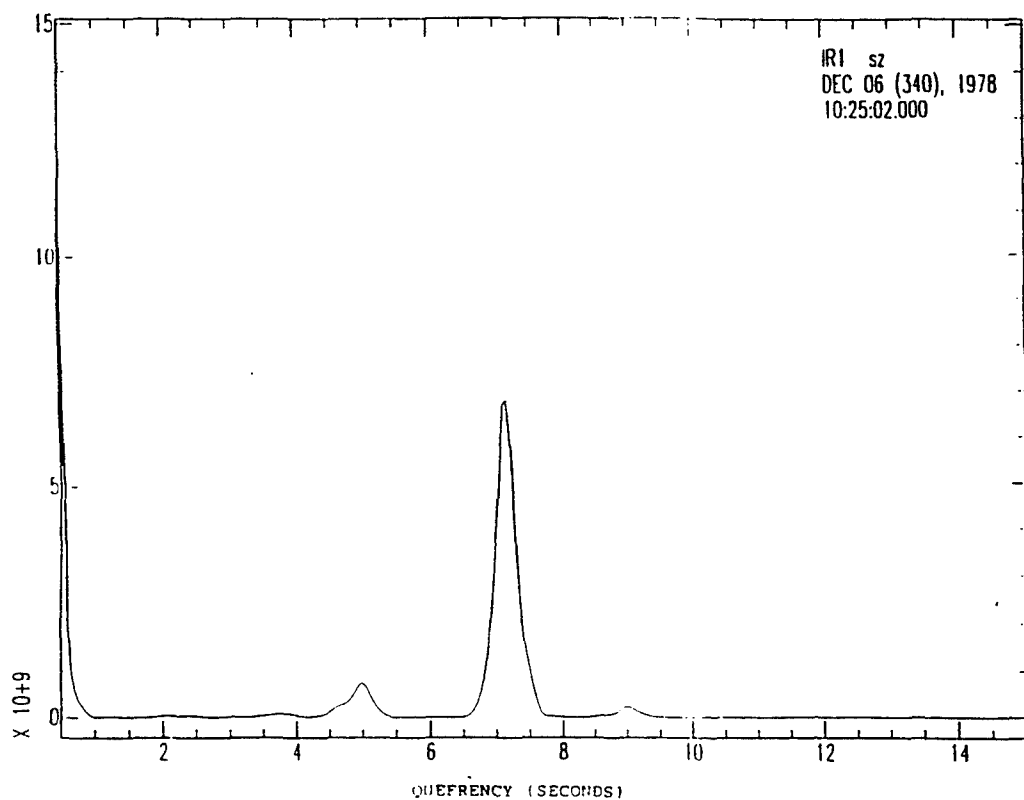
Figure 1b. Stacked cepstra of sub-windows in Figure 1a.
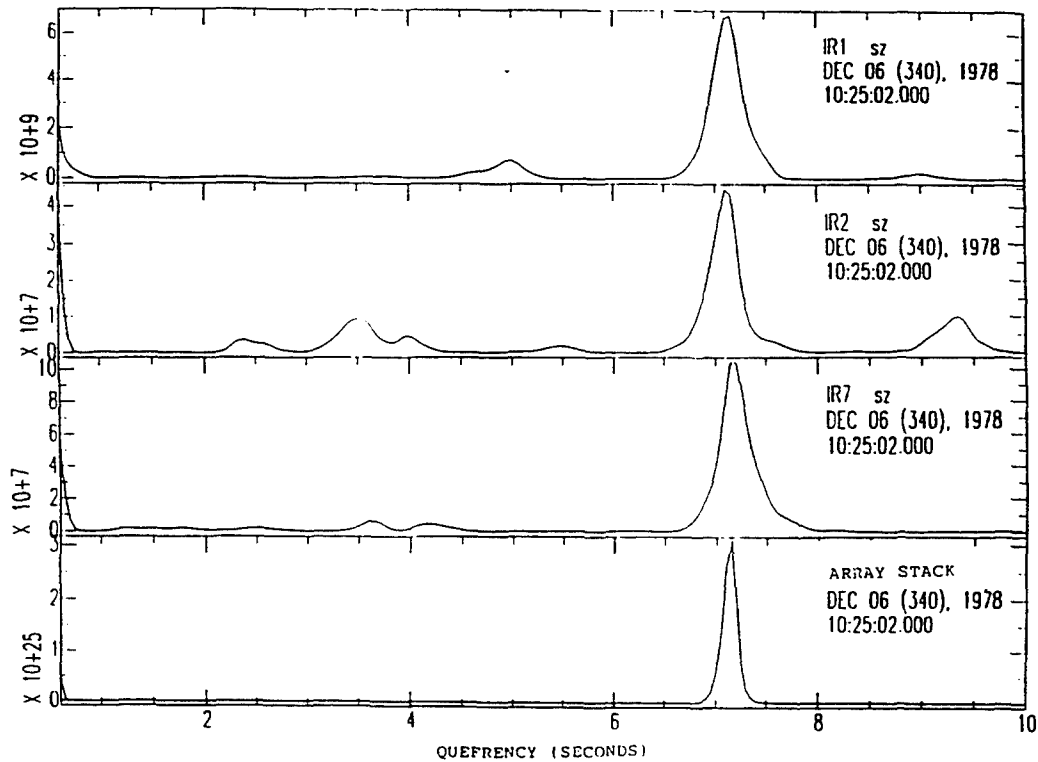
Figure 2. Individual cepstra stacked over three stations in the ILPA array for the event shown in Figure 1a.

826
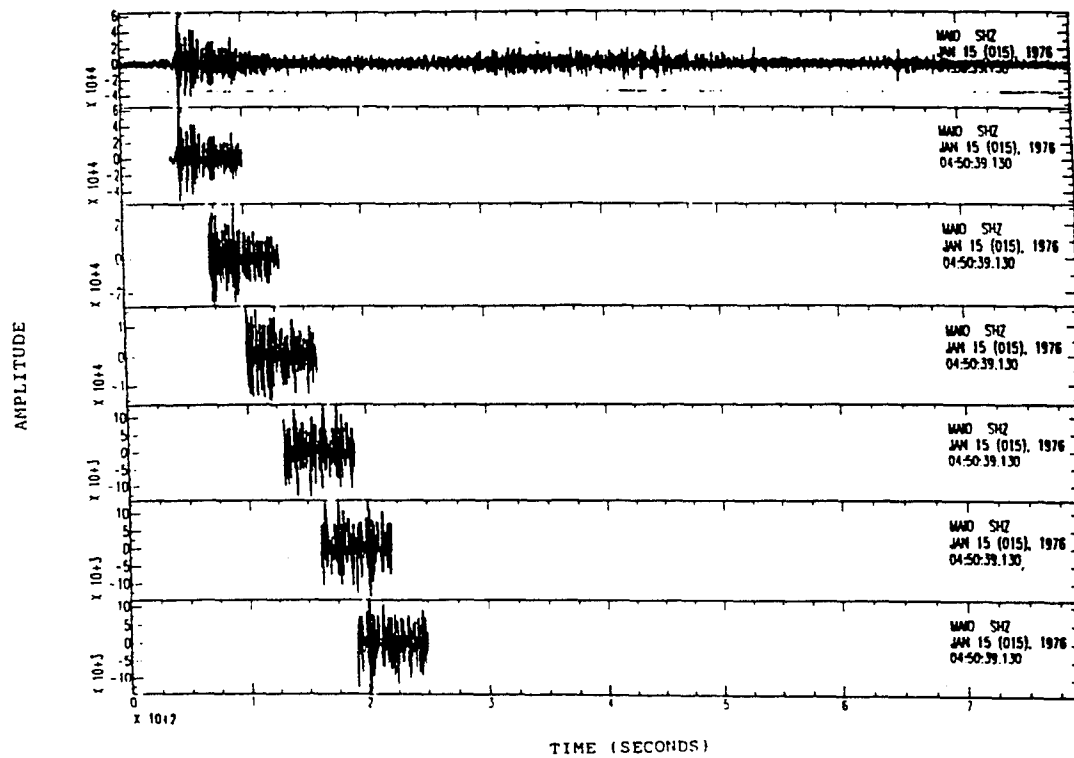
Figure 3a. Signal observed at MAIO for a mb 5.2 underground explosion at Degelen and the sub-windows used for cepstral stacking. Distance = 19.2 deg.
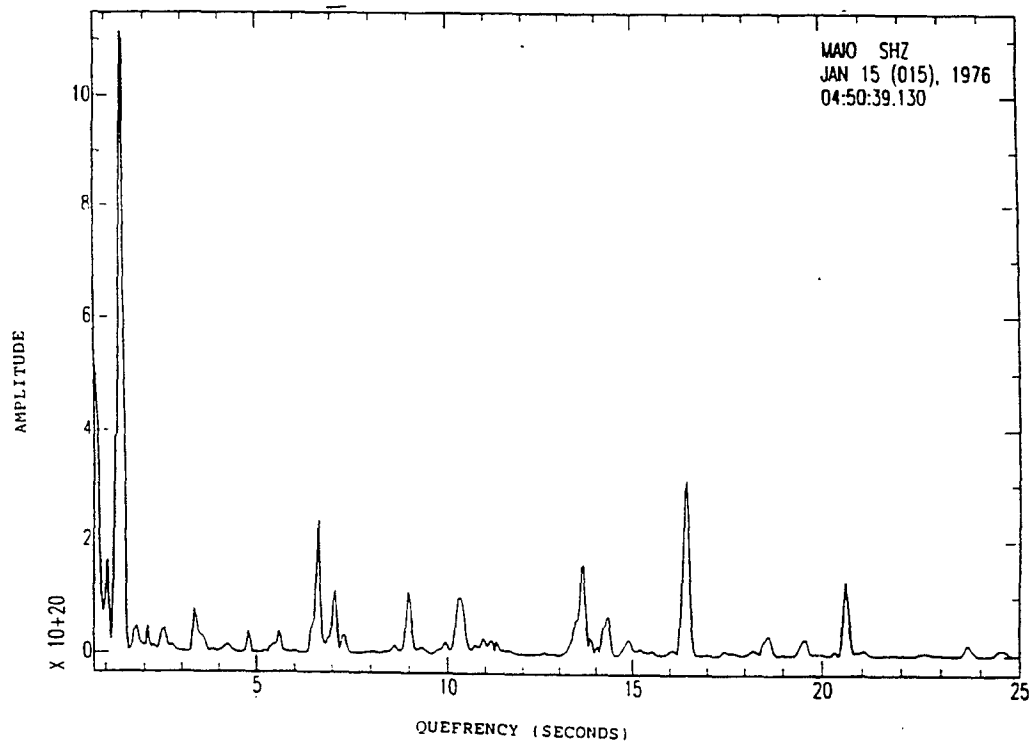
Figure 3b. Stacked cepstra for the STS explosion shown in Figure 3a.

827
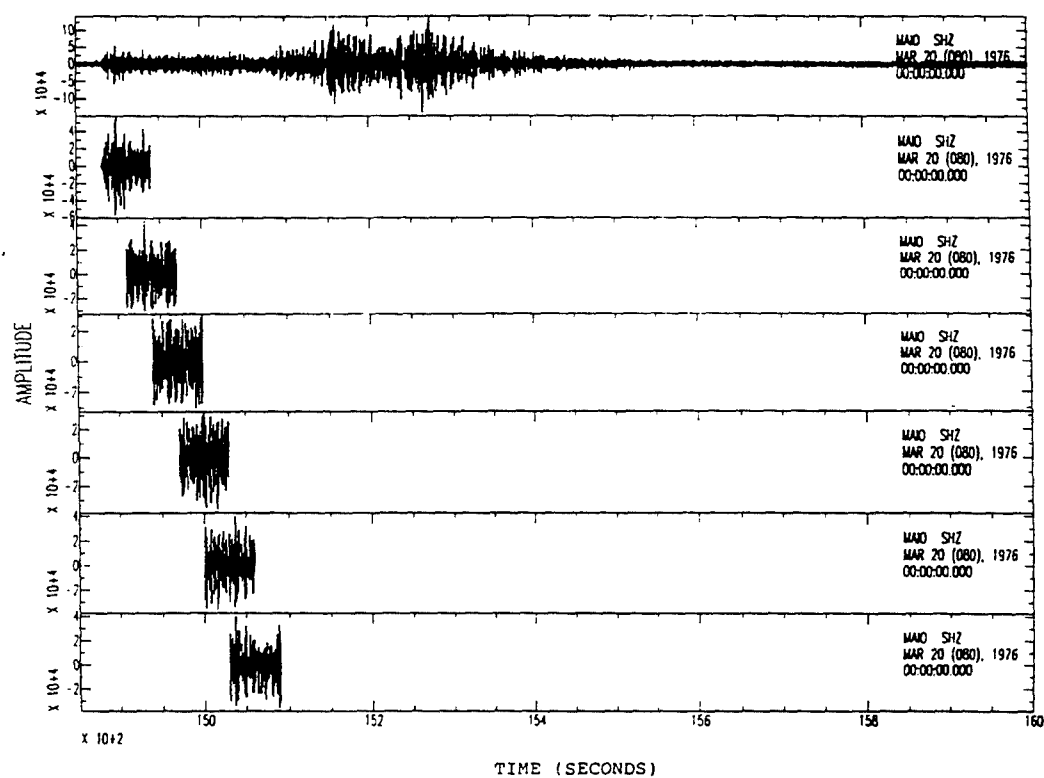
Figure 3c. Signal observed at MAIO for a mb 5.1 earthquake near Degelen and the sub-windows used for cepstral stacking. Distance = 18.8 deg.
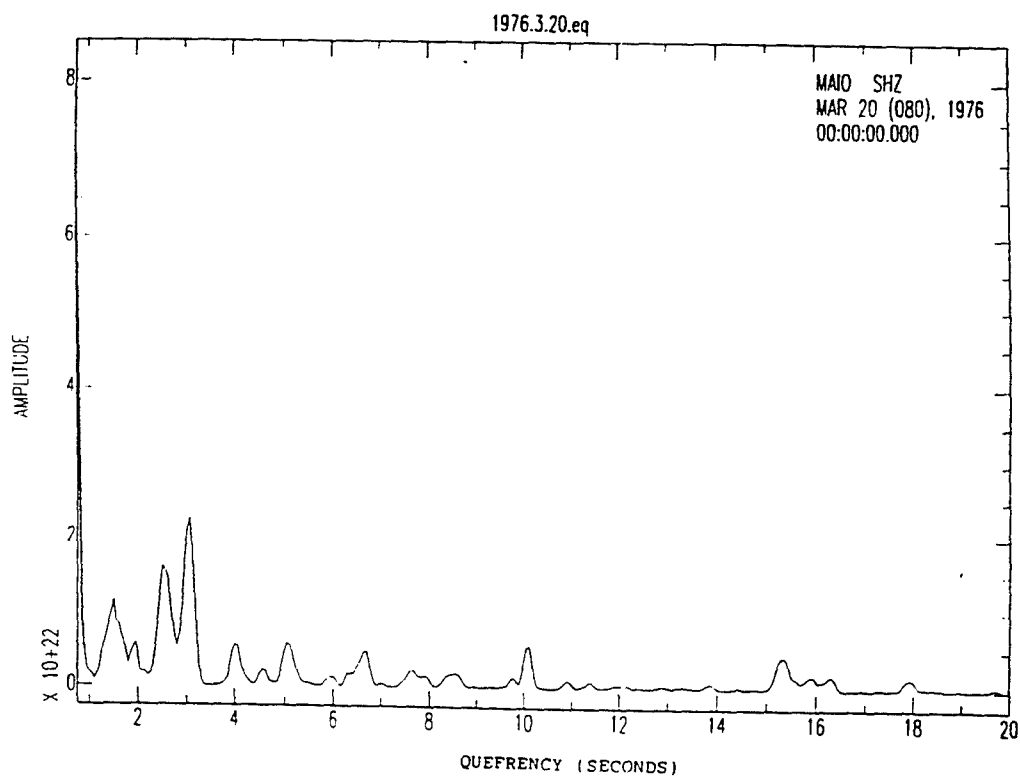
Figure 3d. Stacked cepstra for the STS earthquake shown in Figure 3c.
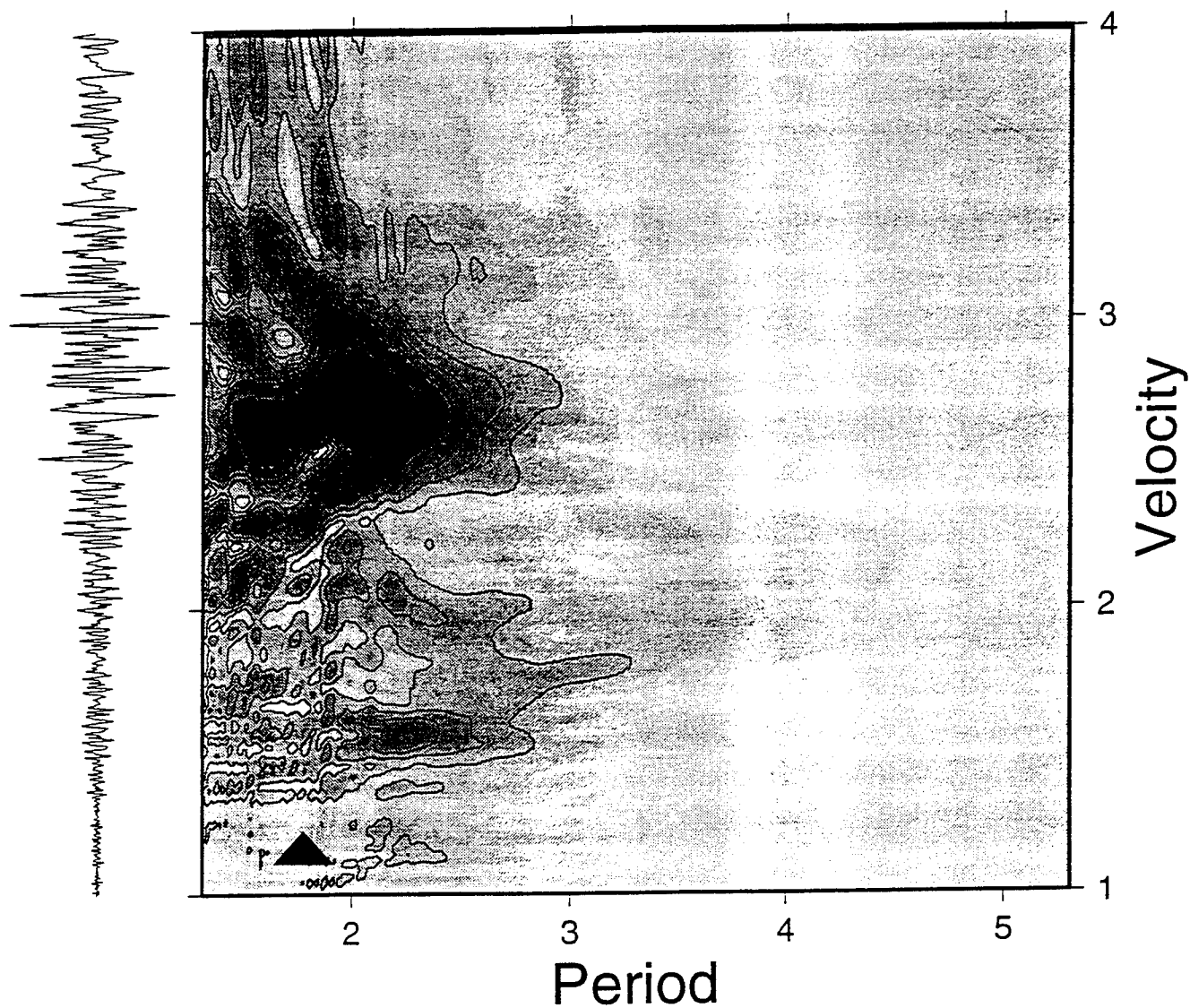
Figure 4. NBF of vertical component data recorded at the regional station DRW, about 160 km southwest of the shot point. Note the spectral null at period of about 1.8 sec in both Lg (velocity about 2.7 km/sec) and Rg (velocity about 1.5 km/sec).
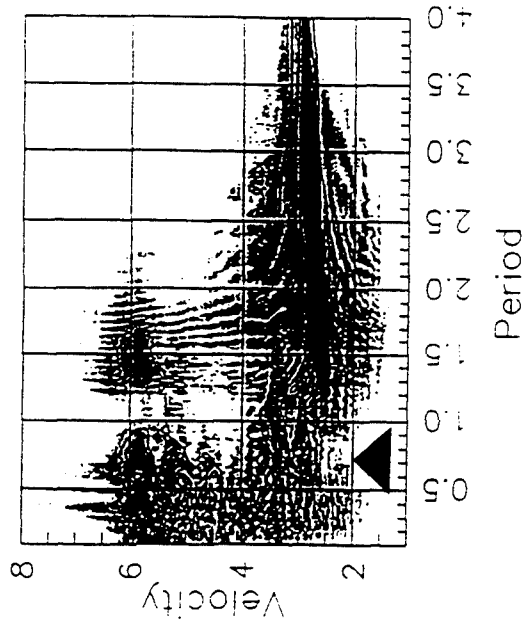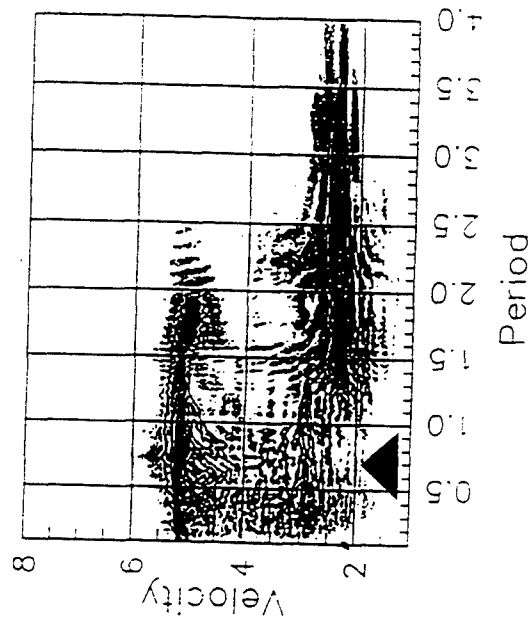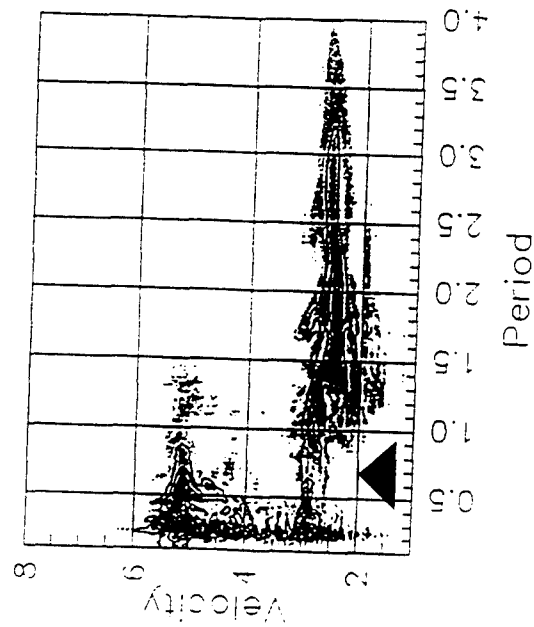
Figure 5. NBF of vertical component data from the Kazakh test site explosion of 14 September 1988 recorded at (a) KSU, 160 km east, (b) KKL, 255 km southwest, and (c) BAY, 255 km northwest, each showing spectral null in the S-wave group or Lg at a period of about 0.7 sec.

Network Detection and Association: Statistical Assessment of Performance

Kevin K. Anderson

Pacific Northwest Laboratory

Abstract

Statistical methods are needed to assess the performance of a global seismic monitoring system. This report considers the problems of estimating the detection capability and identifying misassociations. Detection capability is expressed empirically through a region- and magnitude-dependent detection probability function. Regional network information can substantially improve the estimation of the global network's detection capability. A quantitative measure of the strength of the association of an event is proposed. The proposed amplitude-based measure can be used to discriminate between real events and false associations. It quantifies the agreement among the observed and expected amplitudes of detecting and non-detecting stations.
Key words: network detection capability, association, network magnitude, goodness-of-fit.

Objective

A global seismic monitoring system is judged by its ability to detect and identify suspicious seismic events. Statistical methods are required to assess empirically the performance of all aspects of the monitoring system, from detection to discrimination. This report presents some preliminary research results in the areas of detection and association. Specifically, we report on the use of a catalog of seismic events from a regional network to help assess the detection capability of a global network in that region (Anderson 1995); and we propose a quantitative measure of the strength of event association as a way to identify both real events and false associations.

The global network region-dependent detection capability is expressed as a functional relation between the event magnitude and the probability of detection. Kelly and Lacoss (1969) and Ringdal (1986) have both taken this approach, and used the Gaussian probability distribution function as the basic functional form. We extend these authors' methods and show that event data from regional seismic networks can substantially improve the estimation of the region-dependent detection capability of the global network.

Automated association processes may result in large numbers of so-called false alarms, random phases that are associated to "create" an event where there really wasn't one. False alarms (spurious events) can be a problem for small events detected by relatively few stations. Quantitative measures of the strength of association can be constructed and used to identify false alarms. We propose one measure which is based on Ringdal's (1976, 1986) maximum-likelihood estimation of seismic magnitude. The measure quantifies the agreement among the observed and expected amplitudes of detecting and non-detecting stations.

Preliminary Research Results: Network Detection Probability

The empirically based Gutenberg-Richter magnitude-frequency relation (Gutenberg and Richter 1941) implies that the observed magnitudes of earthquakes in a particular region of homogeneous seismicity are randomly distributed according to a shifted exponential distribution. That is, the observed magnitudes m above some lower magnitude limit of interest m_{min} are well-modeled as a simple random sample from the probability density function

$$\beta \exp(-\beta(m - m_{min})), \qquad m > m_{min}. \tag{1}$$

The choice of m_{min} is important. For the problem of determining the value of β, a value of m_{min} is chosen, such that network detection is complete above it (for example, see Bender 1983). For the problem of estimating the probability of detection as a function of observed magnitude, a value of m_{min} below the magnitude of complete detection is chosen such that the Gutenberg-Richter magnitude-frequency relation is assumed to hold. This m_{min} value is usually greater than or equal to the magnitude of the smallest event observed by the network. The assumption that Equation (1) holds is critical because it serves as "ground-truth" in the estimation of detection probabilities. Non-Gutenberg-Richter frequency-magnitude relationships have been observed (Taylor et al. 1990).

Kelly and Lacoss (1969) derived a maximum likelihood estimation method for the simultaneous estimation of the parameters of the Gutenberg-Richter magnitude-frequency relation and the parameters of a probit model for the probability of detection using continuous magnitude data; that is, they modeled the network detection probabilities $P(m)$ as a function of magnitude m using the Gaussian distribution function

$$P(m) = \Phi((m - c)/d) = \frac{1}{\sqrt{2\pi}} \int_{-\infty}^{(m-c)/d} \exp(-y^2/2)\, dy.$$

They derived their method assuming that, when grouped into non-overlapping magnitude intervals, the number of earthquakes occurring in each interval are independent Poisson random variables. Here, we extend the Kelly and Lacoss (1969) method to provide a joint analysis of two seismic networks.

We assume that two catalogs of seismic events are available covering the same temporal and spatial area; one from a regional network (A) in the region of interest and the other from a large globally distributed network (B). We first consider the case where the two networks' detections in the region of interest are

statistically independent. We assume that event matching between the two catalogs is accurate. We assume that the data available for analysis is a breakdown by magnitude grouping of the number of events detected uniquely or jointly. Y_{ij} is defined as the number of magnitude m_i events of type j, where $j = 1, 2, 3$ corresponds to events detected by both networks, by network A alone, or by network B alone, respectively; and the magnitudes range from m_{min} to m_{max}. Given that the number of earthquakes N has a Poisson distribution with mean λ, the Y_{ij} are independent Poisson random variables with means

$$\exp(\alpha - \beta m_i)p_{ij},$$

where

$$p_{i1} = \Phi((m_i - c_A)/d_A)\Phi((m_i - c_B)/d_B),$$

$$p_{i2} = \Phi((m_i - c_A)/d_A)(1 - \Phi((m_i - c_B)/d_B)),$$

$$p_{i3} = (1 - \Phi((m_i - c_A)/d_A))\Phi((m_i - c_B)/d_B).$$

The parameter α depends on λ and β through

$$\exp(\alpha) = \lambda / \sum_{j=1}^{n} \exp(-\beta m_j).$$

Each network has its own detection probability parameters subscripted by A and B. The parameter c is the 50% detection magnitude and the parameter d affects the steepness of the probability-of-detection curve.

Estimation of the six parameters and their uncertainties can be accomplished by maximum likelihood or by using a two-stage nonlinear least squares approach. A goodness-of-fit test to judge the adequacy of the model can then be performed. Let "hats" indicate parameter estimates, $\hat{Y}_{ij} = \exp(\hat{\alpha} - \hat{\beta} m_i)\hat{p}_{ij}$, and

$$X_{GOF}^2 = \sum_{i=1}^{n} \sum_{j=1}^{3} (Y_{ij} - \hat{Y}_{ij})^2 / \hat{Y}_{ij}.$$

To test the adequacy of the model, X_{GOF}^2 is compared with a chi-square distribution with $(3n - 6)$ degrees of freedom. We estimate $p \times 100\%$ detection thresholds for the two networks as

$$\hat{c}_A + \hat{d}_A \Phi^{-1}(p) \qquad \text{and} \qquad \hat{c}_B + \hat{d}_B \Phi^{-1}(p),$$

where $\Phi^{-1}(\cdot)$ is the inverse of the Gaussian distribution function.

With a simple modification, we can account for one type of dependent networks. Suppose the networks are such that if an event is detected by the global network (B), it is also detected by the regional network (A). In this case, there are no type 3 events, where network B detected, but network A did not; that is, all $Y_{i3} = 0, i = 1, 2, \ldots, n$. This type of dependence is easily accounted for by redefining the p_{ij} as follows:

$$p_{i1} = \Phi((m_i - c_B)/d_B),$$

$$p_{i2} = \Phi((m_i - c_A)/d_A)(1 - \Phi((m_i - c_B)/d_B)),$$

and $p_{i3} = 0$. Using the Poisson model, maximum likelihood estimation or two-stage nonlinear least squares estimation follows as above. Further extensions or modifications, such as replacing the probit probability-of-detection models with other models, are possible.

To demonstrate the method developed above, we considered event catalogs from the Pacific Northwest Seismograph Network (PNSN) and the U. S. Geological Survey (USGS) for 1990-1992 (Anderson 1995). The PNSN has more than 100 stations in the Pacific Northwest.

The three-year PNSN data set analyzed by Anderson (1995) contained 3032 Washington state earthquakes, of which the USGS network detected 123. We determined earthquake matches using location and origin time. For most of the 123 earthquakes, the USGS catalog did not report a network m_b magnitude, so

the PNSN P-coda magnitudes were used in the analysis. The magnitude distribution of these jointly detected events is displayed in Figure 1. No earthquakes were detected by only the USGS. The two networks are not independent, because the USGS receives data from eight PNSN stations by telephone lines in real time (and, in fact, the locations for most of these 123 USGS catalog events are the PNSN locations). Therefore, we analyzed the data using the dependent two-network model.

We had to remove one event from the analysis, a magnitude 3.2 event that was not listed in the USGS catalog. This single "missing" event caused the goodness-of-fit test to reject the model; that earthquake should have been detected by USGS with high probability. Table 1 contains the results of a two-stage nonlinear least squares analysis, with that event ignored. The estimates of the 90% detection thresholds for PNSN and USGS for Washington state are 2.562 and 2.844, with standard errors of 0.224 and 0.028, respectively.

Some caveats must accompany the 90% detection thresholds given above. The analysis was performed to illustrate the statistical method. While one 90% detection threshold might adequately describe the detection capability of the global network in that region, the detection capability of the PNSN regional network is known to be much more spatially heterogeneous. The one 90% detection threshold given for the PNSN is a rough spatial average. Further, the USGS processing is not well-understood; the very sharp cutoff at magnitude 2.5 may merely reflect a procedural decision to exclude events rather than a physical detection limitation.

Table 1: Dependent two-network analysis results: parameter estimates and standard errors

Method	$\hat{\alpha}$	$\hat{\beta}$	$\hat{c}_{PNSN}$	$\hat{d}_{PNSN}$	$\hat{c}_{USGS}$	$\hat{d}_{USGS}$
Two-Stage NLS	9.680	2.407	1.750	0.634	2.607	0.185
	(0.611)	(0.211)	(0.189)	(0.031)	(0.022)	(0.006)

Preliminary Research Results: Measuring Strength of Association

Determining misassociations for a seismic network is challenging. There are two basic types of errors in association. Events may be missing from a network seismicity catalog because the waveforms were not associated or the catalog may contain spurious events, those events which were misassociated based on signals from multiple events. The first type of error, missed association, is different from non-detection. It represents a failure of the association process when there were enough detections to make an association. Events which were missed associations can be discovered through comparison with seismicity catalogs from other networks, or, in the case of explosions, through a ground-truth source. The second type of error, spurious events, may be detected through visualization methods which allow the analyst access to all the information which made up the events. The analyst then bases decisions on his prior experience; he "knows a bad event when he sees one." Quantitative methods of measuring the strength of association are required to reduce the amount of work the analyst must do "by eye." These methods could be used to remove weakly associated events from final seismicity catalogs with or without analyst intervention.

When a spurious event is constructed from the waveforms of multiple events, it is usually the case that the arrival times are consistent, that is, they agree with the expected arrival times from an event placed at the location of the spurious event. By the somewhat random nature of such misassociations, it is expected that other parameters of interest, such as amplitudes and azimuths, would be less consistent, and misassociations could be identified by the larger-than-expected variability among the data from different detecting stations. In less extreme cases, with only a few of the waveforms associated in error, the effect might only be a slight increase in the size of the location error ellipses, or increased uncertainty in network parameter estimates. A goodness-of-fit statistic for the network maximum likelihood magnitude estimate is developed here.

Ringdal (1976) presented a maximum likelihood approach to the estimation of network m_b values. The approach successfully removes the network magnitude bias problem that other studies identified (e.g., Herrin
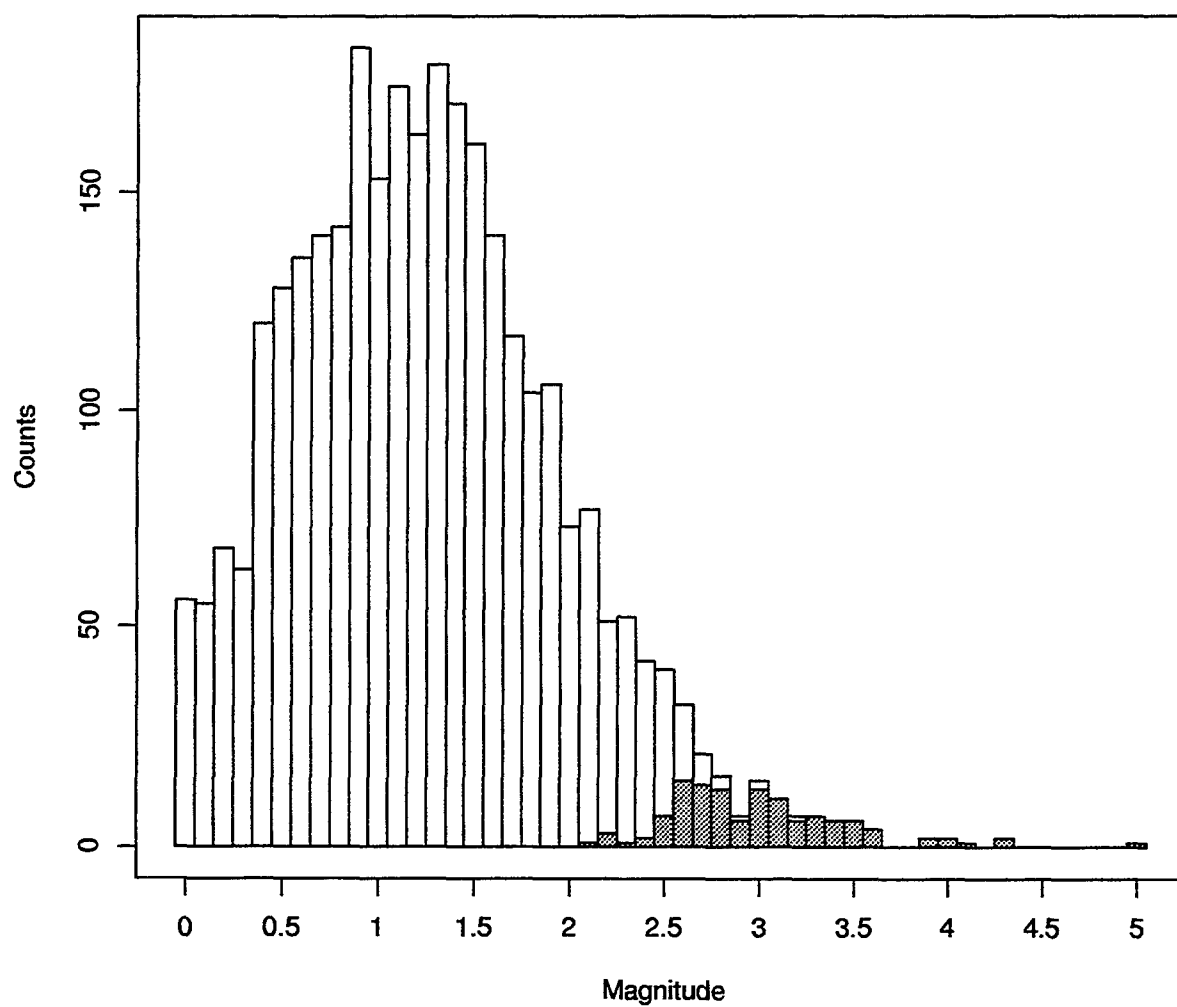
Figure 1: Frequency of State of Washington events, 1990-92, detected by the PNSN and the USGS seismic networks. The unshaded bars represent the number of earthquakes detected by only the PNSN. The shaded bars represent the number of earthquakes detected by both networks.

and Tucker (1972)), by including the information from non-detecting stations. We extend that approach to assess the strength of the association of a seismic event. Since a spurious event may have increased variability in the distance-corrected amplitudes, and may also have no detections at stations that would have detected a real event, we develop a goodness-of-fit statistic that is sensitive to deviations from expected amplitudes and detections.

We assume Ringdal's (1986) model, that for a seismic network of N stations, $g_i, i = 1, 2, \ldots, N$, denotes the P-wave detection thresholds of the stations and $y_i, i = 1, 2, \ldots, N$, denotes the P-wave signals of a seismic event of true bodywave magnitude μ.. We assume that g_i and y_i are Gaussian distributed as follows

$$g_i \sim N(G_i, \gamma_i^2)$$

$$y_i \sim N(\mu - Q_i + B_i, \sigma_i^2),$$

where G_i is the average station detection threshold, Q_i is a distance-depth correction factor (dependent on the locations of the event and the station), B_i is the average station magnitude bias, and γ_i and σ_i are the standard deviations.

Ringdal (1986) includes in the network magnitude estimation only those stations within the teleseismic range of $21°$ to $100°$ from the event. These stations fall into four groups: Group A, stations reporting a P-wave detection and an associated signal level; Group B, stations reporting a P-wave detection with no associated signal level; Group C, stations operable but not reporting a P-wave detection; and Group D, stations which are inoperable or off-line. The Group D stations provide no information and can be omitted from the analysis. We could have defined a fifth group, stations outside the range of $21°$ to $100°$ from the event, and subsequently omitted them from the analysis.

The likelihood function $L(\mu)$ is essentially that described by Ringdal (1986):

$$L(\mu) = \prod_{i \in A} f_i(\mu) \prod_{i \in B} h_i(\mu) \prod_{i \in C} (1 - h_i(\mu)),$$

where

$$f_i(\mu) = \frac{1}{\sigma_i} \phi((\mu - y_i - Q_i + B_i)/\sigma_i)$$

$$h_i(\mu) = \Phi\left(\frac{\mu - G_i - Q_i + B_i}{\sqrt{\sigma_i^2 + \gamma_i^2}}\right)$$

$$\phi(x) = \frac{1}{\sqrt{2\pi}} \exp(x^2/2)$$

and $\Phi(\cdot)$ is the Gaussian distribution function defined earlier. All parameters but μ are known. The network maximum likelihood estimate $\hat{\mu}$ of the event magnitude μ is obtained by numerically maximizing $L(\mu)$. The usual estimate of the variance of $\hat{\mu}$ is the reciprocal of the second derivative of the negative-log-likelihood function evaluated at $\hat{\mu}$.

A goodness-of-fit statistic for the network maximum likelihood magnitude $GOF(m_b)$ is

$$GOF(m_b) = -2\log(L(\hat{\mu})) - \sum_{i \in A} \log(2\pi\sigma_i^2).$$

This goodness-of-fit statistic is approximately distributed as a chi-square random variable with $k = n - \Delta_{GOF} - 1$ degrees of freedom, where n is the number of stations within $21°$ to $100°$ of the event and

$$\Delta_{GOF} = \sum_{i \in B} \chi(h_i(\hat{\mu}) - 0.97) + \sum_{i \in C} \chi(0.03 - h_i(\hat{\mu}))$$

and $\chi(\cdot)$ is the indicator function; if $x \geq 0$, then $\chi(x) = 1$, else $\chi(x) = 0$. The adjustment Δ_{GOF} reduces the degrees of freedom for the stations that provide no information relevant to the magnitude. A large value

836

of $GOF(m_b)$ is evidence that the event is a potential spurious event. Excessive variability in the P-wave amplitudes or missing detections will increase the value of $GOF(m_b)$. An approximate statistical test of the null hypothesis that an event is real is to reject if $GOF(m_b)$ exceeds the appropriate percentile of the chi-square distribution with k degrees of freedom. Using the 95th percentile as the cutoff sets the probability of falsely classifying a true event as spurious at approximately 5 %.

Power studies can be performed to determine the ability of the method to accurately identify spurious events. The power of a statistical test is the probability of rejecting the null hypothesis when it is false. In this case, the power is the probability that the goodness-of-fit statistic $GOF(m_b)$ will indicate that a spurious event is indeed spurious. The power of this test for a particular global network depends on the magnitude and hypocenter of the event, and on how one models a spurious event.

As an example of estimating the power, we considered the globally distributed network of 115 stations described in Ringdal (1986). We modeled a spurious event with a nominal m_b of 3.5 and located at 17°S and 170°E, under combinations of two factors; the first, that the standard deviations of the amplitudes are multiplied by an inflation factor in the range of 1 to 2.5 and second, that as many as two "good" stations did not detect the event, where "good" stations are those that would be expected to detect the event and to provide amplitudes for the the computation of network magnitude. We set the cutoff at the 95th percentile of the chi-square distribution. Further details of the Monte Carlo analysis are omitted. The results from the Monte Carlo analysis are used to generate the three curves in Figure 2. They give the probability of classifying the spurious event as spurious for the range of standard deviation inflation factors and zero, one, or two missing good stations.

Interpretation of the curves is as follows. If all of the stations detect the event as expected and the signal-to-noise ratios are as expected, then the event "looks" real as far as amplitudes are concerned and the probability of classifying the event as spurious is just 5%, the same as for a real event. If all of the stations detect the event as expected and the signal-to-noise ratios are about 1.5 times as expected, then the probability of classifying the event as spurious is about 40%. If two good stations miss the event and the signal-to-noise ratios are about 1.5 times as expected, then the probability of classifying the event as spurious is about 80%. These results indicate the goodness-of-fit statistic $GOF(m_b)$ can provide reasonable identification of spurious events.

Recommendations and Future Plans

The method of Kelly and Lacoss (1969) has been used to determine the region-dependent global network event detection capabilities. We extended the method to include events detected by a regional network. The joint modeling of the detections of the two networks can provide better estimates of the global network's detection probabilities, especially if the number of events detected by the global network is small. The global network's detection capabilities can be tracked in time. The problems associated with matching up events in the two catalogs were not considered here, but may complicate the two-network analysis. The magnitude used in analysis can be the global network magnitude, the regional network magnitude, or some combination of the two.

A goodness-of-fit statistic based on the detection pattern and the amplitudes of the detecting stations was shown to be a reasonable quantitative measure of the strength of event association. Combined with current visualization techniques, the $GOF(m_b)$ statistic can reliably identify misassociated events. Future research will consider including amplitudes and detections from stations at regional distances, within 21° from the event. We will also consider goodness-of-fit statistics based on other seismic parameters, such as azimuth and first motion. The combining of various goodness-of-fit statistics is also an issue. Analysis of catalogs of events from regional networks can also provide information about missed events and spurious events.
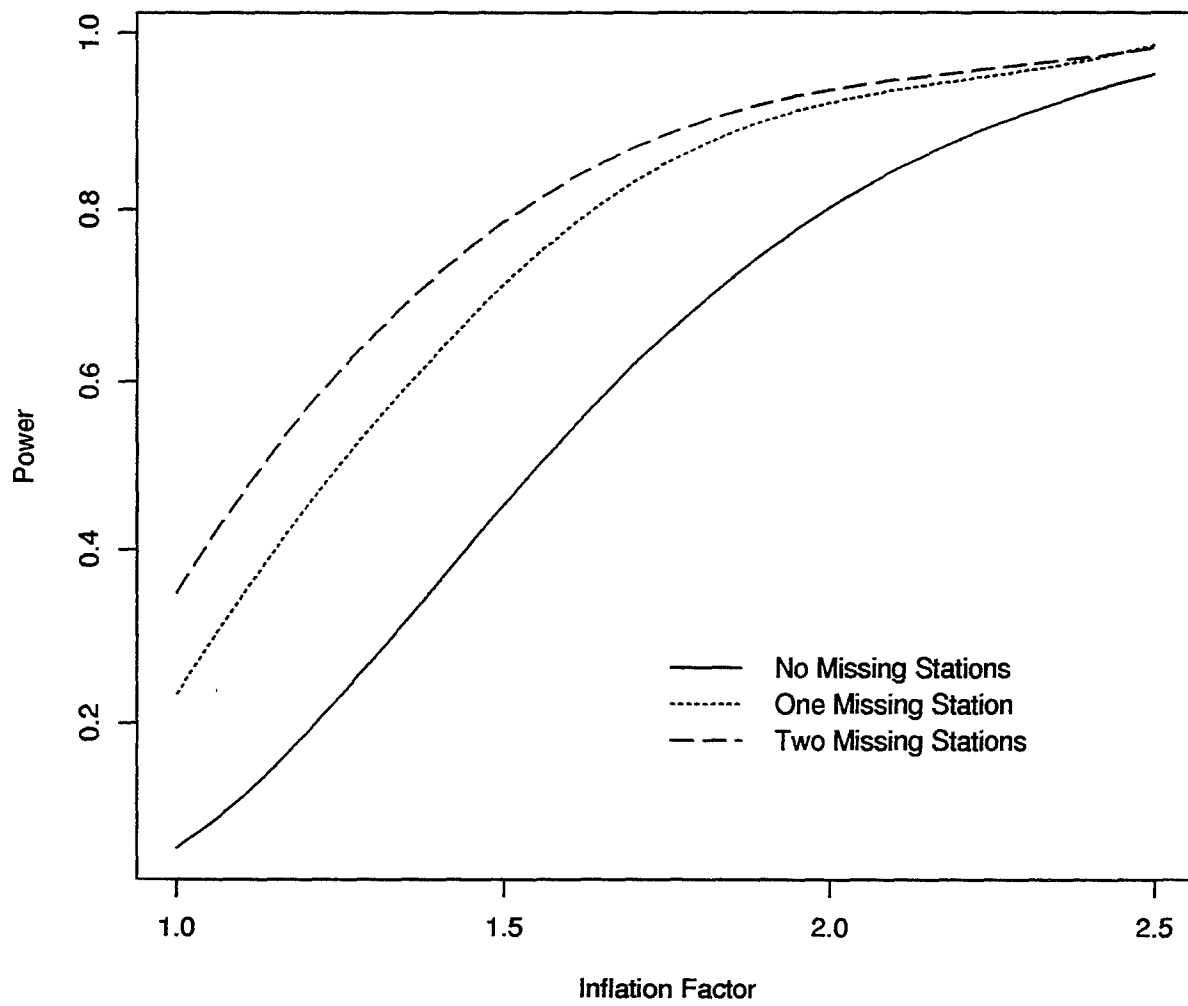
Figure 2: Probability of Identifying Spurious Events.

References

[1] Anderson, K. K. (1995). On the estimation of network detection probabilities, *Technical Report PNL-SA-264180,* Pacific Northwest Laboratory, Richland, Washington.

[2] Bender, B. (1983). Maximum likelihood estimation of b values for magnitude grouped data, *Bull. Seism. Soc. Am.* **73**, 831-851.

[3] Gutenberg, B. and C. F. Richter (1941). Seismicity of the Earth, *Geol. Soc. Am., Spec. Pap.* **34**, 1-133.

[4] Herrin, E., and W. Tucker (1972). On the estimation of bodywave magnitude, *Technical Report to AFOSR,* Dallas Geophysics Laboratory, Southern Methodist University, Dallas, Texas.

[5] Kelly E. J. and R. T. Lacoss (1969). Estimation of seismicity and network detection capability, Technical Note 1969-41, Lincoln Laboratory, MIT, Lexington, Massachusetts.

[6] Ringdal, F. (1976). Maximum-likelihood estimation of seismic magnitude, *Bull. Seism. Soc. Am.* **66**, 789-802.

[7] Ringdal, F. (1986). Study of magnitudes, seismicity, and earthquake detectability using a global network, *Bull. Seism. Soc. Am.* **76**, 1641-1659.

[8] Taylor, D. W. A., J. A. Snoke, I. S. Sacks, and T. Takanami (1990). Nonlinear frequency-magnitude relationships for the Hokkaido Corner, Japan, *Bull. Seism. Soc. Am.* **80**, 340-353.

Detection and Identification of Small Regional Seismic Events

T. J. Bennett, B. W. Barker, M. E. Marshall, and J. R. Murphy
S-CUBED
11800 Sunrise Valley Dr., Suite 1212
Reston, Virginia 22091
Contract No. F 19628-93-C-0093
Sponsored by ARPA

Abstract

Many seismic events detected and located by the prototype International Data Center (IDC) at the Center for Monitoring Research (CMR) are small regional events. However, only very limited experience exists for regional seismic signals from small or decoupled nuclear explosions, which would be important in a CTBT monitoring environment. Furthermore, many of the events currently being reported by the IDC occur in geographical regions for which there is little or no previous seismic monitoring experience with underground nuclear explosion tests. The goal of this research has been to enhance the experience base for the IDC and to identify potential techniques and limitations of IDC seismic monitoring at the low magnitude levels appropriate to a CTBT.

For these investigations we have focussed primarily on application of theoretical source scaling methods to the regional signals from observed underground nuclear explosions and, then, compared the behavior of the scaled regional signals to that from other source types with similar, small magnitudes. During the initial stages of this project, a test database of underground nuclear explosion tests recorded at the Fennoscandian regional arrays was identified. Mueller-Murphy theoretical source scaling was used to scale the array records down to the levels appropriate to CTBT monitoring goals (e.g. 1-kt fully decoupled), and the scaled signals were re-embedded into normal background noise conditions. A copy of this scaled explosion database was provided to CMR for testing capabilities of the existing system, and we performed some independent signal analysis procedures on the waveforms to discern features which could be relevant in identification monitoring at the IDC. In a separate study under this contract, we also investigated seismic identification techniques for some specific events recently detected by the IDC. One such event was the January 5, 1995 seismic event in the central Ural mountains of Russia which had a magnitude of 4.4. Comparisons of L_g/P or S/P ratios and M_S-vs-m_b at selected stations seem to indicate that this event was probably a rockburst or mine tremor.

Key Words: Seismic, Discrimination, Regional, Scandinavia, Explosion, Decoupling, Array.

Objective

Monitoring seismic events at the low magnitude levels appropriate to a CTBT will require the utilization of detection and identification techniques based on observations at regional stations. It will also require extension of discrimination methodology from specific regions within which the regional techniques have been established into new areas which will require calibration. The prototype International Data Center (IDC) at the Center for Monitoring Research (CMR) is routinely detecting and locating seismic events throughout the world as part of the GSETT-3 experiment. Many of the reported events are small and occur in regions where there is little or no direct experience with observations from underground nuclear explosions. Even where such nuclear explosion experience does exist, it is generally for events with magnitudes well above those of most events being reported by IDC. As a result it is difficult to assess potential identification techniques and limitations of IDC seismic monitoring in the context of a CTBT. The primary objective of this investigation has been to make some preliminary attempts to simulate the behavior of regional signals from underground nuclear explosion tests down at the levels of interest for CTBT monitoring (e.g. 1-kt fully decoupled). To accomplish this objective we applied Mueller-Murphy source scaling theory to signals observed at Fennoscandian regional arrays for larger nuclear explosions and then reintroduced the scaled-down signals into the normal seismic background noise. Copies of these simulated nuclear explosion signals were provided to the CMR for testing IDC algorithms, and additional independent studies of the regional signals were conducted to assess potential limitations on detection and identification techniques. A secondary objective of this project has been to investigate seismic characteristics of some specific events reported by the IDC. We have looked at IDC data from selected seismic events and attempted to determine regional signal characteristics which would be useful for identification.

Research Accomplished

At last year's research review meeting, we described the procedures which we have been using to scale regional seismograms from larger nuclear explosions to simulate small and decoupled nuclear tests. The procedures are somewhat similar to the magnitude scaling performed by Kvaerna (1992) to investigate detection threshold monitoring in the vicinity of the Russian test site at Novaya Zemlya (NZ) except we use the more elaborate explosion source scaling theory of Mueller and Murphy (1971). Instead of the simple amplitude reduction produced by magnitude scaling, the explosion source scaling theory produces a combined amplitude reduction and shift to higher frequencies in scaling to lower yield explosions. This scaling operation is represented in the frequency domain as

$$\frac{S_2(\omega)}{S_1(\omega)} = \frac{p_2(\omega)}{p_1(\omega)} \frac{r_{el2}}{r_{el1}} \frac{\omega_{o1}^2 + i\,\omega_{o1}\,\omega - \beta\,\omega^2}{\omega_{o2}^2 + i\,\omega_{o2}\,\omega - \beta\,\omega^2}$$

where r_{el1} and r_{el2} are the elastic radii of the two sources at which the spherically symmetric pressures $p_1(\omega)$ and $p_2(\omega)$ act and

$$\omega_{oi} = \frac{\alpha}{r_{el_i}} \quad \text{and} \quad \beta = \frac{\lambda + 2\mu}{4\mu}$$

with α the P-wave velocity and λ and μ the Lame constants characteristic of the source medium.

We have applied this scaling operation to the seismic records measured at the Fennoscandian regional arrays (viz. ARCESS, FINESS, NORESS) from three large underground nuclear explosions (two at NZ and one PNE north of Arkhangel'sk and east of the White Sea, cf. Figure 1). NORESS was the only operating regional array at the time of the latter event. The NZ explosions both had magnitudes of 5.7 m_b, and the magnitude of the PNE was 5.0 m_b. The epicentral distances from the NZ explosions were approximately 2260 km to NORESS, 1100 km to ARCESS, and 1770 km to FINESS; and the epicentral distance from the PNE to NORESS was 1560 km. So, the recording distances can generally be described as far regional.

Figure 2 shows the source scaling factor as a function of frequency for explosions of four different yields relative to a large explosion. In this case the large explosion has an elastic radius of 685 m corresponding approximately to a yield of 50 kt which is roughly equivalent in magnitude to 5.7 m_b, the magnitude of the NZ explosions. The elastic radii associated with the various scale factors (viz. 186 m, 97 m, 77m and 45 m) correspond approximately to explosion yields of 1-kt fully tamped, 10-kt fully decoupled, 5-kt fully decoupled and 1-kt fully decoupled, respectively. It can be seen from Figure 2 that the theory predicts significant reductions in amplitude for the smaller events. The amplitude reductions are predicted to be much larger at frequencies below about 1 Hz than at high frequencies. The scale factor shows a transition between about 1 Hz, which corresponds to a corner controlled by the larger event being scaled, and a high-frequency corner, which corresponds to and varies with the yield or elastic radius of the smaller event. Comparing the low-frequency levels of the scale factors for 1-kt fully tamped (r_{el} = 186 m) and 1-kt fully decoupled (r_{el} = 45 m), we note the difference is a factor of 70, corresponding to the maximum decoupling factor seen in empirical observations.

In last year's review presentation and in our subsequent report (cf. Bennett et al., 1994), we described in detail and illustrated the steps in the simulation process. After scaling, the modified signals were superimposed on long noise records for each of the arrays. The noise samples used were selected at the time because they seemed to represent some of the longer record segments available which had no apparent signals; subsequently longer noise segments can now be easily accessed in the IDC database for more recent time periods. In our previous presentation we noted that the signals at all three arrays for the 1-kt fully decoupled explosion at distances corresponding to NZ were buried in noise on the broadband records and not apparent. However, we found that at the nearest station (viz. ARCESS at R $\approx$ 1100 km) the regional signals at high frequencies could be brought out of the noise by bandpass filtering. This is illustrated in Figure 3 where we show a narrow bandpass filter analysis of the vertical-component record simulating a 1-kt fully decoupled explosion from NZ recorded at ARAO (using in this case the noise from 04/23/92). The analysis shows little evidence of the regional signals at frequencies below 3 Hz, but strong signals in the 3 Hz to 20 Hz bands. It is apparent from these analyses that most reliable regional methods for detection, location, and discrimination of small or

842
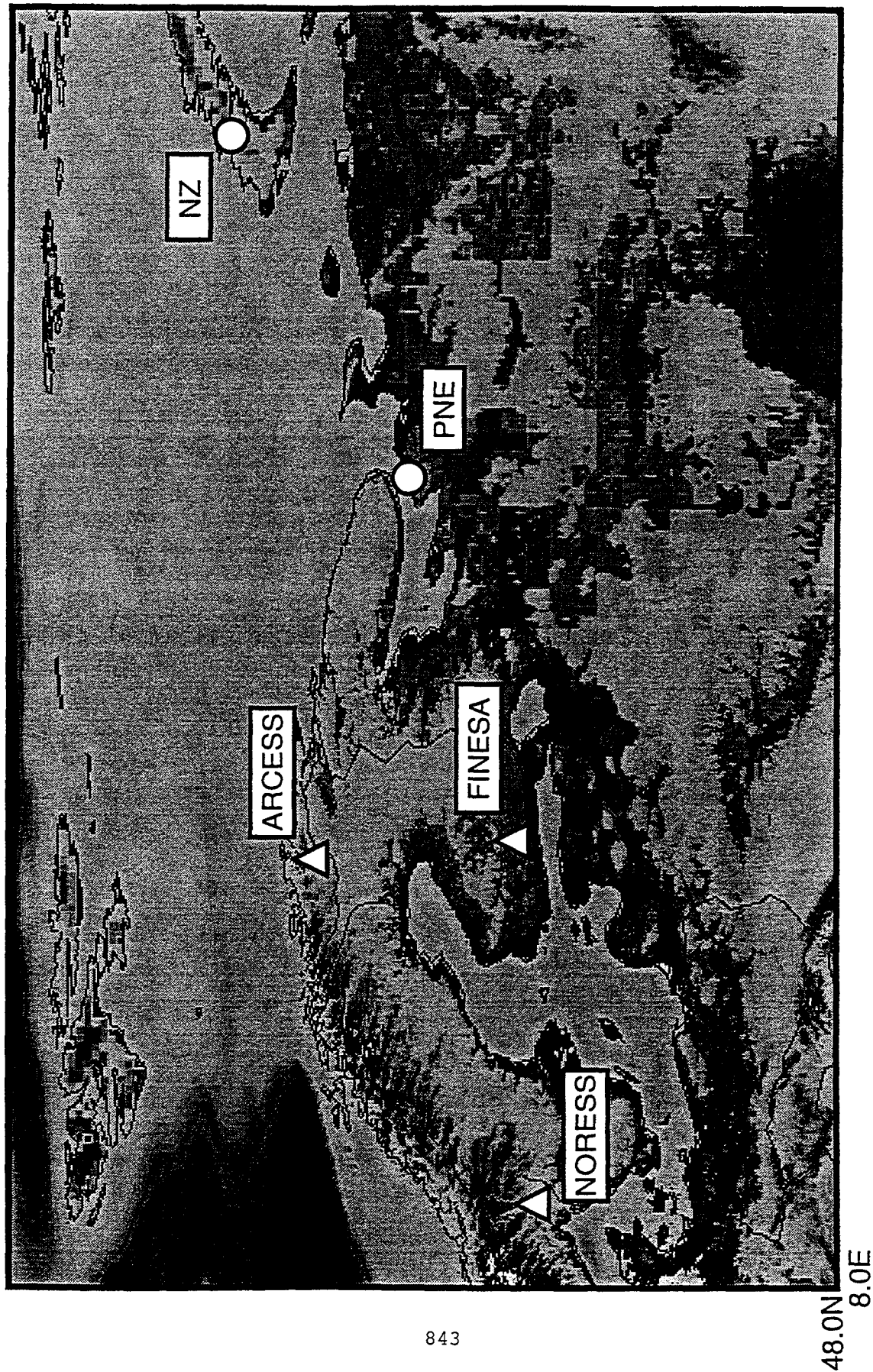
Figure 1. Locations of nuclear explosion sources and ARPA regional array stations.
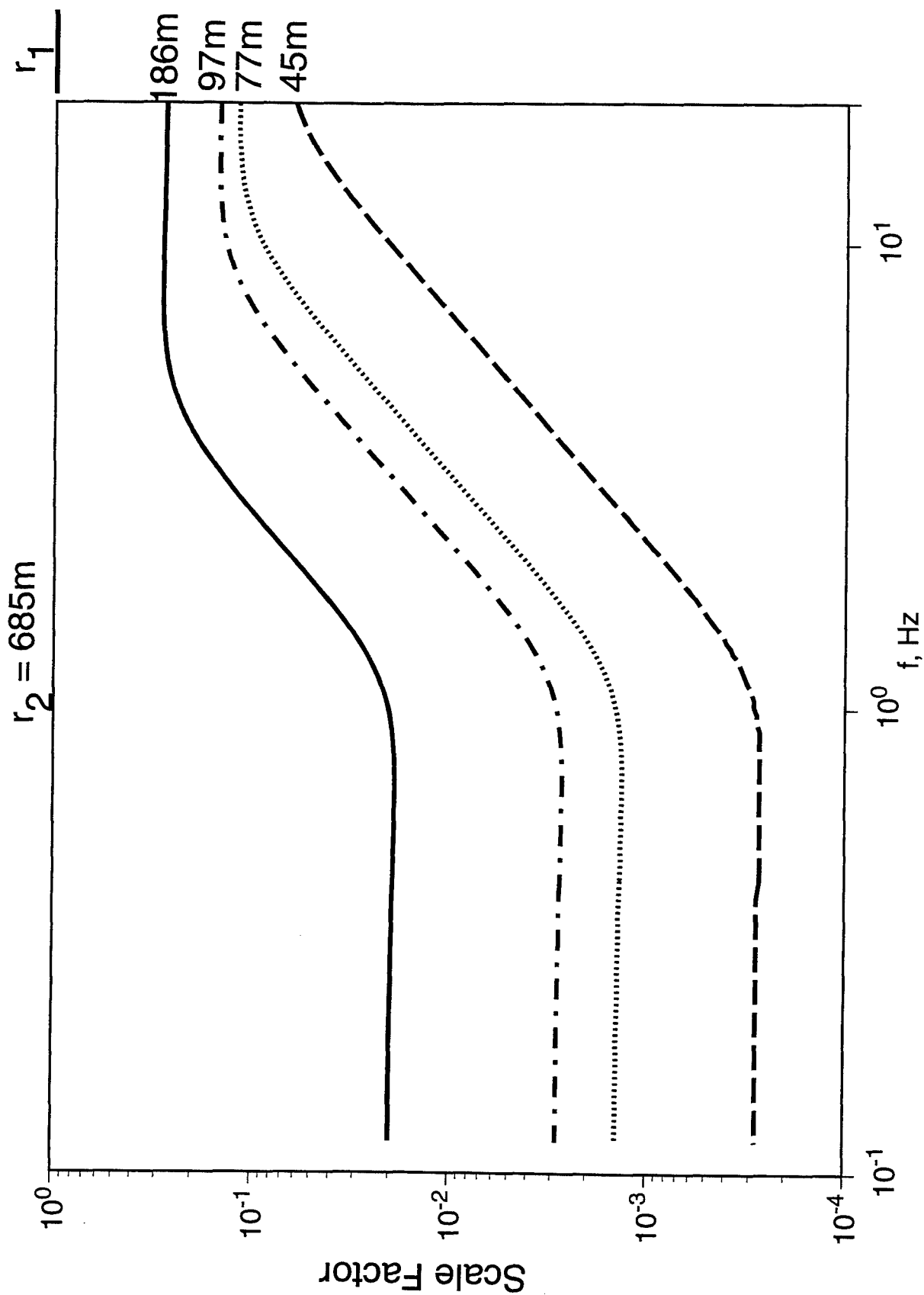
Figure 2. Source scaling factor as a function of frequency for explosions of different yields characterized by their elastic radii (r_1) relative to a larger explosion with an elastic radius of 685m (r_2).
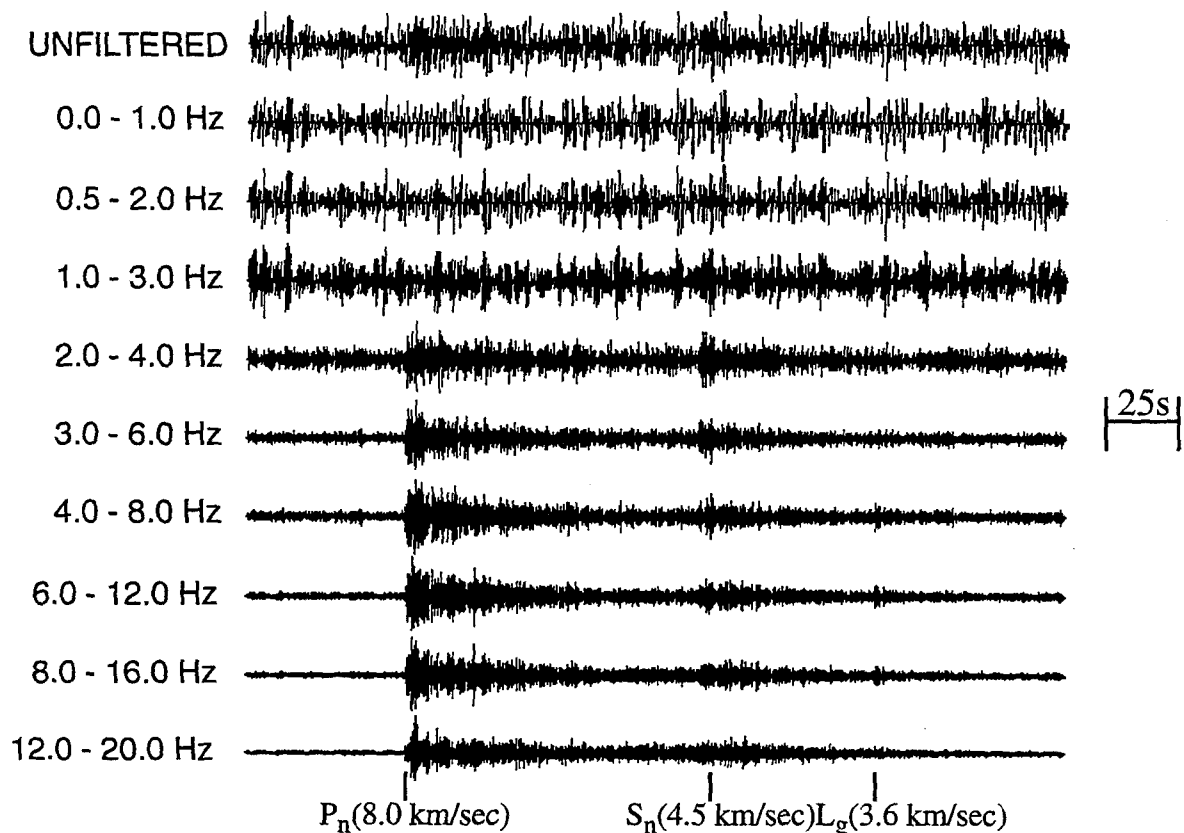
Figure 3. Application of band-pass filter analysis to vertical-component ARA0 recording of the 10/24/90 NZ explosion scaled down to 1kt fully decoupled.
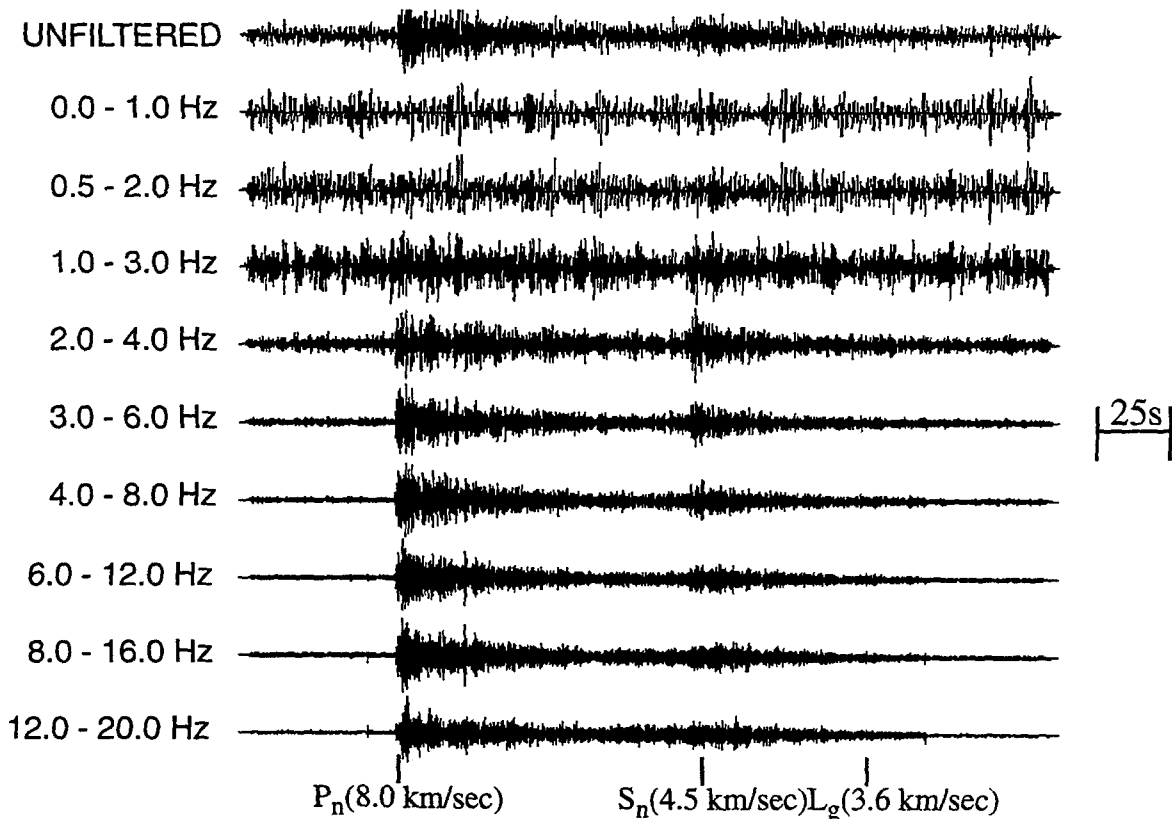
Figure 4. Application of band-pass filter analysis to vertical-component ARA0 recording of the 10/24/90 NZ explosion scaled down to 1kt fully decoupled.

decoupled nuclear explosion tests will need to utilize this higher frequency information.

In our more recent acquisition and analyses of noise segments from the IDC database, we have found that the broadband noise level is sometimes not so high at ARCESS. This seems to agree with observations by Kvaerna (1992) which indicated strong fluctuations in the noise levels and detection threshold at ARCESS by more than one-half magnitude unit during a single month, while the noise levels at the other regional arrays remained more stable. Figure 4 shows the same narrow bandpass filter analysis applied to the simulated ARCESS record for the 1-kt fully decoupled nuclear explosion at NZ with low noise conditions (viz. noise from 04/30/95). In this case the broadband noise on 04/30/95 is about a factor of three to four lower. We see from the broadband (unfiltered) trace at the top that regional P_n and S_n signals are quite apparent on the unprocessed record. The signal-to-noise ratio is roughly a factor of 2.0 for P_n and just above 1.0 for S_n. However, when we look at the individual filter passbands, it is apparent that even at low noise levels some frequency bands will not be useful for detection, location, and identification of small events. In particular, there is still little evidence of the regional signals from the scaled nuclear explosion at frequencies below about 3 Hz; while above 3 Hz signal-to-noise levels are quite high. In fact, maximum amplitudes for the bandpass filter analysis shown in Figure 4 are achieved in the frequency passband from 6 to 12 Hz. The implications again are that regional event characterization methods which make use of high-frequency information in regional seismic signals are likely to be most useful for identifying small or decoupled nuclear explosions at the levels which are currently considered to be of interest for CTBT monitoring.

A test of the relevance of these scaled nuclear explosion data to seismic monitoring like that in the IDC was provided by the 12/31/92 event near NZ (cf. Ryall, 1993). This event of unknown source type had a magnitude of about 2.5 m_b. Therefore, the source size and propagation path for this event should provide a close match to those of our simulated 1-kt fully decoupled NZ explosion. We performed the same bandpass filter analysis shown in Figures 3 and 4 to the ARCESS record for the 12/31/92 event. The results of this comparison were described in detail in the report by Bennett et al. (1994). We observed that above about 3 Hz the simulated decoupled nuclear explosion source produced significantly stronger P signals relative to S (in this case S_n) than the unknown event. The differences become most dramatic in the high frequency passbands (e.g. 6-12 Hz, 8-16 Hz, and 12-20 Hz) where S/P ratios are approximately 1.0 for the unknown event but only about 0.5 for the scaled nuclear explosion records. This behavior for the 12/31/92 event is consistent with that seen for earthquakes and other non-explosion sources in other parts of the world and appears to support the conclusion that the 12/31/92 event was not an explosion.

Another interesting test of seismic monitoring capability with regional stations was provided by the 01/05/95 event in the Ural mountains of Russia. The epicenter of this event reported by the IDC was 59.52 N 56.31 E, and the corresponding magnitude was 4.35 m_b from IDC and 4.7 m_b from PDE. Although this event was located somewhat beyond the normal regional distance range from the Fennoscandian seismic arrays, regional S and L_g phases are apparent on the records at FINESS (R $\approx$ 1660 km), ARCESS (R $\approx$ 1820 km), and NORESS (R $\approx$ 2450 km); and good regional phase signals were observed at closer stations in Russia. Our investigation of this event has focussed on the seismic signals observed at the nearer Russian stations ARU (R $\approx$ 360 km) and OBN (R $\approx$ 1280 km). At station ARU we performed a narrow

bandpass filter analysis on the vertical-component record, as shown in Figure 5. The filtered traces show a strong R_g phase in the 0.5-2.0 Hz passband. Below about 3 Hz the L_g/P ratios are observed to be large (much greater than 1.0), but above 3 Hz the S/P ratios are about 1.0. For comparison we performed the same bandpass filter analyses on the records from three western European events of different source types recorded at station GRFO (located at about the same epicentral distance). The three events include a Polish rockburst, a Netherlands earthquake, and a Swiss munitions blast and were described in the review report for last years PL Seismic Research Symposium. Across the different frequency bands, the filtered traces appear most similar for the Urals event and the Polish rockburst. L_g/P or S/P ratios were seen to be greater than 1.0 for the Polish rockburst at lower frequencies (below about 3 Hz) and about 1.0 at higher frequencies; as we also saw in the Urals event. Although the earthquake also had large L_g/P or S/P at most frequencies, the energy there in the regional seismic phases appeared more dispersed across the different phase windows. The munitions blast produced relatively smaller L_g/P particularly at frequencies near 1 Hz where the blast signals showed a strong P_g. In the longer period bands a single-station M_S of 3.38 was measured for the Urals event at station OBN. Based on these observations at the Russian stations ARU and OBN, we concluded that the 01/05/95 Urals event was clearly shallow considering the strong R_g phase; this might not be consistent with an earthquake source which would likely be deeper. The relatively weak M_S is also more typically seen in explosions and rockbursts, as are the simple P phases. The most diagnostic feature in these comparisons appears to be that the L_g/P and S/P ratios observed at ARU and OBN are large, 1.0 or above in all frequency bands, which is consistent with behavior seen in other parts of the world for rockburst and eathquakes but does not agree with explosion observations. Based on these observations we concluded that the 01/05/95 Urals event was most likely a rockburst, which appears to be supported by damage reports from a Russian mine in the vicinity of the epicenter.

Conclusions and Recommendations

Regional seismic monitoring is likely to be important to detecting, locating, and identifying small events which are of interest under a CTBT. Theoretical source scaling procedures appear to provide a useful tool for helping to understand the issues associated with characterization of small or decoupled nuclear explosions based on regional seismic measurements. The implications from these studies are that the regional methods which are most likely to be effective for detection, location, and identification of small seismic events will be those which utilize the high-frequency information in the regional signals. We are currently pursuing some additional applications of similar theoretical source scaling analyses for nuclear explosions in other tectonic environments. With regard to application of regional characterization techniques to specific events, which are likely to be encountered in IDC monitoring, we have investigated events near NZ and in the Urals. Based on these and similar studies, we have found that some traditional discriminant measures (e.g. M_S vs m_b, depth-based discriminants) may not be reliable for certain classes of events (e.g. rockbursts). We believe that L_g/P and/or regional S/P ratios frequently provide a diagnostic tool for event identification. Such ratios appear to be most robust when they are compared for multiple passbands covering a fairly broad range of
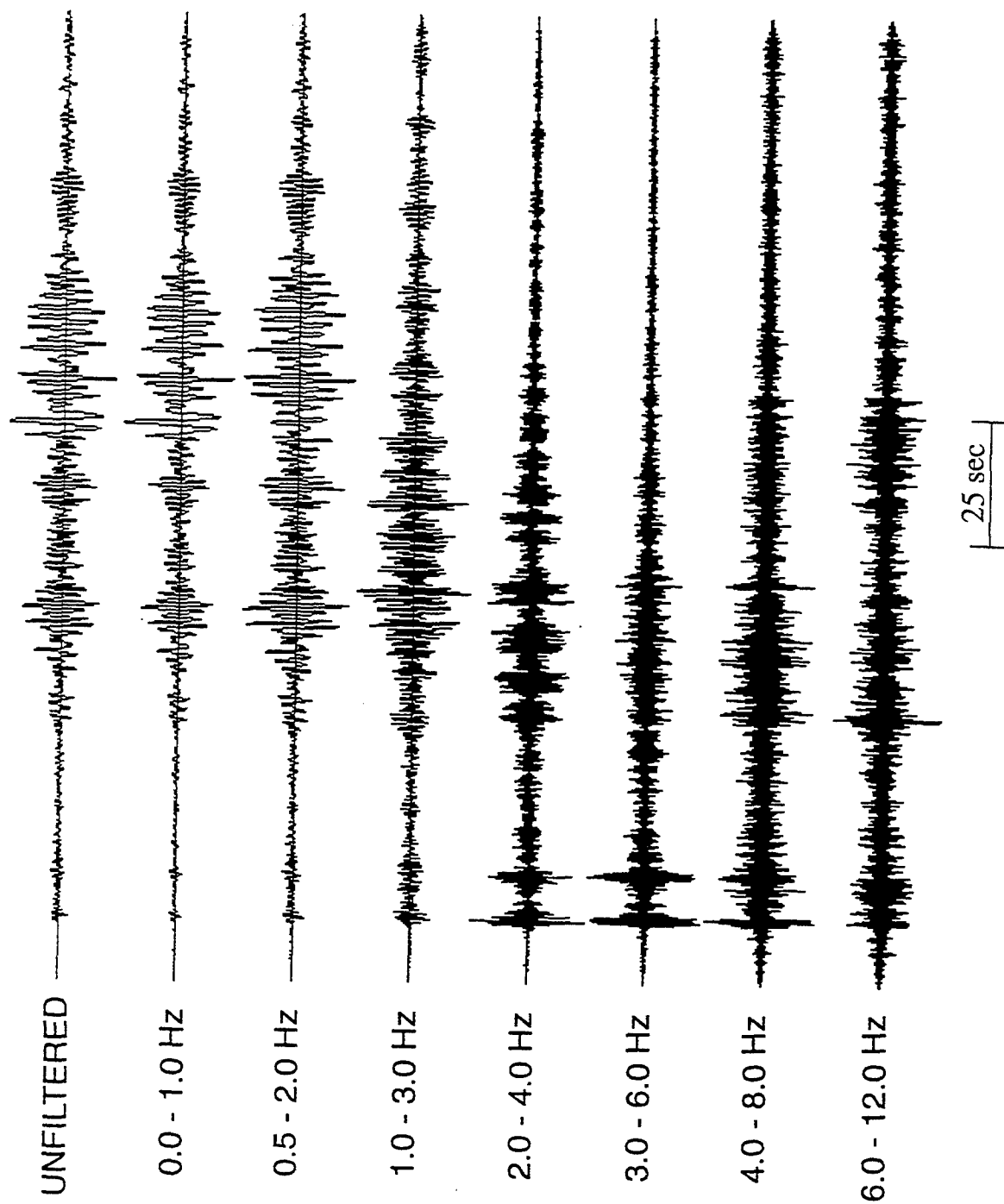
Figure 5. Bandpass filter analysis of the ARU record for the Urals event of January 5, 1995.

848

frequencies. Systematic studies will be needed to confirm transportability of these kinds of regional discriminants into uncalibrated areas.

References

Bennett, T. J., B. W. Barker, and J. R. Murphy (1994). "Investigation of Regional Seismic Discrimination Issues for Small or Decoupled Nuclear Explosions," PL-TR-94-2260. ADA292744

Kvaerna, T. (1992). "Continuous Seismic Threshold Monitoring of the Northern Novaya Zemlya Test Site: Long-Term Operational Characteristics," PL-TR-92-2118, ADA252890.

Mueller, R. A., and J. R. Murphy (1971). "Seismic Characteristics of Underground Nuclear Detonations. Part I. Seismic Spectrum Scaling," Bull. Seism. Soc. Am. 61, pp. 1675 - 1692.

Ryall, A. S. (1993). The Novaya Zemlya Event of 31 December 1992 and Seismic Identification Issues, Executive Summary, Published in Conjunction with the 15th Annual Seismic Research Symposium, 8 - 10 September 1993, Vail, Colorado. PL-TR-93-2160, ADA271458

AN AUTOMATED RAYLEIGH WAVE DETECTION ALGORITHM

Eric P. Chael
Sandia National Laboratories
Albuquerque, NM 87185

Abstract

The desire to operate denser networks in order to monitor seismic activity at lower thresholds leads to greater emphasis on automated data processing. An algorithm for detecting and characterizing long-period Rayleigh wave arrivals has been developed and tested. The routine continuously monitors all directions of approach to a station, in a manner similar to beamforming. The detector is based on cross-powers between the Hilbert-transformed vertical and rotated horizontal signals, so it is sensitive to both the power and polarization properties of the three-component wavefield. Elliptically polarized Rayleigh arrivals are enhanced, while linearly polarized Love waves and body phases are suppressed. A test using one month of data from station ANMO demonstrated that this technique can with high reliability detect Rayleigh arrivals which would be visible to an analyst. The measured arrival times and azimuths are accurate enough to permit automated association of the detections to events in a bulletin.

Key words: detection, Rayleigh wave, surface wave, long period, automated data processing, polarization

Effective verification of a Comprehensive Test Ban will require an extensive seismic network capable of monitoring at a fairly low magnitude threshold. Such a network will generate a large quantity of waveform data and record hundreds or even thousands of events daily. The resulting data analysis burden will force an increased reliance on automated processing. Current networks routinely process short-period (SP) waveforms by computer to automatically detect and associate body arrivals, and then locate the events. Improvements to these routines are necessary in order to improve their reliability. In contrast, the analysis of long-period (LP) waveforms, important for event identification via the $M_S:m_b$ discriminant, remains a largely manual process. First-generation algorithms for automated LP processing have only recently become available. One approach to this problem, currently being tested by the prototype International Data Center under GSETT-3, is to examine the LP signals for the existence of surface waves from known events. An alternate approach, which has been developed and tested for this report, is to continuously scan the LP data for surface arrivals from anywhere. Detected arrivals can then be associated to existing event solutions, or used to help constrain the solutions for events which produce few SP detections.

The Rayleigh detection algorithm discussed here exploits the elliptical polarization of Rayleigh arrivals both to enhance detection sensitivity over that achieved from vertical signals alone, and to decrease the sensitivity to unwanted body or Love arrivals. Several authors have developed algorithms for polarization analysis of seismic waves. Some of these (*e.g.*, Simons, 1988; Samson, 1977) have required knowledge of event location, so that the radial and transverse directions are known *a priori*. Others (*e.g.*, Samson and Olson, 1981) have relied on continuously tracking the dominant polarization direction, in essence dynamically rotating the waveforms to this continually changing azimuth. The method addressed in this work seeks to continuously and independently monitor all directions for Rayleigh arrivals. The technique is comparable to beamforming done for seismic arrays, in which beams are pointed in several different directions then separately scanned for arrivals. Simultaneously watching all directions should offer signal-to-noise improvement compared to tracking only the current dominant direction.

Research Accomplished:

An automated Rayleigh wave detection routine has been designed, and its performance tested using one month of LP data. Three-component long-period or broadband waveforms are required for the Rayleigh detection algorithm. The first step in the processing is to detrend and then bandpass filter the signals. A third-order Butterworth filter with a passband of 0.01 to 0.06 Hz has produced good results. Next, the vertical signal is Hilbert transformed using a 255-point FIR filter (Stearns and David, 1988). This has the effect of phase shifting the vertical waveform by 90°, which converts the elliptical polarization of Rayleigh waves into linear motion. A beneficial side effect of this operation is to change linearly polarized body waves to elliptical polarization, which will de-emphasize them in subsequent processing. At each time step, the 3-by-3 data covariance matrix is calculated over a specified window length. A duration of 80 s has been used for this short-term-average (STA) window, equivalent to 4 cycles at the dominant Rayleigh period near 20 s. The covariance matrix at each time step is then rotated over azimuth from 0° to 85° in 5°

increments. At each azimuth step, the two covariance elements which represent the cross-powers between the vertical and each of the rotated horizontals are extracted. These are used as the STA estimates for the two orthogonal azimuths corresponding to the angle of rotation (0° to 85°) and the direction 90° clockwise from this (90° to 175°). It is not necessary to calculate the covariances for azimuths of 180° to 355°, since the values would simply be the negative of those for 0° to 175°. A strong positive STA response indicates Rayleigh energy with the appropriate retrograde elliptical motion arriving from the specified direction. Using the cross-power between the vertical and horizontal motions should improve the signal-to-noise by about a factor of two (3 dB), compared to using the power on either axis alone. Long-term-averages (LTAs) of each of the STAs are updated at each time step. A recursive scheme was used for the LTA computations, providing exponential weighting of past STAs. The time constant for this weighting was set at 800 s.

A detection function is produced for each look direction by calculating a weighted STA/LTA ratio versus time. Alternatively, one can view the result as a detection surface with an altitude that varies as a function of both azimuth and time. Two weights are applied to the STA/LTA ratios of the cross-powers. The first of these weights is the absolute value of the correlation coefficient between the vertical and the radial signal for a given azimuth. Because the vertical has been Hilbert transformed, it should be well correlated with the horizontal when a Rayleigh wave is arriving from the specified direction. The second weight is based on the relative amplitudes of the vertical and radial components. Its purpose is to emphasize arrivals whose Z and R motions are similar in amplitude. Both of these weights are readily calculated from the elements of the rotated covariance matrix. The detection surface is scanned for peaks exceeding a threshold altitude. When a detection is made, the peak's onset time, amplitude and central azimuth are recorded, along with the peak amplitude of the vertical signal following the detection. The entire Rayleigh detection algorithm was implemented in MATLAB, so it can be easily modified to test different processing details. The current routine should be able to process full-period LP data (1 sps) from roughly 100 stations on a single Pentium-class PC.

Figure 1(a) shows 20 min of LP data from station COL near Fairbanks, AK for an earthquake in the Aleutians. The horizontal components have been rotated to the radial (middle trace) and transverse (bottom trace) directions. A strong Rayleigh wave arrives near 600 s on the LPZ and LPR traces. The LPT signal shows a strong Love arrival near 400 s, with coda extending into the Rayleigh window. This coda contaminates a standard polarization analysis of the Rayleigh wave. Figure 1(b) displays the detection surface produced by these records; the surface is shown for azimuths of 180° to 360°, where the data produce a positive peak. The Rayleigh wave produced a very strong peak at the proper time and azimuth for this event. Note that the large Love arrival had little effect on the surface. The Love coda caused the ridge running to the left from the peak, but did not significantly bias the peak's location. Figure 2(a) shows a much weaker Rayleigh arrival at station ANMO (Albuquerque, NM) from an event in the South Pacific. For this plot the traces were bandpass filtered between 0.01 Hz and 0.06 Hz to enhance the arrival. Again the horizontals have been rotated to radial and transverse, and the Rayleigh wave begins just prior to 600 s. The resulting detection surface in Figure 2(b) shows a prominent peak at the Rayleigh onset time, centered near the correct backazimuth to the event. This peak jumps abruptly from the preceding terrain, despite the relatively low SNR of the arrival on the seismograms. A second

peak occurs near 900 s on the plot, caused by the resurgence in the Rayleigh coda which can be seen on the LPZ trace.

To test the performance of the detection algorithm in routine operation, I processed all of the ANMO data for the month of October, 1993. The resulting detection log was compared to the NEIC event bulletin for this month. A total of 192 detections were reported, of which 157 could be attributed to 108 different events in the bulletin. For those events which caused multiple detections, the trigger corresponding to the Rayleigh onset could usually be readily determined from its time and azimuth. Multiple detections for an event were usually due to fluctuations in the Rayleigh coda, overtone energy preceding the Rayleigh, or S arrivals. Errors in the estimated backazimuths for identified Rayleigh arrivals had a mean of 0° and a standard deviation of 15°. Thus the backazimuth measurements are sufficiently accurate to assist automated association of Rayleigh detections with events. Figure 3 shows the performance of the detector as a function of event magnitude and distance, for all events which had M_S values in the NEIC bulletin. Solid circles represent events which produced Rayleigh detections by the algorithm, open circles events which did not. This plot indicates that the routine can detect Rayleigh waves from most events with M_S over 4 to distances of 30°, with the sensitivity gradually decreasing to an M_S of about 5 at the furthest ranges. The undetected large events at a distance of 108° were aftershocks in the coda of larger events. Adjusting the LTA time constant or changing the logic for ending a previous detection may yield better performance in such cases.

Conclusions and Recommendations:

An algorithm for detecting Rayleigh surface wave arrivals on three-component long-period records has been developed and tested. The routine continuously monitors all directions of approach to a station, in a manner analogous to array beamforming. The detector's response is sensitive to both the power and polarization properties of the wavefield, so that Rayleigh waves are preferentially enhanced over other arrivals. A one-month test of the algorithm with station ANMO demonstrated that it can reliably detect an overwhelming majority of the Rayleigh waves visible on the seismograms, and the detection time and azimuth measures are sufficiently accurate for reliable association to bulletin events.

Further work is needed in three areas. First, estimates of arrival amplitude and period need to be refined, in order to enable accurate automated M_S measurements. Second, better methods for screening non-Rayleigh detections should be developed and tested. Examining a detection's frequency content may be useful here. Finally, more testing is needed to establish the performance for regional events ($\Delta < 30°$), which will become of increasing importance under a CTBT.

References:

Samson, J. C. (1977). Matrix and Stokes vector representations of detectors for polarized waveforms: theory, with some applications to teleseismic waves, *Geophys. J. R. astr. Soc.* **51**, 583-603.

Samson, J. C. and J. V. Olson (1981). Data-adaptive polarization filters for multichannel geophysical data, *Geophysics* **46**, 1423-1431.

Simons, R. S. (1968). A surface wave particle motion discrimination process, *Bull. Seism. Soc. Am.* **58**, 629-637.

Stearns, S. D. and R. A. David (1988). *Signal Processing Algorithms*, Prentice-Hall, Inc., Englewood Cliffs, NJ.
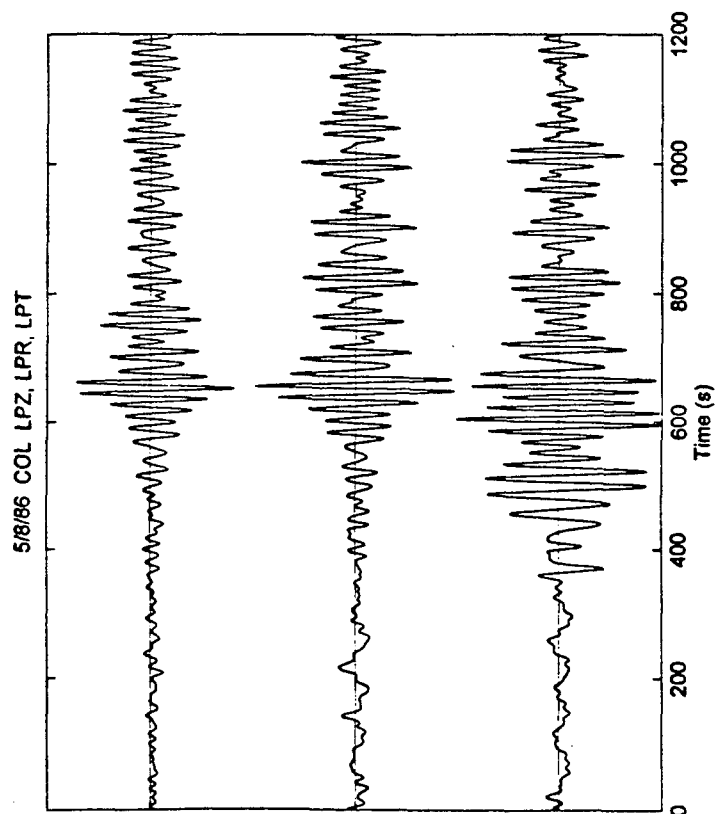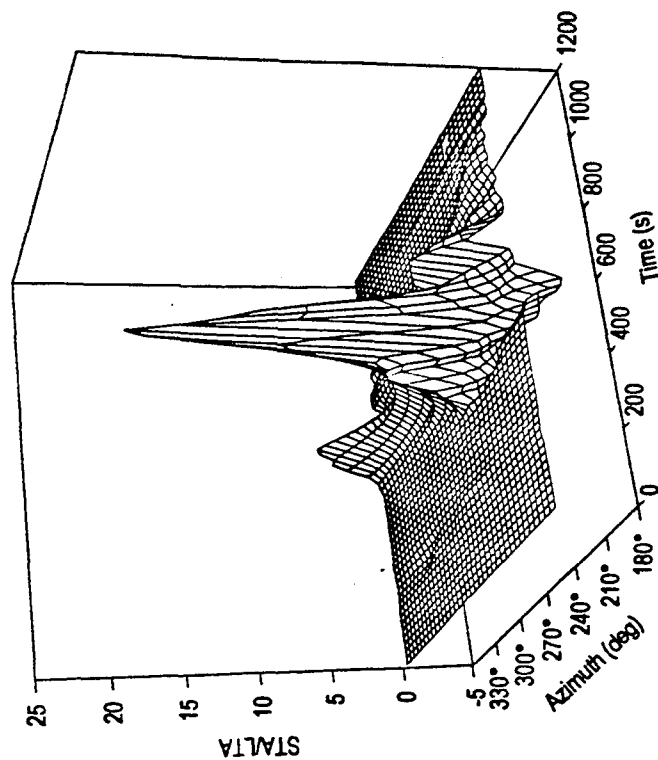
Figure 1. (a) Vertical, radial and transverse records from station COL of an M_S 5.4 earthquake in the Aleutian Islands on May 8, 1986, at a distance of 20° and a backazimuth of 241°. (b) Output of the detection algorithm for the signals shown in (a).

Detector Output for ANMO, 10/7/93

STA/LTA

8
6
4
2
0
-2
-4

330° 300° 270° 240° 210° 180°
Azimuth (deg)

0 200 400 600 800 1000 1200
Time (s)

(b)

10/7/93 ANMO LPZ, LPR, LPT

0 200 400 600 800 1000 1200
Time (s)

(a)
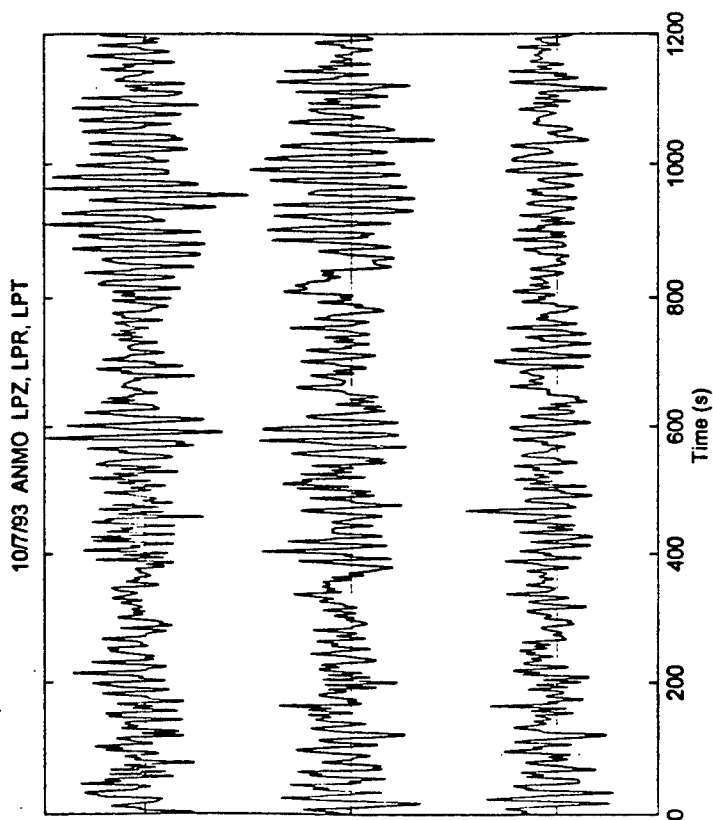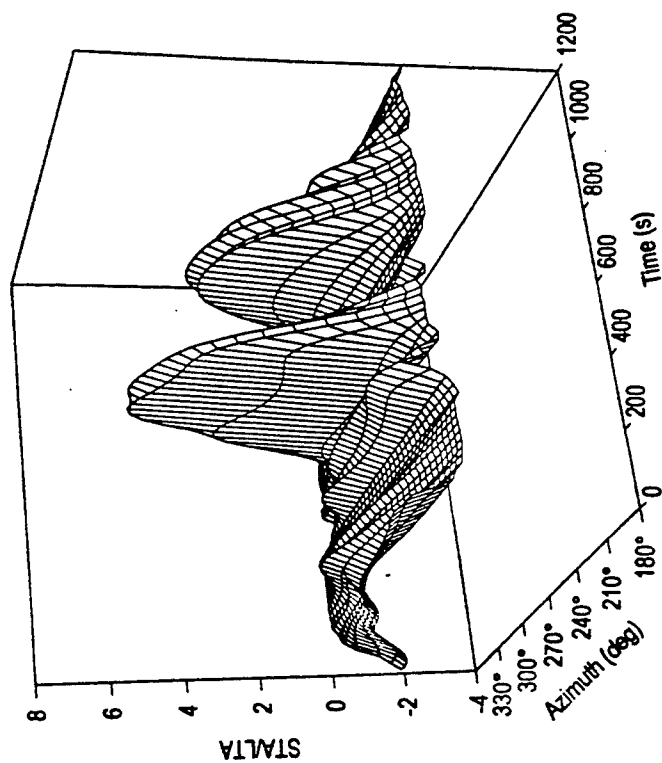
Figure 2. (a) Vertical, radial and transverse records from station ANMO of an M_S 4.3 earthquake in the South Pacific on October 7, 1993, at a distance of 97° and a backazimuth of 232°. (b) Output of the detection algorithm for the signals shown in (a).
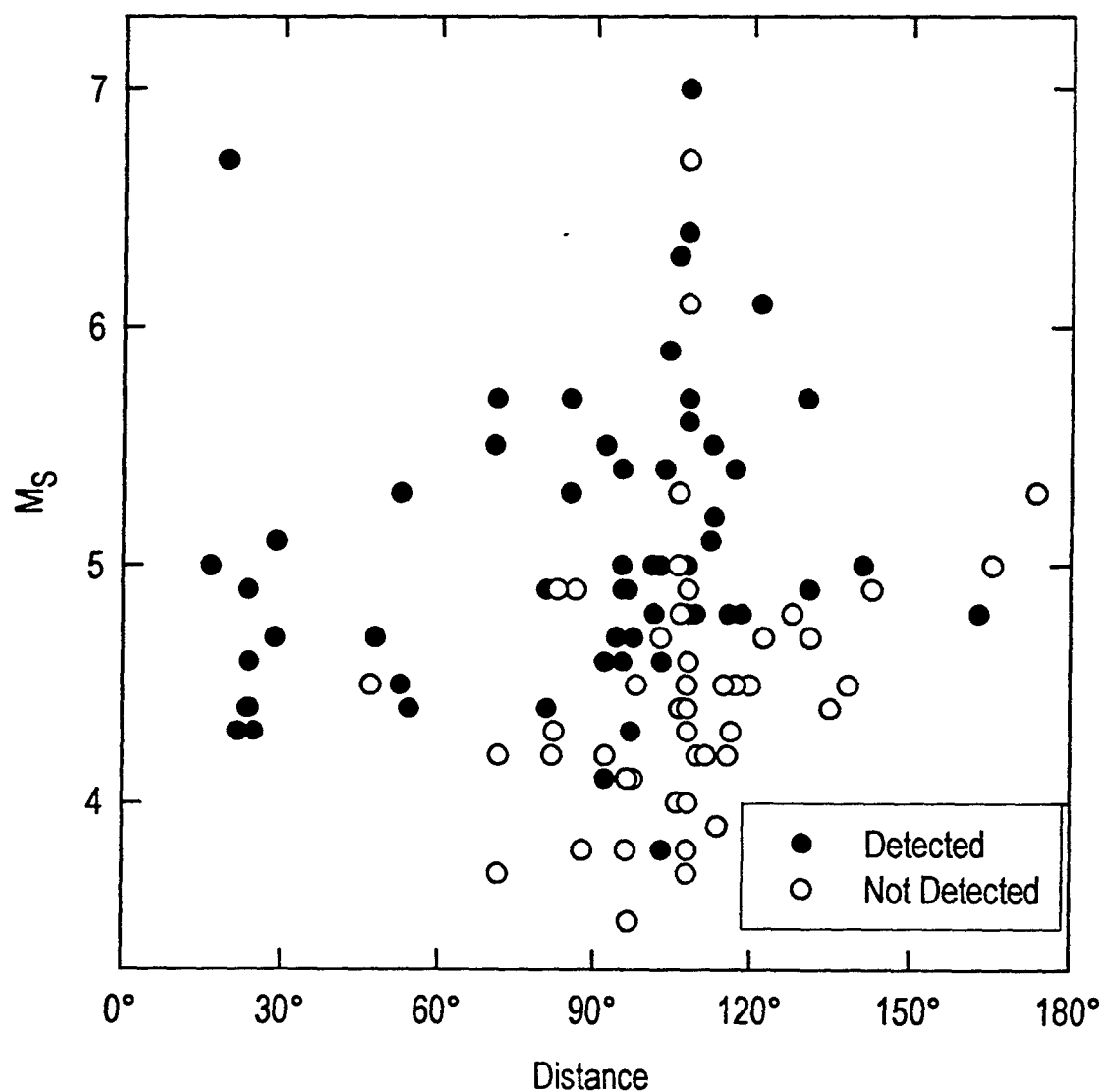
Figure 3. Detector performance as a function of event distance and surface wave magnitude. Solid circles represent events whose Rayleigh waves were detected by the algorithm, open circles indicate that a Rayleigh arrival was not detected.

Statistical Framework for Event Identification and Assessment of Seismic CTBT Monitoring Capability

Mark D. Fisk
Mission Research Corporation, Santa Barbara, CA
and
Henry L. Gray and Gary D. McCartor
Southern Methodist University, Dallas, TX

ABSTRACT

This effort focuses on several main areas regarding event identification within the context of CTBT monitoring: (1) development and integration at the Center for Monitoring Research (CMR) of a software system for event characterization/identification; (2) assessment of regional seismic event identification performance; (3) analysis of GSETT-3 Alpha network data to assess the availability and utility of event characterization parameters for global monitoring; and (4) investigation of robust multi-sensor data fusion techniques for outlier detection and event classification.

We have been implementing a statistical event identification framework. The fundamental methods consist of statistical tests for outlier detection and event classification, as well as algorithms to test appropriate assumptions regarding the data in order to optimize and ensure validity of the results. Our methodology: (1) accurately treats statistical uncertainties of all discriminants used; (2) provides flexibility to incorporate any discriminant and assess its utility objectively; (3) can identify nuclear tests in regions for which relevant ground-truth training data may or may not exist; (4) can function in an automated mode to flag, categorize and/or rank anomalous events; (5) can control the false alarm rate; (6) and provides a rigorous and defensible framework with which to report and justify the results. To also serve as an interactive analysis tool, we have been developing an X Window graphical user interface, featuring a wide range of displays and exploratory data analysis tools. We have applied the methods to seismic events recorded by the ARCESS and GERESS arrays, station WMQ in China, and stations KNB and MNV in the western U.S. Results show that useful monitoring can be performed, currently down to magnitude 3, for regions that are well-covered by at least one seismic station or array. Overall, 91% of explosions were identified as outliers with a false alarm rate slightly higher than the target rate of 1%. In addition to the geological diversity of the regions, these results were obtained for events with a wide range of epicentral distances and magnitudes.

We have also compiled various statistics regarding 1,786 events detected by a set of 30 Alpha stations, currently transmitting data to the CMR, during GSETT-3. We discuss the availability and utility of event characterization parameters, including location (offshore vs. onshore), hypocentral depth and detected depth phases, Ms:mb, and high-frequency regional amplitude ratios.

We have also been addressing the problem of how to best utilize discriminant data from multiple sensors. In general, there are numerous types of seismic and non-seismic (e.g., hydroacoustic and infrasonic) measurements from multiple stations/sensors that can be used as discriminants, and it is not clear from the outset how to best combine this information in a multivariate test for outliers. We have investigated three approaches to this problem. We have derived expressions for the power of each of the three tests and performed a parametric study to determine conditions for which a particular test is favored over the others. We also compared the power of these three tests using actual seismic data from stations KNB and MNV.

Key Words: CTBT, Event Identification, GSETT-3, Alpha Network, Outlier Detection

Statistical Framework for Event Identification and Assessment of Seismic CTBT Monitoring Capability

OBJECTIVE

This effort focuses on several main areas regarding event identification within the context of CTBT monitoring: (1) development and integration at the Center for Monitoring Research (CMR) of a software system for event characterization/identification; (2) assessment of regional seismic event identification performance; (3) analysis of GSETT-3 Alpha network data to assess the availability and utility of event characterization parameters for global monitoring; and (4) investigation of robust multi-sensor data fusion techniques for outlier detection and event classification.

We have been developing a statistical framework to identify seismic events, based on multivariate discriminant analysis. Our approach first utilizes confidence intervals for depth and Ms-mb, and confidence ellipses for location (and eventually hydroacoustic data) to screen events with high confidence that are caused by natural seismicity. Due to current limitations in estimating depth, location and Ms-mb for events below mb ~4.5, analysis of remaining events is based, at least in part, on regional discriminants which include high-frequency Pn/Lg and Pn/Sn. Due to regional variations and the lack of calibration data for nuclear explosions in most regions, we developed a robust multivariate outlier procedure to characterize events relative to previous seismic activity. The outlier method, based on a generalization of the likelihood ratio, has sufficient generality to utilize any combination of teleseismic and regional (as well as non-seismic) discriminants from single or multiple stations. Fisk et al. (1993, 1994) describe the methodology in detail, as well as numerous applications to seismic data. For regions where we do have training data for nuclear explosions, we have also developed a classification procedure (Baek et al., 1995; Fisk et al., 1993).

Fisk et al. (1994) applied the outlier approach to identifying seismic events in diverse geological regions, recorded by the ARCESS and GERESS arrays in Norway and Germany, stations KNB and MNV in the western U.S., and station WMQ in China. Results show that useful monitoring can be performed with this approach, currently down to magnitude 3, for regions that are well-covered by at least one seismic station or array. Overall, 264 of 290 (91%) explosions were identified as outliers and there were 3 false alarms out of 158 earthquakes (1.9%), slightly higher than the target rate of 1%. In addition to the diversity of the regions, these results were obtained for events with a wide range of epicentral distances and magnitudes. Recently we have adapted our multivariate outlier approach to categorize events rather than providing a "yes/no" decision. Categories are intentionally defined in a non-judgemental manner, but with a rigorous probabilistic interpretation, by the degree to which an event differs from previous seismicity in a given region. This approach fuses multivariate data in a composite metric to focus on anomalous events.

RESEARCH ACCOMPLISHED

Analysis of GSETT-3 Data. Recently we have compiled various statistics regarding seismic events detected by a set of 30 Alpha stations currently transmitting data to the CMR, to assess the numbers and characteristics of events that can be expected to be observed by the Alpha network during a given period, including the availability and utility of event characterization parameters that can be used to identify them. Events analyzed include those which occurred between 11 January 1995 and 12 February 1995, during GSETT-3. Regional discriminants and M_S were computed for the events during this period. We examine how many events can be identified with high confidence as due to natural seismicity, based on teleseismic measures of depth, location and M_S:mb. Of the remaining events, we examine how many have useful regional P/S and P/Lg values such that they can potentially be identified. Last, we evaluate the number of remaining ambiguous events which lack adequate discriminant data to identify them.

Figure 1 shows locations of 30 Alpha stations that are currently transmitting data to the CMR, as well as epicentral locations of 1,786 events, which occurred between 11 January 1995 and 12 February 1995 and were reviewed by seismic analysts. Origin, association and event characterization data for these events were retrieved from the *origin, origerr, assoc* and *originamp* tables in the *IDCWDB* database at the CMR. Of the 1,786 events during this period, there were a total of 634 events within regional distance ($\Delta < 20°$) of at least one of the 30 Alpha station.
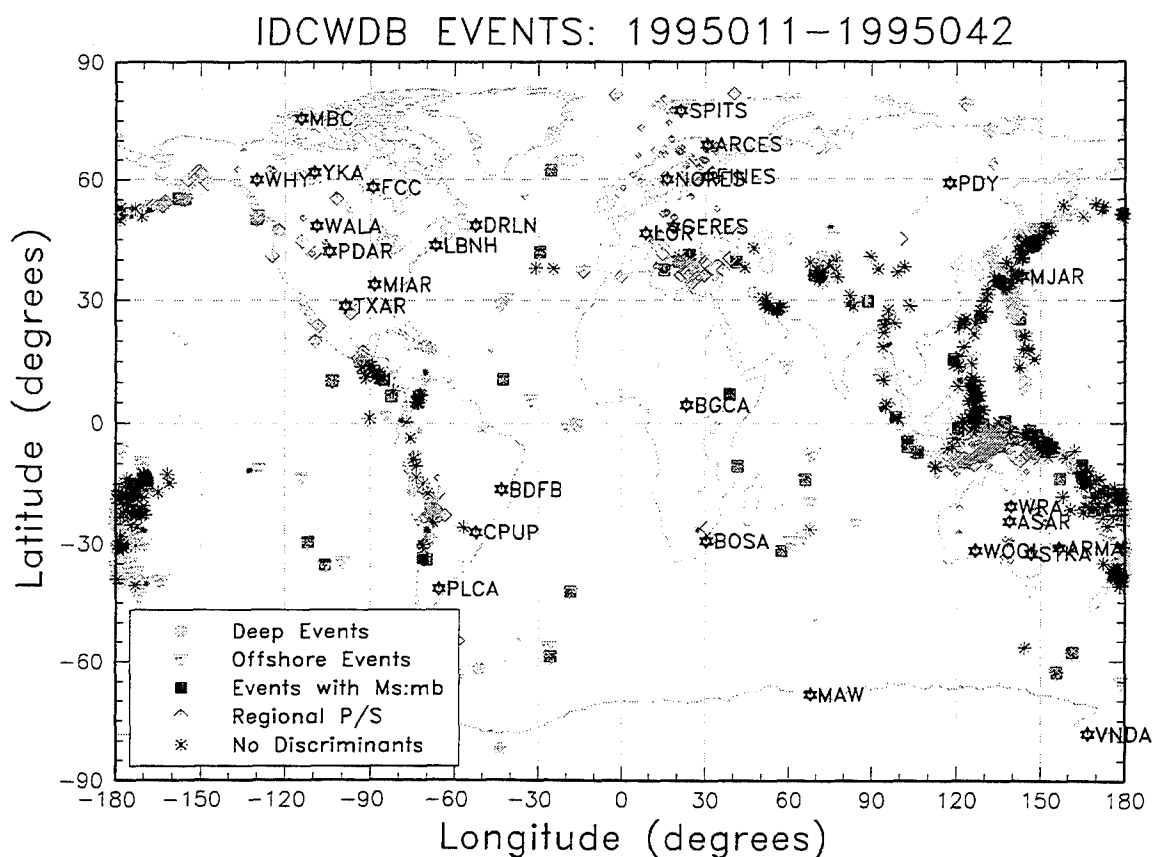
Figure 1. Locations of 30 Alpha stations and 1,786 seismic events recorded between 1995011 and 1995042. Marker types indicate events with various available discriminants or none.

Location Estimates and Uncertainty. Figure 2 shows the distribution of events versus the area of their 90% confidence location ellipses. Roughly half of the events have 90% location ellipses with areas greater than 10,000 km^2. Future use of Beta and Gamma station data, as well as data from future Alpha stations, should help to reduce the size of the location error ellipses. Comparisons by North (1995) of event locations in Canada, based on Alpha station data, to Canadian NDC locations using Beta and Gamma station data indicate that a significant percentage (11/16) of the 90% confidence location ellipses do not contain the Canadian NDC locations, accounting for their uncertainties as well. This may indicate that there are significant biases in location estimates which are not treated in the location uncertainty analysis. Note that of the 1,786 events during this period, 609 have 90% confidence location ellipses entirely offshore.

Depth and Detected Depth Phases. Figure 3 shows the cumulative distribution of events, with and without at least one detected depth phase, versus the upper bound of the 95% depth confidence interval. There were 292 events with 95% depth confidence intervals deeper than 10 km, of which there were 58 with at least one detected depth phase. Thus, using a 95% depth confidence interval, 16% of the events can be classified as deep natural events. If we also require at least one detected depth phase, only 3% of the events can be classified as deep natural events with high confidence.
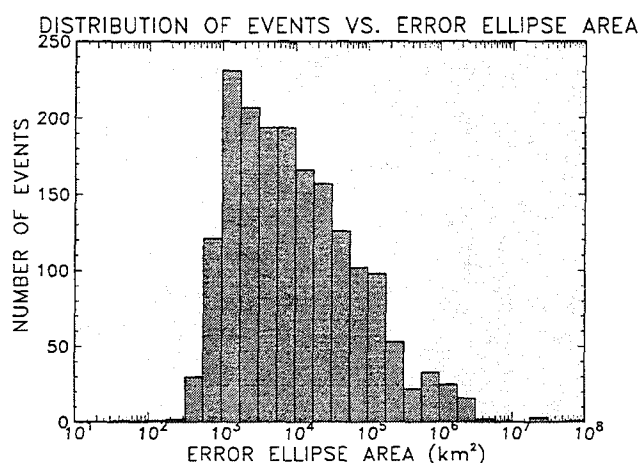
| Figure 2. | Distribution of events versus 90% confidence location ellipse area. | Figure 3. | Cumulative distribution versus upper bound of 95% depth confidence interval. |
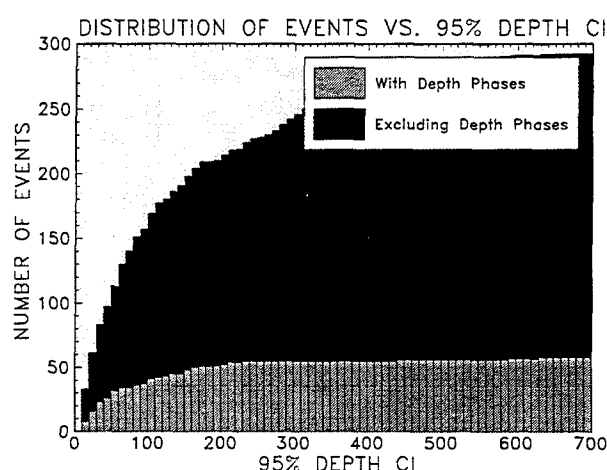
Event Magnitudes and Ms:mb. Of the 1,786 events, there were 1,459, 143 and 398 events for which mb, M_S and M_L, respectively, were measured. Of the events for which mb was measured, all but 35 (roughly 2%) were above mb 3. Comparisons of IDC mb values to those from the QED (Quick Epicentre Determination) of the U.S.G.S. NEIC found that the IDC mb values are about 0.3 units smaller than the QED magnitudes (IDC Performance Report, 3 February 1995). This suggests that roughly 98% of the events are above mb 3.3 and, thus, there are very few mining blasts to contend with for now. Figure 4 (left) shows a scatter plot of M_S versus mb for 143 events for which both mb and M_S were measured. All but 3 of these 143 events fall above the line defined by mb–M_S = 1.2. A similar plot of M_L versus mb is shown on the right of Figure 4. The scatter about the linear trend is greater than one magnitude unit. This has serious implications regarding the usefulness of M_L as an accurate or consistent measure of source size, and will likely require regional calibration.
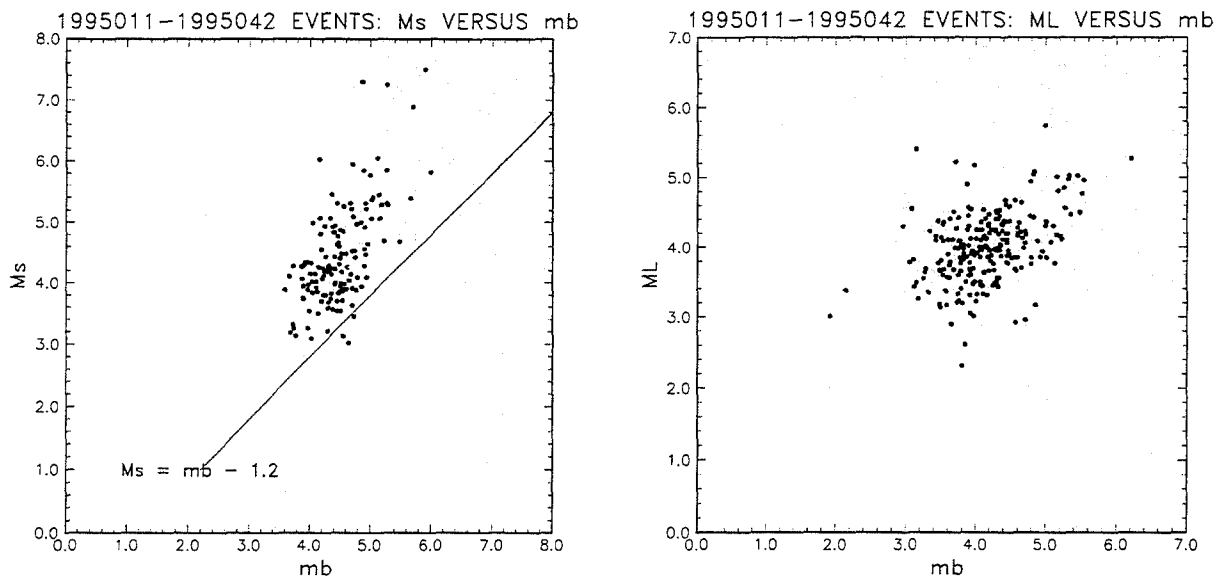
Figure 4. Scatter plots of M_S versus mb (left) and M_L versus mb (right).

High-Frequency Regional Amplitudes. Regional phase amplitudes were computed by automated software at the CMR. Absolute maximum amplitudes were measured on 2-4, 4-6, 6-8 and 8-10 Hz rms beams within predicted group velocity or time windows for Pn, Pg, Sn and Lg. Similar measurements were made of noise amplitudes in predicted pre-Pn, pre-Pg, pre-Sn and pre-Lg windows. The windows for predicted arrivals are used for all regions and stations. Figure 5 shows the number of regional events associated by each Alpha station, those for which Pn/Sn, Pn/Lg, Pg/Sn and/or Pg/Lg were computed, and the subset with SNR greater than 2 for Pn or Pg and Sn or Lg.
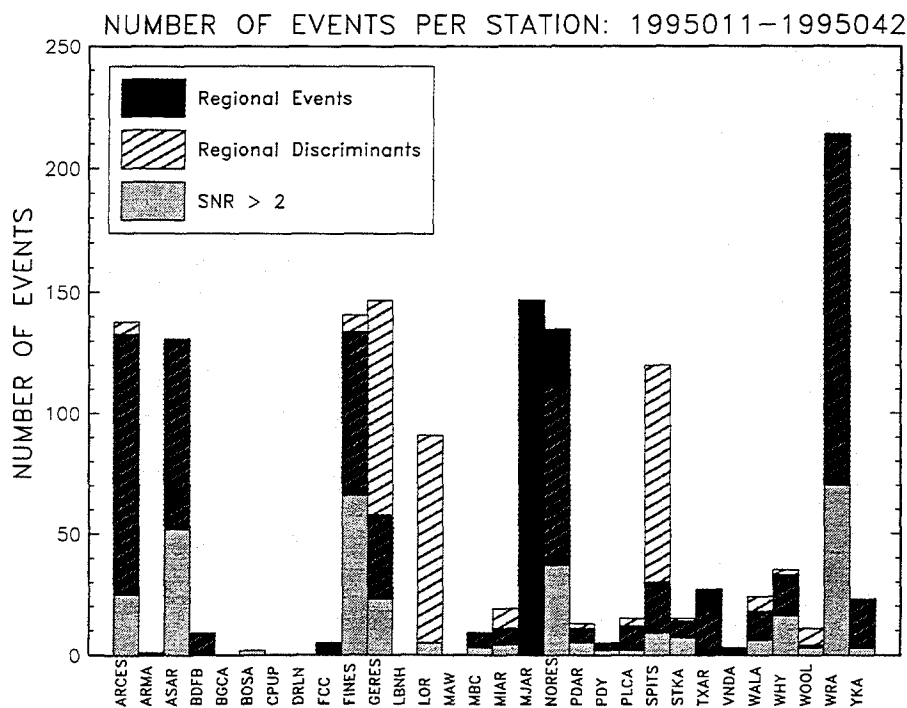
Figure 5. Number of regional events, and those with regional amplitude ratios, per Alpha station.

862

Except for MJAR, regional phase amplitudes were computed for most (487 of 634) regional events. For some stations, the number of events for which regional phase amplitudes were computed (given in the *originamp* table) exceeds the number of associated regional events in the *assoc* table. Only 249 of the 487 events had SNR greater than 2 for at least one regional P phase and Sn or Lg. Thus, less than 40% of the events detected within regional distances have useful high-frequency regional amplitude ratios. Figure 6 shows plots of Pn/Sn in four frequency bands (2-4, 4-6, 6-8 and 8-10 Hz) for each Alpha station. Similar plots (not shown here) exist for Pn/Lg, Pg/Sn and Pg/Lg. The markers are coded by SNR: circles indicate SNR below 2 for either numerator or denominator, while asterisks indicate SNR greater than 2 for both. Note that the majority of amplitude ratios do not satisfy a criteria of SNR > 2 for both numerator and denominator. Examination of the amplitude ratios also indicates that there are a very wide range in values (e.g., from 10^{-4} to 10^{+4} at station WRA) for events which are predominantly earthquakes.
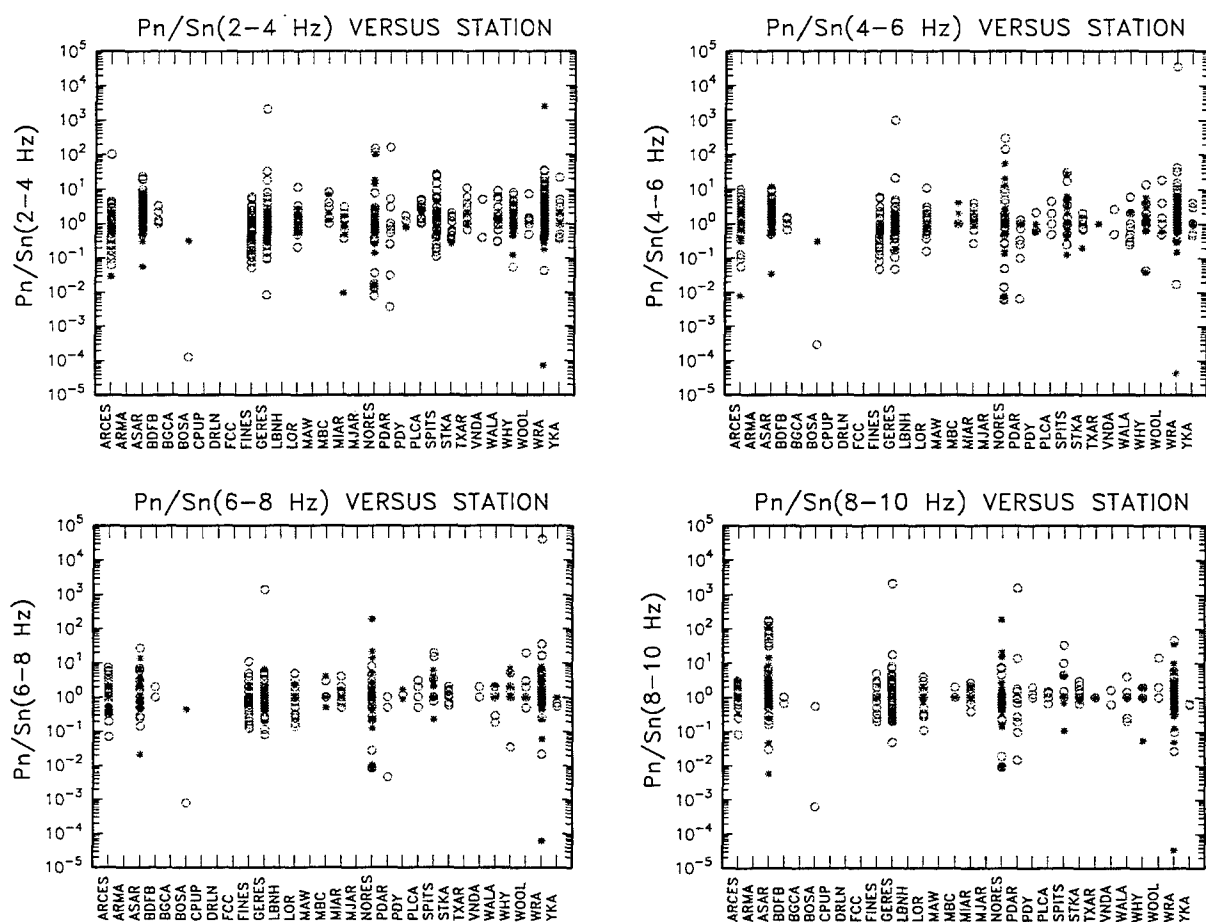
Figure 6. Pn/Sn in 4 frequency bands, plotted by station. Circles indicate SNR < 2, while asterisks indicate SNR > 2.

By studying 12 events with peculiarly high amplitude ratios (e.g., greater than 100), F. Ryall (1995) found the following discrepancies. There are cases for which the predicted phase windows do not correspond to actual phase arrivals or pre-phase noise, leading to anomalous regional phase amplitude measurements. For example, Pn times in the *originamp* table are about 60 sec later than P times in the REB (Reviewed Event Bulletin) for all 12 events except those in N. Europe, where

they are about 30 sec late. As a result, the "Pn" amplitudes in the *originamp* table were measured well into the actual P coda, as were the "pre-Pn noise" amplitudes. Sn times in the *originamp* table are also about 30 sec late at the Australian arrays, while 15 and 5 sec late for two N. European events for which the REB had readings. The automated program measured amplitudes for crustal phases (e.g., "Pg") for events which were deep (e.g., > 190 km) and for which the REB arrivals were P and S. Amplitudes were also calculated for phases that were not associated (i.e., not listed in the REB *assoc* table). Theses discrepancies must be examined more thoroughly and resolved if these measurements are to have valid application to regional event characterization.

Number of Ambiguous Events. Overall, there were 883 events which can be identified by teleseismic measures of depth, offshore location (plus hydroacoustic data eventually) and/or M_S:mb. An additional 166 events have regional discriminants with adequate SNR, although further quality control is needed to validate these measurements. At best there are still 511 teleseismic and 226 regional events which <u>cannot</u> be identified based on available information considered. Figure 7 shows locations and 90% error ellipses of the 511 teleseismic events (asterisks) which cannot be classified as deep or offshore, do not have M_S:mb, and do not have any regional P/S or P/Lg discriminants. The diamonds indicate locations of the 226 regional events which do have at least one regional P/S or P/Lg discriminant, but with SNR less than 2 for either numerator or denominator (or both). Note that many of these events are at far regional to teleseismic distances from existing Alpha stations, but would be well within regional distances of future Alpha stations.
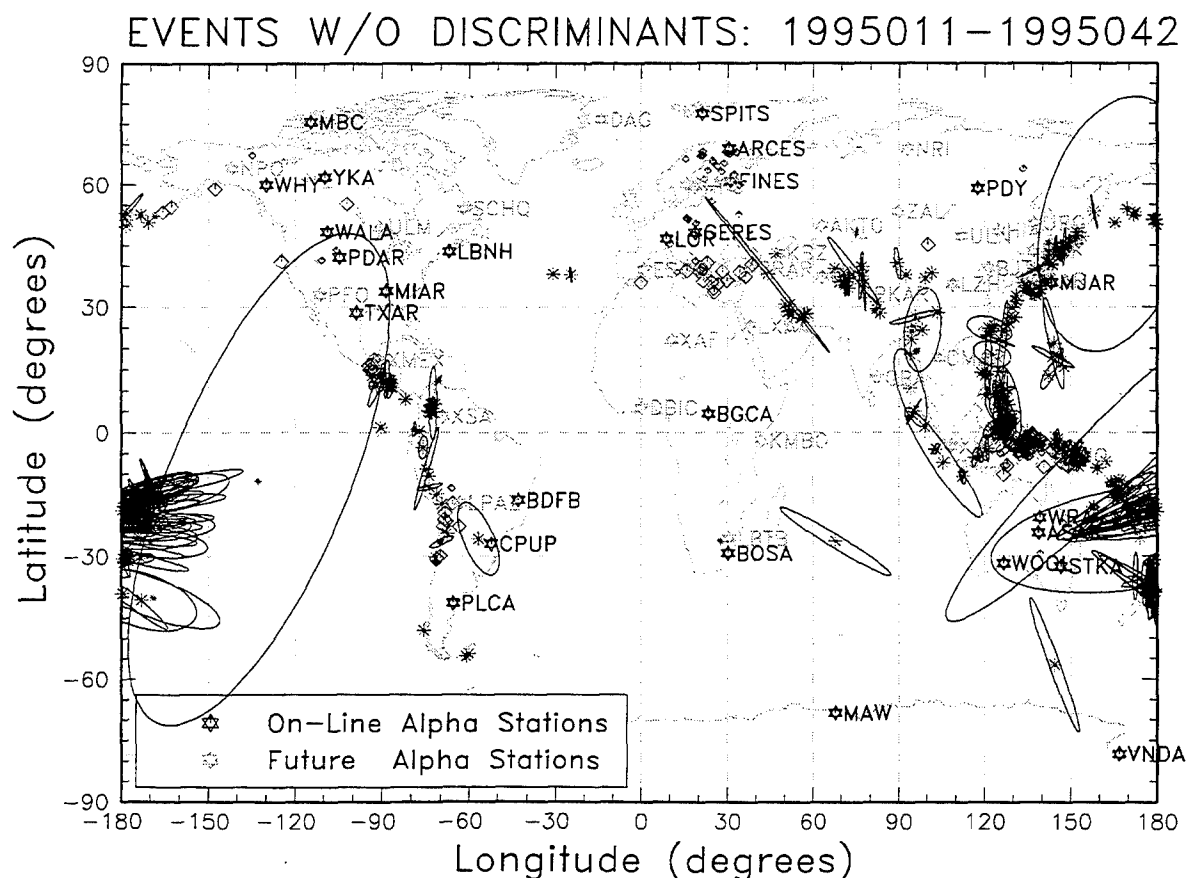
Figure 7. Locations of events for which none of the discriminants are available or have adequate SNR.

There are, however, a significant number of events within regional distances of existing Alpha stations (e.g., from MJAR in Japan) for which no regional phases were associated, even after analyst review. For events which occurred between 1995001 to 1995027, there were only 158 of 444 events within regional distances for which Pn or Pg and Sn or Lg were among the associated phases. Possible explanations for this include (1) regional phase attenuation for events at far regional distances; (2) regional phase blockage (e.g., for events southeast of GERES); (3) deep regional events (e.g., near MJAR) which do not produce crustal phases but whose 95% depth confidence intervals were not deeper than 10 km; and (4) possible phase association errors by the automated system which were not corrected after analyst review. Examples supporting the first three explanations have been found. Study of relevant waveforms is needed to determine whether an analyst could identify regional phases which were possibly missed by the automated system.

Last, Figure 7 shows epicentral location estimates of at least five events which appear to be clearly offshore, e.g., two in the north Atlantic Ocean, one in the south Pacific Ocean, and two in the Indian Ocean (one south and one west of Australia). The two in the north Atlantic are actually in the Azores Island region, while the two in the Indian Ocean and the one in the south Pacific have 90% error ellipses which overlap either Antarctica, Madagascar or North America.

Optimizing Multivariate Evidence for Outlier Detection. We have also been addressing a fundamental problem of how to best utilize multivariate discriminant data from multiple sensors. In general, there are numerous types of teleseismic and regional, as well as non-seismic (e.g., hydroacoustic and infrasonic) measurements from multiple stations/sensors that can be used as discriminants and it is not clear from the outset how to best combine this information in a test for outliers. We have investigated three approaches to this problem. The first (Test 1) is to insert all available features that are thought to discriminate into the outlier likelihood ratio (e.g., Fisk et al., 1993). The second (Test 2) is to perform an optimal weighting of some or all of the discriminants first and then insert the weighted combination(s) into the likelihood ratio. The third (Test 3) is to perform separate tests, based on the likelihood ratio and subsets of discriminants (e.g., for individual sensors), calling an event an outlier if it is found to be an outlier by any of the individual tests. The significance levels of the individual tests in this case must be appropriately modified in order to maintain the overall false alarm rate of the combined results.

We derived expressions for the power of each of these three tests for fixed significance level (i.e., fixed false alarm rate). The power is the probability of identifying an explosion as an outlier. To illustrate how the powers compare for a real situation, we used Pn/Lg measurements in the 6-8 Hz band at stations KNB and MNV for 35 earthquakes and 69 nuclear explosions on the Nevada Test Site. In this case, the estimates of the correlation, standard deviations and differences in the means of the Pn/Lg values for earthquakes and explosions are $\hat{\rho} = 0.228$, $\hat{\sigma}_1 = 0.485$, $\hat{\sigma}_2 = 0.416 = 0.856\hat{\sigma}_1$, $\Delta\hat{\mu}_1 = 1.104 = 2.276\hat{\sigma}_1$, and $\Delta\hat{\mu}_2 = 1.662 = 3.427\hat{\sigma}_1$. Under the assumption of normality (which was shown to be valid) and setting the significance level at $\alpha = 0.01$, the powers of Tests 1, 2 and 3 are 0.922, 0.954 and 0.926, respectively. Test 2 has the greatest power in this case, although all three tests have comparable power. For comparison, the powers of the tests at 0.01 significance level using either one of the stations is 0.363 for KNB and 0.938 for MNV. Thus, combining data from the two stations has far greater power than only using the worst station, comparable or greater power than using only the best station, and does not require that we know which station provides greater power which, in practice, we will not know in most situations.

865

We also performed a parametric study to assess more general conditions for which a particular test is favored over the others. Figure 8 illustrates results of this parametric power comparison. Shown are the differences of the powers of Tests 2 and 1 (left) and Tests 3 and 1 (right) versus correlation (ρ) for $\sigma_1 = \sigma_2 = 1$ (upper) and $\sigma_1 = 1$ and $\sigma_2 = 2$ (lower). Each curve corresponds to various values of $\Delta\mu_1$ and $\Delta\mu_2$ from 0 to 4. The results show that while there are regions of the parameter space (depending primarily on the correlations and separations of the discriminant means for different types of events) for which Test 2 or Test 3 can have the greatest power (e.g., by 5% to 10%), there are many cases for which they can provide dramatically poorer power than Test 1 (e.g., by as much as 90%). Test 1 generally has comparable or greater power than the other two tests over all parameters and there are no situations in which using Test 1 yields dramatically poorer results. Although we will eventually have considerable information regarding discriminant means and the covariance matrix for earthquakes, we will not know the discriminant means for nuclear explosions in most regions. Thus, the most robust procedure is to use Test 1 in which the full vector of discriminants is inserted into the likelihood ratio. This illustrates how fusion of multi-sensor data within a single test, which treats their correlations, provides the most robust results.
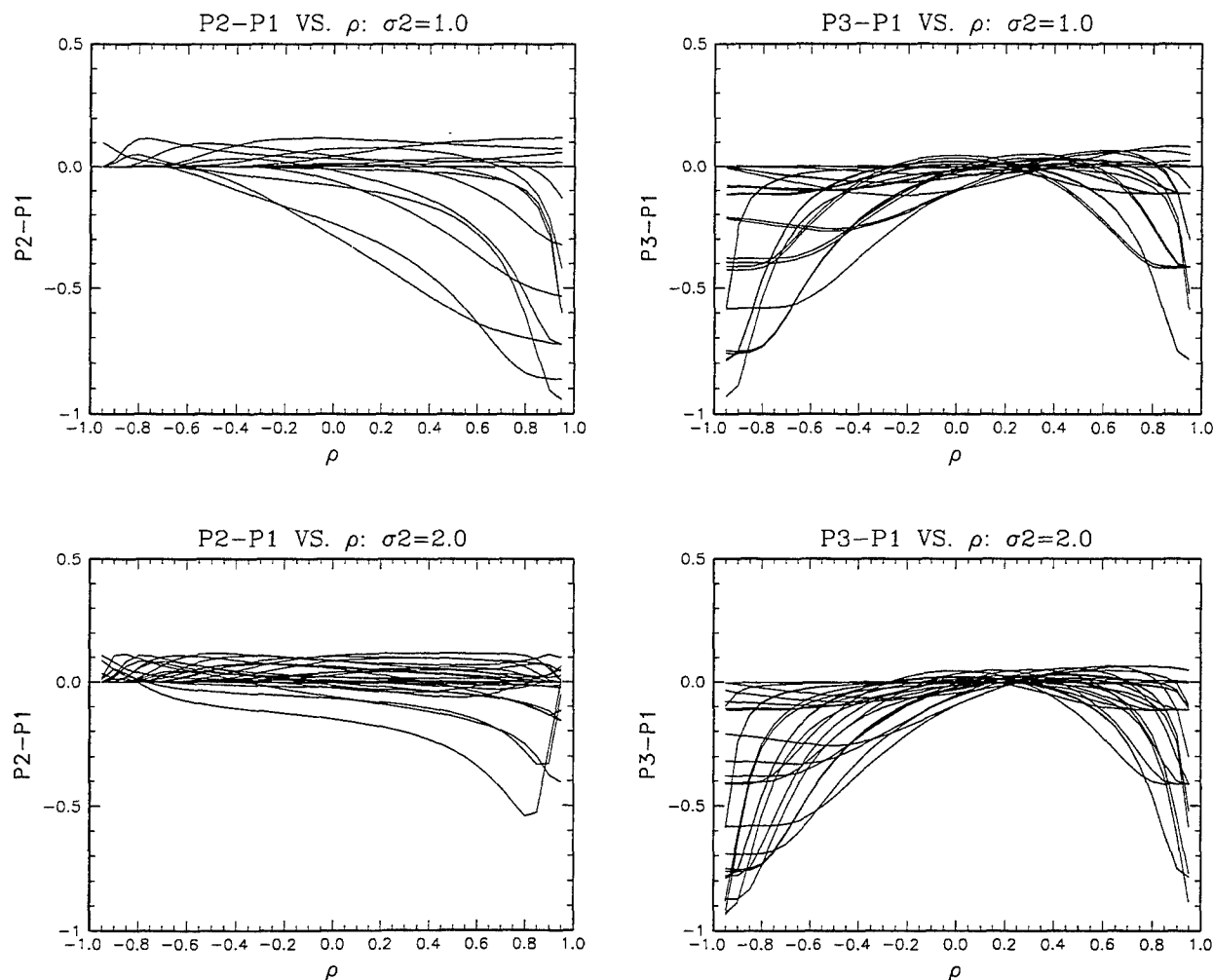
Figure 8. Difference in the power of Tests 2 and 1 (left) and Tests 3 and 1 (right) versus correlation for various values of $\Delta\mu_1$, $\Delta\mu_2$ from 0 to 4, and for $\sigma_1 = \sigma_2 = 1$ (upper) and $\sigma_1 = 1$ and $\sigma_2 = 2$ (lower).

CONCLUSIONS AND RECOMMENDATIONS

Preliminary results show that useful seismic monitoring can be performed with the outlier-detection approach, currently down to magnitude 3, for regions that are well-covered by at least one seismic station or array and provided useful discriminants are available. Results were obtained for diverse geological regions and a wide range of epicentral distances and magnitudes. In our outlier approach, we assume that events above mb 3 are predominantly earthquakes with potentially one or at least a small number of nuclear explosions. That is, we assume that there will be very few chemical mining blast above mb 3. Note that of the 1,459 events between 1995011 and 1995042 with mb measurements, there were only 35 below mb 3. Accounting for the bias of 0.3 units in the IDC mb values relative to QED mb values implies that roughly 98% of the events during this period were actually above mb 3.3. This suggests that the majority of events will fall in the regime where the assumption for application of the outlier test is valid.

Further analysis of GSETT-3 data, however, indicates that there are a significant number of events which cannot currently be processed to identify them based on the incomplete Alpha network and a current lack of sufficient event characterization processing capabilities.

First, requiring that the 95% confidence interval for depth be deeper than 10 km, 292 of the 1,786 events (16%) are classified as deep natural events. If we also require that at least one depth phase be detected (since there may be potential biases in location and depth estimates), only 58 events are classified as deep. Thus, it is important to resolve the issue of biases in location and depth estimates, and to assess whether improvements in associating depth phases can be made.

Second, there are 143 events (8%) with M_S:mb measurements. This relatively low percentage is due to the fact M_S measurements are currently made only for long-period instruments which are limited in number. Future work by S-Cubed includes array processing for broadband instruments, which should lead to a much higher percentage of events with M_S measurements. All but 3 of the 143 events satisfy M_S–mb > 1.2; however, the effect of magnitude biases has yet to be resolved.

Third, 609 events have 90% location error ellipses entirely offshore, but there were no hydro-acoustic (HA) data available to verify that they were not offshore explosions. Future plans by ARPA include collection of HA data and implementation of algorithms to compute relevant event characterization parameters. Incorporating seismic data from Beta stations could lead to smaller error ellipses, thereby improving the capability to classify offshore events with high confidence.

Fourth, there were 487 events for which regional phase amplitudes were computed. Of these, 249 have at least one Pn or Pg phase and one Sn or Lg phase with SNR greater than 2. We found, however, several discrepancies in these measurements, namely, some very large amplitude ratios (e.g., greater than 100) for events which are presumed earthquakes, a peculiarly high number of events with identical regional P phase and Sn or Lg amplitudes in the three highest frequency bands, and some events with amplitudes greater than 1000 but with SNR less than 2. We also found that the theoretical windows used in computing the regional phase and noise amplitudes often do not coincide with the true expected arrivals. These discrepancies must be resolved before these regional discriminants can be used with any degree of confidence.

Overall, there were 883 events which can be identified by teleseismic measures of depth, offshore location and/or M_S:mb. An additional 166 events have regional discriminants with adequate SNR, although further quality control is needed to validate these measurements. At best there are still 511 teleseismic and 226 regional events which <u>cannot</u> be identified based on available information considered. That is, 41% of the events during the period 1955011-1995042 cannot be classified as deep or offshore, and do not have M_S:mb or regional amplitude ratios with adequate SNR.

This situation should improve significantly as the Alpha network nearly doubles and as processing algorithms are integrated. Our future work focuses on integration at the prototype IDC of algorithms, developed by MRC and other ARPA contractors, to compute new event characterization parameters. We will also be implementing our event characterization/ identification subsystem to combine this information optimally. To monitor below mb 3, much of the effort by MRC and other ARPA contractors is directed at implementing reliable automated methods to identify mining blasts. We also plan to extend our outlier approach to test potential nuclear explosions as outliers of a mixture of earthquake, mining blast and rock burst groups. In addition to implementing software for event characterization, our future work will also involve evaluation of monitoring capabilities as the prototype IMS infrastructure evolves.

While our statistical framework has been applied in the past to only seismic discriminants, it possesses the generality and flexibility to incorporate hydroacoustic, infrasonic and other forms of useful discriminant data. Lessons learned from our multivariate outlier analysis indicate that the most robust approach may be to fuse multi-sensor data directly, thereby treating correlations, rather than performing separate tests and then combining the results.

REFERENCES

Baek, J., H.L. Gray, and W.A. Woodward, J. Miller and M.D. Fisk (1995). A Bootstrap Generalized Likelihood Ratio Test in Discriminant Analysis, in press, *Comp. Stat. Data Anal.*

Fisk, M.D., H.L. Gray and G.D. McCartor (1994). Preliminary Assessment of CTBT/NPT Monitoring Capability, PL-TR-94-2300, Phillips Laboratory, Hanscom AFB, MA. ADA293188

Fisk, M.D., H.L. Gray and G.D. McCartor (1993). Applications of Generalized Likelihood Ratio Tests to Seismic Event Identification, PL-TR-93-2221, Phillips Laboratory, Hanscom AFB, MA, ADA279479.

IDC Performance Report - January 15-28, 1995 (February 3, 1995). Available through the Center for Monitoring Research, Arlington, VA.

North, R. (1995). GSETT-3 - Experience and Lessons Learned So Far, paper in *Proceedings of the CTBT Monitoring Technologies Conference*, 15-18 May 1995, Chantilly, VA, Sponsored by ARPA/NMRO, Arlington, VA.

Ryall, F. (1995). Private Communication.

STATISTICAL METHODS FOR
MONITORING NUCLEAR TESTS

H.L. Gray and W.A. Woodward
Southern Methodist University

ABSTRACT

In previous papers, these authors have developed general methodology for detecting outliers. In particular, given a training set of, say, earthquake data, a test of hypothesis for testing whether or not a new observation should be classified as an earthquake was developed. The method was based on a generalized likelihood ratio test which did not require normality assumptions or even continuous data. In the most recent papers the technique was modified to allow missing data. In this paper the methodology is greatly extended to address a variety of issues that arise in a multistation environment. In particular, the method is generalized to allow the inclusion of expert opinion as part of the data and it is extended to allow an outlier to be an outlier to more than one population. Thus, for example, one might have training data from earthquakes and mining explosions and desire to know if an observed event should be classified as belonging to either of these groups or not. With the results of this paper, one can test, at a specified level, whether or not the new observation belongs to the joint population.

Alternative approaches to the generalized likelihood method are also considered for the problems addressed. However, in general, the generalized likelihood approach seems to be the best method of those considered.

Keywords: outlier detection, generalized likelihood ratio, multiple stations, discrimination.

OBJECTIVE:

The goal of this research is to establish the statistical methodology required to automatically detect the occurrence of a nuclear test anywhere in the world, given suitable discriminants.

PRELIMINARY RESEARCH RESULTS:

In previous papers these authors have developed automated methods for detecting outliers based on the generalized likelihood ratio (GLR). Although those methods are reasonably general and robust, they do not address all of the problems which can occur in a multistation, multisensor environment. In what follows, we list several of the problems and their partial solutions.

A) Does adding m stations with p-discriminants create a computing problem?

   Answer: It could, if, for example, $M = p \times m > 200$.

      To be more specific, let $V = $ data vector,
   where
   $$V' = (X_{11}, \cdots, X_{p1}, X_{12}, \cdots, X_{p2}, X_{1m}, \cdots, X_{pm}),$$

   where X_{ij} denotes the discriminant i measured at station j.

Using the generalized likelihood ratio approach involves inversion of an $M \times M$ matrix which could be near singular if care is not taken in selecting the discriminants and the stations.

   Remark: It should be noted that neither stations nor discriminants need to be seismic. Thus, V can be a mixture of seismic and nonseismic data.

Since M could be large in the most general scenario, alternative approaches have and are being considered. Two alternatives which we have thoroughly investigated are based on inverse variance weighting and minimum variance weighting. The advantage of these approaches would be in the computing area, i.e., the data could be significantly compressed and hence reduce computing requirements substantially. Unfortunately extensive simulations show these methods to be unsatisfactory for reasons that are clearly demonstrated by the following example:

   Setting: one discriminant, two stations.
Let
$$X_{1j} = \text{discriminant measured at station } j = 1, 2,$$
$$\mu_j^{(EQ)} = \text{mean of discriminant at station } j \text{ for earthquakes,}$$
$$\mu_j^{(EX)} = \text{mean of discriminant at station } j \text{ for explosions,}$$

and

$$Y = W_1 X_{11} + W_2 X_{12},$$

where $W_1 + W_2 = 1$ and W_1 and W_2 are chosen so that Y will have minimum variance. Y will be referred to as a compressed discriminant. The compressed discriminant, Y, would then be used in the GLR method rather than X_{11} and X_{12}.

<u>Example</u>:   Suppose the earthquake population has

$$\mu_1^{(EQ)} = \mu_2^{(EQ)} = 0$$

$$\sigma_1^{(EQ)} = 1, \quad \sigma_2^{(EQ)} = 2, \quad \rho = .75.$$

(1)

Then it is easily shown that $W_1 = 1.25$, $W_2 = -.25$.

But suppose V is an observation vector from a population defined by

$$\mu_1^{(EX)} = 2, \quad \mu_2^{(EX)} = 10$$

$$\sigma_1^{(EX)} = 1, \quad \sigma_2^{(EX)} = 2, \quad \rho = .75. \tag{2}$$

The observation vector $V' = (X_{11}, X_{12})$ would almost surely be an obvious outlier by the GLR method based on V. However

$$E[Y] = \tfrac{5}{4} E[X_{11}] - \tfrac{1}{4} E[X_{12}]$$

$$= 0. \tag{3}$$

Consequently the compressed discriminant has a mean which is identical to the compressed earthquake mean and since it has the same variance, it is clear that Y cannot be used to discriminate between earthquakes and explosions. Thus the power of a test based on Y in this case would be virtually zero, even though it does have a much reduced variance. Of course, variance reduction is not the goal here, outlier detection is. The GLR approach based on the uncompressed data is effective here and in general because it, in essence, addresses the right problem. Essentially it classifies V as an outlier if it is highly unlikely that it belongs to the hypothesized population.

Having given this example, we should add that it is an extreme one and, in fact, for most cases of interest, the minimum variance method of compressing the data is an effective one. However, since such cases as the previous example can occur, and since at this time we believe the computing requirements for the GLR approach can be handled, we are presently opting to stay with the GLR method on the noncompressed data. We refer to this as the full vector approach. In the future if computing becomes a problem, we believe that it will be possible to develop a

hybrid method based on the Mahalanobis distance that will alleviate the problem described here. Another possible approach is based on principal components, but at the present we are not pursuing that method. Thus the short answer to question A is <u>no</u>.

B) In the previous example we posed the question of an outlier in the form "Is the new observation an earthquake or not?" or "Is the new observation an explosion or not?" That is, "Is the observation a member of a specified group or not?" Of course, the better question might be, "Is the new observation an earthquake or a mining explosion or not?" More generally, the question is, "Is the new observation a member of any one of several groups or not?"

In order to address this problem, we must first make some adjustment to the GLR test. In previous work, it was assumed that the covariance structure of the outlier was the same as the training set population. Even though the GLR method is robust to this assumption, inspection of equation 5 below should make it clear that this would be a poor assumption in this case. To avoid this, we simply make the noninformative assumption that the outlier has a constant distribution over the realistic support of a potential outlier, Z. The generalized likelihood ratio statistic then becomes

$$\lambda_1 = \frac{\sup_\theta L_0(\theta)}{\sup_\theta L_1(\theta)}, \tag{4}$$

where

$$L_0(\theta) = \prod_{i=1}^{n} f(V_i, \theta) f(Z, \theta)$$

and

$$L_1(\theta) = c \prod_{i=1}^{n} f(V_i, \theta),$$

where f is the pdf of the vector V, and c is a constant.

The distribution of λ_1 is then obtained by bootstrapping. Note that if n is sufficiently large, $\lambda_1 \approx f(Z, \widehat{\theta})$, where $\widehat{\theta}$ = maximum likelihood estimate of θ from the training sample. In this event, the bootstrapping can be greatly simplified by just resampling the Z from the training sample. The table below shows that for samples as large as 50 or 60, very little is lost in approximating the significance level α by this reduced bootstrapping and there seems to be a small gain in power.

Table 1. Simulation Results (nominal level $\alpha = .05$)

n	Approximate Level		Approximate Power	
	Full	One	Full	One
15	.065	.118	.568	.729
20	.063	.100	.588	.709
25	.048	.081	.601	.704
30	.051	.084	.609	.718
50	.050	.064	.645	.696
100	.057	.059	.657	.677
150	.061	.057	.664	.703

Suppose we have training data from several different populations. For simplicity, assume training samples from two populations (earthquakes and explosions, for example). The extension to more than two will be obvious. In this case the mixture distribution is given by

$$f(V, \theta) = p_1 g_1(V, \theta_1) + p_2 g_2(V, \theta_2), \tag{5}$$

where $\theta = (p_1, \theta_1, \theta_2)$, $p_1 + p_2 = 1$, and $p_1 \geq 0, p_2 \geq 0$.

In (5) p_1 and p_2 are the mixing proportions and g_1 and g_2 are the pdf's for populations Π_1 and Π_2, respectively. It follows that f is the pdf of the mixed population Π_{12}. Now denote the training sample by the two random samples $V_{11}, V_{12}, \cdots, V_{1n_1} \in \Pi_1$, and $V_{21}, V_{22}, \cdots, V_{2n_2} \in \Pi_2$, where $n_1 + n_2 = n$. We wish to test the hypothesis

$$H_0 : Z \in \Pi_{12}$$
vs.
$$H_1 : Z \notin \Pi_{12},$$

given the random vectors $V_{11}, V_{12}, \cdots V_{1n_1} \in \Pi_1, V_{21}, V_{22}, \cdots V_{2n_2} \in \Pi_2$.

This can now be done by using λ_1 in equation (4) and f in equation (5), where p_1 and p_2 are either given or estimated by the training samples. This method is currently being coded for simulation runs and will be ready to apply to actual data sets by September 1, 1995.

C) The GLR test is essentially a nonparametric test of the hypothesis that $\mu_1 = \mu_2$ vs $\mu_1 \neq \mu_2$. In practice it may be that $\mu_1 \neq \mu_2$, but the deviation is in a direction which doesn't concern us. To be more specific, suppose we wish to test the hypothesis that a new one dimensional observation, Z, is an earthquake. Then we test $\mu^{(EQ)} = \mu_Z$ against $\mu^{(EQ)} \neq \mu_Z$. However, it may be for this particular discriminant that $\mu_Z > \mu^{(EQ)}$ is of no interest, so we would not like to include this possibility in the rejection region. This is not a problem for a small number of events, but for a large number of events maintaining an acceptable false alarm rate could result in a substantial loss of power or detection capability. What is needed is a test which allows a more focused alternative, i.e., in this case the alternative $\mu_1 < \mu_2$. That is, $\mu_{i1} < \mu_{i2}$ for each i. Although this is a simple problem in one dimension, it is difficult in p-space. One approach which we are pursuing to solve this problem is a quasi- Bayesian approach which essentially limits the support of the distribution to regions which are physically plausible. Problems inhibiting this approach have been computational and appear to be solved now by a closed form solution. Confirmation of this will be forthcoming by the time of presentation of this paper. Other approaches to restricting the critical region are being considered but are not sufficiently underway to report on here.

CONCLUSIONS and RECOMMENDATIONS:

Results so far are encouraging. However, one thing is clear: new and better regional discriminants are needed. For regions in which such discriminants become available, the methods discussed and developed here make near optimal use of that data for outlier detection from one or several groups. For regions where such data are lacking, expert opinion may be used in the "Bayesian" GLR method to partially bridge the gap.

REGIONAL SMALL-EVENT IDENTIFICATION USING SEISMIC NETWORKS AND ARRAYS

Michael A.H. Hedlin, Frank L. Vernon,
J.-Bernard Minster & John A. Orcutt

Institute of Geophysics and Planetary Physics,
Scripps Institution of Oceanography,
University of California, San Diego
La Jolla, CA, 92122

ABSTRACT

In view of the importance of small seismic events to a monitored CTBT we have begun a survey of globally distributed regional seismic recordings of earthquakes, quarry blasts and explosions with $m_b \sim 2.5$. The first goal of this project is to test the effectiveness of our automated time-frequency discriminant (ATFD) at distinguishing quarry blasts from single explosions and earthquakes using regional array and network recordings. We intend to use these data to develop and test enhancements of the technique and develop complementary discriminants for use when the ATFD proves to be ineffective. As part of this program we intend to determine if a low frequency spectral signature (perhaps caused by source finiteness) might be used for discrimination at far-regional distances. We will analyze these waveforms using the standard multi-taper estimation technique and a new wavelet based technique that will allow us to process 3-component data and analyze the evolution of spectral amplitude and polarization with time and frequency.

The ATFD uses a binary sonogram which is derived from the original, spectral, sonogram by the application of filters which replace local spectral information with a binary code which simply reflects local spectral highs and lows. The ATFD calculates a two-dimensional Fourier transform of the binary sonogram which reveals the dependence of the binary pattern on frequency *and* time. In view of its resemblance to the cepstrum (which identifies periodicities in single spectra), and the fact that it is derived from onset and coda phases we refer to it as the *coda cepstrum*. We are currently working on an adaptive coda cepstrum which iteratively solves for filters that are optimal for extracting any time-independent pattern that exists in the sonogram of an individual event. We are testing this method using recordings of earthquakes and quarry blasts made by the KNET in Kyrgyzstan.

We have conducted a preliminary analysis of network recordings of calibration explosions and quarry blasts made in Kazakhstan by the NRDC network. Using these data we are currently developing a new discriminant that is based on binary sonograms but takes advantage of the independence of ripple-fire waveform spectra from the recording direction. In essence we perform a three-way cross-correlation between binary sonograms derived from the three orthogonal recording channels.

Key Words: coda cepstrum, ripple-fired quarry blast, binary sonogram, wavelets.

1. Objectives

During the term of our existing contract we will expand significantly research we have conducted into the small-event discrimination problem. Our interest has been in using the spectral characteristics of whole regional waveforms to discriminate ripple-fired from non-ripple-fired events (*incl.* earthquakes and single-event explosions). Our objectives are to apply our *automated* whole waveform time-frequency discriminant (ATFD) to large event populations in varied data sets to test transportability and robustness and to enhance the ATFD with more sophisticated processing. In specific we have the following objectives:

1.1 Robustness and transportability

Apply our existing ATFD (*Hedlin et al., 1990*) to a number of dissimilar, well separated, regional data sets with large populations of ripple and non-ripple-fired events to gauge robustness and regional dependence. We propose to apply the technique to vertical component data from several networks and arrays using low (1 to 20 Hz) and broad (1 to 100 Hz) frequency bands. Particular attention will be paid to the cause of outliers. We propose to determine the extent to which array data can suppress noise and increase the range of the ATFD.

1.2 Software development

Enhance the ATFD via (1) wavelet analysis, (2) more advanced spectral analysis techniques [*e.g.* the statistics of Higher Order Crossings (HOC)], (3) advanced processing techniques to permit full use of modern three-component (3C) networks and arrays. 3C data sets examined under objective 1.1 will be re-analyzed to assess improvement.

1.3 Comparisons with other techniques

Analyze the same data sets, discussed under objective 1.1, with a complementary technique (*e.g.* a "regionally trained" spectral ratio method) to assess relative capabilities under different settings. Our intent is to develop a complementary technique that might be merged through evolutionary programming with our own to provide a more comprehensive, multivariate, discriminant. The time-frequency approach, taken alone, will not discriminate between single-event explosions and earthquakes.

1.4 Low-frequency discrimination

Address the question of what low frequency (*e.g.* 1 to 20 Hz) time-independent signature should be produced by mines that use short (*e.g.* 20 ms) delays especially when delay times are irregular. We willto use "ground truth" data to explain any modulations observed at low frequencies and test the theory that they might be due to temporal finiteness of the source (*Hedlin et al., 1990*).

1.5 Contribution of software to database accessing systems

Develop algorithms that are designed to operate on the CSS 3.0 database structure and will be available to all interested parties.

2. Preliminary Research Results

Under previous Air Force contracts (F19628-87-K-0013 and F19628-88-K-0044) we developed a discriminant that seeks long-lived spectral modulations in major phases and the coda. Long lived modulations can be produced by seismic resonance and by ripple firing. *Hedlin et al (1989)* developed a procedure whereby a binary sonogram is derived from the original, spectral, sonogram by the application of filters which replace local spectral information with a binary code which simply reflects local spectral highs and lows. *Hedlin et al. (1990)* produced a procedure to automatically recognize time independent patterns. This Automated Time Frequency Discriminant (now known as the ATFD) calculates a two-dimensional Fourier transform of the binary sonogram which reveals the dependence of the binary pattern on frequency *and* time. In view of its resemblance to the cepstrum (which identifies periodicities in single spectra), and the fact that it is derived from onset and coda phases we refer to it as the *coda cepstrum*. The binary sonogram and the coda cepstrum form the basis for the preliminary research results described below.

In developing this technique *Hedlin et al. (1989)* used a subset of the 1987 NRDC dataset (Figure 1). The NRDC network was deployed in 1987 in central Kazakhstan and made recordings of calibration explosions and quarry blasts at local and regional distances. To further this analysis we have returned to this dataset and are currently analyzing all recorded events. We are also using data recorded by the KNET. The KNET (Figure 1) is a 10 station telemetered 3C broadband network located in Kyrgyzstan. The network has yielded a large number of recordings of earthquakes and quarry blasts at local and regionals distances.

2.1 The NRDC cross correlation analysis. In Figures 2a and 2b we display sonograms calculated from two recordings in the NRDC dataset (originally published in *Hedlin et al., 1989*). As mentioned above the quarry blast (2b) displays a clear time independent modulation superimposed on the larger spectral features (*e.g.* decay with frequency and time). This modulation is almost certainly due to ripple firing at the source. No modulation is present in the sonogram obtained from the recording of the calibration explosion (2a). By converting each spectral estimate to binary form (using boxcar filters spanning 5.0 and 2.5 Hz; the procedure is described in *Hedlin et al., 1989*) we arrive at the binary sonograms displayed in Figure 3. As expected, this conversion has suppressed the large scale features. The binary sonogram calculated using the quarry blast recording contains an obvious time-independent character. As displayed in Figure 4 this character is largely independent of the recording component - unlike the binary sonograms derived from chemical explosions. Taking advantage of this similarity we are developing a discriminant where we cross correlate the 3 pairs of binary sonograms (E-N, N-Z, Z-E) and compute the average cross correlation at zero lag. A preliminary result of this processing is shown in Figure 5. What we see in this figure is that, overall, the borehole cross correlations are lower - particularly at KSU. This is almost certainly due to the effect of near surface seismic resonance. The borehole sensors were located 100 m beneath the free-surface. Considering the borehole recordings we see that event c (#3) does not have the highest three way cross-correlation, it is somewhat above the average of the quarry blasts population. Events 1 and 10 have clearly failed this test - they have less energy in common between the three channels than the calibration explosions. This is clearly not due to an unusually great range from the station (lower figure) but it appears that no spectral modulation (in the band up to 35 Hz) was produced at the source.
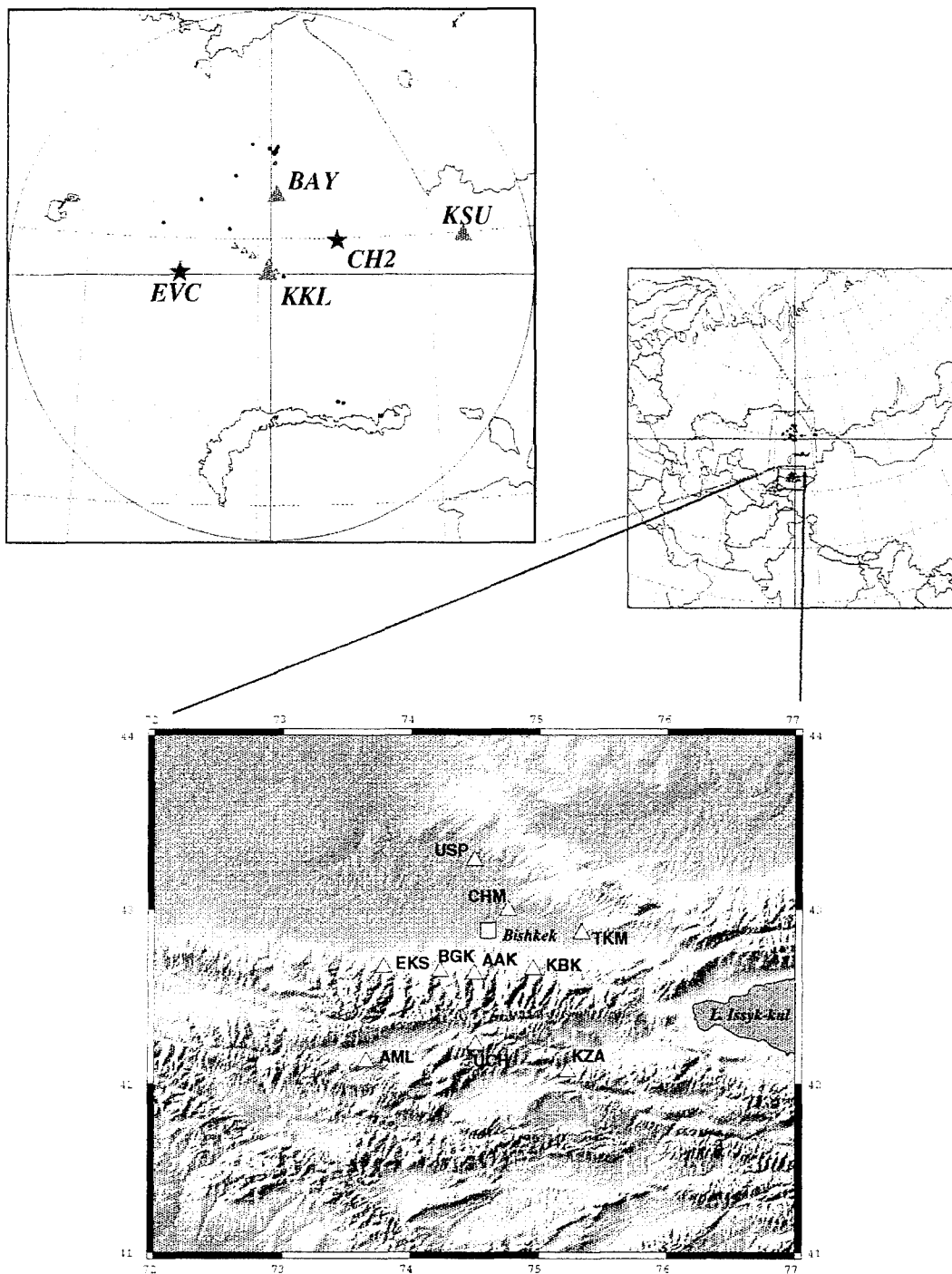
Figure 1. The two datasets considered in this paper come from central Asia. The NRDC dataset (upper left) was collected in 1987. The KNET (lower) is located in Kyrgyzstan on the boundary between the Kazakh platform to the north and the Tien Shan to the sourth.
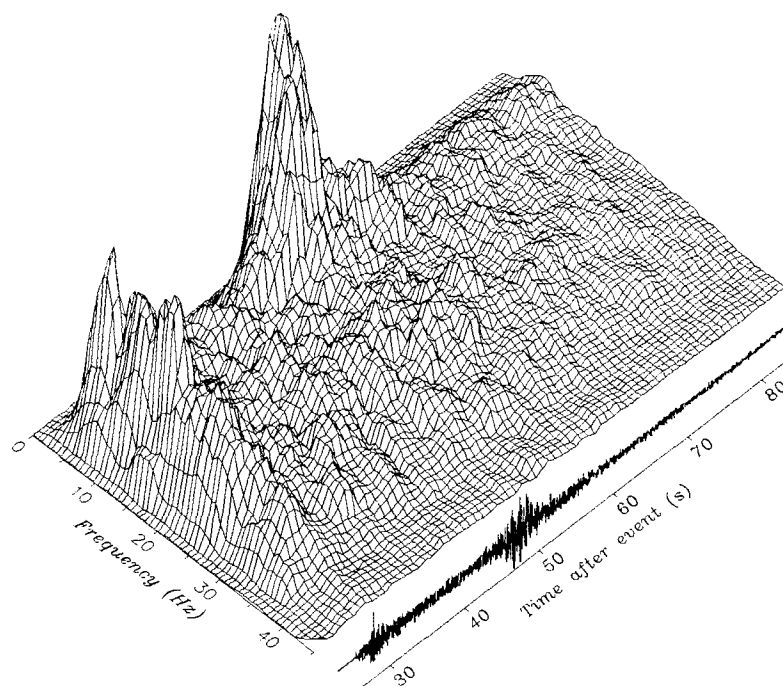
Figure 2a. Seismogram resulting from a single chemical explosion (CH2; Figure 1) detonated in Kazakhstan and corresponding sonogram. The recording was made at a range of 157 km by the vertical component seismometer at Bayanaul.
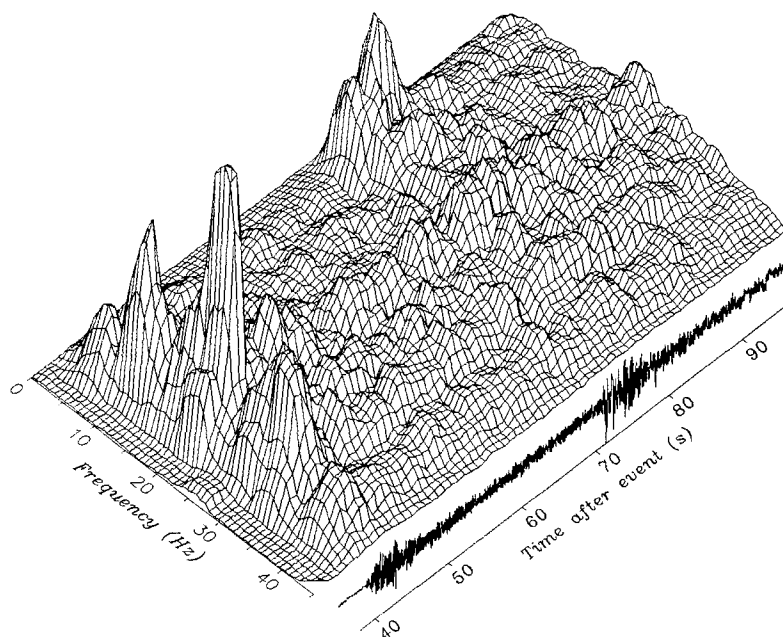
Figure 2b. Seismogram resulting from a ripple-fired quarry blast (EVC; Figure 1) detonated in Kazakhstan and corresponding sonogram. The recording was made at a range of 264 km by the vertical component seismometer at Bayanaul.

879
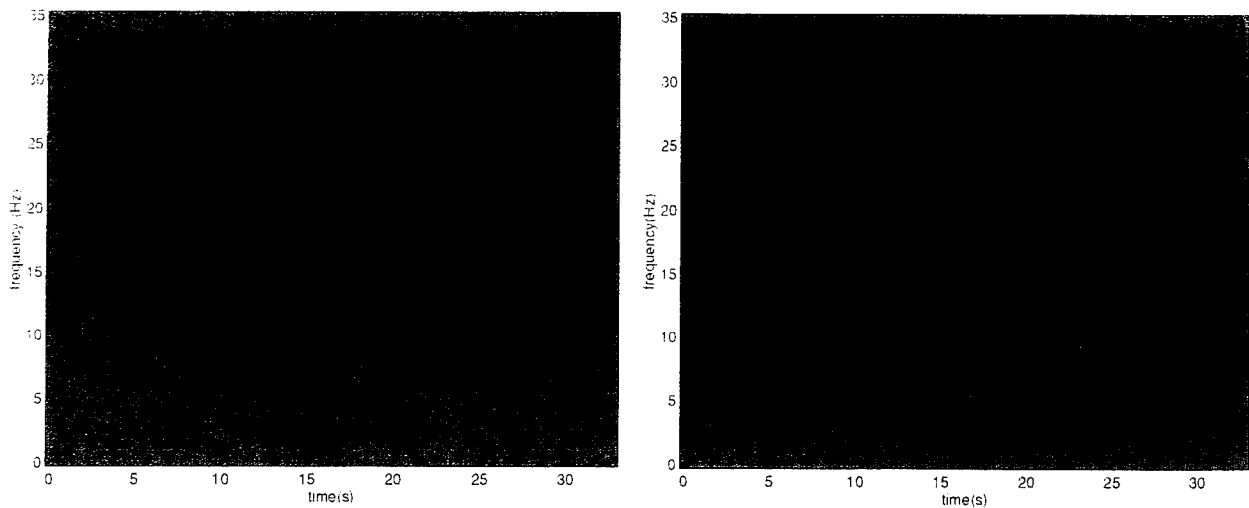
Figure 3. Binary versions of the sonograms presented in Figure 2a (left) and 2b (right).
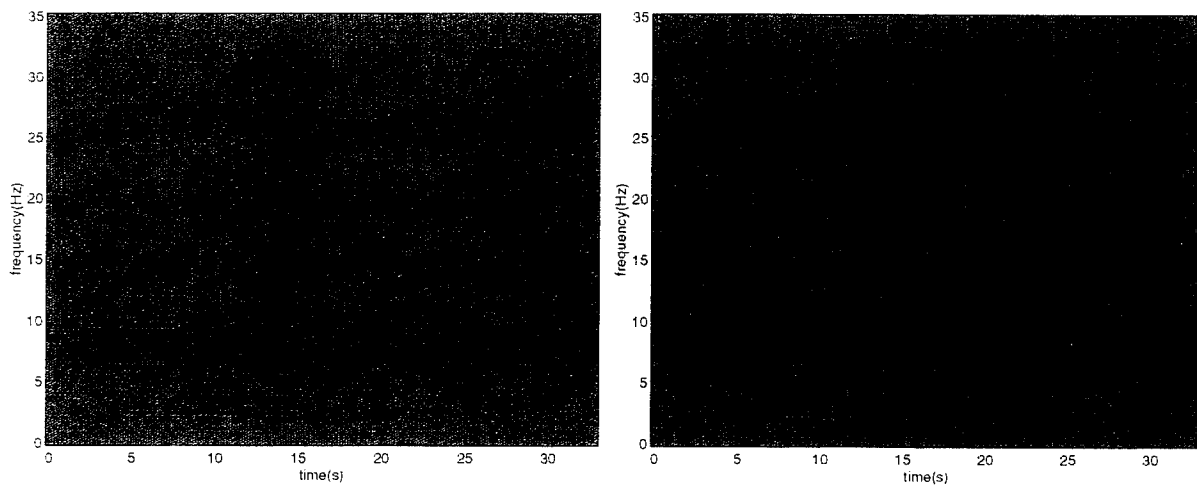
Figure 4. Binary sonograms calculated from the north (left) and east (right) component recordings of event c (Figures 1, 2b and 3).

2.2 An adaptive coda cepstrum calculated using KNET data. One way in which the ATFD might be improved is in the selection of filters used to convert sonograms to binary form. Although quarry blasts come in all sorts of "shapes and sizes" we have, in the past, applied two boxcar filters (via frequency domain convolution) to smooth the spectra and, through differencing, convert them to binary form. The same filters are used for all events. We are currently working on a formalism whereby optimal filters can be obtained for each event. For example, in one approach we make an initial attempt at reducing a sonogram to a binary pattern and, using the information in the resulting coda-cepstrum, iteratively solve for the boxcar filters that will be most effective at extracting the existing time-independent pattern. In Figure 6a we consider a recording of a suspected quarry blast made at 30 km by the KNET station CHM (Figure 1). The sonogram displays significant banding

880
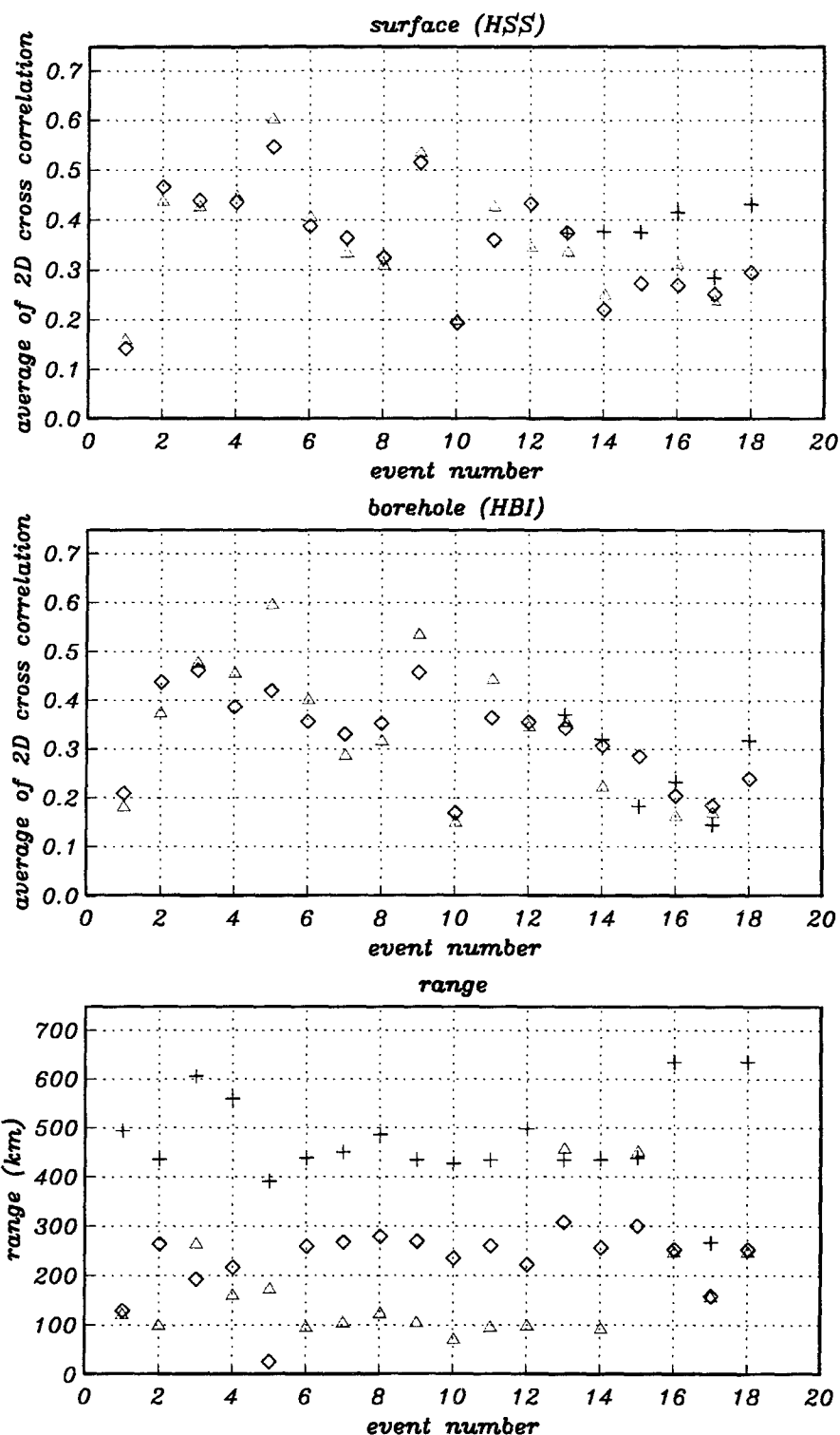
Figure 5. Three way cross correlations from evenst in the NRDC dataset. Events 1 to 15 are quarry blasts, events 16 to 18 are calibration explosions. The events considered in Figures 2 to 4 are #3 and #17. The triangles, diamonds and crosses represent stations BAY, KKL and KSU. Displayed in the upper and middle figure are results from surface high-gain and borehole high-gain sensors., the lower figure shows source-receiver ranges. A perfect match between all three channels would produce an average cross-correlation of 1.0.
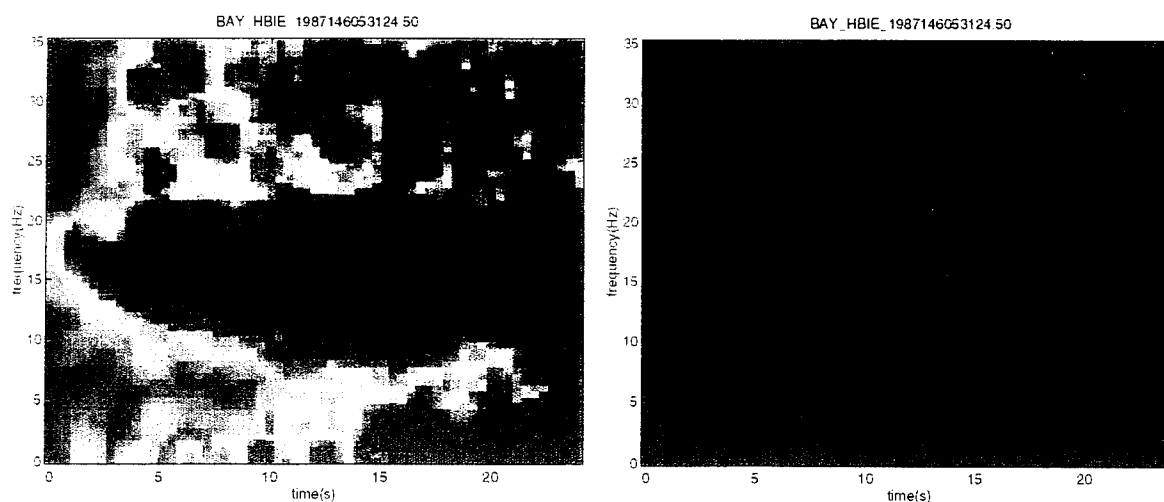
Figure 6a. Sonogram calculated from a CHM recording (east-west high-gain channel) of a nearby quarry blast. A binary sonogram displayed on the right was computed using boxcars spanning 5.0 and 2.5 Hz.

(independent of time). The binary sonogram (calculated using two boxcars of length 5 and 2.5 Hz) has captured much of this time-independent texture. As illustrated in Figure 6b the coda cepstrum has maximum power at a time-independent quefrency of .05 s. The coda-cepstral peaks are roughly half the amplitude of peaks that would be obtained from a pattern that is perfectly independent of time. By iteratively varying the boxcar filters to enhance energy at the peak of the coda-cepstrum we arrive at the binary pattern and the coda-cepstrum shown in Figure 6b. The final filters are clearly better suited to this event. Although the improvement is striking it must be noted that the unhindered algorithm will, sometimes, find time independent energy when essentially none is present. We are currently considering ways to control the process to prevent this. This process of tailoring filters to each event can be viewed as an extension of our goal to train the algorithm to different areas.

3. RECOMMENDATIONS AND FUTURE PLANS

To a large degree our work in the coming year will be directed toward testing and developing discriminants using globally distributed datasets. We plan to continue our work on the KNET and NRDC data and begin analyses of data recorded by the Pinon Flat Broadband Array and the ANZA network (in southern California), the Geyokcha array in Turkmenistan, the Pinedale research facility in Wyoming and numerous stations in the GSETT-3 network. An important aspect of our work will be in explaining why our discriminants fail (*e.g.* events 1 and 10 in Figure 5). For this purpose datasets with ground truth data will be particularly valuable. One dataset we plan to analyze is the Tyrnyauz Mine data (*Stump et al., 1994*). Ultimately we want to determine if a discriminant can be created that is universally applicable, or regionally *trainable* and robust. By analyzing the datasets mentioned above we will be exposing the technique to different mining practice and a different geological setting.
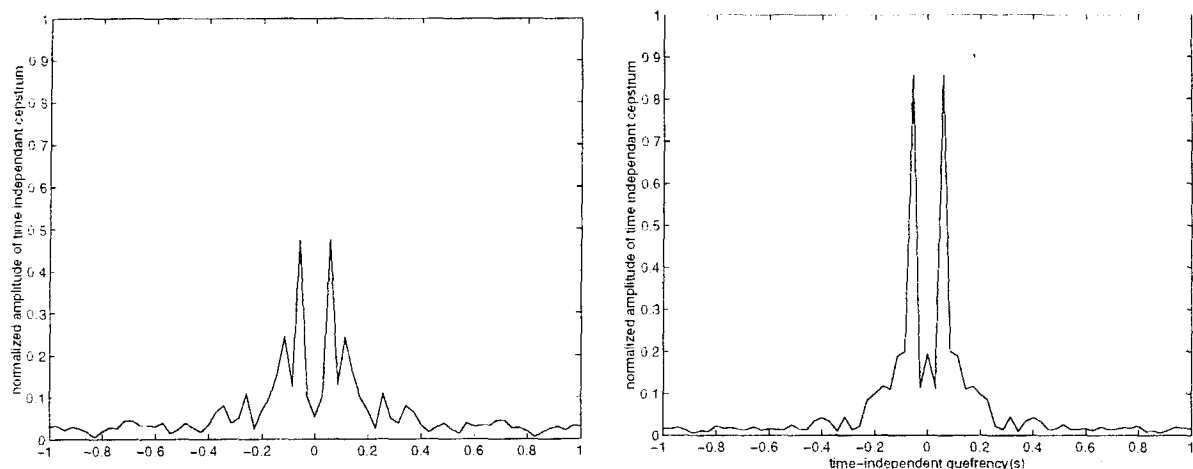
BAY_HBIE_1987146053124.50
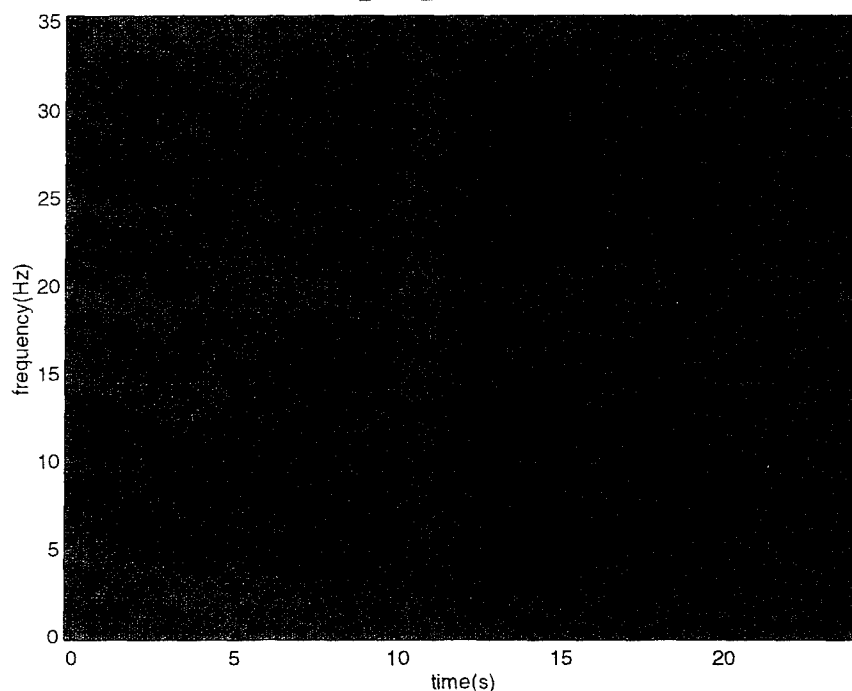
Figure 6b. In the upper left we display the time-independent slice through the coda cepstrum obtained from the binary sonogram displayed in Figure 6a. In the lower part of the figure we display the new binary sonogram obtained using boxcar filters that were chosen after 2 iterations. In the upper right is the final time-independent slice through the coda cepstrum.

In analyzing these data we will, in addition, attempt to answer the following questions:

(1) can earthquakes give rise to time-independent modulations?; (2) under what circumstances will ripple-fired events not yield modulated spectra?; (3) to what extent is success dependent on source-receiver range and azimuth? Using linear superposition theory we will predict the time independent spectral signature that should be present in mine records. Using our ATFD algorithm (*Hedlin*

883

et al., 1990) we will expand the 3-component recordings into time-frequency displays and investigate the correspondence between the expected and observed time independent signatures. We expect significant discrepancies in some events. The same processing will be applied to any earthquake records. Multiple recordings of the same events, obtained at local to regional distances will allow us to determine the effective range of the discriminant.

(4) are short delay (*e.g.* 20 to 30 ms) ripple-fired events capable of generating robust spectral modulations below 20 Hz? There have been a number of observations of a spectral null at low (< 10 Hz) frequencies (*e.g. Gitterman and Van Eck,1993* observing mines at local ranges in Israel). A null is predicted by linear wavefield superposition and is due to source finiteness. If this is detectable in the events in the aforementioned datasets we will attempt to determine if this spectral quality can be used for discrimination at far-regional distances (O 400 km).

(5) how can the discriminant be improved by using 3C data sets? In the past we have used a multi-taper algorithm to expand time series into time-frequency displays. A short sliding window is used to reveal how the spectral content evolves with time. While taking advantage of the multi-taper's proven ability to yield minimally biased spectral estimates from short time series this approach considers each recorded component separately and thus does not constrain particle motion. Furthermore the resolution is invariant with time and frequency. An alternate means to expand a time series into a time-frequency plane is based on wavelets (*Daubechies*, 1990) which scale with frequency and thus yield increasing temporal resolution with increasing frequency. *Lilly & Park, 1995* have derived multiple, leak resistant, wavelets (similar in concept to the tapers used in multi-taper analysis) to expand 3-component recordings into time and frequency dependent displays of spectral power and polarization. We plan to use the method of Lilly and Park to determine whether these wavelet based amplitude and polarization estimates are useful in identifying ripple-fired events from seismic recordings.

4. REFERENCES

Daubechies, I., 1990, The wavelet transform, time-frequency localization and signal analysis, *IEEE Transactions on information theory*, **36**, 961-1005.

Gitterman, Y. & van Eck, T., 1993, Spectra of quarry blasts and microearthquakes recorded at local distances in Israel, *Bull. Seismol. Soc. Amer,* **83**, 1799-1812.

Hedlin, M., Minster, J.G. & Orcutt, J.A., 1989, The time-frequency characteristics of quarry blasts and calibration explosions recorded in Kazakhstan, USSR, *Geophys. J. Int.,* **99**, 109-121.

Hedlin, M., Minster, J.G. & Orcutt, J.A., 1990, An automatic means to discriminate between earthquakes and quarry blasts, *Bull. Seismol. Soc. Amer.,* **80**, 2143-2160.

Kim, W.Y., Simpson, D.W. & Richards, P.G., 1993, Discrimination of earthquakes and explosions in the eastern United States using regional high-frequency data, *Geophysical Research Letters*, **20**, 1507-1510.

Lilly, J.M. & Park, J., 1995, Multiwavelet spectral and polarization analysis of seismic records, manuscript in press with the *Geophysical Journal International.*

Stump, G.W., Riviere-Barbier, F., Chernoby, I. & Koch, K., 1994, Monitoring a test ban treaty presents scientific challenges, *EOS, Trans. of the American geophys. Union,* **75**, 265.

Tribolet, J. M., 1979, Seismic Applications of Homomorphic Signal Processing, Prentice-Hall Signal Processing Series.

PRACTICAL ISSUES IN THE LOCATION OF SMALL EVENTS UNDER A CTBT: POOR STATION COVERAGE AND POORLY KNOWN VELOCITY STRUCTURE

Katharine Kadinsky-Cade, Rong-Song Jih, Anton Dainty and John Cipar
Earth Sciences Division (PL/GPE)
Phillips Laboratory
29 Randolph Rd
Hanscom AFB, MA 01731

ABSTRACT

In regions that do not contain good station coverage, a reasonably well known velocity structure and moderate or large magnitude events (the latter needed for calibration using teleseismic constraints on the location of a master event), it is very difficult to obtain accurate regional event locations. In this situation standard error ellipses generated during event locations may give the impression that an event location is better determined than it really is. False interpretations of the data may be due to a three dimensional velocity structure bias unaccounted for by the method, or simply to phase misidentification. Forward waveform modeling does help constrain the structure, however this approach contains a number of pitfalls. Modeling works best if ground truth is available at several epicentral distances and azimuths. Otherwise an inappropriate model might be constructed by matching synthetic waveforms and arrival times to observed data assumed to be at the wrong location. That model might thereafter be used to locate additional events. Regional arrays, or arrays originally constructed for teleseismic monitoring, can sometimes be used to identify regional phases using frequency-wavenumber (F-K) measurements of phase velocity in short (3-5 second) windows on the seismograms, however this only gives a solution if the signal to noise ratio is high. The F-K method is sensitive to the chosen center frequency and bandwidth, and to three dimensional heterogeneities surrounding the array. Some of these practical issues are discussed in scenarios involving events located within 500 km of a recording station or array. We model seismograms using reflectivity and linear finite difference techniques, assuming flat isotropic layers for simplicity. Phases that can be identified and modeled at these distances include P and S wave reflections and refractions. The Lg phase cannot be used as a phase with fixed group velocity throughout this distance range. This study highlights the importance of developing regional velocity structures for the crust and upper mantle that are well constrained by controlled source experiments.

Key words: phase identification, event location, crustal velocity structure, waveform modeling

OBJECTIVES:

Our objectives are to (1) provide practical solutions to the problem of seismic phase identification in a region sparsely populated by seismic stations, and (2) use these phases to locate seismic events at regional distances. The underlying scientific problem is how to determine an appropriate velocity structure for a region in the absence of ground truth or large well constrained sources that have been located teleseismically.

RESEARCH ACCOMPLISHED:

We consider a generic region in which small infrequent events occur. These might typically be earthquakes or explosions related to mining activity. We assume that only one station or array has recorded these events due to their size. That station or array is situated within 500 km of the sources under study, therefore the crust and upper mantle structure have a strong effect on wave propagation. The question in a CTBT might then be to determine where a specific event X in that region is really located.

The problem is that we do not know the velocity structure in this region. Because of the poor station coverage we cannot perform a joint inversion to reliably obtain velocity structure and event locations, as has been done by Crosson (1976) or by Goins et al. (1981).

If the locations and origin times of the events that have been recorded at the station or array are only approximate, we cannot determine a velocity structure by simply fitting observed phase arrival times with theoretical travel time curves as one would do in a controlled source refraction experiment. Fitting S-P times is not practical either, because seismograms plotted on a travel time (t) versus distance (x) curve are free to move in both the t and x directions due to the unconstrained hypocenter and origin time. If the hypocenter of one of the events is known independently, but the origin time is not precisely known, that event can be used to help construct a travel time curve. In that case the S-P time provides a useful modeling constraint because the position of the seismogram along the distance axis is fixed.

It is possible to assume a starting model for the crust and upper mantle in the region by borrowing a model from another better studied region with similar tectonic characteristics. Continental crust and upper mantle structures have been obtained in a variety of regions around the world (Christensen and Mooney, 1995), and it is often possible to find a reasonable starting structure by analogy with another region. Alternatively, one can determine a starting model using surface waves that have crossed the region under study. Once a starting model has been determined, the whole suite of regional events can be relocated based on that model. Geologically reasonable end-member models can be tested to search for some measure of confidence that includes the effect of the velocity structure. If we perform a joint (relative) relocation of all events using multiple P and S arrivals , the smallest RMS error should correspond to the best of the velocity models considered.

Figure 1 is a set of regional events that have occurred in some arbitrary area. These events can be plotted in record section format only because some crustal structure has been selected and the events have been located accordingly. The lineup of the P and S arrivals gives the impression that the structure can be extracted from this plot by superimposing travel time curves on the plot. However the lineup of the phases has been artificially imposed by the assumption of a specific velocity structure. Other structures and resulting locations will give new positions for the seismograms on the plot and result in phase lineups as well. Ideally some independent information ("ground truth") will help in the selection of the best velocity structure.

In Figure 2 we have plotted synthetic seismograms and travel time curves for two models. The travel time curves constructed here by ray tracing assume a spherically

symmetric homogeneous earth. The one dimensional ray tracing code handles gradients, and is based on Bullen's (1976) treatment of seismic rays in a spherically stratified earth model. We have chosen a surface source, and include direct rays, refracted rays and simple reflections off the Conrad discontinuity and the Moho. We have not plotted phase conversions such as PS or PmS in the travel time curves; they are included in the synthetic seismograms. Model A is composed of the upper few hundred kilometers of the IASP91 earth model (Kennett, 1991; Kennett and Engdahl, 1991). Kennett discussed the limitations of this model recently (Kennett, 1995), pointing out that IASP91 is a convenient hybrid model, but that it was constructed in part by incorporating some artificial constraints. Furthermore it is based on data from a number of different regions, and may not be appropriate for the region under study. The IASP91 model is characterized by a simple two layer crust over an upper mantle with a very weak positive gradient. Model B is generated by replacing the 2 layer crust in the IASP91 model by a 4 layer crust that is more like a crust in a continental shield area. The additional layers add to the complexity of the travel time curve. Another model to test might be a continental shield-type crust overlying a corresponding shield-type mantle. The travel time curves only provide expected arrival times for comparison with the data.

To incorporate amplitude information we turn to waveform modeling. The velocity structure can have a strong effect on amplitudes. For example a strong velocity gradient at the Moho can boost up the amplitudes of the Pn and Sn phases. An appropriate value for Q must be determined as well. Qp and Qs can be determined by trial and error, or by independent spectral or coda decay studies. For each model we construct synthetic seismograms using the linear finite difference and reflectivity methods. The reflectivity code was provided by Harley Benz of the U.S. Geological Survey (Fuchs and Müller, 1971; Benz et al., 1990). The linear finite difference code we use was originally developed at Teledyne Geotech's Alexandria Laboratory (cf. Jih, 1993), and has been modified to include a prototype attenuation operator currently being tested at Phillips Laboratory. In both cases we use an explosion source at the surface. After performing the computation of displacement seismograms we differentiate to get velocity records and apply a high pass filter to simulate short period seismograms. All calculations are done on a Sun Microsystems SPARC20 workstation. Finite difference results are shown in Figure 2. The finite difference calculation is computationally intensive and currently only practical out to 250 km distance for the frequency band of interest. In Figure 3 we have carried the reflectivity calculation out to 500 km for the second model. To avoid instabilities and speed up the calculation we have provided an upper frequency limit of 2 Hz in Figure 5. This simplifies the appearance of the seismograms to some extent. Even with this frequency limitation it is useful to compute seismograms out to 500 km because the 350-500 km distance range helps us constrain the velocity structure of the upper mantle.

If array data are available we can determine apparent velocities of regional phases using frequency-wavenumber (F-K) spectral analysis. Unfortunately it appears that there are some problems inherent in this approach, most likely related to heterogeneity of the crust and resulting frequency dependence of scattering. An example is shown in Figures 4a-4b. This event is a quarry blast from Blåsjø Quarry, recorded at the NORESS array (see Dainty and Toksöz, 1990 for more information). In this case the distance and azimuth of the quarry are known (324 km, 243°; location from Dysart and Pulli, 1987). We have selected two subsets of array stations. Rather than making use of the full complement of NORESS stations we are decimating the array, to see if an array with spacing more appropriate for teleseismic monitoring can effectively see the seismic wavefield decomposed into plane waves at regional distances. We seem to get strong apparently stable spectral peaks, but the phase velocities measured at two different frequencies are quite different from each other. Neither set approximates values expected for a reasonable flat layered structure. We start by selecting 6 array stations, with approximately 2 km spacing between stations, and a center frequency of 1 Hz and bandwith ±10%. Next we select 13 stations with approximately 1 km between stations, and a center frequency of 2

Hz. We should get the same result as in the first case. Instead we find inconsistencies in the phase velocities determined using the different frequency bands. The phase velocities we would expect, based on an IASP91 crust, are Pn-8.1 km/sec, P*-6.5 km/sec, PmP-6.6 Km/sec, Pg-5.8 km/sec, Sn-4.5 km/sec, SmS-3.8 km/sec. If we assume a crustal model such as that of Kanestrom and Haugland (1971), as described by Vogfjord and Langston (1990), we expect slightly higher phase velocities. Here, for example, we should find Pn-8.2 km/sec, PmP-7.3 km/sec, Sn-4.8 km/sec, SmS-4.2 km/sec. We see that the F-K plots give unreasonable results for the first P arrival (Pn) at both frequencies, and questionable results for other phases. Note that the SmS velocity is getting low enough that the corresponding wavenumber is at the borderline of being acceptable for analysis with these values of station spacing, due to possible aliasing.

RECOMMENDATIONS AND FUTURE PLANS

It is clear from the above examples that a combination of raytracing and waveform modeling can be an effective way to characterize regions with few events and fewer stations. It must however be emphasized that waveform modeling without ground truth is subject to misinterpretation. One important factor is the misidentification of phases. This has been mentioned by Vogfjord and Langston (1990). Phases may be missed because they have low amplitude, or mislabeled because of simplified assumptions. For example at short distances (less than 150-200 km) Lg is not a phase with a constant group velocity of 3.5 km/sec. One can instead look for the SmS phase, which can be quite strong and which comprises the beginning of the Lg wavetrain at greater distances. The second factor is the bias provided by the crust and upper mantle. This can be due to anisotropy or to three dimensional effects. For example one factor that may contribute to the difficulty in determining reasonable phase velocities for the Blåsjø Quarry event mentioned above is the presence of the Oslo Graben southwest of the NORESS array (see graben location in Vogfjord and Langston, 1990).

Further work is required to quantify the effects of geologically realistic heterogeneities on travel times and amplitudes. The ability to do rapid relocations using a variety of velocity models through a range of near to far regional distances is important, and we are now focusing our efforts in this area. We are basing our travel time calculations on the tau-p method of Buland and Chapman (1993), for which computation is rapid. If we do not have detailed independent velocity information in an area it seems reasonable to work with a starting one-dimensional crustal model, and quantify how variations in that model would affect our locations. It seems clear that a simple global model like IASP91 is unlikely to be sufficient in specific regions for waveform modeling and reliable locations within a 500 km range.

Use of arrays for regional phase velocity determinations is problematic. Previous work at NORSAR has suggested that P and S energy can be differentiated on F-K plots at NORESS, but that it may sometimes be difficult to separate out phases more precisely from inferred phase velocities (Mykkeltveit and Bungum, 1984; Mykkeltveit et al., 1990). It may be that calibration of each array is necessary as a function of distance and frequency. This is clearly not appropriate in the situation described here in which little if any ground truth is presumed available, and in which we would like to use arrays to constrain crustal structure and identify specific P and S arrivals within the context of that structure.

REFERENCES:

Benz, H., R. Smith and W. Mooney, 1990, Crustal structure of the Northwestern Basin and Range Province from the 1986 PASSCAL seismic experiment, *Jour. Geophys. Res., 95*, pp. 21,823-21,842.

Buland, R. and C. Chapman, 1983, The computation of seismic travel times, *Bull. Seis. Soc. Am., 73*, pp. 1271-1303.

Bullen, K.E., 1976, An introduction to the theory of seismology, Third Edition, Cambridge University Press, Cambridge, U.K., 381 pp.

Christensen, N.I. and W.D. Mooney, 1995, Seismic velocity structure and composition of the continental crust: a global view, *Jour. Geophys. Res.,* 100, 9761-9788.

Crosson, R., 1976, Crustal structure modeling of earthquake data 1. Simultaneous least squares estimation of hypocenter and velocity parameters, *Jour. Geophys. Res.,* *81*, 3036-3046.

Dainty, A.M. and M.N. Toksöz, 1990, Array analysis and seismic scattering, *Bull. Seis. Soc. Am., 80*, 2242-2260.

Dysart, P.S. and J.J. Pulli, 1987, Spectral study of regional earthquakes and chemical explosions recorded at the NORESS array, in Tech. Rep. for the Period 1 April-30 June 1987, *Tech. Rep. C87-03*, Center for Seismic Studies, Arlington, VA, pp 3-21 - 3-24.

Fuchs, K. and G. Müller, 1971, Computation of synthetic seismograms with the reflectivity method and comparison with observations, *Geophys. J. Roy. Astron. Soc., 23*, 417-433.

Goins, N.R., A.M. Dainty, and M.N. Toksöz, 1981, Lunar seismology: the internal structure of the moon, *Jour. Geophys. Res., 86*, 5061-5074.

Jih, R.-S., 1993, User's manual of FD2: a software package for modeling seismological problems with 2-dimensional linear finite-difference method, *Special Topical Report TGAL-93-06*, Teledyne Geotech, Alexandria, VA.

Kanestrom, R. and K. Haugland, 1971, Profile section 3-4 in Deep Seismic Sounding in Europe, A. Vogel, Editor, Swedish Natural Science Research Council, Stockholm, Sweden,76-91.

Kennett, B.L.N.(editor), 1991, IASPEI 1991 Seismological Tables, Research School of Earth Sciences, Australian National University, 167 pp.

Kennett, B.L.N., 1995, The underdetermined earth (IASPEI association lecture), Union of Geodesy and Geophysics XXI General Assembly, Abstracts Week A, July 2-14, Boulder, Colorado, p. A377.

Kennett, B.L.N. and E.R. Engdahl, 1991, Travel times for global earthquake location and phase identification, *Geophys. J. Int., 105*, pp. 429-465.

Mykkeltveit, S. and H. Bungun, 1984, Processing of regional seismic events using data from small-aperture arrays, *Bull. Seis. Soc. Am., 74*, 2313-2334.

Mykkeltveit, S., F. Ringdal, T. Kvaerna and R. Alewine, 1990, Application of regional arrays in seismic verification, *Bull. Seis. Soc. Am., 80*, 1777-1800.

Vogfjord, K.S. and C.A. Langston, 1990, Analysis of regional events recorded at NORESS, *Bull. Seis. Soc. Am., 80*, 2016-2031.
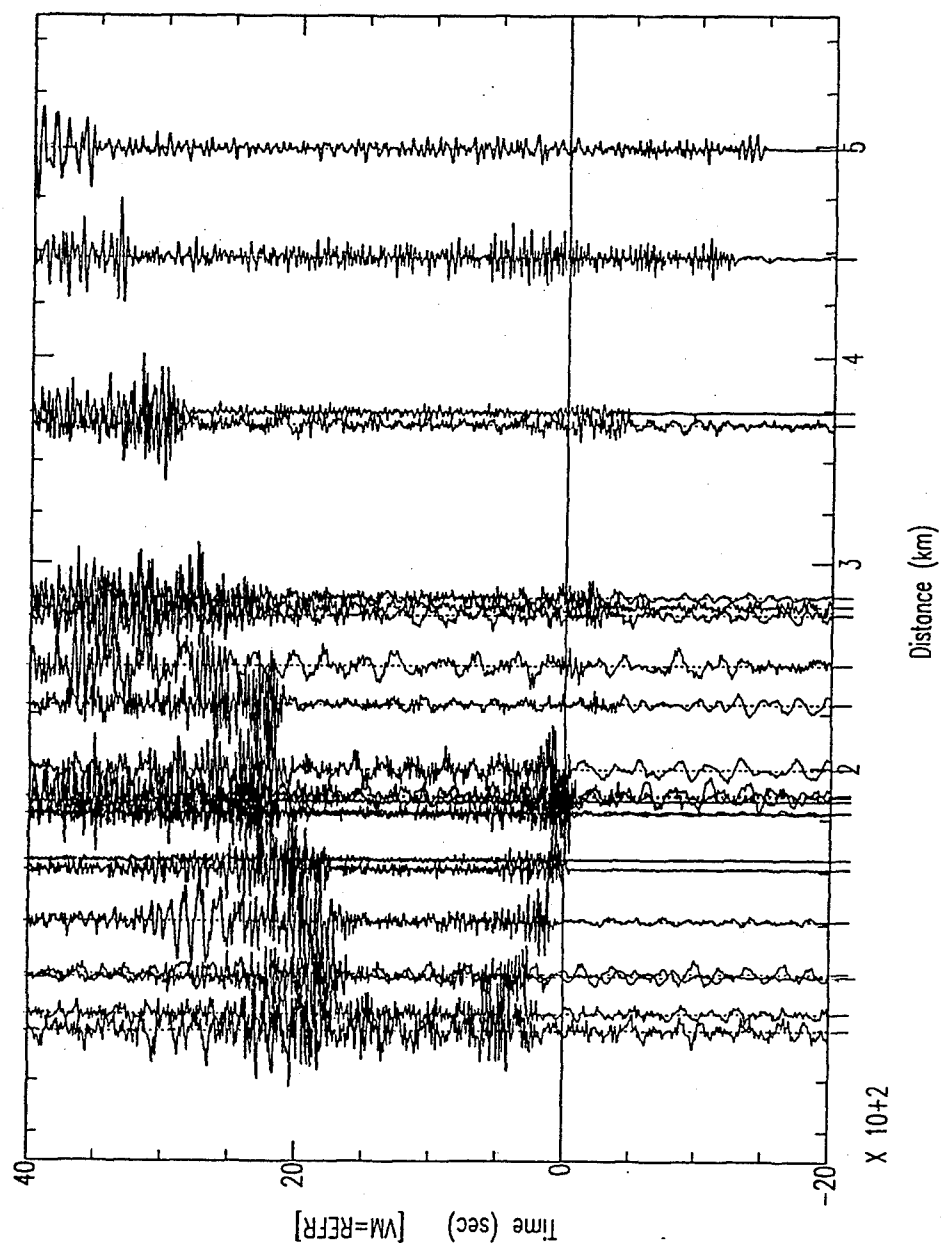
Figure 1.   Regional events in record section format, distance range 0-500 km. A 6 km/sec reduction velocity has been applied.
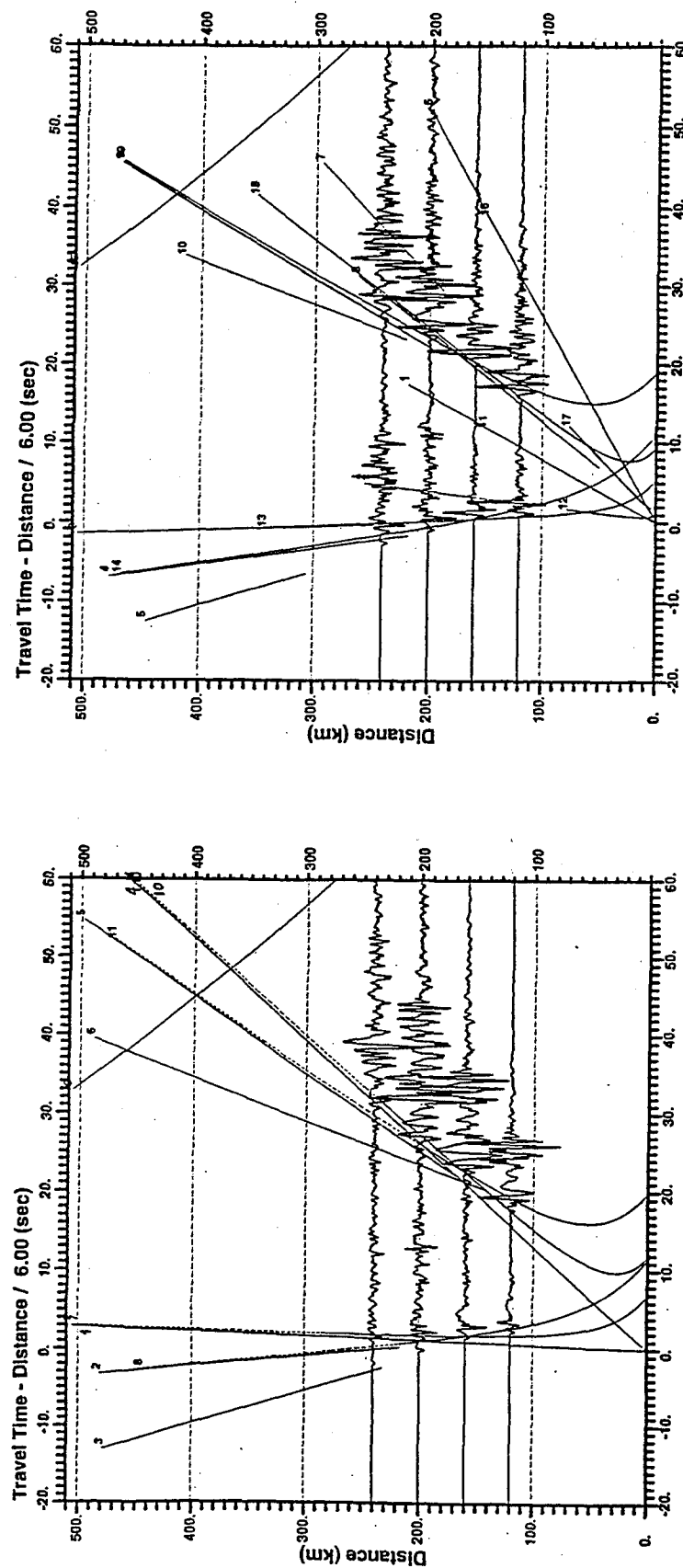
Figure 2. Linear finite difference synthetics overlain by travel time curves. Left: Model A (IASP91). Right: Model B (IASP91 with modified 4 layer crust). Travel time curves from raytracing include direct rays, refractions and reflections. For example Model A includes Pn (#3), P* (2), Pg (#1), $P_{20}P$ (#7), PmP (#8), Sn (#6), S*(#5), Sg(#4), $S_{20}S$ (#10) and SmS (#11).
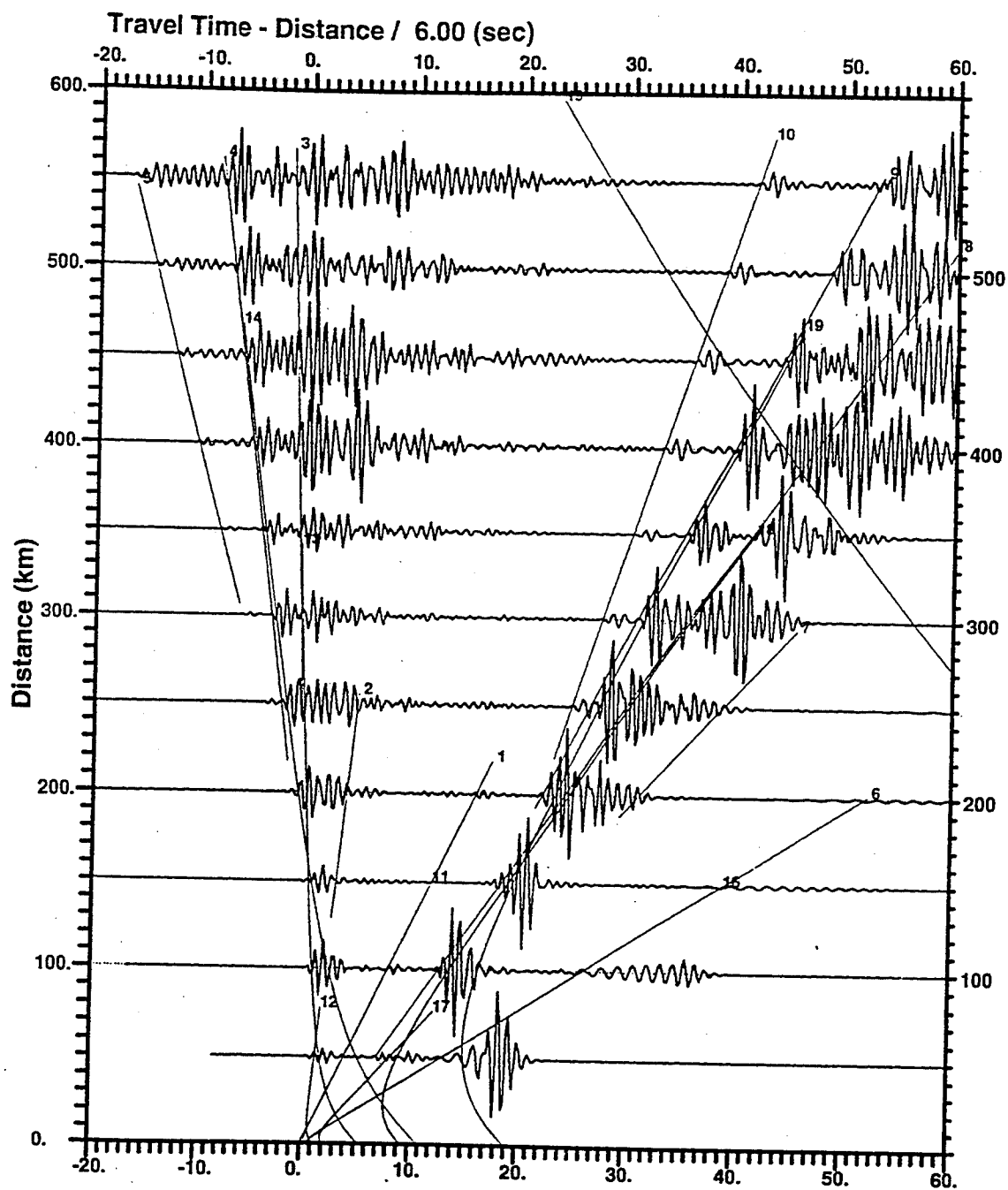
Figure 3.   Reflectivity velocity synthetics overlain by travel time curves for Model B.
             Source is fixed at 0 km depth.
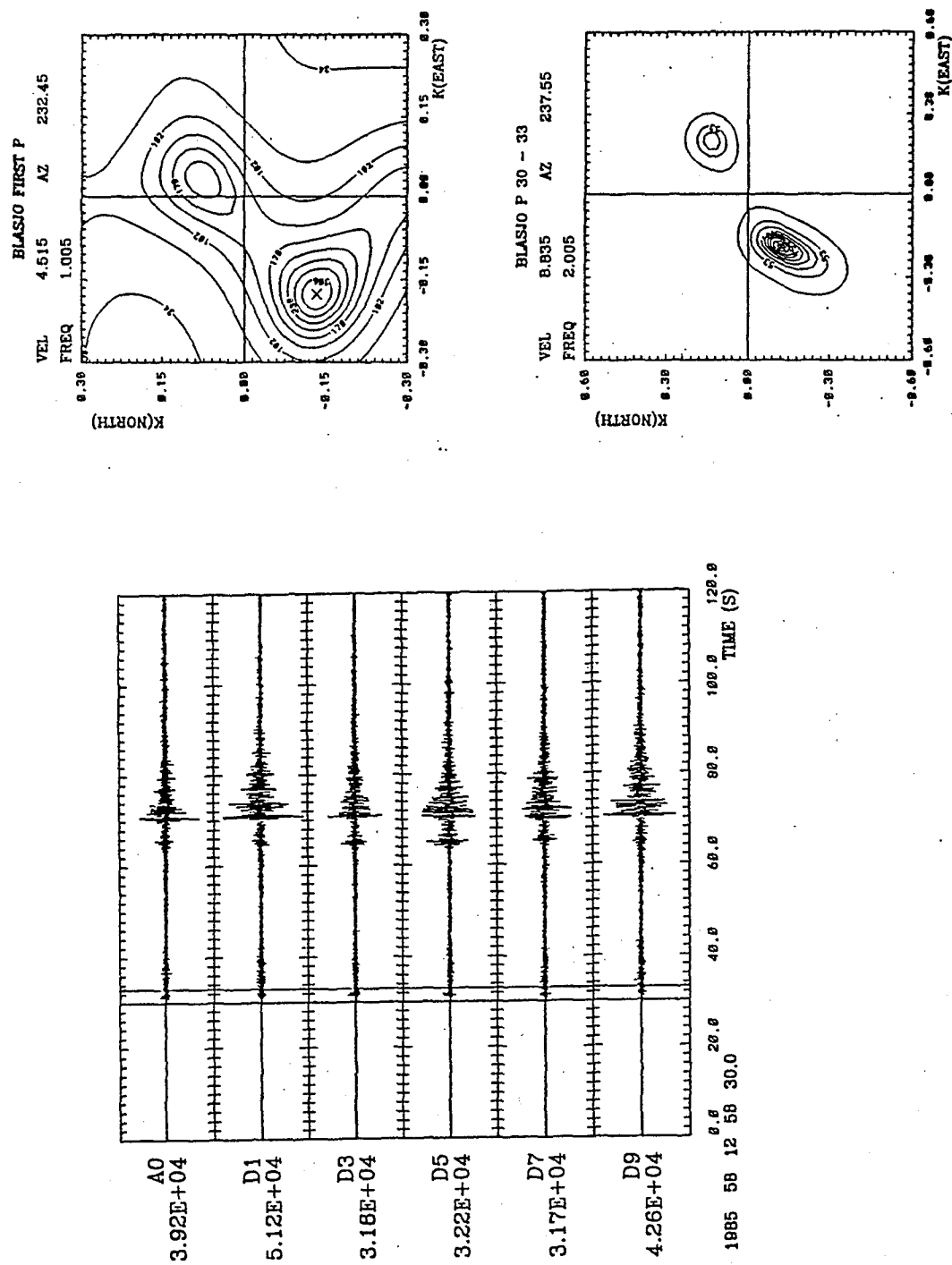
Figure 4a.   NORESS recording of Blåsjø quarry blast. F-K diagrams on the right are for signal in 3 second window shown on left. Upper right: frequency band 0.9-1.1 Hz. Six stations spaced roughly 2 km apart (stations shown on left). Lower right: Frequency band 1.8-2.2 Hz. 13 stations used here (A ring, 3 from C ring, entire D ring), spaced roughly 1 km apart.
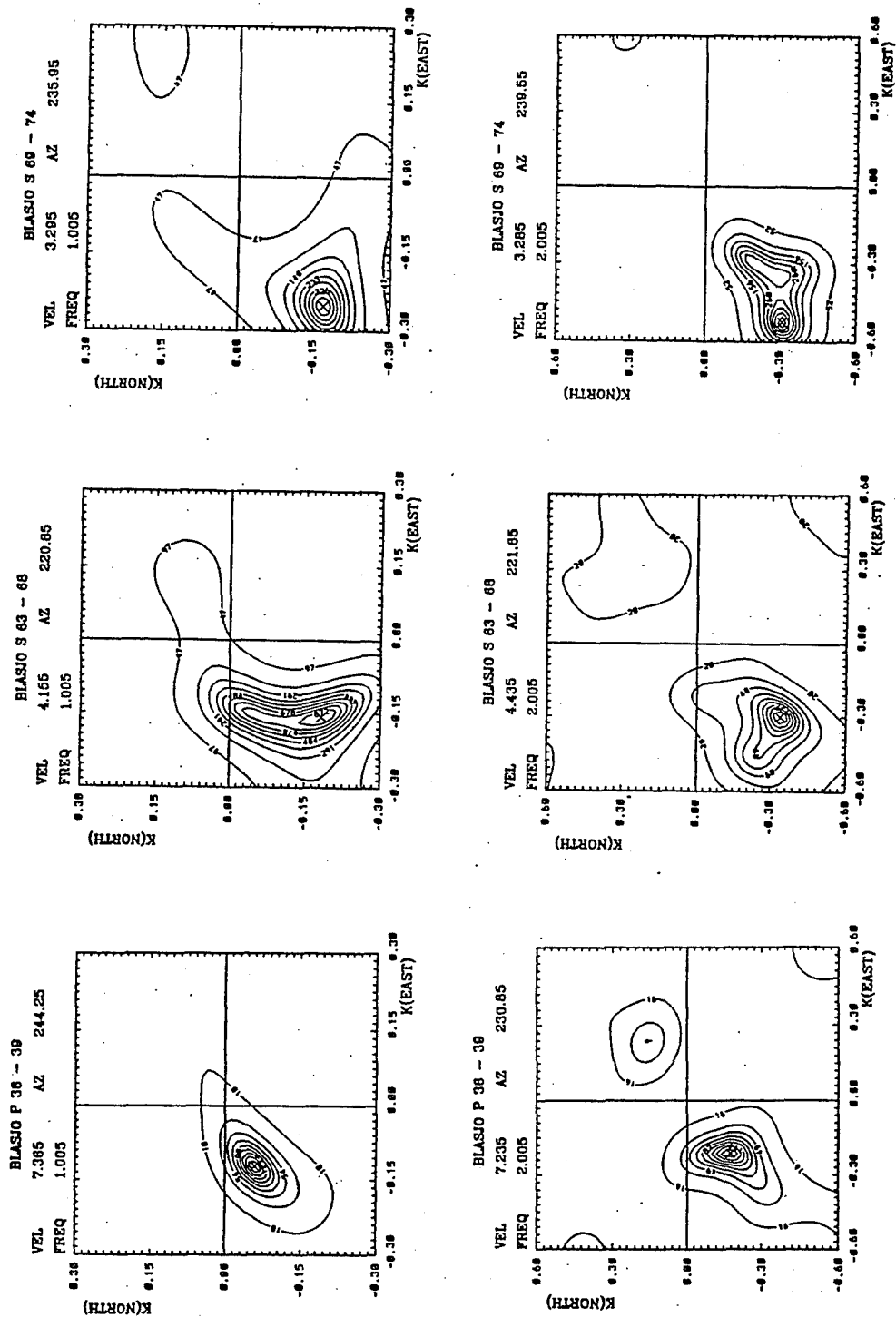
Figure 4b. Continuation of F-K plots from previous figure. Upper set of plots: 1 Hz center frequency, 6 stations. Lower set of plots: 2 Hz center frequency, 13 stations. One P and two S windows shown. Refer to Figure 4a for location of windows along seismic traces.

Effects of Explosion Depth and Crustal Heterogeneity on Lg Waves

H. Keers, K. Vogfjörd, G. Nolet, F. A. Dahlen

Department of Geological and Geophysical Sciences, Princeton University, Princeton, NJ 08544

Contract number: F49620-94-1-0077

ABSTRACT

We use ray theory to model the propagation of Lg waves through 2D and 3D layered crustal models. The layers are homogeneous, and the discontinuities are undulating. The Lg wave train is modelled by multiple S reflections within the crustal layers. The ray tracing system is reduced from a set of linear differential equations to a set of maps. If the medium has three or more discontinuities the number of multiples increases exponentially. Using a binary tree-searching method we systematically keep track of all multiples.

The ray behavior is chaotic for large take-off angles, causing multipathing of the crustal multiples. However, in the presence of mid-crustal discontinuities the rms Lg amplitude is stable, because of the distribution of the energy over a large amount of rays. The simplest case, a one layer over a halfspace model, already contains all the characteristics of wave propagation through the media under consideration.

To examine the source-depth and velocity-structure effects on amplitudes and character of Lg we use wavenumber integration methods in 1-D structures. In particular, we study the ability of shallow explosions to generate S^* and pS rays. Although S^* is a nongeometrical phase it does follow a well defined raypath. In velocity structures, where the peak in the S^* radiation pattern is confined to the crust, signals from explosions within 1 km of the surface, that do not generate spall or significant tectonic release, are likely to be dominated by waves with a very narrow ray-parameter range, coming from the radiation peak of S^*. Observation of Lg waves dominated by such a narrow ray-parameter range may therefore identify the source as explosive, and shallow. Dislocation radiation patterns, or the spalls CLVD term are likely to generate significant S waves over a wider range of ray parameters and therefore not to be confused with S^*.

Effects of Explosion Depth and Crustal Heterogeneity on Lg Waves

OBJECTIVE

The objective of our research is to understand aspects of the excitation of Lg waves and their subsequent propagation through the crust, including 2D and 3D heterogeneous crustal models.

Modeling the Lg wave train is a difficult task, even though measurements of rms amplitude of Lg is stable. We attempt to explain this by modeling Lg as a superposition of supercritically reflected crustal multiples. In our models the crust is multilayered (2D or 3D) and the interfaces are undulating.

We also examine the effect S^* has on amplitudes and character of Lg to determine to what depths and in which types of velocity structures S^* is a significant contributor to Lg.

RESEARCH ACCOMPLISHED

Lg Wave Propagation Through 3D Heterogeneous Structures

To study the propagation of Lg waves through 2D and 3D heterogeneous media we use ray theory. Ray theory is not only very efficient, it also makes the characterization of Lg waves in terms of focusing/defocusing effects, multipathing and traveltimes due to the complicated structure relatively simple. Thus ray theory complements full waveform methods such as finite differences.

Lg waves possess a dual character (e.g. Hansen et al., 1990). On one hand the modeling of Lg waves has proved to be very difficult, on the other hand the Lg wavetrain has been useful to determine seismic moments because rms Lg is a stable quantity, that is relatively independent of regional structure. Using our modeling results we give an explanation for this seemingly contradictory character.

The models that we use are 2D and 3D layered crustal models. The layers are homogeneous, and the discontinuities are undulating. The Lg wave train is modelled by multiple S reflections within the crustal layers. In a flat layered medium the ray-theoretical seismograms are almost identical to the exact synthetics (Keers et al., 1995a). This serves as our justification for the use of ray theory in media with (slightly) undulating interfaces separated by homogeneous layers.

One of the main advantages of using homogeneous layers is that the ray tracing system can be reduced from a set of linear differential equations to a set of maps (Keers et al., 1994). This makes the ray tracing very efficient; it is not necessary to use a Runge-Kutta method and the search for the point where the ray intersects one of the undulating interfaces is reduced to a 1D root-solving problem (even in the three dimensional case). If the medium has three or more discontinuities the number of multiples increases exponentially. Using a binary tree-searching method we systematically keep track of all multiples.

The simplest case, a one layer over a halfspace model, already contains all the characteristics of wave propagation through the media under consideration. In general two regions (by regions we mean take-off angle intervals) are distinguished. One region, corresponding to smaller take-off angles, has regular ray-behavior, and another region, corresponding to the largest take-off angles, has chaotic ray-behavior. In the case of a sinusoidal Moho with a wavelength of 100 km and an amplitude of 1 km the take-off angle intervals are roughly 50°-65° and 65°-90° (the critical angle is close to 50°). The first region is characterized by a low degree of multipathing and a high degree of focusing. The second region is characterized by a large degree of multipathing and consequently a large degree of defocusing The defocusing is caused by the fact that a small change in take-off angle causes a large change in epicentral distance, except at the caustics. However, at the caustics the amplitude is still relatively small (Keers et al, 1995a). It should be noted that the amplitude perturbations due to the undulation are much larger than the traveltime perturbations. Table 1 gives an

indication of the degree of multipathing for the case of a flat Moho, a sinusoidal Moho and a more realistic model, that of the Moho below Germany.

In the case of a more realistic two-layered model with undulating interfaces, the ray behavior remains essentially the same: there exists a regular region corresponding to smaller take-off angles and a chaotic region corresponding to larger take-off angles. All discontinuities are sinusoidal. The surface has a wavelength of 60 km and amplitude of 0.5 km, the midcrustal discontinuity has a wavelength of 160 km and an amplitude of 0.8 km and the Moho has a wavelength of 100 km and an amplitude of 1.5 km. Figure 1a shows the amplitude distribution. This figure is essentially an 'envelope record-section'. It contains only amplitude information; no phase information. The strong focusing in the regular region that was present in the one-layered model is gone. This is due to the reflection and transmission of the multiples at the midcrustal interfaces, which partitions the energy over many multiples. The presence of the chaotic region makes it impossible to identify even the major multiples (SmS, $2SmS$ etc.) at larger epicentral distances. The large degree of multipathing of a certain multiple, like $2SmS$, causes these multiples to consist of many rays, each with a relatively small amplitude, coming in from totally different directions. Each of these multiples is smeared out over a larger time interval and the the maximum amplitude of the dominant rays is low compared to the flat layered case. This explains why the modeling of Lg waveforms has been largely unsuccesful: the waveform is very sensitive to initial conditions (take-off angle) and model parameters.

Figure 2a shows the effect of a 3D sinusoidal Moho. The wavelength is 100 km in both the x and y directions, and the amplitude is 1 km. The figure shows the energy distribution along the x axis. Also shown is the energy distribution for a 2D model with a sinusoidal Moho that has a wavelength of 100 km and amplitude of 1 km. The amount of side scattering can not be ignored, but depends strongly on the model (Keers et al, 1995b). Since this 3D example is for a one-layered model, the focusing of the different multiples plays a dominant role in this figure.

Figure 2b shows the total energy of the Lg wavetrain as a function of epicentral distance for the two models of figure 1. Also plotted is the energy of the waves assuming a $\Delta^{-5/6}$ (Nuttli, 1973) decay of the amplitude (Δ=distance). The undulating two-layered model shows much less focusing especially at larger epicentral distances. This is due to the midcrustal interface. There is still focusing of certain rays, but the reflection and transmission from the midcrustal interface makes these rays much less dominant than in the one-layered model. This explains the stability of rms Lg as observed for many regional events (e.g. Hansen et al., 1990). For models with more layers we can expect the focusing effects to become even less dominant.

Effects of Source Depth and Velocity Structure on the Character of Lg

Discrimination between shallow sources is a difficult task and methods, such as Pg/Lg amplitude ratios and Lg spectral ratios as well as regional $m_b:M_S$, seem to be region dependent and only work for discrimination between shallow explosions and earthquakes deeper than 5 km, and even then there are problems with explosion depths of <1 km. Generation of S waves from explosion sources has generally been attributed to nonisotropic source radiation, spall, tectonic release, or Rg-S scattering in the source region, while S^*, the wave generated by interaction between the curved P wave-front and the surface, has usually been discounted for all but the shallowest sourcs, because of its strong dependence on source depth. However, due to the S^* radiation pattern, in certain structures the amplitude may be significant down to depths of $\sim$1 km, possibly making S^* an added tool to discriminate between shallow sources.

To examine the source-depth and velocity-structure effects on amplitudes and character of Lg we use wavenumber integration methods in 1-D structures. The shortcomings of the simplified structure are overcome by the benefits of a full-wave synthesis, revealing all waves generated by the source and its interaction with discontinuities in the structure; of main interest, of course, is the interaction with the Earth's surface. The characteristics observed in the synthetics are then explained in terms of the radiation pattern of S^*.

A high frequency approximation to the amplitude and phase of the S^* wave was developed by Daley and Hron (1983). In this approximation S^* appears as a spherical wave-front with SV-particle motion, radiated from a point on the surface above the source. Its amplitude is modulated as a function of angle ϕ (measured from the vertical), but is independent of azimuth. The wave exists for $\phi_d = \sin^{-1}(\beta/\alpha) \leq \phi \leq \pi/2$, but the approximation is valid for $\phi_d < \phi < \pi/2$, or $1/\alpha < p < 1/\beta$, where α and β are the mediums P and S

velocities and $p = \sin \phi / \beta$, is the ray parameter. A plot of the radiation function for a frequency of 2 Hz and $\alpha = 4.2$ km/s is shown in Figure 3 (top right). The source depths represented are: 0.1, 0.5, 1.0 and 2.0 km. The amplitude is a maximum at ϕ_d, but decreases to zero at $\phi = 45°$, where the phase also flips by 90°. The amplitude increases again to a smaller maximum, before becoming zero again at 90°. The amplitude decays exponentially with source depht, so for depths greater than 0.5 km, amplitudes are very small at angles above 45°. However, between ϕ_d and 45° the amplitude can be larger than in the original P and the reflected pS wave. To demonstrate, the pS radiation pattern, which exists for reflection angles $\phi < \phi_d$, is also included on the plot.

If the narrow radiation peak of S^* gets trapped in the crust, it may dominate Lg. To demonstrate we calculated synthetics in three different velocity structures, md1, where the peak is radiated into the mantle, md2, where the peak is confined to SmS multiples for source depths down to 1.25 km and, md3, where the peak is confined to turning waves in the crust for source depths down to 1 km. The models have a common Q structure and share a velocity structure below 3 km depth (see Figure 4, lower panel). It is the ratio $\alpha_{source}/\beta_{mantle}$ that determines how much of S^* is trapped in the crust. If $\alpha_{source} < \beta_{mantle}$, all of S^* and some pS are contained in Lg, but when α_{source} increases to $\geq \beta_{mantle}$ the radiation peak starts to go into the mantle. When the critical angle for Moho reflection exceedes $\sim 42°$, no significant S^* can be found in Lg, except for depths ≤ 0.5 km. The angular range of Moho reflections in the three models is indicated on Figure 3 (top right). There it is clear that in md1, most of the S^* radiation peak goes into the mantle and therefore Lg, from a pure explosion source, is expected to decay quickly with source depth. However in md2, all of the radiation peak ends up in Moho reflections, for source depths down to 1.25 km. For this depth range Lg is expected to be of significant amplitude and to be dominated by Moho reflections. In md3, the peak is confined to turning waves in the crust, for source depths down to 1 km. In this depth range Lg is also expected to be significant and dominated by turning waves. These effects are clearly seen in the synthetics: In Figure 4, synthetics are shown at a distance of 500 km for source-depths ranging from 0.1 to 2 km in model md2. Clearly the Lg wave is dominated by the Moho multiples, $2SmS$, $3SmS$ and $4SmS$, and Lg amplitude is significant for source depths down to ~ 1 km. Record sections for an explosion source at 0.5 km depth in the three models are shown in Figure 5, where the expected features are also seen. The md1 record section has smaller amplitude Lg waves than the other models, evenly divided between Moho reflections and turning waves. The frequency content of the Lg wave is also significantly lower than that of the crustal P wave-train. The md2 record section has much larger amplitudes, Lg is dominated by Moho multiples, and there is no significant loss of higher frequencies in Lg. The md3 record section has large amplitude Lg waves of high frequency content, and maximum amplitudes coincide with the arrivals of the turning waves and Moho reflections; the Moho reflections come from pS and the turning waves come from S^*.

Analysis of Array Data

The theoretical results need to be tested against observed data from local and regional events. We have so far selected two regions based on the availability of short-period array data. The regions are: Central Europe, where we make use of the GERESS array, and the Sierra Nevada, where three, 3-component arrays were temporarily operated in 1993. The arrays enable detection of small coherent arrivals and decomposition of the Lg wave train into distinct arrivals with differing phase velocities. The events recorded at GERESS consist of earthquakes and explosions, while most of the events recorded on the Sierra Nevada arrays are earthquakes, but also include the NPE explosion at the Nevada Test Site in September 1993.

CONCLUSIONS AND RECOMMENDATIONS

In 2D and 3D heterogeneous media Lg wave propagation is strongly affected by curved interfaces. The ray behavior is chaotic for large take-off angles, causing multipathing of the crustal multiples. This makes modeling of Lg waves a tidy task. However, in the presence of mid-crustal discontinuities rms Lg is stable, because of the distribution of the energy over a large amount of rays. It should be noted that the undulations used are small (of the order of 1 km). The amplitude behavior will change if the undulations of the Moho become large. Further research is needed to establish this effect. Incorporation of P-S and S-P conversions using our ray-tracing algorithm should make it possible to model Lg wave propagation more realistically.

More detailed Moho maps for regions of interest are also necessary for reliable modeling of Lg in 3D structures. This goal can be achieved by wave-form inversion, using regional seismograms (Das and Nolet, 1995).

In velocity structures, where the peak in the S^* radiation pattern is confined to the crust, signals from explosions within 1 km of the surface, that do not generate spall or significant tectonic release, are likely to be dominated by waves with a very narrow ray-parameter range, coming from the radiation peak of S^*. Observation of Lg waves dominated by such a narrow ray-parameter range may therefore identify the source as explosive, and shallow. Dislocation radiation patterns, or the spalls CLVD term are likely to generate significant S waves over a wider range of ray parameters and therefore not to be confused with S^*. A comparison between data from mining explosions and earthquakes, located in approximately the same area, may serve as a test case for this. GERESS data for events in the Vogtland region in the Czech Republic may be possible candidates.

The completed record section profiles will serve as the data base needed to test the validity of the theoretical calculations and predictions.

REFERENCES

Daley, P. F. and F. Hron (1983). High-frequency approximation to the nongeometrical S^* arrival, *Bull. Seism. Soc. Am.*, **73**, 109-123.

Das, T. and G. Nolet (1995). Crustal thickness estimation using high frequency Rayleigh waves, *Geophys. Res. Lett.*, **22**, No. 5, 539-542.

Hansen, R. A., F. Ringdal and P. G. Richards (1990). The Stability of RMS Lg Measurements and Their Potential for Accurate Estimation of the Yields of Soviet Underground Nuclear Explosions, *Bull. Seism. Soc. Am.*, **80**, 2106-2126.

Keers, H., G. Nolet and F. A. Dahlen, 1995a. Ray Theoretical Analysis of Lg, (submitted to *Bull. Seism. Soc. Am.*).

Keers, H., G. Nolet and F. A. Dahlen, 1995b. Chaos and Lg Waves, EOS, volume 76, no 17, 205.

Keers, H., K. Vogfjörd, G. Nolet and R. Phinney, 1994. Lg Synthesis in Media With Undulating Surfaces by Ray Summation, EOS, volume 75, no 44, 420.

Nuttli, O. W. (1973). Seismic wave attenuation and magnitude relations for Eastern North America, *J. Geophys. Res.*, **78**, 876-885.

Vogfjörd, K. S. (1995). Effects of explosion depth and Earth structure on excitation of Lg: S^* revisited, (submitted to *Bull. Seism. Soc. Am.*).

Table 1	Number of supercritically reflected rays for different Moho models		
epicentral distance (km)	flat Moho	Sinusoidal Moho	Moho below Germany
200	4	4	17
300	6	6	26
400	8	10	53
500	10	14	140
600	12	22	216
700	15	31	218
800	17	56	270

Table 2	layer #	thickness (km)	S-velocity (km/s)	density (g/cm3)
	1	15	3.5	2.7
	2	15	3.9	3.1
	3	∞	4.6	3.3
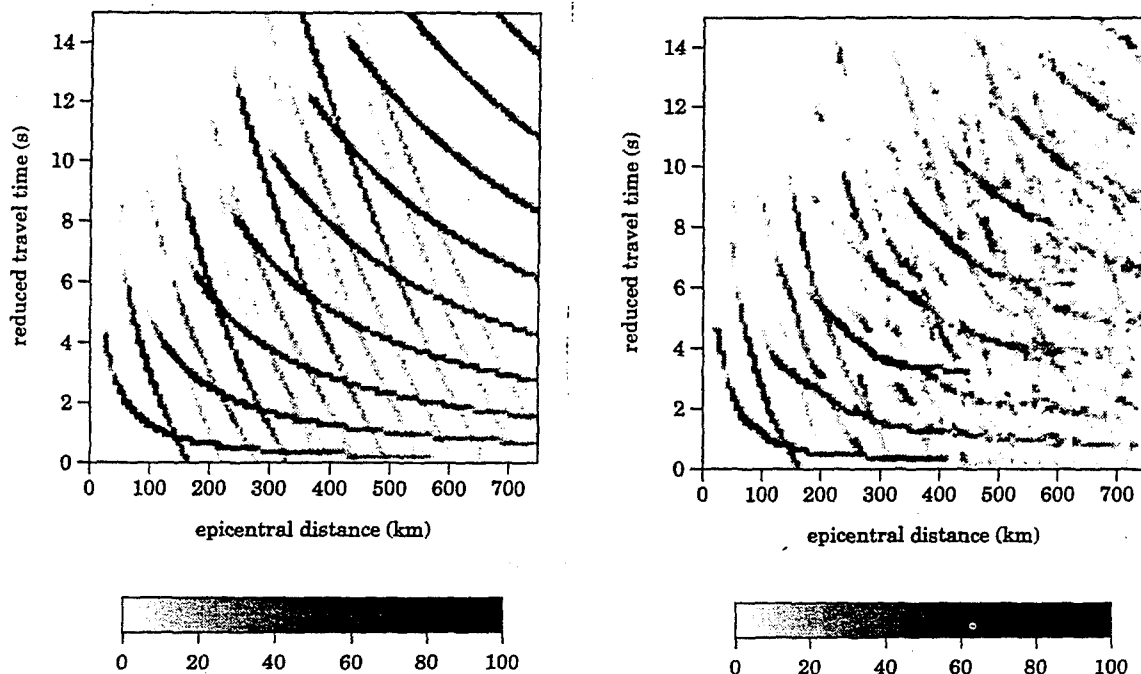
Figure 1. Amplitude distribution for two-layered crustal model with flat interfaces (left) and undulating interfaces (right; see text for the characteristics of the undulations). The amplitudes are scaled with respect to the maximum value (100).
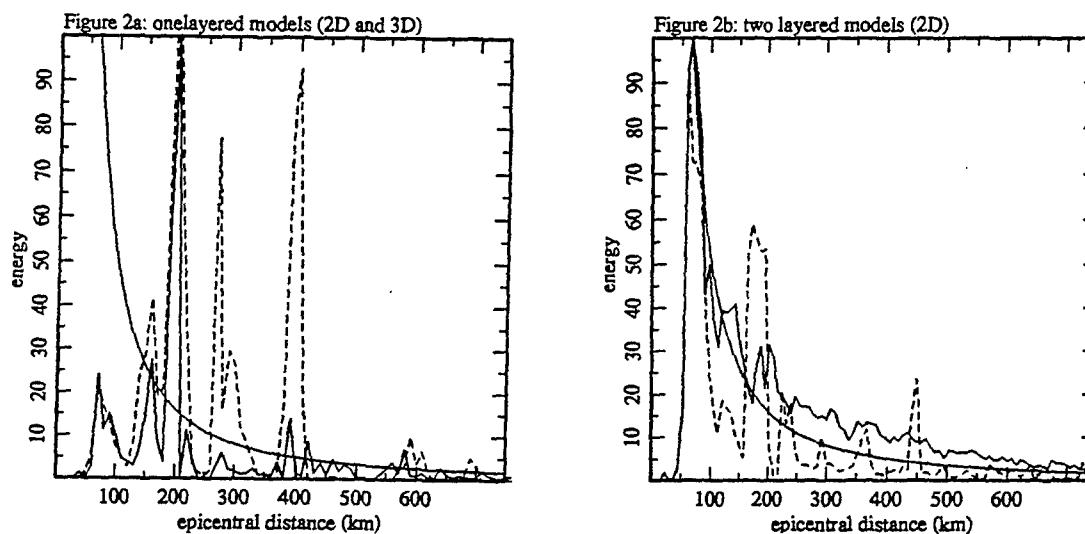
Figure 2a. Energy distribution for a one-layered crustal model with undulating Moho (see text) for 2D (solid) and 3D (dashed) model. The decay of energy according to Nuttli (1973) is also shown (smooth curve).

Figure 2b. Energy distribution for same models as in figure 1: flat model (solid) and model with undulating discontinuities (dashed). The smooth curve is the decay of energy according to Nuttli (1973).
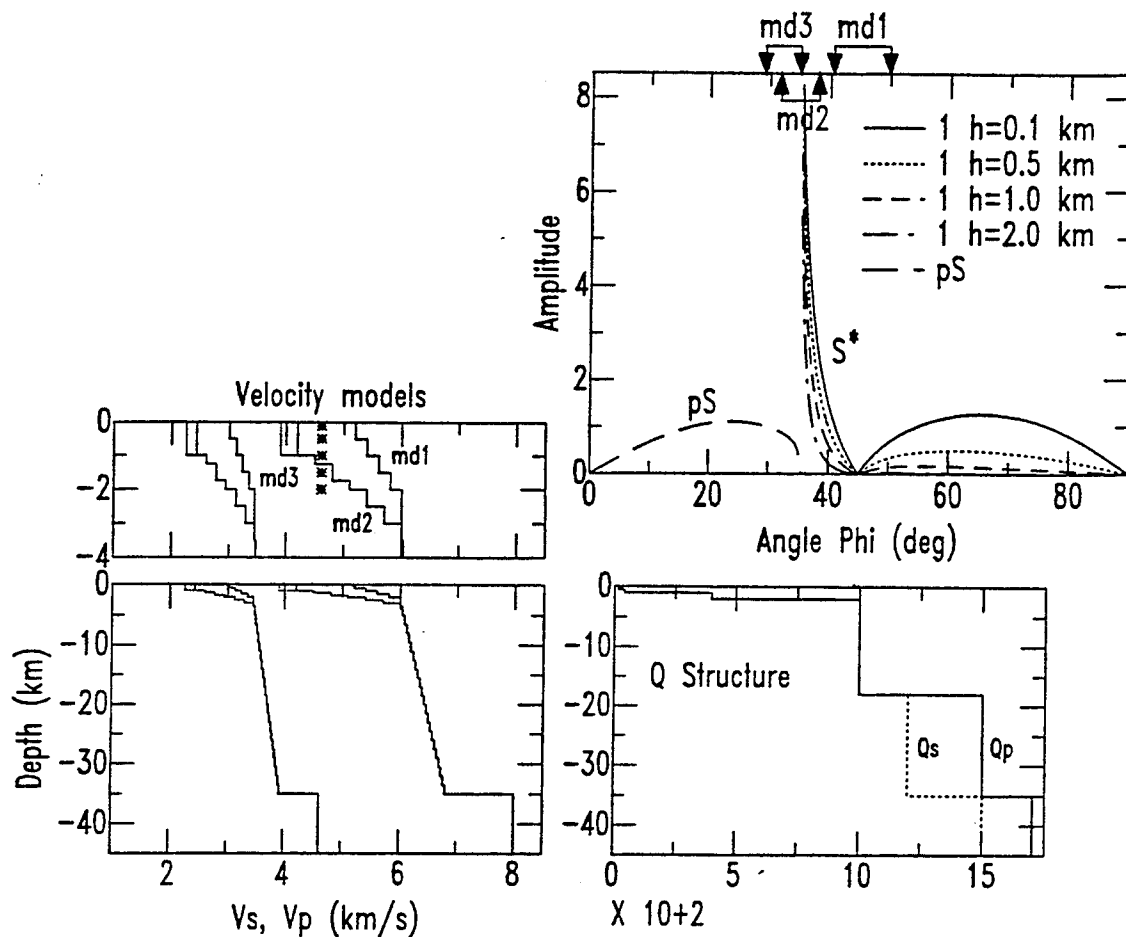
Figure 3. (upper right) S^* radiation pattern at 2 Hz, for various source depths in a medium with $\alpha = 4.2$ km/s. Velocity models (left) and Q structure (lower right) used in the synthetic calculations. Stars, representing some of the source depths used, are positioned at the sub-Moho S velocity, β_{mantle}.
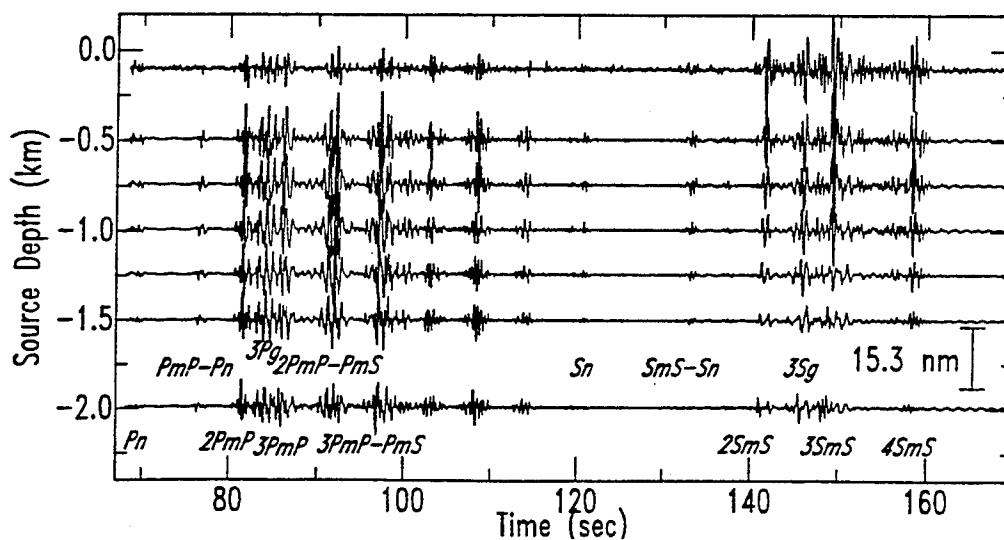
Figure 4. Vertical component synthetic displacement at 500 km distance from an explosion source at various source depths in model md2. The synthetics have a Nyquist frequency of 4 Hz and are convolved with a NORESS-type short-period instrument.
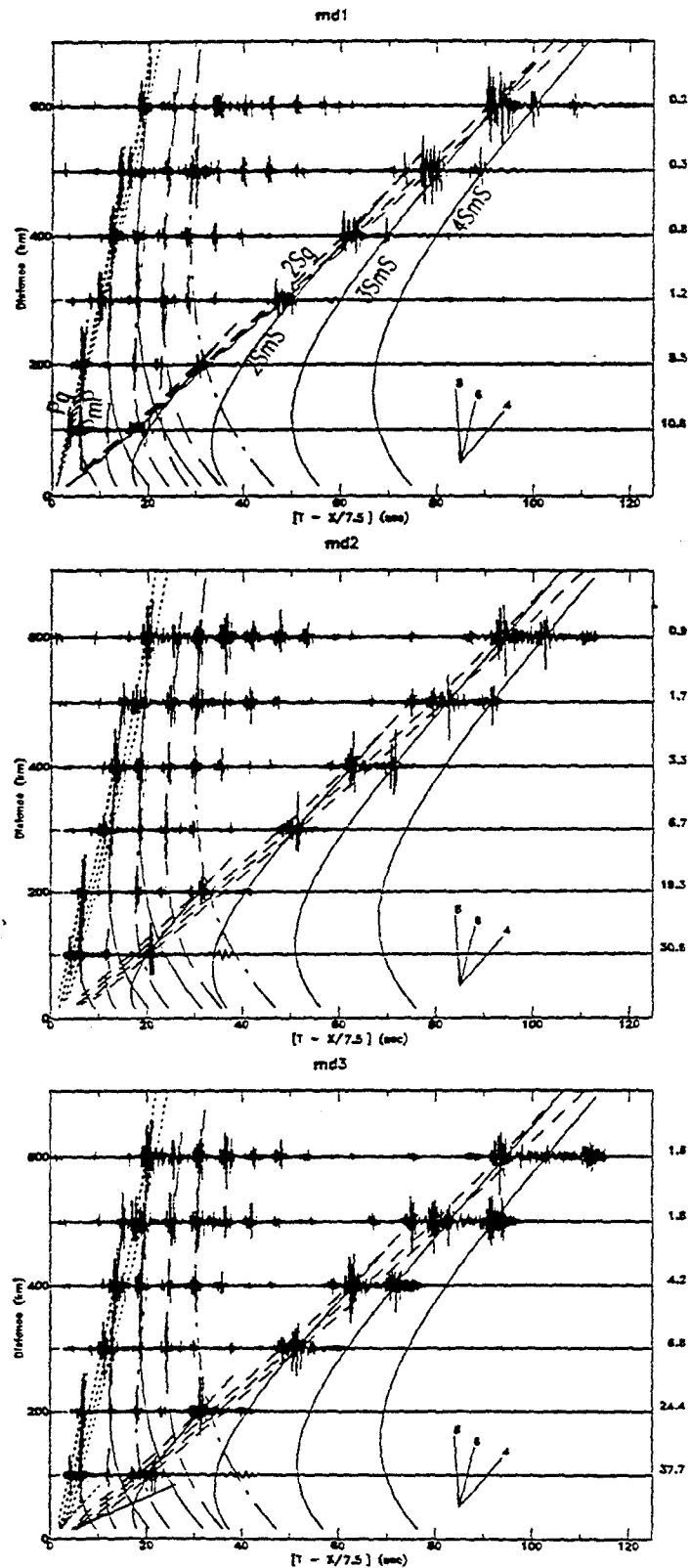
Figure 5. Vertical component synthetic record sections for an explosion depth of 0.5 km in the three models, md1, md2 and md3, with travel-time curves for the major phases superimposed. Amplitudes are normalized to their maxima, shown at the right of each trace. Slopes on the travel-time curves can be read from the velocity template in the lower right corner.

Event Location and Characterisation

B.L.N. Kennett
Research School of Earth Sciences, Australian National University,
Canberra ACT 0200, Australia

ABSTRACT

The accurate location and subsequent characterisation of seismic events is a primary requirement of any verification regime for a test ban treaty. Such procedures depend on the use of good models for the propagation of seismic waves and also accurate picks for identified seismic phases.

An improved radial model of Earth structure has been developed, model *ak135* which provides a very good fit to the empirical travel times for a wide range of seismic phases. The improvements in fit to *S* phases and core phases compared with *iasp91* or *sp6* should improve the accuracy of location procedures exploiting later phases. This representation of the major contribution to teleseismic arrivals needs to be supplemented by correction procedures to allow for the main sources of lateral heterogeneity within the Earth. Ellipticity corrections have been developed for the *ak135* model for a very wide range of phases. A regionalised model for upper mantle corrections is under development as part of a hierarchical scheme of corrections to allow for different influences on the travel times of a wide range of seismic phases.

Precision location requires a good representation of the Earth and also accurate and correctly identified time picks for seismic phases. We have been developing automatic phase detection and recognition procedures which can help with the association of seismic arrivals for use in the location procedures. A pattern recogniton approach has allowed the extraction of phase wavelets whose character can be recognised through the interaction of a number of energy measures applied to three component waveforms.

Subsequent activity will be directed to try to improve the estimation of the depth of seismic events by integrating knowledge of waveform characteristics with estimation of source character.

Event location and characterisation

1   OBJECTIVE

The accurate location and subsequent characterisation of seismic events is a primary requirement of any verification regime for a test ban treaty. Such procedures depend on the use of good models for the propagation of seismic waves and also accurate picks for identified seismic phases.

The objectives of this work are to provide a set of tools which can help with both event location and characterisation. Firstly, through an improved representation of the main radial structure of the Earth and an effective correction procedure for upper mantle heterogeneity. Secondly, through the development of phase detection and recognition procedures which can help with the association of seismic arrivals for use in the location procedures. Thirdly, to try to improve the estimation of the depth of seismic events by integrating knowledge of waveform characteristics with estimation of source character.

2   RESEARCH ACCOMPLISHED

2.1   Earth models for earthquake location

Current methods of locating seismic events depend on the availability of travel-time tables for the major seismic phases which are then supplemented by corrections to allow for lateral heterogeneity within the Earth. Kennett & Engdahl (1991) developed a new radial earth model *iasp91* which was designed for use in event location and phase location by providing a computational summary of observed travel times. The *iasp91* model was best constrained in the mantle and the fits to core phases were not as close as would be desired for optimum utility in location.

New empirical travel-time curves for the major seismic phases, have been derived from the catalogues of the International Seismological Centre by relocating events by using *P* readings, depth phases and the *iasp91* travel times, and then re-associating phase picks for later arrivals. A smoothed set of travel-time tables has been extracted by a robust procedure which gives estimates of the variance of the travel times for each phase branch. This set of smoothed empirical times is then used to construct a range of radial velocity profiles which have been assessed against a number of different measures of the level of fit between the empirical times and the predictions of the models. These measures were constructed from weighted sums of L_2 misfits for individual phases. The weights have been chosen to provide a measure of the likely reliability of the picks for the different phases. The empirical travel-time information has been supplemented by differential times between the various branches for *PKP* picked from broadband digital records.

A new radial model *ak135* has been proposed (Kennett, Engdahl & Buland, 1995) which gives a significantly better fit to the travel-times for a broad range of phases
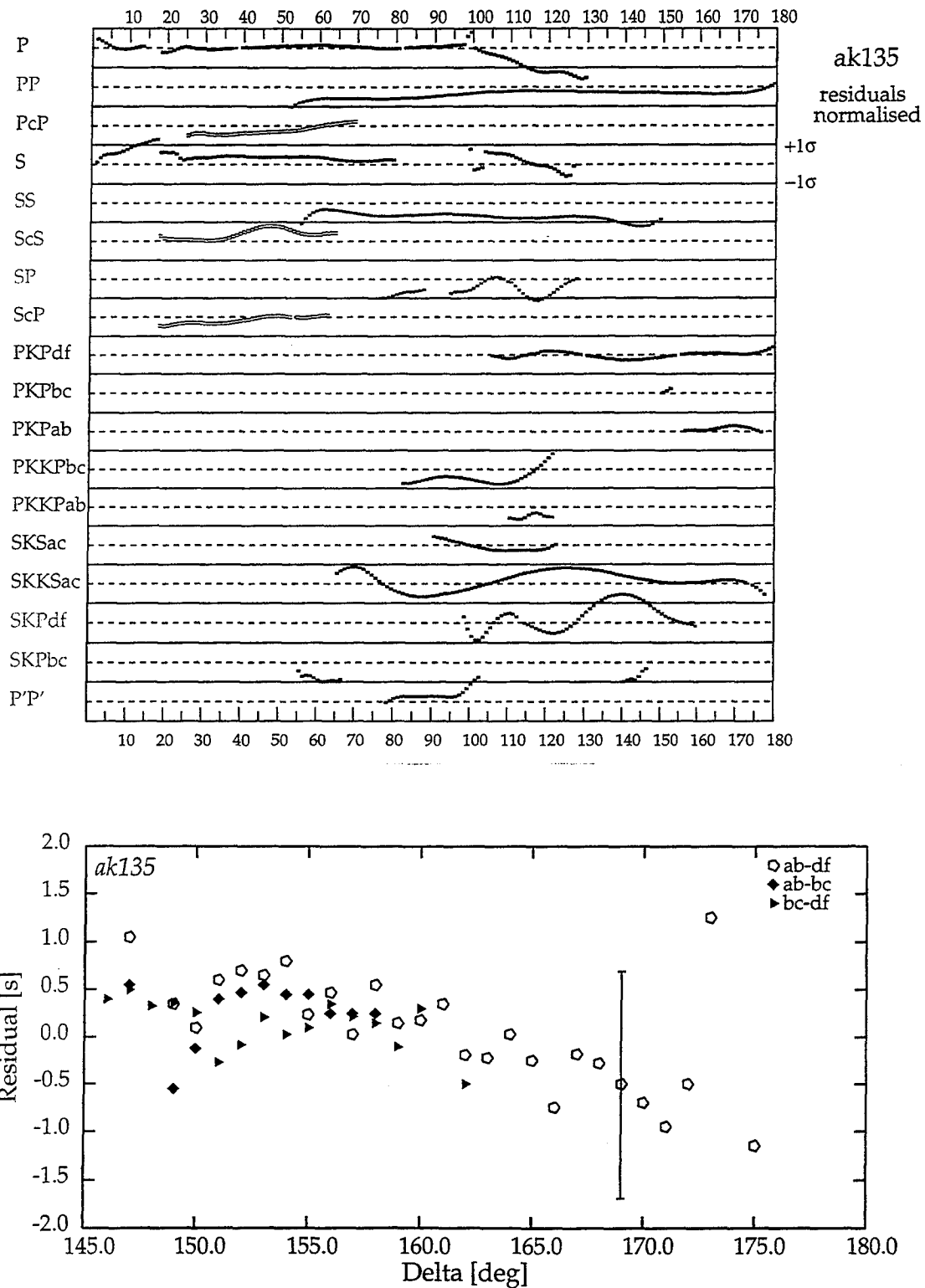
Figure 1. (a) Composite display of the normalised residuals between the travel times predicted for model *ak135* and the smoothed empirical travel times. (b) Differential travel time residuals for core phases for model *ak135* the medians over one degree cells are displayed for each branch.

than is provided by the *iasp91* and *sp6* models. The differences in velocity between *ak35* and these models are generally quite small except at the boundary of the inner core where reduced velocity gradients are needed to achieve satisfactory performance for *PKP* differential time data. The fit achieved with the new *ak135* model to the times for a broad range of phases is illustrated in figure 1, along with the fit to the differential times. A very good fit is achieved to most classes of phases but there are some systematic differences for the surface reflected phases such as *PP, SS* and *SP* which are sensitive to the assumptions made about shallow structure. The model *ak135* retains the same class of upper mantle structure as *iasp91* and is oriented towards a continental structure.

The potential resolution of the velocity structure within the Earth from travel-time information has been assessed with the aid of a nonlinear search procedure in which 5000 models have been generated in bounds about *ak135*. Misfit calculations are performed for each of the phases in the empirical travel-time sets and the models are then sorted using different overall measures of misfit. The best 100 models for each criterion are displayed in a model density plot which indicates the consistency of the different models. The interaction of information from different phases can be analyzed by comparing the different misfit measures. Structure in the mantle is well resolved except at the base, and *ak135* provides a good representation of core velocities.

For global use, the travel-times for the various phases need to be corrected for the influence of the ellipticity of the earth on the propagation path from source to receiver. A full set of ellipticity corrections have been tabulated for all the major phases represented in the *iasp* software.

2.2 Corrections for lateral heterogeneity

A radial earth model such as *ak135* provides a good general description of seismic wave propagation, but the presence of lateral heterogeneity within the Earth leads to systematic errors when seismic events are located. Such errors persist even when the geographic distribution of recording stations provide good azimuthal coverage and are particularly pronounced when locations are determined from a limited number of stations. In the likely verification regime of a test ban treaty, it will not be possible to rely on the statistical effects of large numbers of stations as in the current procedures employed by NEIC and ISC at the present time, but instead there needs to be some way of compensating for the major components of lateral heterogeneity. Since the most accurate location procedures will also make use of a wide variety of seismic phases any correction scheme for lateral heterogeneity should be physically based and adaptable to different classes of wave propagation process.

A hierarchical approach to such a correction scheme is being developed in which a total time correction for a phase is assembled from a number of different constituents. For teleseismic events, at least, the dominant lateral heterogeneity arises in the upper mantle and so the upper mantle contributions to both the near-source and near-receiver portions of the propagation path have to be estimated. An initial correction scheme is being based on a regionalised model of the upper mantle based on tectonic character, which exploits recent advances in the representation and interpolation of three-dimensional fields represented via Delaunay tetrahedra. In the regionalised model the structure for each tectonic province is represented via a radial velocity model and smooth interpolation occurs across a transition zone between regions. Ray-tracing
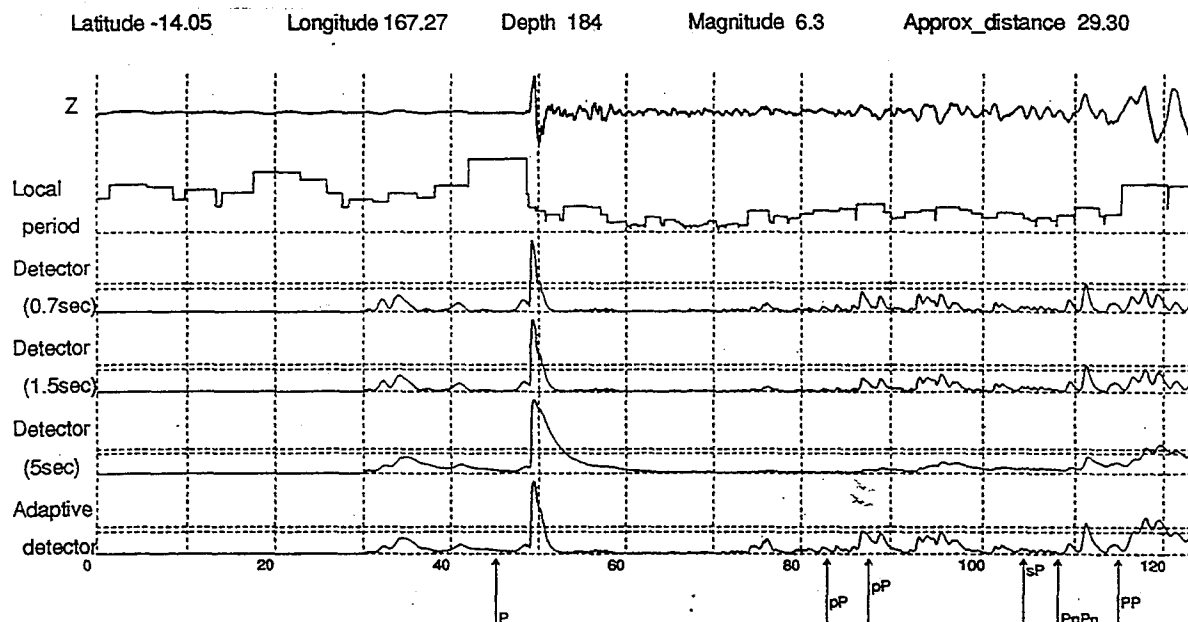
Figure 2. Comparison of phase detectors based on fixed window lengths with an adaptive detector exploiting information on local frequency.

through this simple model provides source-end and receiver-end corrections for upper mantle structure for either *P* or *S* wave legs. Superimposed on these corrections we can then have station specific terms designed to compensate for crustal structure or station elevation.

2.3   Phase recognition

The location of seismic events can be improved if accurate picks can be assigned for later seismic phases, which requires both the detection of an arrival and the recognition of its character. Such phase identifications are particularly valuable if they can be provided in real-time as the seismic disturbance passes across a broadband seismic recording station.

This problem of automatic phase recognition plays an important role in seismogram interpretation, especially in the context of the rapid analysis of large volumes of data in a verification regime. Two different pattern recognition problems are involved. Firstly, we need to separate seismic signals from background noise; then we try to recognise the difference between phase wavelets. Due to the wide range of frequencies for different phases in a broadband seismogram, phase recognition is a context sensitive problem.

An automatic analyzer has been developed which is adaptive to the local waveform background (Tong 1995). The analyzer works on single seismic components using concepts from work in artificial intelligence (especially pattern recognition (Tong, 1995). A seismogram is recognised as a hierarchical structure of subunits - waveform segments - and the features characterising a phase are extracted via a structural analysis.
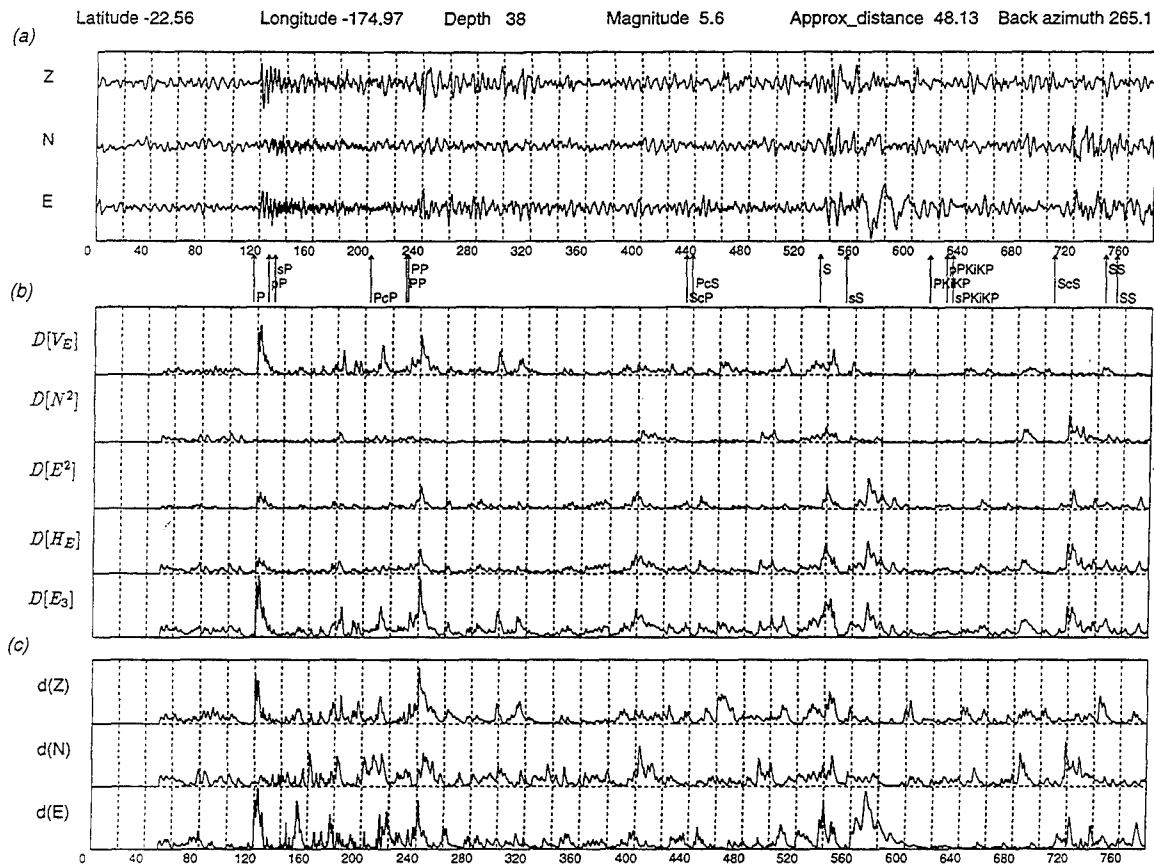
Figure 3. Analysis of broadband records for a shallow Kermadec event recorded in Northern Australia (time scale in seconds): (a) unfiltered broadband records, with indications of the predicted times for phase arrivals using the *iasp91* traveltime tables, (b) phase detectors based on an LTA measure based on total energy and STA measures for various energy contributions from the three-component traces, (c) single component STA/LTA detectors applied to each of the three components separately.

The automatic analyzer recognises the contiguity of an appropriate set of waveform segments and uses this to assign an estimate of the local frequency on the seismic trace. This local frequency information is then used to update the parameters of an STA/LTA phase detection procedure (Fig 2). Following a detection, the pattern recognition analysis separates out the phase contribution by the pattern of waveform segments and then attempts to characterise the extracted phases with a standard Gabor wavelet described by a set of five parameters. The whole analysis procedure requires just a few input parameters and can be accomplished swiftly enough to allow continuous real-time operation.

The analysis procedure is adaptive and can be successfully applied to broadband records with a wide range of frequency content. By coupling the analysis procedure with real time filtering very good results for phase detection and characterisation can be

achieved for weak distant events. The characterisation of phase segments also provides useful information for the comparison of seismograms and is being investigated as a tool for the comparison of observed and synthetic seismograms.

A simple but promising scheme for identifying the physical character of phase arrivals can be constructed by analysing the energy content of the seismic trace as a function of time (Tong & Kennett, 1995). This approach can be used to detect arrivals by comparing the short-term average energy to a long-term average, with averaging windows that are adaptive to the local frequency of the seismic disturbance based on the use of real-time pattern recognition applied to the seismic traces. The phase detector can be tuned to different classes of arrivals by utilising three-component records (fig 3). By comparing the energy on the vertical component of motion to that in the horizontal plane, it is possible to start to separate *P* and *S* arrivals. Phase assignments can be refined by the use of adaptive filtering and by including polarisation information.

With an estimate of the azimuth of propagation it is possible to use approximate projection methods which attempt to compensate for the influence of the free surface (Kennett 1991), since the surface corrections are not a strong function of slowness for teleseismic arrivals. By this means an instantaneous estimate can be made of the relative contributions of *P, SV* and *SH* arrivals which can be very helpful in determining the phase assignment for a particular arrival.

3   FUTURE PRIORITIES

The priorities for future work are to refine location procedures to provide a rapid means of including the influence of lateral heterogeneity within the Earth, and to improve constraints on depth estimation especially for shallower events where the depth phases are not distinct.

The use of regionalised models represents a starting point for a more realistic representation of three-dimensional structure within the upper mantle, derived from a tomographic style inversion. A lower resolution global inversion coupled to a high resolution representation of subduction zones is currently being undertaken to study subduction zone structure but can be readily adapted for location studies. A interesting problem is the appropriate way of filtering the velocities derived from tomography to provide the most effective model for location. It will also be necessary to introduce a priori information in those regions of the upper mantle such as much of the ocean basins for which current sampling by propagation paths are inadequate. Rapid ray-tracing procedures for three-dimensional models will be based on the Delaunay tessellation procedures used to represent the heterogeneous models to allow the testing of simpler correction procedures based on perturbation theory.

For the problem of depth estimation, the most promising route is to make use of comparisons between observed and synthetic seismograms. However this requires an adequate knowledge of the source mechanism. For larger events a number of different techniques can be employed to obtain a point source description of a source. However, for small shallow events the potential resolution of the source mechanism is limited. The inversion procedure needs to couple the source mechanism and depth problem and to try to obtain multiple constraints by exploiting the waveforms and relative amplitudes of many different phases.

ACKNOWLEDGEMENTS

References

Kennett, B.L.N., 1991. The removal of free surface interactions from three-component seismograms, *Geophys. J. Int.*, **104**, 153–163.

Kennett, B.L.N., & Engdahl, E.R., 1991. Traveltimes for global earthquake location and phase identification, *Geophys. J. Int.*, **105**, 429–465.

Kennett B.L.N., Engdahl E.R. & Buland R., 1995. Constraints on seismic velocities in the Earth from travel times, *Geophys. J. Int.*,

Tong C., 1995. Characterisation of seismic phases - an automatic analyzer for seismograms, *Geophys. J. Int.*, in press

Tong C. & Kennett B.L.N., 1995. Towards the identification of later seismic phases *Geophys. J. Int.*, in press

DETECTION, LOCATION AND DISCRIMINATION OF SEISMIC EVENTS BY THE SEISMIC NETWORK OF ISRAEL

A. Shapira, Y. Gitterman, V. Pinsky and A. Malitzky
Seismology Division, The Institute for Petroleum Research and Geophysics,
Holon, Israel.

ABSTRACT

The Israeli Seismic Network (ISN) consists of 36 short period stations distributed throughout the country. In addition, a Broad Band station is operating at the geophysical observatory near Bar Giyyora, Israel (BGIO) and a small aperture seismic array is under construction in the central Negev desert. The ISN is a regional network which aims to monitor the seismicity in the area bounded by latitudes 27.0N - 36.0N and longitudes 32.0E - 38.0E. It is tuned to detect all seismic events of magnitudes ML>2.0 occurring in Israel. Triggered events are routinely analyzed, yielding a seismological bulletin which provides the seismic event source parameters and classifies the events as earthquakes, explosions, possible explosions and distant events. The detection capabilities of the ISN within Israel is proven to be ML>2.0. In many locations around the country, the threshold magnitude is as low as 0.5. Comparisons of the detection performance of the ISN with those of other international organizations has shown the superiority of the ISN in monitoring the eastern Mediterranean and Middle East regions. Less than 10% of the events detected by the ISN are local and regional earthquakes. Most of the detected events are quarry blasts in Israel, Lebanon and Jordan and detonations associated with infrastructure developments. Sonic wave detectors are used to identify quarry blasts. In parallel, ground truth information is used do develop analytical procedures for discrimination. Presently, the azimuth-invariant, low-frequency spectral modulation method is used to identify the quarry blasts and underwater explosions (UWE) caused by ripple firing and bubbling effects, respectively. Furthermore, spectral ratios of the seismic energy between the low frequency band (1-6 Hz) and the higher band (6-11 Hz) are found useful in discriminating between micro-earthquakes and UWE.

Key Words: detection, location, discrimination, seismic network, spectral
             discriminants

INTRODUCTION

The Israeli Seismic Network (ISN) was constructed in 1980, starting with analog recording of about 16 stations. Since 1984, data acquisition has been based on computerized systems. At present, the ISN consists of 36 short period stations distributed throughout the country (see Fig. 1). Six stations are equipped with three component seismometers, whereas the rest are vertical component stations. Continuous analog data from the stations are transmitted by FM telemetry to the central recording site at the Institute for Petroleum Research and Geophysics (IPRG) in Holon. There, the data are digitized (50 samples per second) and checked for event detection. Triggered events are routinely analyzed, yielding a seismological bulletin which provides the seismic event source parameters: origin time, hypocenter coordinates, local and body wave magnitudes, seismic moment, stress drop and radius of the rupture area. Earthquake events are classified as earthquakes, explosions, possible explosions or distant events. The ISN has been designed to monitor only the seismicity of the region and, as such, the Israeli Data Acquisition System (ISDA) is tuned to detect all seismic events of magnitude ML>2.0 which occur in and around Israel.

Bulletin information is provided for the area bounded by latitudes 27.0N - 36.0N and longitudes 32.0E - 38.0E. Events which occur outside this area are not usually analyzed, except for measuring their arrival times at the ISN stations. During 1994 a Broad Band station (an STS2 seismometer and a Quanterra data logger) were installed at the Geophysical observatory near Bar Giyyora, Israel (BGIO). This is currently the only long period station in the region. The data are routinely transferred to the GEOFON network center in Germany, which then makes them available worldwide.

During the past few years we began investigating the capabilities of a local seismic microarray. A simplified experimental version of a short-period vertical component seismic microarray was installed on one of the mountains in the Galilee. During the few months of its operation, we have mastered classical data processing techniques using microarray and have developed a new algorithm for interactive analysis based on phase correlation computations. Encouraged by preliminary results, a new microarray is being installed in central Negev desert.

The following paper provides general descriptions of the methods implemented by the IPRG Seismology Division to detect and locate seismic events and to discriminate explosions from earthquakes. Preliminary results from the microarray as well as preliminary estimations concerning the detection capabilities of the ISN are also presented.

DETECTION OF SEISMIC EVENTS

On line event detection is performed by the ISDA system. The algorithm used is, basically, the detection algorithm developed by Johnson (1979) and slightly modified, i.e. weighting the possible contribution of one-sided pulses in STA and LTA computations and rejection criteria for signals which arrive on the same radio frequency. The detection coefficients have been defined by trial and error, comparing the detection performance of the ISDA with identifications made by seismologists on
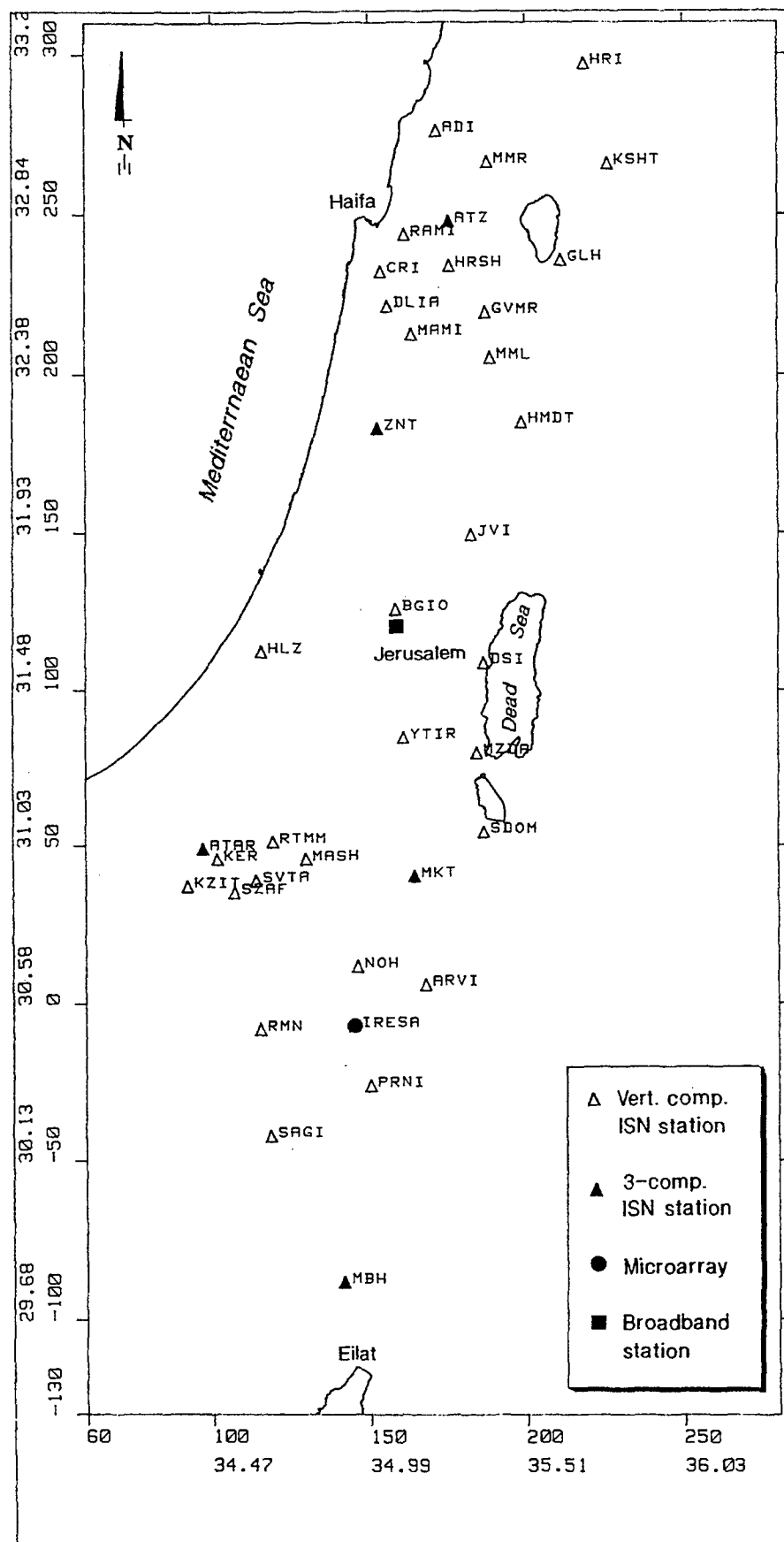
Fig.1 The Israel Seismic Network

continuous analog paper recordings. It has been our aim to ignore small quarry blasts and infrastructure work (which rapidly filled our disks and back-up tapes). Consequently, the ISDA has been tuned to detect only events with magnitudes higher than 1.9 (local scale). Shapira (1992) demonstrated that the detection capabilities of the ISN meet these requirements. It should be noted that in some areas within Israel, either for monitoring a candidate site for a nuclear power plant or for special studies of active faults, a dedicated local network has been installed (usually composed of 6-10 stations) and the magnitude threshold in such cases is much lower; depending on the background noise, it could be $ML \approx 0.5$.

During the last year, interest in detecting seismic events from outside Israel has increased. The JSOP experiment during September-November, 1994 provided some data for a preliminary assessment of ISN detectability. The JSOP (Joint Seismic Observation Program) has been initiated by the USGS, UNESCO and the Council of Europe (through the EMSC-European Mediterranean Seismological Center) to perform seismic monitoring of the Middle East and eastern Mediterranean regions jointly by the seismological centers of Turkey, Lebanon, Cyprus, Israel, Jordan, Egypt, Saudi Arabia and Yemen. The map in Fig. 2 shows the events reported as $ML>3.0$ by at least one of the participating institutions during the period of the experiment and also events not triggered by the ISDA. Evidently, the detectability of the ISN, within regional distances, is azimuth dependent showing lower sensitivity for events directly north or south of Israel. This azimuthal effect is attributed to the elongated, north-south shape of the network. At present, the ISN is the most sensitive seismic network for detecting and locating events in the Middle East.

Another, qualitative, assessment of the importance of the ISN as regards seismic monitoring in the east Mediterranean and the Middle East is inferred from the comparison between the ISN bulletin and recently reported bulletins of the IDC, Washington and the PDE (NEIC, Colorado). During January - April 1995, of the 68 seismic events of magnitude $ML>2.5$ were reported by the ISN for the region 27.0N - 36.0N and 32.0E - 38.0E, only 56% of them were reported by NEIC and IDC. The detection and location capabilities of the ISN within regional distances are currently being re-evaluated after completion of the JSOP data and unification of the data formats by EMSC.

Beyond this region, the detection capabilities of the ISN have not been fully investigated. One of the major obstacles is the lack of a reference system which should include all events above magnitude 3. Nevertheless, as a first order approximation, using PDE data from NEIC for the period 1990-1994, we have analyzed the statistical distribution of the parameter γ_0 satisfying the condition $\gamma_0 > \gamma_i$, given that for any event i:

$$\gamma_i = \frac{10^{m_b}}{\Delta^2} \qquad (1)$$

where Δ is the angular epicentral distance.

As shown in Fig. 3, the 50% and 90% probability levels are $\log \gamma_0 = 1.8$ and $\log \gamma_0 = 3.0$, respectively. However, it should be emphasized that the ISN
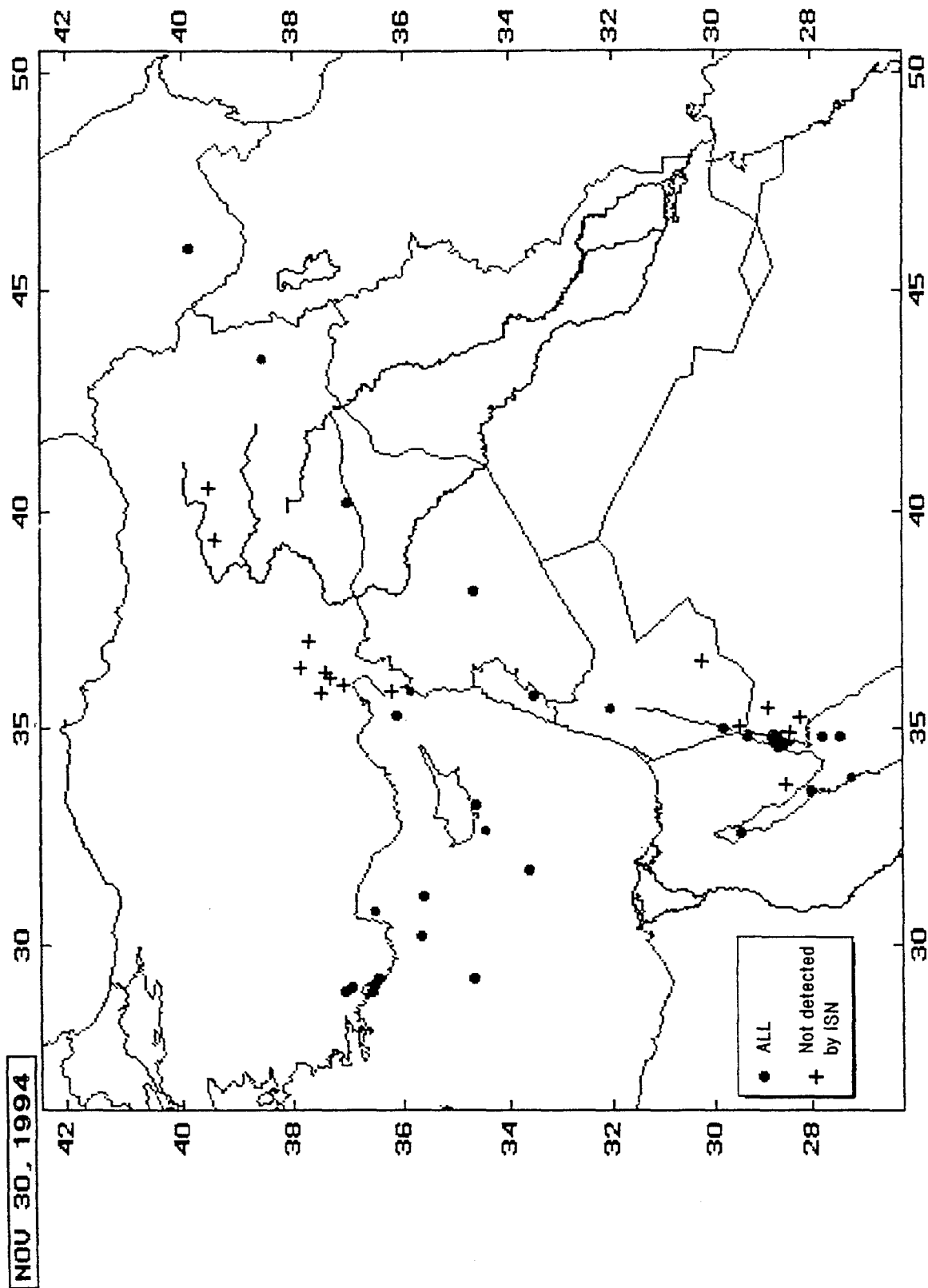
Fig.2 A map of events ($M_L \geq 3.0$) reported during the JSOP experient

NOV 30, 1994

ALL ●
Not detected +
by ISN
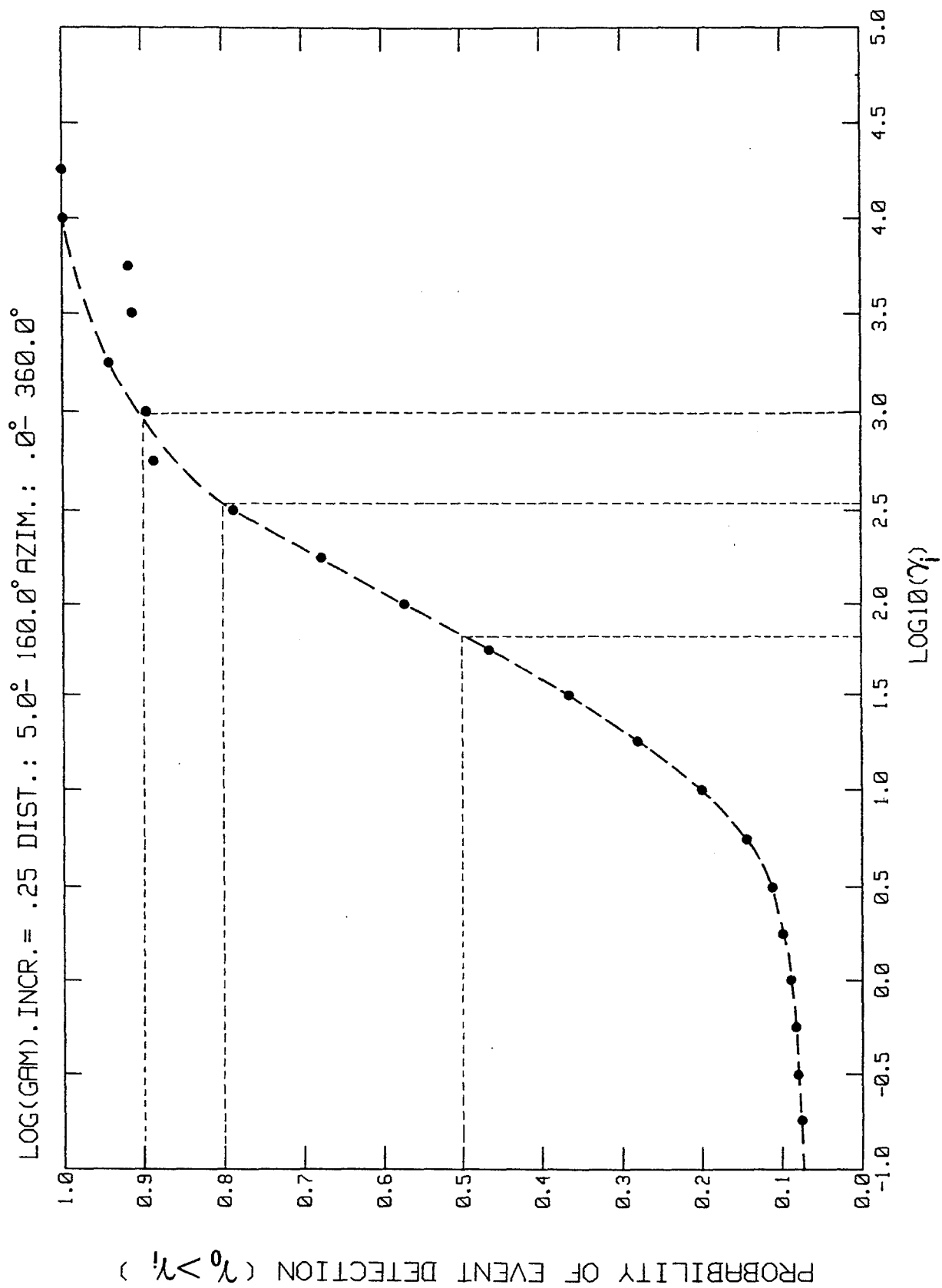
Fig.3 The distribution of a parameter γ

is not currently tuned to detect distant events. With regard to teleseismic distances, the ISN as a system is definitely less sensitive than individual low-noise stations within the ISN. Consequently, the seismic microarray is expected to perform as a much improved detector of events at distances $\Delta > 10°$. Although this statement has not yet been tested, it can be judged by comparing the response curve (Fig. 4) of a typical station in the microarray with that of the most sensitive station in the ISN (station PRNI).

LOCATION OF SEISMIC EVENTS.

The location procedure routinely applied by IPRG is based on a search algorithm (Shapira, 1976, 1980). It is a little more time consuming compared with other procedures (e.g. the Geiger method or Simplex procedure), but is much less affected by the multi-minima behavior of the rms time-residual function. Lacking a basis for comparison, it is difficult to estimate the true uncertainty in the mislocation. Shapira and Du Plessis (1989) demonstrated that, in most cases relevant to ISN conditions, the statistical error estimations (i.e. the error ellipsoid) are questionable and not reliable. Comparing location results of quarry blasts in and around Israel, the accuracy in most cases is better than 3 km. (Location accuracies of quarry blasts in Israel are often better than 1 km).

During the recent JSOP experiment, we had the opportunity to compare ISN results with those obtained using data from neighboring countries (i.e. improving the spatial coverage). The differences are in the order of ±15 km. at epicentral distances of several hundred kilometer; however, as expected, ISN mislocations of hypocenters north and south of Israel are much higher. We have also compared ISN results with those provided by IDC and observed that most of the IDC location results in the region covered by the ISN are erroneous.

The small dimensions of the ISN are not suitable for locating distant events from first arrival measurements. To overcome this difficulty, we plan to incorporate the array techniques using the microarray as well as arrays of stations of the ISN in the analysis. Preliminary studies show that classical F-K analysis does not provide sufficiently accurate results and a new concept, based on the interactive process and phase-correlation procedure, is being tested. The new method has been tested on a few events recorded by the microarray and yield very accurate azimuth determinations (accuracy within 1°) and precise detections of the first P and S arrivals. Experiments in this direction will continue.

DISCRIMINATION OF SEISMIC EVENTS

Less than 10% of the events detected by the ISN are local and regional earthquakes. Most of the detected events are quarry blasts in Israel, Lebanon and Jordan and detonations associated with infrastructure developments. Ground true information from Israeli quarries is routinely collected and is used to verify location results and identifications made by the analysts. In the last year, sonic wave detectors have been installed at some of the ISN stations. The detector is merely a loudspeaker mounted in a resonance box. Many of the man-made events are detected by the loudspeakers, which are used to classify the event as an

917
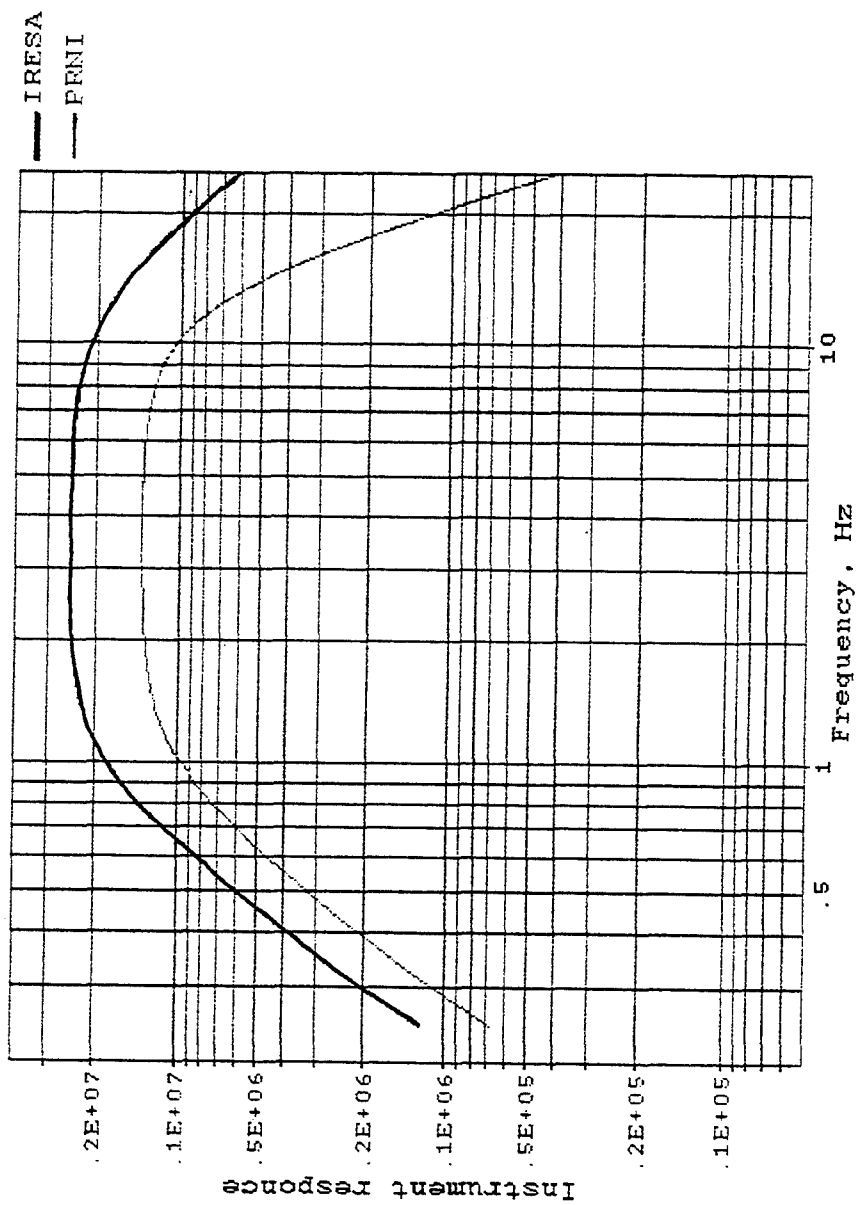
Fig.4 Response curves of the typical station in the microarray and station PRNI (most sensitive station in the ISN)

explosion. This technique is most useful in places where the source is within 40 km of the detector, mainly owing to the fact that the ISDA will trigger only additional 120 sec after the last trigger time.

Analytical discriminators for ISN operations have been tested by Gitterman and van Eck (1993) and by Gitterman and Shapira (1994). The azimuth-invariant, low-frequency spectral modulation (LFSM) method is used to identified the quarry blasts and underwater explosions (UWE) caused by ripple firing and bubbling effects, respectively. Strongly smoothed spectra yield coherent maxima and especially minima in the spectra at different stations, in accordance with the interference phenomenon of the reverberating or ripple firing source. Gitterman and Shapira (1993) also show that spectral ratios of the seismic energy between the low frequency band (1-6 Hz) and the higher band (6-11 Hz) are useful in discriminating between micro-earthquakes and UWE.

REFERENCES

Gitterman, Y. and T. van Eck, 1993. Spectra of quarry blasts and microearthquakes recorded at local distances in Israel, Bull. Seism. Soc. Am., 83:1799-1812.

Gitterman, Y. and A. Shapira, 1993. Spectral discrimination of underwater explosions, Isr. J. Earth Sci., 42:37-44.

Gitterman, Y. and A. Shapira, 1994. Spectral characteristics of seismic events off the coast of the Levant, Geophys. J. Int., 116:485-497.

Johnson, C.E., 1979. CEDAR - an approach to the computer automation of short period local seismic networks, Ph.D. disseration, Calififornia Institute of Technology, Pasadena, Ca.

Shapira, A. and M. Bath, 1976. Location of teleseisms from P- arrivals at the Swedish stations, Seismol. Inst., Uppsala, Report No. 9-76, 25pp.

Shapira, A., 1980. Guidelines for using program LOCHYP, IPRG Rep. S2/567/79-3.

Shapira, A. and A. Du Plessis, 1989. A semi-empirical analysis of hypocenter mislocations, Tectonophysics, 157:301-313.

Shapira, A., 1992. Detectability of regional seismic networks: analysis of the Israel seismic networks. Isr. J. Earth Science, 41:21-25,

PARAMETRIC MODELING AND DETECTION
OF RIPPLE FIRED SIGNALS

Robert H. Shumway
Allan D.R. McQuarrie

Division of Statistics
University of California
Davis, CA 95616

Abstract:

We develop a parametric statistical approach to detecting and estimating the delay and duration parameters of a ripple-fired signal. Such signals are generated by mining blasts with roughly equally spaced charges. Detection of the echo structure induced by ripple firing can serve as a basis for discriminating between mining blasts and nuclear explosions or earthquakes which, in principle, will not contain such echo effects.

The model assumes a noise corrupted signal that can be written as a convolution of source, path and instrument responses with a pulse sequence. The underlying responses are modeled by low order autoregressive moving average (ARMA) models that are consistent with conventional deterministic formulations of source theory and instrument response. The pulse sequence is modeled as a seasonal ARMA process, with the period corresponding to the firing delay and with a model order that is proportional to the signal duration. We use the cepstrum to suggest a range of values for the duration and delay parameters and then search all possible seasonal ARMA models within this range. The final model chosen is the minimizer of the corrected Akaike Information Theory Criterion (AIC_C).

Limited simulations are given to show that both the duration and delay can be estimated effectively with the seasonal ARMA search when the delays are equal and that reasonable estimators are available when the delays are variable. The methodology is applied also to the P phase of a single Scandinavian mining explosion where we obtain reasonable estimators for delay and duration under the assumption of ripple-firing.

Key Words: *Mining explosions, duration and delay, echo detection, cepstra, seasonal ARMA, model selection.*

OBJECTIVE

Regional seismic monitoring and discrimination capabilities that are desirable under a potential Comprehensive Test Ban Treaty (CTBT) can be improved by developing algorithms and new procedures for distinguishing between earthquakes, nuclear explosions and mining explosions of various kinds. Much effort in past discrimination studies has concentrated on extracting various features of the spectrum that are characteristic of earthquakes, nuclear explosions or mine blasts.

One particular spectral feature that characterizes some mining explosions is periodic modulation of the spectrum introduced by ripple-firing. A ripple-fired event involves detonation of a number of mining explosions that are often regularly grouped in space and time. Such explosions, known as quarry blasts, have low magnitudes that may be close to those of nuclear explosions that one might monitor under the CTBT. Hence, procedures for detecting ripple firing can serve as bases for discriminating between mining blasts and nuclear explosions or earthquakes. A number of authors have examined various aspects of this problem and have proposed techniques for analyzing these ripple-fired seismic signals (see Baumgardt and Ziegler, 1988, Hedlin et al, 1990, Chapman et al 1992).

The objective of this study is to develop robust statistical procedures for detecting and characterizing the echo structure induced by ripple-firing. This includes developing maximum likelihood in both the time and frequency domains for the purpose of estimating the parameters corresponding to the delay and duration of a ripple-fired signal as well as the spectrum representing source, path and instrument responses that will be convolved with the ripple-fired signal. We use modern model selection techniques based on Akaike's Information Theoretic Criterion (AIC) to determine the number of pulses and their duration.

PRELIMINARY RESEARCH RESULTS

We have developed a time domain approach to the problem of detecting and identifying the echo parameters associated with a ripple-fired event. The underlying model assumes that a sequence of n signal pulses s_t separated by d will produce an observed process of the form

$$y_t = \sum_{j=1}^{n} \alpha_j s_{t-jd} + n_t \tag{1}$$

where n_t is an additive noise. The observed data is, therefore, characterized in terms of a series of scaled replicas of an underlying signal that last for a total *duration* $(n+1)d$ and are observed at delays $d, 2d, \ldots, nd$. The signal s_t is an underlying process, assumed to satisfy a low-order autoregressive moving average model of the form

$$s_t - \sum_{k=1}^{p} \phi_k s_{t-k} = w_t - \sum_{k=1}^{q} \theta_k w_{t-k}. \tag{2}$$

The characteristics of the signal process are determined by the p autoregressive parameters $\phi_1, \phi_2, \ldots, \phi_p$, the moving average parameters $\theta_1, \theta_2, \ldots, \theta_q$ and the variance σ^2 of the white noise process w_t. In the usual Box-Jenkins approach (see Shumway, 1988, Chapter 3) the model determined by (2) is identified as $ARMA(p,q)$. It is convenient to rewrite (1) and (2) using the backshift operator B, defined as $Bx_t = x_{t-1}$, and we obtain

$$y_t = \alpha_d(B)s_t + n_t \tag{3}$$

and

$$\phi(B)s_t = \theta(B)w_t, \tag{4}$$

where

$$\alpha_d(B) = 1 + \sum_{j=1}^{n} \alpha_j B^{jd}, \tag{5}$$

$$\phi(B) = 1 - \sum_{j=1}^{p} \phi_j B^j, \tag{6}$$

and

$$\theta(B) = 1 - \sum_{j=1}^{q} \theta_j B^j. \tag{7}$$

Now, substituting (4) into (3), we obtain

$$y_t = x_t + n_t \tag{8}$$

where

$$\phi(B)x_t = \theta(B)\alpha_d(B)w_t. \tag{9}$$

The observed process y_t is exhibited in (8) as the sum of noise and a multiplicative $ARMA$ process with a seasonal moving average $\alpha_d(B)$ of order n and season d. The process x_t is identified as the multiplicative seasonal $ARMA$, $ARMA(p,q) \times (0,n)_d$. Under this model scenario, the process of detecting a ripple-fired signal is reduced to looking for a multiplicative seasonal moving average component in an ARMA process, where the order corresponds to the number of pulses and the season corresponds to the delay.

The problem of motivating the model defined by (3) and (4) can be approached by appealing to Dargahi-Noubary (1995), who shows that most deterministic source models, including that of Von Seggern and Blandford (1972) can be generated by a stochastic model of the form (4) with $p = 2$ or $p = 3$ corresponding to the ω^2 and ω^3 models respectively if we take the operator as $(1 - \phi B)^p$. We shall not specialize the operator in hopes that the more general form (6) will help to adjust for instrument response and path effects. Furthermore, these effects can be further mitigated by adding general moving average components of order q.

Although the model suggested by (3) and (4) is not exactly $ARMA(p,q) \times (0,n)_d$ because of the additive noise term, it is well known that $ARMA$ signal plus noise models

are equivalent to pure $ARMA$ models with additional moving average components so we are justified in restricting candidates to models of the multiplicative form. What is required is estimating the ARMA parameters $\phi_1, \ldots, \phi_p, \theta_1, \ldots, \theta_q, \sigma^2$ as well as the amplitudes of the reflections $\alpha_1, \ldots, \alpha_n$. This can be done for a fixed p, q, n and d using nonlinear least squares on the residuals, minimizing

$$\hat{\sigma}^2 = T^{-1} \sum_t \hat{w}_t^2, \tag{10}$$

where w_t can be obtained by solving (9) successively, using y_t in place of x_t. There are generally, an unlimited number of values of p, q, n and d possible so we need a method for deciding which values are most reasonable. A common model selection criterion is the corrected form of Akaike's information criterion (see Hurvich and Tsai, 1989),

$$AIC_C = \log \hat{\sigma}^2 + \frac{T + p + q + n}{T - p - q - n - 2}, \tag{11}$$

where we choose the model that minimizes AIC_C. For the large sample used here, this measure gives the same result as the conventional AIC.

In order to illustrate the above methodology, we consider analyzing two contrived events and a single mining explosion from Scandinavia shown in Figures 1, 2 and 3. The contrived events were simulated by generating an $ARMA(2, 0)$ process of the form

$$s_t - s_{t-1} + .6s_{t-2} = w_t \tag{12}$$

for the signal with $\sigma^2 = 1$. This is Equation (2) with $p = 2, \phi_1 = 1, \phi_2 = -.6$. The process was added and delayed using

$$y_t = a_t x_t + n_t, \tag{13}$$

where

$$x_t = s_t + s_{t-8} + s_{t-16} + s_{t-24} + s_{t-32} \tag{14}$$

which is just a delayed signal with $n = 4, d = 8$, i.e. a signal with four pulses separated by 8 points, leading to a duration of 32 points. To make the output resemble an explosion, the $ARMA$ process was modulated by a function of the form $a_t = \theta_1 \exp\{-\theta_2 t\}$ with $\log \theta_1 = -7, \theta_2 = .01$. The second contrived event, shown in Figure 2 adds five pulses at irregular delays and noise n_t with variance $\sigma_n^2 = (.01)^2$. Figure 3 shows a P-phase from a presumed mining explosion recorded at FINESS in Scandinavia and given by Blandford (1993) in his Table 1.

To analyze these three examples, we search for the best $ARMA(p, q) \times (0, n)_d$ model using $AICC$ and the following general guidelines. The operators (6) and (7) that best emulate the convolution of source, path and instrument response, i.e. p and q in the model, are restricted to low orders. In this case, we took $p = 2, 3, q = 0, 1$, corresponding to values suggested by conventional source models and response functions. These low orders all do a respectable job of emulating the observed spectra. In order to limit somewhat the search over the seasonal components n and d, the spectra, log spectra and cepstra were
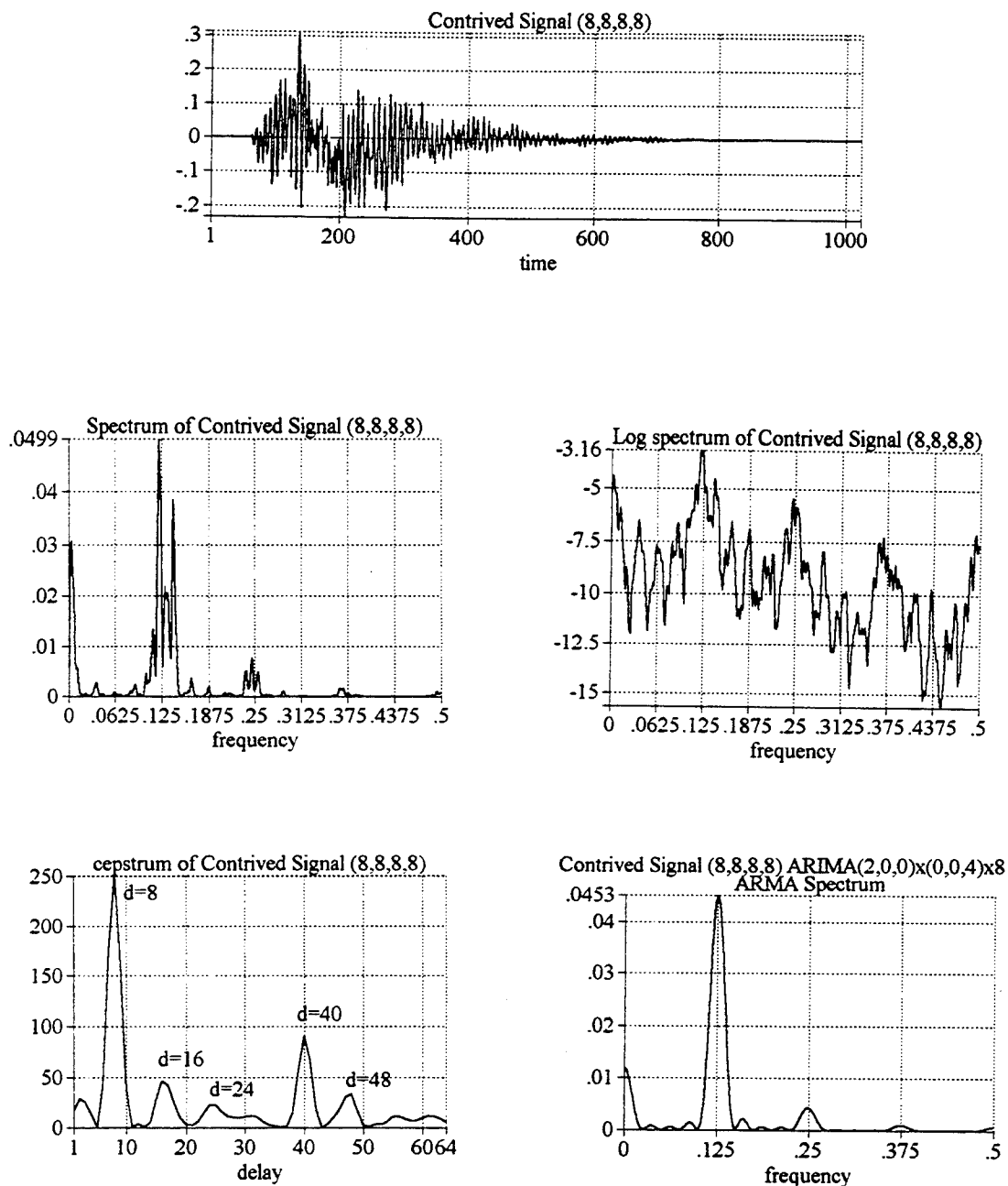
Figure 1. Analysis of a contrived signal composed by modulating an ARMA(2,0) process and delaying using 4 pulses separated by 8 points. Frequency is in cycles/point. Delay is in points.
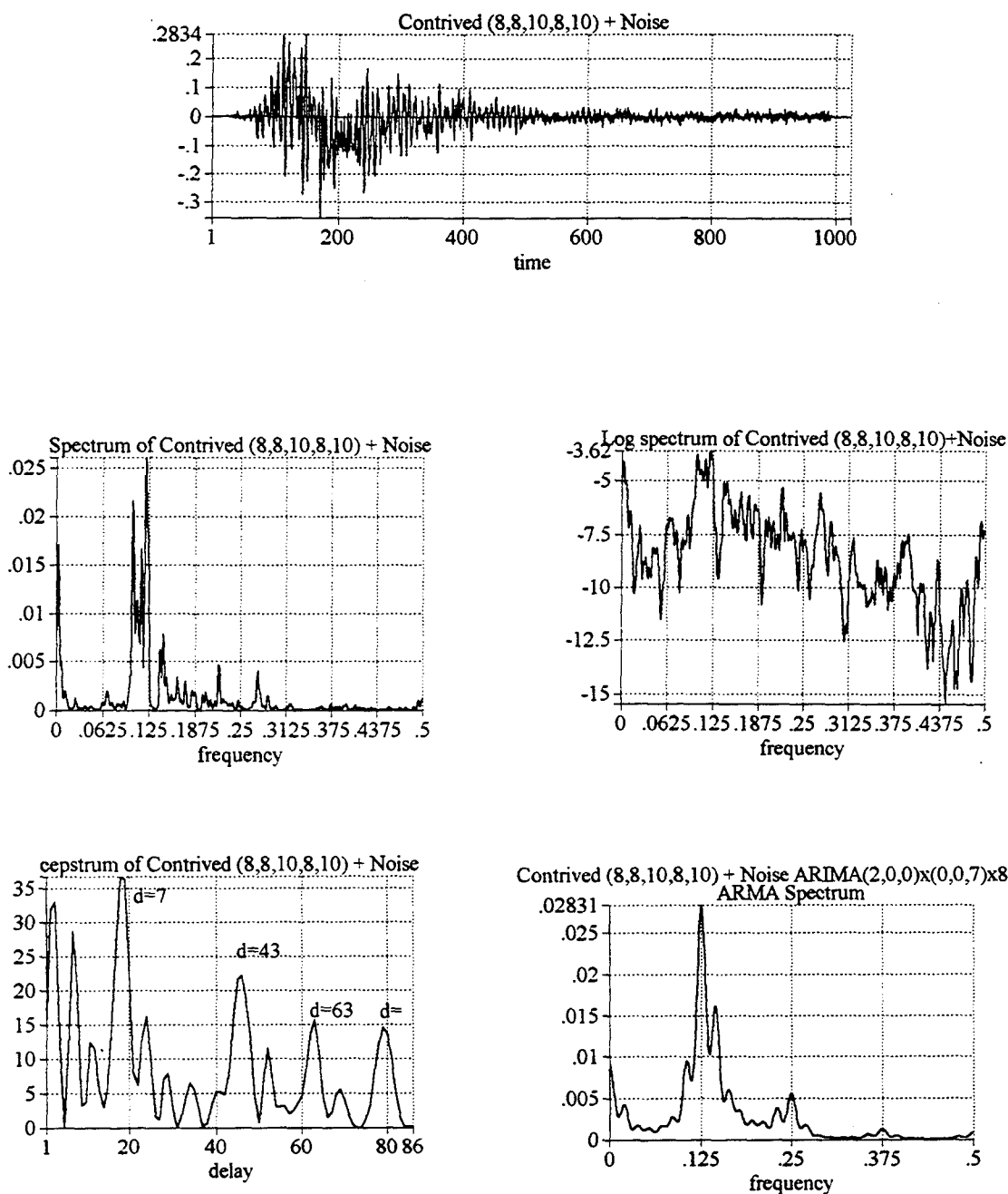
Figure 2. Analysis of a contrived signal composed by modulating an ARMA(2,0) process and delaying using 5 irregularly spaced pulses at intervals 8, 8, 10, 8 and 10 points with additive noise. Frequency is in cycles/point. Delay is in points.
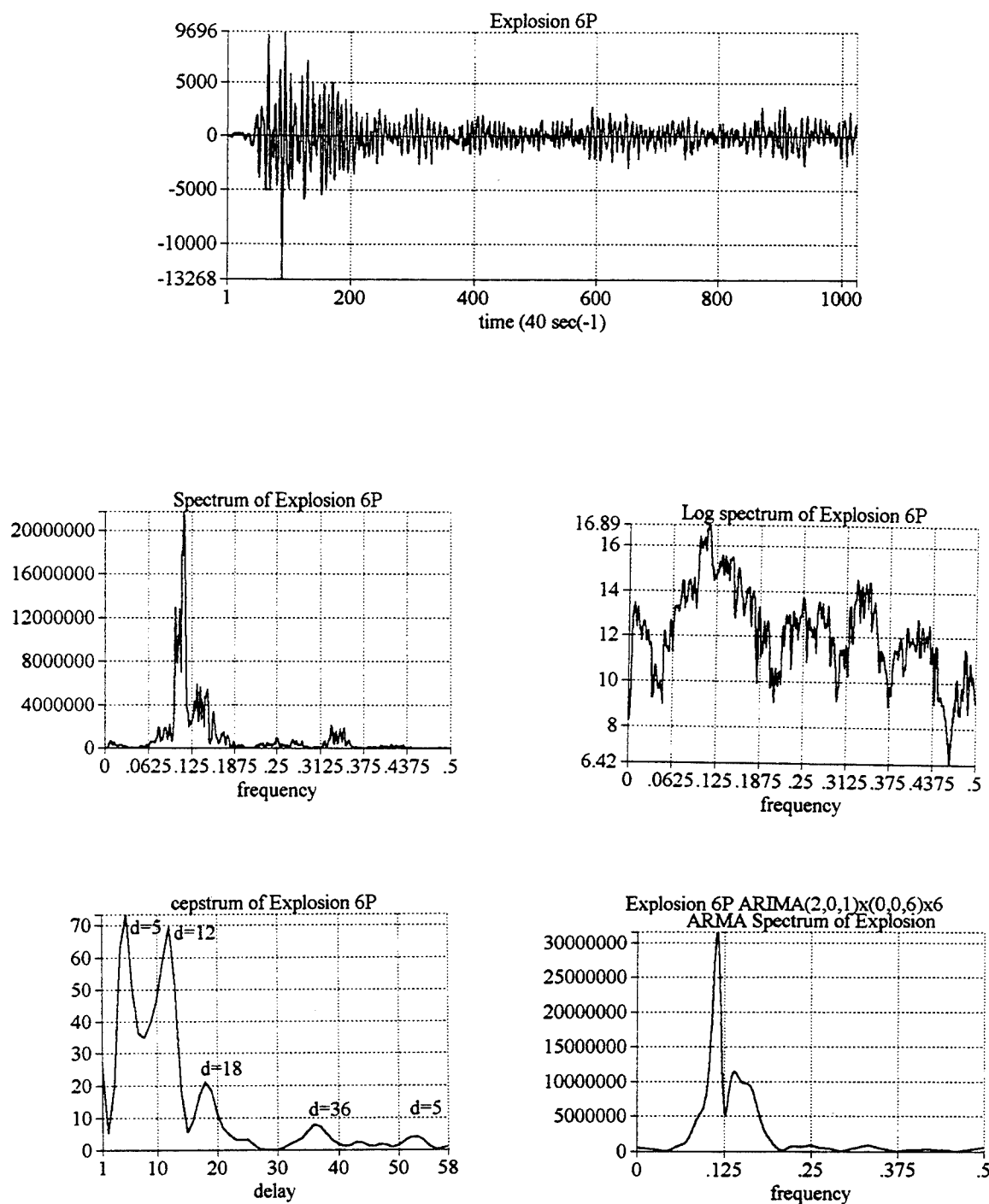
Figure 3. Analysis of a P-phase from a presumed mining explosion recorded at FINESS (F1A1) in Scandinavia (latitude 59.476, longitude 24.1442) dated 12/10/91 with local magnitude 2.59 (see Blandford, 1993, Table 1). Frequency is in cycles per point at 40 sec^{-1} so that the folding frequency corresponds to 20 Hz. Delay is in points or .025 seconds.

computed. The cepstrum, in particular, is helpful in suggesting values for n and d. For example see Bogert et al (1962) who suggested the cepstrum or Baumgardt and Ziegler (1988) who showed, by expansion, the periodicities in the spectrum expected when the spectrum of $x_t = \alpha_d(B)s_t$ is computed. Shumway and McQuarrie (1994) show that when $\alpha_1 = \alpha_2 = \cdots = \alpha_n$, the spectrum of x_t is

$$
\begin{aligned}
P_x(\omega) &= |\alpha_d(e^{-2\pi i\omega})|^2 P_s(\omega) \\
&= \frac{\sin^2(\pi\omega(n+1)d)}{\sin^2(\pi\omega d)} P_s(\omega),
\end{aligned} \tag{15}
$$

where $P_s(\omega)$ is the spectrum of the signal. The cepstrum, i.e. $\log P_x(\omega)$, then will be the sum of the logarithm of the signal spectrum and two other components with periods proportional to d, the delay and nd, the duration.

To begin, consider analyzing the first contrived series shown in Figure 1 which we know to be approximately $ARMA(2,0) \times (0,4)_8$ by inspecting the generating equations (12)-(14). This means that there are 4 pulses of length 8 points in the train leading to a duration of $5 \times 8 = 40$ points. Both the spectrum and the log spectrum show periodicities and we can see the two distinct components in the log spectrum. Computing the cepstrum shows main peaks at 8 and 40 corresponding to the delay and duration. To check the seasonal $ARMA$ search procedure, consider searching the models $ARMA(2-3, 0-1) \times (0, 3-8)_{5-12}$ which indicates looking at $2 \le p \le 3, 0 \le q \le 1, 3 \le n \le 8, 5 \le d \le 12$, i.e. low order $ARMA$ models with seasonal components between 5 and 12 and orders between 3 and 8. Table 1 shows the results obtained from the best seven models under the column Figure 1. We see that the minimum corrected AIC is for the correct model.

The best model has the form of (12)-(14) with the estimated parameters substituted, so that

$$
s_t - .97s_{t-1} + .60s_{t-2} = w_t
$$

becomes the signal model and

$$
x_t = s_t + .99s_{t-8} + .87s_{t-16} + .80s_{t-24} + .71s_{t-32}
$$

gives the estimated reflection pattern. Note that the coefficients are not all near unity because of the exponential modulation of the x_t in the observed data y_t. Table 1 also gives the next best six models and we note that all but one has the correct delay but that the number of pulses and hence, the duration changes. The spectrum implied by this $ARMA(2,0) \times (0,4)_8$ model is shown in Figure 1 and we note that it agrees quite well with the narrow band spectrum (1 % bandwidth).

927

Table 1. Model Summaries: $ARMA(p, q) \times (0, n)_d$

Figure	p	q	n	d	AIC_C
1	2	0	4	8	-7.2546
1	2	0	5	8	-7.2543
1	2	0	6	8	-7.2533
1	2	0	8	8	-7.2523
1	2	0	7	8	-7.2513
1	2	0	3	8	-6.8295
1	2	0	6	6	-6.2294
2	2	0	7	8	-5.7271
2	2	0	6	8	-5.7105
2	2	0	5	8	-5.7028
2	2	0	8	6	-5.6993
2	2	0	7	6	-5.6886
2	2	0	6	9	-6.6858
2	2	0	8	9	-5.6848
3	2	1	6	6	14.3649
3	2	1	4	6	14.3706
3	2	1	5	6	14.3714
3	2	1	3	6	14.3773
3	2	1	3	12	14.3830
3	2	1	4	12	14.3848
3	2	1	5	12	14.3865

When some irregularity in the pulse intervals is introduced as in Figure 2, the cepstrum gives quite ambiguous results. From Table 1, note that the seasonal $ARMA$ search indicates a model with 7 pulses separated by 8 when the correct model has 5 pulses; 3 are separated by 8 points and 2 are separated by 10 points. The duration predicted is $(7 + 1) \times 8 = 64$ points as compared with the known duration of 44 points. The $ARMA$ spectrum shown in Figure 2 is a reasonable version of the narrow band smoothed periodogram. The second best model shows 6 pulses separated by 8 points and an estimated duration of 56 points which seems somewhat closer to the correct model as is the third best model with 5 pulses separated by 8 points. This is a case where the cepstrum gives no insight into the structure but the seasonal $ARMA$ search finds a reasonable model. Again, note that the spacing is easier to estimate than the duration because the number of pulses at a given duration all have about the same value for AIC_C and other durations have generally larger values.

In Figure 3 is shown the P-phase from a single mining explosion along with the spectra, log spectra, cepstrum and $ARMA$ spectrum derived from the best seasonal $ARMA(2, 1) \times (0, 6)_6$ model. The sampling rate is 40 points per second, leading to a folding frequency of 20 Hz corresponding to .5 cycles per point as shown on the graphs in Figure 3. Table 1 shows that the four best models all have a duration of 6 points or $6/40 = .15$ seconds. A

delay of 150 milliseconds (msec.) may be somewhat long for most mining explosions (see Baumgardt and Ziegler, 1988, Hedlin et al, 1990 or Chapman et al, 1992), but it is clear that this sampling rate may not be high enough to pick up in the range 25-50 msec and we may be looking at aliases. Hopefully, there will be data available at higher sampling rates that can unequivocally sort out reflections in the desired ranges.

RECOMMENDATIONS AND FUTURE PLANS

A high priority for this study is obtaining more multiple-phase (P and S arrivals) explosion and earthquake data sampled at a higher rate, say at 100 points per second. We would also like to obtain high quality signals from an array of elements so as to be able to take advantage of replication, as is done in stacking, practiced by both Baumgardt and Ziegler (1988) and Hedlin et al (1990). For this to work, the increased difficulties inherent in replicated $ARMA$ searching may dictate a more semi-parametric likelihood approach in the frequency domain.

There, we would replace the $ARMA$ model for the spectrum by a more non-parametric version, employing the general form

$$P_y(\omega) = |\alpha_d(e^{-2\pi i \omega})|^2 P_s(\omega) + P_n(\omega), \tag{16}$$

where the signal spectrum $P_s(\omega)$ can be estimated non-parametrically using the Whittle likelihood and assuming that broad-band smoothing will eliminate the duration and spacing ripples. We may also be able to assume that the signal-to-noise ratio is constant over frequency and write

$$P_y(\omega) = P_s(\omega)\left(|\alpha_d(e^{-2\pi i \omega})|^2 + \frac{1}{r^2}\right), \tag{17}$$

where $r^2 = P_s(\omega)/P_n(\omega)$ is the signal to noise ratio. If $P_s(\omega)$ is reasonably constant over a broad band, it can be replaced by the smoothed spectrum over that interval in the Whittle likelihood. Such likelihoods can be treated for arrays as in Der et al (1992).

In the frequency domain, we may also consider the possible of taking into account the amplitude modulation function a_t by considering the Whittle likelihood of the time varying spectrum or sonogram. Dahlhaus (1995) has shown that local averaging over time of the Whittle likelihood can be used to estimate parameters of the modulating function.

A final note relates to the fact that the spacing values d will not be the same and, in fact, may be quite variable. In this case, we must replace jd in (1) by d_j so that

$$y_t = \sum_{j=1}^{n} \alpha_j s_{t-d_j} + n_t, \tag{18}$$

where $d_1, d_2, \ldots, d_n$ form a sequence of unequal delay times. Estimating these as parameters seems intractable because of the high dimensionality of the resulting parameter space. An option that expect to try is letting the delay times be random and possibly uniformly distributed on the integers if one makes no specific assumptions about the time

delays. One may also assume that the random time delays are clustered about the points $d, 2d, 3d, \ldots, nd$ in some specified fashion. The integrated likelihood function can then be computed for any preset combination of parameters using Monte-Carlo methods.

References

Baumgardt, D.R. and K.A. Ziegler (1988). Spectral evidence for source multiplicity in explosions: Application to regional discrimination of earthquakes and explosions. *Bull. Seismolog. Soc. of Amer.*, **78**, 1773-1795.

Blandford, R.R. (1993). Discrimination of earthquakes and explosions at regional distances using complexity. *AFTAC-TR- 93-044*, HQ AFTAC, Patrick AFB, FL.

Bogert, B.P., M.J.R. Healy and J.W. Tukey (1962). The frequency analysis of time series for echoes: cepstrum, pseudo-autocovariance, cross cepstrum and saphe cracking. In *Proceedings of a Symposium on Time series Analysis*, ed. M. Rosenblatt. New York: John Wiley.

Chapman, M.C., G.A. Bollinger and M.S. Sibol (1992). Modeling delay-fired explosion spectra and source function deconvolution at regional distances. *Final Report PL-TR-92-2250*, Phillips Laboratory, Directorate of Geophysics, Air Force Materiel Command, Hanscom Air Force Base, MA 01731-3010, *ADA273807*.

Dargahi-Noubary, G.R. (1995). Stochastic modeling and identification of seismic records based on established deterministic formulations. *J. Time Series Analysis* **16** 201-219.

Dahlhaus, R. (1995) Fitting time series models to nonstationary processes. *Beiträge zur Statistik*, Nr. 4, Institut für Angewandte Mathematik, Universität Heidelberg, Heidelberg.

Der, Z.A., A.C. Lees, K.L. McLaughlin and R.H. Shumway (1992). Multichannel deconvolution of short period teleseismic and regional time series. Chapter 9 in *Statistics in the Environmental and Earth Sciences*, A.T. Walden and P. Guttorp (ed., 156-188. Edward Arnold, London.

Hannan, E.J. and P.J. Thomson (1974). Estimating echo times. *Technometrics*, **16**, 77-84.

Hedlin, M.A.H., J.B. Minster and J.A. Orcutt (1990). An automatic means to discriminate between earthquakes and quarry blasts. *Bull. Seismolog. Soc. Amer*, **80**, 2143-2160.

Hurvich, C.M. and C.L. Tsai (1989). Regression and time series model selection in small samples. *Biometrika* **76** 297-307.

Shumway, R.H. (1988). *Applied Statistical Time Series Analysis*, Chapter 5. Englewood Cliffs: Prentice-Hall.

Shumway, R.H. and McQuarrie, A.D.R. (1994). Statistical discrimination studies for nuclear test verification. Final Report, PL-TR-94-2283, Phillips Laboratory, Directorate of Geophysics, Air Force Materiel Command, Hanscom AFB, MA 01731-3010. ADA293572

Von Seggern, D. and R. Blandford (1972). Source time functions and spectra of underground nuclear explosions, *Geophysical J. R. Astro. Soc.*, **31**, 83-97.

WCEDS: A Waveform Correlation Event Detection System

Christopher J. Young, Judy L. Beiriger, Julian R. Trujillo
Sandia National Laboratories
Mitchell M. Withers, Richard C. Aster
New Mexico Institute of Mining and Technology
Luciana Astiz and Peter M. Shearer
University of California, San Diego

ABSTRACT

We have developed a working prototype of a grid-based global event detection system based on waveform correlation. The algorithm comes from a long-period detector (Shearer, 1994) but we have recast it in a full matrix formulation which can reduce the number of multiplications needed by better than two orders of magnitude for realistic monitoring scenarios. The reduction is made possible by eliminating redundant multiplications in the original formulation. In the matrix formulation, all unique correlations for a given origin time are stored in a correlation matrix (C) which is formed by a full matrix product of a Master Image matrix (M) and a data matrix (D). The detector value at each grid point is calculated by following a different summation path through the correlation matrix. The Master Image is a critical component in the detection system because it determines how the data contribute to the detector output at each grid point. Master Images can be derived either empirically or synthetically. Ultimately we will use both types, but for our preliminary testing we have used synthetic Master Images because their influence on the detector is easier to understand.

We tested the system using the matrix formulation with continuous data from the IRIS (Incoroporate Research Institutes for Seismology) broadband global network to monitor a 2 degree evenly spaced surface grid with a time discretization of 1 sps; we successfully detected the largest event in a two hour segment from October 1993. Both space and time resolution results are encouraging: the output at the correct gridpoint was at least 33% larger than at adjacent grid points, and the output at the correct gridpoint at the correct origin time was more than 500% larger than the output at the same gridpoint immediately before or after. Analysis of the C matrix for the origin time of the event demonstrates that while the largest values are due to the expected correlations, there are many significant "false" correlations of observed phases with incorrect predicted phases. These false correlations dull the sensitivity of the detector and so must be dealt with if our system is to attain detection thresholds consistent with a Comprehensive Test Ban Treaty (CTBT). Current research efforts are focussing on this problem.

Keywords: waveform correlation, event detection, master image

INTRODUCTION

As the nuclear treaty verification community moves towards the goal of a Comprehensive Test Band Treaty (CTBT), the demands on event detection systems are changing and indications are that current systems will not be able to meet future needs without significant modifications. The next generation of detection systems must have performance which scales well with an increasing number of stations and should be able to take advantage of the new direction in high-performance computing, parallel processing. As part of the CTBT Research and Development program at Sandia Labs, we have been testing a new type of event detection system, the Waveform Correlation Event Detection System (WCEDS), which may be able to meet these requirements and which has other advantages as well. The technique uses waveform correlation and it has already been used to process 10 years of long-period data to search for "slow" or "silent" earthquakes (Shearer, 1994) and to detect and locate a Chinese nuclear test using broadband data (Wallace, 1994). Neither of these applications has established its true worth as a CTBT-quality event detection system, however.

WAVEFORM CORRELATION EVENT DETECTION

1. Qualitative Theory

The basic premise of this type of system is the idea that if data are sorted to the correct distances for a given event, any phases which are present in the waveforms should be obvious because of the moveouts.
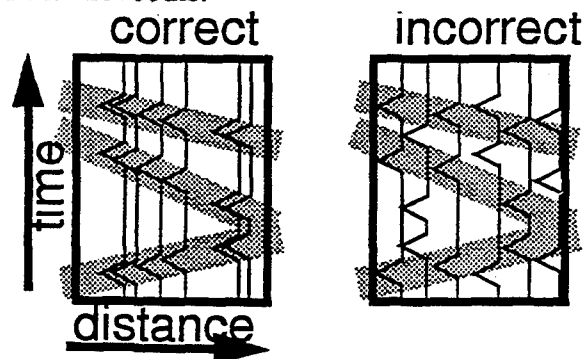
FIGURE 1. A simple example of correctly sorted and incorrectly sorted waveform profiles.

Clearly in the profile on the left the stations are plotted at the correct distances, while in the profile to the right they are not. This simple observation is the basis for the event detection system.

Making an event detection system out of this idea is straightforward. First we must select a network of stations appropriate to the region being monitored. Next we define a grid for the monitored region with a sufficient number of grid points to cover any areas where we think events might occur. Finally, we collect data from each station for the same specified time period (the length is determined by which phases we want to try to observe) and form profiles for each grid point by plotting the data at the appropriate epicentral distances for an event at the grid point. If any of the profiles show the expected moveouts for a seismic event, we declare that an event has occurred at that grid point at the current origin time. To run such a detector continuously through time, we simply repeat this procedure at some regular interval (every 2 minutes for the LP study of Shearer, 1994).

To form an automated system, we use waveform correlation to perform the moveout recognition. Consider two time series X(t) and Y(t). The the dot product of Y(t) with X(t) is:

(Equation 1)

$$Y(t) \bullet X(t) = \sum_{i=1}^{N} X_i Y_i$$

This is the zero time shift correlation of Y(t) with X(t). The greater the similarity, the greater the correlation will be.

I   II   III

X(t)   X(t)   X(t)

Y(t)   Y(t)   Y(t)
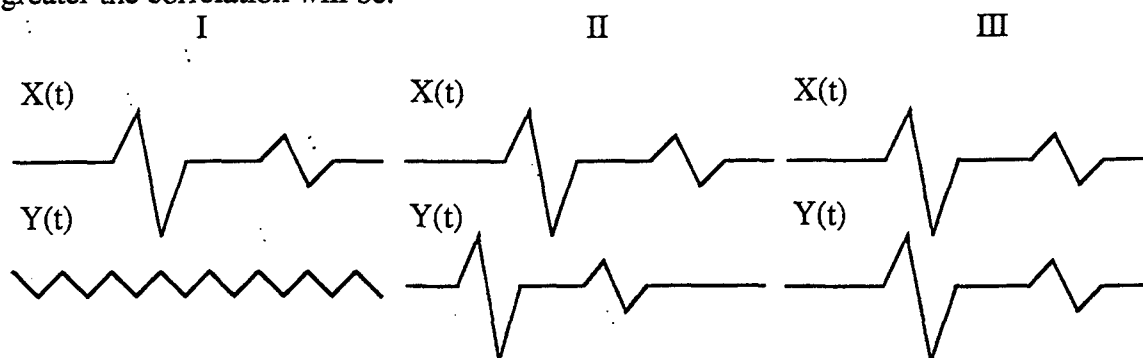
FIGURE 2. Examples of waveform pairs with poor, mediocre, and excellent correlations . Both waveform similarity and correct time alignment are important.

In case I, the waveforms are completely dissimilar and the dot product is small. In case II, the waveforms are similar but the time alignment is poor and the dot product is still small. Finally, in case III the waveforms are similar and they are time aligned so the dot product will be large. Thus, correlation can be used to identify similar waveforms.

For our detector, the data from each station are the waveforms which we wish to identify as valid or invalid with respect to a hypothesized event location (grid point) and origin time. Hence, the correlation waveform must be the expected waveform at the appropriate distance. High correlations (large dot products) will indicate that the observed waveform is consistent with an event at that grid point.

2. Master Images

The expected waveforms can either be derived synthetically or empirically. To derive them empirically, one can take the network data from a large number of events with reliable locations and bin and stack the data (see Shearer, 1991 for details). The correct waveforms emerge quite naturally as a result of averaging the many contributions, and if enough events from different locations are used, expected waveforms for all distances will be generated. If we consider all of the stacked waveforms together they form an image which looks like a plot of travel time curves. An example formed for this project is shown below.
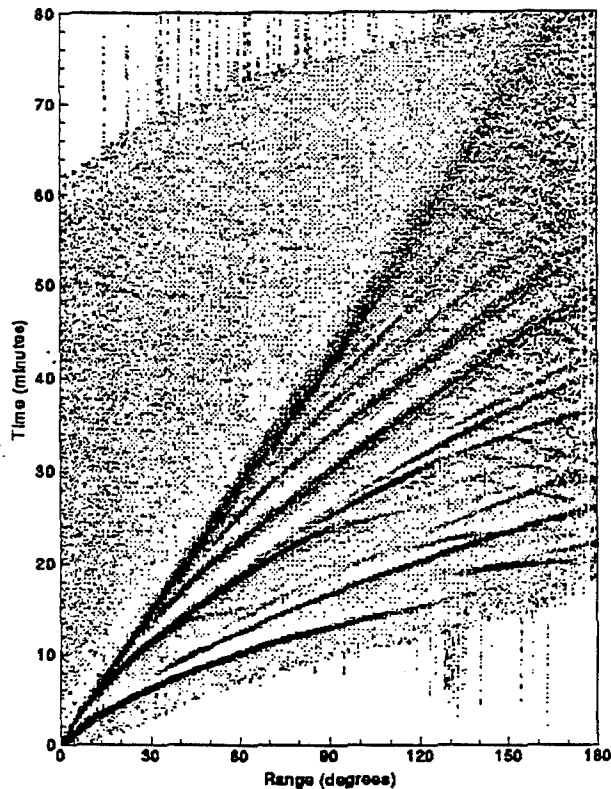
FIGURE 3. An empirical stack using the IRIS BB stations for all events with $M_w > 5.8$ and depth < 50 km.

We will refer to this type of image as a Master Image or MI. Empirically derived MIs have the advantage that the images do not require any phase picks and by definition must produce the true image (assuming that the event locations are accurate). The technique of producing an empirical MI is described in detail in Shearer, 1991. To form empirical MIs for WCEDS, we have gathered all of the IRIS BB data from 1988-1994 for shallow (d < 100 km) events with Mw > 5.8 and for deep (d > 100 km) events with Mw > 5.5. From this, we have formed images for d=0-50 km, 50-150 km, 150-350 km, 350-550 km, and 550+ km.

Unfortunately, the complexity of these images makes them ill-suited for our need to understand the detailed workings of WCEDS. For this reason, we have chosen to use synthetic MIs for our initial testing. Synthetic MIs offer the advantage of being able to control exactly which phases are contained in the image and their relative amplitudes. This information is important because it in turn determines which phases can contribute to an event detection and how they will be weighted. Our synthetic MIs were derived from the IASPEI 1991 travel time tables. Because travel time curves have no duration associated with their phases, the time series for each distance must be convolved with some response function(s) to yield waveforms with correlation windows of finite duration:

FIGURE 4. Transformation of a spike train-style waveform to a waveform that can be used for correlation by means of convolution with a simple response function.

3. Quantitative Theory

3.1 Original Formulation

In the original formulation of the detector (Shearer, 1994), the algorithm is essentially identical to what we have outlined above. For each grid point the data are sorted to the appropriate distance bins and the dot products of each bin with the master image bin are formed and summed to give the detector output at a given gridpoint at a given time:

(Equation 2)

$$E_{gridpoint} = \sum_{i=1}^{N_D} \sum_{j=1}^{N_T} M_{ij} D_{ij}$$

Where M_{ij} is the master image for distance bin i and time point j, D_{ij} is the data for distance bin i and time point j, N_D is the number of distance bins, and N_T is the number of time points to correlate. Thus, for each origin time to be monitored this double summation must be done for all grid points.

For a coarse grid the number of grid points is small (Shearer needed only 416 points for approximately 10 degree spacing on the Earth's surface) and this formulation is acceptable, but for a finer grid the method becomes inefficient (e.g. for our gridding scheme, 1 degree grid spacing for a single surface grid leads to about 41,000 points).

3.2 Matrix Formulation

The number of multiplications needed for the WCEDS processing can be reduced significantly (e.g. 2 orders of magnitude) by using a matrix formulation in which all dot products needed to monitor each grid point for a given origin time are calculated with one full matrix multiplication. The motivation for the matrix formulation is provided by the observation that in the original formulation many redundant dot products are calculated. Consider a given station at a distance of r degrees from the grid point being monitored. This same station will contribute exactly the same dot product to every other grid point the same distance away:
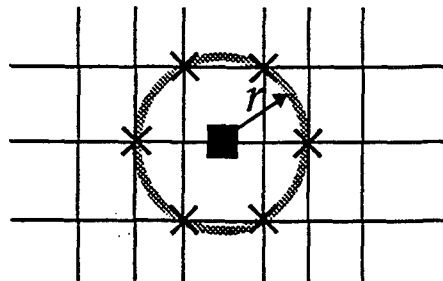
FIGURE 5. A simplified diagram showing that many grid points will lie at the same distance from each station. The shaded circle indicates equal distance from the station (solid square). Six grid points (indicated with Xs) lie at this distance from the station.

Another way to think of this is that each station can only form N_D unique dot products (i.e. it can be dotted once with each of the distance columns of the master image). This suggests a simple shortcut: form all of the possible dot products for each station immediately and then simply look up the dot products needed to monitor each grid point as they are needed. The only thing complicating this formulation is the binning of the station data in the original formulation, which (ironically) was done to limit the number of dot products. If we eliminate the distance binning, however, a much greater gain can be realized.

The matrix formulation is shown graphically below for N_S stations with a correlation window length of N_T points, and a distance discretization of 1 degree for clarity:
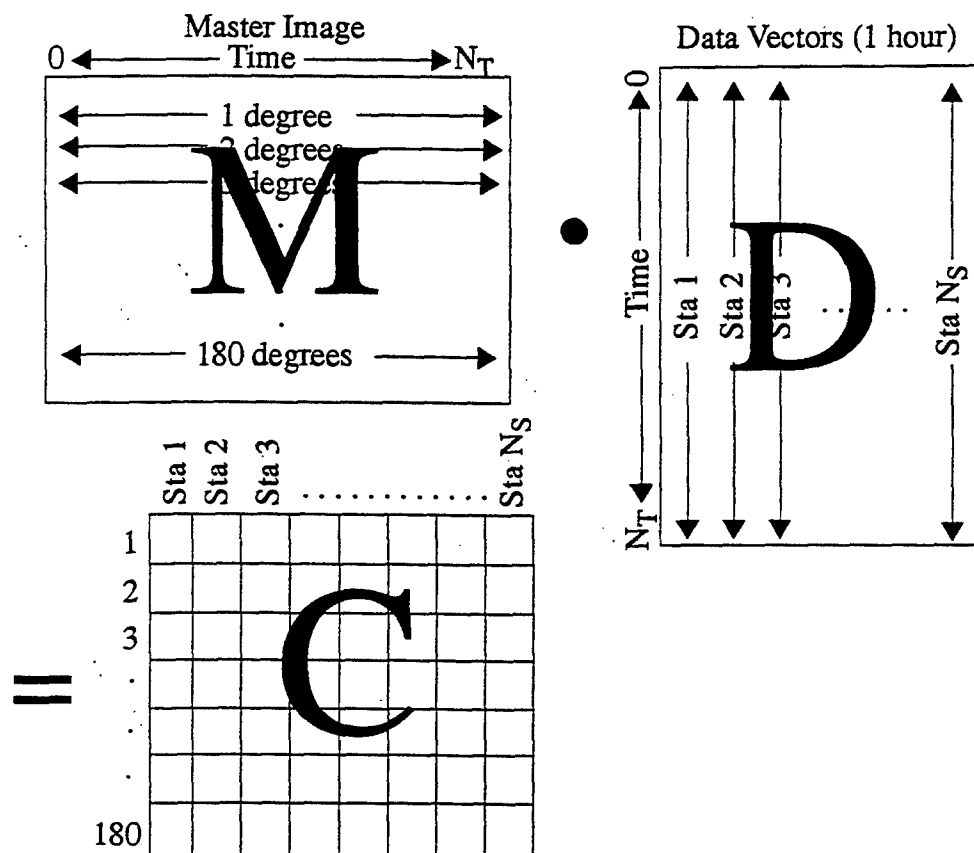
FIGURE 6. The matrix formulation of WCEDS. All of the information needed to monitor each grid point on the earth (contained in the correlation matrix C) can be obtained by forming the full matrix product of the Master Image matrix (M) with the data matrix (D).

Let us compare the number of multiplications needed to monitor a full grid at the surface using both the original and the matrix formulations for a realistic scenario. Let $N_S = 50$, $N_T = 3600$ (a 1 hour correlation window sampled at 1 sps), and using a 1 degree grid spacing (about 41,000 grid points):

- **original formulation**: 41,000 grid points x 50 stations x 3600 time points = 7.38 e09 multiplications. The true number is likely to be somewhat less because of the binning (for each grid point some of the stations will lie in the same distance bin).

- **matrix formulation**: 50 stations x 180 distances x 3600 time points = 3.24 e07 multiplications.

Thus we reduce the number of multiplications by a factor of 227 using the matrix formulation. Even if we assume that binning in the original formulation reduces the number of multiplications at each grid point by as much 50%, the reduction factor is still better than two orders of magnitude.

Once C has been calculated, event detection is simply a matter of referring back to the elements of C. E.g.:

grid point 1 --	Station	Distance	C Matrix Element
	#1	10.6 (11)	C(11,1)
	#2	88.7(89)	C(89,2)
	#3	23.4(23)	C(24,3)
	...	...	...

$$\#50 \qquad 16.7(17) \qquad C(17,50)$$

Correlation for grid point 1 = C(11,1) + C(89,2) + C(24,3) + ... + C(17,50)

The correlations for the rest of the grid points can be calculated in a similar manner.

3.2.1 Importance of Master Images

In general, the output of the detector at a given gridpoint is given by a particular summation path through the correlation matrix:

(Equation 3)

$$E_{gridpoint} = \sum_j^{N_S} C_{ij}$$

Where N_S is the number of stations and i = function(gridpoint, j). From Figure 6, we se that the C_{ij} are a weighted sum of the data D_{lj}:

(Equation 4)

$$C_{ij} = \sum_l^{N_T} M_{il} D_{lj}$$

Where N_T is the number of time points used in the dot products and M_{il} are the elements of the master image. Thus, the master image weights the contributions of the data to the C matrix and thereby to the detector output at each grid point.

4. Example Application

To test the WCEDS prototype, we used a two hour segment of data surrounding an m_b 6.2 event in southern Xinjiang Province, China which occurred at 08:42:32.7 GMT on October 2, 1993. Although there are four other events listed in the PDE for this interval, the Chinese earthquake is by far the largest. The output of our detector reflected this: the maximum value occurs at the grid point nearest to the PDE epicenter of the Chinese event at the given origin time (rounded to the nearest second).
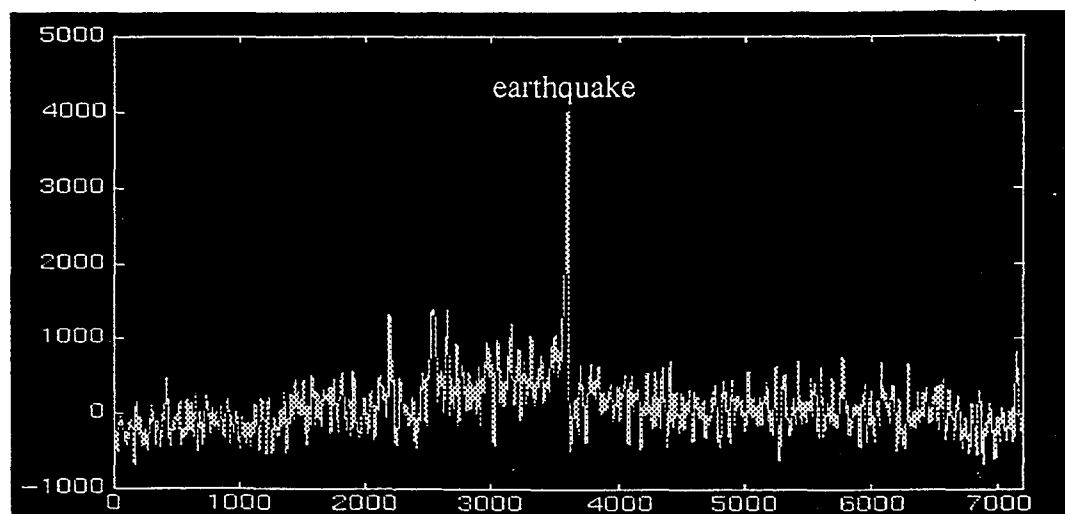
FIGURE 7. Detector output for the grid point nearest the Chinese earthquake for 1 hour before until 1 hour after the event.

Viewing the C matrix sorted for the epicentral grid point well before the event and at the time of the event sorted demonstrates that the correlations are occurring as theorized:

937
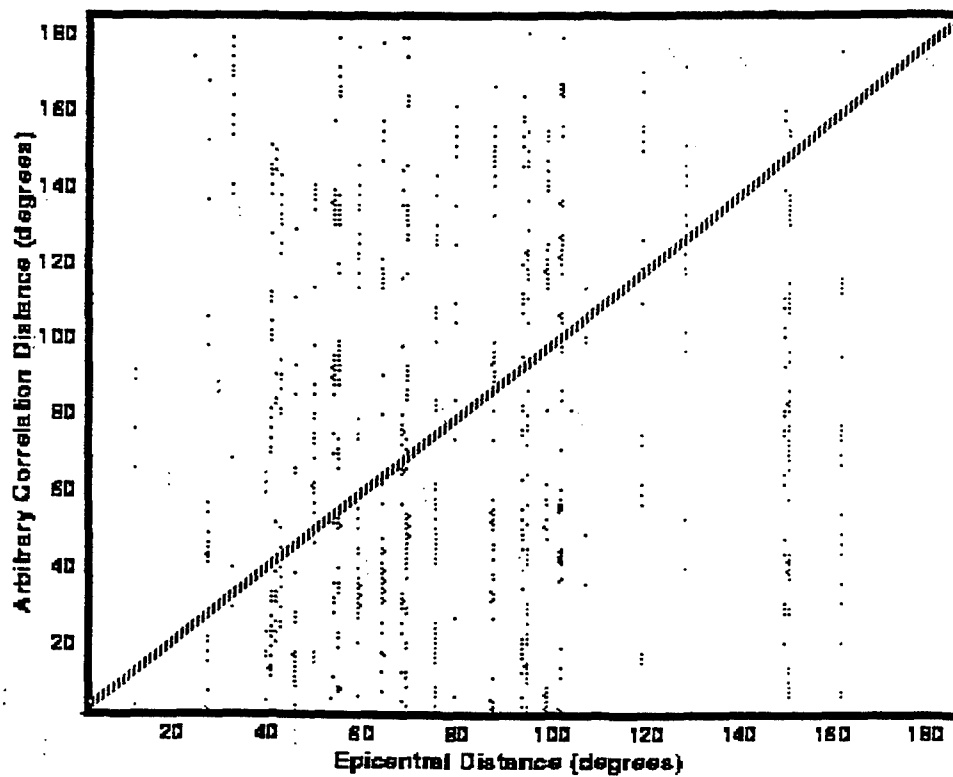
FIGURE 8. C matrix with for an origin time 1 hour prior to the event. The columns have been plotted at the correct distance for grid point nearest to the event location. The dashed line shows the expected positions for the correlations for the event.
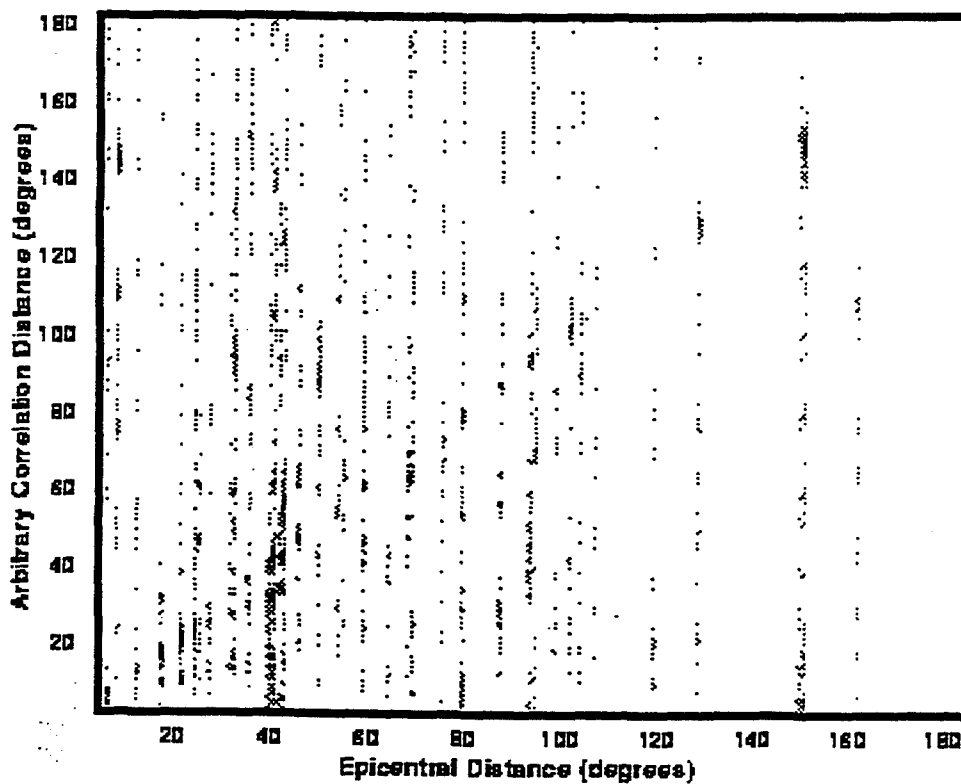
FIGURE 9. Same as Figure 7, but at the correct origin time.

938

FUTURE PLANS

If we examine the above figure carefully it can be seen that in addition to the expected line of correlations along the diagonal, there seem to be several other correlation lines:
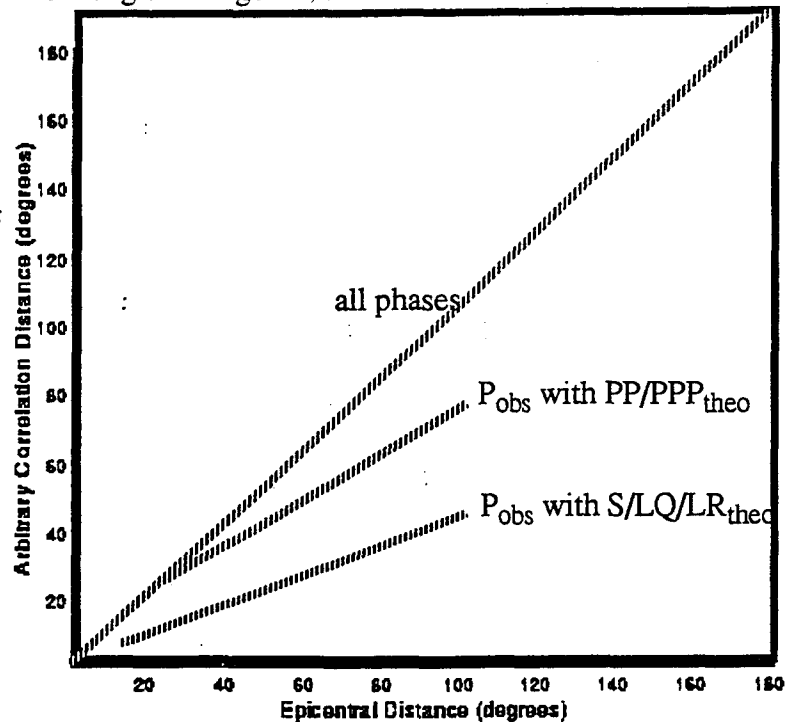
FIGURE 10. Correlation lines observed in Figure 9.

These other lines are the correlations of observed phases with the wrong theoretical phases. In particular, we can pick out P_{obs} with PP/PPP (notice that they begin to split near 40 degrees), and P_{obs} with S/surface waves. The "false" correlations do not contribute as much to the detector as the true correlations because fewer phases contribute:.
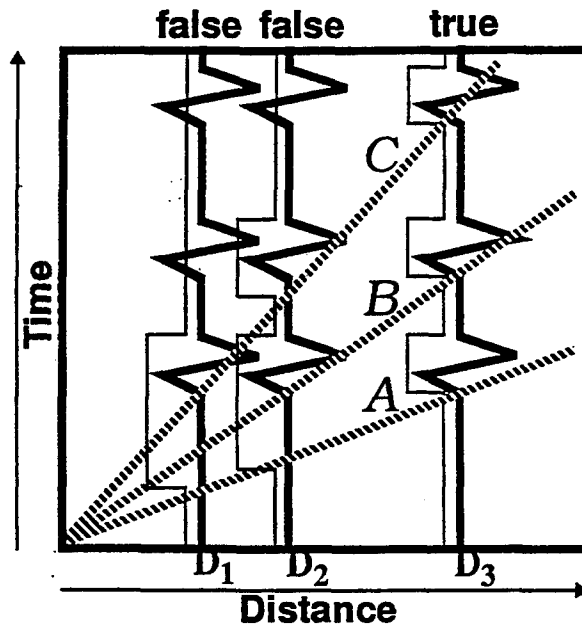
FIGURE 11. True and false correlations of a single observed waveform with theoretical (boxcar) correlation waveforms for a simple system with three phases: A, B, and C. Note that Correlation(D_3) > Correlation(D_2) > Correlation(D_1) because three phases contribute at D_3, two at D_2, and only one at D_1.

939

False correlations do, however, raise the background noise level of the detector because they randomly add to the detector output at grid points when no event is actually occurring. Thus, to lower the detection threshold of our system, we must find a means to eliminate the false correlations, or minimize their effects.

There are two obvious ways of eliminating the false correlations. The most obvious is to go back to the data, zero out the portions where signals were recorded which matched predicted phases for the event, and then recalculate the C matrix and rerun the detector. This method is not difficult to apply, but we would prefer to avoid it because of the recalculation of the C matrix, which we have found to take nearly 90% of the run time for the entire detector. A more computationally efficient method is not to recalculate the C matrix at all, but rather to determine where and when false correlations will occur and to use this information to screen the C matrix whenever running the detector. What we desire is an overlay for the C matrix which will "x" out the elements contaminated by false correlations: we will refer to this as the X matrix.
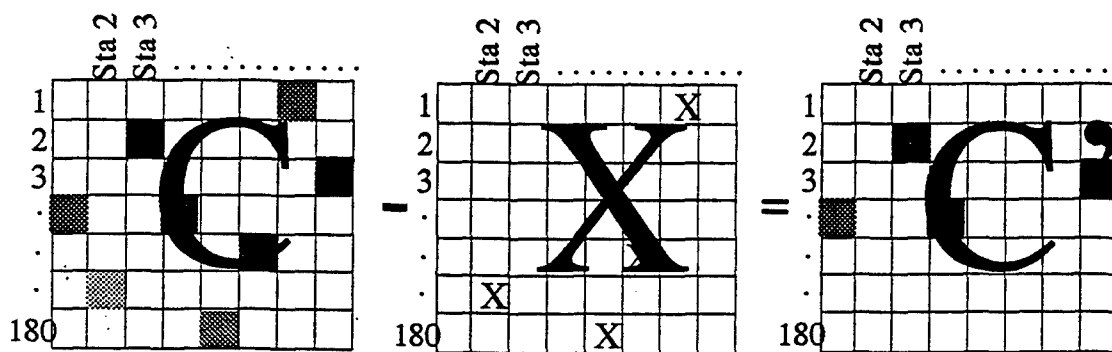
FIGURE 12. An example demonstrating the use of the X matrix to screen nuisance correlations from theC matrix: C - X = C'.

The implementation of the X matrix is one of our active areas of research.

CONCLUSIONS

We have developed a simplified prototype of a Waveform Correlation Event Detection System (WCEDS) which we have used to successfully detect the largest event in a two hour interval from October, 1993 using data from the IRIS broadband global network. The algorithm is based on a long-period detector developed by Shearer (1994) but we have recast it in a full matrix form which can reduce the number of multiplications needed by better than two order of magnitude. Even with the many simplifications which have been made in implementing the prototype, both the performance and the quality of output of the system show great promise. To make WCEDS a CTBT verification system however, will require significant progress in many areas.

REFERENCES

Bache, T. C., S. R. Bratt, J. Wang, R. M. Fung, C. Kobryn, and J. W. Given (1990). The intelligent monitoring system, *Bull. Seismol. Soc. Am.*, **80**, Part B, 1833-1851.

Shearer, P. M. (1994). Global seismic event detection using a matched filter on long-period seismograms, J. Geophys. Res., 99, 13713-13726.

Shearer, P. M. (1991). Imaging global body wave phases by stacking long-period seismograms, J. Geophys. Res., 96, 20353-20364.

Wallace, T. (1994). Chinese nuclear test - June, 1994, *IRIS Newsletter*, **2**, 6.

Determination of Near-Station Crustal Structure and the Regional Seismic Event Location Problem

Lian-She Zhao and Cliff Frohlich
Institute for Geophysics
The University of Texas at Austin
8701 North MoPac
Austin, TX 78759-8397

Since crustal structure strongly influences the character of regional seismic waveforms, a knowledge of near-station crustal structure is necessary for obtaining single-station event locations of small (M~3) seismic events. In this study we demonstrate that it is practical to use a receiver-function method for determining near-station crustal structure; then, we then use this structure as a basis for constructing synthetic waveforms, and determine single-station regional event locations by comparing the synthetic and observed waveforms.

Our receiver-function approach for determining crustal structure utilizes vertical-component P-group waveforms from teleseismic events as input for synthesizing a radial-component waveform for a trial, layered, near-station crustal model. Then, we compare the synthetic and observed radial-component waveforms, and change the crustal model until they are sufficiently similar. To improve efficiency we have implemented several features in our software:
• For synthesizing radial-component waveforms from vertical-component data we employ a theoretical approximation which is exact to second order in the reflection and transmission coefficients; thus, we call this second-order, radial-vertical comparison the SORVEC method;
• For synthesizing reverberation waveforms for a n-layer-over-a-halfspace crustal model we show it is generally sufficient to calculate amplitudes for only (6n+1) carefully selected rays;
• To determine crustal structure we have developed an inversion scheme which utilizes a very fast simulated annealing (VFSA) algorithm which is much faster than grid-search methods, Monte-Carlo methods, or ordinary simulated annealing methods.

Using the SORVEC-VFSA algorithm we have determined flat-layered crustal models beneath 12 seismic stations, one (PAS) in California and 11 in Tibet. To locate regional earthquake near individual stations we use the models using data from teleseismic earthquakes situated at similar azimuths, and determine a crustal model possessing up to five layers. However, often the data fit for 5-layer models is not significantly better than for the 4-layer models; usually the optimal 5-layer models possess two adjacent layers with nearly identical shear velocities which were merged in the optimal 4-layer model.

Finally, using these crustal models we demonstrate that it is possible with single-station data to accurately locate earthquakes with magnitudes of ~3 which occur which occur at distances of up to a few hundred km. We determine the event-station azimuth from phase polarization, then we compare observed seismograms with synthetics constructed at 1-2 km intervals over a range of distances and depths. For a test event occurring in California, our location determined by fitting waveforms recorded at PAS was virtually identical to the location determined by the California network. For a test event in Tibet our location differed significantly from that reported by the ISC.

OBJECTIVES

Our objective is to develop practical methods for locating small (M~3) regional seismic events using single-station waveform data. Our hypothesis is that we can do this by straightforward waveform comparison methods if we know near-station well enough so that we can construct reasonable synthetic wavefomrs. In this study, we make several practical improvements to a previously-developed receiver function method, and, we determine the optimum three- to five-layer crustal velocity structures beneath a number of three-component broadband seismic stations. We then utilize the crustal structures so found to test how well we can determine event locations from single-station recordings of small (M ~ 3) seismic events.

RESEARCH ACCOMPLISHED

Software Development

To locate small seismic events using waveforms recorded at a single seismic station, it is necessary to determine at least three parameters-- these are: 1) the direction of arrival, or azimuth, or the event with respect to the station; 2) the event-to-station distance; 3) the focal depth of the event. Generally different parts of the arriving waveforms are useful for assessing each of these parameters; polarization of the P-group or surface wave group determines the event azimuth; time delays between P, S, and surface wave groups fixes the event distance; while time delays between crustal reverberation phases within the P group provides information about event focal depth. The regional crustal structure-- near the source, along the path, and near the station-- exercises a strong influence on the determination of all these parameters. However, focal depth is usually the most difficult parameter to determine because near-station crustal reverberations may be mistaken for depth phases unless the near-station crustal structure is well known.

Recently, we have been developing practical methods for determining near-station crustal structure using a receiver-function approach (Zhao and Frohlich, 1994; 1995). The essential strategy is to use vertical-component P-group waveforms from teleseismic events as input for synthesizing a radial-component waveform for a trial, layered, near-station crustal model (Figure 1). Then, we compare the synthetic and observed radial-component waveforms, and change the crustal model until they are sufficiently similar. The method is able to determine crustal structure because time-delays and relative amplitudes of radial- and vertical-component phases in the P group coda are strongly affected by the details of near-station crustal layering.

In our software to determine near-station crustal structure we have implemented three features to improve efficiency. First, our scheme for synthesizing and comparing radial-component waveforms from vertical-component data utilizes a theoretical approximation which is exact to second order in the reflection and transmission coefficients; thus, we call this second-order, radial-vertical comparison the SORVEC method. Second, for synthesizing reverberation waveforms for a n-layer-over-a-halfspace crustal model we only calculate the amplitudes for (6n+1) rays (Figure 2). We have performed extensive testing to demonstrate that this provides an adequate fit between data and synthetics for nearly all realistic crustal models; except in pathological cases the (6n+1) rays include all arrivals with amplitudes exceeding 5% of the initial P wave.

Finally, for applying the SORVEC algorithm to determine crustal structure, we have developed an inversion scheme which utilizes a very fast simulated annealing (VFSA) algorithm (Sen and Stoffa, 1991; Zhao et al., 1995). The VFSA inversion is much faster than grid-search

942

methods, Monte-Carlo methods, or ordinary simulated annealing methods. However, VFSA still retains the ability to find the global optimum crustal model that provides a fit between synthetic and real radial-component data, even though the relationship between crustal structure and data fit is highly nonlinear.

Crustal Models Determined from Teleseismic Waveforms

Using the SORVEC-VFSA algorithm described above, we have determined flat-layered crustal models beneath 12 seismic stations, one (PAS) in California and 11 in Tibet. To determine a crustal model at each station we utilized data from several earthquakes with azimuths similar to those of regional earthquakes of interest. For station PAS we evaluated teleseismic waveforms from four earthquakes in Alaska and the Kuriles and found the optimal crustal model with five layers and a total thickness of 26 km (Figure 3). However, only three layers were significant, as the top layer was exceedingly thin (less than 1/2 km), and the shear velocity in the fifth layer did not differ from that in the fourth layer.

For each station in Tibet teleseismic events were available at a variety of different azimuths, so we evaluated 10 or more teleseismic events to determine optimum "average" models. In Tibet the crustal shear velocity typically possessed of a 1-2 km thick lid with velocity of ~1.8 km/sec overlying a 10-30 km thick layer with velocity of 3.-4.0 km/sec. Beneath this was a lower-velocity layer extending to depths of 40-55 km. Beneath all stations the crust is unusually thick by ordinary standards, as the Moho lay at about 70-80 km depth. Although we evaluated the data to find the best-fitting 3-layer, 4-layer, and 5-layer models for each station, often the data fit for 5-layer models was not significantly better than for the 4-layer cases; usually the optimal 5-layer models possessed two adjacent layers with nearly identical velocities which were merged in the optimal 4-layer model.

Seismic Event Location Using Single-Station Data

We have utilized crustal models determined as described above as a basis for locating small seismic events. In California single-station event location is complicated because the crust possesses considerable lateral hetergeneity. However, because the California network possesses a large number of stations, high-quality, independently-determined locations are generally available for comparison with our single-station locations.

Using the crustal model in Figure 3, we relocated a magnitude 3.1 earthquake which occurred on 8 February 1995 near station PAS. After determining the event-station azimuth from phase polarization, we constructed synthetic seismograms at 2 km intervals over a range of distances and at 1 km intervals over a range of depths (Figure 4). The best fit between these synthetics and the PAS vertical- and radial-component waveforms (Figure 4) occurred for distances of 24-26 km from PAS, and focal depths of 5 km. This was virtually identical to the location determined by the California network. Nevertheless, the fit between data and synthetics is not perfect, especially for the initial P phase, which is nearly absent in the data and quite prominent in the synthetics. The fit is quite good, however, for the surface wave group and for the S group, where several prominant crustal reverberations predicted by the crustal model of Figure 3 are evident.

As a further demonstration of the method we relocate an earthquake with m_b of 4.5 which occurred on 10 August 1991 near station AMDO in Tibet. We first determine the station-event azimuth by finding the azimuth which minimizes the signal energy arriving between the P and the S (Figure 5); note that the back azimuth so found (~35°) is significantly different than that (~15°) for the location reported by the ISC (33.87°N, 92.19°E, h = 8 km). Next, we use our

SORVEC-VFSA to determine a crustal structure for AMDO (Figure 6) using a teleseism that occurred on 26 March 1992 in Alaska, chosen because it possessed a similar back azimuth (44°) to the regional event. Finally, using this crustal model we generated synthetics over a range of distances, depths, and focal mechanisms to compare with the vertical and radial waveforms recorded at AMDO for the 10 August 1991 event. The best fit between synthetics and observations occurs for a station-event distance of 190 km and a focal depth of 8 km (Figure 7). While this focal depth is identical to that reported by the ISC, the epicenter differs by about 60 km. Since the closest station used in the ISC location was at a distance 6.6°, we believe that our location is more accurate.

CONCLUSIONS AND RECOMMENDATIONS

• Testing demonstrates that our SORVEC-VFSA algorithm for determining crustal structure from teleseismic waveforms is effective for determining crustal models which consist of three to five flat layers over a halfspace. The algorithm is fast, and generally finds nearly the same optimal crustal model for input data from teleseisms occurring at different azimuths.

• We find that three- or four-layer crustal models generally provide an adequate basis for constructing synthetic seismograms that strongly resemble the waveforms of small-magnitude, real, regional seismic events. We usually are unable to obtain significantly better fits between real and synthetic seismograms by constructing synthetics using crustal models with five or more layers.

• We here test the effectiveness of locating small seismic events with single-station data by determining event-station azimuth from P-group and surface wave polarization, and event-to-station distance and event focal depth by a grid-search comparison of real and synthetic seismograms. In effect this means that event-to-station distance depend on time delays between the P group, S group and surface wave group, while focal depth depends on relative amplitudes and time delays of reverberation phases within the P group. Our preliminary results indicate that using only single-station waveforms we can obtain accurate locations for small events (M ~ 3) at distances of ~100 km or more.

• These results imply that the crustal models we obtain using teleseismic data and the SORVEC-VFSA method are good representations of regional crustal structure at distances of ~100 km or more from the receiving stations. Otherwise it would not be possible to fit waveforms of regional seismic events with synthetics generated using these crustal structures.

References:

Sen, M. K. and P. L. Stoffa, Nonlinear one-dimensional seismic waveform inversion using simulated annealing, *Geophysics, 56*, 1624-1638, 1991.

Zhao, L.-S. and C. Frohlich, Crustal and upper mantle velocity structure beneath seismic stations from modeling teleseismic waveforms, *Proceedings, 16th Annual Seismic Research Symposium, Thornwood, New York*, Air Froce Office of Scientific Research, 400-406, 1994 PL-TR-94-2217, ADA284667

Zhao, L.-S. and C. Frohlich, Teleseismic body-waveforms and receiver structures beneath seismic stations, *Geophys. J. Int.*, (submitted, 1995).

Zhao, L.-S., M. K. Sen, P. Stoffa and C. Frohlich, Application of very fast simulated annealing to the determination of crustal structure beneath Tibet, *Geophys. J. Int.*, (submitted, 1995).
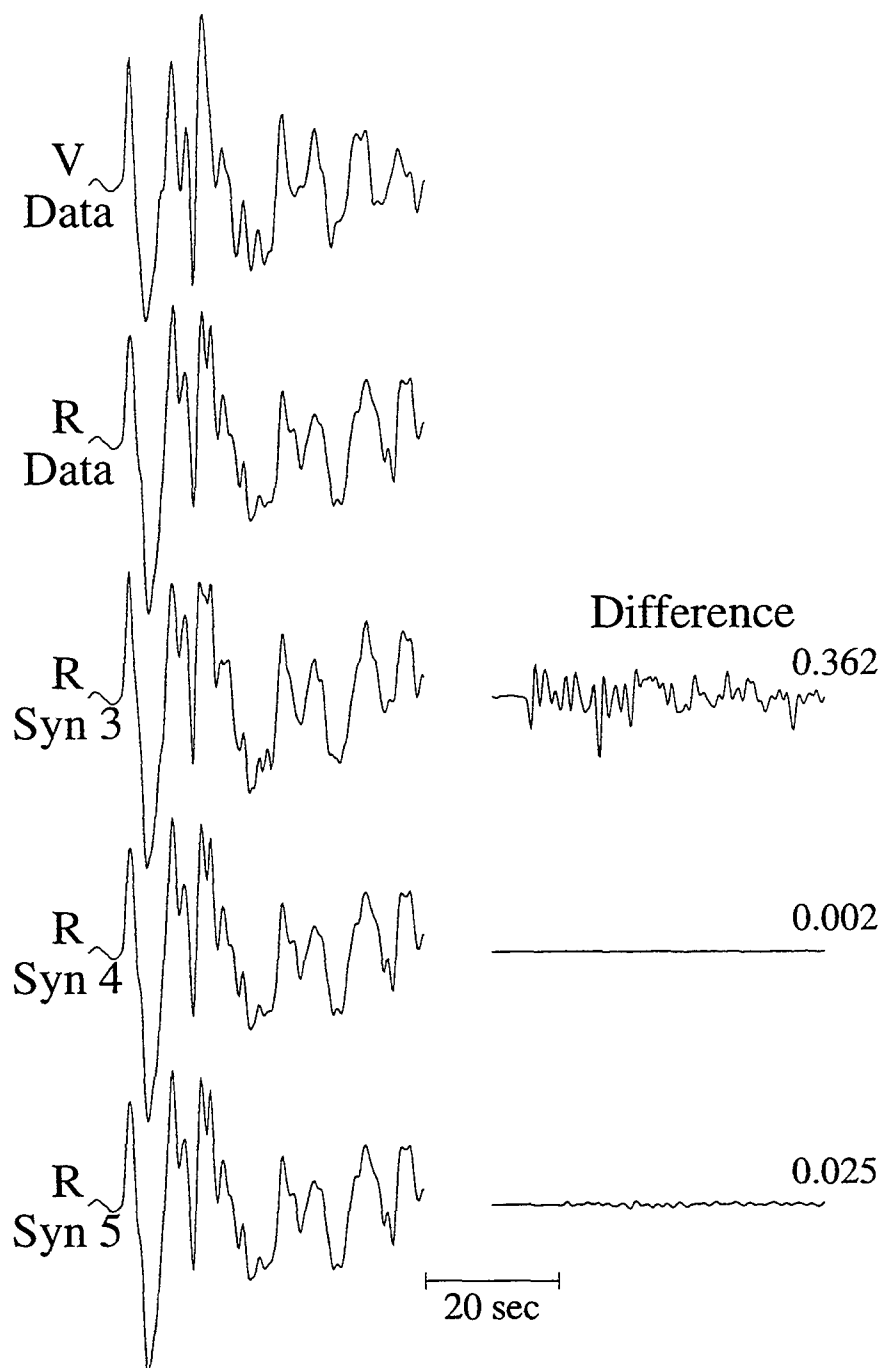
Figure 1. Comparison of radial-component observations with synthetic signals generated for different classes of crustal models with the SORVEC method. Here we use the signal labeled "V" (vertical component of a P wave recorded at station MAQI in Tibet from an earthquake occurring on 17 February 1992) as input for SORVEC to generate a radial-component signal, "R", using the 4-layer-over-halfspace crustal model. Then we test the VFSA inversion method by searching to find the best-fitting crustal models having 3, 4, and 5 layers and the associated radial-component synthetic signals (labeled "Syn 3", "Syn 4" and "Syn 5"). "Difference" column is the difference between the "Radial" signal for the Input crustal structure and the synthetics generated for the best-fitting models; the numbers at right are the misfit, i. e., the amplitude of difference as a fraction of the maximum amplitude of radial component. Note that the 4- and 5-layer models provide excellent fits, whereas the fit for the 3-layer model is significantly poorer.
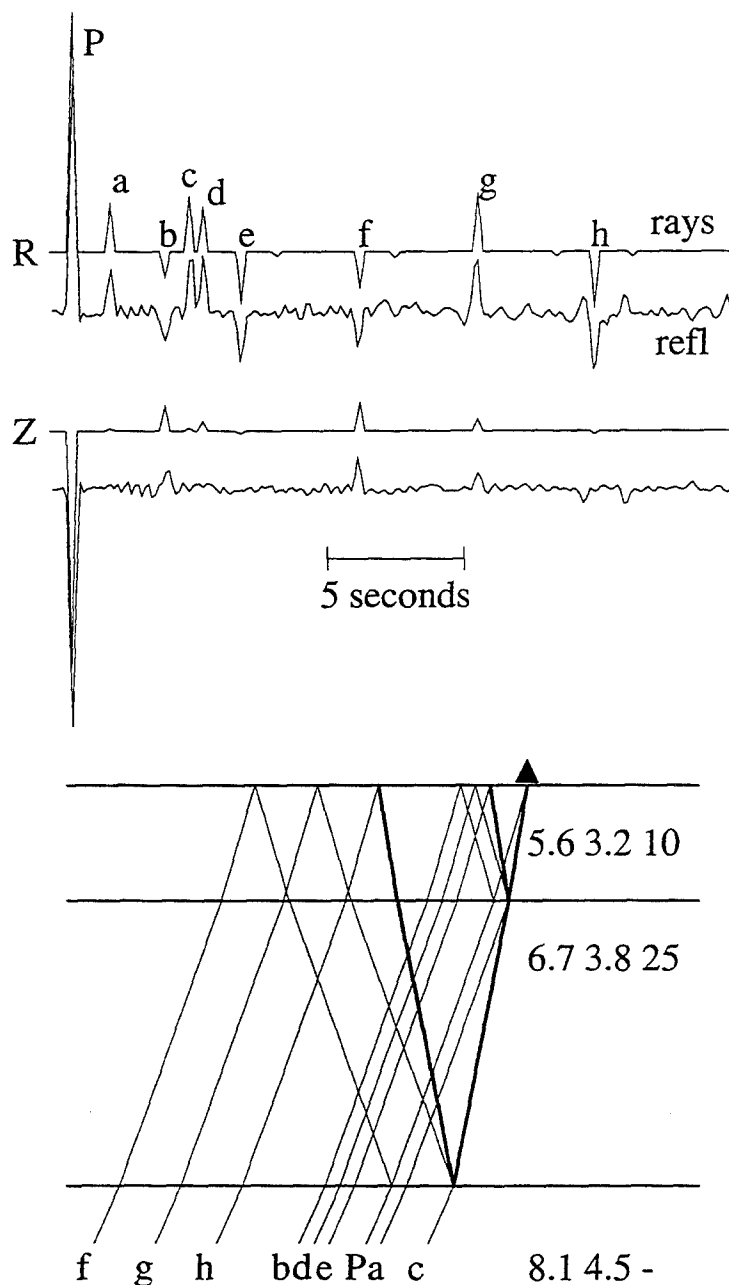
Figure 2. Comparison of radial- (top two traces-- labeled R) and vertical-component (middle two traces-- labeled Z) synthetics generated using generalized ray theory (upper trace in each pair) and with reflectivity (lower trace) for a two-layer-over-a-halfspace model (bottom-- numbers at right represent model P and S velocities and layer thicknesses). Only the nine rays with the labeled ray paths have significant energy.
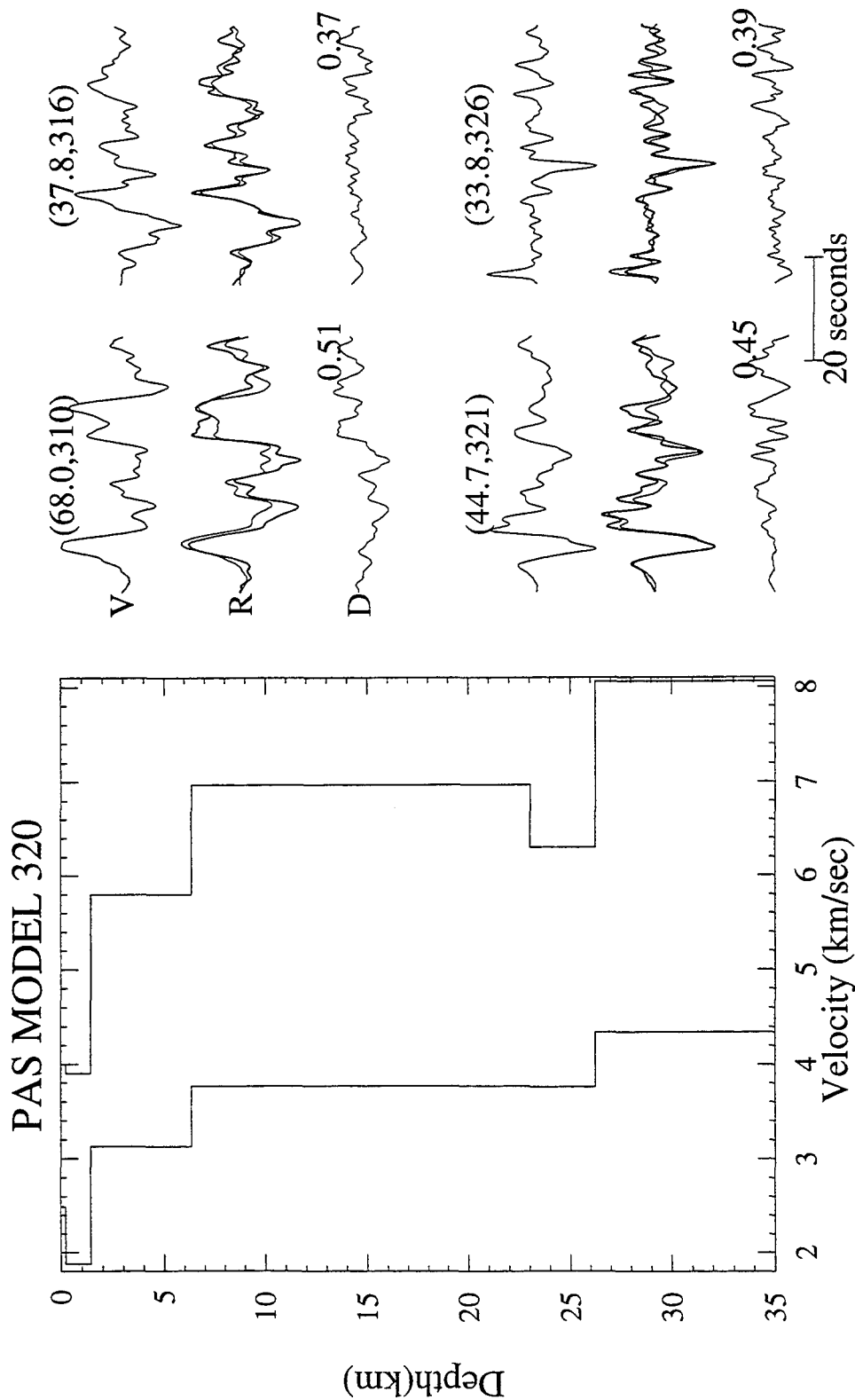
Figure 3. (Left panel) Optimal 5-layer crustal model determined with our SORVEC-VFSA algorithm for station PAS (Pasadena, California). Note that the topmost layer is very thin (< 1/2 km), and that the shear velocity in the fifth layer is indistinguishable from the velocity in the fourth layer. Right panel shows fit between teleseismic waveforms and synthetics generated using the model at left.
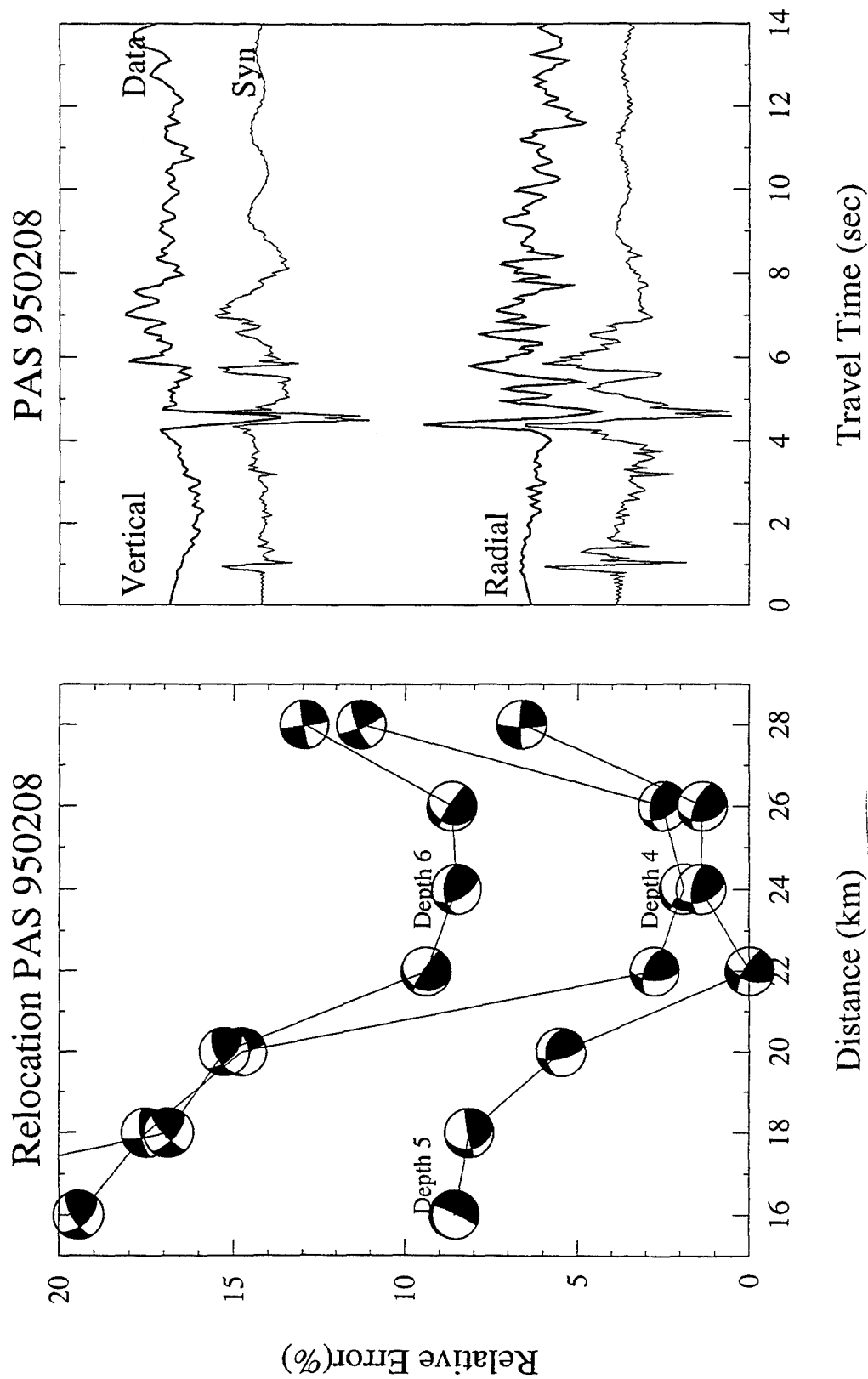
Figure 4. (Left panel) How station-event distance and event focal depth influence fit between data and synthetic waveforms at PAS for the earthquake of 8 Feb. 1995. Relative error is the percentage difference between a normed fit and the optimum fit (0% relative error); best fitting focal mechanism is determined by a grid search for each trial distance and focal depth as indicated by plotted beach-ball mechanism. (Right panel) Comparison of vertical- and radial-component waveforms at PAS (upper traces) with best-fitting synthetics (lower traces).

Back Azimuth Determination
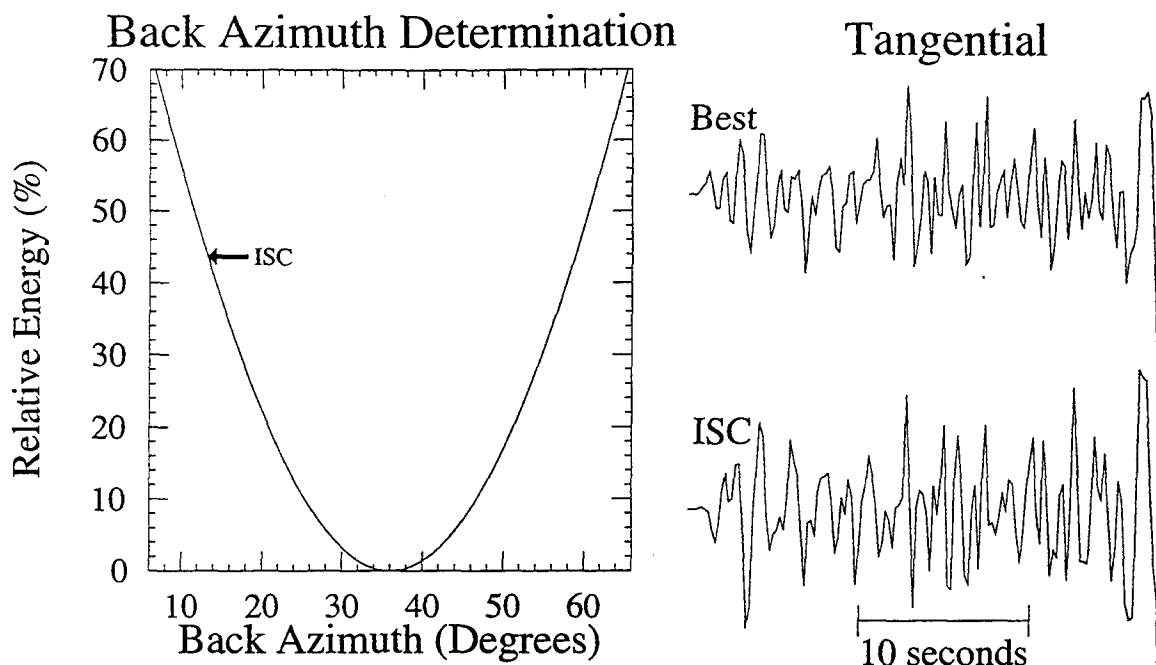
Tangential

Figure 5. (Left panel) Dependence of tangential-component energy of P-group phases on back azimuth chosen for direction of arrival. Earthquake occurred 10 August 1991; station is AMDO in Tibet; energy is determined for the 30 seconds of signal following the initial P arrival. Note that minimum energy occurs for a back azimuth of 35°, while energy is 45% greater for back azimuth corresponding to location reported by the ISC. Right panel shows the tangential-component waveforms for the smallest-energy (top) and ISC-reported (bottom) azimuths.

AMDO MODEL 44
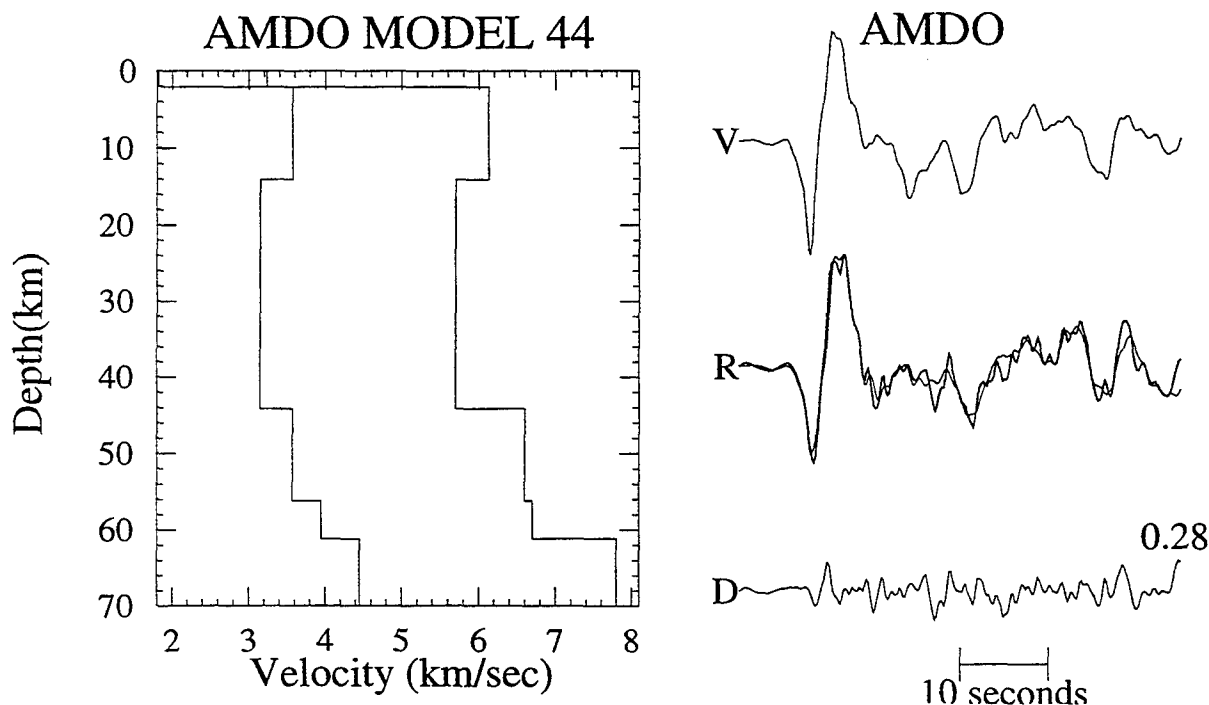
AMDO

Figure 6. (Left panel) Optimum five-layer crustal model determined by the SORVEC-VFSA algorithm for station AMDO in Tibet using waveforms from an earthquake occurring in Alaska on 26 March 1992. (Right panel) Vertical- (V) and radial-component (R) waveforms for this earthquake recorded at AMDO (light lines), and synthstic radial-component waveform (dark line) for the optimum crustal model at left. Trace "D" is the difference between observed and synthetic radial-component waveforms.

949
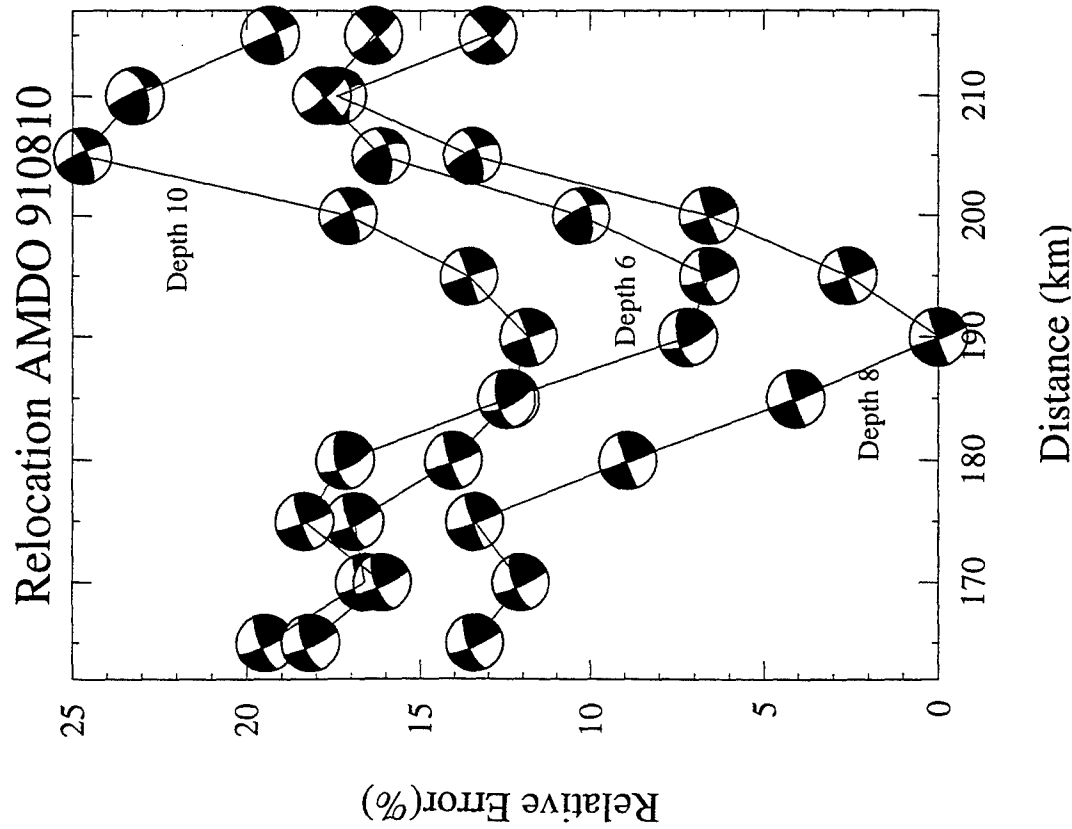
Figure 7. (Left panel) Relative error (i. e., misfit) between observed waveforms and synthetics generated for a range of distances and depths. The earthquake is the regional event of 10 August 1991, and synthetics assume the crustal model of Figure 6; best fitting focal mechanism is determined by a grid search for each trial distance and focal depth as indicated by plotted beach-ball mechanism. (Right panel) Comparison of vertical- (V), radial- (R), and tangential-component (T) waveforms for data (top trace) and synthetics (bottom trace) generated for the best-fitting distance, depth, and focal mechanism as determined in the left panel.

KNOWING THE DEPTH OF A SHALLOW SEISMIC EVENT, HOW OFTEN CAN WE FIND DEPTH PHASES AT REGIONAL DISTANCES?

J. E. Zollweg and D. M. Childs
Boise State University

ABSTRACT

Digital data from 14 events (magnitude 2.4 - 4.5) occurring during the 1981 Elk Lake, Washington earthquake sequence were examined for evidence of phases that could be used to establish focal depths from single recording stations at regional distances. Hypocentral parameters for the Elk Lake sequence are well known as a result of its occurrence within a dense monitoring network. Paths to stations at distances of 130 to 300 km are usually structurally complex. The P_n, P_mP, and P_g phases were found to propagate poorly, and consequently these phases are not promising candidates for use in depth determination. Phases that exhibit depth dependence were found at some stations, but at no station could two P phases be found whose time difference could be used to estimate focal depth. A pair of stations in the same azimuth showed observable time differences between phases that are a function of event focal depth. The time differences are small, 0.1 to 0.3 s for events having a 4 km range of focal depths. Our results suggest that good determination of focal depths from pairs of stations along the same azimuth is possible for events located in small source regions.

Objective

Focal depth determination of seismic events recorded at regional distances is potentially an important means of discriminating between small explosions and earthquakes. We are investigating the frequency with which identifiable crustal phases are recorded, the resolution of depth determination using crustal phases, and the frequency with which any given station can make such determinations.

Methodology

To test potential accuracy of regional phase focal depth determinations and applicability of the methodology to propagation paths through mixed or unknown structure, it would be desirable to study events in a region meeting the following criteria: (1) as many geologic provinces as possible located at regional distances; (2) known gross features of regional velocity structure; (3) widespread crustal seismicity with a good range of focal depths; and (4) well-determined hypocenters due to dense regional seismographic coverage. These conditions are met in the United States' Pacific Northwest.

Our procedure is to take events occurring at different depths in a small region and examine records from single stations for evidence of depth-related phases. We use two techniques. The first is ray-tracing through known structure and attempting to identify arrivals on the seismograms corresponding to the correct travel time for a particular phase. The second is to plot distance-normalized seismograms and look for evidence of phases whose travel-time is a function of depth. The second method is more robust and requires no other input than a known hypocenter.

Our initial analysis has been concentrated on the 1981 Elk Lake, Washington earthquake sequence (Grant et al., 1984). This sequence consisted of over 1000 located events occurring on a nearly vertical right-lateral strike slip fault within the dense seismograph network installed to monitor Mt. St. Helens. More than 80 events were magnitude 2 or greater. These events were recorded by a large number of single-component telemetered stations located at epicentral distances between 150 and 300 km, in several velocity model provinces (see Figure 1). These stations were recorded digitally with 12 bit resolution by the University of Washington. A data set of 14 of the better recorded events (magnitude 2.4 or greater) recorded at about 25 stations has been investigated in detail.

To insure a consistent set of hypocenters, relative relocation of the Elk Lake sequence was performed using P waves at a nearly constant set of stations lying within 50 km of the epicenters and having good azimuthal distribution. Stations known to have large delays or characteristically having poor first arrivals were not used. A different delay model was used than that employed by Grant et al. (1984); it was selected on the basis of considering a 13 May 1981 0504 UTC event (M_L 4.5) as a master event. The locations of the largest events have root-mean-square errors of 0.01 to 0.02 s and are likely to be about the best that can be accomplished with the existing arrival time data. It is believed that location errors for the events we studied are about 200 m horizontally and 400 m vertically. The resulting hypocenters cluster to a greater degree than those of Grant et al. The fault length was 6 km, and the depth range of the aftershock activity was about 7 km. Because of the nearly vertical fault-plane orientation, events occurred having nearly the same epicenter but very different depths.
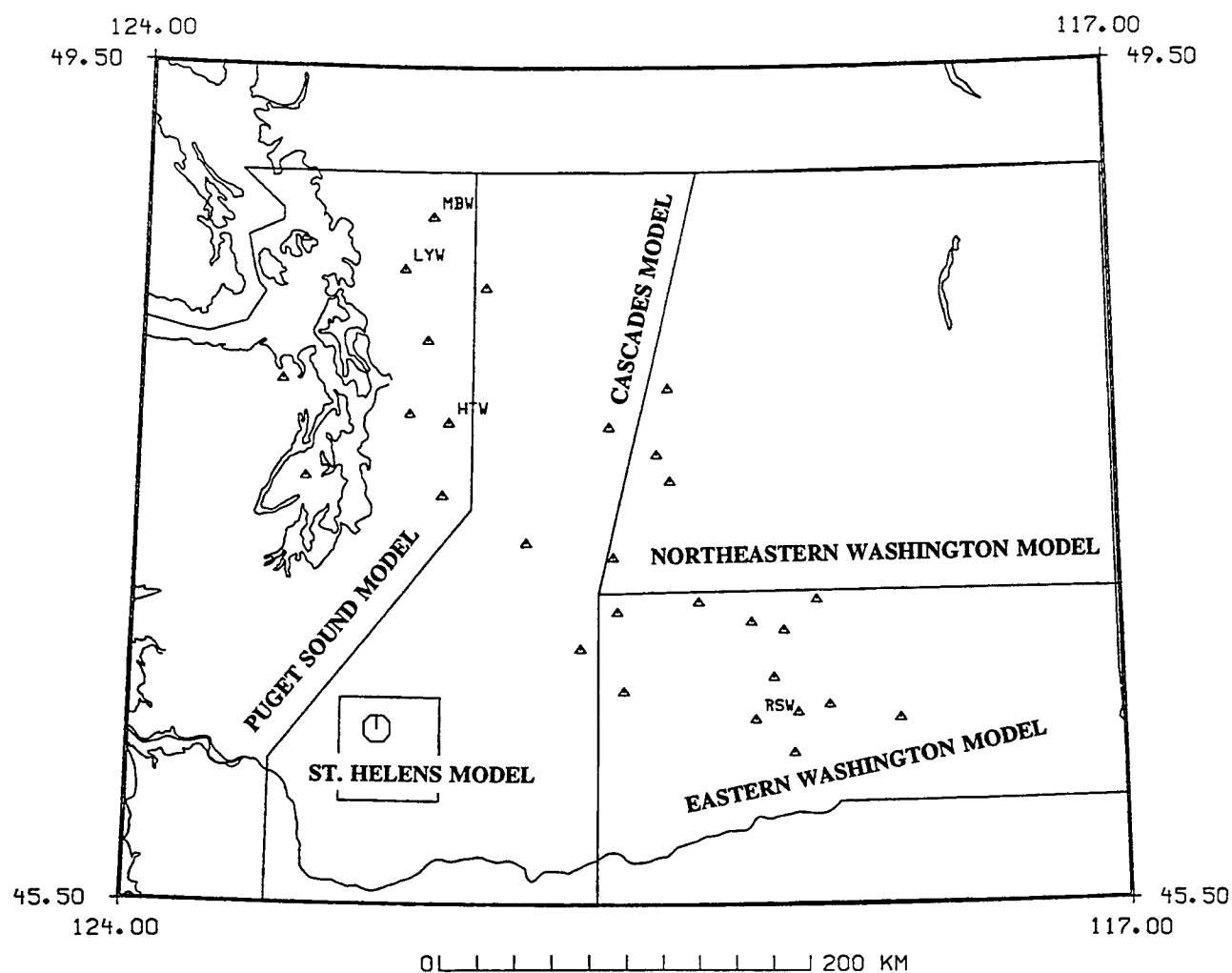
Figure 1. Regions of validity of University of Washington velocity models used in regular seismic event location. Recording stations whose data have been examined in this study are shown by triangles; stations whose data are discussed are identified by station code. The epicenter of the 1981 Elk Lake main shock is shown by an octagon.

The stations selected for study of secondary arrivals were those generally to the north, east and northeast of the epicenters. Ray-tracing of P waves was performed using RAYINVR (Zelt and Smith, 1992). Raypaths to these stations traverse two or three out of four separate crustal regions, as defined by routine University of Washington velocity models (Figure 1).

Seismograms for all stations were examined in a variety of frequency bands. We found that bandpassing the data with corners at 1 and 3 Hz gave the best tradeoff in improving the similarity of different events at the same station while retaining as much high frequency content as possible.

Preliminary Research Results

Complex P waveforms are observed to the north, east and northeast of the epicenters at distances of 130 to 300 km (see Figure 2). Surprisingly, P_n, P_g, and P_mP are weak phases, with P_n usually being near background noise levels for events in the magnitude 3+ range and the latter two phases often being unidentifiable (particularly P_g). Ray-tracing to identify arrivals was not particularly helpful. Some stations had identifiable arrivals, but strong unpredicted phases were often observed and arrivals expected to be strong often were not observed. These observations suggest it will be difficult to make single-station estimates of focal depth based on P waves travelling different crustal paths.

Seismograms for all 14 events were compared at each of the stations plotted in Figure 1. Same-station seismograms were plotted as functions of depth and of epicentral distance, using the well-determined origin times and the expected times of P_g (a phase whose travel time is virtually independent of focal depth at regional distances) to align the traces. At some stations, depth-related phases with small moveouts with respect to depth (of the order of 0.1 to 0.3 s) were observed. The stations having the clearest examples of such phases are identified by their station code on Figure 1. Figure 3 shows an example of a depth-related phase recorded at HTW. Figure 4 shows that the phase travel time is not as closely correlated with epicentral distance as with focal depth.

Since multiple depth-related phases with a differing dependence on depth were not observed on any single station, any determination of focal depth from the data we have studied so far requires 2 or more stations. Stations HTW and MBW were at essentially the same azimuth from the Elk Lake source area, making any time difference between their observed depth-related phases almost entirely a function of depth. Figure 5 shows the time differences, both corrected for small differences in epicentral distance and uncorrected. Both plots are similar, and indicate that there is depth dependence in the time difference. Again, the dependence is small. Nevertheless, we are encouraged that it is observable.

Preliminary Conclusions

Regional phases that have been commonly thought to be useful in focal depth determination (such as P_n, P_g, and P_mP) do not appear to be prominent phases in the data studied to date, making it difficult to estimate depth from a single station. Coherent depth-related P phases are observed at some stations and have travel times that differ by 0.1 to 0.3 s as a function of depth for a small source area. Time differences between such phases observed at two stations along the same azimuth have a similar depth dependence.

954
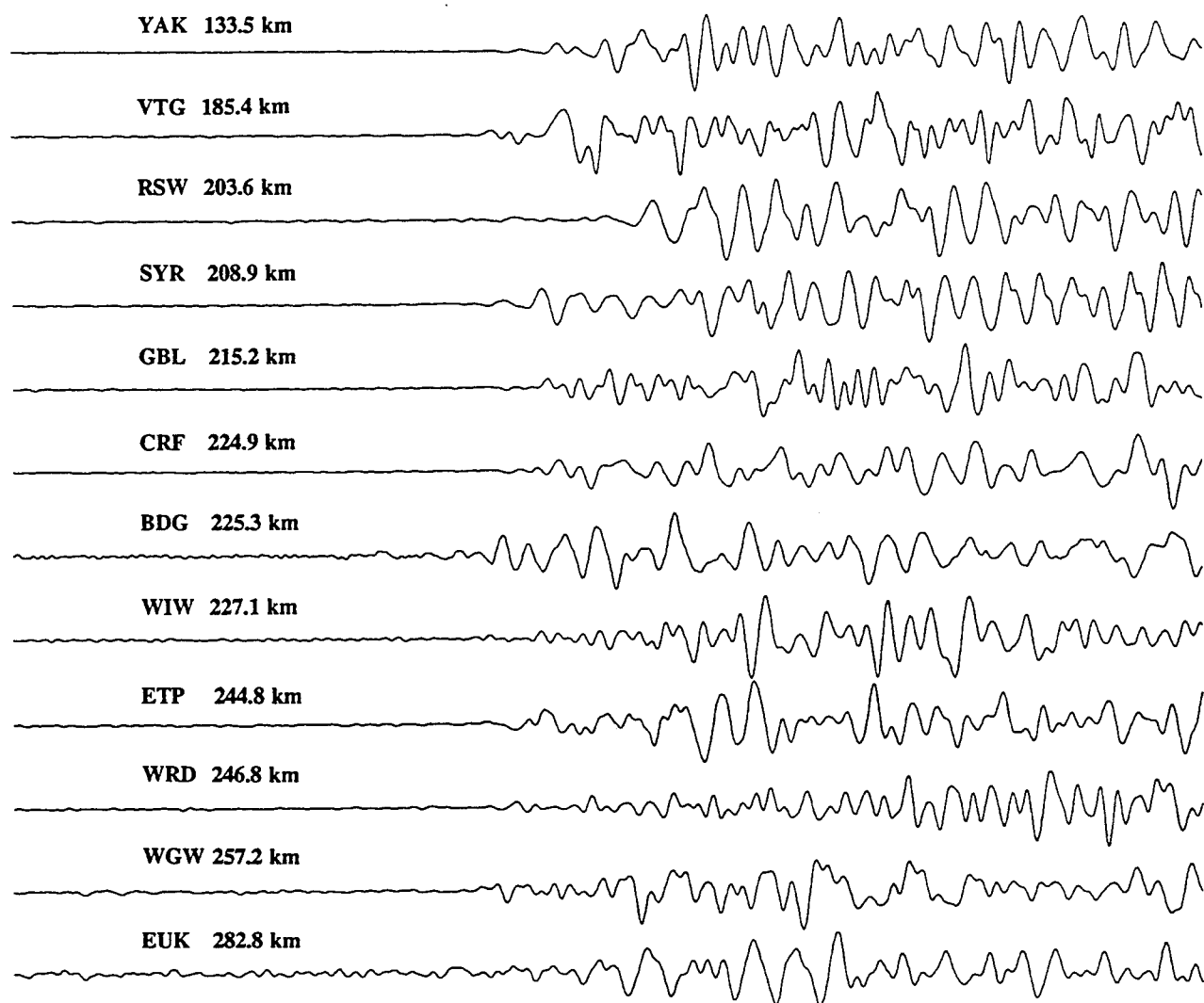
Figure 2. Seismograms from eastern Washington stations for aftershock of 14 February 1981 2127 UTC (magnitude 3.8, depth 7.8 km). Seismograms are 8.5 sec in length and are aligned on the observed first arrival time. Note weak and emergent first arrivals.
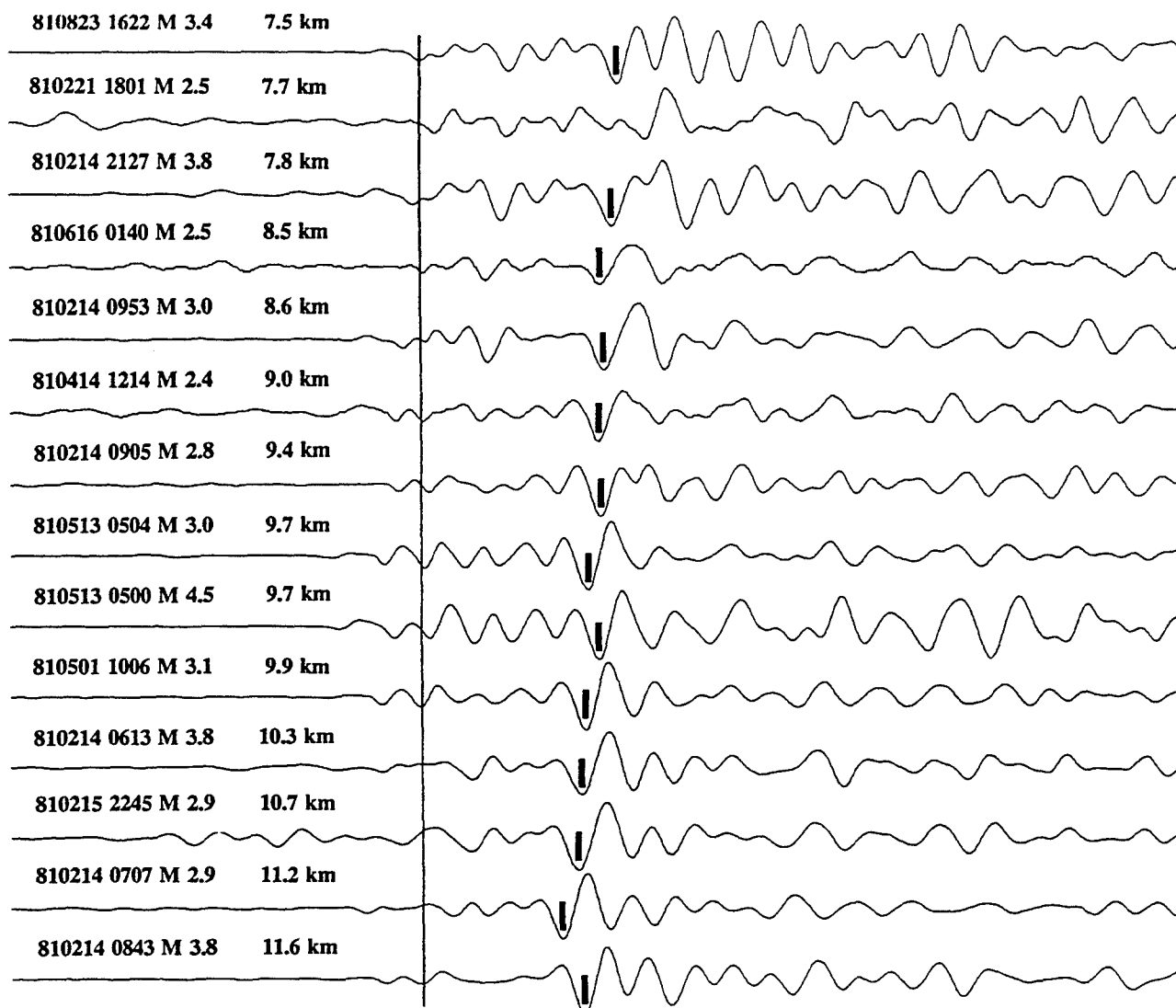
Figure 3. Seismograms from station HTW. Events' focal depths are shown. Seismograms are aligned on the predicted time of a direct wave with a velocity of 6.0 km/s, whose travel-time is nearly constant for the small range of distances and depths involved. Seismograms are 8.5 sec in length and are band-pass filtered with corners at 1.0 and 3.0 Hz. The vertical line is a reference line drawn through the trough of an arrival for the deepest event. Note that the offset from the reference line of an arrival marked with a bar decreases with increasing event depth.

810501 1006 M 3.1	164.1 km	
810513 0500 M 4.5	164.5 km	
810513 0504 M 3.0	164.5 km	
810214 0905 M 2.8	164.8 km	
810823 1622 M 3.4	164.8 km	
810214 0843 M 3.8	165.5 km	
810221 1801 M 2.5	165.9 km	
810414 1214 M 2.4	165.9 km	
810214 2127 M 3.8	166.5 km	
810616 0140 M 2.5	167.1 km	
810214 0707 M 2.9	167.4 km	
810214 0953 M 3.0	167.4 km	
810215 2245 M 2.9	167.8 km	
810214 0613 M 3.8	167.8 km	
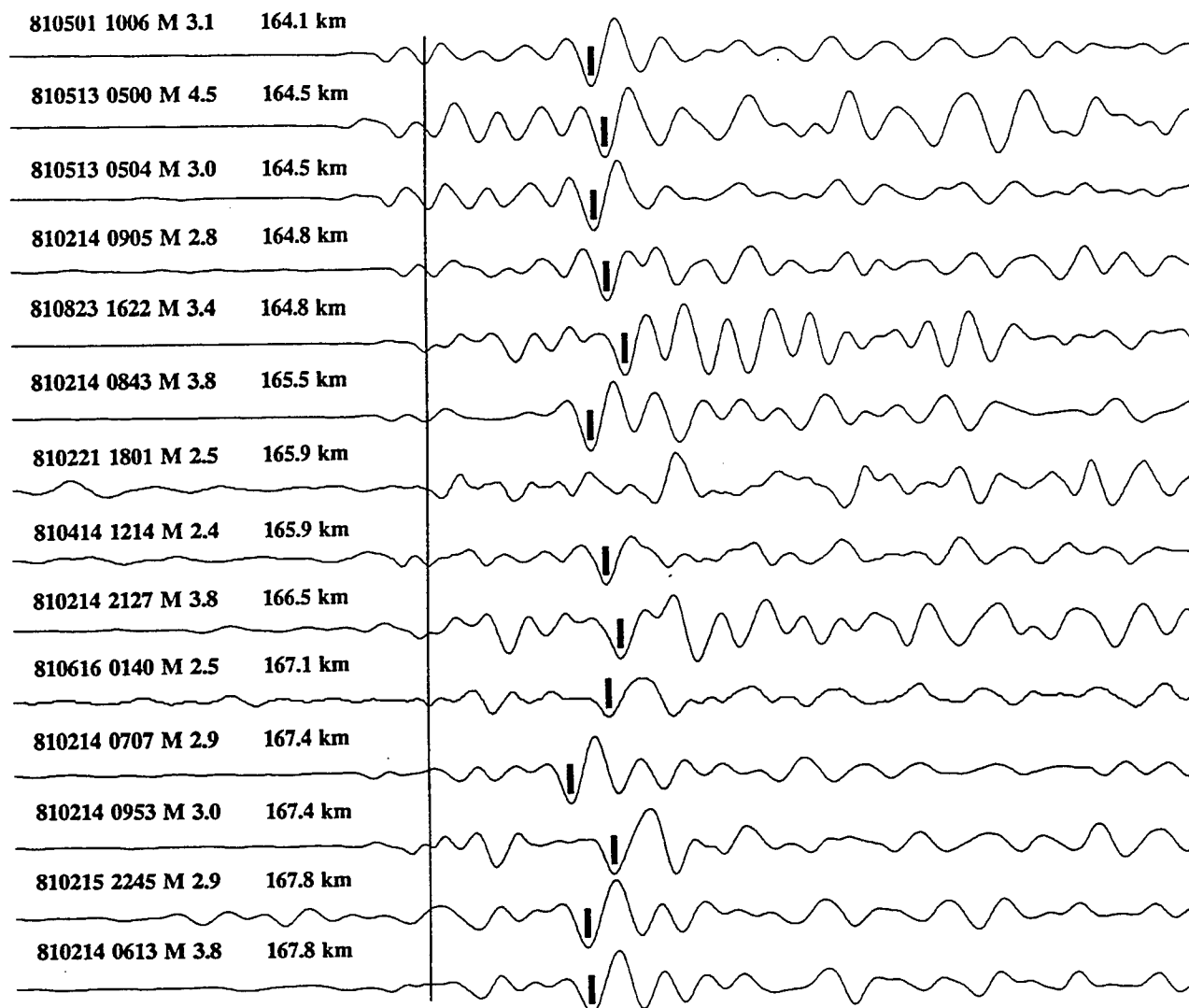
Figure 4. Seismograms from station HTW. Events' epicentral distances are shown. Seismograms are aligned on the predicted time of a direct wave with a velocity of 6.0 km/s, whose travel-time is nearly constant for the small range of distances and depths involved. Seismograms are 8.5 sec in length and are band-pass filtered with corners at 1.0 and 3.0 Hz. The vertical line is a reference line drawn through the trough of an arrival for the deepest event.
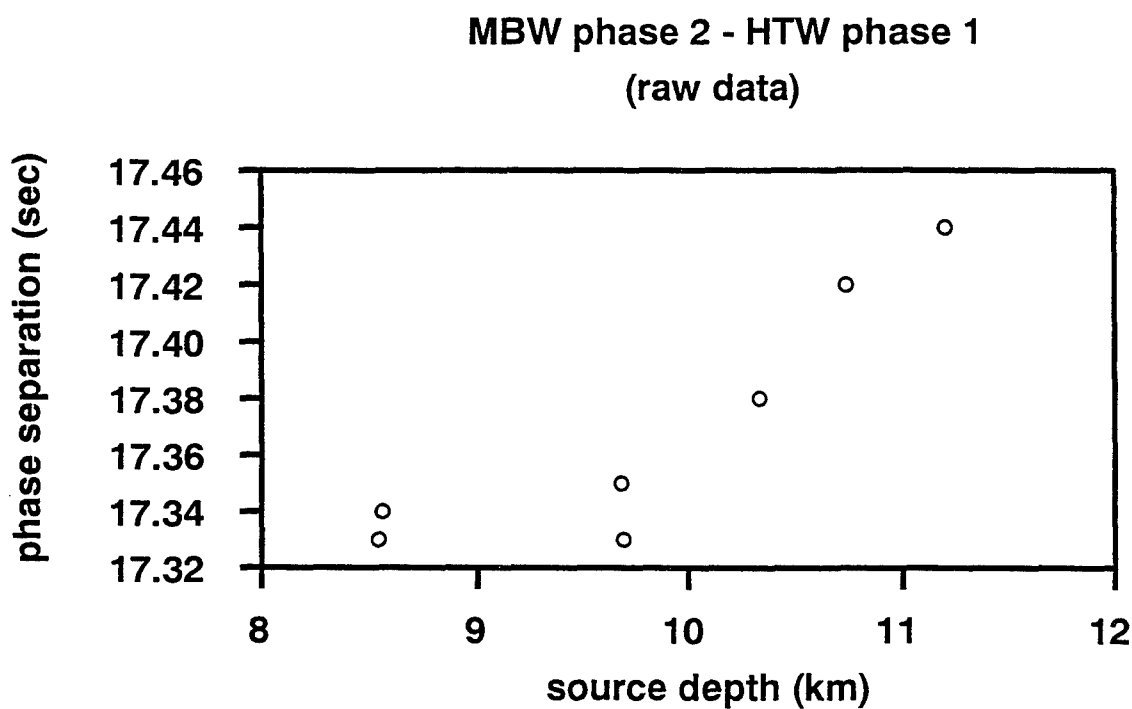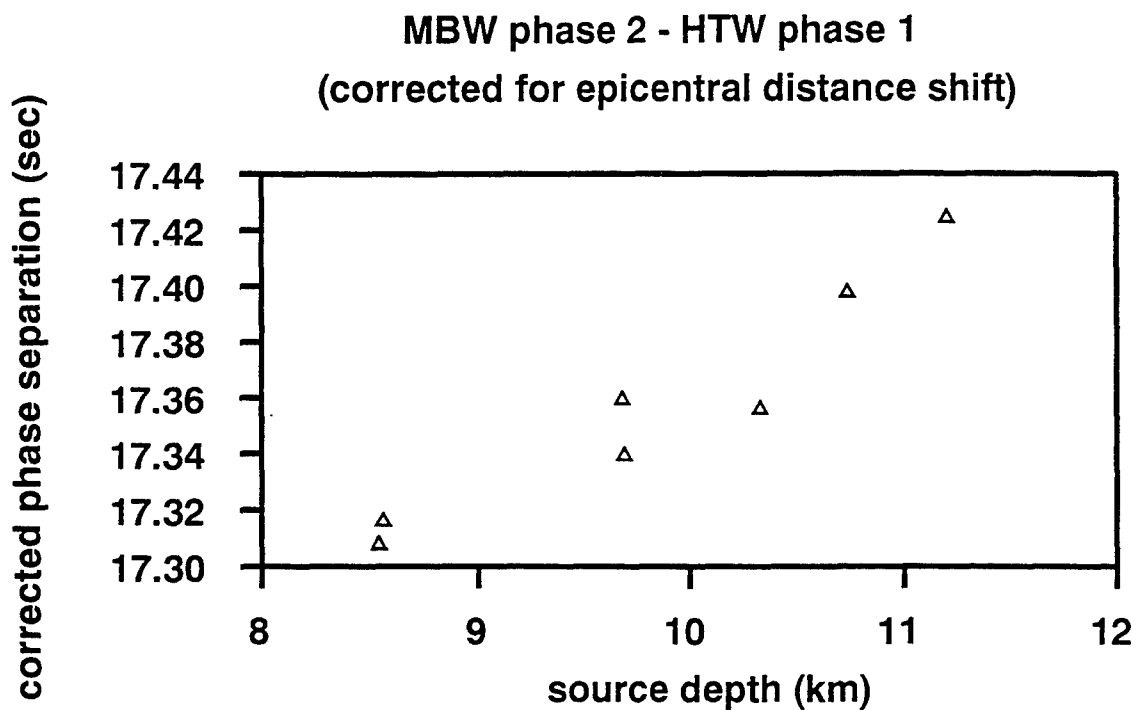
Figure 5. Time differences between secondary phases at HTW and MBW. Top plot shows the differences corrected for epicentral distance shifts using a correction velocity of 6.0 km/s, while the bottom plot shows the raw observations.

The implication for CTBT monitoring is that reliance on P_n, P_g, and P_mP in structurally complicated areas may not be appropriate. While depth-related phases have been found, they are apparent at a minority of the stations examined to date, indicating that site selection for CTBT seismic monitoring may not be trivial. Finally, although the depth-related phases observed to date appear to be capable of fairly good depth resolution over a small area like an aftershock zone, we do not yet know whether they can be traced over a larger region.

Future Plans
We are examining additional earthquake sequences at a variety of depths, in different geological environments, and with larger offset distances.

REFERENCES

Grant, W. C., C. S. Weaver, and J. E. Zollweg (1984), The 14 February 1981 Elk Lake, Washington, earthquake sequence, *Bulletin of the Seismological Society of America* **74**, 1289 - 1309.

Zelt, C. A., and R. B. Smith (1992), Seismic traveltime inversion for 2-D crustal velocity structure, *Geophysical Journal International* **108**, 16 - 34.

ABOUT THE CONTROL OF THE UNDERWATER AND ABOVEWATER NUCLEAR EXPLOSIONS BY HYDROACOUSTIC METHODS.

V.V. Adushkin, B.D. Khristoforov
Moscow, Institute for Dynamics of Geospheres Russian Academy of Sciences

ABSTRACT

The analysis of the experimental data available at the IDG which may be applicable to the problem of the detection and identification of nuclear explosions by modern hydroacoustic methods is represented. These data includes some results of observations of nuclear explosions at the Novaya Zemlya test site; results of measurements of HE with weights to 100 kg at a shallow reservoir; explosions of deep water bombs and mines; modeling of explosions of small charges of HE including underwater explosions in cavities filled by air.

On the basis of the analysis of the experimental data it was shown that methods of hydroacoustic control can be used for the detection and identification of nuclear explosions, which were conducted near bottom or the free surface of water, above water and at reservoir's coast including underground explosions. Application of high sensitive hydrophones established near the bottom of sea with low level of noise, existence of sound channels with small attenuation favor this inspection. From nuclear explosions conducted in confined reservoirs similar to the Bay of Chernaya, hydrophones can received signals in open sea from seismic waves before shock waves in water. These tests shows strong reducing effect of the bottom and free surface of the reservoir on the acoustic efficiency. Thus, it is necessary to conduct a special investigation for determining the advantages and disadvantages of the methods of hydroacoustic control respective to different methods. Special acoustic source function was developed which allows to determine parameters of acoustic signal at large distances before the acoustic wave comes into sound channel. Acoustic signals from various sources of natural and artificial origin: HE, impact of meteorites, earthquakes, tsunami and so on are used for identification of nuclear explosions.

List the key words: water, underwater, abovewater, explosion, HE, control, nuclear, hydroacoustic, method, shock wave, gaseous, bubble, bottom.

ABOUT THE CONTROL OF THE UNDERWATER AND ABOVEWATER NUCLEAR EXPLOSIONS BY HYDROACOUSTIC METHODS.

V.V. Adushkin, B.D. Khristoforov
Moscow, Institute for Dynamics of Geospheres Russian Academy of Sciences

In order to improve hydroacoustic methods of identification and control of underwater and abovewater nuclear explosions available experimental data on hydrodynamic processes in water induced by nuclear and chemical explosions in various conditions are considered. The data are important for construction of a general acoustic source function determining parameters of hydroacoustic waves at large distances from an explosion.

Approximately half of the explosion energy is transferred into shock wave from explosions in unconfined reservoir with the another half remaining in the gaseous bubble and radiated in the consequent oscillations. Energy remaining after dissipation of the shock wave in the near-field zone and energy of the gaseous bubble oscillations propagates at large distances as an hydroacoustic wave. The wave may propagate at large distances due to low attenuation in sound channels. Thus, hydroacoustic methods of control in a number of cases may be preferable. In the real conditions, the energy of acoustic waves in water is decreased by effect of the bottom and free surface of reservoir, that lead to decrease an efficiency of the control. That is why special comparative investigation for determining of advantages and lacks of methods of hydroacoustic control must be conducted. Special source function is helpful to be introduced. This function determines parameters of the acoustic wave coming into a sound channel or for different boundary conditions. In this paper we restricted to a number of experimental data, which showed the influence of real conditions of subwater explosions on its efficiency as a source of acoustic waves.

Specialists from the IDG RAS were taking part in the works of equipment design and measurements of mechanical, seismic and acoustic effects from all nuclear explosions. All the underwater nuclear explosions were conducted in shallow sea, when a large part of explosion energy is transferred into ground and air decreasing intensity of hydroacoustic disturbances. Motion of gaseous bubble was substantially changed as well as emitted into water energy was decreased due to venting of explosion products into the atmosphere. Hydroacoustic disturbances from above water explosions are produced by air shock wave and fall of a water column. The acoustic information on explosion source in known reservoir is obtained from analysis of amplitudes, duration and frequency content of measured signals generated by shock wave and following oscillations of a gaseous babble. The latter generates low frequency acoustic wave characterized by lower attenuation. So, further investigation of the parameters of shock waves and gaseous babbles is of great importance regarding with characteristics of reservoirs, propagation paths in ocean at different condition of explosions , as well as a possibility to conceal and identify the explosions from background noise from nature and technical explosion sources.

Several sets of sensors and recording equipment were designed as well as systems the distant control of the tests and equipment. They were used in natural and model tests with HE at different test sites and laboratory, as well as for investigations of propagation of hydroacoustic signals on large distances at explosions of deep water bombs and mines in sea since 1955.

From the nuclear explosions, the majority of the data for shock wave parameters were obtained by mechanical equipment, which was used in general.

A set of photographic cameras was used in order to record phenomena at the free surface in two perpendicular directions and from above from a plane. Surface waves were also measured by resistive gages with recording of signals onto recording strain gauge. Shock wave parameters in the atmosphere were recorded by a pressure recorder onto smoked paper.

The hydroacoustic signals from the deep water bombs were measured at large distances at ships, submarines and at the coast by different types of high sensitive hydrophones. In these experiments, industrial hydrophones with sensitivity of about 60 V/atm and frequency band above 5 Hz, hydrophones of ships with sensitivity of about 200-500 V/atm and frequency band above 5 Hz, and piezoelectric hydrophones with sensitivity of about 10 V/atm and frequency band above 4 Hz were used.

The investigations of hydroacoustic waves in wide range of distances from nuclear explosions were conducted for 3 underwater (21.9.55.-20 êò, 10.10.57.-small

Fig. 1. A snapshot of the underwater nuclear explosion in 1957.

è 23.10.61 .small), 3 abovewater (13.9.61-small, 27.10.61-small, 22.8.62-small) and 1 coastal explosion on tower with height 15 m(7.9.57.-28 êò). Furthermore, an additional measurements were conducted for 3 underground explosions of large energy (27.10.66.-420 êò, 12.9.73.-2100-1600 êò, 29.8.74.-500-640 êò) at the coast of the strait of Matochkin Char.
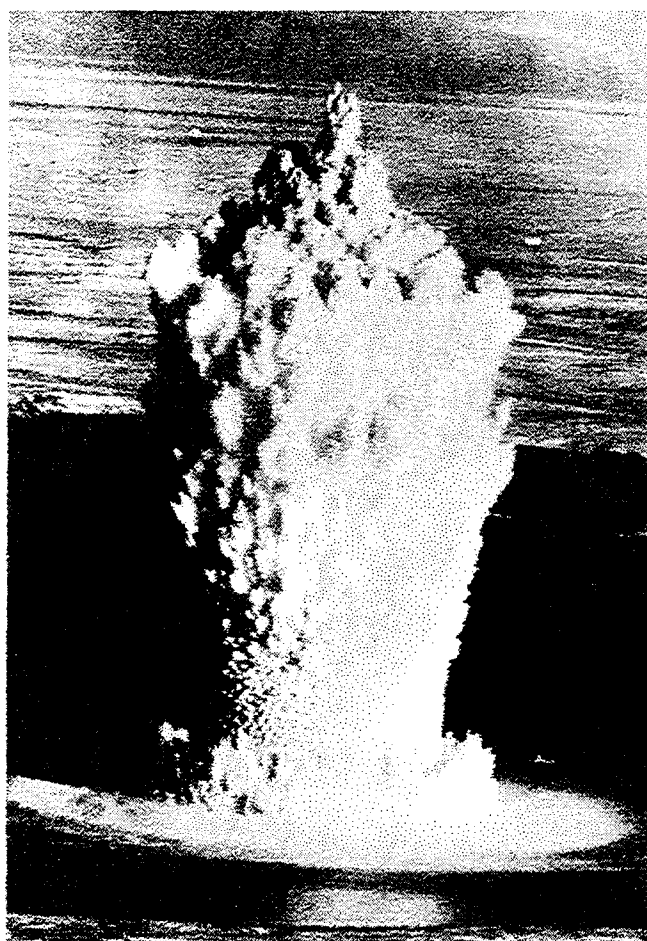
The nuclear device was placed at a depth of 20 to 25 m in the first test. All the underwater explosions were of approximately the same energy and were conducted at scaled depths $H^*=H/R_0 = 2;5;2$ respectively (Ro is the radius of equivalent TNT charge). A snapshot of the underwater nuclear explosion in 1957 is shown in fig. 1. The second explosion was fired at the bottom of the basin and the third at a depth of 20 m. The depth of the Bay of Chernaya beneath the point of the tests was of about 60 m. Therefore all the explosions were conducted in a
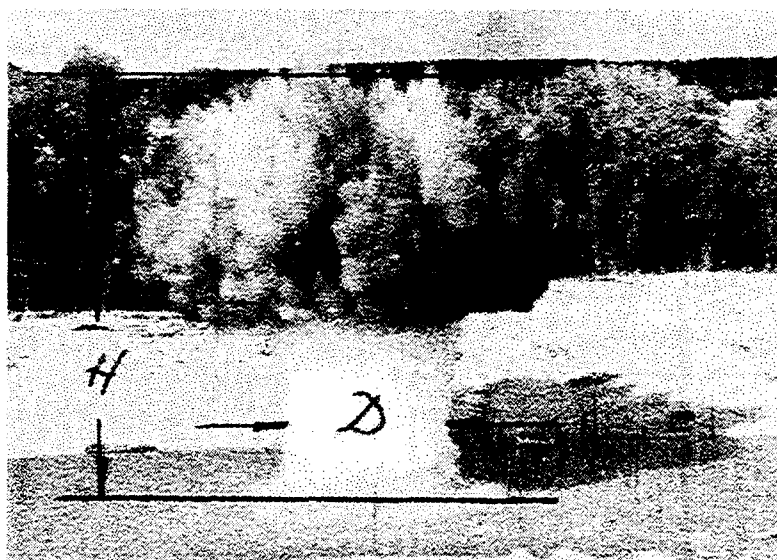
shallow basin conditions. The closest analog of the explosions is the explosion "Baker". It was conducted by USA in July 1946 at the atoll of Bikini at a depth of 60 m. Another explosion, "Vigvam", with TNT equivalent of 30 kT was conducted at a depth of 610 m in a basin 1640 m deep within Pacific on 14.5.55.

Thus, the investigations showed that parameters of hydrodynamic process from explosions of close yields may change by an order of magnitude depending on conditions. HE explosions of different weight were conducted in shallow reservoirs with various types of bottom soils and depths in order to model nuclear explosion. This experiments based on the geometry and energy scaling law. Figure 2 displays a snapshot of an explosion of spherical charge of TNT with weight of 100 kg in the center of reservoir 3 m deep with sandy bottom. Figure 3 shows measured peak overpressure in shock wave against scaled distance from explosions in the centers of reservoirs of different depth. Overpressure and energy of hydroacoustic waves strongly decrease with decrease of the reservoir's depth because of increase of energy part transmitted into the air and ground. At the Black Sea, from explosion of 3000 kg in water with sound velocity gradients, shadow zones and peaks of acoustic signals induced by interference of sound waves in inhomogeneity liquid were observed.

Propagation of hydroacoustic waves at large distances from explosions of deep water bombs was investigated in the Sea of Okhotsk by means of piezoelectric hydrophones in 1-1000 Hz

Fig. 2. A snapshot of an explosion of spherical charge of TNT with weight of 100 kg

Fig. 3. Peak overpressure in atm in shock wave against scaled distance from explosions in the centers of reservoirs of different depth. $H_* = 2R_0$, $4R_0, 12R_0$. Dotted line is a nuclear explosion. R_0 is the radius of equivalent HE charge.
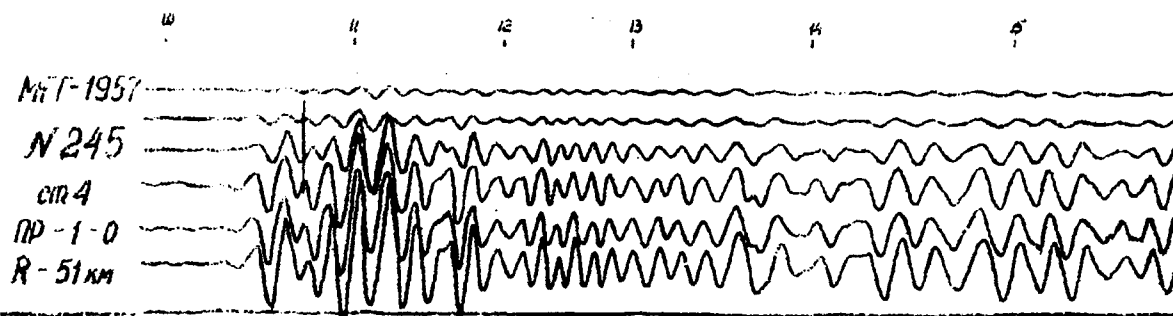
Fig. 4. Typical recordings of initial part of the signals from refracted in water seismic wave near bottom of sea area.

frequency range. The explosions at 10 to 300 m deep were recorded by submarine to a distance of 300 km and different depths.

Typical recordings of initial part of the signals from refracted in water seismic wave are shown in fig. 4. The ratio of signals from shock wave and following pulsation of the gas bubble against distance and depth was investigated from ships. This ratio decreases fast with increasing distance due to attenuation of high frequencies and the signals from the following pulsation become dominating. The waves reflected from the bottom and free surface as well as refracted waves arrive before the direct wave propagating in acoustic channel. The explosions can be detected at distances of several thousand kilometers. Capabilities of identification depend on conditions of the bursts. For example, acoustic signals from pulsation of bubble may not arise at near surface explosion.

Near bottom and near surface explosions, above water explosions, explosions with different volume concentration of energy, including explosions in air cavity for hiding and another questions of subwater acoustics were investigated in laboratory with small HE charges. Figure 5 shows that peak pressure, impulse and energy of shock wave appreciably decrease for an explosion in a cavity with increase of its
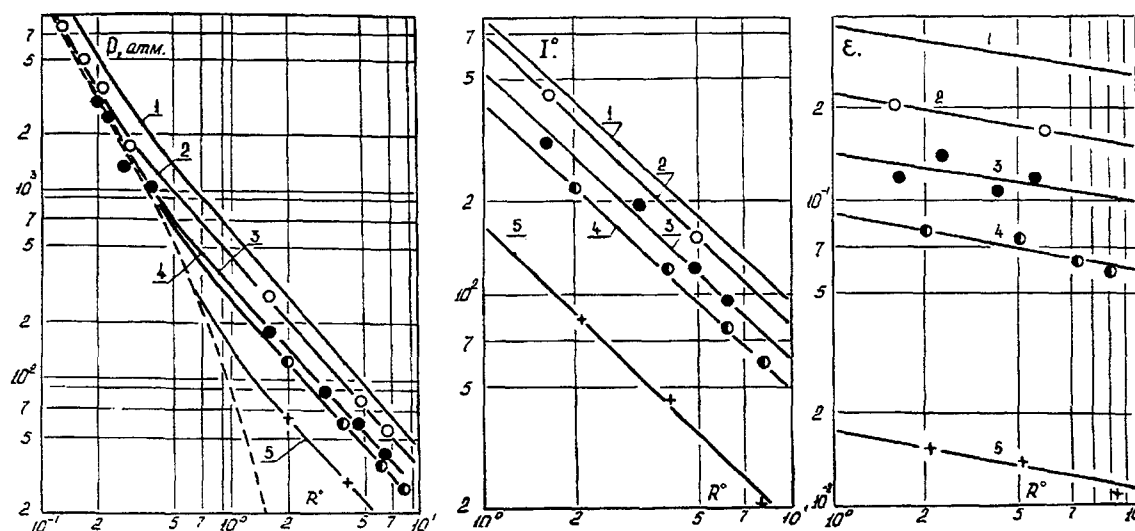
Fig. 5. Peak pressure P in atm, scaled impulse I_* in $kg \cdot s/m^2 \cdot kg^{1/3}$ and ratio of energy of shock wave to explosive energy ε_* versus scaled radius R^0 in $m/kg^{1/3}$ for subwater explosion in air cavity. 1,2,3,4,5 are R_1/R_0=1, 2.64, 3.92, 5.0, 11.9 respectively. R_1 is the radius of cavity.
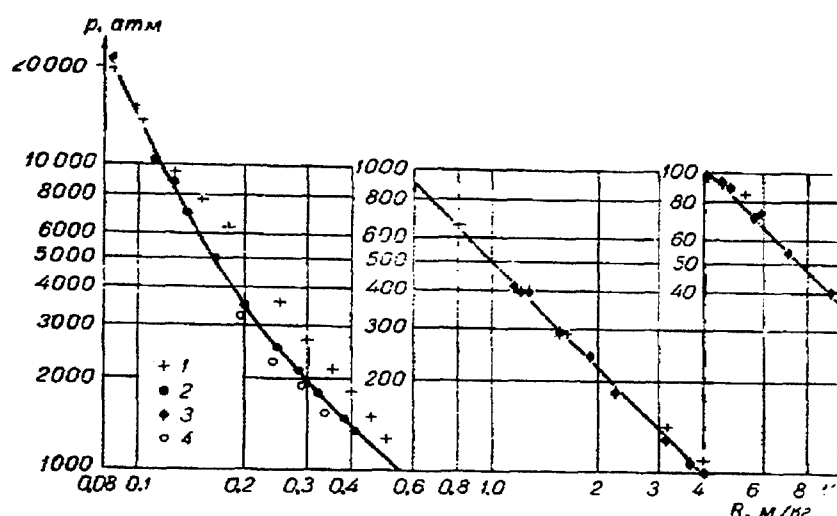
Fig. 6. Peak overpressure in atm in shock wave versus scaled distances in m/kg$^{1/3}$ for explosion of PETN with density of 0.4 g/cm^3.

radius. Accordingly, the energy of hydroacoustic disturbances generated by the shock wave have to decrease at large distances. A problem of similarity of shock waves is considered. It was shown, that shock wave parameters depend on energy concentration, E/V, in the source of an explosion. At increasing the ratio of E/V, the energy propagating at large distances is increased due to increase of a part of initial energy transferred into water by the explosion. This energy reaches maximum value at E/V corresponding to TNT explosion and decreases beyond by two times for nuclear explosion because of energy dissipation in the nearest zone [2-5].

There was an attempt to construct a source function for explosion in unconfined liquid space which determines energy of acoustic disturbances at large distances. In order to construct this function, measured time history of explosion product's radius for PETN with density of 0.4 g/cm^3 was fixed and then wave field in water was calculated numerically. The comparison of predicted and measured data of peak pressure against distance is shown in fig. 6. It can be seen that intensity of hydroacoustic signal at large distances may be determined from the available results of measurements in the nearest zone by such a procedure. Apparently, this method may be used for explosion in shallow reservoir and above water explosion.

In the model experiments with above water explosions, the complicated wave pattern (see fig. 7.) was recorded. The pattern consists from refracted air
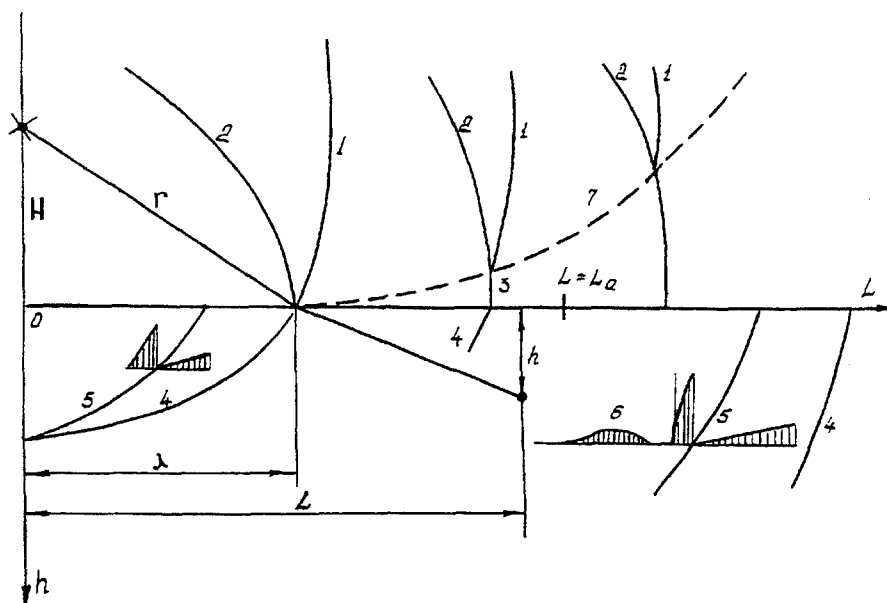
Fig. 7. Wave pattern for above water explosions. 1,2,3 -Direct, reflected and Mach waves in air. 4,5,6-refracted, epicenter and pressured waves in water.

965

wave, epicenter wave, which is generated by a shock of explosive products, and pressured wave, associated with delaying propagation of air wave.

Typical details of the flow and its parameters in the nearest zone are shown in fig. 8 for TNT explosion of 1 KT at the air-water boundary, which was determined for three times by means of model investigations with shock wave velocity in water less, then in air. Pressure in atmospheres (bars) and distances in meters were pointed along vertical and horizontal axis respectively. The results of measurements of shock wave parameters in water at large distances from an explosion of TNT spherical charge of 100 kg in 3 m reservoir at surface are shown in fig. 9. In this case, shock wave velocity in water is larger than in air. Recalculation of this data considering scaling to TNT charge of 1 KT gives following peak values of parameters (in reservoir with a depth of 12 charge's radius): at $R_*=60$ or $R=318$ m - pressure $P_m=72$ atm, duration $\tau_m=3.45$ ms, specific pulse $I_m=1400$ kgs/m^2 and at $R_*=120$ or $R=636$ m - $P_m=27$ atm, $\tau_m=2.6$ ms, $I_m=320$ kgs/m^2.
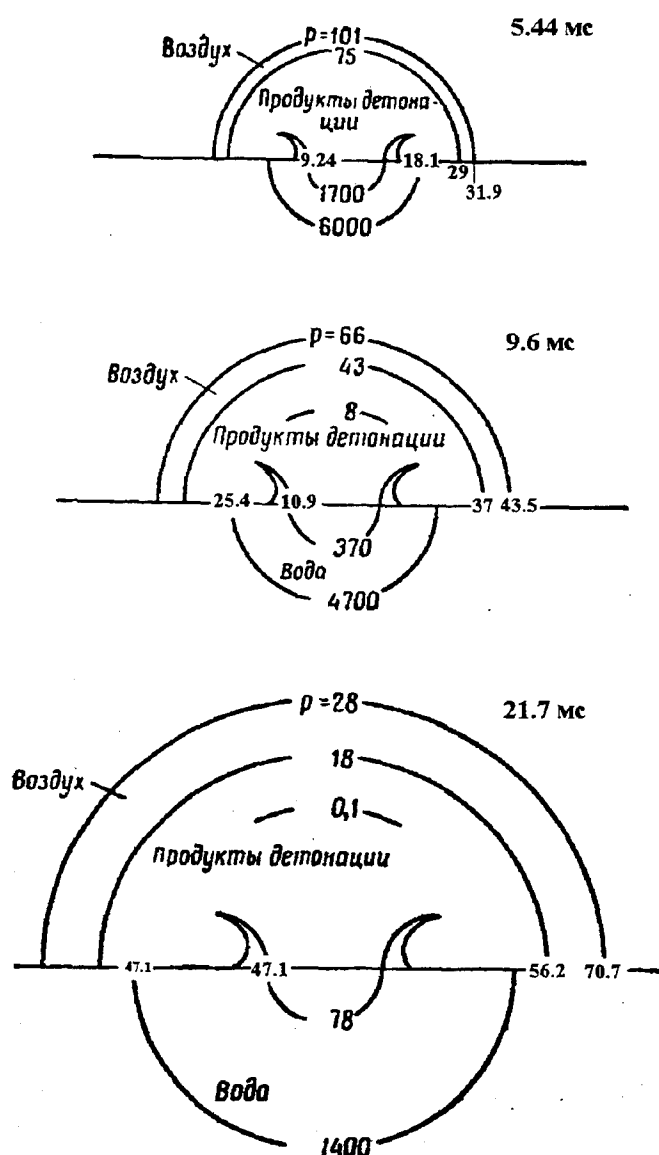
Fig. 8. Typical details of the flow for TNT explosion of 1 KT.

In accordance with the model investigations, the maximum radius of gas bubble is of 157 m and the period of the first pulsation is of 24 s for TNT explosion of 1 KT in unconfined liquid space with ambient pressure of 1 atm. Vertical radius of 170 m and period of 190 s will be for explosion at the free surface. The period increase is due to venting of gaseous products into atmosphere. During this process, pressure in the bubble does not decrease below atmospheric, back motion and subsequent oscillations of the bubble are absent. This may hamper identification of hydroacoustic signals from explosion at large distances.

Modeling of meteorite impacts at the water surface was conducted by means of a shock of high speed plasma jet. The results of measurements of shock wave and bubble were compared with the data from subwater and surface explosion with the aim of determining of TNT equivalent of the impacts

966
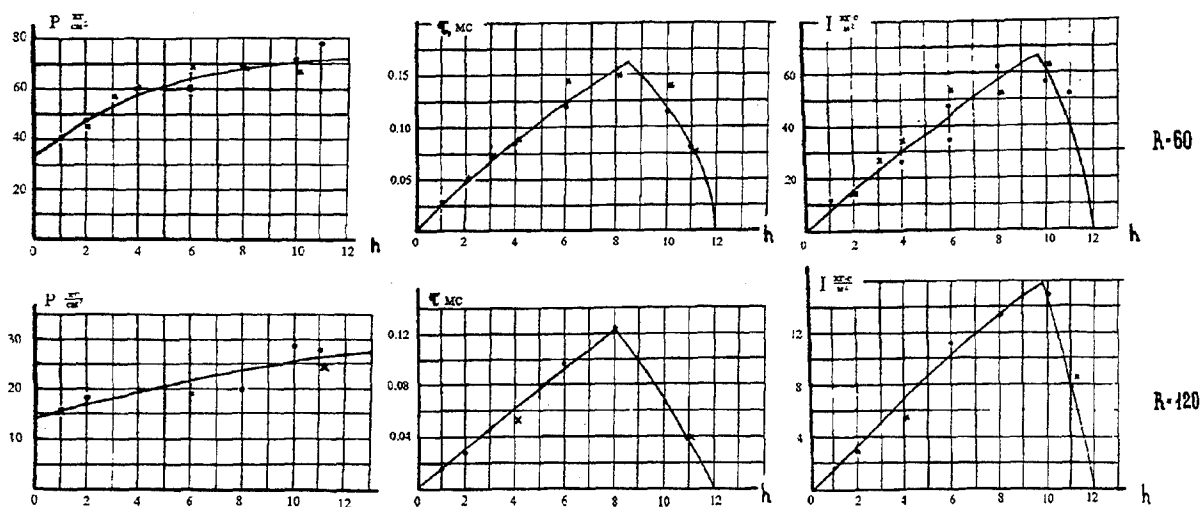
Fig. 9. Peak overpressure in atm, duration in ms and specific impulse in kgs/m² of shock wave in water for an explosion of TNT spherical charge of 100 kg. R∗, h - distances and depth of probe in radius of charge $R_0 = 0.246$ m.

[6]. This investigation may be used for determination of source function and identification of different explosive events.

The investigations and analysis of the experimental data showed that hydroacoustic method of control may be used for detection and identification of nuclear explosions, conducted at different conditions, including near bottom and free surface, near water surface, coasts of opened reservoirs (including underground explosions). Usage of hydrophones based on high sensitivity piezoelectric ceramics with reliable contact to water and relatively low noise level near the sea bottom, existence of sound channels in the majority sea areas characterized by propagation of sound to thousands kilometers with low attenuation favors detection. Hydroacoustic equipment allows to measure waves of seismic origin, traveled in ground, which are recorded before shock wave in water if an explosion was conducted in a confined reservoir like the Bay of Chernaya. It is necessary to use hydroacoustic signals from another natural and artificial sources, such as earthquakes, tsunami, HE and so on for identification of nuclear bursts. It is also necessary to elaborate their source functions which will determine acoustic wave parameters at entrance to waveguide.

REFERENCES

1. V.V. Adushkin, B.D.Khristoforov. Hydroacoustic disturbances at nuclear and chemical explosions. The dynamic processes in geospheres: the high power geophysics. Moscow. Nauka. 1995.
2. Khristoforov B.D. Parameters of Shock Waves and Gaseous Bubbles Arising During Underwater Explosions of Small PETN Charges. ARS Journal Supplement .1962. p.1788-1790.
3. Khristoforov B.D. Underwater explosion in air cavity. PMTF, 1962, No.6, pp.128-132.
4. Khristoforov B.D. About similarityof the shock waves at the explosions in water and air. PMTF, 1963, No. 2, pp.142-146.
5. Korobeinikov V.P., Khristoforov B.D. Underwater explosion. Itogi Nauki i Tekhniki. Gidromekhanika. Vol. 9 Moscow. 1976.
6. Kiselev Y.N., Poklad Y.V. The experimental modelling of meteor impact on water surface. Asteroid Hazard-95 St. Peterburg, ITA RAS 1995, Vol. 2, pp. 62-63.

Seismoacoustic Studies of the Norwegian Sea

Donna K. Blackman and John A. Orcutt

Institute of Geophysics and Planetary Physics
Scripps Institution of Oceanography, University of California San Diego
La Jolla CA 92093-0225

Abstract

The U.S. Navy hydrophone arrays (SOSUS) record seismoacoustic events in a range of frequencies which includes earthquake and explosive sources as well as those relevant to submarine detection, for which they were designed. In the Norwegian Sea we compare detection of seismoacoustic events on SOSUS with seismic detection by the arrays on land in Norway. We also study seismic activity along the spreading centers between Iceland and Svalbard in an attempt to discern any difference in levels of seismicity associated with different sections of the ridge system. Currently, we have assigned archive channels to focus on activity along the Mohns ridge. During March 1995 we recorded many T-phases whose sources have been located along the Mohns ridge using beam steering. Analysis of beamformed data for this continuous one-month period revealed several dozen acoustic events emanating from the southern Mohns ridge and about one third that number from the northern Mohns ridge. Part of this difference is probably due to the choice of beams for the archived data, which emphasizes the southern Mohns ridge, but some of the difference likely reflects the current level of magmatic/tectonic activity. About 10% of the recorded T-phases for this period are preceded by an arrival with greater low frequency content, most likely the P-phase. Approximately two dozen acoustic events were recorded by all channels during the March 95 period suggesting a more distant or larger source, possibly a regional or even teleseismic earthquake. Two of these events correspond to regional events listed in the Center for Monitoring Research (CMR) bulletin, both for which P- and T-phases are observed. The hydroacoustic data have been archived since February 1995 so it is too early to determine systematic patterns in seismic activity or to compile reliable statistics on the relative detection thresholds of the SOSUS system vs the land arrays that can monitor the Norwegian Sea. This work, along with quantitative characterization of the acoustic signals as a function of source parameters, will be the focus of our upcoming investigative year.

1. Objectives

The goal of the investigation in the Norwegian Sea is to assess the usefulness of SOSUS as a tool for seismology and to further our understanding of seismoacoustic wave propagation in ocean basins. Analysis of earthquake detection levels and our ability to characterize both natural and manmade seismic sources will determine how reliably the Navy hydrophone arrays can supplement, or even replace, seismometer arrays on land.

Comparison of the number and types of events recorded by the SOSUS arrays vs those detected by the land arrays is a main focus during this second investigative year. This entails systematic analysis of hydrophone data for continuous time periods as well as directed searches for specific events recorded on land. Along with event detections and source locations, we are developing a catalogue of acoustic arrivals. This catalogue will ultimately be used to quantify the relationship between source parameters and T-phase signal character.

The Norwegian Sea offers a unique setting for assessing SOSUS use for seismology due to the existing combination of seismic activity, instrumentation and varied oceanographic conditions (Figure 1). The different seismic sources in the region provide a range of signal types and locations (e.g. Vogt, 1986): large oceanic earthquakes from transform faults along the plate boundary between Iceland and Svalbard; smaller oceanic earthquakes associated with volcanic eruptions along the rifting portion of the plate boundary; mining explosions on land; slope failure events on the continental shelf. Several types of recordings of Norwegian Sea seismic activity are available from instruments whose capabilities dovetail each other: the Global Seismic Network (GSN); the seismometer arrays in Norway and on Spitsbergen; and the SOSUS acoustic arrays.

2. Research Accomplished

The link to the Norwegian Sea SOSUS system that is required for data archiving was established in February, 1995, through the efforts of Dr. Clyde Nishimura, our colleague at the Naval Research Laboratory in Washington D.C. Useful data began to accrue immediately for 15 of the 16 channels that the archive system can accommodate. For the most part, the first 6 months of data are of good quality allowing us to address several of our initial goals. We were not able to monitor individual hydrophones due to missing wiring diagrams at the site so our initial plans to devote half the archive channels to single phones was modified. Currently we are monitoring 16 pre-formed beams (processed using the U.S. Navy beamforming parameters) from more than one location. We decided to focus our initial efforts on the Mohns ridge, a known source of frequent, low-level seismic activity, and the Jan Mayen transform fault, along which larger earthquakes are generated (Vogt, 1986; observations from the Norwegian arrays). Therefore, our specific choice of beams to monitor in this initial stage reflects this decision.

The array locations are classified so data must be processed at the secure facility at NRL (the Dual Use Analysis Center was designed to accommodate scientific research using SOSUS data (Nishimura and Conlon, 1994). The archive tapes are sent to NRL at 3-4 week intervals, each tape containing 2-3 days worth of 16-channel data. The sampling rate is well above that required for seismic research since marine mammal research is carried out with the same data. In May 1995, tapes for the first 5 weeks of the archive were available so these data were downloaded and the number and types of acoustic arrivals recorded on the various channels was catalogued for a continuous 36-

day period. Subsequently, the corresponding CMR and QED (U.S. Geological Survey's Quarterly Epicenter Determination) bulletins were consulted in order to assess which acoustic events were likely to be regional or teleseismic arrivals.

Events recorded for the 36-day period can be classified in three categories reflecting source region: southern Mohns ridge; northern Mohns ridge; more distant regional or teleseismic events. The events are only generally located at this stage based on which beams showed a signal, which did not and what the relative amplitude of the arrivals was between beams with signal. For these low frequencies, the beams are quite broad. Almost a hundred T-phases emanating from the southern Mohns ridge were recorded, 11 had a preceding P-phase with short duration and lower frequency content. The T-phases varied in amplitude, spectral content and duration. Just over two dozen T-phases were recorded from the northern Mohns ridge area, only one of which had a clear P-wave preceding it. All channels recorded 28 events, 6 of which were preceded by probable P-wave energy. Based on the available CMR listings for this time period, at least two of these all-channel events correspond to known regional earthquakes: a 4.1 mb on the Kolbeinsey ridge and a 2.3 ML on the Knipovich ridge (+'s in Figure 2). Teleseismic arrivals should be observable (Slack and Purdy, 1995, have observed P-waves from several earthquakes of magnitude 5.5 and greater in SOSUS data from Atlantic and Pacific arrays) so we will return to NRL in August to determine if the arrival times correspond to that predicted for the teleseismic QED events during this, and subsequent, periods. Significant low or band pass filtering is usually required to observe teleseismic arrivals through the background noise that pervades near-seafloor hydrophone data (e.g. Blackman et al., 1995). No filtering of the data was attempted during the initial May analysis visit.

The Center for Monitoring Research has agreed to provide a subscription service so that daily bulletins of seismic activity in the Norwegian Sea are automatically sent to us at IGPP. This information provides a rapid means to check event locations and to define time periods during which the hydrophone data may have recorded foreshocks or aftershocks associated with the main event. There have not been any obvious earthquake swarms detected by the Norwegian arrays since late February, 1995. Two events on the plate boundary north of Svalbard may have been related and two events on the Knipovich ridge may be related (Figure 2). For both sets, the two events occurred within a few minutes of each other. CMR lists about twenty events as occurring in the Norwegian Sea between mid-February and mid-July whereas the QED lists 5 events (Figure 2 has different symbols for the different bulletins). Last year we noted a consistent problem where CMR (then CSS) source locations differed from PDE locations by up to 50 km in this region for the 1990-1992 time period. The 1993 addition of the Spitsbergen array improved the match between CSS and PDE locations significantly. These latest data indicate that the CMR locations now match the QED locations rather well in the Norwegian Sea.

Standard techniques can be used to obtain source parameters from the land array data. In contrast, acoustic T-phases are fairly complex with arrival energy often building over a period of many seconds to a maximum and then decaying for as long as a few minutes. This complexity makes the task of using T-phases to determine source parameters rather difficult so we will initially use the land-derived parameters for co-detected events to develop an understanding of how T-phase character (onset time, frequency content, duration, amplitude) reflects source and propagation path parameters. Using code based on HYPOINVERSE but modified (Bryan and Nishimura, 1995) to account for uncertainties typical of T-phase arrivals, we are working to determine how reliably we can locate and parameterize events that are too small to be detected by the land arrays but that are recorded by the hydrophone arrays.

3. Plans for the Upcoming Year

Several upgrades in the archive and recording setup will be necessary for us to achieve our complete set of goals for the project- all are currently possible and, with the cooperation of the Navy and NRL, we expect they can be in place in the near future. The connection for the dead channel should be replaced; the gains should be reset so that high amplitude signals are not clipped; the time stamp in the record header should be verified so that acoustic locations can be accurately compared with seismic locations determined from the land arrays; the wiring diagrams should be located so that we can monitor single hydrophones; and, the clock used for generating a time stamp must be upgraded, preferably using an accurate GPS clock.

Source location using the T-phases is just now being attempted with these data. Much of our efforts in this coming year will be devoted to assessing the accuracy with which we can locate events using the acoustic data. This will entail assessment of pick reliability, appropriateness of the code developed by Bryan and Nishimura for this particular data format (our time resolution is better but the distribution of beams relative to source will vary) and development of modifications optimized for the time/geometry constraints with.which we work.

4. References

Blackman, D.K., J.A. Orcutt, D.W. Forsyth, in press 1995, Recording teleseismic earthquakes using ocean bottom seismographs at mid-ocean ridges, Bull. Seis. Soc. Amer.

Bryan, C.J. and C.E. Nishimura, 1995, Monitoring oceanic earthquakes with SOSUS: an example from the Caribbean, Oceanography 8, 4-10.

Nishimura, C.E. and D.M. Conlon, 1994, IUSS dual use: monitoring whales and earthquakes using SOSUS, Mar. Tech. Soc. 27, 13-21.

Slack, P.D. and G.M. Purdy, 1995, Observations of Mid-Atlantic Ridge earthquake activity using U.S. Navy hydrophone data: progress report, Woods Hole Oceanographic Inst. contribution.

Vogt, P., 1986, Geophysical and geochemical signatures and plate tectonics, in B.G. Hurdle (ed), *The Nordic Seas*, Springer-Verlag, New York, p413.
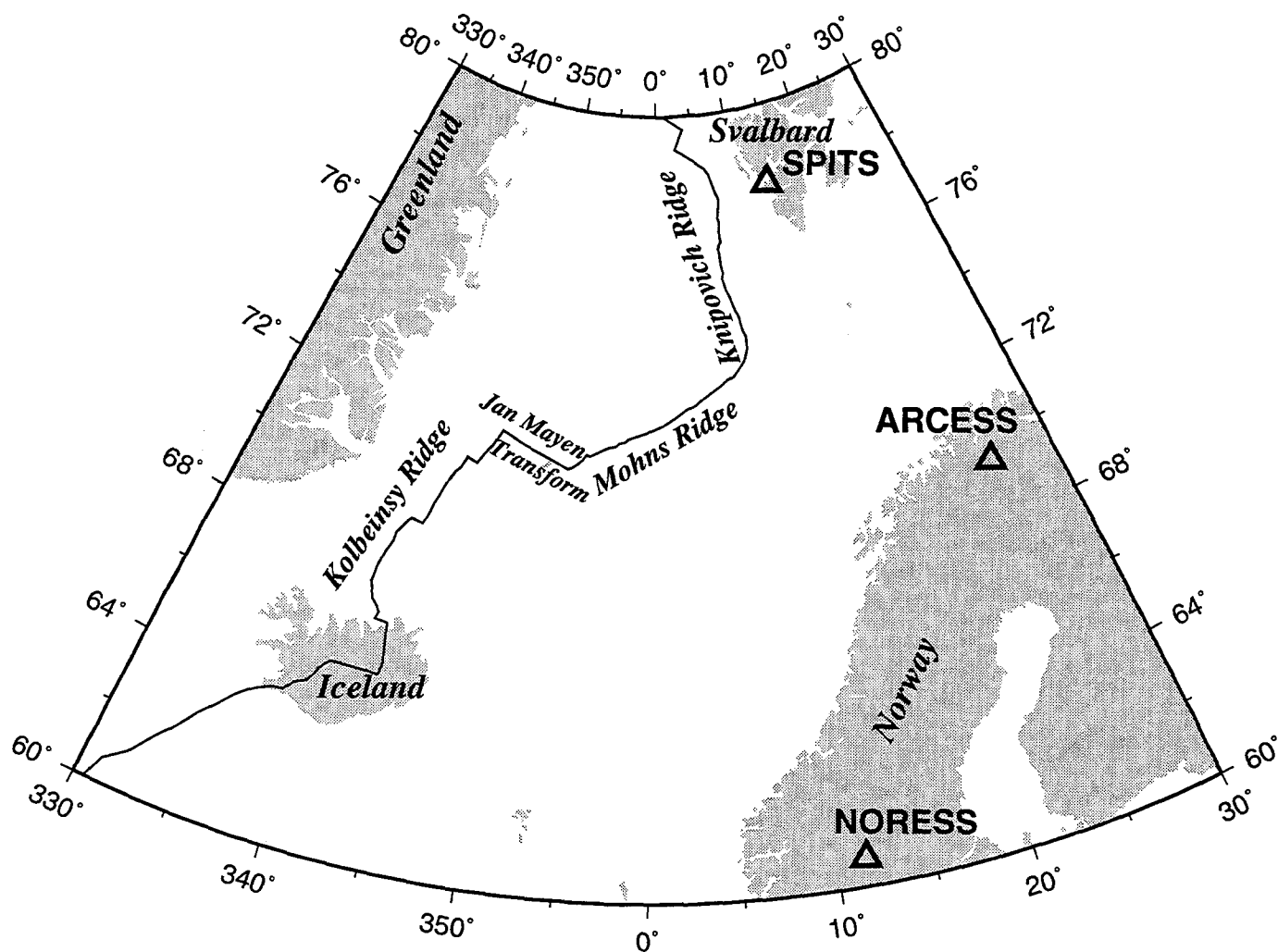
Figure 1. Tectonic setting of Norwegian Sea seismoacoustic study area. Plate boundary is shown by the solid line with spreading centers (Kolbeinsey, Mohns and Knipovich ridges) and transform faults (Jan Mayen) labeled. The Norwegian seismic array locations are indicated by the triangles. 16 channels of beamformed hydrophone data from this area are being archived to characterize acoustic arrivals from local, regional and teleseismic events.
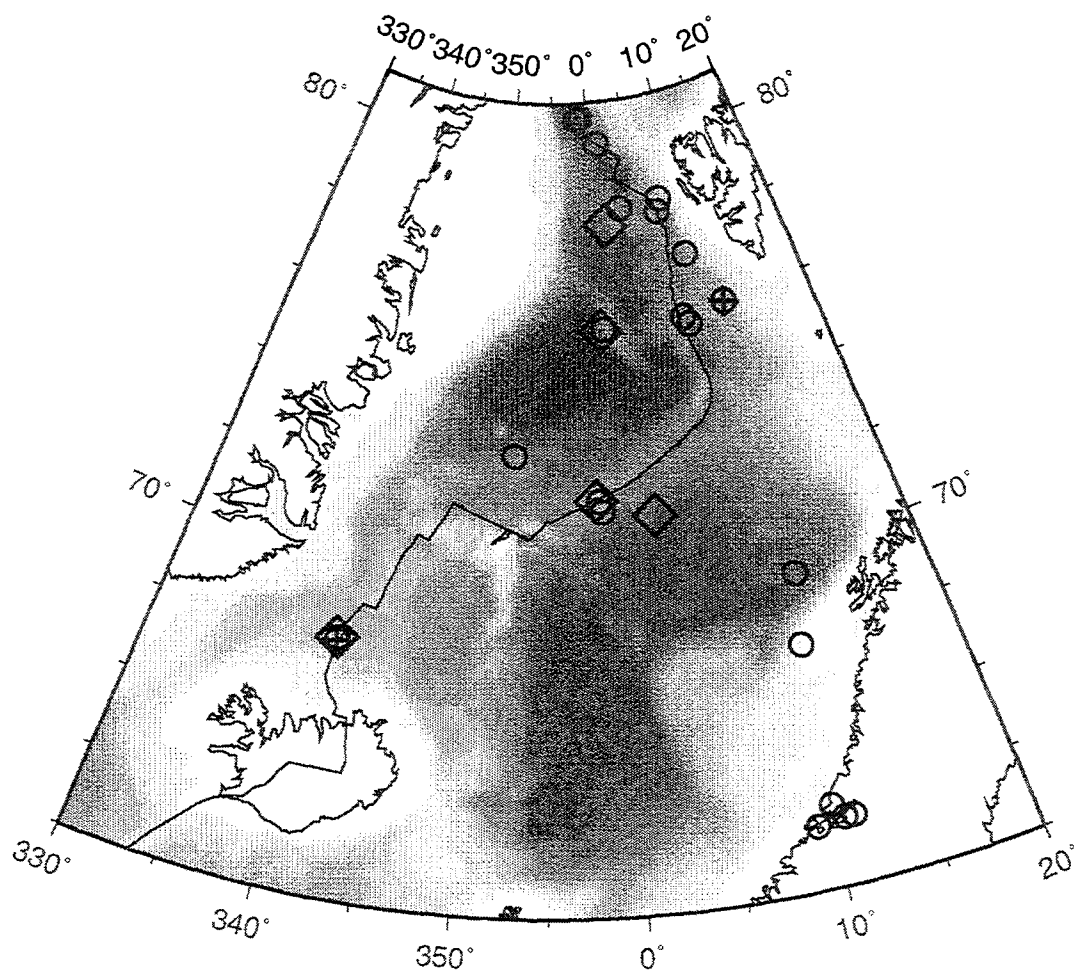
Figure 2. Grayshade of Norwegian Sea bathymetry (darker shades are deepest) and epicenters for earthquakes occurring in the region between mid-February and mid-July 1995. Circles show the location of events listed by CMR; diamonds show locations of events listed in the QED; +'s show the two CMR events that were recorded by SOSUS during March, 1995. One additional March event may have been picked up by SOSUS. The remaining two March CMR events occurred in a region that we were not monitoring with the archived beams.

973

Overview of CTBT Hydroacoustic Studies at LLNL

Abstract

D. Clarke, D. Harris, T. Hauk, R. Leach and J. White*

LLNL conducts a variety of technical and policy studies for DOE in support of hydroacoustic verification technologies for a CTBT. This poster presents an overview of three of the technical studies that have a direct bearing on the performance of hydrophone monitoring systems for detecting and identifying nuclear detonations at sea.

We are developing computer models of the nuclear explosion source of hydroacoustic signals. This model includes the effects of coupling from the strong shock region immediately around the device into the ocean acoustic waveguide (the SOFAR = SOund Fixing and Ranging channel) that propagates acoustic waves to great distances with little attenuation. The model treats both underwater explosions and bursts low in the atmosphere above the ocean surface, and has been used to determine the expected strength of signals from explosions of both types. We describe our current efforts to produce "starter-fields" for acoustic propagation codes that will predict the early-time acoustic signature of explosions observed at ranges of thousands of kilometers.

DOE/LLNL also has operated a data acquisition system at a hydroacoustic station in the North Pacific since April 1993, and has a collection of nearly 2 1/2 years of continuous underwater acoustic recordings. We are using this collection in a study of the feasibility of using earthquake T phases to identify features along the acoustic path that block acoustic propagation. We have extracted observations of T phases from more than 100 earthquakes along the Pacific-Antarctic ridge for this study. We are attempting to characterize the variability of the T phase source to determine the suitability of T phases for obtaining statistical estimates of path attenuation. If path attenuation measurements with T phases are feasible, earthquake observations may help calibrate an installed IMS hydrophone network after several years of observation.

In our third project, we are developing joint detection, location and discrimination algorithms using hydroacoustic and seismic data. We compare observations of explosions (the 1994 Ship Shock trials) and earthquakes at a hydroacoustic station (Kaneohe) and a group of seismic stations along the coast of Southern California. Among other techniques, we use self-organizing neural nets to compare the performance of seismic-only, hydroacoustic-only and seismic-hydroacoustic discrminants.

Modeling Hydroacoustic Propagation for Seismic Events

Catherine de Groot-Hedlin, John A. Orcutt

Institute of Geophysics and Planetary Physics,
Scripps Institution of Oceanography,
University of California, San Diego
La Jolla, CA, 92122

Abstract

The goal of our research is to understand how acoustic energy from underwater earthquakes is coupled to the sound channel and how the sound is propagated from the source to the hydrophone receivers. We intend to compare results from numerical modeling of long-range acoustic propagation to hydroacoustic data. A large suite of hydroacoustic data will be assembled, in order to obtain optimal azimuthal coverage from source to receiver, as well as a wide range of source depths and source parameters. The numerical modeling will involve integrating bathymetric and sound speed databases into the models since sound propagation in the oceans is strongly dependent upon these parameters. Our object is to be able to distinguish between source effects and propagation effects.

We have conducted some simple numerical modeling experiments to compare hydroacoustic signatures for models with and without significant bathymetric interaction along the transmission path. The acoustic wavefield is computed using the parabolic equation method for a large number of frequencies within the band of interest; time domain arrivals are computed by Fourier synthesis of these calculations.

Key Words: hydroacoustic propagation, energy coupling, waveguide, parabolic equation.

Objective

The objective of our research is to analyze hydroacoustic signals from oceanic earthquakes recorded by Navy hydrophone arrays (SOSUS) in the North Pacific and Norwegian Sea, with a view to understanding the coupling of energy to the SOFAR channel and the propagation of acoustic energy from source to receiver. The hydroacoustic signature of any underwater event depends on both the source characteristics and along path propagation effects. In order to discriminate oceanic nuclear tests from submarine earthquakes, it is important to distinguish between source signatures and propagation effects. Both the sound speed within the ocean waveguide and seafloor bathymetry, which limits the depth of the waveguide, strongly affect acoustic signatures recorded on hydrophones. We plan to integrate theoretical predictions of propagation effects with observed acoustic arrivals. Goals include (a) determining the physical mechanisms by which acoustic energy from sources with varying depths is coupled into the sound channel, (b) determining the effects of variations in bathymetry and temperature profiles along the travel path on the received signals, and (c) comparing synthetic responses to data to see if source signatures of various acoustic arrivals can be accurately modeled. This last step includes the assembly of a suite of hydroacoustic array data from a large number of underwater seismic events, in order to obtain optimal azimuthal coverage from source to receiver, as well as a wide range of source depths and source parameters. In this paper we present preliminary numerical modeling results, comparing acoustic signatures for several simple models.

Preliminary Research Results

Advances in methods of computing the acoustic wavefield for slowly varying media make it possible to predict the acoustic signature for a given source to receiver path. We used the acoustic parabolic equation (PE) code of Collins and Westwood (1991) which gives a frequency domain solution of the acoustic wavefield along a travel path with given sound velocity profile and seafloor bathymetry. Strictly speaking, the PE method is exact only for range-independent problems, however, it is accurate for travel paths for which backscattering is negligible and the sound speed varies gradually in the horizontal direction. These assumptions are generally valid for the ocean waveguide. Energy coupling between modes is accounted for by the PE method, thus wave phenomena such as mode conversion and mode cutoff can be accurately modeled. Acoustic phase arrivals are computed by Fourier synthesis of a number of PE calculations within the frequency band of interest.

Synthetic responses were computed at a range of 100 km for a suite of models, each having a sound speed profile as shown in figure 1. For the first model, the source has a depth of 800m, equal to the sound speed minimum, and frequency range from 5-25Hz. The waveguide has a uniform thickness of 5 km. Transmission loss diagrams are shown in figure 2, indicating mode-like transmission of energy at low frequencies, and ray-like transmission at higher frequencies. The synthetic arrivals are shown for various receiver depths in figure 3.

The second model features a ridge centered at 40 km, extending to 1 km from the sea surface. In other respects, the model is exactly like the first. Transmission loss plots are shown in figure 4. Comparing this figure to figure 2, it is obvious that at low frequencies the transmission is barely
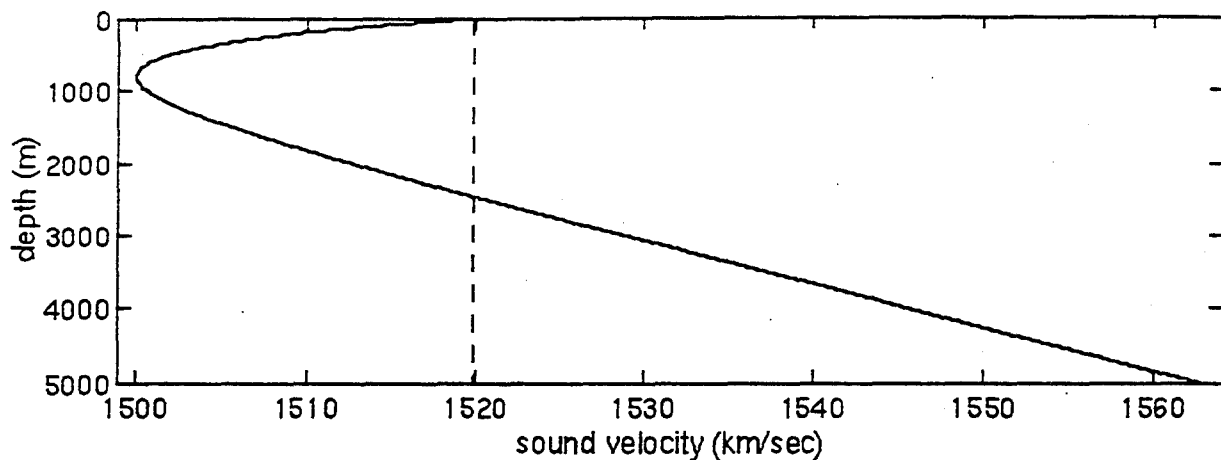
Figure 1. The sound speed profile used for model calculations is shown above. The critical depth, *i.e.* the depth at which the sound velocity equals the velocity at the surface, is approximately 2400m. This depth defines the lower limit of the sound channel.

affected by the ridge, while at high frequencies higher modes are stripped off by the ridge. Lower modes, corresponding to energy concentrated near the sound axis, are unaffected by the ridge at higher frequencies. The time response for a range of 100 km is shown in figure 5, for a series of receiver depths. The time duration of the acoustic phase is shorter than that for the model with no ridge, as shown in figure 3.

Recommendations and future plans

Computations of the time domain signatures of acoustic arrivals for simple models shows that signal duration's are dependent upon properties of the acoustic waveguide. This analysis will be extended to compare results of numerical modeling of long-range acoustic transmission to acoustic signatures seen in hydroacoustic array data and determine where greater modeling accuracy is needed. This will involve using accurate temperature profiles and bathymetric data along the source to receiver path. The bathymetric database used will be the Navy standard DBDB5, available at a grid-spacing of 5 minutes; the Levitus atlas, with a grid spacing of 1 degree, will be used to determine ocean temperature as a function of depth, location and time. These temperature data will be used to understand the effects of seasonal and annual changes in the ocean temperature on acoustic propagation.

For long-range acoustic propagation, the refraction of acoustic energy due to lateral variations in bathymetry and temperature must be taken into account. An efficient approximation to a full 3-D solution for global scale acoustic propagation is the refracted geodesic method of Heaney et al (1991), which can be used to estimate travel time and path of each mode. In this method, adiabatic mode theory (Pierce, 1965) is used to calculate horizontal phase speed for each mode as a function of latitude and longitude. Snell's law is then used to determine the horizontal path taken by each mode. Calculation of the horizontal phase speed, and thus the ray path, takes into account laterally varying bathymetry and ocean temperature. Once the travel path is determined, the parabolic equa-
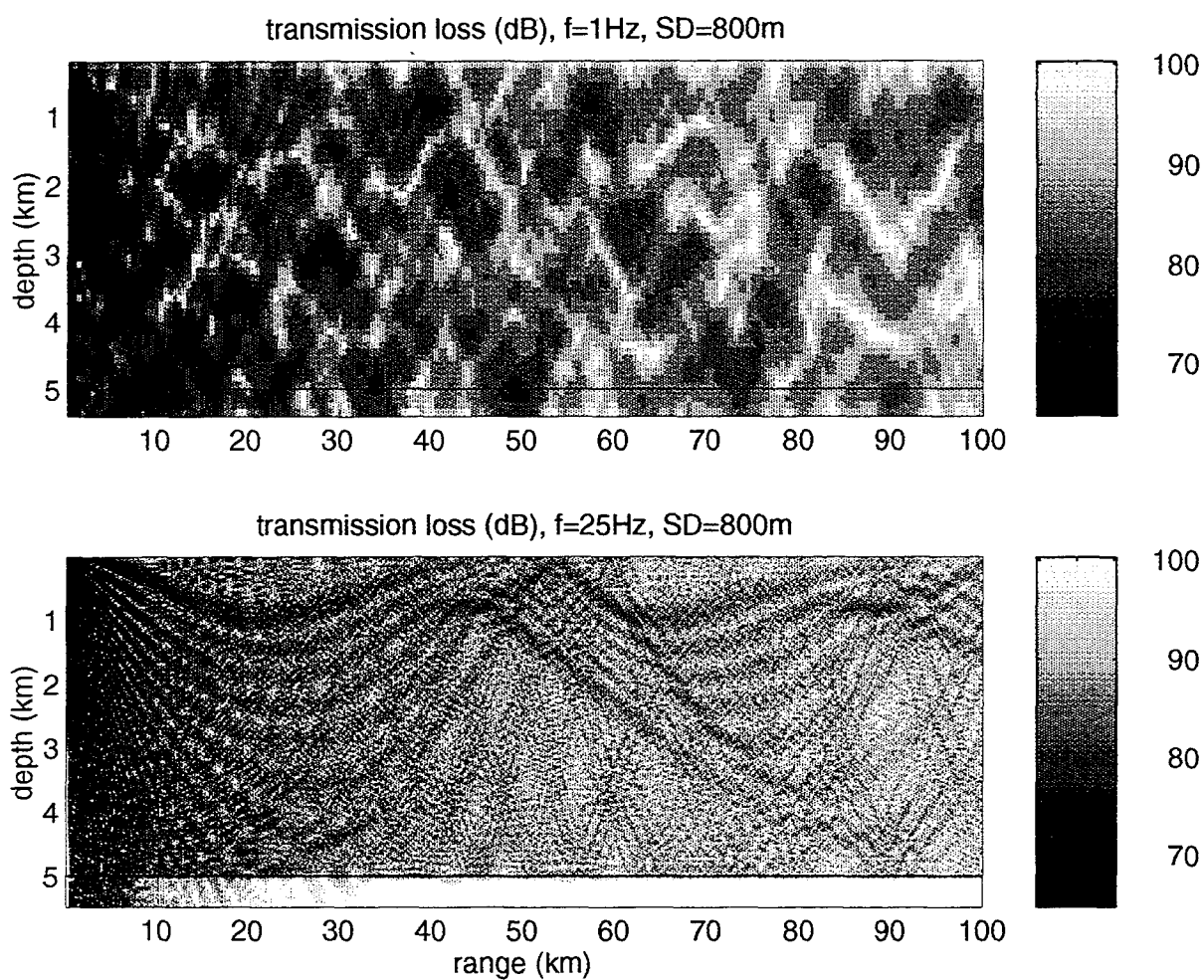
Figure 2. Transmission loss plots for a uniform waveguide with velocity profile as shown in figure 1. The source depth is 800m.
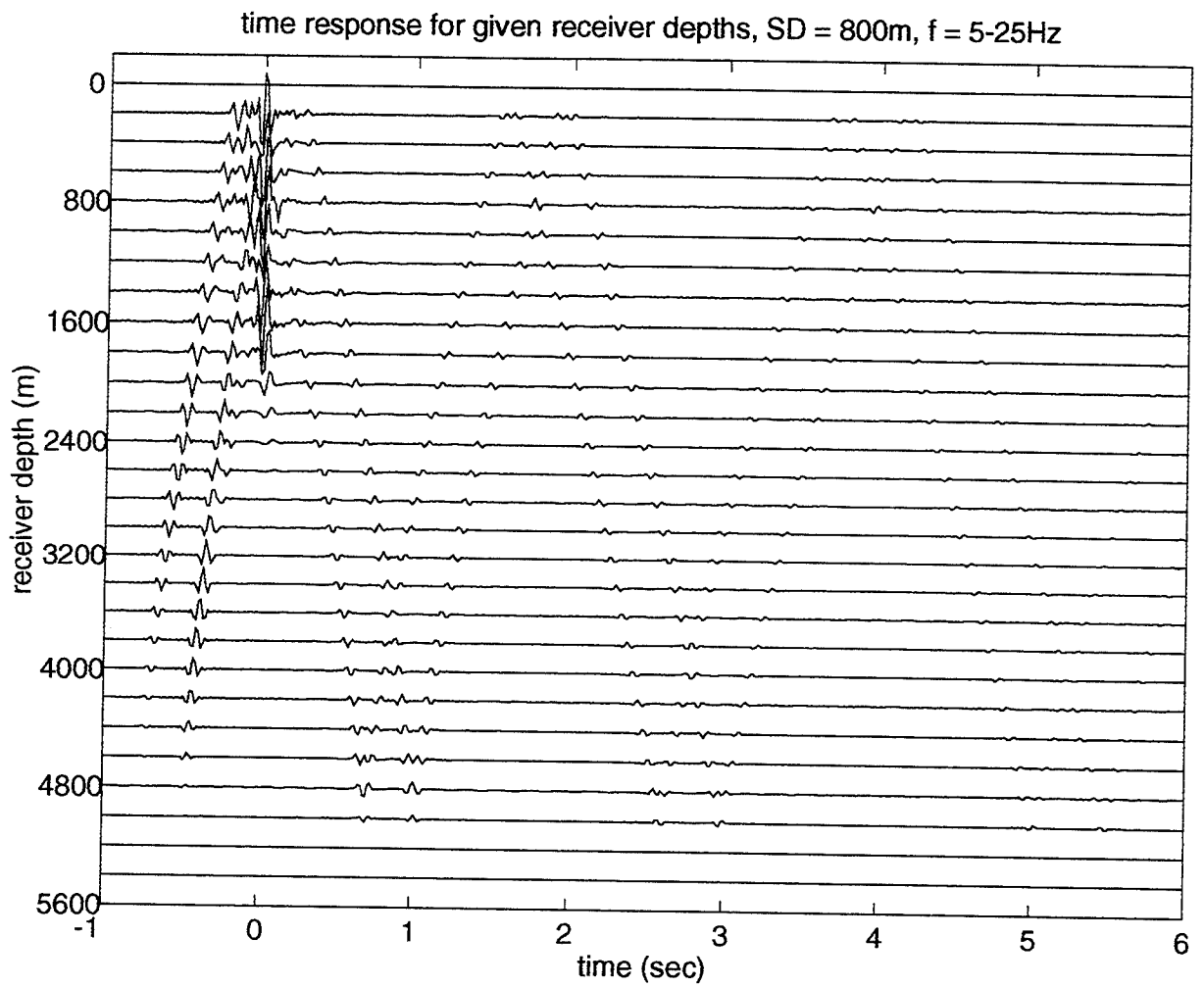
Figure 3. Acoustic signatures at various receiver depths. Times given are reduced times, *i.e.* relative to r/1.5 km/sec.

transmission loss (dB), f=1Hz, SD=800m

transmission loss (dB), f=25Hz, SD=800m
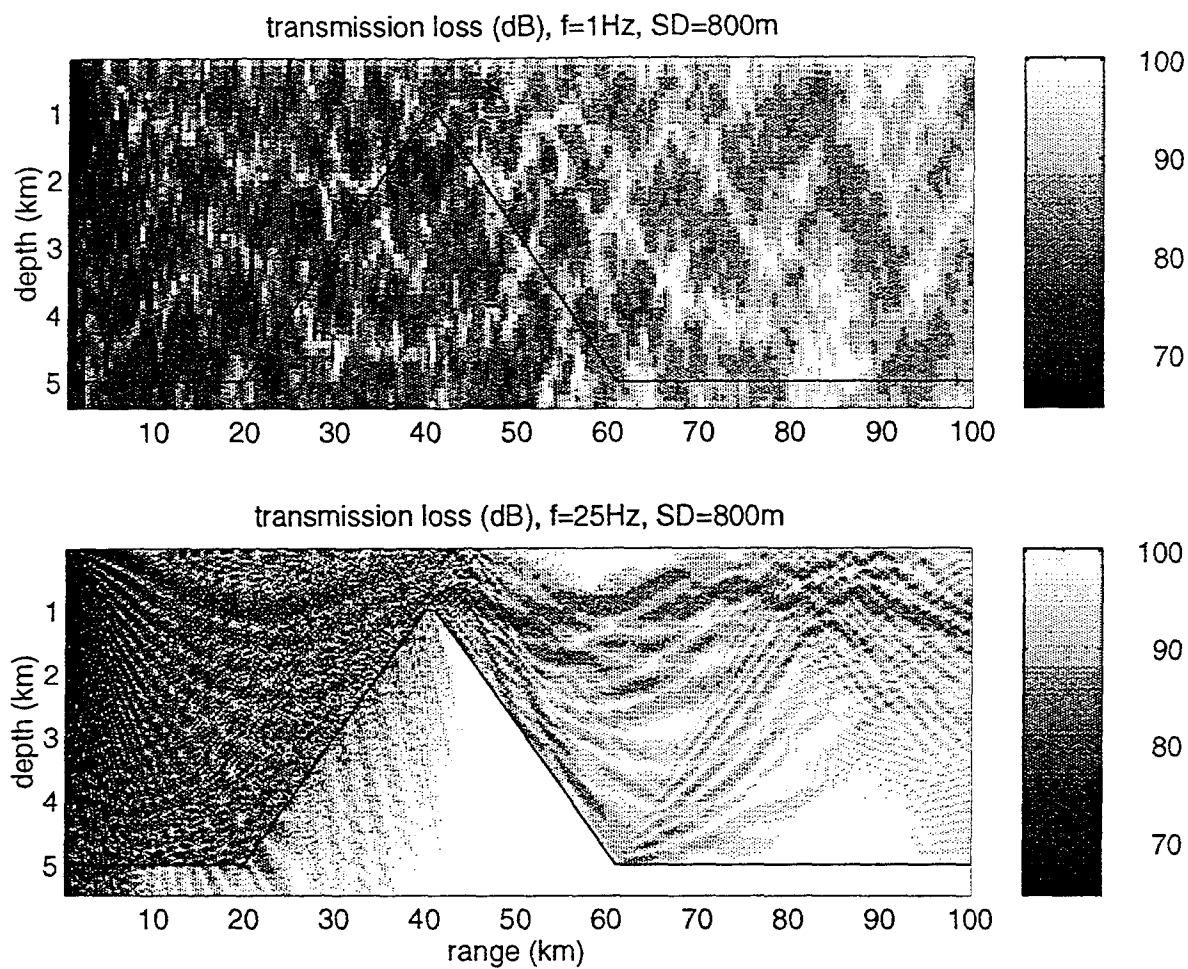
Figure 4. Transmission loss plots for ridge model.

time response for given receiver depths for model with ridge, SD = 800m, f = 5-25Hz
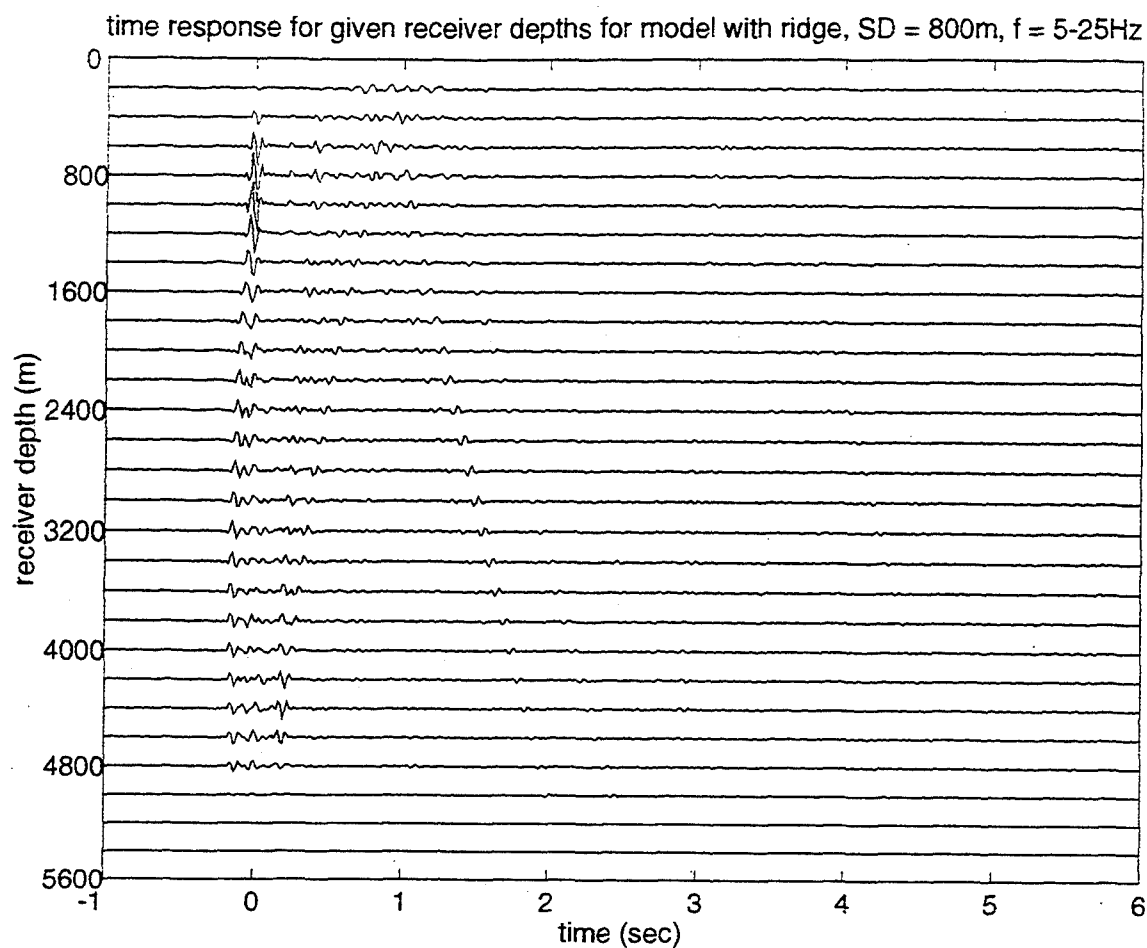
Figure 5. Time domain response for model with ridge extending to near the sound axis.

References

Collins, M.D., 1991, A higher-order energy-conserving parabolic equation for range-dependent ocean depth, sound speed, and density, *J.Acoust.Soc.Am.* ,**89**, 1068-1075.

Heaney, K.D., B.E. McDonald, and W.A. Kuperman, 1991, Perth-Bermuda sound propagation (1960): Adiabatic mode interpretation, *J.Acoust.Soc.Am.*, **90**, 2586-2494.

Levitus, S., 1982, Climatological atlas of the world ocean, *NOAA Professional Paper 13, Rockville, Md.*

Pierce, A.D., 1965, Extension of the method of normal modes to sound propagation in an almost stratified medium, *J. Acoust. Soc. Am.*, **37**, 19-27.

Development of a Comprehensive Coverage Assessment Tool

Greg Duckworth
Kevin LePage
Ted Farrell

Bolt Beranek and Newman, Inc

Contract Pending

Sponsored by DOE

Abstract

BBN has been tasked with developing a comprehensive coverage assessment tool for ocean acoustic monitoring. This tool will facilitate studies into the issues and sensitivities of using acoustic assets in the ocean to support a Comprehensive Test Ban Treaty. These issues include 1) understanding the sensitivity of signal structure to ocean environment variability as manifested through modal coupling, bottom and surface interaction losses and horizontal refraction and diffraction, 2) understanding the sensitivity of signal structure to source characteristics, and 3) designing detection and localization strategies which exploit the the fullest extent our understanding of the source and propagation characteristics.

In the first phase of this effort, the coverage assessment tool, which couples global and basin scale acoustic propagation models together with compatible source functions and an ocean database library, will be developed and benchmarked against available data. Once validated, the tool will be exercised to predict the signal and noise characteristics at existing and notional receiver locations, in order to identify regions where detection will yield particular challenges. Features of this tool will be software modularity and extensibility in order to facilitate the incorporation of new source functions, propagation models, databases and performance assessment modules as they become available.

NUCLEAR TREATY MONITORING
RADIONUCLIDE COLLECTION AND ANALYSIS
BY THE US ATOMIC ENERGY DETECTION SYSTEM

CHARLES F. McBREARTY, JR.
Director, Nuclear Technology
HQ AFTAC

ABSTRACT

This talk will provide an overview of radionuclide collection and analysis as a tool for monitoring nuclear weapons testing. Specifically, it will provide a description of the techniques used currently in AFTAC's nuclear treaty monitoring program as part of the United States Atomic Energy Detection System. A description of the particulate and gaseous sample collection equipment used on the ground and in aircraft, as well as the associated laboratory equipment used in the analysis, will be presented. A review of collection and analysis requirements for the Comprehensive Test Ban Treaty (CTBT) from the USAEDS perspective, and implications of CTB implementation on modes of operation will be addressed. Additionally, the talk will review the current status of on-going field tests of the next generation, automated, ground-based particulate sampler/analyzer, as well as the concepts and status of research and development efforts for the automated, ground-based radioxenon sampler/analyzer. Finally, the talk will cover some of the technical and engineering challenges that still need to be addressed.

DOE RADIONUCLIDE MONITORING SYSTEMS FOR CTBT VERIFICATION

R. W. Perkins
H. S. Miley, and W. K. Hensley

Pacific Northwest Laboratory
Richland, Washington

ABSTRACT

Radionuclide monitoring systems which could be used in monitoring a Comprehensive Test Ban Treaty (CTBT) are being developed and tested at the Department of Energy (DOE) Pacific Northwest Laboratory (PNL). One system is designed to permit automatic near real-time analysis of particulate airborne fission products with a sensitivity of about 2 $\mu Bq/m^3$ of air for the more important signature radionuclides. The second system is designed to measure the noble gas fission products Xe-133 (5.243 day) and Xe-135 (9.10 hour) with sensitivities of about 20 $\mu Bq/m^3$ of air. These systems are designed to operate automatically without maintenance for periods of months to one year or more. A ruggedized model of the particulate radionuclide monitoring system is currently undergoing field test operations at the McClellan Air Force Base. Field tests of the xenon radionuclide monitoring system are planned for early 1996. Both systems provide high sensitivity based on high flow rates and the radioxenon system achieves much high sensitivity than other reported systems based on beta coincidence gamma-ray spectrometric analysis.

Key Words: Radionuclides, Real-Time Monitoring, CTBT Verification

OBJECTIVE

The major objective of the R&D efforts are to develop and demonstrate near real-time monitoring technologies for airborne signature radionuclides which are indicative of nuclear weapons testing in any of the earth's environments. Since the beginning of the nuclear era, analytical technologies have been developed for measuring radionuclides in the atmosphere and in essentially all of the earth's environments. Many of these analytical procedures could be applied directly in monitoring for compliance to a Comprehensive Test Ban Treaty (CTBT); however, they have not been optimized for the spectrum of radionuclide of concern and their labor-intensive nature could impose prohibitive costs and unacceptable delays in data receipt for an International Monitoring System. The DOE focus in developing monitoring technology has been to design systems which could automatically and continuously monitor for those airborne signature radionuclides which provided the best indication of nuclear detonations and which also provide the highest practical sensitivity. The overall objectives have therefore included (1) the identification of the most easily observable and unique radionuclides which would be released from nuclear tests in all of the earth's environments, (2) the selection of practical measurement technologies which were adaptable to near real-time analysis and automation, and (3) the design, construction and testing of practical ruggedized monitoring systems which could operate maintenance-free for periods of months to a year or more, and transmit airborne radionuclide concentrations to National and International Data Centers, as required, at any desired frequency.

RESEARCH ACCOMPLISHED

The goals of this R&D program have been (1) to determine which radionuclides may enter the atmosphere from various nuclear test scenarios, (2) to determine their uniqueness based on other possible sources, (3) to evaluate various measurement alternatives which may be adaptable for automatic near real-time analysis, and (4) to design, construct and test monitoring systems.

A review of signatures from past nuclear detonation monitoring indicates that for ground surface and atmospheric detonation, the full spectrum of fission products enter the atmosphere; however, where underground or underwater detonation are conducted the noble gas radionuclides, and to a much lesser degree, the radioiodines are most likely to be vented.

Thus, in monitoring for compliance to a CTBT, the instrumentation should be capable of measuring the more abundant short-lived fission products from an atmospheric detonation and the more abundant noble gases from a subsurface detonation. The abundance of these radionuclides are summarized in Table 1 for periods of one day, three days, 10 days and 30 days post detonations. The ambient atmospheric concentrations of the shorter lived particulate radionuclides in Table 1 are much lower than the best current detection capabilities of about 1 μBq/m^3 and therefore do not present a background interference to their monitoring. However, the xenon radionuclides, Xe-133 (5.243d) and Xe-135 (9.10 hour) are released to some degree from all operating nuclear reactors and therefore may limit their sensitivities for detecting nuclear detonations. The atmospheric concentration of Xe-133 in the northern hemisphere at mid-latitudes and at a few hundred kilometers from operating nuclear reactors appears to be

about 300 μBq/m^3, whereas backgrounds at higher and lower latitudes in the northern hemisphere are one or two orders of magnitude less and those in the southern hemisphere are at least two orders of magnitude less. The measurement sensitivity of the DOE monitoring system with its sensitivity of about 20 μBq/m^3 should therefore be capable of continuously monitoring the Xe-133 at mid-latitudes in the northern hemisphere and detect significant changes in these concentrations. It should also be capable of detecting concentrations in excess of 20 μBq in the southern hemisphere which would presumably be due to a nuclear detonation or a major nuclear reactor release. The ambient concentrations of the shorter level Xe-135 (9.10 ks) appears to be at least 50-fold lower and its observation at high levels would be suggestive of debris from a nuclear detonation.

The quantities of fission product radionuclides which are produced in even a small (1 Kt) nuclear detonation are considerable, and if such a test were conducted in the atmosphere it should be readily detectable within a few days based on proposed 100 station particulate and noble gas radionuclide monitoring arrays.

Table 2 shows the quantities of two of the major particulate radionuclides, Mo-99 (2.75d) and Ba-140 (12.75d), and the two major noble gas radionuclides Xe-133 (5.243d) and Xe-135 (9.10 hour) which would result from the detonation of a 1 Kt plutonium fission device at one day post-detonation. It also shows what these average concentrations would be if they were diluted by the entire earth's atmosphere and compares their concentrations with the sensitivities which are achievable with the DOE monitoring systems which are being developed and tested. It is clear that atmospheric tests, where 100% of the debris enters the atmosphere, should not be difficult to detect.

Whether denotations occur underground or underwater, only a very small fraction of the total fission products may enter the atmosphere and be transported by turbulent mixing, convective processes and the prevailing winds. In such cases, it is essential to have monitoring systems which provide the highest practical sensitivity. Also, any vented material would be highly enriched in the noble gas radionuclides, and these would be present in ratios proportioned to their independent fission fields which are very different from the "chain yields" which would be generated from precursor radionuclide decay in an atmospheric detonation. The quantities of xenon radionuclides which would be present during the first few minutes following a 1 Kt nuclear plutonium detonation and their ratios on release and during atmospheric transport are shown in Table 3. For an enriched uranium weapon the ratios would be about 1/5 of these values. The ability to measure both the Xe-133 and Xe-135 is thus important since it could serve as a basis for confirming the detonation time of the event where the fissile material was known (plutonium or enriched uranium) or to determine the type of device where the detonation time was known for subsurface tests.

Based on the above factors and other considerations, near real-time and fully automatic monitoring systems are being developed for the continuous measurement of particulate and xenon radionuclides which are indicative of nuclear detonation.

Particulate Radionuclide Analyzer

A particulate radionuclide analyzer which is capable of continuously separating particulate radionuclides from the atmosphere over any specified time period followed by their automatic measurement and transmission of gamma-ray spectral data and specified radionuclide concentrations has been developed and various prototype models have been tested over the last eight months. The initial two prototypes were operated in a connex container near our laboratory at Richland, Washington while the third prototype is currently being tested at the McClellan Air Force Base in Sacramento, California.

These automated particulate radionuclide analyzer has been developed and tested over the past two years. The analyzer draws large volumes of air (15 to 25 m^3/min) through a large area (0.25 m^2), low pressure-drop filter that is subsequently mechanically folded, sealed in a plastic-sieve bag, then positioned at the face of a large-volume, high-resolution germanium detector for gamma-ray spectrometric analysis. The analyzer is equipped to analyze the resulting spectra, transmit the data to a central data repository, accept dial-in commands to perform calibrations, change the sampling schedule, perform various diagnostics, and access stored information and associated information including meteorological data, historical detector performance data, historical system parameters, and all past and present gamma-ray spectral information. During these dial-up sessions, this system can also perform remote software upgrades and do limited mechanical maintenance and repairs. This interrogation/command process can be conducted by network or phone link (hardwired or satcom) using point-to-point protocol.

The product of our design and development efforts is a particulate radionuclide analyzer which consumes about 2500W of power, can process approximately 540 samples between reloading, is about 90 cm x 210 cm, and should cost roughly $100K. Measurement sensitivities for the principal fission products of interest to the CTBT community are about 2 μBq/SCM. Coupled with the expected radionuclide inventory of a 1 Kt detonation and the proposed 100 station world-wide sampling network, any surface or atmospheric nuclear testing should be readily observable. Photographs of the particulate radionuclide analyzer are shown in Figure 1 and include a summary of its operating parameters together with the current joint field test setups at the McClellan Air Force Base.

Xenon Radionuclide Analyzer

The automated xenon radionuclide analyzer is designed to continuously separate the Xe-133 (5.243d) and Xe-135 (9.10 ks) from the atmosphere during eight hours (or other selected) time intervals, measure these radionuclides by low background beta coincidence gamma-ray spectrometry and automatically transmit the gamma-ray spectra and xenon radionuclide concentrations to the National and International Data Centers. The combination of large volume air sampling (40 m^3 /8 hour), the extremely efficient beta coincidence gamma-ray counting (70 to 80%), the very low counter background and the long counting periods (up to 32 hour) permits reliable measurement of both Xe-133 and Xe-135 at concentrations as low as 20 μBq/m^3 of air.

The xenon concentration and purification process involves passing filtered air through a mixed bed of molecular sieve and aluminum oxide for removal of water, carbon dioxide and parts of

the radon. The air stream then passes through a refrigerator where it is cooled to a -100°C and then through an activated charcoal sorption bed maintained at the same temperature for eight hours (or other selected) time periods. At the end of the sampling period, the xenon is thermally desorbed, recaptured and purified on a much smaller sorption bed from which it is transferred to the beta counting cell for beta-coincidence gamma-ray spectrometric analysis. This counting system shown in Figure 2 allows four samples to be measured simultaneously and thus permits continuous eight-hour collections and up to 32-hour counting periods.

RECOMMENDATIONS AND FUTURE PLANS

Both the particulate and xenon radionuclide analyzers are under development, and this will continue together with test programs during the next year and beyond (Figure 3). The particulate radionuclide system is further along in its development and the current ruggedized field version could probably be employed in an actual monitoring operation. Following its testing at the McClellan Air Force Base, and any modifications dictated by these tests, the system will be operated near nuclear reactors such that actual fission product signatures may be observed. Also, optimization studies will be conducted to determine the most practical time intervals for sample collections, sample decay (if any), and counting periods.

Similar tests are planned for the xenon radionuclide analyzer. However, these will be approximately one year later than those planned for the particulate radionuclide analyzer.

We are currently discussing these instrument designs with commercial firms with the objective of having then commercially available for possible use in monitoring a CTBT or for other monitoring applications around nuclear facilities and elsewhere. It is currently planned that the particulate and xenon radionuclide monitoring systems will be commercially available in January and December of 1997, respectively.

Table 1

PRINCIPAL REMAINING FISSION PRODUCTS FROM A 1 kT BURST*
AFTER 1 to 30-DAY DECAY PERIODS (Gamma-ray Emitters)

1-DAY DECAY			3-DAY DECAY		
Radionuclide	Half-Life	%	Radionuclide	Half-Life	%
			Mo-99	2.75 d	9.6
Xe-135	9.089 hr	11.8	Rh-105	1.473 d	8.3
I-133	20.8 hr	7.8	Xe-133	5.245 d	7.3
Zr-97	16.9 hr	6.0	Te-132	3.258 d	6.9
Rh-105	1.473 d	5.4	Ce-143	1.375 d	5.9
Pd-109	13.46 hr	4.4	I-133	20.8 hr	5.9
Ce-134	1.375 d	4.3	Zr-97	16.9 hr	3.1
Mo-99	2.75 d	4.2	I-131	8.041 d	3.1
I-135	6.611 hr	4.2	Ba-140	12.79 d	2.9
Te-132	3.258 d	2.8	Xe-135	9.089 hr	1.9
Sr-91	9.5 hr	2.4	Pd-109	13.46 hr	1.4
Ru-105	4.439 hr	1.5	Ru-103	39.28 d	1.4
Xe-133	5.245 d	1.4	Ce-141	32.51 d	1.3
			Xe-133m	2.19 d	0.42
			Xe-131m	11.9 d	0.0058
10-DAY DECAY			**30-DAY DECAY**		
Radionuclide	Half-Life	%	Radionuclide	Half-Life	%
Xe-133	5.245 d	13.6	Ru-103	39.28 d	12.2
Ba-140	12.79 d	7.9	Ce-141	32.51 d	10.7
I-131	8.041 d	7.0	Ba-140	12.79 d	9.6
Mo-99	2.75 d	6.5	Zr-95	63.98 d	6.3
Te-132	3.258 d	6.2	I-131	8.041 d	4.5
Ru-103	39.28 d	4.8	Xe-133	5.245 d	3.5
Ce-141	31.51 d	4.6	Nd-147	11.06 d	3.4
Nd-147	11.06 d	3.3	Ce-144	284.3 d	1.4
Zr-95	63.98 d	2.2	Ru-106	1.008 yr	1.4
Rh-105	1.473 d	1.2	Te-129m	33.6 d	0.39
Sb-127	3.85 d	0.76	Te-132	3.258 d	0.32
Ce-143	1.375 d	0.69	Eu-156	15.19 d	0.29
Xe-133M	2.19 d	0.23	Xe-131m	11.9 d	0.13
Xe–131m	11.9d	0.05			

Table 2

EXAMPLES OF SOURCE TERMS
FROM 1 kT DETONATIONS
(One-day Post Detonation)

	Half-Life	BQ(x10^{15})	%Abundance
Mo-99	2.75 d	15.3	4.2
Ba-140	12.75 d	3.16	0.87
Xe-135	9.10	42.9	11.8
Xe-133	5.243 d	5.03	1.4

CONCENTRATION IF DILUTED BY EARTH'S ATMOSPHERE
COMPARED WITH DETECTION SENSITIVITIES

	Half-Life	μBq/m^3 on Dilution	Detection Sensitivity, μBq
Mo-99	2.75 d	3600	1
Ba-140	12.75 d	740	1
Xe-135	9.10 hr	10000	20
Xe-133	5.243 d	1200	20

Table 3

XENON-133 AND XENON-135 QUANTITIES AND RATIOS
VERSUS TIME AFTER A 1kT NUCLEAR DETONATION
10^{14} Bq

(Where XENON Gas Venting Occurs Within
5 Minutes After Detonation)

	Half-Life	5 Minutes	4 Hrs	12 Hrs	1 day	3 days	5 days	7 days
Xe-133	5.243 d	0.260	0.254	0.243	0.227	0.175	0.134	0.103
Xe-135	9.10 hr	114	84.6	46.0	18.4	0.477	0.0123	0.000319
Ratio	Xe-135/ Xe-133	440	333	189	81.2	2.72	0.092	0.0031

FIGURE 1

Particulate Radionuclide Analyzer
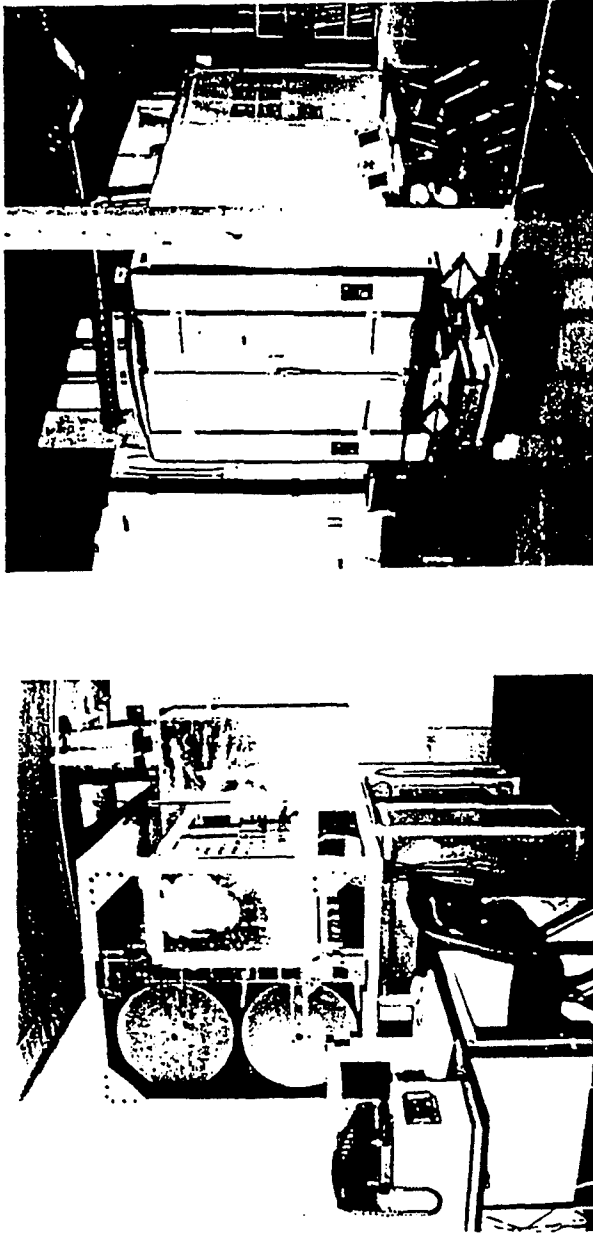
DOE/AFTAC Joint Field Test: McClellan AFB

- FULLY CONTAINED SYSTEM 3 x 3 x 7 FEET MOUNTED IN A COVERED TRAILER (7 x 12 x 7 FEET HIGH)
- BEGAN A 6 MONTH OPERATIONAL TEST IN JULY
- SAMPLES, ANALYZES AND TRANSMITS DATA AUTOMATICALLY
- OPERATIONAL CONTROLS, STATE-OF-HEALTH AND SOFTWARE UPGRADES AVAILABLE BY PHONE-IN

FIGURE 2

Xenon Radionuclide Analyzer

NEAR REAL-TIME ANALYSES OF THE XENON RADIONUCLIDES (ALL OPERATIONS AUTOMATIC)
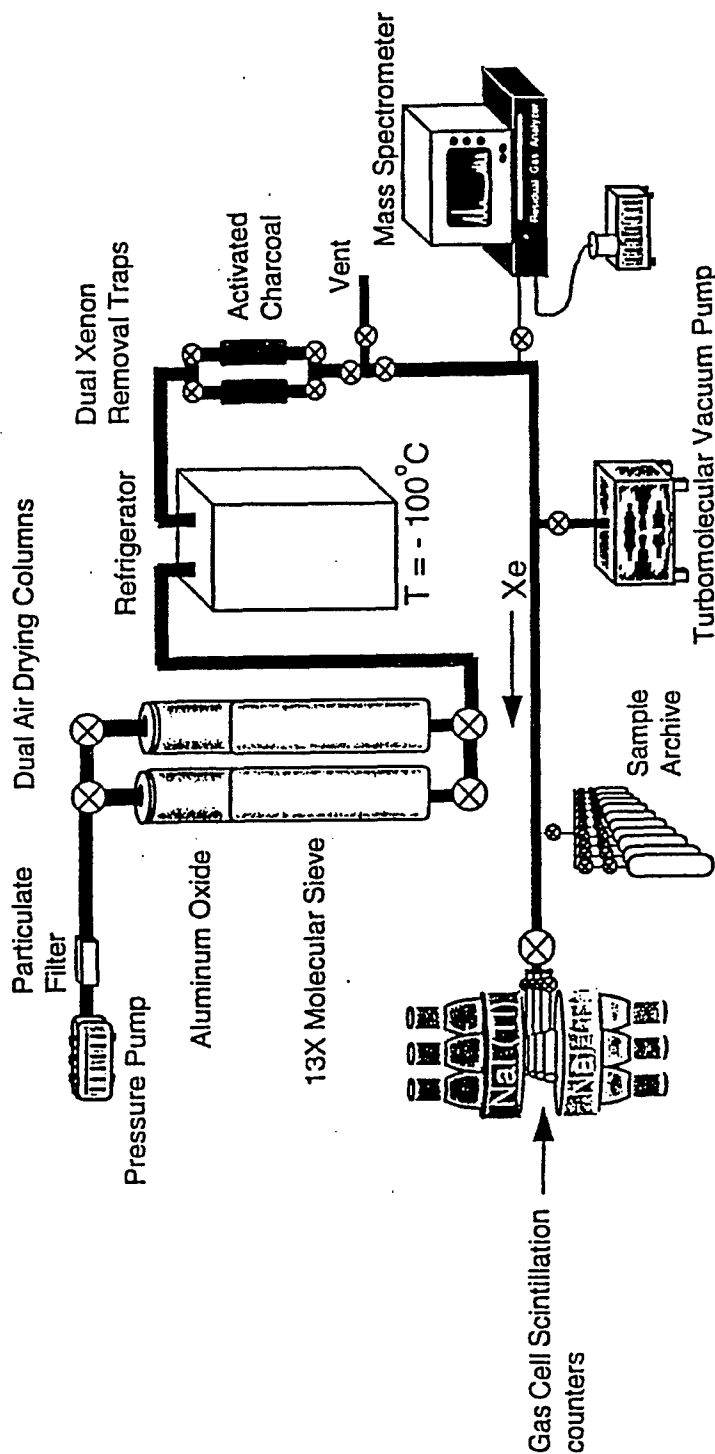
- Designed to continuously separate xenon from the atmosphere at very high flow rates (40 m³ of air per 8-hour collection period) which provides up to 50 fold greater sensitivity than other reported systems performance.

- Employs 8 hour collections versus one to two day collection periods which allow a 5 to 10 fold greater sensitivity for ^{135}Xe (9.1 hr).

- Employs highly efficient and low background beta coincidence gamma-ray spectrometry which provides a 10 fold greater sensitivity than available with other systems.

- Will Automatically transmit the data to NDC for forwarding to IDC.

Figure 3

Xenon Radionuclide Analyzer

Fieldable Fully Automatic Prototype
Near Realtime Analyzer
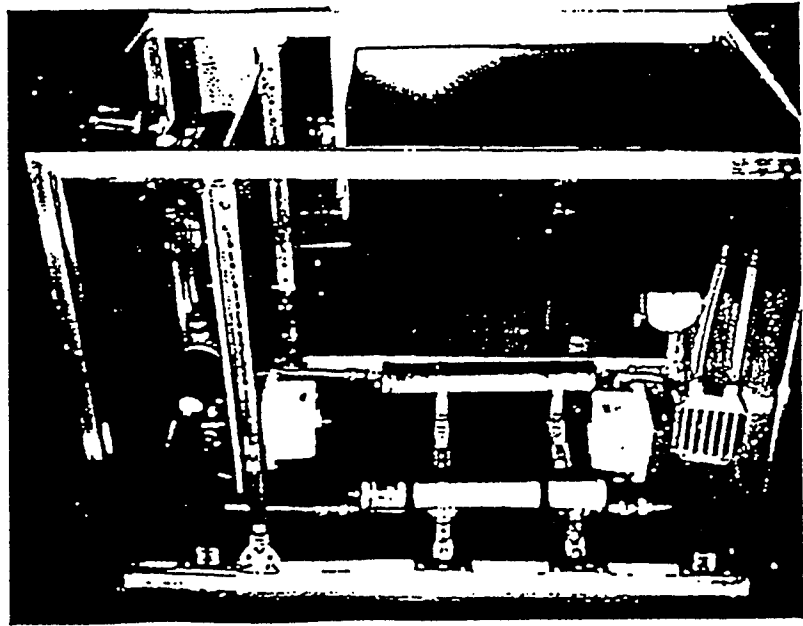
Under Construction For Test In January 1996

- Fully automated sample acquisition, analysis and data transmission

- Portable - 3' x 3' x 7'

- Low power < 2.5 kW power consumption

- 8-hour cycle time

THE HYDROACOUSTIC COMPONENT OF AN INTERNATIONAL MONITORING SYSTEM

ABSTRACT

Joseph K. Schrodt, Dean A. Clauter, and Frederick R. Schult
(Air Force Technical Applications Center
David Harris
(Lawrence Livermore National Laboratory)

The critical issue for the hydroacoustic component of an International Monitoring System (IMS) is its capability for monitoring nuclear explosions in the world's oceans. Factors that affect this capability are number and location of hydroacoustic sensors, placement of sensors, blockage of the hydroacoustic signal due to bathymetric effects, and spatial and temporal variation in hydroacoustic signal propagation due to changes in oceanic properties. This paper provides examples of hydroacoustic monitoring capability from historical data that demonstrates the impact of these factors, and discusses implications from these results on design of a hydroacoustic network.

Specific data processing examples of hydroacoustic detection and discrimination capability are given for hydroacoustic signals from earthquakes and explosions recorded at MILS (Missile Impact Location System) and other hydrophones in the Atlantic and Pacific Ocean. In the 1960's, the United States (U.S.) Navy performed a series of ship sinking explosions underwater as well as a set of explosions that traversed the Aleutian Island chain at a ninety degree angle. Another study is of more recent data from a collection of earthquakes south of Australia and in the Southern Pacific Ocean also detected on MILS and other hydrophones. Examples from all of these data illustrate the blockage effects due to the bathymetric profile and effects of hydroacoustic sensor emplacement on the side or top of, or floated from the top of seamounts into the SOFAR channel on hydroacoustic signal strength.

These data processing examples also demonstrate the high degree of confidence achieved in the discrimination between earthquakes and explosions based on their respective frequency content and presence or absence of an explosion-produced bubble pulse signal. The explosion data exhibit significant frequency content up to the anti-alias filter frequency of seventy Hertz, while the earthquake data shows severe attenuation beyond 20 Hertz and no bubble pulse signals. Potential problems are hydroacoustic signals from volcanic explosions that exhibit explosion-like characteristics and from vented explosions or explosions just above the ocean's surface.

The paper recommends that these historical data provide a basis for a knowledge grid of the ocean that would define for each explosion source position (for example, on a 1- by 1-degree grid) what a hydroacoustic sensor would expect to see. The knowledge grid would contain information from both theoretical detection and location capability models and this type of observed historical data. This could ultimately be combined with a similar seismic and possibly infrasonic knowledge grid to give worldwide detection and location capability for subsurface and low atmospheric nuclear explosions. The paper concludes with a design for the hydroacoustic component that takes into account the use of a combination of assets for monitoring nuclear explosions on a global scale that include seismic, infrasonic, and hydroacoustic networks.

INFRASONIC MONITORING
RODNEY W. WHITAKER
LOS ALAMOS NATIONAL LABORATORY

Abstract

Infrasonic monitoring is a relatively low cost and robust means of monitoring for atmospheric explosions, which was used from the early 1950s through the mid 1970s by the US for monitoring purposes. Source yields anticipated under a Comprehensive Test Ban Treaty monitoring regime are lower than they were during the years of atmospheric testing, with the result that the frequency range of interest is moved to higher values. We present a brief review of infrasound physics and propagation and review the results of recent DOE supported research at Los Alamos National Laboratory. Recent data from large surface explosions is discussed with regard to current monitoring interest. Considerations of synergy among infrasound and other monitoring technologies are presented. Results from earlier work are in good agreement with more recent measurements for kiloton sized explosions. Infrasound continues to be an excellent technology for inclusion in the International Monitoring System for a Comprehensive Test Ban Treaty.

Infrasonic Monitoring
Rodney W. Whitaker
Los Alamos National Laboratory

Infrasound Review and Background

Infrasound signals are regular acoustic signals in that they are longitudinal pressure waves albeit at rather low frequency. Many researchers would place infrasound frequencies in the range of 0.1 to 10.0 Hertz, with corresponding wavelengths of 3300 to 33 meters. As with most wave phenomena, absorption decreases with decreasing frequency and infrasound propagates well in the earth's atmosphere, with geometric loss dominating other losses. This makes infrasound useful in remote monitoring activity such as the CTBT International Monitoring System (IMS). Atmospheric explosions generate a wide spectrum of acoustic frequencies; those in the audible domain are absorbed in the atmosphere and do not propagate to large distance. Lower frequency components are also present, and these do propagate to great distance. As the yield of the explosion decreases, the acoustic energy is concentrated at higher frequency than that for higher yield sources.

Infrasound can be generated by natural and manmade processes; moreover, many sources of audible sound are also sources of infrasound. Some known natural sources include: winds, large scale weather systems, volcanoes, earthquakes, meteors, aurora, and avalanches. Some manmade sources include explosions, helicopters, other aircraft, rockets, and large machinery. Measurements in the Los Alamos infrasound program, working around 1 Hz, have established databases on the acoustic signals from underground nuclear tests, earthquakes and large surface explosions[1-3]. Other organizations have obtained measurements of the acoustic signal from meteors, which can penetrate to lower altitudes where the kinetic energy may be explosively deposited. Meteors are a natural impulsive source and would look like an atmospheric explosion. Large eruptive volcanoes also would appear impulsive; however many would be of large size and would have additional information on origin from the seismic network.

At large range, infrasound signals are oscillatory acoustic signals detected as small pressure variations about the ambient value. Thus in time, a signal would look like positive and negative pressure variations around a zero mean value. The microphone is then a high quality differential pressure sensor not an absolute pressure sensor. In a quiet background, the sensor should be able to measure 0.1 microbars (1 microbar = 1 dyne/cm^2 = 0.1 Pascals). In character, infrasound data is similar to seismic data. For the IMS, sampling rates of no more than 20 samples per second will be sufficient. These are rather low data rates and present no significant data handling or transmission problems.

Detection is accomplished generally with arrays of microphones, and standard array/signal processing techniques are applied to determine source bearings, source power spectra, and correlation coefficients. The sensor can be one for infrasonic frequencies or one for lower frequencies, generally referred to as a microbarograph. Microbarographs were used extensively during the 1960s and 1970s in global networks for detecting atmospheric nuclear

explosions, often at much larger yield than is of interest currently. Infrasound arrays operated by Los Alamos employ a system of porous hoses at each sensor to aid in low level wind noise reduction[4]. This system can be viewed as a generalization of the Daniels pipe used in earlier systems, which emphasized lower frequencies. For a wide band sensor (0.01 to a few hertz) as considered for the IMS, the exact design of the front end noise reduction still needs to be studied to achieve optimum design. The low level wind noise power rises rapidly with lower frequency below a few tenths of a Hertz.

Notional site locations have been made in an expert group report for the Ad Hoc Committee on a Nuclear Test Ban.[5] As final site selection proceeds, it is useful to note that there are some obvious features that one would like to avoid in the selection process. Persistent low level winds of moderate velocity (several meters per second) would have a large background noise level and should be avoided. Locations with ground cover, wooded or shrubs and grass are useful. Sites removed from heavy industry, mining and significant civilization noise are to be preferred. Power requirements are modest and Los Alamos has operated two of its arrays with solar panels and battery backup for several years with minimum maintenance problems. At these locations the analog data are RF transmitted back to a central site for recording using low power (a few watts) VHF transmitters. Snow is generally not a problem and can aid in the wind noise reduction.

In atmospheric wave physics, attention must be given to upper (> 10 km) atmospheric winds, because the wind speed at these heights can be a significant fraction of the sound speed. They can exert an appreciable influence on propagation speed and on surface bounce locations. Northern hemisphere stratospheric winds follow a seasonal pattern, blowing to the east in winter and to the west in summer. Received signal strength is enhanced to the east in winter and degraded to the east in summer. The opposite behavior is seen for propagation to the west. Southern hemisphere stratospheric winds show similar seasonal behavior, with roughly opposite phase. Absolute speeds can be higher in the southern hemisphere in mid summer and mid winter. Work at Los Alamos has provided a normalization procedure to account for the wind effects on measured pressure amplitudes[6].

Recent Surface Explosion Data

As part of the Los Alamos program, long range infrasound measurements of large surface ANFO (ammonium nitrate and fuel oil) explosions have been routinely made[1-3]. We have data from eight tests with charge weights of 24 tons to 4880 tons and ranges of 250 km to 5300 km. These events provide a uniform source set for propagation studies, and our analysis incorporates our wind normalization, giving the amplitude for a zero wind condition. In the attached Figure, the peak to peak normalized amplitude, p_{wca}, microbars, is given as a function of scaled range, where scaled range is actual range, R km, divided by charge weight, W, tons, raised to the 0.5 power. The regression curve is given by

$$p_{wca} = 4.69 X 10^4 (R/W^{0.5})^{-1.36}.$$

998

Interplay with other Technologies

It is not surprising that costs are a significant issue in planning the IMS. Cost saving measures are sought in deployment and operations. Co-location is seen as an obvious method of saving costs in the deployment phase as well as in operations. It will be possible to co-locate two or more technologies at the same location in some instances. There are factors that would prohibit co-location in other instances. Consider for illustration a seismic station and an infrasound station. With seismic using buried sensors and infrasound sensors sitting on the surface, true co-location is possible. However, at a given location the best seismic site may be unsuitable for infrasound because of lack of ground cover and/or low level winds. Low level winds and local topography could make a good seismic site bad for infrasound. With islands where a hydroacoustic ground station might be, one would like to be inland from beach areas to avoid sea breeze and surf noise. In such cases a move of 5 km or so may provide a suitable alternative. This should still be considered co-location and cost savings would still be possible in installation, operations, and data handling. The older global networks did utilize island sites which operated successfully.

For sites that may be rather remote, such as certain island sites, specific dedicated transportation of equipment for initial installation might be expensive. With careful attention to shipping and air schedules, and a little flexibility in deployment schedules, one may be able to use vessels or aircraft which are going to the region of interest anyway, i.e. ships and planes of opportunity. Equipment, for one or more technologies, may be shipped in such cases at some cost savings over dedicated carriers.

It is anticipated that co-location of two sensor types will have benefits in event detection, location and discrimination. Because this type of operation has not been common to date, we must realize that only actual operations can establish the full range of cooperative benefit. With acoustic and seismic paired, each data type can help the other in some background characterization and event identification. This is true when one sensor type sees a suspicious event but the other sensor identifies the event as uninteresting. Differences in travel times for seismic, hydroacoustic and infrasonic data can be exploited to improve event location, when the event is seen by two or more sensor types. The characteristics of infrequent but recurring signals on two different sensors can be learned with time and used to identify (and dismiss as uninteresting) such events. It is likely that the value of such intercomparisons will vary from one site to another and that actual operation will suggest other applications.

Acknowledgment

References

1. "Infrasonic Observations of the Minor Scale High Explosive Test", R. W. Whitaker, J. P. Mutschlecner, S. S.Bunker, and C. A. Painter, 1986, paper J2-6, Proceedings of the 12th International Congress on Acoustics, Toronto, Canada.

2. "Infrasonic Observations of Large-Scale HE Events", Rodney W. Whitaker, J. Paul Mutschlecner, Masha B. Davidson, and Susan D. Noel, 1990, Fourth International Symposium on Long-Range Sound Propagation, NASA-CP-3101.

3. "Miser's Gold", Marie Davidson and Rodney W. Whitaker, 1992, LA-12074-MS.

4. "Comparisons of Noise Reduction Systems", S. D. Noel and R. W. Whitaker, 1991, LA-12008-MS.

5. "Working Group 1 - Verification. International Monitoring System Expert Group Report based on Technical Discussions held from 6 February to 3 March 1995, Part I, Infrasound Monitoring," Ad Hoc Committee on a Nuclear Test Ban, 16 March 1995, Conference onDisarmament, Geneva, Switzerland, CD/NTB/WP.224.

6. "The Correction of Infrasound Signals for Upper Atmospheric Winds", J. Paul Mutschlecner and Rodney W. Whitaker, 1990, Fourth International Symposium on Long-Range Sound Propagation, NASA-CP-3101.
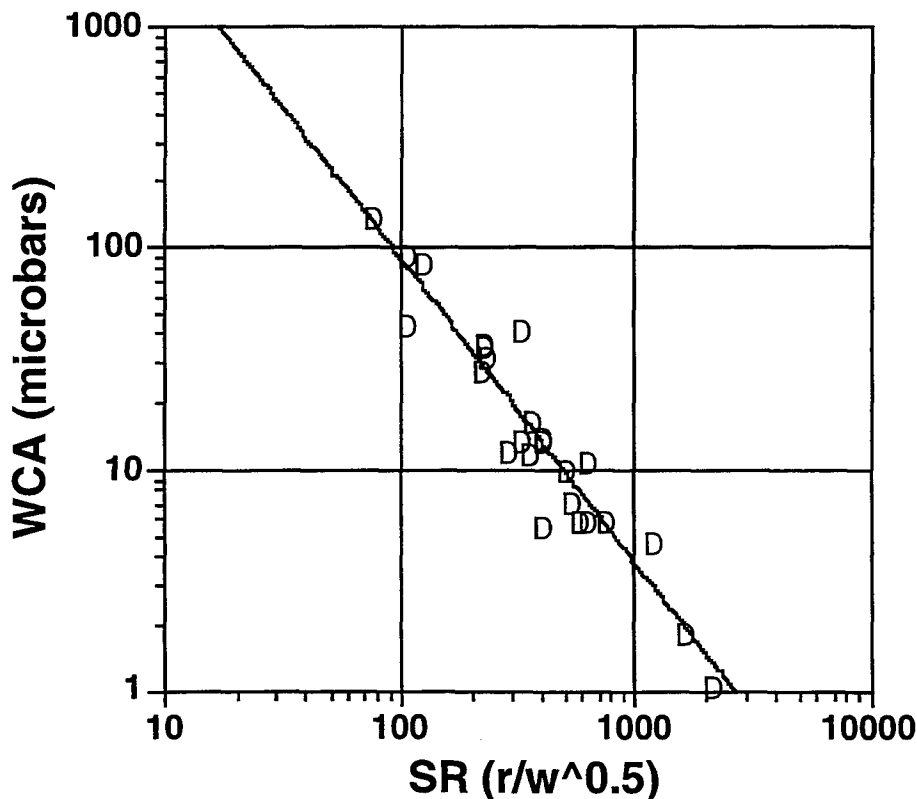
LLNL ON-SITE INSPECTION RESEARCH PROJECT:
A PROGRESS REPORT

J.J. Zucca, C. Carrigan, C. Shultz, A. Smith, J. Sweeney, and W. Pickles
Lawrence Livermore National Laboratory

ABSTRACT

We have been developing four specific technology areas that could be used during on-site inspections under a comprehensive test ban treaty: aftershock monitoring, noble gas monitoring, electromagnetic pulse monitoring, and overhead imagery detection of disturbed ground. Our investigation of aftershocks has shown that the low-frequency aftershocks that have been observed after nuclear tests at the Nevada Test Site are also associated with certain kinds of mining operations such as block caving. Our noble gas detection effort has successfully predicted the travel time of two tracer gases emplaced in the Non-Proliferation Experiment. Our EMP effort has developed a stand-off relationship for EMP sensors from the source and to date, has found that mining explosions do not generate significant low-frequency EMP. Our overhead imagery effort suggests that plant stress from shocked ground above an underground explosion may be detected using a ratio of 690 to 420 microns of visible light.

OBJECTIVE

Under a comprehensive test ban treaty the initial detection capability for treaty violations will come from the international monitoring system (IMS). However, in many evasion scenarios—particularly those including a well-contained underground test—the IMS will not provide conclusive evidence of the nuclear nature of the event. In these cases an on-site inspection (OSI) may be necessary to gather evidence to confirm the nature of the event.

The objective of this project is to identify the phenomenology to be pursued in such inspections and to develop techniques and procedures for use during an OSI. Our project encompasses not only those techniques that would be employed after the occurrence of an ambiguous event, but also those measurements that could be employed during an on-site visit to the site of a declared explosion to confirm its nature.

Out of the many possible OSI methods, we are focusing on improving the effectiveness of a few methods which we feel are critical to the success of an OSI: aftershock characterization, noble gas seepage, low-frequency electromagnetic pulse, and the overhead detection of disturbed ground.

RESEARCH ACCOMPLISHED

Aftershocks. It is well-known that aftershocks occur after large earthquakes and that their occurrence rate decreases with time. Aftershocks from nuclear explosions behave in a similar manner but with the difference that explosion aftershock sequences include varying numbers of low-frequency events (Jarpe *et al.*, 1994; Ryall and Savage, 1969). High-frequency (*i.e.* normal aftershocks) have corner frequencies above 50 Hz, whereas low-frequency events have corner frequencies of a few Hertz. If these low-frequency aftershocks are associated only with underground explosions, then detection of such events during an OSI could help focus the efforts of the inspectors. It is important to know if these events occur in other settings.

A possible analog to rubble zone formation after an underground explosion is a block-caving mine. In this mining technique the ore body is undermined and a collapse is initiated into the mined cavity. As caving operations continue, a rubble zone is formed which extends toward the surface and may intersect it. To see if these low-frequency events are associated with block-caving operations, we deployed a microearthquake network at the Henderson mine in central Colorado, which uses block caving. Figure 1 shows a schematic cross section through the mine. Note that the rubble zone extends to the surface where it has formed a crater approximately 200 m across which is much wider than the rubble zone expected from a underground explosion of a few kilotons. Figure 2 shows an example of the waveforms from the mine compared with some waveforms from an event with similar magnitude from the nuclear test 'Hunter's Trophy' which was conducted at Rainier Mesa at the Nevada Test Site. Note that the low-

frequency events from Hunter's Trophy and Henderson are similar, especially when compared to the shot. The high-frequency content of this waveform suggests that the difference is in the source and not the structure near the station. The low-frequency events are difficult to locate because they are so emergent. Our future work will focus on developing location techniques for these events and seeing if they occur in other types of caving operations.

Noble gas seepage. A key aspect of an OSI will be to search for radioactive gases that are indicative of nuclear explosions. Of these gases, five are potential targets of collection during an OSI: Xenon-135 and -133, Argon-37, Krypton-85, and Tritium which have half lives of 9 hours, 5 days, 35 days, 11 years, and 13 years respectively. Argon-37 is the most attractive target since its half-life is long enough that it will still be detectable after several months, and has a small world-wide background. To test the transport of gas to the surface we placed bottles of two different tracer gases, Helium-3 (^{3}He) and sulfur hexaflouride (SF_6), in or near the explosive cavity of the Nonproliferation Experiment (NPE), an over-buried explosion in which no crater was expected to form. The bottles were crushed at the time of the explosion, releasing the gases.

The first gas to reach the surface was SF_6, in just under two months; the Helium-3 did not reach the surface until a year later. We modeled the transport of the gas to the surface with the flow and transport code NUFT (Nitao, 1993) using measured permeabilities from Rainier Mesa rocks. As an initial condition it was assumed that the gas was forced out significantly into the surrounding rock by the shock wave. We also assumed that a fracture system intersects the initial gas concentration and extends to the surface (Figure 3A). The calculation included the measured surface atmospheric pressure variations so that atmospheric pumping could be included. The model calculations are shown in Figure 3B. It qualitatively predicts the arrival of the tracer gases. If barometric pumping is left out of the calculation, many years are required to transport gas to the surface (not shown). The model also predicts that the arrival of SF_6 before the Helium-3. This difference is apparently caused by the different molecular weights of the two tracers; the heavier SF_6 causes it to have a lower gas diffusivity than the ^{3}He. When barometric pumping is included in the calculations as shown in Figure 3B, flow is mainly along fractures, but diffusion of gas also occurs into the porous matrix of the fracture wall. Gases with higher diffusivity (*i.e.* lower molecular weight) diffuse at a greater rate into the walls of the fracture during up flow. Thus, the higher diffusivity gas is depleted from any upward fracture flow soon after the flow is initiated. This, in turn, delays its arrival at the surface. The molecular weight of the radionuclide gas of main interest to OSI, Argon-37, is bracketed by our results and should have an intermediate arrival time to ^{3}He and SF_6. Our future work will include some model calculation for Argon-37 but primarily focus on collecting the 100 1 samples that will be necessary for detecting Argon-37.

Electromagnetic Pulse. Underground chemical and nuclear explosions in the range of a kiloton yield or greater both generate low-frequency EMP (about 1 Hz) that are observable within several kilometers of ground zero. (Sweeney, 1989; Sweeney, 1994). These signals could be used during cooperative zerotime inspections to confirm the nature of large announced explosions. During this fiscal year we have been gathering data from explosions that LLNL is monitoring for the CTBT program to see if low-frequency EMP is observable from large ripple-fired blasts and from smaller dedicated non-nuclear explosions.

If ELF is to be useful in zerotime monitoring we need to know how far away we can expect to detect signals from an explosion of a given yield. We have assumed that the EMP signal strength falls off as the inverse cube of distance and fit the function to our data base of measured signal levels from nuclear tests to produce the plots shown in Figure 4. To date we have not observed any detectable EMP from mining explosions that we have monitored. This is probably because we cannot deploy our sensors inside the distance indicated in Figure 4.

Overhead detection of disturbed ground. Underground explosions create shock waves in the earth that can reach the surface and create strong ground motion. This motion could create effects on the surface that are observable using overhead imagery. Using the Non-Proliferation Event, we have investigated two such effects, 'fluffing' of the ground surface and plant stress. A comprehensive set of overhead imagery was taken one day before the NPE and for several days after using a low-flying airplane. Acquired imagery included 3 bands of infrared, 8 bands of visible light, and visible-light color photographs. We looked for the 'fluffing' effect by trying to identify systematic changes in surface emissivity in the infrared images—but did not find any changes associated with the NPE (Pickles, 1994).

The plant stress effect is more interesting however. Carter (1993) stressed a variety of plants in a variety of ways and looked at the plant's reflectance. He found that stressed plants show high values of the ratio of visible light of 690 microns to 420 microns. These bands are available in our imagery data and show changes that appear to be associated with the NPE. Figure 5 shows the histograms of pixel values for this ratio for before and after the NPE. Note that there is a significant increase in the ratio for data taken 56 hours after the explosion. The anomaly appears to be gone by the seventh day. Unfortunately the anomaly extends out to the edge of the imaged region, which is approximately 2 km from the NPE or approximately 0.2 G acceleration. We cannot be sure that stressed plants from the NPE are the cause of our observed data, although we did observe that at least one species of plant on Rainier Mesa underwent premature senescence a few days after the NPE. Future work will concentrate on stressing plants from ground acceleration under controlled conditions to see if this effect is reproducible.

1004

CONCLUSIONS AND RECOMMENDATIONS

On-site inspections will be a component of any comprehensive test ban treaty that is concluded in the future. Our work will help make OSIs more effective which benefits the international monitoring regime in two primary ways: 1) an effective OSI regime will give confidence to the requesting party that a violation can be found and assures the inspected party that the inspectors will only search for relevant evidence, 2) a carefully constructed OSI capability will help keep costs to a minimum.

We plan to continue our development of the four technology areas discussed above during FY96 and to make our results available to the international community.

REFERENCES CITED

Carter, A.C., 1993. Responses of leaf spectral reflectance to plant stress, American J. of Botany, 80(3), 239-234.

Jarpe, S., P. Goldstein, and J. Zucca, 1994. Comparison of the Non-Proliferation Experiment aftershocks with other Nevada Test Site events, *Proceedings, Symposium on the Non-Proliferation Experiment, DOE Conf-9404100*, 8-34

Nitao, J.J., 1993. Reference Manual for the NUFT Flow and Transport Code, Version 1.0, UCRL-ID-113520, Lawrence Livermore National Laboratory, Livermore CA.

Pickles, W.L., J.E. Shines, D.L. Hawley, M.D. Pelan, S.B. Brewster, 1994. Low-altitude overhead imagery acquisition pre and post NPE, in Proceedings of the Symposium on the Non-Proliferation Experiment, DOE Conf-9404100, edited by M.D. Denny, Lawrence Livermore National Laboratory, Livermore, CA.

Ryall, A. and W. U. Savage, 1969. A comparison of seismological effects for the Nevada underground test BOXCAR with natural earthquakes in the Nevada region, *J. Geophys. Res.* 74, 4281.

Sweeney, J.J., 1989. An investigation of the usefulness of extremely low-frequency electromagnetic measurements for treaty verification, UCRL-53890 Lawrence Livermore National Laboratory, Livermore, CA.

Sweeney, J.J., 1994. Low-frequency electromagnetic measurements at the NPE and Hunter's Trophy: a comparison, in Proceedings of the Symposium on the Non-Proliferation Experiment, DOE Conf-9404100, edited by M.D. Denny, Lawrence Livermore National Laboratory, Livermore, CA.
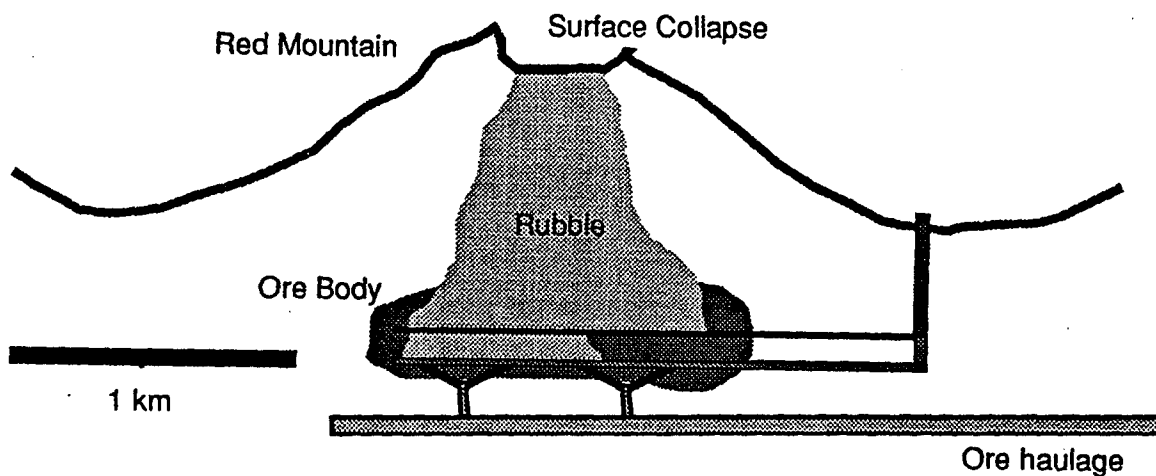
Figure 1.

Schematic cross section of Henderson mine.
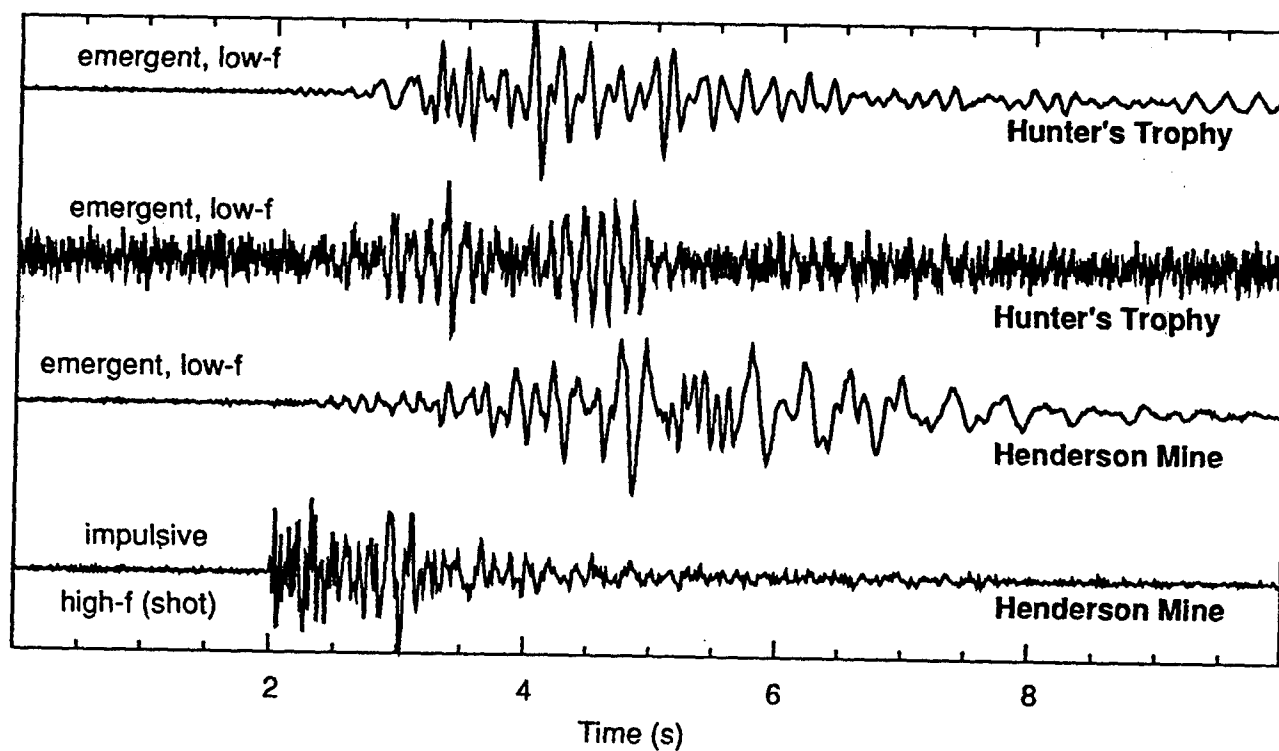
Figure 2.

Aftershocks from the Hunter's Trophy nuclear test compared to microseismic events from the Henderson mine. Hypocentral distance is 1 to 2 km from each event.

A)

B)
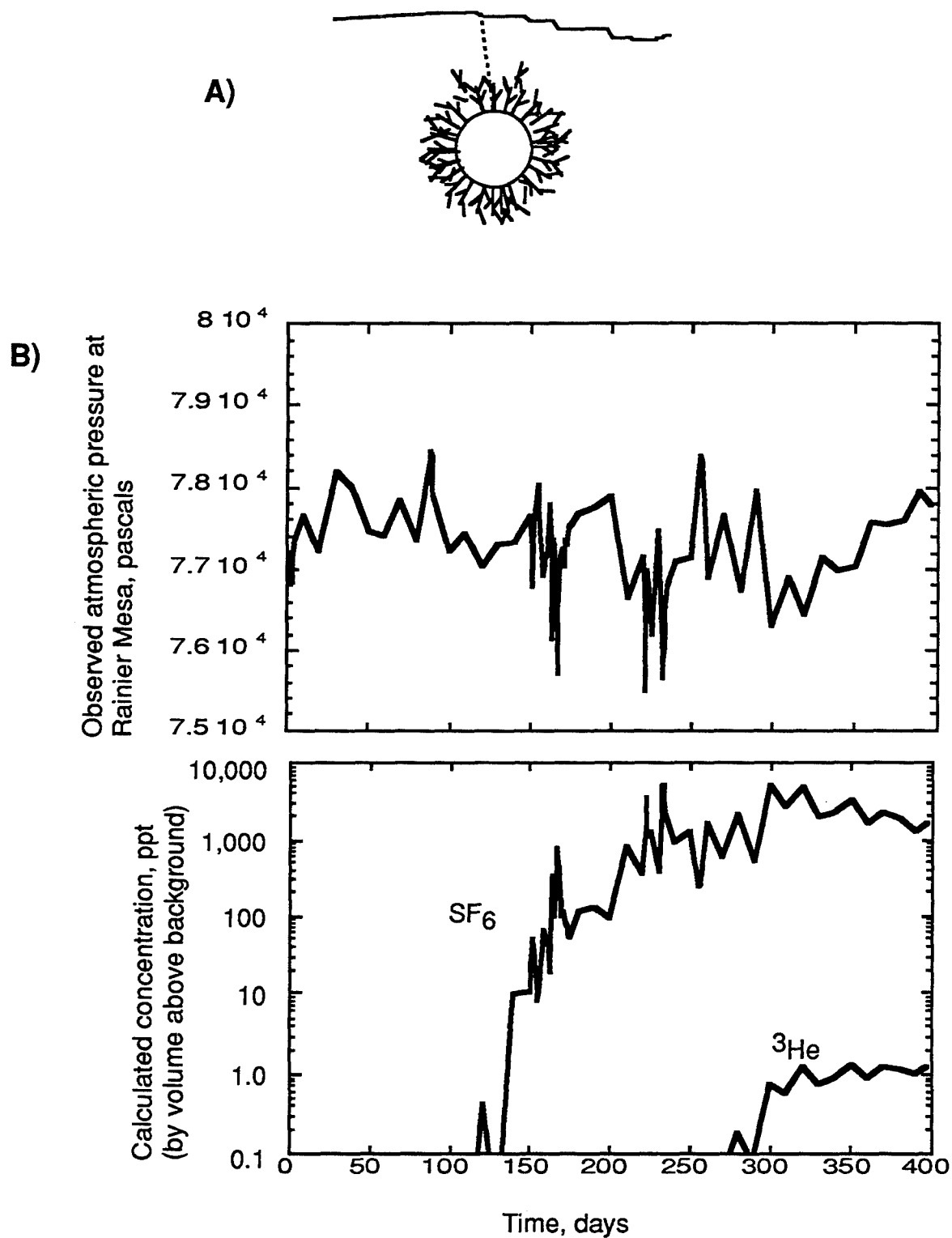
Figure 3

Gas transport model calculations. A) Schematic cross section
showing the starting condition for the model. The gas has been
forced out into the rock along fractures from the explosion. B)
Results of the calculation. The upper panel shows the observed
pressure at Rainier Mesa. Gas was released at zero time.

A)

B)
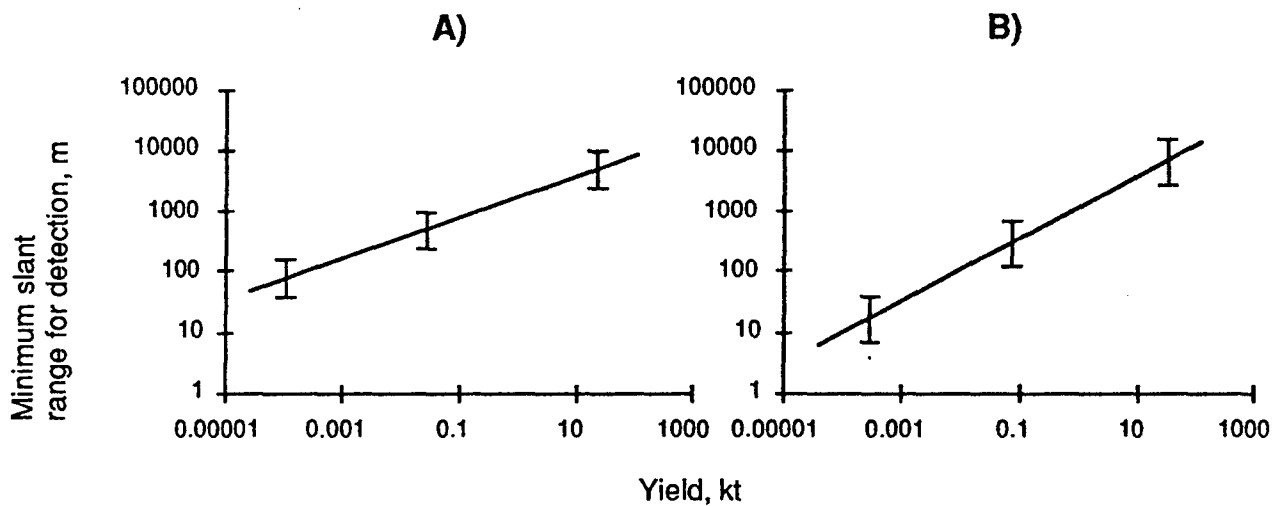
Figure 4.

Calculated minimum slant range standoff distance for detection of electromagnetic pulse from underground explosions: A) Magnetic, B) Electric. In each case the line represents the best fit to the empirical data, the bars indicate uncertainty.

A)   B)   C)
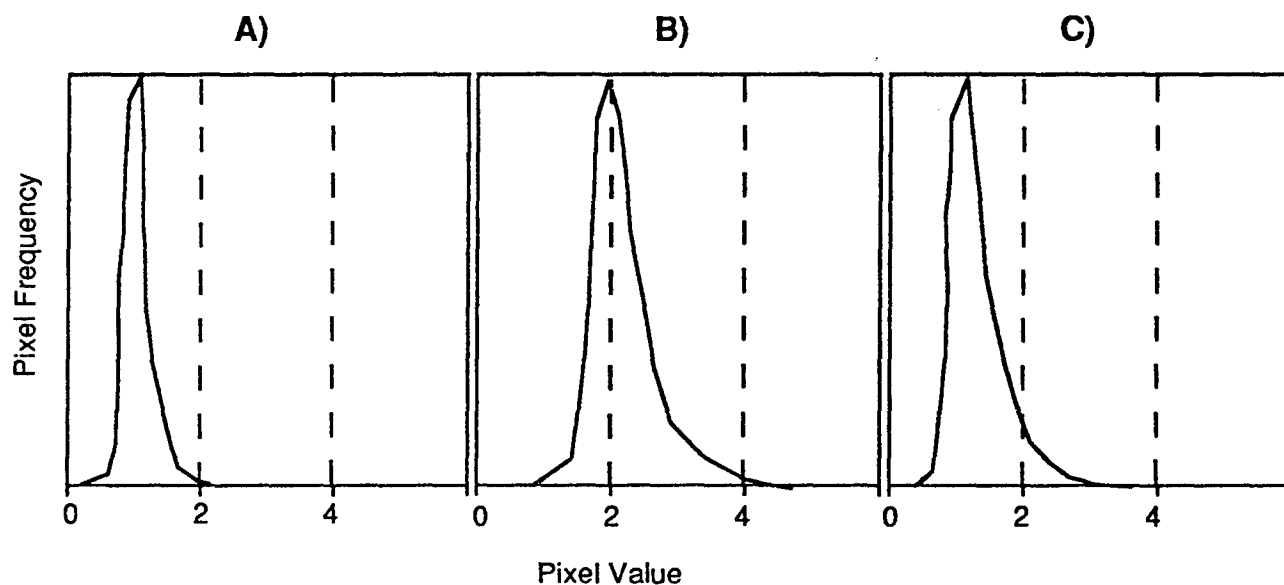
Figure 5.

Histograms of pixel values for the visible light ratio of 690 to 420 microns.
A) Before the NPE. B) 56 hours after C) 7 days after.

An Experimental Characterization of the Non-linear Rheology of Rock

G. N. BOITNOTT

New England Research Inc.

ABSTRACT

A laboratory experimental program is underway to constrain rheological models for deformation of rock in the brittle-damage and moderate-strain regimes. The data will be used to assess the importance and consequences of nonlinearities in mechanical properties which affect the amplitude and spectral character of regional and teleseismic signals. Experiments are being performed to characterize the intrinsic loading path dependence of the deformation of rock subjected to various loading conditions. Cyclic loading tests in unconfined uniaxial compression, torsion, and confined compression are being conducted on a variety of lithologies under conditions expected in the moderate-strain and brittle-damage regimes of an underground explosion. The effect of ambient normal load, water saturation, and loading rate on hysteresis in deformation are being tested directly.

OBJECTIVES

In order to discriminate between underground nuclear explosions and other seismic sources, it is necessary to have confidence in source spectra derived from regional and teleseismic signals. There are four regimes pertinent to the wave propagation problem:

- a near-source, or hydrodynamic regime
- a brittle-damage regime, where rock failure dominates the rheology
- a moderate-strain regime where rock deformation is known to be nonlinear, inelastic, and hysteretic, yet permanent deformation does not occur.
- a far field regime where rock deformation is linear and traditional seismological techniques can be applied.

In this work, we concentrate on studying fundamental issues concerning the deformation of rock in the moderate-strain regime and its transition into the brittle-damage regime.

The objectives are to provide laboratory data for the constraint and development of realistic rock rheologies suitable for modeling wave propagation in the moderate-strain and brittle-damage regimes. The data will be used to assess the importance of nonlinearities on the amplitude and spectral character of regional and teleseismic signals. This information is needed to better understand the extent to which nonlinear material properties in the brittle-damage and moderate-strain regimes are important to regional discriminants and event detection.

In coordination with others, numerical simulations of wave propagation using the developed nonlinear rheologies will be performed to assess the importance of the nonlinearities for problems concerning discrimination, detection, and yield estimation of underground explosions. Comparisons of the simulation results with field data will be made where appropriate.

PRELIMINARY RESEARCH RESULTS

Background

As a result of previous laboratory studies, a general rheological model has been developed for the case of uniaxial stress perturbations in unconfined compression [see *Boitnott*, 1993, 1994]. The model and supporting data provide constraints on the loading path dependence of the deformation for arbitrary loading history, and have provided us with a foundation upon which to develop more general rheologic models.

In order to apply the developed rheology directly to problems of wave propagation from a seismic source, we need to extend the rheology to loading paths expected in the field. Four main goals have been identified. First, we need to extend the rheology to include a wide variety of loading conditions. In order to model shear wave propagation, we need laboratory data to constrain hysteresis in the shear modulus during shear loading. In addition, in order to model compressional wave propagation (including the effects of spherical wavefronts) we need to extend the uniaxial-stress rheology to loading paths which are transitional between uniaxial-strain and uniaxial-

stress. Second, we need to characterize the effects of confining pressure on the rheological models in order to address questions concerning the effect of depth of burial on the seismic signature of an underground explosion. Third, we need to examine in more detail the behavior at reversals in loading direction since the details at the cusps in stress-strain relationship strongly influence the extent to which energy is shifted to higher frequencies. Fourth, we need to extend the stress regime of the rheologies to include the brittle-damage regime.

Developing a More General Rheology

In order to extend the rheology to loading conditions other than uniaxial stress, three types of experiments are being performed. First, unconfined uniaxial stress experiments are being performed during which both axial and radial strain is measured. These experiments are motivated by the need to identify simplifying principles which can be used to extend the uniaxial-stress rheology to the case of arbitrary triaxial stress perturbations. For example, we might hope to model triaxial deformation through the use of superposition arguments, defining a change in stress/strain state as a superposition of a series of hysteretic and non-hysteretic components.

An example of data from an experiment on Sierra White granite is shown in Figure 1. In Figure 1a we see the familiar cusped hysteresis loop between axial stress and axial strain for a cyclic axial load in unconfined compression. In Figure 1b, we plot the corresponding radial strain as a function of axial stress. Note that the radial strain exhibits little (if any) measurable hysteresis. Importantly, this observation rules out the possibility of decomposing an arbitrary deformation into a non-hysteretic dilation and hysteretic distortion, since the data indicates considerable hysteresis in the volumetric strain during perturbations in uniaxial stress.

The observed lack of hysteresis in the radial strain during unconfined compression may however indicate a simplifying principle which may lead to a more general rheology capable of handling the transition from uniaxial-strain to uniaxial-stress loading perturbations. This is of considerable importance in applying the rheological model to propagation of non-planar compressional waves, where the loading path is intermediate (and variable in space in time) between uniaxial-strain and uniaxial-stress. The data in Figure 1b suggests that the radial (Poisson) expansion is largely an elastic phenomena. It follows that the confining pressure required to maintain uniaxial-strain conditions should also be non-hysteretic with respect to axial load. If true, we might hope to develop a rheological model which involves the simple addition of a uni-valued (non-hysteretic) dependence of the axial-strain vs. axial-stress relationship on the hydrostatic component of the stress state.

The notion that the difference between uniaxial-strain and uniaxial-stress loading may be included in the rheology with the rather simple addition of a non-hysteretic confining pressure effect is consistent with some limited observations. In Figure 2 we compare experimental data on Berea sandstone from *Hilbert et al.* [1994] with a simple extension of a rheological model recently developed for the case of unconfined compression. Figure 2a shows a plot of axial strain versus axial stress for uniaxial-stress and uniaxial-strain loading paths on a sample of Berea sandstone. During the overall loading and unloading, small perturbations in axial load were performed to

Sierra White Granite
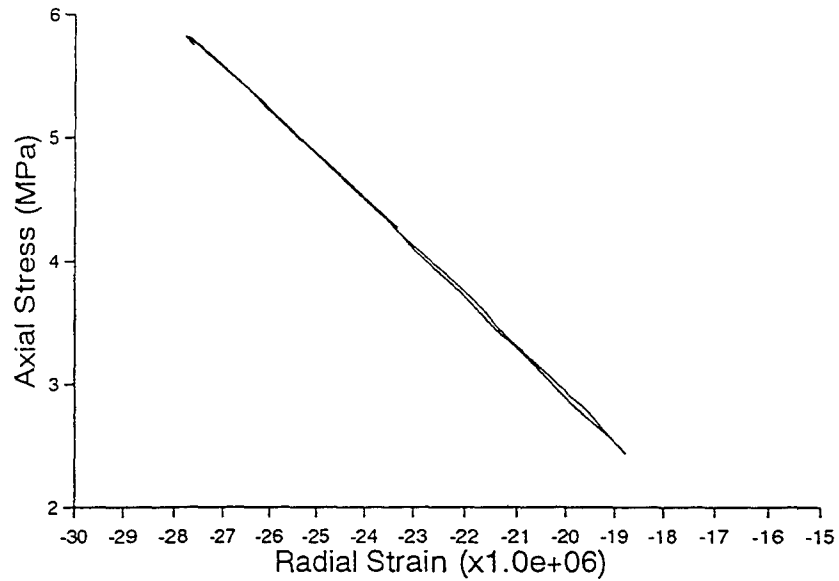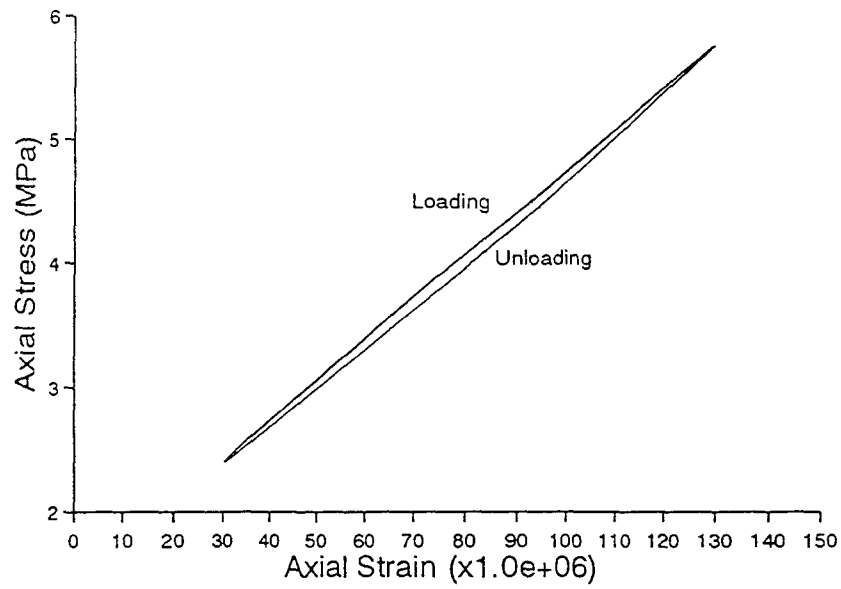
Figure 1: Axial stress versus axial strain and axial stress versus radial strain for cyclic loading of Sierra White granite in unconfined compression. Note the absence of hysteresis in the radial strain. This observation allows for the possibility of a simple model incorporating the effects of confining pressure on the hysteresis in axial strain.
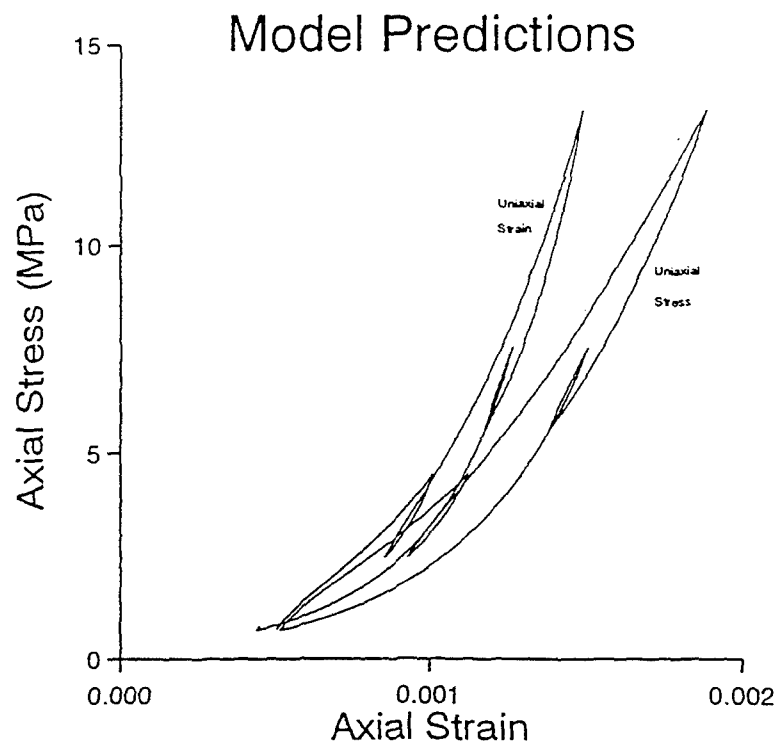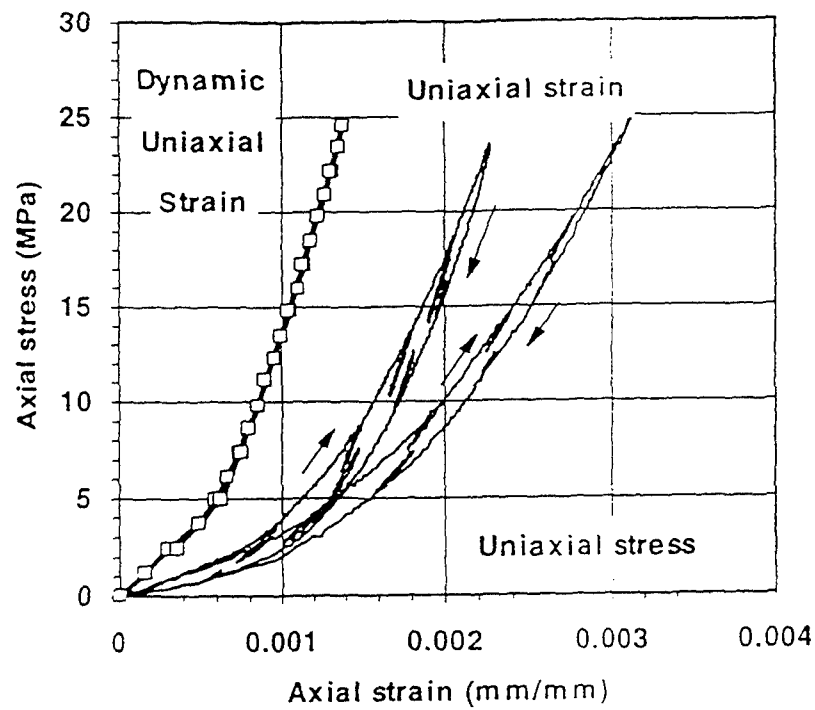
Figure 2: Comparison of Experimental data (from *Hilbert et al.*, 1994) with model predictions for hysteretic deformation in Berea Sandstone. A simple scaling law is used to incorporate the effects of changing confining pressure on the axial stiffness during uniaxial strain loading. The simple model appears to contain many of the features exhibited by the data. Model results are based on experiments using a different sample of Berea sandstone, and thus small quantitative discrepancies between model and data should not to be considered significant.

measure the response to small perturbations in load. Note that the character of the hysteresis is similar for the two loading conditions, and that the difference between the uniaxial-strain and uniaxial-stress behavior is largely the result of the increase in stiffness of the sample as the confining pressure is increased to enforce uniaxial strain conditions.

Model predictions based on the rheological model of *Boitnott* [1993] are shown in Figure 2b for a similar loading path. The peak stress for the model results is somewhat reduced from that of laboratory data since the parameterization of the model is only valid for stresses below 15 MPa. The model results for uniaxial-stress are simply the direct application of the model of Boitnott [1993] applied to the load protocol similar in form to that used by *Hilbert et al.* [1994]. The model results for uniaxial-strain are produced by adding a confining pressure effect to the the uniaxial-stress model. We start by defining the axial stiffness $\eta \equiv \partial\sigma_{11}/\partial\varepsilon_{11}$, where σ_{11} and ε_{11} are the axial stress and axial strain respectively. We then assume that $\eta \equiv \gamma E$, where E is the hysteretic Youngs modulus describing the rheology for uniaxial-stress perturbations, and γ a is scaling factor which is a linear function of the confining stress. The confining stress is assumed to change linearly with axial stress based on the observed lack of hysteresis in the radial-strain / axial-stress relationship as discussed in the context of Figure 1b. The resulting model provides a simple means through which to include confining pressure effects on the axial-stress/axial-strain relationship. Note that the model results compare favorably with the experimental data, illustrating that the scaled rheology is reasonable.

Guided by these observations, experiments are being conducted to constrain the confining pressure effect on hysteresis in uniaxial stress and comparing these results to axial-strain / axial-stress hysteresis during uniaxial-strain experiments. Experiments will be performed on a number of rock types. Once a rheology is developed, its predictive capabilities will be tested by performing a number of experiments using loading paths which mimic (in a quasi-static sense) the expected loading conditions for a spherically propagating compressional wave.

Torsion Experiments

In order to develop similar rheologies for shear wave propagation, torsional experiments are being conducted to constrain hysteresis in the shear modulus as a function of normal load and shear stress history. Experiments are being performed on hollow cylinders of intact sandstone and granite.

Examples of data on Berea sandstone are shown in Figure 3. In Figure 3a, the shear-stress vs. shear-strain relationship is plotted for a cyclic torsional load at a fixed axial load of 5.4 MPa. The frequency of the loading oscillation was 0.01 Hz and data from two different amplitude oscillations are shown. Note the nested nature of the hysteresis loops with amplitude and the fact that the mean slope of the hysteresis loops (i.e. the average shear modulus) decreases with loop amplitude. Figure 3b shows the results of three torsional oscillations at three different axial loads (3.6, 5.4 ,and 7.2 MPa). As expected, the average shear modulus increases, and the width of the hysteresis loops decreases, with increasing axial load.
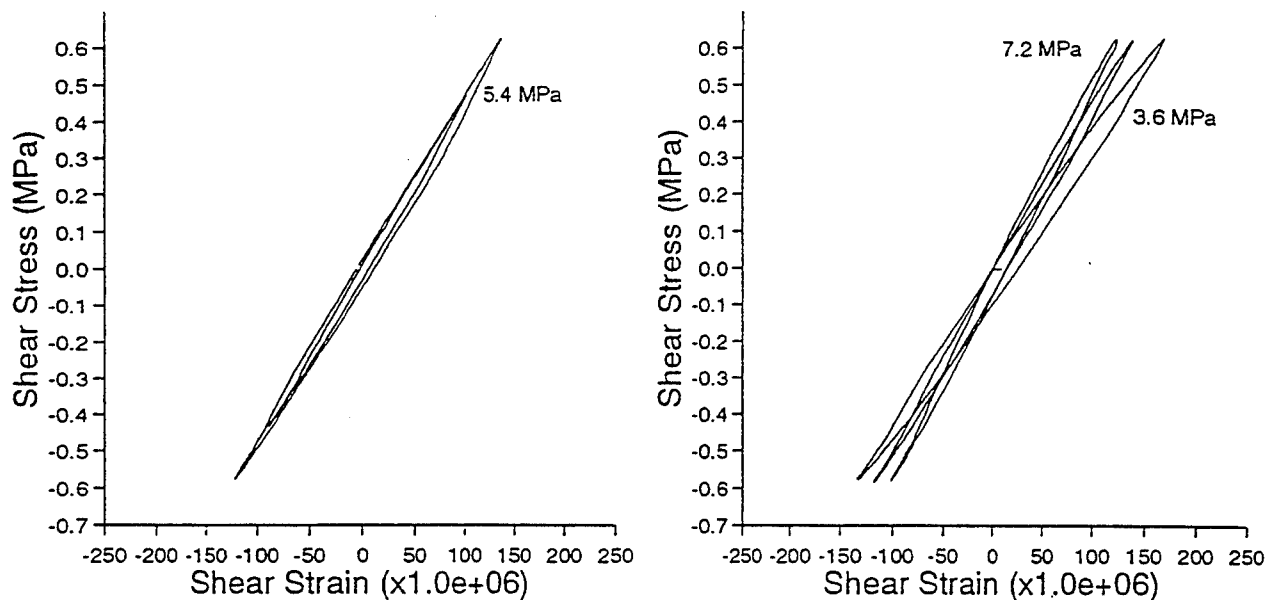
Figure 3: Measured shear stress versus shear strain for Berea sandstone. In the left figure, the effect of shear stress oscillation amplitude is shown at constant axial load (5.4 MPa). Note that the smaller loop is nested within and rotated with respect to the larger loop. In the right figure, the effect of normal load is illustrated, with loops at three different normal loads (3.6, 5.4, and 7.2 MPa). Note that the shear modulus increase and the loop width decreases with increasing normal load.
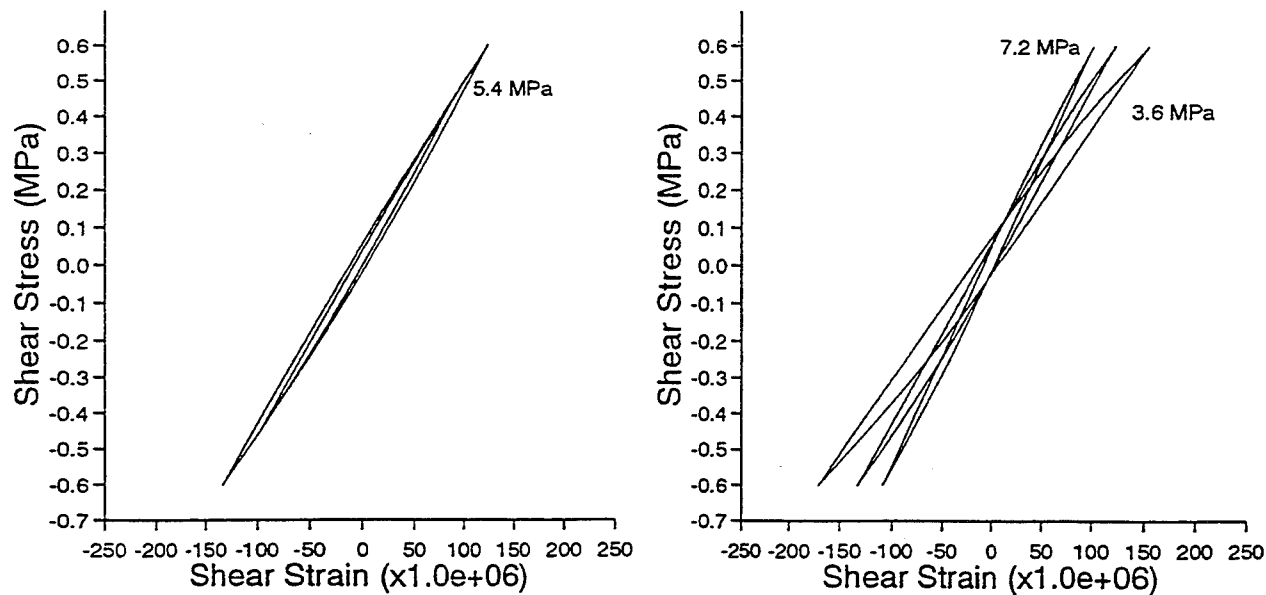
Figure 4: Predicted shear stress versus shear strain for Berea sandstone experiments in Figure 3. A simple "bow-tie" rheology was used to model the data. The model does a good job in producing both the amplitude and axial stress dependence of the deformation.

As we might expect, the hysteresis loops appear to exhibit the same "discrete memory" and "closed-loop" characteristics as noted in studies of hysteresis in Youngs modulus during uniaxial-stress perturbations. Based on this preliminary data, the hysteresis in the shear modulus appears relatively easy to model with only a few parameters. As an example, a simple "bow-tie" model for the shear modulus as a function of shear stress represents the observations fairly well. In the "bow-tie" example, the shear modulus is assumed to follow the form $G = G' - A \cdot |\tau - \tau_r|$, where G' is a function of the axial load (σ_{11}), τ is the shear stress, and τ_r is the shear stress at the last reversal in loading direction. In Figure 4 we plot the predicted stress-strain behavior for the experimental cases shown in Figures 3a and 3b. In Figures 4a and 4b, all the data was modeled using $G' = 2520 + 555\sigma_{11}$ (where G' and σ_{11} are in MPa), and $A = 0.001$ is assumed constant.

Confined Compression and Damage

Preliminary experiments have also been conducted on Barre granite as exploratory experiments for studying the effect of confining pressure on uniaxial stress deformation and for extending the moderate strain regime rheology into the brittle damage regime. Figure 5 illustrates the results of two similar experiments performed at two different confining pressures (0 MPa and 10 MPa respectively).

The experiments shown in Figure 5 consisted of a gradually increasing differential load at fixed confining pressure. During the loading, numerous small perturbations in the load were imposed to measure the unloading stiffness. In these experiments we find that once we enter the damage regime (i.e. differential stress levels above 150 MPa), the stress-strain relationship during cyclic loading exhibits a ratcheting effect, which becomes more pronounced as we approach failure. This ratcheting is thought to reflect time dependent crack growth.

The data is currently being analyzed to help constrain a damage-mechanics based model of rock rheology for the brittle-damage regime (see *Sammis* this issue). In addition the data also provides some preliminary constraint on confining pressure effects in the moderate-strain regime. In Figure 5b, the logarithm of the local Youngs modulus (E) during loading for each experiment is plotted using solid lines and the logarithm of the unloading stiffnesses (E') are plotted using circles. Looking at the data in the moderate-strain regime (differential stresses below 150 MPa), we see that the effect of confining pressure on both E and E' can be modeled with a simple scale factor which is of comparable magnitude for both E and E'. This is consistent with the γ parameter as discussed earlier, although the data indicates that γ is a function of differential stress at low axial loads (a complication ignored in our earlier treatment). Also note that once in the brittle-damage regime, this simple scaling with confining pressure breaks down, as the effect of confining pressure on E develops a more pronounced pressure effect than on E'.
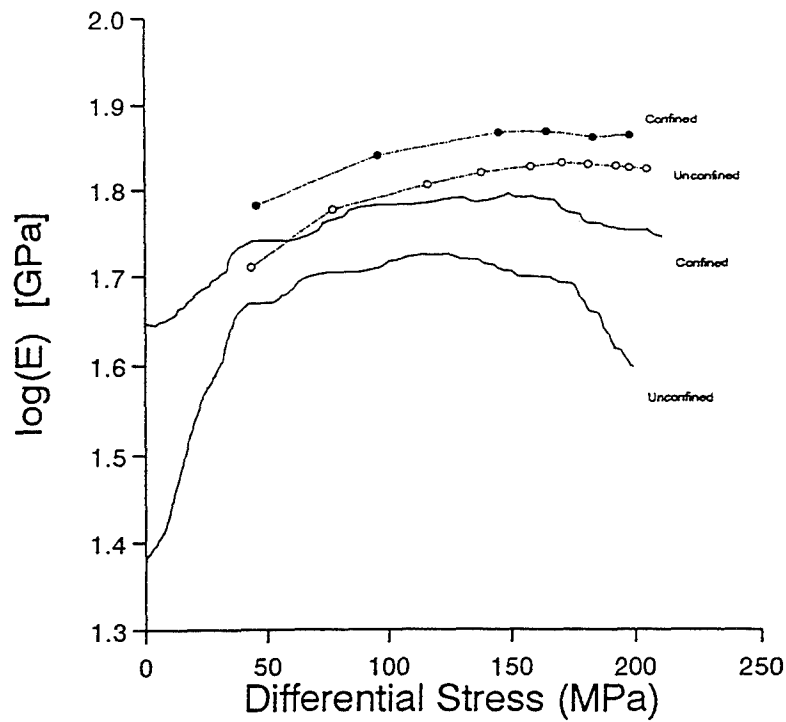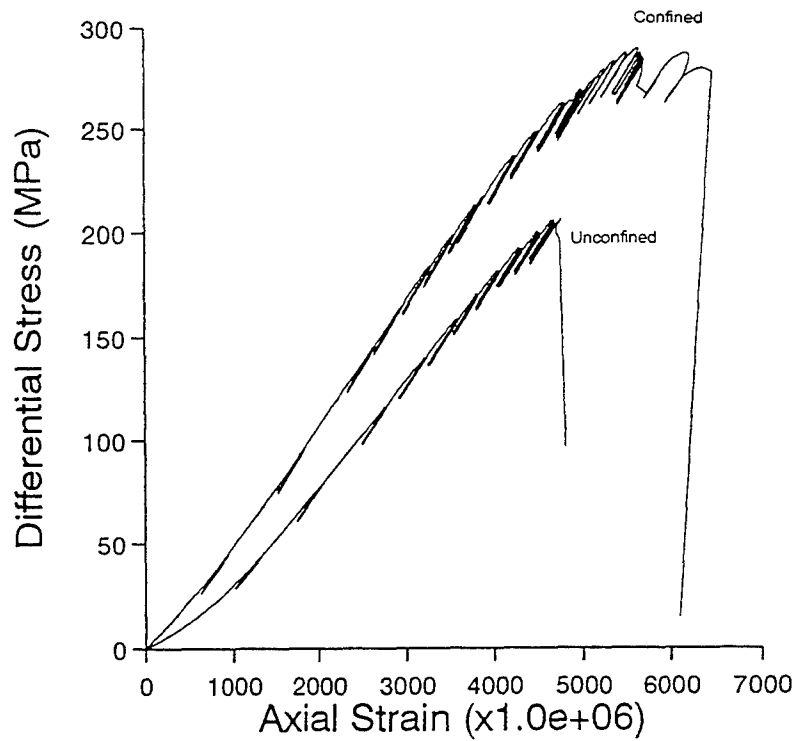
Figure 5: Stress strain data from two uniaxial compression experiments on Barre granite, one unconfined and the other at a fixed confining pressure of 10 MPa. During the loading, perturbations in loading were performed to measure the unloading stiffness. In the lower figure, the logarithm of the Youngs modulus is plotted as a function of differential stress. Solid lines indicating the modulus upon loading and the circles indicate the average modulus during the small cyclic perturbations.

RECOMMENDATIONS AND FUTURE PLANS

The preliminary results shown here are being used to design experiments for constraining rheologies needed to model wave propagation in the moderate-strain and brittle-damage regimes.

Emphasis of future experiments will be placed in a number of important areas. We will improve the quality of torsional data for constraining hysteresis in the shear modulus, so that details of the rheology can be quantified. In addition, based on the preliminary results shown here, we will design and perform experiments to quantify the confining pressure effect on the uniaxial-stress rheology and explicitly test to see if a simple scaling factor (i.e. γ) can be used, along with the uniaxial stress-rheology, to model hysteresis for loading paths transitional between uniaxial-stress and uniaxial strain. The experiments will include testing in the damage regime, and in so doing provide a data set with which to integrate rheologies for the moderate-strain and brittle damage-regimes. We also plan perform additional experiments designed to better quantify the details of the observed cusps in the stress-strain relationship for both shear and uniaxial-stress perturbations. Tests are planned on Berea Sandstone, Sierra White granite, Barre granite, and welded tuff recovered from N-Tunnel at NTS.

REFERENCES

Boitnott, G. N., Fundamental Observations Concerning Hysteresis in the Deformation of Rock with Applications to Nonlinear Attenuation in the Near Source Region, LA-UR-93-3839, 1993

Boitnott, G. N., Experimental Observations of the Rheology of Rock in the Moderate Strain Regime, PL-TR-94-2217, 1994. **ADA284667**

Hilbert, L. B., T. Hwong, N. Cook, K. Kihei, and L. Myer, Effects of Strain Amplitude on the Static and Dynamic Nonlinear Deformation of Berea Sandstone, *in* Rock Mechanics Models and Measurements Challenges from Industry, Proc. 1st N. Amer. Rock Mech. Symp., A.A. Balkema, 1994;

DEVELOPMENT OF A COMPREHENSIVE COVERAGE ASSESSMENT MODEL

Gregory Duckworth
Ted Farrell
Kevin LePage

Bolt Beranek and Newman, Inc.
70 Fawcett St.
Cambridge, Ma 02138

ABSTRACT

BBN has been tasked with developing a comprehensive coverage assessment tool for ocean acoustic monitoring. This tool will facilitate studies into the issues and sensitivities of using acoustic assets in the ocean to support a Comprehensive Test Ban Treaty. These issues include 1) understanding the sensitivity of signal structure to ocean environment variability as manifested through modal coupling, bottom and surface interaction losses and horizontal refraction and diffraction, 2) understanding the sensitivity of signal structure to source characteristics, and 3) designing detection and localization strategies which exploit to the fullest extent our understanding of the source and propagation characteristics.

In the first phase of this effort, the coverage assessment tool, which couples global and basin scale acoustic propagation models together with compatible source functions and an ocean database library, will be developed and benchmarked against available data. Once validated, the tool will be exercised to predict the signal and noise characteristics at existing and notional receiver locations, in order to identify regions where detection will yield particular challenges. Features of this tool will be software modularity and extensibility in order to facilitate the incorporation of new source functions, propagation models, databases and performance assessment modules as they become available.

1. OBJECTIVE

Comprehensive Test Ban Treaty verification requires the ability to monitor (detect, localize, and classify) nuclear testing worldwide. Covert nuclear tests, especially low yield explosions, performed at sea and detonated either in-air or underwater, are difficult to monitor using only land-based seismic sensors since energy from at-sea blasts is poorly coupled to seismic propagation paths. However, such energy often propagates well via waterborne paths, and can be detected at very long ranges using existing underwater surveillance assets such as SOSUS. Thus, a monitoring network comprising both seismic and underwater acoustic receivers can provide an effective and robust monitoring capability. Two key issues for such a system are identification of ocean regions in which propagation conditions prevent existing acoustic sensors from observing covert events, and the design of alternative acoustic sensor systems to provide coverage in such regions.

In August 1995, Bolt Beranek and Newman (BBN) was tasked to begin a twelve month effort to

- develop the initial version of a comprehensive model for evaluation of the ability of underwater sensors to detect and localize the detonation of nuclear devices in or above the ocean;
- validate this initial model by comparing its predictions with measured data; and,
- apply this model to two demonstration problems of operational interest, coverage assessment of selected existing assets, and gap analysis for a selected basin region.

This effort is viewed as the first phase of a multi-year program which will produce a full-capability, validated coverage assessment tool, and will involve more extensive analyses of operational monitoring issues. Deliverables from this initial effort will include both the findings and conclusions of the coverage analyses for the demonstration problems, and the first build of a fully operational and functionally complete software tool for coverage assessment with the following functions and features:

- Estimation of acoustic propagation characteristics (including travel time and attenuation) using state-of-the-art propagation models and high resolution environmental databases.
- Integration of GFI source functions
- Representation of the spatial and signal processing characteristics of acoustic receiver systems.
- Assessment of detection and localization coverage as a function of event yield and altitude/depth based on propagation predictions, receiver characteristics, and ambient noise properties.
- Simulation of received signal time series for examination and assessment of candidate discriminants for waveform-based classification and yield estimation.
- Determination of the confidence bounds for all estimates.

Our technical approach includes exploitation of the state of the art in propagation modeling at both long range (global scale) and medium range (basin scale, with poor coupling to the deep oceans) scenarios, representation of both waterborne propagation and teleseismic energy radiating back into the water column, and bottom and surface boundary interaction effects. We will capitalize on ongoing work in environmental database management software now underway at BBN to provide efficient architectures for incorporating a full spectrum of environmental acoustic databases in the coverage evaluation model, together with powerful visualization and manipulation tools. The model will also incorporate a flexible receiver specification algorithm to allow analyses of different receiver designs under variable noise conditions, and a means to assess the sensitivity of model predictions to environmental variability and model uncertainties.

This investigation will provide a tool for prediction of the signal to noise ratio of a waterborne nuclear event signature observed at the output of an acoustic sensor, and for simulation of the

1020

received waveform itself. This tool will permit assessment of the coverage capability of existing underwater acoustic assets, which can be used both to identify gaps in coverage of particular areas, and to facilitate design of new assets to fill such gaps. This tool also supports operational monitoring, as it will allow the comparison of observed signals with simulated event waveforms (for potential discrimination) and estimation of yield. The user community for this product is expected to include AFPL/Geophysics Directorate, DOE, and AFTAC, as well as researchers at national laboratories and research universities.

2. FUTURE PLANS

Since this contract started in mid-August, the remainder of this paper describes our planned effort.

2.1 Overview of Approach — The development of the computational coverage evaluation tool requires both the resolution of various modeling and technical issues and the implementation of a flexible, extendible, and reusable software system. The approach is summarized below:

- Build a prototype version of the model, taking maximum advantage of existing software modules to achieve an early end-to-end capability. Identify and deal with baseline issues during this initial development process.
- Employ a considered software implementation approach based on a modular architecture and incremental development, test, and integration to ensure a reusable product.
- Validate the initial version by comparing results with measured data. Apply this validated model to two limited-scope test problems of operational interest (coverage assessment of existing assets, and gap analyses of selected basins), iteratively enhance and modify the system.

The result will be a deliverable coverage model, together with the results of the focused coverage evaluation test studies. The details of this approach are described in the following sections.

2.2 Coverage Model Description

The core evaluation metric of the area coverage assessment tool is signal-to-noise ratio (SNR) at the output of a single receiver; this quantity can be represented using the sonar equation for impulsive signals:

$$SNR = ESL - TL - (NL - AG) + PG, \tag{1}$$

where ESL is energy source level, TL is transmission loss (attenuation), NL is noise level, AG is array gain (receiver spatial processing gain), and PG is receiver (temporal) processing gain (all quantities are in dB). SNR is interpreted as the peak value of the receiver output, relative to background, and may be defined for a complete event, or for a single component phase.

A variety of potential metrics might be used to characterize receiver or coverage performance; SNR was selected because it is intuitive, relatively unequivocal, and can be related to a number of other performance metrics, such as detection probability and arrival time accuracy. Calculation of SNR requires computation and combination of the terms on the right-hand side of (1); this process is reflected in the architecture of the computational model, as illustrated in Figure 1. Each of the component blocks of the model is discussed in a subsequent section, as noted in the Figure.

In operation, the area coverage evaluation tool functions as follows. The source function, a "starter field" for linear propagation to long range, defines the ESL over a cylindrical surface in the water column as a function of range, depth, and frequency. This source function is the input to a range dependent propagation model which estimates the complex propagation transfer function, and hence transmission loss (TL) and signal travel time, at multiple frequencies along selected bearings from the event position. The result is the estimated propagation transfer function, for each frequency, to

any selected range and depth along these radials. By interpolating between radials, we can determine received signal level and travel time from any point in the ocean to the receiver location.
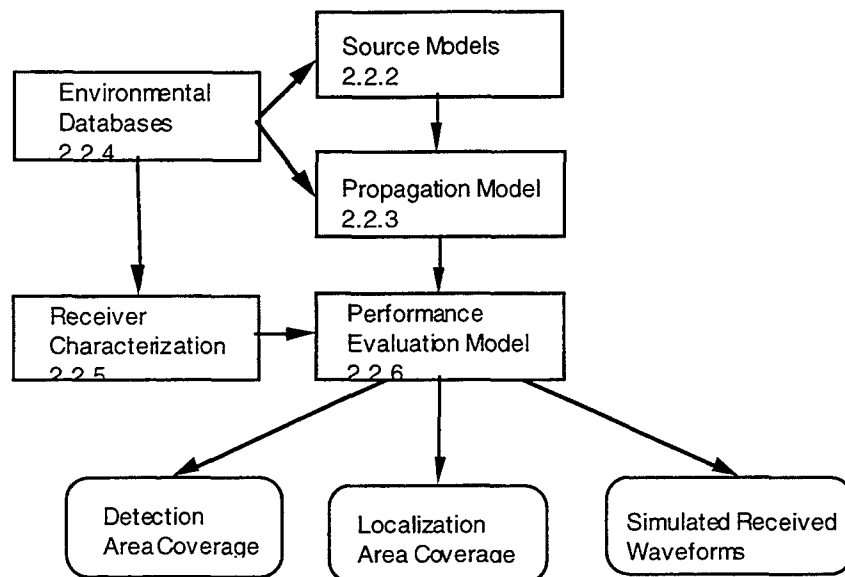
Figure 1. Simplified Block Diagram of Coverage Assessment Model

Receiver spatial and temporal processing characteristics define the array gain, AG, and processing gain, PG. Acoustic receivers typically employ linear arrays of hydrophones and phased-array processing for noise rejection and coarse bearing estimation. These results are combined with the characteristics of the local ambient noise field and the signal to compute SNR using (1). Hence, SNR is specific to both receiver configuration and location for a given event.

Calculation of SNR occurs in the Performance Evaluation module. Single-receiver SNR may be used directly to define detection and localization coverage, converted to another metric, or combined with SNR estimates for other receivers at other locations to compute the performance of an acoustic sensor network. Anticipated data products include geographic contour maps of detection and localization coverage regions, and estimates of the received waveform. Waveform simulation can be very useful for identification of discriminants and model fidelity assessments; the cover of this proposal illustrate the prediction fidelity which can be achieved under some circumstances.

Finally, observe that environmental databases play a central role at all stages of the calculation. Proper use of database information, e.g., selection of the appropriate bathymetry, and a robust interpolation scheme, is a critical development issue.

An advantage of this model implementation is that its modules can be transitioned directly into a nuclear blast detection/evaluation system. For example, given a signal arrival that is both detected and localized, the propagation model can be used to remove the impact of the propagation medium (TL) for each detected arrival, and the resulting ESL estimate can be converted to estimated yield.

2.2.1 Source Models — The principal development effort for the source portion of the model is to couple the GFI source functions to the acoustic propagation medium. The most significant issues are coupling to the bottom, and transmission through the air-sea interface for air blasts. Coupling to ocean bottom seismic waves will be dominated by interactions between the shock and bubble pulse waves and the bottom in the region directly below the detonation. Especially in shallow water, these incident waves will be moderate to strong shock waves. For detonations not too far from acoustically-fast bottom interfaces, up to a third of the radiated sound energy may be coupled into

the bottom and then radiated from it. Those paths which have high group speed due to propagation in the sediment, crustal layers 2 and 3, and the upper mantle result in precursor waves at the receiver. These precursors may provide important classification clues at shorter ranges where they can be detected despite their higher effective attenuation (due to crustal interface roughness and intrinsic attenuation coefficient). They will be particularly important for localization and discrimination at basin scales (ranges < 150 nm).

2.2.2 Propagation Models — Reliable coverage assessment requires an understanding of propagation at both basin and trans-oceanic scales. BBN will employ state of the art acoustic models at these two scales, identify requirements for further model refinement, and explore means of utilizing various ocean environmental databases with these models.

Basin Scale Propagation -- In basin propagation, the signals received from large explosions are typically the sum of seismic phases and dispersive acoustic normal modes. Propagation at low frequencies follows a single horizontal path between the source and receiver. At this scale it will be possible to model the acoustic propagation accurately enough to place precise bounds on the location of the source, and therefore the source strength, using a small number of sensor elements.

Acoustic propagation at basin scales is well understood, and there are a number of models for propagation in range dependent, azimuthally uncoupled environments, an approach termed "N by 2D". Methods for incorporating the elastic sub-bottom are also available for horizontally stratified media and for general range-varying layering under the parabolic approximation. Full three dimensional propagation modeling has recently become computationally feasible, and may be used to model diffraction of sound exiting enclosed basins through narrow outlets. Research issues for the basin scale center on understanding the excitation and subsequent waterborne detection of seismic phases, modeling diffraction of acoustic energy due to highly variable bathymetry, and modeling down slope propagation of acoustic energy out of a shallow region into the basin. In addition, current research addresses integration of database descriptions of the ocean into the various ocean acoustic models, with emphasis on empirical orthogonal functions (EOF) as an efficient basis for representing observed vertical and lateral inhomogeneity in ocean properties.

For predictions at these scales, existing N by 2-D models, such as KRAKEN (a normal mode model) or Finite Element Parabolic Equation (FEPE), and existing seismo-acoustic models, such as OASES, will be used. The importance of deep refracting seismic paths on location and yield estimation will be quantified. The seismo-acoustic models will to investigate the seismic propagation issues, and all propagation models will be used to evaluate horizontal and vertical diffraction effects as mentioned above.

Global Scale Propagation -- At global scales, the geometry of the earth cannot be neglected and the effects of horizontal refraction due to lateral sound speed and bathymetry variations become important. Significant shadow zones can exist between source and receiver, due to the intrusion of continents, islands and shoaling bathymetry into the propagation path. Hence, there will be regions where detonations cannot be observed by specific sensors. Although seismic phases may not be detected at global ranges, horizontal and vertical multi-path may be exploited to help determine the range to the source.

Recent interest in monitoring the temperature of the oceans has required substantial refinement of existing methods of modeling global scale propagation. The assumption that acoustic rays followed great circle paths proved inadequate to describe the signal structure for propagation between sources and receivers half a world apart. Subsequent work has shown that horizontal refraction around continental margins, as well as the non-sphericity of the earth, can account for most discrepancies between the observed signal structure and the previous model predictions. Models employing the parabolic approximation in polar and azimuthal coordinates include the full effects of horizontal

diffraction, provide direct estimates of transmission loss, and hence promise additional insight into the quality of the ray-based horizontal refraction predictions, the present computational standard.

Trans-global acoustic propagation studies will employ state of the art horizontal ray/vertical mode and PE-based acoustic models available from NRL. We will address the sensitivity of travel times, modal content and horizontal multi-path predicted by these models to environmental variability and database interpolation. The adequacy of the adiabatic mode assumption used in ray/mode propagation models will be evaluated given the importance of mode coupling in regions of rapidly varying bathymetry.

The adequacy of a ray model to describe horizontal propagation paths is also a key issue, as is a means of interpreting the absolute shadow zones predicted by ray theory. Also of concern is ray instability, or sensitivity to initial conditions: only if rays are stable can ray models provide good time of flight estimates for hypothetical source locations and available receiver assets. Ray stability will be addressed in concert with the evaluation of database interpolation techniques used to obtain environmental data on the computational grid. Ray sensitivity to interpolation schemes can be as damaging as sensitivity to initial conditions. The tool will enable such sensitivities to be identified by facilitating the comparison between ray and full wave solution techniques.

As with the basin scale problem, the details of the arrival structure at trans-oceanic scales will depend on the modal excitation spectrum of the source function. Basin-scale modeling efforts will aid in identifying the modal mix of the starting field for the trans-global problem. In addition, the local diffraction effects analyzed in the basin scale studies with N by 2-D or 3-D full wave solution techniques will be useful for estimating the global starting field when nuclear devices are detonated in the presence of highly variable bathymetry or in shallow water.

Principal research issues at both scales are summarized in Table 1. For both scales, the sensitivities of the propagation characteristics to the following variables will be addressed as part of the coverage evaluation and model validation efforts:
- Source function and location
- Modal phase velocity structure and variance in the oceans
- Sound speed, bathymetry and bottom properties between the source and receiver
- Bottom, surface, and volume loss mechanisms.

Issue	Basin	Global PE	Global Ray
Transmission loss modeling along horizontal rays			•
Interpretation of absolute shadowing and caustics			•
Adequacy of adiabatic mode assumption for vertical field component		•	•
Sensitivity to database interpolation methods	•	•	•
Travel time and path sensitivity to small perturbations in environmental characteristics			•
Computational efficiency	•	•	•
Seismic phase excitation	•		
Diffraction in variable bathymetry	•	•	•
Down-slope propagation from shallow regions into a basin	•		

Table 1 - Propagation modeling research issues in support of coverage assessment.

2.2.3 Environmental Databases — A critical element for performance prediction is the ability to rapidly visualize, analyze and incorporate large quantities of historical environmental data into numerical propagation, and detection coverage models. BBN has already developed such a database manipulation capability under the ONR Long Term Acoustic Study (LTAS) and ARPA Shallow Water Area Surveillance (SWAS) programs. This geographic information system, called DBTool, comprises a collection of environmental databases, a baseline set of propagation models, and an extensive set of tools for data analysis and visualization. The global databases in DBTool are listed in Table 2; these comprise the baseline for the coverage assessment tool. These databases include information on environmental factors affecting low frequency ambient noise (shipping densities), high frequency ambient noise (wind speed and rainfall), and acoustic propagation (sound speed profiles, bathymetry and sediment characteristics).

Database	Description	Resolution (min)
DBDB-C	Bathymetry	5.0
GDEM	Sound speed profiles	30
LFBL	Low Frequency Bottom Loss	5.0
HWS	Historical Wind Speed	60
HITS	Historical Temporal Shipping	60
ETOPO5	Bathymetry	5.0
NODC	Sound Speed profiles	Variable
GDS	Global Daily Summary (Temp/Precip)	Variable
MGG	Sediment	Variable

Table 2 - DBTool environmental databases to be incorporated in the coverage assessment model

DBTool also provides a means to couple such environmental data directly into various acoustic models using the N by 2D approach for determining geographic coverage, which will be enhanced to support true 3D models for this project. The models currently integrated with the databases include SUNRAY (a BBN-developed range-dependent ray trace model), FEPE, and KRAKEN. Using this system, it is possible to interactively extract, visualize and analyze data for a given region with a graphical user interface. Once the oceanographic data is extracted, N by 2D predictions of the acoustic propagation may be performed by specifying the location of the source and N radials from the source.

2.2.4   Receiver Characterization — This module specifies the acoustic receiver characteristics required for computation of SNR. The baseline receiver model described embodies the essential properties of typical receivers, and may be extended as circumstances indicate. Potential extensions include those required to support fine bearing (arrival azimuth) estimation, or integration windows matched to the anticipated signal envelope (phase structure).

Spatial processing — Typical acoustic receivers employ arrays of hydrophone elements in various configurations, with linear arrays being most common. Such sensors are processed as phased arrays to improve SNR against ambient noise; the spatial processing advantage provided by such a beamformed array is characterized by its array gain, which is the noise level of a beam output relative to an omniphone. Ocean ambient noise over most of the frequency range of concern, 1-200 Hz, is principally due to distant shipping, resulting in a noise field concentrated near the horizontal which varies in both azimuth and frequency. Hence, achievable array gain depends on the spatial distribution of the noise field, the spatial response of the phased array (the beampattern), and the arrival direction of energy from the source (e.g., little spatial gain may be achieved if a dominant noise source lies between the source and the array).

The spatial processing characteristics of the receiver will be specified by the configuration of the array elements (relative position, and absolute location and orientation), and by the processing algorithm used in the beamformer, typically including spatial shading or weighting functions, number of beams formed and pointing directions. These may be summarized by the directional response pattern of the array/beamformer as a function of steering and incident directions, and frequency; this function may be provided or computed from the parameters of the receiver.

Temporal processing — Detection of a nuclear blast event can be characterized as detection of a transient whose bandwidth and duration may be (approximately) known beforehand. A reasonable baseline signal processing chain for such a detection problem is a filter-squarer-integrator: the bandwidth of the filter and the duration of the integrator are matched to expected bandwidth and extent of the transient. Hence, the signal processing portion of the receiver will be characterized by filter bandwidth (plus any frequency shaping, if that is used) and the duration of the integration.

2.2.5 Performance Evaluation Model — The two principal aspects of performance, detection and localization, are addressed in this module.

Detection — Detection performance is characterized by signal-to-noise ratio, SNR, as described in Section 2.2.1. SNR is the (peak) amount of event signal energy captured by the receiving system, relative to the background noise level. Peak signal energy is a function of both the signal properties and receiving system bandwidth and integration time, and also depends on the sensor's spatial response. Background noise level is determined by the spatial distribution of the ambient noise field, the spatial noise response of the receiver, plus the receiver bandwidth and integration time.

Calculation of SNR from (1) is relatively straightforward, but two terms in (1) deserve particular note. The term (NL - AG) represents ambient noise level in a beam, but is calculated by integrating the noise spatial density over the array beampattern. Computation of this value at band center usually suffices; for very broad bands more complex methods must be used. PG represents the gain of the temporal processing receiver, which is typically 10 log (TW), where TW is the time-bandwidth product of the receiver. PG may also include, however, the effects of mismatch to the received signal, e.g., bandwidth mismatch, which will reduce the effective ESL. Depending on the complexity of the received waveforms and the degree of mismatch expected, it may be necessary to determine PG by processing the simulated waveform through the receiver processing chain.

SNR may be transformed into detection probability, but this requires a model for the receiver output statistics. BBN has used a low degree-of-freedom Gaussian (chi-square) distribution to model receiver performance for explosive signals at moderate ranges, but different fluctuation statistics may be encountered at extended ranges. Transformation to probability also requires specification of a detection threshold, which is problematic: transient receiver threshold settings are dominated by false alarm considerations, and are usually determined empirically.

Each individual performance computation yields an SNR value for a fixed receiver configuration and location, and for a fixed event location, yield, and depth/height. Multiple computations provide a set of SNR values which may be presented in various ways. Two data products are envisioned:

- a geographic plot of SNR contours for a specific receiver location/configuration, corresponding to different locations of the event (for evaluation of existing assets); and
- a geographic plot of SNR contours for a specific event location, yield and depth/height for various receiver locations (for evaluation of alternative locations for new sensors).

This methodology may be extended to evaluation of multiple-sensor (field) coverage, by combining the SNR sets computed for different receivers. Potential field performance metrics include: contours of the minimum SNR seen over the field (very conservative); and, for M of N detection criteria, contours of the Mth largest SNR value over the field.

Localization — The most appropriate metric for localization coverage is area of uncertainty (AOU), which summarizes the effect of all the uncertainties in the localization calculation, including model uncertainties, e.g., uncertainties in the assumed propagation speeds. If localization estimates are provided by beam intersection, the AOU is defined by the overlap region of the beams from all arrays which detect the event (have a minimum specified SNR). Alternatively, localization may be based on time difference of arrival of one or more phases at multiple receivers, in which case signal-to-noise ratio, and signal bandwidth/wave shape as well as sensor-event geometries determine AOU. Similarly, range estimates may be obtained from the relative time of arrival of different phases at each array; the AOU is then determined by range intersection uncertainties. BBN has developed AOU computation procedures for similar mixed measurements which occur in multistatic active sonar systems, and will apply these results to the coverage evaluation problem.

2.3 Model Implementation — The model will consists of a shell, written in the C++ object-oriented programming language, and interfaced with existing propagation models written in C or FORTRAN. The shell will employ Matlab for display and analysis of results, and for database interfaces. Careful software design will provide a modular, transportable, flexible architecture which will allow easy inclusion of additional or modified model components or extension to existing models. The bulk of the software development effort will involve the performance modeling shell and integration and enhancement of existing propagation codes; only a modest amount of new code development is anticipated. Development will draw heavily on DBTool, BBN's existing software for management of acoustic performance prediction databases. The target processor for this project will be a dual-processor Sparc-20. If more extensive computational facilities are required, we intend to utilize an existing distributed network of Sun workstations during off-peak hours.

2.4 Coverage Investigations — Two investigations of coverage performance will be performed. These investigations will serve as a testbed for exercise and development of models and analysis capabilities while addressing, on an example basis, problems of practical interest. Incremental enhancements will be made to the model as indicated by the results of these studies.

- Coverage analysis of selected existing assets - For a selected set of existing acoustic surveillance assets (e.g., SOSUS arrays), evaluate detection and localization coverage which is attainable in selected ocean areas. This study employ reciprocity, in which the source event is placed at the sensor location and vice-versa, to achieve a computational efficiency.

- Gap analysis for selected basins - Identify candidate receiver locations and characteristics for the detection of events of specified yield and height/depth in selected basin areas.

These investigations will include the evaluation of confidence or error bounds on predicted performance, and on the intermediate predictions of transmission loss, arrival time, and waveform shape. Although acoustic detection performance in the ocean exhibits statistical fluctuations of practical concern, the effects of database inaccuracies and model imperfections may dominate predictions of performance. BBN will address this issue in two ways. First, performance prediction runs will be made multiple times with perturbed database values to establish an ensemble of "reasonable" predicted values. The objective here is to model the error due to uncertainties in the databases. Second, we will compare predicted values with actual observation of explosive event waveforms, amplitudes, and travel times; this will validate the models by identifying large errors, and establish empirical variability. Presumably, empirical variability will be larger than that due to perturbations, and the residual will comprise the sum of statistical variability and model inaccuracies.

Hydro-Acoustic Monitoring for Nuclear Explosions

Gregory J. Orris and B. Edward McDonald
Naval Research Laboratory
Washington, DC   20375-5200

August 3, 1995

Abstract

Part of the program being designed to monitor the world for violations of the Comprehensive Test Ban Treaty (CTBT) includes the use of a global network of hydrophones. This network would be primarily used to monitor for ocean born nuclear explosions, but could also be used as a secondary tool to monitor for continental violations. One of the requirements to reliably detect and locate treaty violations, as well as determine network performance, will be the capability to model acoustic propagation accurately over distances in excess of 10000 kilometers. The principle of reciprocity and global-scale acoustic propagation models are used to investigate the performance characteristics of proposed hydro-acoustic networks. We describe the models used and demonstrate their use on selected sites.
PACS number: 43.30.Bp, 43.30.Cq

Stability of the P to S energy ratio in the diffusive regime

George C. Papanicolaou*   Leonid V. Ryzhik
Joseph B. Keller
Department of Mathematics, Stanford University
Stanford CA 94305
Internet: papanico@math.stanford.edu, ryzhik@math.stanford.edu, keller@math.stanford.edu

In the presence of inhomogeneities the propagation of elastic wave energy can be modeled by radiative transport equations. This is a good approximation when (i) typical wavelengths are short compared to the overall propagation distance, (ii) correlation lengths are comparable to wavelengths so that the inhomogeneities have appreciable effect and (iii) the fluctuations are weak. The relevant transport equations are derived in [1] starting from the elastic wave equations in an unbounded medium.

There is one consequence of the transport equations that may be important in understanding from first principles the stability of the P/Lg ratio that has proven so useful in yield estimation [2]. This is the fact that over distances (and times) that are long compared to the transport mean free path (transport mean free time), which is the diffusive regime, the P to S energy conversion by the random inhomogeneities equilibrates in a universal way, **independent of the details of the scattering**. There is an equipartition of energy [1] that leads to the relation

$$E_P(t,\mathbf{x}) = \frac{v_S^3}{2v_P^3} E_S(t,\mathbf{x}). \tag{1}$$

Here E_P and E_S are the P and S spatial energy densities, and v_P and v_S are the P and S wave speeds, respectively. For typical values of the P and S speeds this relation becomes $E_S \sim 10E_P$, which is in general agreement with observations.

The above equipartition law was derived when P to S mode conversion is generated by volume scattering. To get the correct equipartition law when Lg waves are present we have to model correctly the elastic wave scattering process in the crustal region and get the relevant radiative transport equations. That is, we must account correctly for the free surface and for the crustal waveguide in the radiative transport approximation. We are studying this problem at present.

References

[1] L. V. Ryzhik, G. C. Papanicolaou and J. B. Keller, Transport Equations for Elastic and Other Waves in Random Media, submitted to the SIAM Journal on Applied Mathematics, September 1995. This paper is available from: http://www-sccm.stanford.edu.

[2] R.A.Hansen, F.Ringdal and P.Richards, The stability of RMS Lg measurements and their potential for accurate estimation of the yields of Soviet underground nuclear explosions, Bull. Seism. Soc. Am., vol 80, 6 pp. 2106-2126, 1990.

STABILITY OF THE P TO S ENERGY RATIO IN THE DIFFUSIVE REGIME

GEORGE C. PAPANICOLAOU, LEONID V. RYZHIK AND JOSEPH B. KELLER

INTRODUCTION

In the presence of inhomogeneities the propagation of elastic wave energy can be modeled by radiative transport equations. This is a good approximation when (i) typical wavelengths are short compared to the overall propagation distance, (ii) correlation lengths are comparable to wavelengths so that the inhomogeneities have appreciable effect and (iii) the fluctuations are weak. The relevant transport equations are derived in [1] starting from the elastic wave equations in an unbounded medium.

There is one consequence of the transport equations that may be important in understanding from first principles the stability of the P/Lg ratio that has proven so useful in yield estimation [2]. This is the fact that over distances (and times) that are long compared to the transport mean free path (transport mean free time), which is the diffusive regime, the P to S energy conversion by the random inhomogeneities equilibrates in a universal way, **independent of the details of the scattering**. There is an equipartition of energy [1] that leads to the relation

$$\mathcal{E}_P(t,\mathbf{x}) = \frac{v_S^3}{2v_P^3}\mathcal{E}_S(t,\mathbf{x}). \tag{1}$$

Here $\mathcal{E}_P$ and $\mathcal{E}_S$ are the P and S spatial energy densities, and v_P and v_S are the P and S wave speeds, respectively. For typical values of the P and S speeds this relation becomes $\mathcal{E}_S \sim 10\mathcal{E}_P$, which is in general agreement with observations.

The above equipartition law was derived when P to S mode conversion is generated by volume scattering. To get the correct equipartition law when Lg waves are present we have to model correctly the elastic wave scattering process in the crustal region and get the relevant radiative transport equations. That is, we must account correctly for the free surface and for the crustal waveguide in the radiative transport approximation. We are studying this problem at present.

OBJECTIVE: RADIATIVE TRANSPORT FOR ELASTIC WAVES

Radiative Transport Equations.

The theory of radiative transport was originally developed to describe how light energy propagates through a turbulent atmosphere. It is based upon a linear transport equation for the angularly resolved energy density and was first derived phenomenologically at the beginning of this century [3,4]. We show in [1] how this theory can be derived from the governing equations for light and for other waves of any type, in a randomly inhomogeneous medium. Our results take into account nonuniformity of the background medium, scattering by random inhomogeneities, the effect of polarization, the coupling of different types of waves, etc. The main new application is to elastic waves, in which shear waves exhibit polarization effects while the compressional waves do not, and the two types of waves are coupled. We also analyze solutions of the transport equations at long times and long distances and show that they have diffusive behavior.

Transport equations arise because a wave with wave vector $\mathbf{k}'$ at a point $\mathbf{x}$ in a randomly inhomogeneous medium may be scattered into any direction $\hat{\mathbf{k}}$ with wave vector $\mathbf{k}$. Therefore one must consider the angularly resolved, wave vector dependent, scalar energy density $a(t, \mathbf{x}, \mathbf{k})$ defined for all $\mathbf{k}$ at each point $\mathbf{x}$ and time t. Energy conservation is expressed by the transport equation

$$\frac{\partial a(t, \mathbf{x}, \mathbf{k})}{\partial t} + \nabla_{\mathbf{k}} \omega(\mathbf{x}, \mathbf{k}) \cdot \nabla_{\mathbf{x}} a(t, \mathbf{x}, \mathbf{k}) - \nabla_{\mathbf{x}} \omega(\mathbf{x}, \mathbf{k}) \cdot \nabla_{\mathbf{k}} a(t, \mathbf{x}, \mathbf{k})$$
$$= \int_{\mathbb{R}^3} \sigma(\mathbf{x}, \mathbf{k}, \mathbf{k}') a(t, \mathbf{x}, \mathbf{k}') d\mathbf{k}' - \Sigma(\mathbf{x}, \mathbf{k}) a(t, \mathbf{x}, \mathbf{k}). \tag{2}$$

Here $\omega(\mathbf{x}, \mathbf{k})$ is the frequency at $\mathbf{x}$ of the wave with wave vector $\mathbf{k}$, $\sigma(\mathbf{x}, \mathbf{k}, \mathbf{k}')$ is the differential scattering cross-section, the rate at which energy with wave vector $\mathbf{k}'$ is converted to wave energy with wave vector $\mathbf{k}$ at position $\mathbf{x}$, and

$$\int \sigma(\mathbf{x}, \mathbf{k}', \mathbf{k}) d\mathbf{k}' = \Sigma(\mathbf{x}, \mathbf{k}) \tag{3}$$

is the total scattering cross-section. Both σ and Σ are nonnegative and σ is usually symmetric in $\mathbf{k}$ and $\mathbf{k}'$. For an acoustic wave the differential scattering cross-section is given by

$$\sigma(\mathbf{x}, \mathbf{k}, \mathbf{k}') = \left((\hat{\mathbf{k}} \cdot \hat{\mathbf{k}}')^2 \hat{R}_{\rho\rho}(\mathbf{k} - \mathbf{k}') + 2(\hat{\mathbf{k}} \cdot \hat{\mathbf{k}}') \hat{R}_{\rho\kappa}(\mathbf{k} - \mathbf{k}') + \hat{R}_{\kappa\kappa}(\mathbf{k} - \mathbf{k}') \right)$$
$$\cdot \frac{\pi v^2(\mathbf{x}) |\mathbf{k}|^2}{2} \delta(v(\mathbf{x})|\mathbf{k}| - v(\mathbf{x})|\mathbf{k}'|), \tag{4}$$

where $\hat{R}_{\rho\rho}$, $\hat{R}_{\rho\kappa}$ and $\hat{R}_{\kappa\kappa}$ are the power spectra of the fluctuations of the density ρ and compressibilty κ defined in [1]. The left side of (2) is the total time derivative of $a(t, \mathbf{x}, \mathbf{k})$ at a point moving along a ray in phase space $(\mathbf{x}, \mathbf{k})$, which means that the frequency of the ray is adjusting to the appropriate local value. The right side of (2) represents the effects of scattering.

The transport equation (2) is conservative because

$$\iint a(t, \mathbf{x}, \mathbf{k}) d\mathbf{x} d\mathbf{k} = \text{const}$$

1031

when the total scattering cross-section is given by (3). For simplicity we will assume that we do not have intrinsic attenuation. However, attenuation is easily accounted for by letting the total scattering cross-section be the sum of two terms

$$\Sigma(\mathbf{x}, \mathbf{k}) = \Sigma_{sc}(\mathbf{x}, \mathbf{k}) + \Sigma_{ab}(\mathbf{x}, \mathbf{k})$$

where $\Sigma_{sc}(\mathbf{x}, \mathbf{k})$ is the total cross-section due to scattering and is given by (3) and $\Sigma_{ab}(\mathbf{x}, \mathbf{k})$ is the attenuation rate.

The reason that power spectral densities of the inhomogeneities determine the scattering cross-section (4) is seen most easily from a Born expansion of the wave equations when the inhomogeneities are weak. This is because the single scattering approximation of (2) and the second moments of the single scattering approximation for the underlying wave equations (the Born expansion) must be the same. The latter are determined by the power spectra of the inhomogeneities. In the same manner we can explain the appearance of the delta function in the cross-section (4) when the random inhomogeneities do not depend on time and therefore the frequencies are unchanged by the scattering. The transport equation (2) arises also when the waves are scattered by discrete scatterers that are randomly distributed in the medium. In this case the scattering cross-section (4) is the same as the cross-section of a single scatterer times the density of scatterers. We will deal only with continuous random media in [1].

Equation (2) has been derived from equations governing the particular wave motion under consideration by various authors such as Stott [5], Watson [6,7,8,9], Barabanenkov et.al. [10], Besieris and Tappert [11], Howe [12], Ishimaru [13] and Kohler et. al. [14] with a recent survey presented in [15]. These derivations also determine the functions $\omega(\mathbf{x}, \mathbf{k})$ and $\sigma(\mathbf{x}, \mathbf{k}, \mathbf{k})$ and show how a is related to the wave field. In [1] we derive (2) and these functions as a special case of a more general theory. We expect that radiative transport equations will provide a good description of wave energy transport when, as mentioned in the Introduction, (i) typical wavelengths are short compared to macroscopic features of the medium (high frequency approximation), (ii) correlation lengths of the inhomogeneities are comparable to wavelengths and (iii) the fluctuations of the inhomogeneities are weak. It is difficult to compare wavelengths with correlation lengths in general because both can vary over very broad and overlapping ranges. Condition (ii) is important because it allows overlapping and therefore strong interaction between the waves and the inhomogeneities, which is the most interesting and difficult case to analyze. In addition to these three conditions, the inhomogeneities must not be too anisotropic because it is well known that in layered random media, for example, we have wave localization even with weak fluctuations, which is quite differnt from wave transport phenomena [16]. When the fluctuations are strong we can have wave localization even when the inhomogeneities are isotropic [17,18].

We also analyze the diffusive behavior of solutions of (2) which emerges at times and distances that are long compared to a typical transport mean free time $1/\Sigma$ and a typical transport mean free path $|\nabla_{\mathbf{k}}\omega|/\Sigma$, respectively. In this regime the phase space energy density $a(t, \mathbf{x}, \mathbf{k})$ is approximately independent of the direction of the wave vector $\mathbf{k}$, $a(t, \mathbf{x}, \mathbf{k}) \sim \bar{a}(t, \mathbf{x}, |\mathbf{k}|)$ and in the simplest, spatially homogeneous case $\bar{a}$ satisfies the diffusion equation

$$\frac{\partial \bar{a}}{\partial t} = \nabla_{\mathbf{x}} \cdot (D \nabla_{\mathbf{x}} \bar{a}) \tag{5}$$

1032

with a constant diffusion coefficient $D = D(|\mathbf{k}|)$ that is determined by the differential scattering cross-section σ and is given in [1]. Diffusion approximatons for scalar transport equations are well known [19], including their behavior near boundaries [20,21]. We show that diffusion approximations are also valid for the more general transport equations that arise for electromagnetic and elastic waves.

Transport Theory for Elastic Waves.

Radiative transport theory was first used in seismology by R.S. Wu [22]. The stationary, scalar transport equation was used to successfully assess scattering and intrinsic attenuation (the albedo) in several papers [23-28] and the time depandent scalar transport equation was used by Zeng, Su and Aki [29], Zeng [30] and Hoshiba [31]. In all these papers the vector nature of the underlying elastic wave motion was not taken into consideration. Mode conversion for surface waves was considered in a phenomenological way by Chen and Aki in [32] and general mode conversion between longitudinal compressional or P waves and transverse shear or S waves was considered by Sato in [33] and by Zeng in [34]. However, the transport equations proposed phenomenologically in [33,34] do not account for polarization of the shear waves. Starting from the elastic wave equations in a random medium we derive in [1] a system of transport equations that accounts correctly for P to S mode conversion and for polarization effects.

Longitudinal P waves propagate with local speed $v_P(\mathbf{x}) = \sqrt{(2\mu(\mathbf{x}) + \lambda(\mathbf{x}))/\rho(\mathbf{x})}$ and transverse shear or S waves that can be polarized propagate with local speed $v_S(\mathbf{x}) = \sqrt{\mu(\mathbf{x})/\rho(\mathbf{x})}$. The corresponding dispersion relations are $\omega_P = v_P|\mathbf{k}|$ and $\omega_S = v_S|\mathbf{k}|$, respectively. The P and S wave modes interact in an inhomogeneous medium because a P wave with a wavenumber $|\mathbf{k}|$ when scattered can generate an S wave with wavenumber $|\mathbf{p}|$ with the same frequency that is, $v_P(\mathbf{x})|\mathbf{k}| = v_S(\mathbf{x})|\mathbf{p}|$, and vice versa. These scattering processes conserve energy and the transport equations for P and S waves energy densities must therefore be coupled. The transport equation for the P wave energy density should be a scalar equation similar to (2) with an additional term that accounts for S to P energy conversion. Similarly, the transport equation for the S wave coherence matrix should be like Chandrasekhar's equation [3] with an additional term that accounts for P to S energy conversion. We show in [1] that this is indeed the case and we determine explicitly the form of the scattering cross-sections in terms of the power spectral densities of the material inhomogeneities.

The coupled transport equations for the P wave energy density $a^P(t, \mathbf{x}, \mathbf{k})$ and the 2×2 coherence matrix $W^S(t, \mathbf{x}, \mathbf{k})$ for the S waves have the form

$$\frac{\partial a^P}{\partial t} + \nabla_{\mathbf{k}}\omega^P \cdot \nabla_{\mathbf{x}}a^P - \nabla_{\mathbf{x}}\omega^P \cdot \nabla_{\mathbf{k}}a^P$$

$$= \int \sigma^{PP}(\mathbf{k}, \mathbf{k}')a^P(\mathbf{k}')d\mathbf{k}' - \Sigma^{PP}(\mathbf{k})a^P(\mathbf{k}) \qquad (6a)$$

$$+ \int \sigma^{PS}(\mathbf{k}, \mathbf{k}')[W^S(\mathbf{k}')]d\mathbf{k}' - \Sigma^{PS}(\mathbf{k})a^P(\mathbf{k})$$

1033

and

$$\frac{\partial W^S}{\partial t} + \nabla_{\mathbf{k}}\omega^S \cdot \nabla_{\mathbf{x}}W^S - \nabla_{\mathbf{x}}\omega^S \cdot \nabla_{\mathbf{k}}W^S + WN - NW$$

$$= \int \sigma^{SS}(\mathbf{k},\mathbf{k}')[W^S(\mathbf{k}')]d\mathbf{k}' - \Sigma^{SS}(\mathbf{k})W^S(\mathbf{k}) \tag{6b}$$

$$+ \int \sigma^{SP}(\mathbf{k},\mathbf{k}')[a^P(\mathbf{k}')]d\mathbf{k}' - \Sigma^{SP}(\mathbf{k})W^S(\mathbf{k}).$$

The differential scattering cross-section $\sigma^{PP}(\mathbf{k},\mathbf{k}')$ for P to P scattering is similar to (4) for scattering of scalar waves and the differential scattering tensor $\sigma^{SS}(\mathbf{k},\mathbf{k}')$ is similar to Chandrasekhar's tensor [3]. They have the form

$$\sigma^{PP}(\mathbf{k},\mathbf{k}') = \sigma_{pp}(\mathbf{k},\mathbf{k}')\delta(v_P|\mathbf{k}| - v_P|\mathbf{k}'|) \tag{7}$$

and

$$\sigma^{SS}(\mathbf{k},\mathbf{k}')[W(\mathbf{k}')] = \{\sigma_{ss}^{TT}T(\mathbf{k},\mathbf{k}')W(\mathbf{k}')T(\mathbf{k}',\mathbf{k}) + \sigma_{ss}^{\Gamma\Gamma}\Gamma(\mathbf{k},\mathbf{k}')W(\mathbf{k}')\Gamma(\mathbf{k}',\mathbf{k})$$

$$+\sigma_{ss}^{\Gamma T}(T(\mathbf{k},\mathbf{k}')W(\mathbf{k}')\Gamma(\mathbf{k}',\mathbf{k}) + \Gamma(\mathbf{k},\mathbf{k}')W(\mathbf{k}')T(\mathbf{k}',\mathbf{k})\}$$

$$\cdot \delta(v_S|\mathbf{k}| - v_S|\mathbf{k}'|), \tag{8}$$

where the 2×2 matrices $T(\mathbf{k},\mathbf{k}')$ and $\Gamma(\mathbf{k},\mathbf{k}')$ are defined by

$$T_{ij}(\mathbf{k},\mathbf{k}') = \mathbf{z}^{(i)}(\mathbf{k}) \cdot \mathbf{z}^{(j)}(\mathbf{k}') \tag{9}$$

and

$$\Gamma_{ij}(\mathbf{k},\mathbf{k}') = (\hat{\mathbf{k}} \cdot \hat{\mathbf{k}}')(\mathbf{z}^{(i)}(\mathbf{k}) \cdot \mathbf{z}^{(j)}(\mathbf{k}')) + (\hat{\mathbf{k}} \cdot \mathbf{z}^{(j)}(\mathbf{k}'))(\hat{\mathbf{k}}' \cdot \mathbf{z}^{(i)}(\mathbf{k})) \tag{10}$$

with $(\hat{\mathbf{k}}, \mathbf{z}^{(1)}(\mathbf{k}), \mathbf{z}^{(2)}(\mathbf{k}))$ the orthonormal propagation triple consisting of the direction of propagation $\hat{\mathbf{k}}$ and two transverse unit vectors $\mathbf{z}^{(1)}(\mathbf{k}), \mathbf{z}^{(2)}(\mathbf{k})$, which in polar coordinates are

$$\hat{\mathbf{k}} = \begin{pmatrix} \sin\theta\cos\phi \\ \sin\theta\sin\phi \\ \cos\theta \end{pmatrix}, \ \mathbf{z}^{(1)}(\mathbf{k}) = \begin{pmatrix} \cos\theta\cos\phi \\ \cos\theta\sin\phi \\ -\sin\theta \end{pmatrix}, \ \mathbf{z}^{(2)}(\mathbf{k}) = \begin{pmatrix} -\sin\phi \\ \cos\phi \\ 0 \end{pmatrix}. \tag{11}$$

The scalar functions σ_{pp} and σ_{ss} are given in terms of power spectral densities of the inhomogeneities in [1] The total scattering cross-sections Σ^{PP} and Σ^{SS} are the integrals of the corresponding differential scattering cross-sections, as in (3), since we assume that there is no intrinsic dissipation.

The coupling matrix N is given by

$$N(\mathbf{x},\mathbf{k}) = \sum_{i=1}^{3} \frac{\partial v(\mathbf{x})}{\partial x^i}|\mathbf{k}|\mathbf{z}^{(1)}(\mathbf{k}) \cdot \frac{\partial \mathbf{z}^{(2)}(\mathbf{k})}{\partial k_i} \begin{pmatrix} 0 & 1 \\ -1 & 0 \end{pmatrix}. \tag{12}$$

The scattering cross-sections for the S to P and P to S coupling terms, σ^{PS} and σ^{SP}, respectively, have the form

$$\sigma^{PS}(\mathbf{k},\mathbf{k}')[W^S(\mathbf{k}')] = \text{Tr}(\sigma_{ps}(\mathbf{k},\mathbf{k}')\mathcal{G}(\mathbf{k},\mathbf{k}')[W^S(\mathbf{k}')])\delta(v_P|\mathbf{k}| - v_S|\mathbf{k}'|) \tag{13}$$

$$\sigma^{SP}(\mathbf{k},\mathbf{k}')[a^P(\mathbf{k}')] = \sigma_{ps}(\mathbf{k},\mathbf{k}')\mathcal{G}(\mathbf{k}',\mathbf{k})[a^P(\mathbf{k}')I]\delta(v_S|\mathbf{k}| - v_P|\mathbf{k}'|)$$

where the tensor $\mathcal{G}(\mathbf{k},\mathbf{k}')$ acts on 2×2 matrices

$$\mathcal{G}(\mathbf{k},\mathbf{k}')[X] = \frac{1}{2}(G(\mathbf{k},\mathbf{k}')X + XG(\mathbf{k},\mathbf{k}')) \tag{14}$$

with the 2×2 matrix G given by

$$G_{ij}(\mathbf{k},\mathbf{k}') = (\hat{\mathbf{k}} \cdot \mathbf{z}^{(i)}(\mathbf{k}'))(\hat{\mathbf{k}} \cdot \mathbf{z}^{(j)}(\mathbf{k}')). \tag{15}$$

The scalar function σ_{ps} is given explictly in terms of power spectral densities of the inhomogeneities in [1].

The geometrical meaning of the 2×2 matrices T, Γ and G that appear in the differential scattering cross-sections (8) and (13) is similar to the one for T that appears in Chandrasekhar's equations [3]. They arise from a single scattering event of P and S waves with wave vector $\mathbf{k}'$ that scatter to P and S waves with wave vector $\mathbf{k}$ and from the fact that the transport equations deal with quadratic field quanitties.

As for the scalar transport equation (3) and Chandrasekhar's equations [3], the elastic transport equations (6) simplify considerably in the regime where the diffusion approximation is valid that is, when the transport mean free path is small compared to the propagation distance. In this regime the P wave energy density $a^P(t,\mathbf{x},\mathbf{k})$ and the S wave coherence matrix $W^S(t,\mathbf{x},\mathbf{k})$ are independent of the direction of the wave vector $\mathbf{k}$, W^S is proportinal to the identity matrix

$$a^P(t,\mathbf{x},\mathbf{k}) \sim \phi(t,\mathbf{x},|\mathbf{k}|), \quad W^S(t,\mathbf{x},\mathbf{k}) \sim w(t,\mathbf{x},|\mathbf{k}|)I \tag{16}$$

and in addition we have the relation

$$\phi(t,\mathbf{x},|\mathbf{k}|) = w(t,\mathbf{x},\frac{v_P|\mathbf{k}|}{v_S}). \tag{17}$$

with ϕ satisfying the diffusion equation (5). The diffusion coefficient $D(|\mathbf{k}|)$ is given explicitly in [1].

The integrated over $\mathbf{k}$ form of the relation (17) is

$$\mathcal{E}_P(t,\mathbf{x}) = \frac{v_S^3}{2v_P^3}\mathcal{E}_S(t,\mathbf{x}) \tag{18}$$

where $\mathcal{E}_P$ and $\mathcal{E}_S$ are the P and S wave spatial energy densities that are related to a^P and W^S by

$$\mathcal{E}_P(t,\mathbf{x}) = \int a^P(t,\mathbf{x},\mathbf{k})d\mathbf{k}$$

and

$$\mathcal{E}_S(t, \mathbf{x}) = \int \mathrm{Tr} W^S(t, \mathbf{x}, \mathbf{k}) d\mathbf{k},$$

respectively. From the point of view of seismological applications of transport theory, relation (18) is important because it predicts universal behavior of the P to S wave energy ratio, in the diffusive regime. When we use the typical S to P wave speed ratio of 1 to 1.7, relation (18) predicts $\mathcal{E}_S/\mathcal{E}_P \sim 10$. This is in general agreement with seismological data and it would be interesting to identify cases where $\mathcal{E}_S/\mathcal{E}_P$ stabilizes. This stabilization, which is derived here from first principles, is reminiscent of the important empirical observation of Hansen, Ringdal and Richards [2] regarding the stabilization of the Lg wave energy.

Research Accomplished: Transport in Unbounded Media, Equipartition

The main accomplishments of the research reported in [1] and summarized here are (i) the derivation from first principles of the correct radiative transport equations for elastic wave motion in unbounded media (2) the demonstration that polarization of shear waves is important and must be taken into consideration and (iii) the demonstration that in the diffusive regime there is a universal P to S wave energy stabilization. This energy equipartition phenomenon, although inuitively clear was not known before and the precise form (1) that it takes is not easy to guess. It is perhaps the simplest instance of many different energy equipartition laws that are valid in other complex situations, such as the ones encountered in crustal wave propagation, that have not been discovered yet.

Relevance: P to S Conversion Stabilization

The relevance to yield estimation is immediate because, as noted in [2] and elsewhere since that paper appeared, P to Lg energy stabilization is the basis for a very successful yield estimation method. We have shown P to S energy stabilization so far, but we believe that the mechanism that controls it, equilibration of multiple scattering effects, is the same for P to Lg stabilization although the precise energy relation analogous to (1) is not known and is likely to be more complicated. The authors of [2] understood qualitatively the role of multiple scattering in the stabilization of P to Lg energy but did not note its universality and independence from the detailed mechanism of the scattering.

Conclusions and Recommendations

The use of transport theory in seismology is a promising research frontier and some very basic issues in yield estimation and other applications have their roots in it and will benefit enormously from a deeper understanding of its implications. An important next step for us is the explicit treatment of P to Lg energy stabilization by modeling the crustal structure in a suitable way and by deriving the transport equations for wave propagation it. Our goal is to get the form of relations like (1) that are valid in this context for the various elastic wave modes.

Acknowledgement

REFERENCES

1. L. V. Ryzhik, G. C. Papanicolaou and J. B. Keller, *Transport Equations for Elastic and Other Waves in Random Media submitted to the SIAM Journal on Applied Mathematics, September 1995. This paper is available from: http://www-sccm.stanford.edu.*.

2. R.A.Hansen, F.Ringdal and P.Richards, *The stability of RMS Lg measurements and their potential for accurate estimation of the yields of Soviet underground nuclear explosions*, Bull. Seism. Soc. Am. **80** no. 6 (1990), 2106-2126.

3. S.Chandrasekhar, *Radiative transfer*, Dover, New York, 1960.

4. H. van der Hulst, *Multiple light scattering vol. I and II*, Academic Press, New York, 1980.

5. P.Stott, *A transport equation for the multiple scattering of electromagnetic waves by a turbulent plasma*, Jour. Phys. A **1** (1968), 675-689.

6. K.Watson and J.L.Peacher, *Doppler shift in frequency in the transport of electromagnetic waves in an underdense plasma*, Jour. Math. Phys **11** (1970), 1496-1504.

7. K.Watson, *Multiple scattering of electromagnetic waves in an underdense plasma*, Jour. Math.Phys. **10** no. 10 (1969), 688-702.

8. C.W.Law and K.Watson, *Radiation transport along curved ray paths*, Jour. Math. Phys. **11** no. 11 (1970), 3125-3137.

9. K.Watson, *Electromagnetic wave scattering within a plasma in the transport approximation*, Physics of Fluids **13** no. 10 (1970), 2514-2523.

10. Yu.Barabanenkov, A.Vinogradov, Yu.Kravtsov and V.Tatarskii, *Applicattion of the theory of multiple scattering of waves to the derivation of the radiative transfer equation for a statistically inhomogeneous medium*, Radiofizika **15** no. 12, 1852-1860. (Russian)

11. I.M.Besieris and F.D.Tappert, *Propagation of frequency modulated pulses in a randomly stratified plasma*, Jour. Math. Phys. **14** (1973), 704-707.

12. M.S.Howe, *On the kinetic theory of wave propagation in random media*, Phil. Trans. Roy. Soc. Lond. **274** (1973), 523-549.

13. A.Ishimaru, *Wave propagation and scattering in random media vol. II*, Academic Press, New York, 1978.

14. I.M.Besieris, W.Kohler and H.Freese, *A transport-theoretic analysis of pulse propagation through ocean sediments*, Jour. Acoust. Soc. Am. **72** (1982), 937-946.

15. Yu.Barabanenkov, Yu.Kravtsov, V.Ozrin and A.Saichev, *Enhanced backscattering in optics*, Progress in Optics **29** (1991), 67-190.

16. M.Asch, W.Kohler, G.Papanicolaou, M.Postel and P.Sheng, *Frequency content of randomly scattered signals*, SIAM Review **33** no. 4 (1991), 519-625.

17. J.Froelich and T.Spencer, *Absence of diffusion in the Anderson tight binding model for large disorder or low energy*, Comm. Math. Phys. **88** (1983), 151-184.

18. P.Sheng, *Introduction to wave scattering, localization, and mesoscopic phenomena*, Academic Press, San Diego, 1995.

19. K.Case and P.Zweifel, *Linear transport theory*, Addison-Wesley Pub. Co, 1967.

20. E.Larsen and J.B.Keller, *Asymptotic solution of neutron transport problems for small mean free paths*, J. Math. Phys **15** no. 1 (1974), 75-81.

21. A.Bensoussan, J.L.Lions and G.Papanicolaou, *Boundary Layers and homogenization of transport processes*, Publ. RIMS **15** no. 1 (1979), 53-157.

22. R.S.Wu, *Multiple scattering and energy transfer of seismic waves – separation of scattering effect from intrinsic attentuation–I. Theoretical Modelling.*, Geophys. Jour. Roy. Astr. Soc **82** (1985), 57-80.

23. R.S.Wu and K.Aki, *Multiple scattering and energy transfer of seismic waves – separation of scattering effect from intrinsic attentuation –II. Application of the theory to Hindu Kush region*, (R.S.Wu and K.Aki, eds.).

24. M.N.Toksöz, A.Dainty, E.Reiter and R.S.Wu, *A model for attentuation and scattering in earth's crust*, PAGEOPH **128** (1988), 81-100.

25. T.L.Shang and L.S.Gao, *Transportation theory of multiple scattering and its application to seismic coda waves of impulse source*, Scientia Sinica, Ser. B. **31** (1988), 1503-1514.

26. K.Mayeda, F.Su and K.Aki, *Seismic albedo from the total energy dependence on hypocentral distance in southern California*, Phys. Eart Planet. Int. **67** (1991), 104-114.

27. T.McSweeney, N.Biswas, K.Mayeda andd K.Aki, *Scattering and anelastic attentuation of seismic energy in central and southcentral Alaska*, Phys. Earth Planet. Int. **67** (1991), 115-122.

28. M.Fehler, M.Hoshiba, H.Sato and K.Obara, *Separation of scattering and intrinsic attentuation for the Kanto-Tokai region, Japan*, Geophys. J. Int. **108** (1992), 787-800.

29. Y.Zeng, F.Su and K.Aki, *Scattering wave energy propagation in a medium with randomly distributed isotropic scatterers*, Jour. Geophys. R. **96** (1991), 607-619.

30. Y.Zeng, *Compact solutions of multiple scattering wave energy in the time domain*, Bull. Seism. Soc. Am. **81** (1991), 1022-1029.

31. M.Hoshiba, *Simulation of multiple scattered coda wave excitation adopting energy conservation law*, Phys. Earth Planet Inter. **67** (1991), 123-126.

32. X.Chen and K.Aki, *Energy transfer theory of seismic surface waves in a random scattering and absorption in half space-medium*, Proc. of 15th annual seismic research symposium (1993), 58-64.

33. H.Sato, *Multiple isotropic scattering model including P-S conversions for the seismogram envelope formation*, Geophys. J. Int. **117** (1994), 487-494.

34. Y.Zeng, *Theory of scattered P-wave and S-wave energy in a random isotropic scattering medium*, Bulletin of Seism. Soc. Amer. **83**, 1264-1276.

DEPARTMENT OF MATHEMATICS STANFORD UNIVERSITY STANFORD CA 94305

THE HYDROACOUSTIC COMPONENT OF AN
INTERNATIONAL MONITORING SYSTEM

Joseph K. Schrodt, David R. Russell, Dean A. Clauter, and Frederick R. Schult
(Air Force Technical Applications Center)
David Harris
(Lawrence Livermore National Laboratory

ABSTRACT: The critical issue for the hydroacoustic component of an International Monitoring System (IMS) is its capability for monitoring nuclear explosions in the world's oceans. Factors that affect this capability are number and location of hydroacoustic sensors, placement of sensors, blockage of the hydroacoustic signal due to bathymetric effects, and spatial and temporal variation in hydroacoustic signal propagation due to changes in oceanic properties. This paper provides examples of hydroacoustic monitoring capability from historical data that demonstrates the impact of these factors, and discusses implications from these results on design of a hydroacoustic network.

Specific data processing examples of hydroacoustic detection and discrimination capability are given for hydroacoustic signals from earthquakes and explosions recorded at MILS (Missile Impact Location System) and other hydrophones in the Atlantic and Pacific Ocean. In the 1960's, the United States (U.S.) Navy performed a series of ship sinking explosions underwater as well as a set of explosions that traversed the Aleutian Island chain at a ninety degree angle. Another study is of more recent data from a collection of earthquakes south of Australia and in the Southern Pacific Ocean. Examples from all of these data illustrate the blockage effects due to the bathymetric profile and effects of hydroacoustic sensor emplacement on the side or top of, or floated from the top of seamounts into the SOFAR (Sound Fixing and Ranging) channel on hydroacoustic signal strength.

These data processing examples also demonstrate the high degree of confidence achieved in the discrimination between earthquakes and explosions based on their respective frequency content and presence or absence of an explosion-produced bubble pulse signal. The explosion data exhibit significant frequency content up to the anti-alias filter frequency of seventy Hertz, while the earthquake data shows severe attenuation beyond 20 Hertz and no bubble pulse signals. Potential problems are hydroacoustic signals from volcanic explosions that exhibit explosion-like characteristics and from vented explosions or explosions just above the ocean's surface.

The paper recommends that these historical data provide a basis for a knowledge grid of the ocean that would define for each hypothetical explosion source position (for example, on a one- by one-degree or finer grid) what a hydroacoustic sensor would expect to see. The knowledge grid would contain information from both theoretical detection and location capability models and this type of observed historical data. This could ultimately be combined with a similar seismic and possibly infrasonic knowledge grid to give worldwide detection and location capability for subsurface and low atmospheric nuclear explosions. The paper concludes with a design for the hydroacoustic component that takes into account the use of a combination of assets for monitoring nuclear explosions on a global scale that include seismic, infrasonic, and hydroacoustic networks.

INTRODUCTION: The oceans cover over 70 percent of the earth's surface with much of the seismic activity from earthquakes and volcanic activity occurring along coastlines, in oceanic ridges, and in the Pacific and Indian Ocean trenches. Hydroacoustic signals propagating from these and other explosion-type oceanic events provide a high-confidence method for monitoring a Comprehensive Test Ban Treaty (CTBT) in the world's oceans. A hydroacoustic system would work in combination with the existing seismic and proposed infrasonic systems to detect, locate, discriminate, and estimate the yield of fully-contained and vented explosions, and explosions just above the ocean's surface.

Several factors contribute to the robust monitoring capability provided by a hydroacoustic system. It is well known and understood that hydroacoustic signals propagate most efficiently as a waveguide phenomena in the SOFAR channel where the sound velocity is at its axis; this results in excellent signal-to-noise ratios for even small events travelling over thousands of kilometers. The velocity of propagation is relatively constant over the broad ocean areas and slow compared to seismic velocities which gives improved location accuracy for oceanic events detected and located by denser seismic and infrasonic systems. The false alarm rate for discriminating fully-contained and vented underwater explosions from submarine earthquakes is low because of the presence of high frequencies beyond 20 Hertz (Hz) in the former case but not the latter one. In addition, fully-contained explosions are uniquely discriminated by bubble pulse signals in the hydroacoustic data; these characteristic signals are produced from expansion and contraction of the gas bubble while it rises to the ocean's surface and are clearly evident even after propagating great distances through the sound channel.

BACKGROUND: At present, there are two fixed-cable hydroacoustic stations offered by the United States as part of the hydroacoustic component of the IMS. These two stations, Wake Island in the Pacific and Ascension Island in the Atlantic, give significant hydroacoustic detection and discrimination capability on a worldwide, oceanic basin scale because of the efficient transmission of sound through water. Each of these stations have unique features that contribute to their excellent monitoring capability. At both the Ascension and Wake Island stations, there are hydrophones far from and near to the islands, all of which are in the SOFAR channel. There are also bottom-mounted hydrophones; however, at Ascension Island, their cable is cut and buried at the shoreline.

The hydrophones at these stations that are far away from the islands in the SOFAR channel are those most useful for detecting explosion signals. The hydrophones closest to the islands but still in the SOFAR channel also are useful in detecting explosion signals but suffer some signal-to-noise reduction from current-induced noise, interfering modes from reflections off the islands, and shadowing effects. The Heard Island Feasibility Test in 1991, in which controlled sources were transmitted in the SOFAR channel from Heard Island in the southern Indian Ocean, demonstrated that attenuated signals were recorded even on hydrophones closest to Ascension Island in the Atlantic Ocean on the back side to the source. The hydrophones on the bottom at these sites are the least useful for detecting explosion signals. These hydrophones are essentially ocean bottom seismometers and are redundant to the planned seismic network. They are also buried in loosely compacted sediment which decouples them from the environment and leads to signal strength loss.

Another type of hydroacoustic asset considered by the IMS but not offered by the U.S. is the sonobuoy configuration. In this case, a hydrophone is suspended from a floating buoy or floated from a moored buoy into the SOFAR channel. This sonobuoy design is essentially in the research and development stage, at present, and not a proven concept particularly for operations in remote regions of the oceans. Typically, present day sonobuoys of this type are used for short time duration experiments to avoid the expense associated with servicing and replacement of the units.

RESULTS: There were a number of experiments done in the 1960's involving underwater explosions whose hydroacoustic signals were recorded on MILS hydrophones at the Wake and Ascension Island facilities as well as other hydrophones. The processed data from these explosions demonstrate the unique capability provided by hydroacoustic assets in a monitoring regime. In particular, these data emphasize the effects of source and receiver blockage as well as sensor position on hydroacoustic signal strength. Comparisons between these explosion data and signals from underwater volcanic eruptions also illustrate problem areas where further research is necessary to resolve discrimination issues.

The first set of data presented is from a series of underwater shots that the U.S. Navy detonated in 1967 on a line that intersected Amchitka Island in the Aleutian Islands. These data were recorded on MILS hydrophones in the Pacific ocean and demonstrated that 1) even with local and long-range partial blockage, the bubble pulse signal was observed at nearly 5000 kilometers, and that 2) bathymetric effects on less than a degree-by-degree scale were important in hydroacoustic signal strength. One series of these explosions was done above, in, and below the SOFAR channel. These data exhibit the expected largest amplitude for the shots in or near the axis of the SOFAR channel.

The second set of data is from a ship (CHASE) explosion off the New Jersey coast that was recorded on both bottom and SOFAR channel MILS hydrophones that were in proximity at Ascension Island. As expected, the hydrophone signal recorded on the SOFAR channel was higher in amplitude than that on the bottom one, but no loss in frequency content, at least to 70 Hz which was the anti-alias cutoff frequency, was observed.

The third set of data is from another CHASE explosion off the California coast that was recorded on Pacific MILS hydrophones. These data were compared to hydroacoustic signals from earthquakes and volcanic eruptions. The major difference between the explosion and earthquake data was in frequency content; the signals from earthquakes were severely attenuated beyond 20 Hz while those from explosions retained significant frequency content up through 70 Hz. The difference in frequency content was not as pronounced between the explosions and volcanic eruptions. The volcanic eruptions are essentially explosive in nature and produce bubble pulse signals, however, the associated hydroacoustic signals are more complex in nature and longer in duration than signals from man-made explosions.

DISCUSSION: The U.S. has proposed a six-station hydroacoustic network to the international community that includes the MILS at Wake and Ascension Island as the U.S. contribution and is capable of recording the types of hydroacoustic signals described in the results section. This network has two stations in each ocean basin principally in the Southern Hemisphere which accounts for the concentration of seismic and radionuclide and other monitoring assets in the Northern

Hemisphere. The network specifically consists of one station each in the southernmost Atlantic and Pacific Oceans, and two in the Indian Ocean as well as the two MILS stations and is illustrated in Figure 1.

This hydroacoustic network, if used in combination with the seismic and proposed infrasonic networks, would provide for detection, location, and discrimination of oceanic events above, at, and below the seismic threshold on a worldwide basis. For oceanic events above the seismic threshold, the hydroacoustic system would provide high-confidence discrimination and improved location of oceanic events. In particular, it would discriminate submarine earthquakes by the absence of high frequency content and bubble pulse signals. The lower uncertainty for hydroacoustic relative to seismic travel times combined with a much lower slowness for the hydroacoustic signal would give improved location estimates, particularly for events in the Southern Hemisphere.

The likely scenario for events below the seismic threshold is that of an explosion in the Southern Hemisphere just above the ocean's surface which should record on multiple infrasonic stations for a one kt explosion. The corresponding infrasonic detections which have a low false alarm rate based on historical evidence would provide azimuths and an approximate origin time for the event. The hydroacoustic travel time prediction should then effectively separate the associated hydroacoustic signals that have illuminated the Southern Hemisphere because of the unique features of the SOFAR channel from false alarm signals due to limited industrial activity that may have also occurred. Azimuths from these infrasonic detections combined with even one associated hydroacoustic travel time that was predicted by these data should significantly improve the location estimate for the event.

CONCLUSIONS and RECOMMENDATIONS: The proposed hydroacoustic network in Figure 1 would provide high-confidence evidence that a one kt explosion had occurred in the world's oceans when operated in a real-time mode. In an event-driven mode, the hydroacoustic system could act in a complementary fashion to the seismic and infrasonic systems for events above and below the seismic threshold, respectively. This would give high-confidence discrimination of submarine earthquakes and improved location estimates for seismic and infrasonic events.

Research studies are required to quantify the improved detection, location, and discrimination capability afforded to the IMS by the hydroacoustic component. Studies should continue on the effects of a number of factors on local hydroacoustic signal strength and long-range hydroacoustic wave propagation. The local effects include current-induced noise and the pinch-out of the SOFAR channel right around islands. Long-range wave propagation effects include partial blockage of the hydroacoustic wave from islands or seamounts that intersect the SOFAR channel as well as lateral heterogeneities in oceanic properties. Once the effects of these factors on hydroacoustic signal strength are quantified, a knowledge grid could be set up for the ocean that would define for each hypothetical explosion source position what a sensor would expect to see. The knowledge grid would contain information from both the theoretical capability models and the types of observed historical data presented here. This could ultimately be combined with a similar seismic and possibly infrasonic knowledge grid to give worldwide detection and location capability for subsurface and low atmospheric nuclear explosions.

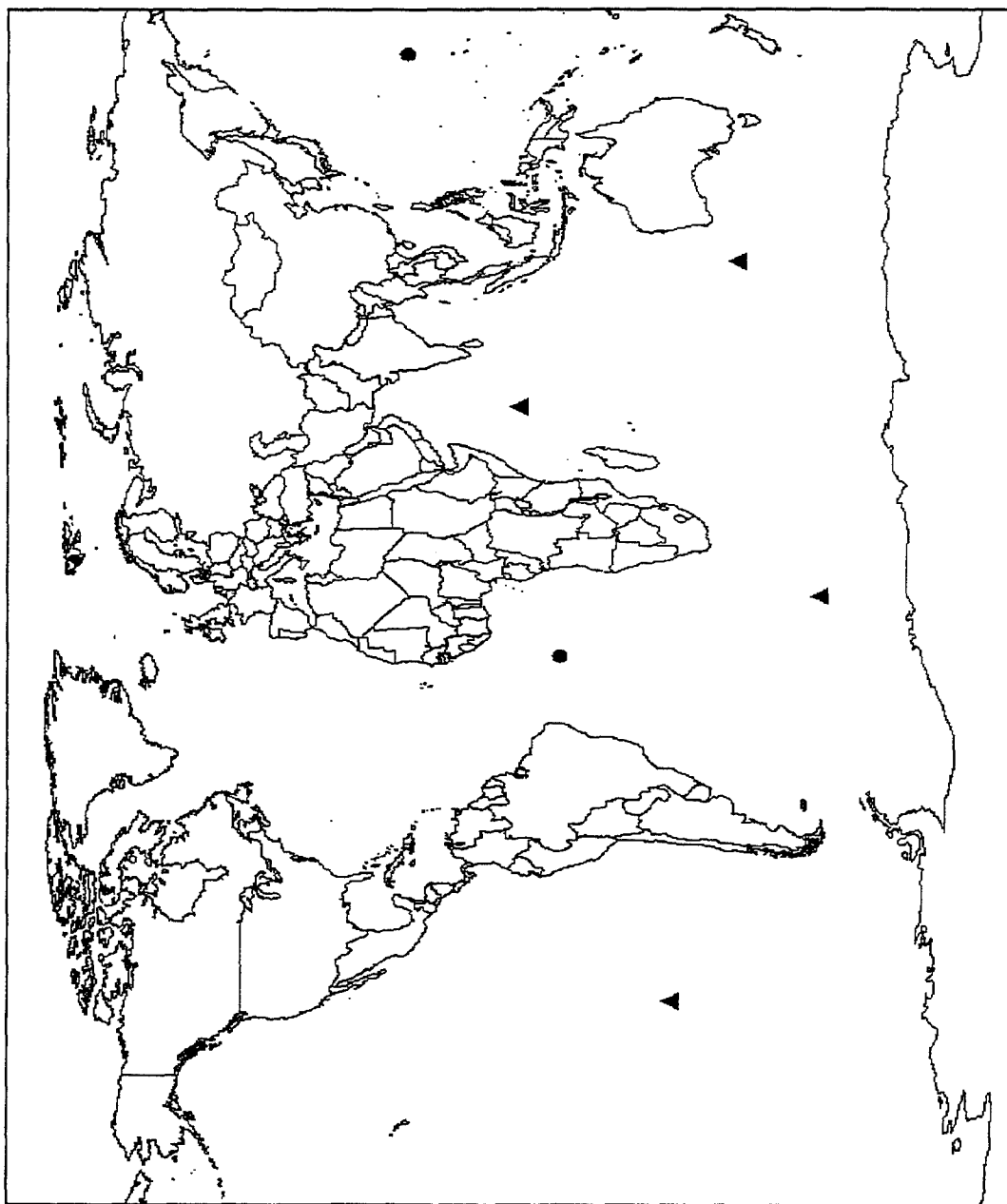Figure 1. Proposed hydroacoustic component for the International Monitoring System. Circles are MILS hydrophones at Ascension and Wake Island and triangles are the proposed hydroacoustic stations.

THE

UNITED STATES

NATIONAL DATA CENTER

BY

Bruce R. Varnum

September 1995

Directorate of Nuclear Treaty Monitoring

Air Force Technical Applications Center

1030 S. Highway A1A

Patrick Air Force Base, Florida 32925-3002

1.0 INTRODUCTION

The United Nations Conference on Disarmament *ad hoc* Group of Scientific Experts (GSE) is conducting the third large-scale technical test, termed GSETT-3, which started on January 1st of this year. The purpose is the continuation of an on-going effort to develop a global system for international monitoring of a Comprehensive Test Ban Treaty (CTBT) which will provide member states with data for their own national monitoring assessment. Accomplishment of this objective requires testing of a system composed of four major components: an International Data Center (IDC), National Data Centers (NDCs) in each member state, a network of seismic stations in each member state, and high speed communications to share the data in near-real time. This paper will discuss the progress of the US efforts to prototype and operate its NDC for GSETT-3. With eight months having elapsed since GSETT-3 began, we are now in a position to attempt a more consistent statistical assessment of the reliability and capability of the US NDC.

2.0 US NATIONAL DATA CENTER

Under the GSE concept for an international monitoring system, each participating member state has several options from which they may choose to develop their own NDC. Member states may choose to cooperate with one or more other states to form a "Regional" Data Center or a regional data concentrator facility; to develop only a raw data transmission capability; or to develop a full-scale NDC. A full-scale NDC, by definition, contains the capability to transmit and process the data, report results to their own national command authorities, and provide a long-term archive of the data. The United States is participating in GSETT-3 by prototyping and operating a full-scale NDC.

The US NDC for GSETT-3 has been established at the Air Force Technical Applications Center (AFTAC) Patrick Air Force Base, Florida. The United States has elected to prototype its NDC with the capability to: fully manage the US network of GSE seismic stations; submit the data from these stations to the IDC; fully process all data received from the IDC; and incorporate data from other AFTAC sources into its database.

The US NDC is currently receiving, and transmitting to the IDC, data from seven US Primary stations, data from eleven US Auxiliary stations, and data from seven southern hemisphere stations. In addition, Supplemental data are being collected and transmitted to the IDC.

2.1 SEISMIC STATIONS

Eight months into the GESETT-3 experiment finds the US NDC receiving data from the seven US planned Primary stations, the seven Southern hemisphere stations, and eleven of the twelve planned Auxiliary stations. These stations were selected for the following rea-

sons: they had the appropriate hardware configuration, they were situated near areas of high seismicity in the US, and they all had low levels of seismic background noise.

2.1.1 Primary Stations (Alpha)

Currently, there are no direct links from any primary stations to the IDC. All Primary data pass through a NDC or a data relay center. For example, CMAR in Thailand and a number of southern hemisphere stations transmit data to the IDC via a relay co-located with the US NDC. Several arrays located in Europe are transmitted through a similar center located in Norway. Most of the links to the IDC, the United States is an example, carry data from several stations located in that particular country. The US NDC is probably the most complex NDC due to its receiving data from the data sources discussed below. Two of the seven US primary stations are arrays, they are TXAR and PDAR. These stations have been operating for the full eight months with some problems encountered and upgrades incorporated. The remaining Primary stations are 3-component stations, they are: Lisbon, New Hampshire (LBNH); Mount Ida, Arkansas (MIAR); Pinon Flat, California (PFO); North Pole, Alaska (NPO); and Vanda, Antarctica (VNDA). The Southern hemisphere stations are sending 3-component data to the US NDC which is then forwarded to the IDC. These stations are: Brasilia, Brazil (BDFB); Bangui, Central African Republic (BGCA); Boshof, South Africa (BOSA); Villa Florida, Paraguay (CPUP); Dimbroko, Ivory Coast (DBIC); La Paz, Boliva (LPAZ); Paso Flores, Argentina (PLCA) and the only array station Chiang Mai, Thailand (CMAR).

2.1.2 Auxiliary stations (Beta)

The following twelve stations were selected using criteria similar to the Primary stations and they are: Albuquerque, New Mexico (ALQ); Blacksburg, Virginia (BLA); Dugway, Utah (DUG); Elko, Nevada (ELK); Ely, Minnesota (EYMN); Kanab, Utah (KNB); Mina, Nevada (MNV); Newport, Washington (NEW); Black Hills, South Dakota (RSSD); Tucson, Arizona (TUC); Tulsa, Oklahoma (TUL); and Tuckaleechee, Tennessee (TLK). Eleven of these stations (all except KNB) are now sending data routinely to the US NDC. Thus, the US NDC's experience with Auxiliary stations is becoming quite extensive, which is also true for a number of the other countries.

2.2 US NATIONAL DATA CENTER ARCHIVES

2.2.1 Overview

The National Data Center Archives (NDCA) is part of the NDC. The NDCA contains both near real-time continuous raw waveform data and historical collections of segmented data organized around selected events, areas, and/or research projects. For the near future-the largest contributor to the NDCA will be raw seismic waveform data being collected during GSETT-3. The NDCA is scheduled to begin archiving all raw GSETT-3 data by September 1995 with an anticipated flow rate of 2-3 Gbytes/day. Ultimately twelve months worth of data will be on-line (or near on-line). It is anticipated that requests for data will be fullfilled within minutes after the system becomes fully operational. After

the twelve months the older continuous data will be migrated off for permanent storage on DAT tapes while segmented event data will be archived on CD-ROM or optical disks.

2.2.2 Scope of the Data Archive

For planning purposes, the maximum daily flow rate to the NDCA is set at 15 Gbytes/day (5.5 terabytes/year). In addition, historical collections of unclassified seismic, and possibly other types, will be incorporated into the NDCA and transferred to optical disk or CD-ROM. These data will not have an additional quality control function performed on them prior to their inclusion.

2.2.3 Data Definition

All seismic, hydroacoustic, and infrasonic data available through the NDCA are in CSS3.0 format as defined in the Technical Report C90-01 of the Center for Seismic Studies. Station parameters include annotations as to the type of geodetic survey and reference spheroid used to locate the instrument sites. The data supplied to the NDCA includes the instrument response, calibration details, and other station specific information so that this information is available to the user.

Data collected as part of the GSETT-3 experiment for primary and auxillary seismic stations will be transmitted to the US NDC, starting in September, using the IDC-defined alpha protocols. These data will be transmitted to the NDCA as close to real time as possible (within 36 hours of the event times). Primary station data will be recorded and archived continuously, while auxiliary station data may be recorded and archived only for specifically requested segments. The NDCA plans to collect and archive continuous data for all auxiliary stations located in the United States.

2.3 DATA DISTRIBUTION

2.3.1 Types of Requests

The anticipation is that there will be two basic types of requests for raw waveform data. The first is for discrete events recorded at all or selected stations and bounded by a maximum of 100 MBytes per request. The second is a global request for all data received for a period extending for minutes, hours, or continuous current data.

The hardware and software being implemented in the US NDC was designed to handle the expected initial exponential growth. Discrete event requests for on-line data may be retrieved directly by the requestor. All other requests will require attention by the US NDC staff and, in general, discrete event-oriented requests will be given priority over global requests. A fully implemented autoDRM is essential to the successful operation of this data distribution scheme and is scheduled to be operational in October.

2.3.2 Request Format

All data must be requested via the GSE2.0 Message submitted by e-mail to a specific account at the US NDC. Users will be able to browse the archive using the World Wide Web Server (web browsers such as MOSAIC, VIDIA, or Netscape will work), and use this information to prepare GSE2.0 message format data requests. Basic Web browsing and basic autoDRM capability are to be installed in September 1995. Except for extenuating circumstances, users will be expected to retrieve "static" files such as station locations, type of instrumentation, and instrument response curves without assistance from the NDC staff. These static files will be maintained on-line and updated daily using data from the IDC. The static file information can be retrieved by downloading from the Web server or by submitting an autoDRM request.

2.3.3 Request Handling Priority

The US NDC is responsible (first priority) for satisfying requests submitted to it by the IDC for US auxiliary and other data. Official government agency requests will be assigned second priority. Small requests from others agencies and individuals will be assigned third priority Very large requests from this last group of requestors will be assigned the lowest priority.

2.3.4 Expected Request Response Time

With retrieval capability currently available at the US NDC, daily subscriptions to IDC products such as the Reviewed Event Bulletin (REB) is available. Authorized government agencies and contractors who require access to continuous waveforms will need to make special arrangements to access the data. Full implementation of the autoDRM and the World Wide Web Server capabilities is planned for January 1996. The goal is to respond to and fulfill all requests less than 100 MBytes of data within a few days of receipt of request.

2.3.5 Security

Data requestors coming in from the Internet will not have accounts on the system, but will be able to browse the archive contents using the World Wide Web Server, submit e-mail GSE2.0 messages , and be able to retrieve data using anonymous ftp.

2.4 US NDC DATA PROCESSING

AFTAC is continuing the development effort for the US NDC to process the data for treaty monitoring purposes. AFTAC has gone on-line earlier this year with the AFTAC Digital Seismic Network (ADSN). The US NDC processing is relying heavily on the ADSN processing. This processing includes the data handling (i.e. array processing) the signal detection process, the signal association process, the estimation process for magnitude, depth process, etc., and the identification processing which relies on processes such as long period (lp) signal processing. The processing structure has its roots in the ADSN

structure, and ultimately in the IDC structure. With the recent reception of some IDC data, the US NDC will begin preliminary processing of those received data during this month (September 1995).

The final products of the ADSN and the US NDC will be different in the final analysis primarily due the end results that are desired. Basically, the NDC exists to support the treaty verification process while the ADSN has added additional features for in-country specific requirements.

2.4.1 Processing Enhancements

The future enhancements relate to the following: the use of regional discriminants, the expanded use of long period data (location for example), the incorporation of more robust association algorithms, and improved signal detectors. Finally, the addition of additional types of data, discussed in the next section, properly fused with the seismic data and processing should improve the results in certain areas if not overall.

2.5 ADDITIONAL DATA SOURCES

The US NDC is currently acquiring additional data that will be sent to the IDC assuming the agreements are put-in-place for GSETT-3. These additional data are: Hydroacoustic, Radionuclide, and Infrasonic. At present these data are being archived at the US NDC, and will be available later in the experiment.

2.5.1 Hydroacoustic

The US will supply supply data from two hydroacoustic arrays located at Ascension Island and Wake Island. Four additional fixed arrays are planned for installation and the data will also be made available. When the pending agreements are put-in-place all these data will be forwarded to the IDC.

2.5.2 Radionuclide

The US has installed two radionuclide monitoring systems at US facilities. These systems are co-located with the seismic stations at Pinedale, Wyoming and North Pole, Alaska. If the GSE agrees that the IDC should experiment with the non-seismic data these data will also be forwarded to the IDC.

2.5.3 Infrasonic

Under a cooperative program with the US Department of Energy, Los Alamos National Laboratory (LANL) to provide infrasonic data from two arrays, the US NDC is currently acquiring and archiving these data. Again, if the GSE agrees that the IDC should experiment with non-seismic data they will be forwarded to the IDC.

3.0 PERFORMANCE SUMMARY

3.1 Contributions to the IDC by the US NDC

Tables and/or graphs are available for the Primary station contributions to the IDC. These graphs show the daily percentage, of the total amount possible, that data are received at the IDC. These graphs do not break down the specific cause for the data outage. Data are available which gives information on the specific cause for the loss of data. Specificly, the data outage is identified to be caused by software, communication problems, station outages, NDC problems, etc. Unfortunately, these data do not identify the software problems or the communication problems to a particular portion of the system.

The most recent statistics which have been compiled are for the four-month period starting on 1 January and ending on 30 April 1995. A total of 6434 unique events were located and reported in the IDC REB for this time period. The US NDC reported defining phases for 57% of these events. The arrays CMAR, PDAR, and TXAR were among the highest contributors to the IDC REB events, these contributions ranged from 23% to 45% of the IDC REB event total. In addition, NPO and BGCA, both 3-component stations, also contributed 30% and 21% of the IDC REB events respectively.

Preliminary results for this four month period indicate the majority of the US NDC stations significantly contribute to associated events located at teleseismic distances from them (epicenters between 20 and 100 degrees). The Southern Hemisphere stations contributed disproportionately high to the events located in the Northern Hemisphere.

Considering all of the US NDC stations, only PDAR and NPO are contributing to regional events. The other stations with high percentages of regional detections, such as CMAR, TXAR, and CPUP, are contributing detections primarily to teleseismic events.

3.1.1 Experience with the IDC Products

In order to further evaluate the US NDC performance, the US NDC personnel subscribe to the IDC bulletins (AEL, ABEL, and REB) as well as the Alpha-status and Comm-status reports. The principal comparison that has been made to date is the United States located events of the REB with the Supplementary Event List (SELs) which is derived from the USGS weekly Preliminary Determination of Epicenters (PDE) bulletins. This bulletin is made up of events occurring only in the US. Thus, the US located events are compared with the SEL events for the same time period. The comparison generally takes into account the basic differences such as station coverage and the deletion of suspected mining blasts from the SEL The comparison of the SEL and REB events was separated into three categories which are the following: events reported by the SEL but not the REB, events reported by both the SEL and the REB, and events reported by the REB but not the SEL.

4.0 CONCLUSIONS

Two years have passed since AFTAC began development of the US NDC. More recently, the US NDC has been supporting the GSETT-3 experiment for over eight months. The NDC is supplying to the NDC nearly all station data which were originally agreed upon. Data outages continue to be a problem with a wide range of causes. Now that nearly all of the Primary and Auxiliary stations are on-line, more effort can be allocated to locating and resolving these problems. In addition, more hardware and software are being brought on-line, as well as upgrading that which has been functioning, lending credence to the reliability numbers originally proposed in the program.

The next four months will be very important as the IDC data will be increasingly available to the US NDC for archiving and processing. This expansion in the amount of data and number of stations will greatly aid the NDC personnel in optimizing the processing algorithms currently available and those scheduled for near-term inclusion. Also the capability for researchers to request and receive large amounts of data from the US NDC will be made available during this time frame.